

TRANSACTIONS

American Society for Metals

VOL. I

1958

TECHNICAL PROGRAM AND REPORTS OF OFFICERS AMERICAN SOCIETY FOR METALS—39th ANNUAL CONVENTION, CHICAGO, NOVEMBER 2-8, 1957

FOR the purposes of record and for the benefit of members who were not in attendance at the Thirty-Ninth Annual Convention of the Society, held in Chicago, November 2-8, 1957, the Programs of the Technical Papers and Educational Lectures together with the Reports of Officers for 1957 are herewith published in full.

ASM SEMINAR ON LIQUID METALS AND SOLIDIFICATION

Saturday, November 2

Palmer House Red Lacquer Room—9 a.m.

Presiding Officer

W. R. Hibbard, General Electric Research Laboratory, Schenectady, N. Y.

Theory and Structure of Liquids—G. Vineyard, Brookhaven National Laboratory, Upton, N. Y.

Properties of Liquid Metals—N. H. Nachtrieb, Institute for the Study of Metals, University of Chicago, Chicago

Thermodynamics and Properties of Liquid Solutions—O. J. Kleppa, Institute for the Study of Metals, University of Chicago, Chicago

Palmer House Red Lacquer Room—2 p.m.

Presiding Officer

J. J. Harwood, Head, Metallurgy Branch, Office of Naval Research, Washington, D. C.

Nucleation—E. M. Pound, Carnegie Institute of Technology, Pittsburgh

Solid-Liquid Reactions—J. Weeks and D. H. Gurinsky, Metallurgy Division, Brookhaven National Laboratory, Upton, N. Y.

Mechanism of Metal Electrodeposition—J. O'M. Bockris, University of Pennsylvania, Philadelphia

Sunday, November 3

Palmer House Ballroom—9 a.m.

Presiding Officer

P. A. Beck, Research Professor of Physical Metallurgy, University of Illinois, Urbana

Mechanism of Crystal Growth—K. A. Jackson, Harvard University, Cambridge, Mass.

Thermal Considerations in Freezing—C. M. Adams, Jr., Massachusetts Institute of Technology, Cambridge, Mass.

Solute Redistribution During Freezing—William G. Pfann, Bell Telephone Laboratories, Murray Hill, N. J.

Palmer House Ballroom—2 p.m.

Presiding Officer

W. D. Robertson, Hammond Metallurgical Laboratory, Yale University,
New Haven, Conn.

Imperfections Resulting From Solidification—John Rutter, General Electric Research Laboratory, Schenectady, N. Y.

Polyphase Solidification—William A. Tiller, Westinghouse Research Laboratory, Pittsburgh

Structure of Ingots and Castings—J. Walker, General Electric Research Laboratory, Schenectady, N. Y.

TECHNICAL PROGRAM OF THE AMERICAN SOCIETY FOR METALS

Monday, November 4

Palmer House Ballroom—9 a.m.

Steel I

Presiding Officers

D. J. Carney, U. S. Steel Corp.

Morris Cohen, Massachusetts Institute of Technology

Electrolytic Extraction of Carbides From Carbon Steel—R. W. Gurry, Quaker Chemical Products Corp., Conshohocken, Pa., J. Christakos, W. M. Kellogg Co., Jersey City, N. J., and C. D. Stricker, American Steel & Wire Division, U. S. Steel Corp., Cleveland

Effect of Manganese on the Curie Point of Cementite—Earl C. Roberts, Associate Professor of Metallurgical Engineering, University of Washington, Seattle, Wash.

Morphological and Phase Changes During Quench-Aging of Ferrite Containing Carbon and Nitrogen—G. Lagerberg, Research Dept., Stora Kopparbergs Bergslags Aktiebolag, Domnarvet, Sweden, and B. S. Lement, Research Staff, Department of Metallurgy, Massachusetts Institute of Technology, Cambridge, Mass.

Some Relationships Between Torsional Strength and Electron Microstructure in a High-Carbon Steel—S. T. Ross, Supervisor, Metallurgical Research, R. P. Sernka, Project Engineer, and Walter E. Jominy, Chief Metallurgist Research, Chrysler Corp., Engineering Division, Detroit

Transformation Structures in Hypoeutectoid Alloy Steels—W. C. Hagel and M. N. Ruoff, General Electric Co., Materials & Processes Laboratory, Schenectady, N. Y.

Palmer House Red Lacquer Room—9 a.m.

Zirconium

Presiding Officers

J. H. Bechtold, Westinghouse Electric Corp.

J. L. Wyatt, Booz-Allen & Hamilton

Powder Metallurgy of Zr-U Alloys—Herbert S. Kalish, Engineering Manager, Metal Fabrication & Assembly, Sylvania Electric Products Inc., Atomic Energy Division, Bayside, N. Y.

A Hot-Hardness Survey of the Zr-U System—W. Chubb, Battelle Memorial Institute, Columbus, Ohio, G. T. Muehlenkamp, General Electric Co., Cincinnati, Ohio, and A. D. Schwoppe, Clevite Research Center, Cleveland

Transformation Kinetics of Zr-U Alloys—D. L. Douglass, Chief Metallurgist, L. L. March, Assistant Chief, and G. K. Manning, Chief, Metallurgical Engineering Division, Battelle Memorial Institute, Columbus, Ohio

Transformation Kinetics and Mechanical Properties of Zr-Ti and Zr-Sn Alloys—R. F. Domagala, Research Metallurgist, Nonferrous Section, D. W. Levinson, Supervisor, Nonferrous Section, and D. J. McPherson, Assistant Manager, Armour Research Foundation of Illinois Institute of Technology, Chicago

Palmer House Crystal Room—9 a.m.

**Joint Session of AEC and ASM on
Conference on the Metal Plutonium**

General Chairman

Arthur S. Coffinberry, Los Alamos Laboratory

Presiding Officers

Glenn T. Seaborg and Cyril Stanley Smith

Discovery of Plutonium in the Cyclotron—Glenn T. Seaborg, University of California

Isolation of Plutonium—B. B. Cunningham, University of California

Research on the Metallurgy of Plutonium at Chicago Metallurgical Laboratory—Sherman Fried, Argonne National Laboratory

Early Work at Los Alamos—Cyril Stanley Smith, University of Chicago

Later Plutonium Metallurgical Research at Los Alamos—Arthur S. Coffinberry, Los Alamos Laboratory

Plutonium Metallurgy at Hanford—O. J. Wick, Hanford Atomic Products Operation

Plutonium Metallurgy at Argonne National Laboratory—Frank G. Foote, Argonne National Laboratory

Studies on Plutonium at Chalk River—O. J. C. Runnalls, Atomic Energy of Canada, Ltd.

Metallurgical Studies on Plutonium in Great Britain—H. M. Finniston, U. K. Atomic Energy Research Establishment, Harwell, England

French Work on Plutonium—E. Grison, Atomic Energy Commission, Saclay, France

Palmer House Ballroom—2 p.m.

Steel II

Presiding Officers

G. H. Enzian, Jones & Laughlin Steel Corp.

R. A. Grange, U. S. Steel Corp.

Some Aspects of the Morphology and Chemistry of Lead in Leaded High-Sulphur Steels—J. W. Thurman and E. J. Paliwoda, Jones & Laughlin Steel Corp., Graham Research Laboratory, Pittsburgh, and E. J. Duwell, Minnesota Mining and Manufacturing Co.

Distribution of Residual Stresses in Carburized Cases and Their Origin—D. P. Koistinen, Research Staff, General Motors Corp., Detroit

Effect of Per Cent Tempered Martensite on Endurance Limit—F. Borik, Research Metallurgist, R. D. Chapman, Managing Engineer, and W. E. Jominy, Chief Metallurgist, Metallurgical Research, Engineering Division, Chrysler Corp., Detroit

Machinability of Type-A Leaded Steels—E. J. Paliwoda, Jones & Laughlin Steel Corp., Graham Research Laboratory, Pittsburgh

Palmer House Red Lacquer Room—2 p.m.

Titanium

Presiding Officers

G. W. Birdsall, Reynolds Metals Co.

E. M. Mahla, E. I. du Pont de Nemours & Co.

Grain Growth and Recrystallization Studies on Commercial Titanium, RC-55, and Alloy, Ti-100A—E. L. Bartholomew, Professor of Mechanical Engineering, University of Connecticut, Storrs, Conn.

Mechanical Properties and Heat Treatment of Ti-Cb Alloys—L. W. Berger, D. N. Williams and R. I. Jaffee, Battelle Memorial Institute, Columbus, Ohio

Evaluation of a New Titanium-Base Sheet Alloy, Ti-4Al-3Mo-1V—R. S. Richards, D. L. Day and H. D. Kessler, Metallurgical Research Division, Titanium Metals Corp. of America, Henderson, Nev.

Mechanical Properties Correlated With Transformation Characteristics of Ti-V Alloys—E. L. Harmon, Research Assistant, A. R. Troiano, Head, Depart-

ment of Metallurgical Engineering, Case Institute of Technology, Cleveland, Ohio, and J. Kozol, Combustion Engineering, Inc., Windsor, Conn.

Factors Affecting the Absorption and Distribution of Hydrogen in Titanium During Acid Pickling—C. R. McKinsey, M. Stern and R. A. Perkins, Metals Research Laboratory, Electro Metallurgical Co., Niagara Falls, N. Y.

Mode of Hydride Precipitation in Alpha Titanium and Alpha Titanium Alloys—Tien-Shih Liu, Titanium Metals Corp. of America, Henderson, Nev., and M. A. Steinberg, Head Metallurgy Department, Horizons, Inc., Cleveland, Ohio

Palmer House Crystal Room—2 p.m.

Joint Session of AEC and ASM on Role of Plutonium in Nuclear Power

Presiding Officers

Edward Epremian and H. M. Finniston

General Statement and the Los Alamos Molten Plutonium Reactor Experiment—R. M. Kiehn, Los Alamos Laboratory

Discussion by Representative of Harwell and Argonne

Argonne Concepts Employing Solid Fuel Elements—Arthur B. Shuck, Argonne National Laboratory

Plutonium Fuels for Power Reactors—S. F. Pugh, U. K. Atomic Energy Authority, England

Fluid Fueled, Fast Power Reactor Concept—Russell E. L. Stanford, Atomic Power Development Association, Inc.

Plutonium Liquid Metal Fuel Reactor—David Gurinsky, Brookhaven National Laboratory

Mixed-Oxide Fuel Concept—W. M. Cashin, Knolls Atomic Power Laboratory

The Hanford Plutonium Recycle Reactor Design Concept—R. M. Fryar, Hanford Atomic Products Operation

Tuesday, November 5

Palmer House Crystal Room—9 a.m.

Mechanical Properties of Steel

Presiding Officers

D. J. Girardi, Timken Roller Bearing Co.

W. T. Lankford, U. S. Steel Corp.

Strain Hardening of Austenitic Stainless Steel—G. W. Powell, Nuclear Metals, Inc., Cambridge, Mass., E. R. Marshall, Associate Professor of Civil Engineering, University of Vermont, Burlington, Vt., and W. A. Backofen, Metals Processing Laboratory, Massachusetts Institute of Technology, Cambridge, Mass.

Effect of Rate of Stress Application and Temperature on the Upper Yield Stress of Annealed Mild Steel—J. A. Hendrickson, Research Assistant, and D. S. Wood, Associate Professor of Mechanical Engineering, California Institute of Technology, Pasadena, Calif.

Some Aspects of Pre-Yield Phenomena in Mild Steel at Low Temperatures—W. S. Owen, Morris Cohen and B. L. Averbach, Massachusetts Institute of Technology, Department of Metallurgy, Cambridge, Mass.

Energy Stored in Ingot Iron Deformed by Torsion at +25, -82 and -185 °C.—T. P. Wang, Research Metallurgist, Wilbur B. Driver Co., Newark, N. J., and Norman Brown, Associate Professor of Metallurgy, University of Pennsylvania, Philadelphia

Palmer House Ballroom—9 a.m.

Metallography

Presiding Officers

J. F. Libsch, Lehigh University

W. A. Reich, General Electric Co.

Classification of Precipitation Systems—R. O. Williams, Cincinnati Milling Machine Co., Cincinnati, Ohio

- Method for the Etching of Metals by Gas Ion Bombardment*—John B. Newkirk and W. G. Martin, General Electric Research Laboratory, Schenectady, N. Y.
- Relation Between Constitution and Ultimate Grain Size in Aluminum—1.25% Manganese Alloy 3003*—Philip R. Sperry, Department of Metallurgical Research, Kaiser Aluminum & Chemical Corp., Spokane, Wash.
- Occurrence of Laves-Type Phases Among Transition Elements*—R. P. Elliott, Research Metallurgist, and W. Rostoker, Assistant Manager, Metals Research Department, Armour Research Foundation of Illinois Institute of Technology, Chicago

Palmer House Exhibit Hall—9 a.m.

**Joint Session of AEC and ASM on
Physical Properties of Plutonium Metal**

Presiding Officers

Eric R. Jette and John Chipman

- Physical Properties of Plutonium Studied at A.E.R.E., Harwell*—J. A. Lee and P. G. Mardon, Harwell, England
- Some Physical and Physico-Chemical Properties of Plutonium Metal Studied at U. K. Atomic Weapons Research Establishment*—A. E. Kay, Aldermaston, England
- First Studies on French-Made Plutonium Metal*—R. Abramson, F. Anselin, R. Boucher, R. Fabre, H. Morti and R. Pascard, Saclay, France
- Dilatometry and Thermal Analysis*—E. M. Cramer, Los Alamos Laboratory
- Sound Velocity Measurements*—H. L. Laquer, Los Alamos Laboratory
- Results of Measurements of Diverse Physical Properties*—T. A. Sandenaw, Los Alamos Laboratory
- Crystal Structures*—W. H. Zachariasen, University of Chicago
- Delta-Prime Phase*—R. O. Elliott, Los Alamos Laboratory
- Corrosion of Plutonium*—J. T. Waber and E. S. Wright, Los Alamos Laboratory

**Industrial Heating Equipment Association
In Cooperation With ASM**

Modern Heating Equipment Speeds Metallurgical Processes

Presiding Officer

E. E. Staples, Hevi-Duty Electric Co.

Palmer House Red Lacquer Room—9 a.m.

- Modernization in Heating for Hot Forming*—P. H. Morse, Sales Manager, Magnethermic Corp.
- Metallurgy of Annealing in Fractional Minutes*—R. K. Wuerfel, Chief Metallurgist and Fellow Engineer, Westinghouse Electric Corp.
- Techniques and Metallurgy of Induction Vacuum Melting*—Walter Jones, Metallurgical Products Division, General Electric Co.
- Convection and Radiation in High-Speed Heating*—R. J. Reed, Application Engineer, North American Manufacturing Co.
- Influence of High-Speed Strip Annealing on Metallurgical Properties*—Gilbert J. Langenderfer, Sales Manager, Heat Treat Division, Surface Combustion Corp.
- Automation in Heating and Quenching*—N. K. Koebel, Director of Research, Manager, Industrial Heat Treating Furnace Division, Lindberg Engineering Co.

Palmer House Red Lacquer Room—2 p.m.

Brittle Fracture

Presiding Officers

J. E. Dorn, University of California

Richard Vanderbeck, U. S. Steel Corp.

- Brittle Fracture of Mild Steel in Tension at -196°C .*—W. S. Owen, Morris Cohen and B. L. Averbach, Massachusetts Institute of Technology, Department of Metallurgy, Cambridge, Mass.

Initiation of Brittle Fracture in Mild Steel—J. A. Hendrickson, Research Assistant, D. S. Wood, Associate Professor of Mechanical Engineering, and D. S. Clark, Professor of Mechanical Engineering, California Institute of Technology, Pasadena, Calif.

Study of the Role of Carbon in Temper Embrittlement—E. B. Mikus, Research Engineer, General Motors Research Staff, Detroit, Mich., and C. A. Siebert, Professor of Metallurgical Engineering, University of Michigan, Ann Arbor, Mich.

Brittle-to-Ductile Transition Temperatures of Binary Chromium-Base Alloys—E. P. Abrahamson II, Research Associate, and N. J. Grant, Professor, Massachusetts Institute of Technology, Department of Metallurgy, Cambridge, Mass.

Palmer House Exhibit Hall—2 p.m.

**Joint Session of AEC and ASM on
Plutonium Alloys and Fuel Elements**

Presiding Officers

A. S. Coffinberry and O. J. C. Runnalls

Phase Diagrams Studied at Harwell—M. B. Waldron, U. K. Atomic Energy Authority, England

Phase Diagrams Studied at Los Alamos—F. W. Schonfeld, Los Alamos Laboratory

Phase Diagrams Published by Russians—F. W. Schonfeld, Los Alamos Laboratory

Review of Intermetallic Compounds—F. H. Ellinger, Los Alamos Laboratory

Aluminum-Plutonium Elements for MTR—R. E. Tate, Los Alamos Laboratory

Plutonium Alloy Preparation at Chalk River—O. J. C. Runnalls, Atomic Energy of Canada, Ltd.

Fabrication of Aluminum-Plutonium Elements for NRX—K. L. Wauchope, Atomic Energy of Canada, Ltd.

Studies of Other Fuel Elements Containing Plutonium—L. R. Kelman and R. J. Dunworth, Argonne National Laboratory

Radiography and Autoradiography of Plutonium and Its Alloys—Dana E. Elliott and G. H. Tenney, Los Alamos Laboratory

Wednesday, November 6

Palmer House Crystal Room—9 a.m.

**Joint Session of AEC and ASM on
Welding of Stainless Steel**

General Chairman

Frank W. Davis

Studies on the Welding of Type-347 Stainless Steel—Reported by V. N. Krivobok, International Nickel Co.

AMERICAN SOCIETY FOR METALS ANNUAL MEETING

Palmer House Ballroom—10 a.m.

Campbell Memorial Lecture

Chairman: Julius J. Harwood, Office of Naval Research, Washington, D. C.
Modern Concepts of Flow and Fracture—Earl R. Parker, University of California

Palmer House Red Lacquer Room—2 p.m.

Stainless Steel

Presiding Officers

G. A. Fritzlen, Haynes Stainless Co.

P. G. Nelson, Budd Co.

Effect of Microstructure and Heat Treatment on the Mechanical Properties of AISI Type-431 Stainless Steel—G. E. Dieter, Research Engineer, E. I. du Pont de Nemours & Co., Experimental Station, Wilmington, Del.

Effect of Aging Cycle on the Properties of an Iron-Base Alloy Hardened With Titanium—T. W. Eichelberger, Metallurgy Department, Westinghouse Electric Corp., Research Laboratories, Pittsburgh

Influence of Nickel on Intergranular Corrosion of 18% Chromium Steels—J. R. Upp, Project Engineer, Wright Air Development Center, Wright-Patterson Air Force Base, Ohio, F. H. Beck, Associate Professor, and M. G. Fontana, Professor, Ohio State University, Columbus, Ohio

Phase Relationships in Austenitic Cr-Mn-C-N Stainless Steels—C. M. Hsiao and E. J. Dulis, Research and Development Laboratory, Crucible Steel Co., of America, Pittsburgh

Carbide Precipitation and Brittleness in Austenitic Stainless Steel—A. Kramer, Research Assistant, and W. M. Baldwin, Jr., Research Professor, Case Institute of Technology, Cleveland

Palmer House Crystal Room—2 p.m.

**Joint Session of AEC and ASM on
Welding in Nuclear Power Generators**

Presiding Officer
Frank W. Davis

Welding Stainless Steels Containing Boron in Excess of 1%—Nicholas Balai, Argonne National Laboratory, and J. M. Gerken, Knolls Atomic Power Laboratory

Joining of Stainless Steel to Zircaloy 2 and 3—Kenneth Koopman, Knolls Atomic Power Laboratory

Welding of Uranium—R. A. Noland and C. C. Stone, Argonne National Laboratory

Thursday, November 7

Palmer House Red Lacquer Room—9 a.m.

Mechanical Properties

Presiding Officers

R. W. Guard, General Electric Co.

H. Y. Hunsicker, Aluminum Co. of America

Effects of Temperature-Time Histories on the Tensile Properties of Airframe Structural Aluminum Alloys—R. E. Fortney, Structures Research Section, and C. H. Avery, Metallurgical Section, Materials and Process Engineering, Northrop Aircraft, Hawthorne, Calif.

Apparatus for Determining the Hardness of Metals at Temperatures up to 3000 °F.—M. Semchyshen and C. S. Torgerson, Climax Molybdenum Co. of Michigan, Office & Experimental Laboratory, Detroit

Mechanical Properties of Forged Chromium—S. A. Spachner and W. Rostoker, Metals Research Department, Armour Research Foundation of Illinois Institute of Technology, Chicago

Deformation and Fracture of Alpha Solid Solutions of Lithium in Magnesium—F. E. Hauser, P. R. Landon and John E. Dorn, University of California, Department of Engineering, Berkeley, Calif.

Palmer House Ballroom—9 a.m.

Thermal Cycling of Uranium

Presiding Officers

H. H. Chiswick, Argonne National Laboratory

W. D. Manly, Oak Ridge National Laboratory

Some Properties of Uranium Low-Titanium Alloys—Daniel J. Murphy, Professor of Metallurgy, University of Arizona, Tucson, Ariz.

Effects of Fabrication and Heat Treatment Variables Upon the Thermal Cycling Behavior of Uranium—S. T. Zegler, R. M. Mayfield and M. H. Mueller, Argonne National Laboratory, Lemont, Ill.

Effects of Cycling Variables Upon Growth Rate of 300 °C. Rolled Uranium—R. M. Mayfield, Metallurgy Division, Argonne National Laboratory, Lemont, Ill.

Growth of Uranium Upon Thermal Cycling—J. E. Burke and A. M. Turkalo, General Electric Co., Research Laboratory, Schenectady, N. Y.

Microstructural Changes of Uranium Upon Thermal Cycling—L. T. Lloyd, Physical Metallurgy Group Leader, and R. M. Mayfield, Metallurgy Division, Argonne National Laboratory, Lemont, Ill.

Palmer House Crystal Room—9 a.m.

**Joint Session of AEC and ASM on
Advanced Metallographic Techniques**

Honorary Chairman

Francis F. Lucas

Presiding Officers

R. J. Gray and D. W. White

Historical Background—Cyril Stanley Smith, University of Chicago

Early Work With Ultra-Violet—Francis F. Lucas, Bell Telephone Laboratories (Retired)

Metallographic Grinding and Polishing—L. E. Samuels, Defense Standards Laboratory, Australia

Revelation of Structures Through Surface Treatment—E. C. W. Perryman, Aluminum Laboratories, Ltd., Canada

Incident Light Microscopy—George L. Kehl, Columbia University

Microradiography, Auto-Radiography and X-Ray Microscopy—Sterling Newberry, General Electric Co.

Electron Microscopy—W. C. Bigelow, University of Michigan

Summary and Critique—Cyril Stanley Smith, University of Chicago

Palmer House Red Lacquer Room—2 p.m.

Physical Metallurgy

Presiding Officers

R. F. Hehemann, Case Institute of Technology

R. I. Jaffee, Battelle Memorial Institute

Grain Boundary Movement in Bicrystalline Aluminum—R. B. Pond, Assistant Professor, and E. Harrison, Research Assistant, Department of Mechanical Engineering, Johns Hopkins University, Baltimore

Growth of Cadmium From Vapor—J. E. McNutt, Engineering Research Laboratory, E. I. duPont de Nemours & Co., Wilmington, Del., and R. F. Mehl, Department of Metallurgical Engineering, Carnegie Institute of Technology, Pittsburgh

Grain Boundary Self-Diffusion of Nickel—W. R. Upthegrove, Assistant Professor of Metallurgical Engineering, University of Oklahoma, Norman, Okla., and M. J. Sinnott, Department of Chemical and Metallurgical Engineering, University of Michigan, Ann Arbor, Mich.

Effects of Oxide Recrystallization on the Oxidation Kinetics of a 62-38 Cu-Ni Alloy—J. A. Sartell, S. Bendel, T. L. Johnston and C. H. Li, Minneapolis-Honeywell Research Center, Hopkins, Minn.

Temperature Stresses in the Two-Phase Alloy, WC-Co—J. Gurland, Assistant Professor, Division of Engineering, Brown University, Providence, R. I.

Palmer House Crystal Room—2 p.m.

**Joint Session of AEC and ASM on
Metallography of Nuclear Materials**

Presiding Officers

R. J. Gray and D. W. White

Metallography of Uranium—R. F. Dickerson, Battelle Memorial Institute, Columbus, Ohio

Metallographic Identification of Inclusions in Uranium—G. L. Kehl, Eric Mendel and Emilio Jaraiz F., Columbia University, School of Mines, New York, N. Y., and Melvin H. Mueller, Argonne National Laboratory, Lemont, Ill.

- Preparation and Metallography of Uranium Carbides*—R. J. Gray, C. K. H. DuBose and W. C. Thurber
Transformation Structures in Uranium-Columbium Base Alloys—F. C. Holtz and R. J. VanThyne, Armour Research Foundation, Chicago
Physical Metallurgical Study of Thorium-Rich Thorium-Uranium Alloys—G. G. Bente, Atomics International, Canoga Park, Calif.
An Adventure in Metallurgy—Micro-Deformation and Fracture in Uranium—T. K. Bierlein and R. E. Hueschen, General Electric Co., Hanford Atomic Products Operation, Richland, Wash. (16-mm. Color and Sound Movie)

**Joint Session of Metal Powder Association and ASM on
Powder Metallurgy**

Palmer House, Room 14—2 p.m.

Presiding Officers

George A. Roberts and Kempton H. Roll

- Current Advances in the Science of Powder Metallurgy*—Joseph E. Burke, Manager, Ceramics Studies, Ceramics Studies Section, and Harold H. Hirsch, Metallurgical Engineer, Materials Application and Evaluation Section, General Electric Research Laboratory, Schenectady, N. Y.
Development of Iron Powder for Powder Metallurgy and Other Uses by the H-Iron Process—Jerome F. Kuznick, Consultant, Kenneth Bruland, Alan Wood Steel Co., Conshohocken, Pa.
Metal Powders to Solid Strip—The Present Status of Commercial Production—William N. Hayden, President, Hayden Metals, Inc., John D. Shaw, President, and Walter V. Knopp, Vice-President, S-K-C Research Associates, Paterson, N. J.

ASM—EDUCATIONAL LECTURE SERIES

Monday and Tuesday, November 4 and 5

All four sessions were held in Room 14, Palmer House

Precipitation From Solid Solution

First Session—9:30 A.M.

Presiding Officer

D. J. Blickwede, Bethlehem Steel Co., Inc., Bethlehem, Pa.

- Introductory and Summary Lectures*—R. F. Mehl, Dean of Graduate Studies, Carnegie Institute of Technology, Pittsburgh
General Theory, Mechanism and Kinetics—J. B. Newkirk, Alloy Studies Research, General Electric Research Laboratory, Schenectady, N. Y.
Precipitation Hardening Aluminum-Base Alloys—W. A. Anderson, Research Metallurgist, Alcoa Research Laboratories, New Kensington, Pa.

Second Session—2:00 P.M.

Presiding Officer

D. H. Ruhnke, Republic Steel Corporation, Massillon, Ohio

- Precipitation Reactions in Carbons and Low-Alloy Steels*—H. W. Paxton, Metals Research Laboratory, Carnegie Institute of Technology, Pittsburgh
Precipitation in Iron-Base Alloys—Adolph J. Lena, Manager, Basic Research Dept., Allegheny Ludlum Steel Corp., Brackenridge, Pa.

Third Session—9:30 A.M.

Presiding Officer

M. R. Meyerson, National Bureau of Standards, Washington, D. C.

- Precipitation Hardening of Copper Alloys*—W. D. Robertson, Hammond Metallurgical Laboratory, Yale University, New Haven, Conn., and Robert Bray, Chase Brass & Copper Co., Waterbury, Conn.
Magnesium Alloys—R. S. Busk, Head, Metallurgical Laboratory, Dow Chemical Co., Midland, Mich.

Fourth Session—2:00 P.M.

Presiding Officer

S. L. Henry, A. O. Smith Corporation, Milwaukee

Some Age-Hardening Characteristics of Ni-Cr Alloys (Nickel-Rich) Containing Aluminum and Titanium—Clarence Bieber and R. J. Raudebaugh, International Nickel Co., Research Laboratory, Bayonne, N. J.*Precipitation in Cobalt-Base Alloys*—Glenn A. Fritzlen, W. H. Faulkner, B. R. Barrett and R. W. Fountain, Haynes Stellite Co., Kokomo, Ind.**Second World Metallurgical Congress****International Panel Discussions**

November 4 to 8 Chicago

All sessions were held in the Sherman Hotel

The following is a listing of the various panel discussions that were part of the Second World Metallurgical Congress Program.

Group No. 1—Steelmaking and Refining**First Session—Iron***Thursday, November 7—Bal Tabarin Room—9:00 A.M.*

MODERATOR: ROBERT L. STEPHENSON, United States Steel Corporation, Monroeville, Pa.

- A. Present Technology of Iron Making
- B. Development in Iron Making
- C. Direct Reduction of Iron

Second Session—Steelmaking*Thursday, November 7—Bal Tabarin Room—2:00 P. M.*

MODERATOR: HOWARD TURNER, Jones and Laughlin Steel Corporation, Pittsburgh

- A. Oxygen in Steelmaking
- B. Vacuum Melting
- C. Vacuum Degassing

Third Session—Solidification of Steel*Friday, November 8—Bal Tabarin Room—9:00 A. M.*

MODERATOR: CHARLES W. SHERMAN, Jones and Laughlin Steel Corporation, Pittsburgh

- A. Ingot Technology
- B. Controlled Nucleation
- C. Continuous Casting

Group No. 2—Nonferrous Refining and Fabrication**First Session—Continuous Casting***Wednesday, November 6—Louis XVI Room—2:00 P. M.*

MODERATOR: CARL E. SWARTZ, Hinsdale, Illinois

Group No. 2—Practical Aspects of Metal Degassing**Second Session***Thursday, November 7—Assembly Room—9:00 A. M.*

MODERATOR: ALBERT J. PHILLIPS, American Smelting and Refining Company, South Plainfield, N. J.

Group No. 3—Metal Fabrication**First Session—Steel Gears***Tuesday, November 5—Crystal Room—9:00 A. M.*

MODERATOR: M. F. GARWOOD, Chrysler Corporation, Detroit
A. Selection of Steel for Gears
B. Fabrication of Gears
C. Operation

Second Session—Selection of Sheet Steel for Formability

Tuesday, November 5—Crystal Room—2:00 P. M.

MODERATOR: RALPH W. E. LEITER, The Budd Company, Philadelphia

Third Session—Machining of Steel

Wednesday, November 6—Crystal Room—2:00 P. M.

MODERATOR: O. W. BOSTON, University of Michigan, Ann Arbor, Mich.
A. Approach to the Problem of Machinability
B. Microstructure as Related to Machinability of Common Constructional Steels
C. Effect of Composition of Constructional Steel on Machinability

Group No. 4—Heat Treatment

First Session—Carburizing

Monday, November 4—Louis XVI Room—9:00 A. M.

MODERATOR: WALTER HOLCROFT, Holcroft Company, Detroit

Second Session—Minimizing Distortion

Monday, November 4—Louis XVI Room—2:00 P. M.

MODERATOR: H. N. BOSWORTH, Bosworth Steel Treating Company, Detroit

Group No. 5—Welding and Joining

First Session—Ship Welding

Monday, November 4—Crystal Room—9:00 A. M.

MODERATOR: D. P. BROWN, American Bureau of Shipping, New York

Second Session—Electrodes

Monday, November 4—Crystal Room—2:00 P. M.

MODERATOR: D. C. SMITH, Harnischfeger Corporation, Milwaukee

Third Session—Stress Relieving and Preheating

Tuesday, November 5—Louis XVI Room—2:00 P. M.

MODERATOR: LEON C. BIBBER, United States Steel Corporation, Pittsburgh

Group No. 6—Inspection and Testing

First Session—Testing in Product Development

Thursday, November 7—Crystal Room—2:00 P. M.

MODERATOR: G. W. STICKLEY, Aluminum Co. of America, New Kensington, Pa.
A. Large Components
B. Medium Size Components
C. Small Size Components

Second Session—Testing for Quality Control After Product Development

Friday, November 8—Room 101—9:00 A. M.

MODERATOR: R. F. THOMSON, General Motors Corporation, Detroit
A. Quality Control on Semi-Finished Product
1. Wrought Materials
2. Cast Materials
B. Quality Control on Component Manufacture
1. Automotive
2. Aircraft

Group No. 8—Metallurgical Research and Education**First Session—Metallurgical Education**

Thursday, November 7—George Bernard Shaw Room—9:00 A. M.

MODERATOR: ROBERT F. MEHL, Carnegie Institute of Technology, Pittsburgh

- A. Physical Metallurgy
- B. Process Metallurgy
- C. Graduate Work
- D. Industrial Training

Second Session—Trends in Metallurgical Research

Thursday, November 7—George Bernard Shaw Room—2:00 P. M.

MODERATOR: CLYDE L. WILLIAMS, Battelle Memorial Institute, Columbus, Ohio

- A. Industrial Research
- B. Government and Government-Sponsored Research
- C. Institutes and Research Consultant Groups
- D. University Research

SECOND ANNUAL AWARDS LUNCHEON

At the Second Annual Awards Luncheon of the American Society for Metals, more than 600 members and guests were present. The meeting was held in the Grand Ballroom of the Palmer House Tuesday November 5, 1957.

Presiding at the luncheon, President Donald S. Clark introduced the persons seated at the top table and then proceeded with the presentation of the awards.

Several organizations in addition to the ASM made the following awards at this luncheon.

American Metal Market Special Award Announcement by—Mr. Archer W. P. Trench

Copper and Brass Mill Industry Award to—Mr. Minoru Yamasaki

Gregory Award to—Messrs. Maurice Faure and Jean Loubignac

Gray Iron Founders' Design Award to—Mr. Harold R. Warsmith

The Henry Marion Howe Medal to—Prof. F. N. Rhines, Mr. W. E. Bond, Miss M. A. Kissel

The ASM Teaching Award to—Dr. Amos J. Shaler

The Francis F. Lucas Metallographic Award by—Dr. Francis F. Lucas

**AWARDS OF DISTINGUISHED LIFE MEMBERSHIP IN THE
AMERICAN SOCIETY FOR METALS**

MR. JOEL HUNTER

MR. ROGER M. BLOUGH

MR. JOSEPH L. BLOCK

MR. I. W. WILSON

MR. EUGENE G. GRACE

DR. JOHN F. THOMPSON

Those seated at the head table were: W. E. Bond, Manager, Metallurgical Department, Pittsburgh Testing Laboratory, Pittsburgh; Frederick N. Rhines, Alcoa Professor of Light Metals, Carnegie Institute of Technology, Pittsburgh; M. A. Kissel, Research Assistant, Metals Research Laboratory, Carnegie Institute of Technology, Pittsburgh; Maurice J. Day, Vice President—Research and Development, Crucible Steel Company of America, Pittsburgh; Walter Holcroft, President, Industrial Heating Equipment Association, Executive Vice President, Holcroft & Company, Detroit; Jean Loubignac, Engineer in charge

Track Shop, Paris Subway, Paris, France; George E. Gregory, President, Gregory Industries, Inc., Toledo, O.; Maurice Faure, Chief Track Engineer, Paris Subway, Paris, France; G. M. Young, Vice President, American Society for Metals, Technical Director, Aluminum Company of Canada, Ltd., Montreal, Canada; Walter H. Wiewel, Sr. Vice President, Crucible Steel Company of America, Pittsburgh; Francis F. Lucas, Winter Park, Florida; E. P. Doyle, Executive Editor, Chicago Herald-American, Chicago; Wm. E. Umstadd, President, Timken Roller Bearing Company, Canton, O.; Walter F. Munford, Assistant Executive Vice President—Operations, United States Steel Corporation, Pittsburgh; Joel Hunter, President, Crucible Steel Company of America, Pittsburgh; Donald S. Clark, President, American Society for Metals, Professor of Mechanical Engineering, California Institute of Technology, Pasadena, California; Roger M. Blough, Chairman, United States Steel Corporation, New York; Philip D. Block, Jr., Senior Vice President, Inland Steel Company, Chicago; I. W. Wilson, Chairman, Aluminum Company of America, Pittsburgh; Herber Fales, Vice President, International Nickel Company, Inc., New York; John S. Marsh, Manager of Research, Bethlehem Steel Company, Bethlehem, Pa.; Archer W. P. Trench, Publisher, American Metal Market, New York; George W. Stamm, Vice President, Crucible Steel Company of America, Pittsburgh; George A. Roberts, President, Metal Powder Association, Vice President, Technology, Vanadium-Alloys Steel Company, Latrobe, Pa.; Carl H. Phil, Secretary, Copper and Brass Research Association, New York; William R. Jarratt, Yamaski, Leinweber and Associates, Royal Oak, Mich.; Ralph Owens, Dean, Illinois Institute of Technology, Chicago; Amos J. Shaler, Head, Department of Metallurgy, Penn State University, State College, Pa.; J. Scott Parrish, Jr., President, Gray Iron Founders' Society, President, Richmond Foundry and Manufacturing Company, Richmond, Va.; Harold R. Warsmith, General Superintendent, Jeffrey Manufacturing Company, Columbus, O.

The address of the meeting was presented by Joel Hunter, President of the Crucible Steel Company of America, entitled "Science and People." This was a very thought provoking address and was well received by this fine audience.

ANNUAL MEETING OF AMERICAN SOCIETY FOR METALS

9:00 A.M. Wednesday, November 6, 1957

Ballroom, Palmer House

The annual meeting was called to order by President D. S. Clark. The order of business was The President's Address; Report of the Treasurer; Report of the Secretary; Report of ASM Foundation for Education and Research; Election of Officers; Campbell Lecture. These reports are printed in the following pages.

ANNUAL ADDRESS OF THE PRESIDENT

DONALD S. CLARK, *President**Thirty-Ninth Annual Meeting, Chicago, November 6, 1957*

THE American Society for Metals is the engineering society of the metals industry and as such it has a distinct educational function. It also has a function of providing services to its members which benefit industry. Since we are an educational group, then we must be concerned with what is going on in the formal training of engineers. I wish to take a few minutes from the usual routine of reporting the activities during the past year to make sure that you know about the changing picture in engineering education.

Engineering is shifting from a strong empirical base toward one which is far more scientific. This shift imposes quite different demands upon the engineer, requiring that he have a more scientific training than heretofore. There have been many instances in which an engineer has been scorned, or made fun of because he has used a scientific approach to engineering problems. Engineering today is requiring men who are better trained in the fundamental sciences and mathematics. This training is necessary if he is to handle the more complex phases of engineering which are based on more advanced science. The time interval between the first concept of a phenomenon and its practical utilization or application is becoming shorter.

Solid state physics has helped us, for example, to understand why electrical conductance in metals is lower than that which is calculated for perfect metal crystals. Likewise it has shown us why metals are a hundred or a thousand times less strong than we compute them to be. The importance of understanding such fundamental concepts becomes clearer and clearer.

Solid state physics is playing an important part in other fields, as for example in transistors, and magnetic materials. Obviously these are becoming highly important and complicated subjects for the engineer to deal with and he will be required to deal with them.

To those who are accustomed to the everyday engineering problems, such as the specification of materials for certain applications, the heat treatment of steel, the processing of ferrous and nonferrous metals, all of this scientific business may sound mystical and quite unreal and not to the point. I assure you it is quite real and it is something that the men who follow you, and not too far off, are going to be dealing with and they are going to make use of these scientific developments for the solution of engineering problems. If this is to be true, a new job knowledge will be required which will involve a better understanding of advanced science. The engineers who are now in our schools must be better thinkers than we are. They must have a greater knowledge of

fundamental sciences; they must be able to handle mathematics to even a better degree than some of us do now. The more mathematically inclined engineer of today may be considered highbrow; the practicing engineer of tomorrow will use higher mathematics with facility and in application to the everyday problems. The technician of tomorrow may take the place of the engineer of today. Also bear in mind that the metallurgist of tomorrow will be called upon to solve problems his professors could not solve, and he will be required to find the solution to problems that we today cannot even imagine.

What I have just said is that we need to develop real thinkers, those who can cope with the important fundamental problems. Are we doing this? In some places, yes! But probably more thought is being devoted to increasing the number of engineers and scientists than to increasing the quality of or providing the opportunity and facilities for the intellectually outstanding young person. Let us not overlook the fact that an increase in quantity cannot make up for inferior quality. Recent developments have made some people ask if there isn't going to be an oversupply of engineers and scientists. My answer is no. There can never be an oversupply of thinkers. Some people say that there would not be a shortage of engineers and scientists if the industrial people would make proper use of them. If fewer engineers were put into administrative or completely nontechnical positions, the situation would be eased. Now this is not a fair statement. In view of our technological developments it becomes more and more necessary for our executives in business to have a background in engineering and science. I think most of our executives who have an engineering background will say that their training supplied them with a foundation that no other training would have given them for their position. Those who have a capacity for administrative positions will move in that direction. Why should we prohibit technically trained people from carrying the scientific approach to administration?

We hear mention made of the fact that many engineers are doing the jobs of technicians, technical aids, draftsmen, mechanics, etc. Don't forget that some graduate engineers do better as technicians than as engineers. Others do best as design engineers, others as high-powered researchers, and others as administrators. Each person on the average does those things for which he is really capable and has the will to do. We are living in a more and more technical period year by year, which means that the demand for technical people will continue to rise. We are living in a world built on physics and chemistry, and on mathematics and engineering and we must have more and more people that understand these things. What we must do is to have a nationwide awakening to this great need of training more engineers and scientists of the thinking variety and the need for every man to have a knowledge of the fundamentals of science and engineering because it is on these prin-

ciples that modern civilization is based. Bringing science and mathematics to more people through a real liberal education may permit us to meet the ever-increasing challenge of our technological expansion. A liberal education is not one limited to the humanities and social sciences, but is one that includes science and mathematics as well. Let us make certain that all of our young people receive at least this liberal education. Let us also make sure that the incentives are great enough to attract the young people who have the capacity, into the general field of Science and Engineering. We must put forth the important *truth* that the technical developments are *dependent* upon research and development in materials and this means we must have more outstanding metal scientists and metallurgists.

I leave these thoughts with you in the hope that each of you will take some action to put these ideas into practice for the benefit of all of us.

Now returning to the ASM. What is it doing? Our chapters throughout the North American Continent all have educational programs of which they can be proud. Furthermore many of the chapters are doing an effective job in bringing information about engineering and metallurgy to the attention of students in our public schools. Your National Officers and Staff are working to provide the chapters and the individual members with educational tools and services.

One of these tools is the Metals Engineering Institute Division of the Society under the direction of Dr. Brasunas. This Division has become an important part of the educational program offered to members as individuals or to groups for in-plant training. This Division will expand rapidly as its value becomes more widely recognized.

The two day seminars on advanced subjects have continued under the sponsorship of the Society. I wish to express our sincere appreciation to the committee in charge and particularly to Dr. Robert Maddin, the Chairman, and to Dr. Bruce Chalmers who was in charge of the program for this year on the subject of Liquid Metals and Solidification.

Another type of seminar has been sponsored by your Society. The first of these was presented at the time of the Western Metal Congress in Los Angeles in March 1957. Some 207 individuals, (44 speakers and 163 registrants) participated in a five day session on the treatment and application of titanium and its alloys.

Your Society has continued to provide funds to the National Science Teachers Association for the administration of the Science Achievement Awards program. This is a service in helping to stimulate interest in the fields of science and engineering in our public schools.

The ASM has assisted 8 universities by providing or making it possible for them to have visiting lecturers in the metallurgical field. These institutions were visited by 8 lecturers of which either the entire amount or a portion of the cost of travel and honorarium of the lecturer was borne by your Society.

All of the professions have an honorary fraternity to which the outstanding students in their respective fields are elected. The metallurgical profession has such a fraternity founded in 1932 at the Michigan College of Mining and Technology. This fraternity is known as Alpha Sigma Mu, signifying as specified by its founders, the Arts and Sciences of Metals. The fraternity has appealed to ASM for assistance in promoting, enlarging, and managing its operations. Your Board of Trustees has agreed to sponsor this fraternity that it may grow and continue to be a means of recognition of the top students in the metallurgical profession.

The Society is providing a service to the United States Air Force by making a survey of the need for a casting design manual. Individuals of the headquarters staff have been assigned to the task of making this evaluation. If the survey indicates the desirability of such a manual, your Society will probably be called upon to prepare this material which will be made available to users and suppliers.

Your Society continues to sponsor the publication of *Acta Metallurgica* which has become an outstanding high powered technical publication. It is truly an international scientific journal devoted to the field of metals under the very able editorship of Dr. Bruce Chalmers.

The ASM has had a committee on Classification of Metallurgical Literature under the chairmanship of Frank T. Sisco. This committee has produced a classification of the metallurgical literature, a gigantic task for which we all express our appreciation. Another committee under the chairmanship of D. C. Hilty has been concerned with Mechanized Literature Searching. The Society is financing a special study through this committee at the Center for Documentation and Communication Research of Western Reserve University. The whole purpose of these two committees is to bring order out of chaos in the classification and retrieval of metallurgical literature. We have now put these two committees together under the leadership of Frank Sisco to whom we again extend our sincere appreciation for his interest and leadership. This new committee is known as the Committee on Metallurgical Documentation.

The American Society for Metals is proud to again be the sponsor of the Second World Metallurgical Congress being held in conjunction with the National Metal Congress in Chicago this year. We are particularly pleased that 535 scientists and engineers from 42 countries are participating in technical discussions. Speaking of Metal Congresses, the Western Metal Congress and Exposition was held in Los Angeles in March 1957. Your Board of Trustees has approved the Southwestern Metal Congress and Exposition to be held in Dallas, Texas between the dates of May 12 and 16, 1958.

I have had the pleasure during the past year of visiting 38 chapters and talking with them about ASM activities as well as engaging in technical discussions. In addition I was privileged to attend regional

conferences in Albuquerque, New Mexico, Jacksonville, Florida, and Boston, Massachusetts. These visits took me into 22 states of the United States and 3 Canadian Provinces. Another 22 chapters were visited by other members of the Board of Trustees, making a total of 60 chapters visited by a National Officer during the year. I assure you that no one can secure a real appreciation of what ASM means until he has visited this many chapters. Such visits are extremely pleasant and stimulating. I finish this year with tremendous pride in our individual chapters and I pay tribute to the officers and executive committees of each chapter for the splendid job they are doing.

During the year three new chapters have been established bringing the total number of chapters to 102. The new chapters which have been formed since the last annual meeting are:

Santa Clara, California, Columbia, South Carolina and Richmond, Virginia.

Last year President Schaefer reported that the Board of Trustees had selected a site for a new headquarters building. Your Board has been engaged in studying plans submitted by architects and have finally agreed upon a general plan which has been submitted by Kelly and Kress and Associates. The details are yet to be presented. We hope that construction can begin sometime in the spring of 1958 and that this unit will be in operation by the spring of 1959. The new facilities are badly needed and will provide a great relief from the present crowded conditions under which the energetic and faithful staff now work.

It is with regret that I record the death of

A. E. White, First President of ASM and one of the 5 founder members of the Society and an Honorary Member.

William P. Woodside, President of ASM in 1939, and one of the five founder members of the Society.

Paul D. Merica, Former Trustee, 25 year member, Honorary Member, and recipient of ASM Gold Medal.

In accordance with custom, I report herewith the awards and outstanding events of the previous National Metal Congress, held in Cleveland in October 1956. The President's Medal was presented to Dr. George A. Roberts; the ASM Medal for the Advancement of Research was awarded to Charles M. White, Chairman of the Board of Republic Steel Corporation; the Sauveur Achievement Award was presented to Edgar H. Dix, Jr. of the Aluminum Company of America; the Gold Medal of the Society was awarded to William H. Eisenman, Secretary of the Society; the Henry Marion Howe Medal was awarded to R. P. Frohmberg of North American Aviation, Inc., W. J. Barnett of General Electric Company, and A. R. Troiano of Case Institute of Technology for their paper on "Delayed Failure and Hydrogen Embrittlement in

Steel"; the Campbell Memorial Lecture was presented by Charles S. Barrett of the Metals Research Laboratory, University of Chicago; the ASM Teaching Award was presented to Ernest F. Nippes, Professor of Metallurgy, Rensselaer Polytechnic Institute. Distinguished Life Memberships were conferred on Mr. R. L. Gray, President, Armco Steel Corporation, Mr. J. L. Mauthe, President, American Steel and Wire Division, United States Steel Corporation, Mr. William B. Umstattd, President, Timken Roller Bearing Company, and Mr. Charles M. White, Chairman of the Board, Republic Steel Corporation. Many of the awards were presented at the first Annual Awards Luncheon at which Mr. Charles M. White presented the principal address on the subject of "Trained Manpower for a Technical Age."

Each year several of the technical societies join with us in the program of the National Metal Congress. I wish to express our appreciation to the American Institute of Mining, Metallurgical and Petroleum Engineers (Metals Branch), Society for Non-destructive Testing, Industrial Heating Equipment Association, Metal Powder Association, and Special Libraries Association who have been the cooperating societies in the present Congress.

During the year I have appointed, with the approval of the Board, many individuals to committees. These committees play an all important part in the national affairs of your Society. I wish to publicly acknowledge this service and to thank all of you for an outstanding job. The membership of the standing committees is given in the Transactions in which this address is published. Some of these members will continue to serve on these committees. I wish them success.

Your Board of Trustees held four meetings this year, March 26, 1957, August 20, 1957, September 5, 1957, and November 5, 1957. I wish to take this opportunity of expressing, for you as members and for myself, our sincere appreciation for the outstanding service of the members of the Board of Trustees of your Society. I wish particularly to pay tribute to the retiring members of the Board. Past President and retiring Trustee, A. O. Schaefer, has been of real help in every facet of Society activities. Trustees G. E. Shubrooks and H. A. Wilhelm have served you well during the past two years. While Treasurer and Trustee C. H. Lorig is not retiring since we expect he will be elevated to the office of Vice-President, I want to express our sincere thanks to him for his service as Treasurer for the past two years. I welcome the new Officers and Trustees who will be elected at this annual meeting, and to tell them that they have a wonderful experience in store for them in working with a wonderful group of men.

No President can give his Annual Report without expressing his most heartfelt thanks to one individual in the organization of ASM. At this point it is probably not necessary for me to even mention this gentleman by name. The President is afforded an opportunity of seeing

the modus operandi of the Secretary and he is appalled by the tremendous energy and efficiency of this man. He is the only Secretary that your Society has ever had. I was interested in the statement which appeared in Volume 1 of the Journal of the American Steel Treaters' Society when Bill first became associated with this predecessor society of the ASM. The following announcement was made at the 1918 meeting. "... The Board of Directors have secured a business manager to devote his entire time to the furtherance of the objectives of our society and to handle the office affairs pertaining thereto in the person of Mr. William H. Eisenman. Mr. Eisenman is possessed of the qualities which begets success in any line of business and further than this, his education and experience have peculiarly fitted him for his position. In securing Mr. Eisenman ... we feel that the society has placed a 'keystone' in the arch of its organization." In this announcement, the Board was completely right, Bill possesses the qualities that beget success and he is truly the keystone of this organization. Every President comes to learn the importance of this keystone. Without it the President's job would be near impossible.

I wish to express to Bill Eisenman my sincere appreciation for his leadership, for his patience, for his creative thinking, and for his understanding of the requirements of our membership. I also express to the entire headquarters staff my thanks for their devotion to an important job very well done.

TREASURER'S REPORT

CLARENCE H. LORIG, *Treasurer*

Fiscal Year Ending August 31, 1957

A GAIN YOUR Society has had a successful financial year. Full details of the fiscal operations of the Society for the year ending August 31, 1957, are included in the Balance Sheet and in the income and expenditure accounts which are presented in the usual form.

The net assets of the American Society for Metals at the close of the fiscal year were \$4,214,431.13, an increase of \$812,782.05 for the period. Approximately 45% of the assets were in the form of stocks, bonds, and land trust certificates which have a total carrying value or cost of \$1,928,358.18. Their approximate market or redemption prices amount to \$2,408,744.26.

Based on approximate market prices, securities owned by the Society comprise 50.5%, or \$1,218,663.11, in common and preferred stocks; 48.2%, or \$1,158,285.00, in bonds; and 1.3% or \$31,796.15, in land trust certificates.

The bonds purchased for the Building Fund, which has been set aside for financing the building of the new headquarters, having a carrying

value of \$1,154,365.63. These bonds are not included among the securities mentioned previously as being owned by the Society. Total assets of the Building Fund amount to \$1,186,400.35.

Total assets of the Society's Foundation for Education and Research amount to \$710,914.04.

The combined assets of all local Chapters of the American Society for Metals are approximately \$340,000.00.

A condensed statement of income and expenses of the Society for the fiscal year is as follows:

Income and Expenses—Fiscal Year Ended August 31, 1957	
Income	\$2,483,347.55
Expense	<u>1,789,548.09</u>
Net Income	\$693,799.46
Income appropriated as authorized by the Board of Trustees:	
For educational purposes.....	\$ 138,500.00
For building fund.....	<u>555,299.46</u>
Total appropriations	\$693,799.46
Unappropriated net income.....	\$000,000.00

In the following table, the approximate income from the various activities of the Society and the disbursements of income are tabulated in terms of percentage of total income.

ASM Income and Its Disposition—Fiscal Year Ended August 31, 1957

	Income (%)	Outgo (%)
Publications	53.7	44.1
National Metal Exposition—Cleveland	20.6	8.9
Western Metal Show—Los Angeles	11.2	4.9
Memberships (net)	7.7	3.1
Dividends and interest earned	4.7	—
Metals Engineering Institute	1.0	1.0
Gain on disposal of securities	0.6	—
General and Administrative	—	7.6
Others	<u>0.5</u>	<u>2.4</u>
	100.0	72.0
Appropriations	<u>—</u>	<u>28.0</u>
	100.0	100.0

Receipts from Publications, the National Metal Exposition in Cleveland, the Western Metal Show, and Memberships (net) accounted for approximately 93% of the total income, while approximately 85% of the total expenses of the Society were for these same activities. The gross dues from memberships amounted to \$318,831.67 of which \$133,724.96 was returned to the local chapters. The net income of the Society was 28.0% of total income during the fiscal year as compared with 24.5% of total income during the preceding year. As mentioned earlier, all of the net income for the year was appropriated for educational purposes and for the building fund.

The appropriations for 1957 from net income were as follows:

Acta Metallurgica	\$ 10,000.00
Teaching Award	2,500.00
Chapter Educational Activities	5,000.00
World Metallurgical Congress	20,000.00
Science Award Program	15,000.00
Visiting Lectureships	1,000.00
Mechanical Literature Searching	15,000.00
Metals Handbook Revision	65,000.00
ASM Foundation for Education and Research	5,000.00
Building Fund	<u>555,299.46</u>
Total	\$693,799.46

It is worth noting that on the expenditure side, the total expenditure for 1957 was \$1,789,548.09, an increase of \$306,221.94 over the expenditure for the preceding year. As against that, the total income for 1957 was \$2,483,347.55, or an increase of \$520,289.23 over the total income for the preceding year. The Society is in the happy position of greatly expanding its services to members while at the same time maintaining its excellent financial position. For this success, we are indebted to Secretary Eisenman to whom we owe a tribute for the leadership, forethought, skill, and good management he has exercised in the past in guiding the affairs of the Society.

Your Treasurer acknowledges his gratitude to the staff of the Society for its kind and generous assistance and cooperation over the past two years. Special thanks are offered to Secretary Eisenman, Assistant Treasurer A. A. Hess, Trust Officers Messrs. W. W. Horner and A. W. Marten of the Cleveland Trust Company, and to the Board of Trustees for their helpful advice and guidance, of which they gave so generously.

The Balance Sheet; the Statement of Income and Expenses; and the Statement of Appropriated Income as audited by the Certified Public Accountants, Ernst & Ernst, appear on pages 23, 24 and 25.

Board of Trustees,
American Society for Metals,
Cleveland, Ohio.

We have examined the balance sheet of American Society for Metals as of August 31, 1957, and the related statements of income and expenses and surplus for the year then ended. Our examination was made in accordance with generally accepted auditing standards, and accordingly included such tests of the accounting records and such other auditing procedures as we considered necessary in the circumstances.

In our opinion, the accompanying balance sheet and statement of income and expenses present fairly the financial position of American Society for Metals at August 31, 1957, and the results of its operations for the year then ended, in conformity with generally accepted accounting principles applied on a basis consistent with that of the preceding year.

Cleveland, Ohio
September 27, 1957

ERNST & ERNST
Certified Public Accountants

BALANCE SHEET

AMERICAN SOCIETY FOR METALS

August 31, 1957

ASSETS		
CASH		\$ 208,508.58
SECURITIES (approximate market or redemption prices aggregate \$2,408,744.26)		
Bonds, stocks, and land trust certificates—		
at cost	\$1,910,879.43	
Accrued interest	17,478.75	1,928,358.18
CASH SURRENDER VALUE OF LIFE INSURANCE		88,365.48
ACCOUNTS RECEIVABLE		
National Metal Exposition—Chicago—		
November, 1957	\$ 105,342.00	
Southwestern Metal Show—Dallas—May, 1958..	38,682.25	
Advertising accounts	33,758.28	
Due from Building Fund	28,501.54	
Miscellaneous	31,311.55	\$ 237,595.62
Less allowance for doubtful accounts	2,000.00	235,595.62
INVENTORIES—at cost or lower		
Bound and unbound books, publications, correspondence courses, etc.....	\$ 244,930.73	
Less allowance for obsolescence.....	6,000.00	238,930.73
OTHER ASSETS		
Officers, employees, and sundry accounts and deposits		20,907.28
BUILDING FUND		
Cash	\$ 22,433.12	
Bonds—at cost (approximate market or redemption prices aggregate \$1,115,415.62)....	1,154,365.63	
Accrued interest	7,084.34	
Land	15,000.00	
Construction in progress.....	16,018.80	\$1,214,901.89
Less amount due operating funds.....	28,501.54	1,186,400.35
REAL ESTATE (at cost less allowances for depreciation)		44,250.00
OFFICE FURNITURE, FIXTURES, AND EQUIPMENT (at cost less allowances for depreciation)		92,593.61
DEFERRED CHARGES		
Prepaid exposition expenses:		
National Metal Exposition—Chicago—		
November, 1957	\$ 70,465.65	
Southwestern Metal Show—Dallas—		
May, 1958	9,070.58	
Development costs applicable to correspondence courses	71,893.20	
Prepaid insurance	9,631.33	
Prepaid sundry expenses.....	9,460.54	170,521.30
		<u>\$4,214,431.13</u>

LIABILITIES, RESERVES, AND SURPLUS

LIABILITIES

Accounts payable:			
For purchases, expenses, etc.....	\$ 77,182.75		
Payroll taxes and taxes withheld from employees	8,462.84		
For apportionment of dues to local chapters..	5,526.97	\$ 91,172.56	
Special contribution—A. S. M. of Tomorrow...		2,500.00	\$ 93,672.56
INCOME APPROPRIATED FOR EDUCATIONAL PURPOSES			177,345.95
INCOME APPROPRIATED FOR BUILDING FUND			555,299.46
RESERVES			
For Metals Handbook.....	\$ 96,380.03		
For conventions	60,000.00		
For dues paid in advance.....	50,000.00		
Campbell Memorial Lecture Fund.....	15,000.00		
H. M. Howe Medal Fund.....	5,000.00		
Sauveur Achievement Award.....	5,000.00		231,380.03
BUILDING FUND			
Reserve			1,186,400.35
DEFERRED INCOME			
National Metal Exposition—Chicago—November, 1957	\$ 568,431.25		
Southwestern Metal Show—Dallas—May, 1958	98,565.00		
Advance receipts on publications.....	727.96		667,724.21
SURPLUS			
Balance at September 1, 1956, and August 31, 1957 (no change during the year)			1,302,608.57
			<u>\$4,214,431.13</u>

STATEMENT OF INCOME AND EXPENSES

AMERICAN SOCIETY FOR METALS

Year ended August 31, 1957

INCOME

Publications	\$1,335,049.77
National Metal Exposition—Cleveland—October, 1956.....	510,299.95
Western Metal Show—Los Angeles—March, 1957.....	278,537.45
Memberships	90,747.71
Dividends and interest earned.....	117,877.25
Metals Engineering Institute.....	13,781.50
Gain on disposal of securities.....	1,080.85
Sundry sales, etc.	1,722.21
Increment and dividends on life insurance.....	2,083.88
Discount earned	1,166.98
TOTAL INCOME	\$2,483,347.55

EXPENSES

Publications	\$1,098,323.05
National Metal Exposition—Cleveland—October, 1956.....	219,244.57
Western Metal Show—Los Angeles—March, 1957.....	121,971.36
General expenses	93,288.10
Memberships	76,704.14
Secretary's office	36,808.27
Transfer of net interest income to building fund.....	31,411.84
Accounting department	30,174.69
Metals Engineering Institute.....	23,781.50
Headquarters	19,445.02
Warehouse	14,367.51
National committees	6,974.56
President's office	5,344.57
Miscellaneous merchandise	5,341.78
Medals, awards, and lectures.....	2,839.77
Trustees	2,672.49
Multigraph department	463.51
Library	391.36
TOTAL EXPENSES	1,789,548.09

NET INCOME—Note A.....\$ 693,799.46

Income appropriated as authorized by the Board of Trustees:

For educational purposes	\$ 138,500.00	
For building fund.....	555,299.46	693,799.46

UNAPPROPRIATED NET INCOME.....\$ —0—

Note A—In addition to expenses shown above, expenditures in the amount of \$123,494.85 were made during the year from prior years' appropriations (see accompanying statement).

STATEMENT OF APPROPRIATED INCOME

AMERICAN SOCIETY FOR METALS

Year ended August 31, 1957

INCOME APPROPRIATED FOR BUILDING FUND

Balance September 1, 1956.....	\$375,442.23
Add amount appropriated during the year.....	555,299.46
	<u>\$930,741.69</u>
Less amount transferred to building fund.....	375,442.23
BALANCE AUGUST 31, 1957	<u>\$555,299.46</u>

INCOME APPROPRIATED FOR EDUCATIONAL PURPOSES

Balance September 1, 1956.....	\$162,340.80
Less expenditures during year:	
World Metallurgical Congress.....	\$38,108.20
Revision of Metals Handbook.....	30,000.00
Mechanical literature searching.....	15,000.00
Science award program.....	15,000.00
Acta Metallurgica.....	8,900.00
Chapter educational courses.....	7,032.25
A. S. M. Foundation for Education and Research.....	5,000.00
Teaching awards.....	2,251.73
Visiting lectureships.....	2,202.67
	<u>123,494.85</u>
Add amount appropriated during year.....	\$ 38,845.95
	<u>138,500.00</u>
BALANCE AUGUST 31, 1957	<u>\$177,345.95</u>

1957 ANNUAL REPORT OF THE SECRETARY

WILLIAM H. EISENMAN, *Secretary*

THE American Society for Metals on October 1, 1957 had a total membership of 28,778, a gain of 1910 members since last October. Of this number 24,522 are regular members, 1547 are student members, 2555 are sustaining members, 116 are honorary and life members and 38 are in the armed forces.

TRANSACTIONS COMMITTEE

Eighteen persons constitute the membership of the TRANSACTIONS Committee for 1957, under the chairmanship of R. D. Chapman, Chrysler Corporation, Detroit. The members of the Committee and their Chapter affiliation are: J. H. Bechtold, Pittsburgh; G. S. Birdsall, Louisville; D. J. Carney, Chicago; Morris Cohen, Boston; J. E. Dorn, Golden Gate; H. J. Elmendorf, Worcester; G. H. Enzian, Pittsburgh; G. A. Fritzlen, Purdue; D. J. Girardi, Canton-Massillon; R. W. Guard, Eastern New York; H. Y. Hunsicker, Cleveland; R. I. Jaffee, Columbus; J. F. Libsch, Lehigh Valley; E. M. Mahla, Wilmington; P. G. Nelson, Philadelphia; W. A. Reich, Detroit, and Ray T. Bayless, Secretary, Cleveland.

During the year the Committee has had three meetings; January 16, May 27-28, September 5, and has a fourth meeting tentatively scheduled for December 2, 1957. The Committee reviewed 106 papers at the first three meetings. Of this number, 71 papers have been approved for

publication in *TRANSACTIONS*; 5 papers were returned to authors for suggested revision and may be returned for re-review; 30 papers were not approved for publication and were returned to the authors with the comments of the Committee and suggestions to the author included.

As the final date for submission of papers for presentation at this Convention had been set at April 15, 1957, arrangements for the technical program at this Convention were made during the May 27-28, 1957 meeting at which time 50 papers were selected for presentation.

Nineteen papers are now in the process of review, and will be considered at the December meeting, along with any new manuscripts received in the interim.

EDUCATIONAL COMMITTEE

Nine persons constitute the membership of the Educational Committee for 1957, under the chairmanship of D. J. Blickwede, Bethlehem Steel Corporation, Bethlehem, Pa. The members of the Committee and their Chapter affiliation are: Richard Doughton, Jr., Pittsburgh; S. L. Henry, Milwaukee; W. T. Lankford, Pittsburgh; E. S. Machlin, New York; M. R. Meyerson, Washington; T. E. Piper, San Diego; D. H. Ruhnke, Canton-Massillon; A. U. Seybolt, Eastern New York; and Ray T. Bayless, Secretary, Cleveland.

The Committee arranged the educational lecture course entitled "Precipitation From Solid Solution" for presentation at this Convention, under the coordination of Richard Doughton, Jr. Eight lectures were presented at four sessions, with an introductory and summary lecture by R. F. Mehl, by the following authors: J. B. Newkirk, General Electric Research Laboratories; W. A. Anderson, Alcoa Research Laboratories; H. W. Paxton, Carnegie Institute of Technology; A. J. Lena, Allegheny Ludlum Steel Corporation; W. D. Robertson, Yale University; Robert Bray, Chase Brass and Copper Co.; R. S. Busk, The Dow Chemical Co.; C. G. Bieber and R. J. Raudebaugh, International Nickel Company; G. A. Fritzlen, W. H. Faulkner, B. R. Barrett, and R. W. Fountain, all of Haynes Stellite Co.

ASM METALS HANDBOOK COMMITTEE

Preparation of Volume I of the new ASM Metals Handbook has gone forward steadily during the past year. Fifty-two committees, totalling 712 members, have held a total of 81 meetings. The remaining 27 committees, totalling more than 400 members, are committed to firm schedules. All of the committee work for Volume I, Properties and Selection of Metals, will be completed in June of 1958.

To assist the numerous committees, the Handbook editorial staff has been increased to five during the year. The headquarters staff consists of Taylor Lyman, editor; Howard E. Boyer, managing editor; Jos. E. Foster, associate editor; James J. Kubbs, associate editor; and Helen Lawton, assistant editor.

SPECIAL LIBRARIES ASSOCIATION

The Metals Division of Special Libraries Association is holding its annual fall meeting in conjunction with the National Metal Congress for the eighth consecutive year. Three technical sessions will be held, featuring "Progress in Nonferrous Metallurgy" (with particular reference to library and documentation problems), "Progress in Ferrous Metallurgy" and "International Aspects of Literature Research." Speakers at the international session will include a number of conferees to the World Metallurgical Congress who will talk about literature services in various European countries.

The Metals Division is also operating a booth at the Metal Show which is designed as a miniature technical library and manned by trained personnel to demonstrate the services provided by special libraries.

ASM MECHANIZED LITERATURE SEARCHING PROJECT

The ASM pilot plant project for mechanized literature searching is now rounding out the second year of the five-year, \$75,000 contract with the Center for Documentation and Communication Research at Western Reserve University.

About 7000 metallurgical literature references have been analyzed and "telegraphic" abstracts prepared. Of these, 2500 have been encoded on paper tape for searching on the experimental searching selector built at Western Reserve University.

Test runs on typical literature searches are now being prepared using this machine on 2500 encoded abstracts from the literature of 1955. Questions for literature searches are being solicited from ASM members who are interested in cooperating in the program.

Another project completed during the summer was the preparation of a fifteen minute, sound, color film entitled "The ASM Metals Information Center of Tomorrow." This film is currently being shown at the National Metal Exposition where an exhibit has been prepared by the Documentation Center to provide information on this project. Copies of the film are available for showing before chapters of the American Society for Metals, educational institutions, library and documentation organizations and other interested groups.

RELATED DOCUMENTATION ACTIVITIES

A new standing committee has been established by the board of trustees to be known as the ASM Metallurgical Documentation Committee. The first meeting of this committee will be held soon. Personnel of the committee is as follows: Frank T. Sisco, New York, Chairman; Wallace R. Brode, Washington; Dolph G. Ebeling, Schenectady; Herman Henkle, Chicago; D. C. Hilty, Niagara Falls; I. H. Jenks, Kingston, Ontario; George A. Roberts, Latrobe, Pa.; A. J. Shaler, Univer-

sity Park, Pa.; John W. W. Sullivan, New York; E. E. Thum, Cleveland; Marjorie R. Hyslop, Cleveland.

This committee supersedes two previous special committees of the society—namely the Mechanized Searching Committee under the chairmanship of D. C. Hilty, Manager, Metals Research Laboratories, Electro Metallurgical Company, and the ASM Committee on Literature Classification under the chairmanship of Frank T. Sisco, Director of the Engineering Foundation.

The latter committee, during the past year, has completed the project for which it was organized—namely a revision of the ASM-SLA Classification of Metallurgical Literature, first published in 1950. The text for the revised edition is now in preparation for publication.

TRANSACTIONS

Since the last National Metal Congress, Vol. 49 and Vol. 49A of the TRANSACTIONS were published and distributed in June to those of our members requesting them. Volume 49 totals 1061 pages and contains the 1956 Edward De Mille Campbell Memorial Lecture; 44 technical papers and their discussions; the president's, secretary's, and treasurer's reports for 1956; a report of the 1956 Convention; a list of ASM Chapters and officers, and other current items of record.

Volume 49A contains 14 papers (372 pages) presented at the Seminar on "Creep and Recovery" held on Saturday and Sunday, October 6 and 7, 1956, during the National Metal Congress and Exposition in Cleveland. This Seminar was sponsored by the American Society for Metals, the subject being selected by a committee appointed by the Board of Trustees. The personnel of this committee was: P. A. Beck, Chairman, Peoria; B. L. Averbach, Boston; M. B. Bever, Boston; Bruce Chalmers, Boston; R. L. Cunningham, Ottawa Valley; Pol Duwez, Los Angeles; John Fisher, Eastern New York; E. R. Jette, Los Alamos; J. S. Koehler, Urbana; Robert Maddin, Philadelphia; A. S. Nowick, New Haven; Thornton Read, Jr., New Jersey. The preparation and coordination of the series of subjects and solicitation of authors was conducted by Robert Maddin.

PREPRINTS OF TRANSACTIONS PAPERS

The Board of Trustees of the American Society for Metals, at their August, 1956 meeting, authorized the quarterly preprinting of technical papers that have been approved by the TRANSACTIONS Committee.

Under this new plan, 71 papers have been preprinted at three different times, and made available to the membership. Lists of the preprints, and notice of their availability, appeared in the March, August, and October issues of METALS REVIEW. The total number of pages in the three series of preprints produced so far this year is 1626. Approximately 51,500 copies of the preprints have been distributed free to members who have requested them.

METAL PROGRESS

Metal Progress' editorial production for the fiscal year (892 pages) almost exactly equalled that of the preceding year, and is about 20% greater in volume than the average of the last few, 1950 to 1955 inclusive. Advertising patronage (2164 pages) reached an all-time high, exceeding last year by 16.5%. The year 1945 was the next best in advertising patronage (2045 pages).

The January issue, as for several years past, has contained a review of international progress in metallurgy. So many good articles are available on this theme that the main portion of this year's January issue was confined to 15 papers from foreign authors. A similar series of papers reviewing similar noteworthy advances in the United States and Canada filled the September 1956 pre-convention issue. It is planned to continue this arrangement—the January issue will be a review of foreign progress, and the pre-convention issue will be a review of progress on this continent.

At the risk of slighting some very meritorious contributions during the last 12 months, the following noteworthy articles might be mentioned:

- Concentrates for Iron Blast Furnaces,
by E. C. Wright
- Metal Powder Rolling and Hot Pressure Bonding,
by Samuel Storheim
- Ferrosilicon Manufacture at Marietta,
by E. E. Thum
- Improved Foundry Compositions,
by A. Wittmoser
- Less Sulphur in Deoxidized Steel,
by H. W. McQuaid and Norman P. Goss
- Crack-Free Welds in High-Temperature Piping,
by Henry M. Soldan and Charles R. Mayne
- Effects of Slack Quenching of Steel,
by D. J. Blickwede and R. C. Hess
- Metals for Fast Flight,
Report from Western Metal Congress
- Superpurity Aluminum,
by E. A. Bloch and P. H. Muller
- New Magnesium Alloys for High Temperature,
by T. E. Leontis

There were also a dozen or so excellent papers on heat treating equipment and methods secured through the Industrial Heating Equipment Association.

Readership surveys of Metal Progress have been made at quarterly intervals by the Eastman Research Organization for the past five years. "Eastman Index" figures for reader interest, reader attention, and value to reader are above the corresponding composite figures for the 30 business publications currently being surveyed by that organization.

METALS REVIEW

During the twelve months from October 1956 through September

1957, Metals Review published a total of 796 pages, an increase of 56 pages over the total for the previous year. Of these 796 pages, 368, or 46.3% were devoted to ASM Review of Metal Literature; 283 pages, or 35.4%, were devoted to chapter and membership activities, special features and headquarters activities; and 145 pages, or 18.3% were devoted to the Employment Service Bureau. These figures represent an increase in each division of 8, 3 and 16%, respectively, over the previous year's figures.

The Student Members Placement Service, usually carried as a special feature in the February issue, was dropped this year because the unusually good employment opportunities for graduating metallurgists greatly decreased the need for this service.

Adhering to the recent changes in the Constitution, which state that preprint papers be publicized on a quarterly basis, the March and August issues carried the first two lists.

A new monthly feature, Men of Metals, joined the already existing features, which include Compliments, New Films, Chapter and Special Meeting Calendars, and Meet Your Chapter Chairman. A total of 432 chapter reports were received and published during this period.

In January the cover format was changed to feature a portrait of a prominent ASM member, with an article regarding his accomplishments in the lead-off pages of the magazine. In July the page size was changed to accommodate standard advertisement requirements.

BOOKS

During the past fiscal year 35,393 books published by the Society were sold to members of the Society and others. This figure includes 1965 ASM METALS HANDBOOKS, 1778 METALS HANDBOOK SUPPLEMENTS printed in 1954, 2675 METALS HANDBOOK SUPPLEMENTS printed in 1955, and 3378 TRANSACTIONS.

During this period 8 titles were added to the publication list. They are:

TRANSACTIONS VOL. 49
CREEP AND RECOVERY
DUCTILE CHROMIUM
EFFECT OF RESIDUAL ELEMENTS ON THE PROPERTIES OF
METALS
FATIGUE DURABILITY OF CARBURIZED STEEL
BASIC METALLURGY VOL. II
ASM REVIEW OF METAL LITERATURE VOL. 13
TRANSACTIONS INDEX

The following books are now in preparation:

TRANSACTIONS VOL. 50
LIQUID METALS AND SOLIDIFICATION
PRECIPITATION FROM SOLID SOLUTION

ASM REVIEW OF METAL LITERATURE VOL. 14
ASM-SLA METALLURGICAL LITERATURE CLASSIFICATION
INTERNATIONAL (SECOND) EDITION
STORY OF THE 2ND WORLD METALLURGICAL CONGRESS
THE METAL THORIUM
THE METAL MOLYBDENUM
INTRODUCTION TO REACTOR METALLURGY
HIGH-TEMPERATURE METALS FOR AIRCRAFT AND MISSILES
MAN, METALS AND MODERN MAGIC
POWDER METALLURGY IN NUCLEAR ENGINEERING

SEMINAR COMMITTEE

Fourteen persons constitute the membership of the Seminar Committee for 1957, under the chairmanship of Robert Maddin, University of Pennsylvania, Philadelphia. The members of the Committee and their Chapter affiliation are: B. L. Averbach, Boston; P. A. Beck, Peoria; M. B. Bever, Boston; Bruce Chalmers, Boston; Pol Duwez, Los Angeles; John Fisher, Eastern New York; J. J. Harwood, Washington; W. R. Hibbard, Jr., Eastern New York; J. S. Koehler, Peoria; Thornton Read, Jr., New Jersey; W. D. Robertson, New Haven; R. L. Smith, Philadelphia; F. L. Vogel, Philadelphia, and Ray T. Bayless, Acting Secretary, Cleveland.

During the year the Committee held one formal meeting in New Orleans on February 24, 1957, at which time the subject for the 1958 Seminar was unanimously selected. With W. R. Hibbard as coordinator, the 1958 Seminar will be held on "Magnetic Properties of Metals and Alloys".

SEMINAR ON LIQUID METALS AND SOLIDIFICATION

The Seminar on "Liquid Metals and Solidification" was arranged into four sessions this year, two on Saturday and two on Sunday, and was an outstanding success in every respect. A capacity audience filled the meeting rooms for the presentation of 12 papers by the following authors: G. Vineyard, Brookhaven National Laboratory; N. H. Nachtrieb, Institute for the Study of Metals of University of Chicago; O. J. Kleppa, Institute for the Study of Metals; E. M. Pound, Carnegie Institute of Technology; J. Weeks and D. H. Gurinsky, Brookhaven National Laboratory; J. O'M. Bockris, University of Pennsylvania; K. A. Jackson, Harvard University; C. M. Adams, Jr., Massachusetts Institute of Technology; W. G. Pfann, Bell Telephone Laboratories; John Rutter, General Electric Research Laboratory; W. A. Tiller, Westinghouse Research Laboratory, and J. Walker, General Electric Research Laboratory.

The preparation and coordination of the series of subjects and solicitation of the speakers were under the direction of Bruce Chalmers.

SCIENCE ACHIEVEMENT AWARDS

Since 1952, ASM has underwritten the costs of many thousands of Science Achievement Awards in Junior and Senior High Schools throughout the country. Counting those students who submitted outstanding entries which merited Certificates and Honorable Mention Awards, close to 5000 boys and girls have been aware of this ASM Educational program. Over 700 of the winners each received cash or U.S. Bonds ranging from \$25 to \$100.

The National Science Teachers Association administers this Award program from Washington, D.C., with ASM funds amounting to \$15,000 annually.

Twenty of the \$100 U.S. Bonds go annually to students whose entries are concerned with metals and their importance to progress.

Judging of the entries is carried out on a regional basis. In each of eight geographical areas, the best of all entries are selected, then sent to Washington where a special committee makes a final selection of fifteen winners in each area or region—a total of 120 U.S. Bonds. All of the winners with entries or projects on the subject of metals are automatically considered for one of the 20 awards of \$100 U.S. Bonds in addition to their first award. Thus a total of 140 U.S. Bonds are awarded each year.

The program which covered the 1956–57 School year was the largest ever completed. 60,000 announcements of the program were mailed from Washington—nearly one-half going to Science Teachers who were members of NSTA.

2,121 Science Teachers requested a total of 26,968 sets of entry material for their students and 2,941 entries were completed and sent in to the regional judging committees. Of these, 1,186 merited Certificates of excellence, and 140 were selected to receive U.S. Bonds.

ASM \$2000 TEACHING AWARD

Twelve \$2,000 Metallurgy Teaching Awards have been made since the program was established in 1952. Designed to encourage and reward the young teacher of metallurgy, the award is made to one individual each year who, in the opinion of the judging committee, has turned in the best teaching performance in the metallurgy curriculum. The candidate must be under 40 years of age at the close of program in which the candidate's name is submitted.

Sponsorship of a candidate can be presented by any educational group or by any ASM Chapter. Selection of a winner is made by a special committee appointed by the Board of Trustees of ASM.

Seven candidates for the ASM Teaching Award were considered during the current (1956–57) year. The Awards Committee selected Amos J. Shaler, Penn State University, as the winner.

ASM VISITING LECTURESHIPS

Since the program's beginning in 1952, 48 Distinguished Scientists and Engineers have been sent by ASM to various Colleges and Universities as Visiting Lecturers. Selection of these special lecturers is made by the schools themselves. After their selection ASM invites the lecturer to conduct, at ASM expense, a two-day lecture series on a subject in which the lecturer is known to specialize. ASM also compensates the lecturer for the time spent on the campus of the visited school.

Average annual cost of the Visiting Lectureship Program to ASM is \$2,878.82.

TRAVELING METALLOGRAPHIC EXHIBIT

The winning entries in the annual ASM Metallographic Exhibit, held during the National Metal Congress, are mounted and sent to as many ASM Chapters and Schools as can be reasonably scheduled. Each year 15 to 25 Chapters and Schools are on the schedule, many of them making use of the Exhibit at a meeting which includes a well-known specialist on Metallography as the principal speaker.

Since the program's beginning in 1954-55, over seventy ASM Chapters and Schools have used the Traveling Exhibit as a part of their special meetings or symposia. All transportation costs are paid by ASM.

CAREER PUBLICATIONS

While many of the ASM Educational efforts contribute to Career promotion—particularly the Science Achievement Awards and the attendant printed material, the Teaching Award, the Visiting Lectureships and the Metallographic Exhibit—certain publications have a more direct application. Two of the principal Career publications are:

Your Career in the Metallurgical Profession

(95 page Illustrated)

Does Engineering Appeal to You?

(7 page accordion fold)

Over 50,000 of the 95 page Booklets have been distributed during the past ten years. These go, for the most part, to High School Science Teachers as a result of requests from them. Many thousands also go to Chapters and Schools for use in promoting the Metallurgical profession. In addition, hundreds of these Booklets are sent upon request from talented Senior High School students who have indicated interest in Metallurgy. Special mailings are made to winners of ASM Scholarships and the winners in the Metals division of the Science Achievement Awards program. Miscellaneous mailing to Metalworking firms and other individuals account for many more.

The Booklet has recently been revised and brought up-to-date and the new edition is expected to be off the press before the first of the year.

300,000 of the 7-page Accordion Fold Leaflets have been distributed since it was prepared six years ago. An average of over 1000 are mailed each month to Schools, Chapters and individual students who request them. The leaflet is a condensed version of the Booklet and provides for mass distribution at economical cost.

CHAPTER STUDENT AFFAIRS

Student Affairs is becoming more and more important to ASM Chapters. During the year, special effort has been made to bring about the appointment of a Student Affairs Committee in the ASM Chapters. 73 of the 104 Chapters now have a Student Affairs Committee and the National Office has established close working relationship with the Chairman in order to make the best use of all information which accumulates in Cleveland as a result of statistical results from sources other than ASM and from success reports of Chapters which might be applied in other Chapters.

INCOME SURVEY

Early in 1957 the ASM Advisory Committee on Metallurgical Education conducted a survey of Metallurgists' income. The results of that survey have been announced and will later be published in Metal Progress.

5,861 questionnaires were mailed to a list of metallurgists and Chief Metallurgists who are members of ASM.

2,985 replies were received—better than 50%.

For the entire 2,985 who replied, the average annual salary was \$10,620.

2,707 Metallurgists reported B.S. Degrees, with an average salary of \$10,284. 117 Metallurgists reported having M.S. degrees, with an average salary of \$10,714. Those with Doctor's degrees had average salaries of \$13,840. 80 reported no College degree, with average salaries of \$8,770.

Out of the nearly 3,000 replies, only 52 reported salaries of less than \$6,000 a year. A further analysis of these 52 replies shows that the individuals had only 2.7 years experience. Only one reply covered an income of less than \$5,000 a year—and that was for a 1957 graduate with no experience.

Experience counts, according to the survey. For Metallurgists with 30 to 35 years experience, the average salary was \$14,770. With 25 to 30 years experience, the average was \$13,682. Those with 20 to 25 years experience were receiving an average annual salary of \$12,704. 15 years experience commanded an annual salary of \$11,698, while the

ten year men were getting on the average \$10,410. With six to ten years experience, the salary was an average of \$7,447.

The average beginning salary for Metallurgists in 1957 was \$4920 a year.

The highest salary reported by the entire survey was \$50,000 annually.

More Metallurgists are engaged in manufacturing activities than any other field. Research accounted for the next greatest number of Metallurgists. Basic metal plants, administration and laboratory were next in that order.

ASMFER SCHOLARSHIPS

Fifty-six Colleges and Universities are today participating in the annual Scholarship program. Through each of these schools the ASM Foundation for Education and Research makes a \$400 Scholarship in Metallurgy.

Since the program was established in 1953, a total of 248 Scholarships have been given by the Foundation.

Close to \$100,000 has been used for this purpose—\$99,200 to be exact. The Scholarship funds are sent to the school, the selection of a winner is made by the school and the funds passed along to the Award winner.

Each Scholarship winner receives a handsome Certificate along with the cash award. Ceremonies for the award presentation are usually held under the auspices of the local ASM Chapter. When there is no ASM Chapter in the vicinity of the winner's school, the Metallurgy Department Head is asked to make the presentation for ASM. Publicity releases for all the Scholarship winners are sent to the home town of the winner.

A breakdown of the annual ASMFER Scholarships follows:

1953-54	—42	Scholarships
1954-55	—48	Scholarships
1955-56	—49	Scholarships
1956-57	—53	Scholarships
1957-58	—56	Scholarships

Fourteen schools have been added to the original list—the most recent additions being: University of Maryland, North Carolina State College, Hamilton College in Canada, Youngstown University, University of Alberta in Canada, San Jose State College and the University of Oklahoma.

Qualifications for Scholarship participation by schools are that a degree in metallurgy be offered as a result of a full day-time course in this Engineering subject.

METALLOGRAPHIC EXHIBIT

The Twelfth Annual ASM Metallographic Exhibit is notable for the establishment of the Francis F. Lucas Award for excellence in metal-

lography. First recipient of this \$500 award, endowed by Adolph I. Buehler, president of the company that bears his name, is T. K. Bierlein and B. Mastel, Hanford Atomic Lab. General Electric Co., Richland, Wash. The award was presented at the Annual Awards Luncheon on November 5, by Francis F. Lucas, widely known microscopist for many years at Bell Telephone Laboratories, in whose honor the award was established.

Competition for this honor was keen, with over 500 entries now on display at the National Metal Exposition—more than double the number in any previous metallographic exhibit. In keeping with the Second World Metallurgical Congress, more than 150 entries were received from foreign metallographers.

As in past exhibits, medals have also been presented for Best in Class and Honorable Mention in each of twelve classifications. The entry designated Best in Show by the judging committee automatically receives the Lucas Award.

All prize-winning entries will again be assembled in a traveling exhibit for shipment to ASM chapters and engineering schools during the winter season.

EDUCATIONAL FILMS

The three films produced under the guidance of the Educational Committee and distributed through the National Headquarters office have been constantly in demand during the last year with peak usage occurring in the fall-to-spring season. Various ASM Chapters and other educational groups have used the three films 310 times, itemized as follows:

METAL CRYSTALS	125 times
IRON-CARBON ALLOYS	118 times
HEAT TREATMENT OF STEEL	67 times

A new 30-minute color and sound film by the ASM and ASMFER has been produced and will be available for showing by the Chapters and Schools this fall. Its subject is "How Metals Behave."

EDUCATIONAL AID TO CHAPTERS

In March a new **SPEAKERS DIRECTORY** was sent out to the officers of all ASM Chapters. Half as bulky as the 1956-57 edition, because of its new format, the 1957-58 Speakers Directory contains 25% more listings. There are 741 individual listings of speakers available to the Chapters, and 129 individual film listings. Both listings include a subject index, and all individual listings have a brief descriptive note.

A revised edition of the **EDUCATIONAL COURSES** available for Chapter use was also distributed to the Chapters in March of this year.

SLIDES for use in connection with educational lecture courses conducted by the Chapters were provided to 21 Chapters.

From November 1956 to October 1957, allowances from the EDUCATIONAL ASSISTANCE FUND have been granted to 68 Chapters.

ASM REVIEW OF METAL LITERATURE

On January 1, 1957 the preparation of the ASM REVIEW OF METAL LITERATURE was transferred from Battelle Memorial Institute, Columbus, Ohio, to the Center for Documentation and Communication Research at Western Reserve University in Cleveland. The work of searching the literature and preparing the annotations has been effectively conducted at Battelle Memorial Institute since the service was instituted in 1944. The principal reason for making the change at this time was so that the work on the abstracting service could be more effectively correlated with the ASM Machine Literature Searching Project being conducted as a five-year pilot plant experiment at Western Reserve's Documentation Center. Preparation of the Review of Metal Literature at Western Reserve is an interim arrangement, and the entire project will be transferred to ASM headquarters when the development work is completed.

The abstracting staff at Western Reserve University is being assisted by the John Crerar Library of Chicago, where some 2500 scientific and technical publications are searched monthly for articles of metallurgical interest.

The REVIEW OF METAL LITERATURE continues to be published as a monthly feature of METALS REVIEW. The monthly installments were again correlated into the thirteenth bound volume, covering the literature of 1956. Volume 13 contains 859 pages and 8329 annotations and is accompanied by an author and subject index.

METALS ENGINEERING INSTITUTE

The Metals Engineering Institute has been in operation since April 1, 1957. During these seven months and without any advertising we have received several thousand inquiries from all over the United States and many parts of the world. The MEI has accepted over 300 registrations from 23 states. Comments from students already enrolled have been decidedly laudatory and indicate favorable reception of future courses.

A sizable proportion of the registrants comes from industrial groups in Cincinnati, Wallingford, Conn., Cleveland, and Los Angeles. Several more in-plant training programs are pending. A consultation service is being provided to training directors who want a program that will combine parts of several MEI courses and thus be "tailor made" to suit their particular requirements.

The March, 1957, Titanium Conference, which was directed by the Metals Engineering Institute, was an overwhelming success. The five-day seminar was conducted during the Western Metal Congress in

Los Angeles. Attendance was well over 150 and included one registrant from Germany, two from France, two from England, several from Canada, and quite a number from various branches of the armed forces.

The courses now available include:

Elements of Metallurgy	by Ralph Edelman
Heat Treatment of Steel	by George Melloy
High Temperature Metals	by Claude Clark
Titanium	by Walter Finlay

By January 1, 1958 the following will be ready:

Metals for Nuclear Power
Stainless Steels
Electroplating
Gray Iron Foundry Practice
Steel Foundry Practice
Steel Plant Processes
Oxy-Acetylene Welding
Primary and Secondary Recovery of Lead and Zinc

Thus far, the MEI has received from its course authors 279 lessons. This is approximately half of the proposed 585 lessons. (585 for 39 courses.)

Of these, 107 have been edited and 53 have been printed. The printed lessons are now in use to serve the MEI students. The ASM membership will be kept informed of the progress of the Metals Engineering Institute (the Home Study School of the Metals Industry) through news articles in the METALS REVIEW.

NATIONAL METAL CONGRESS

The National Metal Congress was again a cooperative activity of the Society for Non-Destructive Testing, the American Mining, Metallurgy and Petroleum Institute, the Industrial Heating Equipment Association, the Metal Powder Association and the Atomic Energy Commission, joining with the ASM in the presentation of an outstanding program—with 84 sessions and the presentation of 240 technical papers.

It has been definitely granted that the high calibre of the papers makes the Congress the most outstanding scientific gathering in the metals industries.

NATIONAL METAL EXPOSITION

The National Metal Exposition now being held in the International Amphitheatre covers 18% more space than any of the 38 shows that have preceded it. The exhibitors make the Exposition a great laboratory of the Metal Congress—so we not only hear and learn about the new metal developments but also see the latest processes and methods in production, fabrication, and testing. The Exposition is an important part of this Great Educational Congress, and we are under deep obliga-

tion to the hundreds of exhibitors who have arranged such attractive, interesting and enlightening presentations of their process and products.

ASM OF TOMORROW

I am delighted to be able to report to you that the Cleveland architectural firm of Kelly and Kress and Associates has presented a design for the national headquarters building which received the approval of all the committees through which it was necessary to pass before reaching the Board of Trustees. The design and proposal received the unanimous approval of the officers and trustees of the Society.

Working drawings are now being completed, and at the present time the contractors, Gillmore-Olson, Inc., of Cleveland, are working on site problems such as water, roads, sewage and electricity.

Already they are building retaining walls and will begin grading an access road within a couple weeks so this road will be available for hauling in equipment and material so erection of the building may be started in early spring.

Borings have been taken; a well has been drilled, and a more than adequate flow of A-1 drinking water has been secured.

I would like to describe the building, but I have not yet been able to assemble words which would adequately describe the wonderful dome and plans so that anyone would understand.

When we talk about a dome, the first thing most people visualize is the dome on the white house, and when we talk about a dome 250 feet in diameter at the base, supported on five pylons, with the top of the geodesic sphere 110 feet in the air, well it is just a little beyond imagination. We have ordered a scale model of the dome and of the building and as soon as it is completed we will either put it in a trunk and travel around the country so that our members can see it, or we will make a picture of it and publish it in the ASM publications.

Of this you can be sure—It is going to be a building of which you may be justly proud and at the same time it is going to be a building which will be so unusual that no one else but the ASM would build it. It will typify the Society and what it stands for and become its trademark.

Most of you will have an opportunity to see it, when you attend the convention in Cleveland next October.

Building will start in the spring of 1958, and we have been promised occupancy of the 50,000 square-foot building in the spring of 1959.

THE 2ND WORLD METALLURGICAL CONGRESS

Two years ago the staff at ASM prepared an outline of activities for the 2nd WMC and since that time that event has been in our thoughts continuously. It is difficult to realize that the activities of this great gathering are now in full function. We were delighted at the cordial

reception and acceptance of the ASM's invitation to the metal scientists of the free world—253 came two weeks early to participate in the industrial and educational tours to plants and institutions between New York and Chicago. These Conferees were joined in Chicago by another group of 251 Overseas Conferees to attend and participate in the Second World Metallurgical Congress.

This Congress was certainly well timed coming at a period when changing world conditions activated the free nations into a desire to exchange and pool their scientific knowledge and achievements in the common problems of mutual interest.

However, forming a brain power alliance is nothing new to the ASM and many of our Overseas guests. In 1951 at Detroit the ASM sponsored the First WMC when for the first time there came to America a group of metal scientists not from one country alone but from every free nation in which metal has a part. Over 500 came in '51 in the spirit that the Congress was a two-way street and the exchange of technical and scientific knowledge was desirable for conservation as well as for collective security and defense.

The WMC of 6 years ago was the first informal pooling of scientific knowledge of properties and fabrication of metals ever held on a world-wide basis.

The results were indeed significant and satisfying so much so that the European Metallurgical Congress was held in 1955 in England, Germany, Belgium, and France, with many other countries such as Italy, Sweden, Spain and others extending post invitations to the visiting scientists.

So now again the ASM has brought together and salutes this gathering as the Metal Science Brains of the Free World and recognizes this group as a key component of the brain power pool which now has official government backing.

It seems to me desirable that this World Congress should consider the possibility and need for closer cooperation among the metal scientists of the free world. It will, of course, be up to the Government to arrange and erect a formal organization—

However, the continuance of the exchange at these World Congresses on nonclassified subjects should be on a closer basis and perhaps at more frequent intervals.

In order that more intensified cooperation and exchange of ideas may be secured, the Board of Trustees will meet with representatives of the 20 Overseas Societies participating in the 2nd WMC in order that they may report to their officers and membership the suggested possibility of formulating a cooperating organization with the ASM to accomplish the purposes outlined above.

I sincerely hope the firm friendly basis upon which these World Metal Congresses have been established may lend itself to the rapid accomplishment of a closer union of the free countries of the World.

**American Society for Metals Foundation for Education and
Research
Annual Report of the President**

ADOLPH O. SCHAEFER, *President*

THIS REPORT covers the twelve-month period beginning September 1, 1956, and ending August 31, 1957.

It has again been the policy of the ASMFER to provide scholarships at all accredited colleges and universities on this Continent offering day-school degree courses in metallurgy or metallurgical engineering. This utilizes the major portion of the funds available each year.

During the past year three more institutions of higher learning were added to those receiving scholarships, making the total 56. Those added include the University of Oklahoma, San Jose State College, and the University of Alberta.

ASMFER scholarships amount to \$400.00 each. Consideration has been given to increasing this amount, and it is possible that the size of the Foundation will someday permit this, but it has appeared necessary to keep the scholarships at this figure for the present.

A list of the institutions granting scholarships, in 1956-57, with the winners names is as follows:

1956-57 WINNERS ASM FOUNDATION SCHOLARSHIPS, WITH
SCHOOLS AND HOME TOWNS

School	Winner	School	Winner
University of Alabama	Wm. M. House University, Ala.	Cornell University	B. D. Woloson Horsesheds, N. Y.
University of Arizona	John F. Peck Phoenix	Drexel Institute of Technology	Geo. A. Kurisky Kingston, Pa.
University of British Columbia	Christopher Huntley Vancouver, B. C.	Hamilton College	Frank Kurth Hamilton, Ont.
University of California	Daniel Green San Francisco	Illinois Institute of Technology	John L. Ledman Chicago
Carnegie Institute of Technology	James E. Bennett Cambridge, Ohio	University of Illinois	Robert Janninck Chicago
Case Institute of Technology	Stephen A. Kish Cleveland	University of Kansas	Jas. L. Jellison Johnson, Kans.
University of Cincinnati	Gerald L. Shawhan Cincinnati	University of Kentucky	Geo. D. Raven-croft Ashland, Ky.
Colorado School of Mines	Victor Kerlins Denver	Lafayette College	Nicholas D. Koopman Saylorsburg, Pa.
Columbia University	H. D. Guberman Bronx, N. Y.		

School	Winner	School	Winner
Laval University	Marc Levesque and Marc Lamontagne Quebec City, P. Q.	University of Pittsburgh	Robert C. Royle Dravosburg, Pa.
Lehigh University	Wm. G. Beattie Philadelphia	Brooklyn Polytechnic	Albert M. Imgram Garden City, N. Y.
Massachusetts Institute of Technology	Owen Deveraux Lexington, Mass.	Purdue University	Richard S. Stenberg South Bend, Ind.
McGill University	H. Daniel Petit Montreal, P. Q.	Queen's University	John G. McCubbin North Bay, Ont.
University of Maryland	Edwin E. Maust Hyattsville, Md.	Rensselaer Polytechnic	Richard D. Betts Altamont, N. Y.
Michigan College of Mines	Lawrence D. Bandy Lewiston, Mich.	South Dakota School of Mines	Allan G. Hins Parkston, S. Dak.
Michigan State College	Harry L. Murphy E. Lansing, Mich.	Stanford University	Jeffrey L. Morby Reno, Nev.
University of Michigan	Michael Tokar Ann Arbor, Mich.	University of Tennessee	Lanny K. Walker Greenville, Tenn.
University of Minnesota	Leon V. Kremer Wells, Minn.	Texas Western College	Dan R. Boyd Abilene, Tex.
Missouri School of Mines	Richard Fabiniak and Thaddeus Fabiniak Lancaster, N. Y.	University of Toronto	J. R. Carruthers Toronto, Ont.
Montana School of Mines	John P. Hager Big Timber, Mont.	University of Utah	Gordon R. Dorny Salt Lake City, Utah
New York University	David Seidman Flushing, N. Y.	Virginia Polytechnic Institute	Donald A. Mannas Alexandria, Va.
North Carolina State	Martin Luther Tyson, Jr. Cary, N. C.	Washington State	David R. Stiefbold Pullman, Wash.
University of Notre Dame	John R. Marshall Jerome, Ind.	University of Washington	Arthur Ellis Hall Yakima, Wash.
Ohio State University	James A. Clym Columbus, O.	Wayne University	Theodore Gottlieb Detroit
University of Pennsylvania	Frank R. Earley Cologne, N. J.	University of Wisconsin	Chas. J. Speerschneider Green Bay, Wis.
Pennsylvania State University	John W. Andrews Camillus, Pa.	Yale University	Nicholas Error, Jr. Salem, Oreg.
		Youngstown University	Anthony B. Strines Youngstown, O.

One Fellowship was awarded this year, and this went to George W. Pearsall, who is enrolled at the Massachusetts Institute of Technology.

It is understood that this Fellowship will be extended for another year should Mr. Pearsall's work this year be satisfactory, which it undoubtedly will be.

ASMFER has considered many ways to advance the cause of metallurgical research and education. It has, this year, tried two new approaches. A motion picture, illustrating metallurgical principles and techniques has been prepared in collaboration with the ASM and the cooperation of the metallurgical staff of the Massachusetts Institute of Technology. This color film with sound will be available soon for public distribution and presentation.

ASMFER has noted with interest a report made by a special independent committee under the chairmanship of Dr. George A. Roberts, a past-president of ASM and ASMFER. This Committee is known as the Special Committee on Manpower for the Metallurgy and Ceramics Professions. This Committee, in a very comprehensive report has recommended a number of worthwhile activities. Included among them is one to prepare a booklet for the use of science teachers in secondary schools which serves as a guide to help the teachers obtain information on the Metallurgy and Ceramics professions.

This booklet will describe the various metallurgical vocations, and the education necessary for each. It will provide material for field projects, list charts, film, and film slides available for teaching. Perhaps of most value, the proposed booklet will describe in detail the services teachers can obtain from the local chapters of technical societies in counseling and advising students, in available awards, speakers, science fairs, and many other valuable aids in presenting our field of science to the youth of our continent.

ASMFER has agreed to finance the publication of such a booklet, and a committee under the chairmanship of Walter R. Hibbard, Jr., of the General Electric Co. is engaged in assembling the necessary information.

A statement of the finances of the American Society for Metals Foundation for Education and Research is appended to this report. In brief, the principal, all of which has been contributed by the ASM, has been increased to the sum of \$689,016.15 by an additional grant of \$5,000.00 from the American Society for Metals, and by smaller sums from the disposal of securities and the sale of rights.

The income from securities during the fiscal year has been \$34,302.34, partially offset by expenses of \$2,419.53.

Expenditures for the year include the scholarships awarded both last year and this, totalling \$43,200.00, our fellowship of \$4,200.00 and our contribution towards the aforementioned motion picture.

No report such as this could be complete without paying tribute to the excellent cooperation and the work which is done by the headquarters staff of the American Society of Metals. Walter Morrison, in

BALANCE SHEET
AMERICAN SOCIETY FOR METALS FOUNDATION
FOR EDUCATION AND RESEARCH—November 30, 1957

ASSETS		
CASH ON DEPOSIT		
The Cleveland Trust Company:		
Income cash	\$ 10,725.85	
Principal cash	<u>5,762.69</u>	\$ 16,488.54
MARKETABLE SECURITIES (approximate market prices aggregate \$805,498.14)—Note A.....		
		701,189.61
OTHER INCOME ASSET		
Accrued bond interest.....		<u>3,478.22</u>
		<u>\$721,156.37</u>
LIABILITY AND FUNDS		
PRINCIPAL OF ENDOWMENT FUND		
Grants from American Society for Metals.....	\$690,346.10	
Net profit on disposal of securities.....	<u>1,606.20</u>	\$691,952.30
UNAPPROPRIATED NET INCOME		<u>29,204.07</u>
		<u>\$721,156.37</u>

NOTE A—Securities obtained by grant from American Society for Metals are stated at market price at July 15, 1952. Subsequent additions are at cost.

STATEMENT OF INCOME AND EXPENSES AND
UNAPPROPRIATED NET INCOME
AMERICAN SOCIETY FOR METALS FOUNDATION
FOR EDUCATION AND RESEARCH—Year ended November 30, 1957

INCOME		
Dividends and interest earned.....		\$ 34,433.34
EXPENSES		
Fiscal agent's fees and services.....	\$ 1,722.29	
Scholarship certificates	531.49	
Professional services	400.00	
Board of Trustees.....	163.69	
Miscellaneous	<u>3.43</u>	2,820.90
	NET INCOME	\$ 31,612.44
Unappropriated net income at beginning of year.....		<u>28,791.63</u>
		60,404.07
Scholarship awards	\$ 22,000.00	
Graduate Fellowship award.....	4,200.00	
Share of cost of film on metallurgy.....	<u>5,000.00</u>	31,200.00
	UNAPPROPRIATED NET INCOME	
	NOVEMBER 30, 1957	<u>\$ 29,204.07</u>

Board of Trustees,
 American Society for Metals Foundation
 for Education and Research, Cleveland, Ohio.

We have examined the balance sheet of American Society for Metals Foundation for Education and Research as of November 30, 1957, and the related statement of income and expenses and unappropriated net income for the year then ended. Our examination was made in accordance with generally accepted auditing standards, and accordingly included such tests of the accounting records, and such other auditing procedures as we considered necessary in the circumstances.

Securities were confirmed to us by The Cleveland Trust Company, agent.

In our opinion, the accompanying balance sheet and statement of income and expenses and unappropriated net income present fairly the financial position of American Society for Metals Foundation for Education and Research at November 30, 1957, and the results of its operations for the year then ended, in conformity with generally accepted accounting principles applied on a basis consistent with that of the preceding year.

Cleveland, Ohio
 December 11, 1957

ERNST & ERNST
 Certified Public Accountants

particular, is tireless in maintaining the correspondence and the records of this Foundation in excellent condition.

The field of metallurgical education and research is one of acknowledged national importance. Our cause is a worthy one. It is a privilege to be associated with a Foundation which is effectively serving our industry and our country.

ELECTION OF OFFICERS

PRESIDENT CLARK: We will now proceed with the election of officers. Complying with the Constitution, I appointed in March 1957 the following Nominating Committee selected from a list of candidates suggested by the eligible chapters prior to March 1, 1957:

CHAIRMAN—Robert M. Brick—Chicago Western

Francis C. Albers, Rome
Edward E. Hall, Northwestern
Pennsylvania
Herbert S. Kalish, Long Island
Robert W. Lindsay, Penn State

R. E. Lorentz, Jr., Chattanooga
Benjamin F. Rassieur, St. Louis
William E. Taylor, Phoenix
Walter P. Wallace, Columbia Basin

The Nominating Committee met on May 21 and 22 in Chicago and made the following nominations:

FOR PRESIDENT

G. M. Young, Technical Director, Aluminum Co. of Canada, Ltd.—
1 year

FOR VICE-PRESIDENT

Clarence H. Lorig, Technical Director, Battelle Memorial Institute—
1 year

FOR TREASURER

Robert H. Aborn, Director, E. C. Bain Research Laboratory, U. S.
Steel Corp.—2 years

FOR TRUSTEES

John H. Hollomon, Manager, Metallurgy and Ceramics, General Elec-
tric Research Laboratory—2 years
E. E. Stansbury, Department of Metallurgy, University of Tennessee—
2 years

Complying with the Constitution, the Secretary has informed me that no additional nominations were received prior to July 15, 1957 for any of the vacancies appearing on the Board. Consequently, the nominations were closed. I now call upon the Secretary to carry out the provisions of the Constitution with respect to the election of officers.

SECRETARY EISENMAN: Conforming with the provisions and requirements of the Constitution of the American Society for Metals, I hereby cast the unanimous vote of the members for the election of the aforementioned candidates who were nominated on May 22, 1957.

PRESIDENT CLARK: Has any member present anything to bring before the annual meeting for the good of the Society? If not, then a motion to adjourn is in order. The meeting is adjourned.

EDWARD DEMILLE CAMPBELL MEMORIAL LECTURE

At 10:30 President Clark reconvened the meeting and presented Dr. Julius J. Harwood, Head, Metallurgy Branch, Department of the Navy, Office of Naval Research, Washington, the chairman of the Edward DeMille Campbell Lecture. Dr. Harwood introduced Dr. Earl R. Parker, Professor of Metallurgy, University of California, Berkeley, California, who presented the thirty-second lecture in honor of Professor Campbell. The lecture was entitled "Modern Concepts of Flow and Fracture," and is published in full in this volume of TRANSACTIONS beginning on page 52.

ASM ANNUAL DINNER

On Thursday evening, November 7, members, guests and friends assembled in the Grand Ballroom of the Palmer House for the Annual Dinner of the Society. The attendance was in excess of 700 persons.

Those seated at the speakers table were: Dr. E. Eugene Stansbury, Professor of Metallurgical Engineering, University of Tennessee, Knoxville, Tennessee; Dr. John H. Hollomon, Manager, Metallurgical Research Department, General Electric Research Laboratory, Schenectady, New York; Dr. George A. Fisher, Jr., Manager, St. Louis Technical Section, The International Nickel Company, Incorporated, St. Louis, Missouri; Francis F. Lucas, Bell Telephone Laboratories, retired; James P. Gill, President, Vanadium Alloys Steel Company, Latrobe, Pa.; Arthur Clarage, President, Columbia Tool Steel Company, Chicago Heights, Illinois; Clarence H. Lorig, Technical Director, Battelle Memorial Institute, Columbus, Ohio; Dr. John Chipman, Head, Metallurgy Department, Massachusetts Institute of Technology, Cambridge, Massachusetts; G. M. Young, Technical Director, Aluminum Company of Canada, Limited, Montreal, Quebec, Canada; Dr. Zay Jeffries, Retired Vice President of General Electric Company Chemical Division, Pittsfield, Massachusetts. Dr. Donald S. Clark, Professor of Mechanical Engineering, California Institute of Technology, Pasadena, California; Dr. Tokushichi Mishima, Professor Emeritus, University of Tokyo, Member, Japan Academy, Tokyo, Japan; Adolph O. Schaefer, President, Pencoyd Steel & Forge Corporation, Philadelphia, Pennsylvania; Bradley Stoughton, Professor Emeritus, Lehigh University, Bethlehem, Pennsylvania; Anthony Post, Joint Assistant Secretary, The Iron & Steel Institute, London, England; Carl E. Swartz, Consulting Metallurgist, Hinsdale, Illinois; Dr. Harley A. Wilhelm, Professor of Chemistry, Iowa State College, Ames, Iowa; Dr. Robert H. Aborn, Jr., Director, Edgar C. Bain Laboratory for Fundamental Research, Monroeville, Pennsylvania; Allen G. Gray, Technical Editor, *Steel*, Cleveland, Ohio; William H. Eisenman, Secretary, American Society for Metals, Cleveland, Ohio.

ALBERT SAUVEUR ACHIEVEMENT AWARD

In 1934 the Board of Trustees of the Society established an award in honor of Dr. Albert Sauveur, distinguished metallurgist and for many years an honorary member of the Society. The award was created to recognize a metallurgical achievement which has stood the test of time and has stimulated others along similar lines to the extent that a marked basic advance has been made in the metal arts and sciences. The 1957 candidate was Professor Tokushichi Mishima. In presenting the candidate, Past President Adolph O. Schaefer read the citation of Professor Mishima's accomplishments. President Donald S. Clark then conferred the award. The citation is:

The improvement of strong permanent magnets, magnets which may be prescribed for strength and tailored for shape and size, is due to the insight, the patience and the enterprise of Prof. Tokushichi Mishima, Japan's most eminent living metallurgist, who shares in our Second World Metallurgical Congress, as he did in our First, and here now is to receive the Albert Sauveur Achievement Award of the American Society for Metals for his "pioneering metallurgical achievements which have stimulated organized work along similar lines to such an extent that a marked basic advance has been made in metallurgical knowledge."

Professor Mishima's pioneering accomplishments were with the ternary alloys of iron, nickel and aluminum lying in the range 18 to 30% nickel, 8 to 15% aluminum, and the remainder iron.

Professor Mishima noted, interpreted and understood why a magnetized high-nickel steel became nonmagnetic after heating to high temperature and slow cooling. This irreversibility lay with its A_3 phase transformation. He judged that the addition of aluminum would eliminate that magnetic block. It did! By determining suitable quenching and tempering rates for optimum compositions he achieved residual magnetisms ranging to the high values of 5500 to 11,000 oersteds.

This was March, 1931, the month after his 38th birthday. He was a doctor of engineering and assistant professor of Tokyo Imperial University's Faculty of Engineering, in charge of metallography and physical metallurgy, the sciences for which our Professor Albert Sauveur had pioneered.

He was also married into a family which had adopted him in the gentle pattern we remember from Greek and Roman history—for example, Julius Caesar's adopting and naming as heir the boy who became the Emperor Augustus. Tokushichi Mishima, whose given name means "Seven Virtues," named his new magnetic alloy series simply with the initials MK of his paternal and adoptive families.

Also he took out the first of his 54 patents throughout the world, read his first of 22 papers at the next convention of the Iron and Steel Institute of Japan, and perfected the magnetic quaternary alloy by adding cobalt to the original ternary. All this within a single year! Between 1933 and 1945 he published nothing because the Japanese Army "classified" all his work. Since then he has resumed publishing steadily, his latest appearing in 1955 under the title of "Process of Sintering M-K3 Magnet (Fe-Al-Ni-Co-Cu)"—a quinary alloy, note.

He is a leading member, councilor or chairman of many of his government's advisory groups, such as those on Aeronautical Technology, Atomic Energy, and Introduction of Foreign Technologies.

HONORARY MEMBERSHIP AWARD

The Board of Trustees of the Society nominated to Honorary Membership Dr. William Hume-Rothery, Professor, Department of Metallurgy, Oxford University, England.

Unfortunately he was unable to be present at this banquet meeting when the formal award was made. However, Anthony Post, Assistant Secretary, Iron and Steel Institute, London was present to receive the award for Dr. Hume-Rothery.

Past President, Dr. Bradley Stoughton read the citation which nominated Dr. Hume-Rothery to Honorary Membership and presented Mr. Post. The citation is:

Dr. Hume-Rothery has been a pioneer and a leader in the development of a scientific basis for the traditionally empirical arts of metallurgy. He has demonstrated, by means of a monumental amount of experimental and theoretical work, and in collaboration with numerous colleagues and students who thereby achieved scientific maturity, that the phase diagrams of alloy systems could be understood, and even predicted, in terms of the sizes of the atom and their electron contribution to the alloy.

His many writings, aimed at all levels of scientific sophistication, have led to a rapid acceptance of the idea that a scientific approach to the understanding of metals would be industrially and intellectually rewarding.

The science of metals owes a great debt to the skill, determination and scientific insight of Hume-Rothery.

CONFERRING OF THE ASM MEDAL FOR THE ADVANCEMENT OF RESEARCH

The ASM Medal for the Advancement of Research for 1957 was awarded to Roy Carnegie McKenna, Chairman of the Board of the Vanadium-Alloys Steel Company.

Due to the fact that Mr. McKenna was unable to be present at this dinner meeting, ASM Past President James P. Gill, a business associate of Mr. McKenna, received the award on his behalf.

In presenting the candidate for this award Arthur T. Claridge, President of Columbia Tool Steel Company, read the citation engrossed on the scroll which accompanies the medal. President Donald S. Clark then presented the medal and scroll to Mr. Gill for transmittal to Mr. McKenna. The citation is:

For as long as the American Society for Metals has been promoting the arts and sciences relating to the metal working industry, metallurgical research has been a prime function of the Vanadium-Alloys Steel Company and the executive leader responsible has been and still is Roy Carnegie McKenna, who at the age of 32, became president. In the spring of 1919 he organized a metallurgical and research department, believing that metallurgical science was essential to a prosperous metals industry.

But perhaps his outstanding contribution was an outgrowth of his belief in full delegation of responsibility to qualified heads of various management departments. The responsibility for the research department was therefore completely separated from the operating, sales, or chemical departments. Such separate organizational status was soon adopted by all competitors and later by the tonnage steel industry.

Papers published within the first three years of the new department's operation disclosed for the first time the detailed chemical analyses of tool steels and he was an author of one of these early papers. Other noteworthy achievements of Vanadium-Alloys Steel Co.'s research department are high-carbon, high-chromium steels (in the 1920's), a detailed study in the 1930's of the carbides in high speed steels, the widely used air hardening, hot work die steel (1933), investigations on the transformation characteristics and partition of elements in high speed steels (in the 1940's), the high-carbon, high-vanadium tools now known as "super high speed steels" (in the 1935-1945 decade), and the postwar introduction of the free machining tool steels, improved cemented carbide cutting materials, (1928-1938), and in recent years, a process for making pre-alloyed steel powders by atomization.

Perhaps the most obvious, but by no means the most important, demonstration of his support of metallurgical research is the Research Laboratory building in Latrobe built in 1945.

For such achievements as these the Board of Trustees of the American Society for Metals has awarded its 1957 Medal for the

Advancement of Research to Roy Carnegie McKenna, of Latrobe, Pennsylvania. The award is specifically in recognition of his contributions toward the establishment of effective and independent research in the metal sciences and of his support and belief in the free, unhampered exchange of information in metallurgical technology especially in the field of tool materials and of specialty alloy steels.

CONFERRING OF THE ASM GOLD MEDAL

The GOLD MEDAL which was established by the Board of Trustees of the Society in 1943 had been awarded ten previous times to individuals for their outstanding metallurgical knowledge and great versatility in the application of science to the metal industry, as well as for their exceptional ability in the solution of diversified metallurgical problems. The recipient of 1957 ASM GOLD MEDAL was Dr. John Chipman, Head of the Department of Metallurgy, Massachusetts Institute of Technology, Cambridge, Mass. Past President, Dr. Zay Jeffries presented Dr. Chipman to President Donald S. Clark to receive this award. In making this presentation he first read the citation engrossed on the scroll which accompanies the medal. The citation is:

If any one man can be said to personify the field of metallurgy, that individual is John Chipman. Not only through gifted teaching and inspired research, but through wise professional leadership, he has helped lift metallurgy to a highly respected plane of science and engineering, wherein metallurgists can discharge their obligations to society and nation with satisfaction, noteworthy effect, and due reward. At a time when it was popular to accentuate the many intriguing facets of metallurgy, John Chipman expounded the unity of metallurgy; in curriculum, in publications, and in action, he has striven to bridge the gap that tends to separate physical and process metallurgy, theory and practice, science and engineering.

In particular, Dr. Chipman has been a pioneer in the application of physico-chemical principles to the production and refining of metals. He might be called "the father of metallurgical thermodynamics." His fundamental papers on slag control, oxidation and deoxidation, sulphur reactions, gas-metal equilibria, and high-temperature chemistry have done much to initiate similar research in other laboratories, and have provided industry with a quantitative approach to many aspects of metallurgy. This basic viewpoint is being carried forward by Dr. Chipman's associates and evergrowing ranks of students; it is now reflected in the teaching and practice of metallurgy in all parts of the world.

Notwithstanding these varied pursuits, Dr. Chipman has de-

voted much time to government and professional activities. During World War II, he was Chief of the Metallurgy Section of the Manhattan District Project at the University of Chicago where the first nuclear reactor was placed in operation. He later became Director of the corresponding Metallurgical Project at M.I.T. As President and Trustee of the American Society for Metals, he participated vigorously in the establishment of the ASM Foundation for Education and Research, which has since contributed on a broad front to enhance the stature of metallurgy and to attract students into the field.

One could dwell at length upon the impressive list of honors and medals that have been bestowed upon Dr. Chipman in this country, England, Sweden and Italy. But perhaps the greatest tribute to his vision and attainments is the M.I.T. Department of Metallurgy which he has led for the past 11 years. This lively group has grown to a faculty of 27 members, a student enrollment of 100 undergraduates and 130 graduates, and a publication rate of about 70 papers per year. The range of activity covers almost every aspect of metallurgy, from mineral engineering to metal physics, and reflects the eminent position that John Chipman has conceived for metallurgy.

In recognition of this leadership, the American Society for Metals is proud to confer upon Dr. Chipman its 1957 Gold Medal.

MODERN CONCEPTS OF FLOW AND FRACTURE

(1957 Edward De Mille Campbell Memorial Lecture)

BY EARL R. PARKER

INTRODUCTORY REMARKS

TODAY is the day set aside by the American Society for Metals to honor the work and memory of a great metallurgist and teacher—Edward De Mille Campbell. His contributions were extensive and great, although they were made under the most trying of circumstances. He was blinded by an explosion which occurred during a laboratory examination of steel. At the time of this tragedy, he was only 28 years old. Professor Campbell was a man of great courage and a person whom young metallurgists would do well to emulate. After he became blind, he devoted more than a quarter century of his life to the training of students and to the extension of knowledge through research. He conducted about 75 research projects and all but three of these were carried out after his accident. At the time of his death, he was Head Professor of Chemistry and Metallurgy and Director of the Chemical Laboratory at the University of Michigan. The great honor of presenting this commemorative address has been bestowed upon me today. I can only say that I am deeply thankful for this privilege and for the opportunity to spend my life, as Professor Campbell did, in helping to train young men in the field of metallurgy.

INTRODUCTION

Prior to about 1940, availability of adequate materials was not the limiting factor in the construction of new machines. Since then, many machines and devices have been designed that cannot be built because of the lack of suitable materials. Some examples of today's requirements are high-temperature semi-conductors, structural materials high in strength and low in weight, and others that can withstand high tensile stresses at temperatures that would melt steel or the "super alloys."

Can the engineer rise to the challenge and produce the substances required by the atomic age? It appears that the answer must be "No," if past developmental methods and practices are followed. It is only necessary to review the progress made, for example, in gas turbine alloys. During the last fifteen years, millions and millions of dollars were spent on "high-temperature alloy development." To what avail?

This is the Thirty-second Edward De Mille Campbell Memorial Lecture, presented by Earl R. Parker, Professor of Metallurgy, University of California, Berkeley, California. The lecture was presented November 6, 1957, during the Thirty-ninth Annual Convention of the Society, held in Chicago.

A few new alloys were formulated and marketed but the maximum operating temperature was barely raised 93 °C (200 °F) and at least half of this gain was due to better mechanical design and better quality control of the metallic parts.

The lack of progress in this instance is in large part due to the same basic fault that retards progress in many other fields, namely, inadequate understanding of the basic physical processes which control the behavior of materials. Consequently, investigators were almost invariably forced to fall back on the empirical approach, trial and error—the same method used by metallurgists since prehistoric times.

Many of the advances in metallurgy for the last 150 years have been associated with chemical technology. Today, however, the situation is different. Metallurgy has reached the point where advancement depends upon our knowledge about solid-state physics. To cite a specific example, the transistor resulted from fundamental advances on the theoretical side; it produced a technological revolution in electronics. A similar example is the permanent magnet made of extremely fine magnetic powders, an "invention" due to theoretical advances which predicted from fundamental knowledge that such materials could actually exist. Clear-cut examples of this kind are limited in number at present but they are prototypes of those forthcoming within the next decade. Solid-state science will unquestionably play a major role in the discovery or *invention* of new materials.

Another major contribution of solid-state science is an improved understanding of the behavior of existing materials, which will extend their use. While the sudden arrival of a new material is a dramatic event, tremendous technological advances may be expected to result merely from the systematic scientific analysis of materials and processes in current use. In fact, new materials and applications are most likely to occur as the by-product of a deeper understanding of the behavior of old familiar metals, alloys and mixtures.

To appreciate the potential utility of solid-state science, it is necessary to remember that the properties of materials fall into two classes—those that are structure sensitive and those that are not. Since one of the metallurgist's functions is to control structure, he thus has potential control over one set of properties. About the other set, however, he can do nothing; he is powerless to change the elastic constants, density, specific heat, and heat of fusion or sublimation. On the other hand, tremendous variations are possible with ductility and strength.

The metallurgist must look forward into a new era of technology. In the decade following World War II, many new metals and metal-oids became important. Germanium and high purity silicon revolutionized the electronics industry; a whole new light metal industry grew up around titanium; zirconium emerged from a laboratory curiosity to become a metal vital to the nuclear engineering program; uranium (al-

most unknown in 1940) and plutonium (an amazing man-made chemical element) formed the basis of atomic energy.

The big lesson to be learned from this roster of new metals is that a host of new materials, and many of them nonmetallic, is appearing on the scene. There are too many combinations of elements possible for us to investigate them all by trial and error methods. Even though actual test results will provide the background information necessary to select the new materials, intelligent application of basic principles is the only feasible means of attacking the problems ahead.

With this as a general introduction, I should like to review in this Campbell Memorial Lecture for 1957 the concepts of flow and fracture that have slowly developed during the past two decades and to show how these concepts can lead to the development of new or improved materials as well as to provide a better understanding of the behavior of those now in commercial use.

DISLOCATIONS

By 1926 physicists had learned enough about the forces holding atoms together to make some reasonable estimates of the theoretical strength of perfect crystals. Frenkel (1)¹ calculated from basic physical principles that the shear stress required to cause one plane of atoms to slip over an adjacent one should be about one-sixth of the shear modulus. The equation he derived is the following:

$$\sigma_m = b/a \times G/2\pi$$

where σ_m is the theoretical stress required to cause all atoms in a plane to move from their normal lattice positions to the nearest set of identical positions, b is the spacing between atoms in the slip direction, a is the spacing between rows of atoms in the direction perpendicular to the slip movement, and G is the shear modulus of the material. Since a and b are very nearly equal, the theoretical shear strength of a crystal should be about $G/2\pi$. This is about a million times higher than the measured strength of single crystals and more than ten times stronger than the strongest alloys. Refinements in calculations lead to theoretical yield strength values of about $G/30$ (2) but even this figure was far higher than measured strengths.

Following the early theoretical work, an attempt was made to explain the observed low yield strengths by assuming that thermal fluctuations produced local stresses in the crystal lattice of sufficient magnitude to start slip (3). It was subsequently shown, however, that thermal fluctuations cannot alter the order of magnitude of the theoretical yield strength and so this approach was abandoned (4). In the next step it was assumed that crystals contained flaws that made them weak. This was not an entirely new concept because Griffith (5) in 1921 had pub-

¹ The figures appearing in parentheses pertain to the references appended to this lecture.

lished his classical theory of cracks to account for the mechanical behavior of glass. Furthermore, x-ray diffraction experiments had shown clearly that real crystals are relatively imperfect and that they were made up of tiny mosaic blocks slightly misaligned with their neighbors (6). It seemed reasonable to assume, therefore, that the weakness of crystals was due to some sort of structural imperfection. The problem thus resolved itself into the question: What sort of crystalline defect had the characteristics necessary to explain the plastic behavior of metals? The answer was provided in 1934 by Taylor (7), Orowan (8),

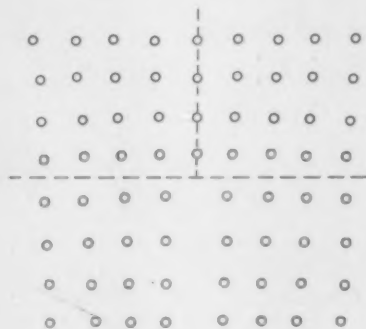


Fig. 1—Sketch of Section through a Simple Cubic Lattice Showing Nature of Structural Defect Called an Edge or Line Dislocation.

and Polanyi (9) who independently concluded that the defect conceived by Prandtl (10) and Dehlinger (11) about 1928 had the required properties. This imperfection has since become known as an *edge* or *line* dislocation. An elementary form of dislocation is shown in Fig. 1. Here it consists of an imperfect square grid, the top half of which contains one more vertical row of atoms than does the bottom half. In a three-dimensional model there would be a large number of identical planes evenly spaced in front of and behind the one shown; thus the defect would consist of a missing sheet of atoms. A straight line through the lattice at the top of the missing sheet of atoms would coincide with the region of maximum lattice disturbance. It is for this reason that this type of imperfection is called a *line* or *edge* type of dislocation. Above and below the dislocation line, the lattice spacing gradually returns to its normal value. In the center of the dislocation the lattice is extremely distorted. The atoms are squeezed together above the horizontal plane containing the discontinuity (the slip plane) and below it they are spread apart. The shear stresses are maximum on this plane. It is this halo of stress that causes dislocations to interact with other dislocations and with other lattice discontinuities such as

grain boundaries, sub-boundaries, solute atoms, and particles of a second phase. Fortunately, the laws of elastic behavior can be applied and thus analyses of the various dislocation reactions can be made. The results of such work are summarized in several texts on this subject (2,12,13).

This paper will show how experimental confirmation of the dislocation theory is gradually being accumulated and to indicate how theory can guide research to improve engineering materials. Before proceeding, however, it will be necessary to introduce several more important

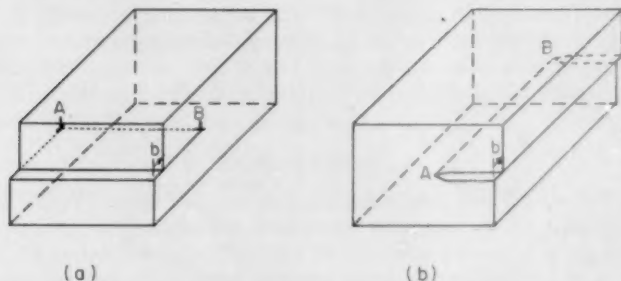


Fig. 2—Sketches Showing How Slip Can Occur in a Crystal by Movement of (a) An Edge Dislocation from Front to Back or (b) A Screw Dislocation from Right to Left.

concepts. One of these is the screw dislocation, invented by Burgers (14) in 1939. Unlike the edge dislocation, which extends *perpendicular* to the direction of slip, the screw dislocation is a lattice discontinuity extending *parallel* to the slip direction. This second type of dislocation permits a wave of plastic flow to travel through the lattice in a direction at right angles to that of the lattice translation. Fig. 2 illustrates how this can happen. In this figure the vector representing the slip direction and distance is indicated by arrows. This vector is designated by the letter, *b*, and is called the Burgers vector.

Another concept of importance is that of the "Frank-Read source." For nearly half a century it has been known that plastic flow occurs by slip on close-packed planes and that the direction of closest atomic approach is the slip direction. Furthermore, deformation has long been known to be concentrated in bands or "slip lines," easily visible by eye or with a low power microscope. In 1948, Heidenreich and Shockley (15) showed that slip bands in aluminum consisted of layers of individual slip lines separated by about 2000Å of unslipped material. They found the amount of slip on each active plane to be about 2000Å. Subsequent work has shown that the interband spacing and glide distance vary with temperature, strain-rate, and material but the fact remains that on a single slip plane the atoms slide past each other many unit

spacings before slip stops. The important questions are, how and why does slip stop after hundreds of unit slip jumps have taken place?

The first question was answered satisfactorily in 1950 by Frank and Read (16) who conceived of a mechanism whereby an unlimited amount of slip could result from the action of a single dislocation line. The Frank-Read concept of a dislocation source is based upon the assumption that dislocations form in crystals during growth. These grown-in dislocations were presumed to be complicated in that they

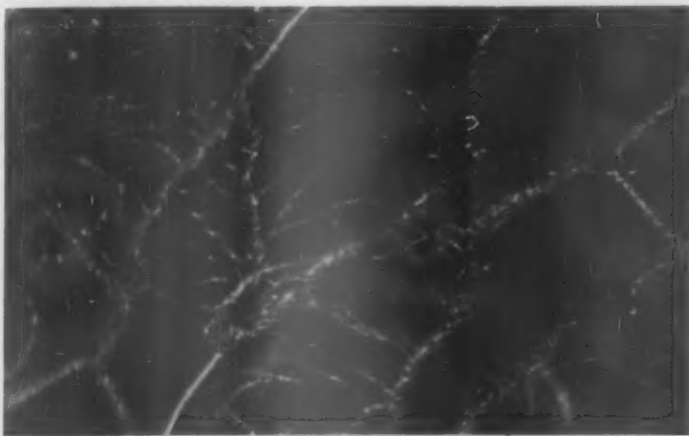


Fig. 3—Photograph of a Lithium Fluoride Crystal Showing Part of a Three-Dimensional Dislocation Network That Formed during Solidification (Courtesy Jack Washburn).

did not lie entirely on a single slip plane. In fact, some dislocation lines were presumed to have portions lying in planes where slip was virtually impossible. The validity of this assumption has since been verified by many workers. Fig. 3 is a photograph showing a grown-in dislocation network in a lithium fluoride crystal. The complex three dimensional nature of the dislocation substructure is evident from this picture. A simplified sketch of a single dislocation in the form of a loop is shown in Fig. 4(a). Only one portion of this dislocation line lies in the slip plane; it is this portion that generates an avalanche of dislocation when an appropriate stress is applied. The details of the generation process will be discussed shortly. As a prelude to this discussion it is necessary to point out that dislocations can move through the lattice on any plane but the shear stress necessary to cause motion is different for each plane; the maximum and minimum stresses may vary by several orders of magnitude. It is natural, therefore, that slip will almost invariably occur on those planes that require the minimum stresses for dislocation

movements; these are the characteristic "slip planes" observed to operate when crystals are deformed. Rarely does the stress rise high enough to move dislocations on the "non-slip" planes.

The portion of the dislocation line lying on the slip plane can move freely when a shear stress is applied whereas the remainder of the line remains immobile in the lattice. This phenomenon is illustrated by the series of sketches in Fig. 4, which show a dislocation line in the form of a rectangular loop and how the portion of this dislocation line lying on the slip plane moves across this plane as the stress is gradually increased. Defects like the dislocation loop shown in (a) of this figure would exist whenever a patch of atoms is missing from a lattice. The dislocation loop would be the closed line constituting the border between the missing patch and the remainder of the lattice. Since only the portion of the line lying in the slip plane could move through the lattice at low stress levels, this portion would move forward as the stress was gradually increased. The remainder of the line would lie immobile in the lattice and so the junctions of the movable and fixed portions would act as anchor points for the movable portion. Thus the stress would force the movable portion to expand into the slip plane to form a loop, much the same as a soap bubble expands outward from a pipe while at the same time remaining anchored around the rim of the pipe. A dislocation loop expanding under the action of a stress must contain portions of screw as well as edge dislocations. Part of the loop must expand sideways in order for the loop to grow and this sideways growth can only occur by the motion of a screw-type dislocation through the lattice. Furthermore, portions of the dislocation loop moving in opposite directions are always of the same kind but opposite in sign, so that when the looping is nearly complete and the screw components moving inward in (d) and (e) of Fig. 4 finally touch, they annihilate each other. Thus the loop becomes "disconnected" from the source and the source is "regenerated," as shown in (f), (g), and (h) in the figure.

Once a complete loop has formed on a slip plane it can move freely away from the Frank-Read sources, expanding continuously as it moves through the lattice until it meets some obstacle such as a sub-boundary, grain boundary, or precipitated particle. In the meantime, the stress continues to act on the source and additional dislocation loops form and grow in the slip plane. These loops follow each other in rapid succession, as is indicated in Fig. 5 which is a sketch of a slip plane containing a number of concentric loops originating from a single source. A Frank-Read source, once activated, should continue to operate indefinitely. Why, then, is the number emanated limited to the few hundred observed on each active slip plane? The answer seems to be that the loops cannot expand freely because they encounter obstacles that stop their movement. This leads to the phenomenon of

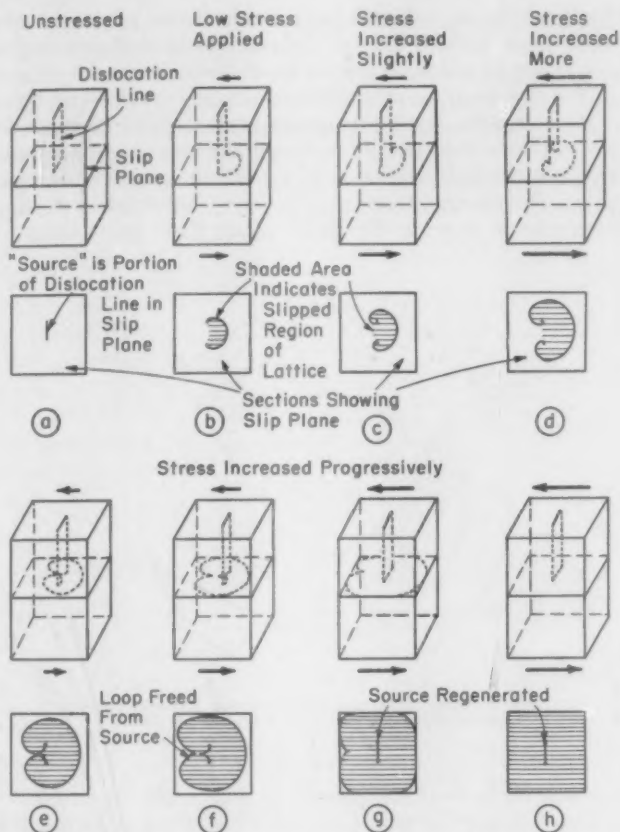


Fig. 4—Sketches Showing How a Dislocation Can Be Generated by the Action of a Stress When a Crystal Contains a Grown-In Dislocation Loop, Part of Which Lies in a Slip Plane. (a) Shows the grown-in loop formed by a missing patch of atoms; (b) Shows how the portion of this loop lying in the slip plane is bowed outward by the stress; (c) through (e) Show how the size of the dislocation line in the slip plane is increased as the stress is raised and how it remains anchored at the points where the grown-in loop leaves the slip plane; (f) through (h) Show how the growing slip dislocation breaks away from the source and how the source is regenerated.

strain hardening which will be described in the next section. Before terminating this discussion, however, a few more comments about the merits of the dislocation theory are in order.

The idea of dislocations originated from efforts to explain the plastic behavior of metals but surprisingly enough it has found equal merit in explaining how crystals grow from a liquid or vapor. The growth rate of a perfect crystal from a vapor or liquid can be predicted theoretically

and it has been shown that on a perfect crystal face growth could not occur until a new nucleus formed. Calculations have shown that such a nucleus would be stable only when its diameter exceeded about 100 atoms (17). However, the probability of forming a nucleus of this size is very low unless the degree of supersaturation exceeds about 50%. Thus it was shown theoretically that a perfect crystal should grow almost infinitely slowly in a solution or vapor of low supersaturation.

In reality crystals are known to grow rapidly even when the degree of supersaturation is relatively small. How, then, could theory and

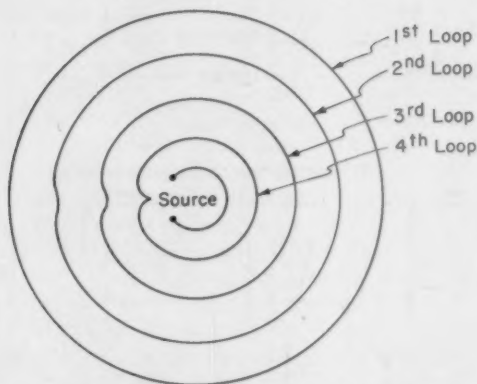


Fig. 5—Sketch of a Slip Plane Showing a Series of Dislocation Loops Forming from a Frank-Read Source.

experiment be reconciled? The answer to this perplexing problem was provided by Frank (17) who postulated that the rapid growth rate of crystals was due to the presence of screw dislocations on the growing faces. As can be seen from Fig. 6, growth could occur easily on imperfect faces because atoms could become firmly attached to the crystal at the step provided by the screw dislocation since there they would be attached to two or more atoms. The screw dislocation permits this kind of growth to continue indefinitely because the step moves forward as each new row of atoms is deposited and in this way it spirals around the screw dislocation as a pivot point. The step always remains because it is a basic feature of the helical crystal surface. It can easily be seen that the addition of an entire plane of atoms to the growing face will raise the surface by one atomic distance but will not change the configuration. Many experiments have shown clearly that rapid crystal growth at low degrees of supersaturation is due to the presence of screw dislocations (18-23) and, conversely, crystal growth

studies have confirmed the existence of screw dislocations, which previously had existed only in theory.

In regard to the experimental verification of the existence of edge dislocations, work reported in 1952 (24) provided the first visual evidence that such crystal defects existed and that they behaved under stress as theory required.

Dislocation theory shows that in a crystal containing a surplus of edge dislocations with the same sign, the dislocations tend to align

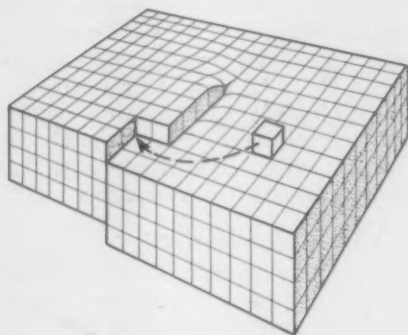


Fig. 6—Sketch Showing How a Screw Dislocation Can Form a Step on a Crystal Face.

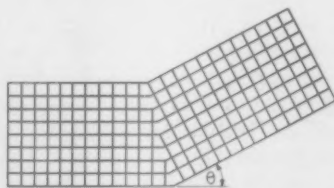


Fig. 7—Sketch Showing the Nature of an Edge Dislocation Boundary in a Simple Cubic Lattice.

themselves one above the other in a plane perpendicular to the slip direction (2,12), as shown in Fig. 7. This array constitutes a dislocation boundary, which is a small angle crystal boundary of the simplest type. The adjoining portions of the crystal differ in orientation by a small angle θ which is equal to the slip distance divided by the distance between dislocations. This kind of boundary can be introduced in a single crystal by plastic bending followed by annealing. Heating a bent crystal to a temperature near its melting point allows the dislocations to migrate through the lattice and to collect in positions of minimum potential energy, as shown in the figure. A boundary of this type in a

zinc single crystal can be seen by eye or with a microscope looking down on the top of the crystal. With appropriate lighting, one side of the crystal will appear light and the other dark. Thus it is easy to determine the location of the boundary and to observe its action when subjected to a stress. Since this kind of boundary consists of dislocations introduced by plastic flow, it should move when subjected to a shear stress. Experiments performed to check this conclusion yielded positive results (24), as Fig. 8 shows. A shear stress caused the boundary to move in one direction; when the direction of stressing was reversed, the boundary moved in the opposite direction and passed its original location. Observation of the motion of dislocation boundaries constitutes direct visual evidence that dislocations do exist and that they move when subjected to a shear stress, as postulated by theory. More recently, additional visual evidence confirming the existence and behavior of dislocations has been obtained by Gilman (25,52), Hirsch (26), and others. In the following section, strain hardening will be discussed in terms of the action of dislocations.

STRAIN HARDENING

What occurs within a metal to make it harder and stronger when it is strained plastically? This question has perplexed man since the dawn of the metal age and only recently has an understanding of this phenomenon become possible. It has become increasingly clear that strain hardening is caused by dislocations interacting with each other and with barriers which impede their progress through the lattice.

The problem of hardening is complicated because hardening involves the action of large groups of dislocations and group behavior is complex because of the large number of ways in which dislocations can arrange themselves. One of the main problems has been to decide which interactions were important and which were trivial. Part of the trouble has been caused by the confusion arising from misleading experimental results. A review of some of the important information will facilitate this discussion.

For many years it has been known that hexagonal metal crystals strain harden at a slower rate than do crystals of cubic metals. It was presumed that this difference was due to the fact that hexagonal metals generally slip on only one plane whereas cubic metals, because of the high degree of the lattice symmetry, slip with equal ease on many planes. Simultaneous slip on intersecting planes is more complicated and should cause greater work hardening than simple slip. The difference in strain hardening characteristics is shown clearly when the stress-strain relationship for various crystals is represented by the following equation:

$$\epsilon = (\sigma/h)^n$$

where ϵ is the strain, σ the stress, h a constant called the coefficient of

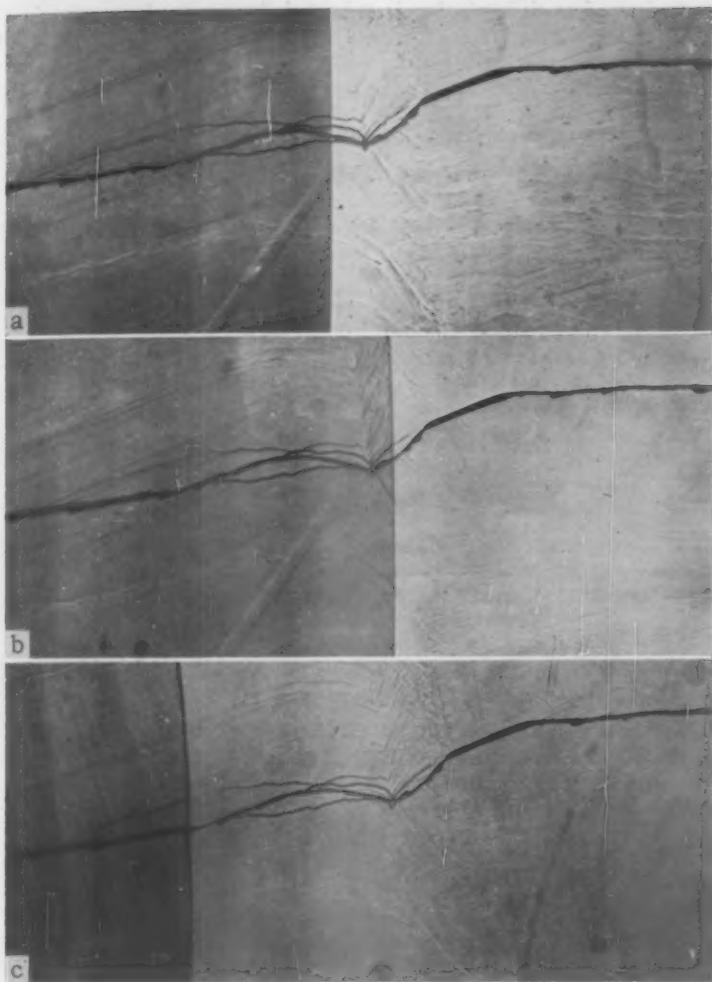


Fig. 8—Stress-Induced Motion of a 2-Degree Dislocation Boundary in a Zinc Crystal at Room Temperature. (a) Original position; (b) Moved 0.1 mm to the right; (c) Moved back 0.4 mm by reversing the direction of applied stress. Irregular horizontal line is a small step in the cleavage surface which forms a convenient reference mark. $\times 50$.

work hardening, and m a constant that is approximately one for hexagonal metals and two for the cubic ones. Cottrell (2) has analyzed data by Schmid and by Boas for magnesium and aluminum single crystals. His results, reproduced in the following table, show that the

coefficient of work hardening is substantially smaller for magnesium than for aluminum.

Temperature ° K	90	290	370	470	570
Coefficient of work hardening, h , in millions of dynes/cm ²	100	50	300	6	1
	Mg	Al			
	700	400		230	180

Furthermore, it is well known that the amount of lattice distortion produced by a given amount of shear strain differs markedly from hexagonal and cubic crystals. Both zinc and cadmium crystals, deformed as much as 100% in shear, diffract x-rays as though the lattice were still

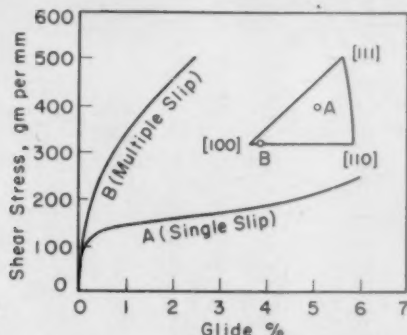


Fig. 9—Stress-Strain Curve for High Purity Aluminum Crystal Showing Difference in Rate of Strain Hardening for Single and Multiple Slip (Lücke and Lange (32)).

relatively perfect; diffraction spots from aluminum or copper crystals, deformed much smaller amounts, almost invariably exhibit severe asterism, showing that the lattice is broken up into subgrains differing slightly from each other in orientation. It might be concluded, then, that if a cubic crystal were forced to slip on only one family of planes, it would then have a stress-strain curve like that of a hexagonal metal. However, the early work on single crystals (27) did not bear out this conclusion. Many tests had been made on single crystals oriented so that slip should occur on only one family of planes. The results of such tests invariably showed high rates of strain hardening for cubic crystals. More recently, however, careful experiments have been performed in which slip has been confined to a single set of planes (28-32). In all such cases, the rate of strain hardening has been low—corresponding to that obtained with the hexagonal metals. It is now known that it is very difficult to produce slip on a single set of planes in a cubic crystal even when the crystal orientation has been carefully selected so that flow should occur on only one slip system. The test conditions used in the early work were too crude to produce simple slip. Hence

the conclusion was drawn that the rate of strain hardening was invariably much greater for cubic metals than for those having hexagonal structure. Simple slip is unstable in cubic crystals and tends to change to double slip. Conditions which favor simple slip are high purity, low temperature, and absence of surface oxide films (28-32). Fig. 9 shows both single slip and multiple slip stress-strain curves obtained by Lücke and Lange (32) for aluminum single crystals. The instability of simple slip in cubic crystals is a phenomenon that deserves considerable attention. It is undoubtedly a fairly complex subject but a brief discussion of some of the factors involved may help to provide an understanding of the phenomenon. This problem can be approached in a rather straightforward manner by considering the changes first that occur during the process of simple slip and how these can lead to double slip in cubic metals.

Plastic flow has often been described as a process similar to the sliding of cards in a deck but this analogy is much too simple. The main difficulty is that strain hardening should not take place when deformation occurs by the ideal simple process. Furthermore, in the absence of strain hardening, slip, once started on a single plane, would continue on the activated plane until the entire crystal was sheared apart. This, of course, seldom if ever occurs in reality. However, it is closely approached under certain circumstances. Fig. 10 shows a photograph of zinc single crystals that had been subjected to low stresses for prolonged periods of time at elevated temperatures. Under these conditions, dislocations were activated on only a few planes. These dislocations were only temporarily held up at imperfect regions in the crystal lattice and in time the trapped dislocations were able to escape, thence to continue to the specimen surface where they could produce a slip offset. As successive dislocations escaped, new ones were generated and thus slip continued on each active plane until the huge slip offset shown in the photograph developed. Just how dislocations can escape around barriers at elevated temperatures will be discussed in detail under the subject of creep which is presented in a subsequent section of this paper.

Returning now to the mechanism of strain hardening during simple slip, as early as 1938 Burgers and Burgers (33) showed that dislocations piled up in a slip plane, because of barriers that interfered with their motion through the lattice, would develop a "back stress" which would oppose the applied stress. The back stress would reduce or cancel the applied stress acting on the source. Thus when a hundred or so dislocations had been generated the source would cease to operate. This theory was developed by Kochendörfer (34) and Laurent (35) into a detailed theory which explained in a satisfactory manner the strain hardening that occurs during simple slip. Experimental verification of this concept was provided in 1953 (36). Single crystals of zinc were

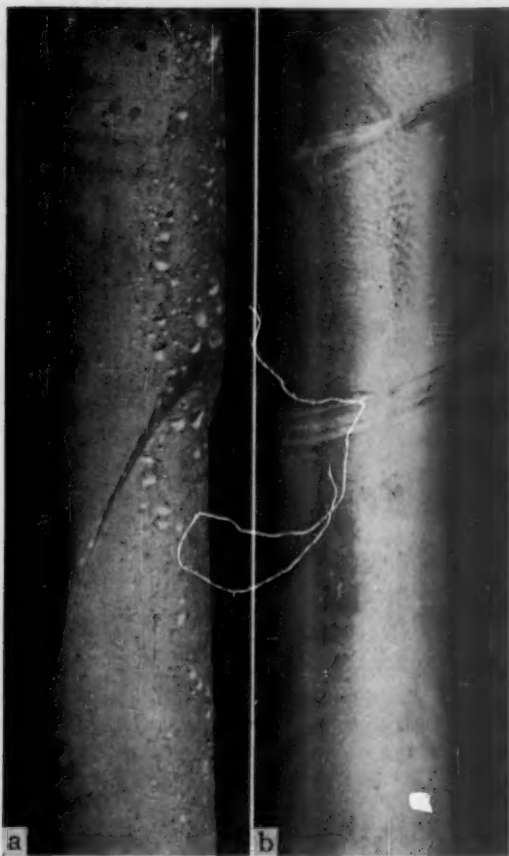


Fig. 10—Zinc Single Crystals Showing Extensive Slip on Few Planes. These crystals were subjected to low stresses for long times at elevated temperatures.

sheared first in one direction and then in the reverse direction. The resulting stress-strain curve is shown in Fig. 11. The curve for the reverse direction has been plotted on the positive stress scale but indicated by an arrow below the curve to indicate that the strain direction had been reversed. The strain is plotted on a continuous or total strain scale to assist in illustrating the behavior. The important features to note are that the yield stress in the reverse direction had been lowered below the yield stress of the annealed crystal by approximately the same amount that strain hardening had raised the flow stress in the

forward direction. This is exactly what should happen if all of the strain hardening were due to the back stress produced by piled up dislocations. Such dislocation, while prevented from moving in the forward direction, are free to move in the reverse direction and indeed tended to move apart even at zero stress because of their repulsive interaction. Furthermore, when the stress direction was reversed, dislocations of the opposite sign could have been created at the same

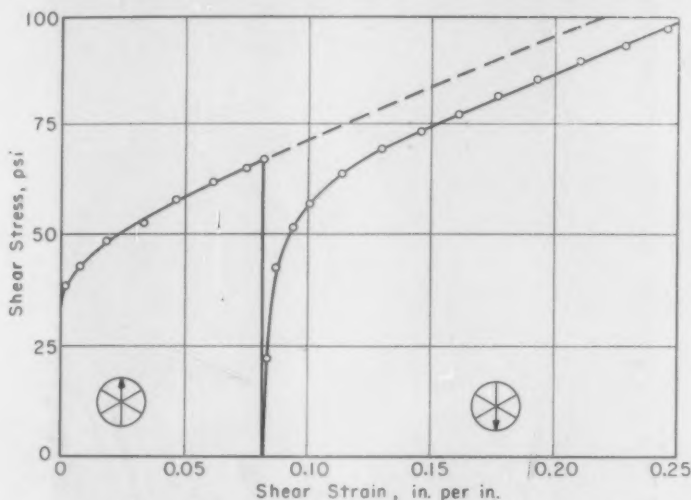


Fig. 11—Effect of Reversing Strain Direction during Testing on the Stress-Strain Curve of a Zinc Crystal. Test temperature was -196°C (-320°F). Arrow in circles shows relative strain directions. Dashed line shows probable course of curve had strain been continued in original direction.

sources that were responsible for strain in the first direction. These would react with the original dislocations to "unslip" the lattice. This "unslipping" is one source of the familiar Bauschinger effect; it actually softens the metal, as shown by the second curve in Fig. 11 which falls below the extension of the first curve. The process of "unslipping" was actually observed to occur, as is shown in Fig. 12 which consists of a series of photomicrographs taken of the same field after successive strain reversals. Because of the oblique lighting used, slip lines appeared dark when the slip offset was made by a strain in the forward direction and light in the reverse direction.

Since experimental evidence shows clearly that crystals strained in simple shear are weakened as much in the reverse direction as they are strengthened in the forward direction, it may be concluded that the only work hardening process that operates in simple shear is that due to the back stress of piled up dislocations.

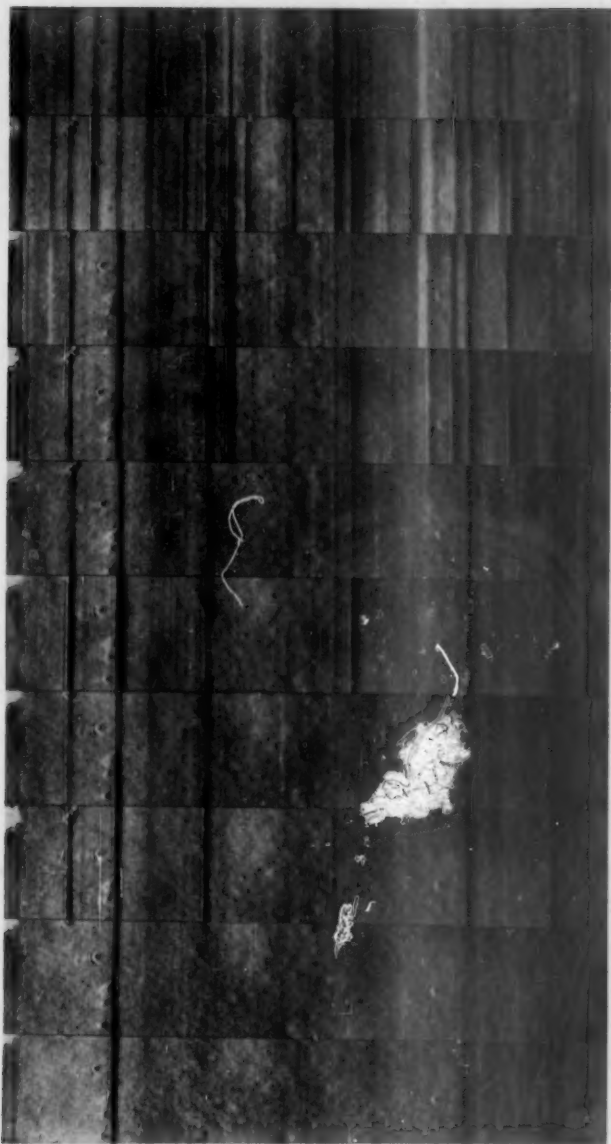


Fig. 12—A Series of Photomicrographs of the Same Area on a Zinc Single Crystal Subjected to Many Strain Reversals. Oblique illumination made slip bands appear dark for slip in one direction and light for the opposite direction. Note that some bands appear to unslip or even reverse direction of slip in succeeding frames; Direction of straining reversed between each frame. $\times 1000$.

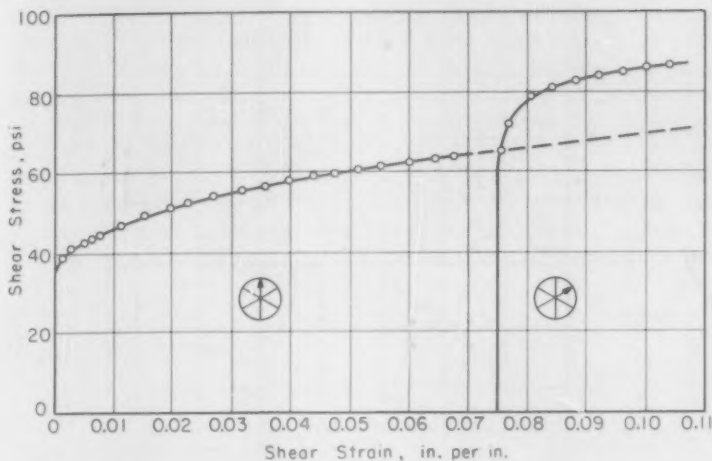


Fig. 13—Effect of Changing Strain Direction in Zinc Single Crystal to New Slip Direction 60 Degrees from the Original Direction. Test temperature -196°C (-320°F). Arrows in circles show relative strain directions.

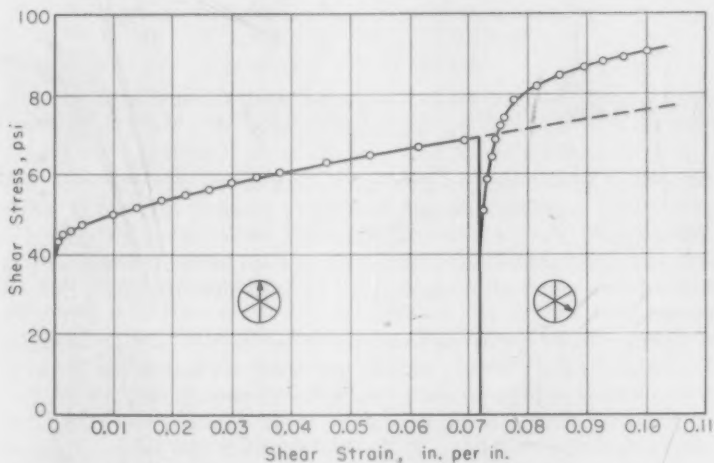


Fig. 14—Effect of Changing Strain Direction in Zinc Single Crystal to New Slip Direction 120 Degrees from the Original Direction. Test Temperature -196°C (-320°F). Arrows in circles show relative strain directions.

It is important to appreciate the significance of the back stress concept of strain hardening because it is this stress that is effective in stopping the generation of dislocations even in the more complex case of multiple slip. The difference between single or simple slip and multiple

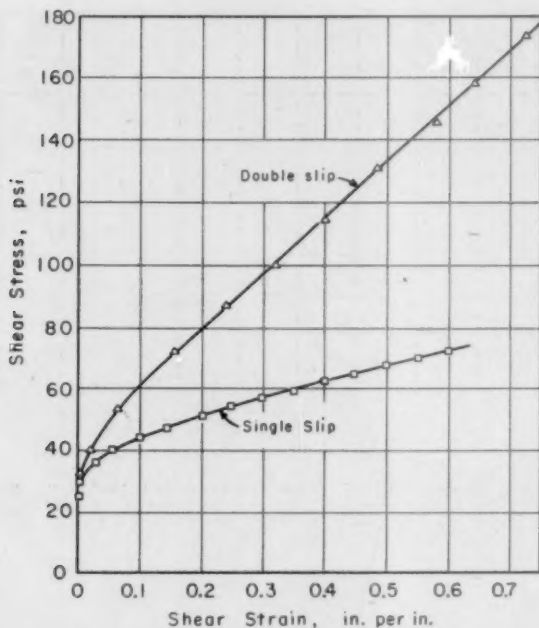


Fig. 15—Stress-Strain Curves for Zinc Single Crystal Showing Difference in Rate of Strain Hardening for Single and Double Slip. Test temperature 25 °C.

slip is that in multiple slip dislocations originating on intersecting slip planes may combine with one another to produce a resultant lattice displacement that is not in a slip direction. When this occurs, the dislocations are immobilized because the applied stress is inadequate to move the resulting dislocation in the nonslip direction of its Burgers vector.

The simplest type of such dislocation interaction is that occurring in zinc wherein slip occurs on only one plane but may occur in any of three directions. Figs. 13 and 14 show the stress-strain curves obtained by first deforming a single crystal of zinc in one direction, then interrupting the test and changing the slip direction to a new slip system at 60 degrees or 120 degrees to the first. The stress-strain curve as continued in the new direction rises well above the extension of the first curve. The effect of dislocation interaction on the rate of strain hardening is reconfirmed by the results in Fig. 15 which shows two stress-strain curves for zinc single crystals—one deformed by single slip and the other deformed by double slip. The one subjected to double slip hardened more than twice as rapidly as did the one strained in simple

shear. When slip occurs on two intersecting planes, as was the case with one of the tests with aluminum crystals shown in Fig. 19, the effect of dislocation interaction on the rate of strain hardening is much more pronounced than is the case for double slip on a single plane.

Lomer (37) has shown that dislocations on intersecting planes in a face-centered cubic metal can attract one another and combine when their Burgers vectors are suitably oriented. Two straight dislocations having Burgers vectors $\frac{1}{2}a[101]$ and $\frac{1}{2}a[011]$ can unite to form a new dislocation having the vector $\frac{1}{2}a[110]$. The new dislocation is of the edge type and can glide only in the plane (001), because this

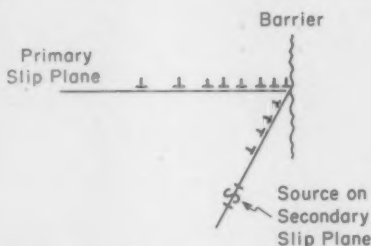


Fig. 16—Sketch Showing How Dislocations Piled Up at Barrier in Cubic Crystal Can Activate Source on Intersecting Slip Plane.

plane contains both the direction of the dislocation line and its Burgers vector. Since the cube plane is not a slip plane, the new dislocation cannot move. Immobile dislocations (called sessile dislocations) interfere with mobile dislocations gliding on the active slip planes. Reactions of the type indicated above occur in face-centered cubic crystals wherever slip planes cross each other. As slip progresses in such crystals, more and more sessile dislocations form. Thus the average distance between barriers decreases with increasing strain so that dislocations spreading out from sources travel shorter and shorter distances as straining is continued. The basic cause of strain hardening is still the back stress due to piled up dislocations but the mean free path is decreased because the sessile dislocations are effective barriers.

At this point it is possible to discuss the reason for the difficulty encountered in trying to produce simple slip in cubic metals. It will be recalled that almost invariably multiple slip occurs when such crystals are strained even though the crystal is oriented so that slip should occur on only one plane. The difficulty occurs because of the multiplicity of equivalent slip systems and because of local secondary stresses induced by dislocations piled up at barriers. Fig. 16 indicates how a pile-up of dislocations at a barrier on a (111) slip plane can induce a shear stress on a ($\bar{1}\bar{1}1$) plane of sufficient magnitude to activate a source on that

plane. The stress on the secondary source can be as high as $n/8$ times the stress that activated the original source, where n is the number of dislocations piled up in the primary slip plane. Thus local slip is induced to occur on two slip planes. The dislocations moving on these planes can interact, as previously shown, to form sessile dislocations which are very effective new barriers. Furthermore, the dislocations of opposite sign generated at the new source are relatively free to move through the lattice and thus become available to interact with other dislocations moving on the family of planes constituting the primary slip system.

Strain hardening is caused by the back stress produced by piled up dislocations whether the deformation occurs by simple or by double slip. With double slip, however, the rate of strain hardening is high because dislocations interact and become immobilized; thereafter they interfere with the free motion of active dislocations.

RECOVERY

When metal is deformed at room temperature and then reheated to successively higher temperatures, several changes occur to relieve the acquired state of strain. Dislocation loops tend to become smaller and some may even disappear. This process happens rather rapidly and when it occurs the hardness drops, the internal stresses practically disappear, and the electrical resistivity is lowered. The best demonstration of this recovery process is that provided by Washburn (38). He deformed one centimeter thick single crystals of zinc by dropping a 0.2 gram indenter on the basal plane. This produced indentations that extended completely through the crystals. The deformed region consisted of a flat cone having a half angle of approximately 80 degrees. Before the recovery treatment was started, the surface layer where the impact occurred was cleaved off to remove the excessively distorted material.

In indentations of this type, deformation occurs by slip on the three equivalent systems in the basal plane. In Washburn's experiments, the maximum shear strain in the radial direction amounted to approximately 2.5%. A careful examination failed to reveal any evidence of nonbasal slip. When the dimpled specimens were heated to successively higher temperatures, the structural changes shown in Fig. 17 occurred. Sharp radial and circumferential boundaries formed soon after the heating was started and at 300 °C (570 °F) the boundaries were clearly defined. At this temperature, the circumference of the dimple had shrunk considerably and a flat area had formed at the center. The boundaries were in noncrystallographic directions, showing that the structure contained dislocations of more than one Burgers vector. As the heating proceeded, dislocations of opposite sign combined and the dislocation structure became simpler. Boundaries that did not lie at right angles to a slip direction shortened and disappeared. Finally, just

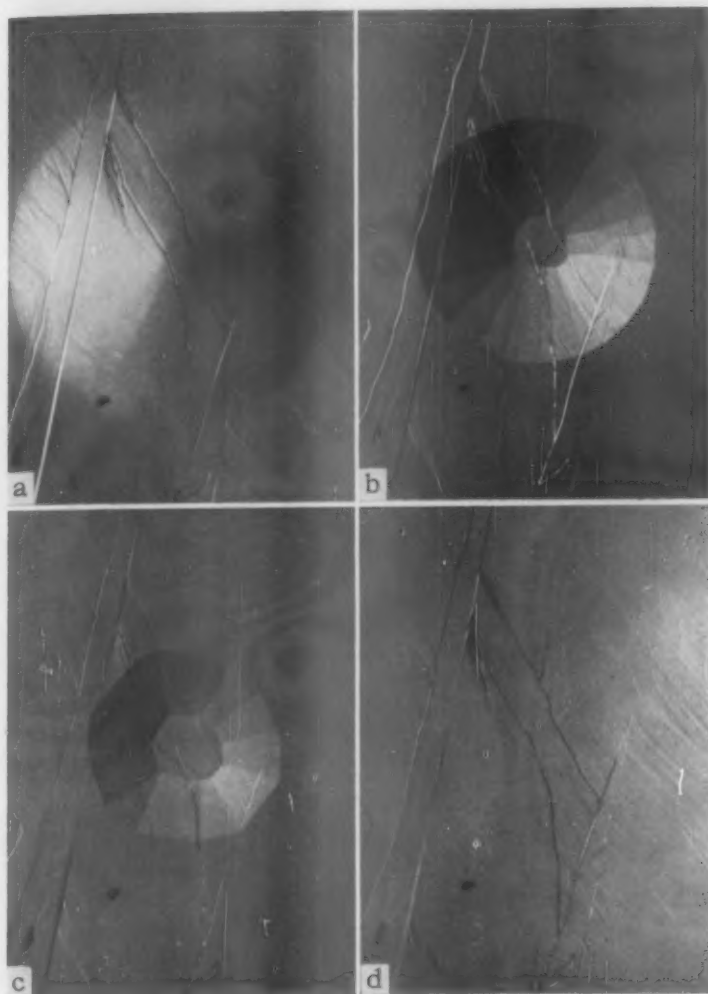


FIG. 17—Micrographs Showing How a Dimple in a Zinc Crystal Disappears during Recovery. (a) Dimple before reheating; (b) After heating to 300 °C (570 °F); (c) After heating to 350 °C (660 °F); (d) After heating to 400 °C (750 °F). Diameter of dimple in (a) was about one millimeter. (Washburn (38)).

before the complete disappearance of the dimple, the remaining boundaries became oriented at right angles to the slip directions, showing that the screw components had completely disappeared. The remaining edge dislocations joined at nodes, as can be seen in Fig. 18. Upon heat-

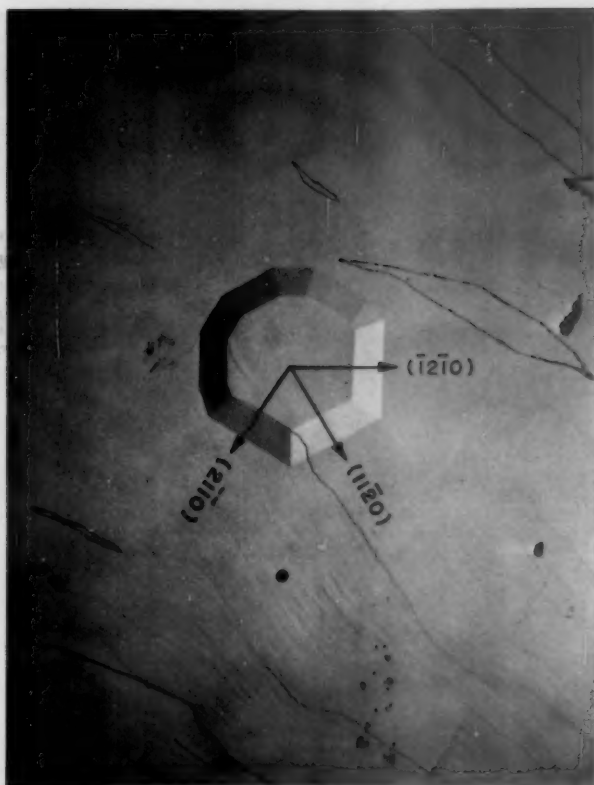


Fig. 18—Micrograph Showing Final Stage in the Disappearance of an Indentation during Heating. The most stable boundaries are those at right angles to directions of the type $[2110]$. (Washburn (38)).

ing to 400°C (750°F), the dimple completely disappeared. These experiments demonstrate clearly that plastic deformation with strains as high as $2\frac{1}{2}\%$ can, under certain conditions, be completely recovered by annealing.

A second recovery process is the combination and annihilation of dislocations of opposite sign. Washburn's (38) experiment also provided evidence that this type of recovery actually does occur when cold-worked metal is heated to elevated temperatures. This process, however, generally requires the movement of dislocations in the direction perpendicular to the slip plane by a process known as "climb." Dislocation climb is necessary before unlike dislocations can unite because they are generally not located on the same plane.

In order for dislocations such as the one indicated schematically in Fig. 1 to climb out of the active slip plane, lattice vacancies must deposit all along the dislocation line. When this occurs, the line will move one plane higher in the lattice. A continuation of this process will cause the dislocation to migrate onto other parallel planes far removed from the plane on which it was generated. It is also possible for dislocations to migrate downward in the lattice. This can occur by the deposition of rows of atoms on the dislocation line. The climb process is relatively slow and its temperature dependence is exponential because its rate is governed by self-diffusion.

A third phenomenon contributing to recovery is the rearrangement of like dislocations into a boundary like that shown schematically in



Fig. 19—Sketch Illustrating Change in Structure of Small Angle Boundary Produced by Heating. (a) Before heating; (b) After heating to a temperature high enough for rapid dislocation climb.

Fig. 7. As theory predicted, such an array of dislocations constitutes a low energy metastable configuration. Boundaries of this kind form only where there is an excess of dislocations of one sign and only when these cannot collapse and disappear. The configuration of dislocations in the cold-worked material is indicated schematically in Fig. 19(a). This is a high energy arrangement which is converted by heating to the lower energy structure shown in (b) of this figure. Details of experiments and theory related to this process have been reviewed by Cahn (39).

As predicted by theory and demonstrated experimentally by Washburn (40), a dislocation boundary of the type shown in Fig. 19(a) should not be a barrier to moving dislocations because each dislocation coming into one side of the boundary would force an identical dislocation to leave the other side. A boundary of the type shown in Fig. 19(b), however, is an effective barrier for moving dislocations.

Substructure boundaries are very stable. They remain in deformed metals even after heating to temperatures far above the normal recrystallization temperature. For example, in zinc single crystals such boundaries are even stable at temperatures approaching the melting point; in nickel, sub-boundaries remain in polycrystalline material even after heating to temperatures in excess of 800°C (1470°F); and in

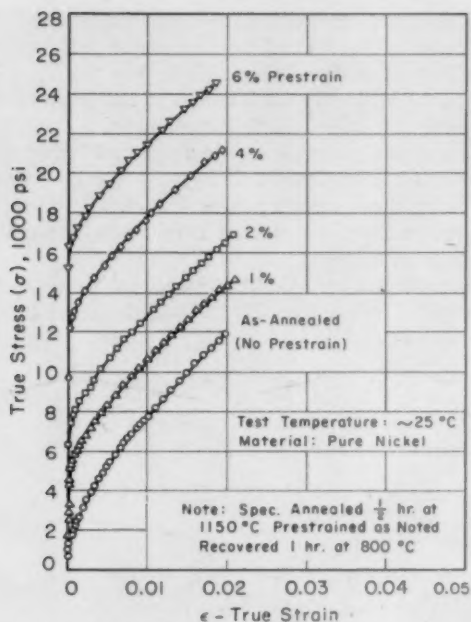


Fig. 20—Effect of Small Angle Boundaries Developed within the Grains of Polycrystalline Nickel (by a Prestrain and Anneal Treatment) on the Stress-Strain Curve.

steel they remain even at temperatures near the alpha-gamma transformation. Because sub-boundaries are relatively stable and because they resist penetration by moving dislocations, it is possible to increase the strength of annealed commercial materials by introducing a substructure in the grains. An example of the change in strength that can be thus produced is shown in Fig. 20. Polycrystalline nickel (41) was pre-strained various amounts and then reheated one hour at 800°C (1470°F). The amount of substructure increased with increasing amounts of pre-strain and the yield strength increased proportionally.

Similar experiments were performed with steel (42). Fig. 21 shows how effectively the yield strength of a medium carbon steel can be increased by the introduction of a substructure and Fig. 22 shows a series of stress-strain curves for another mild steel which illustrates the effect of the annealing temperature after prestraining. It is well known that the yield strength can be increased by cold working but when this is done the transition temperature, as measured by V-notch Charpy specimens, is invariably raised as is shown in Fig. 23. When the cold-worked material is reheated to produce a substructure, however, the embrittle-

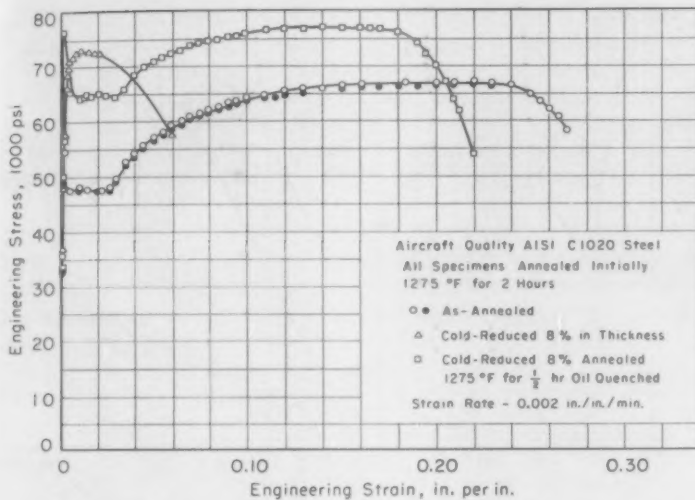


Fig. 21—Effect of Substructure on the Stress-Strain Curve of Aircraft Quality 1020 Steel.

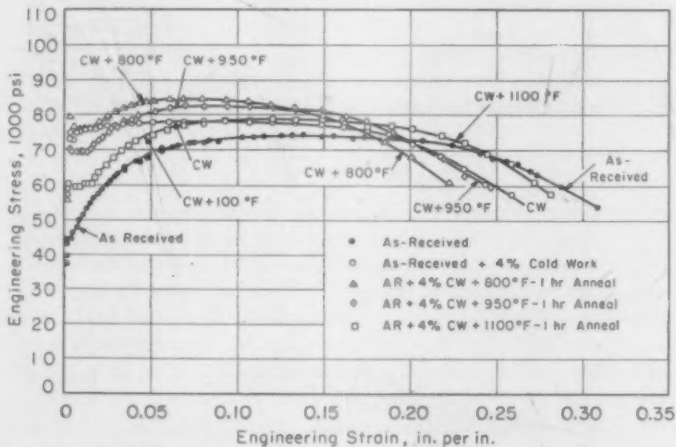


Fig. 22—Improvement in Stress-Strain Characteristics of Mild Steel Which Can be Achieved by Introduction of a Substructure.

ment produced by the cold work is reduced or eliminated, as shown in Fig. 24. The 15-foot pound transition temperature for the material cold worked 4% and reheated to 593 °C (1100 °F) was as low or lower than that of the as-received material. As shown by the curves in Fig. 22,

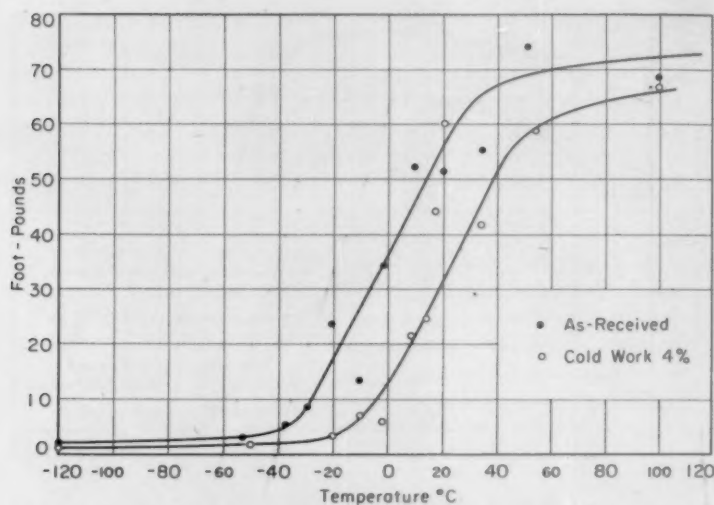


Fig. 23—Change in V-Notch Charpy Energy-Temperature Curve Caused by 4% Cold Work. Steel same as that used for tests in Fig. 22.

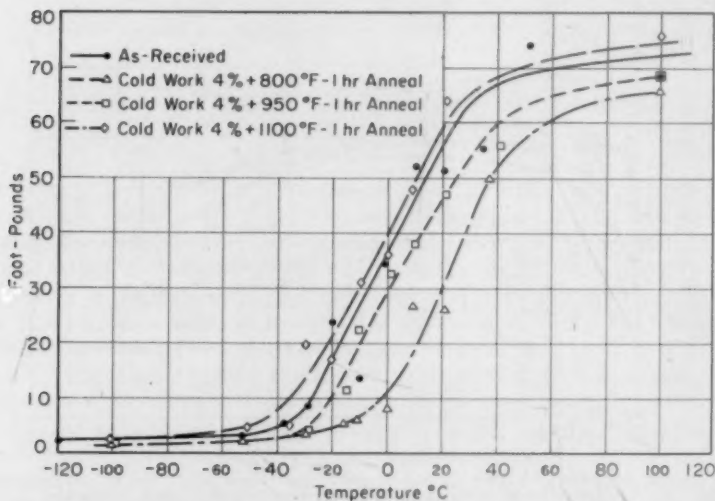


Fig. 24—Change in V-Notch Charpy Energy-Temperature Curve Caused by Reheating Cold Worked Metal to Various Temperatures. Steel same as that used for tests in Fig. 22.

however, this same treatment raised the yield strength of the material by over 30%.

It is evident from the results presented that recovery is now fairly

well understood and that fundamental studies of recovery processes can lead to substantial improvements in commercial materials. To summarize, there are three processes known to occur during recovery; namely (a) collapse of dislocation loops; (b) annihilation of dislocations of opposite sign by combination thereof; and (c) the formation of substructure boundaries by dislocations of the same sign. The first two processes soften the material, the third strengthens it.

CREEP

Many theories of creep have been postulated to explain the behavior of metals at elevated temperatures. They can be separated into the following three groups because of the basic assumption made in regard to the rate-controlling process of creep:

1. Those that assume that activation of the dislocation source is the rate controlling step.
2. Those that assume that the movement of the dislocations (or "flow units") from one potential energy trough in the lattice to the next equivalent position is the rate-controlling step.
3. Those that assume that escape of dislocations around barriers is the rate-controlling step.

A brief review of the important theories will be presented to illustrate the historical development of this subject.

Andrade Theory—In 1914 Andrade formulated the following empirical relationship between strain and time in a creep test. In his equation, "e" is the strain, "t" is the time, and "A" and "B" are empirical constants.

$$e = At^{1/3} + Bt$$

This was the first attempt to express the creep behavior of metals in quantitative terms and was far advanced for this early date.

Becker Theory—In 1925 Becker attempted to formulate a theory of creep based on what seemed to be a sound theoretical approach. He assumed that local stress fluctuations occurred in the lattice because of thermal vibrations and the maxima of these fluctuations acted to overcome the local yield strength of the crystal lattice. In this theory it was presumed that it was the motion of a plastic wave through a perfect lattice that limited the rate of creep—an erroneous assumption as has since been shown.

This theory predicted a variation of the critical shear stress with temperature that was in marked disagreement with the measured change in yield strength. This meant that thermal stress fluctuations are only partially responsible for the low yield strength values actually observed. Other criticisms are that the entropy effect was ignored and strain hardening was neglected. Becker's equation is the following:

$$\dot{\epsilon} = C\epsilon \frac{-(\sigma_0 - \sigma)^2 v}{2GkT}$$

where

$\dot{\epsilon}$ = strain rate
 σ_0 = yield strength at 0°K
 σ = applied stress
 v = volume involved in stress fluctuation
 G = shear modulus
 k = Boltzmann's constant
 T = absolute temperature

Orowan Modification—In 1947 Orowan modified the Becker theory by introducing the stress concentration factor, "q." He reasoned that, because of crystalline defects, the local stress was much higher than applied stress, σ . Therefore he replaced σ by $q\sigma$, where q is much greater than one. Orowan also introduced a term, $\phi(\epsilon)$, which takes strain hardening into account. His equation is given below:

$$\dot{\epsilon} = C\epsilon \frac{-(\sigma_0 + \phi(\epsilon) - q\sigma)^2 v}{2GkT}$$

Actual test data did not follow the above relationship. The implication of the analysis is that dislocations could be moved through the lattice by normal stresses only when aided by thermal lattice vibrations. It has since been found that dislocations move freely through a relatively perfect crystal lattice and are only held up by barriers or when they react with other dislocations to form sessiles. Furthermore, the function $\dot{\epsilon} = f(\sigma, \epsilon, T)$ implies that a mechanical equation of state exists, and this has been proved to be untrue.

Exhaustion Theories of Creep—Theories have been proposed by Mott and Nabarro (43) and also by Smith (44) which assume that *activation of the source* is the rate controlling step in creep. In 1948 Smith proposed that a large number of dislocations exist in an annealed material. These dislocations were presumed to be weakly locked within the metal but were freed by thermal activation at elevated temperatures and thus could be moved by relatively small stresses. The number of dislocations was presumed to diminish during transient creep and no new dislocations were supposed to have been generated. In Smith's analysis the creep rate was given by:

$$\dot{\epsilon} = aC \int_{E=0}^{E=\infty} f_e \lambda^3 e^{-E/kT}$$

where

a = elongation per unit slip process
 C = constant
 $f_e = (E, t_e)$ = energy distribution at $t = 0$
 t = time
 $\lambda = C\epsilon^{3/kT}$
 k = Boltzmann's constant
 T = absolute temperature
 E = activation energy

when $f(E, t_0) = \text{constant} = c$
 $\dot{e} = a c k T \{1 - e^{-\sigma_1}\}$

Mott and Nabarro derived the following expression for exhaustion creep when precipitated particles were present:

$$\dot{e} = \frac{-A(\sigma_1 - \sigma)^{3/2}}{kT} N a L p \nu e^{A(\sigma_1 - \sigma)^{3/2}} \text{ is the activation energy for the "process"}$$

where a = interplanar spacing
 L = distance between precipitated particles
 ν = frequency factor
 p = factor to account for an avalanche occurring
 N = density of dislocation
 $A(\sigma_1 - \sigma)^{3/2}$ is the activation energy for the "process"
 σ is the applied stress
 σ_1 is the internal stress restraining motion
 A = constant
 $3/2$ exponent comes from assumption that internal stress field is sinusoidal rather than constant

From their analysis they concluded that part of the creep curve resulted from exhaustion creep and that pure exhaustion creep would occur at low temperatures and low stresses. The strain due to exhaustion creep was calculated to be:

$$\epsilon = CT^{2/3}(\log \nu t)$$

Since the development of the exhaustion theories, experiments have shown that the density of dislocations *increases* rather than decreases during the early stages of creep. Hence these theories are of no consequence.

Kauzmann Rate Process Theory—In 1941 Kauzmann (45) proposed a theory of creep based on rate theory. He did not specify the "unit" involved in the flow process; his theory did not involve or require a specific physical picture. This theory assumed that motion through the lattice was the rate-controlling step in creep; as mentioned previously, this assumption is not valid.

In Kauzmann's theory, flow takes place by the movement of "flow units" past each other in a potential field having maxima and minima. His equation is:

$$\dot{e} = C e^{\Delta S/R} e^{-E/RT} \sinh(qA\sigma/kT)$$

where E = energy of activation
 ΔS = the entropy of activation
 C = constant
 R = gas constant
 T = absolute temperature
 A = area of projection of flow unit
 $2l$ = distance between two successive potential minima
 k = Boltzmann's constant
 σ = applied stress
 q = stress concentration factor

This equation does not correlate with facts in any simple manner.

Values of qAl obtained experimentally show both stress and temperature dependence. The higher the temperature and the lower the stress, the larger the value of qAl . It was unreasonable to assume that this was due to larger values of q or l , so Kauzmann assumed that A increased. This assumption is inconsistent with the present concept that dislocation pile-ups become smaller the higher the temperature and the lower the stress. This theory was advanced for its time but suffered from the limitation of an inadequate physical picture of the creep process.

Nowick and Machlin Rate Theory (46)—In 1947 these investigators developed an improved rate theory by introducing the concept of dislocations. *Generation* was assumed to be the rate-controlling step. They assumed that in steady state creep an equilibrium existed between the number of dislocations generated and the number that disappeared. They further assumed that dislocations were generated only one lattice distance long at crystal defects where stress concentrations existed. These tiny dislocations were presumed to grow to full-size dislocations during motion. This treatment is a combination of Becker's theory, in which the energy barrier is expressed in terms of stresses, and Eyring's rate theory which introduces a frequency factor; it also leads to a hyperbolic sine dependence of the creep rate on stress. The entropy effect has been taken account of by assuming that the atoms near the source must oscillate in the proper crystallographic direction and by considering the number of atoms at the source that must oscillate in phase in order to generate a dislocation. Their formula is very similar to that proposed by Kauzmann. The main difference is that the heat of activation is expressed in terms of an internal stress. In addition, work hardening has been considered by introducing a "back stress" which results from piled up dislocations. Their work is a definite improvement over Kauzmann's but it still failed to define creep behavior accurately. The main reason for this, as subsequent work has shown, is that *generation* of dislocations is not the rate determining step in the flow process.

Kochendörfer Theory—In 1938 Kochendörfer (47) developed a theory based on the concept of dislocations. He assumed that the *generation* was the creep limiting step in the process. The number of dislocations generated was given by a formula of the Becker type, including a strain-hardening term. Mosaic blocks played a major role in this theory. He assumed that the first dislocations formed move through the mosaic block rather easily until they reached the block boundary where they became immobilized. Other dislocations followed and were stopped by the stress fields of those already piled up. Hardening resulted because of the back stress on the "source" produced by the dislocation pile-up. According to Kochendörfer, the back stress increased the activation energy required for the formation of *new* dislocations. Hardening, therefore, occurred as a consequence of an increase in the

activation energy required for *generation* rather than *propagation* of dislocations.

Kochendörfer was remarkably perceptive considering the early date of his work. He postulated that many dislocations would form and move on each active slip plane. Many years later this was observed by Heidenreich and Shockley to be true and eventually the Frank-Read source was invented to explain the observed behavior. He also forecast the important role played by substructure boundaries. The difficulty with this theory was that he assumed that *generation* of dislocations limited the creep process. As will be discussed in detail later, it now appears rather clear that high temperature creep is controlled by the rate at which piled up dislocations can climb out of their original slip planes.

Cottrell's Theory of Atmosphere of Solute Atoms—Cottrell (2) showed that solute atoms cluster around dislocations to form an "atmosphere." At low stresses, the "atmosphere" may diffuse with the dislocations and thus permit the dislocations to move slowly through the lattice. A theory of creep based on this picture has been formulated but it is not generally applicable.

Polycrystalline Materials—In addition to flow within the grain of a polycrystalline aggregate, flow can also occur because of grain boundary sliding. A grain boundary is merely the surface of contact between two crystals fitting together as well as their different orientations will allow. Boundaries consist of areas of "good" fit and areas of "bad" fit.

An analysis of grain boundary shearing made by Mott (48) in 1948 yielded the following equation:

$$\dot{\epsilon} = 2\nu a e^{-nL(1-T/T_m)/kT} \sinh \sigma n a \omega / ZkT$$

where

- a = lattice constant
- ν = frequency of atomic vibration
- ω = area per atom
- n = number of atoms in area of good fit
- σ = applied stress
- k = Boltzmann's constant
- T = absolute temperature
- T_m = melting temperature
- L = latent heat fusion per atom

Mott assumed that the shear stress was carried primarily by the areas of good fit and that these areas were sheared and thus disordered. Disordering, however, involves an increase in entropy (i.e., a positive change) whereas the entropies of activation found experimentally have been *negative*.

Kê Analysis—Kê (49) observed that the activation energies for grain boundary slip and creep in polycrystalline aggregates were approximately the same as that for volume diffusion. Kê proposed a model in which the boundary was presumed to extend in three dimensions

rather than in two, as in Mott's theory. The disordered groups of atoms were considered as diffused holes.

Kê's analysis led to the following equation:

$$\dot{\epsilon} = C n e^{-u/kT} \sinh (b\sigma/kT)$$

which for low values of stress reduces to:

$$\dot{\epsilon} = C n b \sigma / kT e^{-u/kT}$$

In these equations

b = constant

n = density disordered groups

the other symbols are the same as those used previously.

Kê's theory did not include an entropy term, but the inclusion of

$$e^{\Delta S/k}$$

would lead to a negative entropy—a definite advantage over Mott's equation. Subsequent experimental work has confirmed the concept that grain boundary shearing really occurs so that creep is actually a two-fold process in polycrystalline metals.

Recent Theories—There have been a number of additional attempts to formulate creep theories in recent years but of these the contribution by Weertman (50) shows the most promise. In 1955 he developed a theory of steady state creep based on the dislocation climb process proposed by Mott in 1951. His analysis resulted in the following expression for creep rate, which includes the stress dependence as well as the temperature dependence:

$$\dot{\epsilon} = C (\sigma^a/kT) e^{-u/kT}$$

where C and a are constants

σ = stress

k = Boltzmann's constant

T = absolute temperature

It is interesting to note that this is the equation Dorn (51) found empirically to satisfy creep data obtained at low stresses and at temperatures above 0.4 of the melting point. The great advance made by Weertman was due to the fact that he assumed that *the rate controlling step in the creep process was dislocation climb*.

This presentation completes the abbreviated summary of creep theories and so other pertinent information concerning creep will be discussed next.

Shape of Creep Curve—In the first portion of a normal creep curve the rate decreases continuously with time; in the second part the rate is nearly constant; and in the third stage the creep rate increases continuously. Fig. 25 shows a series of ordinary creep curves. It has long been thought that the first and second stages involve two different creep

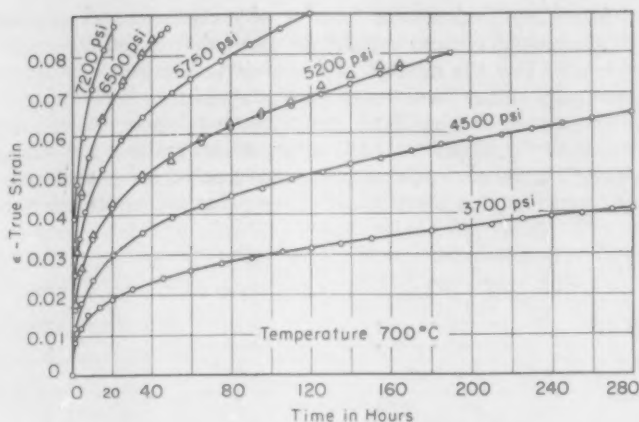


Fig. 25—Constant Stress Creep Curves for High Purity Nickel Tested at 700 °C.

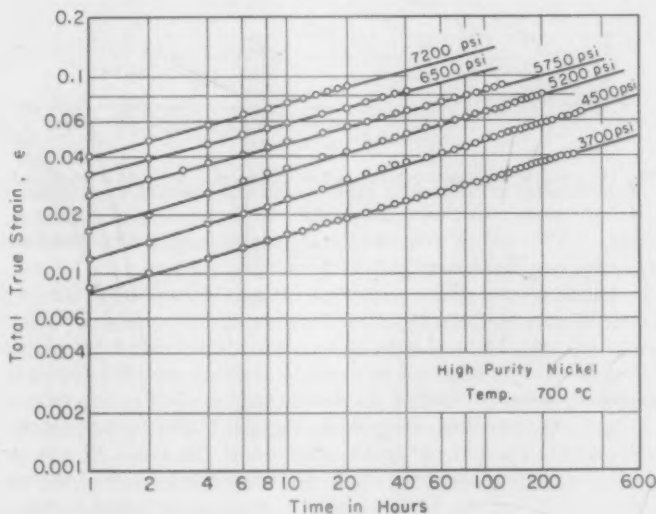


Fig. 26—Log-Log Plot of Curves Shown in Fig. 25.

processes. In the exhaustion theories, it was assumed that the first stage was associated with the disappearance of dislocations from the crystal lattice. The second portion, which is nearly linear, was presumed to prevail when an equilibrium condition existed wherein dislocations escaped to external surfaces at the same rate that new ones were gen-

erated internally. Exhaustion theories of creep, as previously mentioned, are invalid because measurements of dislocation density have shown clearly that the number of dislocations in a metal undergoing creep increases rather than decreases. Furthermore, when creep curves of the type shown in Fig. 25 are replotted on a log-log scale, straight lines result as Fig. 26 shows. Also, x-ray studies made at various positions along the creep curve have shown that a substructure is developed during creep and that the amount of the substructure increases con-

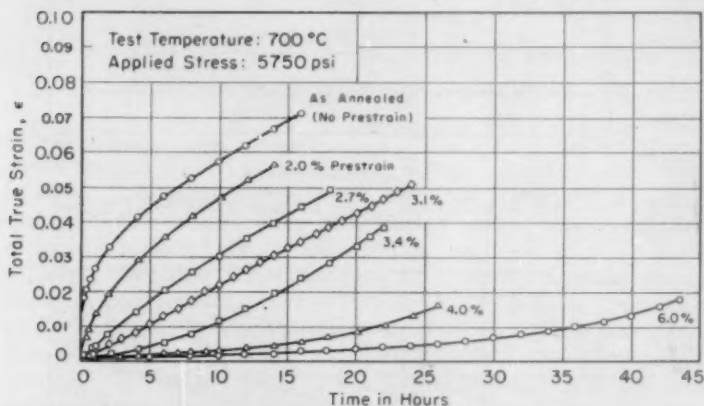


Fig. 27—Effect of Substructure Introduced by Prestraining Indicated Amounts and Annealing at 800 °C (1470 °F) on Shape of Creep Curve for High Purity Nickel.

tinuously during the first stage of creep, approaching a constant value characteristic of the second stage.

The bending over of the creep curve can be accounted for on the basis of the substructure developed during the creep test because increasing amounts of substructure result in decreasing rates of creep. This has been demonstrated by tests in which controlled amounts of substructure were introduced prior to initiation of the creep tests. Results which illustrate this are shown in Fig. 27. The creep rate decreased with increased amounts of substructure and the shape of the creep curve was strongly dependent upon the substructure state of the material. As Fig. 27 shows, it is possible to change the creep curve of a metal from its normal concave downward shape to a straight line, or even to make it concave upward (a condition that arises when more than the equilibrium amount of substructure is introduced prior to initiation of the creep test).

The next question that will be discussed is the mechanism which controls the creep process—dislocation climb. Although there are some cases wherein the creep rate is not controlled by the dislocation climb

process, by far the majority of instances have climb as the rate controlling step; this is particularly true at temperatures above about 0.4 of the absolute temperature melting point.

Dislocation Climb—Many experiments have been made to determine the activation energy for creep. Dorn (51) has summarized these results and shown that the activation energy for creep is almost invariably equal to the activation energy for self-diffusion. This is strong evidence, but not conclusive, that climb occurs and that the rate of climb is diffusion controlled. There is also a great deal of evidence that dislocation climb occurs during the annealing of cold-worked metals (2, 39). Also,

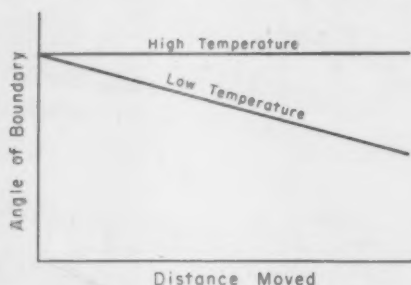


Fig. 28—Sketch Indicating How Angle of Dislocation Boundary Changed When Moved by Applying Stress at Low and at High Temperature.

Gilman and Johnston (52) have presented visual evidence that dislocations in lithium fluoride do climb out of their slip planes at elevated temperatures. Perhaps the most direct evidence that mobile dislocations can detour around barriers that trap them is provided by studies of dislocation boundaries moving under the action of stress at both low and high temperatures. As shown in Fig. 28, the angle of a dislocation boundary decreases as it is moved through the lattice at low temperatures (53). This decrease is due to the loss of dislocations from the boundary as it moves forward. The dislocations lag behind the boundary at the points in the lattice where they meet interference but remain attached to the boundary in other regions; they therefore exert a back stress on the boundary. As a result of this action, the stress must be increased continuously as the boundary is moved forward; when the stress is held constant, boundary motion stops. Under constant stress at elevated temperatures, however, the boundary continuously moves forward, or creeps, at a uniform rate. Furthermore, as shown in Fig. 28, the angle of the boundary remains constant as the boundary moves forward. Dislocations are trapped at barriers at both low and high temperatures but because they are able to climb at elevated temperatures, they are able to escape from the barriers and continue to

move through the lattice. The rate at which they can do this, however, is controlled by self-diffusion. It is interesting to note that for zinc crystals the activation energies for creep, boundaries motion, and self-diffusion parallel to the "c" axis, are all equal.

The mechanism of climb and how it influences creep is indicated schematically in Fig. 29. Climb gives dislocations a second degree of freedom so that they are able to move through the lattice in directions that are not coincident with their Burgers vector.

Grain Boundary Shearing—In polycrystalline materials the creep process is somewhat more complicated because of the presence of grain boundaries. It has been known for many years that adjacent grains in

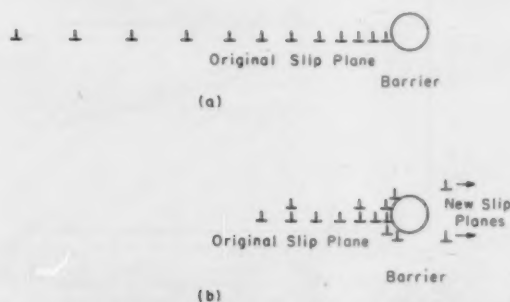


Fig. 29—Sketch Illustrating (a) How Barrier Can Cause Dislocations to Pile Up on Slip Plane and (b) How Climb Permits Dislocations to Detour around Barriers.

a polycrystalline aggregate can move past one another by shear at or near the boundary separating them. It has long been thought that this process contributed substantially to the creep of polycrystalline metals, particularly at high temperatures. Grain boundary shearing has been used to explain why fine-grained materials creep faster at elevated temperatures than do the same materials with a coarse-grained structure, whereas at low temperatures fine-grained material is invariably stronger than coarse-grained material because the boundaries interfere with the motion of dislocations. Fig. 30 shows the effect of grain size on the creep strength of brass (54). These data illustrate the typical grain-size effect found with almost all materials. Some recent work, however, has shed considerable doubt on the validity of the explanation of the grain-size effect. Investigations by several groups (55,56,57) have shown that grain boundary sliding does occur but that it cannot possibly contribute more than about 10% to the total creep strain. Under these circumstances, grain boundaries should be effective barriers to moving dislocations at high temperatures as well as low temperatures; hence, fine-grained material should be stronger in creep

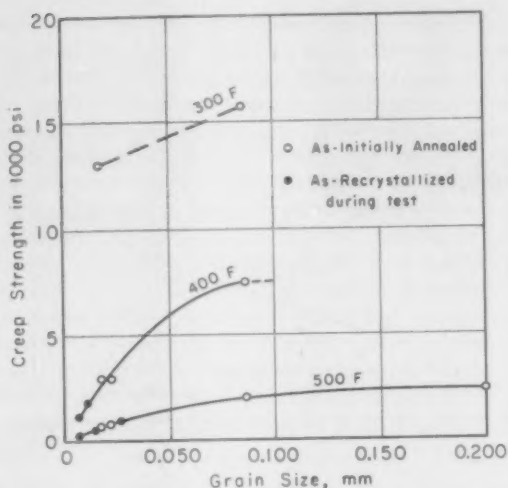


Fig. 30—Effect of Grain Size on Stress Required to Produce Creep Rate of 0.01% Strain Per 1000 Hours for 70-30 Brass (Burghoff, Blank, and Maddigan (54)).

than coarse-grained material. Since this has not been found to be so in most of the experimental work reported in the literature, it is evident that there is some other factor involved which has not received adequate attention. Since continuous flow at high temperatures depends upon dislocation climb and this phenomenon is dependent upon the rate at which vacancies can condense on edge dislocations, an examination of the factors that influence vacancy diffusion may lead to a better understanding of creep.

The equilibrium vacancy concentration in a crystal lattice, and hence the volume diffusion rate, is only influenced by temperature. The situation is different in a grain boundary, however, because the structure of the boundary varies with the relative orientations of adjacent grains. The more disorganized the boundary structure, the faster the diffusion rate along the boundary. Experiments have shown that boundary diffusion may be very much faster than volume diffusion. Vacancies responsible for the climb of dislocations piled up near grain boundaries may travel relatively large distances along the boundary and only short distances through the lattice before uniting with piled-up dislocations. Thus, the rate of dislocation climb, and hence the creep rate, should depend upon the structure of the adjacent boundary. In fine-grained materials wherein many large angle boundaries exist, climb may be rapid and the creep rate high. The same material when heated to a high temperature to coarsen the grain structure prior to a creep test will

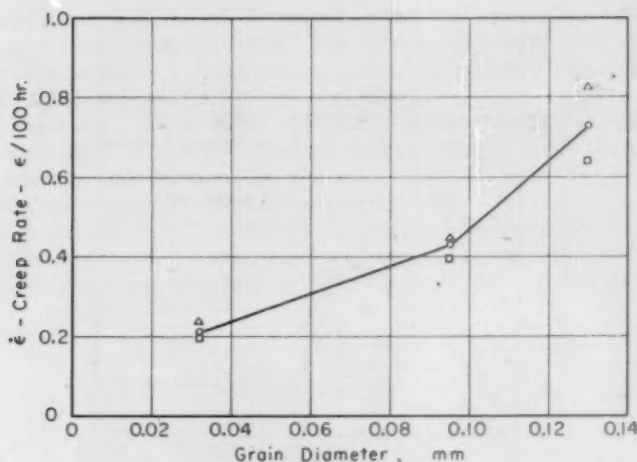


Fig. 31—Creep Rate Versus Grain Diameter for Randomly Oriented Polycrystalline Copper Tested at 400 °C (750 °F).

retain very few of the high energy boundaries because such boundaries tend to disappear during grain growth (58). The grain boundaries that remain are lower energy boundaries along which vacancy diffusion is relatively slow. The dislocation climb process should, therefore, be slower in the coarse-grained material because of the lower mass transport rate along the lower energy boundaries. Thus the "grain size effect" may not be a geometric problem at all but one having to do with diffusion rates of vacancy along the boundaries in the polycrystalline aggregate. In the past, grain size effects have been investigated on materials heated to successively higher temperatures to enlarge the grain size. In all such investigations, two factors—not one—were changed. The grain size was increased but the nature of the grain boundaries was also altered. The second effect has been generally ignored and this has led to seemingly faulty conclusions regarding the grain size effect. This hypothesis is substantiated by the results shown in Fig. 27 which show that when low energy boundaries, such as those that exist in a low-energy substructure, are introduced into the material the creep rate is correspondingly lower. Furthermore, in a recent investigation (59) wherein extreme care was taken to retain a random grain orientation in polycrystalline copper treated to produce different grain sizes, it was found that the creep rate increased with increasing grain size just as it should if the nature of the boundaries was maintained constant as the grain size was altered. These results are summarized in Fig. 31.

Recognition of the fact that grain boundaries may act as highways along which atoms or vacancies can be transported to produce climb helps resolve another perplexing creep problem, namely, that alloying elements do not have the same influence on strength at high and low temperatures. For example, phosphorous is very effective in increasing the strength of steel at low temperatures but relatively ineffective at elevated temperatures, whereas molybdenum is a relatively impotent solid solution strengthener at low temperatures but is strongly effective at high temperatures. Both kinds of atoms are immobile at low temperatures and, when concentrated in boundaries, both can block the motions of dislocations. At the high temperatures, however, the phosphorous atoms can diffuse rather freely but the molybdenum atoms remain substantially immobile. Thus, phosphorous would not change the rate of vacancy migration along boundaries at high temperatures by any significant amount, whereas molybdenum would tend to block such movement and thus reduce the amount of material transported along the boundary.

SOLUTION HARDENING

Mechanisms of Solution Hardening—Until rather recently, solution hardening has been thought to be due to the lattice disturbances caused by randomly distributed solute atoms. Theoretical treatments by Cottrell (2), Suzuki (60), Fisher (61), and others have shown that solution hardening is very likely due to small groups of solute atoms concentrated in the lattice, and not due to those randomly dispersed.

Cottrell (2) has pointed out that internal stresses due to randomly dispersed solute atoms should have almost no hardening effect. If a dislocation line is considered as a rigid linear discontinuity, then along its length there will be equal numbers of positive and negative stress fields due to solute atoms. Half of these act to move the dislocation line forward and half urge it in the backward direction. Thus, these randomly alternating stress fields would nearly cancel and, therefore, dislocations could move through the alloy crystal almost as easily as they could move through a crystal of the pure metal. As Mott and Nabarro (62,63) have shown, however, dislocation lines are not rigid. They may assume a smoothly curved form, but only on a scale that is large compared with atomic dimensions. When the regions of lattice distortion are far apart, the dislocation line may bend or even loop around the highly stressed areas. When the distance between stressed regions approaches atomic dimensions, the dislocation line can no longer curve around the stressed regions because of the high energy required to produce sharp curves in a dislocation line.

The energy of a dislocation has been estimated by Mott and Nabarro (43) as about Gd^3 per unit length of a dislocation line, where G is the shear modulus and d is the atomic spacing (Gd^3 is of the order of a few

electron volts). As Cottrell (2) has pointed out, a dislocation may be considered to have a tension

$$\tau = Gd^2$$

acting along its length and tending to shorten it. The shape assumed by a dislocation in an internal stress field is given by

$$\tau/\rho = \sigma_1 d$$

where ρ is the minimum radius of curvature in the region of the internal stress σ_1 . Combination of the two equations yields

$$\rho/d = G/\sigma_1$$

The radius of curvature in atomic distances is equal to the shear modulus divided by the internal stress. For a radius of curvature approaching atomic dimensions, the internal stress would have to be about as large as the shear modulus. Reasonable estimates indicate that the maximum stress around a solute atom is of the order of $G/100$. Thus, it appears fairly clear that solution hardening cannot be due to stress field surrounding individual randomly distributed solute atoms.

Since solution hardening cannot be accounted for on the basis of randomly distributed solute atoms, it might be due to concentrations of these atoms in the lattice or else to collections of them in substructure boundaries and grain boundaries. The assumption that hardening is due to inhomogeneous distribution of solute atoms leads to several theories of solution hardening; each of these will now be discussed in detail.

Cottrell Mechanism—Cottrell has proposed a mechanism of hardening in which the solute atoms form an atmosphere around dislocations. Atoms above a positive dislocation are compressed and those below are expanded. The strain energy due to this distortion can be reduced by the collecting of large substitutional solute atoms in the expanded region or small ones in the compressed volume. Similarly, interstitial solute atoms causing local lattice expansion will tend to collect in the expanded region of the dislocation. Atoms producing unsymmetrical distortion may relieve shear stresses (2) as well as the hydrostatic stresses due to the volume change. Substitutional atoms generally produce symmetrical distortion and hence can only relieve hydrostatic stresses.

Only very small quantities of solute elements are required for the formation of a Cottrell "atmosphere." Since the maximum dislocation density in a highly cold-worked metal is of the order of 10^{12} per square centimeter, only 0.1% of solute atoms is sufficient to form a concentration of one solute atom per atom distance along the dislocation lines. In annealed metals, the concentration of dislocations is much lower; even in 99.999% pure metals there may be enough solute atoms to form an atmosphere.

The effect of an atmosphere of foreign atoms around dislocations is to raise the stress required to make the dislocations move. When a dislocation is moved away from its atmosphere, the region of the lattice containing the atmosphere is raised to a high energy state because of the high concentration of foreign atoms in this region. Since the extra energy needed to bring about this condition must be supplied by the external load, it is evident that the yield strength must be higher when Cottrell "atmospheres" have formed around the dislocations responsible for plastic flow. Once separated from the atmosphere, the dislocations can move freely and the stress required for continued flow is lower than that required to initiate flow. The sharp yield point phenomenon found in iron containing a small amount of carbon is apparently due to the formation of an atmosphere of carbon atoms around dislocations (64). The theory of solution hardening due to the interaction of solute atoms with dislocations has been developed to a high state by Cottrell (2) and co-workers. They have made calculations of interaction energies, have shown how temperature should influence yield strength, how strain aging in iron is accounted for, and the probable effect of such an atmosphere on slow creep wherein the creep is controlled by diffusion of the atmosphere along with the slow moving dislocations. Consequently, there is little to be gained by further discussion of this subject herein. It is sufficient to say that this phenomenon seems to be well established as a mechanism of solution hardening.

Suzuki Mechanism—A similar mechanism of solution hardening that is not so well known has been proposed by Suzuki (60). His hardening mechanism is also based upon the concentration of solute atoms around dislocations but in a manner that differs from that proposed by Cottrell. This theory relies upon the interaction of solute atoms with dissociated dislocations in the close-packed planes of the face-centered cubic and close-packed hexagonal crystals. Shockley (15) has shown that ordinary edge dislocations are unstable in a close-packed plane because the energy of the dislocation is lowered when it dissociates into two half dislocations of shorter Burgers vector. A dissociated dislocation is shown by Fig. 32 wherein the atoms of one plane are represented by squares and those in the plane above by circles. The regular hexagonal array is indicated by the lines. During the normal process of slip, the atoms in the plane above would traverse the path indicated by the arrows on the right-hand side of the figure. Moving toward the left, the displacement along the slip path gradually diminishes until a region is reached wherein the displacement is one-half of the slip distance. This is a metastable region in the lattice which will vary in extent for different materials; it may range from a few atom distances to perhaps 50 (15). Within this region a stacking fault exists because a face-centered cubic crystal assumes a close-packed hexagonal structure (or in a hexagonal crystal it becomes face-centered cubic) having a thickness of

about two atom planes. The two half dislocations formed by the dissociation reaction move apart because of the repulsive forces arising from the interaction of the stress fields surrounding them. The farther they move apart, the more extensive becomes the stacking fault. Since energy is required to form or extend a stacking fault, the half dislocations will cease to move apart when the energy released by such movement is less than that required to form the additional area of the stacking fault between them. The lattice to the left of the hexagonal region shown in Fig. 32 gradually assumes the normal configuration as the distance from the dislocation is increased.

Thermodynamic reasoning leads to the conclusion that the concentration of solute atoms in the hexagonal region will differ from the average when equilibrium is established between this region and the surrounding face-centered cubic material. This heterogeneous distribution of solute atoms will then cause hardening just as the Cottrell atmosphere does in body-centered cubic metals (where half dislocations do not form). In the face-centered cubic crystals it is rather unlikely that the formation of a hexagonal layer would cause appreciable volumetric disturbance. Hence the concentration of solute atoms therein would depend upon "chemical" (Suzuki) interaction rather than upon interaction energies due to lattice distortion (Cottrell's mechanism). Around each of the half dislocations, however, the lattice would be distorted. Therefore, both types of interaction are theoretically possible in face-centered cubic and hexagonal metals. Suzuki cited the work of Allen, Schofield and Tate (65) in support of his theory (see Figs. 33 and 34). Quoting from Suzuki (60), "These facts would be understood by the present theory in taking account of Hume-Rothery's law. Namely, the relative free energy of these alloys with close-packed hexagonal structure against those with face-centered cubic structure depends only upon the electron concentration, and the free energy of face-centered cubic structure depends only upon the electron concentration, except for a term proportional to the concentration. The critical shear stress . . . is, therefore, a function of electron concentration and is independent of the chemical species of constituents." Suzuki also pointed out (a) that the chemical-type interaction is considerably weaker than the interaction due to lattice distortion, and (b) that thermal fluctuations have little effect upon the behavior of extended dislocations because such dislocations might have to migrate as much as fifty atomic distances to escape from their atmosphere, whereas migration of only a few atom distances would free a dislocation in iron from its atmosphere of carbon atoms.

Fisher Mechanism—Fisher has proposed that short-range ordering provides a substantial contribution to solution hardening, particularly at high solute concentrations. When plastic flow occurs, the local ordered regions intersecting the slip planes are disordered by the flow

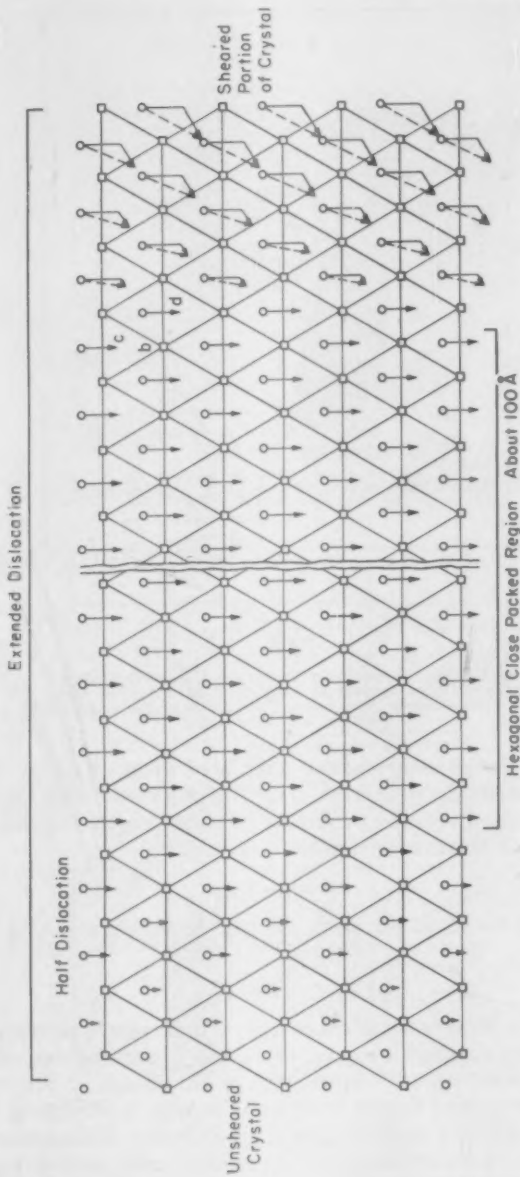


Fig. 32—Extended Dislocation in Face-Centered Cubic Crystal Consisting of a Strip of Hexagonal Close-Packing Bounded by Two Extended Half-Dislocations.

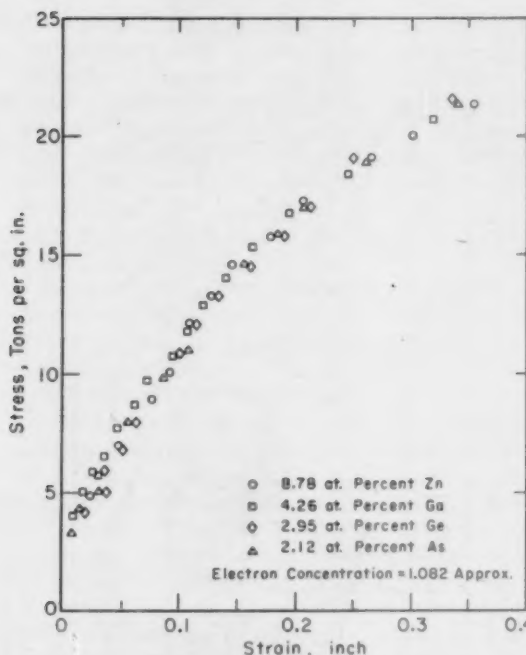


Fig. 33—True Stress-Strain Curves for Copper-Zinc, Copper-Gallium, Copper-Germanium, and Copper-Arsenic Alloy Wires of Approximately the Same Electron-Atom Ratio (Allen, Schofield, and Tate (65)).

process. If γ is the energy of the disordered interface, τ the resolved shear stress, and b the magnitude of the Burgers vector, then the energy change associated with the movement of a unit length of a dislocation through a unit distance is given by

$$\Delta E = \gamma - b\tau$$

ΔE is zero at the stress level that will just disorder a region by plastic flow. Hence

$$\tau_0 = \gamma/b$$

Fisher (61) estimates the misfit energy, γ , to be about the same as the twin boundary energy for copper, i.e., about 20 ergs per square centimeter. Therefore, $\tau_0 \approx 10^9$ dynes/cm², or 15,000 psi. At low temperatures where a fixed degree of order is frozen in, hardening due to short-range ordering should be nearly independent of temperature. It follows from Fisher's analysis that clustering would provide a similar strengthening effect.

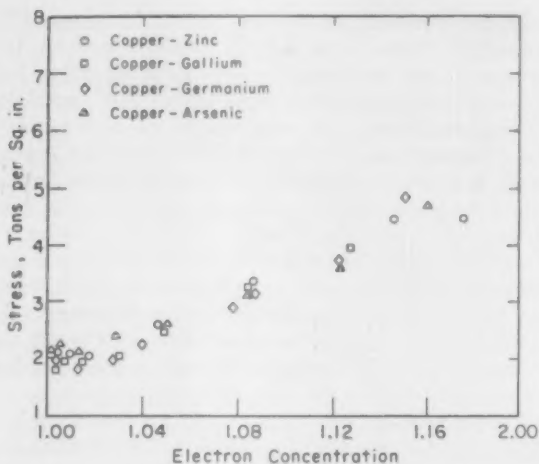


Fig. 34—Effect of Electron Concentration on the Yield Strength of Copper Alloys (Allen, Schofield, and Tate (65)).

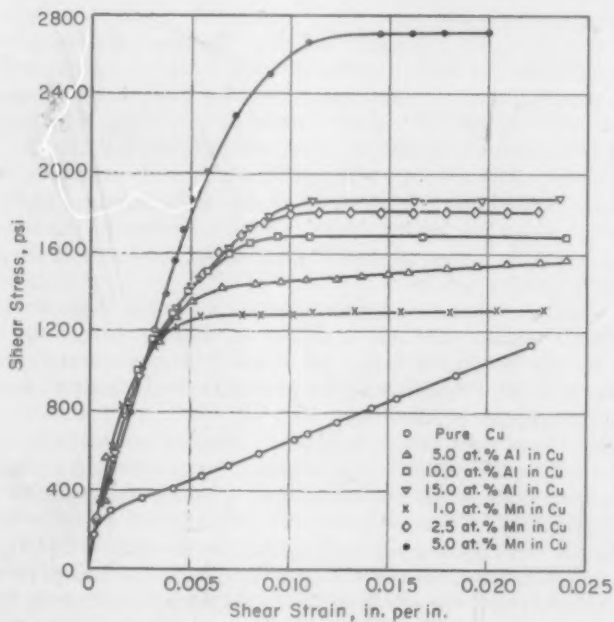


Fig. 35—Stress-Strain Curves for Single Crystals of Copper and Copper Alloys Tested in Simple Shear at Room Temperature (Wiseman (66)).

Hardening by Interstitial Atoms—As Cottrell has shown (2), carbon atoms accumulate around dislocations in iron. These atoms, being tiny, also tend to concentrate in the rarified regions of the crystal boundaries in aggregates. Sub-boundaries, or grain boundaries, containing an atmosphere of carbon atoms are much more effective barriers to the movement of dislocations than they otherwise would be. As was shown in Fig. 22, the introduction of sub-boundaries by plastic flow and heating increased the yield point of steel very markedly. This fact, along with other evidence (42), shows rather clearly that the main cause of solution hardening due to interstitial atoms is the effect that these atoms have on dislocation barriers, such as substructure boundaries and grain boundaries. Interstitial solution hardening is well understood (2) and so no more time will be devoted to it here. The story is different, however, with substitutional hardening which will be discussed in the next section.

Hardening by Substitutional Atoms—At present there is no satisfactory theory capable of explaining solution strengthening due to substitutional elements. In general, it may be said that solid solutions are stronger than pure metals and that the strengthening effect increases with increasing alloy content; however, the mechanism responsible for the strengthening is not yet clearly understood. Some recent experiments (66) have shed considerable light on the mechanism of solution hardening by substitutional atoms. In this work, single crystals of copper, copper manganese, and copper aluminum alloys were tested in simple shear. Typical stress-strain curves are reproduced in Fig. 35 for copper and for several alloys. The elastic limit was found to be relatively unaffected by alloying, being about 200 pounds per square inch in all cases. The plastic portion of the stress-strain curves consisted of two parts, one at low strains where the rate of strain hardening was very high and the second at strains above about 0.5% where the rate of strain hardening was much lower.

One conclusion that can be drawn from this work is that pinning of Frank-Read sources does not contribute to solution hardening. The reason for this conclusion is that the elastic limit of the material, i.e., the stress at which Frank-Read sources begin to become active, is substantially unaffected by alloying.

A second important conclusion is that dislocations pass with equal ease through the lattices of all of the crystals. The slope of the low strain region of the stress-strain curves is the same for all alloys and all concentrations tested. Hence, alloying does not affect the rate of work hardening in this region. Pratt (67) has shown that plastic flow in this portion of the stress-strain curve is associated with dislocations moving through the lattice to the sub-boundary walls but not penetrating them. At the knee of the stress-strain curve, where the slope decreases markedly, the dislocations break through the sub-boundary walls and there-

after slip spreads at a fast rate throughout the entire crystal.

The effect of solute elements on the stress-strain curve is to raise the knee of the curve to higher values of stress. The solute atoms therefore appear to produce solution hardening by strengthening of the sub-boundary walls. Thus, substitutional solution hardening seems to be caused by the same process that produces interstitial solution hardening, namely, the strengthening of sub-boundaries or grain boundaries by the accumulation of solute atoms therein.

HARDENING IN TWO-PHASE SYSTEMS

The cause of hardening in two-phase systems has not been elucidated to any significant extent, principally because solution hardening has been so puzzling. Plastic flow must occur in the ductile matrix of the alloy containing the dispersed hard phase. If the plastic behavior of a saturated solution is not clearly understood, then it is obviously impossible to understand the behavior of such a substance when it contains a dispersed second phase. Now that an understanding of the mechanism of solution hardening seems to be at hand, it may be possible to attack the problem of plastic flow in a two-phase system with some assurance of success. This has not yet been done, however.

FRACTURE

There are a number of different kinds of fracture, including cleavage, shear, fatigue, intergranular, and stress-corrosion, and very little is known about any of them. One basic fact is clear, however, namely that fracture is a two-stage process involving, first, nucleation of a crack and then, second, growth of the crack. Theories describing growth processes are relatively simple to devise; indeed, a number have already been formulated. It is the origin of the crack nucleus that presents the real problem at present.

For example, how do dislocations act to form a crack nucleus in a ductile material that fails by shear? Similar questions apply to all of the other types of fracture and, as yet, there are no satisfactory answers. There is an encouraging note, however, because in current work a combination of theory and experiment is providing an understanding of how such crack nuclei can form to cause brittle cleavage fractures at low temperatures. According to dislocation theory, groups of dislocations piled up at barriers such as a grain boundary induce local tensile stresses which approach the theoretical cleavage strength of the material. Predictions based on this theory, e.g., the effect of grain size, are in good agreement with experimental results and it should not be very long before brittle cleavage behavior is well understood.

Recent work on the origin of fracture nuclei in fatigue has been very illuminating. Experiments have shown that at least with some metals cracks develop on the surface and crack nucleation seems to be associ-

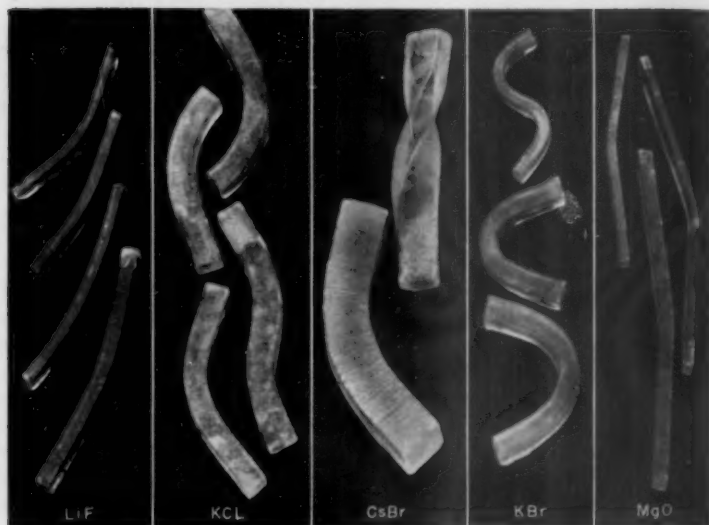


Fig. 36—Ceramic Single Crystals Bent at Room Temperature.

ated with multiple slip. Thompson, Wadsworth, and Louat (68) have shown that with polycrystalline copper subjected to reversed stresses, periodic removal of the surface layer prolonged fatigue life indefinitely. In other experiments (69), single crystals of zinc were subjected to cyclic straining in simple shear. In a room-temperature test, with a strain amplitude of 1%, the crystal was unharmed even after three million cycles or 6,000,000% accumulated plastic strain!

Through these experiments, some of the conditions necessary to avoid fatigue have been disclosed. The fundamental studies of fatigue are progressing rapidly and the present indications are that an understanding of the basic processes leading to fatigue will soon be forthcoming.

In regard to ductile shear-type fractures, and to some extent stress-corrosion cracking, the theoretical picture is still vague and unsatisfactory. Both of these classes of fracture involve nucleation and growth of cracks but at present there is no acceptable picture of either how cracks get started or how they grow.

NONMETALLIC CRYSTALS

From the accumulated knowledge about flow and fracture processes, it seemed reasonable to conclude that certain nonmetallic materials, particularly cubic ionic crystals, should exhibit plastic properties like

those normally associated with metals. The early work by Joffe (70) on sodium chloride and later work on silver chloride (71) strongly supported this conclusion. A rather large fundamental program has recently been initiated at the University of California to explore the possibility of making certain refractory ceramic materials ductile at room temperature. The early results have been encouraging. Many cubic ionic crystals have been tested and to date all have been found to be ductile, or could be made so, at 70 °F.

The most encouraging results of all are those obtained with magnesium oxide. Single crystals of this material could be bent through substantial angles without fracture at room temperature (see Fig. 36). Surface elongations up to 20% have been obtained in some of the bend tests. It now appears that there is a good chance that a number of useful ductile ceramic materials will be developed within the next few years.

CONCLUSION

Perhaps enough has been said—even though in rather general terms—to indicate that metal scientists are working along lines which will build the foundations for new and useful materials of construction with unexampled properties. A little reflection will indicate that the Edisonian “try everything” program is hopelessly inadequate in this day of rapid advance. The chance that such an approach would be worth what it costs is practically zero. The achievements of the solid-state physicists during the last fifteen years have been exceedingly encouraging and I hope that this brief account of modern concepts of flow and fracture has clearly illustrated one point—we are at last learning something about why metals are so weak!

ACKNOWLEDGMENTS

I should like to express my appreciation for the splendid assistance of my co-workers at the University of California without whose help the work discussed herein could not have been done. In particular, I extend my thanks to Jack Washburn, Thomas Hazlett, Alvin Gorum, Leslie Seaborn, Rosa Hansen, Margaret Janzen, Elizabeth Little; and to Thomas L. Johnston, Cho Hsien Li, and Eugene Edwards who have left the University staff. Also, I am deeply indebted to the Office of Naval Research, the Atomic Energy Commission, and the Air Force Office of Scientific Research for the financial assistance that made much of the work possible. Specifically, I should like to thank Irvin Kramer, Julius Harwood, David Lillie, Edward Epremian, and Charles Yost for their understanding and assistance.

References

1. J. Frenkel, "Zur Theorie der Elastizitätsgrenze und der Festigkeit kristallines Körper," *Zeitschrift für Physik*, Vol. 37, 1926, p. 572.
2. A. Cottrell, *Dislocations and Plastic Flow in Crystals*. Clarendon Press, Oxford, 1953.
3. R. Becker, "The Plasticity of Amorphous and Crystalline Substances," *Physikalische Zeitschrift*, Vol. 26, 1925, p. 919.
4. R. Becker and W. Boas, "Dependence of Speed of Flow on Temperature: Cu," *Metallwirtschaft*, Vol. 8, 1929, p. 317.
5. A. A. Griffith, "The Phenomena of Rupture and Flow in Solids," *Philosophical Transactions*, Royal Society, Vol. A221, 1921, p. 163.
6. C. G. Darwin, "The Theory of X-Ray Reflection," *Philosophical Magazine*, Vol. 27, 1914, pp. 315, 675, "The Reflection of X-Rays from Imperfect Crystals," *Philosophical Magazine*, Vol. 43, 1922, p. 800.
7. G. I. Taylor, "The Mechanism of Plastic Deformation of Crystals," *Proceedings*, Royal Society, Vol. A145, 1934, p. 362.
8. E. Orowan, "Plasticity of Crystals. IV Further Foundation for the Dynamic Plasticity Law," *Zeitschrift für Physik*, Vol. 89, 1934, pp. 605, 614, 634.
9. M. Polanyi, "Form of Lattice Distortion That May Render a Crystal Plastic," *Zeitschrift für Physik*, Vol. 89, 1934, p. 660.
10. L. Prandtl, "Ein Gedankenmodell zur kinetischen Theorie der festen Körper," *Zeitschrift für angewandte Mathematik und Mechanik*, Vol. 8, 1928, p. 85.
11. U. Dehlinger, "Theory of Recrystallization of Pure Metals," *Annales de Physique*, Vol. 5, 1929, p. 749.
12. T. Read, *Dislocations in Crystals*, McGraw-Hill, New York, 1953.
13. J. Friedel, *Les Dislocations*, Gauthier-Villars, Paris, 1956.
14. J. M. Burgers, "Some Considerations on the Fields of Stress Connected with Dislocations in a Regular Crystal Lattice," *Proceedings*, Koninklijke Nederlandse Akademie van Wetenschappen, Vol. 42, 1939, pp. 293, 378.
15. R. D. Heidenreich and W. Shockley, "Study of Slip in Al Crystals by Electron Microscope and Electron Diffraction Methods," *Report on Strength of Solids*, London: Physical Society, 1948, p. 57.
16. F. C. Frank and W. T. Read, "Multiplication Processes for Slow Moving Dislocations," *Physiological Reviews*, Vol. 79, 1950, p. 722.
17. W. K. Burton, N. Cabrera, and F. C. Frank, "Role of Dislocations in Crystal Growth," *Nature*, Vol. 163, 1949, p. 398.
18. L. J. Griffin, "Observation of Unimolecular Growth Steps on Crystal Surfaces," *Philosophical Magazine*, Vol. 41, 1950, p. 196.
19. A. R. Verma and S. Amelinckx, "Spiral Growth on Carborundum Crystal Faces," *Nature*, Vol. 167, 1951, p. 939.
20. A. J. Forty, "Observation of Growth of Cadmium Iodide from Aqueous Solution," *Philosophical Magazine*, Vol. 42, 1951, p. 670.
21. I. M. Dawson and V. Vand, "Observation of Spiral Growth-Steps in n-paraffin Single Crystals in the Electron Microscope," *Nature*, Vol. 167, 1951, p. 476.
22. A. J. Forty, "Growth Spirals on Magnesium Crystals," *Philosophical Magazine*, Vol. 43, 1952, p. 481.
23. S. Amelinckx, "Growth Spirals Originating from Screw Dislocations on Gold Crystals," *Philosophical Magazine*, Vol. 43, 1952, p. 562.
24. J. Washburn and E. R. Parker, "Kinking in Zinc Single Crystal Tension Specimens," *Journal of Metals*, Vol. 194, 1952, p. 1076.
25. J. J. Gilman, "Etch Pits and Dislocations in Zinc Monocrystals," *Transactions*, American Institute of Mining and Metallurgical Engineers, Vol. 206, 1956, p. 998.
26. P. B. Hirsch, R. W. Horne, and M. J. Whelan, "Direct Observations of the Arrangement and Motion of Dislocations in Aluminum," *Philosophical Magazine*, Vol. 1, Ser. 8, No. 7, July 1956, p. 677.
27. E. Schmidt and W. Boas, *Kristallplastizität*, J. Springer, Berlin, 1935.
28. R. Maddin, C. H. Mathewson, and W. R. Hibbard, "Unpredicted Cross-slip in Single Crystals of Alpha Brass," *Transactions*, American Institute of Mining and Metallurgical Engineers, Vol. 175, 1948, p. 86; "The Active Slip

- Systems in the Simple Axial Extension of Single Crystalline Alpha Brass," *Transactions, American Institute of Mining and Metallurgical Engineers*, Vol. 185, 1949, p. 527.
29. E. N. daC. Andrade and C. Henderson, "The Mechanical Behavior of Single Crystals of Certain Face-Centered Cubic Metals," *Philosophical Transactions*, Royal Society, Vol. A244, 1951, p. 177.
 30. F. Röhm and A. Kochendörfer, "Recent Results with Respect to Work-Hardening During Plastic Deformation of Crystals. I Shear Stressing of Long Crystals," *Zeitschrift für Metallkunde*, Vol. 41, 1950, p. 265.
 31. G. Masing and J. Raffelspieper, "Mechanical Recovery of Aluminum Monocrystals," *Zeitschrift für Metallkunde*, Vol. 41, 1950, p. 65.
 32. K. Lücke and H. Lange, "The Shape of the Solidification Curve of High-Purity Aluminum Crystals and the Formation of Deformation Curves," *Zeitschrift für Metallkunde*, Vol. 43, 1952, p. 55.
 33. W. G. and J. M. Burgers, Second Report on Viscosity and Plasticity, *Proceedings*, Academy of Sciences, Amsterdam, 1938, p. 200.
 34. A. Kochendörfer, *Plastische Eigenschaften von Kristallen und Metallischen Werkstoffen*, J. Springer, Berlin, 1941.
 35. P. Laurent, "The Theory of Plasticity of Metals and Alloys," *Revue de métallurgie*, Vol. 42, 1945, pp. 79, 125, 156, 194, 230.
 36. E. H. Edwards, J. Washburn, and E. R. Parker, "Some Observations on the Work Hardening of Metals," *Transactions, American Institute of Mining and Metallurgical Engineers*, Vol. 197, 1953, p. 1525.
 37. W. M. Lomer, "A Dislocation Reaction in the Face-Centered Cubic Lattice," *Philosophical Magazine*, Vol. 42, 1951, p. 1327.
 38. J. Washburn, "Experimental Observations Concerning the Collapse of Dislocation Loops During Annealing," *Transactions, American Institute of Mining and Metallurgical Engineers*, Vol. 206, 1956, p. 189.
 39. R. W. Cahn, "Internal Strains and Recrystallization," *Progress in Metal Physics*, Vol. 2, 1950, p. 151.
 40. J. Washburn, "Effect of Structure of Dislocation Boundaries on Yield Strength," *Transactions, American Institute of Mining and Metallurgical Engineers*, Vol. 203, 1955, p. 675.
 41. Betsy Ancker and E. R. Parker, "Quantitative Substructure and Tensile-Property Investigation of Nickel Alloys," *Transactions, American Institute of Mining and Metallurgical Engineers*, Vol. 200, 1954, p. 1155.
 42. E. R. Parker and J. Washburn, "Effects of Impurities and Imperfections on Mechanical Properties," Book—*Impurities and Imperfections*, American Society for Metals, 1955.
 43. N. F. Mott and F. R. N. Nabarro, "Dislocation Theory and Transient Creep," Report of a Conference on Strength of Solids, *The Physical Society*, London, 1948, p. 1.
 44. C. L. Smith, "A Theory of Transient Creep in Metals," *Proceedings, Physical Society*, Vol. 61, 1948, p. 201.
 45. W. Kauzman, "Flow of Solid Metals from the Standpoint of the Chemical Rate Theory," *Transactions, American Institute of Mining and Metallurgical Engineers*, Vol. 143, 1941, p. 57.
 46. A. S. Nowick and E. S. Machlin, "Quantitative Treatment of the Creep of Metals by Dislocation and Rate-Process Theories," N.A.C.A. Tech. Note 1039, Apr. 1946; "Dislocation Theory as Applied by N.A.C.A. to the Creep of Metals," *Journal of Applied Physics*, Vol. 18, 1947, p. 79.
 47. A. Kochendörfer, "Theory of Crystal Plasticity," *Zeitschrift für Physik*, Vol. 108, 1938, p. 244.
 48. N. F. Mott, "Slip at Grain Boundaries and Grain Growth in Metals," *Proceedings, Physical Society*, Vol. 60, 1948, p. 391.
 49. T. S. Kê, "Stress Relaxation Across Grain Boundaries in Metals," *Physiological Reviews*, Vol. 72, 1947, p. 72.
 50. J. Weertman, "Theory of Steady-State Creep Based on Dislocation Climb," *Journal of Applied Physics*, Vol. 26, No. 10, 1955, p. 1213.
 51. J. E. Dorn, "Some Fundamental Experiments on High Temperature Creep," *Journal of the Mechanics and Physics of Solids*, Vol. 3, 1954, p. 85.

52. J. J. Gilman and W. G. Johnston, "Observations of Dislocation Glide and Climb in Lithium Fluoride Crystals," *Journal of Applied Physics*, Vol. 27, No. 9, 1956, p. 1018.
53. D. W. Bainbridge, C. H. Li, and E. H. Edwards, "Recent Observations on the Motion of Small Angle Dislocation Boundaries," *Acta Metallurgica*, Vol. 2, 1954, p. 322.
54. H. L. Burghoff, A. I. Blank, and S. E. Maddigan, "The Creep Characteristics of Alloys at Elevated Temperatures," *Proceedings, American Society for Testing Materials*, Vol. 42, 1942, p. 668.
55. D. McLean, "Grain Boundary Slip During Creep of Aluminum," *Journal, Institute of Metals*, Vol. 81, 1952, p. 293.
56. H. C. Chang and N. J. Grant, "Inhomogeneity in Creep Deformation of Coarse Grained High Purity Aluminum," *Transactions, American Institute of Mining and Metallurgical Engineers*, Vol. 197, 1953, p. 1175.
57. B. Fazan, O. D. Sherby, and J. E. Dorn, "Some Observations on Grain Boundary Shearing During Creep," *Transactions, American Institute of Mining and Metallurgical Engineers*, Vol. 200, 1954, p. 919.
58. P. A. Beck, "Annealing of Cold Worked Metals," *Advances in Physics*, Vol. 3, 1954, p. 245.
59. R. E. Peterson and E. R. Parker, unpublished work.
60. H. Suzuki, "Chemical Interaction of Solute Atoms with Dislocations," *Science Reports, Research Institute, Tohoku University, Japan*, A-Vol. 4, No. 5, 1952, p. 455.
61. J. H. Fisher, "On the Strength of Solid Solutions," *Acta Metallurgica*, Vol. 2, No. 1, 1954, p. 9.
62. N. F. Mott and F. R. N. Nabarro, "An Attempt to Estimate the Degree of Precipitation Hardening with a Simple Model," *Proceedings, Physical Society, London*, Vol. 52, 1940, p. 86.
63. F. R. N. Nabarro, "The Mechanical Properties of Metallic Solid Solutions," *Proceedings, Physical Society, London*, Vol. 58, 1946, p. 669.
64. F. R. N. Nabarro, "Mechanical Effects of Carbon in Iron," *Report on a Conference on Strength of Solids*, Physical Society, London, 1948, p. 38.
65. N. P. Allen, T. H. Schofield, and A. E. L. Tate, "Mechanical Properties of α -Solid Solutions of Copper With Zinc, Gallium, Germanium and Arsenic," *Nature*, Vol. 168, 1951, p. 378.
66. C. Wiseman, E. R. Parker, and T. H. Hazlett, "Substitutional Solid Solution Strengthening of Copper Alloys," 16th Technical Report, Atomic Energy Commission, Project AT(11-1)-34, Project No. 29, Univ. Calif., June 1957.
67. P. L. Pratt, "Strain Hardening of Single Crystals," Atomic Energy Research Establishment, Harwell, England, Report M/R 883, March 1952.
68. N. Thompson, N. Wadsworth, and N. Louat, "The Origin of Fatigue Fracture on Copper," *Philosophical Magazine*, Vol. 1, 8th series, No. 2, Feb. 1956, p. 113.
69. Unpublished work at the University of California.
70. A. Joffe, M. W. Kirpitschewa, and M. A. Lewitsky, "Deformation and Strength of Crystals," *Zeitschrift für Physik*, Vol. 22, 1924, p. 286.
71. J. F. Nye, "Plastic Deformation of Silver Chloride. I Internal Stresses and the Glide Mechanism," *Proceedings, Royal Society*, Vol. A198, 1949, p. 191.

ELECTROLYTIC EXTRACTION OF CARBIDES FROM CARBON STEEL

BY R. W. GURRY, J. CHRISTAKOS AND C. D. STRICKER

Abstract

Repetitive extraction of the same carbon steel, heat treated to contain very fine carbides, and chemical analysis of the residue have served to evaluate many factors pertaining to the conditions of extraction. This work has led to a simple, effective apparatus and technique for the electrolytic extraction of carbides from carbon steel.

Tests show that the proposed method results in less decomposition of the carbide than other established methods. The performance of the new method upon steels tempered over a range of temperature is demonstrated. (ASM International Classification S11f; CN, 14-18)

THE PURPOSE of this investigation was to determine the variation in extent of carbide decomposition accompanying variation of the individual factors constituting the conditions under which carbides may be electrolytically extracted from carbon steel. It was expected that this information would form a basis for the selection of a more satisfactory extraction method, and would indicate the effect of a deviation in the technique. Some of the knowledge gained may be of value in the extraction of carbides from other steels and in the extraction of oxidic and other inclusions.

Carbides can be considered as decomposing in two ways during extraction. In one, iron, manganese, and other elements are dissolved but carbon is left behind as a kind of soot; in the other, carbon is evolved as gas or is dissolved along with the other elements. Chemical analysis of the residue does not give complete knowledge of the extent of decomposition. In addition, some comparison must be made between the amount of carbide found and that known to exist in the weight of steel extracted. In view of this we determined to devise a simple experimental technique that would permit a good measurement of the total weight of residue, as well as an analysis of a sample thereof.

To investigate the effect of a variation in extracting conditions a

A paper presented before the Thirty-Ninth Annual Convention of the Society, held in Chicago, November 4-8, 1957. The authors, R. W. Gurry, J. Christakos, and C. D. Stricker, formerly with United States Steel Corporation, Fundamental Research Laboratory, are now associated with: Quaker Chemical Products Company, Conshohocken, Pennsylvania; Esso Research Laboratories, Linden, New Jersey; and United States Steel Corporation, American Steel & Wire Division, Cleveland, Ohio, respectively. Manuscript received June 15, 1956.

standard steel sample is needed. A medium carbon steel with considerable manganese was selected in order to gain hardenability and, thus, uniformity of constitution after heat treatment. The heat treatment was determined in the following way. The steel was austenitized, quenched to martensite, and then tempered for 24 hours at one of a series of temperatures. The resulting specimens were extracted by the best method known to us at the time, the electrolytic method of Klinger and Koch (1)¹ using a neutral citrate solution, and the carbide residues analyzed chemically. From the results a heat treatment was selected which gave a considerable, but not excessive, decomposition of carbide during extraction. This treatment was applied to all specimens used in the development work, with the purpose that a variation in extracting conditions would produce an easily detected variation in the amount or the composition of the extracted carbide residue. In the course of the investigation runs were made under conditions duplicating those of other well known methods and the results compared. Finally, some of the most promising combinations of extracting conditions were applied to specimens representing a variety of heat treatments, to evaluate their effectiveness.

COMPOSITION AND HEAT TREATMENT OF THE SPECIMENS

All extractions reported here were made on an aluminum-killed, carbon steel, SAE 1045, of the following composition: 0.45% C, 0.80% Mn, 0.027% P, 0.032% S, 0.24% Si, 0.01% Cu, 0.01% Ni, 0.02% Cr and 0.015% acid-soluble Al. Specimens $\frac{3}{8}$ inch in diameter and varying from $2\frac{1}{2}$ to 4 inches long were machined from hot-rolled bar stock $1\frac{1}{8}$ inch in diameter. The $\frac{3}{8}$ inch diameter was chosen since this was the maximum that could safely be converted completely to martensite upon quenching. All specimens were austenitized in vacuum for $\frac{1}{2}$ hour at 1700 °F, quenched in brine, and tempered 24 hours. The tempering temperature was 800 or 900 °F for the development work, but covered a range from 210 to 1300 °F in the final testing of the methods. At 900 °F and below specimens were tempered in deoxidized lead; at higher temperatures they were heated in evacuated Pyrex tubes. Previous to extraction a specimen was always pickled in HCl.

THE APPARATUS AND ITS MANIPULATION

The extraction cell shown in Fig. 1 represents the final stage in a long development series. The specimen A is suspended through a threaded connection, containing a lock washer, to the stainless steel rod B, which in turn is supported by pressure of the coil spring C against the removable collar D. A short piece of rubber pressure tubing will serve in place of the coil spring. A motor-driven, cam-controlled, leaf-spring-powered hammer E raps sharply and continually against the top of the rod, thus

¹ The figures appearing in parentheses pertain to the references appended to this paper.

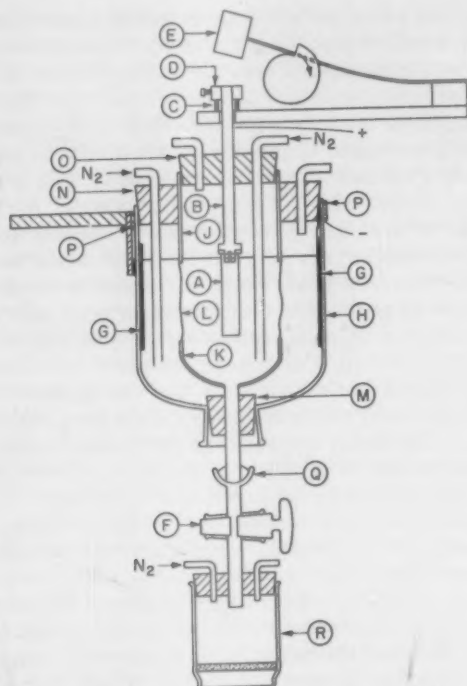


Fig. 1—Extraction Cell.

violently accelerating the specimen and jarring off the isolated particles. In case the anolyte is not flowing these settle down upon the closed large-bore stopcock F.

The cathode G is a copper sheet lining the container H which consists of an inverted one-liter bottle with its bottom cut off. Anolyte and catholyte are separated by the glass parts J and K, but electrically connected through the regenerated-cellulose, tubular dialysis membrane L which fits tightly over them. The bottom of the cathode chamber is closed by the rubber stopper M, and the tops of the two chambers by the rubber stoppers N and O. The wire to the cathode is adequately sealed simply by hammering flat the section which is squeezed between the stopper and the glass wall. Nitrogen is admitted below the surface of the liquid and exhausted from both chambers by glass tubes. Rubber extensions are attached to all outlet tubes to prevent back-diffusion of air. The cell is clamped to a ring stand by a special brass clamp P consisting of a screw-tightened band around the cell brazed to a small vertical bracing plate which in turn is brazed to the clamping rod.

In carrying out a run, the wet dialysis tubing is fitted over the glass parts J and K, which already carry the stoppers N and M, respectively. This assembly is then inserted into the bottle, stopper M seated, and the stopcock attached by means of the ball joint Q. The catholyte is admitted through the nitrogen inlet, and the anolyte is poured through the open top. The stopper O is set in position and the nitrogen flush started in both chambers. The nitrogen used in this work contains about 1% of hydrogen, added to simplify purification; it is passed over copper at 750 °F and then through a tower containing phosphorus pentoxide. After flushing the solutions for a few minutes, the weighed specimen, which has been pickled in HCl and quickly rinsed with water, is fastened to its support rod, and this thrust through the rather tightly fitting hole in stopper O, which is then seated. The electrolysis current is turned on immediately. The current was usually rectified A.C. controlled by a rheostat, but sometimes a lead storage battery was used. The hammering device, which is clamped to the same ring stand as the cell, is lowered, the collar secured, and the motor turned on. A final adjustment in position of the hammering device centers the specimen and sets its top just above the liquid level. A drop of glycerine will serve to lubricate the stopper where the rod passes through. The current was usually set at about 0.5 ampere and the run normally continued for about 18 hours.

At the appointed time the D.C. supply is turned off and the hammer stopped. A fine-porosity fritted Pyrex crucible R, mounted atop a filter flask, is attached below the stopcock, as shown, and nitrogen is passed through. By reversing the nitrogen inlet and outlet connections to the cathode chamber, the catholyte is forced out of the cell and replaced by nitrogen. After the crucible is flushed with nitrogen, suction is applied to the filter flask, the collected residue is brought down and the anode solution filtered in a nitrogen atmosphere by manipulation of the stopcock. Up to this point no air has entered either the cell or the crucible. Now the stopper O is lifted and the specimen as well as the anode chamber quickly rinsed with 5% sodium citrate solution, adjusted to pH 5 by addition of HCl. Any residue still clinging to the specimen rod is removed with a small stiff nylon brush and washed down with more citrate solution. Now the whole cell assembly is raised from the crucible. The residue on the frit is washed for 10 minutes with successive small additions of water, and finally for 5 minutes with absolute methyl alcohol.

While the residue is still quite wet with alcohol the crucible is transferred to a small vacuum desiccator and evacuated for $\frac{1}{2}$ hour with an aspirator pump. The wet handling in air and the flushing of the air from the desiccator by the evaporating alcohol result in an essentially unoxidized residue. The residue can be stored thus in vacuum for an extended period, or it can be exposed immediately to air for weighing and

analysis. The controlled manner in which the residue is exposed to air and the experimentation which led to it are described in a later section. Separate portions of the residue were taken for analysis for carbon, iron and manganese, and occasionally for sulphur. Carbon was determined by combustion, iron and manganese by titration, and sulphur gravimetrically. Homogenization previous to analysis, by gently breaking up the residue in an agate mortar and passing through a 100-mesh sieve, was found unnecessary after extensive testing.

The apparatus described above was effective, convenient to use, and trouble-free. With the electrolytes used, to be described later, no ferric hydroxide was encountered, except under certain extreme experimental conditions. The hammer proved to be an effective means of knocking the isolated residue from the specimen. A good determination of the total weight of residue is obtainable simply by weighing the crucible with and without residue. Anolyte and catholyte of different composition can readily be used. By introducing another tube through the stopper of the anode chamber to bring in fresh solution and fitting the bottom of the crucible with a stopper and an outlet tube, the anolyte can be made to flow continuously. Of course, in such a case, the nitrogen inlet and outlet to the crucible are closed during the electrolysis. It will be seen that the extraction cell is quite versatile; it can be made to reproduce the essential features of most electrolytic methods.

With a continuously flowing anolyte, a device such as that shown in Fig. 2 is needed to supply the solution at constant level. Here the reservoir bottle A feeds solution to the constant level cup B through the syphon tube C, and this, in turn, to the anode chamber D through the syphon tube E, as demanded by the controlled outlet at the bottom of the anode chamber. The level control is established in the cup B by a device limiting the access of air to the reservoir bottle. When the liquid level in cup B falls below the rim of the hemispherical glass bulb F, a bubble of air rises through the tube G and thus enters the reservoir bottle, permitting a corresponding volume of solution to escape through the syphon C. The level is precisely controlled because, in operation, no sooner does it fall below the rim than it is reestablished by solution from the hemisphere. There is no delay in this due to friction of liquid passing through tubing, and, accordingly, no over-shooting. The tubing G must, of course, be of sufficiently large diameter, about 8 millimeters inside, to permit the bubble to rise through the liquid in it. The bulb H and the screw clamp J prevent the column of liquid in G being driven over into the bottle A by a large bubble. The clamp J is adjusted so that the level in G rises slowly due to the action of a rising bubble, and thus time is provided for the bubble to reach the surface before the liquid reaches the clamp. The opening at K assists in adjusting the pressure originally and is closed during operation of the device. The stop-cock L prevents overflow of the cup due to temperature fluctuation

when the device is idle. The cup is covered by a stopper to keep out dust, atmospheric pressure inside being maintained by the open tube M.

With a continuously flowing anolyte a rather long vertical tube of small bore must be connected to the bottom of the crucible to provide the necessary suction, and a stopcock must be inserted in it to control the flow. A simple alteration of an oblique-bore stopcock, namely, filing a V-notch of decreasing depth, half-way round the plug from each end

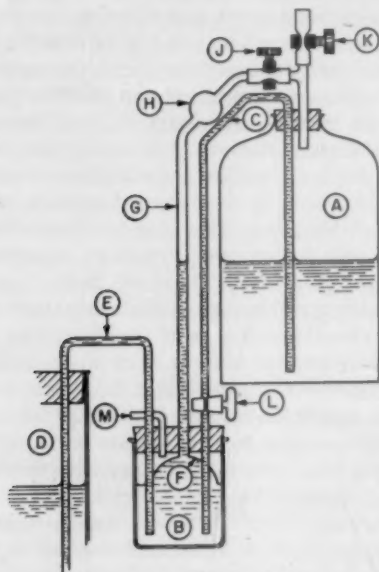


Fig. 2—Device Supplying Liquid at Constant Level.

of the bore, increased the extent of rotation of the plug from off to on, and thus greatly eased the achievement of a proper adjustment of the flow. An alternative regulation of flow was by insertion of a suitable length of fine capillary instead of the stopcock. If the residue is very fine its gradual accumulation on the frit may cause an intolerably great decrease in the flow. In such a case a satisfactory arrangement is to increase the suction by connecting an aspirator pump to a large bottle which serves as a collecting vessel for the waste anolyte, also making a corresponding adjustment of the throttling stopcock or capillary. In working with a strongly acid anolyte some gas is produced in the crucible which, unless an escape is provided, prevents replenishment of liquid in the crucible and results in deterioration of the residue. A sufficiently large tube, about 8 millimeters I.D., between the cell and the

crucible will eliminate the difficulty. Stopcock F (Fig. 1) on this tube is superfluous with a flowing anolyte, and the constriction which it introduces can thus be eliminated. Insertion of a suitably shielded calomel-glass electrode pair through the stopper O into the anolyte and connection through a commercial pH controller-recorder to a solenoid valve in the crucible outlet provides an automatic control of the flow. Many runs in the near-neutral pH range, not reported in this paper, were made using this means of control.

THE ELECTROLYTE

The electrolytes used cover a wide range of composition and include alcoholic as well as aqueous solutions. The composition of the anolyte is given in Tables I through IV, along with the composition of the resulting carbide residue. In the runs reported here the catholyte was almost always a solution of a cadmium salt, with anion the same as that of the anolyte. Usually a single solution was made up and part used for anolyte and part for catholyte, the total amount of salt added being about one and one-half times that required to sustain the deposition reaction at the cathode.

It is highly desirable to maintain a fairly constant pH during extraction to assist in the avoidance of contamination on the one hand or solution of the residue on the other. Evolution of hydrogen at the cathode and the attendant drift toward higher pH can be avoided by suitable

Table I
Aqueous Iodide Extraction of 0.45% Carbon, 0.80% Manganese Steel,
Tempered 24 Hours

Tempering Temp. °F	Electro- lyte	Normality Iodide Ion	Anolyte pH		Anode C.D. amp./cm ²	Residue Analysis				C Yield, % 100 (Wt. C in res.)
			Initial	Final		% C	% Mn	% Fe	Sum	
1300	CdI ₂	0.8	6.1	3.0	0.025	6.4 ₄	5.6	86.1	98.1	99.8
1300	CdI ₂	0.8	5.9	2.4	0.030	6.5 ₀	5.5	85.3	97.3	100.0
1200	CdI ₂	0.8	5.8	3.1	0.021	6.4 ₄	5.6	84.4	96.4	99.9
1200	CdI ₂	0.8	5.9	2.8	0.018	6.4 ₀	5.5	84.4	96.3	99.1
1100	CdI ₂	0.8	5.8	3.3	0.028	6.8 ₂	7.0	85.9	99.7	104.3
1100	CdI ₂	0.8	6.0	3.7	0.032	6.6 ₂	6.9	82.9	96.5	103.8
1100	CdI ₂	0.8	5.7	4.0	0.017	6.6 ₀	5.5	84.4	96.5	100.6
1100	CdI ₂	0.8	5.8	3.8	0.019	6.5 ₄	6.5	83.5	96.5	100.9
1100	CdI ₂	0.8	5.8	4.1	0.026	6.8 ₁	6.9	83.2	96.9	99.4
1100	CdI ₂	0.8	5.5	3.9	0.020	6.3 ₄	6.9	86.6	99.9	98.2
1000	CdI ₂	0.8	5.9	4.2	0.017	6.7 ₁	5.5	84.4	96.6	99.6
1000	CdI ₂	0.8	5.8	2.9	0.019	6.4 ₄	5.7	84.4	96.5	95.6
1000	CdI ₂	0.8	5.3	3.5	0.023	6.4 ₄	5.7	84.9	97.0	95.2
1000	CdI ₂	0.8	5.6	4.2	0.022	6.4 ₄	5.7	84.1	96.2	94.8
900	CdI ₂	0.8	6.3	4.6	0.019	6.5 ₀	3.8	84.4	94.7	95.2
900	CdI ₂	0.8	5.9	3.7	0.020	6.8 ₁	3.8	84.4	95.0	98.7
900	CdI ₂	0.8	6.2	4.6	0.025	6.4 ₄	3.9	85.3	95.6	—
900	CdI ₂	0.8	6.2	4.2	0.017	6.7 ₀	4.0	86.2	96.9	97.1
900	CdI ₂	0.8	6.1	4.2	0.023	6.4 ₄	3.9	85.3	95.7	96.8
900	CdI ₂	0.8	4.8	4.2	0.020	6.4 ₄	3.9	86.2	96.6	96.8
900	CdI ₂	0.8	6.0	4.4	0.022	6.3 ₄	4.0	86.2	96.6	92.3
900	CdI ₂	0.8	6.1	3.7	0.026	6.7 ₄	4.0	82.6	93.3	97.8

Table I (Continued)
Aqueous Iodide Extraction of 0.45% Carbon, 0.80% Manganese Steel,
Tempered 24 Hours

Tempering Temp. °F	Electro- lyte	Normality Iodide Ion	Analyte pH		Anode C.D. amp./cm ³	Residue Analysis				°C Yield, % 100 (Wt. C in res.)
			Initial	Final		% C	% Mn	% Fe	Sum	
Change in Concentration										
900	CdI ₂	1.6	5.5	3.3	0.024	6.4 ₂	3.9	86.1	96.5	96.5
900	CdI ₂	0.6	6.0	4.1	0.019	6.6 ₂	4.0	85.3	96.0	—
No Hammer										
900	CdI ₂	0.8	6.2	3.0	0.021	6.6 ₂	3.7	81.8	92.1	89.7
900	CdI ₂	0.8	6.0	3.8	0.019	6.7 ₂	3.7	84.5	95.0	90.8
N ₂ Bubbled Over Specimen										
900	CdI ₂	0.8	6.1	4.6	0.019	6.7 ₂	3.8	80.9	91.5	97.6
900	CdI ₂	0.8	6.1	4.4	0.024	6.6 ₂	4.1	81.9	92.6	97.7
Change in Current Density										
900	CdI ₂	0.8	5.8	4.2	0.21	6.8 ₂	3.8	82.8	93.4	97.6
900	CdI ₂	0.8	5.5	3.3	0.19	6.8 ₂	3.8	82.1	92.7	99.8
900	CdI ₂	0.8	6.0	4.3	0.11	6.4 ₂	4.0	85.3	95.7	93.8
900	CdI ₂	0.8	6.0	4.2	0.045	6.4 ₂	3.9	84.4	94.7	94.1
900	CdI ₂	0.8	6.1	4.9	0.0057	6.2 ₂	3.8	86.1	96.1	89.6
900	CdI ₂	0.8	5.0	4.4	0.0046	6.6 ₂	4.0	84.7	95.4	96.0
900	CdI ₂	0.8	6.0	4.7	0.0036	6.5 ₂	3.8	85.3	95.7	93.2
Change in pH										
900	CdI ₂	0.8	3.2	4.4	0.019	6.4 ₂	3.8	86.1	96.3	94.0
900	CdI ₂	0.8	3.3	4.5	0.026	6.6 ₂	3.8	85.3	95.7	94.1
800	CdI ₂	0.8	6.4	4.7	0.019	6.6 ₂	2.6	80.5	89.8	86.8
800	CdI ₂	0.8	5.8	5.0	0.018	6.5 ₂	2.4	80.9	89.8	87.8
800	CdI ₂	0.8	5.8	4.7	0.021	7.1 ₂	2.7	85.3	95.1	98.3
800	CdI ₂	0.8	5.8	—	0.018	6.6 ₂	2.7	84.4	93.8	92.6
800	CdI ₂	0.8	5.7	4.7	0.019	7.0 ₂	2.8	83.2	93.0	89.8
No Hammer										
800	CdI ₂	0.8	6.5	3.4	0.018	6.5 ₂	2.4	81.3	90.2	81.9
800	CdI ₂	0.8	6.1	3.1	0.021	6.6 ₂	2.3	81.2	90.2	83.1
700	CdI ₂	0.8	6.0	4.8	0.021	7.0 ₂	1.9	81.8	90.7	91.4
700	CdI ₂	0.8	6.0	4.3	0.016	7.4 ₂	2.0	81.8	91.2	87.3
700	CdI ₂	0.8	6.2	4.4	0.005	7.2 ₂	1.9	81.8	91.0	89.8
210	CdI ₂	0.8	5.6	2.1	0.029	29.	—	—	—	104.
As- Quenched	CdI ₂	0.8	5.6	4.0	0.023	31.3	2.0	27.2	60.4	88.

choice of the cation. Hydrogen, ammonium and alkali metal ions are normally rejected as the principal cation in the catholyte for this reason. Preliminary runs, not reported, were made using zinc, tin, lead, nickel, cobalt, copper and cadmium cations. The solubility relations are satisfactory for all except lead and tin. Few lead salts are soluble in water or alcohol, and stannous solution must be rather strongly acid to prevent precipitation of hydroxide. Copper and cadmium gave no observable gas evolution under the experimental conditions; cobalt and nickel gave only a little. Of the two ions with highest cathode efficiency cadmium is much to be preferred for the following reasons: it does not precipitate hydroxide readily, permitting use of a near-neutral solution; the citrate is soluble and the metal is not precipitated upon contact with the steel anode, so that complications do not arise from diffusion of the cation through the diaphragm into the anode chamber even when a

Table II
Aqueous Chloride Extraction of 0.45% Carbon, 0.80% Manganese Steel,
Tempered 24 Hours at 900° F

Tempering Temp. °F	Electro- lyte	Normality Of Chloride Ion	Anolyte pH		Anode C.D. amp./cm ²	Residue Analysis				C Yield, % 100 (Wt. C in residue)
			Initial	Final		% C	% Mn	% Fe	Sum	
900	CdCl ₂	0.8	6.0	4.3	0.018	6.2 ₁	3.8	84.5	94.5	80.4
900	CdCl ₂	0.8	4.9	4.7	0.019	6.2 ₀	3.8	85.3	95.3	78.2
900	CdCl ₂	0.8	6.1	4.8	0.032	6.2 ₄	3.7	85.3	95.2	81.6
900	CdCl ₂	0.8	5.9	4.8	0.027	6.4 ₂	3.9	80.8	91.1	81.9
Change in Concentration										
900	CdCl ₂	1.2	6.1	5.0	0.023	6.6 ₁	4.0	83.1	93.8	78.2
900	CdCl ₂	1.2	6.0	5.7	0.023	6.7 ₀	4.0	83.4	94.1	92.3
No Hammer										
900	CdCl ₂	0.8	6.0	4.9	0.040	6.5 ₁	3.7	83.6	93.8	70.6
Change in Current Density										
900	CdCl ₂	0.8	5.7	4.1	0.18	6.7 ₁	3.8	81.3	91.8	87.9
900	CdCl ₂	0.8	5.7	4.3	0.16	6.9 ₀	3.7	81.9	92.5	82.7
900	CdCl ₂	1.2	6.2	5.4	0.072	6.4 ₁	3.6	78.6	88.7	73.6
900	CdCl ₂	1.2	4.1	5.3	0.0074	6.9 ₁	4.1	84.2	95.2	80.8
900	CdCl ₂	1.2	6.2	5.7	0.0040	6.6 ₁	3.5	80.8	91.0	95.0
Change in pH										
900	HCl ^a	5.0	-0.6 ^b	-0.6	0.022	12.7 ₁	—	74.9	—	26.6
900	HCl ^a	2.0	-0.2 ^b	-0.2	0.020	8.2 ₀	1.2	81.4	90.8	55.7
900	HCl ^a	1.4	0.0 ^b	0.0	0.024	7.8 ₁	3.6	80.6	92.1	55.6
900	CdCl ₂ (HCl 1.2)	0.2	1.0	1.0	0.015	7.6 ₁	—	82.4	—	28.2
900	HCl ^a	0.23	1.2 ^c	1.4	0.025	7.7 ₁	—	—	—	19.4
900	HCl ^a	0.014	2.1	2.5	0.020	7.6 ₁	—	68.5	—	25.8
900	HCl ^a	0.014	2.3	2.4	0.022	8.1 ₁	4.3	75.7	88.2	42.7
900	CdCl ₂	1.2	2.2	4.4	0.017	6.9 ₁	4.0	81.8	92.7	77.0
900	HCl ^a	0.10	3.1 ^c	4.2	0.018	6.6 ₁	4.2	79.5	90.4	64.2

a. Flowing anolyte.

b. pH calculated from composition.

c. Flow of anolyte restricted, so that pH was not that of incoming solution.

Table III
Miscellaneous Aqueous Extractions of 0.45% Carbon, 0.80% Manganese
Steel, Tempered 24 Hours at 900° F

Tempering Temp. °F	Electro- lyte	Normality of Anion	pH		Anode C.D. amp./cm ²	Residue Analysis				C Yield, % 100 (Wt. C in residue)
			Initial	Final		% C	% Mn	% Fe	Sum	
900	CdBr ₂	0.8	6.1	4.5	0.023	6.6 ₀	4.0	86.2	96.8	89.2
900	CdBr ₂	0.8	6.0	4.1	0.015	6.5 ₁	3.8	84.5	94.8	87.8
900	CdBr ₂	0.8	5.9	5.0	0.004	6.6 ₀	3.8	83.6	94.0	84.0
900	CdBr ₂	0.4	6.1	4.7	0.025	6.2 ₁	3.7	85.3	95.2	88.1
900	CdBr ₂	0.6	6.0	4.5	0.020	6.1 ₁	4.0	85.3	95.5	89.0
900	CdI ₂	0.2	6.0	4.4	0.014	6.1 ₁	3.9	85.3	95.4	—
	CdCl ₂	0.6								
900	CdI ₂	0.2	5.9	4.1	0.020	6.4 ₁	3.7	85.5	95.6	91.2
	CdCl ₂	0.4								
900	CdI ₂	0.4	6.5	6.5	0.015	8.2 ₁	4.0	80.5	92.7	97.2
	Na citrate	0.5								
900	KBr	0.1	7.2	6.6	0.016	7.5 ₀	3.5	82.8	93.8	97.2
	KI	0.036								
900	Na citrate	0.5	7.0	4.2	0.021	7.0 ₁	3.9	84.7	95.6	89.2
	KBr	0.1								
900	KI	0.036	7.2	6.3	0.020	8.5 ₀	3.5	82.0	94.0	97.6
	Na citrate	0.5								
900	NaCl	0.8	7.2	6.3	0.020	8.5 ₀	3.5	82.0	94.0	97.6
	NH ₄ citrate	0.044								
900	NH ₄ Cl	0.1								

a. Flowing anolyte.

b. Klinger and Koch anolyte composition.

Table IV
Alcoholic Extraction of 0.45% Carbon, 0.80% Manganese Steel, Tempered 24 Hours

Tempering Temp. °F	Electrolyte	Normality of Ion	Anode C.D. amp./cm ²	Residue Analysis				C Yield, % 100 (Wt. C in residue)
				% C	% Mn	% Fe	Sum	
900	CdI ₂	0.8	0.023	6.4 ₀	3.8	86.2	96.4	91.3
900	CdI ₂	0.8	0.020	6.4 ₁	2.5	83.6	92.5	92.2
900	CdI ₂	0.8	0.020	7.2 ₁	3.4	86.9	97.5	87.1
900	CdI ₂	0.8	0.020	6.9 ₁	3.3	87.8	98.1	96.6
900	CdI ₂ ^a	0.8	0.022	7.0 ₁	3.5	86.9	97.5	86.2
900	CdI ₂ ^a	0.8	0.009	7.3 ₀	3.6	86.9	97.8	87.7
800	CdI ₂ ^a	0.8	0.018	8.2	2.8	83.3	94.3	96.4
800	CdI ₂ ^a	0.8	0.014	7.4 ₀	2.9	83.3	93.6	91.4
800	CdI ₂ ^a	0.8	0.025	7.6 ₁	2.5	86.0	96.1	—
800	CdI ₂ ^a	0.8	0.023	7.0 ₁	2.5	86.9	96.4	—
800	CdI ₂ ^a	0.8	0.021	7.6 ₁	2.8	86.0	96.4	—
800	ZnCl ₂ ^b	1.2	0.020	7.2 ₁	2.8	85.1	95.1	100.0
800	ZnCl ₂ ^{b,c}	1.2	0.012	8.1 ₁	2.2	81.5	91.8	—
800	ZnCl ₂ ^b	1.2	0.018	7.2 ₁	2.5	86.9	96.6	—
800	ZnCl ₂ ^b	1.0	0.027	7.1 ₀	2.3	84.5	93.9	—

a. CdI₂ dried by heating at 250°F; alcohol dried by treating with magnesium and distilling.

b. ZnCl₂ dried by heating to 570°F in vacuum.

c. H₂ instead of N₂ to flush cell.

citrate anolyte is used. A factor of some practical significance is the ability of the cation to give a uniform deposit on the cathode, free from trees of crystals which would penetrate the diaphragm and endanger the proper completion of a run. Of the cations, cadmium, tin and lead have a propensity for treeing. In spite of this disadvantage, which is minimized by a cathode sufficiently large and well separated from the diaphragm, as shown in Fig. 1, cadmium is preferred by us as the ion to carry out the cathode reaction.

EXTRACTION DATA

The data in Tables I through IV pertain to runs made with the apparatus shown and by the technique described. Very few runs have been discarded due to failure. It will be realized that an alteration in the apparatus or in the technique of handling the residue will generally affect the amount or analysis of the residue, and many runs which for some reasons are not comparable to those above are not reported. The necessity of evaluating a factor over again after making a change in conditions makes development tedious, but was found necessary in many instances.

In the tables, the electrolyte and initial concentration shown were used for both anolyte and catholyte except when the anolyte flowed continuously. In such a case, the electrolyte listed is the anolyte and the catholyte was a solution of cadmium chloride, 0.8 N in chloride ion. The pH listed was measured by glass electrode except in strongly acid solution where it was computed from the concentration. In the extractions reported there was no mechanical stirring of either anolyte or catholyte, but in earlier work both were tried. The only stirring, aside from the jarring by the hammer, was from the rising nitrogen bubbles;

in two runs this was accentuated by letting the rising bubbles strike the anode.

Duplicate extractions show some variation in analysis. Most of this is due to lack of complete homogeneity of the steel, but some is attributable to analytical error. As is to be expected, the determination of carbon gave the greatest error; replicate analysis of a homogenized residue indicated a variation of about $\pm 0.1\%$ C. The "carbon yield" shown in the last column of Tables I to IV is calculated from weight and carbon content of both extracted steel and residue, and indicates the extent to which carbon was preserved, either as carbide or soot, during the extraction. Usually a blank in the tables indicates that a determination was impossible because of insufficient sample, but sometimes simply that no measurement was made.

VARIATIONS IN THE EXTRACTING CONDITIONS

Many interesting effects will be observed in comparing the various data in Tables I through IV. Some of the more striking results, pertaining to extraction of the very fine carbides in the steel tempered 24 hours at 900 °F, have been summarized in Table V. Each entry in the "analysis" and "carbon yield" columns represents the average of all pertinent data in the previous tables. In computing the carbide composition from the residue analysis, account is taken of the fact that some of the manganese is combined with sulphur. The amount of sulphur found in residues extracted by the normal iodide method was about 0.80 times that present in the steel; specifically the recovery varied from 0.73 to 0.87 and, as would be expected, showed no systematic variation with tempering temperature. In making the correction to the manganese content of the residue, all of the sulphur is assumed to be associated with manganese. Moreover, in Table V, the same manganese correction, as determined by the normal iodide method, is applied to all other residues. To simplify a comparison of the results, the quantities listed in the last three columns have been calculated, namely the percentages of carbide decomposed with and without preservation of carbon, and the percentage contamination of the residue. The calculation of this latter considers a residue to be uncontaminated if it consists exclusively of carbide, sulphide and carbon. It should be remembered that the results pertain to extraction of very fine carbides from plain carbon steel, specifically that tempered 24 hours at 900 °F.

The relative effect of the halide anions is shown by the first group in Table V. As far as complete decomposition is concerned iodide is by far the best, bromide next, and chloride worst. However, iodide and bromide extraction preserved a little more carbon as soot than did the chloride. Attempts to substitute chloride or bromide for part of the cadmium iodide, Table III, seemed to give intermediate values, as might be expected.

Table V
The Effect of a Variation in Extraction Conditions Upon the Extent of Carbide Decomposition and of Contamination of the Residue. Summary of Some Data in Tables I through IV—Steel Tempered 24 Hours at 900° F.

	Ave. Analysis of Residue			Corr. Sum (%)	Carbide Comp.			C Yield (a) %	Carbide decomposed (b) %		Contamination (c) %
	% C	% Mn	% Fe		% C	% Mn	% Fe		decomposed to carbon (b)	completely decomposed (d)	
"Normal" iodide method	6.57	3.91	85.1	94.9	6.93	3.42	89.7	96.4	3.3	3.6	4.0
"Normal" hammer method	6.57	3.90	85.1	95.1	6.91	3.40	89.7	88.5	2.8	11.5	3.8
"Normal" chloride method	6.27	3.80	84.0	93.4	6.72	3.35	89.9	80.5	0.4	19.5	5.5
Iodide electrolyte	6.68	3.87	83.4	93.3	7.16	3.43	89.4	97.1	6.4	2.9	5.6
8 times normal C.D.	6.81	3.75	81.6	91.5	7.45	3.37	89.2	85.3	8.7	14.7	7.4
Chloride electrolyte	6.73	3.7	83.2	92.9	7.25	3.3	89.5	90.3	7.0	9.7	6.0
Iodide electrolyte	6.52	3.7	83.6	93.1	7.00	3.3	89.7	70.6	3.1	29.4	5.8
1 wt. % KI anolyte	7.85	3.6	80.6	91.4	8.59	3.2	88.2	55.6	12.3	44.4	7.5
1 wt. % NaOH anolyte	7.87	3.75	81.7	92.6	8.50	3.33	88.2	97.2	20.7	2.8	6.3
Klingner-Koch anolyte	6.91	3.35	86.4	96.0	7.20	2.80	90.0	90.2	6.4	9.8	2.9
Iodide electrolyte											
alcoholic solution											

(a) "Normal" conditions are defined as follows: electrolytic cell, that shown in Fig. 1, with hammer operating; anolyte and catholyte, same aqueous solution of minimum salt with concentration of anion 0.8 N., initial pH about 6.0; current density, about 0.02 amp./cm²; residue washed 15 min., evacuated, and exposed to air in controlled manner.

(b) For normal iodide method:

$$\% \text{ Mn with S in residue} = \frac{0.80(0.032)(54.9)(\text{Wt. steel})}{(32.06)(\text{Wt. residue})}$$

where 0.80=fraction Mn recovered in residue; 0.032=%S in steel; 54.9=at. wt. Mn.; and 32.06=at. wt. S.

Sulfide content of other residues taken the same as that found by the normal iodide method; % Mn with S=0.67, % MnS in residue=1.06.

(c) Does not include S or Mn associated with S.

$$(d) \% \text{ C Yield} = \frac{\text{Wt. C in steel}}{100 (\text{Wt. C in residue})}$$

(e) Percentage of the carbide that is decomposed with carbon preserved = C Yield (1-6.69/% C), where 6.69 is the stoichiometric carbon content of cementite, and % C is that listed under "carbide composition."

(f) Percentage of the carbide that is decomposed completely = (100-C Yield).

(g) For this purpose, MnS is not considered a contaminant. The percentage contamination is, therefore, 100 minus the sum of the percentages of C, Mn, Fe,* and S in the residue. It is considered to be principally oxygen.

A great increase in current density, second group, resulted in some increase in total decomposition (the sum of the two tabular values) for both iodide and chloride. However, with chloride the increase in decomposition to soot was much greater, as was also the decrease in complete decomposition. In the normal range of 0.015 to 0.03 ampere per square centimeter a variation in current density had no effect. A decrease from the normal current density did not seem to give any consistent improvement.

The beneficial effect of the hammer is shown by the next group in Table V. For both iodide and chloride solutions, failure to use the hammer resulted in considerable increases in both types of decomposition as well as some increase in contamination. Other methods of removing the carbide from the anode were formerly employed. One was an oscillating rubber wiper, and the other a rotation of the anode at 8000 to 10,000 r.p.m. Of the two, the latter was more effective, but no more so than the hammer; it required considerable maintenance and gave trouble in causing the anode solution to foam. The latter was largely eliminated by addition of a drop of *n*-octyl alcohol. The hammer required no maintenance, gave no trouble, and was much simpler to use with the required exclusion of air from the apparatus.

The effect of acidity was investigated only with chloride anion and is reported in Table II. Only a single run at pH zero is included in Table V, this corresponding to 5% by weight HCl, one of the commonly used electrolytes in acid extraction. High acidity greatly increases both types of decomposition. In several cases there was so little residue that a complete analysis was impossible. Variation of pH in the range 4 to 6 seemed to have no noticeable effect on the residue from the steel tempered at 900 °F, nor did catching the residue in glycerine. Even a somewhat lower pH than this is not detrimental to large carbides, as evidenced by the early entries in Table I. These same data, for higher tempering temperature, also indicate an unexpected tendency of the anode solution to become somewhat more acid during the extraction. In general, a given set of extracting conditions tends always to produce about the same final pH, regardless, within reasonable limits, of the initial pH.

The Klinger and Koch anolyte, and other citrate solutions as well, gave a great decomposition to soot, although the carbon yield was very good. With the apparatus and technique used, no advantage can be taken of the ability of the citrate to cut down on contamination by holding iron in solution.

One way of avoiding the danger of hydroxide precipitation without resorting to acid or citrate is to carry out the electrolysis in alcoholic solution. Accordingly, a considerable number of extractions were made in absolute methyl alcohol. The number of salts that can be used, however, is very much restricted by solubility and by availability in water-

free form. With alcohol the cellulose membrane could not be used because it had a very high resistance. A new one-piece anode chamber embodying a cylindrical section of fritted Pyrex, 2 inches I.D., was procured and with this the extraction could be carried out without difficulty. Most of the alcoholic runs made have been deleted from Table IV because of a change in technique of handling the residue. Although, in general, there does seem to be a very slight decrease in amount of contamination with alcohol, the extent of both types of carbide decomposition are decidedly worse.

Some other factors are of relatively minor importance. A variation in concentration of anion had no appreciable effect over the range used. The concentration of cation had no effect as long as it was great enough to avoid hydrogen evolution. Bubbling nitrogen over the specimen, although noticeably accentuating the electrolytic attack at the areas of impingement by decreasing concentration polarization, seemed to result only in a slight increase in the amount of contamination, as indicated by a lower value for "sum" in Table I.

HANDLING OF THE RESIDUE

The chemical analysis, and even to some extent the x-ray electron diffraction analysis, of an extracted residue is dependent not only upon the conditions under which the extraction was carried out, but also upon the manner in which the residue is handled between extraction and analysis. This includes such details as the washing of the residue, stabilizing it to air, and storing it.

Washing

After the anode solution is filtered through the fritted crucible the residue is washed with solvent to remove any soluble material, particularly salts of iron. As regards the technique of washing, it should be mentioned that it is advantageous to add the solvent in successive small portions, allowing the liquid to nearly disappear before each addition. However, if the residue goes to dryness it will oxidize, usually to a detrimental degree; the residues from the lower tempering temperatures are pyrophoric.

Since both finely divided iron carbide and soot are known to be very surface-active and, therefore, tend to adsorb a considerable amount of material from the extracting solution, the question arises as to how long a residue in the crucible should be washed with solvent to prepare it for analysis. In Table VI are the results of washing experiments on residues extracted in alcoholic solution from the same steel used above, tempered 24 hours at 800 °F. Each successive 5-minute portion of the wash alcohol was analyzed for iron colorimetrically by the thiocyanate method. Based on the results shown, a 15-minute period of washing was considered adequate.

Table VI
Iron Content of Alcohol after Washing Residue From Steel Tempered
24 Hours at 800°F^a

5 to 10 min.	10 to 15 min.	15 to 20 min.	20 to 25 min.
17. mg. Fe	2. mg. Fe	0.4 mg. Fe	—
2.7	0.15	0.13	0.11 mg. Fe
3.2	0.44	0.13	0.12
5.4	0.62	0.57	0.11
1.5	0.62	0.20	0.25
28.5	3.8	0.12	0.075
35.1	1.6	0.17	0.075

a. Weight of residue varied from 0.6 to 0.7 grams. Volume of alcohol wash varied from 15 to 25 cc. for each 5 minute period. First 5 minute wash was discarded.

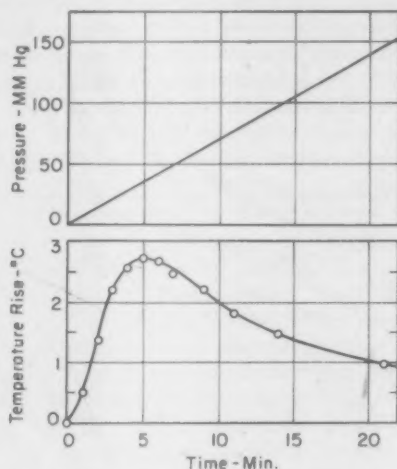


Fig. 3—Temperature Rise of Residue (800 °F Temper, 24 Hours) Upon Slow Admission of Air to Evacuated Desiccator.

Stabilizing by Slow Oxidation

To be weighed and analyzed at all conveniently a residue must be dry and exposed to air. It occurred to us that if the residue were oxidized very gradually it would not heat up and burn, and, moreover, the thin oxide film on each particle would make the residue relatively stable in air and alter the analysis only to a minimal extent. Accordingly, a copper-constantan couple was sealed into the lid of a vacuum desiccator so that the temperature of the residue could be followed during exposure to air. The couple was made of extremely fine wire to minimize the conduction of heat away from the junction. A manometer was also connected to the desiccator. The procedure was to place a fritted crucible, containing a residue moist with alcohol, into the desiccator, replace the lid with the couple junction buried in the residue, and im-

mediately draw a vacuum with an aspirator pump. After a period of time air was admitted slowly through a constricted glass tube, and the temperature of the residue are measured as a function of time. The readings for a typical case are plotted in the lower part of Fig. 3. Pressure readings as a function of time serve to calibrate the constriction, and a portion of this curve, which is linear over a wide range, is also reproduced in Fig. 3.

The results on eleven residues using two quite different constrictions are summarized in Table VII, the first entry representing the data of Fig. 3. In some cases after initially pumping down with the aspirator, the evacuation was continued with an oil pump; this caused no noticeable difference in behavior. With use of the constrictions the rise in temperature was in every case small, and, in any case, was quite satisfactory as judged by: (a) the lack of any change in appearance of the residue during oxidation; and (b) the lack of any detectable analytical

Table VII
Temperature Rise of Residue from Steel Tempered at 800°F for 24 Hours
During Controlled Admission of Air to Evacuated Desiccator

Type of Pump for Evacuation	Time for Max. Temp. Rise	Max. Temp. Rise	Air Pressure at Max. Temp. Rise
Constriction A			
Oil	5 min.	2.7°C	35 mm.
Oil	5	2.2	35
Oil	5.5	12.2	37
Oil	3.5	7.2	34
Oil	4	2.1	27
Oil	4.5	2.1	31
Aspirator	4	5.8	27
Aspirator	7	2.4	47
Aspirator	8	0.8	56
Constriction B			
Oil	13.5	4.6	9
Aspirator	10	3.2	6

variation. The observed variation in temperature rise probably reflects the difference in extent of oxidation of the residues during washing, which was done in the open air, although with solvent cooling. A rapid admission of air a few minutes after the maximum temperature had been reached caused no appreciable rise in temperature. Also, admission of air a second time, after evacuation, gave no thermal effect. Moreover, it seemed to make no difference whether the air admitted to the desiccator was dried or not. The temperature rise was independent of the time the residue was stored in vacuum, at least from $\frac{1}{2}$ hour to 60 hours, showing that storage in vacuum, after evaporation of alcohol from a wet residue, is quite protective.

The results above indicate that a residue is oxidized to a slight and somewhat variable degree during the normal extraction and washing procedure used. The rapid and detrimental further oxidation upon ex-

posure of the dried residue to air can be effectively reduced by the technique described. During oxidation under conditions which prevent overheating, the residue acquires a thin, but protective, oxide film in a very short time and at very low oxygen pressure. Although for the residues tested both constrictions A and B seem suitably fine, other coarser constrictions gave considerably more heating and were rejected. It is possible that a more finely divided residue would require a finer constriction, but perhaps the unavoidable preoxidation during extraction and washing would eliminate the necessity of this.

To determine the extent of oxidation of a residue during controlled exposure to air the following experiment was performed. A crucible was fitted, bottom and top, with rubber stoppers and a length of fine capillary inserted through the top stopper. This crucible containing a wet residue from steel tempered 24 hours at 800 °F, with stoppers in place, was put in the desiccator and evacuated. Now purified nitrogen instead of air was admitted and the dry residue weighed in nitrogen. Air was kept out of the capillary by the technique of bringing the crucible into the air still slightly cool from alcohol evaporation, and taking the weight just previous to the time of temperature equilibration. The crucible was replaced in the desiccator, evacuated, and air admitted through constriction A in controlled manner. The increase in crucible weight, allowing for difference in buoyancy of nitrogen and air, is the weight of oxygen picked up by the residue. In one case it was 11.6 milligrams per gram of residue, and in another, considered better, it was 15.7 milligrams per gram. If we consider the particles to be uniform in size and to have an average diameter of about 0.06 microns, as indicated by electron micrographs of such a residue, the area per gram comes out to be 1.4×10^5 square centimeters. Dividing the above weight increase, 15.7 milligrams, by this area we calculate the oxygen uptake of the carbide as 0.12 micrograms per square centimeter, a figure about one-third that obtained upon exposure of a reduced, rolled steel surface to air. The difference may reflect the different response of carbide and iron to the same treatment or, more likely, it may be largely due to the fact that the carbide was already partially oxidized by previous treatment when weighed in nitrogen.

Oxidation During Storage

After controlled exposure to air, described above, several residues from the steel tempered 24 hours at 800 °F were stored under different conditions at room temperature and the further oxidation following by observing the gain in weight. The results for some typical samples are shown in Fig. 4. A residue stored in the atmosphere oxidized more rapidly than one kept in a desiccator which was opened frequently for weighing, and this in turn more rapidly than one kept in an unopened desiccator. As mentioned previously, samples stored in

vacuum, at least up to 60 hours, did not oxidize appreciably, as judged by the rise in temperature upon controlled exposure to air.

On the type of plot shown, weight gain against square root of time, a straight line is obtained if the oxidation process is controlled by diffusion through an oxide film whose character does not change with time. None of the cases in Fig. 4 follow such a law, particularly in view of the fact that, for such a comparison, the zero on the ordinate scale

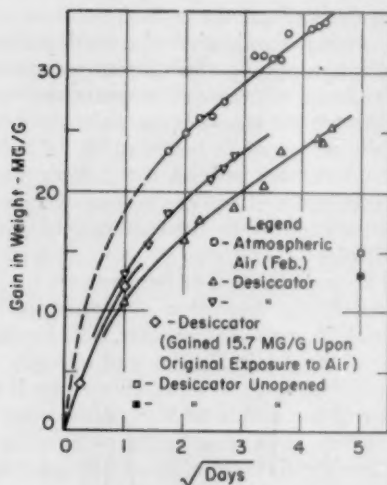


Fig. 4—Gain in Weight, after Original Exposure to Air, of Residues from Specimens Tempered at 800 °F During Storage in Air under Various Conditions.

should be depressed to pertain to the reduced material. After an initial transient period of about two days, the oxidation is approximately parabolic, i.e., linear with square root of time.

The curves of Fig. 4 are very similar to those of Winterbottom (2), who measured the extent of oxidation of iron in air by the polarized light method of determining film thickness. He found an almost instantaneous growth of a 20 Å film of magnetite, equivalent to 0.29 micrograms of oxygen per square centimeter, upon exposure to air at 20 °C. For our residue with 0.06 micron average particle size this same film would give a weight increase of 40 milligrams per gram of residue (to be compared with our value of 15.7 milligrams, which is admittedly too low.) After 20 days at 20 °C the film had grown to about 38 Å, which, for our residue, would correspond to an additional weight increment of 36 milligrams per gram. This is of the same order as our weight increase. Winterbottom's curves also indicate parabolic oxida-

tion after about 2 days, and he also finds moisture in the air to increase the rate of oxidation. The latter fact is somewhat surprising in view of the fact that no water is incorporated in the oxide.

From the above it appears that the best way to store a residue previous to analysis is in vacuum—specifically, the original vacuum in which the residue is dried after washing. Then when further work is to be done on the residue, it can be slowly exposed to air with the formation of the minimum film necessary to make it stable to air. The thickness of the magnetite film on the particles from such a treatment is of the order of 20 Å, and is, no doubt, quite reproducible. A procedure almost as good for most purposes would be to store it in air in a desiccator, in which case the film would increase by about 3 to 7 Å during the first 24 hours, and by about 7 to 15 Å during the first 25 days, depending upon the dryness of the air. The residues reported in this paper were stored in air in a desiccator, opened periodically to admit others, for periods from a few hours to about a month.

EFFECT OF A VARIATION IN TEMPERING TEMPERATURE

Results from Table I on all normal aqueous iodide extractions from steels tempered 24 hours at temperatures from 700 to 1300 °F are summarized in Table VIII. Aqueous iodide extraction was considered best because it gave the least total decomposition of carbide. In Table VIII the carbide composition is computed after correcting the manganese content for that combined with sulphur, using the sulphur recovery factor of 0.80, as outlined in Table V and the discussion thereof. Other quantities are computed as described in Table V.

With higher tempering temperature the carbide particles are larger and, therefore, less subject to decomposition. The results shown at the top of Table VIII indicate the capability of the aqueous iodide method under favorable circumstances. As the tempering temperature is lowered, decomposition increases, particularly below 900 °F, the two types keeping pace with each other, for the most part. The extent of contamination of the residue also increases, and in a smooth manner. It is interesting to note that only in the case of a specimen tempered below about 800 °F does the total percentage of carbide decomposition exceed the sulphide decomposition, 20%, assuming, of course, that all sulphur in the residue is sulphidic.

Some of the results from Table VIII are plotted against tempering temperature in Fig. 5. Total decomposition of carbide is the sum of the two types tabulated. Although some lack of consistency is evident, the trends are quite definite. As expected, carbon content, total carbide decomposition, and residue contamination all increase with lower tempering temperature, the change being more pronounced below, say, 1000 °F. The maximum in the curve for manganese content is readily explainable as follows. As it precipitates during quench, the carbide has

Table VIII
Testing of the "Normal" Aqueous Iodide Extraction Method on Specimens of the
Steel Tempered 24 Hours at Each of Several Tempering Temperatures^(a)

Tempering Temp., °F	Ave. Analysis of Residue		% Mn corr. for MnS ^(b)		Sum corr.	Carbide Comp.		C Yield %	Carbide decomposed to carbon %	Carbide completely decomposed %	Contamination %
	% C	% Mn	% Fe	% Mn	% C	% Mn	% Fe				
1300	6.47	5.55	85.7	4.92	97.1	6.67	88.3	99.9	-0.3	0.1	1.9
1200	6.42	5.55	84.4	4.92	95.7	6.70	88.2	99.5	0.1	0.5	3.3
1100	6.64	6.62	84.4	5.99	97.0	6.85	87.0	101.2	2.4	-1.2	2.0
1000	6.50	5.65	84.5	5.00	96.0	6.77	88.0	96.3	1.1	3.7	3.0
900	6.57	5.91	85.1	3.24	94.9	6.93	89.7	96.4	3.3	3.6	4.0
800	6.80	2.64	82.9	1.91	91.6	7.33	90.6	91.1	8.0	8.9	7.2
700	7.22	1.93	81.8	1.14	90.2	8.00	90.7	89.5	14.7	10.5	8.5

^(a) This tabulation is based on the average of the data on all runs in the first group at each tempering temperature in Table I. A description of "normal" extraction conditions, as well as of the several column headings will be found in footnotes to Table V.

^(b) Calculated as described in Table V.

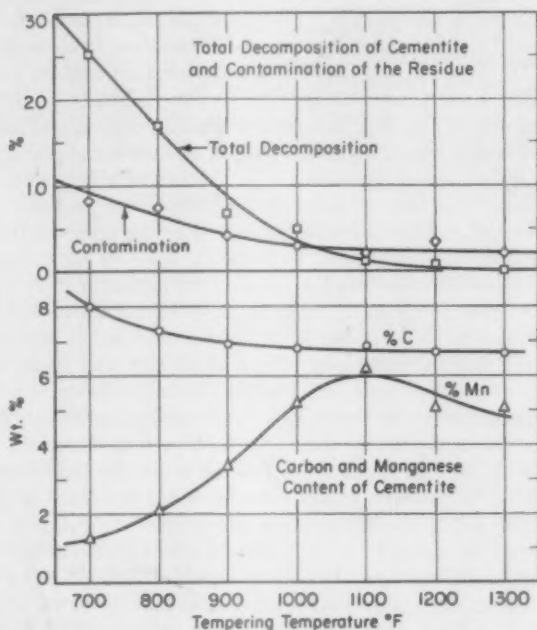


Fig. 5—Results on Application of Aqueous Iodide Extraction Method to 0.45% Carbon, 0.80% Manganese Steel Tempered 24 Hours at Various Temperatures. Data from Table VIII.

a manganese-iron ratio approaching that in the original steel, which, in the present case, would correspond to about 0.8% manganese in the carbide. During tempering the carbide picks up manganese by diffusion, and the higher the temperature the more will be picked up in the 24 hours, so long as the equilibrium value is not approached. At about 1100 °F and higher the 24-hour period is sufficient for the equilibrium manganese content to be nearly reached and, accordingly, the values found in this range reflect the fact that the equilibrium values decrease with rising temperature. This has been verified in another investigation, to be published.

For the most part, the residues consist of carbide, sulphide and soot, and, to the extent that they do, we consider them free of contamination. Attempts to dry the residue by heating in air at 230 °F resulted only in a slight increase in weight due to oxidation, indicating the original moisture content to be nil. Residues from electrolytic extraction are generally found to contain a considerable percentage of silica or silicic acid resulting from oxidation and hydration of the silicon in the steel during extraction. The percentage of silica in the residue due to non-

metallic inclusions in the steel is usually very small. Four of the residues, extracted by the normal aqueous iodide method from steel tempered at 900 °F, were analyzed for silica and cadmium, and the content found to be nil in every case. This freedom from silica is particularly surprising in view of the fact that, in the final technique evolved, the residue is not washed with alkaline solution to remove silicic acid, as is the commonly accepted procedure. The absence of silica in our residues may be due to a low anodic operating potential accompanying the use of a high concentration of iodide anions, or to the essential freedom of our electrolyte from dissolved oxygen. In spite of these negative results, silica must be considered a possible contaminant with the use of some electrolytes, particularly the more acid ones or those with a low halide concentration. With a cupric catholyte, not used in the experiments reported here, a small percentage of copper was found in the residue. A major contaminant, and one that is unavoidable, is oxygen. A 20 Å film of magnetite on the residue from steel tempered at 800 °F, assuming the average particle size to be 0.06 μ , would amount to an oxygen impurity of 4%. Even for a residue from the steel tempered 24 hours at 1300 °F, whose average particle size is about 0.4 μ (giving an area of 2.0×10^4 centimeters square per gram), at 20 Å film would contribute 0.6% of oxygen. It is probable that, after storage for a month, the total percentage of oxygen would be about twice these values. For the residues from steel tempered at 800 °F, as summarized in Table VIII, carbon, manganese and iron total 92.3%; including sulphur, the sum is 92.8%. Of the remaining 7.2%, a large fraction is thus probably attributable to oxygen. The residues from steel tempered at 1300 °F total, with sulphur, 98.1%, and again it appears that oxygen is probably the major contaminant.

In the oxidation of carbide during exposure to air and during storage the question arises as to what happens to the carbon. If carbon is lost from the residue a decrease in the carbon to iron ratio will accompany oxidation. Our ability to determine this is poor. In the first place, a large fraction, probably over 50%, of the oxidation occurs during initial exposure to air and before any analysis can be made. Secondly, a small variation in the carbon content is not discernible with certainty since the accuracy of this determination is not high. After three years storage in a desiccator, each of two residues from the steel tempered 24 hours at 900 °F was found to have decreased in carbon to iron ratio by about 1%. This is, of course, within analytical error, but, if real, signifies a slight loss of carbon during oxidation. In any case, the carbon loss during a reasonable storage period is negligible, and, therefore, the relative proportions of carbon, iron, and manganese are not affected. As far as the usual chemical analysis is concerned, then, oxidation of a residue results only in an increase in oxygen content (contamination) and a corresponding decrease in the percentage of each of the other constituent elements.

SUMMARY

In studying the effect of a variation in extracting conditions it is desirable to employ a steel whose carbide particles are fine enough to undergo appreciable decomposition. Thus, the resulting differences in amount and composition of the residue are made greater and subject to more accurate evaluation. In the development work reported in this paper, repetitive extractions were carried out on a 0.45% carbon, 0.80% manganese steel made martensitic and then tempered 24 hours at 900 °F; residues were quantitatively recovered and chemically analyzed. A simple but effective apparatus and technique were developed for the electrolytic extraction of carbide from carbon steel.

An electrolyte consisting of an aqueous solution of cadmium iodide was found to give a minimum of decomposition. With the iodide solution and with other conditions optimum, this constituting our so-called "normal" iodide method, only 6.9% of the fine carbide in the above described steel was decomposed. With bromide solution the decomposition was twice as much, and with chloride, three times as much. The Klinger and Koch citrate electrolyte gave about three and a half times the decomposition of the iodide, and 5% by weight HCl over eight times. Extraction in anhydrous alcoholic solution more than doubled the decomposition. The iodide was also quite insensitive to a large variation in current density.

A hammering device was found to be very effective in preventing the accumulation of a carbide layer upon the anode during extraction. Failure to use this resulted in two and a half to five times the carbide decomposition, depending upon the electrolyte. The amount of impurity in the residue was quite small. The chief source of contamination was oxidation subsequent to extraction, and this was minimized by an effective procedure in which the residue is exposed to air slowly, under controlled conditions.

The iodide extraction method was tested on a series of specimens of the same steel, tempered over a range of temperature. The extent of carbide decomposition varied in a continuous manner, from nil for a 24 hour tempering at 1300 °F to 25.2% for a 24 hour tempering at 700 °F.

References

1. P. Klinger and W. Koch, "Beitrag zur electrolytischen Bestimmung von nichtmetallischen Einschlüssen im Stahl," *Archiv für Eisenhüttenwesen*, Vol. 11, 1937/38, p. 569.
2. A. B. Winterbottom, "Optical Studies of the Oxidation of Iron at Temperatures in the Range 20-265 °C," *Journal, Iron and Steel Institute*, Vol. 165, May, 1950, p. 9.

DISCUSSION

Written Discussion: By L. J. E. Hofer, chief, Physical and Catalytic Chemistry Section, Branch of Coal-to-Oil Research, U.S. Bureau of Mines, Pittsburgh.

This extensive study of the preparation of carbide extracts from carbon steel is indeed welcome. Electrolytic extraction has in the past been mainly "rule of thumb," and the effects of procedural variables on the results were largely unknown. The data presented show that real confidence may be placed on the results, even when the carbides are in a high state of subdivision, if the indicated precautions are taken. The reviewer suggests only that powder diffraction data on the extracts would improve the paper and would prove beyond doubt that extracts are truly iron carbides and not mixtures of iron carbide, free carbon, and iron. In specimens tempered at the low temperature ranges, it is quite possible that carbides other than cementite will be present. This in itself would be of interest.

The paper opens several new fields of inquiry. Among these may be mentioned the concentration of alloying elements in the carbide phase. The authors already have obtained some provocative data showing the concentration of manganese in the carbide phase. The concentration during 24-hour tempering in a 0.45% C steel is about 8.1-fold at 1300 °F and 3.1-fold at 800 °F. This technique will also lead itself to the determination of various phases in the tempering sequence. Recently Okada² has published data on iron carbide extracts in which the χ -iron carbide phase seems to be identified quite unambiguously by both powder diffraction analysis and Curie point. Such results could have been obtained only with difficulty without the concentrating effect of electrolytic extraction.

Authors' Reply

We wish to thank Dr. Hofer for his kind remarks. With reference to diffraction measurements, we, of course, did subject the residues to X-ray and, in some cases, to electron diffraction. The resulting patterns showed: (a) the complete absence of metallic iron in all residues, and (b) the presence of cementite as the only carbide phase in specimens tempered at 700 °F and above. The carbide phases in the untempered specimens and those tempered at 210 °F were not identified.

As regards the use of the extraction method, we have applied it to steels of different manganese content tempered at various times and temperatures. Measurements performed on the residues have yielded an analysis of size distribution as a function of tempering conditions, the equilibrium distribution coefficient of manganese between cementite and ferrite as a function of temperature and manganese content of cementite, and the Curie Point of cementite as a function of manganese content. These results are in process of publication.

² Okada, Minoru, "Some Fundamental Researches in Welding Metallurgy of Steel," Department of Welding Engineering, Osaka University, 1955.

EFFECT OF MANGANESE ON THE CURIE POINT OF CEMENTITE

BY EARL C. ROBERTS

Abstract

By determining the curves showing the gradual loss of cementite ferromagnetism with temperature for three series of annealed steels, a generalized graph relating the Curie temperature of the cementite to the manganese content of the cementite has been drawn. The manganese content for the cementite was determined by chemical analysis of the extracted residue from the steels. It is shown that the percent manganese in the cementite of an annealed steel is a function of both the manganese and carbon percentages of that steel. Empirical equations are presented to show the relationship between the manganese content of the cementite (a) the manganese content of the steel, (b) the manganese content of the ferrite phase, (c) the Curie temperature of the cementite. (ASM International Classification: P16d, 2-10; ST, Mn)

SINCE Karsten (1)¹ first reported isolating a "carboniferous compound" in 1824, investigations pointed towards a better understanding of the nature and behavior of cementite in ferrous materials are too numerous to mention, and good review articles are available (2,3). Studies of the alloying of cementite with manganese seem to have started with Arnold and Read's (4) investigation in which the carbides in manganese-bearing steels were extracted by electrolysis and analyzed chemically. Their conclusion was that the weight percent manganese in the cementite varied linearly with the weight percent manganese in the steel, the concentration ratio being about 5 to 1 for steels with manganese contents of less than 4%. Later work by Maurer and Hartmann (5) and more recently by Houdremont, Koch and Wiester (6) also indicated linear variations in the manganese percentages but suggested a 4:3 and 4:1, respectively, for the cementite manganese to steel manganese ratio.

Jacobson and Westgren (7) indicated that manganese reacts with carbon to form Mn_3C which is isomorphous with Fe_3C and forms a continuous series of solid solutions with it. Yoshisaki's recently re-

¹ The figures appearing in parentheses pertain to the references appended to this paper.

A paper presented before the Thirty-Ninth Annual Convention of the Society, held in Chicago, November 4-8, 1957. The author, Earl C. Roberts, is Associate Professor, Metallurgical Engineering, University of Washington, Seattle 5, Washington. Manuscript received October 16, 1956.

ported work (8) indicates that Arnold and Read's suggested double compound ($3\text{Fe}_3\text{C} \cdot \text{Mn}_3\text{C}$) occurring in steels containing more than 4% manganese is questionable, and a continuous intermetallic solid solution apparently is formed. This same conclusion was reached by Cheve-nard and Portevin (9) in 1925 from studies of approximately 4.5% carbon, manganese-bearing cast irons.

Since P. Curie's (10) determination of the variation in magnetic intensity of iron with increasing temperature, it has been discovered that cementite shows an analogous temperature dependence on change of magnetic intensity (11). The familiar A_0 of the iron-cementite equilibrium diagram, which is called the Curie temperature of cementite, has been determined from the magnetic intensity-temperature curve.

A number of alloying elements and particularly carbide forming elements are known to replace iron in the cementite lattice (12) and to change the Curie temperature of the cementite. Until now this has been done for manganese-bearing cast irons (8,9) manganese steels transformed to pearlite and bainite (13) but apparently not for steels in the fully annealed or spheroidized condition.

EXPERIMENTAL PROCEDURE

One high purity iron-carbon alloy (14) and three series of steels of different carbon percentages were chosen as specimen sources. (See Table I.) Each series was relatively constant with respect to the man-ganese percentage and all steels had been especially prepared so as to

Table I

Specimen Number	Analysis of Steels					Analysis of Cementite			% Mn		Curie Temp., °F
	% C	% Mn	% P	% S	% Si	% Mn	% Fe	% Mn	% Fe		
0M-1	0.96	*	*	*	*	—	—	0	0	406	
3M-1	0.72	0.27	0.021	0.023	0.22	1.60	83.8	1.88	328		
3M-2	0.93	0.27	—	—	0.29	1.25	86.5	1.42	362		
3M-3	1.07	0.25	0.011	0.014	0.23	1.25	84.5	1.46	364		
5M-1	0.25	0.57	—	—	—	3.28	80.2	3.93	286		
5M-2	0.75	0.50	0.007	0.020	0.27	2.68	84.8	3.06	307		
5M-3	0.94	0.47	0.013	0.030	0.21	1.98	84.2	2.30	321		
5M-4	1.13	0.59	0.006	0.018	0.24	2.25	84.5	2.60	328		
5M-5	1.37	0.52	0.006	0.017	0.28	1.95	86.1	2.21	332		
8M-1	0.16	0.81	0.011	0.024	0.05	5.00	76.5	6.14	206		
8M-2	0.20	0.93	0.012	0.036	0.26	6.95	72.3	8.76	137		
8M-3	0.49	0.83	0.010	0.039	0.21	4.60	78.9	5.51	233		
8M-4	0.53	0.87	0.015	0.028	0.29	5.16	77.9	6.21	193		
8M-5	0.84	0.80	0.009	0.026	0.24	3.28	82.5	3.82	265		
8M-6	0.98	0.98	0.018	0.032	0.19	3.20	83.5	3.69	281		

*Silicon and Oxygen <0.01% others <0.001%

have a minimum residual alloy content. All analyses were made on chips from the bar stock used. A piece from each steel was machined to a cylindrical specimen 3 inches long with a 0.240 (± 0.001) inch diameter to provide uniformity for magnetic testing. A small diameter

hole, $\frac{3}{4}$ inch in depth, was drilled into one end of each specimen to allow the introduction of the (Pt-Pt-10% Rh) thermocouple used to determine the specimen temperature.

If either the cementite is very fine or the steel is in a cold-worked condition, variations in the Curie temperature are found (15). In order to avoid difficulty from these effects and to achieve as close to an equilibrium state in the steels as possible, each specimen of steel, following machining and cleaning was sealed in an evacuated glass tube and annealed for 100 hours at 1200 °F. This is well within the time-temperature range used by Bain, Davenport and Waring (16) in their studies of the iron-manganese-carbon equilibrium diagram.

Magnetic measurements were made on the steels using the magnetometer of a combination magnetometer-dilatometer that has been previously described (17). A constant applied field strength of 300 gauss was used. This rather low field strength was used, as greater sensitivity in Curie temperature determinations has been found with low field strengths than with high (18).

Following these measurements the specimens were made the anodes in a modification (19) of a special double electrolytic cell containing a neutral anolyte solution (20). In all specimens except one, more than 90% of the amount of cementite present in the steel (as calculated from the carbon percentage of the steel) was obtained by electrolysis.

EXPERIMENTAL RESULTS AND DISCUSSION

The summarizing plots of magnetic deflection versus temperature curves for the three series of steels and for the high purity iron-carbon alloy are shown in Figs. 1, 2, 3 and 4. The experimental points shown in the latter figure have not been included on the other graphs for the sake of clarity. Each curve represents the best average plot of the data obtained by first slowly heating (~ 5 °F/min.) the specimen to above the cementite transition and then slowly cooling back to room temperature. The data of Fig. 4 was taken primarily to establish a singular Curie temperature for high purity cementite. This is usually given as 210 °C (410 °F).

The method of Curie temperature selection used is shown in Fig. 1 on the curve obtained for specimen 3M-1. This simply involved the location of an intersection between a line coincident with the main slope of the curve and a second line extrapolated back from the constant value reached when the ferromagnetic to paramagnetic conversion of the cementite is complete.

Tested by application to the high purity cementite curve, this method gave a value of 406 °F (208 °C). This temperature thus closely corresponded to the quoted value and for the purposes of this investigation represented a more accurately located reference point than if the latter had been arbitrarily selected.

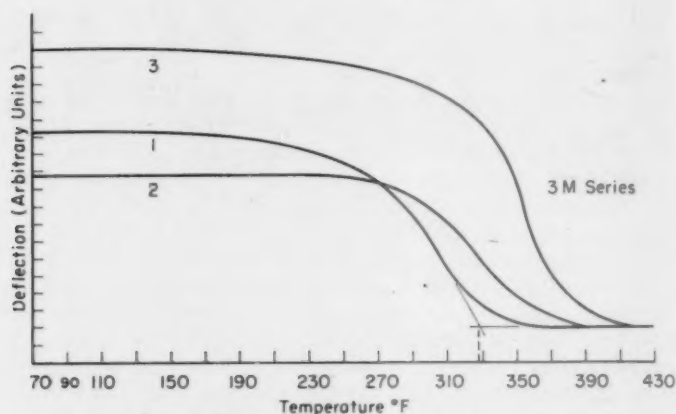


Fig. 1—Magnetometer Deflection Versus Temperature Plots for Steels Containing Approximately 0.3% Manganese.

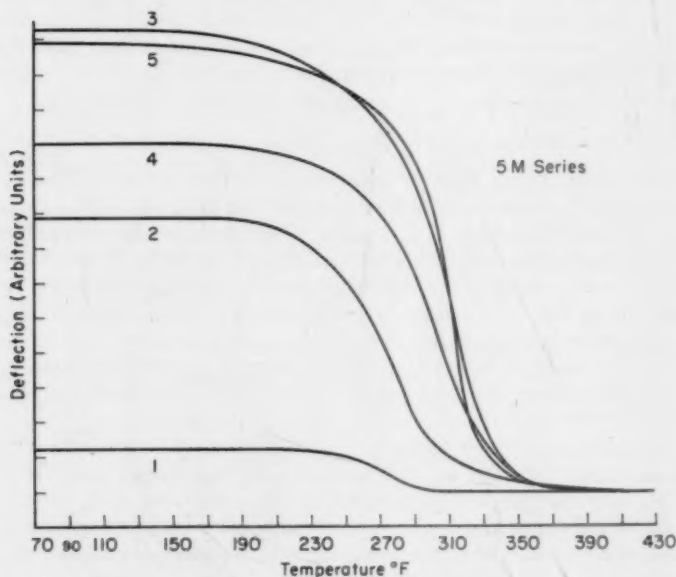


Fig. 2—Magnetometer Deflection Versus Temperature Plots for Steels Containing Approximately 0.5% Manganese.

Fig. 5 is a plot showing the relationships between the determined Curie temperature of the cementite and the manganese content of the carbide. Relatively little difference was found if the analyzed cementite

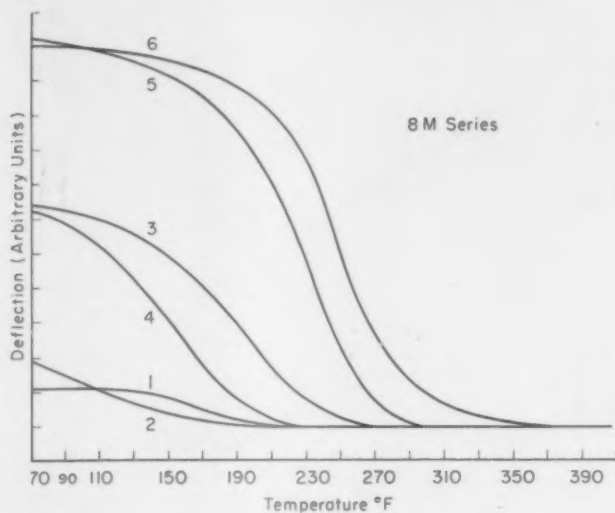


Fig. 3—Magnetometer Deflection Versus Temperature Plots for Steels Containing Approximately 0.8% Manganese.

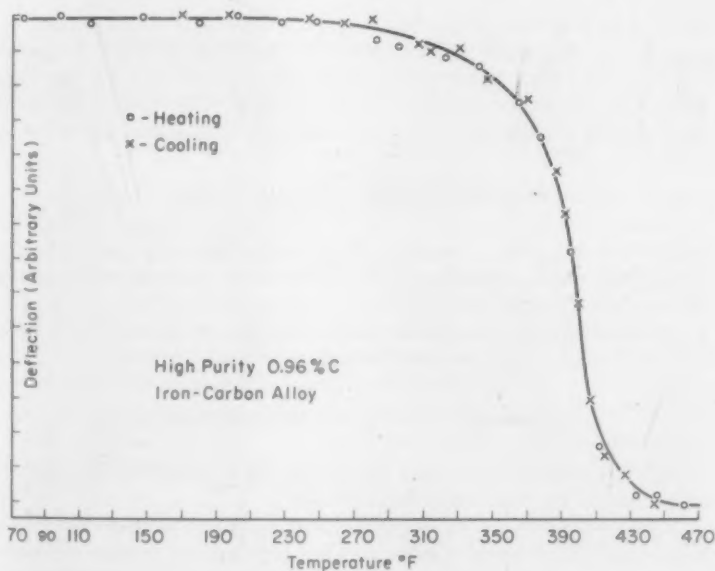


Fig. 4—Magnetometer Deflection Versus Temperature Plot for High Purity Iron—0.96% Carbon Alloy.

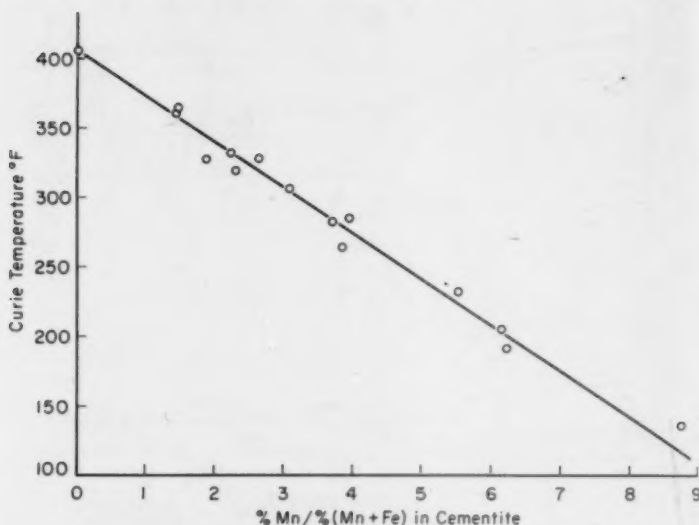


Fig. 5—Change in Curie Temperature (°F) with Increasing Weight Percentages of Manganese in the Cementite.

manganese contents or the ratio of the weight percent manganese to total metal ion weight percentage in the cementite were plotted. This latter factor better represented the factors contributory to the magnetic behavior, as the calculated carbon content of the cementite varied only slightly (Equation 1) for the range of manganese values in the specimens studied.

$$\text{Wt.\% C in carbide} = 6.680 + 0.0011 (\text{Wt.\% Mn in carbide})$$

Equation 1

Equation I applies for manganese contents between 0 and 50%, the latter being the composition point where more complex carbides may possibly enter the picture (3).

The relationship between the Curie temperature in degrees Fahrenheit and the analyzed percent manganese in the cementite is given by Equation 2:

$$\text{Curie Temp. (°F)} = 406 - 39.3 (\text{Wt.\% Mn in cementite})$$

Equation 2

This simplified expression allows an approximate calculation if either one of the two variables is known.

A possibly more fundamental relationship exists between the Curie temperature in degrees Kelvin and the ratio of the number of manganese atoms to the total number of metallic atoms per atom of carbon. This is shown in Fig. 6.

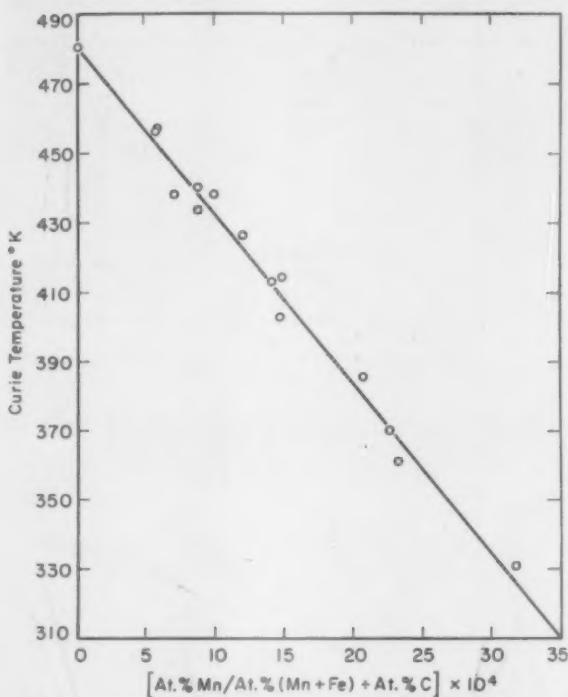


Fig. 6—Change in Curie Temperature (K) as a Function of the Atomic Percentages of Manganese and Carbon in the Cementite.

Of some practical importance is the relationship between the percentages of manganese in the steel and manganese in the cementite. Although previously shown as a straight line (4,5,6), the data obtained in this investigation indicate that a curvilinear relationship is followed. A very marked dependence on the percent carbon in the steel was also observed. The Mn (steel)/Mn (cementite) relationship obtained for the approximately 1% carbon steels and the corresponding Curie temperature/Mn (cementite) relationship are shown in Fig. 7.

By simple analysis it was found that, for the experimental results obtained in this work, the manganese percentage of the steel was related to the manganese percentage of the cementite by a parabolic expression:

$$\% \text{ Mn}_{(c)} = \sqrt{\% \text{ Mn}_{(s)} / k - A} \quad \text{Equation 3a}$$

The value of A was determined graphically and k was easily seen to be a function of the carbon percentage of the steel. The empirical ex-

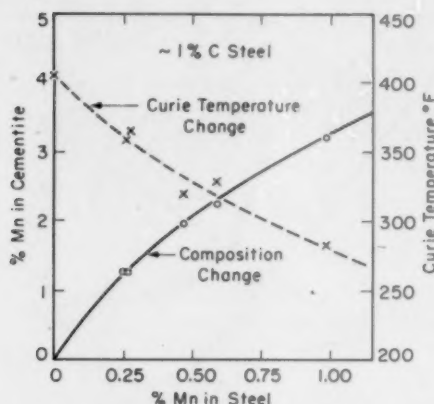


Fig. 7—Relationship Between the Percent Manganese in the Steel and both the Percent Manganese in the Cementite and Curie Temperature of the Cementite for Approximately 1% Carbon Steels.

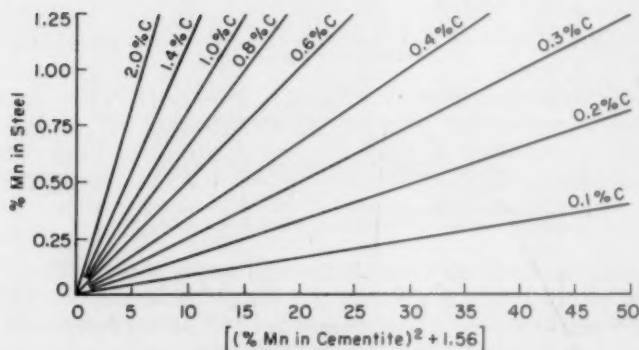


Fig. 8—Relationship Between Percent Manganese in the Steel and Percent Manganese in the Cementite for Steels of Various Carbon Content.

pression that best fitted the available data is given by Equation 3b.

$$\% \text{ Mn}_{(c)} = \sqrt{\% \text{ Mn}_{(s)} / 0.0833\% \text{ C}_{(s)} - 1.56} \quad \text{Equation 3b}$$

All percentages used in these equations are weight percentages.

A direct evaluation can be made by the use of the graph in Fig. 8. This graph has been drawn so as to cover only the limited data range available as a result of this research. Results from broader composition ranges will be necessary before its extension in two dimensions can be justified.

Table II
Calculated Cementite Manganese Percentages from Steel Manganese Percentages

Specimen Number	% Manganese in Cementite (Analyzed)	% Manganese in Cementite (Calculated)
3M-1	1.60	1.71
3M-2	1.25	1.39
3M-3	1.25	1.16
5M-2	2.68	2.54
5M-3	1.98	2.10
5M-4	2.25	2.17
5M-5	1.95	1.73
8M-2	6.95	7.35
8M-3	4.60	4.68
8M-4	5.16	4.26
8M-5	3.28	3.14
8M-6	3.20	3.24

Table III
Calculated Cementite Manganese Percentages from Ferrite Manganese Percentages

Specimen Number	% Manganese in Ferrite	% Manganese in Cementite (Analyzed)	% Manganese in Cementite (Calculated)
3M-1	0.119	1.60	1.73
3M-2	0.104	1.25	1.42
3M-3	0.074	1.25	1.14
5M-2	0.240	2.68	2.40
5M-3	0.239	1.98	2.16
5M-4	0.261	2.25	2.04
5M-5	0.186	1.95	1.56
8M-2	0.808	6.95	8.51
8M-3	0.536	4.60	4.44
8M-4	0.525	5.16	4.22
8M-5	0.466	3.28	3.16
8M-6	0.610	3.20	3.34

Table II shows the results of the application of this equation to the experimental data. Although in one instance the application resulted in an error of about 18% for the calculated value as compared to the analytical result the overall error is only about 6%. It should be pointed out that the silicon percentage of the steel seemed quite important. In the two specimens for which the equation failed, the silicon percentage was either low or undetermined. Fortunately, in most of the specimens, the silicon percentages varied between 0.19 to 0.29% and therefore were practically within the normal range for steels; e.g., 0.20 to 0.35%.

The obtaining of a reasonably satisfactory relationship between the cementite manganese and the total manganese of the steel suggested that an analogous expression might be obtained for the distribution of manganese between the ferrite and cementite phases of the steel.

Since a detailed record of the weights of the specimens before and after electrolysis and the weights of cementite obtained from them was kept, the ferrite manganese percentages were easily calculable. Such

percentages can be related to the cementite manganese percentages by Equation 4.

$$\% \text{ Mn}_{(c)} = \sqrt{\% \text{ Mn}_{(f)} / 0.0556\% \text{ C}_{(a)}} \quad \text{Equation 4}$$

Fig. 9 shows the graphic evaluation of this equation. Table III shows the calculated versus analyzed percentages of manganese in the cementite assuming that the weight percent ferrite is known.

The results given for the calculated percentages of manganese in

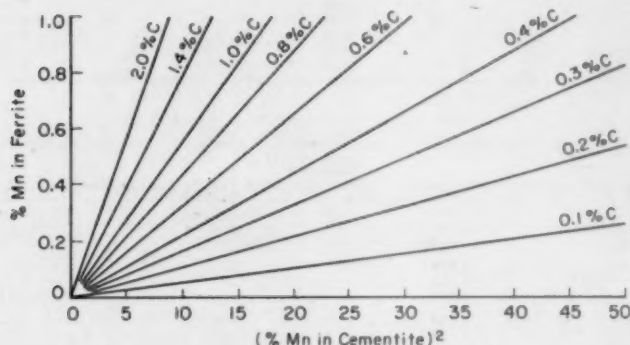


Fig. 9—Relationship Between Percent Manganese in the Ferrite and Percent Manganese in the Cementite for Steels of Various Carbon Contents.

the carbide in Table III are not within the limits of accuracy of the similar data in Table II. This is to be anticipated as some error undoubtedly enters in the calculation of the percent manganese in the ferrite.

CONCLUSIONS

1. A linear relationship exists between the Curie temperature and (a) the manganese content of the cementite, (b) the percent manganese over total metal ion percentage of the cementite in annealed steels. The Curie temperature decreases as the cementite manganese increases.

2. The data indicate a relationship between the manganese percentage in the cementite and (a) the manganese content of the steel, (b) the percent manganese in the ferrite phase. Empirical equations developed from limited experimental data allow calculations to be made. The results so obtained compare favorably with those obtained from chemical analysis.

ACKNOWLEDGMENT

The author wishes to express his thanks to Dr. Morris Cohen, Professor of Physical Metallurgy at Massachusetts Institute of Tech-

nology, for initially suggesting the problem and for advice and encouragement during the investigation.

References

1. K. Karsten, "On the Carbides of Iron," *Archiv fur Bergbau und Huttenwesen*, Vol. 8, 1824, p. 3.
2. J. B. Austin, "The Effect of Changes of Condition of Carbides on Some Properties of Steel," *TRANSACTIONS, American Society for Metals*, Vol. 38, 1947, p. 28.
3. H. J. Goldschmidt, "The Structure of Carbides in Alloy Steels," *Journal, Iron and Steel Institute*, Vol. 160, 1948, p. 345.
4. J. O. Arnold and A. A. Read, "The Chemical and Mechanical Relations of Iron, Manganese and Carbon," *Journal, Iron and Steel Institute*, Vol. 81, 1910, p. 169.
5. E. Maurer and F. Hartmann, "On the Quantitative Determination of Iron Carbides in Plain Carbon Steel," *Zeitschrift fur Anorganische Chemie*, Vol. 136, 1924, p. 75.
6. E. Houdremont, W. Koch and H. J. Wiester, "On the Processes of Transformation in Chromium and Manganese Steels," *Archiv fur das Eisenhuttenwesen*, Vol. 18, 1945, p. 147.
7. B. Jacobsen and A. Westgren, "On Nickel Carbide and its Relation to the Other Carbides of the Series of Elements Scandium-Nickel," *Zeitschrift fur Physikalische Chemie*, Vol. 20, Series B, 1933, p. 316.
8. H. Yoshisaki, "On the Carbides in Manganese Steels," *Science Reports of Tohoku University*, Vol. 6, Series A, No. 5, 1954, p. 469.
9. P. Chevenard and A. Portevin, "Dilatometric Analysis of Alloys," *Revue de Metallurgie*, Vol. 22, 1925, p. 361.
10. P. Curie, "Magnetic Properties of Materials at Various Temperatures," *Annales de Chemie et de Physique*, Vol. V, Series 4, 1895, p. 289.
11. K. Honda and T. Murakami, "On the Thermomagnetic Properties of the Carbides Found in Steels," *Science Reports of Tohoku Imperial University*, Vol. 6, 1917, p. 23.
12. C. S. Barrett, *Structure of Metals*, 2nd Edition, 1952, p. 247, McGraw-Hill Co., New York.
13. F. Wever and K. Mathieu, "On the Transformations of Manganese Steels," *Mitteilungen, Kaiser Wilhelm Institut fur Eisenforschung*, Vol. 22, 1940, p. 9.
14. Supplied by Dr. C. S. Roberts, formerly Research Assistant at Massachusetts Institute of Technology.
15. R. L. Sandford and C. A. Ellinger, "Thermomagnetic Analysis and the A. Transformation in 0.75 per cent Carbon Steel," *TRANSACTIONS, American Society for Steel Treating*, (American Society for Metals), Vol. 31, 1931, p. 83.
16. E. C. Bain, E. S. Davenport, and W. S. N. Waring, "The Equilibrium Diagram of Iron-Manganese-Carbon Alloys of Commercial Purity," *Transactions, American Institute of Mining and Metallurgical Engineers*, Vol. 100, 1932, p. 228.
17. O. Zmeskal and M. Cohen, "Simultaneous Measurements of Magnetic and Dilatometric Changes," *Revue of Scientific Instruments*, Vol. 13, 1942, p. 346.
18. O. Zmeskal, "The Tempering of High Carbon High Chromium Steels," Sc. D. Thesis, Massachusetts Institute of Technology, 1941.
19. E. C. Roberts, "Creep Properties of 4.5% Chromium Steels in the Annealed and Tempered Condition," Sc. D. Thesis, Massachusetts Institute of Technology, 1952.
20. D. J. Blickwede and M. Cohen, "The Isolation of Carbides from High Speed Steel," *Transactions, American Institute of Mining and Metallurgical Engineers*, Vol. 185, 1949, p. 578.

DISCUSSION

Written Discussion: By A. G. Molinder, chief metallurgist, Uddeholm Co., Munkfors Works.

In the column "Analysis of Cementite" in Table I the total metal ion content $\%Mn + \%Fe$ in no case reaches higher figures than 88%. Yet the author uses the analyzed manganese content as a measure of the manganese content of the carbide. It might have been better to use the expression

$$\%Mn_{(c)} = \frac{\%Mn_{(a)}}{\%Mn_{(a)} + \%Fe_{(a)}} \cdot (1 - 0.067) \quad (1)$$

where index (a) means analyzed metal ion content.

In a Fe-Mn-C-diagram the composition points for the ferrite, the cementite and the total steel analysis must lie on a straight line. Thus

$$(\%Mn_{(c)} - \%Mn_{(f)}) \cdot \frac{\%C_{(a)} - \%C_{(f)}}{\%C_{(c)} - \%C_{(f)}} = \%Mn_{(a)} \quad (2)$$

where $\%C_{(a)}$, $\%C_{(f)}$ and $\%C_{(c)}$ means carbon content of the steel, the ferrite (abt. 0.05%) and the cementite (abt. 6.67%) respectively.

Equation IIIb and IV in the paper do not follow this relationship.

It would be interesting to know if the author has looked for any other carbide than $(Fe, Mn)_3C$ in the steel investigated. The manganese contents of the cementite in the specimens 8M-1, 8M-2, 8M-3 and 8M-4 are so much higher than those of the specimens 8M-5 and 8M-6 that it can be suspected that an other carbide than cementite may be present.

Author's Reply

The author appreciates Mr. Molinder's interest and careful resumé of this work. In answer to his first remark, the equation submitted by Mr. Molinder is more accurate than that used by the author, but the additional correction factor is of relatively small significance for the major portion of the data. Admittedly this factor would become of increasing importance as the manganese content of the cementite increased, but in the range of compositions studied its use exerts little, if any, influence on the slope of the line in Fig. 5.

Equations IIIa, IIIb and IV are empirical determinations which seem to fit data reasonably well. The author wonders whether the complex equation suggested by Mr. Molinder might be carrying the mathematical analysis beyond the limits of experimental error—particularly for substances which are not pure Fe-Mn-C alloys.

In answer to the discussor's inquiry regarding the presence of other carbide phases, it can be reported that all the extracted residue from each of the steels was ferromagnetic at room temperature. This would indicate that other carbides, which should have developed under the conditions of heat treatment if they were stable phases, were either not present or were also ferromagnetic. The likelihood of the latter circumstance is very small.

MORPHOLOGICAL AND PHASE CHANGES DURING QUENCH-AGING OF FERRITE CONTAINING CARBON AND NITROGEN

By G. LAGERBERG AND B. S. LEMENT

Abstract

The quench-aging of a Fe-C alloy (0.016% carbon), a Fe-N alloy (0.084% nitrogen), and two Fe-C-N alloys (0.021% carbon, 0.028% nitrogen and 0.023% carbon, 0.011% nitrogen) was studied by means of light microscopy, electron microscopy, and electron diffraction. The following two-stage reactions were found to occur: ferrite supersaturated with carbon $\rightarrow \epsilon$ -carbide \rightarrow cementite; ferrite supersaturated with nitrogen $\rightarrow \alpha''$ -nitride $\rightarrow \gamma'$ -nitride; ferrite supersaturated with both carbon and nitrogen $\rightarrow \epsilon$ -carbonitride \rightarrow cementite. At relatively low aging temperatures, only the first stage was observed; whereas both stages occurred at intermediate temperatures. At relatively high aging temperatures, the first stage is apparently omitted and the final products form directly from ferrite. The early stage of precipitation was found to involve the formation of films at ferritic subboundaries corresponding to a subgrain size of 10^{-4} to 10^{-6} centimeters. These films may be due to segregation of solute atoms which migrate to the subboundaries. Rapidly localized thickening of these films and the eventual formation of platelets from the thickened portions was observed. The subboundary films disappeared in favor of the platelets before the start of the second stage. In Fe-C-N alloys, a higher nitrogen content apparently results in both greater stability of the ϵ -phase and a larger average particle size of the cementite phase. (ASM International Classification N7a; CN)

INTRODUCTION

QUENCH-AGING of mild steel is accompanied by marked changes in physical properties. These changes are now generally understood as being due to the decreasing solubilities of carbon and nitrogen

This paper is part of a thesis submitted by G. Lagerberg in partial fulfillment of the degree of Master of Science in Metallurgy (August 1955) Massachusetts Institute of Technology.

A paper presented before the Thirty-Ninth Annual Convention of the Society, held in Chicago, November 4-8, 1957. Of the authors, G. Lagerberg is associated with the Research Dept., Stora Kopparbergs Bergslags Aktiebolag, Domnarvret, Sweden, and B. S. Lement is associated with the Research Staff, Division of Sponsored Research, Department of Metallurgy, Massachusetts Institute of Technology, Cambridge, Massachusetts. Manuscript received February 18, 1957.

in ferrite with decreasing temperature. The respective solubility curves have been determined by various investigators (1-5).¹ On quenching ferrite, carbon and nitrogen are retained in supersaturated solution. During subsequent aging, the solute atoms are rejected from the solution in the form of carbides or nitrides.

During recent years the reactions occurring during quench-aging have been studied by means of various techniques. On the basis of internal friction measurements, it was reported by Dijkstra (3) and by Wert (6,7) that carbon precipitated as cementite in a single stage at all temperatures whereas nitrogen precipitated in two stages forming α'' -Fe₁₆N₂ (8) and γ' -Fe₄N successively. Possible evidence of a two stage process during carbon precipitation was later reported by Krisement (9) who observed a heat effect below 218-230 °C (425-445 °F) in making a calorimetric study of the carbon solubility in ferrite. He attributed this effect to ϵ -carbide formation mainly because Jack (10) demonstrated that this phase formed during the first stage of tempering of carbon martensite.² Tsou, Nutting, and Menter (12) in an electron diffraction study of an ingot iron containing 0.025% carbon and 0.006% nitrogen found that ϵ -carbide formed at 200 °C (390 °F) whereas cementite formed at 300 °C (570 °F) or higher.

Wert (6) was able to fit his internal friction data on the kinetics of the early stage of precipitation of carbon and of nitrogen to a Johnson-Mehl type equation. According to Zener (13), one of the parameters in this equation should be a function of the shape of the precipitated particles. If diffusion controlled growth alone is involved, the time exponent should be 3/2 for spheres and 5/2 for plates. Assuming a negligible incubation time, Wert obtained values of the time exponent that indicated that carbide particles precipitate as spheres whereas nitride particles precipitate as plates. Radavich and Wert (14) claimed to have confirmed this in an electron microscopic study. On the other hand Tsou, Nutting, and Menter (12) found electron microscopic evidence of plate-like carbides formed on aging ingot iron.

Not much is known about the nature of precipitates formed in ternary Fe-C-N alloys. Wert (15) reported that carbon and nitrogen precipitated simultaneously in specimens having the same concentration of both carbon and nitrogen in solid solution (0.015%), the rate of precipitation being the same as that of the element which precipitates faster out of a binary alloy. This indicated that the precipitate formed as a carbonitride. Jack (16) observed that ϵ -carbonitride formed on tempering carbon-nitrogen martensite and proposed that ϵ -carbide and ϵ -nitride are isomorphous. He also obtained some evidence (8) that the precipitate formed during the first stage of martensite tempering

¹ The figures appearing in parentheses pertain to the references appended to this paper.

² ϵ -carbide formed during tempering of carbon martensite has the approximate formula Fe_{2.4}C according to Lement (11).

was ϵ -carbonitride if the carbon-nitrogen ratio exceeded 0.5 and α'' -carbonitride if the ratio was less than 0.5.

The object of the present investigation was to obtain more definite information regarding the morphology and lattice structure of precipitates formed on quench-aging. The morphological changes occurring during quench-aging of Fe-C, Fe-N, and Fe-C-N alloys were followed by means of light and electron microscopy. Electron diffraction was employed for the identification of the precipitated phases.

Experimental Procedure

A Fe-C alloy, a Fe-N alloy, and two ternary Fe-C-N alloys were prepared from a high purity iron made by the National Research Corporation. This iron contained 0.004% carbon, 0.0005% nitrogen, and 0.013% oxygen, and was furnished in the form of a hot-rolled bar $\frac{5}{8}$ -inch in diameter. Subsequent decarburizing, carburizing or nitriding treatments were carried out on slabs $\frac{1}{8}$ -inch thick and $\frac{1}{4}$ -inch wide machined from the rolled bar and on $\frac{1}{4}$ -inch diameter cold-swaged bars. Table I gives information on the chemical composition

Table I
Chemical Composition and Grain Size

Alloy	%C	%N	Grain Size ASTM No.
Fe-C	0.016	nil	1
Fe-N	0.005	0.084	1
Fe-C-N	0.021	0.028	3-4
Fe-C-N	0.023	0.011	1

and grain size of the four alloys made. In general, the alloy preparation and the subsequent aging treatments of separate specimens consisted of the following steps:

- (a) Anneal 20 minutes at 860 °C (1580 °F) in evacuated vycor tubes to obtain a uniform grain size.
- (b) Gas treatments:
 - a) decarburizing—36 hours at 710 °C (1310 °F) in wet hydrogen
 - b) carburizing—24 hours at 675 to 710 °C (1245 to 1310 °F) in hydrogen saturated with n-heptane at room temperature
 - c) nitriding—48 hours at 580 °C (1075 °F) in ammonia-hydrogen mixtures.
- (c) Homogenizing:
 - a) after carburizing—20 hours at 720 °C (1325 °F) in evacuated vycor tubes
 - b) after nitriding—24 hours at 580 °C (1075 °F) in nitrogen

- c) after nitriding and carburizing—24 hours at 710 °C (1310 °F) in nitrogen
- (d) Solution treatment—15 minutes at 715 °C (1320 °F) in nitrogen followed by quenching in 10% sodium hydroxide at about 0 °C.
- (e) Aging—90 to 472 °C (195 to 880 °F) range in oil or salt baths.

The gas treatments used were selected on the basis of obtaining as uniform a concentration of the solute element as possible. Estimates of the times required were obtained from tables given by Darken and Gurry (17) for nonsteady-state diffusion in objects of various shapes. In preparing the ternary alloys, the problems of how to introduce carbon without removing previously introduced nitrogen and vice versa were faced. The method finally adopted consisted of alternately nitriding and carburizing using successively shorter times, the final operation being carburizing. After carburizing treatments, about $\frac{1}{64}$ -inch was machined off the surface of the specimens in order to get rid of any cementite layer that might have formed. The specimens used for quench-aging were in the form of either $\frac{1}{4}$ -inch squares or rounds both $\frac{3}{32}$ -inch in thickness.

For the metallographic preparation of the specimens, electrolytic polishing was employed using a solution of 19 parts glacial acetic acid and 1 part of perchloric acid. The current density was about 1 ampere per square centimeter and the time of polishing 20 to 30 seconds. The polishing usually produced a smooth surface with slight if any etching attack. The specimens were etched in 1% nital for about one minute and examined with a light microscope. All light micrographs were taken with slightly oblique illumination and the direction of the incident light is from top to bottom of the light micrographs presented.

Replicas for electron microscopy were dry stripped from the etched specimens, rotary shadowed with chromium at an angle of 27 degrees and examined in an RCA model B electron microscope. Electron diffraction using the reflection method was carried out using a diffraction lens in place of the projector lens in the electron microscope. The voltage employed was 60 kilovolts corresponding to a wavelength of 0.049 Å. The electron beam is reflected off the polished and etched specimen surface at a very low incident angle, which allows protruding particles such as carbides or nitrides to give a more intense diffraction pattern than the matrix.

Experimental Results

In analyzing the results, attempts were made to correlate the microstructural changes observed during quench-aging with the reported kinetics of precipitation. Previous internal friction studies (3,6,7,15)

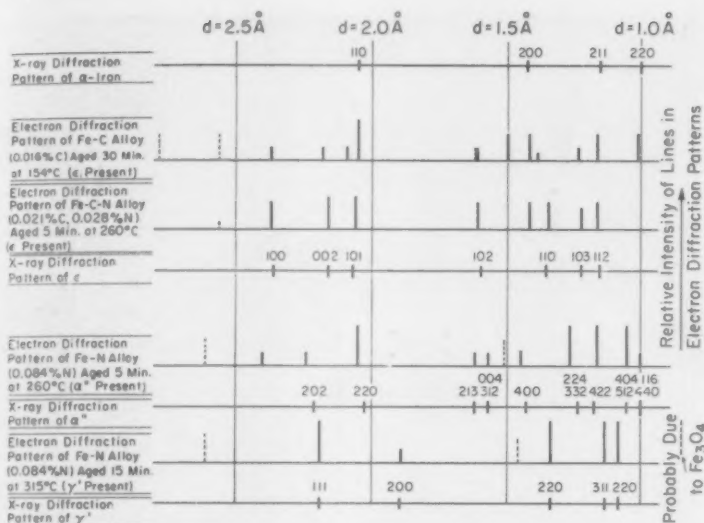


Fig. 1—Identification of Phases Detected by Electron Diffraction Carried Out in Reflection.

seem to supply sufficient data to enable reasonably good estimates of the times required for complete precipitation of carbon and nitrogen at various aging temperatures.

Fig. 1 is a chart illustrating the identification of phases in selected quench-aged specimens by electron diffraction in reflection. This was done by a comparison of the d -values and relative intensities obtained by electron diffraction with corresponding data obtained by x-ray diffraction. The latter information with respect to the ϵ , α'' , and γ' phases was taken from the work of Jack (10,19,20). Similar information by Jack on cementite (10) was used although not included in Fig. 1. Frequently, diffuse lines believed to be due to Fe_3O_4 (indicated by dotted vertical lines) and occasionally unidentified lines were encountered in the electron diffraction pattern. The presence of α -iron lines was detected after aging treatments which resulted in precipitated particles of a relatively small size. Presumably, as particles grow and protrude further out of the matrix after etching, the ferrite matrix makes less of a contribution to the electron diffraction pattern. The approximate relative intensities of the x-ray diffraction lines of the various phases taken from the work of Jack are not indicated in Fig. 1.

The Fe-C alloy (0.016% Carbon)—After quenching from 715 °C (1320 °F), the microstructure of the Fe-C alloy containing 0.016% carbon was found to consist of very slightly mottled ferritic grains as

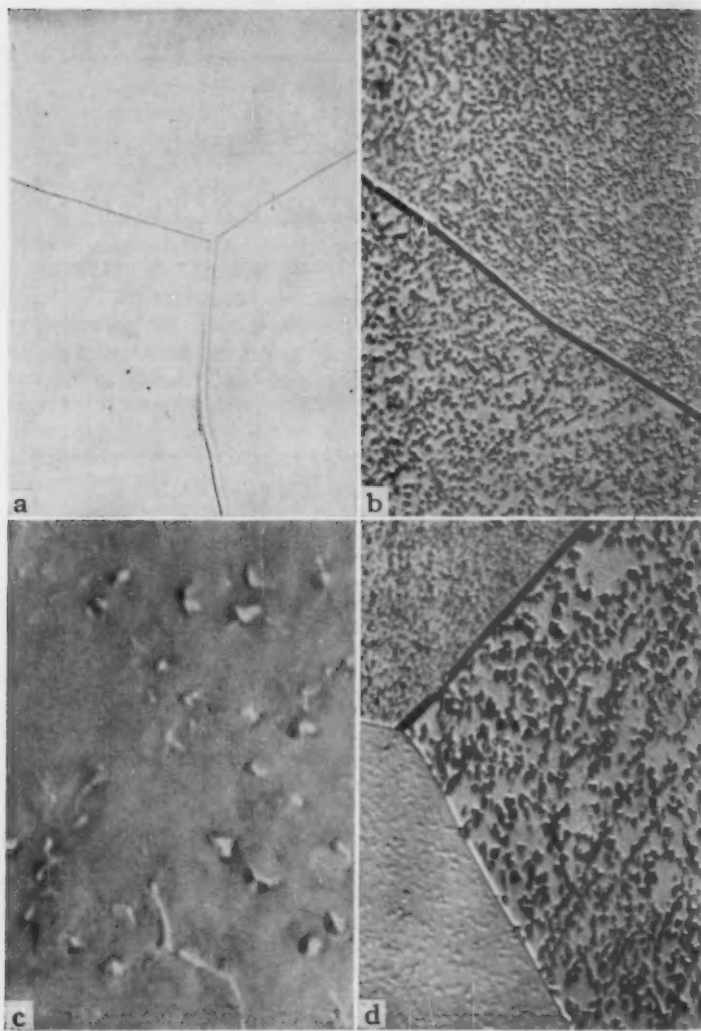


Fig. 2—Microstructural Changes on Aging Fe-C Alloy Containing 0.016% Carbon Quenched from 715 °C (1320 °F). (a) Light micrograph at $\times 1500$. As-quenched; (b) Light micrograph at $\times 1500$. Aged 5 days at 90 °C (195 °F); (c) Electron micrograph at $\times 2500$. Aged 5 days at 90 °C (195 °F); (d) Light micrograph at $\times 1500$. Aged 12 hours at 154 °C (310 °F).

shown in Fig. 2a. However, examination in the electron microscope of a replica from this specimen failed to reveal any structural feature within the grains. The electron diffraction pattern of the same specimen

consisted of a set of fairly strong and spotty rings corresponding to α -iron. The spottiness is apparently due to the fact that only a few grains were irradiated.

Aging at 90 °C (195 °F)—According to previous investigations, complete precipitation would be expected to occur in about 16 hours. During the course of aging, the mottled structure of the quenched condition was found to coarsen. Distinct particles could be observed after about 24 hours. Fig. 2b shows densely spaced particles in a specimen aged for 5 days. The corresponding electron micrograph in Fig. 2c reveals irregularly shaped particles often elongated to give the appearance of films. The diffraction pattern of this specimen exhibited both the spotty α -iron rings, and a set of rings composed of a few very weak spots elongated circumferentially. The latter reflections were found to correspond to ϵ -carbide. The weak elongated spots may be due to a preferred lattice orientation of the ϵ -carbide particles with respect to the ferritic matrix.

Aging at 154 °C (305 °F)—Complete precipitation would be expected to occur in about 2 hours. Examination with the light microscope revealed changes similar to those observed for aging at 90 °C (195 °F) although the rate of the process had increased considerably. After 30 minutes particles could be distinguished. The structure in Fig. 2d shows definite particles obtained on aging for 12 hours. The three grains in this micrograph appear to differ with respect to the size of the particles. This is believed to be due mainly to the anisotropy of the etching characteristics of ferrite (18) and probably also to the relative orientations between elongated particles and the ferrite matrix. The diffraction pattern of the specimen aged for 30 minutes indicated the presence of ϵ -carbide. After aging for 12 hours, a large number of somewhat spotty rings corresponding to cementite was observed.

Aging at 205 °C (400 °F)—Complete precipitation would be expected to occur in about 20 minutes. After aging for 2 minutes, the mottled structure still prevailed although distinct particles could be observed in some grains. Electron micrographs at 2 minutes, 15 minutes, and 8 hours are shown in Figs. 3a,b,c, and d. After 2 minutes (Fig. 3a), films which appear discontinuous and nonuniform in thickness have formed at what is believed to be subboundaries. Portions of these films give the impression that they represent a stage in the initial formation of separate particles. After 15 minutes (Fig. 3b), definite particles appear. The films are still present but appear thinner and even less continuous. Fig. 3c shows another area of the same specimen in which particles predominate. The apparent variation in the extent and nature of precipitation in different areas is believed to be due to the orientation effects previously mentioned. After aging for 8 hours (Fig. 3d), plates aligned in specific directions were observed. This implies definite habit orientation relationships with the matrix. The diffraction

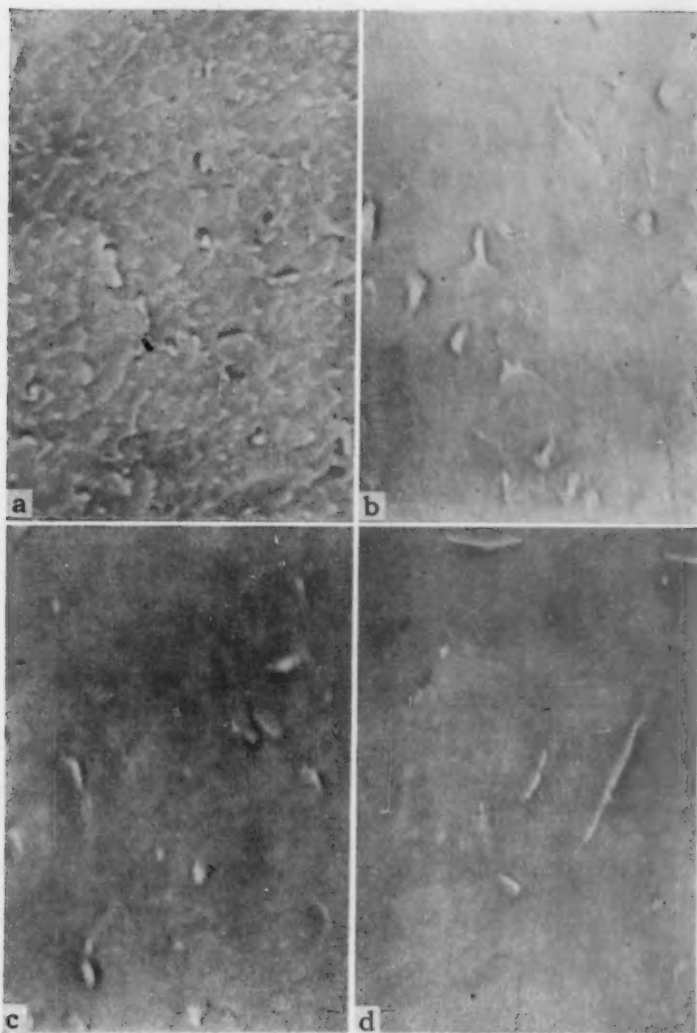


Fig. 3—Microstructural Changes on Aging of Fe-C Alloy Containing 0.016% Carbon Quenched from 715 °C (1320 °F). (a) Electron micrograph at $\times 25,000$. Aged 2 minutes at 205 °C (400 °F); (b) Electron micrograph at $\times 25,000$. Aged 15 minutes at 205 °C (400 °F); (c) Electron micrograph at $\times 25,000$. Aged 15 minutes at 205 °C (400 °F); (d) Electron micrograph at $\times 25,000$. Aged 8 hours at 205 °C (400 °F).

pattern obtained after aging for 15 minutes showed weak rings corresponding to ϵ -carbide. After aging for 1 hour or longer, the diffraction rings observed corresponded to cementite.

Aging at 315 and 472 °C (600 and 880 °F)—Complete precipitation would be expected to occur in about 2 minutes at 315 °C (600 °F) and in less time at 472 °C (880 °F). The structures obtained after aging at 315 °C (600 °F) for 5 and for 30 minutes were found to be similar. As shown in Fig. 4a, the structure after the latter treatment consists of particles distributed uniformly within the grains. Fig. 4c shows plate-like particles formed after aging at 472 °C (880 °F) for 5 minutes. In this case, a preferential growth at grain boundaries is evident. Electron micrographs of the precipitates formed on aging at 315 and 472 °C (600 and 880 °F) revealed particles in the shape of plates (Figs. 4b and 4d). The latter figure shows carbide plates at a ferrite grain boundary. All of the diffraction patterns obtained after aging at 315 and 472 °C (600 and 880 °F) indicated the presence of cementite.

The Fe-N alloy (0.084% nitrogen, 0.005% carbon)—The observations of the as-quenched condition were similar in all respects to the corresponding observations for the Fe-C alloy with the exception that occasionally small areas of martensite could be observed at the ferritic boundaries. In these cases, the nitrogen solubility in ferrite at the solution temperature of 715 °C (1320 °F) was probably exceeded to a slight extent. Under such conditions some austenite would form at ferritic boundaries and then transform to martensite on subsequent quenching.

Aging at 90 °C (195 °F)—Complete precipitation of nitrogen would be expected to occur in about 10 hours. The structure obtained upon aging for 6 hours is shown in the light micrograph of Fig. 5a. No significant change in this condition was observed after aging for 24 hours. Electron micrographs for these times are shown in Figs. 5b and 5c respectively and exhibit discontinuous films of nonuniform thickness. At the longer aging time, portions of the films give the impression of plate-like particles to an increasing extent and films are less prevalent. By electron diffraction, no indication of the existence of a precipitate in these two specimens could be found.

Aging at 154 °C (310 °F)—The precipitation was probably completed after 1 hour at this temperature. After aging for 2 minutes the structure was coarsely mottled, and after 5 minutes short closely spaced plates characteristic of α'' could be observed. Upon aging for 2 hours, the plates had increased somewhat in size and decreased in number. Regions adjacent to ferrite grain boundaries were often found to be free from precipitates.

Aging at 205 °C (400 °F)—The electron micrographs in Figs. 6a and 6b show the precipitates formed on aging for 5 minutes and 2 hours respectively. At the shorter time (Fig. 6a), plates of irregular shape which seem to be associated with subboundaries are present. No evidence of subboundaries was found at the longer time (Fig. 6b). This micrograph shows two sets of plates each of which appears to have a

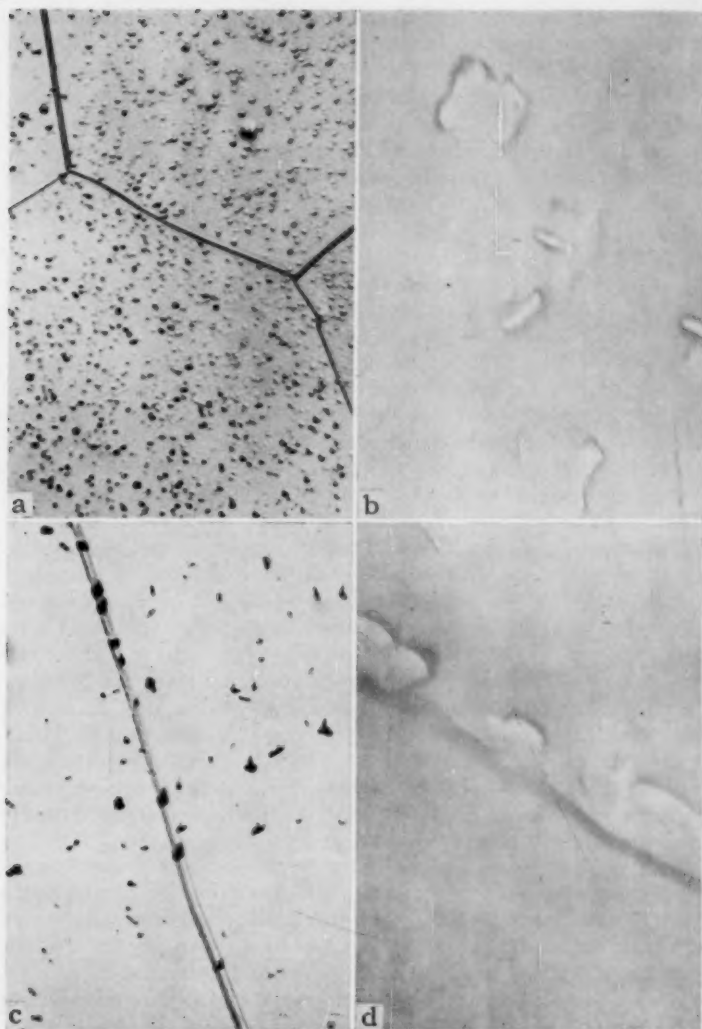


Fig. 4—Microstructural Changes on Aging of Fe-C Alloy Containing 0.016% Carbon Quenched from 715 °C (1320 °F). (a) Light micrograph at $\times 1500$. Aged 30 minutes at 315 °C (600 °F); (b) Electron micrograph at $\times 25,000$. Aged 30 minutes at 315 °C (600 °F); (c) Light micrograph at $\times 1500$. Aged 5 minutes at 472 °C (880 °F); (d) Electron micrograph at $\times 25,000$. Aged 5 minutes at 472 °C (880 °F).

common orientation. One set seems to have formed at a small angle with the specimen surface.

Aging at 260 °C (500 °F)—According to Dijkstra's results (3),

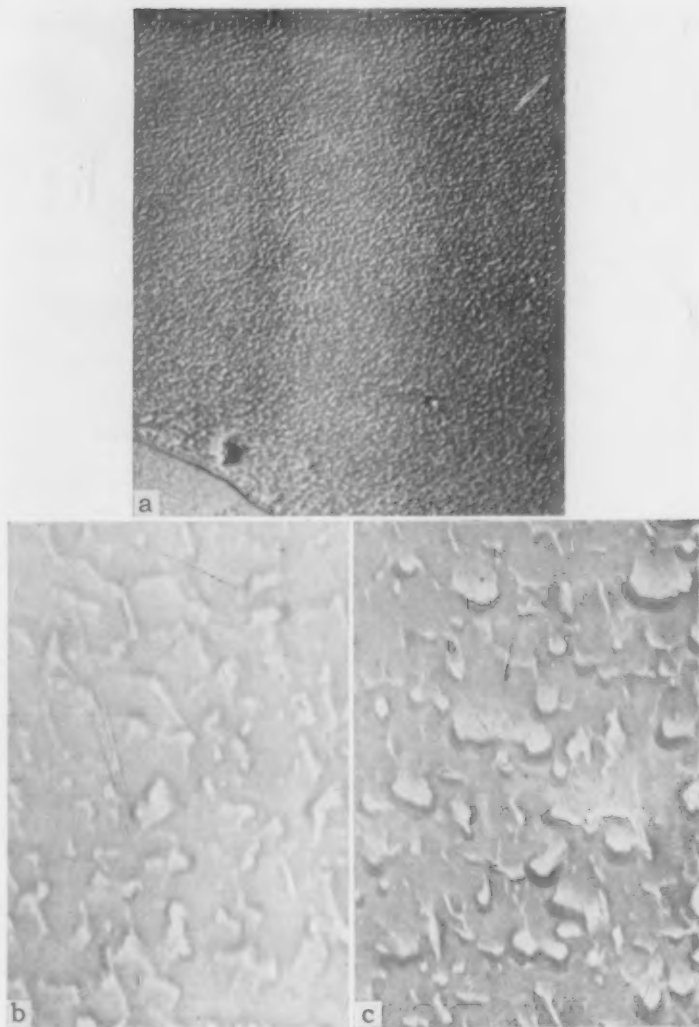


Fig. 5—Microstructural Changes on Aging of Fe-N Alloy Containing 0.084% Nitrogen Quenched from 715 °C (1320 °F). (a) Light micrograph at $\times 1500$. Aged 6 hours at 90 °C (195 °F); (b) Electron micrograph at $\times 25,000$. Aged 6 hours at 90 °C (195 °F); (c) Electron micrograph at $\times 25,000$. Aged 24 hours at 90 °C (195 °F).

only the metastable nitride would be expected to form at the previously discussed temperatures. At 260 °C (500 °F), however, both the metastable and the stable nitrides should form successively. It was estimated

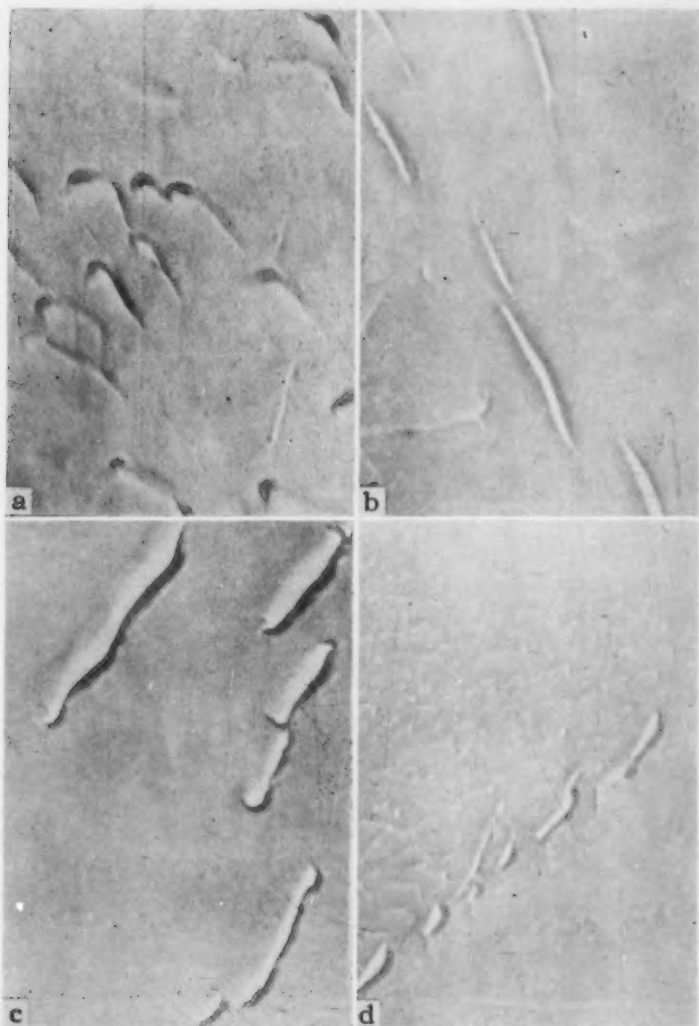


Fig. 6—Microstructural Changes on Aging of Fe-N Alloy Containing 0.084% Nitrogen Quenched from 715 °C (1320 °F). (a) Electron micrograph at $\times 25,000$. Aged 5 minutes at 205 °C (400 °F); (b) Electron micrograph at $\times 25,000$. Aged 2 hours at 205 °C (400 °F); (c) Electron micrograph at $\times 25,000$. Aged 5 minutes at 260 °C (500 °F); (d) Electron micrograph at $\times 25,000$. Aged 5 minutes at 260 °C (500 °F).

that a few minutes is required to reach metastable equilibrium, whereas 1 hour is required to reach stable equilibrium. In agreement with Dijkstra's findings, the structure after aging for 5 minutes, shown in

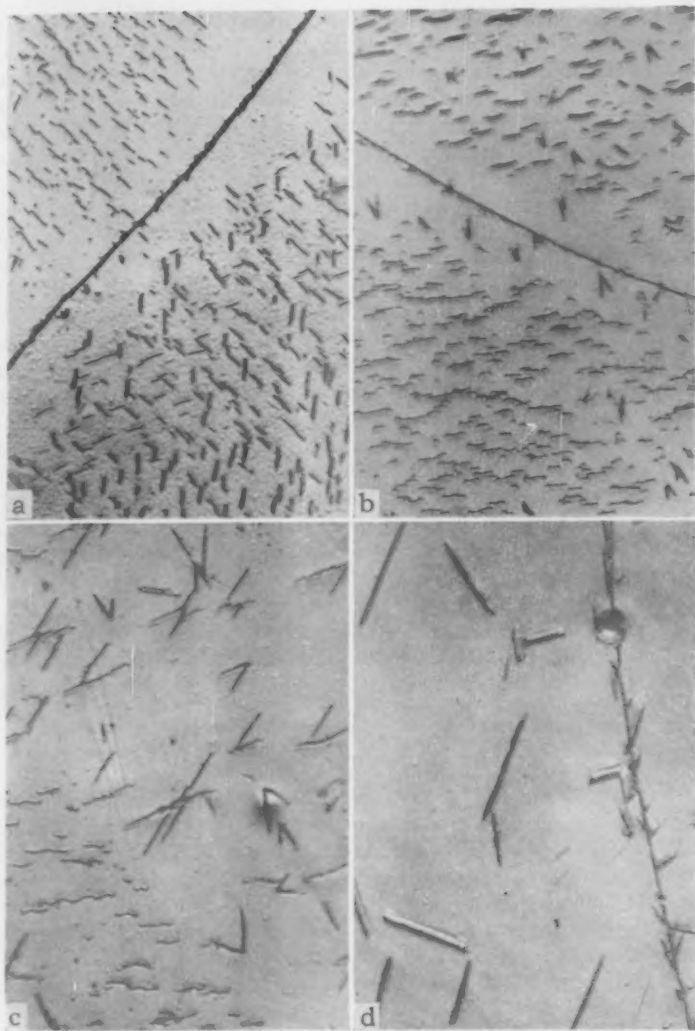


Fig. 7—Microstructural Changes on Aging of Fe-N Alloy Containing 0.084% Nitrogen Quenched from 715 °C (1320 °F). (a) Light micrograph at $\times 1500$. Aged 5 minutes at 260 °C (500 °F); (b) Light micrograph at $\times 1500$. Aged 15 minutes at 260 °C (500 °F); (c) Light micrograph at $\times 1500$. Aged 2 hours at 260 °C (500 °F); (d) Light micrograph at $\times 1500$. Aged 15 minutes at 315 °C (600 °F).

Figs. 7a and 6c, consisted of wavy plates somewhat longer than those observed at lower temperatures although similar in shape and oriented in a maximum of three directions within a given grain. Regions adja-

cent to grain boundaries were often free from plates (Fig. 7a). It was not possible to decide whether this is due to re-resolution of α'' accompanying the initial formation of γ' at grain boundaries or to a lower rate of nucleation of α'' at these regions. Occasionally, however, some type of precipitate was found right at the grain boundaries (Fig. 6d). The substructure visible in the left grain of this electron micrograph was a rather infrequent feature. The diffraction pattern consisted of spotty rings, the strongest of which corresponded to α'' . This confirms the x-ray results of Jack (8,19). After aging for 15 minutes, dark etching straight plates (V-shapes) were frequently found present in addition to the α'' plates as shown in Fig. 7b. The electron diffraction pattern of this specimen exhibited rings corresponding to α'' as well as to γ' — Fe_4N (20). With increasing aging time, the γ' plates increased in size and number at the expense of α'' plates. The α plates were still present after 2 hours (Fig. 7c), whereas only γ' plates could be observed after 4 hours.

Aging at 315 °C (600 °F)—Stable equilibrium would be expected to be established in less than 1 hour. After 15 minutes only γ' plates were found as shown in Fig. 7d. It would appear from this micrograph that the γ' plates preferentially nucleate at grain boundaries and at non-metallic inclusions. All the strong rings of the diffraction pattern of this specimen were due to the γ' phase. The weak superlattice reflections of γ' reported by Jack (20) were not observed.

The Fe-C-N Alloys—In the as-quenched condition, the ferrites of the two ternary Fe-C-N alloys appeared similar to the ferrite of the binary alloys in the same condition. The changes observed during quench-aging were as follows:

Fe-C-N alloy (0.021% Carbon, 0.028% Nitrogen)

Aging at 90 and 154 °C (195 and 310 °F)—Complete precipitation of carbon and nitrogen would be expected to occur in about 16 hours at 90 °C and in about 1 hour at 154 °C (310 °F). The morphological changes during aging at these temperatures were found to be similar to the corresponding changes in the binary alloys. Coarsening of the mottled structure and the eventual development of a finely dispersed precipitate was involved. With the light microscope, well defined particles were observed after 15 hours at 154 °C (310 °F). Fig. 8a is an electron micrograph that shows the presence of films and possibly plate-like particles presumably associated with subboundaries after 24 hours at 90 °C (195 °F). A diffraction pattern of this specimen did not reveal the presence of any precipitate. However, patterns obtained after 4 and 15 hours respectively at 154 °C (310 °F) both showed a set of weak but essentially continuous rings which were apparently due to ϵ -carbonitride which is isomorphous with ϵ -carbide.

Aging at 205 °C (400 °F)—Complete precipitation of carbon and

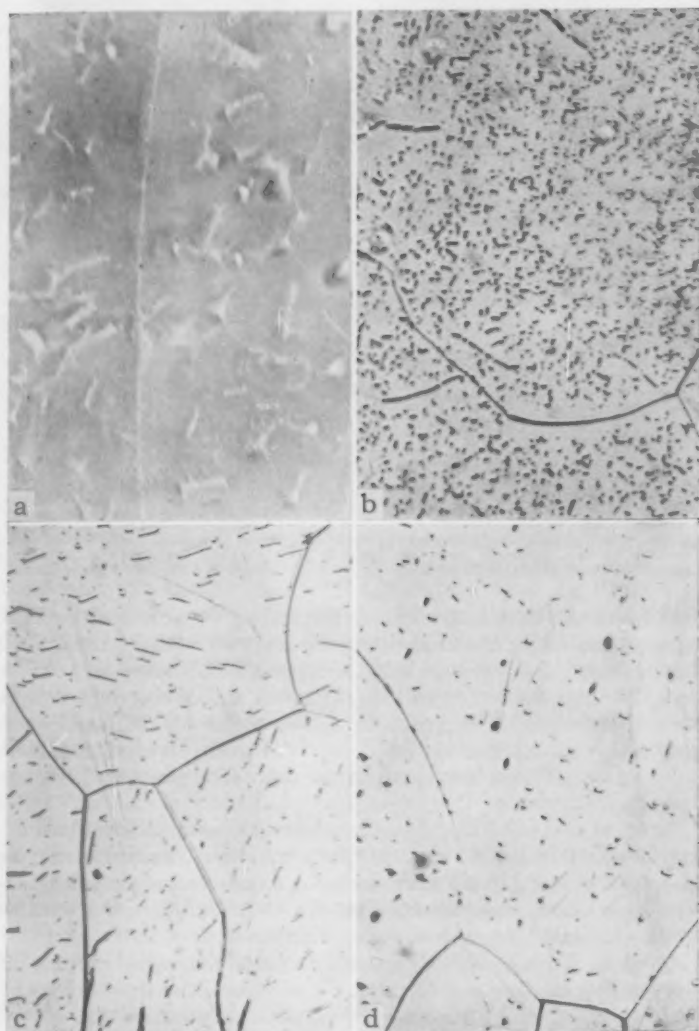


Fig. 8—Microstructural Changes on Aging Fe-C-N Alloy Containing 0.021% Carbon, 0.028% Nitrogen Quenched from 715 °C (1320 °F). (a) Electron micrograph at $\times 25,000$. Aged 24 hours at 90 °C (195 °F); (b) Light micrograph at $\times 1500$. Aged 2 hours at 260 °C (500 °F); (c) Light micrograph at $\times 1500$. Aged 15 minutes at 315 °C (600 °F); (d) Light micrograph at $\times 1500$. Aged 10 minutes at 365 °C (690 °F).

nitrogen should occur in about 20 minutes. Closely spaced and somewhat elongated particles were observed after aging for 5 minutes, 15 minutes and 2 hours. Diffraction patterns of these three specimens ex-

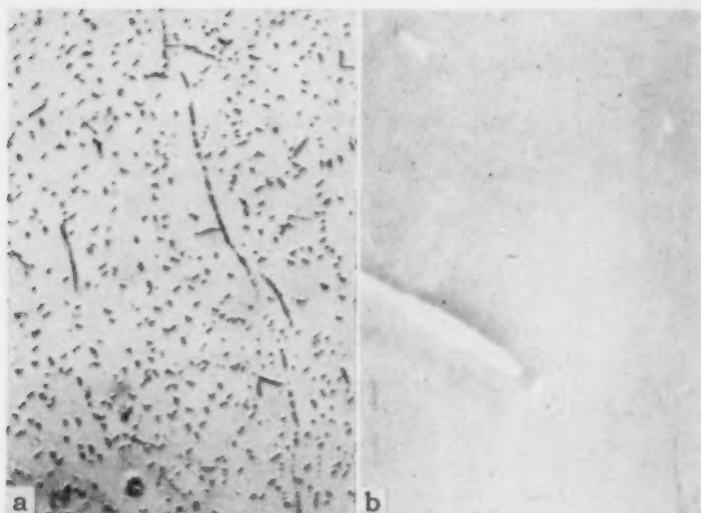


Fig. 9—Microstructural Changes on Aging Fe-C-N Alloy Containing 0.023% Carbon, 0.011% Nitrogen Quenched from 715 °C (1320 °F). (a) Light micrograph at $\times 1500$. Aged 2 hours at 260 °C (500 °F); (b) Electron micrograph at $\times 25,000$. Aged 2 hours at 260 °C (500 °F).

hibited almost continuous rings corresponding to ϵ -carbonitride. The rings became stronger and sharper with increase in aging time. Since there is probably a preferred habit orientation relationship between the precipitate and the ferrite matrix, the continuity of the rings may be due to the smaller ferritic grain size of this alloy (ASTM No. 3-4) as compared to the other alloys (ASTM. No. 1). The irradiation of more grains by the electron beam permits the precipitate phase to diffract in many more directions.

Aging at 260 °C (500 °F)—Complete precipitation would be expected to occur in about 5 minutes. The precipitates obtained after aging for 5 minutes and 2 hours were similar and consisted of elongated particles often located at subboundaries (Fig. 8b). The diffraction patterns strongly indicated the presence of ϵ -carbonitride.

Aging at 315 °C (600 °F)—Complete precipitation of carbon and nitrogen should occur in 5 minutes. Fig. 8c shows the structure resulting from aging for 15 minutes. Two types of precipitates are visible; small particles and large plates. After aging for 2 hours, the large plates decreased in number. Diffraction patterns of both specimens indicated that only cementite was present.

Aging at 365 °C (690 °F)—After aging for 10 minutes, only small platelets were observed (Fig. 8d) similar in appearance to that in the Fe-C alloy given a corresponding aging treatment. The diffraction pattern of the Fe-C-N specimen indicated the presence of cementite.

Fe-C-N Alloy, 0.023% C, 0.011% N

The morphology of the precipitates formed on aging this alloy was found to be similar to that described in the previous section. The only difference was that whereas both fairly large plates and small plate-like particles gradually developed during aging at 260 °C (500 °F), only the small plate-like particles appeared on aging at 315 °C (600 °F). Figs. 9a and 9b show large plates and small plate-like particles after aging at 260 °C (500 °F) for 2 hours. The large plates are often surrounded by an area devoid of precipitates. Electron diffraction revealed ϵ -carbonitride to be present on aging at 154 °C (310 °F) for 15 hours and at 205 and 260 °C (400 and 500 °F) for 2 hours. At 315 °C (600 °F) and higher, only cementite reflections were obtained.

DISCUSSION OF RESULTS

As revealed by the electron microscope, a striking similarity exists with respect to the morphological changes associated with precipitation at low aging temperatures in the four alloys studied. Irrespective of whether carbon atoms or nitrogen atoms or both are present in supersaturated solution, the initial stage of precipitation seems to involve the migration of solute atoms to subboundaries at which films of an unknown character are formed.³ The subgrains have a size of 10^{-5} to 10^{-4} centimeters comparable to the size reported for mosaic blocks and differ from the substructure delineated by veining which is much coarser. The films may represent either a precipitate which lacks the ability to produce a diffraction pattern of detectable intensity or else an enrichment of solute atoms within solid solution without the actual formation of a new phase. The latter possibly may be due to Cottrell atmospheres at dislocations. The films appear discontinuous and can be observed to thicken almost from the beginning of aging. Eventually plate-like particles develop from the thickened portions of the films. This is accompanied by gradual disappearance of the unthickened portions. At low aging temperatures, remnants of the films may be present long after the precipitation reaction should be complete. It is likely that the transition from films to plate-like particles occurs at places where the habit plane of the precipitate coincides with the subgrain interface. The platelet thus formed would be expected to follow its habit plane during subsequent growth and eventually depart from the subboundary. In view of the fact that films have been observed to be in the process of disappearing, the growth of platelets may be to some extent dependent on the supply of solute atoms from the adjacent films.

The analysis by Wert (6) of the difference in kinetics for precipitation of carbon and nitrogen is not supported by the present investi-

³ Similar results have been obtained for the first stage of tempering of martensite by Lement, Averbach and Cohen (21). In this case a subboundary precipitate identified as ϵ -carbide was formed.

gation. The precipitation reaction seems more complicated than just a growth of particles of definite geometrical shapes that is controlled by isotropic diffusion. Furthermore, the shape of carbides, nitrides, and carbonitrides seems to be plate-like almost from the beginning of precipitation; whereas Wert concluded that carbides precipitate in the form of spheres and nitrides precipitate in the form of plates.

During quench-aging of the Fe-C alloy below about 205 °C (400 °F), precipitation was found to occur in two stages:

ferrite supersaturated with respect to carbon \rightarrow ϵ -carbide \rightarrow cementite. However, ϵ -carbide is present for definitely longer times than estimated for the complete carbon precipitation. This implies that the transition from ϵ -carbide to cementite occurs after virtually all of the carbon in the supersaturated ferrite solution has precipitated out. The concentrations of carbon in ferrite in equilibrium with ϵ -carbide and cementite respectively are both very low at these temperatures. This probably explains why a two stage process has generally not been observed in the precipitation curves obtained by internal friction measurements. The fact that no significant difference in the morphology between ϵ -carbide and cementite was observed in the present investigation could mean that ϵ -carbide transforms to cementite in situ. However, this mode of transition is not believed to happen during the tempering of martensite (21).

When nitrogen is present in addition to carbon, the ϵ -phase apparently becomes more stable. The electron diffraction results indicated that ϵ -carbonitride was the only phase present in the two Fe-C-N alloys studied after aging at 260 °C (500 °F) for 2 hours even though it is estimated that complete precipitation of carbon and nitrogen should have occurred within 5 minutes.⁴ After aging at 315 °C (600 °F) which was the next temperature used, cementite alone was observed to form. Thus a transition from ϵ -carbonitride to cementite would be expected to occur at some temperature in the range of 260 to 315 °C (500 to 600 °F). Accordingly, the sequence of precipitation reactions in the Fe-C-N alloys is believed to be as follows:

ferrite supersaturated with both carbon and nitrogen \rightarrow ϵ -carbonitride \rightarrow cementite (carbonitride).

The presence of large plates and small particles on aging the low nitrogen alloy at 260 °C (500 °F) (Figs. 9a and 9b) and the high nitrogen alloy at 315 °C (600 °F) (Fig. 8c) suggests that two types of precipitate form simultaneously. However, electron diffraction indicated that only ϵ -carbide was present in the former case, and that only cementite was present in the latter. The apparent discrepancy between

⁴ The stabilizing effect of nitrogen may explain why Tsou, Nutting and Menter (12) did not find cementite after aging their ingot iron. (0.026% carbon and 0.006% nitrogen) at 200 °C (390 °F).

the microscopic and diffraction evidence could be explained in any of the following ways:

(a) Precipitated particles form with the same lattice structure but possess different growth rates because of different nitrogen contents.

(b) The precipitated particles go through a stage during which they are coherent with the ferrite lattice. When some of the particles become large enough, they lose their coherency and grow more rapidly.

(c) For an unknown reason, only one type of precipitate produces a diffraction pattern of detectable intensity.

The cementite formed on aging the *low nitrogen* Fe-C-N alloy at 315 °C (600 °F), is similar in appearance to the cementite formed in the binary Fe-C alloy after a corresponding treatment. This similarity would imply that no appreciable amount of the nitrogen comes out of solution. This is supported by the fact that the solubility of nitrogen in ferrite at 315 °C (600 °F) (5) is about equal to the nitrogen content of the alloy (0.011% nitrogen). It is known that the effect of carbon on the nitrogen solubility is negligible at 250 °C (480 °F) (15) and this may also hold for 315 °C (600 °F). The large plates formed at 315 °C (600 °F) in the *high nitrogen* Fe-C-N alloy seem to represent the major amount of precipitate and it is likely that they make the principal contribution to the cementite diffraction pattern. Taking the nitrogen solubility of the ferrite to be about 0.011% at 315 °C (600 °F), the equivalent of 0.017% nitrogen should be contained in the cementite phase. Hence, the large plates are believed to be carbonitrides with the lattice structure of cementite. After aging the same alloy at 365 °C (690 °F), the cementite appeared similar to that formed in the binary Fe-C alloy after a corresponding aging treatment. In this case, a large part of the nitrogen apparently remains in solid solution due to the increased nitrogen solubility of the ferrite.

The observations on the precipitation in the binary Fe-N alloy confirm the two stage process proposed by Dijkstra (3). The metastable phase is α'' in accordance with Jack (8) and the sequence of precipitation reactions are as follows:

ferrite supersaturated with nitrogen $\rightarrow \alpha''$ -nitride $\rightarrow \gamma'$ -nitride. Because of their characteristic appearance, the metastable and stable nitrides can be easily distinguished metallographically. The transition which apparently involves the nucleation and growth of γ' simultaneously with the re-solution of α'' appears to occur after comparatively short aging times at temperatures in the vicinity of 260 °C (500 °F). At lower temperatures, only α'' was observed although γ' might form in specimens that are aged long enough. Although only γ' was observed at 315 °C (600 °F), it is possible that α'' may have existed for a short time during the early stage of precipitation since the nitrogen content (0.085%) of the binary Fe-N alloy appreciably exceeds the nitrogen solubility of the ferrite in equilibrium with α'' (0.065%) (5).

CONCLUSIONS

1. The initial stage of aging at relatively low temperatures in the Fe-C, Fe-N, and the two Fe-C-N alloys studied consists of the formation of films of variable thickness at subboundaries in the ferritic matrix corresponding to a subgrain size of 10^{-4} to 10^{-8} centimeters. On continued aging, preferential thickening of the films was found to culminate in the formation of platelets of a metastable phase which apparently grow at the expense of the adjacent subboundary films.

2. On aging each alloy at an intermediate temperature, a transition eventually occurs from the metastable to the stable precipitate which also takes the form of plates but larger in size. At relatively high aging temperatures, some evidence of direct formation of the stable precipitate was obtained.

3. Depending on the type of supersaturation of the ferrite, the stages of aging are as follows:

ferrite supersaturated with carbon $\rightarrow \epsilon$ -carbide \rightarrow cementite;

ferrite supersaturated with nitrogen $\rightarrow \alpha''$ -nitride $\rightarrow \gamma'$ -nitride;

ferrite supersaturated with both carbon and nitrogen $\rightarrow \epsilon$ -carbonitride \rightarrow cementite.

4. In the Fe-C alloy, the transition of ϵ -carbide to cementite occurs after virtually all the carbon in the supersaturated ferrite solution has precipitated out.

5. Due apparently to increased nitrogen content, the ϵ -phase that forms in the Fe-C-N alloys is more stable than in the Fe-C alloy.

6. In the Fe-C-N alloys, the presence of nitrogen in cementite promotes the formation of relatively large plates.

ACKNOWLEDGMENTS

The authors wish to express their appreciation to Professor Morris Cohen for invaluable help in the completion of this investigation; to Miss Miriam Yoffa for her skillful aid in the metallographic aspects of the work; to Marc Richman for his assistance in heat treating. The authors are also indebted to the Instrumentation Laboratory of MIT for financial support of this investigation.

References

1. C. A. Wert, "Solid Solubility of Cementite in Alpha Iron," *Journal of Metals*, Vol. 1, October 1950, p. 1242.
2. J. K. Stanley, "The Diffusion and Solubility of Carbon in Alpha," *Journal of Metals*, Vol. 1, October 1949, p. 752.
3. L. J. Dijkstra, "Precipitation Phenomena in Solid Solutions of Nitrogen and Carbon in Alpha Iron Below Eutectoid Temperature," *Journal of Metals*, Vol. 1, March 1949, Sec. 3 (Transactions), p. 252.
4. V. G. Paranjpe, M. Cohen, M. B. Bever and C. F. Floe, "The Iron-Nitrogen System," *Journal of Metals*, Vol. 2, February 1950, p. 261.

5. J. D. Fast and M. B. Verrijp, "Solubility of Nitrogen in α -Iron," *Acta Metallurgica*, Vol. 3, March 1955, p. 203.
6. C. A. Wert, "Precipitation from Solid Solutions of C and N in Alpha-Iron," *Journal of Applied Physics*, Vol. 20, October 1949, p. 943.
7. C. A. Wert, *Thermodynamics in Physical Metallurgy*, 1950, p. 178, American Society for Metals, Cleveland.
8. K. H. Jack, "The Ageing of Nitrogen-Ferrite," Lecture in Stockholm, March 1955.
9. O. Krisement, "Ausscheidung von Kohlenstoff aus α -Eisen," *Arkiv fur Fysik*, Vol. 7, 1953, p. 353.
10. K. H. Jack, "Structural Transformations in the Tempering of High Carbon Steels," *Journal, Iron and Steel Institute*, Vol. 169, September 1951, p. 26.
11. B. S. Lement, "Appendix B—The Mechanism and Kinetics of the First Stage of Tempering," *TRANSACTIONS, American Society for Metals*, Vol. 45, 1953, p. 597.
12. A. L. Tsou, J. Nutting and J. W. Menter, "The Quench-Aging of Iron," *Journal, Iron and Steel Institute*, Vol. 172, October 1952, p. 163.
13. C. Zener, "Theory of Growth of Spherical Precipitates from Solid Solution," *Journal of Applied Physics*, Vol. 20, October 1949, p. 950.
14. J. Radavich and C. A. Wert, "Study of Precipitates of C and N in Iron with an Electron Microscope," *Journal of Applied Physics*, Vol. 22, April 1951, p. 367.
15. C. A. Wert, "Precipitation Out of Dual Solid Solutions of Carbon and Nitrogen in Alpha-Iron," *Acta Metallurgica*, Vol. 2, May 1954, p. 361.
16. K. H. Jack, "The Iron-Carbon-Nitrogen-System," *Royal Society of London, Proceedings*, Vol. 195 A, November 1948, p. 41.
17. L. S. Darken and R. W. Gurry, *Physical Chemistry of Metals*, 1953, p. 445, McGraw-Hill Book Co., New York.
18. A. Hultgren, A. Josefsson, E. Kula and G. Lagerberg, to be published.
19. K. H. Jack, "The Occurrence and the Crystal Structure of α -Iron Nitride; a New Type of Interstitial Alloy Formed During the Tempering of Nitrogen—Martensite," *Proceedings, Royal Society of London*, Vol. 208 A, August 1951, p. 216.
20. K. H. Jack, "The Iron-Nitrogen System: The Structures of Fe_3N and Fe_2N ," *Proceedings, Royal Society of London*, Vol. 195 A, November 1948, p. 34.
21. B. S. Lement, B. L. Averbach and Morris Cohen, "Microstructural Changes on Tempering Iron-Carbon Alloys," *TRANSACTIONS, American Society for Metals*, Vol. 46, 1954, p. 851.

DISCUSSION

Written Discussion: By Dr. J. Nutting, Department of Metallurgy, Cambridge University, England.

I should like to congratulate the authors upon a very interesting and timely investigation. Evidence in favor of a two-stage decomposition of carbon super saturated ferrites has also been obtained by Pitsch and Lücke^{*} using internal friction techniques. This, together with the authors' evidence, seems to establish beyond doubt the transformation supersaturated ferrite \rightarrow

ϵ — carbide \rightarrow cementite.

I am not completely in agreement with the interpretation by the authors of their experimental evidence on the mode of formation of ϵ — carbide and ϵ'' nitride. Mr. E. Smith, Mr. R. G. Baker and I have been following the precipitation of vanadium carbide and molybdenum carbide from alloy ferrites and we have found

^{*} W. Pitsch and K. Lücke, *Archiv für Eisenhüttenwesen*, Vol. 27, 1956, p. 45.

structures very similar to those found by the authors if we used plastic replicas, but by using direct carbon or direct carbon extraction replicas, we were able to detect plate-like precipitates earlier than with plastic replicas. It was, however, still impossible to follow the initial formation of these precipitates. Part of the difficulty would appear to be that immediately prior to the formation of a new phase the etching characteristics of the matrix may be such that they do not indicate directly the nature of the impending phase changes.

Although I agree with the authors' views that prior to the formation of ϵ or α'' phases zones of carbon or nitrogen enrichment occur analogous to the formation of G.P. [1] zones in Al — 4% copper alloys, I do not believe that we can see these by using etching and replica methods. In order to investigate this phenomenon further we shall have to resort to direct examination of thin foils of the metal in high resolution electron microscopes.

Authors' Reply

The authors wish to thank Dr. Nutting for pointing out that there is now internal friction evidence favoring a two-stage reaction during the aging of ferrite supersaturated with carbon. At the time the present investigation was started, the results of internal friction measurements appeared to support a single stage reaction even though two types of carbide were reported to occur.

In view of the observations made on the precipitation of alloy carbides from ferrite by Dr. Nutting and his associates, the significance of the films that the authors found by their examination of plastic replicas is open to question. It would certainly be worthwhile to study quench-aging of ferrite containing C or N by both carbon replica techniques and direct examination of thin metal foils.

SOME RELATIONSHIPS BETWEEN TORSIONAL STRENGTH AND ELECTRON MICROSTRUCTURE IN A HIGH CARBON STEEL

BY S. T. ROSS, R. P. SERNKA AND W. E. JOMINY

Abstract

Austempered and quenched and tempered SAE 51100 steel samples were tested to failure in torsion. All oil-quenched samples were tempered in the 400–550 °F range. Austempering was also done in this range. The torsional yield strength-hardness relationship was plotted for both austempered and quenched and tempered samples. Austempered data were linear over the whole hardness range investigated (Rockwell C-53—C-60) and generally ductile fractures were exhibited. For quenched and tempered samples, the plot was linear up to Rockwell C-57.5 above which there was much data scatter. Brittle fractures were noted for these specimens.

Representative samples of each heat treatment were examined with the electron microscope. Regions of weakness in the form of percarbide films and elongated cementite particles in martensite needle boundaries were observed in those quenched and tempered samples which displayed erratic yield strength results. No such films or elongated particles were noted in austempered samples. Electron diffraction patterns of carbide particles were made from extraction replicas of samples representing both heat treatments. The Hagg type Fe_3C and cementite were identified. (ASM International Classification Q1a, 2–14, M21e; AY)

PREFACE

PREVIOUS WORK by the authors (1)¹ has shown that percarbide films surrounding tempered martensite needles may be an assignable cause of erratic fatigue and torsion test data in higher hardness ranges. Correlation was established between endurance limit and torsional yield strength properties when considered as functions of tempered hardness. Included in the work were plots of torsional yield strength versus hardness for six medium carbon, low alloy steels which

¹ The figures appearing in parentheses pertain to the references appended to this paper.

A paper presented before the Thirty-Ninth Annual Convention of the Society, held in Chicago, November 4–8, 1957. Of the authors, S. T. Ross is managing engineer, Metallurgical Research; R. P. Sernka is project engineer; W. E. Jominy is chief metallurgist—Research, Chrysler Corporation, Detroit. Manuscript received April 15, 1957.

showed considerable scatter and low strength for samples tempered below about 500 °F. This corresponds with the tempering range in which several authors have shown the presence of the iron percarbide identified as epsilon (2-4). Work reported by the ASTM Subcommittee on Electron Metallography (5) illustrates the electron microstructure of the martensite resulting from tempering below 550 °F as well as that of isothermally obtained lower bainite. These structures resemble each other closely. They differ mainly in that lower bainite

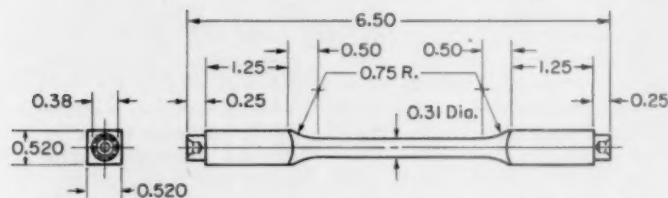


Fig. 1—Torsion Test Specimen Before Final Machining.

needles are not surrounded by the percarbide films common to martensite tempered for short periods of time in the same range of temperature. Therefore, it was considered possible that torsion test data could show less scatter for isothermally transformed samples as compared to samples quenched and tempered in the same heat treatment range.

SAE 51100 steel was selected for this investigation. It has a low M_s temperature as is common with high carbon steels. Thus, a relatively wide range of temperature was available for austempering above the M_s and in the area where epsilon carbides have been shown to form both in lower bainite and in tempered martensite.

SPECIMEN PREPARATION

All samples were prepared from the same heat of SAE 51100 steel having the following chemical analysis: C-1.02, Mn-0.34, P-0.009, S-0.018, Si-0.28, Cr-1.00. Prior to machining, as-received 1-inch rounds were annealed for 1½ hours at 1750 °F. Torsion test bars were roughed out to the dimensions shown in Fig. 1, with the exception that 0.020 inch grind stock was left on the square sections. Their gage lengths were machined to a surface finish of 10-50 microinches. The bars were plated with 0.0005 inch of copper to prevent decarburization during subsequent heat treatment. Mild steel rollers were fastened to each end of the bars to enable them to be rotated during the subsequent oil quench. All specimens were austenitized at 1800 °F for 1 hour in a neutral atmosphere received from an endothermic gas cracker. Quenching of the samples to be tempered was done in agitated, room temperature oil, while the bar rotated about its longitudinal axis. All oil-

Table I
Specimen Heat Treatment

Specimen No.	Austempering Temperature °F	Time Hours	Tempering Temperature °F	Time Hours	Avg. Hardness Rockwell C
1-3			As-quenched		62.2
4-6			500	3¼	57.7
7-9	550	2			53.0
10-12	500	3¼			56.4
13-15			550	2	57.3
16-18	450	6½			58.6
19-21			550	200	53.6
22-24			450	6½	59.0
25-27			As-Quenched & Cold Treat		65.0
28-30			500	18	57.2
31-33	400	24			59.9
34-36			400	24	59.2
37-39			400	10	59.5
40-42			600	1	55.4
43-45			600	1¾	55.9

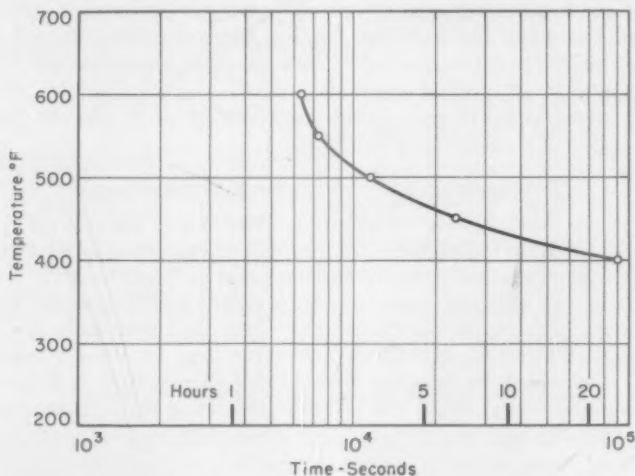


Fig. 2—SAE 51100 Steel Isothermal Transformation Diagram—End of Bainite Transformation Line.

quenched samples, with the exception of samples 1, 2 and 3, were cold-treated immediately at -105°F for 30 minutes. Heat treatment details are given in Table I.

It was desired to austemper for a time sufficient to allow complete decomposition to bainite at temperatures from 400°F up to about 550°F . The procedure of Davenport and Bain (6) was used to determine the austempering time necessary to obtain these structures. Fig. 2 is the I-T plot of the end-of-bainite transformation for SAE 51100 steel obtained experimentally. All of the oil-quenched specimens were tempered in this same temperature range. Some were tempered for times

equivalent to those required for austempering. The balance were tempered to hardnesses equivalent to those obtained at austempering temperatures. The copper plate was stripped from the samples after heat treatment. Finish grinding of the square sections was specified to result in true, flat and parallel surfaces. These square sections were gripped by the jaws of the torsion test machine.

METALLOGRAPHIC PROCEDURES

Specimens representative of each heat treatment were sectioned through their gage lengths, perpendicular to the longitudinal axes. This was done with an abrasive cut-off wheel, while the specimens were immersed in coolant. Metallographic mounting and polishing were followed by etching with 4% picric acid plus 0.1% zephiran chloride in ethyl alcohol. Final polishing and etching were repeated until disturbed metal layers resulting from prior metallographic preparation were removed. Formvar and parlodion replicas were dry-stripped and supported on 200 mesh copper grids. Replicas were chromium-shadowed in vacuum at an incident angle of about 45 degrees. Electron micrographs were taken at an original magnification of $\times 6900$ and were enlarged to $\times 30,000$ for final printing.

INTERPRETATION OF ELECTRON MICROGRAPHS

Previous work by the authors (1), Teague and Ross (8) and the ASTM (5) have reported the electron microstructures of steel samples both austempered and quenched and tempered in the 400–550 °F range. Lower bainite obtained by austempering at 400–550 °F has been found to consist of ferrite needles containing fine, discrete carbide particles oriented at about 60 degrees to the needle axes by those mentioned above. This structure has been found in both plain carbon and common alloy constructional steels. The electron diffraction work of Austin and Schwartz (2) and the electron diffraction data of Fisher (9) have identified these carbides as either a percarbide or cementite, depending on the time and temperature of heat treatment. Tempered martensite has been shown to consist also of ferrite needles containing the same fine carbide particles, but with a somewhat lower degree of orientation with respect to needle axes. However, martensite needles have been found to be enveloped by a percarbide film after tempering for 1–3 hours below about 550 °F (1,8). These films have not been found to be associated with lower bainite needles. Figs. 8, 10, 12 and 15 are representative electron micrographs of lower bainite found in the austempered samples. Figs. 7, 9, 11, 13, 14, 16, 17, and 18 are of structures typical of the tempered martensite samples. The arrows in Fig. 7, 11 and 16 point out percarbide films and those in Figs. 9, 13 and 14 indicate films that have begun to dissolve with time and re-precipitate as cementite. Fig. 7 represents the structure of martensite tempered for

1 hour at 400 °F, and was added for comparison purposes, since its percarbide films are complete and have not begun to dissolve. The interpretation of these structures agrees with those suggested in the references cited above.

TORSION TESTING

A 2000 inch-pound torsion test machine was used. Special jaws, described previously (1), engaged the square sections of the test bars. All bars were twisted to failure at a rate of 0.1 revolution per minute.

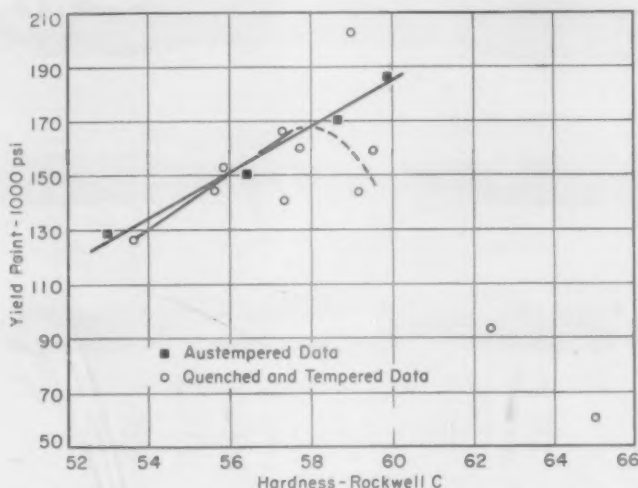


Fig. 3—Relationship Between Torsional Yield Strength and Hardness for SAE 51100 Steel, Austempered and Quenched and Tempered Samples.

Torsional yield strength was regarded as a function of the force in inch-pounds which resulted in 1.0 degree offset. The ultimate strength in psi was calculated using the formula for maximum shear stress: $S = 16M/\pi d^3$ as published* by Timoshenko and Lessells (14). However, the method of Nadai (7) was employed in calculation of torsional yield strength values, since the formula

$$S = 1/2\pi r^3 [\theta (dm/d\theta) + 3M]$$

takes into account the shape of the stress-strain (torque-twist) curve.**

* Symbols in this formula have the following meaning:

S is maximum shear stress in psi
M is torque at fracture in inch pounds
d is test bar diameter in inches.

** Symbols in this formula have the following meaning:

S is shear stress in psi
r is test bar radius in inches
 θ is the angle of twist in the test bar
M is the torque in inch pounds.

Torsion test data and the resulting fracture types are given in Table II. Significantly, data from the three samples austempered in each manner display more consistency than do comparable data obtained from quenched and tempered samples. The ΔS column is the stress difference in 1000 psi between torsional yield and ultimate strength. Fig. 3 is a plot of the torsional yield strength values and corresponding Rockwell C hardness readings obtained during this investigation. Each

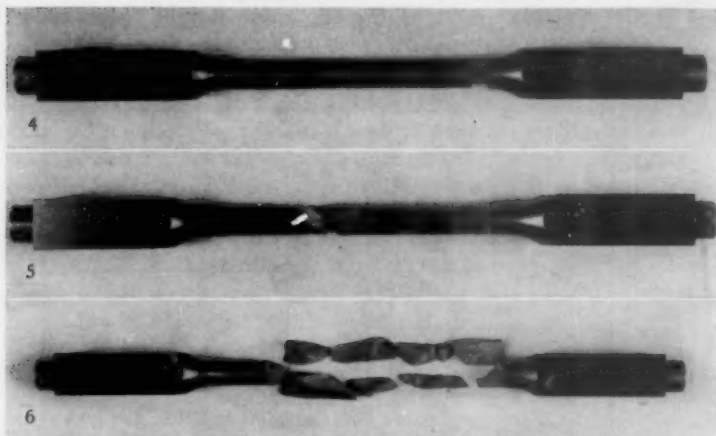


Fig. 4—Fracture Type A, SAE 51100 Steel Torsion Test Bar.
Fig. 5—Fracture Type C, SAE 51100 Steel Torsion Test Bar.
Fig. 6—Fracture Type B, SAE 51100 Steel Torsion Test Bar.

point is an average of the three sets of values resulting from tests of the three samples given each heat treatment. The data representing the austempered series of samples are linear in nature, without significantly great scatter in the hardness range investigated. However, the data obtained from the quenched and tempered samples show linear relationship only to about Rockwell C-57.5, at 167,000 psi. At higher hardness values, these data are erratic. This scatter has been represented by a dashed curve, bending in a downward direction.

Three fracture types were noted. Type A was a typical shear fracture on planes perpendicular to specimen axes as shown in Fig. 4. Type C was a tensile failure along helical planes at 45 degrees to specimen axes as shown in Fig. 5. Fracture Type B was regarded as a combination shear and tensile failure. Bars exhibiting this type of failure shattered into many small pieces, some of which contained shiny shear surfaces parallel to the longitudinal specimen axes. As is shown in Fig. 6, the balance of these fracture surfaces are similar in appearance to the Type C tensile fracture surfaces.

Table II
Torsion Test Data

Spec. No.	Heat Treatment	Yield Strengths 1" Offset, 1000 psi	Avg. Yield Strength 1000 psi	Ultimate Strengths 1000 psi	Avg. Ult. Strength 1000 psi	Fract. Type	S, 1000 psi Stress Difference—Yield Str. to Ult. Str.
1-3	As-Quenched	102.0, 98.7, 79.0	93.2	102.0, 98.7, 79.0	93.2	C	0
2-7	As-Quenched—Cold Treat	63.1, 56.0	59.5	63.1, 56.0	59.5	C	0
32-36	Quench & Temper, 400° F., 24 Hrs.	138.4, 122.0, 172.0	144.1	138.4, 122.0, 172.0	137.9	B	13.8
37-39	Quench & Temper, 400° F., 10 Hrs.	155.0, 182.7, 141.8	159.8	155.0, 216.5, 143.2	171.6	B	11.8
22-24	Quench & Temper, 450° F., 6½ Hrs.	207.7, 221.0, 181.0	203.2	207.7, 221.0, 273.0	223.3	B	64.0
4-6	Quench & Temper, 500° F., 3¼ Hrs.	164.2, 164.2, 158.0	162.1	253.0, 259.0, 158.0	223.3	B	61
28-30	Quench & Temper, 500° F., 18 Hrs.	112.0, 190.2, 128.5	143.6	112.0, 190.2, 128.5	143.6	B	0
13-15	Quench & Temper, 550° F., 2 Hrs.	184.3, 165.0, 148.0	165.8	184.3, 263.0, 148.0	198.4	B	32.6
19-21	Quench & Temper, 550° F., 200 Hrs.	133.6, 112.1, 135.8	127.2	220.0, 112.1, 223.0	185.0	B	57.8
40-42	Quench & Temper, 600° F., 1 Hr.	145.3, 140.2, 154.9	146.8	240.0, 227.3, 265.0	224.1	B	97.8
43-45	Quench & Temper, 600° F., 1½ Hrs.	150.0, 150.6, 158.3	153.0	220.0, 246.5, 220.0	228.8	B	75.8
31-33	Austemper, 400° F., 24 Hrs.	192.3, 185.0, 181.5	186.3	220.0, 206.5, 208.0	211.5	B	25.2
16-18	Austemper, 450° F., 6½ Hrs.	168.5, 171.5, 171.5	170.5	276.4, 276.4, 267.0	273.3	A	102.8
10-12	Austemper, 500° F., 3¼ Hrs.	153.0, 150.8, 151.7	151.8	249.5, 251.0, 246.5	249.0	A	97.2
7-9	Austemper, 550° F., 2 Hrs.	132.2, 124.6, 129.0	128.6	238.0, 196.5, 223.0	219.2	A	90.6

ELECTRON DIFFRACTION

Samples 9, 15, 18, 24, 29, 36 and 45 were investigated by means of electron diffraction in order to corroborate identification of the carbide phases present. The specimens were sectioned and polished in the usual manner. Then, extraction replicas were prepared from them using the method of Fisher (9). Briefly, this technique involves polishing and etching as for standard electron metallography. The samples are then coated with parlodion films. A heavy re-etch is accomplished through the permeable films, dislodging some of the percarbide and cementite particles. Some of these dislodged particles remain with the parlodion films which are then dry-stripped from the samples. Thus, the carbides are removed from the surface of the sample, while maintained in their relative positions. Selected-area electron diffraction patterns were obtained from these replicas. Fig. 19 is a typical pattern, and Fig. 20 is a corresponding electron micrograph of its extraction replica. Interplanar spacings (d values) and Miller indices of the diffraction patterns are labelled. The diffraction results are presented in Table III.

Good correlation has been found between the experimentally obtained patterns and the $d_{h,k,l}$ values reported for the Hagg-type percarbide,

Table III
Electron Diffraction Data

Sample No.	Heat Treatment	Phase Identification
9	Austemper—550°F.—2 Hrs.	Fe ₃ C and Hagg Fe ₃ C
15	Quench & Temper—550°F.—2 Hrs.	Fe ₃ C and Hagg Fe ₃ C
18	Quench & Temper—550°F.—2 Hrs.	Fe ₃ C and Hagg Fe ₃ C
29	Quench & Temper—500°F.—18 Hrs.	Hagg Fe ₃ C, Trace Fe ₃ C
24	Quench & Temper—450°F.—6½ Hrs.	Hagg Fe ₃ C
36	Quench & Temper—400°F.—24 Hrs.	Fe ₃ C and Hagg Fe ₃ C
45	Quench & Temper—600°F.—1¼ Hrs.	Fe ₃ C
18	Austemper—450°F.—6½ Hrs.	Hagg Fe ₃ C and Fe ₃ C

Fe₂C, which is described as being orthorhombic (13). Although the presence of cementite, Fe₃C, is a complicating factor in pattern analysis, correlation of relative intensities produced results considered to be reliable. Existence of the Hagg form of percarbide is consistent with data published by Anderson (11) and Hofer and Cohn (10). These authors showed that hexagonal epsilon percarbide is unstable above about 450 °F and that it will decompose to the more stable Hagg percarbide in the temperature range of our investigation. The effect of time at temperature and alloy content have not been evaluated fully for this phenomenon.

DISCUSSION

The torsion data as plotted in Fig. 3 show instability when consideration is given to the higher hardness range of the quenched and tempered

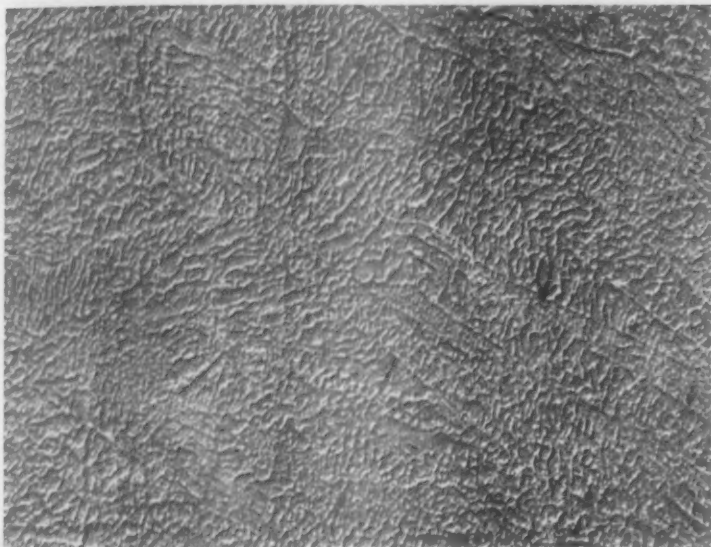


Fig. 7—SAE 51100 Steel, Oil-Quenched and Tempered at 400 °F. For 1 hour. Many fine percarbide particles and films in a matrix of supersaturated ferrite are seen. The films, outlining martensite needles, are noted by arrows. $\times 30,000$.

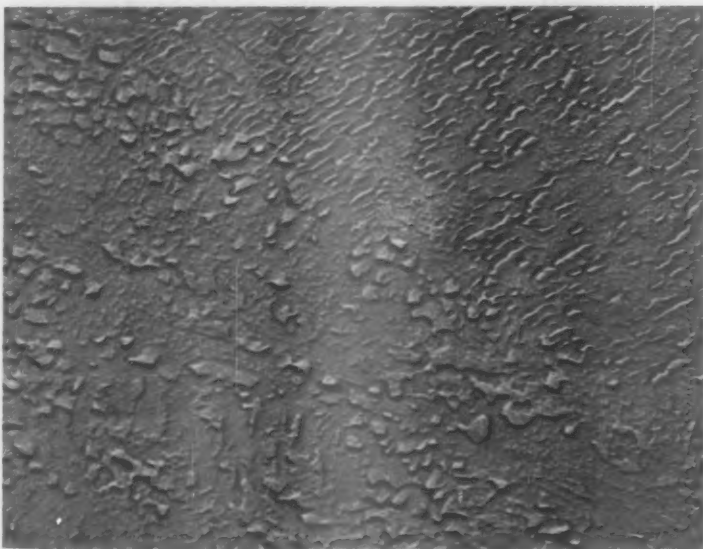


Fig. 8—SAE 51100 Steel, Austempered at 400 °F. For 24 hours. The lower bainite contains percarbide and cementite particles in a matrix of ferrite. No films are noted. $\times 30,000$.

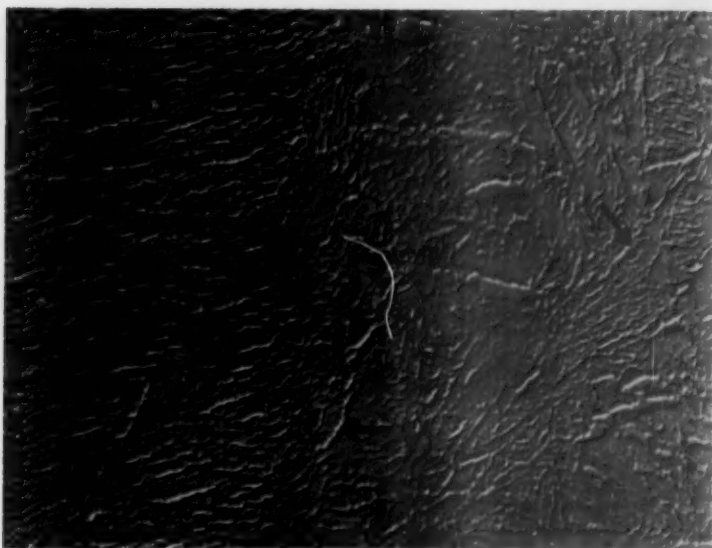


Fig. 9—SAE 51100 Steel, Oil-Quenched and Tempered at 400 °F. For 24 hours. Beginning of solution of some pearlite films and precipitation of cementite is noted by arrows. The remaining structure consists of fine pearlite particles in a matrix of supersaturated ferrite. $\times 30,000$.

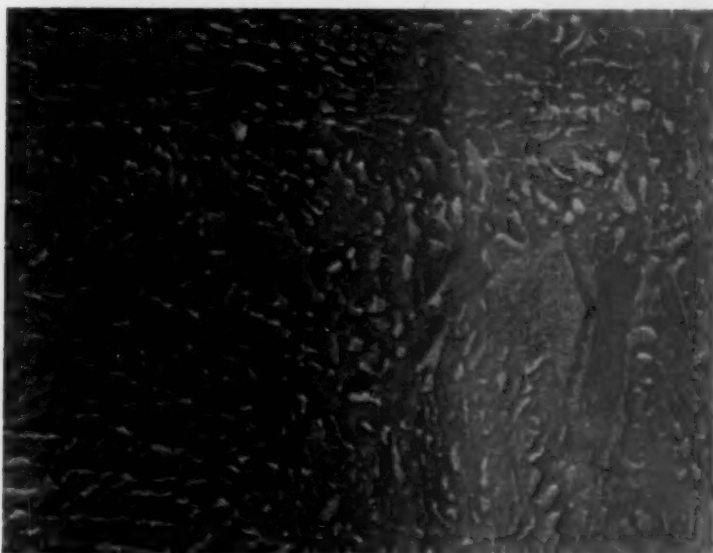


Fig. 10—SAE 51100 Steel, Austempered at 450 °F. For 6½ hours. A typical lower bainite structure containing pearlite and some cementite particles in a matrix of ferrite. $\times 30,000$.

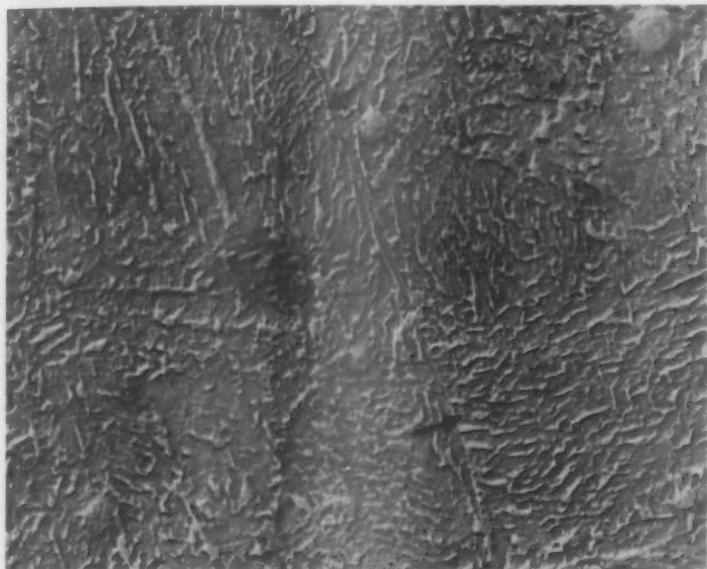


Fig. 11—SAE 51100 Steel, Oil-Quenched and Tempered at 450 °F. For 6½ hours. The structure consists of fine pearlite particles, and some films, noted by arrows, in a matrix of supersaturated ferrite. Elongated cementite particles are also present. $\times 30,000$.

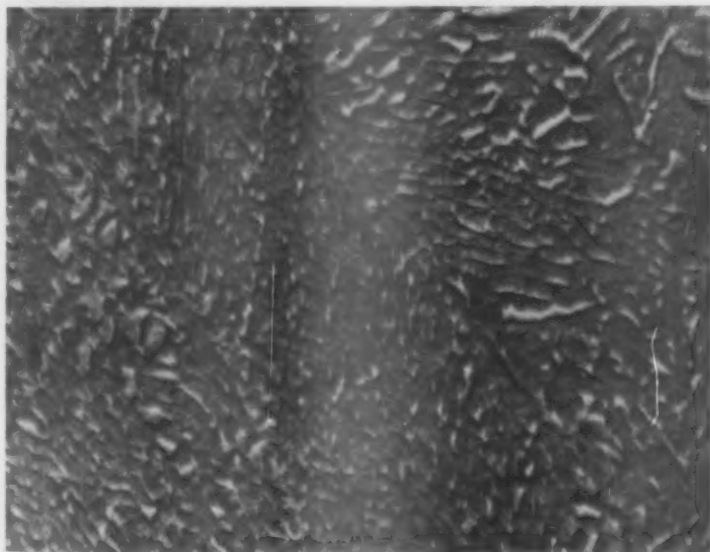


Fig. 12—SAE 51100 Steel, Austempered at 500 °F. For 3¼ hours. Bainite needles, not outlined by films, and containing pearlite and cementite particles in a ferrite matrix are seen. $\times 30,000$.

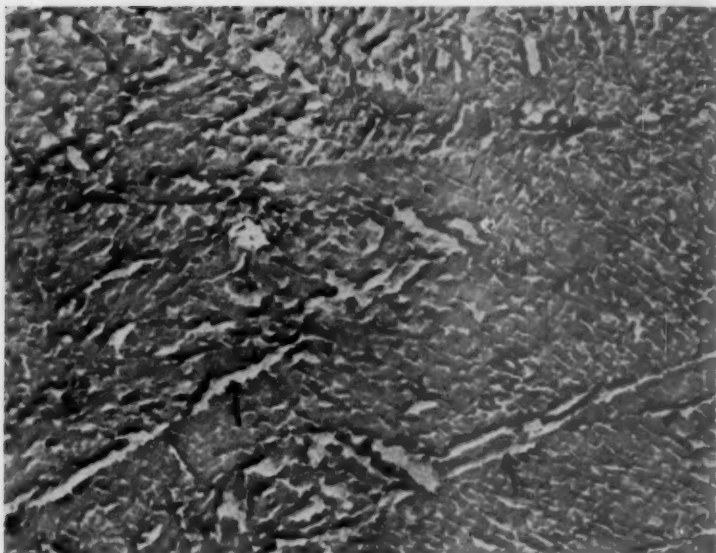


Fig. 13—SAE 51100 Steel, Oil-Quenched and Tempered at 500 °F. For 3¼ hours. Fine percarbide particles in a matrix of supersaturated ferrite are present. Elongated cementite particles at former martensite needle boundaries are noted by arrows. $\times 30,000$.

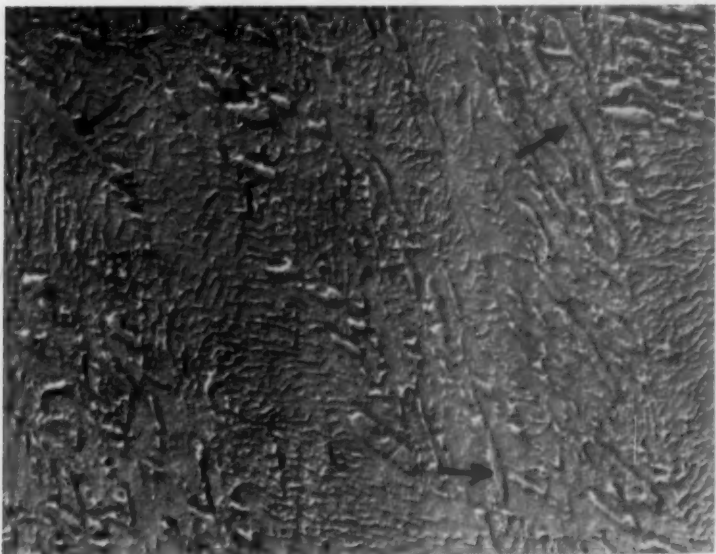


Fig. 14—SAE 51100 Steel, Oil-Quenched and Tempered at 500 °F. For 18 hours. The structure contains some fine percarbide particles and elongated cementite which is indicated by arrows. The matrix is supersaturated ferrite. $\times 30,000$.

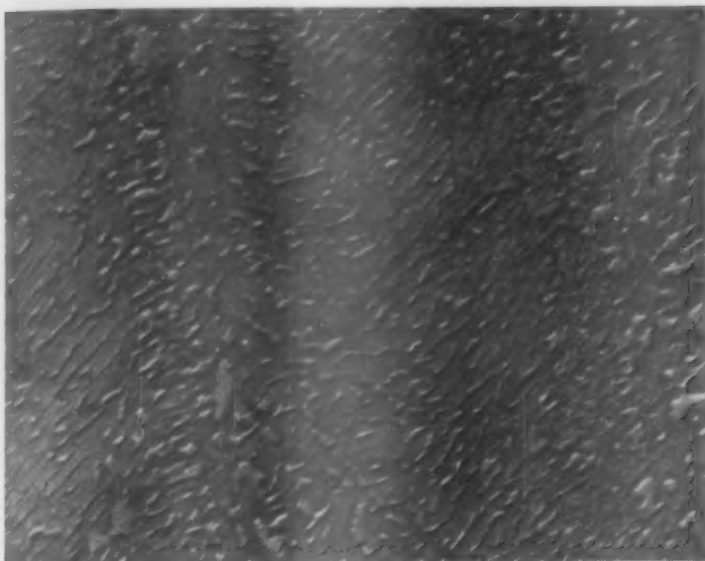


Fig. 15—SAE 51100 Steel, Austempered at 500 °F. For 2 hours. Bainite containing cementite and percarbide particles oriented at about 60 degrees to the needle axes is seen in a matrix of ferrite. $\times 30,000$.

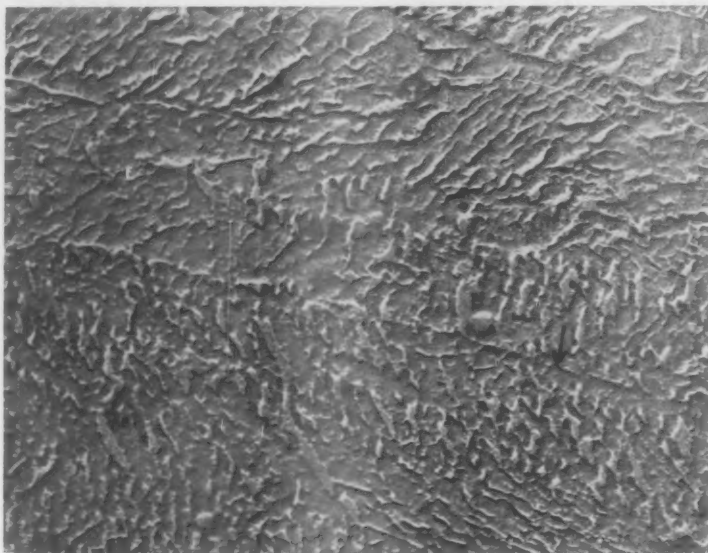


Fig. 16—SAE 51100 Steel, Oil-Quenched and Tempered at 550 °F. For 2 hours. Although the percarbide films have begun to be replaced by cementite, some still remain as indicated by the arrow. The remaining structure is percarbide and cementite particles in a matrix of supersaturated ferrite. $\times 30,000$.

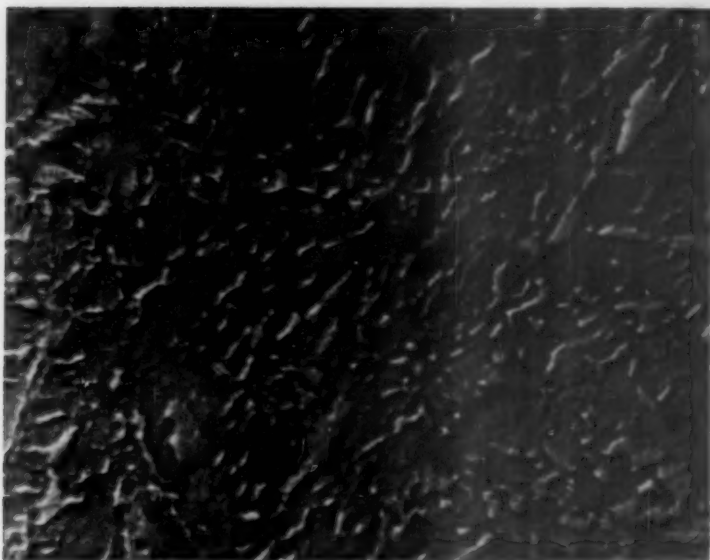


Fig. 17—SAE 51100 Steel, Oil-Quenched and Tempered at 550 °F. For 200 hours. A structure of cementite in saturated ferrite is seen. Coalescence of elongated cementite particles has occurred. $\times 30,000$.

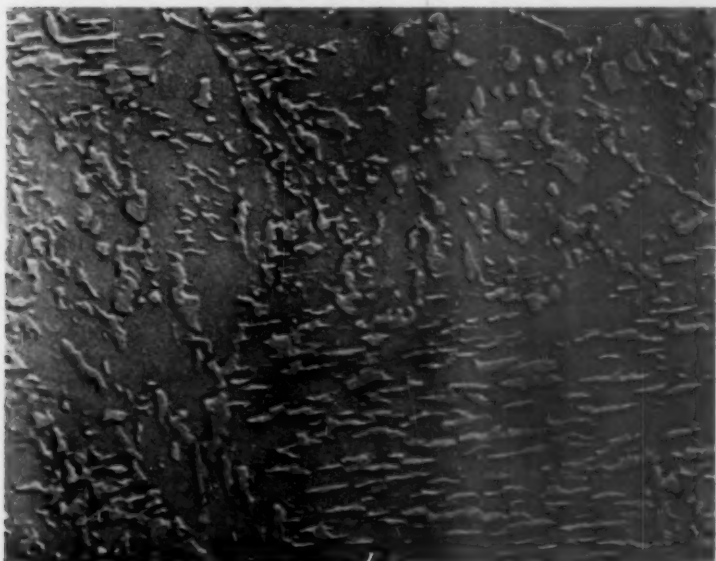


Fig. 18—SAE 51100 Steel, Oil-Quenched and Tempered at 600 °F. For 1½ hours. Cementite particles in a matrix of saturated ferrite are seen. $\times 30,000$.

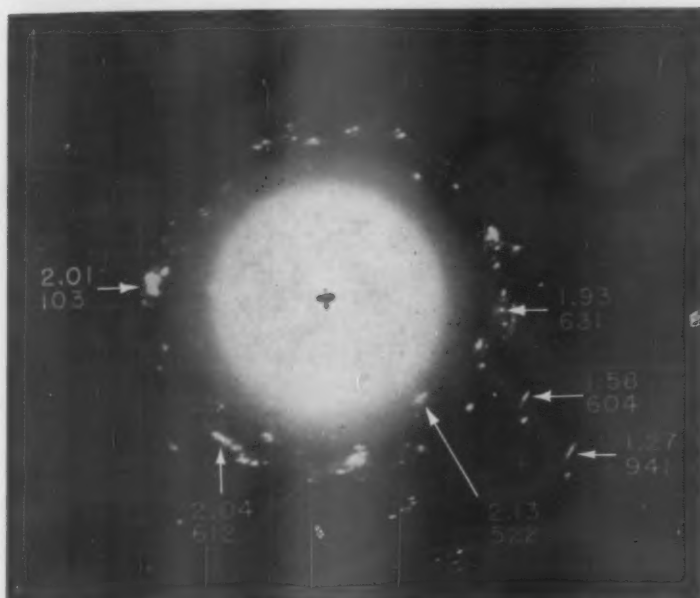


Fig. 19—Electron Diffraction Pattern of SAE 51100 Steel, Austempered at 550 °F. For 2 hours. Some $d \cdot a \cdot t$ values and Miller indices are noted.

series. This agrees with the work of Olleman, Wessel and Hull (12) on a high carbon tool steel, as well as with the work of the authors (1) on six medium carbon, low alloy steels. However, such behavior is not apparent when the series of austempered samples is considered. These data display linearity over the entire hardness range investigated. Further, Table II shows that the data obtained for each austempering temperature are more consistent, indicating much less tendency to scatter.

Interpretation of the electron micrographs published in this paper indicate that there are two possible structural causes for torsion test data scatter of the quenched and tempered series of samples. The first is the presence of percarbide films around martensite needles tempered below 550 °F for relatively short periods (1 to 3 hours). The second is the presence of elongated cementite particles in the needle boundaries of the martensite tempered in the same range of temperature, but for longer times (3 to 24 hours). Each phenomenon results in regions of weakness through which failure can occur, in torsion, at lower-than-expected values. These low values occur even after long tempering times. Such phenomena are not associated with austempering in the same hardness range. With the exception of the percarbide films and elongated cementite particles, the electron microstructures of the two series of samples are markedly similar.

It is admitted that residual quenching stresses may also play a part in erratic data behavior. No determination was made of such stress, although it was considered that the longer tempering times used in this investigation should have decreased the amount of residual stress and thus resulted in less data scatter or brittleness. We observed no such decrease in the samples tempered for 24 hours, and even 200 hours.

From Table II it can be seen that the stress difference (ΔS) be-



Fig. 20—Electron Micrograph of Extraction Replica. Replica of SAE 51100 Steel, austempered at 550 °F. For 2 hours. Black regions are carbides from which the pattern in Fig. 19 was made.

tween torsional yield and ultimate strength is greatest for the austempered and higher temperature tempered samples. Correlation of these data with Fig. 3 suggests that samples exhibiting high ΔS values are most likely to be found on the linear portions of the curves.

Consideration of the fracture types resulting from torsion testing also indicated that regions of weakness are present in samples quenched and tempered to high hardness values. Brittleness, as exemplified by tensile and shattering fractures, types B and C, occurred in all bars representative of data instability. Generally, the austempered bars broke with the more ductile type A fractures. When examined by electron microscopy, those same bars that failed in brittle fashion in regions of data instability, were found to contain films or elongated particles around tempered martensite needles.

CONCLUSIONS

1. The torsional yield strength versus hardness relationship for quenched and tempered SAE 51100 steel is linear up to about Rockwell C-57.5. Above this hardness the data reflect instability. The same relationship is linear for austempered SAE 51100 steel over the entire range of hardness studied from Rockwell C-53 to C-60.
2. When tested in torsion, austempered SAE 51100 steel fails with a ductile fracture at higher hardnesses than does quenched and tempered SAE 51100 steel.
3. Percarbide films and elongated cementite particles result in regions of weakness which are possible causes of erratic torsion test data for quenched and tempered SAE 51100 steel.
4. Austempered SAE 51100 steel contains no percarbide films or other microstructural regions of weakness such as elongated cementite particles.
5. The percarbide which exists in the samples investigated has been identified as the orthorhombic Hagg-type Fe_2C .
6. Torsion test data show less scatter for SAE 51100 steel austempered in the 400–550 °F range than for quenched and tempered SAE 51100 steel samples heat treated in the same range of temperature.

References

1. S. T. Ross, R. P. Sernka and W. E. Jominy, "Some Relationships Between Endurance Limit and Torsional Properties of Steel," *TRANSACTIONS, American Society for Metals*, Vol. 48, 1956, p. 119–139.
2. A. E. Austin and C. M. Schwartz, "Electron-Diffraction Study of Iron Carbides in Bainite and Tempered Martensite," *Proceedings, American Society for Testing Materials*, Vol. 52, 1952, p. 592.
3. K. H. Jack, "Structural Transformations in the Tempering of High Carbon Steels," *Journal, Iron and Steel Institute*, Vol. 169, 1951, p. 26–36.
4. G. Hagg, "Powder Photographs of a New Iron Carbide," *Zeitschrift für Kristallographie*, Vol. 89, 1934, p. 92–4.
5. "Electron Microstructure of Tempered Bainite and Tempered Martensite in Steel," Fourth Progress Report of Subcommittee XI of Committee E-4, *Proceedings, American Society for Testing Materials*, Vol. 54, 1954, p. 568.
6. E. S. Davenport and E. C. Bain, "Transformation of Austenite at Constant Subcritical Temperatures," *Transactions, American Institute of Mining and Metallurgical Engineers*, Vol. 3, 1930, p. 117–144.
7. A. Nadai, *Plasticity*, 1931, McGraw-Hill Co., New York.
8. D. M. Teague and S. T. Ross, "Electron Microstructure of Bainite and Tempered Martensite in Steel," *Proceedings, American Society for Testing Materials*, Vol. 55, 1955, p. 590.
9. R. M. Fisher, "Electron Microstructure of Steel by Extraction Replica Technique," *Techniques for Electron Metallography*, 1954, p. 49, American Society for Testing Materials, Philadelphia.
10. L. J. E. Hofer and E. M. Cohn, "Some Reactions in the Iron-Carbon System: Application to the Tempering of Martensite," *Nature*, Vol. 167, 1951, p. 977.
11. R. B. Anderson, *Advances in Catalysis*, Vol. V., 1953, Academic Press, Inc.
12. R. D. Olleman, R. T. Wessel and F. C. Hull, "A Study of Factors Controlling Strength in the Torsion Test," *TRANSACTIONS, American Society for Metals*, Vol. 46, 1954, p. 87–99.

13. K. H. Jack, "Binary and Ternary Interstitial Alloys," *Proceedings, Royal Society*, Vol. 195, 1948, p. 56.
14. S. Timoshenko and J. M. Lessells, *Applied Elasticity*, 1925, Westinghouse Press, Pittsburgh.

DISCUSSION

Written Discussion: By D. J. Girardi and W. E. Littmann, The Timken Roller Bearing Co., Canton, Ohio.

The authors are to be commended for this contribution of data on the fracture behavior of high carbon steel at various hardness levels.

A study of the data given in Tables I and II suggests several questions. Was there any measurable degree of plastic strain for those samples having ultimate strengths identical with the "yield strengths," for example the specimens numbered 34 and 35 in Table II, or did they fracture before reaching one degree of plastic twist?

It is interesting to see how the data of Tables I and II look plotted in a slightly different way, distinguishing between those quenched and tempered samples for which the authors' $\Delta S = 0$ and those showing measurable ductility as indicated by the value of ΔS . Where all three specimens having a given heat treatment showed $\Delta S > 0$, the average strengths were plotted in Fig. 21. Wherever one or

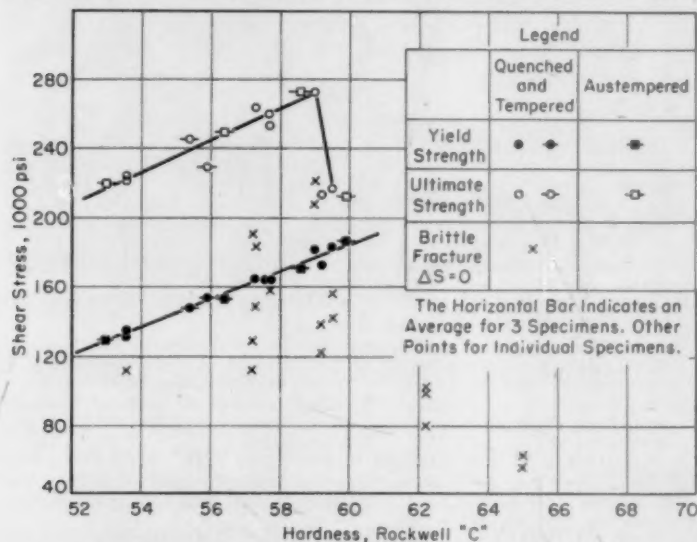


Fig. 21—Relationship of Yield Strength (1 Degree Offset) and Ultimate Strength to Hardness for Torsion Tests of 51100 Steel from the Authors' Tables I and II.

more of the specimens showed $\Delta S = 0$, the points were plotted for each specimen to avoid averaging values for brittle and ductile specimens as indicated by the value of ΔS . It can be seen from Fig. 21 that the yield and ultimate strengths for all of the quenched and tempered samples which showed some ductility follows

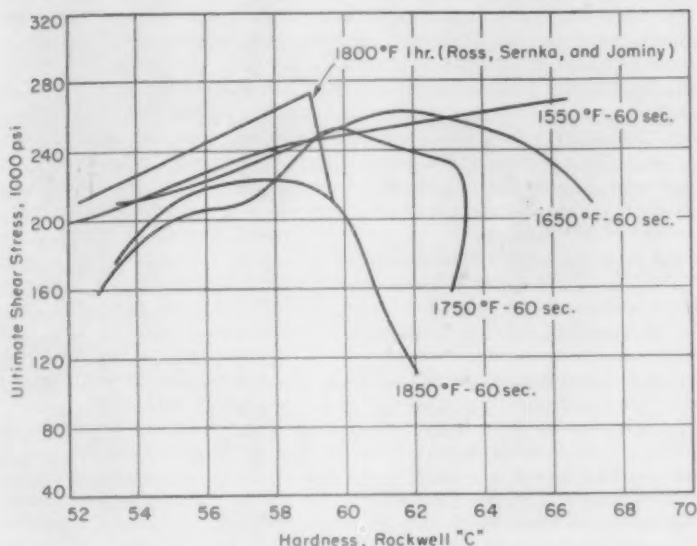


Fig. 22—Relationship of Ultimate Strength and Hardness for Torsion Specimens of 51100 Steel According to Emmons and from Fig. 21.

the same linear relationship of yield strength to hardness as the austempered samples despite the presence of carbide films present from the tempering treatments used.

The ultimate strength data for the ductile samples indicate an abrupt loss of ductility above Rockwell C-59 for both austempered and quenched and tempered samples. Some torsion tests of 51100 steel by Emmons² may shed some light on the reason for this behavior. In Fig. 22 the ultimate shear stress at fracture calculated from the ultimate torques as reported in Emmons' paper is plotted against hardness for each series of samples quenched from various austenitizing temperatures. The curve representing the authors' data for ductile samples from Fig. 21 is included for comparison. It appears that the brittle fracture behavior at high hardness levels is due to some factor which increases in severity with austenitizing temperature. Furthermore, the high ultimate strengths and ductility shown up to the maximum hardness of Rockwell C-66.5 for the samples quenched from 1550 °F indicate that high carbon steel is not always brittle near its maximum hardness.

The data compared in Fig. 22 thus indicate that the observed brittle fracture behavior found in the authors' samples austenitized at 1800 °F should not be present to the same degree at the lower austenitizing temperatures used in most applications of 51100 steel.

Written Discussion: By B. S. Lement, Division of Sponsored Research, Massachusetts Institute of Technology, Department of Metallurgy, Cambridge, Mass.

² J. V. Emmons, "Some Physical Properties Of Hardened Tool Steel." *Proceedings, American Society for Testing Materials*, Vol. 31, 1931, p. 47.

The authors are to be congratulated for establishing a correlation between the brittle behavior of SAE 51100 steel subjected to torsion and the occurrence of both carbide films and elongated particles at martensitic boundaries. The correlation of mechanical properties with microstructure is a difficult area of physical metallurgy and each advance in knowledge requires a great deal of painstaking work. This is particularly true when dealing with extremely fine particles which require the high resolution of an electron microscope in order to be observed.

I wonder if, in addition to carbide shape and distribution, the authors have considered the possible effect of the matrix solid solution on the observed brittle behavior in torsion. Based on the work of Werner,* the carbon content of the matrix of bainite formed isothermally at 400 °F in an iron-carbon alloy is probably less than 0.05% where it is necessary to temper 1 hour at 500-550 °F in order to deplete the carbon content of martensite in this alloy to the same level. Since the "torsional instability" attributable to the martensite structure in SAE 51100 steel persists on tempering up to about 550 °F, it seems likely that for equal hardness levels above about Rockwell C-57.5 a bainite structure has the advantage of a lower matrix carbon content in addition to a better carbide distribution.

The identification of the Hagg carbide by electron diffraction resurrects an old controversy. Although it seems indisputable that the Hagg carbide can form in synthetically prepared iron carbides, the bulk of x-ray and electron diffraction work carried out in the past has indicated that only epsilon carbide and cementite form during the tempering of iron-carbon martensite. This difference in behavior can be rationalized on the basis that the presence of the martensite solid solution alters the free energy relationships so that the kinetics of Hagg carbide formation during tempering become unfavorable. To make a positive identification of Hagg carbide as a product of tempering is very difficult because of the relatively small number of diffraction lines obtainable, the closeness of the d-values attributable to cementite, and the possible effects of fine particle size and lattice strain on line intensities.

Assuming that the Hagg carbide does form a tempering as claimed by the authors, some clarification seems needed with respect to the sequence of carbide formation. The structure shown in Fig. 7 for a 1 hour temper at 400 °F is described as showing fine percarbide particles and films and is similar to structures previously shown by the authors to result by tempering at even lower temperatures. The fine percarbide particles were also shown in Fig. 9 which corresponds to a 24 hour temper at 400 °F and found to exist after tempering at higher temperatures. Since the fine percarbide particles formed after 24 hours at 400 °F were identified by electron diffraction as the Hagg carbide, does this mean that the Hagg carbide occurs after a 1 hour temper at 400 °F as well as after tempering at lower temperatures? Do the authors have any electron diffraction evidence of the transition of epsilon carbide to Hagg carbide? If both epsilon carbide and Hagg carbide occur during tempering, the similarity in their appearance based on the electron microstructures presented by the authors would imply that the transition occurs *in situ* rather than re-solution of epsilon concurrent with precipitation of Hagg carbide.

* G. E. Werner, B. L. Averbach and Morris Cohen, "Matrix Phase in Lower Bainite and Tempered Martensite," *Transactions, American Institute of Mining and Metallurgical Engineers*, Vol. 206, p. 1484. Note: The estimates of carbon content of the matrix are based on the measured c/a ratios. However, it is possible for the matrix to have a body centered cubic structure with the same lattice parameter as ferrite (2.866 ± 0.003 Å) and still contain an appreciable amount of carbon in solid solution (perhaps as much as 0.1%).

Authors' Reply

The authors thank Doctors Girardi, Littman, and Lement for their comments and additions to our paper. In answer to Girardi and Littman, specimens which are reported as having identical yield and ultimate strengths broke while in the straight line portion of the torque-twist curve. No plastic deformation was noted.

Girardi and Littman's replot of the yield strength vs. hardness and ultimate strength vs. hardness data is interesting. We agree with the relationship which they established for ultimate strengths. The decrease in ultimate strength at hardness levels higher than Rockwell C-59.0 might be expected when considering fracture types which were obtained. The highest hardness austempered samples broke with the semi-brittle shattering effect whereas the remaining austempered samples displayed the ductile shear failure. Analysis of yield strength values on an individual sample basis as attempted by Girardi and Littman does not seem consistent with good practice. One would expect some of the individual quenched and tempered sample data to fall on the straight line established for the austempered samples. However, as pointed out by Fig. 21, the majority of the quenched and tempered samples do not display a linear relationship; only 8 of the 26 points representing these samples fall on the line. Fig. 21 clearly points out quenched and tempered data scatter and instability in the higher hardness range. The authors feel one could not expect much yield strength reliability for parts made from SAE 51100 steel and oil quenched and tempered to Rockwell C-57-60.

The increase in ductility at higher hardness levels for parts austenitized at lower temperatures may be a function of the amount of carbon in solution as a result of the hardening treatment. As Emmons pointed out and, as we also noted, complete solution of spheroidal carbides does not take place until about 1800 °F for the times under consideration. We chose the austenitizing temperature of 1800 °F to be certain that all the carbides were in solution before quenching.

In reply to Dr. Lement's discussion, the reported physical properties of SAE 51100 steel were correlated only with carbide morphology and not with matrix condition. The authors recognize that the amount of carbon remaining in solution will influence strength and we agree with Lement that bainite produced by austempering may have a matrix more conducive to ductile behavior at high hardnesses than does tempered martensite, but this may be due to residual stresses in the martensite.

Although epsilon carbide has been identified in pure iron carbon alloys, the effect of alloy content and time at temperature on carbide formation has not been thoroughly evaluated. Mr. J. Pomey* and Pomey and Coudray,** using thermomagnetic techniques have reported the transition of epsilon carbide to Hagg carbide with increasing time at temperature for both tempered martensite and bainite. The Hagg carbides identified in our paper were found in samples tempered from 2 to 24 hours and we believe this is sufficient time to produce the more stable Hagg carbide. Pomey* has also shown that the presence of silicon and nickel in a 0.7% carbon steel will result in the initial formation of epsilon carbide during the bainitic transformation. With further time at temperature the epsilon was shown to transform to Hagg carbide. If nickel and silicon were absent or present in small amounts, Hagg carbide is the first to form, according to Pomey.

* J. Pomey, "Carbide Formation During the Bainite Transformation in Steel," *Comptes rendus*, June 14, 1954, p. 2318-20.

** J. Pomey and R. Coudray, "Carbide Formation During the Tempering of Martensite," *Comptes rendus*, July 6, 1953, p. 62-64.

TRANSFORMATION STRUCTURES IN HYPOEUTECTOID ALLOY STEELS

By W. C. HAGEL AND M. N. RUOFF

Abstract

Detailed optical- and electron-microscopic observations were made of the morphological aspects of both isothermal and cooling transformations in laboratory Ni-Mo, Cr-Mo-V and Ni-Cr-Mo steels containing 0.3% carbon. Transformation curves were obtained by varying isothermal-reaction temperatures from 1300 to 700 °F (705 to 370 °C) and cooling rates from 9 to 30,000 °F per hour; resultant structures are more continuous and intermixed in nature than existing classifications indicate. Although diffusion and interfacial-energy effects are paramount at high temperatures and slow cooling rates, strain energy and nucleation site effects dominate at lower temperatures and faster cooling rates. Globular alloy carbides precipitate at the edges of advancing proeutectoid-ferrite plates, and fine carbide rods precipitate within lower bainite needles in a multiplicity of directions suggestive of spontaneous shearing. (ASM International Classification: N8g; Ay)

INTRODUCTION

IT IS WELL KNOWN that the widely useful mechanical properties of tonnage and specialty steels—even after additional tempering, annealing or high temperature service—basically depend on the structures resulting from commercially practicable cooling rates. As a consequence, the solid-state reactions occurring during austenite decomposition have received, and should receive, more attention than transformations in any other alloys of a single base metal. Although some of the fundamental principles and experimental facts reviewed by Mehl and Hagel (1)¹ to account for the formation of pearlite are applicable to the formation of proeutectoid ferrite and bainite, Geisler (2) and Aaronson (3) have found that these latter reactions await a better understanding of morphology-controlling factors such as diffusion, interfacial energy, strain energy and nucleation site before any proposed mechanism can be regarded with confidence.

¹ The figures appearing in parentheses pertain to the references appended to this paper.

A paper presented before the Thirty-Ninth Annual Convention of the Society, held in Chicago, November 4-8, 1957. The authors, W. C. Hagel and M. N. Ruoff, are associated with Materials and Processes Laboratory, Large Steam Turbine-Generator Department, General Electric Co., Schenectady, New York. Manuscript received April 15, 1957.

Direct evidence for certain effects of the aforementioned factors is obtainable if one employs the higher resolution and depth of focus of an electron microscope. Progress reports compiled by the ASTM (4,5,6) sought to establish suitable electron-microscopy techniques for iron-base alloys and to provide the standard electron microstructures of an isothermally transformed plain carbon eutectoid steel. Schrader and Wever (7) concluded that upper bainite growing in a 0.48% carbon-1.98% manganese steel consists of parallel feathers of ferrite sheathed by carbon-rich austenite which may eventually precipitate as cementite between the feathers; Hehemann and Troiano (8) have referred to their electron micrographs as partial confirmation of the Hultgren mechanism (9) where a special kind of ferrite forms and enriches the surrounding austenite in carbon so that cementite appears at the austenite-ferrite interface. Coheur and Habraken (10) studied bainite with an electron microscope and observed that fine striations, apparently parallel to the octahedral planes of austenite, appear within lower bainite needles; the ASTM (5) interpreted these same striations as carbide platelets at a constant 55-degree angle to the major bainite needle axis. The reaction products which appear in end-quench hardenability bars have been identified by Ross, Sernka and Jominy (11).

Since the optical observations of Carpenter and Robertson (12) in 1931, little new knowledge has been gained of cooling structures *per se*. Most investigators direct their attention solely on the more simple isothermal reactions and assume correlation with cooling behavior based on the requirement that high and low temperature transformations are either completely additive or completely independent. However, if the rate of transformation at any temperature depends upon the amount of transformation which has taken place at some higher temperature, isothermal transformation curves are inadequate for describing cooling behavior. To provide the correct heat treatment of five hypoeutectoid Ni-Mo, Cr-Mo-V and Ni-Cr-Mo deep-hardening steels, both isothermal and cooling transformation curves were determined; the hundreds of specimens gathered under such controlled conditions were subsequently given a thorough optical and electron microscopic examination to uncover the structural details needed for mechanistic interpretations.

EXPERIMENTAL PROCEDURE

Material

Steel compositions are listed in Table I; each value is the average of six wet-chemical or spectrographic analyses. All heats were melted under argon in an induction furnace, cast as 100-pound ingots, given a three-to-one forging reduction and homogenized by holding for 12 hours at 2000 °F (1095 °C).

Transformations

Both the isothermal and cooling transformation techniques used here have long been standard procedure. Specimens measuring $0.12 \times 0.50 \times 1.00$ inches were machined from billet interiors for isothermal transformation. The 1% chromium-1% molybdenum-0.2% vanadium steel was austenitized in a graphite-muffle furnace by holding for 45 minutes at 1750 °F (955 °C), and the other four low vanadium steels were austenitized by holding for 45 minutes at 1600 °F (870 °C). No banding, residual carbides, excessive decarburization or other inhomogeneities were observed after these treatments. Resulting austenite grain sizes are also listed in Table I. Held within ± 5 °F at equilibrium temperatures of 700, 800, 900, 1000, 1100, 1200 and 1300 °F (370,

Table I
Steel Compositions

Designation	C	S	P	Mn	Si	Ni	Cr	Mo	V	Al	ASTM Grain Size
2.6Ni-0.4Mo	0.30	0.021	<0.02	0.52	0.18	2.64	<0.05	0.37	—	<0.015	5
3.6Ni-0.5Mo	0.30	0.014	<0.02	0.41	0.28	3.64	<0.05	0.47	—	0.058	6
1Cr-1Mo-0.2V	0.26	0.025	<0.02	0.72	0.29	0.11	1.01	1.04	0.23	<0.015	6
2Ni-1.3Cr-0.5Mo	0.33	0.014	<0.02	0.52	0.11	2.02	1.34	0.47	0.09	0.040	6
3Ni-2Cr-0.7Mo	0.26	0.024	<0.02	0.41	0.22	2.91	1.98	0.69	—	<0.015	5

425, 480, 540, 595, 650 and 705 °C), large commercial salt pots were used to prevent recalescence effects during specimen immersion. Isothermal reaction times were measured with a stop watch from the moment of insertion, and reactions were terminated at suitable logarithmic intervals by quenching in salt brine.

Cooling transformations were performed in a Leitz dilatometer using 2.0-inch long \times 0.141-inch diameter cylindrical specimens. Heating rate to the above austenitizing temperatures was 54 °F per hour; the continuous cooling rates were 9, 18, 54, 108, 216, 910, 3,000 and 30,000 °F per hour. Sufficiently fast cooling rates could not be developed with this apparatus to determine M_s and M_f temperatures directly. However, formulae for calculating B_s , B_f , M_s and M_f temperatures have been derived by Steven and Haynes (13); since calculated B_s and B_f temperatures do compare favorably with experiment, the same type of calculations for M_s and M_f temperatures should be equally valid. All dilation curves were recorded on photographic film, and cooling transformation start and stop temperatures were measured at observed inflection points with an accuracy of ± 10 °F.

To provide approximate Ae_1 and Ae_3 temperatures, as-tempered specimens were heated for 60 hours at 50-degree intervals from 1100 to 1500 °F (595 to 815 °C); specimen hardnesses after quenching give an indication of austenitizing characteristics as shown in Fig. 1. Above the Ae_1 , hardness increases as austenite (or martensite on cooling)

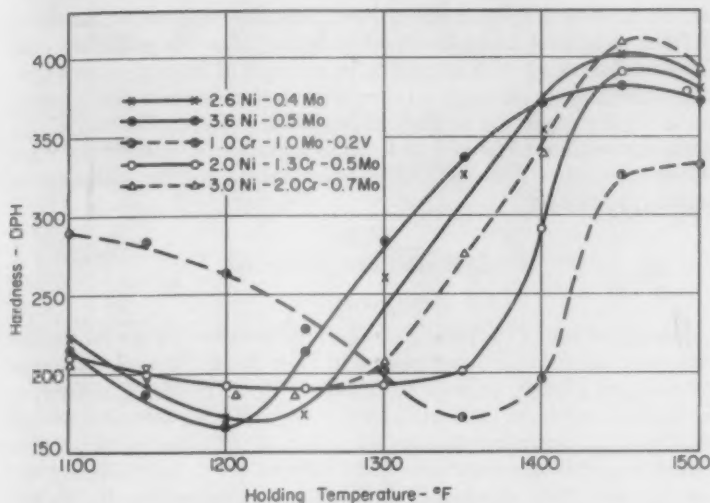


Fig. 1—Steel Hardnesses on Quenching from a Series of Temperatures after Holding for 60 Hours.

forms; above the A_{e3} , hardness decreases as austenite grain growth occurs. Both Ni-Mo steels have the lowest A_{e1} and A_{e3} temperatures and the 1% chromium-1% molybdenum-0.2% vanadium steel has the highest; further additions of nickel in the Ni-Cr-Mo steels again depress these temperatures.

Structures

Isothermal and dilatometer specimens were mounted in cold-setting plastic and sectioned to expose their 0.12 × 0.50-inch and 0.141-inch cross sections respectively. Water cooling was employed in all cutting, grinding and polishing operations to avoid tempering. Smooth surfaces were obtained mechanically by using a Carnauba-wax wheel for intermediate polishing and Gamel cloth with fine alumina for final polishing. Specimens were etched with 2% Nital for both optical and electron microscopy; at least two etching times were used to evaluate the effect of etch depth on microstructural appearance. Isothermal specimens were studied in detail at 1500 diameters with an oil-immersion optical objective and at 2000 to 60,000 diameters with a Philips 100 KV electron microscope to establish time for 1% transformation and to follow further morphological changes until complete impingement. After cooling to room temperature, all dilatometer specimens were examined both optically and with the electron microscope.

For the latter instrument, lightly etched specimens were strip-cleaned

five times with a 3% parlodion film. Negative replicas of the metal surfaces were then taken by direct stripping of a 1% parlodion film. Vacuum shadowing with chromium at an angle of 20 degrees was generally satisfactory, although a lower angle best delineates fine particles and a higher angle the ferrite subboundaries. By application of the extraction-replica technique (14), fine particles of interest were removed for further size distribution observations and for transmission electron diffraction.

EXPERIMENTAL RESULTS

Transformations

Isothermal start (1%) and cooling transformation curves for the five hypoeutectoid alloy steels are plotted in Figs. 2 to 6. No isothermal stop curves were plotted, because these points were frequently difficult to distinguish and have little useful value to justify an intensive search. Most high temperature reactions would become stabilized at about 80% completion after a week's time (6×10^5 seconds). Approximate A_{e1} and A_{e3} temperatures taken from Fig. 1 and calculated B_s , B_t , M_s and M_t temperatures are added to the ordinate of each graph. Alloy variations were so chosen as to cause decreasing calculated B_s temperatures. Although isothermal transformations occurred at only 100-degree intervals and cooling transformations took place over a range of cooling rates, hardenability increased within this group of steels to give a complete morphological sequence for all time-temperature conditions of austenite decomposition.

Using the method of Grange and Kiefer (15) for predicting the start of cooling transformations from isothermal start curves, one can calculate the dotted lines shown in Figs. 2 to 6. Agreement with experiment is good at the maximum experimental B_s temperatures measured on using a cooling rate of 910 °F per hour; predicted curves for faster rates lie either above or below experimental curves, and predicted curves for slower rates are always high. The cross-hatched zone in Fig. 2 represents the range between surface and 0.25-radius cooling rates, as found experimentally by Timo and Goldhoff (16), on air cooling a 45-inch diameter cylinder; the cooling rates used in this investigation are depicted as interrupted lines in Fig. 3. Since some preferred orientations remained in the specimens from the original forging reduction, x-ray patterns of retained austenite were too spotty for a quantitative determination. However, dilatometer-curve and microstructural examinations showed that the maximum amount of retained austenite also appeared in each steel after cooling at about 910 °F per hour. In sequence from the 2.6% nickel-0.4% molybdenum steel to the 3.0% nickel-2.0% chromium-0.7% molybdenum steel, these maxima in retained-austenite content were approximately 0, 5, 10, 15 and 25%.

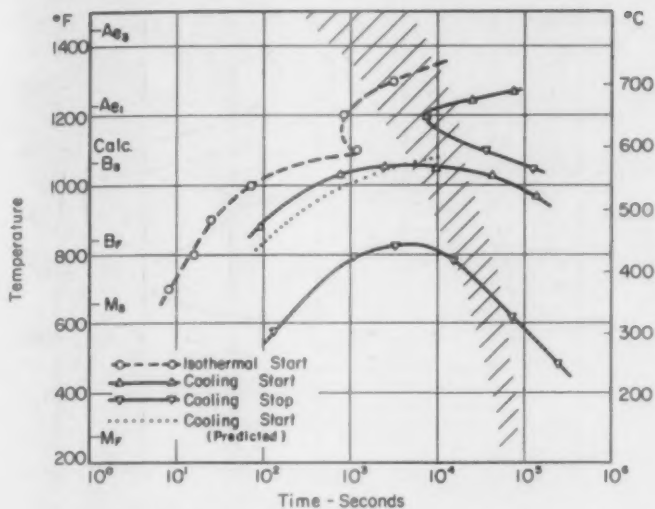


Fig. 2—Isothermal and Cooling Transformation Curves for 2.6Ni-0.4Mo Steel Austenitized at 1600 °F (870 °C). Cross-hatched zone shows range of cooling rates measured on air cooling a 45-inch diameter cylinder.

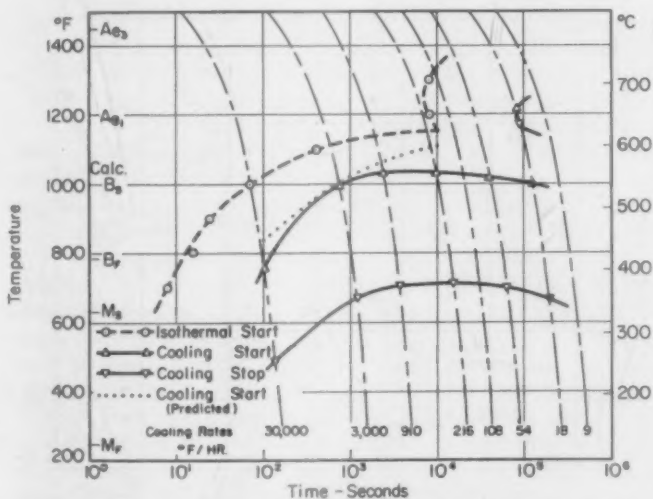


Fig. 3—Isothermal and Cooling Transformation Curves for 3.6Ni-0.5Mo Steel Austenitized at 1600 °F (870 °C). Interrupted lines show experimental cooling rates employed.

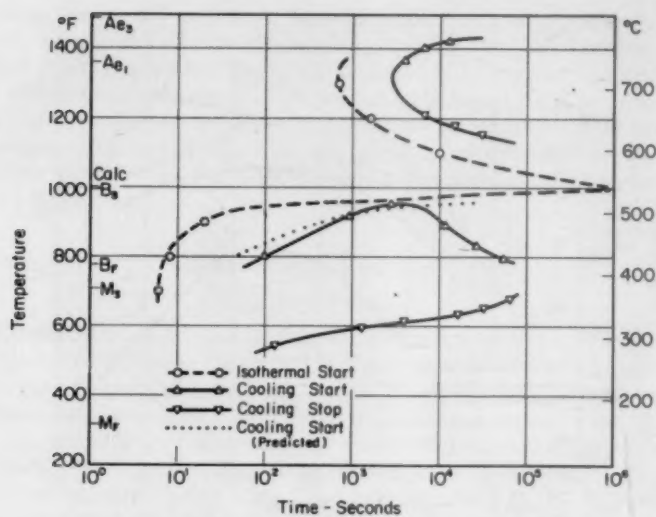


Fig. 4—Isothermal and Cooling Transformation Curves for 1.0Cr-1.0Mo-0.2V Steel Austenitized at 1750 °F (955 °C).

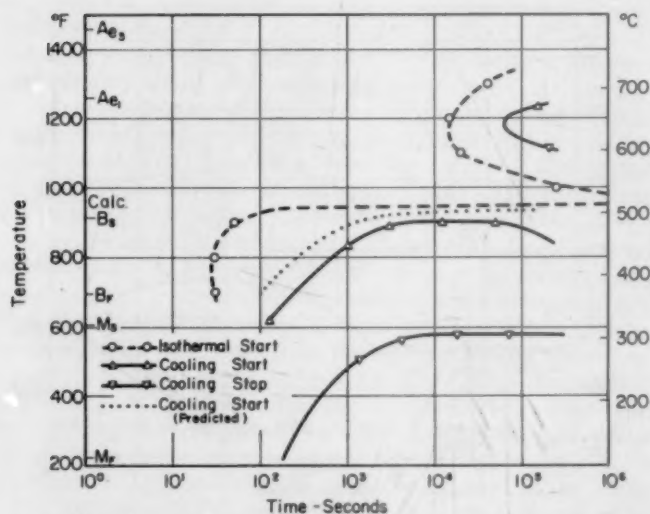


Fig. 5—Isothermal and Cooling Transformation Curves for 2.0Ni-1.3Cr-0.5Mo Steel Austenitized at 1600 °F (870 °C).

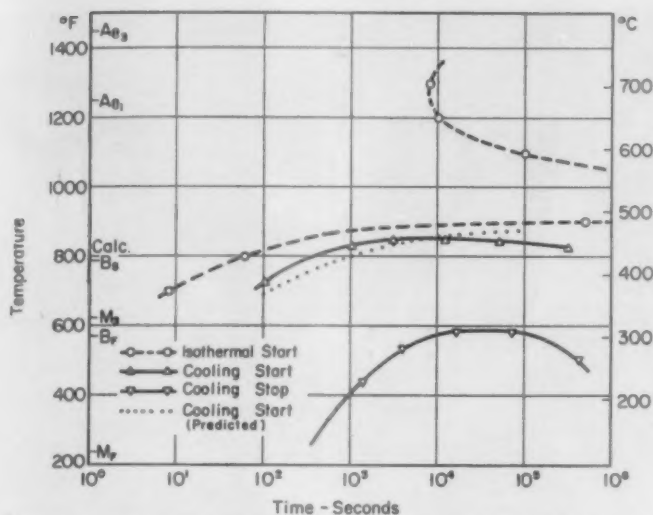


Fig. 6—Isothermal and Cooling Transformation Curves for 3.0Ni-2.0Cr-0.7Mo Steel Austenitized at 1600 °F (870 °C).

Structures

Examples of representative isothermal and cooling transformation structures are shown in Figs. 7 to 25. All electron micrographs are mounted so that shadowing direction is from the upper-right corner; apparent craters are to be interpreted as elevations on the etched metal surface. Fortunately, the presence of the carbide-forming elements, chromium, molybdenum and vanadium, promotes substructure revealing carbide precipitation at all temperatures.

The isothermal reaction just above the Ae₁ temperature for each steel is the formation of rounded carbide-containing ferrite crystals extending from and along austenite grain boundaries (Fig. 7). With increasing time an occasional idiomorph appears, and the existing ferrite thickens and contains an alloy carbide dispersion reminiscent of well spheroidized pearlite.

From the Ae₁ to ferrite knee temperatures, portions of the advancing ferrite crystals become angular to the extent that arms protrude and engulf pools of austenite (Fig. 8); concurrently, alloy carbides nucleate and grow at austenite-ferrite interfaces depending on available diffusion short circuits. No carbide-free ferrite was observed even after very short isothermal transformation times; with further growth, one could see the carbide traces of consumed austenite pools. Carbide content in proeutectoid ferrite roughly increased in sequence from the 2.6%

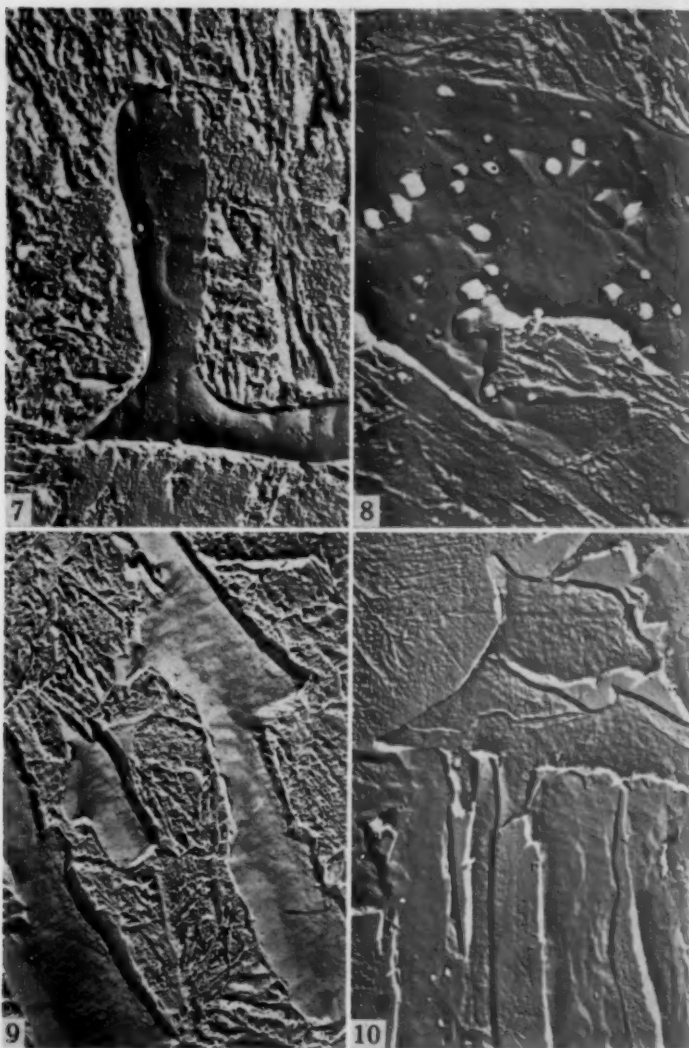


Fig. 7—3.6Ni-0.5Mo Steel Isothermally Transformed for 5.5×10^4 Seconds at 1300 °F (705 °C). Rounded carbide-containing ferrite crystals appear above the A_{c1} temperature. $\times 8000$.

Fig. 8—3.0Ni-2.0Cr-0.7Mo Steel Isothermally Transformed for 1.0×10^4 Seconds at 1200 °F (650 °C). Below the A_{c1} , angular ferrite arms engulf austenite pools; formation of (Fe, Cr)_mMo_nCa occurs at austenite-ferrite interface. $\times 8000$.

Fig. 9—2.6Ni-0.4Mo Steel Isothermally Transformed for 2.0×10^4 Seconds at 1100 °F (595 °C). Above the bainite-shelf temperature, austenite-ferrite interfaces become more linear and assume an orientation relationship. $\times 8000$.

Fig. 10—3.6 Ni-0.5Mo Steel Isothermally Transformed for 5.0×10^4 Seconds at 1000 °F (540 °C). Clean bainite initially forms, and carbides later precipitate behind the interface. $\times 8000$.

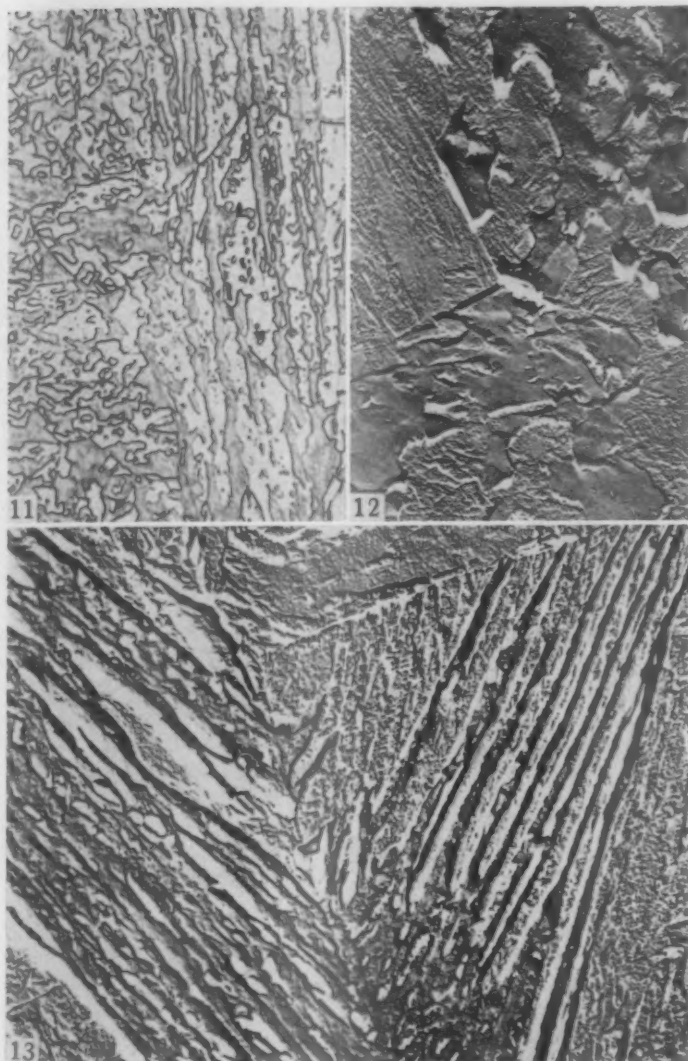


Fig. 11—2Ni-1.3Cr-0.5Mo Steel Isothermally Transformed for 1.0×10^4 Seconds at 900 °F (480 °C). Optical micrograph shows gross features of clean-bainite morphology, including "apparent" growth across grain boundaries. $\times 1000$.

Fig. 12—3.0Ni-2.0Cr-0.7Mo Steel Isothermally Transformed for 5.5×10^4 Seconds at 800 °F (425 °C). Higher alloy content promotes clean-bainite formation at lower temperatures. $\times 8000$.

Fig. 13—2.6Ni-0.4Mo Steel Isothermally Transformed for 30 Seconds at 900 °F (490 °C). Here one sees the typical advancement of upper bainite feathers and ensuing formation of carbides at ferrite-ferrite interfaces. $\times 8000$.

nickel-0.4% molybdenum to the 3.0% nickel-2.0% chromium-0.7% molybdenum steel. The 3.0% nickel-2.0% chromium-0.7% molybdenum specimen whose structure is shown in Fig. 8 was electrolytically digested, and the remaining residue gave a strong x-ray diffraction pattern for face-centered cubic $M_{23}C_6$ of lattice parameter $a_0 = 10.56 \text{ \AA}$. These alloy carbides are probably $(Fe, Cr)_{21}Mo_2C_6$, since $a_0 = 10.64 \text{ \AA}$ for pure $Cr_{23}C_6$ (17) and $a_0 = 10.52 \text{ \AA}$ for pure $Fe_{21}Mo_2C_6$ (18). Nonlamellar pearlite appeared only in the 2.6% nickel-0.4% molybdenum steel after long time isothermal holding.

From the ferrite knee to bainite-shelf temperatures, proeutectoid ferrite assumes an orientation relationship which gives the conventional pseudomorphic crystal structure of allotropic transformations. As seen in Fig. 9, the austenite-ferrite interfaces become more linear and lie fairly parallel to octahedral austenite planes. A convenient orientation guide is the experimental fact (2) that martensite needles form parallel to octahedral austenite planes in steels containing from 0 to 0.4% carbon. Although austenite-ferrite interfaces frequently appear to be dark etching under an optical microscope, higher magnifications disclose that there is a beveled region extending back about 2000 \AA from the interface. Interface-nucleated alloy carbides were observed in the proeutectoid ferrite to a lesser degree as temperature decreased.

Along the upper level of the bainite shelf, clean bainite plates soon form (Figs. 10, 11 and 12); after an indeterminant incubation period, a few carbides precipitate at scattered nucleation sites well behind the advancing interface. The names of X constituent or probainitic ferrite have long been applied to this structure, but such a distinction of degree from the general bainite reaction seems unnecessary. Use of the extraction-replica technique makes it possible to distinguish carbides from small slivers of transformed or retained austenite. The apparent carbon-rich sheath of austenite first noted by Schrader and Wever (7) could well be an etching artifact; further etching of the same specimen seen in Fig. 10 disclosed martensitic structure up to the edge of each interface. No sheaths are observable in the deeper etched specimens of Figs. 12 and 13; no carbides were found at austenite-ferrite interfaces at temperatures below the bainite shelf. Clean bainite plates frequently give the impression that they grow across austenite grain boundaries; as shown in Fig. 11, a plate may touch a boundary at or across from its point of origin and finish its development in an adjacent grain if the respective octahedral planes are so matched. Sometimes only a low angle boundary shift within the ferrite (Fig. 12) is all that is needed to affect continuation. The interphase interfaces of clean bainite are more irregular than those of other higher or lower temperature structures.

At lower temperatures, the familiar morphology of upper bainite is evident at austenite grain boundaries (Fig. 13). Advancing feathers of

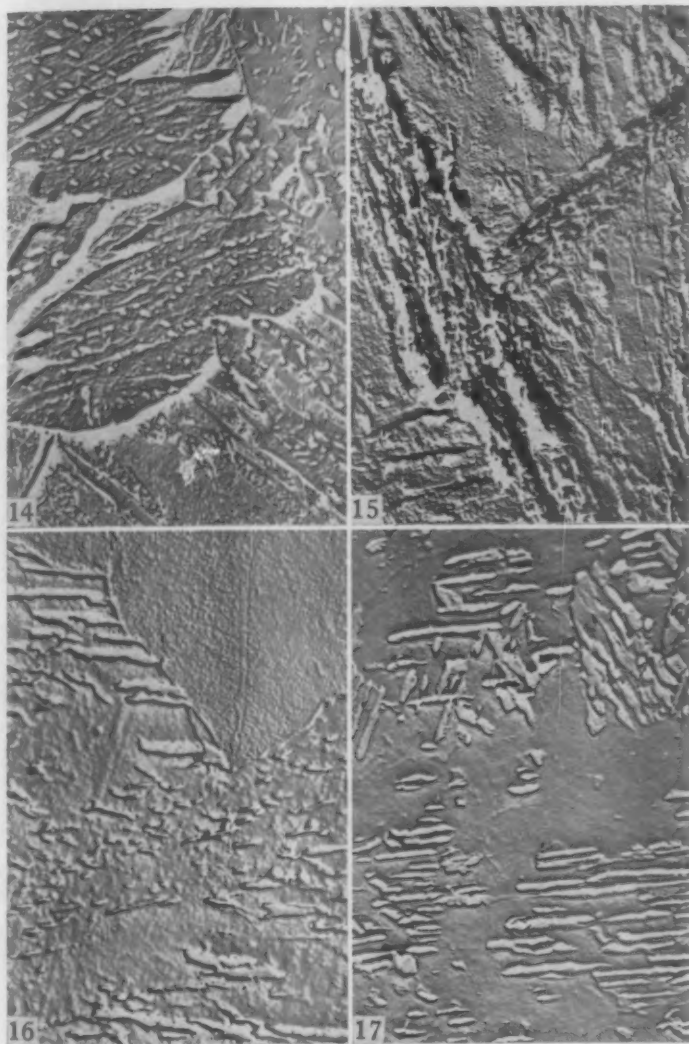


Fig. 14—2.6Ni-0.4Mo Steel Isothermally Transformed for 30 Seconds at 800 °F (425 °C). Sheaves of lower bainite are connected by ferrite-ferrite interfaces; carbides are oriented 60 degrees to direction of major bainite needle axis. $\times 8000$.
 Fig. 15—2.6Ni-0.4Mo Steel Isothermally Transformed for 30 Seconds at 700 °F (370 °C). No carbides are visible within distorted low temperature bainite. $\times 8000$.
 Fig. 16—1.0Cr-1.0Mo-0.2V Steel Cooled at Rate of 54 °F per hour. Electron micrograph shows carbide lamellae forming at tip of proeutectoid-ferrite plate. $\times 8000$.
 Fig. 17—1.0Cr-1.0Mo-0.2V Steel Cooled at Rate of 216 °F per hour. Less proeutectoid ferrite is present and the remaining austenite transforms to Widmanstätten pearlite. $\times 8000$.

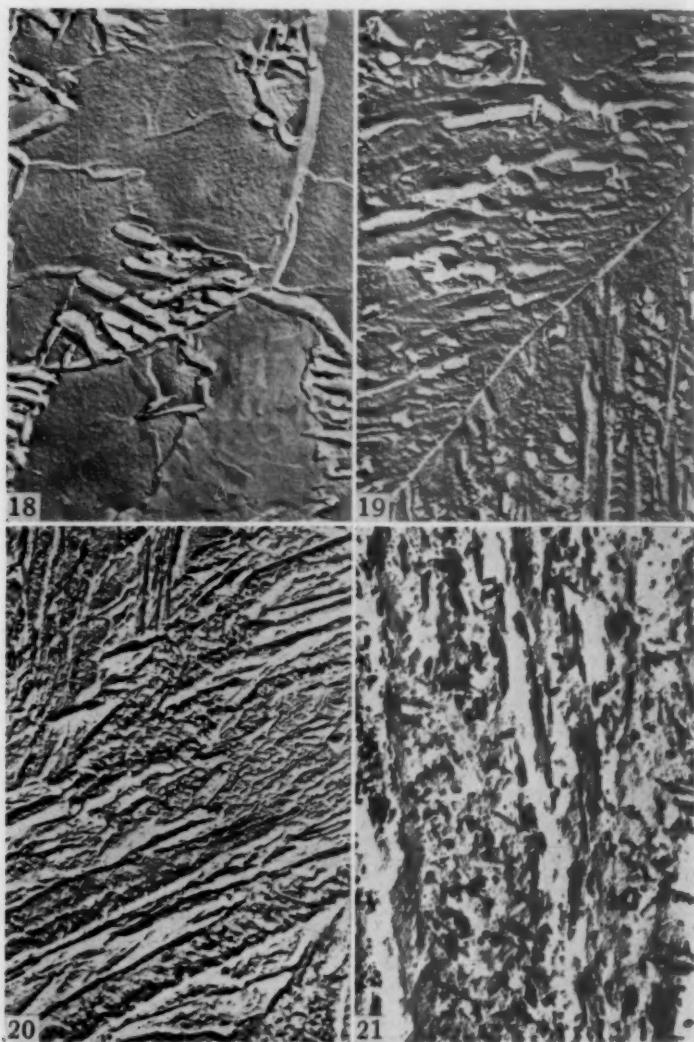


Fig. 18—3.6Ni-0.5Mo Steel Cooled at Rate of 910 °F per hour. Clean bainite appears and some pearlite forms in untransformed austenite. $\times 8000$.

Fig. 19—1.0Cr-1.0Mo-0.2V Steel Cooled at Rate of 3000 °F per hour. Upper bainite containing ferrite-nucleated carbides appears at grain boundaries. $\times 8000$.

Fig. 20—1.0Cr-1.0Mo-0.2V Steel Cooled at Rate of 30,000 °F per hour. Bainite needles in martensitic matrix show cross-striated carbides. $\times 8000$.

Fig. 21—Extraction Replica of Surface Seen in Fig. 20. Carbide rods are oriented 0, 60 and 120 degrees with main direction of bainite needle. $\times 20,000$.

ferrite extend along octahedral planes of austenite, and carbides can be observed a finite distance behind the junction of two ferrite feathers and a sliver of austenite. With time the aligned carbides grow by carbon diffusion through the ferrite until they become spherical, but, in disagreement with the Hultgren mechanism, no carbide growth was found to occur by the direct consumption of retained austenite.

In lower bainite, groupings of intragranular needles known as sheaves (19) can be observed initially. The sides of these connected needles somewhat resemble a stress catenary, and within them are carbides oriented at an angle of about 60 degrees to their lengthwise direction (Fig. 14). Isothermal transformation just above the M_s temperatures provides acicular dark-etching bainite much like tempered martensite in appearance. At high magnifications, one can see a carbide dispersion exhibiting one, three, four and possibly more striation directions on each bainite needle surface with decreasing temperature. Eventually the needles become so distorted internally that no discrete carbide particles are observable (Fig. 15). The austenite (or martensite on quenching) located adjacent to bainite needles at all temperatures appears to be essentially undisturbed, partially indicating, along with the high number of striation directions, that most of the deformation accompanying bainite formation occurs in the ferrite.

Formation of carbide-containing massive ferrite at high temperatures and nonlamellar pearlite at lower temperatures results from using cooling rates slow enough to pass through the ferrite nose. On cooling, the rate of growth of proeutectoid ferrite apparently decreases with time until carbide nuclei grow into austenite from the austenite-ferrite interface and promote the continuation of fast growing pearlite (Fig. 16). With faster cooling rates, less proeutectoid ferrite appears, and the remaining austenite transforms to Widmanstätten pearlite at a higher temperature. The carbide-ferrite orientation relationship of Fig. 17 suggests carbide nucleation on the octahedral planes of austenite; orientation adjustments within the slower forming ferrite would then be accomplished by the observed subboundary formation. When cooling rates intersect the maximum B_s hump, clean bainite first appears, and some of the remaining austenite transforms to lamellar pearlite (Fig. 18). At faster cooling rates, the low temperature transformation provides upper bainite in which the carbides are aligned along ferrite-ferrite interfaces (Fig. 19). Still faster cooling rates produce multi-striated bainite needles in a martensitic matrix whenever the steel's M_s temperature exceeds its B_f temperature (Fig. 20).

Fig. 21 shows an extraction replica taken from the same specimen used for Fig. 20. The carbides are distinctly rodlike in appearance, and, with this cooling rate, they are oriented 0, 60 and 120 degrees to the major bainite-needle axis. Note also the fine spheres or discs present in the adjacent martensite which may result from tempering during

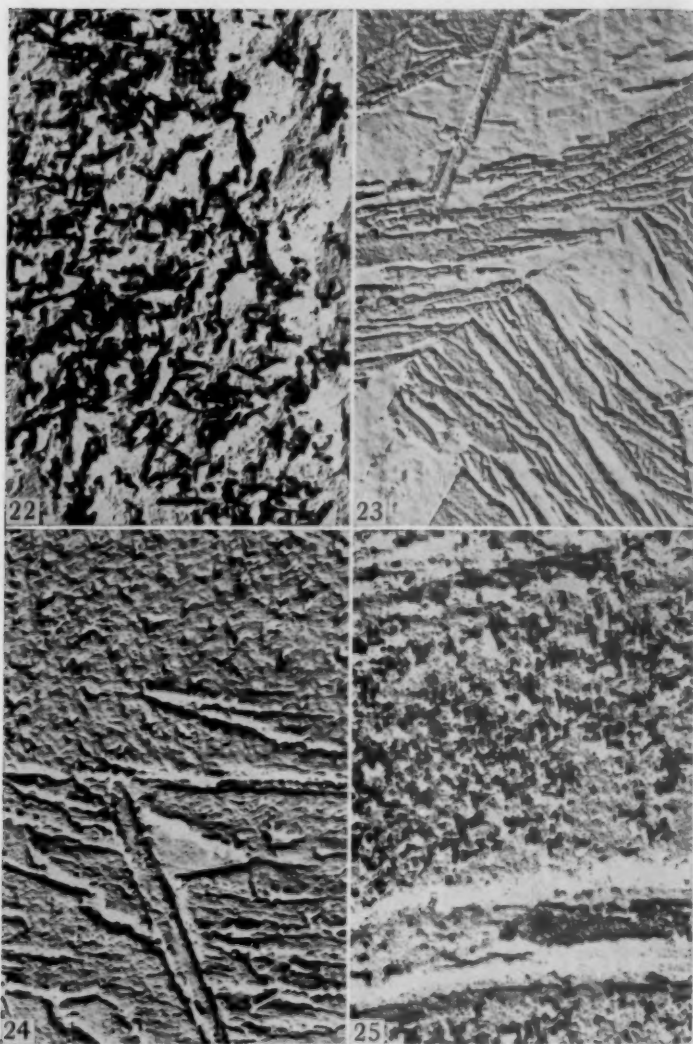


Fig. 22—Extraction Replicas of 3.0Ni-2.0Cr-0.7Mo Steel Cooled at Rate of 30,000 °F per hour. Carbide rods are oriented in a multiplicity of directions on transformation at lower temperatures. $\times 20,000$.

Fig. 23—Brine-Quenched 1.0Cr-1.0Mo-0.2V Steel. Carbide-free martensite showing sub-boundary structure was obtained. $\times 8000$.

Fig. 24—Specimen Seen in Fig. 23 Tempered for 1 Hour at 400 °F (205 °C). Numerous carbide spheres or disks appear in tempered-martensite needles. $\times 20,000$.

Fig. 25—Extraction Replica of Surface Seen in Fig. 24. Separated particles are definitely not like rods present in Figs. 21 and 22. $\times 20,000$.

further cooling. In the 3.0% nickel-2.0% chromium-0.7% molybdenum steel possessing higher hardenability so that a lower temperature transformation occurs at the same fast cooling rate (30,000 °F per hour) given the 1.0% chromium-1.0% molybdenum-0.2% vanadium steel, extraction replication shows rods carefully lifted from their actual positions and oriented in five or more directions (Fig. 22). This indicates that precipitation occurred on dodecahedral, or even higher order, planes of the ferrite; slip in ferrite is known to take place along {110}, {112}, {123} planes in the $\langle 111 \rangle$ directions.

Similarity of the size-distribution of rods extracted from lower bainite to the "straws" mentioned by Aborn (20) as forming during the quench-tempering of low carbon martensites caused the authors to investigate further the carbides produced during low temperature tempering. To insure the formation of pure martensite, a thin specimen of the 1.0% chromium-1.0% molybdenum-0.2% vanadium steel was rapidly quenched in brine, and the resulting structure seen in Fig. 23 shows subboundaries resulting from intricate and varying transformation stresses and the presence of no carbides whatsoever. Tempering of this specimen for 1 hour at 400 °F (205 °C) precipitated numerous carbide spheres or disks (Figs. 24 and 25) of much finer size distribution than the lower bainite rods seen on previous extraction replicas. Transmission electron diffraction patterns of the particles extracted from lower bainite and tempered martensite all have five characteristic lines which can be best indexed as orthorhombic M_3C . Within the errors of this technique, the identification of M_3C is not conclusive, but the data do show that neither face-centered cubic $M_{23}C_6$ nor hexagonal epsilon carbides are present.

SUMMARY AND CONCLUSIONS

The isothermal and cooling transformation curves for these alloy steels show an upper knee for proeutectoid ferrite, a region of very slow reaction and a lower knee for bainite. Structurally, however, there are many similarities which existing classifications obscure. At high temperatures, the dominating morphology-controlling factors are diffusion and interfacial energy; at low temperatures, strain energy and nucleation site dominate. At any intermediate temperature, all these factors may be present, and the observed structure depends on their relative influence. In hypoeutectoid plain carbon, nickel or manganese steels that contain no carbide-forming elements, there is a single upper knee below which no pearlite appears and bainite forms only after long time isothermal holding. Addition of carbide-forming elements will retard the upper knee by requiring alloy-carbide precipitation at advancing austenite-ferrite interfaces and accelerate the lower knee by promoting stress-relieving carbide precipitation at ferrite-ferrite interfaces and slip traces within the strained ferrite. The same reasoning applies to

cooling transformations with the exception that Widmanstätten pearlite forms on slow cooling, possibly as the result of carbide nuclei growing into untransformed austenite when proeutectoid-ferrite growth decreases.

As a result of the foregoing experimental work, a number of conclusions may be drawn:

1. The formulae derived by Steven and Haynes for calculating B_s and B_f temperatures and the method of Grange and Kiefer for predicting the start of cooling transformations from isothermal start curves provide fair agreement with independent experiments.
2. Concurrently with proeutectoid-ferrite growth in steels containing appreciable amounts of carbide-forming elements, globular alloy carbides precipitate at advancing austenite-ferrite interfaces.
3. There is no positive evidence for the existence of carbon diffusion gradients or retained austenite sheaths adjacent to ferrite plates and bainite needles.
4. After a short incubation period, globular carbides precipitate at scattered nucleation sites behind advancing clean bainite interfaces.
5. Aligned carbides precipitate in upper bainite a finite distance behind the junction of two ferrite feathers and a sliver of austenite.
6. Extraction replication of the carbide rods in lower bainite shows that they are oriented in a multiplicity of directions, indicating considerable shearing during the transformation.
7. Carbide spheres or discs of a finer size distribution than lower bainite rods initially appear on tempering martensite.

ACKNOWLEDGMENT

The specimens given an electron microscopic examination were prepared and photographed by R. E. Smith.

References

1. R. F. Mehl and W. C. Hagel, "The Austenite-Pearlite Reaction," *Progress in Metal Physics*, Vol. 6, 1956, p. 74. Pergamon Press Ltd., London.
2. A. H. Geisler, "Crystallography of Phase Transformations," *Acta Metallurgica*, Vol. 1, 1953, p. 260.
3. H. I. Aaronson, "Effects of Nucleation Site Upon Precipitate Morphology," *Institute of Metals*, Monograph and Report Series, No. 18, 1955, p. 47.
4. "Electron Microstructure of Steels. First Progress Report of Subcommittee XI, ASTM Committee E-4 on Electron Metallography," *Proceedings*, American Society for Testing Materials, Vol. 50, 1950, p. 444.
5. "Electron Microstructure of Bainite in Steels. Second Progress Report of Subcommittee XI, ASTM Committee E-4," *Proceedings*, American Society for Testing Materials, Vol. 52, 1952, p. 543.
6. "Techniques for Ferrous Electron Metallography. Third Progress Report of Subcommittee XI on Electron Metallography," *Proceedings*, American Society for Testing Materials, Vol. 53, 1953, p. 505.

7. A. Schrader and F. Wever, "On the Question of Adapting the Electron Microscope for a Structural Investigation of Steel," *Archiv für das Eisenhüttenwesen*, Vol. 23, 1952, p. 489.
8. R. F. Hehemann and A. R. Troiano, "The Bainite Transformation," *METAL PROGRESS*, American Society for Metals, Vol. 70, No. 2, 1956, p. 97.
9. A. Hultgren, "Isothermal Transformation of Austenite," *TRANSACTIONS*, American Society for Metals, Vol. 39, 1947, p. 915.
10. P. Coheur and L. Habraken, "A Study of Lower Bainite with the Electron Microscope," *Revue Universelle des Mines, de la Metallurgie des Travaux Publics, des Sciences et des Arts Appliqués à l'Industrie*, Vol. 94, March 1951, p. 107.
11. S. T. Ross, R. P. Sernka and W. E. Jominy, "An Electron Metallographic Study of the Dependence of Microstructure on Hardenability," *TRANSACTIONS*, American Society for Metals, Vol. 47, 1955, p. 727.
12. H. C. H. Carpenter and J. M. Robertson, "The Formation of Ferrite from Austenite," *Journal, Iron and Steel Institute*, No. 1, 1931, p. 345.
13. W. Steven and A. G. Haynes, "The Temperature of Formation of Martensite and Bainite in Low-Alloy Steels," *Journal, Iron and Steel Institute*, Vol. 183, 1956, p. 349.
14. R. M. Fisher, "Electron Microstructure by the Extraction-Replica Technique," American Society for Testing Materials Special Publication No. 155, 1953, p. 49.
15. R. A. Grange and J. M. Kiefer, "Transformation of Austenite on Continuous Cooling and Its Relation to Transformation at Constant Temperature," *TRANSACTIONS*, American Society for Metals, Vol. 29, 1941, p. 85.
16. D. P. Timo and R. M. Goldhoff, unpublished research.
17. A. Westgren, "Complex Chromium and Iron Carbides," *Nature*, Vol. 132, 1933, p. 480.
18. F. R. Morral, G. Phragmen and A. Westgren, "Carbides of Low Tungsten and Low Molybdenum Steels," *Nature*, Vol. 132, 1933, p. 61.
19. H. I. Aaronson and C. Wells, "Sympathetic Nucleation of Ferrite," *Transactions*, American Institute of Mining and Metallurgical Engineers, Vol. 206, 1956, p. 1216.
20. R. H. Aborn, "Low Carbon Martensites," *TRANSACTIONS*, American Society for Metals, Vol. 48, 1956, p. 51.

DISCUSSION

Written Discussion: By E. P. Klier, Syracuse University, Research Institute, Syracuse, N. Y.

Some twelve years ago we reported metallographic evidence of carbon diffusion gradients adjacent to ferrite-bainite structures in plain carbon steels.² The photomicrograph in Fig. 26, we believe, can be interpreted in no other way. Carbon diffusion gradients can be developed just as strikingly in high carbon steels as we have reported elsewhere.^{3,4}

More recently we have been determining the cooling transformation diagrams and hardenability of certain relatively deep hardening steels. Limited results of our cooling transformation studies on 4340 steel are presented in Fig. 27.

In Fig. 27 the CT diagrams for a given 4340 steel are presented after austenitizing at 1550 and 1500 °F. For practical purposes the CT diagrams are equivalent. Further the hardenability curves obtained from the CT specimens are closely

² E. P. Klier and Taylor Lyman, *Transactions*, American Institute of Mechanical Engineers, Vol. 158, 1944, p. 394/419.

³ E. P. Klier, *Transactions*, American Institute of Mechanical Engineers, Vol. 162, 1945, p. 186/195.

⁴ E. P. Klier and Volker Weiss, *Transactions*, American Institute of Mechanical Engineers, Vol. 203, 1955, p. 707/709.



Fig. 26—0.36% Carbon Steel Quenched From 1100 to 570 °C (2010 to 1060 °F), Held for 1 Second and Quenched to Room Temperature. Etched in dilute Picral. Arrows indicate diffusion gradients. $\times \approx 5000$.

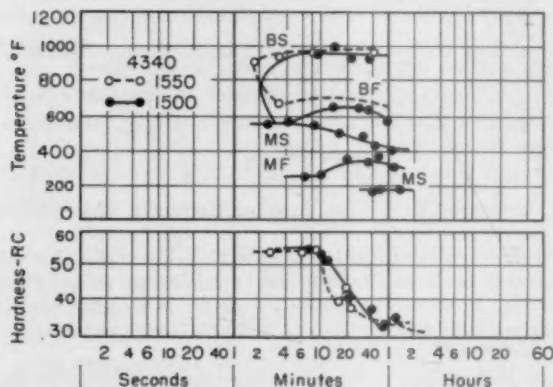


Fig. 27—Cooling Transformation Diagrams for 4340 Steel Heat No. 1, After Austenitizing at 1500 and 1550 °F. The hardenability curve was determined from the dilatation specimens for the elapsed time to cool to 200 °C (390 °F).

related. However, if the hardenability of the steel for the two austenitizing temperatures is determined with a 2.5×8 -inch specimen⁸ the hardenability curves are as given in Fig. 28. Clearly there is indicated a severe reduction in harden-

⁸ E. P. Klier, Volker Weiss and George Sachs, *Transactions, American Institute of Mechanical Engineers*, 1957, in press.

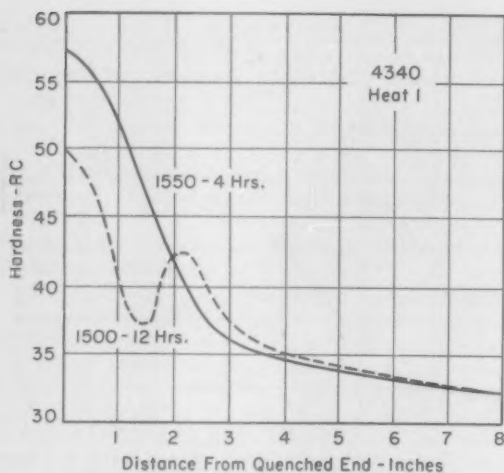


Fig. 28—End-Quench Bar Hardenability for 4340 Steel Heat No. 1, Austenitized as Indicated. Hardenability bar = 2.5 inch round \times 8 inches.

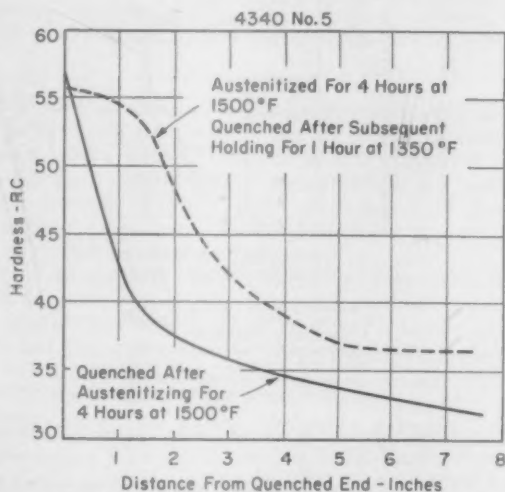


Fig. 29—End-Quench Bar Hardenability for 4340 Steel Heat No. 5, Austenitized as Indicated. Hardenability bar = 2.5 inch round \times 8 inches.

ability by this test for the lower austenitizing temperature and this is in contrast to the trends predicted by the CT diagrams. We have previously stated our belief that the rate of cooling through the critical range affects the hardenability of a 4340 steel⁴ and two experiments were conducted to confirm this effect.

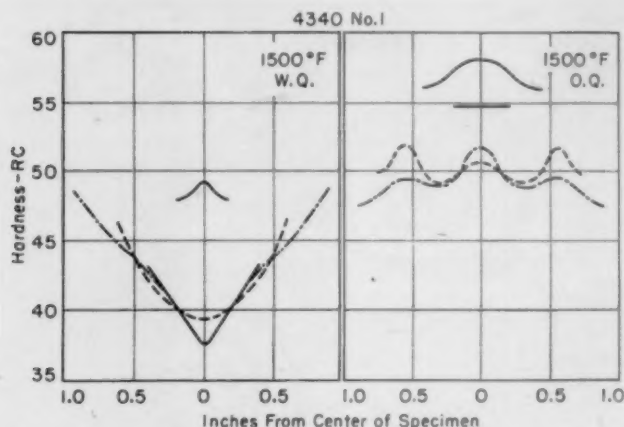


Fig. 30—Hardness Traverses of Quenched Rounds of 4340 Steel Heat No. 1, Austenitized at 1500 °F and Quenched as Indicated.

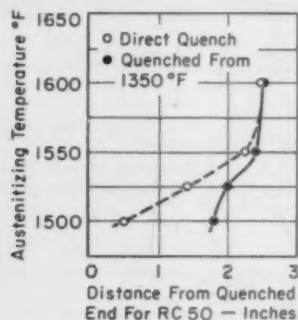


Fig. 31—Jominy Distance for $R_c = 50$ After the Indicated Austenitizing Treatments. Hardness bar = 2.5 inch round \times 8 inches. Stabilized specimens were furnace cooled to 1350 °F and quenched.

The first experiment consisted in comparing the hardenability of the 4340 steel on direct quenching from 1500 °F with that measured for austenitizing at 1500 °F followed by furnace cooling to 1350 °F and end-quenching from the latter temperature. The results are presented in Fig. 29, where it is evident that the stepped treatment has markedly increased the end-quench hardenability.

The hardenability of the 4340 steel following austenitizing and directly quenching from 1500 °F in the large end-quench specimen was low. The CT diagrams indicated, however, that a moderate reduction in the cooling rate should lead to increased hardenability. To explore this possibility two sets of cylindrical hardenability specimens were austenitized at 1500 °F; the first was water-quenched while

the second was oil-quenched. The data are presented in Fig. 30. It is, indeed, interesting that the oil-quenched specimens possess greater hardenability than do those water-quenched. The reduction in hardenability is due to the formation of ferrite in the water-quenched rounds.

The effect described above is dependent on the austenitizing temperature and for a 4340 steel this dependence is given in Fig. 31. These data clearly indicate that the hardenability behavior of a steel is an extremely complex phenomenon and that caution must be exercised in predicting hardenability from CT diagrams.

Written Discussion: By F. E. Werner, Metallurgy Department, Westinghouse Research Laboratories, Pittsburgh.

From the data given in Fig. 1, it appears that at the temperatures taken to be A_{cs} there is a considerable quantity of residual carbides still out of solution. The hardness level shown corresponds to only about 0.15% carbon in solution^a compared to approximately 0.30% in the steels as a whole. (Closer estimates are not possible since the nitrogen contents are not reported.) The authors report that at the final austenitizing temperature there were no residual carbides present; thus, the as-quenched hardness versus temperature curve must take a sharp rise between the apparent plateau in Fig. 1 and 1600 °F (1750 °F for the 1 Cr-1 Mo-0.2 V). The effect of the solution of carbides would greatly outweigh any small contribution of grain size to the hardness. Actually, the writer would be surprised if the grain size changes appreciably while many residual carbides are present. In this connection, have the authors made grain size measurements to verify their statement that an increase in grain size decreases the as-quenched hardness?

Authors' Reply

Subsequent to these discussions, the authors re-examined the specimens used and the data gathered during this investigation. No residual, undissolved carbides could be found in electron microstructures of the 1 Cr-1 Mo-0.2 V steel austenitized for 45 minutes at 1750 °F and of the other four low vanadium steels austenitized for 45 minutes at 1600 °F. Furthermore, electrolytic digestion (using 10% HCl in alcohol) of similarly austenitized specimens quenched in brine and liquid air yielded no carbide residues.

In Table II are presented data which should provide further clarification. Carbon determinations of each steel were reconfirmed in a micro-combustion apparatus, and nitrogen analyses were performed colorimetrically in accord with the micro-Kjeldahl technique. The empirical relationship of Nehrenberg, Payson and Lillys,^a i.e., $\log \text{Rockwell C hardness} = 2.182 + 0.469 (\log C) + 0.108 (\log C)^2 + 0.164 (\log N) + 0.025 (\log N)^2$ where C and N are the respective carbon and nitrogen contents in weight percent, was used to calculate the maximum hardness which can be attained in fully martensitic steels free from residual carbides and nitrides. Hardness measurements (Rockwell C) were made of water quenched specimens held for 60 hours at 1450 °F and of additional brine and liquid-air quenched specimens held for two hours at 1450 and 1900 °F and for their normal austenitizing treatments. A hardness correlation of the latter group of specimens with calculated values is within experimental error.

Originally, a holding time of 60 hours was used for all data shown in Fig. 1

^a A. E. Nehrenberg, Peter Payson and Peter Lillys, "Effect of Carbon and Nitrogen on the Attainable Hardness of Martensitic Steels," *TRANSACTIONS, American Society for Metals*, Vol. 47, 1955, p. 785.

Table II
Calculated and Measured Quenched Hardness

Designation	Interstitial Weight Percent		Calculated Maximum Hardness	Rockwell C Hardness			
	Carbon	Nitrogen		Quenched in Water 60 hrs @ 1450 °F	Quenched in Brine and Liquid Air 2 hrs @ 1450 °F	Normal Austenitizing	2 hrs @ 1900 °F
2.6 Ni-0.4 Mo	0.30	0.007	53.6	41.0	53.5	53.2	48.5
3.6 Ni-0.5 Mo	0.30	0.007	53.6	39.0	53.0	52.8	49.0
1 Cr-1 Mo-0.2 V	0.26	0.006	50.4	32.7	46.2	49.5	40.0
2.0 Ni-1.3 Cr-0.5 Mo	0.33	0.007	55.4	39.8	56.0	53.0	52.1
3.0 Ni-2.0 Cr-0.7 Mo	0.26	0.005	50.0	42.0	50.2	50.5	50.0

to provide the best approximation of the A_{e1} ; actually, only about two hours are required to determine the A_{e2} . Although the usual precautions were taken, some high temperature decarburization of the small specimens used to obtain 60-hour data points may have occurred; however, larger specimens held for shorter holding times have shown that the A_{e2} temperatures plotted in Figs. 2 to 6 are still valid. Quenched hardness decreases above the A_{e1} , and the only structural change to be detected is an increase in grain size, e.g., the ASTM grain size of specimens held for two hours at 1900 °F is 2-3. Similar changes were noticed during a study of austenitizing characteristics of modified 12-chromium alloys.⁷

Although slow-etching, structureless regions were frequently observed to outline ferrite plates and bainite needles, further deep etching would reveal lower bainite or martensite adjacent to or, at the most, 400 Å from the interface. It is possible that earlier electron-microscopic observations of a carbon-rich sheath, approximately 5000 Å wide, were made on specimens where the effect of etch depth and/or shadowing angle on microstructural appearance had been incompletely evaluated. Those regions behind an advancing interface which may be carbides, slivers of martensite or retained austenite are also subject to misinterpretation. Use of extraction replicas disclosed that they are principally carbides, but an occasional stripping of two-phase regions would yield no extracted particles and thusly indicated the presence of martensite or austenite.

The metallographic evidence which Dr. Klier presents is not incontestable; it would be of interest to learn whether the 5000 Å "diffusion gradients" observed are reproducible when examined at higher magnifications. On reviewing the references Dr. Klier mentions, one notes that his interpretation is based on measurements of the tetragonality of martensite after quenching from an isothermal transformation temperature. For a steel containing 3% chromium and 0.38% carbon, c/a values of 1.019 to 1.022 are reported⁸ which, according to Honda and Nishiyama,⁹ correspond to a carbon content of 0.5 to 0.6%. More recent data¹⁰ show that these c/a values correspond only to a carbon content of 0.42 to 0.49% and are not indicative of a significant carbon enrichment. The other 1% chromium-0.4% molybdenum and 1% chromium steels, for which tetragonal splits are reported,⁸ respectively contain 0.42% and 0.44% carbon. An attempt by Hehemann

⁷ W. C. Hagel and E. F. Becht, "Structural Stability of Modified 12-Chromium Alloys," *Transactions, American Society of Mechanical Engineers*, Vol. 78, 1956, p. 1439.

⁸ E. F. Klier and T. Lyman, "The Bainite Reaction in Hypoeutectoid Steels," *Transactions, American Institute of Mining and Metallurgical Engineers*, Vol. 158, 1944, p. 394.

⁹ K. Honda and Z. Nishiyama, "The Nature of the Tetragonal and Cubic Martensites," *Science Reports, Sendai*, Vol. 21, 1932, p. 299.

¹⁰ F. E. Werner, B. L. Averbach and M. Cohen, "The Tempering of Iron-Carbon Martensite Crystals," *Transactions, American Society for Metals*, Vol. 49, 1957, p. 823.

and Troiano¹¹ to detect tetragonal splits under similar conditions was unsuccessful.

Since hardenability refers to a performance characteristic of a steel, i.e., its ability to be hardened in certain sizes under certain cooling conditions, the latter portion of Dr. Klier's discussion lies beyond the scope of this investigation. However, some of his results may be confusing to the reader and require further interpretation. It has long been recognized that hardenability increases with increasing carbon content, alloy-element content (with the exception of cobalt), austenite grain size and austenite homogeneity; such factors as smaller section size and the increased cooling power of a quenching medium can promote deeper hardening in a steel of given hardenability, but they do not change hardenability. It does not seem likely that a decreased cooling rate through the critical range would change hardenability, except by providing increased austenite homogeneity. Dr. Klier's Fig. 6 simply shows that hardenability increases with increasing austenitizing temperature (or austenite grain size) and with an interrupted hold at 1350 °F (or increased austenite homogeneity). His concept of increasing hardenability by decreasing cooling rate delusively results from comparing cooling media rather than the true cooling histories of the specimens whose hardness traverses are plotted in Fig. 5. Although the average cooling rate of water is more rapid than oil, the duration of a water-vapor envelope may have allowed a sufficiently slow cooling rate for the low hardness specimen to form proeutectoid ferrite within an intermediate temperature range.

¹¹ R. F. Hehemann and A. R. Troiano, Authors' Reply to Discussion of "Stabilization of the Bainite Reaction," *Transactions, American Institute of Mining and Metallurgical Engineers*, Vol. 203, 1955, p. 707.

SOME ASPECTS OF THE MORPHOLOGY AND CHEMISTRY OF LEAD IN LEADED HIGH SULPHUR STEELS

BY J. W. THURMAN, E. J. PALIWODA AND E. J. DUWELL

Abstract

An experimental ingot of leaded high sulphur steel has been examined, with the aid of microradiography, in both the as-cast and hot-rolled conditions. It appears that virtually all the lead can be revealed by a microradiographic technique. The processes of solidification cause the lead to become entrapped in the same inter-dendritic regions in which manganese sulphide (and other non metallics) form. Thus, lead and manganese sulphide remain in close physical association in the steel. It follows that the distribution of lead is very similar to that of sulphur and other segregating elements. The distribution and size of lead particles is a function of the time required for solidification in relation to the settling rate of lead globules as defined by Stokes' Law. Rolling extends the sulphide inclusions into the familiar lenticular shape and the associated lead typically appears as sheaths or "tails" at each end of the elongated nonmetallic. Lead not associated with an inclusion is extended into a thin stringer. In the absence of reliable evidence of chemical combination, it is concluded that most, if not all, of the lead is present in the elemental form. (ASM International Classification N12c, M23n; Ay, Pb)

INTRODUCTION

IT HAS BEEN known for some twenty years that the machinability of steels may be significantly improved by the addition of small amounts of lead (1,2).¹ It is generally recognized that lead and iron are immiscible in both the liquid and solid states and it is to be expected that the lead added will be present as fine particles of the elemental metal. The lead appears to have but slight effect on mechanical properties. The enhanced machinability conferred by the lead is thought to be a result of internal lubrication which reduces friction at the tool/chip interface (3). It is evident that the desired improvement in

¹ The figures appearing in parentheses pertain to the references appended to this paper.

A paper presented before the Thirty-Ninth Annual Convention of the Society, held in Chicago, November 4-8, 1957. Of the authors, J. W. Thurman and E. J. Paliwoda are associated with the Jones & Laughlin Steel Corporation, Pittsburgh, and E. J. Duwell is associated with Minnesota Mining and Manufacturing Company. Manuscript received May 8, 1957.

machining quality is dependent on the dispersion of lead throughout the steel and on its mode of occurrence. Methods for the study of morphology are therefore of importance.

Little has been published on the microdispersion and mode of occurrence of lead in steel (4,5,6,7). This probably reflects the difficulty of obtaining useful data with the methods available. Various tests, including exudation or "sweat" tests, printing methods, and standard metallographic procedures, have been used to assure favorable lead distribution, however, none of these tests are altogether satisfactory. Sample preparation for metallographic study is exceptionally difficult because of the fine dispersion of the lead constituent and its extreme softness. Standard etching procedures have failed to delineate a lead constituent satisfactorily. Recourse may be had to converting the lead to salts whose distinctive color may be recognized by observation under polarized light. These include the iodide, (8,9) dichromate, chromate, (2) and "dithizonate." (10) Of these, the last is the most satisfactory, but they all suffer from the disadvantage that the lead constituent is converted into a reaction product which (with the possible exception of the "dithizonate") conveys a false impression of the size and shape of the particle. Also extremely fine particles or stringers in a rolled product may not be resolvable.

The failure of standard metallographic techniques to reveal lead suggested to early workers that the lead was present in a submicroscopic state. Later work (6,7) indicated that at least some of the lead could be accounted for by particles which could be resolved at moderate magnifications. Nead, Sims, and Harder (11) using a micro sweat test, reported that a portion of the lead was associated with sulfide inclusions in high sulphur steels.

MICRORADIOGRAPHY

In some other work, unexplained variations in the machinability of leaded high sulphur steels were encountered. These were thought to be due to differences in lead dispersion. Attempts to obtain data by existing metallographic methods which would correlate satisfactorily with machinability tests met with only indifferent success. Consequently, these methods were supplemented with microradiography as suggested for studies of this sort by Clark and Gross (12) and others. The present paper describes the microradiographic technique employed and its application to the examination of an experimental commercial sized ingot of Type "A" steel both in the as-cast condition and after various amounts of reduction by hot rolling.

Radiography is a process of photographically recording the variations in intensity of an x-ray beam caused by differential absorption on passage through a nonhomogeneous object. Highly absorbing regions within the object thus appear as "shadows" on a photographic plate.

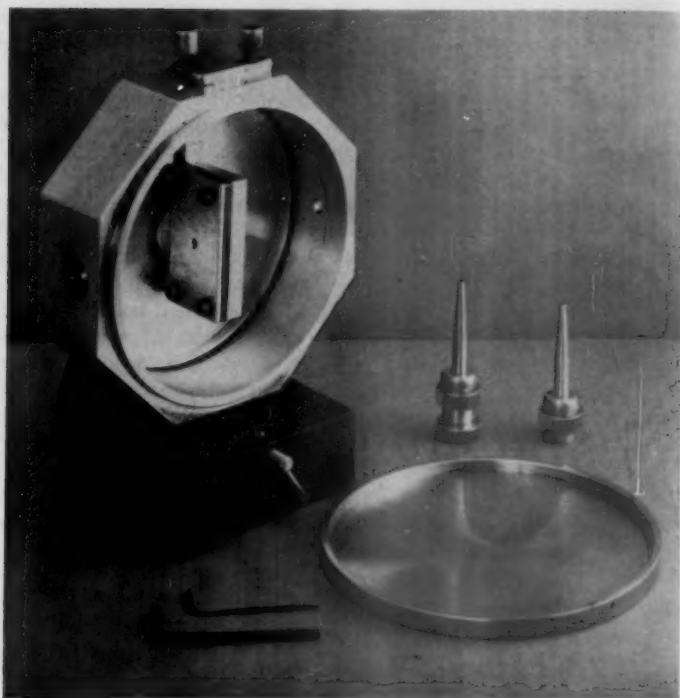


Fig. 1—Flat Plate Camera Mounted for X-Ray Exposure.

If a high resolution emulsion is used so that details on a microscopic scale can be resolved by subsequent magnification of the image, the process is called microradiography. Microdispersion of lead and the appearance of manganese sulphide inclusions, which are of interest in the present work, can be clearly revealed in this way.

Since the image obtained is produced by structural details in three dimensions, it is necessary to restrict the thickness of the sample to a few times the average dimensions of the constituents to be observed in order to eliminate confusion from overlapping. Thickness is also limited by the requirement of a convenient exposure time. For steel, it has been found that foils 0.0035 inch in thickness permit most inclusions to be readily distinguished from their surroundings and the exposure time with the radiation used is in the neighborhood of one half hour. Such foils may be prepared by mounting a flat sample in a magnetic chuck and carefully grinding to the proper thickness with a narrow soft wheel. They may be polished but this is not necessary since light grinding marks do not seriously hamper interpretation.

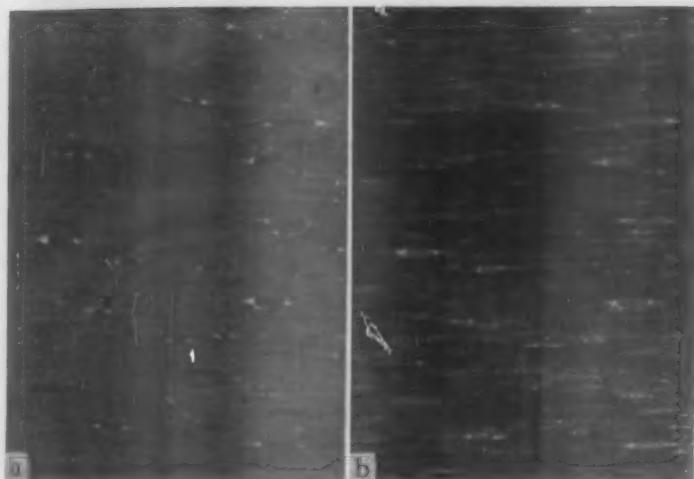


Fig. 2—Microradiographs of Hot-Rolled Type "A" Steel. $\times 100$. (a) Cr $K\alpha$ Radiation. (b) Co $K\alpha$ Radiation.

It is important to maintain close contact between the thin sample and the emulsion in order to obtain maximum resolution. This has been done by the use of a simple flat plate camera which was conveniently mounted in a Debye-Scherrer powder camera as illustrated in Fig. 1. Diffraction can occur if a crystallite within the sample is in proper orientation, however, diffraction and absorption effects can be readily distinguished, in cases of doubt, by slight rotation of the sample.

Magnification attainable is limited by the grain of the photographic emulsion. With the use of Kodak 649-0 spectroscopic plates, processed in D-19 developer, magnifications considerably in excess of the $\times 100$, selected as standard here, could be obtained without undue graininess. Negatives were magnified with a standard metallograph, using transmitted light. Contact prints were made from the metallographic plates. Since these prints are from a third photographic process, they correspond in appearance to the original radiographic image.

The decrease in intensity of an x-ray beam on passing through matter is exponentially related to the distance traversed and to the mass absorption coefficient of the substance. The absorption coefficient increases rapidly with wave length until a sharp discontinuity is reached at an "absorption edge" where the coefficient abruptly decreases and then starts again to rise slowly. This is the longest wave length which excites the K, L, or M spectra of the irradiated element. The wave length of the absorption edge is unique for each element, and this fact, in theory, permits the unequivocal identification of a segregated element. Thus,

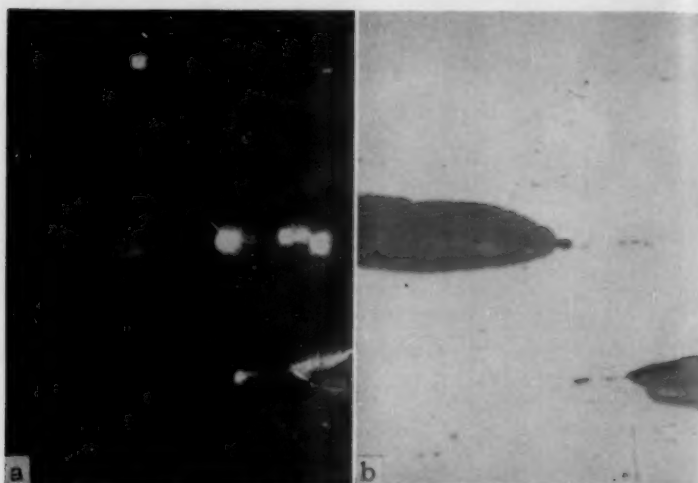


Fig. 3—Photomicrographs of Same Area as Fig. 2. (a) Etched in Potassium Dichromate-Acetic Acid. Polarized Light. $\times 1000$. (b) Same Field as (a) Lightly Repolished Un-etched $\times 1000$.

in the present work, comparison of microradiographs prepared with Co $K\alpha$ and Cr $K\alpha$ radiation permits positive identification of manganese sulphide inclusions. Since the wave length of the Co radiation is on the short wave length side of the K absorption edge of manganese, this element is an effective absorber. Manganese sulphide inclusions therefore appear lighter than the steel matrix. With chromium radiation the reverse is true and manganese sulphide appears dark.

The mass absorption coefficient increases rapidly with atomic number. Lead is therefore highly absorbing and particles of lead or a lead compound appear nearly white using either of the above radiations.

These effects are illustrated in Fig. 2 which represents the same area of a hot-rolled Type "A" steel photographed with chromium $K\alpha$ and Co $K\alpha$ radiation. The latter renders manganese sulphide with a density about midway between that of the steel matrix and lead. Thus detail is somewhat more easily perceived when cobalt rather than chromium radiation is used. For this reason, Co $K\alpha$ radiation was employed in all of the microradiographs prepared in the examination reported here.

It will be observed, in Fig. 2 that the lead is almost exclusively present as sheaths or "tails" at each end of the elongated manganese sulphide inclusions. On the basis of rough calculations it can be concluded with some confidence that virtually all the lead present is resolved by microradiography. Fig. 3 presents photomicrographs at higher magni-

fication, of the same field represented by the microradiographs. Etching with a dichromate solution indicates that the dark appearing material at the ends of the sulphide inclusions is a lead containing constituent. All efforts, in this work, to detect lead compounds by x-ray and electron diffraction methods have failed and it is therefore likely that this dark material is metallic lead. It is probable that ordinary metallographic techniques are at present incapable of developing a faithful reproduction of its true appearance.

EXAMINATION OF AN AS-CAST INGOT OF TYPE "A" STEEL

The methods just described were applied to a detailed examination of an experimental ingot of Type "A" steel in the as-cast condition and after various amounts of reduction by hot rolling. The analysis of the heat was as follows:

C	Mn	P	S	Pb
0.08	0.98	0.046	0.300	0.17

Low carbon ferromanganese was added in the furnace and ladle additions consisted of ferrophosphorus and flowers of sulphur. The lead addition of 6.1 pounds per ton was made to the mold in the usual way in the form of 99.8% pure lead shot, finer than 20 mesh. The experimental ingot was poured in a warm, clean, unpainted, 24 × 24 inch big end down mold with hot top. Ingot weight was 10,400 pounds. Details of the method of adding the lead as well as a discussion of the segregating tendencies of lead and sulphur have been published (13). Results of chemical analyses for lead and sulphur are summarized in the sketch of Fig. 4.

Fig. 4 also depicts the method of sampling the ingot for radiographic examination. Foils, perpendicular to the vertical axis, were prepared at each of the locations indicated by squares. Samples were so cut that a surface immediately adjacent to the foil was prepared for metallographic examination. Structures representative of those observed are presented in Figs. 5 through 9 in which the microradiograph and the photomicrograph of the companion surface are displayed side by side at the same magnification.

One of the more striking features of the micrographs is the extremely fine size of the inclusions in those portions of the ingot which have cooled rapidly. This was apparent in varying degrees in all samples from near the surface of the ingot and all the samples from the extreme bottom. Fig. 5 which is from the outside surface at the top of the ingot, is representative. It will be observed that the inclusions delineate a structure by having become entrapped in interdendritic fillings. This appears to represent the junction between the "chill zone" and the "columnar zone". The dendritic character of the distribution is much less pronounced in the accompanying photomicrograph.

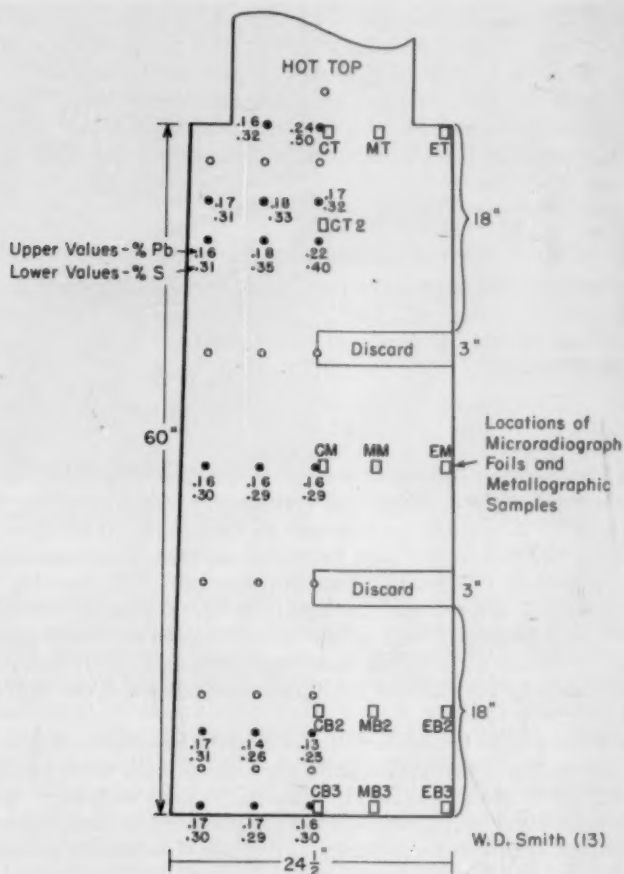


Fig. 4—Sketch of the Type A Ingot Studied.

As the interior of the ingot is approached the inclusions become larger and the crystallites which they outline are likewise larger and equiaxed. Fig. 6, which is taken midway between edge and center from the middle part of the ingot, is representative. It will be observed that the lead constituent is confined to the same areas as the manganese sulphide. For the most part the lead particles are globular. They appear to be mainly in physical contact with the sulphides, although occasional ones are seen to exist independently. Within the interdendritic regions the distribution appears to be quite random. This is more clearly evident when the spatial arrangement of the inclusions is observed by stereo-

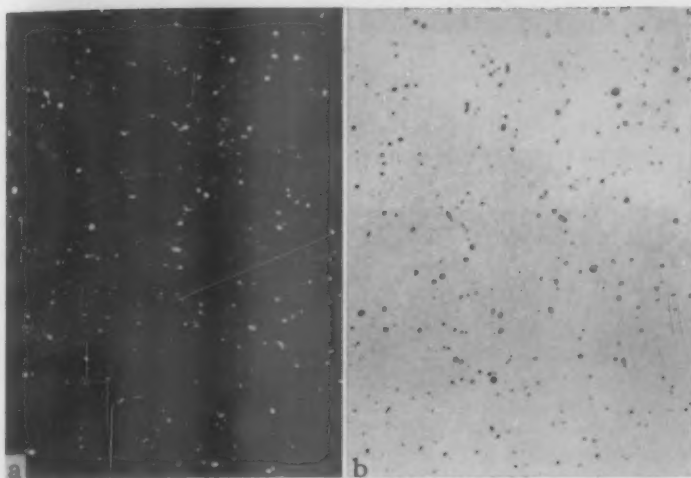


Fig. 5—Sections Near Outside Surface at Top of Ingot (Sample ET) (a) Microradiograph Co K α $\times 100$. (b) Photomicrograph $\times 100$.

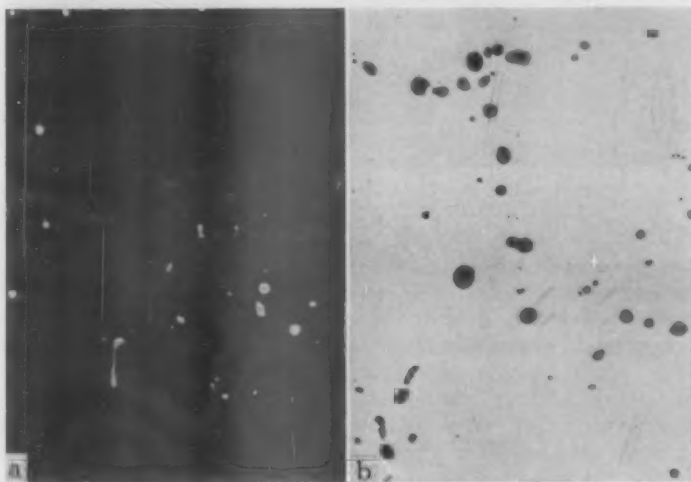


Fig. 6—Section Midway Between Surface and Center From Middle of Ingot (Sample MM) (a) Microradiograph Co K α $\times 100$. (b) Photomicrograph Unetched $\times 100$.

scopic examination. This may be done by making two exposures with the x-ray beam at equal but opposite angles to the normal. The resulting images are then superimposed, either with an instrument or, after some

practice, with the unaided eye. Such a stereoscopic pair is illustrated in Fig. 7.

It is not within the subject matter of this report to examine the nature of the sulphide inclusions. It was somewhat surprising to note, however, that they are not predominately of a globular nature, but appear more typically to be elongated or vermiform. The shape assumed

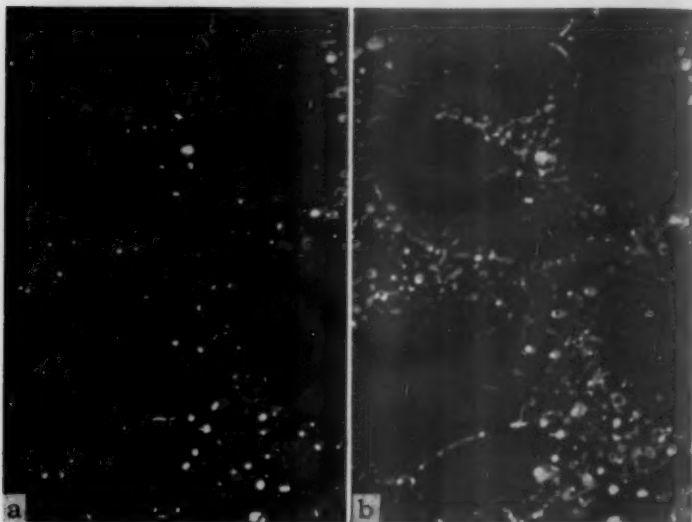


Fig. 7—Stereoscopic Pair of Microradiographs Taken From the Center Portion of the Middle of the Ingot (Sample CM) Co K α Radiation Original Magnification $\times 100$.

by sulphide inclusions is probably related to differences in plasticity at the time of solidification. The last metal to freeze in the interdendritic spaces is, obviously, a very complex system. Among the factors influencing the shape and distribution of sulphides are such things as departures from stoichiometric proportions, presence of foreign solutes, and traces of a ternary (or higher) eutectic. The intersection of a plane with the irregular shapes observed is roughly circular. Thus metallographic examination of a polished surface conveys the false impression that the inclusions are almost entirely globular. The apparent two-phase nature of nearly all the sulphide inclusions is of interest. It would be natural to ascribe this to concentration gradients of manganese and presence of oxides, however, it is difficult to account for the observed photographic density in this way.

A typical variation in inclusion nature from inside to outside of the ingot is illustrated in Fig. 8 which represents sections from the edge,

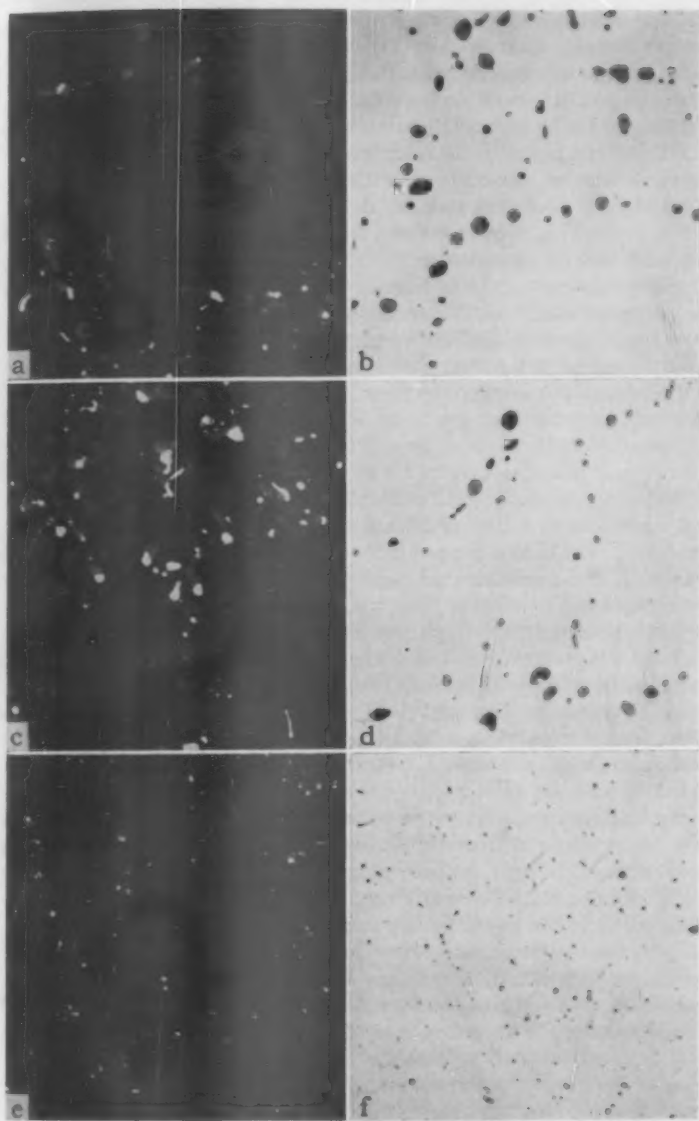


Fig. 8—Horizontal Section Nine Inches From Bottom of Ingot $\times 100$. (a and b) Center. (c and d) Midway. (e and f) Edge. (a, c and e) Microradiographs Co K α Radiation. (b, d and f) Photomicrographs.

middle, and center of the ingot at a distance of nine inches from the bottom surface. Comparison of the microradiographs with the photomicrographs demonstrates that the dark material in the latter is largely lead. (Distinction between lead and "oxysulphides" is not clearcut by metallography in ordinary illumination).

The interpretation of the micrographs appears to be rather straightforward. The lead shot added to the ingot is quickly reduced to a very small particle size by the action of the gun, agitation of the molten metal, and rapid melting. Since lead and iron are virtually immiscible in both the solid and liquid states, a 2-phase system is quickly established in which the second phase is initially very finely dispersed. The liquid lead droplets would tend to settle out at a rate defined by Stokes' Law. During the settling period, however, there is evidently a tendency toward agglomeration since large particles of lead are invariably found in the bottom portions of the ingot which are discarded. Thus Stoke's Law tends to maintain the required dispersion since larger particles are rapidly lost through sinking. The settling is hindered first by turbulence and convection currents in the molten metal and later by the onset of solidification. In the zones at the surface of the ingot, solidification is almost immediate and small lead particles are forced into interdendritic areas before the tendency to agglomerate has increased size greatly. A similar mechanism causes fine sulphides to precipitate in the same regions. Chemical studies indicated that the lead content at the surface was moderately high and rather uniform. In areas which are molten for a longer time one finds larger particles as a result of agglomeration while settling and, at the same time, a lower lead content. Thus the size of particle and the amount of lead retained is a function of the time required for solidification in relation to the settling rate. This mechanism would account for the observed lower efficiencies of lead additions with increasing carbon content (13). It was noted that the lowest lead contents were in the center of the ingot near the bottom. It is just this region which would remain molten longest in big end down mold practice. Similar considerations explain the rather large particle size with higher lead contents near the top of the ingot. This region just under the hot top is molten for a relatively long time, permitting settling and agglomeration. However, solidification is well advanced somewhat lower in the ingot and high lead contents are entrapped. Examination of samples from the bottom surface of the ingot indicate that, in spite of the fine dispersion shown, a chill zone does not form in the center portions since lead was found down to the actual surface. Lead additions are not started immediately at the beginning of the pour and thus rapid freezing must not occur until the mold is partially filled and some lead has had an opportunity to settle out. In this way large particles are occasionally found associated with an otherwise fine dispersion.

If the lead and sulphur contents are plotted over areas of interest in the ingot, the two plots are almost exactly parallel. This might be interpreted as evidence for the formation of lead sulphide or of mutual solubility at elevated temperature with subsequent precipitation. Thermodynamic reasoning, however, suggests that neither of these is probable. Considerable effort has been expended in an attempt to detect the presence of lead compounds by means of x-ray and electron diffraction. Only lead and manganese sulphide have been found so far and it seems safe to conclude that the lead present is largely, if not entirely, elemental lead. This implies that lead and manganese sulphide, although segregating by different mechanisms, are forced into the same areas as a result of the fact that both are trapped in the last metal to solidify in interdendritic spaces. It is possible that the surface energies are such that the lead wets manganese sulphide forming in the "mushy" interdendritic material. In any event, it appears that the close association of the two is due to purely mechanical influences and, to this extent at least, is fortuitous.

EXAMINATION OF BARS ROLLED FROM INGOT OF TYPE "A" STEEL

Bars, $3\frac{1}{2} \times 4$ inch were cut from each of twelve locations represented by micrographs and these were hot-rolled. Foils and metallographic samples were taken after 50%, 75%, 90%, and 98% reductions. A typical sequence of structures is illustrated in Fig. 9. It will be noted that as rolling proceeds the manganese sulphide inclusions gradually assume the lenticular shape which is characteristic of hot-rolled high sulphur steels. The shape of the resulting inclusions is determined by their malleability at steel rolling temperatures which, in turn, is probably related to the degree of oxidation of the steel. It has been shown (15,16) that best machinability is obtained with globular sulphides rather than elongated stringers. Also best properties are obtained in the case of leaded steels when the lead is present as relatively massive particles, along with globular sulphides, rather than thin stringers or extremely fine particles. It will be observed in Fig. 9 that as rolling progresses the position of the lead particles is changed and that they eventually assume the form of sheaths at the ends of the elongated sulphide inclusions. This condition is typical of leaded high sulphur steels. The effect appears to be mechanical. At steel rolling temperatures the lead is molten and the liquid metal in contact with the nonmetallic inclusion is forced by rolling stresses to each end of the less plastic sulphide by a sort of extrusion process. This effect is shown more clearly by the higher magnification photomicrographs of Fig. 10. (It will be recognized that not all regions which appear bright under polarized light are lead particles and that observation in color is necessary to distinguish the lead.)

Occasionally, a sulphide inclusion completely enveloped with lead

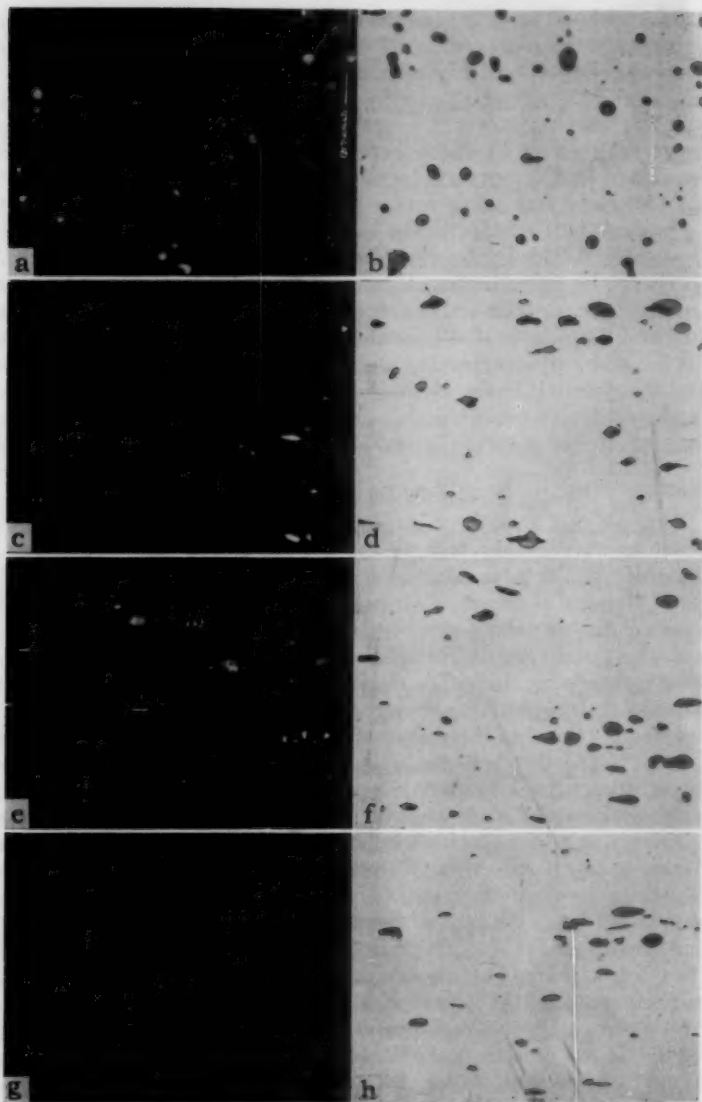


Fig. 9—Influence of Hot Rolling on Lead and Sulphide Inclusions. (a, c, e and g) Microradiographs Co K α \times 100. (b, d, f, and h) Photomicrographs. (a and b) As-cast. (c and d) 50% Reduction. (e and f) 75% Reduction. (g and h) 90% Reduction.

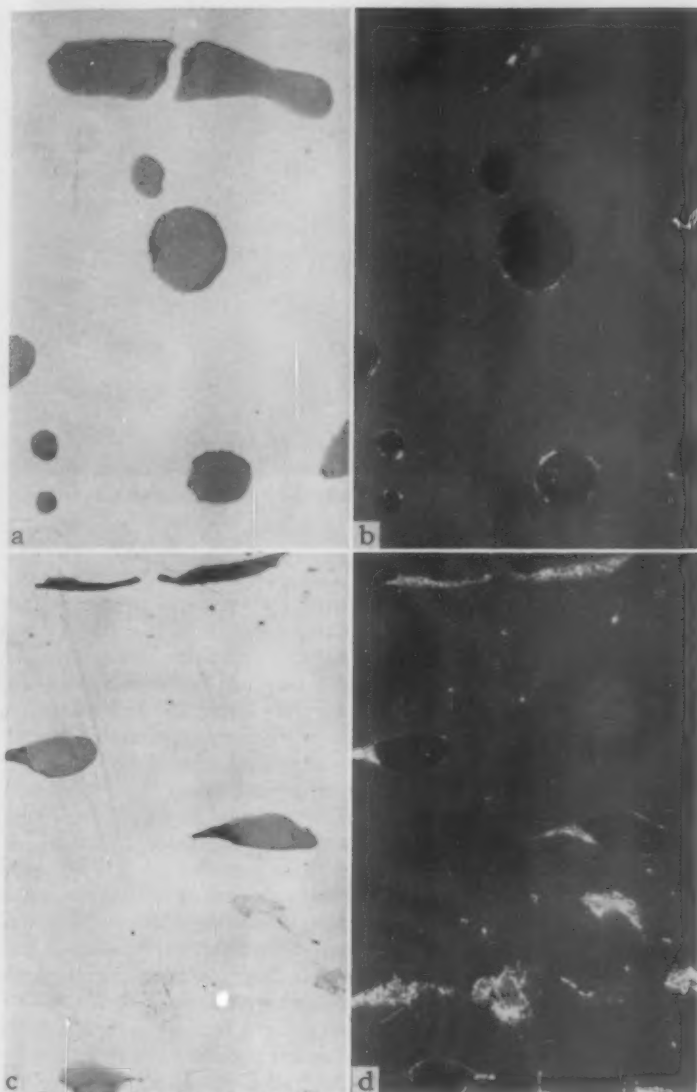


Fig. 10.—(a and b) As-Cast. Ordinary light and polarized light. (c and d) Reduced 90% By Hot Rolling Ordinary light and polarized light. $\times 500$. Etchant: Dithizone.

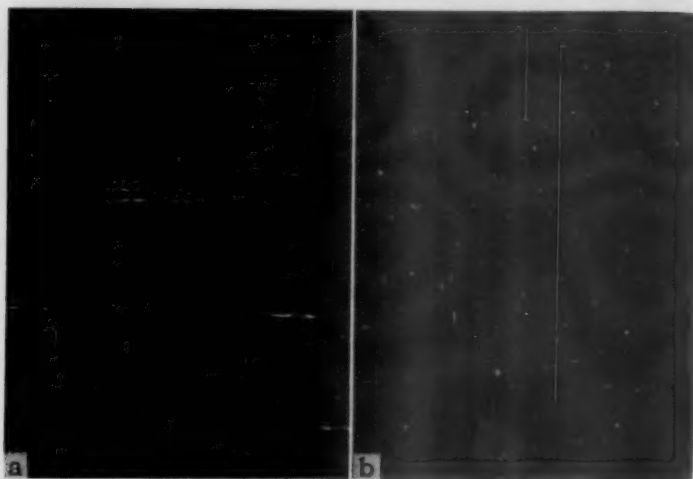


Fig. 11—Microradiographs of Low Sulphur Leaded Steel Co K α Radiation. $\times 100$.
(a) Longitudinal section. (b) Cross section.

is observed. Apparently this is caused by variation in the relative amounts of lead and sulphide present as one inclusion. It will be evident that there is an interrelationship between the masses of the inclusion constituents during solidification and subsequent hot working. In general, sulphide inclusions which are severely elongated and broken up during rolling exhibit fine "tails". Conversely, oval type sulphides retain relatively massive lead particles as sheaths. Examples of the types of inclusion just described are given in another publication (16).

As may be observed in the microradiographs of the as-cast ingot, there are occasional lead particles which are not associated with sulphide inclusions. During hot working these particles are severely elongated and appear ultimately as very fine stringers of lead. An example of this may be seen in Fig. 9. Fig. 11 represents typical lead inclusions in a rolled low sulphur steel. Although the ratio of the amount of lead to nonmetallic material is much greater in this case there is still a tendency for the lead to be associated with nonmetallics.

It has been reported that, aside from a slight grain refining effect, the influence of lead on the normal mechanical properties of rolled leaded steels is negligible. However, since the lead is extended during rolling into the form of either stringers of lead or sheaths associated with non-metallics, it might be anticipated that a measureable difference would be found between properties as determined longitudinally and transversely to the rolling direction.

SUMMARY

Microradiography is a useful tool for the investigation of the morphology of leaded steels and, especially when used in combination with standard metallographic methods, is capable of producing information.

The distribution of lead in the as-cast ingot closely follows that of other segregating elements, particularly sulphur. This is a result of mechanical processes occurring during freezing which force lead and nonmetallic inclusions into the same interdendritic areas.

No evidence of lead compounds has been obtained by x-ray or electron diffraction methods. It is therefore concluded that the lead is present largely, if not entirely, in the elemental form. The close association of lead with manganese sulphide apparently is not a result of chemical reaction or mutual solubility at elevated temperature.

The distribution of lead and the size of lead particles is a function of the time required for solidification in relation to settling rate of lead particles.

Rolling elongates the manganese sulphide inclusions and at the same time forces the associated lead particles to each end of the inclusion where they exhibit the typical appearance of lead sheaths or "tails."

ACKNOWLEDGMENT

It is a pleasure to acknowledge the assistance of the authors' associates at the Graham Laboratory for J&L Research and particularly to thank F. R. Turner for his careful metallographic work.

References

1. F. Robbins, "Character and Performance of Lead-Bearing Steels," *Iron Age*, Vol. 142, No. 20, 1938, p. 28-33.
2. F. Robbins and G. Caskey, "A Discussion of Leaded Steels," *TRANSACTIONS, American Society for Metals*, Vol. 27, 1939, p. 887-992.
3. M. E. Merchant, "Metal Cutting Research—Theory and Application," *Machining—Theory and Practice*, 1950, p. 5-44, American Society for Metals, Cleveland.
4. L. Northcott and D. McLean, "The Structure and Segregation of Two Ingots of Ingot Iron, One Containing Lead," *Journal, Iron and Steel Institute*, Vol. 148, 1943, p. 429-441.
5. C. Graham, "Examination of Two Ingots of Free-Cutting Steel, One Containing Lead and the Other Lead Free," *Journal, Iron and Steel Institute*, Vol. 151, 1945, p. 273-275.
6. W. Bardgett and R. Lismer, "Mode of Occurrence of Lead in Lead Bearing Steels and the Mechanism of the Exudation Test," *Journal, Iron and Steel Institute*, Vol. 151, 1945, p. 281-301.
7. T. Schofield, "Microscopical Examination of Lead-Bearing and Lead Free Steels and Ingot Irons," *Journal, Iron and Steel Institute*, Vol. 151, 1945, p. 277-280.
8. K. Volk, "Metallographic Proof of Lead in Steel," *Archiv fur das Eisenhüttenwesen*, Vol. 16, 1942, p. 81-84.
9. A. V. Vegesack, "Method of Etching for Identification of Lead in the Microstructure of Free-Cutting Steels Alloyed with Lead," *Jernkontorets Annaler*, Vol. 126, 1942, p. 559-564.

10. A. E. Gerds and C. W. Melton, "New Etch Spots Leaded Steels," *Iron Age*, Vol. 178, No. 9, August 30, 1956, p. 86-87.
11. J. Nead, C. Sims, and O. Harder, "Properties of Some Free Machining Lead-Bearing Steels," *Metals and Alloys*, Vol. 10, March 1939, p. 68-73; April 1939, p. 109-114.
12. G. Clark and S. Gross, "Technique and Applications of Industrial Micro-radiography," *Industrial and Engineering Chemistry*, Analytical Edition, Vol. 14, 1942, p. 676-683.
13. W. D. Smith, "Manufacture of Leaded Steel," American Institute of Mining and Metallurgical Engineers National Open Hearth Conference, April 8, 1957.
14. L. H. Van Vlack, "Correlation of Machinability with Inclusion Characteristics in Resulphurized Bessemer Steels," *TRANSACTIONS, American Society for Metals*, Vol. 45, 1953, p. 741-757.
15. E. J. Paliwoda, "The Influence of Chemical Composition on the Machinability of Rephosphorized Open Hearth Screw Steel," *TRANSACTIONS, American Society for Metals*, Vol. 47, 1955, p. 680-691.
16. E. J. Paliwoda, "Machinability of Leaded Type A Steels," *TRANSACTIONS, American Society for Metals*, This Volume, 1958, p.

DISCUSSION

Written Discussion: By Francis W. Boulger, Chief, Division of Ferrous Metallurgy, Battelle Memorial Institute, Columbus, Ohio.

The authors have carried out an outstanding study on a very interesting and difficult subject. It is gratifying to my associates that they confirm the findings of Gerds and Melton that lead exists as envelopes and tails attached to the sulphide inclusions. Although one expects insoluble impurities to be concentrated in interdendritic areas during freezing it is helpful to have both radiographic and metallographic evidence supporting this view. The authors should be complimented on the high quality of their microradiographs. We have used similar techniques in studies on aluminum alloys containing lead and bismuth and recognize the difficulties they must have encountered in their work.

The authors' statement that x-ray and electron diffraction studies support the opinion that lead exists in steel in the elemental state is particularly important. Others have deduced this from thermodynamic data but there seems to be no prior experimental work on this subject.

The reader is apt to be impressed by the large number of lead-coated particles visible in the microradiographs of Figs. 5 and 11. Have the authors attempted to determine, by point counting techniques, the spacing and average size of the particles? It is possible to estimate the thickness of the lead films on sulphides by comparing the apparent volumes of the particles with the known lead contents of the samples.

In connection with the authors' statement immediately preceding the summary, it may be pertinent to mention that I have found significant differences in machining properties among specimens oriented differently in plates of resulphurized steel. Probably this is also true of plates made from leaded steels. On the other hand, the effects of lead on directional variations in tensile properties may be unimportant. Inclusions do not have much effect on strength and transverse ductility probably depends more on rolling practice than on inclusion content.

Written Discussion: By Frank W. Luerksen, Chief Research Engineer, Inland Steel Company, Research and Development, East Chicago, Indiana.

First, let me congratulate the authors on a thought-provoking manuscript. This paper adds knowledge to the technology of leaded steels which should certainly aid in improvements in their manufacture.

A matter which I feel is in need of discussion and clarification is that of possible solubility of lead in liquid iron. The authors' statement, "It is generally recognized that lead and iron are immiscible in both the liquid and solid states", cannot be proven by direct data. It seems to me that the authors have shown data which are difficult to interpret as representing anything other than solidification from a solution of lead in liquid iron.

Let us first examine the statements and data of the authors and then inspect some unpublished data on leaded steels. The authors observe that lead particles are closely associated with manganese sulfide inclusions in their ingot samples. One would expect to find close association of lead, sulphur and manganese in steel were they all rejected from common solution in iron during the solidification process. The fact that elemental lead rather than a lead compound is found associated with MnS in the inclusions can be explained by the relatively stronger association of manganese and sulphur in the prior impure liquid.

The authors found on chemical examination of a 10,400-pound high sulphur leaded ingot that the patterns of lead and sulphur segregation were identical or nearly so. A large volume of data accumulated on semi-killed ingots of high sulphur leaded steel at Inland show the same trend. Although the authors do not state this directly, I suspect that in their data as in ours, very strong segregation patterns are apparent. The "V" and "inverted V" segregates are as clearly identified by lead analysis and lead printing in a split ingot as by sulphur printing. Very important in this discussion is that a large upright cone of negative lead segregation exists close to the bottom of these ingots whereas, the ingots are strongly positively segregated toward the top. For instance, at the 80% ingot height, of 10 drillings from edge to edge on the center face of a split ingot the lead analyses ranged from 0.191% lead to 0.273% lead with the lowest concentration at the edge. In contrast, at the 15% ingot height, of 10 drillings from edge to edge the lead analyses ranged from 0.240% lead to 0.14% lead with the higher concentrations close to the edge and the lower concentrations at the center. These segregation data strongly indicate the presence of solubility in the liquid lead-iron system.

Recently, A. Peters of the Metallurgical Department of Inland Steel Company experimented with lead additions to a rimmed ingot. This was a 22.5×24.5 -inch ingot which was allowed to rim for 13 minutes to a 4-inch rim thickness. Again, the segregation of lead and sulphur were alike. The average lead in the rim zone was 0.145% lead while that of the core was 0.254% lead. Moreover, the profile of lead concentration, edge to center, had the same shape as that for sulphur. One would certainly expect an extremely low lead concentration in the rim zone if lead were present as a fine dispersion due to washing by the strong currents set up by the rimming action. On the contrary, one finds appreciable lead in the rim of the ingot.

The data presented here are, in the opinion of the discussor, adequate evidence for solubility of lead in liquid iron. Furthermore, the solubility limit should be in excess of the 0.145% lead of the rim zone, and may be as much as several times that great.

Authors' Reply

The authors wish to thank the discussers for their interest in this work and for their thoughtful comments.

It is true, as Mr. Luerrson suggests, that the immiscibility of lead and iron has not been proved by direct data; indeed, thermodynamically, *complete* immiscibility probably does not exist in any system. It was recognized that the segregation observed could be explained either on the basis of limited solubility or by means of the mechanism proposed. It is believed, however, that the observations presented are more logically interpreted in terms of virtually complete immiscibility for the following reasons: If lead is being precipitated from solution it would be expected that the observed range of particle size would be similar to that occurring in other systems displaying liquid solubility; for example, graphite in cast iron, or manganese sulfide in steel. On the contrary, lead particles are observed to range from a very small microscopic size to quite large macroscopic globules, occurring in the bottom of the ingot which must be discarded for this reason. It is difficult to account for such agglomeration, obviously occurring in the liquid, except on the basis of negligible solubility. Moreover, if the solubility were anything like 0.145%, it would be expected that almost all of the lead in the "chill zone", which is essentially a quenched material, should be in the form of a uniform and extremely fine—possibly submicroscopic—precipitate. This is not observed. An attempt to establish definitely whether or not there is more than negligible solubility of lead in iron should be a rewarding field of study.

The authors are gratified to learn that their work confirms similar work carried out by Mr. Boulger and his associates. Some efforts were made to employ point counting techniques but the attempt was abandoned since it was felt that the results were not quantitatively significant. An attempt to estimate the thickness of the lead films on sulfides would probably entail an almost prohibitive amount of work to be statistically reliable. Even then the results would be of doubtful significance because of the relatively wide variation of structure among the inclusions. It was interesting to learn of Mr. Boulger's work on variation of machinability characteristics as influenced by orientation. Little appears to have been published on this. We are in complete agreement with the comment that normal inclusions, per se, have only a minor influence on mechanical properties.

THE DISTRIBUTION OF RESIDUAL STRESSES IN CARBURIZED CASES AND THEIR ORIGIN

BY D. P. KOISTINEN

Abstract

The residual stress distributions in carburized cases on SAE 8620, 1118, 1018, and 5140 steels were studied using a precision x-ray diffraction technique. Maximum residual compression is shown to occur at 50 to 60% of the total case depth. The residual stress distributions through the carburized cases were correlated with the crystalline phase compositions as determined by x-ray diffraction studies and with the carbon distribution. It is shown that the experimental data support the theory that the origin of the compressive stress in the case lies in the sequence in which transformations occur in the case and in the core. The introduction of carbon delays the martensite transformation in the case until after the core has transformed. The subsequent transformation and accompanying growth of the case is opposed by the previously transformed core, resulting in compressive stresses in the case and tensile stresses in the core. The magnitude of the compressive stress in the case is governed by the extent of transformation to martensite. (ASM International Classification Q25h, N8, J28; CN, AY)

INTRODUCTION

THE PRACTICE of carburizing the surfaces of steel parts has been utilized for some time to obtain extremely hard, long wearing surfaces on easily fabricated low carbon steels and on low alloy steels where the combination of surface hardness and high strength and toughness in the core prove to be valuable under certain types of applied stresses.

In addition, it has come to be increasingly recognized that as a valuable by-product to these case-hardening treatments, residual compressive stresses will generally be found in the hardened surface layers. Since the benefit to be derived from these residual compressive stresses in fatigue applications depends on the exact magnitude and depth distribution of the stress, it was thought worthwhile to study the stress

A paper presented before the Thirty-Ninth Annual Convention of the Society, held in Chicago, November 4-8, 1957. The author, D. P. Koistinen, is associated with the General Motors Corporation Research Staff, Detroit. Manuscript received April 22, 1957.

distribution in carburized cases using the precision x-ray diffraction method for hardened steel which has recently become available.

Furthermore, the stress distribution through the carburized case was correlated with the carbon distribution as determined chemically and with the crystalline phase composition as determined by an accurate x-ray diffraction method. A widely held theory of the origin of these residual stresses is that "the hardened case is in compression resulting from its greater tendency to expand during the hardening transformation, and from the resistance of the core to this expansion . . ." (1)¹. It is assumed, in this theory, that the case has a greater tendency to expand during the hardening transformation due to its higher carbon content. Thus, the point of maximum compression should be at or near the point of maximum carbon content, that is, the surface. The studies reported here, however, show that the point of maximum compression is at 50-60% of the total case depth. Furthermore, it can be shown that there is probably relatively little variation with carbon of the expansion during the martensite transformation. For example, on the basis of the lattice parameters of austenite and tetragonal martensite corrected, from thermal expansion data, to the M_s temperature, Houdremont and Krisement (2) have calculated the relative change in volume $\Delta v/v$ during the martensite transformation as a function of carbon content. They found that $\Delta v/v$ varied from 2.78 at 0.4% carbon to 2.91 at 1.0% carbon and back to 2.86 at 1.4% carbon. In view of the possible inaccuracies in some of the assumptions which were made, Houdremont and Krisement concluded that the small variation in $\Delta v/v$ with carbon may not be real and that "It is quite possible that at the martensite temperature, $\Delta v/v$ is constant, independent of the % carbon".

The evidence in the present paper supports a different theory which ascribes the development of the compressive stresses in the hardened case to the sequence of the transformations of the austenite to the various products that form in different portions of the case and core. In this theory, the introduction of carbon in the surface layers has the primary effect of lowering the martensite start (M_s) temperature of the case and thus delaying the transformation of the case austenite to a lower temperature and correspondingly later time than the transformation of the austenite in the core. Thus, as the core transforms into either isothermal transformation products or low carbon martensites, the accompanying growth of the core is accommodated by plastic deformation of the austenite case. During the subsequent transformation of the case to martensite, the accompanying growth of the case is opposed by the previously transformed core, resulting in compressive stresses in the case and tensile stresses in the core.

¹ The figures appearing in parentheses pertain to the references appended to this paper.

EXPERIMENTAL TECHNIQUES

The residual stresses reported here were determined using the x-ray technique proposed by Christenson and Rowland (3) with minor modifications. The accuracy of this technique as applied in our laboratory has been checked by showing correlation with mechanical dissection techniques and the reproducibility has been found to be ± 5000 psi (4). When necessary, corrections calculated by elastic theory have been made for stress relief due to parting the specimen from a larger section and for stress changes due to removal of stressed surface layers.

The crystalline phase compositions of the samples studied in this work were determined by the integrated x-ray diffraction line intensity technique proposed by Averbach and Cohen (5) and modified by K. E. Beu (6). Recent evaluations of this technique have shown that the reproducibility is better than ± 1 volume % and that the accuracy is almost within the reproducibility limits (7).

Metal removal for studies with depth was accomplished by electrolytic polishing. Hundreds of quantitative determinations of residual stresses and phase composition have been made on steel surfaces prepared by electropolishing and no anomalous results ascribable to the electropolishing have been observed.

Where reported, the carbon content was determined by chemical analyses of chips machined from bars from the same steel stock, heat treated simultaneously with the specimens to be used for x-ray diffraction measurements. Each carbon content reported is the average carbon content of the finite layer of chips removed and hence this value is plotted at the mid-point of the layer.

Most of the samples examined were 0.250-inch thick with a case of approximately 0.040-inch on both sides. The SAE 8620 steel specimen was 0.500-inch thick with a 0.050-inch case on both surfaces. As will be shown later, these section sizes are small enough that there are no large thermal gradients in the temperature range that transformations occur, while being thick enough to provide sufficient core thickness to support the compressive stresses in the cases.

EXPERIMENTAL RESULTS

One specimen studied was an SAE 8620 steel block, $1\frac{5}{8}$ inches by $1\frac{5}{8}$ inches by $\frac{1}{2}$ inch carburized at 1680 °F for $7\frac{1}{2}$ hours in an atmosphere of 125 cu.ft./hr. of Rx gas enriched with 0.8 cu.ft./hr. of natural gas (0.85–0.95% carbon potential) to a total case depth of 0.045 inches–0.055 inches. The block was quenched from the carburizing temperature into S-7 oil at 110 °F and then tempered at 300 °F for $\frac{1}{2}$ hour. A beam specimen, $\frac{1}{2}$ inch by $1\frac{5}{8}$ inch by 0.100 inch was then parted from the center section of one $1\frac{5}{8}$ inch by $1\frac{5}{8}$ inch faces of the block. The parting stress relief was determined by x-ray diffraction

measurements before and after parting and by means of an SR-4 gage glued to the center of the beam specimen during parting. The parting stress relief as determined by these two methods was the same.

Measurements of the residual stress and the phase composition were made on the surface and after electropolishing to prescribed depths. The residual stresses were then corrected for the parting stress relief and for the stress in the removed layers. Results of these studies are given in Fig. 1. No undissolved carbides were observed in this specimen and thus the phase composition is presented in terms of volume %

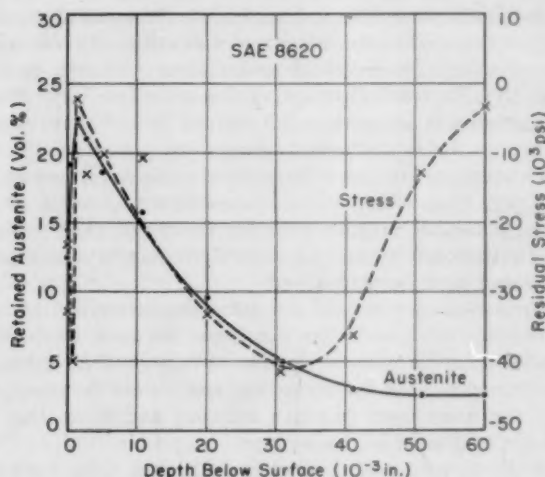


Fig. 1—Residual Stress and Retained Austenite Distributions Through a Carburized Case on SAE 8620 Steel.

retained austenite. Except for the first 0.002 inches, the retained austenite content of the case decreases in a smooth curve to the nominal case depth (0.050 inches) and then becomes constant in the core. The surface was decarburized to a depth of 0.002 inches as indicated by the decreased retained austenite content and by the narrower martensite x-ray diffraction lines in the patterns obtained in this region. This decarburized layer is detectable by electron metallography as shown in a paper by Rouze and Grube (8). Since this specimen was heat treated in a batch type gas carburizing furnace, this decarburization presumably occurred in the time interval between the breaking of the furnace atmosphere and the quenching of the specimen.

When the residual stress distribution through the carburized case is plotted on the same graph as the amount of retained austenite, a close correlation between the two sets of data is observed. Between the

surface and approximately 0.030 inches, the amount of retained austenite completely controls the residual stress distribution. That is, the greater the extent of transformation to martensite, the greater the compressive stress. Maximum compression occurs at 0.030 to 0.035 inches and below this point the stress rises rapidly toward tension. At the point of maximum compression (approximately 60% of the total case depth) the carbon content must be 0.5% or less. This can be deduced from the carbon versus depth relationships in Figs. 3 and 4. Even without the results of Houdremont and Krisement, it does not seem reasonable that the addition of 0.3% carbon to the core carbon content of 0.2% would cause sufficient change in the expansion during transformation to generate large compressive stresses. Thus the carbon expansion theory for the generation of the compressive stresses fails to give a reasonable explanation for maximum compression occurring so deep in the case.

Examination of the data on the carburized SAE 8620, however, gives support to the theory that the stress is the result of the sequence of the transformation. It is possible to make an accurate estimate of the M_s temperature of the steel at any depth in the carburized case from the amount of retained austenite measured at that depth. This is accomplished by using a general equation for the extent of transformation of austenite to martensite as a function of the difference between the M_s temperature and the ultimate quenching temperature (T_q) recently discussed by Koistinen and Marburger (9). This equation is,

$$V = e^{-0.00013(M_s - T_q)} \quad \text{Equation 1}$$

where V is the volume fraction retained austenite. This equation has been shown to hold for plain carbon and low alloy steels which have been water-quenched. When this equation is applied to oil quenched specimens, the slightly greater amount of austenite retained after oil quenching results in the M_s temperatures calculated from this equation being too low by about 30 °F. Since this is a consistent error, however, differences between M_s temperatures should remain highly significant.

The M_s temperatures calculated from the retained austenite as a function of depth for the carburized case on the SAE 8620 steel are shown by Curve A in Fig. 2. As can be seen, the difference of 0.3% carbon between the core carbon content and the carbon content at the point of maximum compression (approximately 0.030 inch) results in a change in M_s temperature of approximately 130 °F. Superimposed on the M_s temperature versus depth curve are shown experimental cooling curve data for the quenching of SAE 9420 steel into S-7 oil at 120 °F as reported by Weinman, Thomson, and Boegehold (10). The data have been replotted as temperature versus depth curves at various times after the beginning of the quench. The cooling curve data were obtained on a 1-inch diameter cylinder which, according to French

(11), should correspond to a 0.67-inch thick plate. Since the SAE 8620 steel plate was $\frac{1}{2}$ -inch thick, the cooling curve data probably represents a more severe (in terms of temperature gradients during cooling) situation than existed during the quenching of the SAE 8620 steel. It is apparent from these data that the core reached its M_s temperature well before the major portion of the case started to transform and at the instant that the point of maximum compression (0.030 inch)

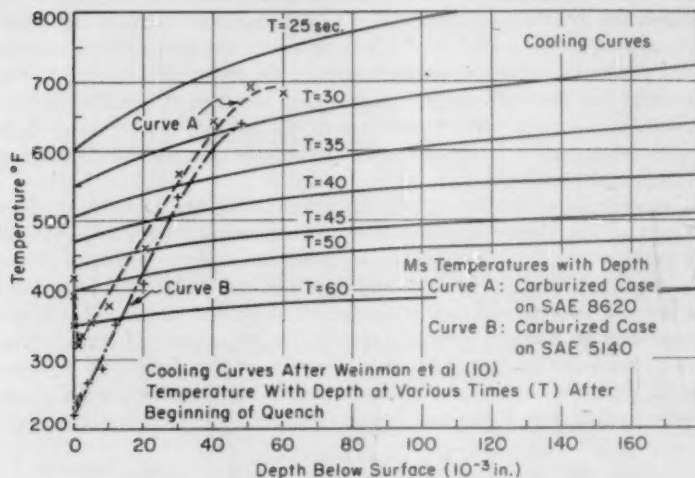


Fig. 2—Cooling Curves During a Quench into S-7 Oil at 120 °F Superimposed on M_s Temperature Distributions Through Carburized Cases on SAE 8620 and SAE 5140 Steels.

reached its M_s temperature, the adjacent area in the core was at least 100 °F below its M_s temperature and hence (according to the equation for extent of transformation) at least 50% transformed. It, therefore, seems that transformations occur through the case in the proper sequence to generate the compressive stresses observed.

Of additional interest in this specimen is the distribution of stress in the decarburized surface layer. As the amount of retained austenite decreases from 0.002 inch to the surface, a stress distribution is found that is very similar, except for the depth scale factor, to the distribution inward between 0.002 inch and the case-core boundary. That large compressive stresses are found in the decarburized surface layer is additional evidence that it is unlikely that the compression is due to a greater tendency of the case to expand during the hardening transformation because of its higher carbon content.

In view of the interesting results obtained on this sample it was decided to enlarge the study to a series of other steels. Samples of various

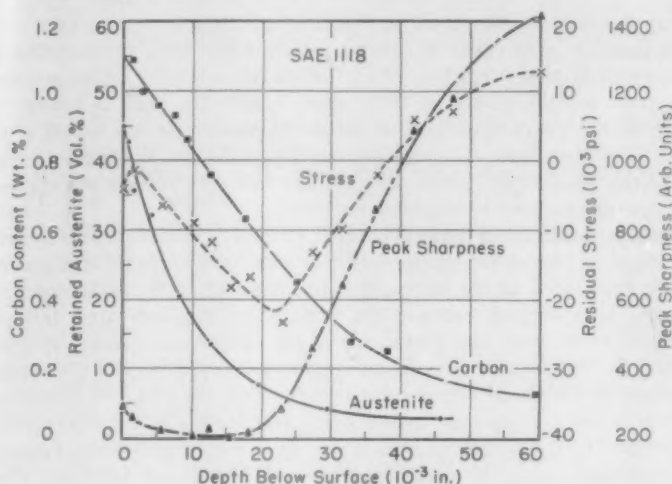


Fig. 3—Residual Stress, Retained Austenite, Carbon Content, and X-Ray Diffraction Peak Sharpness Through a Carburized Case on SAE 1118 Steel.

steels used in industrial applications were carburized in an industrial continuous four-zone furnace supplied with 1000 cu.ft./hr. Rx gas enriched with 75 cu.ft./hr. natural gas and 75 cu.ft./hr. ammonia and quenched in 130 °F S-7 oil from 1525 °F. The carburizing potential of the atmosphere in this furnace was extremely high and most samples showed surface layers of iron carbide (Fe_3C) indicating that the carbon potential of the atmosphere was in excess of the limit of solid solubility of carbon in the austenite. The nitrogen content of the cases studied dropped smoothly from about 0.25% at the surface to about 0.05% at the case-core boundary. Since the amount of nitrogen was small compared to the amount of carbon, in the following discussions the influence of the nitrogen has been considered only as supplementary to the effects due to the carbon. The specimens were tempered at 300 °F for $\frac{1}{2}$ hour.

The results obtained on a specimen of SAE 1118 carburized as described above are shown in Fig. 3. This graph shows four curves corresponding to the four different types of information obtained on this single carburized case. The curves on this graph should be each associated with the appropriate scale factors on the ordinate. As before, retained austenite and residual stress distribution are plotted as functions of depth. Also plotted as functions of depth are the carbon content as determined from chemical analyses, and a curve labelled "Peak Sharpness". A brief explanation of this last curve is in order. As a consequence of obtaining accurate intensity distributions across the

x-ray diffraction lines used for the determination of residual stresses, it is possible to calculate a number which is inversely proportional to the width of the diffraction line; that is, this number is large when the peak is narrow and is very small where the peak is broad. In general, the diffraction lines of tempered martensite are broad while the diffraction lines of ferrite are narrow and thus, the measurement of "Peak Sharpness" yields information as to the phases present and the transformations which have occurred.

In this specimen of SAE 1118 steel (Fig. 3) no surface effects were observed and hence the retained austenite content drops off in a smooth curve from 45% at the surface to approximately 3% in the core. As before, in the region between the surface and approximately 60% of the case core depth, the magnitude of the compressive stress is determined by the amount of retained austenite. Comparison of the carbon content and residual stress curves shows that the point of maximum compression corresponds to the point where the carbon content has decreased to 0.5%. Below this depth the stress rises rapidly towards tension and seems to correlate well with the curve labelled "Peak Sharpness". Since the diffraction peak begins to get sharper in the same region that the carbon content drops below 0.5%, it can be assumed that the increasingly sharp diffraction peak in this region reflects the presence of increasing amounts of isothermal transformation products (ferrite, pearlite, and bainite) and martensite formed at high temperature and tempered during the quench. Hence, the increasing peak sharpness indicates qualitatively the relative extent of transformation to martensite or isothermal transformation products. Maximum compression occurs at the point of most complete transformation to martensite; at greater depths the amount of martensite is restricted by prior transformation to isothermal products and closer to the surface the amount of martensite is restricted by incomplete transformation of the austenite. Since there is also a growth associated with the isothermal transformation, the fact that transformation from austenite to martensite results in compressive stresses must be due to the sequence of the transformation. That is, since the martensite in the case forms at a lower temperature and a later time than the isothermal transformation products in the core the associated growth is opposed by the already transformed core.

This theory of the formation of the compressive residual stresses is further confirmed in the results given in Fig. 4. These data were obtained in studies on SAE 1018 steel, carburized simultaneously with the sample given in Fig. 3. Four sets of data are presented in Fig. 4 for this carburized case. The complete control which the extent of transformation to martensite exercises over the amount of compressive stress is shown at several points in this sample. Because of the high carburizing potential of this furnace a surface layer consisting of 19%

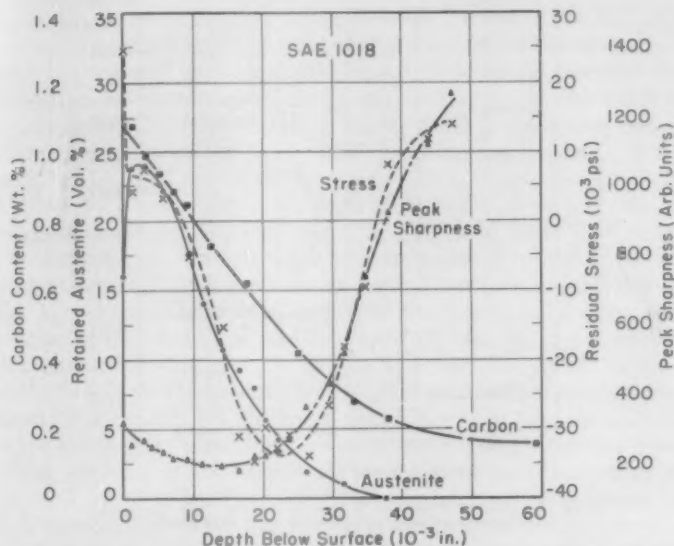


Fig. 4—Residual Stress, Retained Austenite, Carbon Content, and X-Ray Diffraction Peak Sharpness Through a Carburized Case on SAE 1018 Steel.

iron-carbide (Fe_3C), 16% retained austenite, and the remainder martensite was detected. The iron carbide actually exists as a discontinuous surface film as shown in the paper by Rouze and Grube (8). The percentage phase composition reported here is actually a weighted average over the finite layer penetrated by the x-ray beam. Thus, in the surface layer the total amount of martensite formed is low compared to other regions in the case and correspondingly a tensile stress (+29,000 psi) was detected. For the next 0.006 inch the retained austenite content is reasonably constant indicating a saturated carbon content at the carburizing temperature, and correspondingly, the stress in this region is a constant. Below this depth the retained austenite drops off and correspondingly the stress becomes more compressive as more martensite is formed. As before, maximum compression is obtained at the point where the carbon content is approximately 0.5%. In the region below the point of maximum compression the diffraction peak becomes sharper as more isothermal transformation products occur and correspondingly the stress gets less compressive. The residual stress curve crosses the zero line at the case-core boundary as defined by the amount of retained austenite becoming zero (indicating complete transformation to isothermal products).

A further significance of the "Peak Sharpness" curve is illustrated in Fig. 5. A correlation between the x-ray diffraction peak sharpness

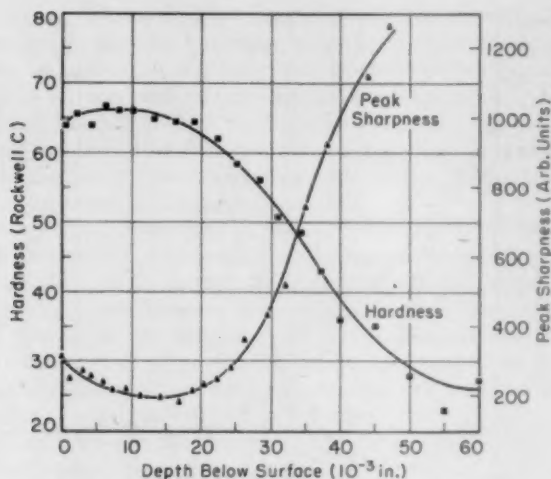


Fig. 5—Microhardness and X-Ray Diffraction Peak Sharpness Through a Carburized Case on SAE 1018 Steel.

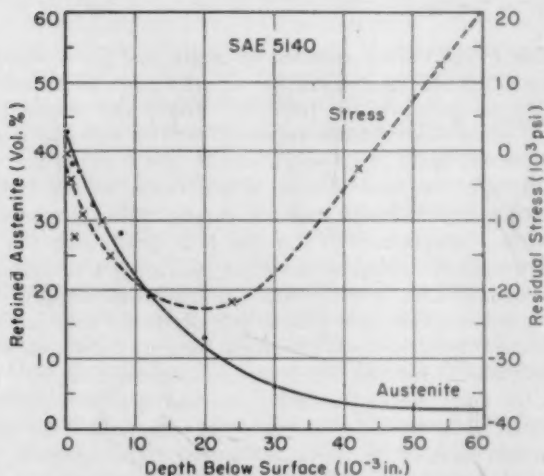


Fig. 6—Residual Stress and Retained Austenite Distributions Through a Carburized Case on SAE 5140 Steel.

and the Rockwell C hardness was obtained for this sample of carburized SAE 1018 steel. The Rockwell C hardness data was obtained by conversion of diamond pyramid hardness measured with a Bergsman

Microhardness Tester using a 100-gram load. These data are part of a larger study on the microstructure and hardness of various carburized cases being reported by Rouze and Grube (8). It can be seen that the peak sharpness curve is almost an exact inverse of the Rockwell C hardness curve. The large scatter in the hardness in the core is due to the large grain size of the isothermal transformation products in the core.

The results obtained on a specimen of higher core-carbon content carburized simultaneously with the SAE 1118 and SAE 1018 steels are shown in Fig. 6. Though fewer data are available on this specimen of carburized SAE 5140 steel, some general conclusions may still be made. Microhardness measurements and electron metallographic examination of this specimen established that it was through-hardened with a martensitic structure in both case and core (8). As in the other samples, however, the residual stress shows maximum compression at approximately 50% of the case depth. Since both the case and the core are martensitic, the compressive stress must result entirely from the time sequence of the martensite transformations. Application of Equation 1 relating the % retained austenite at room temperature to the M_s temperature shows that the M_s at the point of maximum compression is more than 200 °F lower than the M_s temperature at the case-core boundary (see Curve B in Fig. 2). Hence, assuming that there are no greater temperature gradients with depth than are shown in Fig. 2, the martensite transformations at the case-core boundary occurred well before the beginning of the transformations at the point of maximum compression.

CONCLUSIONS

Some general conclusions may be drawn from these studies:

1. The magnitude and distribution of the compressive stress at every depth in a carburized case is determined by the extent of the transformation to martensite and the sequence in which these transformations occur.
2. Maximum compression occurs at 50 to 60% of the total case depth. In low carbon core samples studied this corresponds very closely to the point at which the carbon content drops below 0.5%.
3. The reversal in the sign of the residual stress from compression in the case to tension in the core occurs at or very near the case-core boundary.
4. Proceeding outward through the case from the case-core boundary to the point of maximum compression, the stress becomes more compressive due to sequence of the transformations to isothermal transformation products or to martensite.
5. Proceeding outward through the case from the point of maximum compression to the surface, the magnitude of the compressive stress

decreases as the amount of martensite is restricted by incomplete transformation of the austenite.

6. On some carburized specimens thin surface films may occur in which there are wide variations in phase compositions and correspondingly wide variations in residual stress.

ACKNOWLEDGMENTS

The author wishes to thank D. N. Callahan who made the retained austenite measurements, R. P. Mitchell who made the residual stress measurements, S. R. Rouze and T. R. McKinney for permission to use their data on microhardness, W. Keesaer of Buick Motor Division, General Motors Corporation, who furnished some of the samples, and W. L. Grube and R. E. Marburger for many valuable discussions.

References

1. G. T. Williams, "Selection of Carburizing Steel, Case Depth and Heat Treatment," *Metals Handbook*, American Society for Metals, 1948, p. 681.
2. E. Houdremont and O. Krisement, "Supercooling of Transformation Processes as a Basis for the Martensite Transformation," *Archiv für das Eisenhüttenwesen*, Vol. 24, January, February 1953, p. 53. Brucher Technical Translation No. 3339.
3. A. Christenson and E. Rowland, "X-Ray Measurement of Residual Stress in Hardened High Carbon Steel," *TRANSACTIONS*, American Society for Metals, Vol. 45, 1953, p. 638.
4. M. H. Miller, E. R. Mantel and W. S. Coleman, "An Evaluation of the X-Ray Diffraction Method of Stress Measurement," Paper No. 411, *Proceedings*, Society for Experimental Stress Analysis, (in Press).
5. B. L. Averbach and M. Cohen, "X-Ray Determination of Retained Austenite by Integrated Intensities," *Transactions*, American Institute of Mining and Metallurgical Engineers, Vol. 176, 1948, p. 401.
6. K. E. Beu, "Modifications of an X-Ray Method for the Measurement of Retained Austenite Concentrations in Hardened Steels," *Transactions*, American Institute of Mining and Metallurgical Engineers, Vol. 194, 1952, p. 1327.
7. K. E. Beu, "The Sensitivity, Reproducibility, and Accuracy of X-Ray Diffraction Measurements of Retained Austenite," *Proceedings*, American Society for Testing Materials, Vol. 55, 1955, p. 630.
8. S. Rouze and W. L. Grube, "Electron Metallography of Carburized and Carbonitrided Cases," Submitted to American Society for Metals for publication.
9. D. P. Koistinen and R. E. Marburger, "Extent of the Austenite-Martensite Transformation in Pure Iron-Carbon Alloys," Paper No. CA 7 Bulletin, American Physical Society, Vol. 2, 1957, p. 122.
10. E. W. Weinman, R. F. Thomson and A. L. Boegehold, "A Correlation of End-Quenched Test Bars and Rounds in Terms of Hardness and Cooling Characteristics," *TRANSACTIONS*, American Society for Metals, Vol. 44, 1952, p. 803.
11. H. J. French, *The Quenching of Steels*, p. 42. American Society for Steel Treating, (American Society for Metals), Cleveland.

DISCUSSION

Written Discussion: By J. E. Campbell, Battelle Memorial Institute, Columbus, Ohio.

We wish to congratulate Mr. Koistinen and his associates for making an im-

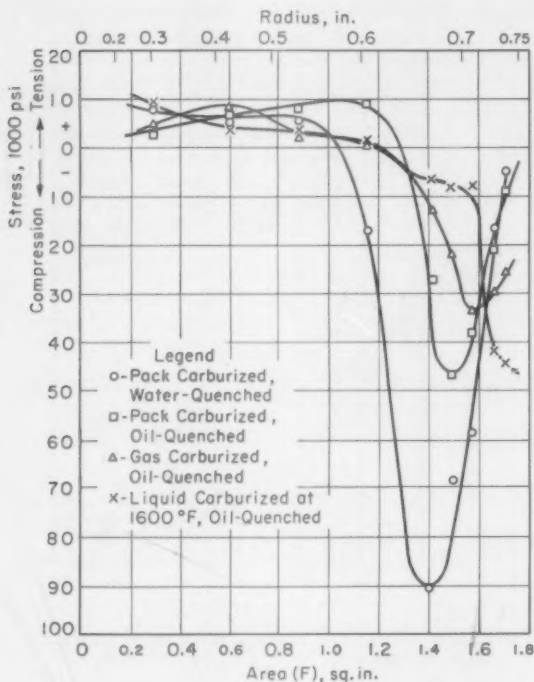


Fig. 7—Tangential Stress Patterns for 1½-Inch Diameter 8620 Bars After Carburizing and Quenching.

portant contribution to the field of ferrous metallurgy. The techniques reported in this paper are not only significant in evaluating residual stresses and explaining their origin, but also in evaluating the quality of carburized cases. I am sure that many have seen thin decarburized surface layers on cases under the microscope and wondered how they occurred. The techniques described provide a quantitative measure of the effects of this decarburization or the effects of carbides at the surface of the case if they are present. The corresponding residual stress patterns show the high, and presumably undesirable, stress gradients that exist within the first 0.002 inch from the surface when the surface carbon level is either too low or too high as compared to the carbon content at greater depths.

The residual stress pattern in Fig. 1 in the paper for 8620 steel, gas-carburized and oil-quenched, agrees exceptionally well at depths over 0.010 inch with data reported for round bars by Campbell and McIntire* in 1953. Tangential stress curves for carburized 8620 steel 1½ inches diameter are shown in Fig. 7. This work was done as part of a comprehensive investigation on residual stresses for Springfield Armory. Residual stresses in round bars were determined by tedious

* J. E. Campbell, and H. O. McIntire, "How to Develop Favorable Stress Patterns," *Iron Age*, Vol. 172, No. 22, November 26, 1953, p. 102-105.

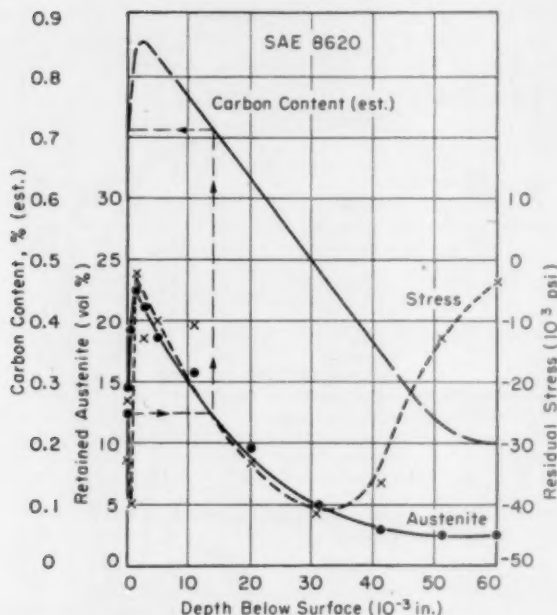


Fig. 8—Residual Stress and Retained Austenite Distributions Through a Carburized Case on SAE 8620 Steel.

measurement of strains resulting from successive boring and grinding operations on thin disks cut from heat treated bars. This was a modification of the procedure often referred to as the Sach's method. The x-ray diffraction technique is much less time consuming and permits a more complete survey of the stresses near the surface than the Sach's method. The explanation given by Mr. Koistinen for the compressive stresses in a carburized case was also advanced in the above reference, and we were gratified to learn that the current work led to the same explanation.

The results of the study reported in Mr. Koistinen's paper show the relationships that exist between carbon contents in the case, hardness, retained austenite, residual stress, M_s temperature, temperatures in the case at a given instant during quenching, and peak sharpness for carburized steels of several compositions. From the data given, we can employ these relationships to estimate the carbon content curve for the 8620 steel in Fig. 1 as shown in Fig. 8. The retained austenite is shown to be about 12½% at the surface which corresponds to the retained austenite at 0.014 inch below the surface. This corresponds to a carbon content of about 0.72% which, in turn, should correspond to the carbon content at the surface as shown by the arrows in Fig. 8. If this is true, the small amount of decarburization required to give high stress gradients could not be detected metallographically, and the x-ray diffraction method appears to be a practical method for determining its presence. Furthermore, if the retained austenite is at a maximum value at

the surface, decarburization or carbides which produce high stress gradients near the surface have been avoided in the heat treatment.

In addition to the method used by the author, M_s temperatures can be calculated from the compositions of the various layers in the case (ASM Handbook, 1948, p. 611) if the carbon contents are known. With these data, curves similar to A and B in Fig. 2 can be determined.

Discussion of the above relationships could be carried much farther than this. However, with information from recent studies on carburizing becoming available, we are in a much better position to understand what is desired in a carburized case for maximum service performance.

THE EFFECT OF PER CENT TEMPERED MARTENSITE ON ENDURANCE LIMIT

BY F. BORIK, R. D. CHAPMAN AND W. E. JOMINY

Abstract

The effect of microstructure on the endurance limit of the following steels has been investigated: SAE 1340, 4042, 4340, 5140 and 80B40. Using different quenching media and by changing the cross section of the quenched bars, various amounts of martensite were produced by continuous cooling.

A relationship appears to exist between the amount of martensite obtained in the "as-quenched" condition and the endurance limit of low alloy steels. This correlation is based on steels with carbon content in the range of 0.39-0.45% and about the same tempered hardness (Rockwell C-36), but with different hardenabilities.

This relationship shows that the endurance limit drops with the presence of small percentages of nonmartensitic products. As the per cent of martensite decreases below 85%, the endurance limit is not as sensitive to microstructure.

The results indicate also that the endurance limits of the above steels as determined in tests with R. R. Moore machines were nearly the same for a given amount of martensite when tempered to a given hardness irrespective of their hardenability. (ASM International Classification: Q7a, N8p, 3-21; CN, AY)

INTRODUCTION

THE CORRELATION of microstructure with the mechanical properties of steel was object of extensive investigation in the past. A survey of work in this vast field shows an absence of a systematic study that would focus attention to the martensite content with respect to its influence on the fatigue properties of steel.

In the early twenties, Moore and Kommers (1)¹ were among the first to recognize qualitatively the influence of quenching and tempering temperature and the time of tempering upon the fatigue limit of steel. More than a decade later, Cazaud and Persoz (2) elaborated

¹ The figures appearing in parentheses pertain to the references appended to this paper.

A paper presented before the Thirty-Ninth Annual Convention of the Society, held in Chicago, November 4-8, 1957. Of the authors, F. Borik is Research Metallurgist, R. D. Chapman is Managing Engineer—Metallurgical Research, and W. E. Jominy is Chief Metallurgist—Metallurgical Research, of the Chrysler Corporation, Detroit. Manuscript received May 3, 1957.

on the conclusions of Moore in their classical work on fatigue in which they correlated the fatigue properties with the heat treatment of about forty different steels. According to their investigation, the ratio of endurance limit and the rupture strength f/R varied with the microstructure. The ratio for steels with fully ferritic or tempered martensitic microstructures was around 0.60, with austenitic or pearlitic microstructures 0.40. The ratio was found to vary with carbon content in mixed microstructures of pearlite and ferrite, decreasing from 0.63 to 0.38 with increase in carbon content. For steels with untempered martensite, the ratio varied from 0.23 to 0.47 depending upon the severity of quench, being lower for more drastic quenches. Although they concluded that this ratio assumed intermediate values for mixed microstructures, being between those of the individual microconstituents, no attempt was made to correlate the structures and their mixture with the absolute values of the endurance limits.

More recently, Hollomon and his co-workers (3) studied the effect of microstructure on mechanical properties of NE 8735 and SAE 3135. They produced microstructures of tempered martensite (martensite being obtained on continuous cooling) and microstructures prevalently pearlitic (plus ferrite) and bainitic by isothermal transformation and in correlating them with the fatigue properties, they generally concluded: (a) that the endurance limit of steels having the same tensile strength depended upon structure, through the effect of structure on the yield strength and (b) that steels having a tempered martensitic structure had fatigue properties superior to those of steels with other structures for a given tensile strength. In general, this seemed to answer the question of choice between fully martensitic and mixed microstructures.

Liedholm (4) noted in his study of delayed quench transformation of SAE 4330 steel that the mechanical properties, and especially the fatigue strength, were not radically lowered by the ferrite rejection. Even with 51% rejected ferrite and appreciable amounts of bainite, the lowering of the fatigue strength amounted to only about 8%. He drew his conclusion from a plot of endurance limit versus the time of delayed quench. During this type of quench, he produced martensitic microstructures containing no ferrite, trace of ferrite, a few per cent of ferrite, about 10% ferrite, about 50% ferrite plus bainite and maximum amount of ferrite compatible with the cooling cycle. On the basis of his result, Liedholm rejected the popular failure diagnosis charging fatigue crack to the occurrence of ferrite rejection in the failure area of heat treated parts. He seems to be first to mention the relative amounts of the microconstituents in their relation to fatigue properties.

Among the recent investigators, Hodge and Lankford (5) did a commendable work on SAE 4340 steel for which they established a curve showing the dependence of the fatigue limit on the percentage

Table I

	1340	4042	4340	5140	80B40*
Carbon	0.45	0.40	0.43	0.39	0.42
Manganese	1.68	0.90	0.76	0.79	0.98
Phosphorous	—	0.011	—	0.02	0.018
Sulfur	—	0.025	—	0.029	0.026
Silicon	0.22	0.27	0.28	0.29	0.30
Nickel	—	0.07	1.65	—	0.35
Chromium	—	0.11	0.82	0.79	0.31
Molybdenum	—	0.28	0.25	—	0.13
Copper	—	0.05	—	—	—
Round Dia. (inches)	2	1½	1½	2	2

*This steel contained No. 79 Grainal (4 lbs. per ton) of the following composition: 25% Va, 10% Al, 15% Ti, and 0.20% B.

of upper bainite plus martensite obtained during isothermal transformation followed by an oil quench. The points represented 1%, 5%, 10%, 20% and 50% upper bainite, 5% ferrite and 5% pearlite (+8% ferrite). According to the authors' conclusions, the fatigue properties of SAE 4340 steel were lowered somewhat by the presence of 50% upper bainite or 5% pearlite (plus 8% ferrite) but were not significantly affected by the smaller percentages of upper transformation products. Hodge and Lankford expressed belief that the results obtained in terms of transformation products formed isothermally could be applied to the mixed microstructures ordinarily obtained upon continuous cooling.

According to the history of this study, it seemed that the question about the influence of relative amounts of tempered martensite versus tempered mixed structures was not resolved to satisfaction. Most investigators implied their preference for tempered martensitic microstructure to structures with predominantly transformed structure in fatigue applications. In order to support, disprove or supplement their findings, it was felt that results on more than one or two steels would render basis for more specific conclusions.

It was, therefore, the purpose of our investigation to determine the endurance limit of five low alloy steels quenched to varying percentages of martensite obtained on continuous cooling as opposed to those obtained by isothermal transformation. The continuous cooling method was chosen because of its general industrial practicability.

MATERIAL AND HEAT TREATMENT

Five hot-rolled steels were used for the specimen preparation, namely SAE 1340, 4042, 4340, 5140 and 80B40. The check analyses of their composition and the sizes of the rounds are recorded in Table I. The rounds, 3 to 4 feet long, were normalized at 1650 °F in a neutral atmosphere. The time of normalizing in hours at heat was numerically equal to the cross sectional size in inches. The SAE 80B40 was normalized at 1600 °F for 3 hours.

The objective was to find a quenching condition and a proper size bar that would produce representative amounts of martensite, yet could be tempered to Rockwell C—36. This tempered hardness still allowed the heat treated bars to be machined into fatigue specimens.

Generally, the procedure was divided into five steps:

- (a) Correlation of hardness and per cent martensite as determined from the end quenched bars.
- (b) Preparation of step bars that were quenched from the austenitizing temperature into quenching media of various quench severity.
- (c) Quenching and tempering of sets of dummy bars the size and the heat treatment of which was based on results in step (b).
- (d) Heat treatment of endurance bar specimens.
- (e) Final machining and testing of the fatigue specimens.

End Quench Bars

An end-quenched bar was made for each steel and ground 0.015 inches deep on two opposite sides. The ground surfaces of the bars were polished and etched with 4% picral and the percentage of martensite metallographically determined along the bar by four independent observers. The readings were averaged and the resulting curves for the martensite versus the distance from the quenched end were superimposed on the hardenability curves in order to establish their relationship (Figs. 1 to 5). No attempt was made to determine the nature of the nonmartensitic product. Although mixtures of ferrite, pearlite and bainite were identified, their relative amounts at the high stage of transformation were difficult to resolve.

Nevertheless, from other work done in our laboratory with the electron microscope (6) we believe that the decomposition products near the quenched end of the hardenability bar are probably mixtures of bainite and ferrite. At the higher decomposition percentages, the structures are most likely mixtures of ferrite, bainite and pearlite.

STEP BARS AND QUENCHING MEDIA

Originally in this study attempts were made to obtain a predetermined amount of martensite. Several step bars were turned, copper plated, and quenched into different media. These quenching media were still water, oil, a "Pagoda quench" described by Zurburg (7), trichlorethylene, liquid tallow at 200 °F and still air. After quenching the step bars from 1550 °F into these various media, a size was selected with a particular quench to give the desired microstructure. The microstructure referred to a location at $\frac{1}{8}$ inch radius from the center. This location corresponded to the outer fiber of the minimum diameter

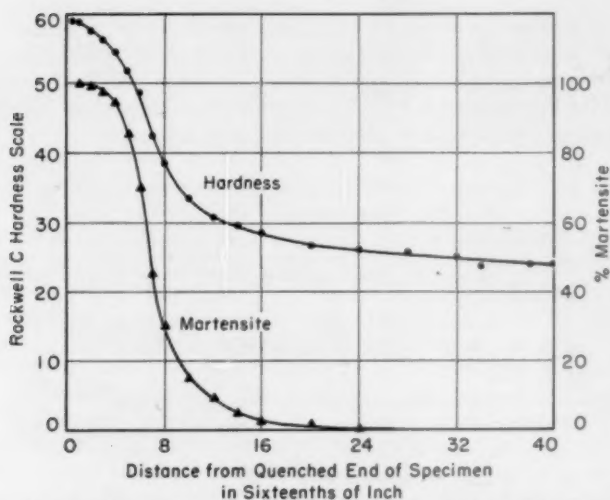


Fig. 1—Hardness Versus Per Cent Martensite on End Quench Bar of SAE 1340.

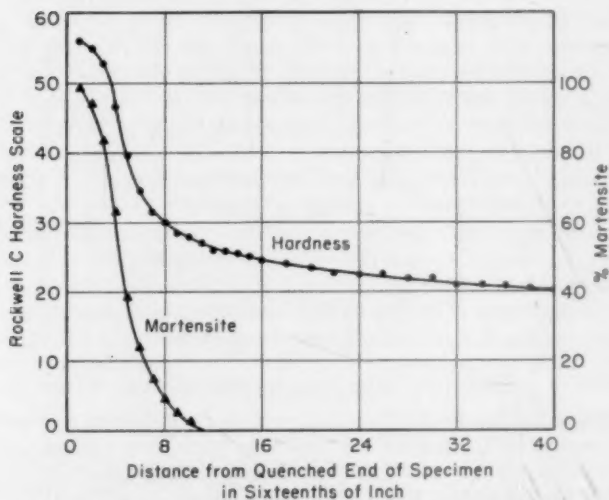


Fig. 2—Hardness Versus Per Cent Martensite of End Quench Bar of SAE 4042.

of the fatigue specimens which were later to be machined from the heat treated bars. It was found very difficult to obtain an exact predetermined per cent of martensite. This required many trials since duplica-

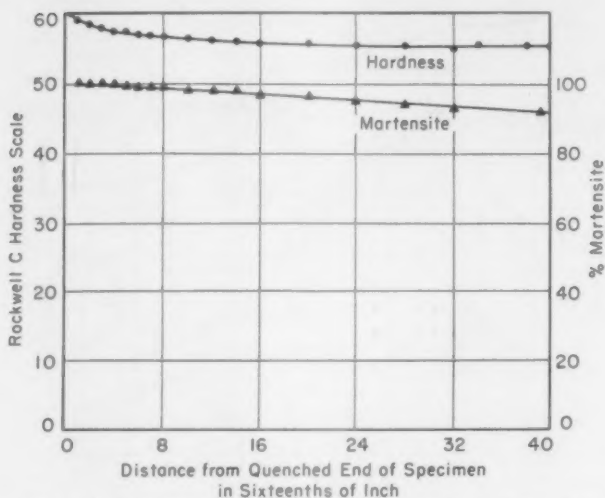


Fig. 3—Hardness Versus Per Cent Martensite on End Quench Bar of SAE 4340.

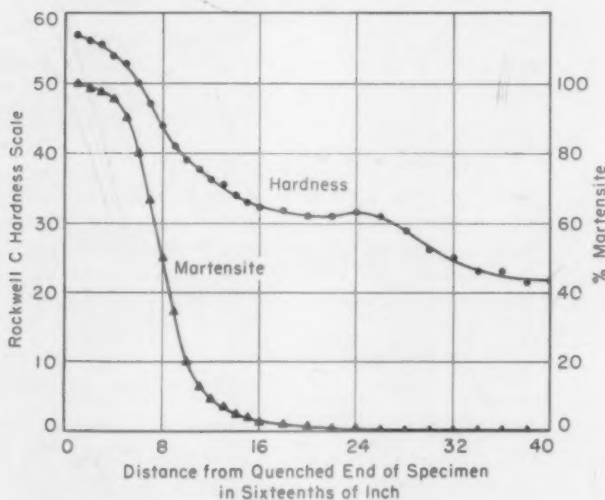


Fig. 4—Hardness Versus Per Cent Martensite on End Quench Bar of SAE 5140.

tion of quenching is known to give somewhat erratic results. After the first three steels (SAE 4042, 5140 and 80B40) had been run indicating the nature of the martensite versus endurance limit curve, we felt that

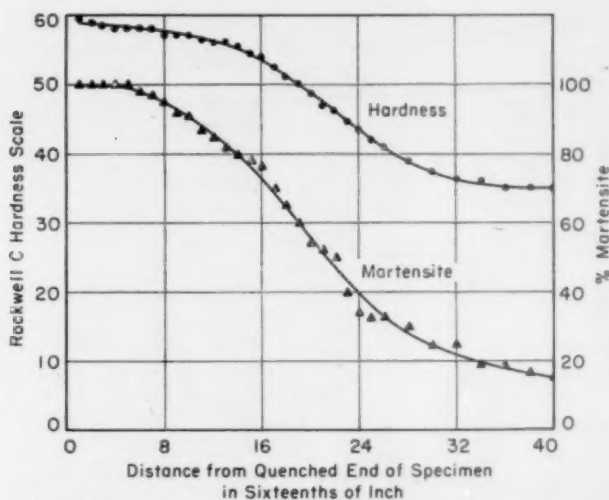


Fig. 5—Hardness Versus Per Cent Martensite on End Quench Bar of SAE 80B40.

Table II

Steel	Series	Selected Quench	Selected Size (inches)	As-Quenched Hardness Rockwell C	% Martensite
4042	A	Pagoda Quench at Room Temperature	.27	56.2	100
	B	Still Oil Quench at Room Temp.	.50	54.3	95
	C	Still Oil Quench at Room Temp.	.68	52.3	85-90
	D	Pagoda Quench at Room Temperature	.95	45.6	70
	E	Pagoda Quench at Room Temperature	1.18	39.2	35
5140	F	Pagoda Quench at Room Temperature	.26	56.6	99.5
	G	Still Liq. Tallow at 200°F.	.42	55.0	97
	H	Same as above	.55	46.0	60-65
	I	Same as above	.65	39.0	20
**80B40	J	Pagoda Quench at Room Temperature	.27	59.0	100
	K	Still Liq. Tallow at 200°F.	.63	57.5	90
	L	Still Water Quench at Room Temp.	2.00	56.5	85
	M	Still Oil Quench at Room Temperature	2.00	48.0	50-55
	N	Same as above	3.00	38.5	25
4340	P	Hot Air in 5 cu. ft. insulated container	1.00	43.7	40
1340	Q	Pagoda Quench at Room Temperature	.28	59.5	100
	R	Still Oil Quench at Room Temperature	1.25	37.2	25

**J and K series were austenitized for 1 hour, L and M for 3 hours and N for 4 hours at 1525°F. J series were stress relieved after quenching at 550°F for 1 hour to avoid cracking. The 3 inch dia. size of the N series was done by shrink fitting a 1/2 inch thick sleeve of SAE 1020 steel around a 2-inch diameter bar.

Table III

Steel	Series	Hardness As Quenched Rockwell C	Tempered (1 Hr. at deg. F.)	Average Tempered Hardness Rockwell C
4042	A	56.2	960	36.4
	B	54.3	950	36.3
	C	52.3	945	35.6
	D	45.6	815	35.0
	E	39.2	655	33.0
5140	F	56.6	910	37.0
	G	55.0	928	35.0
	H	46.0	865	34.0
	I	39.0	775	34.5
80B40	J	59.0	960	36.5
	K	37.5	945	36.5
	L	56.5	940	36.5
	M	48.0	880	36.5
	N	38.5	750	36.3
4340	O	58.0	1060	34.5
	P	43.7	920	36.7
1340	Q	59.5	850	39.1
	R	37.2	710	35.4

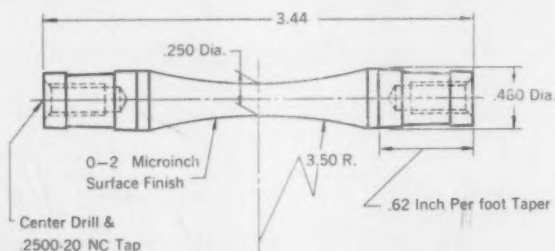


Fig. 6—Fatigue Bar Ground After Heat Treatment.

an approximate predetermined percentage was sufficiently satisfactory to indicate whether other steels fit on this curve. Of course, after quenching, the amount of martensite formed was carefully determined. For these reasons the series of SAE 1340 and 4340 were heat treated to a hardness that could still be tempered to Rockwell C—36 and the per cent of martensite was determined secondarily. The selected sizes and the quenching media along with the "as-quenched" hardness and percentage of martensite are shown in Table II.

TEMPERING OF SELECTED SIZES

On the basis of results in Table II, six bars for each series were machined to the selected sizes and given the predetermined heat treatment. They were tempered at successively higher temperatures, water-quenched, and their hardness measured after every tempering step until the desirable hardness level was reached (Rockwell C—36). The tempering temperatures for each series and the average tempered hardness are listed in Table III.

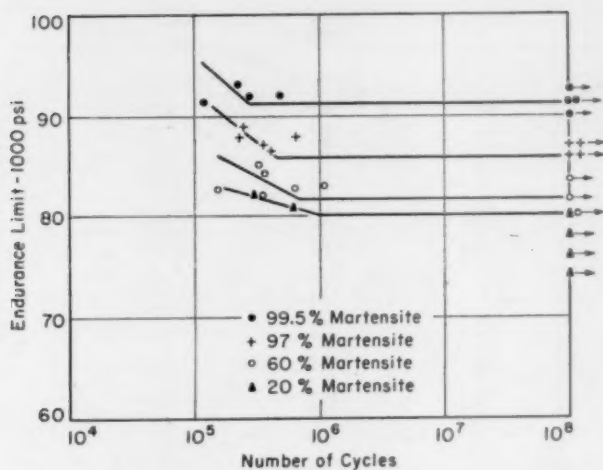


Fig. 7—S-N Curves of SAE 5140 Specimens with Various Amounts of Martensite, and Tempered to Rockwell C-36.

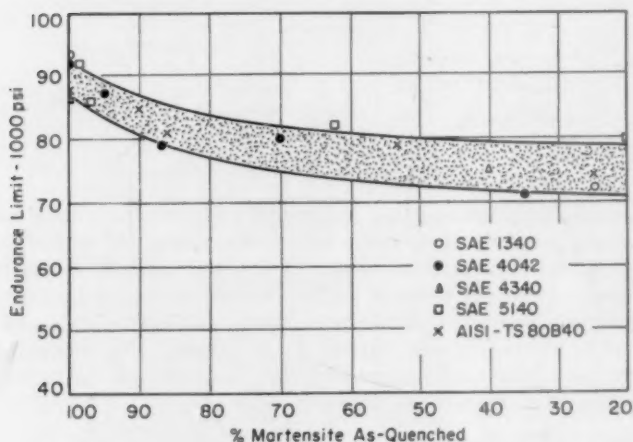


Fig. 8—Endurance Limit Versus Per Cent "As-Quenched" Martensite in Specimens Tempered to Rockwell C-36.

PREPARATION OF THE FATIGUE TEST SPECIMENS

About 12 to 15 samples were prepared for each series and processed according to the selected schedule as indicated in Tables II and III. Each series had 3 pilot samples that were successively cut up and rechecked for hardness and microstructure after each heat treating step.

After the heat treatment, the samples were machined and carefully ground to R. R. Moore fatigue specimens (Fig. 6). They were super-finished to the surface roughness specification of 0-2 microinches, inspected and their minimum diameter measured on the optical comparator.

TESTING OF THE FATIGUE BARS

The fatigue bars were tested in R. R. Moore fatigue testing machines (10,000 rpm type). After completion of each test, the fractures of the samples were ground off and the tempered hardness rechecked. The run-out specimens with over 100 million cycles were cut in half and

Table IV
Endurance Test Data

Steel	Series	Endurance Limit (psi)	% Martensite "As-quenched"
SAE 4042	A	92,000	100
	B	87,000	95
	C	79,000	85
	D	80,000	70
	E	71,000	35
SAE 5140	F	91,000	99.5
	G	86,000	97
	H	82,000	60-65
	I	80,000	20
AISI TS-80B40	J	88,000	100
	K	85,000	90
	L	81,000	85
	M	79,000	55
	N	74,000	25
SAE 4340	O*	86,500	100
	P	75,000	40
SAE 1340	Q	93,000	100
	R	72,000	25

*Data taken from Garwood, Zurburg and Erickson (7)

their hardness checked similarly.* The results of the fatigue tests of each steel were used to plot the S-N curves. A typical family of S-N curves for SAE 5140 steel is illustrated in Fig. 7. The endurance limits of the series with their respective amounts of "as-quenched" martensite are shown in Table IV, and graphically represented in Fig. 8.

DISCUSSION OF RESULTS

Results of all the testing are illustrated in Fig. 8 and show the relationship of endurance limit versus per cent martensite obtained on continuous cooling and tempering to a common hardness of Rockwell C-36. The data are represented as a band since there is a certain amount of scatter in the data points. Nevertheless, from this curve it can be seen that a few percentages of nonmartensitic products cause

* These values are those reported in Table III. In any series of fatigue bars the hardness variation was ± 0.5 Rockwell C.

a rather rapid drop in the endurance limit. Below 85% martensite, there appears to be little change in endurance limit as the curve flattens out.

For several years now metallurgists have been discussing the effect of the percentage of martensite at various positions in the quenched section sizes of parts. Some feel that we should have 90% martensite at the $\frac{3}{4}$ radius for parts used in bending or in torsion; others used the figure of 80% martensite at the $\frac{3}{4}$ radius. From the data in Fig. 8, it appears that the 90% figure may be a more realistic one inasmuch as the higher endurance limit would be obtained with this per cent of

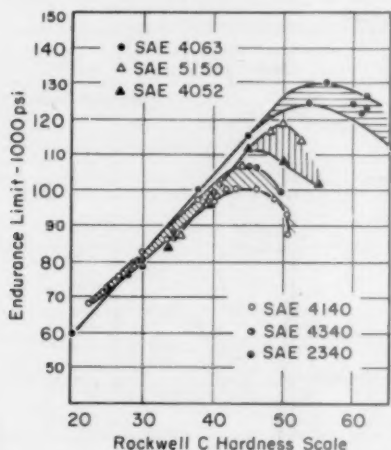


Fig. 9—Endurance Limit of Specimens Tempered to Various Hardness.

martensite. Further, from our data, it appears that it would not make very much difference whether the figure of 80% or 50% were used, since there is little drop in the endurance limit between 80% and 50% martensite.

It was surprising to find from this investigation that a small per cent of nonmartensitic products adversely effected the endurance limit. For this reason the advantage of having 100% martensite at the surface of a part subject to fatigue stresses is clearly apparent.

An effort was made to correlate our data with that of Hodge and Lankford (5), who had studied the effect of microstructure obtained by isothermal transformation. Unfortunately, no correlation could be found. However, on further studying the work of the authors, who had tempered their bars to Rockwell C-34, some discrepancies seem to exist. With a hardness of Rockwell C-34 their endurance limit, using

a figure of 50% of the ultimate strength as a criterion, should be approximately 80,000 psi. Their data show an endurance limit of 72,000 psi, which seems low for the hardness of Rockwell C-34. However, our data on 100% tempered martensite are supported by findings of Garwood and his co-workers (7). They presented a correlation of the endurance limit of six low alloy steels with the tempered hardness (Fig. 9). The endurance limit values at Rockwell C-36 fall between 88,000 and 93,000 psi which range conforms very well with the result as determined in this investigation.

We recognize that more steels and more hardness ranges should be investigated to further study this important behavior of quenched and tempered steels. Perhaps a more precise method for measuring the percent martensite in the as-quenched condition may be worked out. The electron microscope covers so small a field that it is not effective in determining the percentage of martensite. Our method of taking the average of the careful determinations of four qualified metallographers seems as satisfactory as present methods permit.

SUMMARY

A relationship was found to exist between the percent of martensite formed on quenching and tempering to Rockwell C-36 and the endurance limit. It is further shown that a small percentage of nonmartensitic structure has a deleterious effect on the fatigue strength of the steels tested. Below 85% martensite the endurance limit is effected very little by microstructure.

In the application of hardenability to design, some specifications require 90% martensite at the $\frac{3}{4}$ radius. In less stringent specifications 80% martensite is required and in still less, 50% martensite is required. Provided that 100% martensite is obtained at and just below the surface there appears to be little difference between the 50% and 80% martensite requirement at the $\frac{3}{4}$ radius. The 90% martensite would give a higher endurance value at this point.

If the surface is less than 100% martensite the endurance limit drops off rather sharply to the 95% value and less sharply to the 85% value.

ACKNOWLEDGMENT

At this occasion, the authors wish to express their thanks to the Chrysler Corporation for permission to publish the results of this research. They are equally indebted to the staff members of the Metallurgical Research Department of the Chrysler Corporation, especially H. V. Holst for his help and cooperation during the course of this study.

References

1. H. F. Moore and J. B. Kommers, *Fatigue of Metals*, First edition, 1927, p. 205. McGraw-Hill Book Co., Inc., New York.

2. F. Cazaud and L. Persoz, *La Fatigue Des Metaux*, 2nd edition, 1943, Chapter V, Dunod, Paris 92 rue Bonaparte (VI).
3. J. H. Hollomon, L. D. Jaffe, D. E. McCarthy and M. N. Norton, "The Effects of Microstructure on the Mechanical Properties of Steel," *TRANSACTIONS, American Society for Metals*, Vol. 38, 1947, p. 807-847.
4. G. A. Liedholm, "Experimental Studies of Continuous Cooling Transformations," *TRANSACTIONS, American Society for Metals*, Vol. 38, 1947, p. 188-189.
5. J. N. Hodge and W. T. Lankford, "Influence of Non-Martensitic Transformation Product on Mechanical Properties of Tempered Martensite," Technical Note 2862, National Advisory Committee for Aeronautics, Dec. 1952.
6. S. T. Ross, R. P. Sernka and W. E. Jominy, "An Electron Metallographic Study of the Dependence of Microstructure on Hardenability," *TRANSACTIONS, American Society for Metals*, Vol. 47, 1955, p. 727-742.
7. M. F. Garwood, H. H. Zurburg and M. A. Erickson, "Correlation of Laboratory Tests and Service Performance," *Interpretation of Tests and Correlation with Service*, 1951, p. 1-77. American Society for Metals.

DISCUSSION

Written Discussion: By J. M. Hodge, Chief Research Engineer—Alloy Steels, United States Steel Corporation, Monroeville, Pa.

The results reported in this paper are in a field of real importance to the users of heat treated alloy steels, and the authors are to be congratulated on the well conceived and extensive research job that they have done.

The authors have mentioned in discussing their results, the paper published by Dr. W. T. Lankford and myself, reporting the results of studies of the effects of nonmartensitic products on the mechanical properties of tempered martensite which were carried out as a joint effort by a number of laboratories under the sponsorship of the Chrysler Standardization Committee. The authors state that they were unable to find any correlation between their results and the results reported in this paper and that a number of apparent discrepancies seemed to exist. I would like to point out that the results of the two investigations do have much in common and to discuss briefly some of the factors that may be involved in the discrepancies which were noted.

The first of these factors, which has also been mentioned by other discussors, is the fact that, in neither of these studies, were there enough specimens to permit a statistical evaluation of the results. There is, therefore, necessarily some uncertainty about the quantitative results of both studies.

The principal difference between the approach of the authors, and that of the work reported by us lies in the use of controlled continuous cooling to establish the microstructures in the first instance and of partial isothermal transformation in the work which we reported. We believe that, for a single steel of a given hardenability, the two methods would give similar answers. Our work was on a 4340 steel and, if the 4340 results are isolated from those of the other steels in the authors studies, it will be seen that the answers obtained in the two investigations are similar. At 40% martensite, the authors show a decrease in endurance limit of about 12% and in our studies, a decrease of 13% was found when the microstructure was 50% martensite. Our studies, however, showed that the effect of the nonmartensitic products varied with the nature of the product, with 5% of pearlite, being about as effective as 50% of bainite in lowering the endurance limit. Thus, steels of lower hardenability, in which the nonmartensitic products

were pearlitic or were formed at transformation temperatures higher than that for bainite, might exhibit lower endurance limits for a given microstructure in terms of percentage of martensite. This could explain the apparent larger effect of small percentage of nonmartensitic products that was found for some of the steels investigated by the authors as compared to the rather minor effect found by us.

In regard to the rather large discrepancy between the endurance limit for the 4340 steel with a fully tempered martensitic structure which we investigated and that of the 4340 steel investigated by the authors, we can only comment that there are obviously a number of factors other than gross microstructure which can markedly affect the endurance limits of quenched and tempered alloy steels. We do not believe, however, that this discrepancy is, in itself, significant in regard to the effects of nonmartensitic products on endurance limit which was the subject being investigated in both studies.

Written Discussion: By T. J. Dolan and G. M. Sinclair, Department of Theoretical and Applied Mechanics, University of Illinois, Urbana, Illinois.

In general, the trends of the data and the results contained in this paper are in good agreement with the conclusions drawn by the writers as presented in a previous ASTM paper.* The authors have obtained more detailed information in terms of the influence of *per cent* of martensite on fatigue strength. In our earlier work, the exact percentages of martensite were not determined, but the same trends were observed. That is, tempered martensitic structures definitely had some superiority in fatigue when all specimens were tempered to the same hardness level.

One point of especial interest emphasized by the authors is that a very small percentage of nonmartensitic decomposition products had a relatively large effect in lowering fatigue limit; additional higher percentages of nonmartensitic products had relatively little effect. In our studies, four different steels were given a variety of heat treatments and all specimens tempered back to the same hardness of about 100 Rockwell B (a considerably lower hardness level than that utilized in the present paper). However, even at this low hardness level, small amounts of a proeutectoid ferrite in a matrix of tempered martensite lowered the static and fatigue properties. Thus randomly dispersed islands of the weaker constituent proved to be significant in affecting the fatigue limit. Larger amounts, as represented by a pearlitic type of structure, were *not* particularly effective in further lowering of the fatigue limit.

It should also be pointed out that there was a large change in the V-notch Charpy impact transition temperature when the microstructure was less than 100% tempered martensite. That is, the tempered martensitic structures had good impact properties as represented by low transition temperatures compared with the values obtained when other decomposition products were allowed to form.

It is also of interest to point out that in our previous work sets of notched specimens were tested to determine whether the fatigue strength reduction caused by the presence of a stress raiser was significantly different for tempered martensitic structures as compared with those having other decomposition products present. In general, it was found that the martensitic type structures exhibited

* G. M. Sinclair and T. J. Dolan, "Some Effects of Austenitic Grain Size and Metallurgical Structure on the Mechanical Properties of Steel," *Proceedings, American Society for Testing Materials*, Vol. 50, 1950, p. 587.

higher fatigue strength for notched specimens as well as for the unnotched or "par" values.

In appraising the effects of heat treatment, however, data of the type shown in Fig. 9 of the paper should be re-emphasized. They indicate that for practical application, small changes in the final hardness of the part are as effective in producing a change in the fatigue limit as is the presence of small amounts of a nonmartensitic product in an otherwise completely martensitic structure. Furthermore, since it is practically impossible to produce a component of a machine without having some abrupt changes in section such as holes, fillets, keyways, etc., (or in many instances, such parts will contain rough-machined, as-forged, or partially decarburized surfaces) all of which produce a much greater harmful effect on the fatigue limit of the finished component than does a slight change in the metallographic constituents of the metal. In other words, a small percentage of non-martensitic constituents may produce a 10 or 15% lowering of the endurance limit, whereas a sharper fillet (or a small amount of decarburization on the surface) can readily produce a 50% lowering of the endurance limit. Thus, the final geometry, method of surface processing, and the final surface chemistry in the finished product, may often prove to be more important than the selection of an alloy or heat treatment in an attempt to produce 100% martensite.

One criticism that might be offered of the present paper (and also of the writers' previous work) is the lack of sufficient specimens to attempt to evaluate statistically the most probable value of endurance limit and the reliability of the data obtained. Since data of the type shown in Fig. 7 are inherently statistical in nature, wide variations in the actual experimental data would be obtained if tests were repeated with new groups of samples. In recent years, a good deal more emphasis has been placed upon testing larger groups of samples as representative of the population to enable a determination of the mean fatigue limit and the confidence limits on this value. The significance of differences measured between individual groups can only be appraised on the basis of statistical methods.

Authors' Reply

The authors would like to thank Mr. Hodge for his very valuable remarks concerning this paper. His assertion that results of his study of the SAE 4340 steel and our work are principally in agreement is very interesting.

Because our endurance limit values were so much higher than those of Hodge's, we thought comparison between the two was hazardous. However, we think it is very interesting that in spite of the large difference, the percentage drop, as calculated by Hodge, is comparable between our 40% martensite value and their 50% martensite value. As Mr. Hodge states, and with which we agree, other factors than gross microstructure can markedly affect endurance limits.

The authors wish to express their thanks to Messrs. Dolan and Sinclair for their excellent comments on this paper. It was gratifying to learn that our data on the microstructural effect upon the endurance limit were supported by the findings of their study showing an analogous behavior when steels were tempered to a different hardness level. Also, we were very interested in their mention of a similar trend for tempered martensitic series having better impact properties than those containing transformed microstructures.

As to the judgment of the degree in which the microstructure influences the endurance limit, we agree that there are other factors governing the fatigue be-

havior of quenched and tempered steel parts. However, the purpose of our investigation was to resolve the effect of microstructure. We intended merely to qualify the choice of an alloy or heat treatment more quantitatively than it was done in the past by saying a given microstructure is "better", "worse" or "makes no difference" under repeated stresses. We agree with Professor Dolan's discussion that the nature of the fatigue data is such that it requires statistical treatment.

Such a procedure calls for a large number of samples. Our inability to comply with the statistical approach stems from the difficulty in the preparation of the fatigue specimens. In many instances the cross-sectional sizes of the heat treated blanks were large in diameter and in order to machine a fatigue bar from the center of such blanks, careful grinding in a coolant was required to penetrate the hard skin to the machinable core. To prepare large quantities of such fatigue specimens would be time consuming and costly.

We would like to encourage other investigators to make further tests of the effect of microstructure, particularly in the high hardness range, and feel that the subject is of sufficient importance to justify additional studies. We would, however, like to caution those who do this that great care must be exercised to obtain the correct percentage of transformed products in each fatigue specimen. We have found that quenching must be most carefully controlled and that very small factors in quenching can vitiate the microstructural condition. It would be unfortunate to make a great many samples for statistical analysis but to have microstructural differences in these samples.

THE MACHINABILITY OF TYPE A LEADED STEELS

By E. J. PALIWODA

Abstract

The machining uniformity of Type A leaded steels appears to be subject to the same chemical composition variables which affect the machinability of nonleaded open-hearth free cutting steel. As in the case of C-1213 steels, oval sulphide inclusions are favorable to the machinability of Type A steels with stringer-like sulphides being less effective. Lead inclusion mass appears to be dependent on sulphide inclusion nature with fine lead tails being associated with fine stringer-like sulphides. The somewhat greater machinability index range of Type A material as compared to regular screw stock may, in part, be due to a size effect of the inclusions present with both massive lead tails and oval sulphides being favorable to machining quality (lower tool-chip friction).

Decreased carbon, silicon and manganese or increased sulphur and lead contents are beneficial to the cutting quality of Type A steels. The machinability advantages of phosphorus and nitrogen cannot be evaluated by means of the turning rate test employed. (ASM International Classification G17k, 1-10; CN, Pb)

INTRODUCTION

THE ADDITION OF lead to steel results in low tool-chip friction which permits the use of fast machining rates and favors the formation of superior as-machined finishes. (1,2)¹ Since lead and iron appear to be mutually insoluble in both the liquid and solid states, lead is added to the mold in such a manner as to minimize its segregation (3). The rate and timing of the addition coupled with control of the teeming temperature are utilized to produce steels with a satisfactory distribution of lead. Exudation tests, x-ray fluorescence analysis and chemical analysis checks are employed as controls for discarding portions of the product containing either low or excessively high lead contents.

¹ The figures appearing in parentheses pertain to the references appended to this paper.

A paper presented before the Thirty-Ninth Annual Convention of the Society, held in Chicago, November 4-8, 1957. The author, E. J. Paliwoda, is associated with Jones & Laughlin Steel Corporation, Graham Research Laboratory, Pittsburgh. Manuscript received May 13, 1957.

Despite these controls, it has been shown that there are subtle microscopic differences in lead or lead compound particles in high sulphur steels (4). The relative mass of the lead particles is affected by rate of solidification of the parent ingot, association or lack of association with other nonmetallics, and the malleability of the sulphides. Attempts were made to establish whether machining variability of leaded high sulphur steels is related to sulphide and lead inclusion nature and whether factors pertinent to the machinability of regular screw stock would also be operative in the leaded high sulphur grades.

MACHINABILITY TESTING

Experience has shown that rate of machining or tool life and as-machined finish are the major considerations in the production of premium screw steels. Other factors, such as chip character, are usually of secondary consideration. The measurement of rate of cutting in the laboratory studies consisted of turning 2 cubic inches of metal at progressively increased speeds, usually 10 surface feet per minute increments. With cutting conditions constant at $\frac{1}{16}$ inch depth of cut and a 0.003 inch feed, the highest turning speed possible without exceeding a prescribed wear of the relatively soft cutting tool is termed the machinability index. Details of the testing procedure have been described previously (5).

The test endpoint is determined by projecting a 50-diameter image of the tool tip on the screen of an optical comparator (Fig. 1). Extensions of the relatively unaffected edges of the tool tip are used to gage the amount of wear with $\frac{1}{16}$ inch being considered the test endpoint. The machinability index is expressed in surface feet per minute calculated on the basis of the machined bar diameter. It should be recognized that the machinability indices are obtained with a relatively soft cutting tool and that these cutting rates are appreciably below those normally employed in commercial machining.

The principal disadvantage of the pilot machinability test is that, as is true of any turning rate test, no information is obtained as to chip character, surface finish or dimensional accuracy. Thus, an accurate evaluation of the contributions of phosphorus and nitrogen to machinability is not possible since their effects lie largely in the area of these factors.

EXPERIMENTAL RESULTS

A series of 1 to 1 $\frac{1}{4}$ inch cold drawn rounds representing several production sources were obtained from commercial and experimental leaded ingots. Table I contains the chemical composition and machinability indices for the Type A steels involved. Metallographic examinations were made on the steels and Fig. 2 illustrates the observed relationship between machinability rating and sulphide inclusion na-

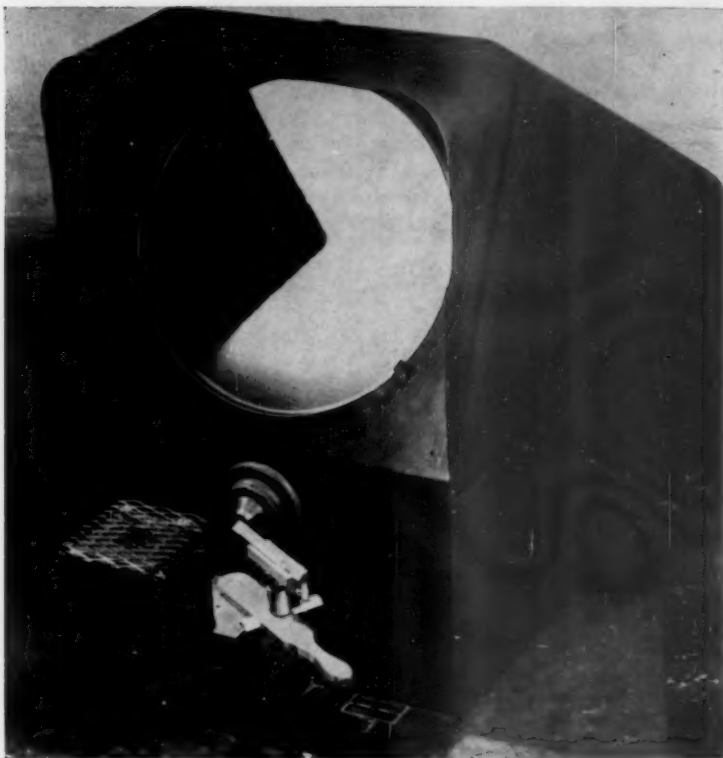


Fig. 1—Method of Determining Tool Wear. Following each turning test, a magnified image ($\times 50$) of the cutting tool is projected on the screen of an optical comparator. Extensions of the relatively unaffected edges of the test tool are employed to gage tool tip wear. The highest speed of turning 2 cubic inches of metal that produces a $1/16$ -inch or less tool tip wear is termed the machinability index.

ture. It can be noted that, as in the case of regular screw steels, oval sulphides are favorable to machining quality, while stringer-like sulphides appear to be less effective in promoting cutting quality. The addition of lead does not appear to alter sulphide inclusion nature noticeably, since the inclusion character of the Type A steels is similar to that observed in C-1213 material.

The variation in machinability indices, shown in Table I, is somewhat greater than that encountered in steels such as C-1213 or B-1113. Since all Type A steels, whether from commercial or experimental ingots, were subjected to sweat tests and exhibited satisfactory lead dispersion, differences in the macroscopic distribution of lead were believed to be of minor significance. Attention was directed to lead dis-

Table I
Chemical Composition and Machinability Indices

No.	C	Mn	P	S	Si	Pb	Soluble N	Machinability Index
1	0.11	1.36	0.060	0.302	0.020	0.28	0.006	90
2	0.09	0.98	0.059	0.318	0.009	0.26	0.007	150
3	0.07	0.91	0.050	0.293	0.006	0.21	0.007	180
4	0.08	1.08	0.061	0.237	0.014	0.19	0.007	130
5	0.08	1.11	0.064	0.254	0.011	0.22	0.008	130
6	0.10	1.23	0.051	0.293	0.015	0.23	0.008	110
7	0.07	0.95	0.059	0.301	0.004	0.18	0.008	180
8	0.10	0.98	0.063	0.337	0.002	0.18	0.008	150
9	0.09	0.81	0.058	0.332	0.014	0.17	0.008	170
10	0.08	1.06	0.054	0.313	0.005	0.17	0.008	140
11	0.09	1.05	0.059	0.336	0.010	0.24	0.008	170
12	0.08	1.04	0.055	0.315	0.006	0.25	0.008	150
13	0.09	0.97	0.063	0.282	0.010	0.26	0.003	160
14	0.11	0.98	0.070	0.292	0.009	0.30	0.004	160
15	0.09	1.00	0.067	0.310	0.009	0.31	0.005	160
16	0.10	1.14	0.056	0.308	0.010	0.24	0.007	140
17	0.09	0.84	0.048	0.294	0.020	0.25	0.007	140
18	0.06	0.90	0.062	0.282	0.011	0.24	0.004	180
19	0.09	1.03	0.065	0.225	0.002	0.21	0.004	150
20	0.09	1.05	0.052	0.225	0.006	0.20	0.005	160
21	0.08	0.85	0.046	0.259	0.006	0.20	0.006	160
22	0.08	0.88	0.051	0.285	0.006	0.15	0.006	140
23	0.08	0.86	0.046	0.256	0.014	0.20	0.004	150
24	0.08	0.85	0.050	0.270	0.012	0.18	0.004	160
25	0.09	1.03	0.043	0.190	0.013	0.13	0.005	130
26	0.09	1.04	0.053	0.232	0.007	0.14	0.005	130
27	0.08	1.04	0.044	0.189	0.011	0.21	0.005	130
28	0.07	1.02	0.045	0.192	0.013	0.13	0.005	130
29	0.07	0.97	0.052	0.255	0.013	0.13	0.006	160
30	0.07	0.96	0.050	0.250	0.018	0.18	0.003	160
31	0.07	0.97	0.052	0.255	0.009	0.13	0.006	160
32	0.08	0.97	0.050	0.255	0.011	0.19	0.009	160

person on a microscopic scale as a factor contributing to the machining differences.

In order to investigate the microdispersion of lead in steel, various suggested etchants (6-8) were employed with indifferent success. Subsequently, microradiography was employed to establish the distribution of the lead or lead compound particles which would be visible at one or two hundred magnifications. The procedure involved has been described in other work (4). Briefly, the absorption of the x-rays by a 0.0035 inch thick foil is recorded photographically on fine grain spectroscopic plates. The negative is enlarged and a "shadow" of the structure is obtained. Cobalt K α radiation which falls at the K absorption edge of manganese was employed to obtain microradiographs of both sulphide (manganese) and lead inclusion character. By virtue of the enlargement and printing process, the microradiographs shown exhibit lead as the white areas and sulphides as the areas of intermediate density. The microradiographs represent the inclusion characteristics of the steels at a depth of $\frac{1}{16}$ inch into the bar which corresponds to the metal in contact with the tool during machinability testing.

Microradiographs of a number of steels tested are included in Fig. 3. It can be observed that virtually all of the visible lead or lead compound particles are associated with sulphide inclusions. Although the existence of lead compounds is not precluded by work to date, only elemental

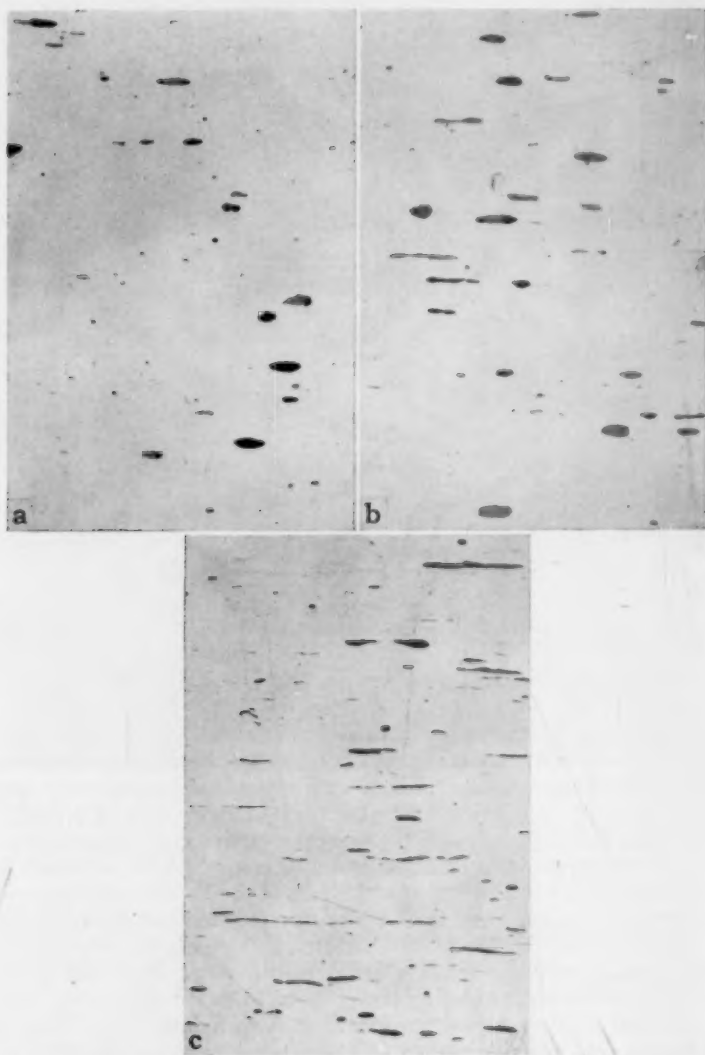


Fig. 2—Machining Quality of Type A Steels As Influenced by Sulphide Inclusion Nature ($\times 100$). (a) Machinability index 180; (b) Machinability index 130; (c) Machinability index 90. In Type A steels, oval sulphides are favorable to machining quality. Either the mass of the oval sulphides, as suggested by Merchant (12) and Van Vlack (11), or composition differences associated with such inclusions promote tool-chip lubrication thereby improving cutting quality.

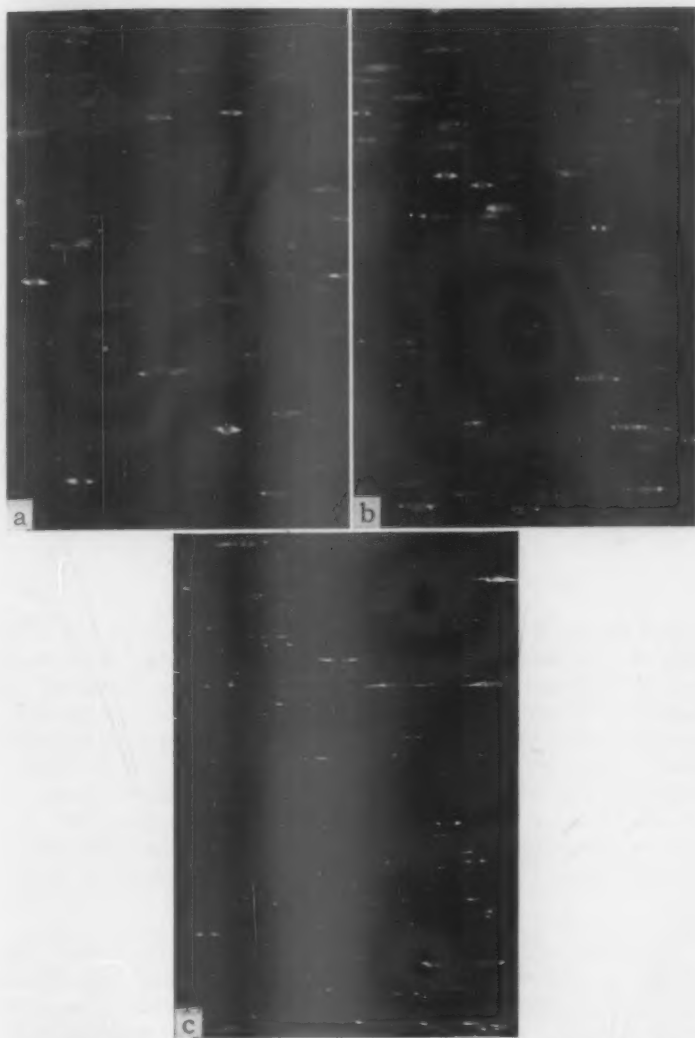


Fig. 3—Inclusion Characteristics Versus the Machinability of Type A Steels ($\times 100$). (a) Machinability index 180; (b) Machinability index 130; (c) Machinability index 90. The interdependence of lead and sulphide inclusion mass may be responsible for the somewhat wider machinability rating ranges within leaded grades as compared to regular high sulphur screw steels. If the size effect suggested by Merchant (12) is operative, the complementary action of lead and sulphide inclusion size may be the reason for the larger machinability index range of leaded screw steel grades. Although lead inclusion size is probably independent of its composition, the size effect is not regarded as conclusive due to the possible effects of lead segregation within acceptable sweat test specifications.

lead has been identified consistently by electron and x-ray diffraction (4). For purposes of clarity, the lead-containing particle will be termed elemental lead. Lead occurs as sheaths, tails or envelopes on many of the sulphide inclusions present. In addition to the relationship between machining quality and sulphide inclusion nature illustrated in Fig. 3, there appears to be a correlation between lead particle size and sulphide inclusion nature. Massive oval sulphides exhibit massive lead sheaths while elongated stringer-like sulphides, particularly those which appear to have broken up during rolling, show correspondingly fine lead tails. Details of the effect of hot working on lead dispersion have been described in detail by Thurman, et al (4).

Since the effectiveness of sulphide inclusion nature in promoting machining quality appears to be similar in both regular and leaded high sulphur steels, multiple correlation analysis was employed in an effort to establish whether the same composition variables are operative in both instances. It was possible to ascribe 73% of the machining variance of Type A steels to differences in chemical composition. The relationship obtained is expressed as follows:

$$\text{Machinability Index} = 265 - 600 (\%C) - 1300 (\%Si) \\ - 100 (\%Mn) + 100 (\%S) + 100 (\%Pb)$$

DISCUSSION OF RESULTS

Two factors, the mutual insolubility of lead and iron as well as the mass interdependence of the inclusions present, should permit at least a qualitative comparison of chemical composition effects in regular and leaded high sulphur steels. Past work indicates that composition effects on machinability vary depending on the steelmaking practice employed. (9-11). Consequently, it is not surprising that the data for Type A steel differ somewhat from observations made on Bessemer grades. On the other hand, present results appear to be in agreement with composition effects observed in C-1213 steels despite the difference in phosphorus and nitrogen levels of the two grades involved.

Sulphur and Lead

The nature of the sulphide inclusions present in free-cutting steels exerts a marked effect on machining quality while minor variations in the amount of sulphur present at these levels appear to be a secondary factor. A similar effect may exist for lead in that the microdispersion of the element may overshadow minor differences in the amount present. The influence of a 0.01% increase in lead was found to be + 1 index point for Type A steels.

A somewhat greater machinability index range for the leaded screw steel as compared to high sulphur grades may stem from the interdependence of sulphide and lead inclusion mass. The difference in the

mass of inclusions was suggested as the reason for the relationship between machining quality and sulphide inclusion nature. (11,12) Sulphide inclusion composition, however, may be equally important. Lead particle size is probably independent of its composition; hence, if the size effect is significant, the machinability advantages of massive oval sulphides may be complemented by the presence of relatively massive lead tails. Conversely, fine stringer-like sulphides with correspondingly fine lead tails would be less effective in promoting machinability. The

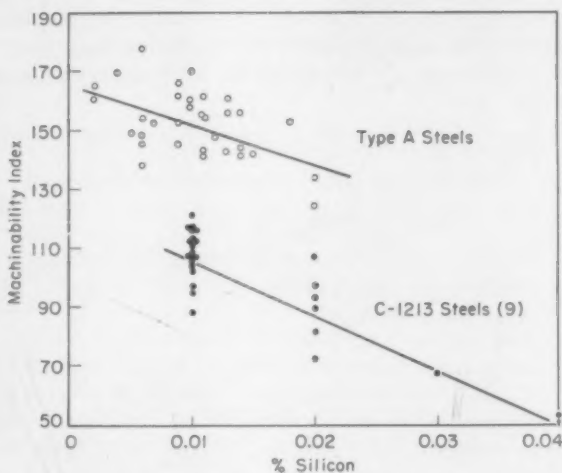


Fig. 4—A Comparison of the Influence of Silicon Content on the Cutting Quality of Type A and C-1213 Steels. Decreased silicon in Type A steels, as in the nonlead C-1213 grade, is beneficial to machining quality. Lower silicon contents in the subject grade favor the formation of the more effective oval type sulphides with correspondingly massive lead tails.

size effect, however, cannot be considered conclusive since variations in macroscopic distribution of lead (acceptable sweat tests) may be important.

In open-hearth regular and leaded stock, the effects of a 0.01% increase in sulphur are $1\frac{1}{2}$ and 1 index point respectively.

Silicon

The effect of an 0.01% decrease in silicon in Type A steels was found to be + 13 as compared to + 18 index points in regular C-1213 material (Fig. 4). These data appear to be in fairly good agreement, particularly in view of the slightly higher manganese content of the leaded stock. Increased silicon favors the formation of elongated stringer-like sulphides in both grades and affects lead microdispersion in Type A steels through its effect on the sulphides. It should be noted that the total

silicon values employed include both the elemental form and silicon combined as silicates. Results of regular high sulphur steel investigations indicate that occasional screw steels can exhibit high total silicon contents with oval sulphide inclusions and correspondingly excellent machining quality (9,10). Similar exceptions to the effect of silicon have recently been observed in Type A steels and it is presumed that the element can be present in screw steels in a form which does not materially affect machining quality.

Carbon

The effect of carbon appeared to be similar in both Type A and C-1213 steels (Fig. 5). In both instances, decreased carbon appears to

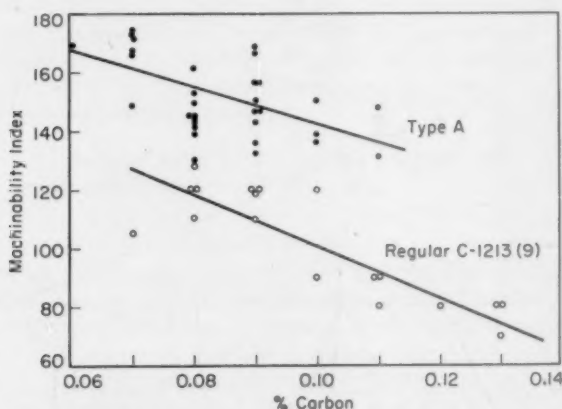


Fig. 5—The Influence of Carbon Content on the Machining Quality of C-1213 and Type A Steels. In the graph, the machinability indices of the Type A and C-1213 steels are corrected for variations in chemical composition exclusive of carbon contents. It can be noted that the effect of carbon in the two grades is similar despite differences in nitrogen and phosphorus levels.

be beneficial, being rated at $8\frac{1}{2}$ and 6 index points per 0.01% carbon for the regular and leaded grade respectively. The role of carbon appears to be similar to that of silicon in that lower carbon contents appear to favor the formation of the more effective oval sulphides with correspondingly more massive lead sheaths or tails.

Manganese

Decreased manganese in Type A steels is mildly beneficial and its effect was rated at 1 index point per 0.01%. Due to the fairly wide range of manganese contents present, its over-all effect is pronounced in terms of machining variations in the Type A steels.

Phosphorus and Nitrogen

Phosphorus and nitrogen are, to some extent, complementary in contributing to the work embrittlement of steel (13). The elements are added to screw steels to promote a more favorable cutting action with its inherent advantages to finish, chip characteristics and dimensional accuracy. It should be emphasized that single point turning tests do not accurately define the benefits derived from these elements, and results may actually be misleading when applied to a complete evaluation of machinability. It is likely that the level of phosphorus and nitrogen desired in any screw steel grade is a function of the tool-chip friction as well as the types of machining operations to which the steel is subjected.

SUMMARY

The effects of chemical composition variations on the machinability of leaded high sulphur steels parallel the effects of the elements in regular screw stock. Oval sulphides favor the machining quality of leaded steels while stringer-like nonmetallics appear to be less effective. The bulk of lead in the subject steels occurs as envelopes or sheaths associated with the sulphides. The mass of the lead tails is, to some extent, dependent on sulphide malleability. The machinability rating variations within Type A steels may be due to a size effect, with both fine stringer-like sulphides and corresponding fine lead tails being unfavorable. Due to the interdependence of sulphide and lead particle size, however, the size effect of inclusions is not considered to be conclusive.

Decreased carbon and silicon favor the formation of oval sulphide inclusions with correspondingly massive lead tails and are beneficial to the cutting quality of Type A stock. This is consistent with published results on open hearth C-1213 steels. Machinability is favored by lower manganese contents. Exclusive of inclusion variation, lead and sulphur appear to have a similar beneficial effect of about + 1 index point per 0.01% increase of the element. Phosphorus and nitrogen, within the limits of this work, do not appear to influence the quality of Type A steels.

References

1. J. Nead, C. Sims and O. Harder, "Properties of Some Free Machining Lead Bearing Steels," *Metals and Alloys*, Vol. 10, March 1939, p. 68-73, 109-114.
2. J. D. Armour, "Metallurgy and the Machinability of Steels," *Machining—Theory and Practice*, 1950, p. 123-168, American Society for Metals, Cleveland.
3. O. Harder, U. S. Patent No. 2,197,259 (April 16, 1940).
4. J. W. Thurman, E. J. Paliwoda and E. J. Duwell, "Some Aspects of the Morphology and Chemistry of Lead in Leaded High Sulphur Steels," *TRANSACTIONS, American Society for Metals*, this volume, 1958.

5. A. C. Cruickshank, U. S. Patent No. 2,269,360 (January 6, 1942).
6. A. V. Vegesack, "Method of Etching for Identification of Lead in the Microstructure of Free-Cutting Steels Alloyed with Lead," *Jernkontorets Annaler*, Vol. 126, 1942, p. 559-564.
7. K. Volk, "Metallographic Proof of Lead in Steel," *Archiv für das Eisenhüttenwesen*, Vol. 16, 1942, p. 81-84.
8. A. E. Gerds, and C. W. Melton, "New Etch Spots Leaded Steels," *Iron Age*, Vol. 178, No. 9, August 30, 1956, p. 86-87.
9. E. J. Paliwoda, "The Influence of Chemical Composition on the Machinability of Rephosphorized Open Hearth Screw Steel," *TRANSACTIONS, American Society for Metals*, Vol. 47, 1955, p. 680-691.
10. F. W. Boulger, H. A. Moorhead and T. M. Garvey, "Superior Machinability of MX Explained," *Iron Age*, Vol. 167, No. 20, May 17, 1951, p. 90-95.
11. L. H. Van Vlack, "Correlation of Machinability with Inclusion Characteristics in Resulphurized Bessemer Steels," *TRANSACTIONS, American Society for Metals*, Vol. 45, 1953, p. 741-757.
12. M. E. Merchant, "Metal Cutting Research—Theory and Application," *Machining—Theory and Practice*, 1950, p. 5-44, American Society for Metals, Cleveland.
13. G. H.ENZIAN, "Some Effects of Phosphorus and Nitrogen on the Properties of Low Carbon Steel," *Journal of Metals*, February 1950, p. 346.

DISCUSSION

Written Discussion: By Francis W. Boulger, Chief Division of Ferrous Metallurgy, Battelle Memorial Institute, Columbus, Ohio.

Mr. Paliwoda is to be congratulated on this concise and valuable contribution to the literature on the machinability of free-cutting steels. He is one of the few investigators in this field who makes use of multiple correlation analyses, a powerful tool for determining the effect of composition on machining practices. We too find this procedure particularly helpful.

The results of studies on free-cutting steels in our laboratories are in good agreement with those presented in this paper. The work by Melton and Gerds mentioned by the author was done in connection with a study on similar steels. That study also showed that lead occurs as a coating around the sulphides. There is little doubt that differences in the size and shape of sulphide inclusions account for most of the variations in machining properties of steels of closely similar composition. Larger sulphide inclusions are associated with better machinability in both leaded and non-leaded free-cutting steels. The effects of the various elements on the machinability ratings based on soft cutting tools seem to be in fairly good quantitative agreement with their effects on ratings based on constant-pressure lathe tests.

Written Discussion: By G. Dementis, Research and Development Department, Inland Steel Company, East Chicago, Indiana.

The preceding article was reviewed with a great deal of interest in view of the semi-proprietary position of the Inland Steel Company in connection with leaded steels. This interest dates back to the original development of leaded steels which was a joint effort of the Inland Steel Company and Battelle Institute.

When the methodology and results reported in this article are compared to those reported in other technical articles and those encountered in our investigations, some areas of difference are noted.

To assess machinability, the author uses a tool wear test utilizing a degraded tool. Our own experimental work, which has been confirmed by the work of Bryden² and others, would indicate problems arising from a technique such as this. Tool failure patterns appear to be of two distinct classes. Failure patterns in the steels of higher chemical hardness show a relatively constant rate of tool wear as machining progresses. In the case of steels of lower hardness, test tools would fail catastrophically through a galling or welding type of failure. In other words, tool wear and tool life are not very closely related, especially when comparing steels of varying hardness. In an effort to eliminate potential errors introduced from differences in tool materials, an attempt to use a standard closer to actual production tools (18-4-1 tool material) is used in all our research.

It is especially interesting to notice the results of applying correlation techniques to the assessment of the effect of chemistry on the "machinability index". A similar equation developed independently some time ago by E. S. Madrzyk of Inland is as follows:

$$\begin{aligned} \text{Cutting Speed in ft/min.} &= 267 - 1400 (\%C) + 93 (\%Mn) + 77 (\%S) \\ (60 \text{ Min. Tool Life}) &\quad + 77 (\%Pb) - 527 (\%P) - 7078 (\%N) \end{aligned}$$

This equation points out what we believe to be the important influence of phosphorous and nitrogen on machinability. Silicon is not considered as a variable in this equation because of its stability in our current steelmaking practices.

As pointed out in the preceding article, a rather substantial amount of unexplained variance still remains when computed and experimental values are compared. Unfortunately, this use of linear regression techniques as a method of predicting machinability is open to question. The Inland machinability equation was finally discarded because of the feeling that the mathematical conditions for linear regressions do not appear to be adequately met. These conditions call for both linear relationships and independence of the variables. Generally neither of these two conditions are present. For example, the manganese level tends to be a function of the sulphur level. But perhaps more seriously, tool life is not a linear function of elements such as sulphur and lead. It is reasonably certain that the relationships of both lead³ and sulphur⁴, to machinability are more nearly parabolic. The relationship of other chemical elements to machinability also appear to be parabolic in nature.⁵ This fact would negate the linear regression method of prediction used. It would appear at the present time that it is necessary to use more involved mathematical approaches to be able to adequately predict machinability from the chemistry of the material.

Author's Reply

The author is indebted to Messrs. Boulger and Dementis for their interesting discussions of this paper. The similarity of results obtained by the machinability test reported in this work and by the constant pressure lathe test developed at Battelle is noteworthy since there are basic differences in the manner of testing.

² H. L. Bryden, "Comparative Machinability of B1113-C1213-C1120 HR-C1120 CD and C1119 Steels," *Transactions, American Society of Mechanical Engineers*, Vol. 79, May 1957, p. 915-919.

³ J. Nead, C. Sims, and O. Harder, "Properties of Some Free Machining Lead Bearing Steels," *Metals and Alloys*, Vol. 10, March 1939, p. 68-73, 109-114.

⁴ F. W. Boulger, H. A. Moorhead, and T. M. Garvey, "Superior Machinability of MX Explained," *Iron Age*, Vol. 167, No. 20, May 17, 1951, p. 90-95.

⁵ W. W. Gilbert, "Economics of Machining," *Machining—Theory and Practice*, 1950, p. 465-485 (Fig. 7). American Society for Metals.

The hazards of broad interpretation of accelerated turning rate tests, even those carried out on automatic screw machines, are aptly demonstrated by Bryden's work and by the turning rate equation presented by Mr. Dementis. The influence of hardness level on the manner of tool failure such as that cited was first observed in our laboratory some twenty five years ago during extensive accelerated machinability tests on a 4-spindle automatic screw machine. Accelerated machinability tests proved to be a satisfactory measure of Bessemer steel performance in commercial operations but failed as gages of machining quality when low phosphorus open hearth screw steels were included in the comparison. Under such conditions, the test ratings for C-1120 and even C-1020 were comparable to those for premium Bessemer screw steels, whereas actual companion production runs in consumer plants markedly favored the Bessemer material. This and other subsequent observations led originally to the use of fixed tool wear indices for open-hearth grades as opposed to complete tool failure for Bessemer material and finally to the restriction of accelerated machinability test comparisons to screw steel grades containing similar hardness or shear strength levels. In view of the many facets of machinability, such restricted machinability test comparisons are followed by consumer trials whenever possible. The present machinability test procedure as a reflection of screw steel performance in commercial plants was illustrated in a prior publication on C-1213 steels. In the present work, despite differences in phosphorus, nitrogen and lead contents, it was found that carbon and silicon exert a similar influence on machining quality and sulphide inclusion nature of Type A and C-1213 steels. These findings with respect to sulphide inclusion nature are in good agreement with other recent machinability works on free cutting steels and suggest that the primary shortcoming of accelerated machinability tests is usually the broad interpretation to which such results are subjected.

The possibility of more complex relationships between machining quality and individual elements is an important point. References were cited by Mr. Dementis to illustrate that the influence of sulphur and lead are more nearly parabolic. In these same references, however, it can be noted that in the sulphur range from 0.19 to 0.34% and in the lead range from 0.13 to 0.31% (compositions representing present data) the relationships are reasonably linear and no serious errors should arise from the use of linear regression analysis. In the original treatment of the data presented, the possibility of curvilinear relationships was of concern since such a relationship was observed for a composition variable in a study of another leaded grade. As a result, early work consisted of graphical multiple correlation and after a series of successive approximations it was found that linear relationships could be employed.

THE POWDER METALLURGY OF ZIRCONIUM-URANIUM ALLOYS

BY HERBERT S. KALISH

Abstract

An investigation was made of methods for fabricating zirconium-uranium alloys by powder metallurgy techniques. Both uranium and zirconium powders were made by the hydride process. It was found that the best materials could be obtained by making mixtures of -325 mesh uranium powder and -325 mesh zirconium hydride powder and compacting at 50 tsi. The compacts were vacuum sintered. In the case of the alloys rich in zirconium, high density was readily obtained even sintered well below the melting point, whereas alloys in the range of 40% and more uranium required sintering very close to the melting point to obtain high density. It was found that the zirconium-uranium system was particularly amenable to powder metallurgy and homogeneous alloys were obtained in all compositions. Densities of better than 97% of theoretical were obtained for all compositions. The alloys also had reasonable ductility and high strength. A peak in strength was found at 80 w/o uranium. A correlation is made between microstructure and some of the physical properties obtained. (ASM International Classification: H general; Zr, U)

INTRODUCTION

THE USE OF powder metallurgy fabrication techniques for forming uranium (1)¹ and zirconium (2) has been reported. Both of these metals are of interest for nuclear reactor use, and information on the alloys between zirconium and uranium is also of interest in the nuclear materials field.

The development of powder metallurgy techniques as a zirconium fabrication method has been presented in a number of previous articles (2,3,4). It was shown in these papers that the use of zirconium hydride for compacting and sintering was superior in all respects to the use of zirconium powder, i.e., zirconium powder which had been made by vacuum decomposition of zirconium hydride powder. For this investigation, therefore, it was decided to use zirconium hydride powder ex-

¹ The figures appearing in parentheses pertain to the references appended to this paper.

A paper presented before the Thirty-ninth Annual Convention of the Society, held in Chicago, November 4-8, 1957. The author, Herbert S. Kalish, is Engineering Manager, Metal Fabrication and Assembly, Sylvania-Corning Nuclear Corporation, Bayside, New York. Manuscript received February 18, 1957.

Table I
Particle-size Distribution, Density, Apparent Density and Gas Analysis of Zirconium Hydride and Zirconium Powder Made from Crystal Bar

Particle size, microns	Zirconium hydride powder	Zirconium powder from vacuum decomposition of hydride
0-1	10.2	1.5
1-2	10.4	2.8
2-3	13.5	2.0
3-4	19.2	4.3
4-5	8.3	3.8
5-6	5.0	5.4
6-8	5.4	6.6
8-10	1.8	5.5
10-12	1.1	5.3
12-14	1.3	3.6
14-16	1.5	5.5
16-20	1.8	8.0
20-30	7.7	15.4
30-44	10.5	19.4
>44	2.3	8.9
Photolumetric average size, micron	10.3	20.0
Particle density, g/cm ³	5.72	6.59
Apparent density, g/cm ³	2.2	2.0
Oxygen content, percent	0.2	0.3
Nitrogen content, percent	0.01	0.01

clusively. The methods of making uranium powder by the hydride process have been reported by Hausner and Zambrow (1). The methods used in this investigation for making the powders, mixing, compacting and sintering, are described under "Experimental Procedure".

The investigation of the powder metallurgy of zirconium-uranium alloys entailed a determination of whether it would be feasible to make all compositions across the phase diagram by powder metallurgy methods, the optimum fabricating conditions and the properties of the powder metallurgy material.

EXPERIMENTAL PROCEDURE

Zirconium crystal bar, i.e., zirconium made by the iodide process, was hydrided for 20 hours at 800 °C (1470 °F) and furnace-cooled in a flow of 12 cfh of purified hydrogen. The massive zirconium hydride was hand pulverized in a steel mortar and pestle until it was fine enough to pass through a 325 mesh screen. The grinding operation was done in air. The average particle size, particle size distribution, particle density and gas content of zirconium hydride powder as used in this investigation and zirconium powder made from the vacuum decomposition of the hydride is shown in Table I.

Uranium powder was produced by hydriding massive uranium wafers for 3 hours at 225 °C (435 °F) in purified hydrogen followed by vacuum decomposition of the hydride, in the same furnace tube, for about 1 hour at 440 °C (825 °F). The actual time of hydriding and decomposition depends upon the size of the charge. For this work 200 grams of wafers, cut into halves or quarters from discs about 2 inches

in diameter and $\frac{1}{8}$ inch thick, were used as the charge. Hydriding of larger charges takes somewhat longer, e.g., $5\frac{1}{2}$ hours for a 600-gram charge. Vacuum decomposition was carried on until the pressure in the system was reduced to 35 microns of mercury. This decomposition required 1 hour for the 200-gram charge and a slightly longer time for the larger charges. The loosely sintered cake thus obtained was hand pulverized in a steel mortar and pestle contained in an argon drybox until the powder was fine enough to pass through a 325 mesh screen. The pyrophoric properties of uranium and uranium hydride powder makes it difficult to obtain particle size analysis. Even though the uranium powder is ground to -325 mesh particles, it is composed of very fine particles as were originally formed as UH_3 . Any larger particles are, in reality, agglomerates of particles mostly smaller than one micron (1).

All subsequent operations were done in an argon atmosphere, including the loading of the furnace tube. The proper charges of uranium and zirconium hydride powders were weighed out and tumble-mixed in glass bottles for 2 hours. It has been found that a satisfactory mixture is obtained for all compositions with this mixing procedure.

A charge of the proper amount of powder mixture to obtain the desired compact size was weighed out and placed in a rectangular, single-action, come-apart die. Compacts were pressed to a size of $3 \times \frac{1}{4} \times \frac{1}{8}$ inch at 50 tsi. The compacts were placed in a graphite boat, which was covered; and the boat was put into a sillimanite furnace tube. These furnace tubes have glass-to-sillimanite seals. A ground glass joint with a stopcock attached was used to close off the furnace tube so that the tube could be carried to the furnace without exposure of the charge to air. The furnace was evacuated to a pressure of about 2×10^{-5} millimeters of mercury, and the charge heated to the sintering temperature in 2 to 3 hours. Decomposition of the hydride during the heating cycle caused the pressure to increase to about 1 millimeter. The pressure again began to decrease at about 1000°C (1830°F) until a pressure of 2×10^{-5} millimeters was reached at the sintering temperature. Sintering temperatures of 1120, 1170, 1210, 1260, 1320 and 1370°C (2050, 2140, 2210, 2300, 2410, 2500°F) for 10 hours and 1170 and 1320°C (2140 and 2410°F) for 3 hours were used in this investigation.

The samples of all compositions as removed from the furnace after being sintered have extremely bright metallic surfaces. The high uranium content samples will begin to tarnish, however, after a few days of exposure to the air.

THE USE OF URANIUM OR URANIUM HYDRIDE POWDER

It was considered possible that uranium hydride powder might be superior to uranium powder for the preparation of these alloys, analogous to the superiority of zirconium hydride powder over zirconium.

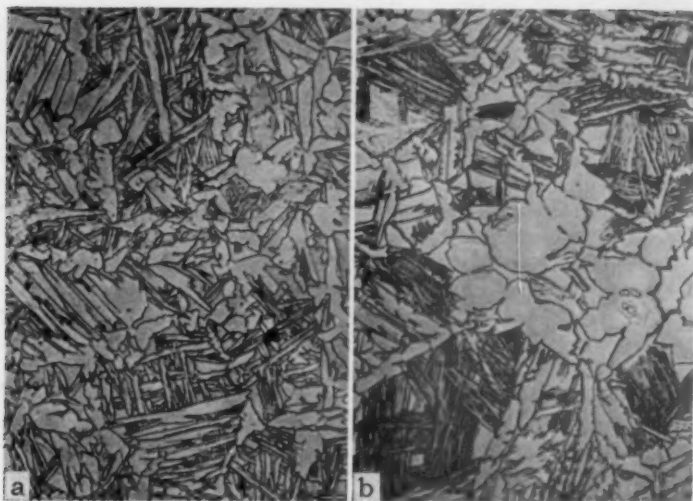


Fig. 1—20 Weight % Uranium-Zirconium Alloy Made from a Mixture of —325 Mesh Zirconium Hydride and —325 Mesh Uranium or Uranium Hydride Powders Compacted at 75 tsi and Sintered 10 Hours at 1260 °C (2300 °F) in High Vacuum. a. Uranium powder used in the mixture. b. Uranium hydride powder used in the mixture. (Note white areas indicative of zones high in oxygen.)

Investigations were made to determine the feasibility of using uranium hydride powder.

It was found that, after the powder mixtures were made in the inert atmosphere drybox, compositions containing up to 20 weight % uranium could be safely handled in the air in the powder condition for short periods of time.

Compacts of 10 and 20 weight % uranium powder in zirconium hydride powder, or uranium hydride powder in zirconium hydride powder, were made in the following way: the powders were weighed out and tumble-mixed, and charges for pressing weighed out in the argon drybox. The powder charges were placed in the die in air, leveled and pressed. Immediately after being pressed, the compacts were returned to an argon atmosphere until they were loaded into the boat and furnace tube. This loading operation was done in air. It was found that such a treatment was as good as the previously outlined method of complete argon handling (essential for uranium contents higher than 20 weight % uranium) when uranium powder was used. Loading in air, however, was found detrimental when uranium hydride powder was used. The data are shown in Table II. These data show that full density is attained in both cases, but that the hardness was higher where UH_3 powder was used, indicating oxygen pick-up. This was further

Table II
Comparison of Properties of Sintered Zirconium-Uranium Alloys Made from
-325 Mesh Zirconium Hydride Powder and -325 Mesh Uranium or Uranium
Hydride Powder. Powder Mixtures Were Compacted at 75 Tsi and
Sintered 10 Hours at 1260 °C (2300 °F)

Uranium Content, Weight %	U Powder Type	Hardness, Rockwell B	Density, g/cm ³
0	—	100.7	6.54
10	U	104.8	6.98
10	UH ₃	106.4	6.98
20	U	105.3	7.49
20	UH ₃	107.3	7.47

verified by the microstructure, as shown in Fig. 1. The white areas of Fig. 1b are typical of the use of oxidized uranium powder in these mixtures.

Since powder mixtures of high uranium content must be handled entirely in an argon atmosphere, an investigation was carried out to determine if the UH₃ powders can be used under these conditions, i.e., where processing is carried out entirely in an argon atmosphere. The results of this investigation are summarized in Table III. These data show that better sintered density can be attained when uranium powder is used.

The inferiority of the uranium hydride powder in regard to sintered density for this process can be attributed to the tremendous shrinkage which must occur during sintering. A comparison of the pressed density of zirconium hydride-uranium compacts made from either UH₃ or uranium powder is shown in Fig. 2. The pressed density of the com-

Table III
Comparison of Sintered Zirconium-Uranium Alloys Made from -325 Mesh
Uranium Hydride or Uranium Powders Mixed With -325 Mesh Zirconium
Hydride Powder Compacted at 50 Tsi and Vacuum Sintered for 10 Hours

Composition, Weight % Uranium	Sintering Temp., °C	Sintered Density, g/cm ³		Linear Shrinkage, %	
		Powder type		Powder type	
		U	UH ₃	U	UH ₃
10	1170	6.93	6.92	8.93	9.67
10	1260	6.96	6.94	9.13	9.90
20	1170	7.45	7.45	8.83	10.73
20	1260	7.45	7.48	9.43	10.70
30	1170	8.01	7.99	8.87	11.20
30	1260	8.08	8.02	9.13	11.47
40	1170	8.67	8.60	8.57	12.27
40	1260	8.73	8.64	9.13	12.40
50	1170	9.51	9.41	8.37	13.10
50	1260	9.60	9.47	9.17	13.47
60	1170	10.53	10.43	8.60	14.17
60	1260	10.59	10.53	9.27	14.63
70	1170	11.97	11.85	9.37	15.87
70	1260	12.04	11.97	9.60	16.30
80	1170	13.63	13.41	9.53	17.33
80	1260	13.63	13.71	10.27	17.67
90	1170	15.91	15.37	10.40	18.67

pacts high in uranium hydride powder is indeed low relative to that of compacts made from uranium powder. The net result of this is that unusually high shrinkage must take place during sintering, if full density is to be attained. In Fig. 3, it is clear that the shrinkage which occurs during sintering of zirconium hydride-uranium powder compacts is little affected by composition. The slight decrease in shrinkage which occurs at about 50% uranium is due to the fact that these alloys

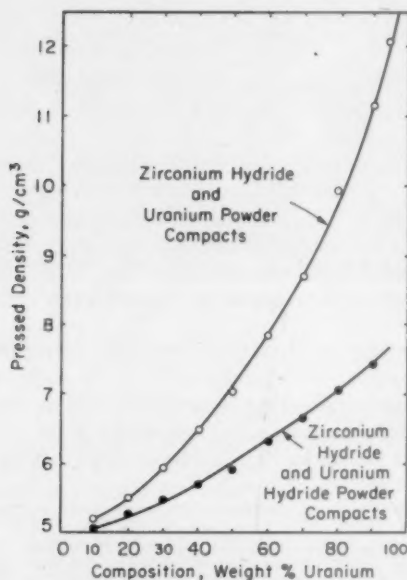


Fig. 2—The Pressed Density of Zirconium Compacts Made from Mixtures of -325 Mesh Powders Pressed at 50 tai.

do not densify completely at this temperature. The increase in shrinkage at higher uranium compositions simply reflects a slightly lower relative pressed density which occurs with increasing uranium content. This point will be discussed more fully in Section IV (A) on densification.

The shrinkage of zirconium hydride-uranium hydride compacts during sintering shows a tremendous increase with increasing uranium hydride content. So severe is this effect that cracks frequently develop during the sintering of these high uranium compacts. The linear shrinkage is approximately the same in all directions. Thus, the shrinkage of 16 to 18% linear represents a volume shrinkage of about 40 to 45%. This can be attributed to two factors:

(a) the large volume change which occurs when UH_3 decomposes to uranium, and (b) the extreme fineness of the UH_3 powder.

The true density of UH_3 is 10.9 grams per cubic centimeter compared to 19.05 grams per cubic centimeter for uranium. Calculation reveals that if one had pure UH_3 and decomposed it to pure uranium, one must get a volume shrinkage of 43%. This, then, could account for almost all the shrinkage, eliminating the second factor entirely and

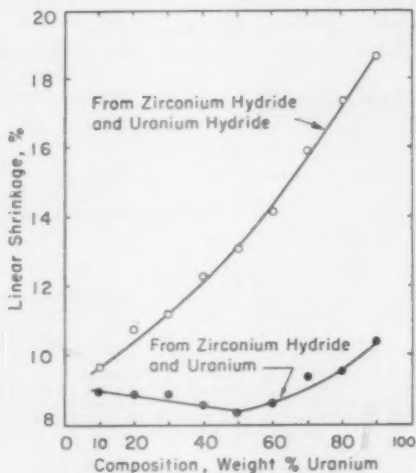


Fig. 3—The Linear Shrinkage of Zirconium-Uranium Alloys Sintered for 10 Hours at 1170 °C (2140 °F) in Vacuum from Mixtures of -325 Mesh Powders Compacted at 50 tsi.

even eliminating normal shrinkage of a powder compact to the sintered product. Apparently, some lower hydride or a combination of hydrides is present, rather than UH_3 . Even so, the shrinkage of this uranium hydride powder, as made, is too great to permit proper sintering. It should be questioned, then, as to why the use of zirconium hydride does not give rise to the same trouble. The answer is that if solid ZrH_2 , the highest hydride of zirconium, is made, it will shrink only 14% in volume upon decomposing to pure zirconium.

In addition to the unfavorable high shrinkage when uranium hydride powder is used, it was found that homogenization was much delayed over that occurring with uranium powder. This would necessitate longer sintering times or higher sintering temperatures to attain results similar to those obtained with the use of uranium powder. It was decided, therefore, that zirconium-uranium alloys should be made from powder mixtures of zirconium hydride and uranium.

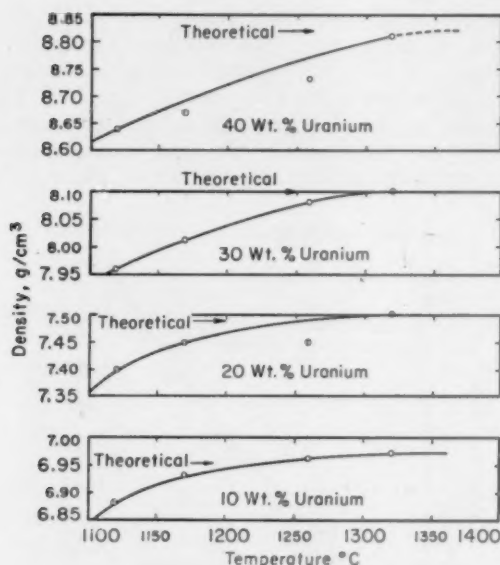


Fig. 4—The Effect of Sintering Temperature on the Sintered Density of Zirconium-Uranium Alloys. Samples compacted at 50 tsi from mixtures of -325 mesh zirconium hydride and -325 mesh uranium powders and sintered for 10 hours in high vacuum.

DISCUSSION OF RESULTS

The properties of the zirconium-uranium alloys can be expected to depend upon the following five factors:

1. Density of the sintered compact.
2. Degree of homogenization of the alloys.
3. Oxygen and nitrogen pick-up during processing.
4. Grain size.
5. Phase changes.

The above five factors can be controlled to some extent by processing variables, but one cannot optimize all of these factors simultaneously. In the discussion below, the role these factors play in the properties of these alloys will be described.

Densification of the Sintered Compact

The mechanism of densification during sintering of a pure metal depends largely upon the self-diffusion of the metal. In a binary alloy system, it depends upon the self-diffusion of both metals and the inter-diffusion of the two metals, as well as upon the phase changes which occur at the sintering temperature.

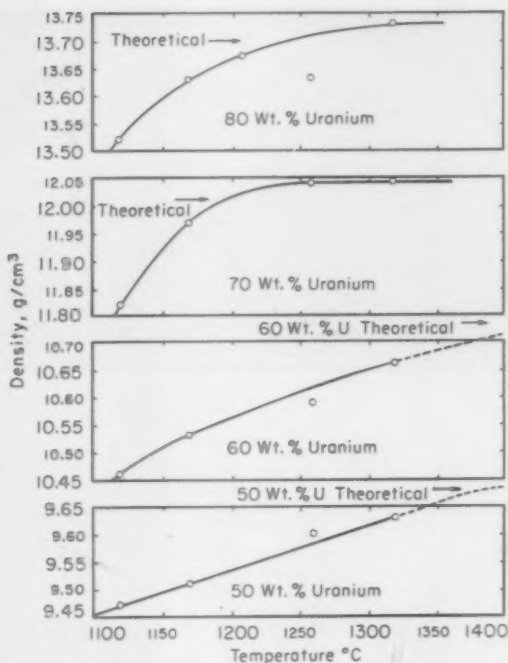


Fig. 5—The Effect of Sintering Temperature on the Sintered Density of Zirconium-Uranium Alloys. Samples compacted at 50 tsi from mixtures of -325 mesh zirconium hydride and -325 mesh uranium powders and sintered for 10 hours in high vacuum.

The zirconium-uranium phase diagram (Fig. 10) shows that a continuous solid solution of gamma uranium and beta zirconium, both body-centered cubic, exists across the system at temperatures above 860°C (1580°F) and up to the solidus line. This is a most suitable condition for sintering. It appears further that the diffusion of zirconium in uranium, or vice versa, is so rapid that no liquid phase forms when powder mixtures of these metals are sintered well above the melting point of pure uranium.

The density of alloys up to 40% uranium as a function of sintering temperature is shown in Fig. 4. It is apparent that as the uranium content increases, a higher sintering temperature is required to attain full density. This is brought out further in Fig. 5. A sintering time of 10 hours has been selected as standard for this work because it is the longest sintering time thought practicable. Shorter sintering time necessitates higher temperatures to attain the same amount of homogenization and density. The use of temperatures much in excess of those

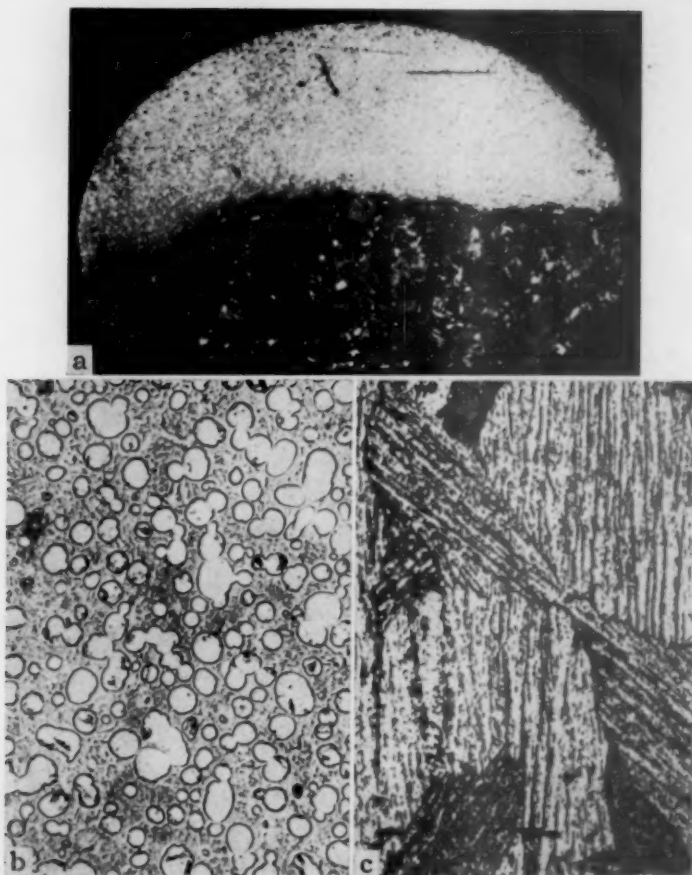


Fig. 6—90 Weight % Uranium-Zirconium Alloy Which Melted During Vacuum Sintering for 10 Hours at 1260 °C (2300 °F). Compact pressed at 50 tsi from a mixture of -325 mesh zirconium hydride and uranium hydride powders. (a)—Cross section of melted compact. $\times 30$. (b)—Upper region of the above compact. $\times 250$. (c)—Lower region of the melted compact. $\times 250$.

needed for the 10-hour sintering results in excessive oxygen pick-up in the case of the zirconium-rich alloys, and would result in melting in the case of the uranium-rich alloys since those of 80% uranium and more must be sintered close to the melting point.

When considerable melting occurs in the compacts, the result is generally a separation of the alloy into layers, even though the cooling is quite rapid. This is shown nicely in Fig. 6 where the complete metallographic difference is apparent in the top and bottom of the

sample. Analysis reveals that the upper portion of the sample is 15.3 weight % zirconium and the lower portion is 6.98 weight % zirconium. Assuming a pure binary system, one finds that at 1260 °C (2300 °F), a 10% zirconium alloy, according to the phase diagram, should have solid of the composition 15% zirconium and liquid of about 5% zirconium. This fulfills the analysis nicely and indicates that the solid present, which was richer in zirconium and hence of

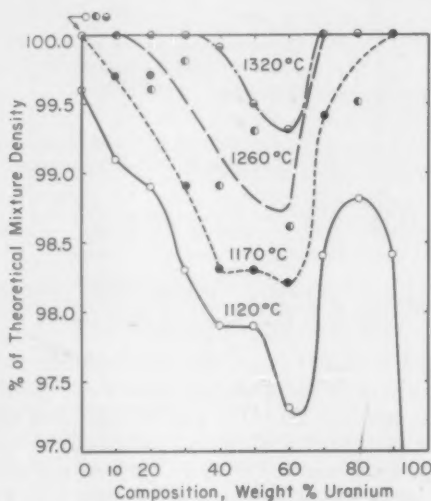


Fig. 7—Isotherms Showing the Effect of Uranium Content on the Densification of Zirconium-Uranium Alloys Sintered 10 Hours at Various Temperatures. For compacts pressed at 50 psi from mixtures of -325 mesh zirconium hydride and -325 mesh uranium powders.

lower density, floated to the top of the liquid. Subsequent freezing of the alloy did not permit homogenization to take place. If these alloys are to be made by a melting technique, the danger is always present that with freezing of insufficient rapidity, there will be a separation of the constituents. When very little melting occurred, i.e., just above the solidus, there may have been some slight distortion in the compact shape, but there was no such separation into layers.

In order to clarify the effect of composition on the sintered density of these alloys, Fig. 7 was drawn. Up to 80% uranium the trend is quite normal in that the alloys of intermediate composition have the lowest density relative to ideal at any given sintering temperature. At 80%, however, there is a strange occurrence in that the alloys above this composition do not sinter to high densities unless they are sintered

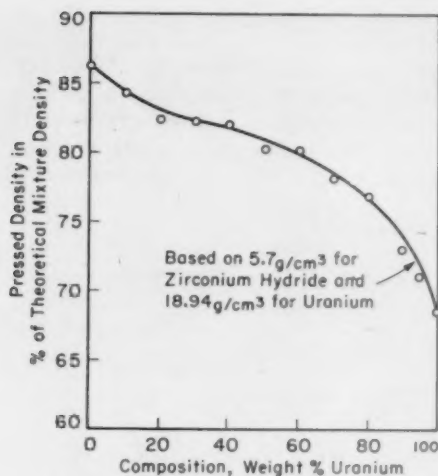


Fig. 8—The Effect of Composition on the Pressed Density of Zirconium Hydride-Uranium Mixtures Compacted at 50 tsi from -325 Mesh Powders.

very close to the melting point. Thus, the wide spread between the 1120 and 1170 °C (2050 and 2140 °F) isotherms at 90% uranium becomes tremendous at 95%. At 1170 °C (2140 °F), this alloy, viz., 95%, will melt and at 1120 °C (2050 °F), it will hardly sinter. In order to sinter this alloy, then, it is necessary to use a temperature of 1150 °C (2100 °F), which is just below the solidus line. This has been done, and densities approaching theoretical have been obtained.

Table IV
The Densities of Zirconium-Uranium Alloys Made by Powder Metallurgy and Made by Melting

Weight Percent Uranium	Theoretical mixture (low hafnium) (calculated)	Densities, g/cm ³		
		Melted and rolled, normal hafnium (2-3% hafnium)	Powder Metallurgy Normal hafnium (2-3% hafnium)	Powder Metallurgy Low hafnium
0	6.50	6.54	6.59	6.51
1	6.54		6.64	
3	6.63		6.63	
4	6.68	6.72	6.76	
6	6.77	6.83	6.79	
10	6.95	6.99	6.98	6.97
14	7.17	7.16	7.24	
16	7.27	7.20		
20	7.48			
22.3	7.63			
30	8.10			7.50
40	8.82			8.10
50	9.68			8.82
60	10.73	10.40		9.63
70	12.02			10.72
80	13.70			12.10
90	15.90			13.71
95	17.30			15.91
				16.81

In Fig. 7, the basis of the percent of theoretical density shown was the mixture density of the two metals. Calculated mixture densities can generally be used only as a preliminary guide. Ordinarily, in a binary system, phases will be formed which have a different density from that calculated from a simple mixture. The data from this investigation, as shown in Table IV, however, indicate that the calculated mixture density is very close to the true density.

From Fig. 7 one can determine the optimum sintering temperature for any zirconium-uranium composition. In addition, one can ascertain the density which will occur at sintering temperatures lower than optimum. For higher compacting pressures or more favorable compact shape, i.e., lower wall area to pressing area ratio, the isothermal lines would move upward. A lower compacting pressure or less favorable compact shape would displace the isothermal lines downward.

In Fig. 8 is shown the relative pressed density of zirconium hydride-uranium powder compacts. It is clear from this curve that as the uranium composition increases, the relative pressed density decreases appreciably. The decrease in density due to the increase in uranium content can be explained by the extremely fine particle size of the uranium powder compared to that of zirconium hydride powder, as discussed under "Experimental Procedure", i.e., the finer the average particle size of any given metal powder, the lower will be the pressed density of the powder compact. Even so, it is surprising and indeed fortunate to find that the green strength of uranium-rich compacts is very good.

Zirconium hydride powder presses to unusually high relative pressed densities for a brittle powder, but it does not have good green strength. This matter has been discussed in detail by Kalish, et al (6). Uranium or uranium-rich powder compacts, on the other hand, have excellent green strength but low relative pressed density (1).

Homogenization and Structure

All the uranium-zirconium compositions homogenized relatively rapidly. As the uranium content is increased from 0 to 30 weight % uranium, homogenization time increases; but, even at 30 weight %, a homogenized alloy is obtained in about 1 hour at 1300 °C (2370 °F). In general, the microstructure of the alloys shown in Fig. 9 corresponds to the latest versions of the zirconium-uranium phase diagram (Fig. 10); and, in fact, certain observations that were made in this powder metallurgy study aided in the determination of the diagram (5).

The microstructures indicate a two-phase region across the diagram, although a single-phase δ -region has been reported at about 50 weight % zirconium. Transformation to this single phase is known to be very sluggish, if it exists, so that it is not unusual to find two phases present at every composition in the microstructures shown in Fig. 9. The phase diagram (5) shows two eutectoids: one at about 94 weight % uranium,

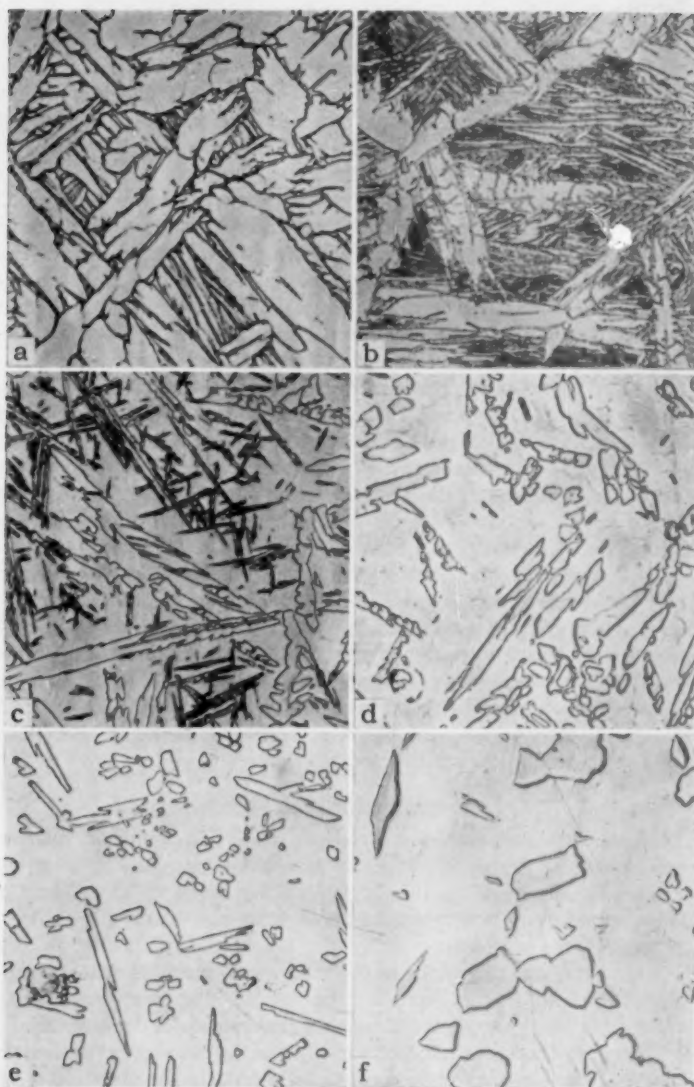


Fig. 9—The Microstructure of Zirconium-Uranium Alloys Made by Powder Metallurgy Methods. Compacts pressed at 50 tsi from a mixture of -325 mesh zirconium hydride and -325 mesh uranium powders and sintered 10 hours at 1370 °C (2500 °F) in vacuum. $\times 250$. (a) 10 Weight % Uranium; (b) 20 Weight % Uranium; (c) 30 Weight % Uranium; (d) 40 Weight % Uranium; (e) 50 Weight % Uranium; (f) 60 Weight % Uranium.

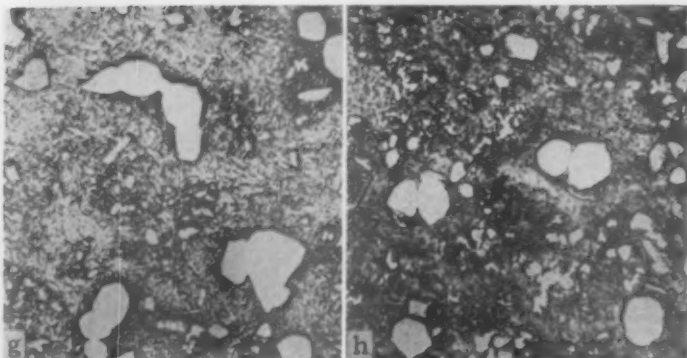


Fig. 9 (Continued)—The Microstructure of Zirconium-Uranium Alloys Made by Powder Metallurgy Methods. Compacts pressed at 50 tsi from a mixture of -325 mesh zirconium hydride and -325 mesh uranium powders and sintered 10 hours at 1370 °C (2500 °F) in vacuum. $\times 250$. (g) 70 Weight % Uranium; (h) 80 Weight % Uranium.

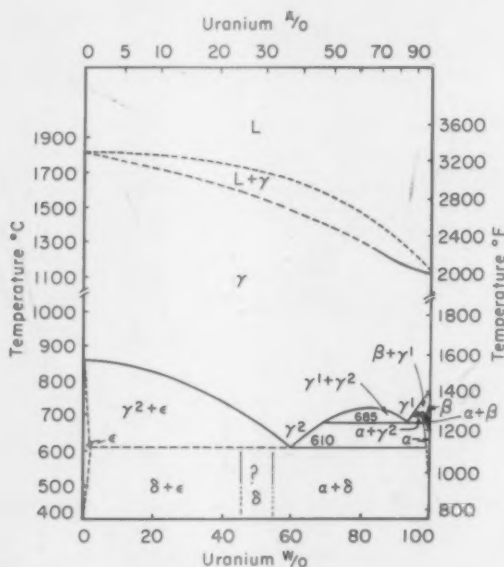


Fig. 10—The System Zirconium-Uranium.

at 685 °C (1265 °F), and the other at about 60 weight % uranium, at 610 °C (1130 °F). According to the diagram, the eutectoid of γ_1 decomposing to $\alpha + \gamma_2$, subsequently decomposes at 610 °C in the eutectoid reaction of γ_2 to $\alpha + \delta$ (or $\alpha + \epsilon$). The microstructure as shown

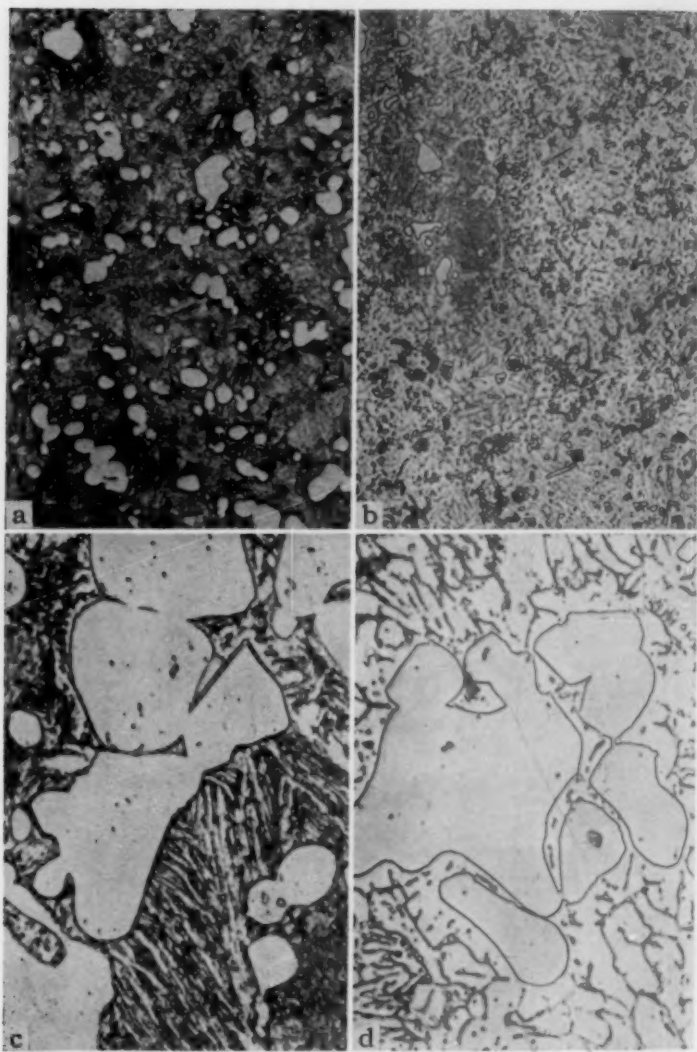


Fig. 11—The Microstructure of Zirconium-Uranium Alloys. Compacts pressed at 50 tsi from a mixture of -325 mesh zirconium hydride and uranium powders and sintered 10 hours in high vacuum. (a) 90 Weight % Uranium—Sintered at 1170 °C (2140 °F). $\times 250$; (b) 95 Weight % Uranium—Sintered at 1120 °C (2050 °F). $\times 250$; (c) Same as (a) $\times 1000$; (d) Same as (b) $\times 1000$.

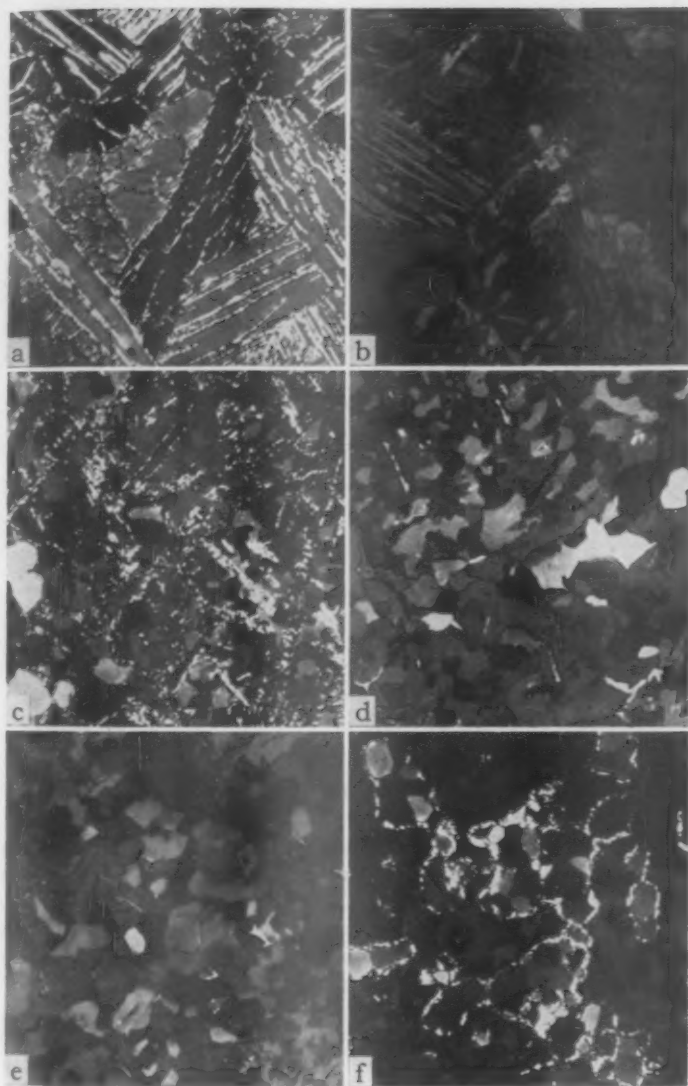


Fig. 12—The Grain Size of Zirconium-Uranium Alloys Sintered 10 Hours at 1170 °C (2140 °F) in High Vacuum. Compacts pressed at 50 tsi from a mixture of -325 mesh zirconium hydride and uranium powders. Polarized light. $\times 250$. (a) 10 Weight % Uranium; (b) 20 Weight % Uranium; (c) 30 Weight % Uranium; (d) 40 Weight % Uranium; (e) 50 Weight % Uranium; (f) 60 Weight % Uranium; (g) 70 Weight % Uranium; (h) 80 Weight % Uranium; (i) 90 Weight % Uranium.

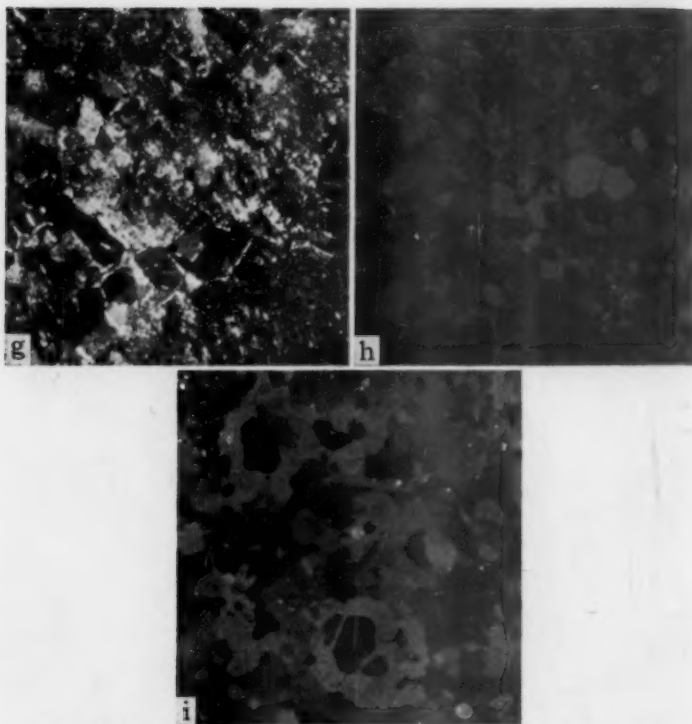


Fig. 12 (Continued)—The Grain Size of Zirconium-Uranium Alloys Sintered 10 Hours at 1170 °C (2140 °F) in High Vacuum. Compacts pressed 50 tsi from a mixture of -325 mesh zirconium hydride and uranium powders. Polarized light. $\times 250$. (g) 70 Weight % Uranium; (h) 80 Weight % Uranium; (i) 90 Weight % Uranium.

in Fig. 11, however, indicates that the eutectoid structure persists even though x-ray analysis indicates that the two phases present are α -uranium and ϵ (α -zirconium). The other eutectoid is shown in the phase diagram at 60 weight % uranium, whereas, from the microstructures in Fig. 9, one would place it in the vicinity of 20 weight % uranium. The reason for this discrepancy in the location of the second eutectoid composition is not clear.

Grain Size

The grain size of the zirconium-uranium alloys can be shown nicely in polarized light at any composition, as indicated in Fig. 12. The grain size of the 10 and 20 percent uranium alloys is of the order of 100 microns, and the grain size of the uranium-rich alloys up to 90% uranium is about 15 microns. Longer sintering times or higher sinter-

ing temperatures than the 10 hours at 1170 °C (2140 °F), shown in Fig. 12, result in very little increase in grain size.

Properties of the Alloys

The sintered alloys were evaluated for the following properties in addition to density: electrical resistivity, hardness, ductility, and ultimate tensile strength. The electrical resistivity and hardness are shown as a function of composition in Fig. 13 for samples sintered at 1120 °C

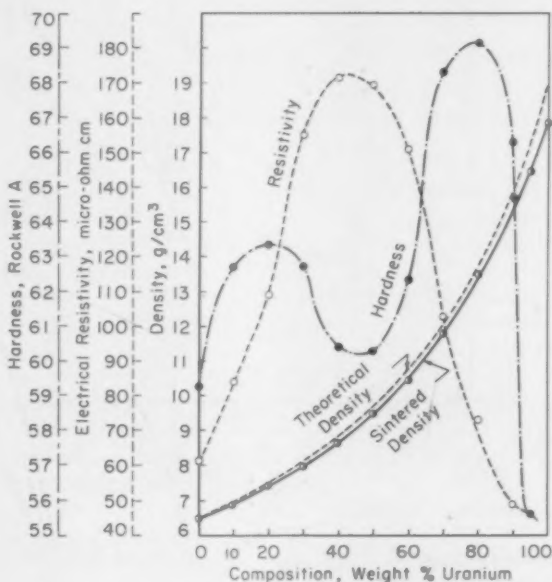


Fig. 13—Properties of Zirconium-Uranium Alloys Sintered at 1120 °C (2050 °F). Compacts pressed at 50 psi from a mixture of -325 mesh zirconium hydride and -325 mesh uranium powders sintered in high vacuum for 10 hours at 1120 °C (2050 °F).

(2050 °F). Since densification was not complete, the data shown in Fig. 13 are not the optimum obtainable for the alloys. The optimum properties are shown in Fig. 14. It is immediately apparent that the trends in regard to composition are the same and that any intermediate sintering temperature would show similar trends.

A comparison of Fig. 13 and 14 reveals that as the alloys approach the optimum, the hardness increases and the resistivity decreases for any given composition. This is simply a function of the pore removal by densification. The specific effect of sintering temperature on the electrical resistivity is very complex and varies for each individual

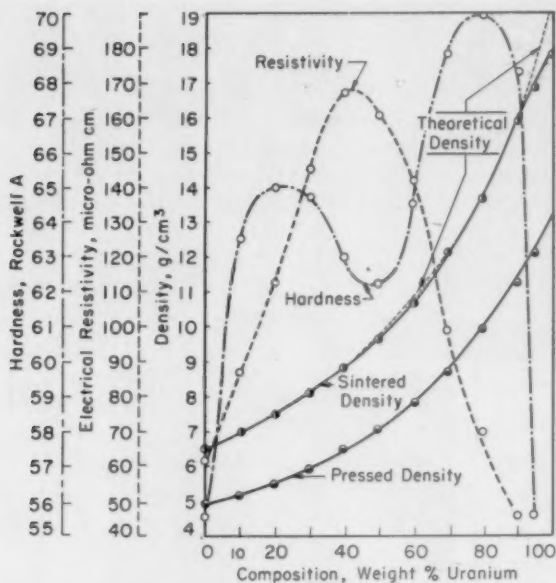


Fig. 14—Properties of Zirconium-Uranium Alloys Made Under Optimum Sintering Conditions. Compacts pressed at 50 tsi from a mixture of -325 mesh zirconium hydride and -325 mesh uranium powders sintered in high vacuum for 10 hours as following: 0 Weight % Uranium—1170 °C (2140 °F), 10 to 70 Weight % Uranium inc.—1320 °C (2410 °F), 80 Weight % Uranium—1260 °C (2300 °F), 90 Weight % Uranium—1170 °C (2140 °F), 95 Weight % Uranium—1120 °C (2050 °F).

composition. In general, however, it can be stated that the following occurs at any composition:

1. Densification decreases the electrical resistivity and increases the hardness.
2. Alloying of any type tends to increase the resistivity and to increase the hardness.
3. The pick-up of gaseous impurities tends to increase the resistivity and to increase the hardness.

Thus, the optimum sintering condition can generally be determined by the minimum hardness and resistivity commensurate with the maximum density.

Having established the optimum sintering condition, one can examine the properties of the various alloys (as shown in Fig. 14). Although density was thoroughly discussed earlier, it is interesting to note the two places where deviation from the theoretical density occurs.

Table V
Properties of Zirconium-Uranium Alloys Made by Powder Metallurgy Methods
from Mixtures of -325 Mesh Zirconium Hydride and Uranium Powders
Compacted at 50 Tsi and Sintered 10 Hours in Vacuum at Optimum Temperatures

Composition, Weight % Uranium	Sintering Temp., °C (Optimum)	Sintered Density, g/cm ³	Hardness, Rockwell A	Cold Red- uction to first sign of edge cracking, percent	Resistivity, Microhm-cm
0	1170	6.51	55.5	57	61.1
10	1320	6.97	63.5	42	87.1
20	1320	7.50	65.0	33	112.4
30	1320	8.10	64.7	30	145.0
40	1320	8.82	63.0	36	167.0
50	1320	9.63	62.2	37	160.3
60	1320	10.72	64.5	39	141.4
70	1320	12.10	68.8	30	98.9
80	1280	13.71	69.9	46	69.7
90	1170	15.91	68.3	44	45.9
95	1150	16.81	39.6	46	46.2

The continuous increase and then the decrease in resistivity can best be accounted for by the presence of the intermediate δ -phase. Although x-ray diffraction did not reveal this phase at the high uranium compositions, it was in strong evidence at compositions from 40 to 60 weight % uranium.

Based upon the assumption of the existence of the δ -phase, it would be expected to have high resistance relative to the two-component, solid solutions; and this would account for the peak in the resistivity curve at the intermediate compositions.

The hardness curve in Fig. 14 reveals considerable information about the properties of these alloys. The increase up to 20% reflects the eutectoid which has been quite definitely identified. The decrease at the intermediate compositions shows that the δ -phase is relatively soft, compared to the eutectoid at 20 weight % uranium, as well as that at the high uranium compositions.

Table V shows the optimum sintering temperature for each composition and the properties of the as-sintered samples. The alloys are

Table VI
Properties of Zirconium-Uranium Alloys Made from Mixtures of -325 Mesh
Zirconium Hydride and Uranium Powders Compacted at 50 Tsi and Sintered
10 Hours at 1120 °C (2050 °F) in Vacuum

Composition, Weight % Uranium	Sintered Density, g/cm ³	Hardness, Rockwell A	Resistivity, Microhm-cm	Ultimate Tensile Strength, psi	Elongation, percent
0	6.47	59.3	61.3	54,000	13.2
10	6.88	62.7	83.8	89,000	15.5
20	7.40	63.3	109.1	96,000	17.0
30	7.96	62.7	154.5	66,000	13.5
40	8.64	60.4	171.4	73,000	12.2
50	9.47	60.3	169.2	83,000	14.5
60	10.46	62.3	150.7	89,000	14.5
70	11.82	68.3	102.9	116,000	16.2
80	13.52	69.1	72.9	120,000	16.0
90	15.66	66.3	48.9	114,000	17.5
95	16.44	55.6	46.2	72,000	13.5

all relatively ductile and can be cold worked to a considerable degree. It is interesting to note that in the zirconium-rich region, the alloys have a decrease in ductility along with an increase in hardness because of the eutectoid. The δ -phase is quite ductile, and the uranium-rich alloys have good ductility.

The tensile strength data shown in Table VI were determined on ordinary rectangular cross sectional specimens having no reduced gage length section. The samples were tested in the condition in which they were removed from the furnace, with no machining. Of course, they broke in the grips. These data are extremely conservative, then; and it can be expected that the tensile strength and elongation would be higher, if actual standard tensile bars were used. In addition, these specimens were made at something less than the optimum condition (compare densities with those of Table V) so that samples sintered at the optimum temperature would have even better tensile properties. The two maxima in tensile strengths at 20 and 80% uranium again are evidence for the eutectoid at the zirconium-rich end and the eutectoid at the uranium-rich end of this binary system.

CONCLUSIONS

1. Zirconium-uranium alloys, in apparently all compositions, can be made homogeneous and of relatively high density by powder metallurgical methods.
2. For best properties by the powder metallurgy approach, these alloys should be made from -325 mesh zirconium hydride and -325 mesh uranium powder mixtures.
3. Zirconium-uranium alloys of all the compositions investigated in this study have high tensile strength and ductility.
4. All these alloys can be machined and hot or cold worked.
5. All the zirconium-uranium alloys studied in this investigation and made by powder metallurgical methods are fine-grained.

ACKNOWLEDGMENTS

This paper is based on work done for the Atomic Energy Commission under Contract AT-30-1 GEN-366. The author wishes to thank the Commission for permission to publish this work.

The author is indebted to Henry H. Hausner, under whose supervision this work was carried out, and to Robert P. Wittmann, Harry Woods, Eleanor Jurasek and Robert E. King, who participated in this investigation.

References

1. Henry H. Hausner and John L. Zambrow, "The Powder Metallurgy of Uranium," *Nuclear Science and Engineering*, Vol. 1, 1956, p. 92.
2. Henry H. Hausner, Herbert S. Kalish and Roswell P. Angier, "Powder Metallurgy of Zirconium," *Transactions, American Institute of Mining and Metallurgical Engineers*, Vol. 191, 1951, p. 625.

3. Herbert S. Kalish, "Ductile Zirconium by Powder Metallurgy," *Materials and Methods*, Vol. 37, 1953, p. 101-103.
4. H. H. Hausner and H. S. Kalish, "Powder Metallurgy of Zirconium," *The Metallurgy of Zirconium*, National Nuclear Energy Series, Division VII-Vol. 4, 1955, p. 280. McGraw-Hill Book Company, New York.
5. H. A. Saller and F. A. Rough, "Compilation of U. S. and U. K. Uranium and Thorium Constitutional Diagrams," Battelle Memorial Institute, June 1, 1951 (BMI-1000) p. 66-67. Technical Information Service, United States Atomic Energy Commission.
6. H. S. Kalish, H. H. Hausner and R. P. Angier, "The Physical Properties of Sintered Zirconium," Sylvania Electric Products Inc., March 31, 1951 (SEP-44), T. I. D. of United States Atomic Energy Commission.

DISCUSSION

Written Discussion: By Henry H. Hausner, Vice President, Nuclear Engineering Division, Penn-Texas Corporation, New York City.

Herbert Kalish is to be congratulated on the fine job he has done on zirconium-uranium alloys prepared by powder metallurgy.

In his paper he emphasized that "better sintered density can be attained when uranium powder is used", instead of uranium hydride. This, however, is not quite correct for specimens with up to 20% uranium in the alloy. Up to this percentage the density of the alloy is practically identical whether uranium metal or UH_3 is used, as Kalish himself has shown in Table III; on account of the relatively small percentage of the uranium component there is also very little difference in shrinkage.

According to my own experience, there is, however, another difference in the alloys made from uranium powder and uranium hydride powder, respectively. The specimens prepared from the hydride show small cracks which are probably due to the complicated reactions going on during sintering of mixtures made from both of the hydrides. At an already low sintering temperature (approximately 200°C) (390°F) UH_3 decomposes; however, the decomposition at this temperature does not contribute to shrinkage because the main component, ZrH_2 , is still present in its original form and the decomposition of UH_3 results in the formation of uniformly distributed voids in the compact. Whether the highly reactive H_2 from the decomposition of UH_3 reacts at this temperature with ZrH_2 is not known as yet. During the sintering interval between 300 – 600°C (570 – 1110°F), uranium bonds to the probably still stable ZrH_2 . Above this temperature, however, H_2 is released during decomposition of the ZrH_2 and although the reaction rate between uranium and hydrogen at this temperature is rather small, a certain formation of UH_3 will occur. The void formation at low temperature and formation of UH_3 with its larger volume at elevated temperature, however, results in the formation of stresses and cracks which are highly undesirable.

Written Discussion: By J. J. Kearns and D. A. Harp, Westinghouse Electric Corporation, Bettis Atomic Power Division, Pittsburgh.

This paper is certainly a detailed and thorough study of the powder metallurgy of an alloy system of great interest to the nuclear reactor industry. It represents a significant contribution.

The author has attributed the presence of two phases in the 50 and 60 weight % uranium alloys to sluggish transformation. In light of the results of a recent study

on the effect of oxygen on U-Zr alloys,⁸ the second phase is undoubtedly oxygen-stabilized alpha zirconium. In our work, alpha zirconium has been observed to exist up to at least 900 °C (1650 °F) in 50 and 60 weight % uranium-alloys containing less than 1000 ppm O₂. These alloys prepared by the powder metallurgy process contain at least 1000 ppm since the zirconium hydride itself contains 2000 ppm.

A more recent U-Zr phase diagram has been published for which the stability and existence range of the intermediate epsilon phase have been established.⁹ In the new diagram, the composition of the eutectoid at the zirconium side of the diagram is shifted to higher zirconium content. This fact supports the authors interpretation of certain microstructures which did not agree with the earlier phase diagram.

Written Discussion: By Arthur A. Bauer, W. Chubb, and F. A. Rough, Battelle Memorial Institute, Columbus, Ohio.

The data presented in this paper represent one of the significant pioneering contributions in the field of uranium-alloy powder metallurgy. The discussion presented below is concerned primarily with interpretation of the system and is based upon increased knowledge of the system acquired as the result of fairly recent investigations. It is intended primarily as an addendum to the data presented.

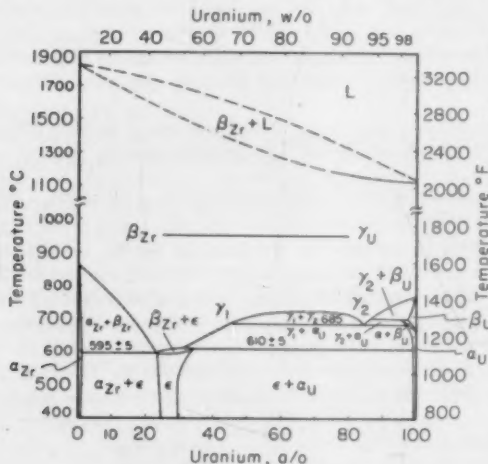


Fig. 15—Zirconium-Uranium Constitutional Diagram.

The hardness curve presented by Mr. Kalish shows hardness peaks occurring in the vicinity of 20 and 80 weight % uranium. Qualitatively similar behavior is obtained on cast and wrought alloys when furnace cooled from the gamma-phase region. It should be realized that hardness is not static in these alloys and hardness curves apply for only a single condition of heat treatment. Marked variations from the curves shown can be obtained by changing the cooling rate.

⁸ H. A. Saller, F. A. Rough and A. A. Bauer, "The Effect of Oxygen on Zirconium-Uranium Epsilon-Phase Alloys," Second Nuclear Engineering and Science Conference 1957.

The hardness peaks are interpreted in this paper as resulting from eutectoid decomposition at or near the two compositions given above. However, the phase diagram, as recently determined³ for this system and shown in Fig. 15, shows that eutectoids, or more exactly, eutectoid and monotectoid decompositions occur at about 40 and 92 weight % uranium, respectively.

The hardness peaks observed are, consequently, primarily a product of dispersion hardening. In uranium-rich alloys, this dispersion consists of alpha-uranium and epsilon and in zirconium-rich alloys of alpha-zirconium and epsilon. The much

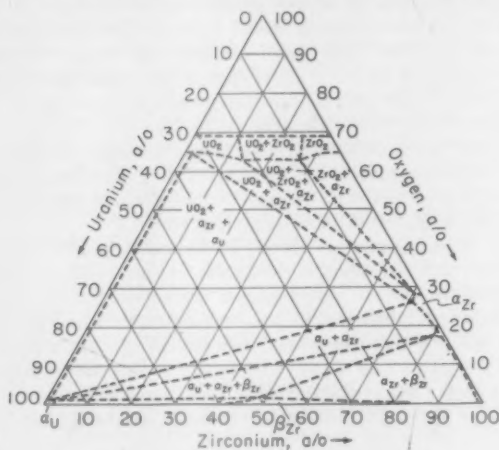


Fig. 16—Tentative Zirconium-Uranium Oxygen Ternary Section at 650 °C (1200 °F).

finer dispersion in the uranium-rich alloys is responsible for the comparatively high hardness exhibited by these alloys. As concluded by Mr. Kalish, the intermediate epsilon phase, when transformed by furnace cooling, is soft and ductile.

The structure exhibited by the 20 weight % uranium alloy, and interpreted by the author as a eutectoid structure, is produced as a consequence of the acicular nature of alpha zirconium precipitated from the beta-zirconium solid solution on furnace cooling. This acicular nature is well illustrated by the structures shown for the 10, 20, and 30 weight % uranium alloys. Variations in relative amount of alpha zirconium formed and in the temperature at which precipitation occurs with increasing uranium content are responsible for the number and size of alpha-zirconium plates nucleated and grown.

Mr. Kalish also reports that two-phase structures are observed across the system in spite of the existence of the intermediate single-phase region and interprets this as resulting from sluggish and incomplete transformation of the gamma uranium-beta zirconium solid solution to the intermediate phase. In reality, this decomposition is known to occur quite rapidly.⁴ The two-phase structures are

³ H. A. Saller, F. A. Rough, and A. A. Bauer, "The Effect of Oxygen on Zirconium-Uranium Epsilon Phase Alloys," Second Nuclear Engineering and Science Conference, Preprint No. 57-NESC-20, March 11-14, 1957.

⁴ J. J. Kearns, "Transformation Kinetics of Uranium-Zirconium Alloys Containing 50 and 60% Uranium," Presented at Second World Metallurgical Conference, American Institute of Mining and Metallurgical Engineers, November 5, 1957.

instead a product of oxygen and nitrogen contamination of the alloys rather than partial transformation.³ The effect of oxygen, and nitrogen which act similarly, on the constitution of these alloys is illustrated by the partial uranium-zirconium-oxygen ternary diagram shown in Fig. 16. The phase relationships shown at the temperature of 650 °C are similar to those observed at lower temperatures except that the beta-zirconium phase decomposes to the intermediate epsilon phase. At higher temperatures, the beta-zirconium limits in the binary uranium-zirconium system expand; however, the phase is still extremely limited as to oxygen solubility, and small amounts of oxygen produce alpha zirconium in alloys of all composition. In this connection, it should be noted that the maximum oxygen solubility at 660 °C (1220 °F) in beta zirconium is only between 500 and 600 ppm. Based on knowledge of the effect of oxygen on the constitution of these alloys, oxygen in excess of 1500 ppm is probably present in the alloys of intermediate composition prepared for the studies reported here.

Therefore, the second phase appearing in the 50 weight % alloys is a direct consequence of the oxygen present. Similarly, the massive light colored particles appearing in the alloys of high uranium composition are alpha zirconium precipitated during the high temperature sintering anneal.

The tensile values reported are similar to those exhibited by cast and wrought alloys. The fairly constant values of elongation measured with changes in uranium content are unusual, however. Much higher elongations for the terminal metals and alloys and lower values for the intermediate compositions are generally observed with cast and wrought alloys. The low elongations reported here, for zirconium in particular, may result from oxygen pickup during preparation. The reason for the higher values observed at intermediate compositions are less easily explained unless the particular heat treatments accompanying sintering are responsible.

Author's Reply

I should like to thank Dr. Hausner for his interesting comments. It is true that up to about 20% uranium the use of uranium hydride would be perfectly acceptable, aside from the tendency of the fine UH_3 particles to oxidize. Even at higher uranium compositions, the uranium hydride yields densities almost as good as uranium powder. It is primarily the large linear shrinkage which I consider objectionable. This large difference in linear shrinkage has been quite definitely shown. In applications where such shrinkage is not objectionable, the use of uranium hydride can very definitely be considered.

I think the possible reactions between ZrH_2 and UH_3 are quite clear. The UH_3 begins to decompose at 200 to 300 °C (390 to 570 °F), but it decomposes rapidly only at 400 to 500 °C (750 to 930 °F). At this temperature, the zirconium is quite saturated with hydrogen and therefore the hydrogen coming from the UH_3 will have no effect on the zirconium hydride. Decomposition of the UH_3 is quite complete by the time the temperature reaches 600 °C where significant decomposition of zirconium hydride begins. The hydrogen coming from the zirconium hydride cannot react with the uranium metal at 600 °C (1110 °F) and particularly at 800 to 900 °C where hydrogen is emitted rapidly because the decomposition pressure of UH_3 at this temperature would be tremendous. Uranium would not pick up hydrogen even under a high hydrogen pressure at 800 to 900 °C (1470 to 1650 °F)—it certainly cannot react when the hydrogen is present at a partial pressure of 1/760 of an atmosphere.

I want to thank Messrs. Kearns and Harp for their comments which further clarify the reason for the presence of the second phase in the 50 and 60 weight % uranium-zirconium alloys.

Their comments in comparing the microstructures to the more recent uranium-zirconium phase diagram are also appreciated.

The discussion of Bauer, Chubb and Rough is very helpful and adds a great deal to this paper.

The more recent version of the zirconium-uranium phase diagram as presented by Bauer, et al, is actually in better agreement with the information found in the work on the powder metallurgy of zirconium-uranium alloys. The eutectoids in this diagram are much closer to those that one would place as a result of examination of the structures of the powder metallurgy specimens.

While it is true that the hardness peaks shown might be considered primarily the result of dispersion hardening, it is indeed the eutectoid and monotectoid compositions which create the condition for the dispersion hardening.

I appreciate the comments on the transformation kinetics of the epsilon phase. At the time that this paper was written, there was considerable question about whether this phase even existed and certainly no knowledge about the transformation kinetics or the effect of oxygen and nitrogen.

The conclusion and supporting zirconium-uranium-oxygen ternary phase diagram by Bauer, et al, that the reason for retention of two phases in the vicinity of 50 weight % uranium-zirconium is a direct consequence of oxygen is well taken.

In regard to the tensile values reported, it was encouraging to hear that they are similar to those exhibited by cast and wrought alloys. The discrepancy in elongation for the data shown in this paper compared to that found in cast and wrought materials can be explained by the type and condition of the specimens. The fact that the tensile specimens were ordinary rectangular bars tested in the as-sintered condition and which invariably broke in the grips is good reason to expect lower elongation values for the relatively ductile material such as pure zirconium or zirconium low in uranium. This is undoubtedly one factor and the oxygen content is another factor in creating lower elongation values. The elongation data as an indication of ductility is roughly backed up in the paper by comparing the elongation of Table VI with the cold reduction to first sign of edge cracking, as shown in Table V. Since this indicates considerable ductility in these alloys at the intermediate compositions, the only plausible explanation for the better ductility than is generally observed with the cast and wrought alloys is the particular heat treatment in furnace cooling from the sintering temperature, as suggested by Bauer, et al.

A HOT-HARDNESS SURVEY OF THE ZIRCONIUM-URANIUM SYSTEM

By W. CHUBB, G. T. MUEHLENKAMP, AND A. D. SCHWOPE

Abstract

A complete hardness survey of the zirconium-uranium system has been made at temperatures from room temperature to 900 °C (1650 °F). The composition of maximum hardness increases from 40 atomic % zirconium at room temperature to 60 atomic % zirconium at 600 °C (1110 °F). At 700 °C (1290 °F), the hardness data indicated the presence of the beta uranium phase in alloys containing 95 and 100 atomic % uranium. This phase was found to be unusually hard. At 900 °C (1650 °F), maximum hardness of the gamma zirconium-uranium solid solution was found to occur at about 50 atomic %. (ASM International Classification Q29p, M24b; Zr, U)

INTRODUCTION

ZIRCONIUM has been mentioned many times as a structural material for thermal reactors, and it has been reported that zirconium was used in the STR (the reactor of the submarine, Nautilus) (1).¹ Recently, it was announced that the design of the nation's first nuclear power station at Shippingport, Pennsylvania, calls for a seed core containing zirconium-uranium alloy plates clad with Zircaloy (2). The design of a prototype boiling-water reactor power plant also calls for a fuel element of either uranium diluted with zirconium and clad with Zircaloy or just uranium clad with Zircaloy (3).

In connection with this type of interest in zirconium-uranium alloys for the production of power, it was thought desirable to survey the entire system with respect to mechanical properties. Such a survey might disclose an alloy of optimum properties and it might disclose compositions to be avoided. While hardness measurements are necessarily crude and cannot be interpreted in terms of ductility, they are quite adequate as a measure of relative strength. In a survey program

¹ The figures appearing in parentheses pertain to the references appended to this paper.

This work was performed under AEC Contract W-7405-eng-92.

A paper presented before the Thirty-Ninth Annual Convention of the Society, held in Chicago, November 4-8, 1957. Of the authors, W. Chubb is associated with Battelle Memorial Institute, Columbus, Ohio; G. T. Muehlenkamp and A. D. Schwoppe, formerly with Battelle, are now associated with General Electric, ANP Division, Cincinnati, Ohio; and the Cleve Research Center, Cleveland, Ohio, respectively. Manuscript received December 7, 1956.

of this type, hardness measurements at elevated temperatures can be extremely valuable as a guide for design and fabrication. A sharp drop in hardness with increasing temperature often indicates the upper limit of usefulness of a particular alloy. A certain hardness level, say 10 to 30 DPH, may indicate the maximum hardness level at which alloys may be hot-rolled with the available equipment. Another hardness level, say 2 DPH, may designate the hardness-temperature relation for forging. Obviously, such data, even though crude, are far better than no data when handling alloys for the first time. Such data are readily obtained by means of hardness measurements; the first tests perhaps being made on small castings and later more refined measurements being made on wrought materials. The ease with which a complete hardness survey of an alloy system can be made gives hardness measurements a distinct advantage over other methods of mechanical-property measurement.

APPARATUS

Hardness at elevated temperatures were determined in apparatus designed to handle easily oxidized metals in a vacuum at temperatures up to 1000 °C (1830 °F) (4). A diagram showing the essential features of the machine appears in Fig. 1. The diagram shows an elevation view of a cross section of the machine. The vacuum and accessory port is on the extreme left; the specimen-positioner-rod assembly is on the right; a dead-weight loading system occupies the upper half; and the movable pedestal is shown in the lower center. The center of the drawing shows an annular, wire-wound resistance furnace and surrounding radiation shields. The outer walls are water-cooled and vacuum tight. Rubber O-rings and gaskets at each joint allow the machine to be opened for repairs or to change specimens.

All parts of the machine exposed to elevated temperatures are made of stainless steel or ceramic; the remainder are made of brass or other conventional materials. The pedestal is ceramic and contains the control thermocouple. It is rigidly supported by a stainless steel block, a stainless steel bellows, and a heavy steel screw. Furnace temperature is maintained by a voltage control system regulated by the control thermocouple. The sapphire-tipped indenter is heated to essentially the same temperature as the specimen. The sapphire has a Vickers pyramid tip.

In operation, the chamber is evacuated to an absolute pressure of less than 5 microns of mercury, and the specimen resting on the pedestal is heated to some temperature as determined by the control thermocouple. The specimen is moved into place under the indenter column by means of the positioner rod, which is then retracted from the furnace. The pedestal is raised until the specimen contacts the indenter and raises the indenter column off a microswitch. The indenter column,

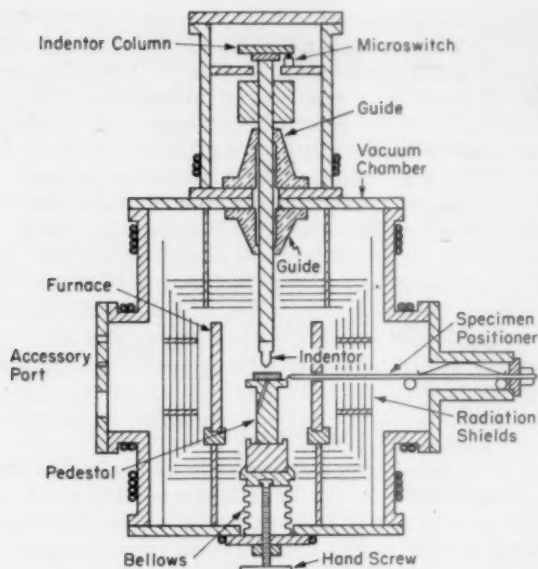


Fig. 1—Vacuum Hot-Hardness Machine.

which weighs approximately 1 kilogram, is allowed to remain in contact with the specimen for approximately 10 seconds. The pedestal is then lowered and the process is repeated. Friction between the stainless steel indenter column and the brass guides is equivalent to less than 10 grams.

MATERIALS

The zirconium used in preparing the alloys mentioned in this report was Foote Mineral Company, Grade 1, iodide zirconium. Some alloys were prepared with "Derby" uranium; others were prepared with "Fernald" uranium. Some alloys were prepared by arc melting; others were prepared by induction melting. The results do not show any consistent effects or trends attributed to these differences in preparation.

All alloys were reduced to $\frac{1}{8}$ -inch sheet by rolling in the gamma range at temperatures between 700 and 930 °C (1290 and 1705 °F). Prior to testing, all alloys were heated for 24 hours at 575 °C (1065 °F).

RESULTS OF EXPERIMENT

The results of the hardness tests are shown in Table I. The results

Table I
Hardness of Zirconium-Uranium Alloys

Nominal Alloy Composition			Hardness (DPH), kg./mm. ² at Temperature, °C										Type of Uranium and Melting Method(a)
At. % U (Balance Zr)	Wt % U (Balance Zr)	Room	300	500	600	650	700	750	800	850	900		
0	0	113	53	33	22	—	16.6	12.5	9.3	7.2	1.4	D-A	
0	0	138	58	39	27	—	14.5	11.1	8.7	8.4	2.6	F-I	
4	10	246	195	85	32	—	9.8	6.1	4.4	4.2	2.8	D-A	
8.5	20	235	182	102	51	—	25	16.4	8.2	2.9	2.0	F-I	
8.5	20	252	188	102	51	—	—	6.4	3.6	2.7	2.1	D-A	
14	30	283	185	136	56	—	16	7.3	5.0	4.2	3.7	F-I	
14	30	298	249	168	28	—	10.5	7.3	4.3	3.2	—	D-A	
20	40	295	255	172	75	—	10	7.4	5.7	4.8	4.1	F-I	
20	40	302	264	194	96	—	9.7	6.8	5.4	4.1	3.6	D-A	
20	40	311	271	178	100	—	10.0	6.3	5.4	3.6	3.6	D-I	
27	50	272	242	183	92	—	11.9	8.2	7.0	4.9	4.9	F-I	
27	50	264	262	192	101	—	10.9	8.5	6.9	5.9	5.9	D-A	
36	60	279	251	211	96	—	12.8	10.4	8.6	7.6	7.1	F-I	
36	60	364	337	249	81	—	15.7	12	9.9	—	—	D-A	
36	60	242	247	224	104	—	18.0	15.2	11.5	—	—	D-I	
48	70	350	293	219	75	—	16.9	13.5	9.5	—	7.3	F-A	
48	70	370	320	245	73	—	23	19.0	12.5	10.8	8.5	F-A	
60	80	411	341	212	57	—	15.4	12.8	13.6	—	—	D-A	
60	80	391	341	209	90	—	26	13.1	14.8	11.2	8.9	D-A	
60	80	385	318	213	77	—	22	13.3	15.7	—	8.4	F-I	
60	80	431	354	213	77	—	23	10.6	12.1	—	8.4	F-I	
60	80	359	359	209	80	—	25	15.0	11.9	—	7.3	D-I	
77	90	359	359	129	26	—	4.6	10.6	8.6	—	5.9	D-A	
77	90	363	258	159	68	—	14.0	9.6	7.1	5.2	2.2	F-I	
88	95	307	181	106	49	—	7.6	5.4	4.4	3.0	3.0	D-A	
88	95	347	139	118	38	—	6.4	4.7	3.6	2.7	2.3	F-I	
95	98	283	155	85	49	—	35	3.9	2.3	2.0	1.7	D-A	
100	100	249	91	29	14.5	—	33	—	—	—	—	D-A	
100	100	263	144	49	23	—	43	—	—	—	—	D-A	
100	100	200	68	23	13	—	31	—	1.7	—	0.6	D-A	
100	100	265	117	37	18.7	—	33	28	—	—	—	F-I	
100	100	—	—	—	—	—	33	23	0.79	—	0.72	F-I	
100	100	—	—	—	—	—	12.7	23	—	—	—	F-I	

(a) D=Derby uranium
F=Fernald uranium
A=Arc-melted alloy
I=Induction-melted alloy

for each composition and selected temperatures have been averaged and plotted as Fig. 2. Isotherms are shown for hardnesses at room temperature, 300, 500, 600, 700, 800, and 900 °C (570, 930, 1110, 1290, 1470 and 1650 °F). Appropriate phase relationships have been indicated for certain curves.

The room temperature curve shows a maximum hardness at approximately 60 atomic % (80 weight %) uranium. As the temperature

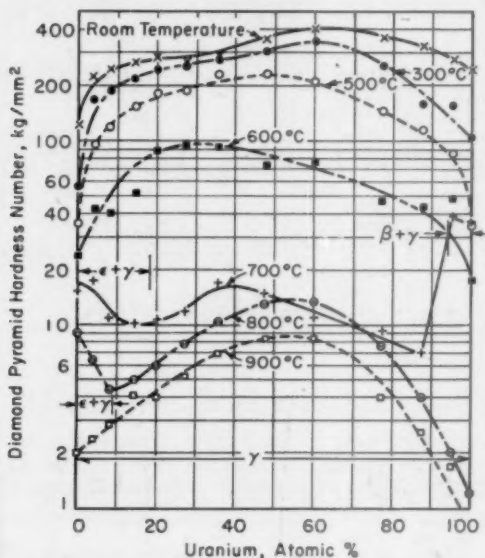


Fig. 2—Hardness Isotherms in the Zirconium-Uranium System.

is increased, this peak shows a tendency to shift to a lower percentage uranium alloy. It is also interesting to note that the hardness of the pure metals falls off much more rapidly with increasing temperature than does the hardness of the intermediate alloys.

The curve at 600 °C (1110 °F) is complicated by the appearance of the gamma phase in the zirconium-rich alloys. This also occurs in a temperature range where the hardness of all zirconium-uranium alloys changes very rapidly with changes in temperature. The result is a series of erratic points. A pronounced maximum occurs at the approximate location of the delta phase field, however.

The curve at 700 °C (1290 °F) shows the effect of the occurrence of the hard and intractable beta-uranium structure. The curves at 700, 800, and 900 °C (1290, 1470 and 1650 °F) show the effect of the

gradual appearance of the gamma phase at the expense of the low temperature structures with increasing temperature. At 650 °C (1200 °F), the hardest and most stable gamma alloy occurs at approximately 35 atomic % (60 weight %) uranium. At higher temperatures, this peak shows a tendency to shift to a higher percentage uranium alloy.

Fig. 3 shows part of the uranium-zirconium phase diagram (5,6). Superimposed upon this diagram are averages of the hardness values shown in Table I. It is interesting to note that the gamma plus gamma

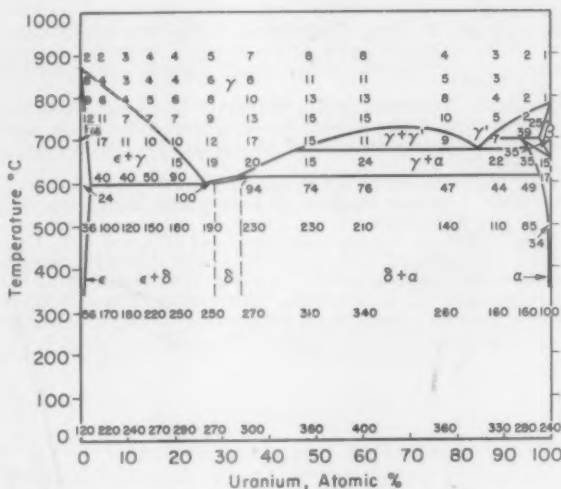


Fig. 3—Hardness-Temperature Relationships in the Zirconium-Uranium System. Hardness in DPH.

prime phase field shows lower hardness than gamma of the same composition at a higher temperature. Between 650 and 760 °C (1200 and 1400 °F), the beta-uranium structure is by far the hardest of all zirconium-uranium alloys. Alloys containing beta uranium undoubtedly are more difficult to roll than other compositions in this system.

CONCLUSIONS

1. A hardness survey of the zirconium-uranium system shows a maximum hardness at room temperature at about 60 atomic % (80 weight %) uranium. With increasing temperatures up to 600 °C (1110 °F), this maximum tends to shift toward 30 atomic % (50 weight %) uranium. Between 500 and 600 °C (930 and 1110 °F) this maximum corresponds to the approximate location of the delta phase field.

2. The beta uranium phase is much harder than any other zirconium-uranium alloy in the temperature range from 650 to 760 °C (1200 to 1400 °F).

3. Maximum hardness of the gamma zirconium-uranium solid solution at 650 °C (1200 °F) occurs at about 36 atomic % (60 weight %) uranium. With increasing temperature up to 900 °C (1650 °F), this maximum tends to shift toward 50 atomic % (75 weight %) uranium.

References

1. H. Etherington, R. C. Dalzell, and D. W. Lillie, "Zirconium and Its Application to Nuclear Reactors," *The Metallurgy of Zirconium*, 1955, Chapter 1, McGraw-Hill.
2. J. W. Simpson and M. Shaw, "Description of the Pressurized Water Reactor Power Plant at Shippingport, Pennsylvania," *Proceedings, International Conference on the Peaceful Uses of Atomic Energy*, United Nations, Vol. 3, 1955, p. 211-226.
3. J. M. Harrer, A. S. Jameson, and J. M. West, "The Engineering Design of a Prototype Boiling Water Reactor Power Plant," *Proceedings, International Conference on the Peaceful Uses of Atomic Energy*, United Nations, Vol. 3, 1955, p. 250-262.
4. W. Chubb, "The Contribution of Crystal Structure to the Hardness of Metals," *Transactions, American Institute of Mining and Metallurgical Engineers*, Vol. 203, Jan. 1955, p. 189.
5. H. A. Saller and F. A. Rough, "Compilation of U.S. and U.K. Uranium and Thorium Constitutional Diagrams," *BMI-1000* (Battelle Memorial Institute), June 1955, Department of Commerce, Washington, D. C.
6. A. N. Holden and W. E. Seymour, "Intermediate Phase in the Uranium-Zirconium System," *Transactions, American Institute of Mining and Metallurgical Engineers*, Vol. 206, October 1956, p. 1312.

TRANSFORMATION KINETICS OF ZIRCONIUM-URANIUM ALLOYS

BY D. L. DOUGLASS, L. L. MARSH, JR., AND G. K. MANNING

Abstract

The transformation kinetics of zirconium alloys containing 8.85, 11.1, 14.3, and 20.7 weight % uranium have been determined by metallography and x-ray diffraction. The effect of increasing uranium content in the alloys was to retard alpha zirconium precipitation and to accelerate the precipitation of epsilon, an intermediate phase.

Direct quenching of the 8.85, 11.1, and 14.3 weight % alloys resulted in the formation of alpha prime, a martensitic alpha-zirconium structure. Some epsilon prime (super-saturated epsilon) was observed in all the alloys; however, the 20.7 weight % alloy was essentially 100% epsilon prime in the quenched condition.

An unusual structure, tentatively called bainitic alpha, was observed in several of the 8.85 and 11.1 weight % alloys which were isothermally transformed at 550 °C (1020 °F) or lower.

The data are presented in the form of T-T-T curves. (ASM International Classification: N6, N7; Zr, U)

INTRODUCTION

FIG. 1 shows the zirconium-uranium phase diagram as determined by Saller and Rough (1).¹ The high temperature body-centered cubic zirconium phase (beta) is isomorphous with the high temperature uranium phase (gamma). The eutectoid composition, containing 44 weight % uranium, decomposes to alpha zirconium, a hexagonal close-packed zirconium containing less than 1 weight % uranium in solid solution, and to epsilon, an intermediate phase of unknown crystal structure and questionable composition limits. Some investigators (2) index the structure as hexagonal with $a_0 = 8.71$ and $c_0 = 9.19$ Å, whereas others (3) index the phase as cubic with $a_0 = 10.69$ Å. Present composition limits extend from 43 to 58 weight % uranium.

Oxygen stabilizes alpha zirconium (4) and has the effect of raising the beta/beta plus alpha transus in the zirconium-oxygen system from

¹The figures appearing in parentheses pertain to the references to this paper.

A paper presented before the Thirty-Ninth Annual Convention of the Society, held in Chicago, November 4-8, 1957. Of the authors, D. L. Douglass is Principal Metallurgist, L. L. Marsh, Jr. is Assistant Chief, and G. K. Manning is Chief, Metallurgical Engineering Division, Battelle Memorial Institute, Columbus, Ohio. Manuscript received April 19, 1957.

865 °C (1590 °F) for pure zirconium to 1940 °C (3525 °F) at 2 weight % oxygen. Consequently, the purity of the zirconium used in fabricating the alloys markedly affects the transus temperature. This probably accounts for some of the anomalous results reported by early investigators.

EXPERIMENTAL PROCEDURES

Alloy Preparation

Westinghouse Grade 1 crystal bar zirconium and center-cut biscuit uranium were double arc-melted in vacuum in water-cooled copper crucibles. The ingots were broken down by forging at 800 °C (1470 °F) and by rolling to 1/2-inch diameter rods at 750 °C (1380 °F). The chemical analyses of the alloys are listed in Table I.

Heat Treatment

Heat treatments were performed in two manners. Isothermal-

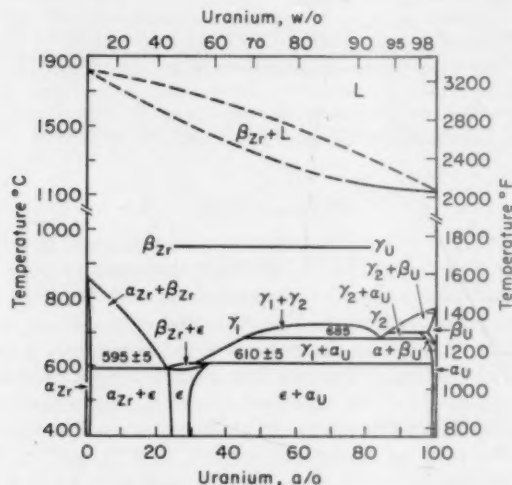


Fig. 1—Zirconium-Uranium Constitutional Diagram.

Table I
Chemical Analyses of Alloys

Nominal	Uranium, weight %	Actual	Oxygen, weight %	Hydrogen, weight %	Carbon, weight %
7		8.85	0.0219	0.0025	0.11
10		11.1	0.0196	0.0029	0.16
15		14.3	0.0396	0.0038	0.13
20		20.7	0.0232	0.0033	0.28

transformation specimens were $\frac{3}{16}$ -inch diameter cylinders, $\frac{1}{4}$ -inch high, and were individually sealed in $\frac{1}{4}$ -inch diameter Type 304 stainless steel tubing. The ends of the capsules were crimped shut and then welded. The capsules were attached to Nichrome wire and suspended in a salt bath at 950 °C (1740 °F) for 1 hour. This temperature was sufficient to insure that the alloys were single phase (beta) at the end of the solution treatment. The capsules were then quenched into an intermediate salt bath maintained at the desired temperature, held for a given time, and water quenched to room temperature. Studies of direct quenching specimens were made by sealing samples in Vycor tubes in vacuum, solution treating, and quenching by immediately smashing the capsule in ice water.

M_s Determination

A gas-quenching technique similar to that used by Greninger (5) was used to detect the thermal "arrest" associated with the martensitic transformation of alpha zirconium. A small specimen, $\frac{1}{4} \times \frac{1}{8} \times 0.040$ inch, was attached to a plunger by means of a spot-welded thermocouple. The plunger was actuated through a Wilson seal in the top of a vacuum chamber. The specimen was solution treated in a small furnace in the vacuum chamber and was then raised by the plunger into a blast of precooled helium (-77 °C). The time-temperature curve was recorded on a Sanborn high speed recorder. The break in the curve (modified thermal arrest) was taken as the M_s point.

Metallography

Samples were mounted in Bakelite, ground through a 600-grit silicon carbide wheel, polished with Blue Diamond abrasive on a Forstman cloth, and etched with a solution of 30-ml HNO₃, 30-ml lactic acid, and 6 drops HF.

X-Ray Diffraction

Diffraction patterns were made with a 57.3-millimeter Debye camera on a rotating sliver, 0.025 inch in diameter, tapered to a fine point. The slivers were etched from bars $\frac{1}{16}$ -inch square with a solution consisting of 15-milliliter lactic acid, 20-milliliter HNO₃, and 10-milliliter HF. Filtered radiation was used with an iron target on all samples but three. Manganese radiation was used on three samples in order to separate some questionable lines in the back-reflection area.

High temperature diffraction patterns were made in a vacuum camera on a thin sliver sample. The sample was solution treated in the camera, cooled to the desired transformation temperature by reducing the current to the furnace, and subjected to the x-ray beam. Cooling from the solution treating temperature of 1000 to 500 °C (1830 to 930 °F) required about 30 seconds.

RESULTS AND DISCUSSION

The time-temperature-transformation diagrams for the four alloys were shown in Figs. 2 through 5. The curves were drawn on the basis of metallographic examination correlated with x-ray diffraction results. Interpretation of the microstructures was complicated by the presence of phases which formed during the final quench rather than during the isothermal treatment, i.e., alpha prime and epsilon prime. Enrichment of the beta phase during isothermal precipitation of alpha caused additional difficulties in interpreting the final microstructure.

Isothermal Precipitation of Alpha

Transformation of beta to alpha proceeded rapidly at high temperatures, initiating within 1 minute for all alloys. The "knee" of the curves occurred between the beta/beta + alpha transus and the eutectoid temperature for all alloys, decreasing from about 700 °C (1290 °F) for the 8.85 weight % alloy to about 620 °C (1150 °F) for the 20.7 weight % alloy. Increasing uranium content retarded the initiation of the reaction from 10 seconds for the 8.85 weight % alloy to about 60 seconds for the 20.7 weight % alloy at the knee. The curves extended below the eutectoid temperature until intersection occurred with either the M_s , B_s (bainite-start temperature), or the E'_s (start of epsilon prime transformation). Below the eutectoid temperature, increasing uranium content was even more effective in retarding alpha precipitation. Transformation started at 400 °C (750 °F) within 100 minutes in the 14.3 weight % alloy, but did not start in 10,000 minutes in the 20.7 weight % alloy at the same temperature.

The alpha precipitate was coarser the higher the transformation temperature. Furthermore, the alpha precipitate appeared to coalesce and coarsen when the specimens were held isothermally for extended periods of time. These two effects are illustrated for the 8.85 weight % alloy in Figs. 6 through 9. All microstructures are at a magnification of $\times 1000$; thus, direct size comparison may be made.

Alpha which formed at 650 °C during 120 minutes was barely resolvable at $\times 1000$. However, considerable coalescence occurred during a transformation period of 1400 minutes as shown in Fig. 6. Short-time structures obtained at 700 °C (1290 °F) correspond to those obtained by long treatments at 650 °C (1200 °F) as seen in Figs. 7 and 8, representing transformation times of 60 and 6200 minutes, respectively, for the 8.85 weight % alloy. The structure obtained at 750 °C (1380 °F) for a transformation period of 5800 minutes, Fig. 9, consisted of a very coarse precipitate of alpha in a matrix of epsilon prime. The epsilon prime formed during the final quench from 750 °C (1380 °F) and is indicative of beta enrichment during alpha precipitation.

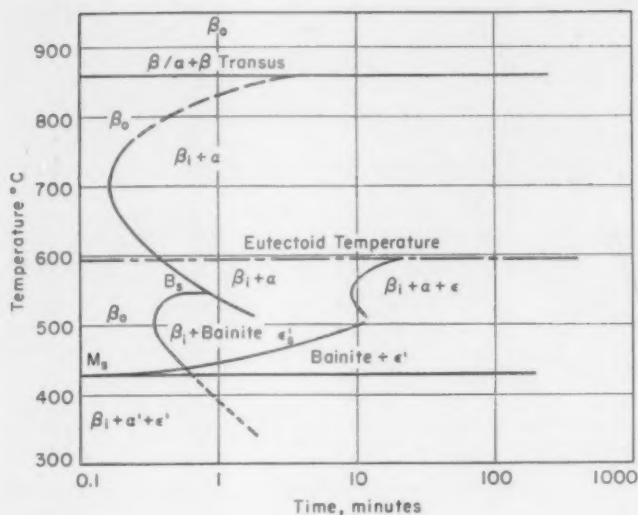


Fig. 2—Time-Temperature-Transformation Diagram for a Zirconium-8.85 Weight % Uranium Alloy.

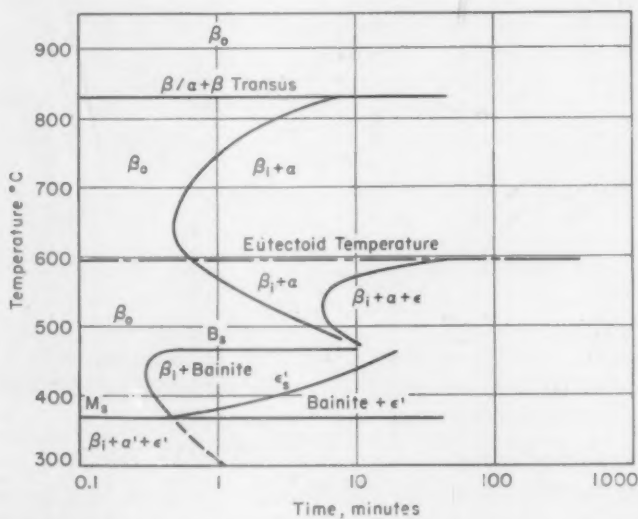


Fig. 3—Time-Temperature-Transformation Diagram for a Zirconium-11.1 Weight % Uranium Alloy.

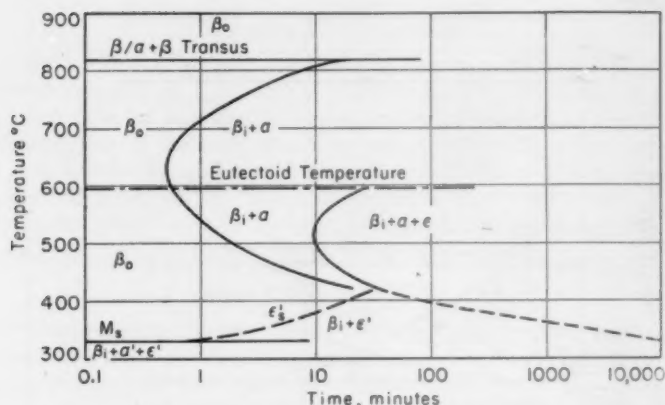


Fig. 4—Time-Temperature-Transformation Diagram for a Zirconium-14.3 Weight % Uranium Alloy.

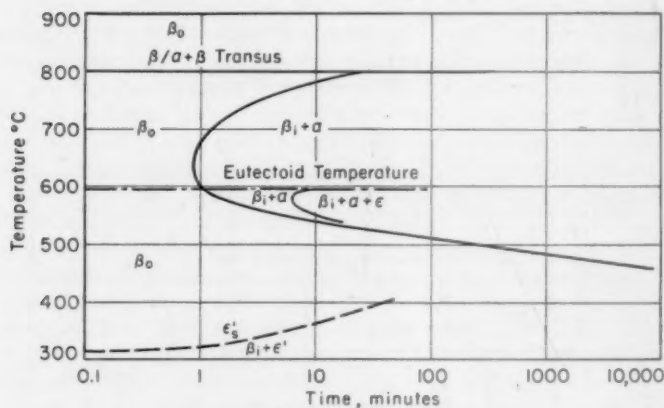


Fig. 5—Time-Temperature-Transformation Diagram for a Zirconium-20.7 Weight % Uranium Alloy.

Transformation of the 11.1 weight % alloy produced similar structures as observed in the 8.85 weight % alloy. Precipitation of alpha appeared to be complete within 1400 minutes, but additional time resulted in considerable coarsening of the alpha phase.

The 14.3 weight % alloy transformed similarly to the 11.1 weight % alloy at 650 °C (1200 °F). However, at 750 °C (1380 °F), the 14.3 weight % alloy precipitated alpha initially as a grain boundary network with a small amount appearing within the grains as individual platelets. The 8.85 and 11.1 weight % alloys showed a Widmanstätten

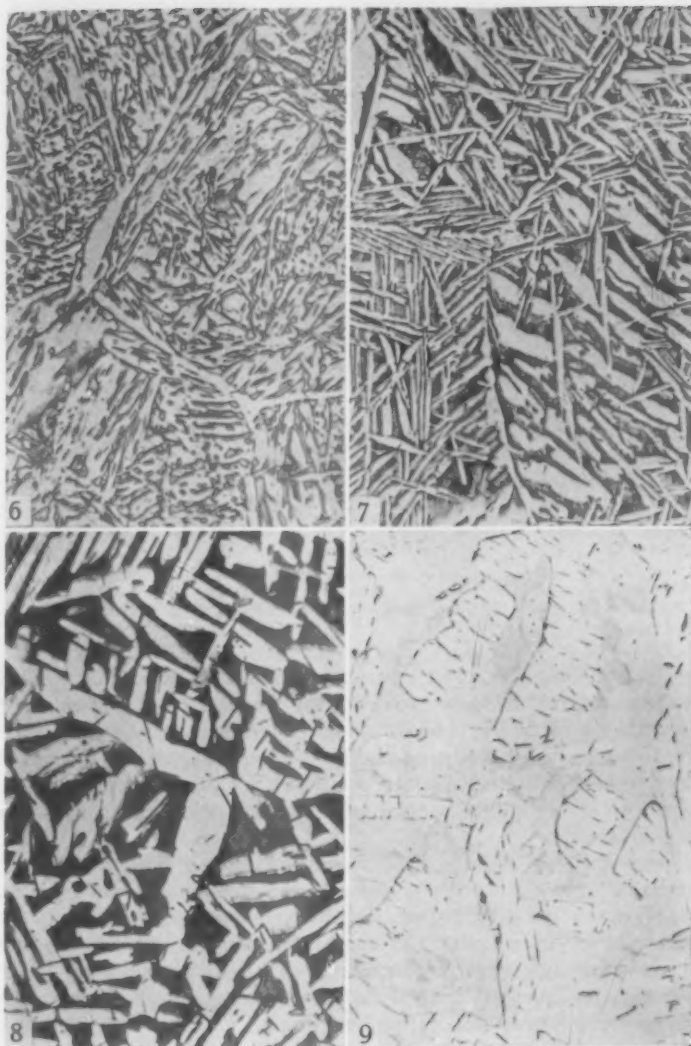


Fig. 6—8.85 Weight % Uranium Alloy Isothermally Transformed 1400 Minutes at 650 °C (1200 °F).

Fig. 7—8.85 Weight % Alloy Isothermally Transformed 60 Minutes at 700 °C (1290 °F).

Fig. 8—8.85 Weight % Alloy Isothermally Transformed 6200 Minutes at 700 °C (1290 °F).

Fig. 9—8.85 Weight % Alloy Isothermally Transformed 5800 Minutes at 750 °C (1380 °F).

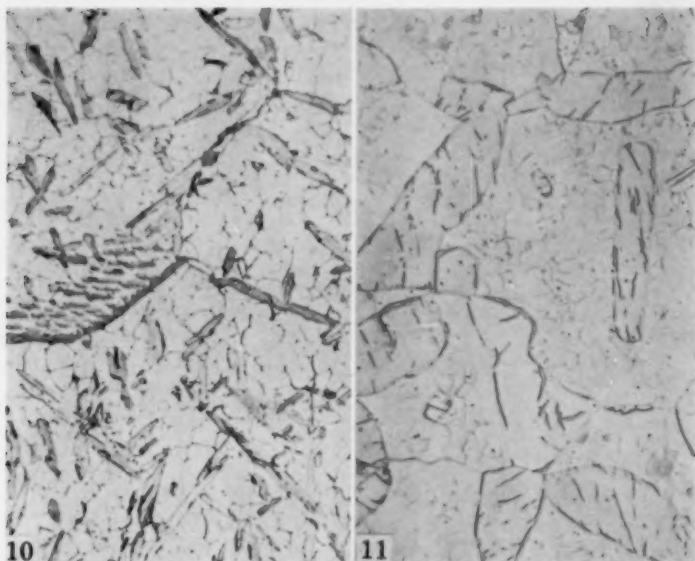


Fig. 10—14.3 Weight % Alloy Isothermally Transformed 5 Minutes at 750 °C (1380 °F).

Fig. 11—14.3 Weight % Alloy Isothermally Transformed 5800 Minutes at 750 °C (1380 °F).

precipitation of alpha. Once again, the matrix of the alloys was epsilon prime as determined by x-ray diffraction results. Micrographs of this alloy are shown in Figs. 10 and 11 for transformation times of 5 and 5800 minutes, respectively. Considerable alpha was present after 5 minutes at temperature. It appeared that little further nucleation had occurred by 5800 minutes, but agglomeration had taken place after about 1000 minutes.

Precipitation of alpha in the 20.7 weight % alloy at 650 °C (1200 °F) proceeded as a combination Widmanstätten precipitation and as a grain boundary precipitation. Samples held at temperature for 120 and 6200 minutes are shown in Figs. 12 and 13. The amount of alpha appeared constant, but coalescence had occurred.

It may be concluded from the type of precipitate which dominated the microstructures that alpha precipitation generally occurred by a Widmanstätten mechanism, i.e., a simple cooperative gliding of a group of atoms. In other words, a group of atoms in the body-centered cubic parent phase undergoes a slight shearing action and becomes a plane of the hexagonal close-packed precipitate. The shape of the particles, thin platelets, is the shape of lowest strain energy. However, opposition to the formation of platelet particles results from the surface

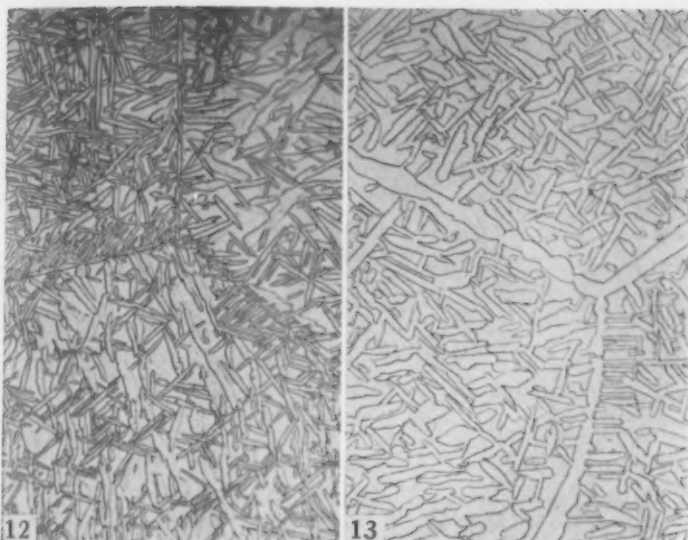


Fig. 12—20.7 Weight % Alloy Isothermally Transformed 120 Minutes at 650 °C (1200 °F).

Fig. 13—20.7 Weight % Alloy Isothermally Transformed 6200 Minutes at 650 °C (1200 °F).

energy which is a minimum for a spherical shape. Thus, the final shape is dependent upon the mode of diffusion, the strain energy, and the surface energy. According to the observed structures, cooperative translation seems to dominate over bulk diffusion, minimum strain energy dominates at short times of transformation, and the minimum surface energy dominates for long holding times.

Alpha Prime and Bainitic Alpha Transformations

Alloys containing 8.85, 11.1, and 14.3 weight % uranium transform to a martensitic alpha during a direct quench from the beta region to room temperature. This behavior has been noted by others also (6). Alpha prime is a distorted, supersaturated, close-packed hexagonal alpha zirconium. Temperatures for the start of alpha prime formation, M_s , as determined by the modified thermal arrest are 8.85 weight % uranium— 430 ± 10 °C, 11.1 weight % uranium— 370 ± 10 °C, and 14.3 weight % uranium— 325 ± 10 °C. No alpha prime was observed in the 20.7 weight % alloy with the quenching conditions employed in this investigation, although it has been reported by Chubb and co-workers.

X-ray diffraction patterns of alpha prime showed a diffuse pattern

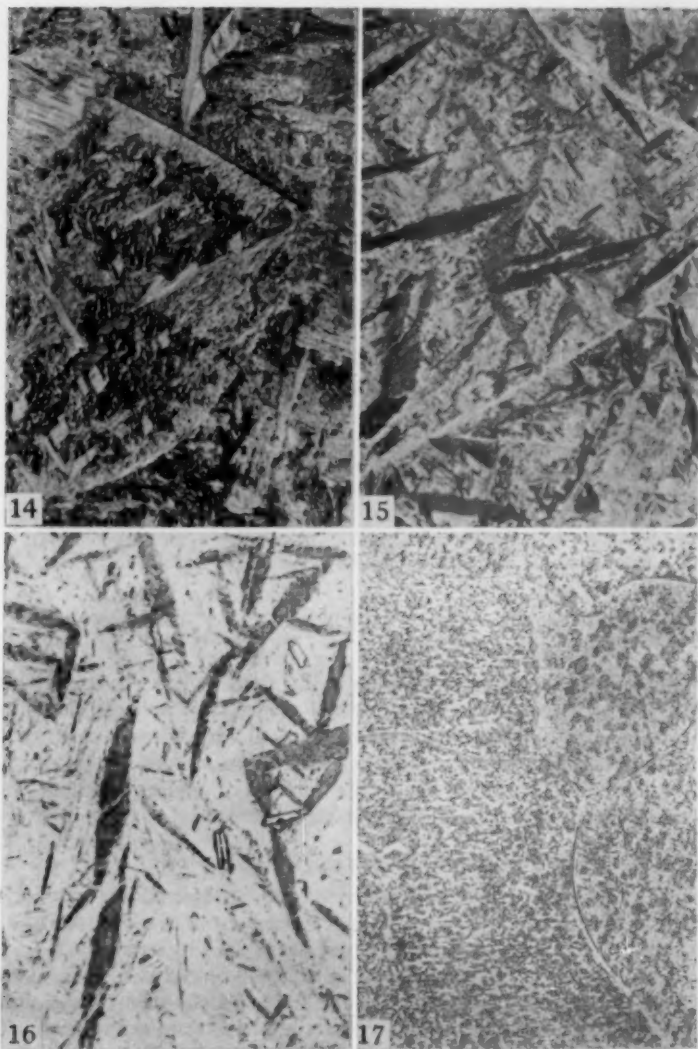


Fig. 14—8.85 Weight % Uranium Alloy Water-Quenched from 1000 °C (1830 °F).

Fig. 15—11.1 Weight % Uranium Alloy Water-Quenched from 1000 °C (1830 °F).

Fig. 16—14.3 Weight % Uranium Alloy Water-Quenched from 1000 °C (1830 °F).

Fig. 17—20.7 Weight % Uranium Alloy Water-Quenched from 950 °C (1740 °F).

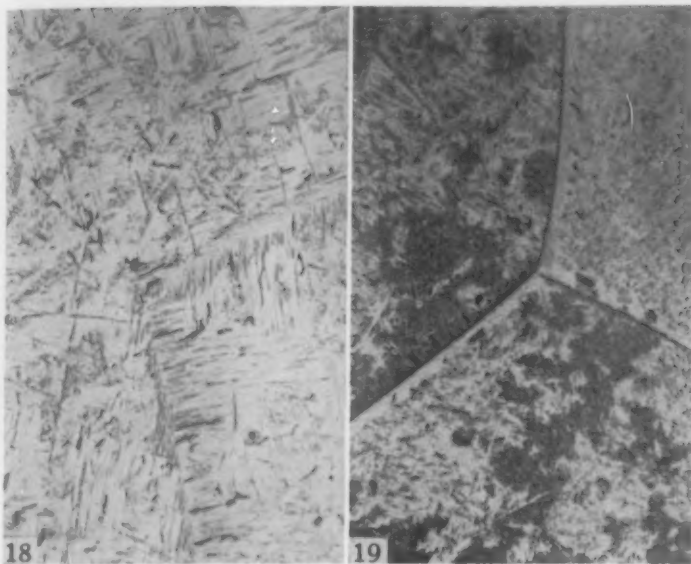


Fig. 18—8.85 Weight % Uranium Alloy Isothermally Transformed 2 Minutes at 350 °C (660 °F) and Water-Quenched.

Fig. 19—8.85 Weight % Uranium Alloy Isothermally Transformed 2 Minutes at 400 °C (750 °F) and Water-Quenched.

of alpha with considerable line broadening. The diffuseness of the lines prevented a determination of the lattice-cell constants as a function of uranium content. It is believed, however, that the alpha prime had the uranium content of the beta phase from which it formed. Traces of epsilon prime were detected in samples quenched from 1000 °C (1830 °F). More rapid cooling would have suppressed formation of this phase as reported in Reference 6.

The nature of the epsilon-prime phase is controversial. It appears to form very rapidly and could nucleate either athermally or isothermally. The curves for the start of epsilon-prime transformation are drawn so that they approach the M_s curves and intersect the ordinate, 0.1 minute.

The degree of supersaturation believed to exist in alpha prime would seemingly involve a hardening reaction due to the formation of martensite. Little hardening was observed and may be explained by the lack of coherency between alpha prime and the parent beta phase. The observed hardening may be traced to oxygen contamination of the alpha zirconium. Microstructures of the quenched alloys are shown in Figs. 14 through 17. Alpha prime is the dominant phase for alloys containing up to 14.3 weight % uranium. The 20.7 weight % alloy was essentially 100% epsilon prime. An interrupted quench to tem-

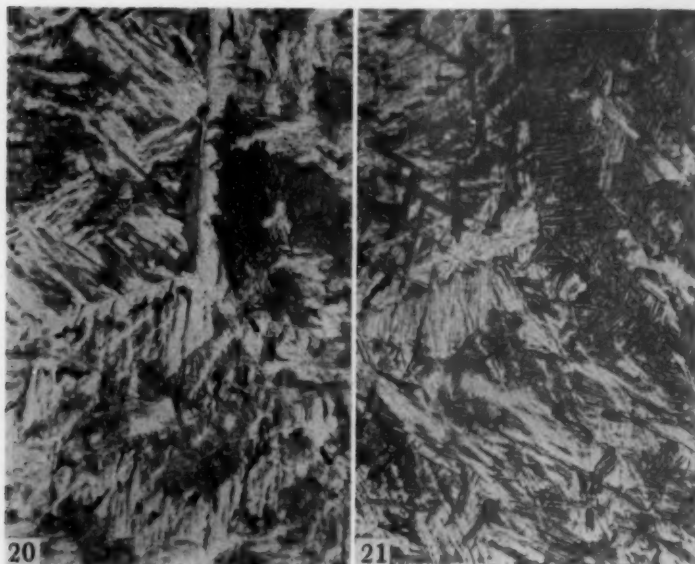


Fig. 20—8.85 Weight % Uranium Alloy Isothermally Transformed 1560 Minutes at 400 °C (750 °F).

Fig. 21—8.85 Weight % Uranium Alloy Isothermally Transformed 5500 Minutes at 350 °C (660 °F).

peratures below the M_s temperature resulted in smaller alpha-prime needles which appeared to have variable etching characteristics. Examples are shown in Figs. 18 and 19 for holding times of 2 minutes at 350 and 400 °C for an 8.85 weight % alloy. Fig. 18 is an example of the coarser structure and less dark-etching constituent due to a greater fraction of alpha prime formed by the quench to 350 °C (660 °F) than by a quench to 400 °C (750 °F). Fig. 19 shows more dark-etching alpha prime, the dark needles being formed during the final quench to room temperature.

The effect of long times on the alloy at these temperatures was to either temper the alpha prime that formed during the initial quench; to isothermally transform the retained beta; or to have no effect on the beta, in which case additional alpha prime formed during the final quench. Examples of the structural changes incurred by "tempering" of the alpha prime or by additional isothermal transformation (formation of bainitic alpha) may be seen in Figs. 20 through 22. The nature of the additional transformation is not definitely discernible on the basis of present data; however, a phase has been observed which has some characteristics of lower bainite found in steels. This structure, Fig. 22, shows large lenticular particles of alpha with a precipitate within the

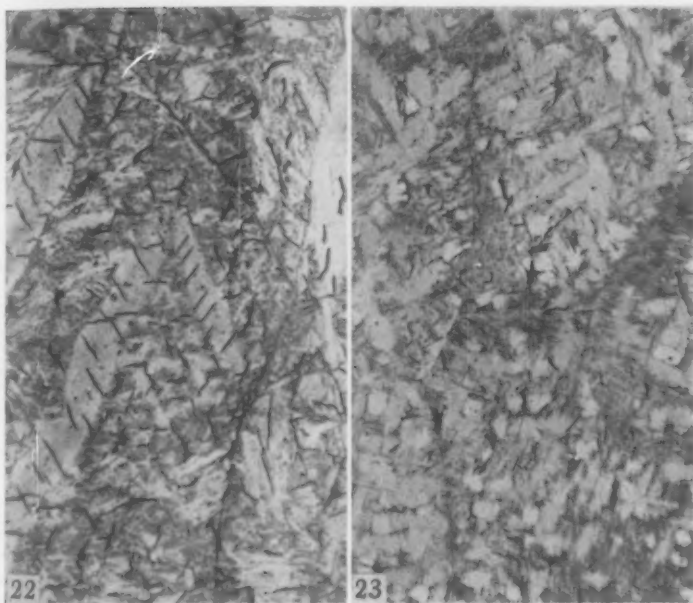


Fig. 22—8.85 Weight % Uranium Alloy Isothermally Transformed 6200 Minutes at 450 °C (840 °F), Illustrating Bainitic Alpha (Lenticular Phase).

Fig. 23—14.3 Weight % Uranium Alloy Isothermally Transformed 10 Minutes at 350 °C (660 °F) α' Formed by the Initial Quench to 350 °C (660 °F). This reaction was immediately followed by the transformation of the remaining $\beta \rightarrow \epsilon'$.

lenses. It is thought that the angular precipitate within the alpha particles is epsilon and was nucleated from the alpha phase. The bainitic type structure was also observed in a 11.1 weight % alloy transformed at 400 °C (750 °F).

The highest uranium content alloy to form alpha prime was the 14.3 weight % alloy. However, an appreciable amount of epsilon prime was formed along with the alpha prime as shown in Fig. 23. The epsilon prime is the equiaxed, light-etching phase.

Isothermal Precipitation of Epsilon

Alpha forms prior to epsilon in all four alloys investigated. Consequently, epsilon forms from a beta which is enriched in uranium. The precipitation of epsilon was restricted to a rather narrow temperature range for times of less than 6000 minutes. X-ray diffraction results showed that epsilon prime was formed at temperatures below 450 to 500 °C (840 to 930 °F), depending upon the alloy content. High temperature x-ray work showed that equilibrium epsilon formed at 500 °C (930 °F) for a 20.7 weight % alloy within 2 hours. However,

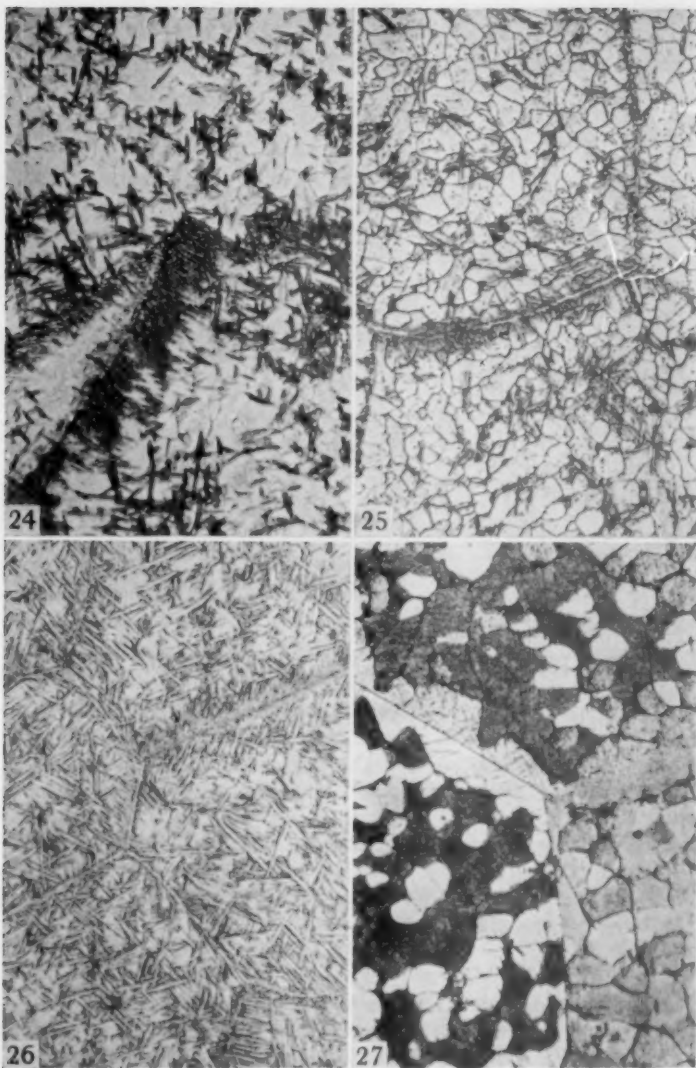


Fig. 24—20.7 Weight % Uranium Alloy Transformed 2 Minutes at 580 °C (1075 °F).

Fig. 25—20.7 Weight % Uranium Alloy Isothermally Transformed 140 Minutes at 500 °C (930 °F).

Fig. 26—20.7 Weight % Uranium Alloy Isothermally Transformed 1080 Minutes at 500 °C (930 °F).

Fig. 27—20.7 Weight % Uranium Alloy Transformed 5800 Minutes at 350 °C (660 °F).

other samples which had been held for intermediate times at 500 °C (930 °F) and then quenched to room temperature gave a strong epsilon prime diffraction pattern. This means that some beta transformed to equilibrium alpha plus epsilon at temperature and that the remaining untransformed beta formed epsilon prime during the final quench. Thus, epsilon prime either nucleates athermally from the highly enriched beta, or very rapid isothermal transformation of the enriched beta-to-epsilon prime may take place. Additional experiments with varied cooling rates are needed in order to see if the ratio of beta/epsilon prime is constant. If the ratio were constant, it could be concluded that epsilon prime formed athermally.

Precipitation of epsilon initiated within 6 to 10 minutes in the temperature range of about 550 to 595 °C (1020 to 1100 °F) for a 20.7 weight % alloy. However, for times of less than 6 minutes, alpha precipitated first, and epsilon prime formed during the final quench. See Fig. 24. The dark phase, alpha, precipitated in a Widmanstätten pattern within the prior beta grains. The remaining beta transformed to a fine grain structure of epsilon prime (light etching phase). At a lower temperature, 500 °C (930 °F), alpha precipitated first, followed by epsilon. Transformation for 140 minutes for a 20.7 weight % alloy resulted in alpha precipitation (Fig. 25), whereupon the final quench formed the fine grain epsilon prime. A holding time of 1080 minutes (Fig. 26) caused considerable alpha formation and equilibrium epsilon as determined by x-ray diffraction.

No epsilon or alpha were observed in the 20.7 weight % alloy at 350 °C (660 °F) within 5800 minutes. Fig. 27 shows this alloy which is essentially 100% epsilon prime. A very small amount of alpha formed during the quench from 950 to 350 °C (1740 to 660 °F). The fine grain structure of epsilon prime etched differentially. Some grains appeared mottled, whereas others etched clearly. Additional work is necessary to discern the nature of this behavior.

CONCLUSIONS

The following conclusions may be drawn from this investigation.

(a) Alpha precipitation is strongly retarded by increased amounts of uranium, particularly at temperatures in the range of 350 to 500 °C (660 to 930 °F).

(b) Alpha prime (martensitic alpha) is formed during a direct quench from the beta region to room temperature in alloys containing up to 14.3 weight % uranium. No alpha prime was observed in the 20.7 weight % alloy.

(c) A supersaturated epsilon was formed by direct quenching from the beta region. The transformation appears to be nucleated very rapidly under isothermal conditions or may possibly nucleate athermally.

(d) Bainitic alpha formed in alloys containing 8.85 and 11.1 weight % uranium during isothermal transformation below 550 °C (1020 °F).

(e) Equilibrium epsilon formed isothermally at temperatures below the eutectoid after alpha precipitation had occurred.

ACKNOWLEDGMENTS

The excellent work of George Wheeler in the preparation of innumerable photomicrographs is gratefully acknowledged. Thanks are given to J. Robert Doig for x-ray diffraction analyses.

This work was performed under AEC Contract No. W-7405-eng-92.

References

1. H. A. Saller and F. A. Rough, "Compilation of U. S. and U. K. Uranium and Thorium Constitution Diagrams," Battelle Memorial Institute 1000, June 1955.
2. F. A. Rough, A. E. Austin, A. A. Bauer and J. R. Doig, "The Stability and Existence Range of the Zr-U Epsilon Phase," Battelle Memorial Institute 1092, 1956.
3. M. H. Mueller, "The Delta Phase in the U-Zr System," Research in Progress Abstracts, American Institute of Mining and Metallurgical Engineers Fall Meeting, 1955.
4. R. F. Domagala and D. McPherson, "System Zirconium-Oxygen," *Journal of Metals*, Vol. 6, No. 2, Feb. 1954, p. 238.
5. A. B. Greninger, "The Martensite Thermal Arrest in Iron-Carbon Alloys and Plain Carbon Steels," *TRANSACTIONS, American Society for Metals*, Vol. 30, 1942, p. 1.
6. H. A. Saller, F. A. Rough and W. Chubb, "Survey of Heat Treatment Response of Some Zirconium-Uranium Alloys," Battelle Memorial Institute 1096, 1956.

DISCUSSION

Written Discussion: By J. J. Kearns, Westinghouse Electric Corp., Bettis Atomic Power Division, Pittsburgh.

Along with the TTT diagrams which give a complete picture of the transformation kinetics, the authors also show some very interesting photomicrographs. Of particular interest to the writer are the several photomicrographs which reveal the subcell or domain structure of the epsilon prime phase. The domain size is large enough to be easily resolved at X1000. Such large domain size is striking since the data indicate that in certain cases these domains formed in the exceedingly short time period during the quench from the isothermal transformation temperature. Also, the temperature of formation must have been as low as 300 to 400 °C (570 to 750 °F). Such characteristics are quite different from those associated with domain formation in a 50 weight % uranium alloy with which the writer is familiar.² Domains form in this alloy by nucleation and growth of epsilon particles. However, domains of resolvable size form in a short time (several seconds) only when samples are quenched directly from the Beta (or Gamma) region to temperatures above 500 °C (930 °F). At lower temperatures or when

²J. J. Kearns, "The Transformation Kinetics of Uranium-Zirconium Alloys Containing 50 and 60 weight % Uranium", WAPD-T-417, American Institute of Mining and Metallurgical Engineers Fall Meeting, 1957.

samples are quenched to room temperature and reheated, development of resolvable domains requires much longer periods of time. This low temperature behavior is believed to result from a very high ratio of nucleation to growth rate. Epsilon particles apparently form but are submicroscopic. Coalescence and growth to resolvable domains occur only after lengthy periods of heating. At 500 °C (930 °F), for example, it requires about 2 months.

I would like to know if the authors feel that the domains revealed in their photomicrographs have the same origin as those formed in the 50 weight % uranium alloy, and if so, if uranium content is responsible for the different kinetics.

Authors' Reply

Mr. Kearns has pointed out a very interesting piece of data in his zirconium-50 weight % uranium alloy with regards to the long periods of time required to obtain resolvable domains of epsilon. Before answering the question posed by Mr. Kearns the authors would like to make some additional comments on the epsilon phase.

The phase has been the center of controversy for some time. It was originally thought that the phase was a metastable one and should not appear on the phase diagram. Later work by Bauer, et al., (2) showed that zirconium and uranium powders held for long times below the temperature at which beta was a stable phase formed epsilon, and that it was therefore an equilibrium phase. The crystal structure of the phase has been uncertain until recently. Mueller³ has indexed the phase as hexagonal, AlB_2 ($c32$) structure, with a c/a ratio of about 0.6. The range of homogeneity extends from about Zr_3U to about Zr_5U .

The mechanism by which this phase forms from the beta phase is still unresolved. Furthermore, in zirconium-rich alloys ($>80\%$), both equilibrium epsilon and epsilon prime were formed during the transformation of beta at subcritical temperatures. The epsilon prime, epsilon supersaturated with zirconium, is obviously a transition structure between beta and epsilon. Decomposition of epsilon prime proceeded by the rejection of equilibrium alpha until equilibrium epsilon existed.

A transition lattice is to be expected when a marked difference exists between parent phase and the equilibrium phase, or when complicated atomic movements are required for transformation. Certainly, the two equilibrium phases, beta and epsilon, whose structures are body-centered cubic and hexagonal ($c/a = 0.6$), respectively, fulfill this criterion. An orientation relationship exists between the two equilibrium phases, but it was not possible to determine the orientation relation between beta and the transition phase because the beta was not retained by quenching in this composition range, and high temperature x-ray cameras were unavailable.

In our work, it was observed that epsilon prime formed very rapidly, during a direct quench, but that equilibrium epsilon could also be formed first at temperatures above the ϵ' . The domain sizes encountered were always of the same order of magnitude regardless of the time or temperature of isothermal transformation. From these observations we concluded that the phase formed by some mechanism other than by nucleation and growth involving the deposition of individual atoms. If the latter had been true, a size effect would have been detected as a function of

³ M. Mueller, private communication.

time. The rapid formation precluded the diffusion of zirconium out of the lattice and resulted in supersaturation of epsilon with zirconium.

The apparent speed and diffusionless nature of the reaction suggest the possibility of the so-called "massive" transformation.^{4, 5, 6} The criteria of a massive transformation are rapid rates of formation, intermediate to martensitic and nucleation-growth reactions; the same composition as the parent phase; noncoherency; and a disregard for prior parent grain boundaries, i.e., noncoherent interface movement involving the consumption of neighboring grains. Although the latter was not definitely discernible, the other criteria were noted.

It appears that the alloy Mr. Kearns described formed equilibrium epsilon by a nucleation and growth process, and that the author's alloys formed a supersaturated epsilon by some process intermediate to martensitic and nucleation-growth processes, in addition to isothermal formation of epsilon by normal nucleation and growth.

The reason for this difference in alloys of different uranium content is uncertain. It appears that a critical composition range is required to form supersaturated epsilon, and that alloys both richer or poorer in uranium than this critical composition range formed equilibrium epsilon by nucleation and growth.

A complete answer to Mr. Kearns's question would require a detailed knowledge of the mechanism of transformation. Inasmuch as this system is not readily amenable to fundamental study it is difficult to disentangle the many simultaneous reactions and to discern the mechanism by which epsilon forms.

⁴ A. J. Phillips, "The Alpha-Beta Transformation in Brass," *Transactions, American Institute of Mining and Metallurgical Engineers*, Vol. 89, 1930, p. 196.

⁵ A. B. Greninger, *Transactions, American Institute of Mining and Metallurgical Engineers*, Vol. 133, 1939, p. 204.

⁶ D. Hull and R. D. Garwood, "The Diffusionless Transformation of Metastable Beta-Brass," Paper from *The Mechanism of Phase Transformations in Metals*, Institute of Metals, London, 1956, p. 219.

TRANSFORMATION KINETICS AND MECHANICAL PROPERTIES OF Zr-Ti AND Zr-Sn ALLOYS

By R. F. DOMAGALA, D. W. LEVINSON AND D. J. MCPHERSON

Abstract

Three Zr-Ti and three Zr-Sn alloys based on sponge zirconium were prepared by arc melting and forging. Transformation kinetics of these alloys were investigated. The decomposition $\beta \rightarrow \alpha$ occurred so rapidly it was not possible to construct TTT curves. The Zr-Ti compositions, prototypes of α and β isomorphous alloys, demonstrated a general lack of response to heat treatment. Significant improvements in impact strength and optimum conditions for other mechanical properties were developed by finish-forging 5 and 15% titanium alloys in the $\alpha + \beta$ field. A correlation between hardness and tensile strength was observed.

The peritectoid prototype alloys, zirconium-4, 7.5 and 11% tin, were subjected to several heat treatments designed to establish their response characteristics. The 4% tin composition showed promise as a potentially weldable material; however none of the alloys qualify as "heat treatable" alloys. (ASM International Classification: N6, N7, Q general, Zr, Ti, Sn)

INTRODUCTION

THIS PAPER presents a portion of the result of a program (1,2)¹ designed to systematically study the kinetics of transformation and related mechanical properties of prototype Zr-X binary alloys. The object of this program was to provide a sound basis for a scientific approach to the realization of optimum properties in binary zirconium alloys. Alloys of Zr-Mo (eutectoid), Zr-Sn (peritectoid) and Zr-Ti (α and β isomorphous) were prepared and studied. The data herein are confined to the Zr-Sn and Zr-Ti prototype alloys. The eutectoid type alloys have been discussed previously (3).

MATERIALS AND PROCEDURES

Sponge zirconium (Hf-free) in the form of $-\frac{1}{2}$ inch \pm 40 mesh pieces was used to prepare all ingots. The arc-melted hardness of a

¹ The figures appearing in parentheses pertain to the references appended to this paper.

A paper presented before the Thirty-Ninth Annual Convention of the Society, held in Chicago, November 4-8, 1957. Of the authors, R. F. Domagala is Research Metallurgist, D. W. Levinson is Supervisor, Nonferrous Section, and D. J. McPherson is Assistant Manager, Metals Research Department, Armour Research Foundation of Illinois Institute of Technology, Chicago. Manuscript received January 10, 1957.

Table I
Summary of Chemical Analyses

Material	Analysis						
	% O	% N	H	% C	% Fe	% Ti	% Sn
Zr (as-received)	0.13*	0.02	49 ppm*	0.023	0.042		
Zr (melted and forged)	0.12	0.02	65				
Zr-5 Ti*						5.0	
Zr-15 Ti*	0.15		160			15.0	
Zr-35 Ti*						35.5	
Zr-4 Sn*	0.14	0.01	96				3.9
Zr-7.5 Sn*							7.2
Zr-11 Sn*	0.13						11.1

*Analysis on 100-gram arc-melted ingot

*Analysis on doubly melted and forged rod

small button of this zirconium was found to be VPN 168. An analysis of this material is included in Table I.

Alloy ingots were prepared by a double melting technique. First, three 5-pound ingots of each alloy composition were arc-melted in a nonconsumable electrode arc furnace. Charges for these melts were weighed out in 300-gram lots. They were fed into a water-cooled copper melting chamber, a little at a time, by a hopper and feed mechanism which formed an integral part of the furnace assembly. After melting, the ingots were ground to remove any surface defects. A subsequent forging operation was performed to convert the ingots into 1-inch diameter rods. The forged rods were centerless ground to eliminate all surface contamination. The bars were then threaded and tapped to permit joining and remelting of each composition into a single ingot by the consumable electrode melting technique.

Open anvils were employed for all forging operations, specimens being preheated in an electric furnace. The open anvil technique was necessary because of the volume of scale which formed during forging. This scale caused serious surface defects in the pieces when a final swage-forge operation was attempted. The furnace temperatures employed during forging ranged from 1095 °C (2000 °F) to a maximum of 1235 °C (2250 °F).

After the second melting operation, the large ingot of each composition was forged to 1-inch diameter. The rod was then cut into calculated lengths to produce, on subsequent forging, an equal number of tensile and impact blanks and a sufficient number of transformation study specimens. For the TTT investigation, rods were forged to $\frac{3}{8}$ -inch diameter and ground to $\frac{3}{16}$ -inch; for tensile bars a $\frac{5}{8}$ -inch diameter rod was formed; for impact specimens the stock was forged to $\frac{5}{8}$ -inch square.

Attempts to establish TTT charts principally utilized resistometric techniques. It has been demonstrated for titanium and zirconium base alloys (3,4,5) that the decomposition of the beta phase is associated with a significant change in resistivity. It was also shown that a TTT

diagram can be constructed by carefully following these changes in a plot of resistivity versus annealing time for specimens isothermally quenched from the beta field. Such evaluation of resistivity data must be verified initially by metallographic checks.

Tensile and impact blanks were heat treated after transformation kinetics were investigated. Treatments included various quenches from the beta field as well as isothermal quench and quench and reheat anneals. One tensile and one impact bar of each alloy were always treated together; never more than one such set was treated at a time. Specimens were handled in one of three ways:

1. For short time isothermal quench anneals the test blanks were attached to titanium rods by means of molybdenum wire and "beta-ized" in a Globar furnace under a dynamic helium atmosphere for 30 minutes. The samples were then isothermally quenched into a deoxidized lead bath or second furnace (depending upon the temperature) and annealed for the desired time followed by water quenching.
2. For long time isothermal anneals the entire treatment including the "beta-izing" was conducted with the specimens in evacuated Vycor or Quartz bulbs. The beta treating time was increased to 45 minutes and a water quench at the conclusion of the anneal was standard.
3. Quench and reheat treatments were made by "beta-izing" bare specimens in a helium atmosphere as in No. 1 above. After water quenching from the beta field, the blanks were sealed in evacuated bulbs, annealed and water-quenched.

Standard $\frac{1}{4}$ -inch shoulder type tensile and "V" notch Charpy impact specimens were machined from heat treated blanks, $\frac{5}{8}$ -inch round and $\frac{5}{8}$ -inch square, respectively.

The metallographic techniques employed in the program were standard. Button heads of tested tensile bars were rough polished down to 0000 grit silicon carbide paper. The samples were then electropolished. A solution containing 59% methyl alcohol, 35% butyl cellusolve and 6% perchloric acid was used. Current densities of ~ 1 ampere per square inch were maintained for 30 seconds. Finally, the samples were etched with a solution of $\sim 10 - 20\%$ HNO_3 and $10 - 20\%$ HF in glycerine.

RESULTS AND DISCUSSION

Pure zirconium, as well as many dilute zirconium alloys, may transform on quenching from the high temperature beta phase (b.c.c.) to the low temperature alpha phase (h.c.p.) with extreme rapidity. In zirconium alloys, when a needle-like martensitic configuration occurs, the term alpha-prime (α') is used to describe the transformation structure.

Table II
Mechanical Property Data for Sponge Zirconium

Treatment	UTS (psi)	Elongation %	Reduction in Area %	Impact Strength (ft-lbs)	VPN (20 Kg)
1025 °C WQ	109,000	13	40	11.5	282
1025 °C AC	100,000	17	41	3.5	204
1025 °C FC	74,000	12	21	4.5	161
1025 °C WQ					
900 °C-60 minutes WQ	101,000	14	36	6.0	230
1025 °C					
900 °C-60 minutes WQ	84,800	18	48	12.5	216
1025 °C WQ					
750 °C-1000 minutes WQ	73,700	17	32	9.0	172
1025 °C					
750 °C-1000 minutes WQ	79,400	18	35	—	186
Forged at 900 °C from ½-¼ inch					
900 °C-60 minutes—>AC	79,400	16	40	2.0	199

With increasing alloy content in certain zirconium systems, the high temperature beta phase may finally be retained on quenching from above the $\beta/\alpha + \beta$ boundary. When such retained beta structures are subsequently reheated or transformed by step-quenching below the $\beta/\alpha + \beta$ boundary, equilibrium phases are formed which may be alpha or alpha plus another phase (compound and/or beta).

In view of the impurity content of all sponge zirconium and its possible influence on mechanical properties, a heat treatment versus property study for unalloyed sponge was made. Tensile and impact properties were obtained for material processed in an identical manner to the alloy ingots so a better comparison could be made.

The sponge zirconium ingot was prepared by melting in the non-consumable electrode furnace. The absence of alloying agents precluded the necessity for double melting and the ingot was, therefore, forged directly to rods for tensile and impact blanks.

Gas analysis of the forged rod is included in Table I. Mechanical property data for the sponge zirconium ingot are shown in Table II. Some variation in tensile properties, impact strength and hardness was observed; however, a generally ductile condition was preserved regardless of treatment. The 900 °C (1650 °F) level at which some of the specimens were treated lies in the $\alpha + \beta$ field for sponge zirconium. The $\alpha \rightarrow \beta$ transformation temperature for pure zirconium is ~ 865 °C (1590 °F). A metallographic study of slices of the forged rods which were annealed at temperatures between 700 and 1025 °C (1290 and 1877 °F) showed the transformation "range" to extend from ~ 800 to ~ 975 °C (1470 to 1787 °F). The microstructural appearance of the specimens varied from a martensitic (α') type structure to a coarse alpha configuration, depending on the annealing treatment. The α' structure provided the strongest condition.

Zirconium-Titanium Alloys

Titanium and zirconium form a complete series of α as well as β

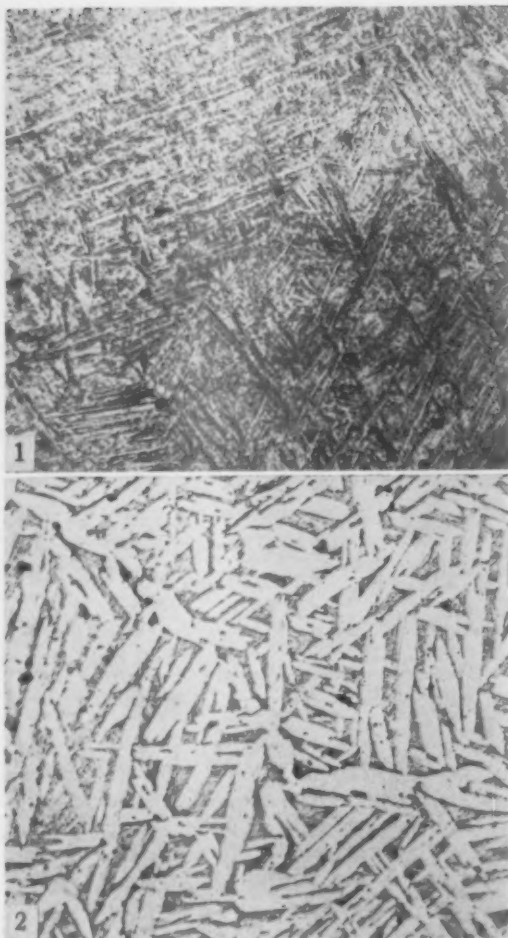


Fig. 1—Zr—5% Titanium 950 °C (1740 °F) WQ. A completely transformed beta structure (α'). $\times 250$.

Fig. 2—Zr—5% Ti. 950 °C (1740 °F) 800 °C (1470 °F), 1000 min. WQ. After a long hold at 800 °C, the alpha particles have grown in size. The matrix is α' . $\times 250$.

solid solutions (6). A narrow $\alpha + \beta$ field drops from the transformation temperature of zirconium (865 °C) to a minimum of ~ 535 °C at 35% titanium. With sponge base alloys, this nominally narrow $\alpha + \beta$ field was somewhat broadened, especially at low (5%) titanium levels. In

Table III
Mechanical Property Data for Zr-5% Ti Alloy

Treatment	UTS (psi)	Elongation (%)	Reduction in Area (%)	Impact Strength (ft-lbs)	VPN (20 Kg)
950°C WQ	97,500	15	41	10.0	225
950°C AC	83,900	23	42	3.5	193
950°C FC	76,700	8	12	3.0	184
950°C					
800°C-5 minutes WQ	94,100	18	28	14.0	216
950°C					
800°C-180 minutes WQ	88,400	24	50	10.0	225
950°C WQ					
800°C-180 minutes WQ	92,000	10	37	10.0	209
950°C					
800°C-1000 minutes WQ	86,000	24	47	12.0	218
950°C					
700°C-5 minutes WQ	88,700	21	46	11.0	243
950°C					
700°C-180 minutes WQ	85,000	15	29	12.0	220
950°C					
700°C-2500 minutes WQ	82,500	21	35	10.0	197
950°C					
650°C-1000 minutes WQ	80,700	22	43	13.0	197
950°C					
650°C-1000 minutes WQ	93,700	15	40	9.0	213
950°C					
600°C-5 minutes WQ	88,500	19	38	13.0	226
950°C					
600°C-180 minutes WQ	88,700	18	43	12.0	225
950°C					
500°C-5 minutes WQ	89,200	17	34	14.0	236
950°C					
500°C-180 minutes WQ	86,000	18	31	14.0	243
950°C					
500°C-1000 minutes WQ	81,800	24	28	14.0	195
Forged at 800°C ($\alpha + \beta$) from $\frac{1}{8}$ - $\frac{1}{4}$ inch					
800°C-60 minutes AC				19.5*	204
600°C-180 minutes WQ	90,400	22	49	21.5	
				20.5	209

*Three impact bars tested

the present work, alloys containing 5, 15 and 35% titanium were prepared and tested. Analytical data are shown in Table I.

Resistivity experiments were conducted but failed to yield data which could be used to construct a TTT chart. The as-quenched (from β) resistivity was the same as the resistivity of bars isothermally quenched into the α or $\alpha + \beta$ field and held for times up to one week. Specimens undoubtedly transformed during the isothermal quench and remained essentially unaffected with time (6). Metallographic evaluation of slices from the treated resistivity rods showed that the structures were essentially α' , coarsened to various extents depending upon the temperature and time of isothermal annealing. The shortest tempering treatment was always 0.2 minutes; the transformation $\beta \rightarrow \alpha$ occurs in less than this time and must be followed with dynamic techniques. Although the usual transformation curves were not established, a mechanical property versus heat treatment study was pursued and the results are shown in Tables III, IV and V.

The as-quenched strength and hardness of the 5% titanium alloy

Table IV
Mechanical Property Data for Zr-15% Ti Alloy

Treatment	UTS (psi)	Elongation (%)	Reduction in Area (%)	Impact Strength (ft-lbs)	VPN (20 Kg)
950°C WQ	155,000	2	2	5.0	284
950°C AC	127,000	4	12	5.5	256
950°C FC	113,000	4	4	3.0	255
950°C OQ	150,000	2	2	4.5	273
950°C					
600°C-5 minutes WQ	135,000	4	3	6.0	264
950°C					
600°C-180 minutes WQ	113,000	11	28	6.0	260
950°C					
600°C-1000 minutes WQ	117,400	14	16	8.0	236
950°C					
500°C-5 minutes WQ	140,000	2	2	7.0	279
950°C					
500°C-180 minutes WQ	139,000	2	6	6.0	280
950°C WQ					
500°C-180 minutes WQ	134,000	1	0	3.5	298
950°C					
500°C-1000 minutes WQ	117,000	17	16	6.0	244
950°C WQ					
500°C-1000 minutes WQ	150,000	2	2	4.5	284
950°C					
500°C-10,000 minutes WQ	118,000	11	17	7.0	249
950°C WQ					
500°C-10,000 minutes WQ	143,000	4	4	6.0	268
Forged at 650°C ($\alpha + \beta$) from $\frac{1}{4}$ in					
650°C-60 minutes AC					
500°C-180 minutes WQ	132,000	11	33	10.0	257

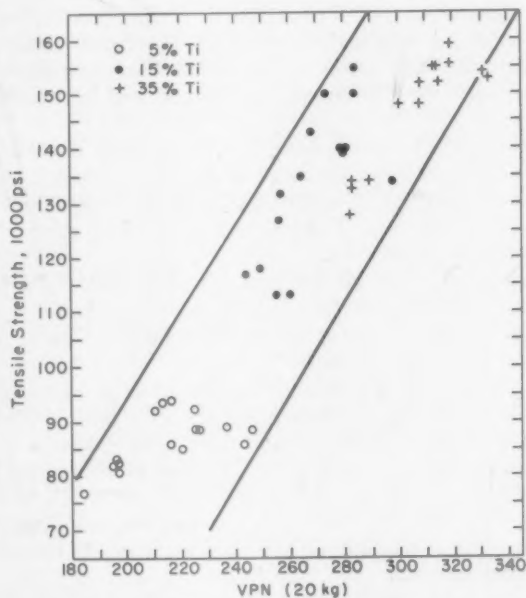


Fig. 3—Correlation Between Hardness and Strength for Zr-Ti Alloys.

Table V
Mechanical Property Data for Zr-3.5% Ti Alloy

Treatment	UTS (psi)	Elongation (%)	Reduction in Area (%)	Impact Strength (ft-lbs)	VPN (20 Kg)
950°C WQ	148,000	3	2	5.5	300
950°C AC	158,500	1	0	3.5	319
950°C FC	128,000	6	12	1.5	282
950°C OQ	155,000	1	1	3.0	314
950°C					
500°C-5 minutes WQ	152,000	1	3	4.0	315
950°C					
500°C-180 minutes WQ	155,000	1	2	3.0	314
950°C					
500°C-1000 minutes WQ	133,000	2	1	2.5	283
950°C					
500°C-10,000 minutes WQ	134,000	3	5	2.5	289
950°C WQ					
500°C-10,000 minutes WQ	152,000	2	1	5.0	308
950°C					
400°C-5 minutes WQ	153,000	1	2	3.5	334
950°C WQ					
400°C-5 minutes WQ	148,000	2	1	3.0	309
950°C					
400°C-180 minutes WQ	154,000	1	0	3.5	331
950°C					
400°C-1000 minutes WQ	134,000	5	2	2.5	283
950°C WQ					
400°C-1000 minutes WQ	159,000	0	0	3.5	319

were slightly higher than those of any of the other specimens. The impact strength and tensile ductilities were correspondingly lower in the as-quenched condition. Furnace or air cooling provided no significant improvement in mechanical properties. Specimens water quenched from the beta field and subsequently reheated were stronger and less ductile than equivalent isothermally quenched and heat treated specimens.

The variation in properties can be attributed to structure. Fig. 1 shows the water-quenched structure of this alloy, which is completely martensitic α' . On quenching to and holding at 800°C (1470°F), α forms and grows; Fig. 2 shows a 5% titanium alloy after 1000 minutes at 800°C (1470°F).

"Transformation" anneals conducted at 700, 650, 600 and 500°C (1290, 1200, 1110 and 930°F) influenced the mechanical properties only slightly. As expected, the longer the annealing time at any level, the more ductile the specimen.

The most beneficial treatment of the 5% titanium alloy was the one shown last in Table III. The tensile and impact blanks which had been forged to $\frac{5}{8}$ -inch (rounds and squares) were reheated to 800°C ($\alpha + \beta$) and forged to $\frac{1}{2}$ -inch stock. The bars were then subjected to a heat treatment consisting of 1 hour at 800°C (1470°F) and 3 hours at 600°C (1110°F). This treatment provided the best compromise of tensile strength and ductility. It also yielded a low hardness and the highest impact strength.

The tensile, impact and hardness data for the 15% titanium alloy are shown in Table IV. There was a general lack of ductility in tensile

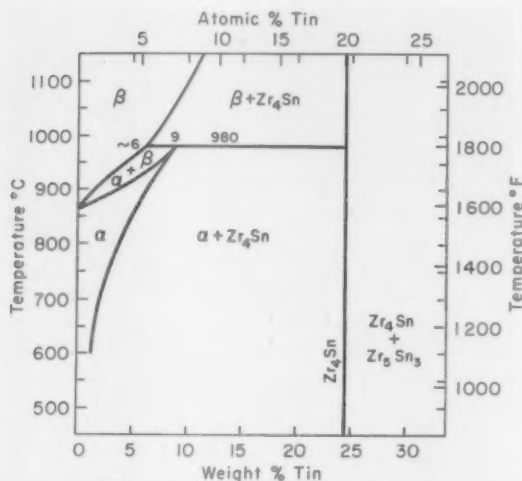


Fig. 4—Partial Diagram Zirconium-Tin System (7).

bars water-quenched from the beta and subsequently reheated. The various cooling rates from beta did not provide any improvement in properties. As with the 5% titanium composition, forging from $\frac{5}{8}$ to $\frac{1}{2}$ -inch in the $\alpha + \beta$ field yielded the best compromise in properties. Again, the highest impact strength was developed by this treatment.

Increases in ductility and decreases in hardness and tensile strength were also experienced with this alloy isothermally annealed below the $\alpha + \beta/\alpha$ boundary. Significant variations in strength and ductility were found according to the length of holding. While the as-quenched specimen had 155,000 psi tensile strength and only 2% elongation, annealing at 500 and 600 °C (930 and 1110 °F) for various lengths of time caused a gradual softening and decrease in strength. After 1000 minutes at 600 °C (1110 °F) the ultimate tensile strength fell to 117,000 psi, while the tensile elongation increased to 14%. The changes in impact strength were slight; an increase from 5 to 8 ft-lbs were observed.

The Zr-35% Ti displayed the same trends as the other two titanium compositions. Insignificant property changes (Table V) were experienced when the specimens were held at 400 or 500 °C (750 or 930 °F) for as long as 3 hours. When the time was increased to 1000 minutes (16 $\frac{2}{3}$ hours), however, a drop in tensile strength to 133,000 psi from the water-quenched value of 148,000 psi was noted. Slight changes in tensile ductility and hardness were also observed, however, usable ductility was not developed in this composition by any heat treatment. A reasonably good correlation between hardness and tensile strength seems to exist for Zr-Ti alloys and is shown in Fig. 3.

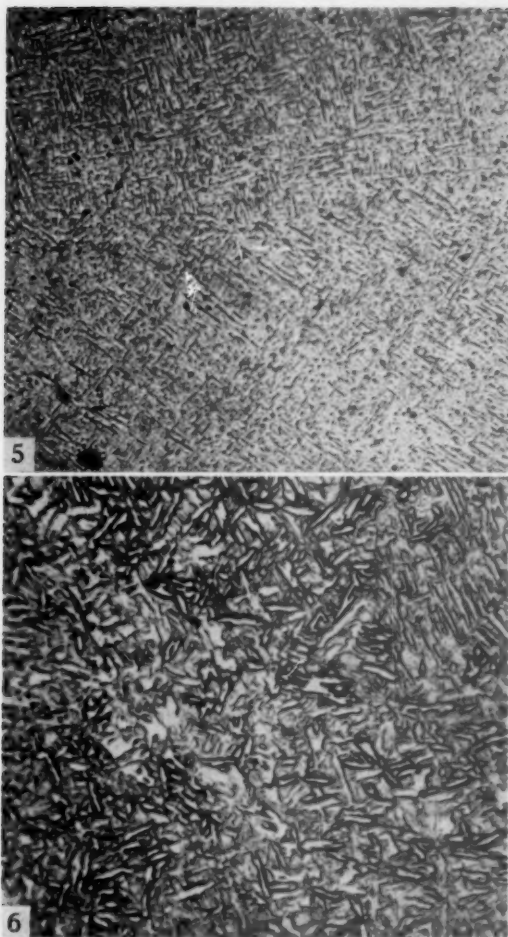


Fig. 5—Zr—4% Sn. 1025 °C (1878 °F) WQ. This alloy has completely transformed on quenching from the beta field. $\times 250$.

Fig. 6—Zr—4% Sn. Forged from $\frac{3}{4}$ to $\frac{1}{4}$ inch at 975 °C (1787 °F) ($\alpha + \beta$). 975 °C—60 min \rightarrow AC + 700 °C (1290 °F) 30 minutes, WQ. An all α structure. $\times 250$.

Zirconium-Tin Alloys

Phase relationships in the zirconium-rich region of this system are shown in Fig. 4. This diagram is based on iodide-base alloys (7). No definitive boundary placement study was carried out with sponge-base

alloys. A cursory survey of the $\beta/\alpha + \beta$ and $\alpha + \beta/\alpha$ lines using only the 4% tin alloy showed a broadening of the $\alpha + \beta$ region (to both higher and lower temperatures).

In the work with these peritectoid prototype alloys, three compositions, nominally 4, 7.5 and 11% tin were employed. Analyses are included in Table I.

An attempt was made to establish transformation curves for the Zr-Sn alloys. While the resistivity of specimens isothermally quenched from the beta field increased with increasing tin content, no major changes in resistivity were encountered in any alloy regardless of the isothermal "transformation" temperature or length of holding time. The shortest transformation anneal conducted was 1 minute. In some cases a very slight downward trend in resistivity was noted at short times (up to 10 minutes), followed by a rise to the original value. Such variations were never great, amounting to only about 2% and were considered to be of no significance toward the construction of a TTT chart. Metallography of slices of the heat treated rods was carried out concurrently. The lack of change in electrical properties was in part corroborated by the appearance of structures. In each alloy, transformation of beta seemed to have occurred with extreme rapidity. Configurations of α' and/or α were always observed.

It seems that the transformation from beta to alpha in these alloys proceeds by the same mechanisms operative in the Zr-Ti compositions. It can only be concluded that whatever the mechanism, the transformation occurs very rapidly and the techniques employed were not sensitive enough to provide data for the construction of a TTT chart.

The intermediate phase Zr_4Sn , an equilibrium component of all three alloys at some temperatures, could never be positively identified in the microstructures, although it must have precipitated during many of the treatments employed. The inability to identify Zr_4Sn stemmed from the presence of rather large quantities of a peppery impurity phase in the alloys. This impurity phase is by no means unknown in zirconium and zirconium-rich alloys; it seemed more prevalent in the 4 and 7.5% tin alloys than in the 11% tin composition. Its appearance, however, somewhat resembled that of equilibrium Zr_4Sn as observed in the original phase diagram determination. Assuming Zr_4Sn did precipitate but could not be metallographically identified because of the peppery phase, the absence of resistivity changes becomes difficult to explain. The only apparent conclusions are that the Zr_4Sn did not precipitate in any of the treatments, or that the quantity of Zr_4Sn present was not great enough to influence the specimen's resistivity. An alternative, which is exceedingly unlikely but should not be overlooked, is that Zr_4Sn precipitates on any quenching operation, in which case neither resistivity nor microstructural changes would be anticipated.

In view of the negative results of the transformation kinetics study,

Table VI
Mechanical Property Data for Zr-4% Sn Alloy

Treatment	UTS (psi)	Elongation (%)	Reduction in Area (%)	Impact Strength (ft-lbs)	VPN (20 Kg)
1025°C WQ	142,000	13	33	7.5	203
1025°C AC	104,000	16	39	—	—
1025°C FC	90,800	15	29	3.5	191
1025°C					
925°C-5 minutes WQ	120,000	17	44	6.5	197
1025°C					
925°C-30 minutes WQ	104,500	19	46	8.5	204
1025°C WQ					
925°C-30 minutes WQ	113,500	16	47	8.0	202
1025°C					
850°C-30 minutes WQ	93,500	18	38	7.0	205
1025°C WQ					
850°C-30 minutes WQ	108,000	14	33	8.5	207
1025°C					
800°C-1000 minutes WQ	94,300	18	40	8.0	191
1025°C					
700°C-5 minutes WQ	122,000	17	37	11.5	207
1025°C					
700°C-30 minutes WQ	110,000	18	42	10.5	208
1025°C					
600°C-1000 minutes WQ	103,000	17	37	7.0	211
1025°C					
500°C-5 minutes WQ	123,000	15	42	7.5	205
1025°C					
500°C-30 minutes WQ	128,000	12	29	10.0	199
1025°C WQ					
500°C-30 minutes WQ	137,000	12	39	9.0	207
1025°C					
500°C-1000 minutes WQ	101,000	17	40	9.5	194
1025°C WQ					
500°C-1000 minutes WQ	133,500	12	34	9.0	215
Forged at 975°C ($\alpha + \beta$) from $\frac{3}{8}$ - $\frac{1}{2}$ inch					
975°C-60 minutes AC					
700°C-30 minutes WQ	98,600	17	45	8.0	203

heat treatment of tensile and impact blanks was aimed at bringing out the property differences which might result from "tempering" during the isothermal holds. The mechanical properties of these alloys are given in Tables VI, VII, and VIII.

The mechanical property data for the 4% tin composition are shown in Table VI. The tensile strengths for the quench and reheat treatments are slightly higher than the strengths for isothermally quenched specimens. Although these modest variations exist, there is essentially little difference between the properties developed by any heat treatment. Forging tensile and impact blanks in the $\alpha + \beta$ field from $\frac{5}{8}$ to $\frac{1}{2}$ -inch offered no change in mechanical properties. The general retention of ductility and small hardness variation makes this alloy attractive as a weldable material if not as a heat treatable alloy.

Two typical microstructures are shown in Figs. 5 and 6.

The Zr-7.5% Sn specimens subjected to quench and reheat treatments were invariably stronger and harder than isothermally quenched specimens. The data are given in Table VII. Fig. 7 is a typical microstructure for this alloy.

The mechanical property data for the Zr-11% Sn composition are

Table VII
Mechanical Property Data for Zr-7.5% Sn Alloy

Treatment	UTS (psi)	Elongation (%)	Reduction in Area (%)	Impact Strength (ft-lbs)	VPN (20 Kg)
1125°C WQ	156,000	4	9	6.0	347
1125°C AC	124,000	10	23	4.0	275
1125°C FC	114,000	10	18	4.0	251
1125°C					
1000°C-5 minutes WQ	135,000	12	30	3.0	279
1125°C					
1000°C-30 minutes WQ	156,500	2	1	3.0	294
1125°C WQ					
1000°C-30 minutes WQ	146,000	10	30	7.5	317
1125°C					
950°C-5 minutes WQ	137,000	3	0	2.0	300
1125°C					
950°C-180 minutes WQ	120,000	19	22	4.0	304
1125°C					
900°C-30 minutes WQ	124,000	7	9	5.0	267
1125°C					
850°C-5 minutes WQ	114,000	13	19	3.0	242
1125°C					
850°C-180 minutes WQ	117,000	14	21	6.0	253
1125°C					
800°C-30 minutes WQ	114,000	16	33	6.5	272
1125°C					
700°C-5 minutes WQ	135,000	11	21	7.0	293
1125°C WQ					
700°C-5 minutes WQ	166,000	9	28	6.0	343
1125°C					
700°C-30 minutes WQ	123,000	16	38	7.5	275
1125°C					
700°C-1000 minutes WQ	116,000	15	29	4.0	246
1125°C WQ					
700°C-1000 minutes WQ	153,000	7	19	4.5	325
1125°C					
600°C-30 minutes WQ	119,000	14	29	7.5	289
1125°C					
500°C-5 minutes WQ	119,000	13	24	5.5	305
1125°C					
500°C-1000 minutes WQ	124,000	12	17	4.0	270

Table VIII
Mechanical Property Data for Zr-11% Sn Alloy

Treatment	UTS (psi)	Elongation (%)	Reduction in Area (%)	Impact Strength (ft-lbs)	VPN (20 Kg)
1250°C WQ	142,000	13	22	4.5	327
1250°C AC	150,000	7	13	4.0	321
1250°C FC	113,500	1	0	1.5	286
1250°C					
1100°C-30 minutes WQ	138,000	11	24	2.5	332
1250°C					
1050°C-5 minutes WQ	136,000	12	22	3.0	304
1250°C					
1050°C-180 minutes WQ	136,000	11	23	2.5	309
1250°C					
950°C-5 minutes WQ	131,000	13	31	2.5	301
1250°C					
950°C-30 minutes WQ	132,000	7	1	4.0	289
1250°C					
950°C-180 minutes WQ	125,000	11	17	2.5	282
1250°C					
800°C-5 minutes WQ	132,000	5	5	3.0	301
1250°C					
800°C-180 minutes WQ	121,000	2	3	1.5	282
1250°C					
600°C-5 minutes WQ	139,000	6	5	4.0	303
1250°C					
600°C-180 minutes WQ	140,000	8	9	3.5	304
1250°C					
500°C-30 minutes WQ	142,000	9	11	3.5	295

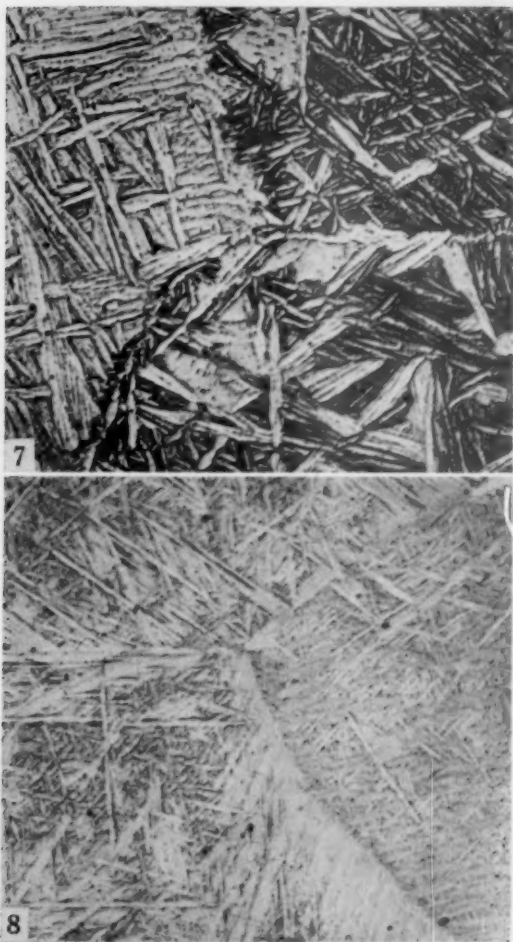


Fig. 7—Zr—7.5% Sn. 1125 °C→500 °C, 1000 minutes, WQ.
An intimate $\alpha + \text{Zr}_4\text{Sn}$ structure. $\times 250$.

Fig. 8—Zr—11% Sn. 1250 °C→1100 °C, 30 minutes, WQ. This specimen was quenched into the $\beta + \text{Zr}_4\text{Sn}$ field. Large α or α' needles have formed. They must result from the final quench. $\times 250$.

shown in Table VIII. This alloy provided the smallest range of properties among the three tin-bearing compositions.

Regardless of the treatment conducted in the $\beta + \text{Zr}_4\text{Sn}$ field, identical properties were observed and the structure shown in Fig. 8 is

typical of those observed for this condition. A rather unusual transformation structure is present. Positive interpretation of this structure is difficult. It would seem that on quenching from beta into the $\beta + \text{Zr}_4\text{Sn}$ field, something occurs which permits the formation of rather large alpha areas on the final quench. It is possible that a precipitation of small particles of Zr_4Sn nucleates alpha. Alternatively, it may be that the step-quench technique effectively slows the cooling rate so that the alpha particles may grow in size.

SUMMARY

Transformation kinetics and response to heat treatment of Zr-Ti and Zr-Sn binary alloys were investigated. The results of this study may be itemized as follows:

1. No TTT diagram could be constructed for alloys containing 5, 15 and 35% titanium. The $\beta \rightarrow \alpha$ transformation occurs rapidly, probably by a martensitic mechanism (6).
2. Isothermal quench and quench and reheat annealing treatments performed on mechanical test blanks of the three Zr-Ti alloys always resulted in a change from as-quenched properties to a weaker, more ductile condition. Appreciable ductilities were developed in the 5 and 15% titanium alloys. A significant improvement in the impact strengths of these two compositions was found for bars finish-forged in the $\alpha + \beta$ field. A hardness-tensile strength correlation for these three alloys was established.
3. No TTT curves could be constructed for the Zr-Sn peritectoid prototype alloys. The decomposition of β into α seemed to proceed as rapidly as in the Zr-Ti alloys.
4. The 4% tin alloy exhibited a very small range of hardness but a measurable variance in tensile properties. This composition holds some promise for certain applications despite (or because of) its lack of heat treatability.
5. The 7.5% tin alloy exhibited the widest range of properties of the Zr-Sn alloys. The smallest array of mechanical properties was shown by the 11% tin composition.

ACKNOWLEDGMENTS

The authors wish to express their thanks to the Atomic Energy Commission, sponsors of this work under contract No. AT(11-1)-315, for permission to publish this paper. Special thanks are due to L. Murphy for the metallographic work and to H. L. Nurnberg, Project technician.

References

1. R. F. Domagala and D. J. McPherson, "A Study of the Mechanisms of Heat Treatment of Zirconium-Base Alloys," United States Atomic Energy Commission Report No. 2, Summary (C00-207), Aug. 3, 1955.
2. R. F. Domagala and D. W. Levinson, "A Study of the Mechanisms of Heat Treatment of Zirconium-Base Alloys," United States Atomic Energy Commission Report No. 3, Summary (C00-211), July 17, 1956.
3. R. F. Domagala, D. W. Levinson and D. J. McPherson, "Transformation Kinetics and Mechanical Properties of Zr-Mo Alloys," Submitted for Publication American Institute of Mining and Metallurgical Engineers, Aug. 1956.
4. D. J. DeLazaro and D. W. Levinson, "Correlation Between Microstructure and Resistivity of Transforming Ti-Mn Alloys," *Transactions, American Institute of Mining and Metallurgical Engineers*, Vol. 200, 1954, p. 1089.
5. D. W. Levinson and W. Rostoker, "Structural Changes of Commercial Titanium-Base Alloys on Heat Treatment," WADC-TR-54-244, May 1954.
6. P. Duwez, "Allotropic Transformation in Ti-Zr Alloys," *Journal of Institute of Metals*, Vol. 80, 1952, p. 525.
7. D. J. McPherson and M. Hansen, "The System Zirconium-Tin," *TRANSACTIONS, American Society for Metals*, Vol. 45, 1953, p. 915.

DISCUSSION

Written Discussion: By A. H. Roberson, United States Department of the Interior, Bureau of Mines, Region 1, Albany, Oregon.

The authors have presented some interesting data on the mechanical properties of titanium-zirconium alloys which supplement and extend earlier results developed by the Bureau of Mines.³

The fact that some of the Bureau alloys which were water quenched or furnace cooled from 950 °C (1740 °F) exhibited lower ultimate strengths and greater elongation may have been due to the sheath-forging of all specimens.

The data presented today was derived from specimens that had been forged in air at 1095 to 1235 °C (2000 to 2255 °F).

It has been our experience that a 35 weight % titanium alloy, (50 a/o) has high affinity for oxygen and nitrogen. It would appear that the high temperature exposure to air may have resulted in more than a surface contamination, which could not be removed by grinding.

The heat treat schedule outlined on page 3 of the paper includes protection in a dynamic helium atmosphere. It is suggested that unless the helium had been purified the alloys might gather any residual oxygen or nitrogen from the gas. As a result, some hardening may have taken place.

Authors' Reply

Admittedly, no oxygen or nitrogen analyses were run for the Zr-35% Ti alloy. No contamination was suspected for the following reasons:

- (a) No alpha case was observed metallographically on any of the tensile test specimens or any of the resistivity specimens.
- (b) If some surface contamination did occur during heat treatment, it should have been removed during machining inasmuch as the 3/4-inch round bars were machined to 1/4-inch at the test section.

³ E. T. Hayes, A. H. Roberson and O. G. Paasche, "Zirconium-Titanium System Constitution Diagram and Properties," U. S. Bureau of Mines Report of Investigation 4826, November 1951.

- (c) The lower ductility and increased strength for the 35% Ti composition follows the pattern which is expected of the Zr-Ti alloys.
- (d) Analysis of the Zr-15% Ti alloy showed no oxygen contamination.

Although the reference cited by the discussors was not immediately available to the authors, the work of Hayes, Roberson and Paasche is cited in the book, *Metallurgy of Zirconium*, by B. Lustman and F. Kerze (p. 514). The mechanical property data presented therein are in fairly good agreement with the results of this work.

SOLUBILITY OF CARBON IN THORIUM

BY ROBERT MICKELSON AND DAVID PETERSON

Abstract

The solubility of carbon in thorium has been investigated and the limit of solubility has been determined at four temperatures. Thorium-carbon samples, containing from 0.025 to 1.23 weight percent carbon, were prepared by arc melting sponge thorium with high purity graphite. X-ray data, hardness readings, and metallographic examinations of heat treated specimens were combined to obtain the following solubility limits: room temperature—0.35% carbon, 800 °C—0.43% carbon, 1018 °C—0.57% carbon, and 1215 °C—0.91% carbon. (ASM International Classification N12 p; Th, C.)

INTRODUCTION

CARBON has been found to be the most effective alloying element in changing and improving the mechanical properties of thorium metal. Peterson (1)¹ reports that additions of carbon to thorium increase the hardness and tensile strength without seriously reducing ductility. The investigation of the solubility of carbon in thorium was undertaken to provide basic information of value in understanding the effect of carbon on the physical properties of thorium.

The thorium-carbon system has been investigated by Chiotti (2), who reports that thorium monocarbide is the stable phase in equilibrium with thorium at room temperature. Thorium and thorium monocarbide are reported to be completely soluble in the liquid and solid states at elevated temperatures. The exact limits of the solubility of carbon in thorium were not extensively investigated. Saller (3) investigated the solubility of carbon in thorium and found considerable variation between the results of x-ray diffraction and metallographic examination. His conclusion was that the metallographic results were more accurate.

EXPERIMENTAL

Preparation of Samples

The thorium-carbon samples used in this investigation were prepared by arc melting in a water-cooled copper crucible. The crucible

¹ The figures appearing in parentheses pertain to the references appended to this paper.

The authors, Robert Mickelson and David Peterson are associated with the Institute for Atomic Research, Department of Chemistry, Iowa State College, Ames, Iowa. Manuscript received June 15, 1956.

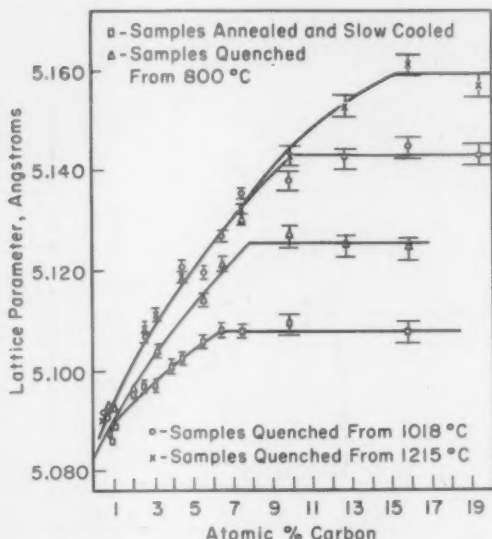


Fig. 1—Lattice Constants of Thorium-Carbon Samples with Various Heat Treatments.

was evacuated to less than 0.1 micron and filled with purified helium. A piece of zirconium metal was then melted to remove any oxygen or nitrogen still present in the furnace. The samples, which weighed about 100 grams, were prepared by melting Ames sponge thorium and dissolving high purity graphite in the molten metal. Each sample was turned and remelted three times to insure homogeneity.

The thorium sponge and the thorium-carbon samples were chemically analyzed for carbon and nitrogen. The thorium sponge contained 0.026 weight percent carbon and 0.026 weight percent nitrogen. The average nitrogen content of the seventeen samples was 0.032 weight percent. The thorium sponge and five thorium-carbon samples were spectrographically analyzed for eleven different impurities.

Heat Treatment

Samples used to determine the room temperature solubility limit were heated in a quartz tube evacuated to less than 0.02 micron. The samples were held at 900 °C (1650 °F) for 6 hours and cooled to room temperature over a period of 5 days.

A molybdenum tube resistance furnace was adapted to quench samples into molten Wood's metal placed on the furnace base directly beneath the cylindrical heater. The heating was done under a vacuum of 0.4 micron or lower. The samples were supported on a thorium disk

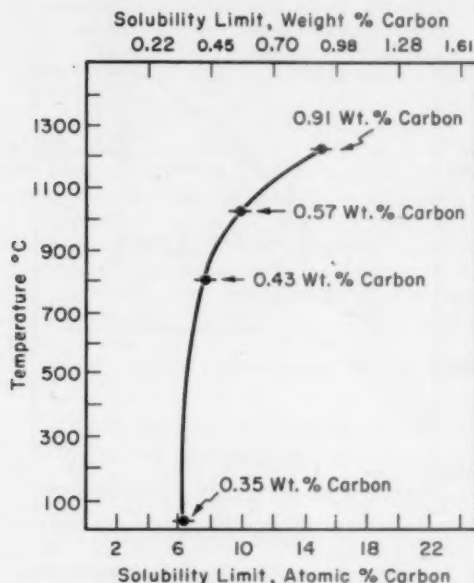


Fig. 2—Solubility of Carbon in Thorium of Various Temperatures.

which was allowed to fall into the quenching vessel with the samples. Since heating and quenching were done under vacuum and the samples were in contact only with thorium, the chances for contamination of the samples were reduced. The samples were held at temperature for 30 minutes or more before quenching. The Wood's metal was maintained at 80–100 °C (175–210 °F).

X-ray Study

Lattice parameter determinations were made on a North American Phillips back-reflection camera which has a diameter of 12 centimeters. Samples containing less than 0.1 weight percent carbon were hot-rolled to $\frac{1}{16}$ inch sheet and shaped to the circumference of the camera before undergoing heat treatment. Samples containing more than 0.1% carbon were too brittle to roll and blocks $\frac{1}{16}$ inch thick and $\frac{1}{4}$ inch wide were used in the x-ray camera. In every instance, before the sample was exposed it was vigorously pickled in dilute nitric acid which contained a small amount of hydrofluoric acid. This pickling was performed to remove the surface metal which might have become contaminated during heat treatment.

Thorium oxide lines appeared on most of the x-ray photographs. These lines were more sharply defined than the thorium lines and, con-

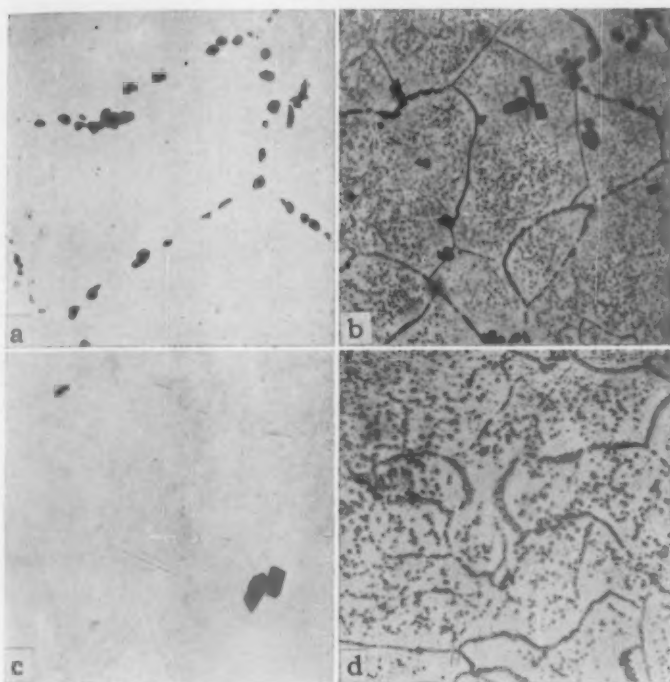


Fig. 3—Thorium-Carbon Samples. Nitric acid etch. $\times 500$. (a)—0.30% carbon. Slow-cooled. (b)—0.408% carbon. Slow-cooled. (c)—0.350% carbon. Quenched from 800 °C. (d)—0.736% carbon. Quenched from 800 °C.

sequently, they could be measured with greater accuracy. Thus, thorium oxide was used as an internal standard to eliminate systematic errors in the determination of the lattice constant. If the thorium oxide lines indicated that there was an appreciable error in a given film, this error was eliminated by a graphical extrapolation against $\sin^2 \theta$.

The samples of thorium containing more than 0.5% carbon were very coarse-grained, particularly when quenched from the higher temperatures. As a result, the x-ray diffraction patterns were very spotty and the accuracy of film measurement was poor. Since massive samples were used, there was no way of eliminating this difficulty.

A maximum random error in the measurement of the lattice constant was calculated from a reasonable assumed error in measuring the film. A larger assumed error was used for samples containing more than 0.5% carbon because of the spotty lines from these samples. The systematic error in many of the determinations was less than this maximum random error and, in these cases, no correction was made.

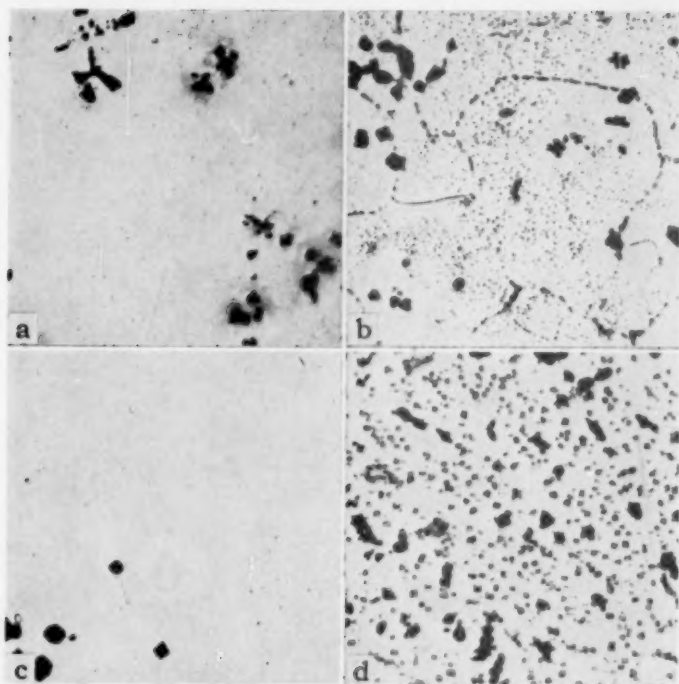


Fig. 4—Thorium-Carbon Samples. Nitric acid etch. $\times 500$. (a)—0.408% carbon. Quenched from 1018 °C. (b)—0.736% carbon. Quenched from 1018 °C. (c)—0.736% carbon. Quenched from 1215 °C. (d)—0.959% carbon. Quenched from 1215 °C.

Metallographic Examination

The samples for metallographic examination were ground on 320, 400, 500, and 600 grit paper. They were polished with Linde B on Microcloth. Etching was used to improve the contrast between thorium monocarbide and thorium. The presence of thorium carbide could usually be detected before etching, but the improved contrast made the pictures clearer. The etching solution was 2 molar nitric acid, 0.02 molar hydrofluoric acid, and 0.005 molar thorium nitrate. The etching solution was applied by swabbing for ten to thirty seconds.

RESULTS AND DISCUSSION

The spectroscopic analyses of the thorium metal used in preparing the samples and of a number of the samples are given in Table I. Most of these results are an upper limit since the actual content was below the limit of measurement of the methods used. The chemical analyses of the thorium-carbon samples for nitrogen and carbon are presented in

Table I
Spectroscopic Analysis of Thorium-Carbon Samples

Sample Number	Impurity Content ppm										
	Be	Al	Ca	Mg	Si	Fe	Mn	B	Cd	Zn	Zr
Sponge	<20	<25	<50	<20	<50	40	<20	0.75	<0.2	110	<110
1	<20	<25	<50	<50	<50	35	<20	<0.3	0.3	<10	<100
2	<20	<25	<50	<50	<50	30	<20	<0.3	<0.2	<10	<100
3	<20	<25	<50	<20	<50	105	<20	0.45	2.1	12	<100
5	<20	<25	<50	<20	<50	35	<20	<0.3	0.3	<10	<100
6	<20	<25	<50	<20	<50	45	<20	<0.3	<0.2	<10	<100

Table II
Analysis and Hardness of Thorium-Carbon Samples

Sample Number	Nitrogen Content, ppm	Carbon Weight Percent	Content Atomic Percent	Rockwell A Hardness			
				Heated at 900 °C and slow cooled	Quenched from 800 °C	Quenched from 1018 °C	Quenched from 1215 °C
1	471	0.025	0.47	23	—	24	25
2	344	0.054	1.03	—	27	29.5	—
3	344	0.026	0.49	26	—	—	28
4	203	0.035	0.67	—	—	—	—
5	482	0.042	0.81	—	—	29	—
6	241	0.104	1.98	—	38	36	—
7	301	0.132	2.49	—	—	—	43.5
8	1,015	0.163	3.06	38	44	48.5	50
9	332	0.208	3.87	41.5	—	48.5	—
10	293	0.239	4.44	44	—	52	54
11	253	0.300	5.50	46	49	51	—
12	224	0.350	6.36	50	54	55.5	—
13	143	0.408	7.37	—	—	60	—
14	215	0.556	9.82	53	—	62.5	—
15	178	0.736	12.59	55	58.5	64	—
16	168	0.959	15.78	57.5	60	64	—
17	182	1.228	19.40	—	—	66.5	—

Table III
Lattice Constants of Thorium-Carbon Samples

Sample Number	Carbon Content, Weight Percent	Heated at 900 °C and Slow-Cooled	Lattice Parameter, Angstroms		
			Quenched from 800 °C	Quenched from 1018 °C	Quenched from 1215 °C
1	0.025	5.0871	5.0877	5.0920	5.0900
2	0.054	5.0886	5.0922	—	—
3	0.026	5.0871	5.0875	—	5.0867
4	0.035	5.0873	5.0926	5.0905	—
5	0.042	5.0859	—	—	—
6	0.104	5.0953	5.0958	—	—
7	0.132	5.0964	—	5.1064	5.1075
8	0.163	5.0966	5.1033	—	5.1107
9	0.208	5.1004	—	—	—
10	0.239	5.1020	—	5.1203	5.1183
11	0.300	5.1058	5.1140	5.1196	—
12	0.350	5.1077	5.1211	5.1272	5.1216
13	0.408	5.1077	5.1305	5.1356	5.1325
14	0.556	5.1092	5.1270	5.1380	5.1433
15	0.736	—	5.1250	5.1425	5.1532
16	0.959	5.1077	5.1243	5.1447	5.1613
17	1.228	—	—	5.1436	5.1573

Table II. The oxygen content of these samples was not determined but must have been above the solubility limit since thorium oxide was observed in the microstructures of all these samples. The thorium oxide

content was probably between 1 and 2%. In graphing the results of this investigation, the error in the carbon analysis was assumed to be 5% of the absolute value of the carbon content.

The solid solubility limits of carbon in thorium were established from the x-ray data and confirmed by microscopic examination. The observed lattice constants of the samples after various heat treatments are reported in Table III and are plotted in Fig. 1 against the carbon content. The solubility limit at each temperature was taken as the carbon content above which there was no further increase in lattice constant. The experimental error is indicated by horizontal and vertical lines through each point.

The solid solubility limits of carbon in thorium are shown in Fig. 2 as a function of temperature.

The solubility limits established by x-ray methods were checked by microscopic examination. Thorium carbide could be identified as small particles which tend toward a square form. The thorium oxide particles were much larger and darker in color.

Figs. 3 and 4 show samples above and below the solubility limit at each temperature. These pictures show the precipitation of thorium carbide in samples above the solubility limits.

An anomalous effect was observed in samples which contained less than 0.35% carbon and hence were not saturated with carbon. These quenched samples showed an increase in lattice constant over the slow-cooled samples of the same carbon content, and, up to 1000 °C (1830 °F), the higher quenching temperatures resulted in an increased lattice constant. A similar effect was observed in the increased hardness of unsaturated samples quenched from various temperatures. The most likely explanation is that the samples were saturated with nitrogen at room temperature and heating to higher temperatures caused more thorium nitride to dissolve in the thorium. Thorium nitride has been reported by Chiotti (2) to be appreciably soluble in thorium at elevated temperatures.

CONCLUSIONS

The solubility of carbon in thorium was established as 0.35% at room temperature, 0.43% at 800 °C, 0.57% at 1018 °C, and 0.91% at 1215 °C. Increasing the carbon content causes an increase in the hardness of thorium by solid solution hardening. An impurity in these samples, believed to be nitrogen, caused an increased lattice constant and hardness of quenched alloys below the carbon solubility limit.

References

1. D. Peterson and R. F. Russi, unpublished work, Iowa State College, Ames, Iowa, 1952.
2. P. Chiotti, "Thorium-Carbon System," Atomic Energy Commission Report No. AECD-3072, 1950.
3. L. H. Grenell and H. A. Saller, "The Solubility of Carbon in Thorium," Atomic Energy Commission Report No. TID-1071, 1946.

DISCUSSION

Written Discussion: By W. C. Lilliendahl, advisory engineer, Metals Research, Westinghouse Electric Corporation, Bloomfield, New Jersey.

A determination of the solubility of carbon in thorium is of metallurgical significance because this is one of the few impurities which in small amounts produce lattice hardening by interstitial solution.

The authors of this paper have presented extensive data to support their conclusions. The actual solubilities are determined from the expansion of lattice parameters and the range of solubilities determined metallographically by the appearance of a carbide phase.

There are a few points which suggest that the results are indicative of a three component system probably thorium, thorium carbide and thorium nitride.

Chiotti,¹ has identified two carbides of thorium and also shown that nitrogen dissolves in thorium metal and that the solubility increases with increasing temperature. This fact has been recognized by the authors.

Referring to Table II of the text the nitrogen content of the samples varies from 143 to 1015 ppm with an average nitrogen content of 320 ppm. As 600 ppm nitrogen corresponds to approximately 1 atomic % and the contribution to lattice expansion is of the same order of magnitude as carbon it would appear that its effect would be significant. The authors do not clarify this point in their article.

It would also seem that if a third component were not present the plateaus shown in Fig. 1 of the text would emanate from a single rising curve instead of three separate branches as shown in the drawing.

Regarding the metallographic studies on the rejection of a carbide phase at grain boundaries, Lagerberg and Joseffson,² in similar studies on the influence of grain boundaries on the solubility of nitrogen in alpha iron report an increase in solubility with decreasing grain size. It would be of interest to know if the authors have noted such a dependence in the case of thorium.

Authors' Reply

The comments of Dr. Lilliendahl regarding the effect of nitrogen on the observed lattice constants are quite valid. The samples were prepared from the purest thorium which was available for this investigation. Although the nitrogen content was significant, it was fairly constant in most of the samples. It would be quite interesting to determine whether the increase in hardness and lattice constant for quenched thorium samples below the carbon solubility limit was due to the nitrogen content of the samples. This seems to be a reasonable explanation but it certainly has not been proven.

The effect of grain size on the solubility of carbon in thorium was not investigated by the authors because of the difficulty in controlling the grain size of thorium-carbon samples. The arc-melted structure had a large grain size which could not be decreased by cold working due to the lack of ductility in samples containing more than 0.1 weight percent carbon.

The authors wish to thank Dr. Lilliendahl for his kind and constructive comments.

¹ P. Chiotti, "Thorium-Carbon System," Atomic Energy Commission Report No. AECD-3072, 1950.

² G. Lagerberg and A. Joseffson, "Influence of Grain Boundaries on the Behavior of Carbon and Nitrogen in Alpha Iron," *Acta Metallurgica*, Vol. 3, 1955, p. 236.

THORIUM-ZIRCONIUM AND THORIUM-HAFNIUM ALLOY SYSTEMS

BY E. D. GIBSON, B. A. LOOMIS AND O. N. CARLSON

Abstract

The thorium-zirconium and thorium-hafnium systems have been studied by electrical resistance, thermal, microscopic and x-ray methods and phase diagrams have been proposed for each. The thorium-zirconium system was investigated extensively by high-temperature x-ray methods.

The thorium-zirconium system exhibits a minimum in the solidus at 1350 °C (2460 °F) and 25 weight % zirconium, a monotectoid reaction at 910 °C (1670 °F) and 25 weight % zirconium, and a eutectoid reaction at 650 °C (1200 °F) and 69 weight % zirconium. There is a small solid immiscibility loop above the 910 °C horizontal extending from 25 to 37 weight % zirconium.

The proposed thorium-hafnium system consists of a eutectic, a eutectoid and an inverse peritectic reaction. The eutectic reaction occurs at 1450 °C (2640 °F) and 25.7 weight % hafnium, the eutectoid reaction at 1295 °C (2360 °F) and 8.9 weight % hafnium, and the inverse peritectic reaction at about 1600 °C (2910 °F) and 96 weight % hafnium. At room temperature the maximum solubility of hafnium in a thorium is 4.9 weight % while there is little if any solubility of thorium in a hafnium. (ASM International Classification: M24b; Th, Zr, Hf)

INTRODUCTION

RECENT STUDIES of thorium and its alloys have been promoted because of the possibility of using this metal in nuclear reactors. The work herein reported is the result of such an investigation performed as part of a program on the study of the alloying behavior of thorium in combination with other reactor materials.

The initial studies on the thorium-zirconium system were performed by Carlson (1)¹ in 1950 at which time a tentative diagram was proposed. This proposed diagram, shown in Fig. 1, was based primarily upon microscopic evidence and thermal data. The present investigation was undertaken to clarify the uncertain regions and to propose a complete phase diagram for the thorium-zirconium system.

¹ The figures appearing in parentheses pertain to the references appended to this paper.

The authors, E. D. Gibson, B. A. Loomis and O. N. Carlson, are associated with the Institute for Atomic Research and Department of Chemistry, Iowa State College, Ames, Iowa. Manuscript received April 8, 1957.

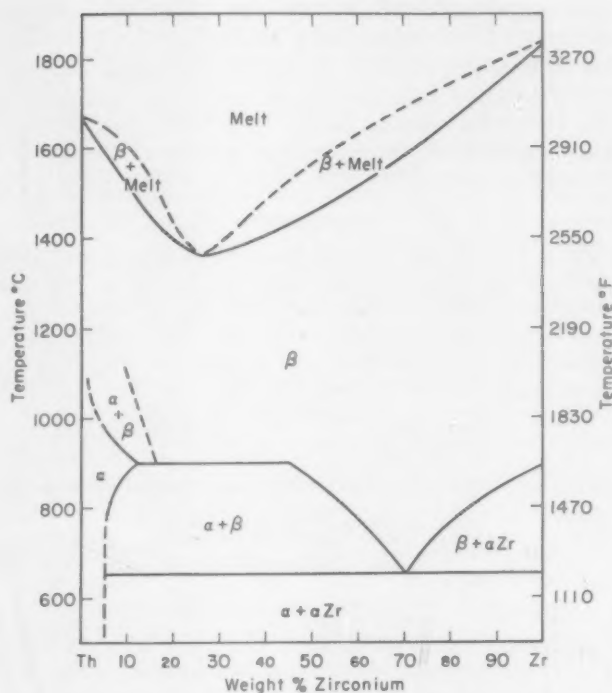


Fig. 1—Tentative Thorium-Zirconium Phase Diagram Proposed by Carlson in 1950.

Because of the well known similarity between zirconium and hafnium, the authors also undertook the investigation of the thorium-hafnium system. This was done in order to ascertain whether or not this system was analogous to that of thorium-zirconium as might be expected from a comparison of the properties of zirconium and hafnium summarized in Table I.

Table I
Some Physical Properties of Thorium, Hafnium and Zirconium

Property	Thorium	Hafnium	Zirconium
Allotropy	FCC to BCC at 1400°C	HCP to BCC reported (2,3, 4) from 1310°C to 1950°C	HCP to BCC at 854°C
Atomic Radii*	1.79 Å	1.60 Å	1.61 Å
Melting Point	1700°C	2130°C	1845°C
Lattice Constants			
Room Temperature	a=5.08 Å	a=3.197 Å	a=3.232 Å
Form		c=5.057 Å	c=5.147 Å
High Temperature	a=4.11		a=3.61 Å
Form			

* Calculations from the lattice constants of room temperature phase.

EXPERIMENTAL METHODS

Alloys were prepared by arc melting and the phase reactions occurring in these alloys were investigated by electrical resistance measurements, differential cooling curves, x-ray diffraction studies, and microscopic examination. In the thorium-zirconium investigation considerable emphasis was placed upon high temperature x-ray methods.

Materials

The alloys used in this investigation were prepared from thorium sponge, crystal bar hafnium and crystal bar zirconium. The thorium sponge was prepared by the bomb reduction of ThF_4 with calcium and is generally referred to as Ames thorium (5). The crystal bar hafnium was prepared by the Foote Mineral Company from hafnium sponge which was prepared by the authors (6). The zirconium was Grade A crystal bar obtained from Westinghouse Corporation. An analysis of these materials is given in Table II.

Table II
Chemical Purity of Thorium, Hafnium
and Zirconium Used in Alloy Preparation

Metal	C	O	N	Weight % Impurity			Be	Zr	Hf
				Al	Si	Fe			
Thorium	0.037	0.012	0.015	0.009	0.009	0.014	0.003	trace	—
Hafnium	0.03	—	0.009	trace	trace	0.01	trace	0.01	Major
Zirconium	0.01	0.02	0.001	0.003	0.003	0.02	—	Major	0.004

Alloy Preparation

Alloys were prepared by arc melting weighed amounts of the desired metals into 50 to 100 grams buttons. Melting was carried out under an atmosphere of purified helium in a water-cooled copper crucible employing a tungsten electrode. Since the weight change as a result of melting was small, the nominal composition was close to that as determined by chemical analysis. Alloys of thirty-five different compositions were prepared for use in the study of the thorium-hafnium system, and the thorium content of each was determined by chemical analysis. An equal number of thorium-zirconium alloys were also prepared for further investigation of this system and chemically analyzed for the thorium and zirconium present.

Electrical Resistance Measurements

Electrical resistance versus temperature data were obtained by the use of a continuously recording apparatus designed and constructed by Chiotti (7). The alloy specimen was formed into a rod which was clamped between two electrodes and heated by passing a high current through it. The potential developed between two probes which made

contact with the specimen was recorded directly, as resistance, on a Brown Elektronik potentiometer. The temperature of the sample was determined at frequent intervals by sighting with an optical pyrometer on a small hole drilled in the specimen. Resistance was then plotted graphically as a function of temperature.

Thermal Analysis

Cooling curves were obtained by means of a differential thermocouple circuit with one thermocouple junction in the alloy specimen and the other in a neutral body. The specimen temperature and the temperature difference between the two bodies were recorded simultaneously on a Brown Elektronik X-X potentiometer. In studying the relatively low temperature transitions in the thorium-zirconium system, chromel-alumel thermocouples were used, but in the thorium-hafnium system, tungsten-niobium thermocouples were employed.

The solidus curves of both systems were determined by observing the temperature at which melting first occurred in a bar or rod of the alloy. This temperature was measured by sighting with an optical pyrometer on a small hole drilled in the bar and observing continuously during heating until liquid first appeared in the hole. The alloy was heated by passing a high current through the bar while the bar was clamped between two water-cooled electrodes.

Heat Treatment and Microscopic Examination

In the study of the thorium-zirconium system all quenches were carried out from temperatures below 1100 °C (2010 °F). The specimens to be heat treated were annealed in an evacuated quartz tube in a resistance furnace, helium was admitted to the system and then the samples were immersed in water. However, in the thorium-hafnium system a large number of samples were quenched from temperatures above 1200 °C (2190 °F). The thorium-hafnium samples were supported on a beryllia disk inside a tantalum tube furnace and maintained at the desired temperature for 3 to 5 hours. A jet of helium gas which had been cooled by liquid nitrogen was impinged on the sample thus producing very rapid cooling rates. Where slow cooling of the specimen was desired the same furnace was employed for annealing and the power to the furnace was gradually decreased.

Samples for microscopic examination were ground on silicon carbide papers of successively decreasing grit size, and polished on a Microcloth-covered wheel using a water suspension of Linde A abrasive. With alloys containing greater than 30% hafnium* the addition of a drop or two of hydrofluoric acid to the abrasive greatly reduced the polishing time and aided in removal of scratches and films.

Several different etchants were used in the investigation of these

*All compositions refer to weight percentages.

alloys. For examining thorium-hafnium alloys, the thorium-rich alloys were etched electrolytically in a solution containing 100 parts formic acid, 2 parts of hydrochloric acid and 1 part hydriodic acid. The samples were etched for 8 seconds in this solution at a current density of 0.152 amperes per square centimeter and 12 volts. Hafnium-rich alloys were etched by swabbing the specimen with a solution containing 6 parts glycerine, 2 parts HNO_3 and 1 part HF.

Thorium-zirconium alloys were etched electrolytically in a solution containing 125 ml HNO_3 , 0.5 ml HF and 3 gm $\text{Th}(\text{NO}_3)_4$ diluted to 1 liter with H_2O .

X-ray Investigations

X-ray data constitute a significant part of this investigation and serve as much of the basis for the diagrams proposed for these systems. The solubility limits at room temperature were determined in the conventional manner by measuring lattice constants as a function of alloy composition. The lattice constants were determined from powder patterns taken on a back-reflection precision camera. The powder samples used were annealed filings taken from carefully annealed and slowly cooled alloys.

High temperature x-ray studies were carried out by use of an x-ray camera designed by Chiotti (8). It is specifically designed to replace the regular room temperature specimen holder on the North American Philips high angle goniometer. The alloy specimen with dimensions $1 \times \frac{3}{8} \times \frac{1}{8}$ inch was cut from the massive alloy and positioned in a groove of similar dimensions in the surface of a tantalum bar. The specimen and tantalum bar were surrounded by a tantalum tube furnace and enclosed within an evacuated chamber.

In the thorium-hafnium investigation the specimen temperature was measured by means of an optical pyrometer sighted on a small hole in the bar just below the specimen. However, in the thorium-zirconium alloy studies which involved a maximum temperature of only 1000 °C a Pt/Pt-10% Rh thermocouple was spot welded to a thin tantalum sheet which was in turn spot welded to the specimen. A standardization of the temperature measurement was made with a pure silver specimen in the x-ray camera. The lattice constant of the silver was experimentally determined as a function of the measured temperature. Results obtained by this method were compared graphically with similar data taken by Hume-Rothery and Reynolds (9) and more recently by Mauer and Bolz (10). Analyses of the data showed that an accuracy of ± 10 °C should be placed on the temperature measurement. The transformation temperature of zirconium was determined using this method and the value obtained was 854 °C (1569 °F) which is in good agreement with the accepted transformation temperature of crystal bar zirconium.

THORIUM-ZIRCONIUM SYSTEM

Data obtained on the thorium-zirconium system* from examination of microstructures of quenched alloys and high temperature x-ray studies are plotted on the partial phase diagram shown in Fig. 2. A discussion of the various regions of the system and how the boundaries of these regions were determined will be presented in detail in this section.

Confirmation of $\alpha + \beta'$ Region

The existence of a two-phase region corresponding to that identified as $\alpha + \beta'$ (Fig. 2) was postulated in the early work on this system as

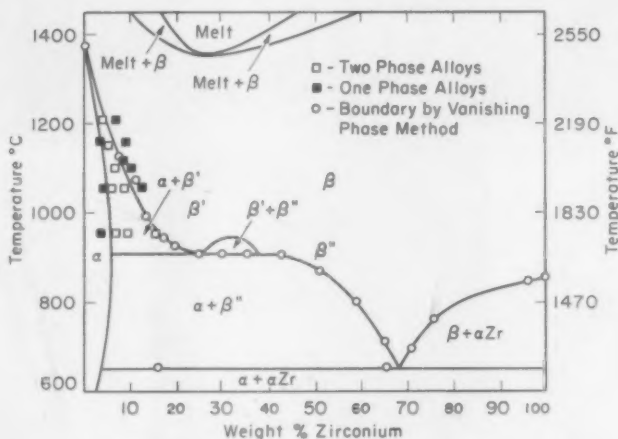


Fig. 2—Partial Thorium-Zirconium Phase Diagram with Plot of Data.

shown in Fig. 1. In later work a series of alloys of compositions which extended across this region were quenched from 950, 1050, 1100, 1150, and 1200 °C (1740, 1920, 2010, 1150 and 2190 °F). Typical microstructures for the series of quenches from 1150 °C (2100 °F) are shown in the accompanying photomicrographs. A 3.0% zirconium alloy (Fig. 3) is interpreted as a single-phase alloy which was quenched from within the α solid solution region; a 5.0% zirconium alloy (Fig. 4) contains approximately equal amounts of each phase, and an 8.5% zirconium alloy (Fig. 5) is a single-phase alloy quenched from within the β' solid solution region. The impurity phase present in all three alloys is ThO_2 which is commonly observed in thorium metal.

* This work is reported in greater detail in the M.S. thesis of E. D. Gibson, "Investigation of the Thorium-Zirconium System With Emphasis on High Temperature X-Ray Techniques," Iowa State College Library, Ames, Iowa.

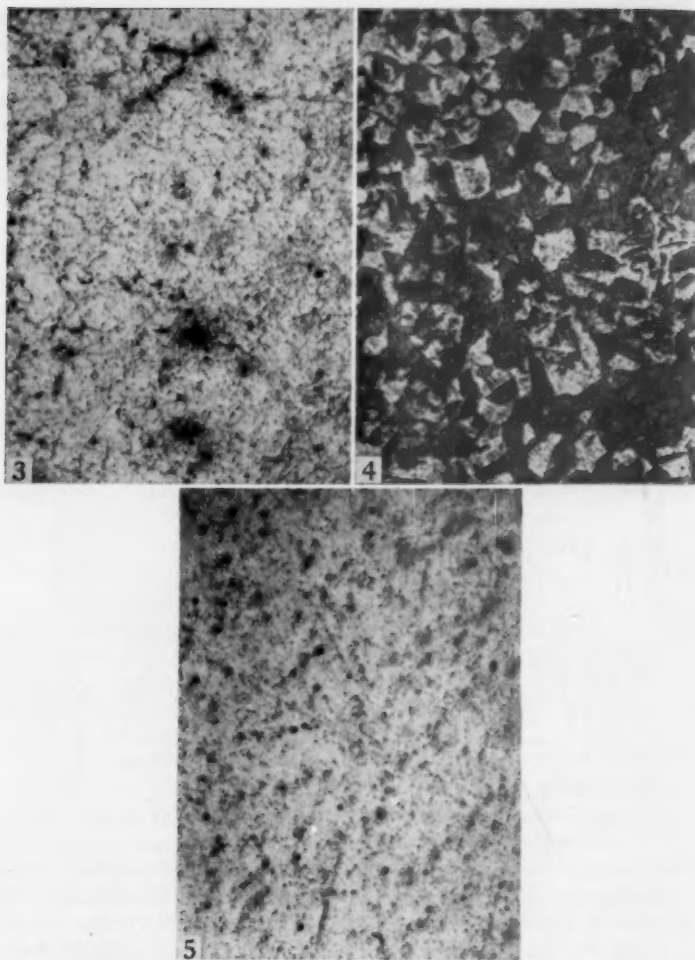


Fig. 3—3.0% Zirconium Alloy. Annealed for 12 hours and quenched from 1150 °C (2100 °F). One phase, α solid solution. Electrolytic etch. $\times 250$.

Fig. 4—5.0% Zirconium Alloy. Annealed for 12 hours and quenched from 1150 °C (2100 °F). α phase (light areas) plus β' solid solution. Electrolytic etch. $\times 250$.

Fig. 5—8.5% Zirconium Alloy. Annealed for 12 hours and quenched from 1150 °C (2100 °F). One phase, β' solid solution. Electrolytic etch. $\times 250$.

The boundaries of this region were also determined by high temperature x-ray techniques, and are in good agreement with those estimated from the microscopic evidence. The limit of solid solubility of

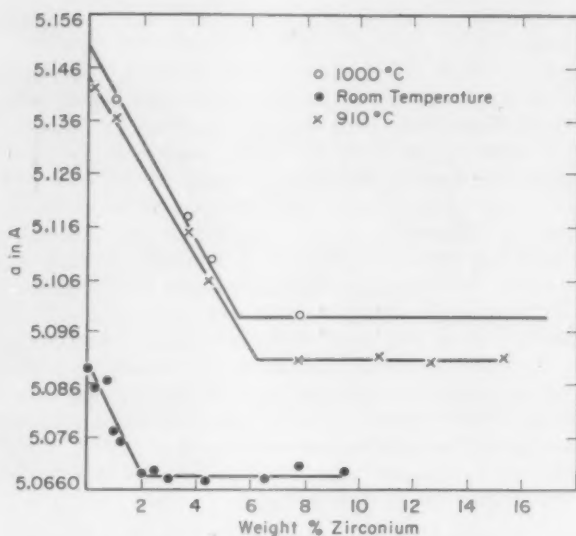


Fig. 6—Curves Showing Solubility of Zirconium in Thorium at Room Temperature, 910 and 1000 °C (1670 and 1830 °F).

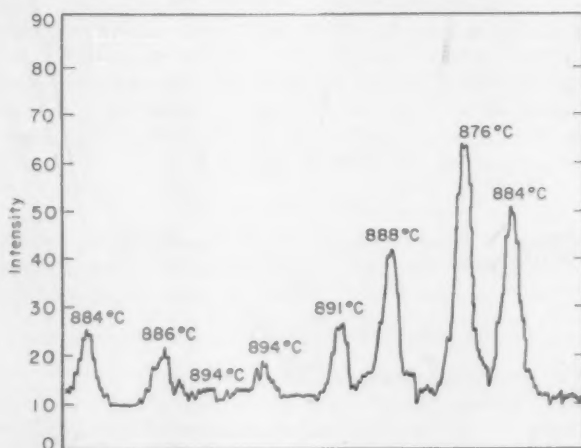


Fig. 7—Vanishing Phase Pattern of 40.8% Zirconium Alloy. Intensity of Th(III) reflection during transformation from FCC to BCC.

zirconium in α thorium at 910 °C (1670 °F) was determined to be 6.3% zirconium as shown by the lattice constant versus composition plot of Fig. 6. The curve at 1000 °C (1830 °F) is of the same form and indi-

cates a decrease in solubility to approximately 5.5% zirconium at 1000 °C (1830 °F).

The upper $\alpha + \beta'$ to β' boundary was determined by a vanishing-phase method. In general this method involved elevating the temperature of the alloy specimen to a temperature near the boundary in question and scanning the x-ray diffraction pattern of the high temperature camera to identify the phases present. As the boundary was crossed slowly, one of the phases which was present below the boundary disappeared. Conversely, as the temperature was lowered from above the boundary the phase reappeared. The disappearance and reappearance of the FCC phase on the thorium side of the eutectoid and of the HCP phase on the zirconium side were used as criteria for the determination of the $\alpha + \beta'$ to β' and $\alpha\text{Zr} + \beta$ to β boundaries, respectively. A typical pattern illustrating this vanishing method of boundary determination is shown in Fig. 7. The (111) reflection of the FCC phase in a 40.8% zirconium alloy was scanned at various temperatures and can be seen to disappear completely at 894 °C (1640 °F) upon heating and to reappear upon cooling. This and other points obtained in this manner are plotted in Fig. 2.

Confirmation of β Solid Solution Region

The extent of the β solid solution region above 910 °C (1670 °F) was still somewhat in question since data from the earlier investigation (1) indicated that a two-phase field might exist in this area at about 50% zirconium. Lattice constant measurements taken in the present investigation at 1000 °C (1830 °F) show that the solid solution region begins at about 20% zirconium and extends to the zirconium end of the system. The lattice constants of the BCC solid solution phase as a function of composition are given in Table III.

Solid Immiscibility Loop

The inflection in the $\alpha + \beta$ to β boundary in the thorium-zirconium diagram as originally proposed suggested that a region of solid immiscibility was imminent or actually present above the 910 °C

Table III
Lattice Constants of BCC Phase at 1000 °C

Alloy Composition % Zr	Lattice Constant in Å
19.8	3.91
24.8	3.88
26.7	3.84
40.8	3.79
50.9	3.74
58.4	3.70
75.4	3.66
100	3.61

A graphical plot of lattice constant versus atomic % zirconium gives a linear relationship across this region of the system.

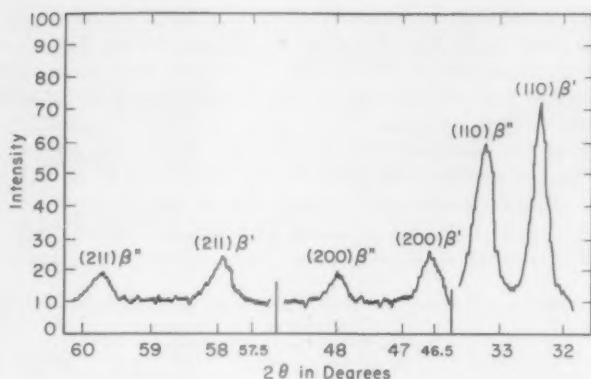


Fig. 8a—29.7% Zirconium Alloy, High temperature pattern taken at 914 °C (1680 °F) showing peaks from both β' and β'' phases.

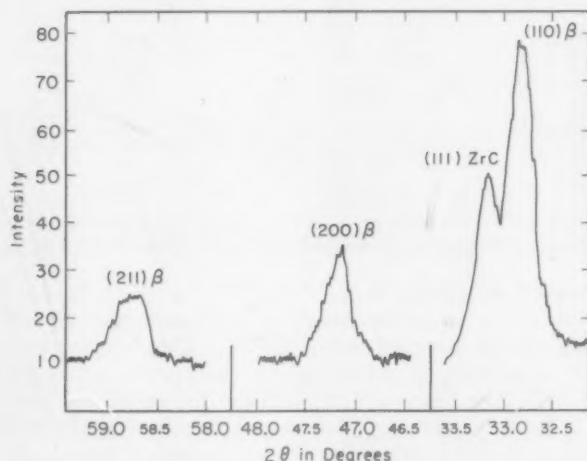


Fig. 8b—29.7% Zirconium Alloy, High temperature pattern taken at 955 °C (1750 °F) showing one BCC phase.

(1670 °F) horizontal. The theoretical treatment of such a tendency is given by Ricci (11). With this tendency to be considered, experimental investigation of the region of the system near 900 °C (1650 °F) and 30% zirconium was undertaken. Rogers (12) confirmed the presence of a horizontal at 910 °C (1670 °F) by electrical resistivity measurements but failed to detect any evidence for a solid immiscibility loop above it. Likewise, attempts at retaining a two-phase microstructure by quenching alloys from just above the horizontal failed to yield evidence for such a loop.

Finally studies were undertaken with the aid of a high temperature x-ray camera to identify the phase or phases present just above the horizontal. Examination of a 29.7% zirconium alloy at six different temperatures from 887 to 955 °C (1630–1750 °F) revealed phase relationships which indicated that a region of solid immiscibility does exist about this horizontal. A typical x-ray diffraction pattern of the 29.7% zirconium alloy taken at 914 °C (1680 °F) is shown in Fig. 8a. This pattern shows clearly reflections from two BCC phases differing only slightly in lattice constant. The data in Table IV show how the lattice constant of these phases become more nearly equal as the

Table IV
Lattice Constants of BCC Phases

Alloy Composition % Zirconium	Temperature °C	a' in Å	a'' in Å
15.73	959	3.94	
15.73	928	3.92	
15.73	920	3.91	
15.73	916	3.90	
15.73	890		3.76
24.84	915	3.89	
29.69	887		3.75
29.69	914	3.89	3.77
29.69	923	3.88	3.79
29.69	935	3.85	3.80
29.69	945	3.84	3.82
29.69	955	3.84	
34.46	923	3.88	3.79
40.85	876		3.73
40.85	923		3.77
50.95	885		3.74
50.95	914		3.75
50.95	935		3.75
50.95	959		3.76

temperature is raised and finally merge into one BCC phase at 955 °C (1750 °F) with a lattice constant value lying somewhere between those of the two phases observed within the loop. This is illustrated by the other diffraction pattern in Fig. 8b. An enlargement of this portion of the system is shown in Fig. 9 and includes the lattice constants of the phases at the various temperatures together with points indicating the temperature at which one of the phases disappears upon heating and reappears upon cooling.

Terminal Solid Solubility at Room Temperature

The solid solubility of zirconium in thorium at room temperature was estimated from a plot of lattice constant versus per cent zirconium. The lattice constants were calculated from diffraction patterns taken with a precision back-reflection type camera and were considered to be reproducible to ± 0.0005 Å. The graphical plot is shown in Fig. 6 in which the solubility limit lies at approximately 2% zirconium.

Similar work done on the zirconium end of the system places the limit of solid solubility of thorium in zirconium at 0.5% thorium or

Table V
Zirconium Lattice Constants

Alloy Composition % Zirconium	a in Å	c in Å
0	3.2375	5.1376
0.5	3.2310	5.1527
3.83	3.2315	5.1524

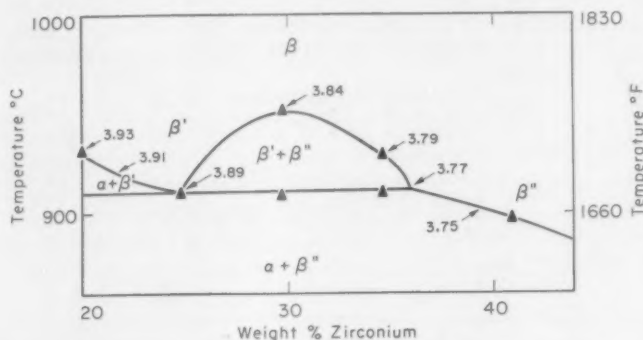


Fig. 9—Enlarged Portion of Solid Immiscibility Loop in Thorium-Zirconium System Showing Lattice Constants of Different BCC Phases at Various Temperatures.

less. The data listed in Table V show a decrease in the "a" value and increase in the "c" value upon the addition of small amounts of thorium to zirconium.

THORIUM-HAFNIUM SYSTEM

A phase diagram is proposed for the thorium-hafnium alloy system* as presented in Fig. 10. This diagram is based on data obtained from electrical resistance measurements, thermal analysis, x-ray investigations and the examination of microstructures. There is a eutectic reaction occurring at 1450 °C (2640 °F) and 25.7% hafnium and a eutectoid reaction occurring at 1295 °C (2360 °F) and at 8.9% hafnium. An inverse peritectic is postulated to occur at 1600 °C (2910 °F) and 96% hafnium.

Electrical Resistance and Cooling Curve Data

Electrical resistance versus temperature curves show clearly that there is a phase transition in the binary alloys at 1295 °C (2360 °F) as indicated by a discontinuity in the resistance curves on all alloys of compositions between 5 and 98% hafnium. The magnitude of the

* This work is reported in greater detail in the M.S. thesis of B. A. Loomis, "Thorium and Hafnium Phase Diagram," Iowa State College Library, Ames, Iowa.

break increased with decreasing hafnium content of the alloy. These data are shown as plotted points in Fig. 10. There is another break in the resistance-temperature curves at 1450 °C (2640 °F) occurring in most of the alloys studied, and one in hafnium-rich alloys at 1600 °C (2910 °F). An abrupt change in resistance was also observed in the unalloyed hafnium at 1735 °C (3155 °F), which was considered to be

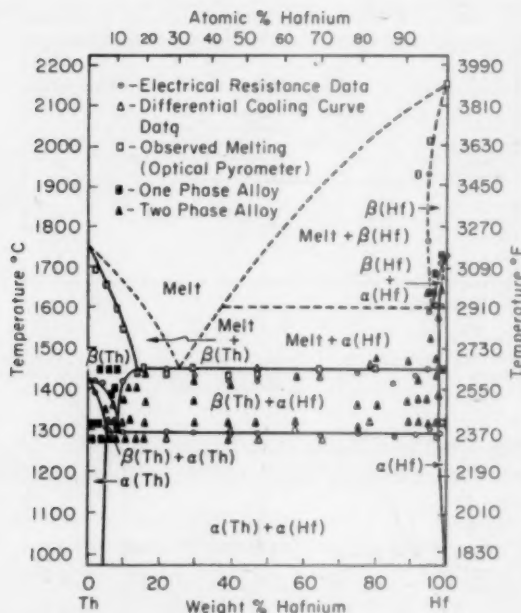


Fig. 10—Plot of Data and Proposed Thorium-Hafnium Phase Diagram.

associated with the α to β transformation in hafnium metal. A similar transformation in thorium at 1400 ± 25 °C has been reported by Chiotti (13).

A large thermal arrest was observed at about 1300 °C (2370 °F) in differential heating and cooling curves and a second arrest was detected at the 1450 °C (2640 °F) temperature horizontal in alloys containing 47.8, 65.4 and 77.6% hafnium. These data are likewise plotted in Fig. 10.

Eutectic Reaction

Microstructures and thermal analyses of as-arc-melted alloys indi-

cated that there was a eutectic reaction occurring at 1450 °C (2640 °F) and at a composition of 25.7% hafnium. Fig. 11 is a photomicrograph of the 25.7% hafnium eutectic alloy and Fig. 12 of an 80.0% hafnium alloy showing primary hafnium in a eutectic matrix. A 16.3% hafnium alloy (Fig. 13) contains primary transformed β thorium solid solution plus a small amount of eutectic. On the basis of this and other microscopic evidence the solubility limit of hafnium in β thorium has been placed at 13% hafnium at the eutectic temperature. This coincides with the point of intersection of the solidus curve and the eutectic horizontal as determined from melting point observations (see Fig. 10).

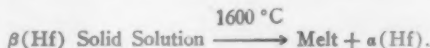
Eutectoid Reaction

A eutectoid reaction occurs at 1295 °C (2360 °F) in which β thorium solid solution containing 8.9% hafnium decomposes into α (Hf) plus α (Th). In addition to the evidence from electrical resistance and cooling curve data there is microscopic evidence for the existence of the eutectoid reaction. Fig. 14 is a photomicrograph of a 9.9% hafnium alloy whose composition is near that of the eutectoid. This same alloy is shown in Fig. 15 after quenching from 1370 °C (2500 °F) above the eutectoid horizontal, and in which there now appears to be β (Th) plus a small amount of primary α (Hf). As can be seen from Fig. 10 several alloys were examined microscopically after quenching from the various phase regions and from different temperatures in the vicinity of the eutectoid.

Evidence for the β (Th) plus α (Hf) region in the system is the microscopic appearance of alloys which were annealed and quenched from this region. A typical structure is that of a 57.7% hafnium alloy shown in Fig. 16 as quenched from 1430 °C (2600 °F). Approximately equal areas of the phases identified as β (Th) and α (Hf) are present in this alloy. The prolonged annealing prior to quenching has eliminated all of the eutectic structure of the alloy.

Inverse Peritectic Reaction

Evidence for the presence of an inverse peritectic reaction is somewhat inconclusive and therefore is represented by dashed lines in the proposed diagram. This reaction proceeds upon cooling according to the following reaction:



As was described earlier, electrical resistance data indicated the presence of a horizontal at 1600 °C (2910 °F) in hafnium-rich alloys which is somewhat lower than the 1735 °C (3155 °F) resistance break observed in unalloyed hafnium. High temperature x-ray investigation of crystal bar hafnium and thorium-hafnium alloys containing 94.7, 91.4

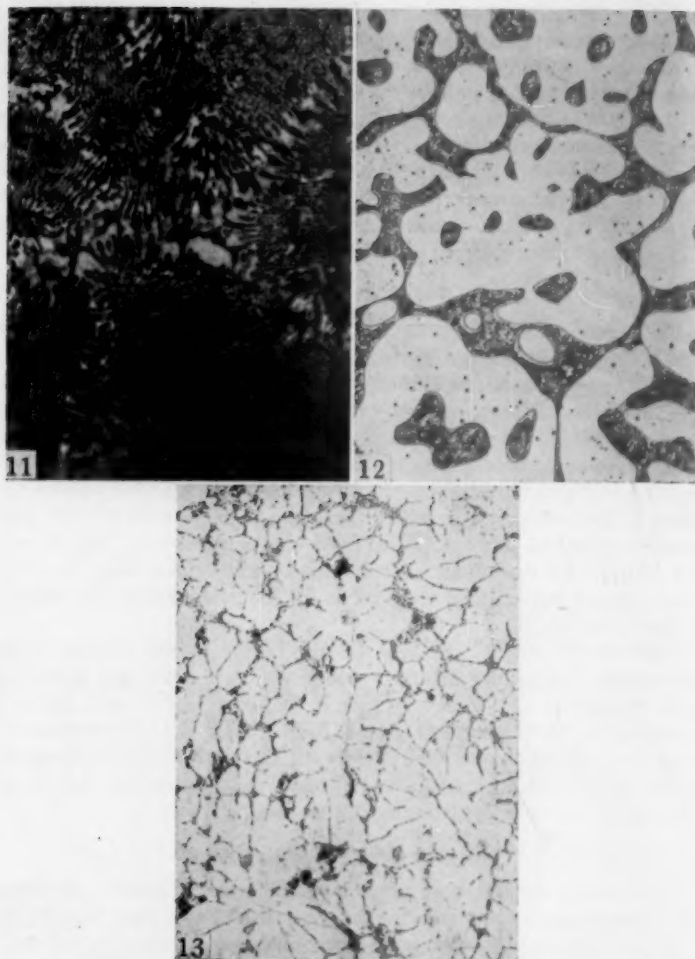


Fig. 11—25.7% Hafnium Alloy. As arc-melted. Complete eutectic structure. Etchant: Glycerine-HF-HNO₃. $\times 500$.

Fig. 12—80.0% Hafnium Alloy. As arc-melted. Primary α (Hf) plus small amount of eutectic. Etchant: Glycerine-HF-HNO₃. $\times 500$.

Fig. 13—16.3% Hafnium Alloy. As arc-melted. Transformed β (Th) plus eutectic along grain boundaries. Etchant: Glycerine-HF-HNO₃. $\times 500$.

and 69.6% hafnium revealed that all three alloys contained the hexagonal, α (Hf), phase up to 1450 °C (2640 °F).

The alpha phase was present up to 1500 °C (2730 °F) in pure haf-

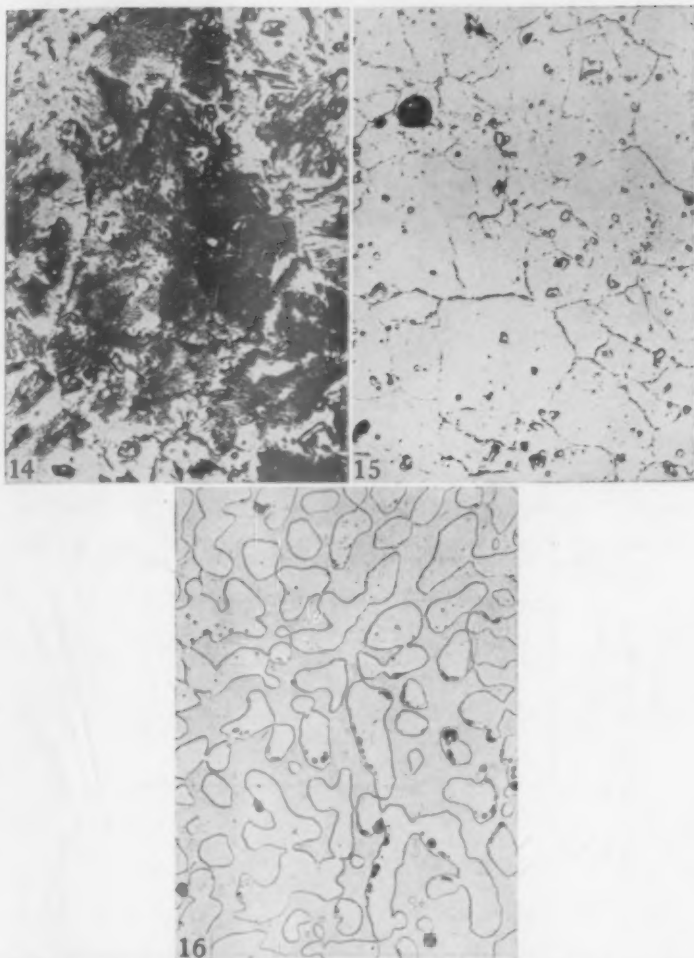


Fig. 14—9.9% Hafnium Alloy. Slow cooled from 1425 to 1260 °C (2600 to 2300 °F). α (Hf) (small globular areas) in eutectoid matrix. Electrolytic etch. $\times 250$.

Fig. 15—9.9% Hafnium Alloy. Quenched from 1370 °C. β (Th) plus small amount of α (Hf). Electrolytic etch. $\times 250$.

Fig. 16—57.7% Hafnium Alloy. Annealed and quenched from 1430 °C (2605 °F). Clear areas of β (Th) in a matrix of α (Hf). Etchant: Glycerine-HF-HNO₃ $\times 250$.

nium, the upper limit of the high temperature camera employed in this investigation. A 96.4% hafnium alloy was quenched from 1630 °C (2965 °F) above the horizontal, which as can be seen from Fig. 17 was

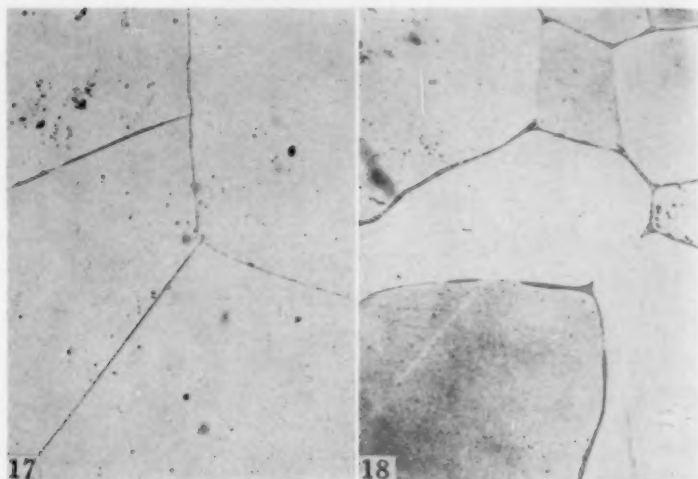


Fig. 17—96.4% Hafnium Alloy. Quenched from 1630 °C (2965 °F). Transformed β (Hf). Etchant: Glycerine-HF-HNO₃. $\times 250$.

Fig. 18—96.4% Hafnium Alloy. Quenched from 1475 °C (2685 °F). Grains of α (Hf) surrounded by quenched melt. Etchant: Glycerine-HF-HNO₃. $\times 250$.

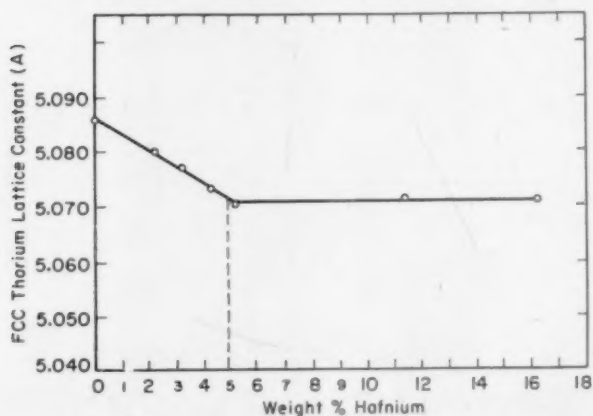


Fig. 19—Plot of Lattice Constant of α (Th) Against Hafnium Content for Alloys at Room Temperature.

from within a one-phase region. However, when this same alloy was quenched from 1475 °C (2685 °F), a temperature below the horizontal, it contained two phases (Fig. 18) interpreted as α hafnium surrounded by quenched liquid. A 94.7 and 97.5% hafnium alloy also exhibited this difference in microstructure when quenched from above and below

the 1600 °C (2910 °F) horizontal. On the basis of the above data an inverse peritectic has been postulated at a composition of about 96% hafnium and at a temperature of 1600 °C (2910 °F).

Terminal Solid Solubility

The maximum solubility of hafnium in α thorium at room temperature was estimated at 5% hafnium from a plot of lattice constant versus composition as is shown in Fig. 19. The solubility limit at higher tem-

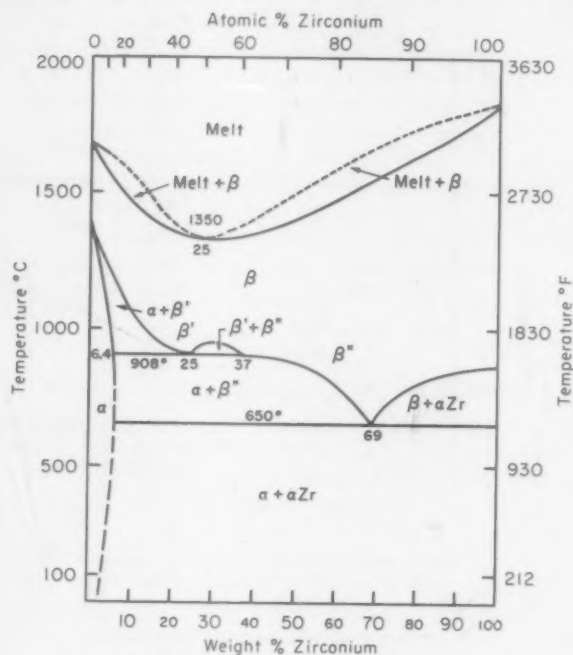


Fig. 20—Thorium-Zirconium Equilibrium Diagram.

peratures was estimated from microstructures of quenched specimens.

The lattice constants of the α (Hf) phase in a 94.7% hafnium alloy were $a = 3.202$ Å and $c = 5.061$ Å. The corresponding lattice constants of the crystal bar hafnium were determined to be $a = 3.197$ Å and $c = 5.057$ Å. Since the addition of thorium has such a slight effect upon the lattice constants of α hafnium, solid solubility of thorium in hafnium at room temperature is considered to be insignificant. However, microstructures of alloys quenched from elevated temperatures indicate that there is appreciable solubility, perhaps as high as 2% thorium, at the eutectic and eutectoid temperatures.

DISCUSSION

Phase diagrams have been proposed for both the thorium-hafnium and thorium-zirconium systems and are shown in Figs. 20 and 21. At first glance, the systems would appear to be very dissimilar contrary to the expected analogous alloying behaviour of zirconium and hafnium as was discussed in a preceding section of this paper. However, upon

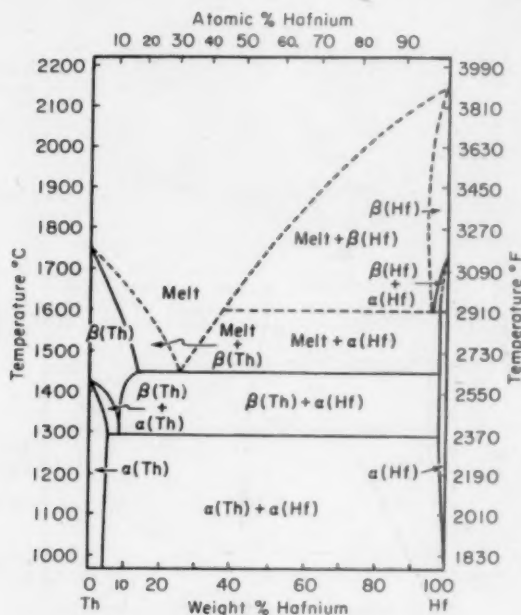


Fig. 21—Thorium-Hafnium Equilibrium Diagram.

closer examination several similarities become apparent. Both systems show minima in their melting curves, lowering of the thorium transformation by either monotectoid or eutectoid formation and limited terminal solid solubility in β thorium. Furthermore, if one could expand the $\beta' + \beta''$ solid immiscibility loop in the thorium-zirconium system to such a size that it intersected the solidus, this system would then closely resemble the proposed thorium-hafnium. The principal differences would thus appear to be in the size of the solid immiscibility loop above the eutectoid horizontal and in the relative stability of the hexagonal phase in the two systems.

A factor which could explain the difference in the extent of solid

Table VI
Atomic Radii and Percentile Differences in Thorium, Hafnium and Zirconium

Metal Couple	Atomic Radii		Percentile Difference R
	r_1	r_2	
FCC Thorium-HCP Zirconium	1.79	1.61	10.6
BCC Thorium-BCC Zirconium	1.78	1.56	13.1
FCC Thorium-HCP Hafnium	1.79	1.60	11.2
BCC Thorium-BCC Hafnium	1.78	1.52	15.8
HCP Zirconium-HCP Hafnium	1.61	1.60	0.6

solubility between the BCC lattices in the two systems is the atomic size factor. While there appears to be little, if any, difference in the relative size of the zirconium and hafnium atoms in the room temperature crystal lattice, as listed in Table I, there may be considerable difference in their relative sizes in the high-temperature lattice. Duwez (2) has estimated the high-temperature lattice constant of hafnium to be 3.50 Å considerably smaller than the value of 3.61 Å reported for zirconium. Duwez's value was obtained by extrapolation across a two-phase region of the hafnium-columbium alloy system, but it is probably a fairly good approximation. If these lattice constants are used to calculate the atomic radii for BCC hafnium and zirconium, the percentile difference in atomic radii shown in Table VI are obtained. The percentile difference, R, is defined by the relation:

$$R = 100 (r_1 - r_2) / r_{avg}$$

where r_1 and r_2 are the atomic radii of the respective components in the system and r_{avg} is the arithmetic mean.

The atomic radii of BCC thorium and BCC zirconium differ by only 13.1% which is well below the maximum difference of 15% set forth by Hume-Rothery as a condition for complete miscibility between isomorphous crystals. On the other hand, BCC thorium and BCC hafnium differ in their atomic radii by 15.8% and thus exceed the limiting conditions for complete solid solubility. Hence, if Hume-Rothery's rule is applied rigorously to these two systems it would explain the differences in extent of solid solubility between the high temperature crystal forms.

Another factor which undoubtedly contributes to the dissimilarity in the systems is the pronounced difference in the transformation temperatures of hafnium and zirconium. Whereas the melting point of hafnium is only slightly higher than that of zirconium, its transformation temperature is twice that of zirconium. This higher transformation temperature opposes the stabilization of β hafnium by eutectoid formation as occurs in the thorium-zirconium system which probably results in the somewhat analogous inverse peritectic reaction in thorium-hafnium alloys.

SUMMARY

Phase diagrams of the thorium-zirconium and thorium-hafnium sys-

tems were constructed on the basis of electrical resistance, thermal, microscopic and x-ray evidence. The characteristic features of the thorium-zirconium system are as follows:

1. There is a minimum in the solidus curve at 1350 °C (2460 °F) at a composition of 25% zirconium.
2. A monotectoid reaction occurs at 910 °C (1670 °F) and at 25% zirconium. A solid immiscibility loop lies above the 910 °C horizontal and extends from 25 to 37% zirconium.
3. There is a eutectoid at 650 °C (1200 °F) and 69% zirconium.

The salient features of the thorium-hafnium system were established as follows:

1. A eutectic reaction occurs at 1450 °C (2640 °F) and 25.7% hafnium.
2. A eutectoid reaction occurs at 1295 °C (2360 °F) and 8.9% hafnium.
3. An inverse peritectic reaction is postulated at 1600 °C (2910 °F) and 96% hafnium.
4. The limit of solubility of hafnium in a thorium at temperatures below 650 °C is 4.9% hafnium.

ACKNOWLEDGMENTS

The authors wish to express their appreciation to Dr. Premo Chiotti for his suggestions and advice concerning the electrical resistance measurements and high temperature x-ray studies. Thanks are due to Mr. Ed Borders, Mr. Don Westlake and Mr. Kenneth Hood for their assistance in the metallographic and other experimental work, and to the analytical chemistry group of the Ames Laboratory for the chemical analyses.

References

1. O. N. Carlson, "Some Studies on the Uranium-Thorium-Zirconium Ternary Alloy System," *U. S. Atomic Energy Report*, AECD-3206, 1950, p. 31.
2. P. Duwez, "The Allotropic Transformation of Hafnium," *Journal of Applied Physics*, Vol. 22, 1951, p. 1174.
3. C. Zwikker, "Modificatieveranderingen Bij Zirkoon En Hafnium," *Physica*, Vol. 6, 1926, p. 361.
4. J. D. Fast, "The Allotropic Transformation of Hafnium and a Tentative Equilibrium Diagram of the System Zr-Hf," *Journal of Applied Physics*, Vol. 23, 1952, p. 350.
5. O. N. Carlson, P. Chiotti, G. Murphy, D. Peterson, B. A. Rogers, J. F. Smith, M. Smutz, M. Voss and H. A. Wilhelm, "The Metallurgy of Thorium and Its Alloys," *Reactor Technology and Chemical Processing*, Vol. 9, 1956, p. 74.
6. O. N. Carlson, F. A. Schmidt and H. A. Wilhelm, "Preparation of Zirconium and Hafnium Metals by Bomb Reduction of Their Fluorides," *Journal of the Electrochemical Society*, Vol. 104, 1957, p. 51.
7. P. Chiotti, "Measurement of the Electrical Resistance of Metals and Alloys at High Temperatures," *Review of Scientific Instruments*, Vol. 25, No. 9, 1954, p. 876.

8. P. Chiotti, "Adaptation of a Geiger-Counter X-Ray Diffractometer for High-Temperature Investigations," *Review of Scientific Instruments*, Vol. 25, No. 7, 1954, p. 683.
9. W. Hume-Rothery and P. W. Reynolds, "A High Temperature Debye-Scherrer Camera, and its Application to the Study of the Lattice Spacing of Silver," *Proceedings of the Royal Society*, Vol. A167, 1938, p. 25-34.
10. F. A. Maurer and L. H. Bolz, "Measurement of Thermal Expansion of Cermet Components of High Temperature Diffraction," *National Bureau of Standards*, Report No. WADC 55-473.
11. J. E. Ricci, "The Phase Rule and Heterogeneous Equilibrium," 1951, p. 175, D. Van Nostrand Co., Inc., New York.
12. B. A. Rogers, unpublished work, Ames Laboratory of the U. S. Atomic Energy Commission, Ames, Iowa, 1952.
13. P. Chiotti, "High Temperature Crystal Structure of Thorium," *Journal of the Electrochemical Society*, Vol. 101, 1954, p. 567.

GRAIN GROWTH AND RECRYSTALLIZATION STUDIES ON COMMERCIAL TITANIUM, RC-55, AND ALLOY, Ti-100A

By E. L. BARTHOLOMEW, JR.

Abstract

The influences of prior to deformation grain size, amount of cold deformation, annealing temperature and time on the grain size of cold-worked and annealed titanium (RC-55) and alloy (Ti-100A) were investigated. Isothermal annealing of cold-rolled titanium (RC-55) was also carried out to establish recrystallization rates and to investigate grain growth in the absence of recrystallization.

Both titanium (RC-55) and alloy (Ti-100A) exhibit excessive coarsening tendencies when annealed following a critical amount of plastic deformation. Annealing temperature and prior to deformation grain size are shown to influence the magnitude of this coarsening. The grain coarsening is attributed to strain induced boundary migration. The activation energies for 30 to 70% recrystallization of 30% cold-rolled RC-55 are in the range, 74 to 79 K cal./g. atom. The activation energies for 30 to 70% transformation to coarsened structure by strain-induced boundary migration of 12% cold-rolled RC-55 are in the range, 33 to 35 K. cal./g. atom. (ASM International Classification N3, N5, 2-14, 3-18; Ti)

INTRODUCTION

THE LARGE crystal size frequently developed in metals and alloys which have been annealed following a small amount of plastic deformation (critical deformation) has been the object of numerous investigations (1,2,3).¹

Extensive fabrication of titanium and its alloys by cold forming methods like rolling, deep drawing, stretch forming and wire drawing is anticipated. The required annealing attendant to these operations can well be expected to embrace occasionally those critical conditions leading to crystal sizes which might be prohibitively large in view of

This study was supported by the Ordnance Corps, under cognizance of Springfield Ordnance District, with technical supervision by the Watertown Arsenal Laboratory.

¹ The figures appearing in parentheses pertain to the references appended to this paper.

A paper presented before the Thirty-Ninth Annual Convention of the Society, held in Chicago, November 4-8, 1957. The author, E. L. Bartholomew, Jr., is professor of Mechanical Engineering, University of Connecticut, Storrs, Connecticut. Manuscript received November 20, 1956.

either subsequent forming operations or service requirements. For these reasons it appeared desirable to evaluate the annealing behavior of titanium with respect to critical deformation in the hope that resulting information could be of some value in guiding fabrication procedures.

EXPERIMENTAL

Grain size studies were made on commercial purity sponge titanium, RC-55 and commercial Ti-100A, having the following chemical analysis:

	RC-55	Ti-100A
Carbon	0.08	0.036
Nitrogen	0.049	0.054
Iron	0.08	0.20
Silicon	0.03	0.04
Tungsten	0.144	0.010
Oxygen	0.121	0.169

Annealing temperature, annealing time, prior to deformation grain size and magnitude of cold working below and above that of the observed critical deformation were all varied to evaluate their influence on resulting annealed grain size. Details of these experiments on grain size behavior are summarized in Table I.

Table II indicates the corresponding details of experimentation in conjunction with isothermal annealing of RC-55.

RESULTS AND DISCUSSION OF GRAIN SIZE STUDIES

Rolled-Annealed RC-55 and Ti-100A

The results of cold rolling and annealing RC-55 and Ti-100A of

Table I
Summary of Experiments Carried Out on Titanium,
RC-55 and Alloy, Ti-100A

Deformation Ranges	Grain Size Studies Annealing Temperatures	Annealing Times
RC-55—FINE PRIOR CRYSTAL SIZE—COLD-ROLLED		
3% to 30% Reduction in thickness	1100 to 1500 °F inclusive at 100 °F intervals	½ hour, 1½ hours, 3 hours
RC-55—COARSE PRIOR CRYSTAL SIZE—COLD-ROLLED		
3% to 40% Reduction in thickness	1200 to 1500 °F inclusive at 100 °F intervals	1½ hours
Ti-100A—FINE PRIOR CRYSTAL SIZE—COLD-ROLLED		
3% to 35% Reduction in thickness	1100 to 1500 °F inclusive at 100 °F intervals	½ hour, 1½ hours, 3 hours
Ti-100A—COARSE PRIOR CRYSTAL SIZE—COLD-ROLLED		
3% to 35% Reduction in thickness	1200 to 1500 °F inclusive at 100 °F intervals	1½ hours

Table II
Summary of Experiments Carried Out on Titanium, RC-55

Deformation	Isothermal Annealing	
	RC-55—FINE PRIOR CRYSTAL SIZE—COLD-ROLLED Annealing Temperatures °F	Annealing Times
12% Reduction in thickness	1200, 1300, 1400	10 seconds through 2½ hours
30% Reduction in thickness	1100, 1200, 1300	10 seconds through 3 hours

fine prior to rolling crystal size intended to show the influence of annealing temperature, annealing time and magnitude of cold rolling on the final annealed grain size are given in plot form in Fig. 1 through Fig. 6. With reference to these plots, it will be noted that more scatter of datum points is found in the deformation range between the critical deformation and about 20% deformation. In this range crystal sizes were mixed.

Representative photomicrographs of structural changes observed in Ti-100A are shown in Figs. 7, 8, and 9. While these structures are for Ti-100A, identical structural changes were encountered in RC-55.

The beginning of coarsening was experienced in all cases at deformations below the critical deformation. The level of critical deformation coincides with the datum points for peak crystal sizes. This partial coarsening represented in Fig. 9 necessarily led to a grossly mixed crystal size such that evaluations were meaningless. Consequently, all curves are dotted from the largest deformation at which no evidence of coarsening at center section was found to the peak values of crystal size where the structure was noted to be essentially completely coarsened.

The use of a single curve to represent grain size as a function of deformation for all annealing temperatures and times beyond deformations of approximately 16% suggests that resulting grain size is a function of deformation only. Channon and Walker (4) report a similar finding in connection with their recrystallization studies on alpha brass.

Microstructures

Fig. 8 is typical of as received structure in Ti-100A and representative of prior to rolling structure in RC-55. Comparison of Fig. 8 with Fig. 7 gives a representative indication of the structural change observed as a result of annealing critically deformed RC-55 and Ti-100A.

Particular attention is invited to Fig. 7 and the irregularly shaped crystals shown which were experienced in both RC-55 and Ti-100A in this deformation range. The boundaries are curved and highly irregular; a condition normally found in cases of grain boundary migration and not usually associated with recrystallization. Annealed struc-

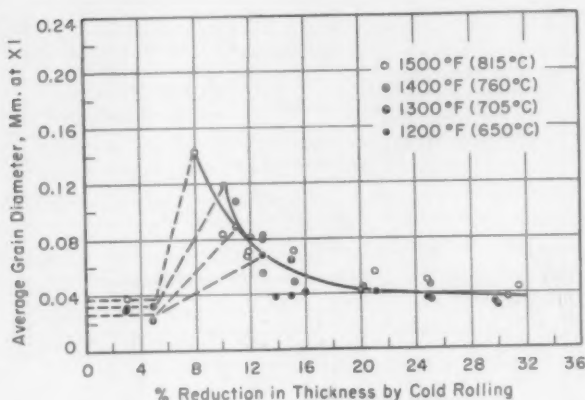


Fig. 1—Effect of Annealing Temperature and Amount of Deformation by Cold Rolling on Average Crystal Diameter of RC-55. Fine prior grain size. Annealing time $\frac{1}{2}$ hour.

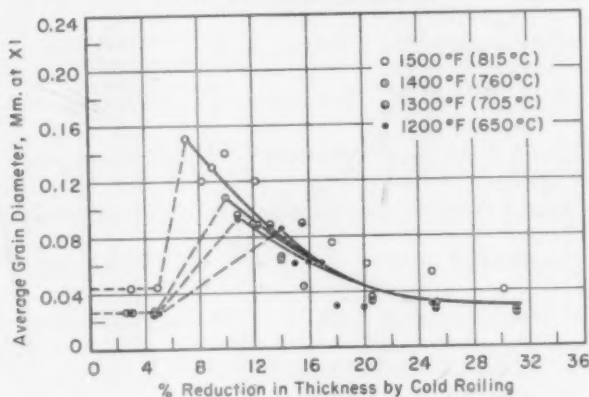


Fig. 2—Effect of Annealing Temperature and Amount of Deformation by Cold Rolling on Average Crystal Diameter of RC-55. Fine prior grain size. Annealing time $1\frac{1}{2}$ hours.

tures noted in the deformation range between the critical deformation and approximately 20% were seen to consist of a mixture of curved boundary crystals and straight sided crystals. Above 20% deformation crystals were typical of recrystallized structure and were of appearance typified in Fig. 8.

Strain induced growth in the absence of recrystallization has been observed in brass by Maddigan and Blank (5), by Burke and Shiau (6) and in aluminum by Beck and Sperry (7). It is proposed that strain induced boundary migration could be the mechanism by which the structure shown in Fig. 7 is developed. In order to shed more light

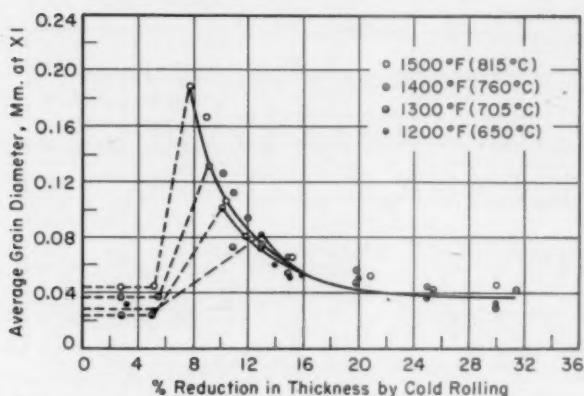


Fig. 3—Effect of Annealing Temperature and Amount of Deformation by Cold Rolling on Average Crystal Diameter of RC-55. Fine prior grain size. Annealing time 3 hours.

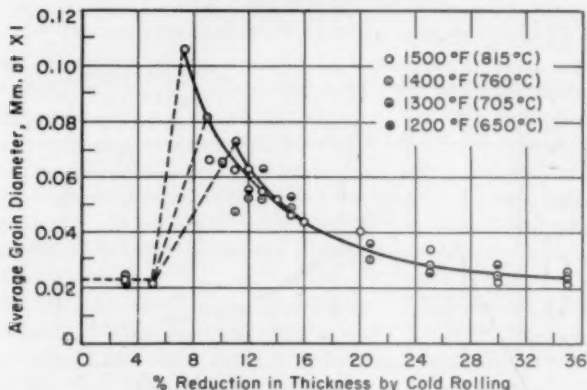


Fig. 4—Effect of Annealing Temperature and Amount of Deformation by Cold Rolling on Average Crystal Diameter of Ti-100A. Fine prior grain size. Annealing time $\frac{1}{2}$ hour.

on this behavior, the isothermal annealing of RC-55 was undertaken. The results of this work are to be discussed later in this paper.

Effect of Large Prior to Rolling Grain Size

Large prior to rolling crystal size in RC-55 was developed by subjecting the as received stock to a rolling and annealing treatment which according to earlier work should develop a grain size of 0.090 millimeters at $\times 1$. Samples of this metal so treated were evaluated and the resulting grain size was found to be between 0.080 and 0.093 millimeters at $\times 1$.

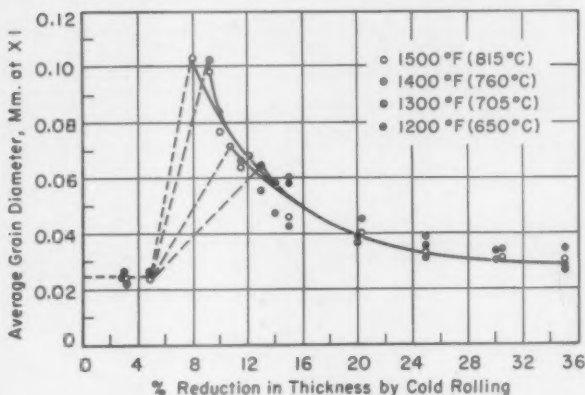


Fig. 5—Effect of Annealing Temperature and Amount of Deformation by Cold Rolling on Average Crystal Diameter of Ti-100A. Fine prior grain size. Annealing time 1½ hours.

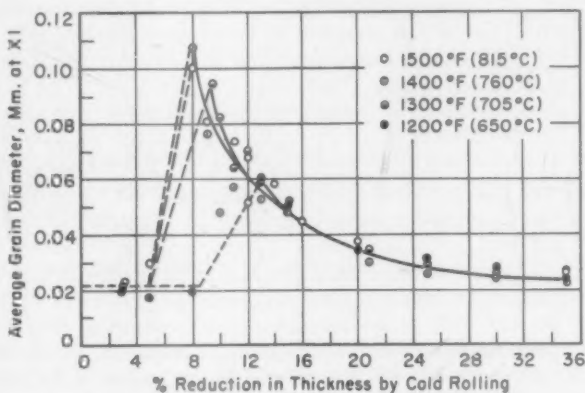


Fig. 6—Effect of Annealing Temperature and Amount of Deformation by Cold Rolling on Average Crystal Diameter of Ti-100A. Fine prior grain size. Annealing time 3 hours.

When a series of these coarse grain size specimens was rolled and annealed as listed in Table I and evaluated, no significant coarsening was observed.

A definite refinement in grain size, however, was measured above deformations of approximately 20%. Microstructures in this deformation range showed evidence of recrystallization.

Since results of roll-anneal experiments on the large grain size RC-55 indicated that a prior to rolling grain size could be large enough to preclude coarsening at deformations less than those result-

Table III
Comparison of Grain Size Behavior in Rolled Annealed Ti-100A of Fine and Large Prior to Rolling Grain Size

Ti-100A—Average prior to rolling grain size—0.020 to 0.025 mm. at $\times 1$		
Annealing Temp. °F	Max. Ave. Grain Diameter mm. at $\times 1$	Critical Deformation at max. grain diameter % Reduction in thickness
1500	0.10	8.0
1400	0.10	9.5
1300	0.071	11.0
1200	0.064	13.0
Ti-100A—Average prior to rolling grain size—0.049 mm. at $\times 1$		
Annealing Temp. °F	Max. Ave. Grain Diameter mm. at $\times 1$	Critical Deformation at max. grain diameter % Reduction in thickness
1500	0.084	13.0
1400	0.068	15.0
1300	0.070	15.0
1200	0.056	18.7

* All annealing for a period of 1½ hours.

ing in recrystallization, the alloy, Ti-100A, of an intermediate grain size was then rolled and annealed as reported in Table I. The salient features of these results are summarized and compared with fine prior to rolling grain size data in Table III. They are seen to be in accordance with the behavior predicted by thermodynamic analysis.

RESULTS AND DISCUSSION—ISOTHERMAL ANNEALING OF RC-55

In view of the consistent evidence of grain growth without recrystallization discussed in the preceding, isothermal anneals of cold-rolled RC-55, outlined in Table II, were carried out. Fig. 10 shows the isothermal recrystallization curves for RC-55 cold-rolled 30% reduction in thickness and annealed at 1100, 1200 and 1300 °F. Plots of the times for 30, 50 and 70% recrystallization as a function of the reciprocal absolute annealing temperature are given in Fig. 12. The corresponding rate curves for RC-55 cold-rolled 12% reduction in thickness and annealed 1200, 1300 and 1400 °F are shown in Fig. 11. Natural logarithms of times for 30, 50 and 70% transformation to coarse crystals as a function of reciprocal absolute temperature for this 12% cold-rolled and annealed series are also plotted in Fig. 12.

Fig. 13 is representative of the microstructure in RC-55 after 30% cold rolling. Fig. 14 shows a partial transformation of this cold-rolled structure after 1200 seconds at 1100 °F. The much smaller equiaxed crystals in the transformed areas are typical of those encountered in metals undergoing what has been customarily referred to as recrystallization.

Fig. 15 shows RC-55 after a cold rolling of 12%. Fig. 16 is taken from one of these specimens after annealing for 720 seconds at 1200 °F

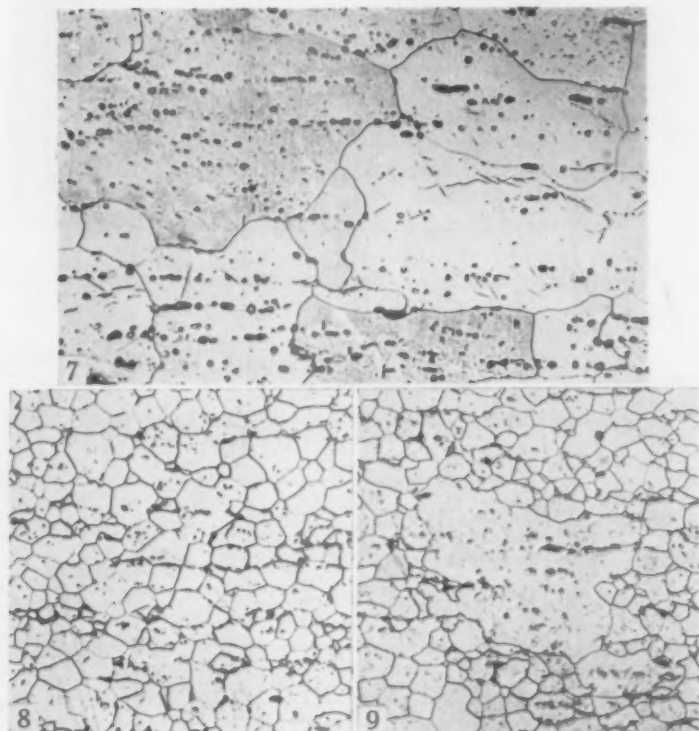


Fig. 7—Ti-100A Rolled 8% Reduction in Thickness and Annealed at 1500 °F for 1.5 Hours
Fig. 8—Ti-100A As-Received.
Fig. 9—Ti-100A Rolled 6% Reduction in Thickness and Annealed at 1500 °F for 1.5 Hours.
All Specimens Etched in Aqueous HF. $\times 250$.

and illustrates the partial transformation to abnormally large irregularly shaped crystals. Comparison of Fig. 14 with Fig. 16 in terms of the drastic differences in size and shape of transformed areas leads one to the conclusion that different phenomena are operative in the two cases.

Still further experimental evidence in substantiation of this conclusion is to be had from the calculations of activation energies for transformation in 12% cold-rolled and annealed titanium and the 30% cold-rolled and annealed titanium. The activation energy from the line representing 30% transformation by annealing following a 30% cold rolling is calculated to be 79 K cal./gm. atom, 74 K cal./gm. atom at 50% transformation and 78 K cal./gm. atom at 70% transformation. This is in reasonable agreement with the values reported by Liu and Margolin (8) from hardness measurements on 60% cold-rolled and annealed

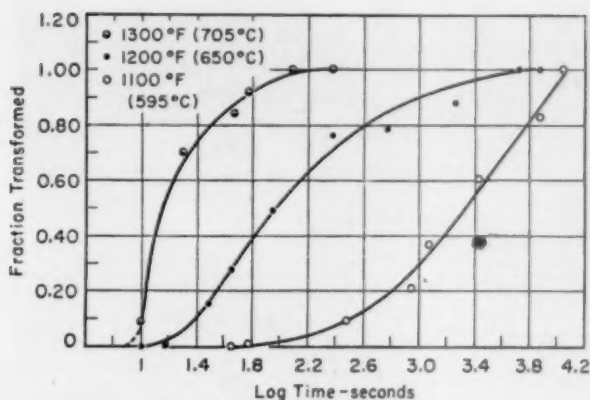


Fig. 10—Isothermal Reaction Rate Curves for Cold-Rolled 30% and Annealed RC-55.

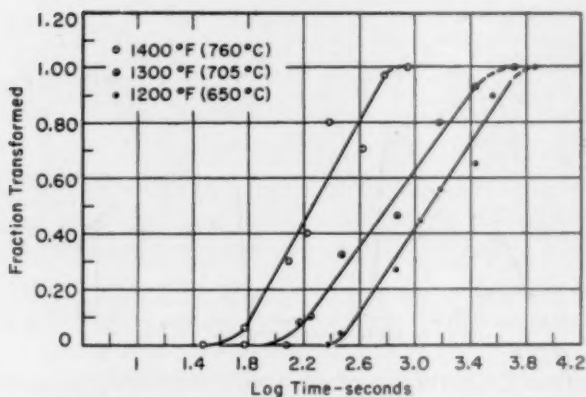


Fig. 11—Isothermal Reaction Rate Curves for Cold-Rolled 12% and Annealed RC-55.

low alloy content binary titanium alloys. The corresponding activation energy calculated for the 12% cold-rolled and annealed RC-55 is 35 K cal./gm. atom at 30 and 50% transformation and 33 K cal./gm. atom at 70% transformation. It is believed that considerable significance can be attached to these differences in activation energy values. There is little doubt that the process by which the transformation pictured in Fig. 14 has taken place is by what is customarily known as recrystallization. Thus, 74-79 K cal./gm. atom represents the activation energy of recrystallization for 30% cold-rolled RC-55. If the process by which transformation during annealing following a 12% cold rolling

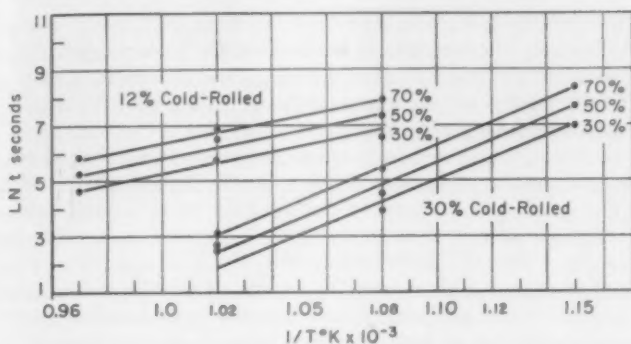


Fig. 12—Time for 30%, 50% and 70% Transformation Versus Reciprocal Absolute Temperature for 12% and 30% Cold-Rolled Annealed RC-55.

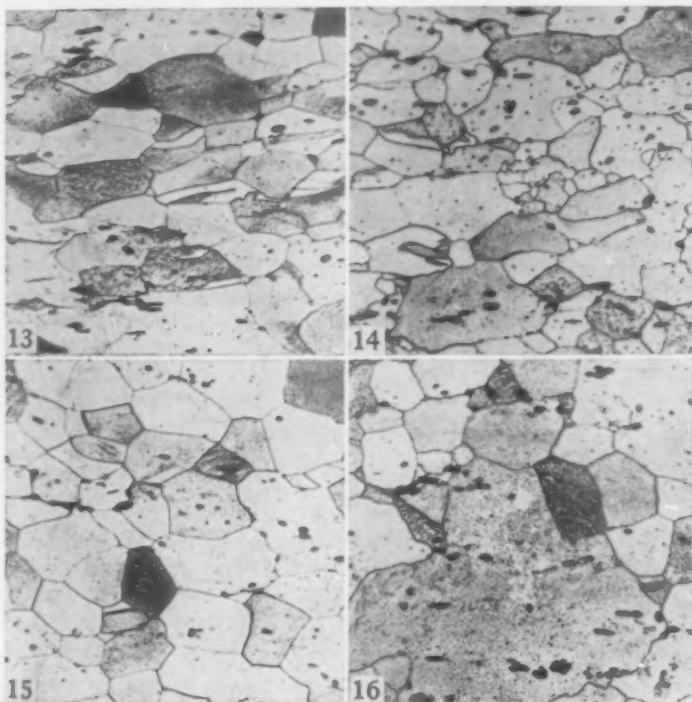


Fig. 13—RC-55 Cold-Rolled 30%.

Fig. 14—RC-55 Cold-Rolled 30% Annealed 1200 Seconds at 1100 °F.

Fig. 15—RC-55 Cold-Rolled 12%.

Fig. 16—RC-55 Cold-Rolled 12% Annealed 720 Seconds at 1200 °F.

All Specimens Etched in Aqueous HF. $\times 500$.

is also recrystallization, then the corresponding activation energy should be higher. The fact that it is considerably lower suggests that a transformation mechanism other than recrystallization is operative. It is believed that this value represents the activation energy for strain induced grain boundary migration.

That recrystallization of the titanium does not appear to proceed spontaneously when annealing follows small deformations, while boundary migration does, may be analyzed in terms of the related general thermodynamics. A small fraction of the total work expended in cold rolling a metal is stored within it as strain energy (9). When annealing temperatures provide sufficient atomic mobility, this stored energy accounts for the diminution in free energy accompanying the transformation, be it boundary migration or nucleation and growth in the recrystallization reaction. In recrystallization the formation of a relatively strain-free nucleus is accompanied by the formation of a new surface between it and the strained matrix. This means that the net free energy of recrystallization consists in a summation of energy terms, one of which is positive, representing the increase in free energy of new surface. It is true that the increasing curvature of boundaries during strain induced boundary migration represents an increase in interfacial free energy. However, it is probable that the magnitude of the former is greater than the latter when many nuclei form. Thus, stored energy resulting from critical deformations may be high enough to offset the positive interfacial energy change associated with boundary migration but not sufficient to offset the higher interfacial energy involved in nucleus formation. If the stored energy increase with increasing deformation is gradual enough, as appears to be the case with titanium, the deformation ranges in which either process may occur are correspondingly separated and either may be made to operate exclusively of the other.

CONCLUSIONS

The following statements summarize the results of experiments reported in this paper:

1. RC-55 and Ti-100A of fine prior to deformation grain size exhibit excessive coarsening when cold-rolled to a given level of so-called critical deformation and subsequently annealed. Prior to rolling grain size and annealing temperature influence the magnitude of both the critical deformation and the peak crystal size.
2. Titanium, RC-55 when critically deformed (8-12% reduction in thickness by cold rolling) and subsequently annealed, develops a structure of large irregularly shaped crystals by the process of strain-induced boundary migration. Normal re-

crystallization takes place when annealing follows cold rolling in excess of 20% reduction in thickness.

3. The activation energies for 30 to 70% recrystallization of 30% cold-rolled RC-55 titanium are in the range, 74 to 79 K cal./gm. atom. The activation energies for 30 to 70% transformation by strain-induced boundary migration of 12% cold-rolled RC-55 titanium are in the range, 33 to 35 K cal./gm. atom.

ACKNOWLEDGMENTS

The author wishes to acknowledge the assistance of John J. Turney in connection with the work on isothermal annealing.

This work was made possible through the financial assistance of the Ordnance Corp. The author is grateful for the advice and encouragement offered by Dr. Laurence S. Foster, Ordnance Material Research Office, of the Watertown Arsenal.

References

1. A. N. Holden, "Preparation of Metal Single Crystals," *TRANSACTIONS, American Society for Metals*, Vol. 42, 1950, p. 319.
2. R. F. Mehl, "Recrystallization," *METALS HANDBOOK*, American Society for Metals, 1948 Edition, p. 259.
3. W. M. Williams and R. Eborall, "Critical Strain Effects in Cold-Worked Wrought Aluminum and Its Alloys," *Journal, Institute of Metals*, Vol. 81, 1952-53.
4. S. L. Channon and H. L. Walker, "Recrystallization and Grain Growth in Alpha Brass," *TRANSACTIONS, American Society for Metals*, Vol. 45, 1953, p. 200.
5. S. E. Maddigan and A. I. Blank, "Recovery and Recrystallization in Longtime Annealing of 70-30 Brass," *Transactions, American Institute of Mining and Metallurgical Engineers*, Vol. 137, 1940, p. 170.
6. J. E. Burke and Y. G. Shiau, "The Effect of Mechanical Deformation on Grain Growth in Alpha Brass," *Transactions, American Institute of Mining and Metallurgical Engineers*, Vol. 175, 1948, p. 141.
7. P. A. Beck and P. R. Sperry, "Strain-Induced Boundary Migration in High Purity Aluminum," *Journal of Applied Physics*, Vol. 21, 1950, p. 150.
8. Y. C. Liu and H. Margolin, "Grain Size Control in Titanium and the Effect Thereon of Various Addition Agents," Final Report to Watertown Arsenal, WAL Report No. 401/105-16, p. 5.
9. M. B. Bever and L. B. Ticknor, "The Energy Stored During the Cold Working of A Gold-Silver Alloy," *Acta Metallurgica*, Vol. 1, No. 2, March 1953, p. 116.

DISCUSSION

Written Discussion: By H. P. Leighly, research metallurgist, Denver Research Institute, Denver, Colorado.

The author presents some interesting ideas, however some doubts are raised as a result of the data presented. Leighly and Walker² found in commercially pure titanium, corresponding to RC-55, that the activation energies for recrystalli-

²H. P. Leighly and H. L. Walker, "Recrystallization and Grain Growth in Commercial Titanium," *Transactions, American Institute of Metals*, Vol. 8, 1954-55, p. 288, TP 120.

zation after 0.15, 0.30, 0.38 and 0.60, fractional reductions in thickness to be 39.4, 38.9, 37.4 and 36.3 k cal/mole which are in general agreement with results of Bartholomew's 12% deformation which, however, disagrees completely with his 30% deformation results. The reason for such a large variation is difficult to discern and such a variation is quite unusual. Would the author describe in detail the method used to measure the fraction recrystallized?

In the case of the large grains in the 12% deformation, it seems doubtful that they could result from strain induced boundary migration for two reasons. In the case of the references cited,^{3,4,5} the materials used were of very high purity and secondly, deformation of the specimen was by elongation. Elongation is probably less severe deformation than cold rolling. I suggest that actually the author is examining instances of coarsening, resulting from recrystallization near the critical deformation and that with less deformation he should get larger and larger grain size until, at least in theory, he should achieve a single crystal such as might result from the strain anneal method for producing single crystals. Leighly and Walker² found no instances of unusually large nonuniform grain size in 15% cold-rolled specimens. Would the author elaborate on the discussion of the coarsening phenomenon inasmuch as this disagrees with the classical representation of recrystallized grain size⁶ after various amounts of deformation.

It is unfortunate that the data presented in Figs. 1 through 6 give the grain size after a finite annealing time period (meaning recrystallization and grain growth) rather than recrystallized grain size. Data presenting the recrystallized grain size as a function of deformation might either confirm or deny the accuracy of the equations derived by Leighly, Walker and Marx.⁷

Author's Reply

The reason for the large difference in recrystallization activation energies between those reported in this paper and those reported by Dr. Leighly may well be found in any or a combination of the following considerations:

1. Dr. Leighly's values are computed on the basis of 100% recrystallization. In view of the diminishing rate at which recrystallization approaches completion, uncertainty as to the difference between samples which still contain a small fraction of distorted metal and one in which distorted metal has "just" disappeared can lead to substantial uncertainty in the time for 100% recrystallization.
2. Deformation by cold rolling is heterogeneous. Because of this, all evaluations leading to data reported in this paper were made longitudinally at a location midway to the nearest 0.01 inch between roll contact surfaces of the sample. At small reductions where large irregularly shaped crystals were experienced in the mid-thickness, outer layers near the rolled surfaces were frequently observed to consist of completely recrystallized fine grained metal.

³ J. E. Burke and Y. G. Shiau, "The Effect of Mechanical Deformation on Grain Growth in Alpha Brass," *Transactions, American Institute of Mining and Metallurgical Engineers*, Vol. 175, 1948, p. 141.

⁴ S. E. Maddigan and A. I. Blank, "Recovery and Recrystallization in Longtime Annealing of 70-30 Brass," *Transactions, American Institute of Mining and Metallurgical Engineers*, Vol. 137, 1940, p. 170.

⁵ P. A. Beck and P. R. Sperry, "Strain-Induced Boundary Migration in High Purity Aluminum," *Journal of Applied Physics*, Vol. 21, 1950, p. 150.

⁶ R. F. Mehl, "Recrystallization," *American Society for Metals—Metals Handbooks*, 1948, p. 259.

⁷ H. P. Leighly, H. L. Walker and J. W. Marx, "Recrystallization and Stored Energy," *Journal of Metals*, June 1953.

3. Initial grain size is known to have a substantial influence on the activation energy of recrystallization, larger initial grain sizes leading to higher values of activation energy. The initial grain size of the titanium used in the reported experiments is at least twice that of the titanium on which Dr. Leighly's values are based.

The method used to measure fraction recrystallized as well as fraction coarsened is standard. Twenty direct projection photographs were taken per sample at mid-thickness to the nearest 0.01 inch. Transformed areas were outlined within a 10 square inch circle and planimeted. Each point on the isothermal transformation curves is the mean of twenty such evaluations. Duplicate runs evaluated by hardness measurements as well as hardness readings on metallographic samples showed reasonable agreement.

It is well known that insolubles block or retard boundary migration. On the other hand, critical dispersions have been found to lead to "exaggerated" growth. In any case, it should be pointed out that large crystals as postulated by the classical minimum nuclei theory must in their growth still surmount such impurity obstacles. At small reductions where critical coarsening is experienced, the driving force for growth from strain energy differences should not favor growth from nuclei or subgrains more than grain boundary migrations.

While not included in this paper by reason of space limitations, the writer has photographs of 12% reduced titanium which photographs of identical crystals before and after annealing show "ghosts" of original boundaries measurably displaced from final boundaries. Since normal grain growth could not accomplish the displacements evidenced here in the short time of 210 seconds and in view of the fact that boundaries show evidence of having moved away from their centers of curvature, it appeared reasonable to postulate a strain induced migration.

MECHANICAL PROPERTIES AND HEAT TREATMENT OF TITANIUM-NIOBIUM ALLOYS

BY L. W. BERGER, D. N. WILLIAMS AND R. I. JAFFEE

Abstract

Niobium has a relatively strong solid-solution strengthening effect in alpha titanium. However, beta titanium stabilized by niobium is very soft and ductile and about equal in strength to unalloyed titanium. Properties of beta-quenched alloys show minimum yield strength, maximum tensile strength, and maximum uniform elongation at about 35% niobium. Strain-transformed martensite was observed in alloys containing 25 to 40% niobium. The beta alloys with 50 or more % niobium are mechanically stable and have characteristically low uniform elongation and small spread between yield and ultimate strengths. There is no increase in hardness associated with martensite formation in Ti-Nb alloys. However, mechanical properties of Ti-Nb alloys may be varied considerably by solution treatment in the alpha-beta field to control amount and composition of the retained beta, and alloys containing 20 to 35% niobium may be appreciably hardened by quenching from the beta field followed by aging. (ASM International Classification Q general, J27a, J27d, Ti, Nb)

INTRODUCTION

WITH THE FUTURE availability of niobium (columbium) looking more promising as a result of recent discoveries of ore deposits in the United States, Canada, and Africa, the outlook for applications of the metal has changed drastically. Instead of seeking ways to conserve the metal, investigators are seriously considering niobium as a structural base material in its own right, chiefly for high-temperature applications (1-3),¹ and as an alloying addition to other metals (4). One of the metals in which niobium might be a valuable alloying element is titanium. In this paper, the results of studies of the mechanical properties of titanium-niobium alloys containing up to 70 weight % niobium are described.

Prior investigations have determined the constitution (5,6) and electrical properties (7) of the titanium-niobium alloys. On the basis

¹ The figures appearing in parentheses pertain to the references appended to this paper.

A paper presented before the Thirty-Ninth Annual Convention of the Society, held in Chicago, November 4-8, 1957. The authors, L. W. Berger, D. N. Williams, and R. I. Jaffee, are associated with Battelle Memorial Institute, Columbus, Ohio. Manuscript received April 12, 1957.

of arc-melted and homogenized alloys, Hansen, et al (5), reported the titanium-niobium phase diagram shown in Fig. 1. The phase diagram shows a beta-isomorphous system with a limited solubility of niobium in alpha titanium and a rather extensive alpha-beta field. At 1100 °F, about 3% of niobium can be dissolved in alpha, while the alpha-beta field extends from 3 to 53% niobium. The beta transus of the titanium-niobium system decreases only moderately with increasing alloy con-

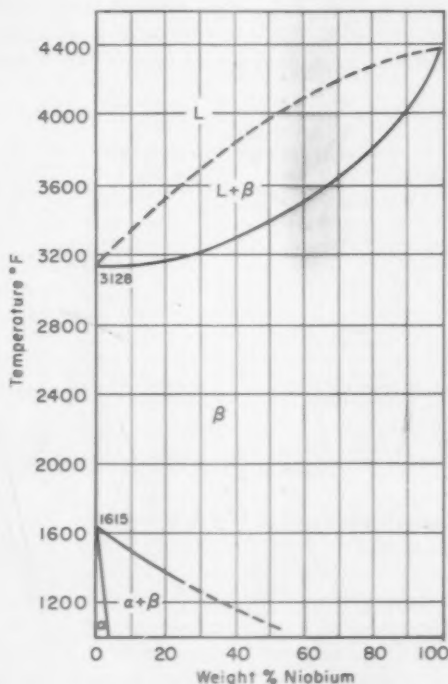


Fig. 1—The System Titanium-Niobium After Hansen et al (5).

tent, indicative of the relatively mild beta-stabilizing action of niobium. On quenching from the beta field, Duwez (6) found that beta titanium is completely retained in alloys containing 36 or more % niobium. A martensite reaction occurs in alloys of lesser niobium content. From the equilibrium diagram, therefore, the binary alloys would appear to offer heat treatment possibilities from the standpoint of both martensite and age-hardening (decomposition of metastable beta) reactions.

EXPERIMENTAL PROCEDURES

Alloy Preparation

A good grade of titanium sponge, of 120 to 140 Brinell hardness, and high purity niobium sheet, specified as 99.4% minimum purity, were used in this investigation. A typical analysis of the latter material is given in Table I.

Binary alloys containing up to 70% niobium were prepared as 35-gram buttons by inert-electrode arc melting on a water-cooled copper hearth, using a static argon pressure of from 15 to 20 centimeters of

Table I
Typical Analysis of Niobium Sheet

Element	Content, weight %
Zirconium	0.5
Tantalum	<0.15
Antimony	<0.005
Iron	<0.005
Magnesium	<0.001
Silicon	<0.01
Nickel	0.006
Aluminum	0.002
Titanium	0.002
Silver	0.002
Calcium	0.001
Copper	0.003
Manganese	0.001
Carbon	0.04
Nitrogen	0.06
Oxygen	0.1

mercury and a current of from 275 to 350 amperes. The copper hearth contained an elongated depression in which to hold the charge, which could be rocked from side to side during melting. This method provided rapid homogenization of the melt by eliminating the need for repeatedly opening the furnace in order to invert the ingots. The buttons were radiographed, and any ingots showing inhomogeneities were remelted until acceptable. Except for excessive spattering while melting the 60 and 70% niobium alloys, no difficulties in melting were encountered. Spot checks on intended compositions of 3, 20, and 60% niobium analyzed 3.7, 19.1, and 60.9%, respectively, indicating relatively good agreement between nominal and actual compositions.

The melted buttons were fabricated by forging in air at 1800 °F to approximately $\frac{3}{8}$ inch square cross section, followed by rolling in air at 1300 or 1500 °F to 0.050-inch sheet. A 10% reduction in thickness per pass was used during the rolling operation. After fabrication to sheet, the alloys were surface cleaned by grit blasting in order to remove loose scale. Sufficient material for property evaluation was then heat treated prior to preparation into test samples.

Heat Treatment

Short-time heat treatments above 1300 °F and all long-time treatments were carried out by encapsulating the samples in sealed Vycor tubes under a partial pressure of argon prior to exposure in the furnace. Other treatments were done in air.

Mechanical Testing

Longitudinal sheet tensile specimens were prepared with a $1.25 \times 0.25 \times 0.040$ -inch reduced section and a gage length of 1 inch. Tensile tests were performed using a platen speed of 0.02 inch per minute, while stress-strain data in the low strain range were obtained by means

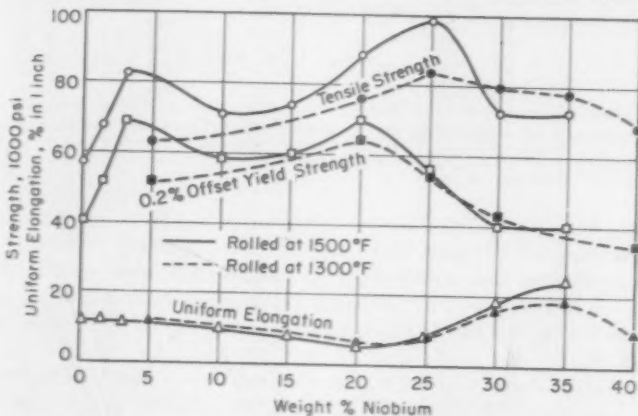


Fig. 2—Tensile Properties of Annealed or Stabilized Titanium-Niobium Sheet Alloys.

of strain gages and a strain indicator. Uniform elongation was measured by taking divider readings at the gage marks during loading up to the maximum tensile load. These readings were also used to calculate flow data. Bend specimens, 0.375 inch wide, were later taken from the undeformed tensile ends. These samples were tested on a series of progressively sharper Vee bend dies having a 105-degree bend angle. Bend ductility is then reported as the ratio of the radius of the last successful bend to the average thickness of the sample tested. Hardness tests were taken on a Vickers machine using a 10-kilogram load, and the average of five impressions is reported for each value. Fabricated and heat-treated samples were mounted on a longitudinal edge prior to indentation.

DISCUSSION OF RESULTS

Mechanical Properties

The mechanical properties of annealed titanium-niobium alloys are

Table II
Hardness and Ductility of Annealed or Stabilized Titanium-Niobium Alloys

Nominal Composition, wt % niobium (Balance Ti)	Vickers Hardness (10-Kg Load)		Total Elongation, % in 1 inch	Reduction in Area, %	Bend Ductility, T
	As Cast	Wrought ^(a)			
Rolled at 1500°F					
None	146	151	35	67	0
1.5	166	181	35	54	0
3	165	188	32	52	0
10	205	191	18	47	0
15	242	197	13	33	0
20	243	222	— ^(b)	30	0
25	207	207	— ^(b)	24	0
30	230	213	21	41	0
35	164	161	28	29	0
Rolled at 1300°F					
5	166	169	24	60	0
20	266	168	— ^(b)	38	0
25	249	175	16	55	0
30	205	210	— ^(b)	42	0
35	162	189	22	48	0
40	189	189	13	28	0

^(a) The unalloyed, 1.5, and 3% niobium alloys were annealed at 1100°F for 1 hour after rolling. The remainder of the alloys were equilibrated and stabilized by holding for one-half hour at 1300°F, furnace cooling to 1100°F, holding one hour, and air cooling.

^(b) Fractured outside gage mark.

shown in Fig. 2 and Table II. Samples containing up to 3% niobium were annealed for 1 hour at 1100 °F, while the remainder of the alloys were equilibrated and stabilized by holding for 0.5 hour at 1300 °F, furnace cooling to 1100 °F, holding for 1 hour, and air cooling. Data are given for two series of alloys, one rolled at 1500 °F and one rolled at 1300 °F.

Titanium-niobium alloys are characterized by low strength and excellent bend ductility. Niobium added in small quantities is a very good alpha solid-solution strengthener. Additions of up to 3% niobium significantly raise strength properties, have little effect on elongation, but lower reduction in area to some degree. Somewhere between 3 weight % niobium and 5 to 10 weight % niobium there is a decline in strength. Further additions, however, result in some alpha-beta strengthening until a maximum in tensile strength is reached at 25% niobium. This maximum is more pronounced in the alloys rolled at 1500 °F than it is in the alloys rolled at 1300 °F.

Up to 20% niobium, strength and ductility parameters are fairly parallel, but from 25 to 40% niobium significant differences are noted. There is a considerable decline in yield strength with a much larger difference between tensile and yield and a noteworthy increase in uniform elongation, which is at a maximum at 35% niobium. These differences are even more striking in the case of the beta-quenched alloys whose mechanical properties are presented in Fig. 3 and Table III. Here it can be seen that the beta-quenched Ti-35Nb alloy has maximum tensile strength, minimum yield strength, and maximum uniform and total elongation. The large gap between tensile and yield strengths

Table III
Hardness and Bend Ductility of Beta-Quenched Titanium-Niobium Alloys Rolled at 1500°F

Nominal Composition, wt % niobium (Balance Ti)	Vickers Hardness (10-Kg Load)		Bend Ductility, T
	As Cast	Wrought(a)	
30	230	179	0
35	164	155	0
40	166	135	0
50	153	138	0
60	176	146	0
70	169	139	0

(a) After rolling, the alloys were held for 2 hours at 1450°F and water-quenched.

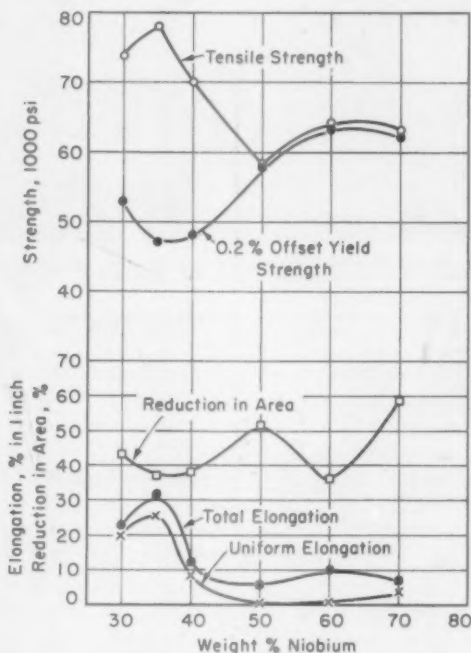


Fig. 3—Tensile Properties of Beta-Quenched (1450 °F) Titanium-Niobium Sheet Alloys.

with attendant increase in uniform elongation is characteristic of strain-induced martensite transformation, which has been observed in binary titanium-molybdenum alloys (8,9) as well as other titanium-base alloys (10).

To verify the formation of strain-induced martensite, all the tensile fractures of the binary alloys were examined microscopically and compared visually with unstrained material. The deformed structures of



Fig. 4—Strain-Induced Martensite in a Ti-35Nb Alloy Near a Hardness Impression. Etchant: 1.5% HF, 3.5% HNO₃, 95% H₂O.

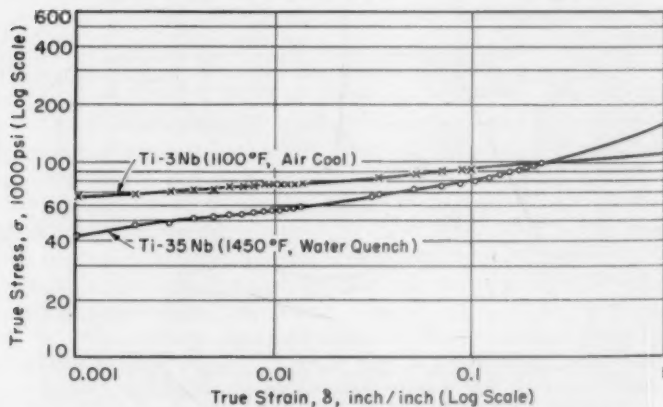


Fig. 5—Flow Curves for Ti-3Nb and Ti-35Nb Illustrating Mechanical Instability of the Beta Phase in the Ti-35Nb Alloy.

Ti-25Nb, Ti-30Nb, Ti-35Nb, and Ti-40Nb all showed the presence of a strain-induced acicular phase, while alloys lower or higher in niobium did not. An example of the appearance of strain-induced martensite in a Ti-35Nb alloy is shown in Fig. 4. Another indication of mechanical instability of the beta phase may be found in the shape of the flow

curve (11), which deviates sharply from a straight line. Fig. 5 shows the flow curves of Ti-3Nb and Ti-35Nb, the former alloy being mechanically stable and the latter alloy being mechanically unstable. The sharp upward slope of the Ti-35Nb curve (at $\delta = 0.11$) may be interpreted as due to work hardening of the alpha prime (martensite) which had formed previously during the earlier flat portion of the curve.

The binary alloys from 50 to 70% niobium are characterized by low strength, high yield to ultimate strength ratio, very low uniform elongation, excellent bend ductility, and a relatively high reduction in area, as shown in Fig. 3 and Table III. These alloys are mechanically stable beta alloys with a very low degree of work-hardening capacity. During the tensile test, necking takes place very shortly after the onset of plastic deformation.

It is interesting to note that the strengths of the stable beta alloys are about equal to that of the unalloyed titanium used in this investigation. The terminal alpha solid solution (Ti-3Nb), on the other hand, is considerably stronger than the soft beta alloys.

The trend in the strengths of the entire series of alloys reported in this paper agree quite well with the unpublished results of Suiter (12), who investigated some five titanium-niobium alloys containing from 10 to 65% niobium, which were tested after vacuum annealing for 16 hours at 1200 °F.

Microstructure

Representative microstructures of binary titanium-niobium alloys are shown in Fig. 6. The structures shown are of alloys rolled at 1500 °F and heat treated as indicated. Annealed Ti-1.5Nb is essentially all alpha, while stabilized Ti-10Nb is alpha-beta. The structure shown in Fig. 6b is typical of an alpha-beta alloy fabricated high in the alpha-beta field. The Ti-25Nb alloy (Fig. 6c), which was worked in the beta field and stabilized in the alpha-beta field, shows alpha plates in a beta matrix. Retention of the acicular alpha after annealing for some time in the alpha-beta field is indicative of the sluggishness of this alloy.

On quenching Ti-30Nb from 1450 °F, alpha prime (martensite) plus retained beta is obtained (Fig. 6d), while the same heat treatment applied to Ti-50Nb results in complete retention of beta (Fig. 6e). The Ti-35Nb alloy showed very little alpha prime in a beta matrix, while the Ti-40Nb alloy was all beta after quenching from the beta field. Both Ti-60Nb and Ti-70Nb as beta quenched show the fibrous and directional structure illustrated in Fig. 6f. On first observation, the structure appears to be worked (not recrystallized). Deeper etching, however, brings out equiaxed beta grains, some of which can be seen in the structure, without removing the wavy appearance. It seems probable that this effect may be caused by freezing segregation of niobium

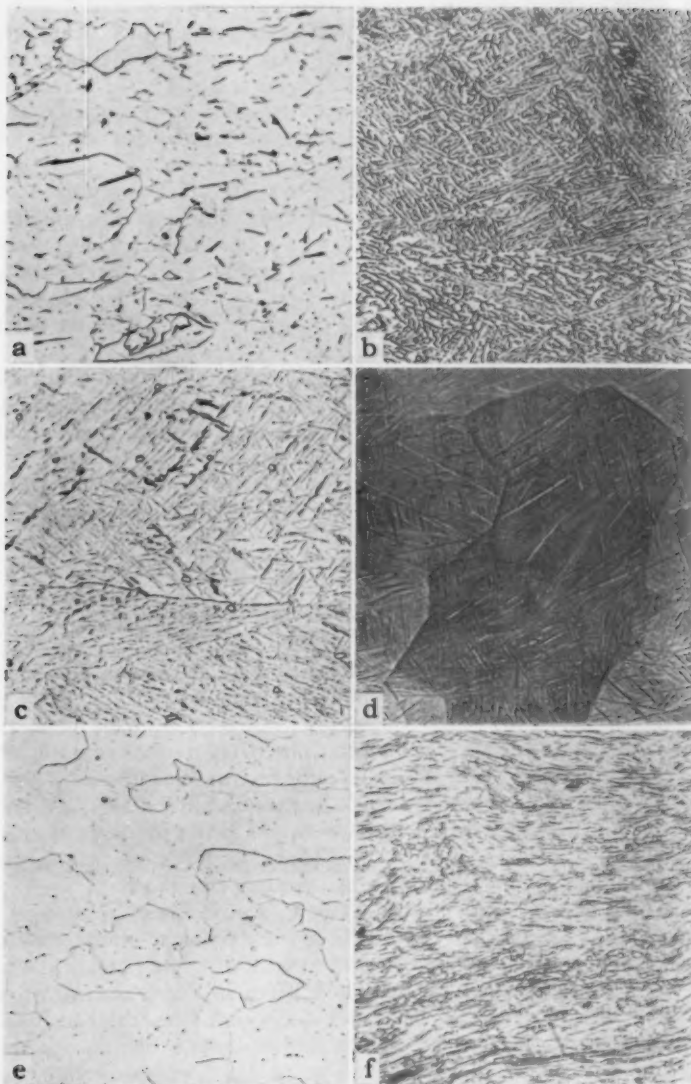


Fig. 6—Representative Microstructures of Wrought Titanium-Niobium Binary Alloys. (a)—Ti-1.5Nb—1 hour at 1100 °F, A.C.; (b)—Ti-10Nb—½ hour at 1300 °F, F.C. to 1100 °F, hold 1 hour, A.C.; (c)—Ti-25Nb—½ hour at 1300 °F, F.C. to 1100 °F, hold 1 hour, A.C.; (d)—Ti-30Nb—2 hours at 1450 °F, W.Q.; (e)—Ti-50Nb—2 hours at 1450 °F, W.Q.; (f)—Ti-70Nb—2 hours at 1450 °F, W.Q. Etchant: a, b, c—1.5% HF, 3.5% HNO₃, 95% H₂O. × 500. d, e, f—Chemical polish in 50% lactic acid, 30% HNO₃, 20% HF; final etch—0.5% HF, 99.5% H₂O. × 250.

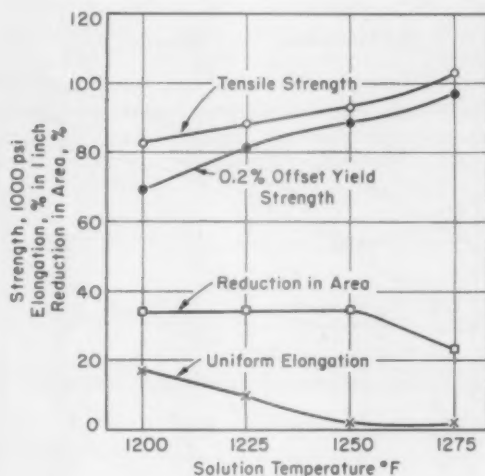


Fig. 7—Effect of Solution Treatment on the Mechanical Properties of Ti-20Nb.

in the as-cast material. Subsequent hot working apparently is unable to even out compositional differences because of the sluggishness of the alloys.

Heat Treatment

In the previous section, it was shown that beta-quenched alloys containing 30 to 40% niobium undergo strain transformation with a corresponding maximum uniform elongation at about 35% niobium. It is to be expected, therefore, that solution treatment of an alloy lower in niobium in the alpha-beta field so as to produce a beta phase of about 35% niobium will improve the uniform elongation of an alpha-beta

Table IV
The Effect of Beta Quenching on the Hardness of Annealed or Stabilized Titanium-Niobium Alloys

Nominal Composition, wt % niobium (Balance Ti)	Vickers Hardness (10-Kg Load)	
	Annealed or Stabilized	Beta Quenched(a)
None	151	138
1.5	181	170
3	188	196
10	191	212
15	197	186
20	222	190
25	207	211
30	213	184
35	161	151

(a) The unalloyed, 1.5, and 3% niobium alloys were held for 1 hour at 1700°F and water-quenched. All other alloys were quenched from 1550°F after being held at temperature for 1 hour.

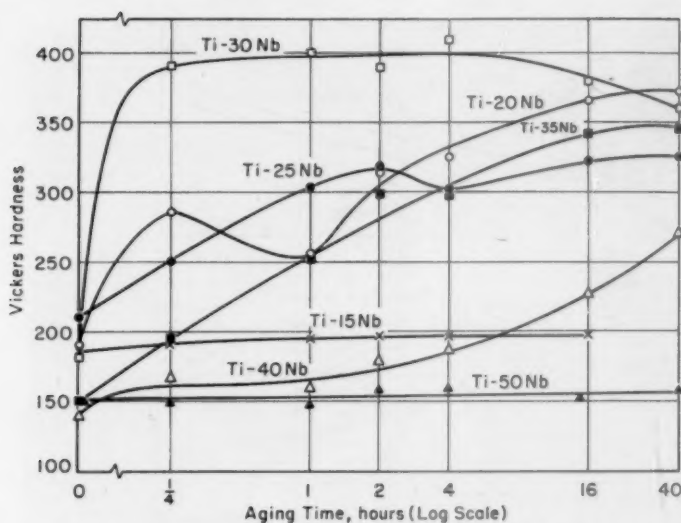


Fig. 8—The Aging Response of Titanium-Niobium Binary Alloys Quenched from 1550 °F and Aged at 800 °F.

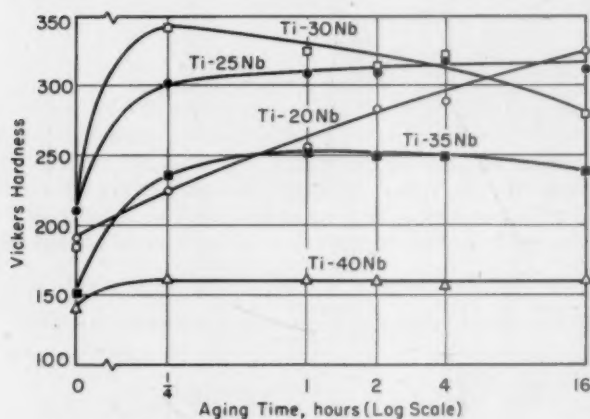


Fig. 9—The Aging Response of Titanium-Niobium Binary Alloys Quenched from 1550 °F and Aged at 900 °F.

alloy. Tensile specimens of Ti-20Nb were solution heat treated at 1200, 1225, 1250, and 1275 °F, which correspond at equilibrium to beta-phase compositions of approximately 38, 35, 32, and 29% niobium, respectively. Samples were held initially at 1325 °F for 4 hours, furnace

cooled to the solution temperature, held for 16 hours, and then water-quenched. The results of these treatments are shown in Fig. 7.

Solution treatments at both 1200 and 1225 °F increase the uniform elongation of the equilibrated and stabilized Ti-20Nb alloy from 5% to 17 and 10%, respectively; the lower temperature resulting in the greater increase. For the samples evaluated, raising the solution temperature lowers the uniform elongation, but also results in considerable

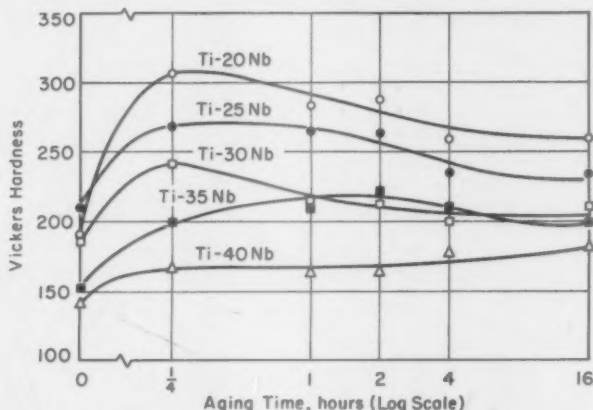


Fig. 10—The Aging Response of Titanium-Niobium Binary Alloys Quenched from 1550 °F and Aged at 1000 °F.

strengthening. Raising the solution heat treatment temperature also results in the formation of a greater amount of beta, which is leaner in niobium and not completely retained on quenching from the solution temperature. The solution studies further indicate that mechanical properties of alloys in the 20% niobium range are quite sensitive to small differences in heat treatment and, probably, fabrication temperatures in the alpha-beta field. This sensitivity might well account for the differences in properties previously noted for alloys rolled at 1500 °F and 1300 °F (see Fig. 2).

In order to ascertain the possible hardening effect associated with the formation of martensite, previously annealed or stabilized samples containing up to 35% niobium were beta quenched and checked for hardness, as shown in Table IV. It is apparent from the data shown that there is no increase in hardness connected with martensite formation.

To explore the possibility of age hardening, alloys containing from 15 to 50% niobium were quenched from the beta field and subsequently aged at 800, 900, and 1000 °F. The results of hardness measurements made during aging are presented in Figs. 8, 9, and 10. Response to low-temperature aging is best at 800 °F and for alloys containing from 20

Table V
Mechanical Properties of 0.040-Inch Sheet Samples of Heat Treated
Binary Titanium-Niobium Alloys

Nominal Composition, wt %	Heat Treatment	Yield Strength, psi		Tensile Strength, psi	Elongation, % in 1 inch		Reduction in Area, %	Vickers Hardness (10-Kg Load)	Bend Ductility, T
		0.1% Offset	0.2% Offset		Uniform	Total			
Ti-20Nb	Equilibrated and stabilized ^(a) 1 Hour at 1550°F, W.Q.; aged at 900°F for 16 hours	58,000	64,000	76,000 ^(c)	6	— ^(b)	38	168	0
Ti-20Nb		121,000	127,000	139,000 ^(c)	3	3	5	325	18.4
Ti-25Nb	Equilibrated and stabilized ^(a) 1 Hour at 1550°F, W.Q.; aged at 900°F for 4 hours	48,000	54,000	84,000	8	16	55	175	0
Ti-25Nb		110,000	119,000	136,000	4	5	8	319	4.7
Ti-30Nb	Equilibrated and stabilized ^(a) 1 Hour at 1550°F, W.Q.; aged at 800°F for 4 hours	39,000	43,000	79,000 ^(d)	16	— ^(b)	42	210	0
Ti-30Nb		— ^(e)	— ^(e)	133,000 ^(d)	0	0	0	409	> 23.4
Ti-35Nb	Equilibrated and stabilized ^(a) 1 Hour at 1550°F, W.Q.; aged at 800°F for 16 hours	105,000	112,000	78,000	18	22	48	189	0
Ti-35Nb		— ^(e)	— ^(e)	135,000	2	3	7	342	9.9

^(a) One hour at 1300°F, furnace cooled to 1100°F, held 1 hour, and air-cooled.

^(b) Fractured on or outside gage mark.

^(c) Fractured at maximum load.

^(d) Fractured before yielding.

^(e) Stress-strain data not available.

to 35% niobium. At 1000 °F, overaging takes place quickly. With increased niobium content above 35%, the beta phase becomes increasingly more stable so that at 800 °F (Fig. 8), the Ti-50Nb alloy shows no response to aging for times up to 40 hours. This alloy is apparently both thermally and mechanically stable. At low niobium contents, up to 15%, there is not sufficient stabilization of the beta phase, and no aging takes place.

A comparison of mechanical properties in the equilibrated and stabilized condition with those produced by selected aging treatments for alloys containing 20 to 35% niobium is presented in Table V. In all cases, strength is considerably increased at the expense of ductility. Extreme brittleness, as seen in the case of the aged Ti-30Nb alloy, as well as the double-hardness peak shown in several of the alloys in Fig. 8, appears to be consistent with omega formation although further confirmation by x-ray methods was not attempted.

ACKNOWLEDGMENTS

The research described in this paper was conducted at Battelle Memorial Institute under the sponsorship of the Kennecott Copper Corporation. Permission to publish these results is gratefully acknowledged. Thanks are due to Drs. Jenness and Croft for their cooperation, advice, and assistance during the course of the research.

References

1. R. L. Orr and D. W. Bainbridge, "The Correlation of High-Temperature Rupture Data for Niobium," Twenty-ninth Technical Report, Series 22, N7-ONR-295, Task Order II, NR-031-048, July 1953.
2. R. T. Begley and M. S. Fredenburg, "Development of Niobium-Base Alloys," First Quarterly Report No. A-2173, Westinghouse Electric Corporation, Aviation Gas Turbine Division, April 1956.
3. H. A. Saller, J. T. Stacy and S. Porembka, "Initial Investigation of Niobium and Niobium-Base Alloys," Battelle Memorial Institute Atomic Energy Commission Report BMI-1003, May 1955.
4. "MST 8A1-2Cb-1Ta Titanium Alloy," Mallory-Sharon Titanium Corporation Alloy Data Sheet November 26, 1956.
5. M. Hansen, E. L. Kamen, H. D. Kessler and D. J. McPherson, "Systems Titanium-Molybdenum and Titanium-Columbium," *Transactions, American Institute of Mining and Metallurgical Engineers*, Vol. 191, 1950, p. 881.
6. P. Duwez, "The Martensitic Transformation Temperature in Titanium Binary Alloys," *TRANSACTIONS, American Society for Metals*, Vol. 45, 1953, p. 934.
7. S. L. Ames and A. D. McQuillan, "The Resistivity-Temperature-Concentration Relationships in the System Niobium-Titanium," *Acta Metallurgica*, Vol. 2, Nov. 1954, p. 831.
8. E. S. Machlin and S. Weinig, "LeChatelier's Principle and Stress-Induced Displacive Transformations," *Acta Metallurgica*, Vol. 1, 1953, p. 480.
9. F. C. Holden, H. R. Ogden and R. I. Jaffee, "Heat Treatment and Mechanical Properties of Ti-Mo Alloys," *Journal of Metals*, Oct. 1956, p. 1388.
10. H. R. Ogden, F. C. Holden and R. I. Jaffee, "Effect of Alpha Solutes on the Heat-Treatment Response of Ti-Mn Alloys," *Journal of Metals*, Jan. 1955, p. 105.
11. F. C. Holden, D. N. Williams, W. E. Riley and R. I. Jaffee, "Flow Properties, Deformation Textures, and Slip Systems of Titanium and Titanium Alloys," TML Report No. 30, Titanium Metallurgical Laboratory, Battelle Memorial Institute, Jan. 1956.
12. J. Suiter, Private Communication.

EVALUATION OF A NEW TITANIUM-BASE SHEET ALLOY, Ti-4Al-3Mo-1V

By R. S. RICHARDS, D. L. DAY AND H. D. KESSLER

Abstract

Sheet from a production-size ingot of a new titanium-base alloy, Ti-4Al-3Mo-1V, was evaluated on the basis of annealed, solution treated, and solution treated and aged properties. Stress stability tests, cold rolling, welding, and actual forming of parts in the solution treated condition were also performed. The optimum solution temperature fell in the range, 1550-1650 °F, which resulted in solution treated properties of 135,000-140,000 psi ultimate tensile strength, 85,000-90,000 psi yield strength, 13-18% total elongation, 8-11% uniform elongation, and 2.5-3.0T bend radius. Final aged properties of 170,000-195,000 psi ultimate tensile strength, 130,000-165,000 psi yield strength, and 6-10% elongation were obtained after solution treatment in the range, 1550-1650 °F. Final aged strengths increased with increasing solution temperature. Fully heat treated sheet exhibited good stability under stress and good creep resistance at 800 °F. The higher heat treated strength levels also showed a short-time strength advantage at temperatures to 1000 °F. (ASM International Classification Q general, J27a; Ti, 4-3)

INTRODUCTION

WITH INCREASING applications for titanium and its alloys in high speed aircraft, it was recognized that a higher strength titanium sheet alloy was required which could be heat treated to a room temperature ultimate strength of 170,000-180,000 psi and would possess good strength and stability under stress in the heat treated condition to temperatures of 800 °F. In an effort to satisfy this requirement, the Ti-4Al-3Mo-1V composition was developed by the Titanium Metals Corporation of America as a moderate strength heat treatable alloy for such sheet applications and is now in semi-commercial production.

An aluminum content at the 4% level was chosen as a balance between good high temperature strength and fabricability, while a total of 3 to 4% of molybdenum and vanadium was selected to provide good heat treat ability and stability of properties at elevated temperatures.

A paper presented before the Thirty-Ninth Annual Convention of the Society, held in Chicago, November 4-8, 1957. Of the authors, R. S. Richards and H. D. Kessler are associated with the Product Development Division, Technical Department, and D. L. Day is associated with the Metallurgical Research Division, Titanium Metals Corporation of America, Henderson, Nevada. Manuscript received May 3, 1957.

These decisions were based upon a large amount of data previously developed at TMCA on the Ti-Al-Mo-V series of alloys.

The Ti-4Al-3Mo-1V alloy was one of those chosen for further study in the Department of Defense titanium sheet alloy rolling program. However, the major objective of this paper is to present results of the extensive evaluation conducted on this composition by TMCA prior to its selection for the government program. This evaluation included numerous tests utilizing a wide selection of annealing, solution treating and aging treatments as well as more limited elevated temperature tensile and stress stability tests. In addition, the effects of cold rolling, welding, and actual forming of parts were studied. The results were obtained on material from a production size ingot of the Ti-4Al-3Mo-1V alloy.

MATERIAL

A 1000-pound ingot of Ti-4Al-3Mo-1V was double vacuum-melted early in 1955. After melting and conditioning, the ingot was press-forged to 8×12 -inch billet size from temperatures of 1750–1800 °F. Blooming to 2×12 -inch random length slab was performed from a heating temperature of 1730 °F.

The slab material was rolled to 0.040 to 0.050-inch gage sheet using commercial mill practice. Finish rolling was initiated at a temperature of 1650 °F and a 37% reduction was achieved during the final rolling operation.

Chemical analyses were made on the ingot and sheet product as follows:

	Al %	Mo %	V %	Fe %	C %	N %	O %	H %
Ingot	4.33	3.08	1.13	0.09	0.02	0.02	—	—
Sheet	4.14	3.07	1.15	0.14	—	0.02	0.15	0.010

These results show that the amounts of alloying elements compared quite well with the intended additions of 4.0% aluminum, 3.0% molybdenum, and 1.0% vanadium.

The beta transus temperature was determined on sheet material by water quenching sheet specimens from temperatures of 1700 to 1850 °F. Metallographic examination showed that the beta transus was about 1780 °F.

EXPERIMENTAL PROCEDURES

Testing Procedures

All specimens were heat treated in air atmosphere furnaces except for a few special samples that were heated to high temperatures in vacuum for a period of 24 hours. Following heat treatment, most of the sheet specimens were lightly sand blasted to remove the heat treating scale. A few annealed and aged blanks were descaled in molten Virgo. Both methods of descaling produced comparable results.

After descaling, the specimens were pickled in a 20% nitric-2% hydrofluoric acid mixture at temperatures to 150 °F. Removal of 0.004 to 0.006-inch from the sheet gage insured a surface free from oxygen contamination.

Tensile specimens were machined following the pickling process, while bend samples ($\frac{3}{4}$ -inch wide) required no machining. Both 1 and 2-inch gage length tensile specimens were used and these were gridded with lines spaced at 0.1-inch intervals so that elongation measurements could be made in various parts of the reduced section. Tests were conducted on a Riehle Universal testing machine at a crosshead speed of 0.05-inch per minute and a microformer extensometer was used to autographically record the strain behavior of the specimens during the initial stage of each test. The strain rate was measured as approximately 0.005-inch per inch per minute up to the yield stress; beyond this point the strain rate increased rapidly to a constant value of about 0.05-inch per inch per minute to failure. After failure, elongation measurements were made with dividers and uniform elongation was obtained by measuring 0.5 and 1.0-inch spans outside the necked region for the one and 2-inch gage lengths, respectively. Local elongation was measured across the fracture utilizing a span of 0.2 inch.

Bend tests were of the guided wrap-around type in which samples were bent to incipient failure on a modified Di-Acro bender with a roller bearing nose wheel pushing the bend strip around the die to a maximum angle of about 120 degrees. Tests were usually made to determine the minimum bend radius (expressed in terms of R/T) to achieve a satisfactory 90 degrees bend after springback.

Heat Treatments

Sheet specimens were given annealing treatments which consisted of heating at temperatures between 1000 and 1500 °F for times up to 1 hour in furnaces which were maintained at the specified temperature, ± 15 °F, followed by air cooling. This material was evaluated by means of tensile and bend tests. Sheet was also evaluated by solution treating over a range of temperatures from 1375 to 1750 °F for $\frac{1}{2}$ -hour followed by quenching in water at room temperature. Solution temperatures were maintained within ± 5 °F. Tensile and bend tests were conducted on the material to determine the effect of solution temperature on these properties. Representative photomicrographs were taken of structures resulting from the various heat treatments.

Tensile properties were obtained after solution treating at 1550, 1600, 1650, and 1700 °F and aging at 900 and 1000 °F, ± 15 °F. In addition, material was solution treated at 1550 °F and aged at temperatures of 850, 900, and 1000 °F for times of 0.25 to 48 hours. Specimens were examined microscopically in an effort to correlate microstructure with aging response.

Elevated Temperature Tensile Tests

Elevated temperature tensile tests were conducted at 400 to 1000 °F on annealed, solution treated and aged, and solution treated, cold rolled, and aged material. Specimens were brought to temperature in an electrically heated tube furnace and equilibrated for approximately 30 minutes. Temperature control was ± 5 °F and uniformity was maintained at ± 5 °F over the gage length. Specimens were then pulled to failure using the same procedure as for room temperature tests.

Stress Stability Tests

Stress-stability tests were conducted at 800 °F for 1000 hours at 50,000 psi on material which had been solution treated at 1550 °F ($\frac{1}{2}$ hr) water-quenched and aged for 12 hours at 850, 900, and 1000 °F. Additional material was solution treated at 1650 °F ($\frac{1}{2}$ hr) water-quenched, aged at 900 and 1000 °F for 24 hours, and tested for stability at 800 °F under a stress of 50,000 psi for 300 hours.

Two indentations were made on each side of stress stability specimens with a Vickers hardness tester to serve as gage marks approximately 1-inch apart within the reduced section. This length was measured with a toolmaker's microscope and the specimens were loaded in lever-type stress-rupture frames. Samples were brought to temperature, prior to loading, by electrically heated tube furnaces with a maximum gradient of ± 5 °F over the gage length. During the tests, temperatures were controlled within ± 5 °F. After the stress stability test was completed, total deformation was measured from the gage marks. The samples were then tensile tested at room temperature to determine if the properties had changed markedly after exposure to stress at elevated temperatures. The stability of the material was determined by the loss in ductility exhibited during the subsequent room temperature tensile test; i.e., good stability is shown by little loss in ductility.

Formability Tests

Bend tests were conducted on material in various heat treated conditions. In addition, full range stress-strain diagrams were obtained for material solution treated at 1550 °F ($\frac{1}{2}$ hr) water-quenched. Some sheet was also tested in the annealed and aged conditions. Full range load-strain curves were obtained by means of a dual range microformer extensometer which recorded the entire strain behavior of the specimens.

Actual bending, stretch forming, and joggling operations were carried out at North American Aviation, Inc., Inglewood, California, on material which had been solution treated by the resistance heating method (1)¹. A more detailed discussion of this solution treating method will be published at a later date.

¹ The figures appearing in parentheses pertain to the references appended to this paper.

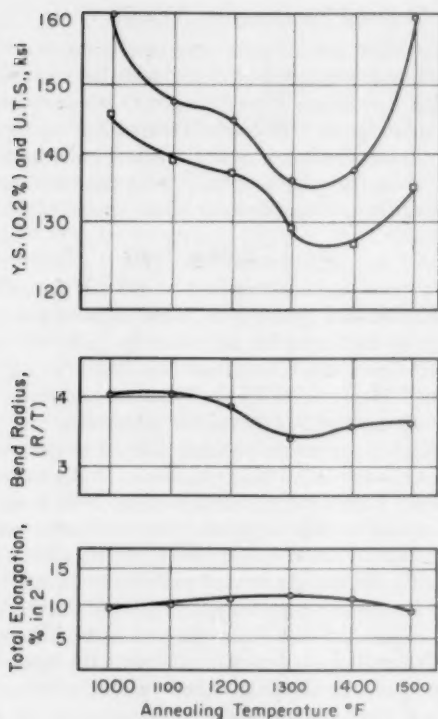


Fig. 1—Effect of Annealing Temperature on the Tensile and Bend Properties of Ti-4Al-3Mo-1V Sheet Annealed 1 Hour and Air-Cooled.

Welding

Annealed material was Heliarc fusion butt-welded without filler using a welding speed of 16 inches per minute at 60 volts and 90 amperes. The welded material was examined on the metallograph and a microhardness survey was taken across the weld zone. Guided wrap-around bend tests on the Di-Acro bender and tensile tests were conducted on both the as-welded and heat treated material.

RESULTS AND DISCUSSION

Annealing Studies

Sheet specimens were given annealing treatments in the range of 1000 to 1500 °F for periods of 8 minutes to 1 hour. Tensile and bend properties are summarized in Fig. 1. Since there were only minor

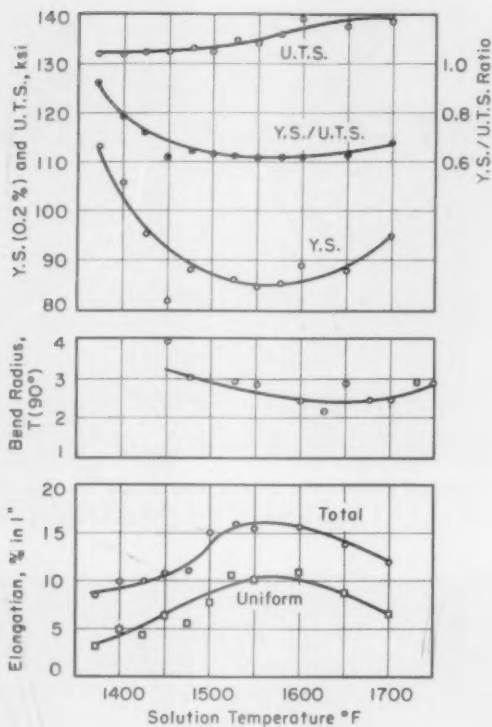


Fig. 2—Effect of Solution Temperature on the Tensile and Bend Properties of Ti-4Al-3Mo-1V Sheet Heated $\frac{1}{2}$ Hour at Temperature and Water-Quenched.

changes in annealed properties with varying times at annealing temperatures, the data for 8, 15, 30, and 60 minute treatments were averaged and graphed as a single point for each temperature in Fig. 1. These results show that a decrease in strength and minimum bend radius was obtained with increasing temperatures to 1300 °F. Above 1400 °F, the strength increased sharply indicating partial transformation of the beta phase during air cooling.

Solution Treatments

Solution treating studies were conducted using solution temperatures from 1375 to 1750 °F and tensile and bend properties are presented graphically in Fig. 2. Of particular interest is the minimum yield strength and minimum yield-to-tensile strength ratio observed at a solution temperature at about 1550 °F. This phenomenon is notable in

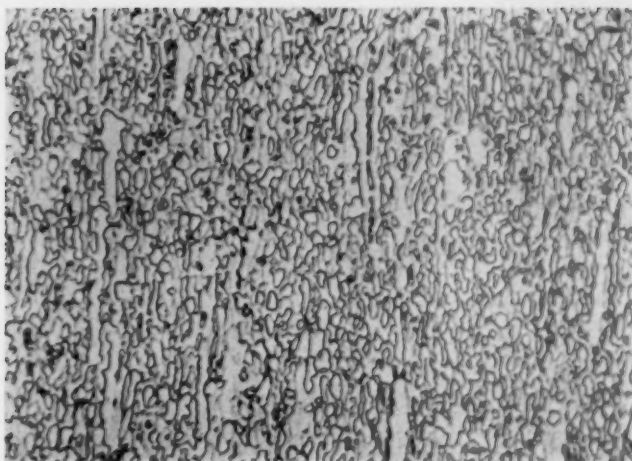


Fig. 3—Ti-4Al-3Mo-1V Longitudinal Section with Rolling Direction Shown Vertically, 1550 °F ($\frac{1}{2}$ hour) Water-quenched. Primary alpha in a continuous beta matrix. 1% HF + 12% HNO₃ etch $\times 750$. UTS 134 ksi; Y.S. (0.2%) 81 ksi; Elong 16% in 1"; Bend 2.9T—90°.

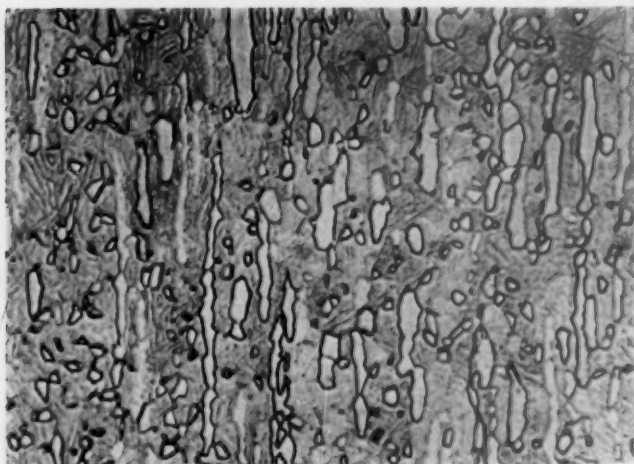


Fig. 4—Ti-4Al-3Mo-1V Longitudinal Section with Rolling Direction Shown Vertically, 1700 °F ($\frac{1}{2}$ hour) Water-quenched. Elongated primary alpha in a partially transformed beta matrix. 1% HF + 12% HNO₃ etch $\times 750$. UTS 138 ksi; YS (0.2%) 95 ksi; Elong 12% in 1"; Bend 2.5T—90°.

this type of alloy and appears to be the result of retained metastable beta. It has been postulated that, during tensile testing or other plastic deformation, a part of the metastable beta transforms to martensite as

a result of a strain-induced reaction (2,3). This apparently manifests itself in a low yield strength, as shown in Fig. 2. The large spread between yield and ultimate tensile strengths is indicative of good formability, as will be discussed in a later section.

It is evident that the maximum tensile elongation (both total and uniform) occurred at solution temperatures which were near the higher temperature end of the minimum yield strength "dip," and that the

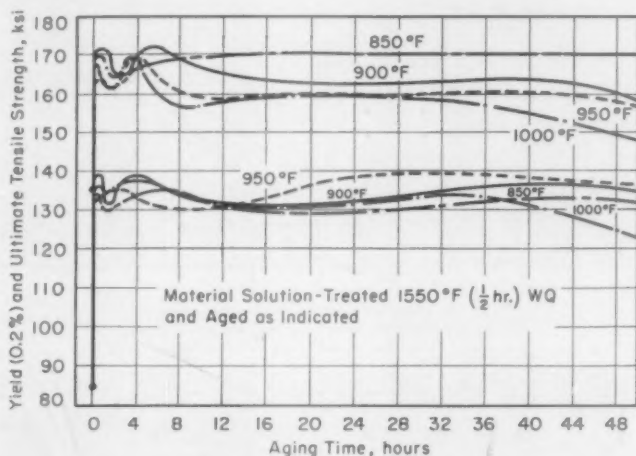


Fig. 5—Effect of Aging Time on the Tensile Properties of Ti-4Al-3Mo-1V Sheet.

bendability improved slightly with increased solution temperatures. The best bendability was obtained at solution temperatures of 1600 to 1700 °F.

Fig. 3 shows the elongated alpha-beta mixture obtained by finish rolling this alloy from 1650 °F and solution treating at 1550 °F ($\frac{1}{2}$ hr) water-quenched, while Fig. 4 shows the microstructure achieved by solution treating the sheet at a higher temperature of 1700 °F. It is interesting to note that good bend properties were obtained for material solution treated at these higher temperatures even though the matrix contained a substantial amount of partially transformed beta. However, the tensile ductility had decreased some from the peak values obtained at solution temperatures of 1550 to 1600 °F.

Aging Studies

The effects of aging time and temperature on the tensile properties of Ti-4Al-3Mo-1V sheet solution treated at 1550 °F ($\frac{1}{2}$ hr) water-quenched are shown in Fig. 5. From these curves it is seen that the strength in an overaged condition (e.g., 12 to 24 hours) decreased with

increasing aging temperatures above 850 °F. Peak strength was obtained after aging at 900 °F for 4 to 6 hours. Two aging peaks and the possibility of a third are shown in Fig. 5 for aging temperatures of 900 to 1000 °F. The observation of these peaks seems reasonable since some rather complex reactions occur during aging. Reactions such as the formation of coherent omega, loss of this coherency, and formation and

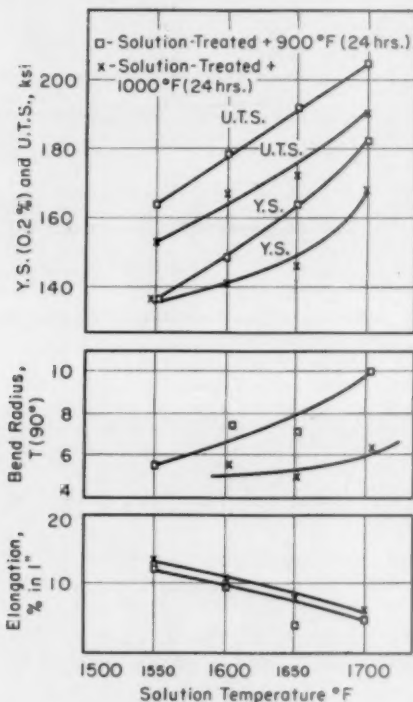


Fig. 6—Effect of Solution Temperature on Longitudinal Tensile and Bend Properties of Aged Ti-4Al-3Mo-1V Sheet.

growth of alpha and enriched beta from the omega (with and without coherency) could easily account for the inflections observed in the aging curves.

The effect of solution temperature on final aged tensile and bend properties is shown in Fig. 6. Aged strength increased with increasing solution temperature which is typical for this type of alpha-beta alloy. Using an aging temperature of 900 °F for 24 hours, the ultimate tensile strength increased from 172,000 to 202,000 psi as the solution temperature was raised from 1550 to 1700 °F. By aging at 1000 °F for 24

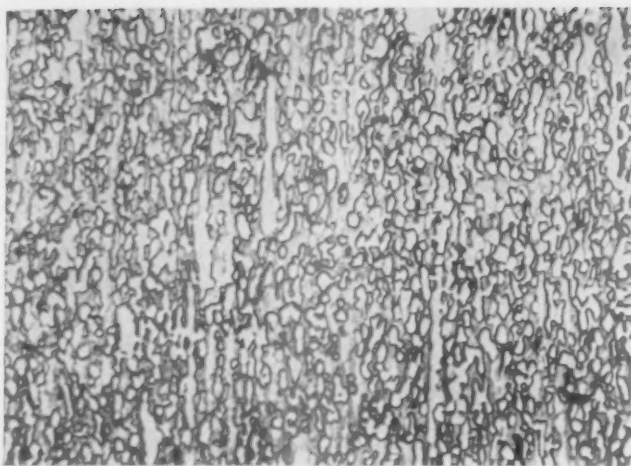


Fig. 7—Ti-4Al-3Mo-1V Longitudinal Section with Rolling Direction Shown Vertically, 1550 °F (½ hour) Water-quenched + 900 °F (4 hours) air-cooled. Primary alpha in a partially aged beta matrix. 1% HF + 12% HNO₃ etch × 750. UTS 175 ksi; YS (0.2%) 143 ksi; Elong 11% in 1".

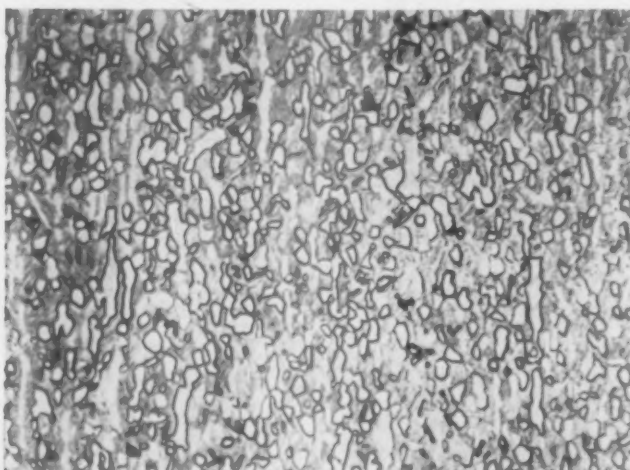


Fig. 8—Ti-4Al-3Mo-1V Longitudinal Section with Rolling Direction Shown Vertically, 1650 °F (½ hour) Water-quenched + 900 °F (24 hours) air-cooled. Primary alpha in an overaged beta matrix. UTS 193 ksi; YS (0.2%) 165 ksi; Elong 7% in 1".

hours, the ultimate strength increased from 161,000 to 190,000 psi for this same range of solution temperatures.

Microstructures of aged specimens, which had been solution treated

at 1550 °F ($\frac{1}{2}$ hr) water-quenched, are represented by the aged structure (900 °F for 4 hours) shown in Fig. 7. The aged structure following solution treatment at a higher temperature of 1650 °F is shown in Fig. 8.

Elevated Temperature Tensile Properties

The elevated temperature tensile properties are plotted in Fig. 9 and 10. Fig. 9 shows elevated temperature tensile properties of material

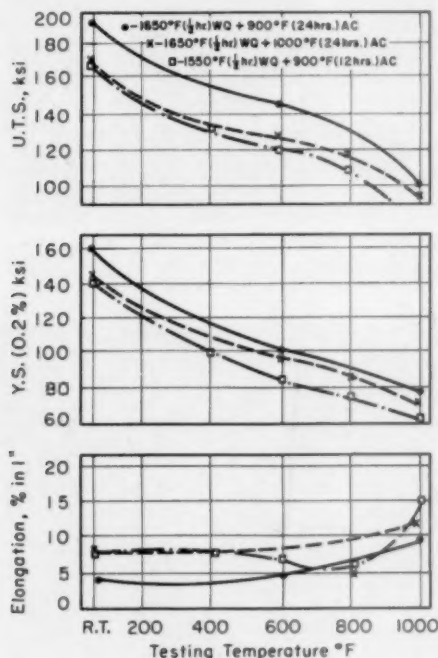


Fig. 9—Elevated Temperature Properties of Ti-4Al-3Mo-1V Sheet Solution Treated and Aged as Indicated (Longitudinal).

which was solution treated at 1650 °F and aged at 900 and 1000 °F for 24 hours as well as those for sheet which had been solution treated at 1550 °F and aged at 900 °F for 12 hours. Comparison of material heat treated to substantially the same room temperature tensile strength level (170,000 psi) shows that the higher solution temperature of 1650 °F resulted in significantly higher elevated temperature strengths to 1000 °F. By heat treating at 1650 °F ($\frac{1}{2}$ hr) water-quenched + 900 °F (24 hours) AC, a strength advantage of 20,000 to 25,000 psi

was obtained (compared to solution treating at 1550 °F for ½ hour and aging at 900 °F for 12 hours) which persisted at 1000 °F.

Elevated temperature tensile properties of Ti-4Al-3Mo-1V as annealed, as solution treated and aged, and as solution treated, cold rolled, and aged, are shown in Fig. 10. Higher room temperature strengths obtained by heat treatment were also observed at higher testing tem-

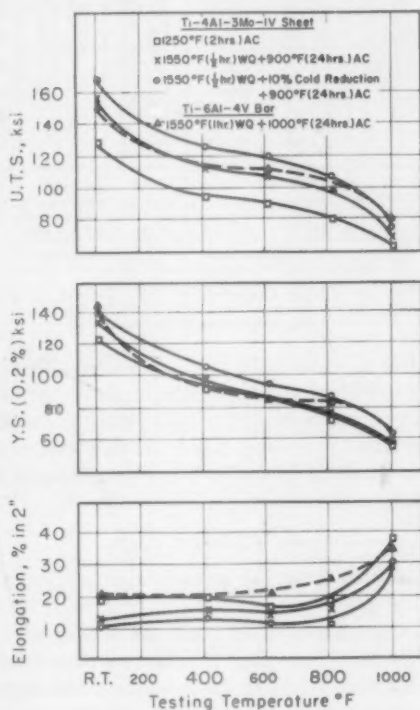


Fig. 10—Elevated Temperature Properties of Ti-4Al-3Mo-1V Sheet and Ti-6Al-4V Bar (Longitudinal Specimens).

peratures, although to a lesser extent. Elevated temperature properties of heat treated Ti-6Al-4V bar are included in Fig. 10 for comparison; properties of Ti-4Al-3Mo-1V sheet were quite comparable to those of Ti-6Al-4V bar as heat treated to about the same room temperature strength level. It is interesting to note that Ti-4Al-3Mo-1V sheet which had been solution treated at 1550 °F, cold-rolled 10% and aged, possessed elevated temperature strengths which were consistently higher than the material which had not been cold-worked. This indicates the

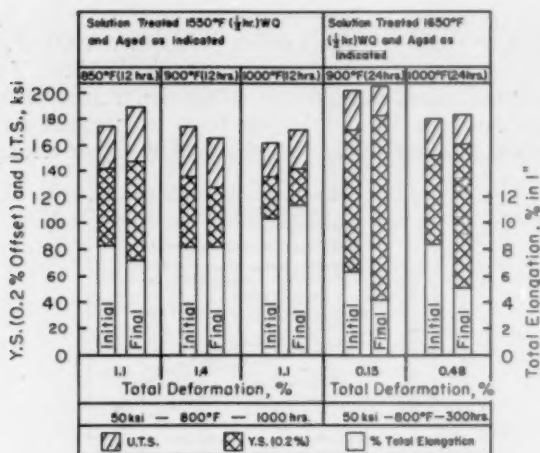


Fig. 11—Tensile Properties of Heat Treated Ti-4Al-3Mo-1V Sheet Before and After Stress Stability Testing as Indicated.

persistence of what appears to be cold work strengthening even after aging at 900 °F for 24 hours. This strength advantage was maintained over the entire temperature range to about 1000 °F, but decreased with increasing temperature of testing. Thus, no deleterious effect on final aged strength was obtained by cold deformation of sheet in the solution treated condition.

Stress Stability Tests

Information obtained from the stress-stability tests is presented in Fig. 11. In the first group of tests solution treated at 1550 °F (1/2 hr) water-quenched, aging times of 12 hours were utilized, since this was considered to be the minimum time to achieve a reasonably stable over-aged condition (see Fig. 5). After stress stability testing for 1000 hours at 800 °F, it can be noted that the ultimate tensile and yield strengths have changed slightly with little change in the tensile elongation. The increase in strength observed for the two specimens, which were aged at 850 and 1000 °F, seems to correlate with the aging curves shown in Fig. 5, i.e., both curves show increased strength with aging times longer than 12 hours. Total plastic deformation in 1000 hours at 800 °F and 50,000 psi averaged 1.2%, showing that the material possesses good creep resistance along with good stability.

The second group of tests was conducted on material which had been solution treated at 1650 °F (1/2 hour) water-quenched and aged at 900 and 1000 °F for 24 hours. Subsequent stability testing for 300 hours at 800 °F under a stress of 50,000 psi increased the yield strength of

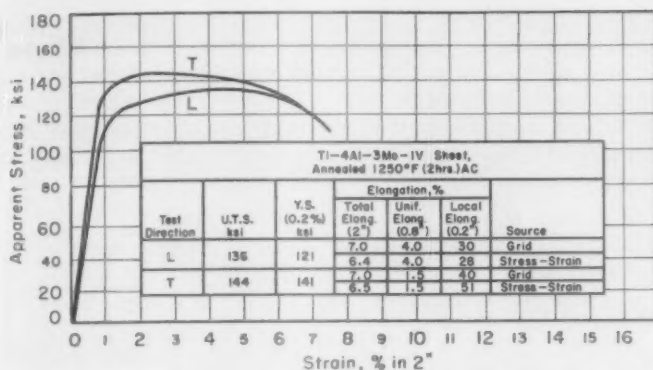


Fig. 12—Full Range Stress Strain Curves for Annealed Ti-4Al-3Mo-1V Sheet.

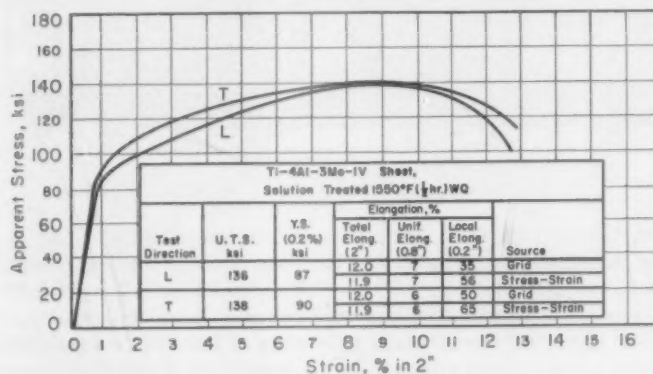


Fig. 13—Full Range Stress Strain Curves for Solution Treated Ti-4Al-3Mo-1V Sheet.

sheet in both aged conditions by approximately 10,000 psi while the elongation dropped slightly. The total deformations of 0.15% for the 900 °F aging treatment and 0.48% for the 1000 °F aging treatment indicate good creep resistance for these high strength heat treatments, although a direct comparison cannot be made with the lower strength heat treated conditions, since they were tested for 1000 hours.

Formability Tests

Bend data have been shown in Figs. 1, 2, and 6 for all three general types of heat treatment; i.e., annealed, solution treated, and solution treated and aged. Full range stress-strain diagrams are presented in Figs. 12 through 14 for the conditions indicated on the diagrams. The gridded tensile elongation data given were obtained by dividers and

0.1-inch grids on the specimens. The uniform elongation values derived from the stress strain diagrams were assumed to be the elongations which occurred just before the maximum load was reached. In curves with "flat" maximum loads (Figs. 12 and 14), the beginning of the "flat" was chosen as the limit of uniform elongation. Elongation values obtained by the two methods of measurement agree reasonably well. The stress-strain diagrams for sheet solution treated at 1550 °F

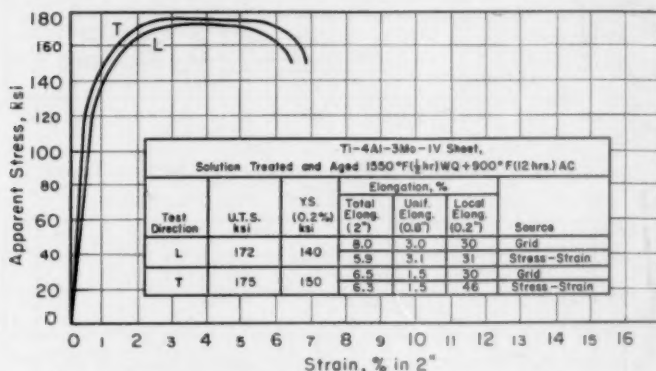


Fig. 14—Full Range Stress Strain Curves for Solution Treated and Aged Ti-4Al-3Mo-1V Sheet.

(Fig. 13) show a continuously rising curve from the yield stress to the ultimate tensile strength which should be of benefit in stretch forming operations because of this work hardening characteristic.

Figs. 12 and 14 show the strain behavior of sheet in the annealed and solution treated plus aged conditions, respectively. A rather pronounced lack of strain hardening beyond the yield stress is seen in the annealed condition. (Fig. 12) in contrast to the continuously rising curves for solution treated material (Fig. 14). Also a significant amount of directionality is shown in the annealed material, while the solution treated sheet exhibited much less directionality.

Four sheets of Ti-4Al-3Mo-1V, each measuring approximately 0.048 × 22 × 25-inches, were resistance solution heated at 1550 °F (1 minute) water-quenched (1). These were acid pickled and sent to North American Aviation, Inc., Inglewood, California, for formability tests and evaluation.

Strips of the material were press brake bent to 4T radius—90 degree angle sections at room temperature. These were subsequently stressed to approximately 70,000 psi and stretch wrapped at a so-called "No. 1 wrap rate". Both outboard and inboard flanges were stretch wrapped satisfactorily. Although exhaustive tests of this type were not con-

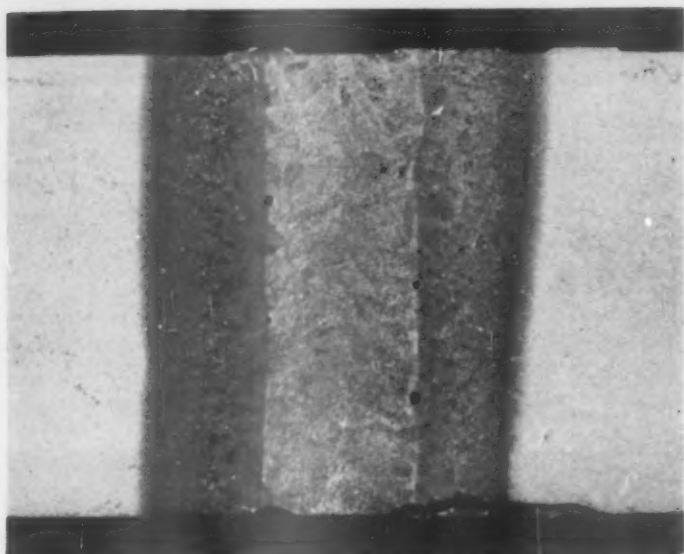


Fig. 15—Surface of Ti-4Al-3Mo-1V Sheet After Heliarc Welding and Etching Showing Weld and Heat Affected Zone.

ducted, it was the opinion of the authors that the material bent and stretched at room temperature as well or better than annealed titanium alloy sheet being formed at that time.

Room temperature joggle tests were made on material bent to 90 degrees on a 4T radius with 1-inch flanges. These pieces were given various tests in which the depth and length of joggle were varied, and the sheet passed tests at a length-to-depth ratio of 2.2. On the basis of these limited joggling tests at room temperature, it was felt that the joggling characteristics of solution treated Ti-4Al-3Mo-1V were at least equal to, if not better than, those of annealed titanium alloy sheet being formed by production methods at the time this investigation was made.

Welding

The as-welded sample was bright and shiny and appeared to be sound and non-porous. However, after a light pickling operation, several voids or pores were evident at the edge of the fusion zone, as shown in Fig. 15. In bend tests made without prior pickling, fractures occurred through some of these holes, the interior surfaces of which were observed to be shiny and apparently free from contamination.

Mechanical properties obtained on the weldment are presented in

Table I
Mechanical Properties of Welded Ti-4Al-3Mo-1V Sheet

(1" Gage Length—Material Welded Without Filler in the Mill Annealed Condition)

Specimen and Treatment	UTS ksi	VS (0.2%) ksi	Elongation, %			Guided Bend Test	
			Total	Unif	Local	R/T	Degrees
Base Material	150	139	12	2	45		
As-received; 1250°F (2 hr) AC	148	144	12	2	45		
As-Welded	145(3)	131	8	2	30		
	135(3)	114	9	1	30		
	142(3)	127	7	2	20		
As Welded plus 1250°F (1 hr) AC	141(3)	133	8	0	20	9.3(2)	70
	132(3)	120	9	1	35	6.2(2)	62
						13.0(2)	90
As-Welded plus 1550°F (½ hr) WQ	129(1)	90	8	2	20	6.0(1)	90
	133(1)	82	8	4	20	3.3(1)	90
						3.0(1)	50
						4.3(1)	90
As-Welded plus 1550°F (½ hr) WQ—1000°F (6 hr) AC	136(1)	129	3	1	10	6.0(1)	62
	135(1)	125	3	1	10	12.3(1)	90

- (1) Specimen broke at edge of weld metal, porosity evident.
 (2) Specimen broke in weld metal.
 (3) Specimen broke in base metal due to nonuniform thickness of weld zone.

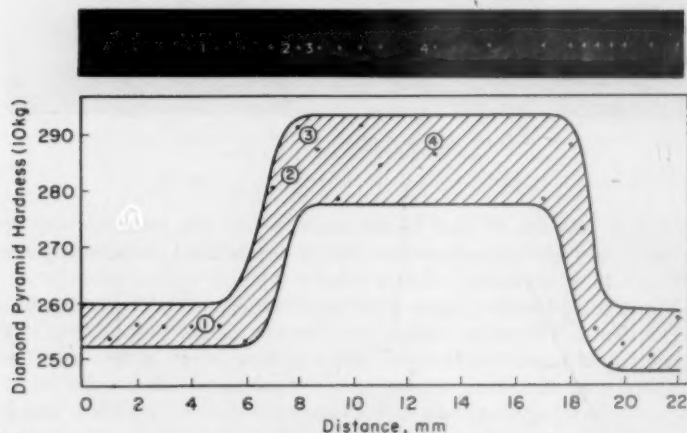


Fig. 16—Hardness Traverse and Etched Section of Heliarc Welded Ti-4Al-3Mo-1V Sheet (as Welded).

Table I. Practically all of the tensile and bend tests failed at the edge of the fused zone, and porosity was evident in all such failures. The presence of this porosity makes comparison of the data less meaningful, but it would appear that the strength of the weld metal approaches that of the base material and might duplicate or exceed it (see hardness curve shown in Fig. 16) if the porosity were eliminated. Of particular interest is the good bendability obtained in the weld following a solution treatment of 1550 °F.

A Vickers hardness survey was made on a longitudinal section across the weld (as received material). The data are presented in Fig. 16

along with a macrograph of the sample, which is presented at a magnification identical to the hardness curve beneath it. In general, the hardness of the weld metal was approximately 30 DPN higher than that of the base metal.

SUMMARY OF RESULTS

Because Ti-4Al-3Mo-1V is a heat treatable alloy, most of the evaluation was performed on the basis of a study of its solution treating and aging characteristics. Particular emphasis was placed on solution treating to achieve a minimum yield-to-tensile strength ratio which occurred at a solution temperature near 1550 °F. However, it was found that higher solution temperatures of 1600–1700 °F resulted in bendability that was comparable to that obtained at 1550 °F, although the solution treated tensile ductility decreased at solution temperatures above 1600–1650 °F. Solution temperatures higher than 1550 °F were required to obtain aged ultimate tensile strengths in excess of 170,000 psi. Little sacrifice in solution treated tensile and bend ductility was observed at a solution temperature as high as 1650 °F which resulted in ultimate tensile strengths of the order of 190,000–195,000 psi after aging at 900 °F for 24 hours. This strength advantage at room temperature (obtained by using a higher solution temperature) also persisted at elevated temperatures to 1000 °F.

Heat treated sheet was found to be stable under stress of 50,000 psi at 800 °F for periods to 1000 hours, although the loss in ductility after elevated temperature exposure under stress was somewhat greater in the higher strength condition obtained by solution treating at 1650 °F. However, no embrittlement was detected. Total creep deformation of material solution treated from 1550 °F and aged at 850 to 1000 °F was in the range of 1.1 to 1.4% at 800 °F after 1000 hours at 50,000 psi. Material solution treated from 1650 °F and aged at 900 and 1000 °F showed deformation from about 0.1 to 0.5%; however, the exposure time was only 300 hours at 800 °F and 50,000 psi, so no direct comparison with the 1550 °F solution treated material can be made at this time.

Limited formability tests on larger resistance solution treated pieces of sheet showed that the material bent satisfactorily at room temperature around a radius of 4.0T and that it could be subsequently stretch wrapped and joggled at room temperature with encouraging results.

A preliminary welding study showed that weld strengths were comparable to those of the base metal, although the as-welded ductility was at a low level. However, post-welding annealing appeared to offer some promise in improving weld ductility, while good bendability (3.3 T) was obtained in the weld following a solution treatment of 1550 °F (½ hr) water-quenched. Porosity in the weldment studied somewhat limited the reliability of test results and did not allow definite conclusions with regard to weldability to be made.

ACKNOWLEDGMENT

The authors wish to thank R. P. Simmons and his staff at the Brackenridge Mill and R. Kazeva and his group in the Brackenridge Research Laboratory of Allegheny Ludlum Steel Corporation for their efforts in the planning, processing, observing, and testing of the material used in this program. Special acknowledgment is also given to North American Aviation, Inc., of Inglewood, California, for the production formability tests.

References

1. Titanium Metals Corporation of America, unpublished data on resistance heating of titanium sheet.
2. F. C. Holden, D. N. Williams, W. E. Riley and R. I. Jaffee, "Flow Properties, Deformation Textures, and Slip Systems of Titanium and Titanium Alloys," Titanium Metallurgical Laboratory, TML Report No. 30, January 31, 1956, p. 24-30.
3. F. C. Holden and R. I. Jaffee, "Beta Transformation in Titanium Alloys," Titanium Metallurgical Laboratory, TML Report No. 25, December 5, 1955, p. 12-14.

DISCUSSION

Written Discussion: By F. A. Crossley, Senior Metallurgist, Armour Research Foundation of Illinois Institute of Technology, Metals Research Department, Chicago.

The Ti-4Al-3Mo-1V alloy represents a forward step in the effort to combine two properties which are basically antagonistic in a single sheet alloy, formability and high strength. It is generally recognized that heat treatments which produce high strength combined with acceptable ductility do not necessarily result in structures which have elevated temperature stress stability. Heat treatments must be carefully designed to meet objectives of strength and stability.

The β phase of an α - β alloy that has been heat treated by solution treating and aging to equilibrium is metastable at all temperatures except that of aging. Whether such a structure will have practical stress stability depends primarily upon the aging temperature and the temperature exposure to stress. Aged β is much less likely to have practical stress-stability if the β phase is not aged to equilibrium at the aging temperature. The equilibrium structure of aged β for the alloy and heat treatments reported in the current paper is discrete α precipitate particles in a β matrix. The microstructures corresponding to such equilibrium aged β would be expected to be dark in appearance using the etchant 1% HF - 12% HNO₃. Applying these considerations to the photomicrograph shown in Fig. 8 suggests that the reason for the loss of ductility and increase in strength in the stress-stability evaluation of the given heat treatment, i.e., 1650 °F - 1/2 hour—water-quenched, 900 °F - 24 hours, is continued aging of the metastable aged β . It is the experience of the author that Ti-Al-Mo alloys solution heat treated and aged at 1000 °F to a condition wherein the aged β is dark after etching (indicating complete α precipitation) suffer no loss in ductility upon exposure

to stress at 800 °F. Aging to conditions which result in a β which is light in appearance has resulted in lack of stress stability.^{2,3}

Have the authors noted that the aged β grains of stress stability specimens which showed loss of ductility were in part dark or wholly dark after etching, compared to unexposed specimens?

The data presented indicates that the β retained by quenching from 1650 °F is more sluggish upon aging than that retained by quenching from 1550 °F. This relationship of increasing thermal sluggishness with increasing solution treating temperatures (over a particular temperature range) has been observed for the Ti-7Al-3Mo alloy and appears to hold for other alloys as well.²

Authors' Reply

The authors appreciate Dr. Crossley's comments and agree with him that heat treatments must be carefully designed to meet objectives of strength and stability.

We have also observed that aged molybdenum-bearing beta phase appears dark after etching as a result of the fine precipitate of alpha, although the degree of darkening is probably dependent on the particular metallographic technique used.

Regarding stability of the alloy after exposure to stress at elevated temperatures, this is a property which must be considered along with the desired strength level and ductility of the heat treated material. An alloy may be overaged sufficiently at higher temperatures or for longer periods of time to exhibit almost perfect stability under stress and yet may possess an undesirable low strength because of the aging treatment used. Thus, from a practical standpoint, a material is considered to be stable if its mechanical properties are not altered beyond certain levels.

The authors have examined a few specimens metallographically after exposure to stress at 800 °F, but have not observed any marked changes due to such exposure. However, these had not exhibited any pronounced degree of instability and, therefore, any differences in the aged beta probably would have been difficult to detect.

It is possible that the beta phase retained by quenching from 1650 °F is more sluggish upon aging than that retained by quenching from 1550 °F, although we have not made a study of this. The aging process is certainly a complex one and would require further investigation to gain a better understanding of this thermal sluggishness.

² F. A. Crossley, W. F. Carew and H. D. Kessler, "Development of Titanium Base Alloys for Elevated Temperature Applications Part II—Ternary Alloys," ASTM Special Technical Publication (to be published).

³ F. A. Crossley, "The 7 Aluminum—3 Molybdenum Titanium Alloy—A Review of Its Development and Properties," Regional Reactive Metals Conference, Southern California Section American Institute of Mining and Metallurgical Engineers, Los Angeles, California, May 28–29, 1957.

MECHANICAL PROPERTIES CORRELATED WITH TRANSFORMATION CHARACTERISTICS OF TITANIUM-VANADIUM ALLOYS

BY E. L. HARMON, J. KOZOL AND A. R. TROIANO

Abstract

Mechanical properties of a series of high purity titanium alloys containing up to 24% vanadium were interpreted on the basis of time-temperature-transformation (TTT) diagrams. Microstructural changes in these alloys resulting from variation of alloy content and heat treatment exerted a profound influence on strength and ductility. Increasing vanadium concentration in alloys consisting entirely of alpha prime resulted in higher strength and notch sensitivity, and lower ductility and impact resistance. Alloys containing substantial quantities of omega in the quenched structures exhibited high strength and low ductility. A quenched 11% vanadium alloy was very ductile and possessed an exceptionally low ratio of yield strength to tensile strength. This exceptional behavior was indicative of stress induced transformation during the tensile test, probably the formation of alpha prime from beta. High levels of ductility and impact resistance were associated with the completely beta structures of the quenched 20 and 24% vanadium alloys.

Alloys containing substantial quantities of retained beta produced good combinations of strength and ductility when aged appropriately. Solution treatment in the alpha-beta region prior to age-hardening produced higher ductility at a given strength level than did solution treatment in the beta region. The difference produced by the two types of solution treatments is associated with the initial precipitation of alpha in the beta grain boundaries after solution treatment in the beta region.

Severe embrittlement was associated with the presence of omega in aged structures. (ASM International Classification: Q27a, Q23p, N7c; Ti, V)

INTRODUCTION

THE MECHANICAL properties of titanium-base alloys are influenced strongly by the types and the amounts of alloying elements and by the particular heat treatments employed. The present investiga-

A paper presented before the Thirty-Ninth Annual Convention of the Society, held in Chicago, November 4-8, 1957. Of the authors, E. L. Harmon is Research Assistant; A. R. Troiano is Professor and Head, Department of Metallurgical Engineering, Case Institute of Technology, Cleveland. J. Kozol is associated with Combustion Engineering Inc., Windsor, Connecticut. Manuscript received April 10, 1957.

tion was undertaken for the purpose of evaluating the effects of the latter two factors upon the mechanical properties of a series of high purity titanium-vanadium alloys. The nature and decomposition kinetics of alpha prime and the decomposition of beta by aging, which previously had been studied for the titanium-vanadium system, provided a basis for interpreting mechanical properties (1,2).¹

At low concentrations of vanadium, quenching of the high temperature body-centered cubic beta phase results in a martensitic transformation into hexagonal alpha prime. This transformation occurs in alloys containing less than about 15% vanadium (3). Alloys containing as much as 7.5% vanadium consist essentially of all alpha prime.

The tendency to retain beta in quenched alloys containing from 7.5 to 15% vanadium increases with higher vanadium concentration, thus permitting the utilization of age hardening type heat treatments. As in other age-hardening systems, under appropriate conditions, an intermediate transition phase is the initial precipitate. The formation of the equilibrium alpha phase and of the transition phase, omega, for a particular alloy can be described on an isothermal time-temperature-transformation diagram by two C-shaped curves intersecting at about 430 °C (805 °F), the upper C-curve depicting alpha precipitation and the lower one delineating the conditions for formation of the metastable transition phase, omega (1). Omega precipitates so rapidly in 12.5, 15 and 17.5% vanadium alloys that brine quenching is unable to suppress it. Hardness values for these alloys after quenching are substantially higher than those for a 20% vanadium alloy which forms no detectable omega upon quenching (2).

Material

The alloys used in this investigation were made from iodide titanium furnished by Watertown Arsenal, and high purity vanadium. The effect of impurities was thereby minimized and a more representative picture was obtained of the inherent characteristics of the binary titanium-vanadium alloys.

Alloys containing 0, 2.5, 7.5, 12.5 and 15% vanadium were prepared by Battelle Memorial Institute and alloys containing 5, 11, 20 and 24% vanadium were melted and fabricated by the Electro Metallurgical Company. In both cases ingots of about 8 pounds each were prepared by arc melting in an inert atmosphere, with a tungsten electrode and water-cooled copper crucible. Except for the unalloyed titanium all the alloys were double melted, with precautions taken to insure uniformity of composition and to avoid contamination. The first group of alloys was finish rolled to ½-inch square bar and the second set was finish rolled to ⅝-inch round bar. The 0, 2.5, and 7.5% vanadium alloys were

¹ The figures appearing in parentheses pertain to the references appended to this paper.

rolled at temperatures in the alpha-beta field, while the remaining alloys were rolled in the beta region.

PROCEDURE

Heat Treatment

Specimens other than those used for dilatometric and metallographic studies were solution treated in high vacuum resistance furnaces at pressures below 5×10^{-5} millimeters of mercury. The dilatometric and metallographic specimens used in the determination of TTT diagrams were solution treated in an argon atmosphere. Aging and isothermal quenching treatments at temperatures up to and including 550 °C (1020 °F) were conducted in salt baths. Lead baths were employed for heat treatments at temperatures greater than 550 °C (1020 °F).

Dilatometric Studies

Isothermal transformation behavior at temperatures up to 550 °C (1020 °F) was investigated with a quenching dilatometer. Dilatometric specimens measured $1\frac{1}{2} \times \frac{1}{4} \times \frac{1}{32}$ inch. Dimensional changes were detected by a differential transformer coupled to a high speed recorder. Six seconds after quenching was the shortest time at which the reaction could be observed with this technique.

Metallography

Metallographic specimens used to supplement information obtained by the dilatometer in studying isothermal transformation behavior were $\frac{1}{2} \times \frac{1}{4} \times \frac{1}{8}$ inch in size. Sectioned tensile specimens were also examined metallographically.

Polishing was done mechanically. The etching reagent was a solution of 3 parts glycerine and 1 part HF followed by a short rinse in dilute HNO₃ to prevent staining.

Tensile Testing

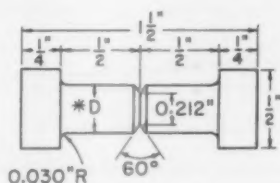
Tensile and notched tensile specimens were rough machined prior to heat treatment, allowing about 0.060 inch on the diameter for removal of contamination. Notching and finish machining were performed after completion of the heat treatment. The notched tensile specimens were of the type shown in Fig. 1.

Tensile testing was performed on a Baldwin-Southwark Testing Machine of 60,000-pounds capacity. A constant head speed of 0.05 inch per minute was maintained. Strain data were obtained during the test by means of a radial strain gage.

Impact Testing

Standard size Charpy V-notch impact specimens were also rough

machined prior to heat treatment, allowing about 0.030 inch on each face. The specimens were ground to finish dimensions subsequent to heat treatment. Testing was conducted on a Sonntag Universal Impact machine with a capacity of 120 ft-lbs and a striking velocity of 17.4 feet per second. Specimens were immersed in a heating or cooling medium for 10 minutes prior to testing at the desired temperature. High flash point oil was used for heating purposes. Liquid nitrogen, mixtures of isopentane and liquid nitrogen, or dry ice and acetone were used as



* D: Determined by Required Notch Depth
Notch Radius: 0.001"

Fig. 1—Notch Tensile Specimen.

cooling media. The estimated elapsed time of transfer from the heating or cooling medium to the testing machine fixture was approximately three seconds.

EXPERIMENTAL RESULTS

Transformation Behavior

Time-temperature-transformation (TTT) diagrams for isothermal decomposition of beta in 12.5 and 15% vanadium alloys were determined previously by Brotzen, Harmon and Troiano, Figs. 2 and 3 (1). In the present investigation the transformation characteristics of alloys containing 20 and 24% vanadium were obtained in a similar manner, Figs. 4 and 5.

The previous work indicated that although omega was present in alloys containing between 12.5 and 17.5% vanadium when quenched from the beta region, there was no hardness or x-ray diffraction evidence of its presence in a quenched 20% vanadium alloy. It is apparent from Figs. 2-5 that both the omega and alpha noses are shifted to longer times with increasing concentration of vanadium thus making it possible to quench past the omega "nose." Since the range of omega formation occurs at shorter times than that for alpha formation, omega precipitates upon quenching, in preference to alpha, in 12.5 and 15% vanadium alloys. That is, the omega C-curves for these alloys are intersected by the cooling curves for rapid quenching, while sufficient time exists to allow cooling past the alpha nose. It might be expected that at

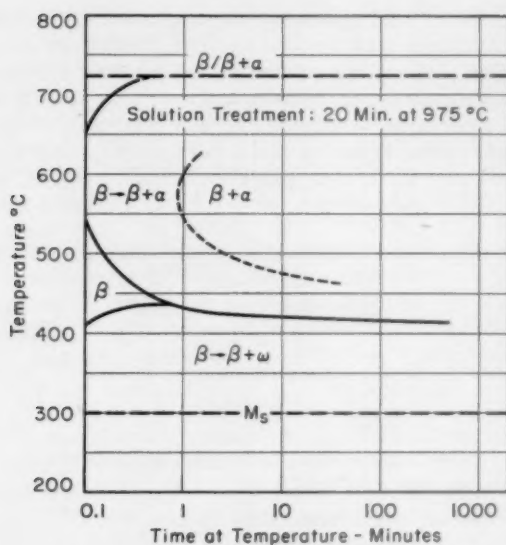


Fig. 2—Time-Temperature-Transformation Diagram for a 12.5% Vanadium-Titanium Alloy After Brotzen Et Al. (1).

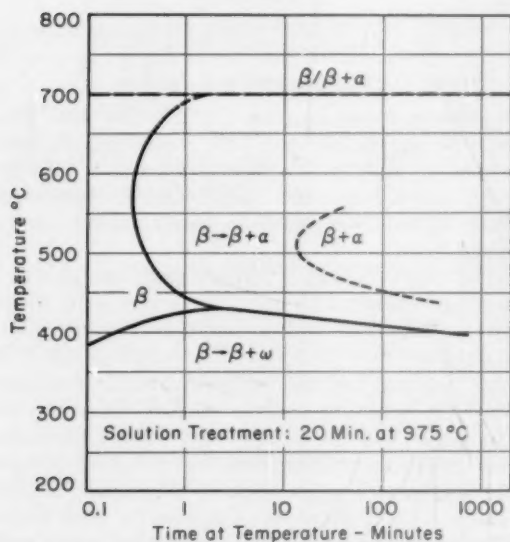


Fig. 3—Time-Temperature-Transformation Diagram for a 15% Vanadium-Titanium Alloy After Brotzen Et Al. (1).

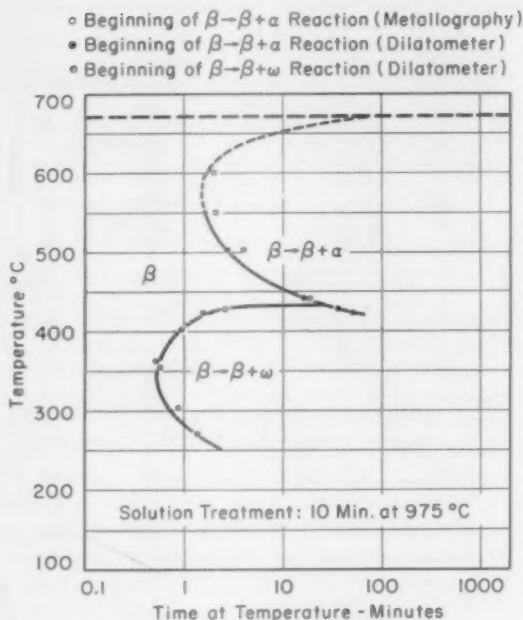


Fig. 4—Time-Temperature-Transformation Diagram for a 20% Vanadium-Titanium Alloy.

a composition somewhat below 12.5% vanadium, the alpha C-curve would be intersected by the cooling curve.

Alpha precipitation in an 11% vanadium alloy appeared to start so rapidly that the beginning of transformation could not be observed with the dilatometric technique employed. However, alpha was not observed in the quenched structure, although alpha prime, beta and traces of omega were detected by x-ray diffraction.

MECHANICAL PROPERTIES

Quenched Alloys

The strength and ductility of quenched alloys varied markedly with vanadium content, Fig. 6. Alloys containing up to about 7.5% vanadium consist essentially of all alpha prime of increasingly finer structure. The initial tensile strength increase, Fig. 6 is therefore associated with solution hardening, increasingly finer structure and correspondingly greater lattice strains accompanying the martensitic transformation at higher vanadium concentrations.

The 7.5% vanadium alloy quenched from the beta region contained

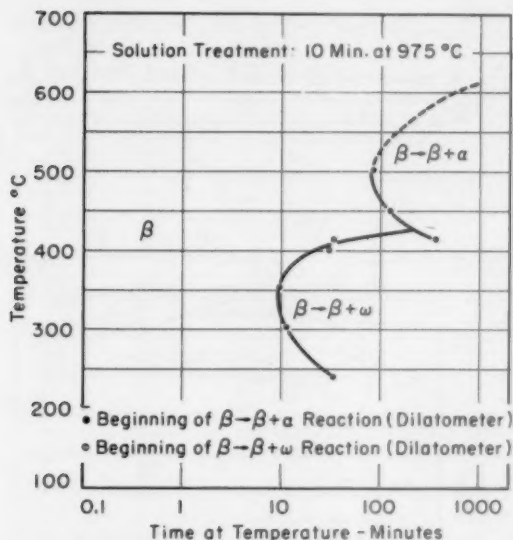


Fig. 5—Time-Temperature-Transformation Diagram for a 24% Vanadium-Titanium Alloy.

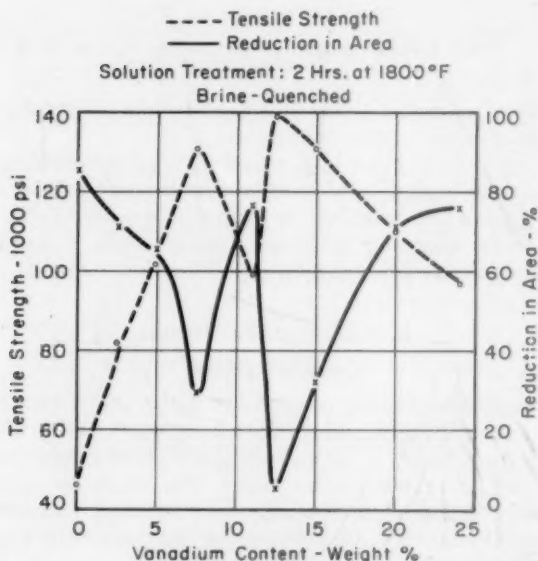


Fig. 6—As-Quenched Strength and Ductility as Functions of Vanadium Content.

Table I
Ratio of Yield Strength to Tensile Strength
For Quenched Titanium-Vanadium Alloys

% V	Yield Strength psi 0.2% Offset	Tensile Strength psi	Y.S./T.S.
0	33,000	49,000	0.67
2.5	63,000	84,000	0.75
5	68,000	100,000	0.68
7.5	95,000	135,000	0.70
11	50,000	105,000	0.48
12.5	98,000	139,000	0.70
15	120,000	131,000	0.92
20	75,000	105,000	0.71
24	86,000	104,000	0.83

what appeared to be a thin network of alpha in the prior beta grain boundaries. This network may have caused the pronounced decrease in ductility near this composition, Fig. 6.

Exceptional tensile properties were exhibited by the 11% vanadium alloy, Fig. 6. The ratio of yield strength to tensile strength of this alloy in the quenched condition is considerably lower than that of any other alloy studied, Table I. Both the high ductility and the low yield-to-tensile ratio are very likely direct results of the formation of alpha prime from retained beta during deformation in the tensile test.

The formation of the omega transition phase in a quenched 12.5% vanadium alloy caused a sharp drop in ductility and rise in tensile strength, Fig. 6. As composition was increased to 15% vanadium the resulting lesser amounts of omega yielded lower strength and improved ductility.

Since the structures of the quenched 20 and 24% vanadium alloys consisted entirely of retained beta, these alloys exhibited a high level of ductility, accompanied by a drop in tensile strength, Fig. 6.

The relative notch ductility* of quenched titanium-vanadium alloys was continually lowered by increasing notch depth**. The area under the curve of relative notch ductility versus notch depth gives a semi-quantitative indication of notch sensitivity in a tensile test; i.e., the greater the area under the curve the lower the notch sensitivity. This value is informative in that it represents the notch behavior integrated over a range of notch severities. Although no data were obtained for the 12.5 and 15% vanadium alloys, it appears from Fig. 7 that the notch sensitivity of the quenched alloys varied with vanadium content in the same general manner as the tensile strength.

The impact behavior of the quenched alloys also reflected the influence of composition. It is apparent in Fig. 8 that the general level

* The relative notch ductility is defined as:

$$\frac{\% \text{ reduction in area of notched specimens}}{\% \text{ reduction in area of unnotched specimens}}$$

** The notch depth is defined as:

$$\frac{(\text{area of unnotched cylindrical section}) - (\text{area at base of notch})}{(\text{area of unnotched cylindrical section})}$$

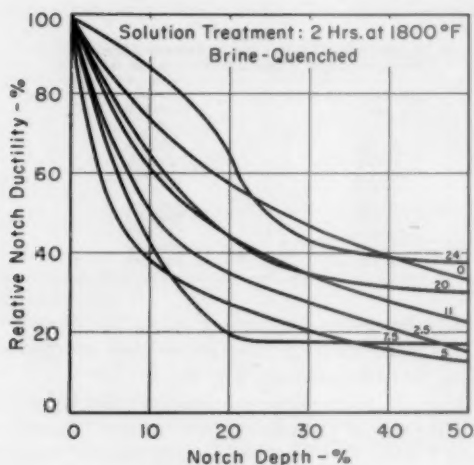


Fig. 7—Relative Notch Ductilities of Quenched Titanium-Vanadium Alloys.

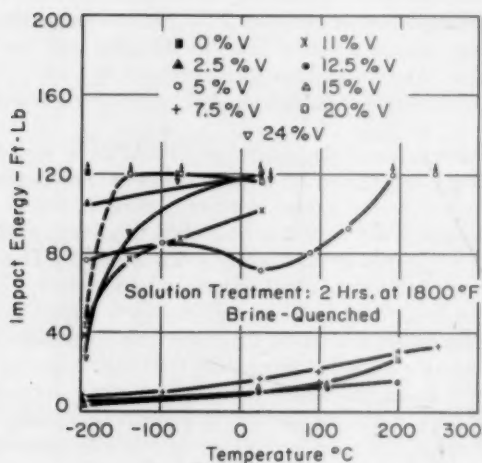


Fig. 8—Impact Transition Curves for Quenched Titanium-Vanadium Alloys.

of impact energy over the entire temperature range studied is shifted with vanadium content in a manner similar to that for reduction in area in a tensile test.

To demonstrate further the similarities in behavior among impact, tensile and notch tensile properties, the impact energy at an arbitrarily

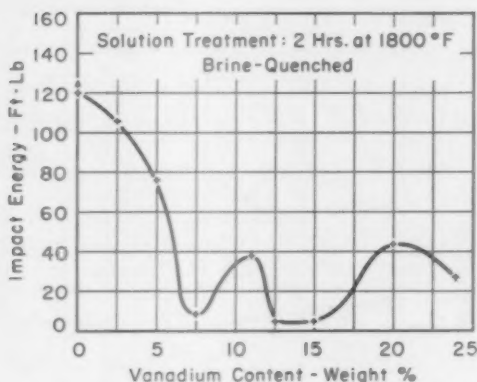


Fig. 9—Impact Energy at -196°C (-321°F) of Quenched Titanium-Vanadium Alloys as a Function of Vanadium Content.

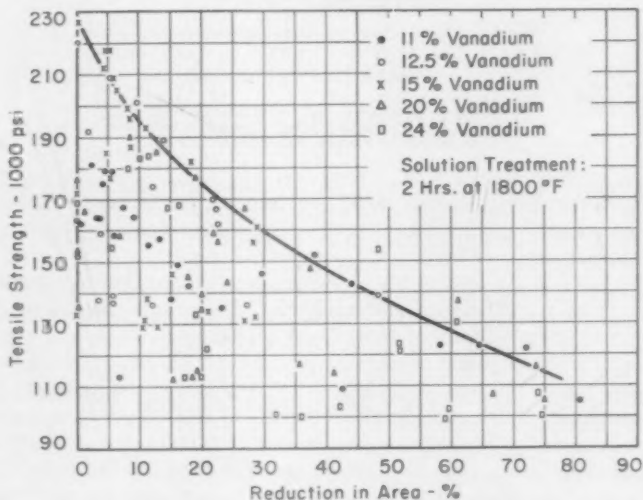


Fig. 10—Tensile Strength versus Reduction in Area for Aged Titanium Alloys Containing from 11 to 24% Vanadium, Solution Treated in the Beta Region.

chosen temperature of -196°C (-321°F) was plotted as a function of vanadium content, Fig. 9. This curve also exhibits a minimum near 7.5% vanadium, and again at about 12.5% vanadium, reaching a maximum at an intermediate composition near 11% vanadium.

Age-Hardened Alloys

A wide range of properties may be obtained by aging of retained

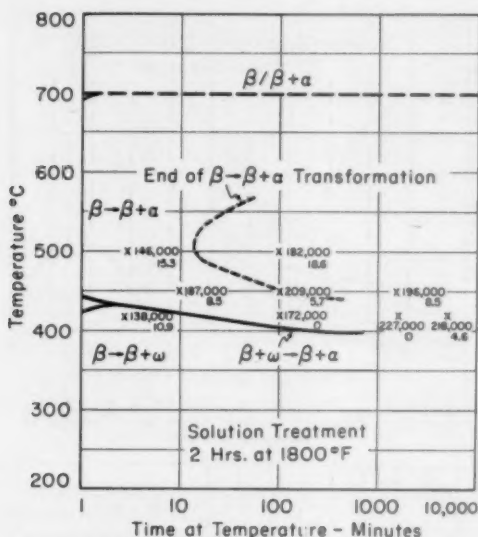


Fig. 11—Tensile Strength and Reduction in Area of a 15% Vanadium Titanium Alloy, Quenched from the Beta Region to Various Aging Temperatures.

beta. Of the alloys studied those containing 11% or more vanadium are particularly susceptible to aging treatments since they retain considerable amounts of beta.

The curve illustrated in Fig. 10 represents the maximum obtainable combinations of strength and ductility for alloys containing 11 to 24% vanadium, solution treated in the beta region and subsequently aged. Except for those points representing quenched 11, 20 and 24% vanadium alloys, all the points which lie on or near this curve represent heat treatments by which considerable amounts of alpha have been precipitated from beta. Sufficient aging at any particular temperature improved the combination of strength and ductility, i.e., the points generally were moved closer to the optimum curve as aging was prolonged. All of the points which lie on the ordinate, i.e., those exhibiting no reduction in area, represent aging treatments at temperatures where omega is known to form. In some cases, however, no ductility is apparent even after omega has disappeared and alpha has formed. This is evident in Fig. 11, which is a reproduction of the TTT diagram for the 15% vanadium alloy, with tensile strength and reduction in area values indicated for the appropriate time and temperature combinations. Aging times of 100 minutes and 1500 minutes at 420 °C (790 °F) produced brittle failures which were short of the maximum load strain.

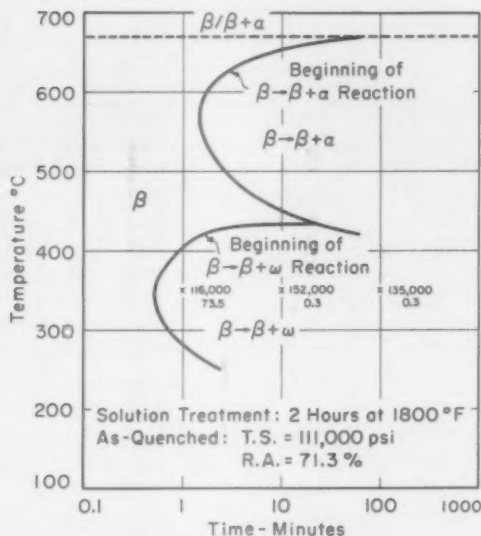


Fig. 12—Tensile Strength and Reduction in Area of a 20% Vanadium-Titanium Alloy Quenched from the Beta Region to 350 °C (660 °F).

The higher tensile strength of the 1500-minute treatment is thus an indication of the restoration of ductility with longer aging time. This is further demonstrated by the improved reduction in area of a specimen aged 5000 minutes at 420 °C (790 °F).

A continuous network of alpha in the beta grain boundaries was apparent after aging at 420 °C (790 °F) for 100 minutes or longer. Prolonged aging increased the amount of alpha precipitated within the grains. Recovery of ductility occurred coincident with increasing general precipitation of alpha. At higher temperatures, where omega is not involved in the decomposition, embrittlement again occurred at short aging times followed by recovery after longer aging times. The embrittlement at these higher temperatures (450 and 500 °C (840–932 °F), in this case) was not as severe as that found at 420 °C (790 °F), Fig. 11. Any specimen, however, which did not have a tensile strength-reduction in area combination lying on or near the curve in Fig. 10 is considered more or less embrittled. Thus, if one locates the tensile strength and reduction in area values of Fig. 11 on the graph of Fig. 10, the course of the disappearance of embrittlement can be followed. The results discussed above for the 15% vanadium alloy are representative of the results of direct quenching to the transformation temperature from the beta region of 11, 12.5, 20 and 24% vanadium alloys. In each case optimum strength-ductility combinations

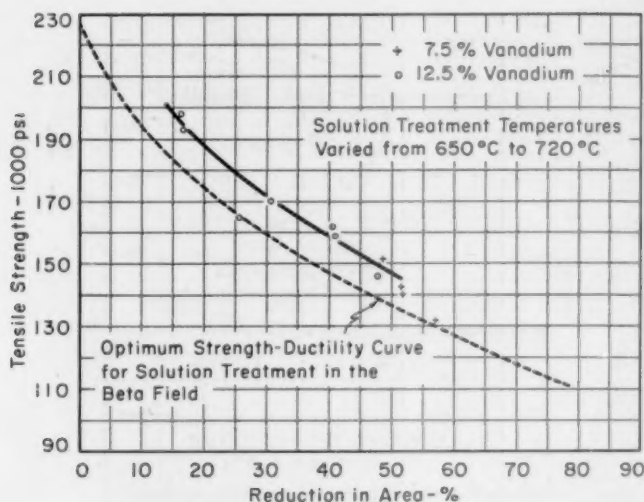


Fig. 13—Tensile Strength versus Reduction in Area for Aged Titanium Alloys Containing 7.5 and 12.5% Vanadium, Solution Treated in the Alpha-Beta Region.

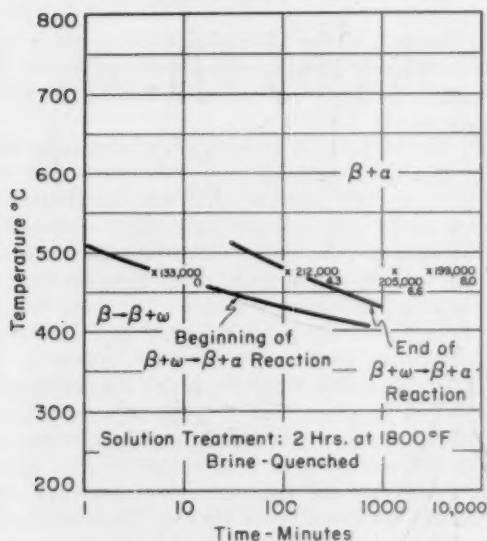


Fig. 14—Tensile Strength and Reduction in Area of a 15% Vanadium-Titanium Alloy, Brine-Quenched from the Beta Region and Aged at 475 °C (885 °F).

upon aging were obtained only after extensive transformation from beta to alpha had occurred. After the optimum curve was attained further aging increased ductility and decreased strength in accord with the curve. Higher strength levels occurred at lower aging temperatures, but the time necessary to attain optimum strength-ductility combinations increased.

Embrittlement caused by omega formation in a 20% vanadium alloy is illustrated in Fig. 12. For an aging time of 1 minute at 350 °C (660 °F), after a direct quench from the solution temperature, the tensile strength increased slightly over the as-quenched value. The ductility, however, did not change significantly. Thus, small amounts of omega appear to have strengthened the alloy slightly without embrittling. Severe embrittlement occurred at longer holding times as more omega was formed. The mechanism by which omega produces embrittlement is not well understood. It is conceivable that the omega phase is extremely brittle, *per se*, because of its low coordination number and that its presence in large amounts, finely distributed, seriously impairs ductility. Another possibility is that the embrittlement is associated with coherency strains between omega and enriched beta. If, on the other hand, embrittlement were due to a network of omega in the beta grain boundaries, it might be possible to prevent this localized precipitation and thereby attain very high strengths with usable ductilities.

Solution treatment of 7.5 and 12.5% vanadium alloys in the alpha-beta region prior to aging was conducted with the expectation that the precipitation of alpha or omega during aging would be less likely to occur within beta grain boundaries if a uniform distribution of alpha were present initially. The tensile test results in Fig. 13 indicate that in several cases the strength-ductility potential after this type of solution treatment is significantly greater than after solution treatment in the beta region. The lowest aging temperature employed which produced these improved strength-ductility combinations was 400 °C (750 °F). Very little omega would be expected to form at this or higher temperatures, so that the results in Fig. 13 apply primarily to the precipitation of alpha. Alpha-beta solution treatment followed by aging for 30 minutes at 350 °C (660 °F), where a considerable amount of omega was expected to form, produced no appreciable ductility in the 12.5% vanadium alloy. The tensile strength and reduction in area of this specimen lie near the ordinate at 140,000 psi in Fig. 13.

The preceding observations indicate that embrittlement associated with grain boundary alpha may be minimized or eliminated by solution treating in the alpha-beta region, but that embrittlement due to omega precipitation is not readily avoided.

The 12.5% vanadium alloy quenched from the alpha-beta region exhibited an excellent tensile strength-reduction in area combination.

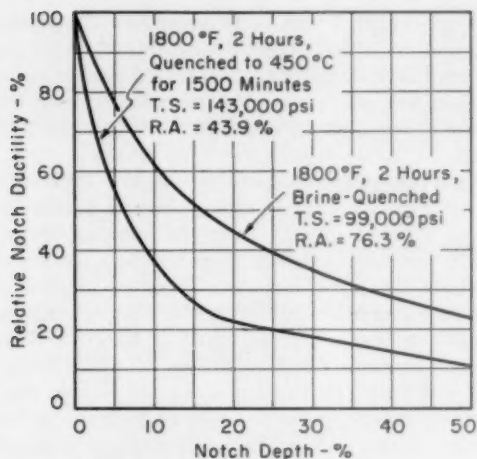


Fig. 15—Effect of Aging on the Notch Sensitivity of an 11% Vanadium-Titanium Alloy.

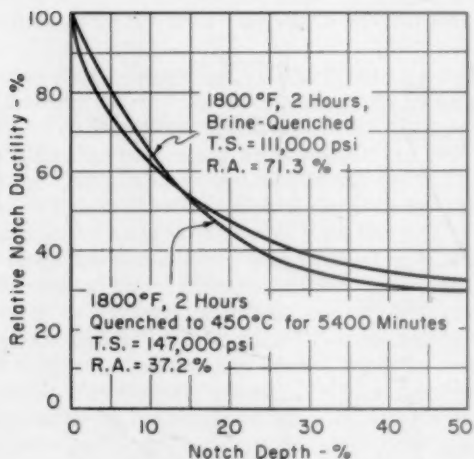


Fig. 16—Effect of Aging on the Notch Sensitivity of a 20% Vanadium-Titanium Alloy.

Subsequent aging merely shifted the tensile strength and reduction in area values along the upper curve of Fig. 13. Thus, the optimum strength-ductility level characteristic of alpha-beta solution treatment is attained regardless of the degree of transformation from beta to

alpha during the aging treatment. This is in marked contrast to the behavior of the all-beta solution treated alloys, for which it was demonstrated that optimum properties were very sensitive to the degree of beta to alpha transformation. These results further incriminate grain boundary alpha as a potential mechanism of embrittlement.

The results of tensile testing of quenched and aged alloys containing from 11 to 24% vanadium were in accord with those obtained for direct quenching to the transformation temperature. For example, Fig. 14 illustrates tensile strength and reduction in area values for the 15% vanadium alloy quenched from the beta region and subsequently aged at 475 °C (885 °F). The TTT diagram for quenching and aging, previously determined by Brotzen, Harmon and Troiano (1), is also included in Fig. 14. Again at longer aging times the tensile strength and reduction in area values move to lower strengths and higher ductilities along the curve of Fig. 10.

In general, quenching and aging instead of direct isothermal transformation permits omega to form at higher temperatures, which may inhibit the subsequent precipitation of alpha (1). Thus, an isothermal TTT diagram determined by direct quenching to the reaction temperature is not necessarily sufficient to allow an evaluation of the effect of quenching and aging upon mechanical properties. Generally, good combinations of strength and ductility can be obtained by either type of treatment if appropriate aging temperatures and times are employed.

Notched Tensile Properties

On the basis of the optimum strength-ductility curve in Fig. 10 representative heat treatments were chosen for further evaluation of mechanical properties. Aging after solution treatment in the beta region and direct quenching to the reaction temperature was performed on 11, 20 and 24% vanadium alloys. The aging treatments selected were 1500 minutes at 450 °C (840 °F) for the 11 and 24% vanadium alloys, and 5400 minutes at 450 °C (840 °F) for the 20% vanadium alloy. These treatments resulted in tensile strength levels around 150,000 psi, substantially higher than the strength level of the quenched material. The notch sensitivities of the 11 and 24% vanadium alloys increased markedly after aging, while that of the 20% vanadium alloy was essentially the same as that for the quenched condition, Figs. 15-17.

Impact Properties

Charpy V-notch impact specimens of the 11, 20 and 24% vanadium alloys were subjected to the same aging treatments as were the notched tensile specimens. The resultant impact transition curves are depicted in Fig. 18. A comparison of Figs. 8 and 18 indicates that the aging treatments employed shifted the impact transition curves of the 11, 20 and 24% vanadium alloys to higher transition temperatures and

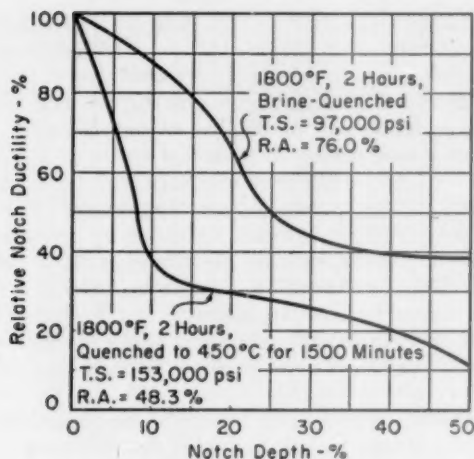


Fig. 17—Effect of Aging on the Notch Sensitivity of a 24% Vanadium-Titanium Alloy.

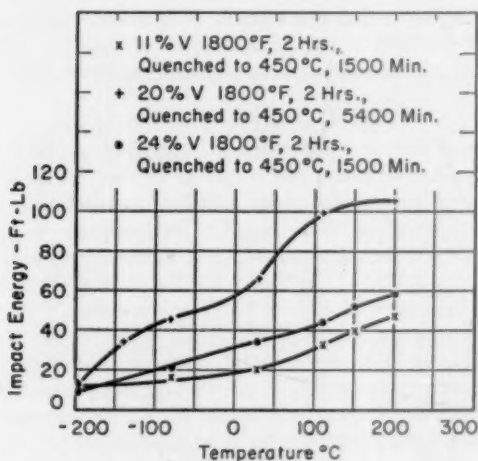


Fig. 18—Impact Transition Curves for Aged Titanium-Vanadium Alloys.

lower impact energies. Again it must be realized that the strength level of the aged material is relatively high. It should be noted that even the lower regions of the transition curves for the aged alloys do not represent poor levels of impact energy. This is especially true of the 20% vanadium alloy.

SUMMARY AND CONCLUSIONS

Microstructural changes in titanium-vanadium alloys resulting from variation of alloy content and heat treatment exert a profound influence on strength and ductility. Quenched titanium alloys containing up to 7.5% vanadium consisted essentially of alpha prime after quenching. For these quenched alloys the tensile strength increased continuously with increasing vanadium concentration, accompanied by a considerable decrease in the ductility and impact energy level. The substantial decrease in ductility appears to be associated with the precipitation of alpha in the boundaries of the original beta grains.

A quenched 11% vanadium alloy exhibited very high ductility and an exceptionally low ratio of yield strength to tensile strength. This exceptional behavior was indicative of stress induced transformation during the tensile test, probably the formation of alpha prime from beta.

As a result of the presence of omega, quenched 12.5 and 15% vanadium alloys exhibited low ductility and impact energy. Increasing vanadium content to 20 and 24% retarded the precipitation of omega sufficiently to allow complete retention of beta on quenching. This resulted in a high level of ductility and impact energy.

Notch sensitivity was evaluated, using as a criterion the effect of increasing notch depth upon the reduction in area in a tensile test. The notch sensitivity of the quenched alloys varied with vanadium concentration in the same general manner as the tensile strength.

Solution treatment in the alpha-beta region prior to age-hardening produced higher ductility at a given strength level than did solution treatment in the beta region. The difference produced by the two types of solution treatments is associated with the initial precipitation of alpha in the beta grain boundaries after solution treatment in the beta region.

Appropriate heat treatments minimized or eliminated embrittlement associated with alpha in the grain boundaries, but embrittlement caused by the presence of omega was not readily avoided.

Using the results of tensile tests as a basis for heat treatment notched tensile and impact properties were determined for 11, 20, and 24% vanadium alloys aged to a strength level of about 150,000 psi. The notch sensitivity in a tensile test was unchanged for the 20% vanadium alloy, but was increased for the 11 and 24% vanadium alloys relative to that for the alloys in the quenched condition. The impact energy level was lowered for all three alloys. However, it should be remembered that the strength level of the aged material was substantially higher than that of the quenched material.

ACKNOWLEDGMENTS

This investigation was sponsored by Army Ordnance Corps, Watertown Arsenal, under Contract No. DA-33-019-ORD-1690. The authors express their appreciation to the Ordnance Corps, Department of the Army, for permission to publish this research. They are also grateful for the cooperation of Watertown Arsenal Laboratory.

References

1. F. R. Brotzen, E. L. Harmon and A. R. Troiano, "Decomposition of Beta Titanium," *Transactions, American Institute of Mining and Metallurgical Engineers*, Vol. 203, 1955, p. 413-419; *Journal of Metals*, Vol. 7, 1955.
2. F. R. Brotzen, E. L. Harmon and A. R. Troiano, "Nature and Decomposition Kinetics of Alpha Prime in Titanium-Vanadium Alloys," *TRANSACTIONS, American Society for Metals*, Vol. 48, 1956, p. 774-782.
3. P. Pietrokowsky and P. Duwez, "Partial Titanium-Vanadium Phase Diagram," *Transactions, American Institute of Mining and Metallurgical Engineers*, Vol. 194, 1952, p. 627-630.

DISCUSSION

Written Discussion: By D. N. Williams, Battelle Memorial Institute, Columbus, Ohio.

This paper presents a timely account of the variation in properties possible with beta titanium alloys. The data is particularly interesting since vanadium is a principal ingredient in several new experimental titanium alloys. On examining the data presented some questions have arisen which cannot be answered clearly without further discussion by the authors. I would appreciate the authors' comments regarding these questions.

1. The 7.5% vanadium alloy quenches to martensite with the presence of a small amount of grain boundary alpha. The nose of the alpha curve, extrapolating from the data given, should probably occur at about 1020-1110 °F (550-600 °C). The Ms temperature of this alloy occurs at about the same temperature. A duplex structure would therefore seem probable. However, the conclusion that grain boundary alpha is embrittling may not be entirely correct. The 5% vanadium alloy was fabricated in the beta field and melted at a different laboratory than the 0, 2.5, and 7.5 vanadium alloys. Is it possible that the 5% alloy is unexpectedly ductile, and that the properties of the 7.5% alloy are representative of martensite containing 7.5% vanadium?

2. The phenomenon of strain transformation has received considerable attention recently. (See, for example, *Mechanical Properties and Heat Treatment of Ti-Nb Alloys*, L. W. Berger, D. N. Williams, and R. I. Jaffee, appearing in this volume of *TRANSACTIONS*.) In the absence of omega, the maximum ductility of the metastable alloy is found to occur at about the minimum composition that completely retains beta. This would be close to 15% vanadium in the Ti-V alloys. Therefore, a peak in ductility would be expected at 15% vanadium. The authors have attributed the absence of this peak to the formation of omega on quenching, which seems quite logical. However, one would expect the 11% alloy to be similarly affected since the tendency toward omega formation should increase as the beta phase becomes less stable. What do the authors think is the most probable explanation for the anomalous ductility observed in this alloy?

3. Aging response of the various alloys is shown on one master plot in the paper. The alloys represented included quite a range of compositions representing

several degrees of beta stability and at least three variations in amount of retained beta. Are the authors able to select the type of alloy which produces the best properties after aging? That is, how stable should the beta be for maximum aging response? The implication of the curve, that all compositions when suitably aged can produce the same strength-ductility properties, seems improbable.

4. Data is reported showing an improvement in ductility in the alloys when solution treated in the alpha-beta field rather than the beta field before aging. Did equivalent aging treatments result in improved strength at constant ductility or improved ductility at constant strength? Also, what was the grain size after the two solution heat treatments?

Authors' Reply

The authors are grateful to Dr. Williams for his interesting comments. We will endeavor to answer his specific questions in the order in which they have been raised.

1. It seems unlikely that the 5% vanadium alloy is unexpectedly ductile. Fabrication in the beta field, if it affects ductility at all, would probably lower it with respect to fabrication in the two-phase field. For this reason, it appears more likely that the ductility of the 7.5% vanadium alloy in the quenched condition is lower than expected of martensite of this composition. The authors have suggested grain boundary precipitation as one possible explanation for this embrittlement.

2. The high level of ductility of the quenched 11% vanadium alloy is possible because very little omega is present. The M_s temperature of this alloy is sufficiently high so that during quenching some martensite will form before the temperature range of omega formation is reached. The martensite present might very well stabilize the remaining beta so that subsequent omega formation is negligible. Another possibility which should be considered is that the rate of omega formation is a maximum at about 12.5% vanadium, and a lowering as well as a raising of alloy concentration will decrease the rate of omega formation. This explanation requires that the free energy-compositional relationship of the supersaturated beta phase governs the kinetics of the omega reaction and also that this free energy-compositional relationship is such that there exists a tendency for segregation into vanadium-rich and titanium-rich regions within the beta phase.

3. It is the authors' conclusion that within the range of alloys studied, between 11 and 24% vanadium, the same strength-ductility combinations after quenching from the beta field can be obtained with any composition, appropriately aged. In other words, the maximum obtainable ductility after quenching from the beta field is the same for all the alloys when and if they can be aged to the same strength level. The 12.5 and 15% vanadium alloys exhibit maximum aging response since, within the relatively narrow range of aging times employed, they generally reached higher strength levels than the other alloys.

4. Strictly speaking, "equivalent aging treatments" cannot be obtained in the same alloy, since the composition of the beta phase in an alloy solution treated in the two-phase field will be different from that after solution treatment in the beta field. Therefore, the alloy will not display the same aging response in both cases. It was observed, however, that solution treatment in the two-phase field produced lower strength and greater ductility than did solution treatment of the same alloy in the beta field, when both treatments were followed by identical aging procedures. The influence of grain size was not evaluated in this investigation, but it is unlikely that differences in grain size can account for the substantial differences in properties obtained by the two types of solution treatments.

FACTORS AFFECTING THE ABSORPTION AND DISTRIBUTION OF HYDROGEN IN TITANIUM DURING ACID PICKLING

BY C. R. MCKINSEY, M. STERN AND R. A. PERKINS

Abstract

The environmental and metallurgical factors which control the absorption and distribution of hydrogen in titanium during acid pickling are discussed. Hydrogen pickup results from corrosion of the metal and can be minimized by passivation of the surface or alteration of the cathodic reaction. Hydrogen pickup in predominantly alpha alloys is shown to be confined to a thin surface layer which is stable at temperatures below 100 °C (210 °F). The presence of beta results in more hydrogen pickup and deeper penetration. The importance of phase distribution is indicated. The significance of surface hydride layers is discussed in terms of the effect on hydrogen absorption, total hydrogen content, and mechanical behavior. (ASM International Classification N15d, L12g; Ti)

INTRODUCTION

HYDROGEN as an impurity in titanium has received considerable attention due to the deleterious effect of minor amounts of this element on the mechanical behavior of titanium and its alloys. Hydrogen can be absorbed at any stage in processing, from production of sponge to fabrication of mill products. The reaction is reversible and hydrogen can be removed by heating in vacuum. This results in an additional cost which might be eliminated through better process control. Many of the problems associated with hydrogen contamination which faced the industry in its early years have been solved, and some effective controls have been developed. However, difficulties still are encountered, and a better understanding of the absorption and effects of hydrogen is required.

The effects of hydrogen contamination have been described by several investigators (1,2,3)¹, and a general summary of embrittlement

¹ The figures appearing in parentheses pertain to the references appended to this paper.

A paper presented before the Thirty-Ninth Annual Convention of the Society, held in Chicago, November 4-8, 1957. The authors are associated with the Metals Research Laboratories, Electro Metallurgical Company, A Division of Union Carbide Corporation, Niagara Falls, New York. Manuscript received April 15, 1957.

phenomena has been prepared (4). The total hydrogen content is not necessarily a criterion of brittle behavior. The distribution of hydrogen, type of alloy, and mechanical conditions imposed are believed to be equally important factors. The absorption of hydrogen at elevated temperatures has received considerable attention and appears to be reasonably well understood (4-9). The absorption of hydrogen at low temperatures also has been studied, and observations in acid-pickling operations and research investigations have developed a general but inadequate knowledge of behavior (4,10-14). Hydrogen pickup is markedly different for various bath compositions, surface conditions, alloy types, and section sizes.

The pickup of hydrogen at elevated temperature can be minimized by effective controls and techniques which have been developed. It is not considered a serious problem at the present time. On the other hand, the absorption of hydrogen at low temperatures in acid-pickling operations has not been explained sufficiently to permit very marked improvements in this critical phase of titanium processing. The purpose of this work is to examine the absorption and distribution of hydrogen at room temperature as a function of the environmental and metallurgical factors and to define more clearly the important variables which must be considered in acid pickling and utilization of pickled materials.

ENVIRONMENTAL FACTORS AFFECTING HYDROGEN PICKUP

When a metal reacts in an acid solution with hydrogen gas evolution, one of the processes which occurs at the surface is reduction of hydrogen ions to form hydrogen gas ($2\text{H}^+ + 2\text{e} \rightarrow \text{H}_2$). This overall process may be considered to occur in two individual steps—reduction of hydrogen ions to form hydrogen atoms ($\text{H}^+ + \text{e} \rightarrow \text{H}$) and combination of two hydrogen atoms on the surface to form hydrogen gas ($\text{H} + \text{H} \rightarrow \text{H}_2$). In addition to forming hydrogen gas, hydrogen atoms in contact with a metal surface may dissolve directly in the metal or in some cases react with the metal to form a hydride. This is the source of hydrogen pickup during pickling.

A concentration of hydrogen atoms at the metal surface constitutes a driving force for the absorption of hydrogen. It may be regarded as an effective surface pressure, although it is not a pressure in the sense normally associated with molecular gases. Darken and Smith (15), who studied hydrogen diffusion through steel during acid immersion, have called this driving force "virtual pressure." They calculate the "virtual pressure" to be of the order of 10^6 to 10^8 atmospheres, many orders of magnitude greater than the hydrogen gas pressure of about one atmosphere which exists above the solution.

From theoretical considerations, it is believed that the "virtual pressure" of hydrogen is a marked function of applied current density dur-

ing cathodic charging (16). The reduction of hydrogen ions to hydrogen atoms can be made to proceed at much higher rates by intentionally making the metal a cathode in acid solutions. The rate of reduction of hydrogen ions is by Faraday's law directly proportional to the cathodic current if no other reduction reaction occurs. If the reaction proceeds at a high rate, the concentration of hydrogen atoms at the metal surface increases. Hence, the "virtual pressure" which is the driving force for absorption of hydrogen atoms also increases.

To determine the importance of this variable on hydrogen pickup by titanium, cathodic charging experiments were conducted at various current densities in a manner which is described in a later section of this discussion. It was found that hydrogen pickup was indeed quite sensitive to applied current density, increasing markedly with an increased rate of reduction of hydrogen ions.

Since, as described above, the rate of reduction of hydrogen ions on a titanium surface influences the driving force for diffusion of hydrogen into titanium, any factor which changes this rate will affect hydrogen pickup. Thus, an increase in the corrosion rate of titanium caused by an increase in acid concentration would be expected to create a greater hydrogen pickup. To check this, titanium sponge, with a high surface-to-mass ratio, was corroded in 1% HCl and 5% HCl for 18 hours at room temperature. The hydrogen pickup from 5% HCl was 3.7 times as high as that found in the 1% acid. A further experiment was conducted to determine whether a corrosion inhibitor which passivated titanium would decrease hydrogen pickup. Ferric ion additions to hydrochloric acid are known to passivate titanium and thus minimize corrosion (17). Since very low corrosion rates do not provide sufficient hydrogen to measure easily by vacuum-fusion analysis, it was necessary to use radioactive hydrogen (tritium) as a measure of hydrogen absorption. Titanium was corroded in tagged 1% HCl with and without ferric ion for 17 hours. The hydrogen pickup, measured by tritium activity, was reduced by a factor of about one hundred when titanium was passivated.

The hydrogen content of titanium will increase during acid pickling, which is a corrosion process, if hydrogen ion reduction is the cathodic process. For example, it is reported that pickling in a 2% HF solution increases hydrogen content considerably. However, if nitric acid is added to the pickling solution, hydrogen pickup is minimized (11,12). This is due to the fact that the primary cathodic reduction reaction during pickling is changed from hydrogen evolution to reduction of nitrate. As long as passivity is not achieved, the pickling process will occur at a rapid rate without appreciable hydrogen evolution. It is important to note in this connection that the electron diffraction studies of Ogawa and Watanabe (18) show that a titanium hydride surface film is formed during immersion of alpha titanium in hydrofluoric,

hydrochloric, sulphuric, or phosphoric acid. In these solutions, hydrogen evolution is the primary cathodic corrosion reaction. An immersion time of only a few seconds is required to produce a hydride on titanium in concentrated hydrofluoric acid at room temperature or hydrochloric acid at the boiling point. Immersion in nitric acid or aqua regia, however, produced a surface film of titanium dioxide (anatase). Titanium hydride surface films have been identified by x-ray diffraction in our Laboratories after corrosion in hydrochloric acid.

METALLURGICAL FACTORS AFFECTING HYDROGEN PICKUP

Room temperature solubility and diffusion rate of hydrogen in alpha and beta titanium are the principal factors which control hydrogen pickup in acid pickling. The alpha/alpha + hydride and beta/beta + hydride boundaries have been derived as mathematical relationships from thermodynamic data by McQuillan (5). The solubility of hydrogen in alpha titanium is less than 20 ppm at room temperature but becomes appreciable at temperatures above 100 °C. The corresponding solubility in beta is 66 ppm and at any temperature is significantly higher than that in alpha. This is a hypothetical boundary, however, and one would expect a different solubility in beta phase due to the presence of elements required to stabilize the beta phase to room temperature.

The diffusion coefficients of hydrogen in both alpha and beta titanium at elevated temperatures have been determined by Wasilewski and Kehl (6). Diffusion of hydrogen is faster in the beta phase than in alpha.

These data indicate that hydrogen pickup would be controlled to a large extent by the amount and distribution of the two phases present in an alloy. Predominantly alpha structures would be expected to pick up hydrogen slowly, forming a concentration of hydrogen in the form of hydride at the surface. This has been demonstrated experimentally by McKinsey and Martin (13) and Otsuda (19). Beta-rich alloys would be expected to dissolve considerably more hydrogen with a much greater depth of penetration under the same conditions. Therefore, the amount of hydrogen absorbed in acid pickling is strongly dependent on structure and on the ratio of surface area to total mass.

A series of experiments were conducted to illustrate more clearly the importance of metallurgical factors such as grain structure, alpha-beta ratio, and alpha-beta configuration on the absorption and distribution of hydrogen and to indicate wherein the ratio of surface area to mass is most significant.

MATERIALS AND PREPARATION

Samples of commercially pure titanium and selected alloys were heat treated to obtain a variety of structures as shown in Table I. The

Table I
Materials and Preparation

Sample No.	Alloy	Heat Treatment	Microstructure	Cathodic Charging Conditions	Hydrogen		Net Increase ppm
					Initial ppm	Final ppm	
A-1	C.P. Ti	1 hr.-775°C.-WQ	Equiaxed: Alpha	A	112	236	124
B-1	Ti-0.21% Fe	1 hr.-775°C.-WQ	Equiaxed: Alpha+2.0% Beta	A	111	334	223
C-1	Ti-0.34% Fe	1 hr.-775°C.-WQ	Equiaxed: Alpha+4.4% Beta	A	97	367	270
D-1	Ti-0.52% Fe	1 hr.-775°C.-WQ	Equiaxed: Alpha+7.8% Beta	A	111	434	323
A-2	C.P. Ti	1 hr.-950°C.-FC	Serrated: Alpha	A	112	280	168
B-2	Ti-0.21% Fe	1 hr.-950°C.-FC	Basket Weave: Alpha+1.0% Beta	A	111	478	364
C-2	Ti-0.34% Fe	1 hr.-950°C.-FC	Basket Weave: Alpha+2.3% Beta	A	97	479	382
D-2	Ti-0.52% Fe	1 hr.-950°C.-FC	Basket Weave: Alpha+4.0% Beta	A	111	547	436
A-3	C.P. Ti	1 hr.-950°C.-WQ	Serrated: Alpha	A	112	247	135
B-3	Ti-0.21% Fe	1 hr.-950°C.-WQ	Acicular: Alpha (+Beta)	A	111	460	349
C-3	Ti-0.34% Fe	1 hr.-950°C.-WQ	Acicular: Alpha (+Beta)	A	97	484	387
D-3	Ti-0.52% Fe	1 hr.-950°C.-WQ	Acicular: Alpha (+Beta)	A	111	575	464
25106	Ti-7% Mn	1 hr.-850°C.-FC to 700°C.-1 hr.-WQ	Beta+25% Alpha*	B	—	12,100	—
25106	Ti-7% Mn	1 hr.-850°C.-WQ	Equiaxed: Beta	B	—	13,600	—
4-1469	C.P. Ti	Mill Anneal	Equiaxed: Alpha	C	15	—	—

*Widmannstätten and Intergranular Distribution

A—10.15-mm. thick sheet, 20% H₂SO₄, 0.088 amp./sq. cm., 20 hoursB—1.8-mm. thick sheet, 20% H₂SO₄, 0.20 amp./sq. cm., 20 hoursC—10.0-mm. dia x 80-mm. long bar, 20% H₂SO₄, 0.10 amp./sq. cm., 48 hours

data for samples A to D are from a previous investigation (13). The samples were charged with hydrogen by making them the cathode in an electrolyte of 10 to 20% sulphuric acid solutions. Platinum anodes were used. The conditions of charging were 20 or 48 hours at a current density of 0.088, 0.10, or 0.20 ampere per square centimeter. Both rod and sheet samples were used. A portion of each sample was prepared for chemical analysis. Total hydrogen was determined by vacuum-extraction techniques.

Distribution of hydrogen was studied by metallographic methods.

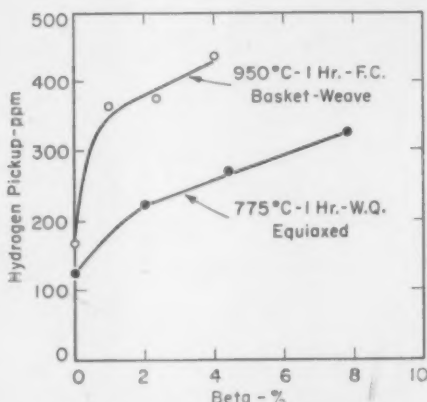


Fig. 1—Effect of Amount and Distribution of Beta on Hydrogen Pickup.

A cross section of each specimen was prepared for study. In order to preserve the edge during polishing, specimens were plated either with copper, iron, or nickel prior to polishing. It was assumed that hydrogen pickup during plating was negligible. Best results were obtained with nickel which had better resistance to the etching solutions than either copper or iron. All samples were etched in 2% HF:23% HNO₃:75% H₂O solution for metallographic examination. The amount of beta phase was determined by lineal analysis or, where calculations permitted, from equilibrium relationships.

RESULTS

Evidence of the importance of microstructure in controlling hydrogen pickup is given in Fig. 1 (13). These data indicate that in predominantly alpha alloys the total hydrogen pickup is directly related to the amount and distribution of beta phase. A network distribution of a very small amount of beta (basket-weave structure) is far more detrimental than a random dispersion of a larger amount of beta phase.

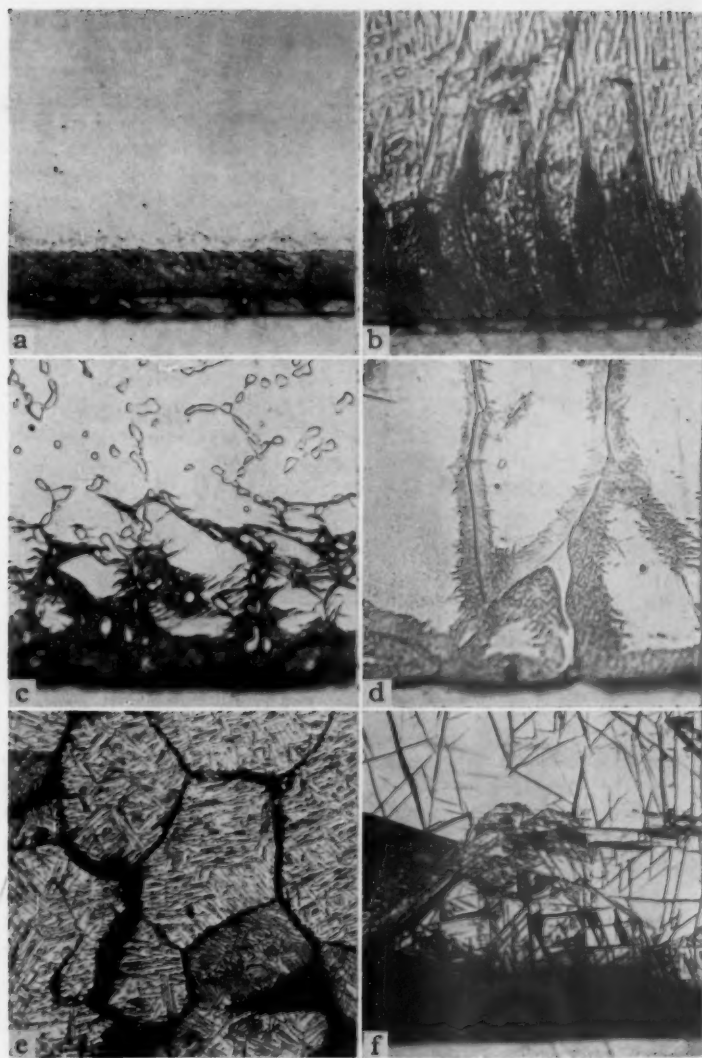


Fig. 2—Effect of Microstructure on Hydrogen Distribution: (a) Alpha Equiaxed $\times 500$; (b) Alpha (+ Beta) Acicular $\times 500$; (c) Alpha + 7.8% Beta Equiaxed $\times 500$; (d) Alpha + 2.3% Beta Basket Weave $\times 500$; (e) Beta + 25% Alpha $\times 100$; (f) Beta Equiaxed $\times 100$.

Composition and heat treatment, therefore, can have a marked effect on susceptibility to hydrogen absorption during acid pickling.

As shown in Fig. 2, hydrogen absorbed by commercially pure titanium or predominantly alpha alloys is concentrated as titanium hydride in a thin surface layer. Under the conditions of these experiments, the layer was 0.010 to 0.020 millimeter thick. As determined in an earlier study (13), the presence of the beta phase resulted in deeper penetration of hydride compared with that obtained in all-alpha struc-

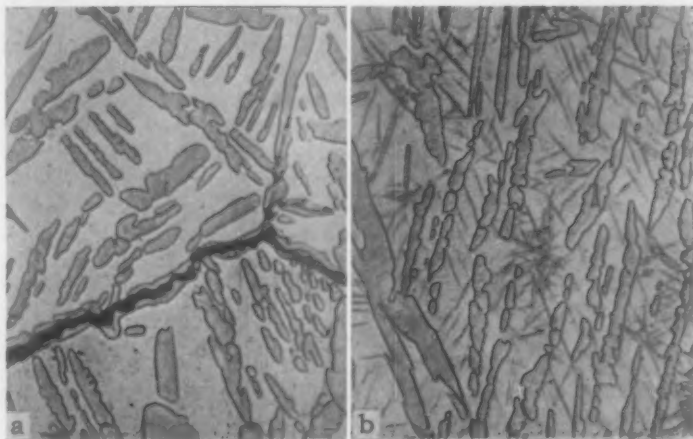


Fig. 3—Structure of Titanium—7% Manganese Alloy Charged with 12,100 ppm Hydrogen. $\times 1000$. (a) Crack in Alpha Phase at Prior Beta Grain Boundary. No Hydride in Alpha; (b) Acicular Markings in Beta Matrix.

tures. Hydrogen penetrated deeper into an alloy with 2.3% beta in a network distribution than in an alloy with 7.8% beta in a random dispersion. The depth of penetration in acicular alpha (martensite) also is greater than that in equiaxed alpha, indicating the presence of retained beta in the acicular structure. This indicates that hydrogen by virtue of its higher solubility and diffusion rate in beta has an easy path of entry. It is interesting to note that in structures where beta is present up to 8% by volume, the hydrogen still is found as hydride needles in the alpha structure adjoining beta particles. This indicates that the beta may be saturated with hydrogen.

A markedly different behavior was exhibited by beta-rich alloys. A titanium-7% manganese alloy heat treated to form a structure of 25% alpha in a beta matrix was charged to a total hydrogen content of 12,100 ppm. The same alloy quenched to form an all-beta structure was charged under the same conditions to 13,600 ppm hydrogen.

Charging conditions were somewhat different from those used with beta-lean alloys so a quantitative comparison of total hydrogen pickup with alloys which are predominantly alpha cannot be made (Table I). The results indicate, however, that the beta-rich alloys are far more susceptible to hydrogen pickup. Large amounts of hydrogen can be absorbed under these conditions. The most significant result of this experiment, however, is the fact that in beta-rich alloys, no surface layers of hydride are formed. In fact, as shown in Figs. 2 and 3, there was no evidence of hydride formation in either the alpha or beta phases in alloys with 12,000 to 14,000 ppm hydrogen. This was checked by both metallographic and x-ray diffraction studies.

The hydrogen dissolved in the beta is far in excess of that predicted by McQuillan's thermodynamic extrapolation of the beta/beta + hydride phase boundary in the titanium-hydrogen binary system (5). The presence of manganese would be expected to modify this phase boundary. Also, beta may be supersaturated, since McQuillan proposed that nucleation of hydride in a body-centered cubic matrix might be extremely difficult, if not impossible (5).

The needle-like structure observed in the beta phase (Fig. 2f) is identical in appearance to martensite (acicular alpha) produced by mechanical deformation of metastable beta and was not present before cathodic charging. The presence of alpha titanium was confirmed by x-ray diffraction. Most likely the acicular markings in the matrix of the beta + 25% alpha alloy (Fig. 3b) are also martensite needles. It appears that the introduction of hydrogen promoted the formation of martensite. A higher incidence of acicular markings in beta near the surface may indicate some gradation in hydrogen concentration. Evidence that the introduction of hydrogen creates internal stress is given by the intergranular cracking developed in the beta plus 25% alpha alloy as a result of cathodic charging. Cracking appeared to be confined to the alpha phase (Fig. 3a).

STABILITY OF HYDRIDE LAYER

Since hydrogen pickup from acid solutions is characterized by the formation of surface layers of titanium hydride in predominantly alpha structures, it is important to know the relative stability of the layer at low temperatures. This effect was studied by metallographic examination of cathodically charged specimens (Heat 4-1469, Table I) heated for different lengths of time at temperatures up to 400 °C (750 °F). Results are shown in Table II and Fig. 4. The specimens contained 15 ppm hydrogen initially, and no trace of hydride needles could be found in the structure. Hydrogen content after charging was not measured but was estimated to be about 90 to 110 ppm.

The hydride layer did not change in appearance on standing several months at room temperature or on heating for 1 hour at 100 °C. After

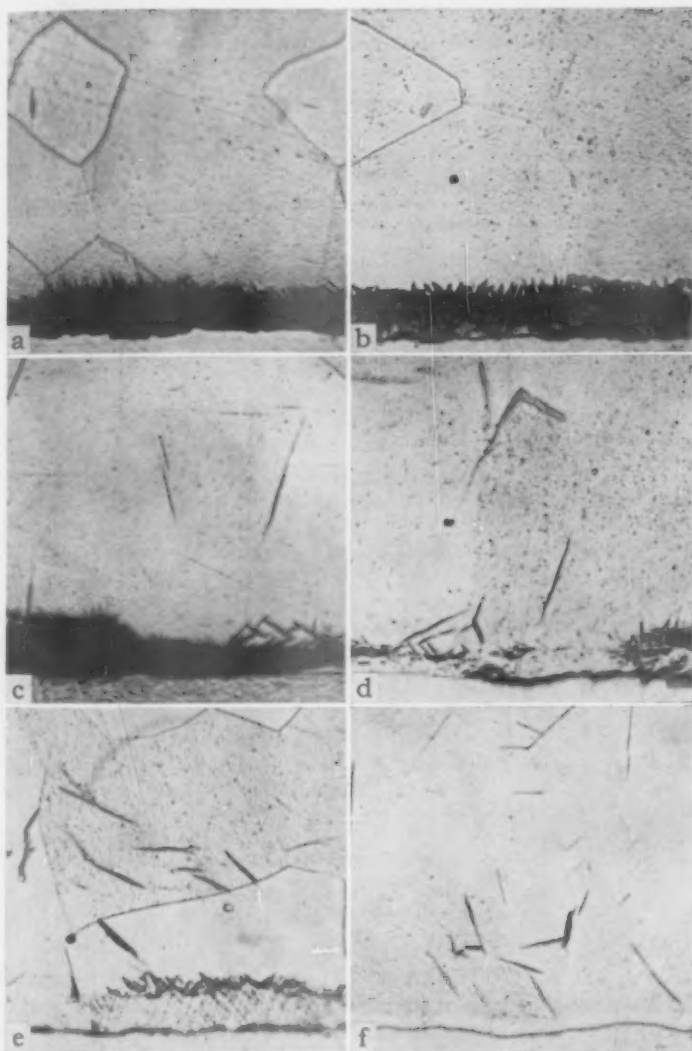


Fig. 4—Effect of Heat Treatment on Stability of Surface Hydride Layer. $\times 500$. (a and b) 100 °C (210 °F); (c and d) 200 °C (390 °F); (e and f) 300 °C (570 °F). (a), (c) and (e) 1 hour. (b), (d) and (f) 24 hours.

24 hours at 100 °C, a few hydride needles were observed in the core to a depth of 0.3 millimeter from the surface, indicating that some dissociation and diffusion had occurred. A similar change was noted after

Table II
Effect of Heat Treatment on Stability of Hydride Layer

Sample No.	Temp. °C.	Temp. °F.	Hydride Layer Thickness-mm. Heating Time-Hr.			Depth of Penetration-mm.* Heating Time-Hr.		
			0	1	24	0	1	24
D-1A	100	210	0.015	0.015	0.015	0	0	0.30
D-1B	200	390	0.011	0.011	0-0.006	0	0.40	3.50
D-2A	300	570	0.015	0-0.006	0	0	1.40	3
D-2B	400	750	0.012	0	0	0	2.70	5

*Distance from surface at which hydride needles were observed in core.

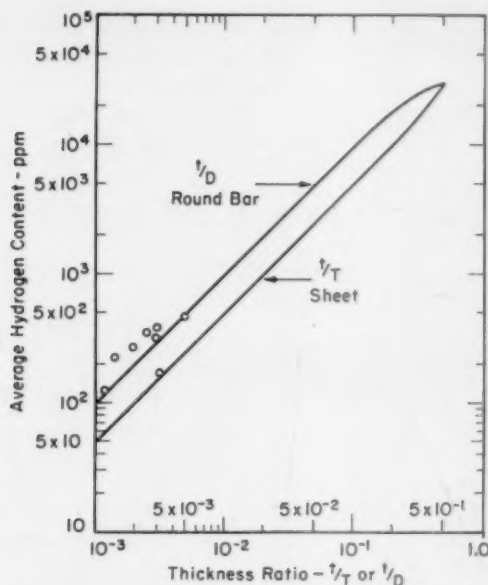


Fig. 5—Effect of Ratio of Hydride Layer Thickness to Total Thickness on Hydrogen Content.

1 hour at 200 °C (390 °F). After 24 hours at 200 °C (390 °F), much of the layer was dissociated, and hydride needles extended well into the core (Fig. 4). Dissociation was not uniform and diffusion appeared to occur both into the core and into the nickel plate. After 24 hours at 300 °C (570 °F), the hydride layer had completely disappeared, and needles were randomly dispersed throughout the specimen. The layer also was completely dissociated after 1 hour at 400 °C (750 °F), but additional time at this temperature was required for uniform dispersion to the center of the 10-millimeter rod sample.

SIGNIFICANCE OF SURFACE HYDRIDE LAYERS

The fact that in predominantly alpha alloys the hydrogen absorbed during acid pickling is concentrated as a very thin surface layer of titanium hydride is of considerable significance, since total hydrogen content generally is taken as the criterion for hydrogen embrittlement. The influence of a surface hydride layer is important since it (a) may restrict total hydrogen pickup by limiting diffusion, (b) contributes to total hydrogen content, and (c) most likely leads to mechanical behavior different from that produced by a uniform hydrogen content.

Gulbransen and Andrew (9) found a different behavior in the absorption of hydrogen at 250 °C (480 °F) compared with that at higher temperatures which they attributed to the presence of a hydride film. No direct measurement of the effect of surface hydride on the diffusion of hydrogen into titanium has been made, however. The cathodic charging experiments indicate that the effect may be significant since large increases in charging time did not result in proportionate increases in the thickness of hydride layers.

A significant effect of surface hydride is the contribution that it will make to total hydrogen content. The total hydrogen content will depend on the ratio of surface area to mass or, more properly, on the ratio of the layer thickness to the total thickness of the material. A relationship expressing the total hydrogen content as a ratio of the layer thickness to total thickness for sheet and bar has been derived as shown below:

$$1) \quad H_T = \frac{(V_L) (\rho_L) (H_L)}{(V_T) (\rho_T)}$$

Sheet	Bar
$H_T = \frac{[2(t/T)] (\rho_L) (H_L)}{(\rho_{T1}) - [2(\rho_{T1} - \rho_L) (t/T)]}$	$2) \quad H_T = \frac{[1 - (1-2t/D)^2] (\rho_L) (H_L)}{(\rho_L) + [(\rho_{T1} - \rho_L) (1-2t/D)^2]}$

where H_T = total hydrogen, ppm.
 H_L = hydrogen in layer, ppm.
 ρ_L = density of hydride layer
 ρ_{T1} = density of titanium
 t = layer thickness
 T = total thickness
 D = total diameter
 V_L = volume of layer
 V_T = total volume
 ρ_T = average density

These derivations are based on a negligible hydrogen content in the material exclusive of the layer and do not take into account possible end or edge effects.

Assuming a hydrogen content of 30,000 ppm for the layer (midway between TiH and TiH₂), density of the layer was calculated to be 3.78 grams per cubic centimeter. Using these values, the equations

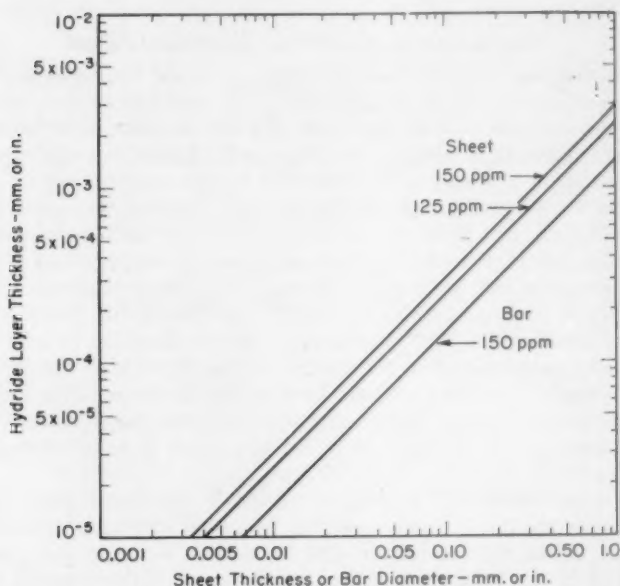


Fig. 6—Maximum Hydride Layer Thickness for 125 or 150 ppm. Hydrogen in Sheet or 150 ppm. Hydrogen in Bar of Varying Total Thickness.

were solved for various assumed values of t/T and t/D , and plotted in two ways as shown in Fig. 5 and Fig. 6. Fig. 5 expresses total hydrogen content as a function of the thickness ratio, while Fig. 6 shows the total layer thickness required for a given sheet or bar thickness to reach total hydrogen contents of 125 and 150 ppm.

These curves serve to illustrate the sensitivity of total hydrogen content to hydride layer thickness and thickness ratios. For example, in 16-gage sheet (0.0625-inch thick) a hydride layer 0.00019-inch thick (ratio = 0.003+) would increase the total hydrogen content by 150 ppm. The same layer thickness on 22-gage sheet (0.03125-inch thick—ratio = 0.006+) would increase total hydrogen by 300 ppm. The hydrogen content effectively is doubled when the thickness ratio is doubled. Thickness ratios were determined for several of the cathodically charged bar specimens of predominantly alpha alloys, and results are plotted in Fig. 5. Although some scatter is evident, agreement with the calculated curve is fairly good.

The existence of surface hydride layers presents a complication in the analysis of acid-pickled material for hydrogen. The actual hydrogen content may be greater or less than that measured depending on how the analytical sample is prepared and the subsequent treatment of the

material. Failure to include the surface of the material or abrasion of the surface in preparing an analytical sample will result in lower hydrogen contents. Similarly, alteration of the surface after analysis may result in a significant change in hydrogen content.

It remains to be demonstrated whether surface hydride layers are detrimental to mechanical behavior. It would seem that mechanical behavior of materials with the same total hydrogen content occurring as a surface layer in one case and as a uniform distribution in the other would be quite different. This subject is of considerable importance and would be a fertile field for detailed investigation.

SUMMARY AND CONCLUSIONS

Hydrogen pickup and distribution in titanium and its alloys during acid pickling are controlled by a variety of interrelated environmental and metallurgical factors. Corrosion of the metal surface results in the formation of hydrogen atoms, which constitute an effective hydrogen pressure and is the driving force for diffusion into the metal. Any factor which alters the rate of reduction of hydrogen will affect hydrogen pickup. It is possible to passivate titanium or to change the cathodic reaction and minimize hydrogen pickup.

Hydrogen pickup by cathodic charging and, hence, by acid pickling in predominantly alpha alloys is characterized by the formation of thin surface layers of titanium hydride. Essentially, all the hydrogen is concentrated in the surface layer. The presence of small amounts of beta, particularly in network distribution, results in more hydrogen pickup and deeper hydrogen penetration. Hydrogen pickup in predominantly beta alloys is characterized by lack of surface hydride layers, rapid hydrogen penetration, and the possibility of extremely high hydrogen contents. High internal stresses also can be developed.

The hydride layer formed on alpha titanium is stable on heating for short times at temperatures up to 100 °C. At higher temperatures, it decomposes in less than 24 hours and hydrogen diffuses into the core.

The thin hydride layers may make a substantial contribution to total hydrogen content and are believed to contain an average of about 30,000 ppm hydrogen. Total hydrogen content of the material depends on the ratio of the layer thickness to total thickness. Analysis of pickled material for total hydrogen will give erroneous results if the original surface is not included in samples for the analysis.

Total hydrogen content is not necessarily a true criterion for expected mechanical behavior, and distribution of the hydrogen should be considered. A material with high hydrogen content, most of which is concentrated at the surface, may be acceptable if the thin surface layer is removed by some mechanical means. In this respect it appears best not to heat acid-pickled material after descaling since heating will result in deeper penetration of hydrogen.

ACKNOWLEDGMENT

The authors gratefully acknowledge the helpful guidance and assistance of the staff of the Metals Research Laboratories, Electro Metallurgical Company. They wish to thank particularly R. G. Myers who was most helpful in conducting the experimental work.

References

1. H. M. Burte, E. F. Erlein, G. T. Halin, R. J. Kotfila, J. W. Seeger and D. A. Wruck, "Hydrogen Embrittlement of Titanium Alloys," *METAL PROGRESS*, American Society for Metals, Vol. 67, No. 5, 1955, p. 115.
2. R. I. Jaffee, "General Physical Metallurgy of Titanium Reviewed," *Journal of Metals*, Vol. 7, 1955, p. 247.
3. H. D. Kessler, R. G. Sherman and J. F. Sullivan, "Hydrogen Affects Critical Properties of Commercial Titanium," *Journal of Metals*, Vol. 7, 1955, p. 242.
4. G. A. Lenning and R. I. Jaffee, "Effect of Hydrogen on the Properties of Titanium and Titanium Alloys," Battelle Memorial Institute, TML Report No. 27, December 27, 1955.
5. A. D. McQuillan, "Hydrogen in Titanium and Its Alloys," Lecture presented at Titanium Metallurgy Course, New York University, September 12, 1956.
6. R. J. Wasilewski and G. L. Kehl, "Diffusion of Hydrogen in Titanium," *Metallurgia*, Vol. 50, 1954, p. 225-230.
7. W. J. Barth and A. L. Field, Jr., "Sodium Hydride Descaling of Titanium," *METAL PROGRESS*, Vol. 68, No. 2, 1955, p. 114-116.
8. H. L. Alexander, H. Farrell and Q. D. Wheatley, "Hydrogen Contamination of Titanium Minimized by Modified Descaling Bath," *METAL PROGRESS*, American Society for Metals, Vol. 69, No. 2, 1956, p. 78-80.
9. E. A. Gulbransen and K. F. Andrew, "Kinetics of the Reaction of Titanium with O_2 , N_2 , and H_2 ," *Transactions*, American Institute of Mining and Metallurgical Engineers, Vol. 185, 1949, p. 741-748.
10. G. A. Lenning, C. M. Craighead and R. I. Jaffee, "Hydrogen Contamination in Descaling and Acid Pickling of Titanium," *TRANSACTIONS*, American Society for Metals, Vol. 48, 1956, p. 726-733. Discussion p. 733-741.
11. H. B. Bomberger, M. B. Vordahl and W. L. Finlay, "How to Avoid Titanium Embrittlement During Pickling," *Materials and Methods*, Vol. 40, No. 12, 1954, p. 105.
12. Rem-Cru Titanium Review, October 1954, p. 7.
13. C. R. McKinsey and R. C. Martin, "The Influence of Small Iron Additions on the Behavior of Titanium," Presented at the American Institute of Mining and Metallurgical Engineers Regional Reactive Metals Conference, Buffalo, March 20, 1956.
14. J. W. Seeger, "Hydrogen Levels in Titanium Alloy Materials Used for Current Aircraft and Engine Production," Presented at a Symposium on Hydrogen Embrittlement, Wright Air Development Center, October 29, 1954.
15. L. S. Darken and R. P. Smith, "Behavior of Hydrogen in Steel During and After Immersion in Acid," *Corrosion*, Vol. 5, No. 1, 1949, p. 1-16.
16. P. VanRysselberghe, *Electrochemical Affinity*, 1955, p. 64, Hermann and Cie, Paris.
17. J. R. Cobb and H. H. Uhlig, "Resistance of Titanium to Sulfuric and Hydrochloric Acids Inhibited by Ferric and Cupric Ions," *Journal*, Electrochemical Society, Vol. 99, 1952, p. 13.
18. S. Ogawa and D. Watanabe, "Electron Diffraction Study on Titanium Attacked by Various Acids," *Science Reports of the Research Institute*, Tohoku University, Vol. 7A, 1955, p. 184.
19. R. Otsuda, "Protective Film on Titanium in Hydrochloric Acid," *Journal*, the Scientific Research Institute, Japan, Vol. 49, December 1955, p. 319-324.

DISCUSSION

Written Discussion: By D. N. Williams, Battelle Memorial Institute, Columbus, Ohio.

The authors are to be congratulated on carrying out an investigation which will do much to explain previously anomalous results obtained in studies of low temperature hydrogen absorption. I should like to raise a mild objection to one of their statements, however. In referring to Fig. 3, the authors state that this structure, representing an 8Mn alloy containing 12,100 ppm of hydrogen, contains no hydride. In my opinion, the very sharp outlining around selected alpha needles is due to a fine hydride interface between the alpha and beta phase. The inability of x-rays to detect hydride would not seem unusual, since x-ray detection of hydride is quite difficult. A fairly large amount of reasonably coarse hydride is required to produce an x-ray indication of the presence of hydride.

To further support this argument, the microstructure in Fig. 7 is of interest.² In this illustration, hydride precipitation in a solution heat treated and aged commercial alpha-beta alloy is shown. Although this sample contains only 200 ppm hydrogen, the tendency toward hydride precipitation at the alpha-beta interface is quite apparent.

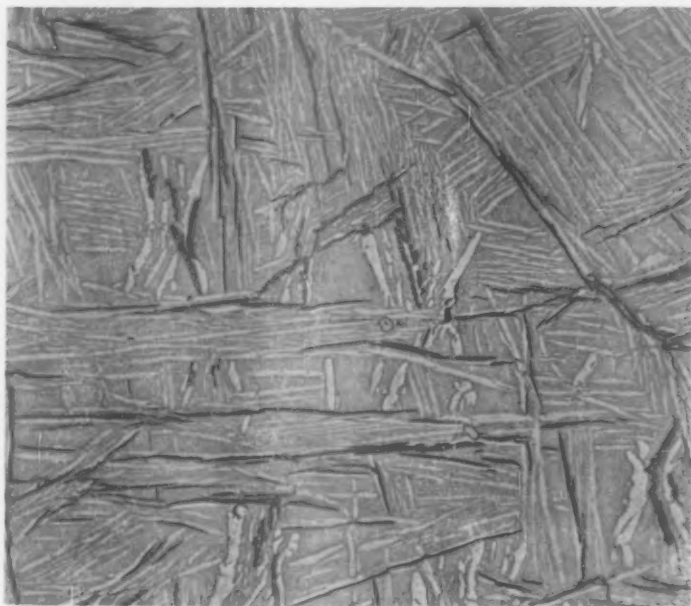


Fig. 7—Ti-2Mo-2Fe-2Cr Containing 200 ppm. $\times 500$

² WADC TR 54-616, Part IV, D. N. Williams, F. R. Schwartzberg, P. R. Wilson, W. M. Albrecht, M. W. Mallett, and R. I. Jaffee.

Authors' Reply

As stated in the text, no surface layer of hydride was formed in the predominantly beta alloy, and there was no evidence of hydride formation within either the alpha or the beta phase. This does not preclude the existence of a fine hydride phase at the alpha-beta interface, and the authors agree that this may be the case. However, it is also possible that an aging treatment after hydrogenation is necessary to produce this effect. The specimen in Dr. Williams' example was both solution heat treated and aged. Also, in recent work by Huber and co-workers,* in which hydrogen distribution was studied by autoradiography, it was found that an aging treatment at 900 °F was necessary to precipitate a hydrogen-rich phase at the alpha-beta interface in a titanium-3% manganese complex alloy after charging with 600 ppm hydrogen and solution heat treating in the alpha + beta field.

* O. H. Huber, J. E. Gates, A. P. Young, M. Pobereskin and P. D. Frost, "Hydrogen Distribution in Heat Treated Titanium as Established by Autoradiography," *Transactions, American Institute of Mining and Metallurgical Engineers*, Vol. 209, 1957, p. 918 to 923.

THE MODE OF HYDRIDE PRECIPITATION IN ALPHA TITANIUM AND ALPHA TITANIUM ALLOYS

BY TIEN-SHIH LIU AND MORRIS A. STEINBERG

Abstract

The modes of hydride precipitation in alpha titanium and alpha titanium alloys have been determined using optical methods on oriented single and large-grained crystals by the two-surface method. Under favorable conditions of hydride precipitation and growth, the appearance of the hydrides in unalloyed and alloyed (Ti-3% Al, Ti-3% Ta, Ti-2% V, and Ti-10% Zr) alpha titanium are basically the same—thin needles. The precipitation tends to take place along slip lines and twin markings, where the surface energies are higher than surrounding areas. The habit planes for hydride precipitation were determined as follows:

Ti and Ti-2% V $(10\bar{1}0)$ $(10\bar{1}1)$

Ti-10% Zr $(10\bar{1}1)$ $(11\bar{2}2)$

Ti-3% Ta $(10\bar{1}1)$ $(11\bar{2}1)$ $(11\bar{2}2)$

Ti-3% Al $(10\bar{1}1)$ $(11\bar{2}1)$ $(10\bar{1}2)$

Crystallographic relationships postulated for unalloyed titanium are

$\{10\bar{1}0\}_{\alpha\text{Ti}}$ $(101)_{\text{TiH}}$ F.C.T.

$\{12\bar{1}0\}_{\alpha\text{Ti}}$ $[011]_{\text{TiH}}$ F.C.T.

$\{10\bar{1}1\}_{\alpha\text{Ti}}$ $(101)_{\text{TiH}}$ B.C.T.

$\{12\bar{1}0\}_{\alpha\text{Ti}}$ $[100]_{\text{TiH}}$ B.C.T.

An explanation of impact brittleness caused by hydride precipitation is presented. (ASM International Classification N7b; Ti)

INTRODUCTION

THE EFFECT of hydrogen on mechanical properties of titanium and its alloys with particular reference to its embrittling behavior has been the object of widespread investigation in the last several years. The objective of the present investigation is to seek better understand-

This work was performed under the auspices of the Metallurgy Branch, Office of Naval Research on Contract No. Nonr-1847 (00).

A paper presented before the Thirty-Ninth Annual Convention of the Society, held in Chicago, November 4-8, 1957. Of the authors, T. S. Liu is former project supervisor, Metallurgy Department, Horizons Inc. and is now at Titanium Metals Corporation of America, Henderson, Nevada. M. A. Steinberg is head, Metallurgy Department, Horizons, Inc., Cleveland. Manuscript received March 27, 1957.

ing of this mechanism of hydrogen embrittlement in titanium and its alloys with particular reference to the modes of hydride precipitation. In order to approach the problem systematically, hydride precipitation in alpha titanium and alpha-titanium alloys was studied.

Micrographic studies of unalloyed alpha titanium and alpha-titanium alloys have revealed the presence of fine markings which have variously been ascribed as precipitated X-phase, etch pits, twins, or hydrogen-rich "rifts" in the structure. The work of Craighead, Lenning and Jaffee (1)¹ has indicated that the precipitation of the hydride TiH is in all probability responsible for the markings.

Due to the inherent characteristics of the constituents involved, especially the low atomic scattering power of hydrogen and titanium, optical and metallographic methods rather than x-ray techniques for the orientation determination of the hydrides were used to study this precipitation. Alloys chosen were all alpha regions of the Ti-Al, Ti-Zr, Ti-V, and Ti-Ta binary systems.

BACKGROUND

In the metal-hydrogen systems, there are four types of interactions between the gas and the metal.

1. With the alkali and alkaline-earth metals, hydrogen forms hydrides of a salt-like nature.

2. With the metals of Group IV B, V B, and VI B, covalent hydrides are formed yielding compounds analogous to the hydrocarbons.

3. A number of metals, such as iron, chromium, nickel, cobalt, platinum, copper, silver, molybdenum, magnesium, and aluminum dissolve hydrogen to form true solutions, as indicated by the fact that.

- a. the hydrogen solubility varies as \sqrt{P} , and
- b. solubility increases with increasing temperature.

4. With the rare-earth metals and titanium, zirconium, thorium, hafnium, vanadium, niobium, tantalum, uranium, and manganese, the solubility varies as \sqrt{P} for certain ranges of values of pressure (P) and this solubility decreases with increasing temperature in certain temperature ranges.

In the case of titanium, the maximum hydrogen solubility in alpha-titanium of 7.9 atomic % is reached at approximately 608 °F. Beyond this temperature the solubility of hydrogen in alpha titanium decreases gradually to zero at the alpha-beta transformation temperature, 1620 °F.

According to Craighead, Lenning and Jaffee (1), the solubility of hydrogen in alpha titanium decreases from 7.9 atomic % at 572 °F to about 0.1 atomic % at room temperature. The hydrogen cannot be re-

¹ The figures appearing in parentheses pertain to the references appended to this paper.

tained by fast quenching. It precipitates as plates at slow cooling rates and as a fine dispersion after quenching.

The results of investigations to date indicate that the precipitated γ phase has a rather wide range of composition—from 48 to 63.3 atomic % according to McQuillan (2). It has generally been accepted that this γ phase is face-centered cubic. Due to the nature of the elements involved, positioning the hydrogen atoms in the lattice by x-ray studies has been impossible. Using iodide titanium with 61.7 atomic % of purified hydrogen, McQuillan (3) obtained a lattice parameter of 4.41 Å.

Neutron diffraction studies by Jaffe (4) indicate that below 500 °F there is a body-centered tetragonal phase with $a_0 = 3.12 \text{ Å}$, $c_0 = 4.18 \text{ Å}$, and with a c/a ratio of 1.34. This investigation is still in progress at the present time.

Similar hydride precipitation was observed by Langeron and Lehr (5) on coarse grained zirconium specimens. Using x-ray diffraction and stereographic manipulations, these investigators concluded that the plane of hydride precipitation in zirconium is of the type $(10\bar{1}0)$. It is interesting to note that this corresponds to the slip plane in zirconium.

No recorded work can be found on the crystallography of hydride precipitation in titanium or zirconium alloys. In the present investigation, the selection of the alloys is such that there is a variation of the axial ratio both above and below that of pure titanium ($c/a = 1.587$) (see Table I).

Hydrogen embrittlement in zirconium was investigated by Young and Schwartz (12). They concluded from observations using an electron microscope that micro-crack formation at the hydride-zirconium interfaces was responsible for the embrittlement in zirconium.

According to Lenning and Jaffee (13) there are two distinct types of hydrogen embrittlement in titanium and titanium alloys. Alpha-type alloys are more susceptible to hydrogen embrittlement at impact speeds. Alpha-beta-type alloys are susceptible to both the impact-type and the strain-aging type of hydrogen embrittlement. It was suggested that the addition of 5% aluminum would increase the hydrogen tolerance of alpha alloys. Another method would be to utilize the higher hydrogen solubility of beta titanium. Thus, the addition of a small amount of a beta-stabilizing element such as molybdenum would also raise the

Table I
Nominal Composition of Alpha Ti Alloys Used and Their c/a Ratios

Nominal Comp.	Actual Composition	c/a	References
Ti-3% Al	2.76% Al	1.592	(6)
Ti-10% Zr	9.54% Zr	1.377	(7), (8)
Ti-3% Ta	2.83% Ta	1.589	(9)
Ti-2% V	2.1% V	1.587	(10), (11)

hydrogen tolerance thus preventing the strain-aging type embrittlement.

From the foregoing discussion, it is evident that while considerable knowledge has been gained on the effect of hydrogen on the properties of titanium and titanium alloys, our knowledge of the actual modes of hydride precipitation, hence the reason for the observed effects, is still lacking.

EXPERIMENTAL PROCEDURE

Materials Used

Titanium metal used in the present investigation was supplied by the Bureau of Mines. It was electrorefined and had a Brinell hardness of 69. The following percentages of impurities were indicated by Bureau of Mines.

Fe	<0.02	Si	0.011	Ni	0.008	O ₂	0.051
Cr	<0.005	Mn	0.03	C	0.005	H ₂	0.014
Mg	0.002	Cu	<0.005	Cl ₂	0.01		
Na	<0.005	Al	<0.04	V	<0.005		

Specimens of iodide titanium purchased from Foote Mineral Co. were used for comparison although alloys were prepared with Bureau of Mines titanium. Vacuum fusion analyses in this laboratory showed the following oxygen, hydrogen and nitrogen contents:

Iodide Ti (Foote)	O ₂ 0.038%	H ₂ 0.010%	N ₂ 0.003%
Bureau of Mines Ti	O ₂ 0.018%	H ₂ 0.001%	N ₂ 0.001%

Elements used for making Ti-alloys were obtained from Alcoa Research Laboratory (Al); Electro Metallurgical Co. (V); and this laboratory (hafnium-free zirconium and electrolytic Ta). The oxygen and hydrogen contents of these materials were very low, below 0.010%. Tank hydrogen was used in this investigation. According to the supplier, it is 99.8 + % pure with a maximum oxygen content of 10 ppm and moisture content of 0.01 milligrams per liter. This hydrogen was further purified by a de-oxygen device and passed through a drying train and heated titanium chips before being introduced into the specimens. Table I lists the nominal composition of the alloys used and their respective axial ratios.

Preparation of Specimens

Alloys of the desired compositions were prepared by the melting of weighed constituents in a nonconsumable electrode arc-melting furnace using argon as a protective atmosphere. The alloys melted into 25-gram buttons, were remelted at least six times. After each melting the button was turned over and remelted to achieve homogeneity as evidenced by subsequent metallographic examination.

These alloys were then rolled flat and sliced in preparation for a strain annealing treatment. For ease in operation, compression by cold

Table II
Grain-coarsening Schedule for α -Ti and α -Ti Alloys Investigated¹

Nominal Composition	Preliminary Annealing	Av. Starting Grain Size, mm	Final Grain Coarsening Anneal	Average Resulting Grain Size, mm
Iodide Ti	3.5 hrs. at 1580°F	0.08	90 hrs. at 1598°F	1.2
B ₂ of M, Ti	4 hrs. at 1598°F	0.31	120 hrs. at 1607°F	2 to 3
Ti 3% Al	5 hrs. at 1607°F	0.09	144 hrs. at 1607°F	0.6 to 1.6
Ti 10% Zr	4.5 hrs. at 1592°F	0.07	120 hrs. at 1500°F	0.4 to 1
Ti 3% Ta	4.6 hrs. at 1547°F	0.114	120 hrs. at 1563°F	0.6 to 1.3
Ti 2% V	3 hrs. at 1563°F	0.08	96 hrs. at 1382°F	1.3
	+2 hrs. at 1202°F	to 0.12		

¹A 1% compression by rolling was used as the critical straining in each case.

²For Ti-2% Al, the strain-annealing cycle was repeated four times; the final starting grain size was 0.4 to 0.6 mm.
 For Ti-16% Zr, the strain-annealing cycle was repeated three times; the final starting grain size was 0.2 to 0.5 mm.
 For Ti-5% Ta, the strain-annealing cycle was repeated four times; the final starting grain size was 0.5 to 0.6 mm.

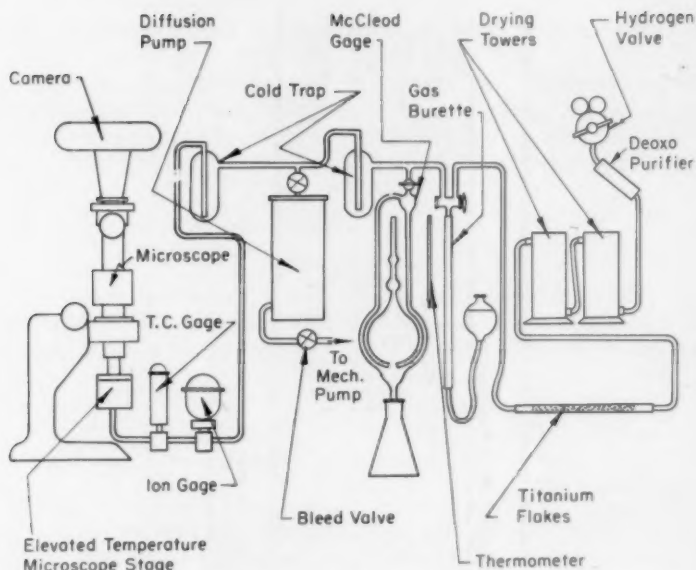


Fig. 1—Schematic Diagram of Modified Sieverts' Apparatus.

rolling was used for critical straining. Since a coarse-grained specimen with a grain size of about 1 millimeter was satisfactory for the present investigation, no attempt was made to investigate the various possibilities of growing single crystals of alpha titanium alloys. In the case of pure titanium, single crystal flakes obtained by fused salt electrolysis in our laboratory were used in conjunction with coarse-grained polycrystalline specimens. The schedules used for grain coarsening of various specimens are given in Table II.

After the optimum grain sizes were reached, the specimens were cut into desired size and shape, chemically etched and electrolytically polished. For hydrogenation in the Sieverts' apparatus, the specimens were weighed before being put into the high temperature microscope stage and furnace.

Hydrogenation Treatment

Two methods of introducing hydrogen into the specimens were used. The first one utilized a modified Sieverts' gas absorption apparatus with an elevated temperature microscope stage incorporated into the system. Fig. 1 is a schematic drawing of the Sieverts' apparatus together with the hydrogen purifying train and the elevated temperature microscope stage (17). Fig. 2 shows a general view of the stage with microscope with recording camera in place.



Fig. 2—Photograph Showing General View of Stage with Microscope and Recording Camera in Place.

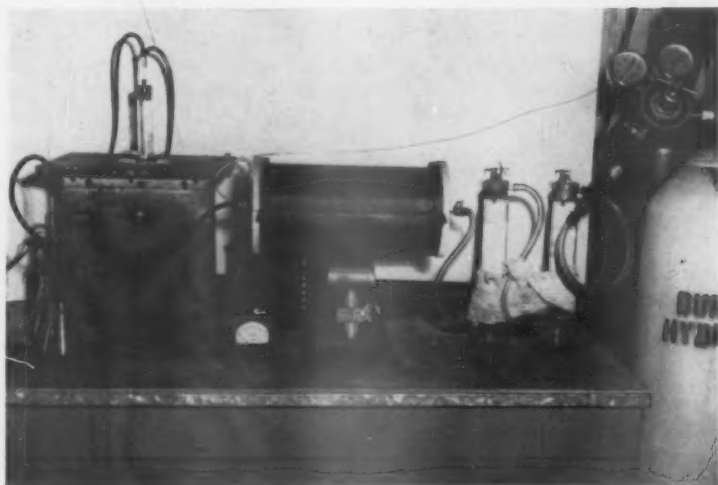


Fig. 3—Photograph of System for Saturation of Titanium with Purified Hydrogen—Continuous Flow.

After the specimens were heated to 1328 °F, a measured amount of dry and purified hydrogen was admitted into the evacuated system. The actual amount of hydrogen absorbed was calculated from the initial and final pressures of the run and the calibrated volume of the apparatus.

The second method of admitting hydrogen into a specimen was to saturate it with a continuous flow of purified hydrogen. In this method, the amount of hydrogen in the resulting specimen was determined by vacuum fusion analysis. Fig. 3 shows a schematic view of the apparatus for these experiments. It was found that using this arrangement, a temperature of 662 to 752 °F followed by furnace cooling in hydrogen was sufficient to cause large sized hydride formation.

Stereographic Analyses

Specimens after hydride formation were examined under the microscope. Although in some cases the hydrides showed up without etching, normally, a supplementary etching brought out the hydride formation more clearly. It was found that a two-step etching procedure yielded best results:

First etch:	2 parts HNO ₃ by vol. 1 part HF 2 parts glycerine	} Modified Remington A Etchant
Second etch:	80 cc H ₂ O 2 cc HF 2 cc HNO ₃	

For the two-surface method of determining the plane of precipitation in the matrix, a grain that straddles two polished surfaces intersecting at a known angle, containing large hydrides, and of sufficient size to be x-rayed, is needed. For this reason, a large number of specimens had to be inspected before one single usable grain was found. Stereographic projection of the planes responsible for the hydride traces were then superimposed on the stereographic projection of the grain being studied. The orientation of the grain was obtained by Laue back-reflection methods. The indices of the hydride plates in terms of the matrix orientation were then determined.

A geometrical consideration of the planes of precipitation was then made to establish possible planes and directions of precipitation of the hydride phase.

EXPERIMENTAL RESULTS

Unalloyed Titanium

Single crystal titanium flakes, produced in our laboratory by fused-salt electrolysis, range in size from ¼ to over 4 inches long and a few mils thick. Fig. 4 is a macroscopic view of these crystals. Various types of line markings were observed. While the majority of these markings

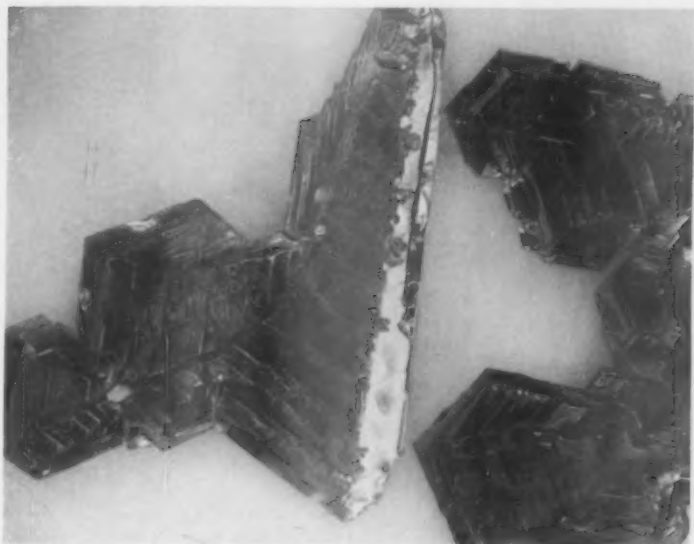


Fig. 4—Macroscopic View of Ti Single Crystals Obtained by Fused Salt Electrolysis.

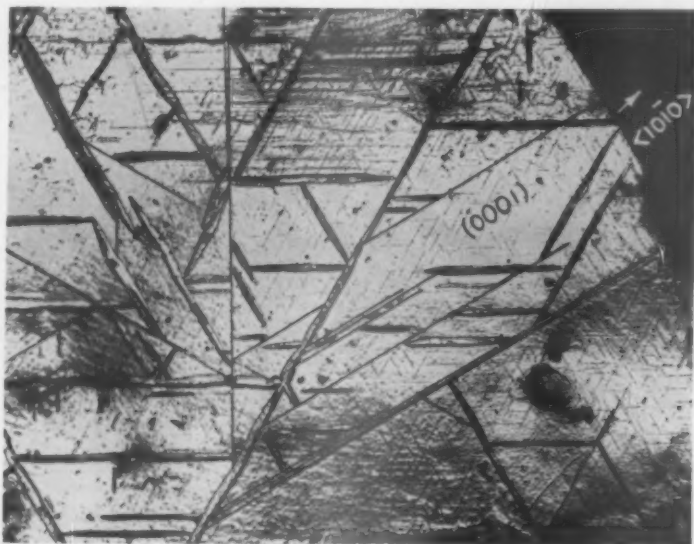


Fig. 5—Twins and Hydride Line Markings on Electrolytically Deposited Ti Crystal Flakes. Etchant: Remington A.

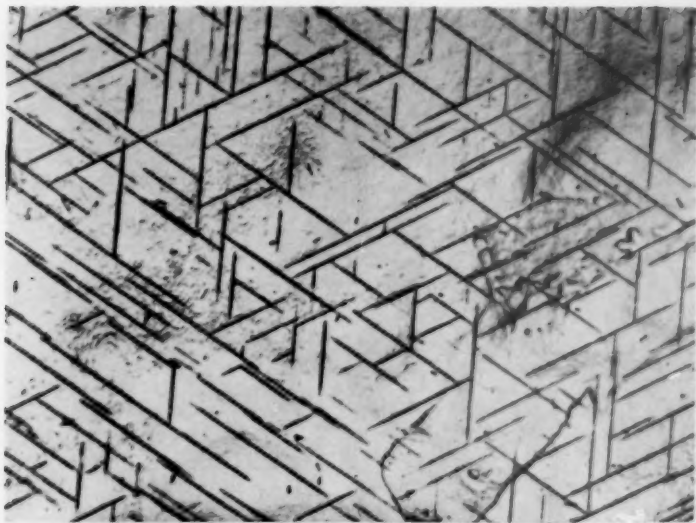


Fig. 6—Hydride Lines Produced by Hydrogenation of High Purity Ti Crystals. Etchant: Remington A followed by etchant B.

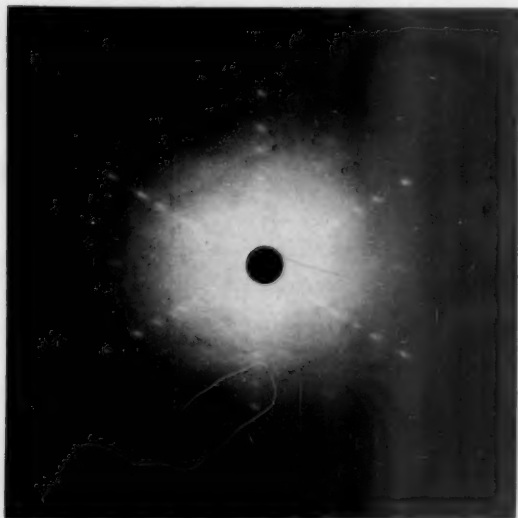


Fig. 7—Laue Back Reflection Pattern of Ti Single Crystal Flakes Taken Perpendicular to the Flat Surface.

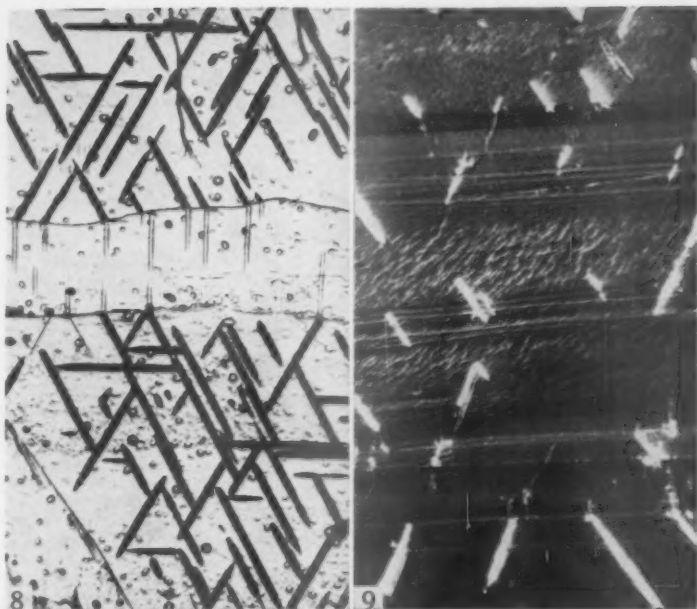


Fig. 8—Enlarged View of Hydrides in (0001) Plane of Titanium Crystal with (1012) Twin Plane Transverse Photograph (Note Hydride Direction Change from Matrix Through Twin as Well as a Second Type of Hydride in Twin). Also hydrides present were formed from residual hydrogen in the titanium and hydrogen pickup in acid treatment. Etchant: Remington A.

Fig. 9—Interaction of Hydride Needles with Twin Traces, After Hydrogenation Treatment and Slow Cooling (Note that Some Hydrides Cross Twins Without Direction Change While Others Have Abrupt Direction Changes Across Twins). (Polarized light). Etchant: Remington A followed by etchant B.

were twins, as characterized by their shape and finite width, there is a second group of needle-like, usually short, line markings. By vacuum fusion analysis, it was found that there is 0.02% hydrogen in the crystal flakes which show these short markings.

To confirm that these short line markings are due to hydride, and hydride alone, several crystal flakes—which showed no short line markings whatsoever and have extremely low hydrogen content—were subjected to a hydriding treatment at temperatures above 572 °F. It was found that these markings can be duplicated after a hydriding treatment at as low as 572 °F. Fig. 5 shows line markings and twins as they appeared on titanium crystal flakes obtained by electrolytic deposition. Fig. 6 indicates these hydride lines produced after hydriding a low hydrogen crystal flake. The similarity of the fine line markings in both cases is clearly noticed. It is thus evident that these fine line markings are due to hydride precipitations.

The crystal flakes so produced were found to be single crystals with

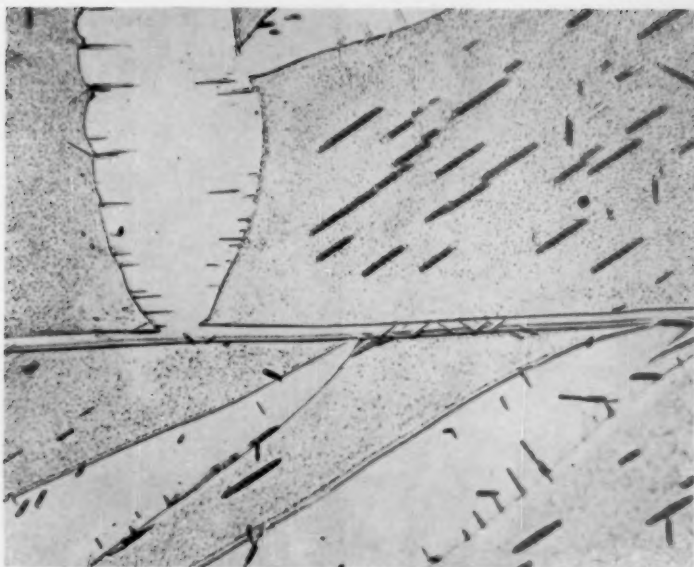


Fig. 10—Hydride Markings on the Basal Plane and Within the Broad ($10\bar{1}2$) and Narrow ($11\bar{2}1$) Twins. Etchant: Remington A and etchant B.

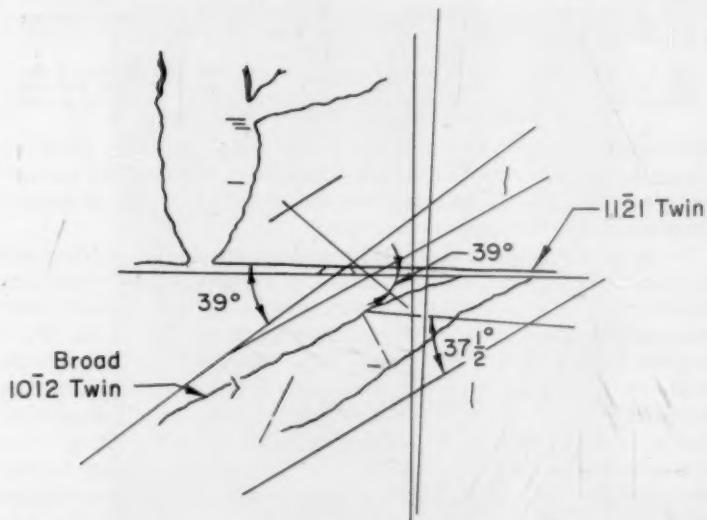


Fig. 11—Tracing of Twins and Hydrides in Photomicrograph of Fig. 10 with the Directions of Hydride Needles.

(0001) basal planes parallel to the flat surfaces, as determined by Laue back-reflection technique and reported elsewhere (14) (Fig. 7). It is interesting to note that the hydride line markings arrange themselves into a definite geometric fashion. They made perfect 60-degree angles with each other as shown in Fig. 8. In this photomicrograph it is also noticed that twin traces and the hydride markings are easily distinguishable.

It is also to be noted that in some cases where the hydride markings meet a twin on the basal plane, there is a definite and abrupt change of the direction of the markings, while in others they cross without any change in direction (see Fig. 9). This indicates that there are at least two different sets of habit planes.

In Fig. 10 the broad twins are identified by the two-surface method as $(10\bar{1}2)$ twins, and the narrow twin running across the picture is a $(11\bar{2}1)$ twin. The close parallelism of the hydride markings to the broad $(10\bar{1}2)$ twins suggests that the habit planes are of the type $(10\bar{1}n)$.

To determine the indices n , use was made of the known angle between the twinned portion of the crystal and that of the matrix, and the measured angle between the hydride markings and the twin boundaries (Fig. 11). From the analyses based on both the $(10\bar{1}2)$ twin traces and the $(11\bar{2}1)$ twin traces on all the crystals examined, stereographic plotting of the data indicates that the two families of habit planes are $(10\bar{1}0)$ and $(10\bar{1}1)$, (Figs. 12 and 13). Fig. 18 is an edge view of one of the crystal flakes. This was taken on a plane closely parallel to a $(11\bar{2}0)$ prism plane. Here the hydride markings run across the twins without any noticeable change in their directions, indicating a prismatic mode of precipitation.

Alpha Titanium Alloys

Generally speaking, under the present experimental conditions, which were made favorable for the growth of the hydrides, the appearance of the hydrides in the alpha titanium alloys studied were similar to those observed in the unalloyed titanium. They all appeared as sharp, thin needles. Fig. 19 shows hydride needles in an unalloyed polycrystalline titanium. This is to be compared with the hydride needles in Ti-3% Al (Fig. 26); Ti-3% Ta (Fig. 23); Ti-10% Zr (Fig. 20); and Ti-2% V (Fig. 21). It was observed that in most cases, the hydride precipitation took place along slip lines and twin traces where the surface energy was higher than in the surrounding matrix.

Ti-10% Zr Alloy—The general appearance of the hydride needles is shown in Fig. 20. The alloy has a network of retained beta throughout the specimen although this did not appear on the surface. Controlled furnace cooling at 50 °F per hour from the all beta range did not elim-

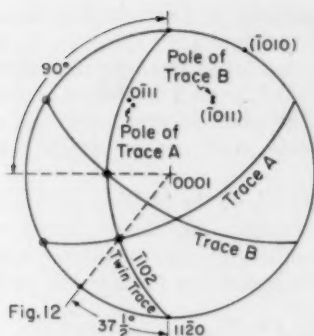


Fig. 12

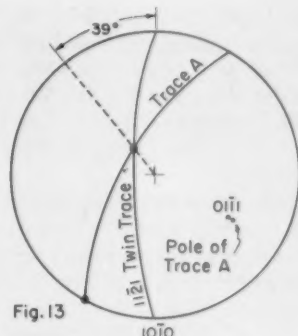


Fig. 13

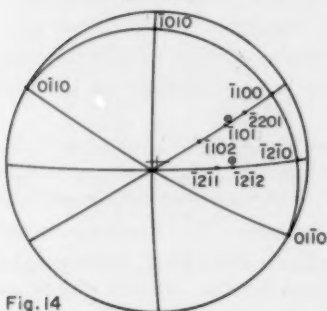


Fig. 14

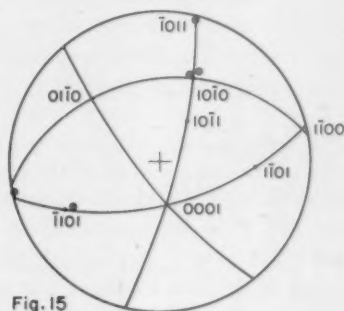


Fig. 15

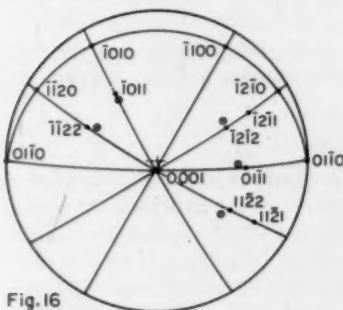


Fig. 16

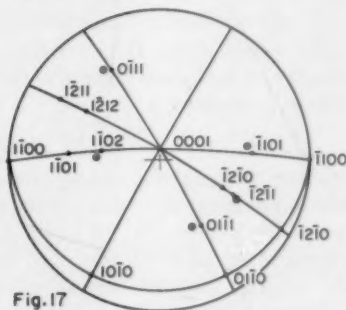


Fig. 17

Fig. 12— $10\bar{1}1$ and $10\bar{1}0$ Type Habit Planes Derived from Basal Plane and $10\bar{1}2$ Twin Traces.

Fig. 13— $10\bar{1}1$ Type Habit Planes Determined from Basal Plane and $11\bar{2}1$ Twin Traces.

Fig. 14—Orientation of a Ti-10% Zr Grain with Poles Responsible for Hydride Traces Superimposed.

Fig. 15—Orientation of a Ti-2% V Grain with Poles Responsible for Hydride Traces Superimposed.

Fig. 16—Orientation of a Ti-3% Ta Grain with Poles Responsible for Hydride Traces Superimposed.

Fig. 17—Orientation of a Ti-3% Al Grain with Poles Responsible for Hydride Traces Superimposed.

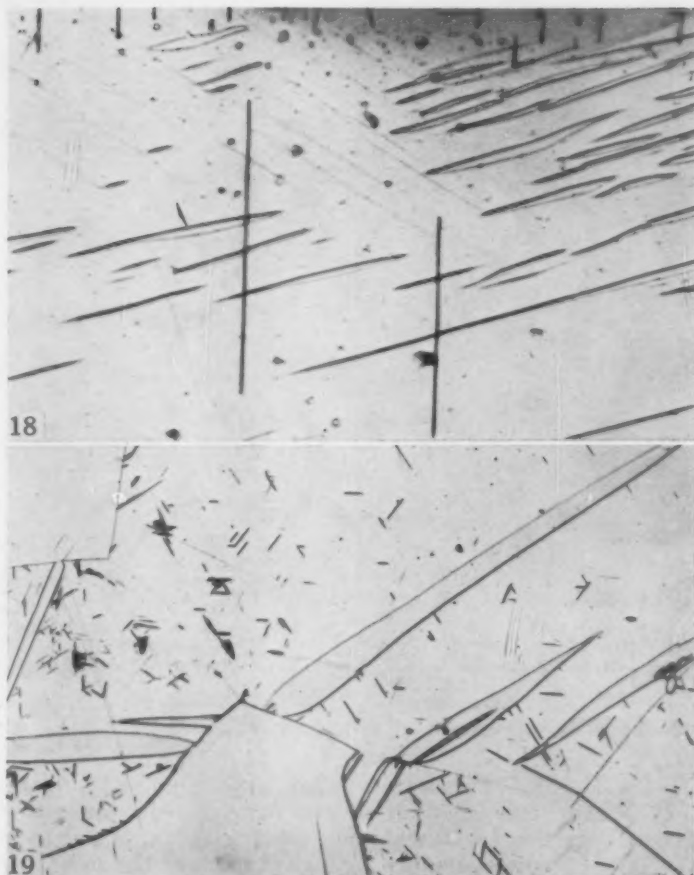


Fig. 18—Edge View of Hydride Precipitation In Unalloyed Titanium. Etchant: Remington A and etchant B.

Fig. 19—Photomicrograph of Polycrystalline Ti After Hydrogenation and Slow Cooling. Etchant: Remington A and etchant B.

inate this network. It was also observed that under identical conditions of introducing hydrogen, there were fewer hydride formations than in the other alloys examined. Due to this fact and the stringent requirements imposed by the two-surface method, some fifteen grains were selected from a large number of specimens for studying. Fig. 14 shows a typical stereographic projection of a grain studied and of the hydride habit planes therein. The data indicated that the habit planes of the

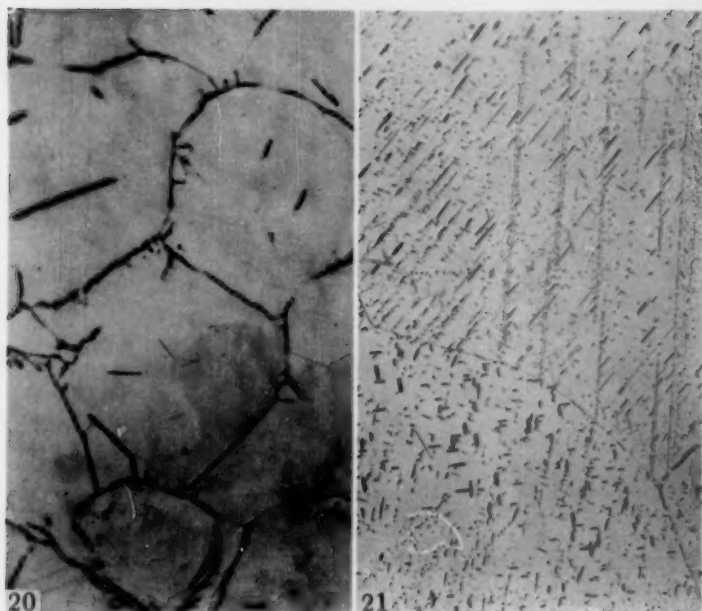


Fig. 20—Large-Grained Ti-10% Zr Alloy After Heat Treatment (See Table II) and Hydrogenation (β Phase Also Present). Etchant: Remington A and etchant B.

Fig. 21—Hydride Precipitation in Ti-2% V Alloy. Etchant: Remington A and etchant B.

hydrides in this particular alloy were represented by $(10\bar{1}1)$ and $(11\bar{2}2)$.

Ti-2% V—Fig. 21 shows the general appearance of hydrides in Ti-2% V alloy. This particular specimen was prepared in the modified Sieverts' apparatus. Due to the limited working distance of high power microscope objectives, a rather small sized specimen had to be used. This reduced the chance of finding suitable usable grains considerably. In addition, the thermal etching of the hydrides as they formed were not satisfactory for observation. For these reasons, the modified Sieverts' apparatus was used only for introducing predetermined amounts of hydrogen into the specimens. Fig. 22 shows the direction of the hydride precipitation in one of the grains investigated. Stereographic projection of the planes responsible for these traces together with the orientation of the grain as determined by back-reflection Laue method is shown in Fig. 15. The data indicate that the habit planes are of the type $(10\bar{1}0)$ and $(10\bar{1}1)$.

Ti-3% Ta—The appearance of hydrides in Ti-3% Ta alloy is shown in Fig. 23. The appearance of the hydrides are not evident until after

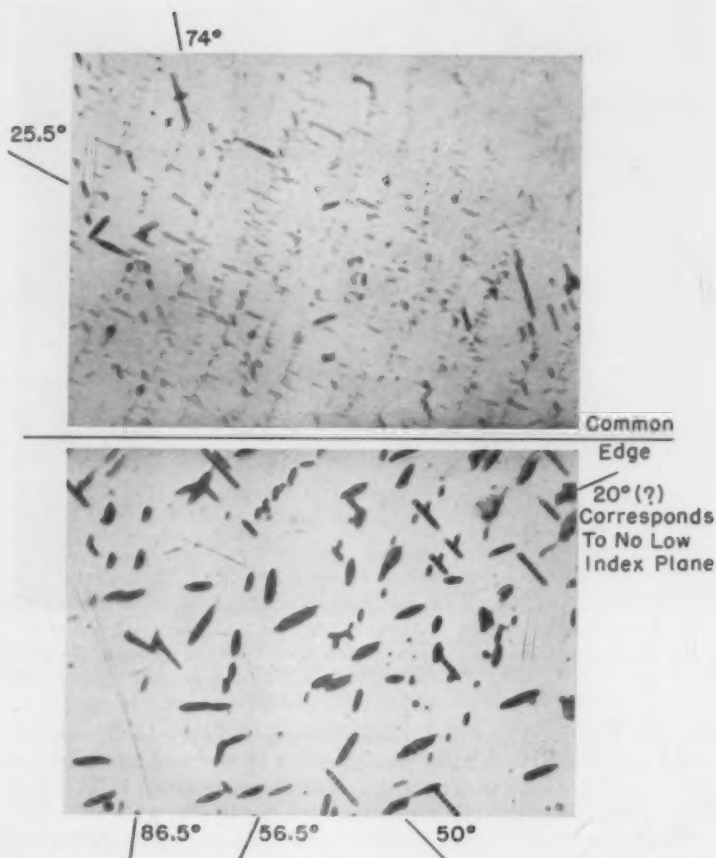


Fig. 22—Hydride Needles on the Face and Edge of a Ti-2% V Grain. Etchant: Remington A and etchant B.

etching. Similar etching applied to specimens prior to hydrogen treatment failed to bring out these needles. Thus the possibility that these needles were caused by etching was ruled out.

Fig. 16 shows the stereographic projection of a typical grain together with the projections of the planes responsible for the traces on two mutually perpendicular surfaces. The habit planes were found to be $(10\bar{1}1)$, $(11\bar{2}1)$, and $(11\bar{2}2)$.

Ti-3% Al—This alloy when treated in hydrogen exhibits superficial films and markings which are sometimes misleading. Fig. 24 shows one type of such markings observed. Another type which occurs is

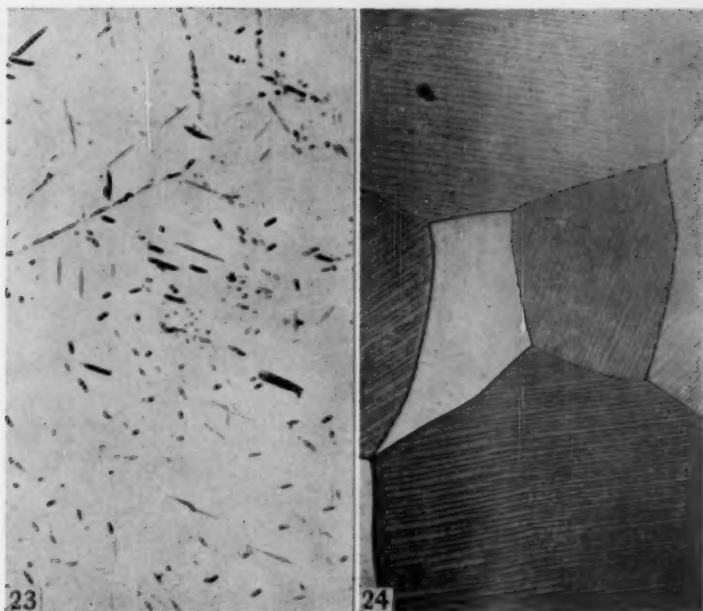


Fig. 23—Hydride Precipitation in Ti-3% Al. Etchant: Remington A and etchant B.

Fig. 24—Surface Appearance of Ti-3% Al Alloy After Treated in Hydrogen (200 ppm H_2). Etched before treatment.

shown in Fig. 25. These films caused a marked change in the response of the specimen to various etchants, but can be removed by electrolytic polishing. After such treatment, the hydride precipitation in Ti-3% Al alloy showed up as short, thin needles, as shown in Fig. 26.

Stereographic projection of typical grains investigated together with the planes responsible for the hydride traces are shown in Fig. 17. The habit planes for hydride precipitation in Ti-3% Al alloy are of the type $(10\bar{1}1)$, $(11\bar{2}1)$ and $(10\bar{1}2)$.

DISCUSSION

Although at 572 °F the solubility of hydrogen in alpha titanium is about 8 atomic % (0.20 wt. %), Craighead, Lenning and Jaffee (15) indicated that the room temperature solubility is less than 0.14 atomic %, and the hydride precipitation cannot be suppressed by fast quenching. From a consideration of the crystal structures of the constituents involved, as will be shown shortly, there seems to be too large a strain for the matrix to sustain without the hydride phase precipitating out.

Alpha titanium is C.P.H. with $a_0 = 2.950$ and $c_0 = 4.683$ A. U. (3).

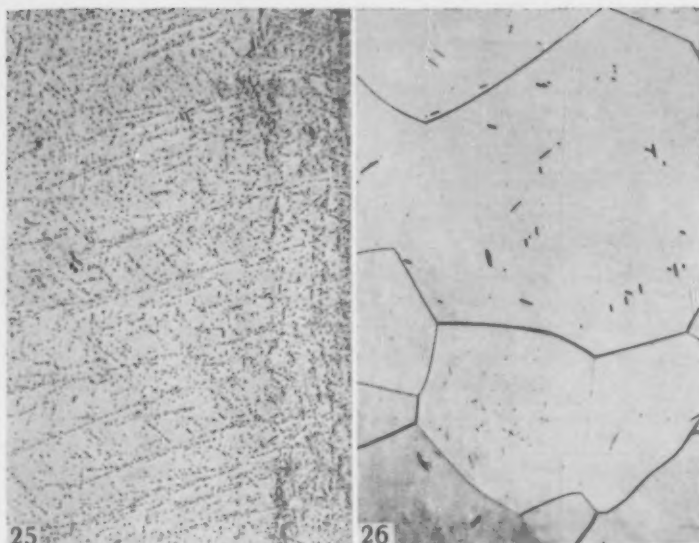


Fig. 25—Surface Appearance of Ti-3% Al Alloy After Treatment in Hydrogen. Un-etched after treatment.

Fig. 26—Appearance of Hydride Precipitation of Above Specimen After Electrolytic Polishing and Etching. Etchant: Remington A followed by etchant B.

The latest information on the crystal structure of the γ phase in the Ti-H system is that obtained by Jaffe (4). By neutron diffraction, the γ -phase structure obtained can be regarded either as B.C.T. with $a_0 = 3.12 \text{ \AA}$, $c_0 = 4.18 \text{ \AA}$, and $c/a = 1.34$ or F.C.T. with $a_0 = 4.42 \text{ \AA}$, $c_0 = 4.18 \text{ \AA}$, and $c/a = 0.946$.

Due to the small size of the hydride precipitates obtainable and the low atomic scattering powers of titanium and hydrogen, it is difficult to establish the lattice orientation relationship between the matrix and the precipitate by diffraction methods. However, from the knowledge of the habit planes obtained optically and a consideration of the lattice types and dimensions, the following are two possible lattice orientation relations between α -Ti and TiH precipitates:

$$\begin{Bmatrix} (10\bar{1}0)_{\alpha\text{Ti}} \\ [\bar{1}2\bar{1}0]_{\alpha\text{Ti}} \end{Bmatrix} \parallel \begin{Bmatrix} (101)_{\text{TiH, F.C.T.}} \\ [011]_{\text{TiH, F.C.T.}} \end{Bmatrix} \quad \text{I}$$

$$\begin{Bmatrix} (10\bar{1}1)_{\alpha\text{Ti}} \\ [\bar{1}2\bar{1}0]_{\alpha\text{Ti}} \end{Bmatrix} \parallel \begin{Bmatrix} (101)_{\text{TiH, B.C.T.}} \\ [100]_{\text{TiH, B.C.T.}} \end{Bmatrix} \quad \text{II}$$

This is shown schematically in Figs. 27a and 27b. It is to be noted that, while in both cases the discrepancy in the habit planes are less than

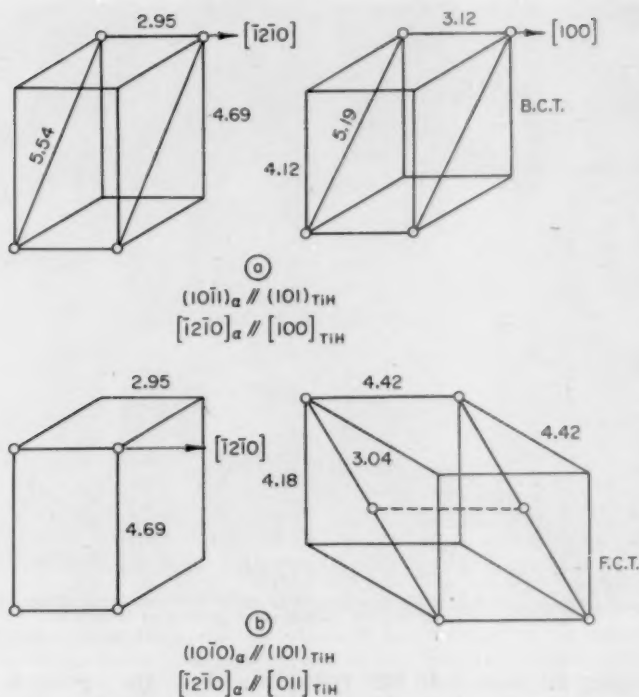


Fig. 27a and 27b—Postulated Lattice Orientation Relations Between Alpha Titanium and TiH Precipitates.

6%, to accommodate the TiH phase in a direction perpendicular to the habit plane would require an expansion of the matrix of some 12% in that direction in the case of $(10\bar{1}1)$ pyramidal type habit planes, and up to 17.9% for $(10\bar{1}0)$ prismatic type habit planes. This can well be the reason that no hydride precipitation can be suppressed by quenching.

It is noticed that the two habit planes for hydride precipitation fall on two of the three possible slip planes for titanium at room temperature. This could conceivably contribute to a shortened nucleation period for the slip process. While in static tests such shortening of the nucleation time does not affect the resultant behavior, the effect would be most noticeable in short duration tests such as impact testing.

Summarizing the results on the habit planes of hydride precipitation, as shown in Table III, it is noticed that in the alpha titanium alloys studied, there is a common habit plane $(10\bar{1}1)$. Since hydride precipitation in a binary titanium alloy involves a ternary system, it is not clear

Table III
Habit Planes of Hydride Precipitation

Alloy	Habit Planes
Ti-10% Zr	(10 $\bar{1}$ 1) (11 $\bar{2}$ 2)
Ti-2% V	(10 $\bar{1}$ 0) (10 $\bar{1}$ 1)
Ti	(10 $\bar{1}$ 0) (10 $\bar{1}$ 1)
Ti-3% Ta	(10 $\bar{1}$ 1) (11 $\bar{2}$ 1) (11 $\bar{2}$ 2)
Ti-3% Al	(10 $\bar{1}$ 1) (11 $\bar{2}$ 1) (10 $\bar{1}$ 2)

whether the precipitated phase is identical in crystal structure and lattice dimension in each case. It is quite possible that (10 $\bar{1}$ 1) is a slip plane that is common to the alpha alloys studied.

According to Langeron and Lehr (5), hydride precipitation takes place along (10 $\bar{1}$ 0) planes in coarse grained zirconium. This corresponds to the slip plane in zirconium at room temperature. The lack of (10 $\bar{1}$ 0) habit planes in Ti-10% Zr alloy is noted. Since zirconium has a high affinity to hydrogen, it might be that the precipitated phase has such a crystal structure and lattice spacing that renders (10 $\bar{1}$ 0) planes in the matrix unfavorable for precipitation.

In studying the habit phenomenon in the martensitic transformation, Machlin and Cohen (16) used a sizeable single crystal Fe-Ni alloy and partially transformed it to martensite. In their case, a favorable condition for the observation of the precipitated phase, i.e., martensite plates, is achieved. To make accurate studies of the path of atom movement during the transformation, titanium specimens of comparable size are needed.

SUMMARIES AND CONCLUSIONS

1. Under favorable conditions of hydride precipitation and growth, the appearance of hydrides in unalloyed and alloyed (Ti-3% Al, Ti-3% Ta, Ti-2% V, and Ti-10% Zr) alpha titanium are basically the same—thin needles.

2. The precipitation tends to take place along slip lines, and twin markings, where the surface energies are higher than their surrounding areas.

3. The habit planes for hydride precipitation in unalloyed alpha titanium and Ti-2% V are of the (10 $\bar{1}$ 0) and {10 $\bar{1}$ 1} types.

4. The habit planes for hydride precipitation in Ti-10% Zr alloy are {10 $\bar{1}$ 1} and {11 $\bar{2}$ 2}.

5. The habit planes for hydride precipitation in Ti-3% Ta alloy are of the {10 $\bar{1}$ 1}, {11 $\bar{2}$ 1} and {11 $\bar{2}$ 2} types.

6. The habit planes for hydride precipitation in Ti-3% Al are of the {10 $\bar{1}$ 1}, {11 $\bar{2}$ 1} and {10 $\bar{1}$ 2} types.

7. Crystallographic relationships

$$\begin{aligned} & \left\{ \begin{array}{l} (10\bar{1}0)_{\alpha\text{Ti}} \parallel (101)_{\text{TiH, F.C.T.}} \\ [\bar{1}2\bar{1}0]_{\alpha\text{Ti}} \parallel [011]_{\text{TiH, F.C.T.}} \end{array} \right. \\ & \text{and} \\ & \left\{ \begin{array}{l} (10\bar{1}1)_{\alpha\text{Ti}} \parallel (101)_{\text{TiH, B.C.T.}} \\ [\bar{1}2\bar{1}0]_{\alpha\text{Ti}} \parallel [100]_{\text{TiH, B.C.T.}} \end{array} \right. \end{aligned}$$

were postulated from lattice type and habit plane considerations.

8. An explanation of impact brittleness caused by hydride precipitation was presented.

ACKNOWLEDGMENTS

This investigation was sponsored by the Office of Naval Research. The authors wish to thank the ONR-Metallurgy Branch staff for their continued interest and support of this investigation.

The authors express their appreciation to the following Horizons Incorporated personnel for their assistance in this research; R. Chill for his experimental aid in carrying out the hydrogenation and single crystal preparation work; W. Whitaker, x-ray diffraction; A. Burnside and R. Baskey, metallography; and A. DeRubeis, photography.

References

1. C. M. Craighead, G. A. Lenning and R. I. Jaffee, "Nature of the Line Markings in Titanium and Alpha Titanium Alloys," *Journal of Metals*, Vol. 4; *Transactions, American Institute of Mining and Metallurgical Engineers*, Vol. 194, 1952, p. 1317.
2. A. D. McQuillan, "An Experimental and Thermodynamic Investigation of the Hydrogen-Titanium System," *Proceedings of the Royal Society*, Vol. 204, 1950, p. 309-323.
3. A. D. McQuillan, "The Titanium-Hydrogen System for Magnesium-Reduced Titanium," *Journal, Institute of Metals*, Vol. 79, 1951, p. 371-378.
4. L. D. Jaffe, "Metallographic Identification and Crystal Symmetry of Titanium Hydride," *Transactions, American Institute of Mining and Metallurgical Engineers*, Vol. 206, 1956, p. 861.
5. J. P. Langeron and P. Lehr, "Preparation of Large Zirconium Crystals and Determination of the Orientation of the Zirconium Hydride Precipitates," *Comptes rendus*, Vol. 245, No. 2, 1956, p. 151-154.
6. E. S. Bumps, H. D. Kessler and M. Hansen, "Titanium-Aluminum System," *Transactions, American Society of Mining and Metallurgical Engineers*, Vol. 194, 1952, p. 609.
7. J. D. Fast, "The Transition-Point Diagram of the Zirconium-Titanium System," *Recueil des Travaux Chimiques des Pays-Bas*, Vol. 58, 1939, p. 973-983.
8. P. Duwez, "Allotropic Transformation in Titanium-Zirconium Alloys," *Journal, Institute of Metals*, Vol. 80, 1951, p. 525-527.
9. D. J. Maykuth, H. R. Ogden and R. I. Jaffee, "Titanium-Tungsten and Titanium, Tantalum Systems," *Transactions, American Institute of Mining and Metallurgical Engineers*, Vol. 197, 1953, p. 231-237.
10. H. K. Adenstedt, J. R. Peqnigot and J. M. Rayner, "The Titanium-Vanadium System," *TRANSACTIONS, American Society for Metals*, Vol. 44, 1952, p. 990-1003.
11. P. Pietrokowsky and P. Duwez, "Partial Titanium-Vanadium Phase Diagram," *Transactions, American Institute of Mining and Metallurgical Engineers*, Vol. 194, 1952, p. 627-630.

12. A. P. Young and C. M. Schwartz, "A Fundamental Investigation of Hydrogen Embrittlement in Zirconium," Battelle Memorial Institute Report No. 1100, Contract No. W-7405-eng.-92, July 27, 1956.
13. G. A. Lenning and R. I. Jaffee, "Effect of Hydrogen on the Properties of Titanium and Titanium Alloys," Battelle Memorial Institute, Titanium Metallurgical Laboratory, Report No. 27, Dec. 27, 1955.
14. T. S. Liu and M. A. Steinberg, "Deformation Mechanisms in Alpha Titanium," Discussion, *Transactions*, American Society for Mining and Metallurgical Engineers, Vol. 200, 1954, p. 697; *Journal of Metals*, May 1954.
15. G. A. Lenning, G. M. Craighead, and R. I. Jaffee, "Constitution and Mechanical Properties of Titanium-Hydrogen Alloys," *Transactions*, American Institute of Mining and Metallurgical Engineers, Vol. 200, 1954, p. 367; *Journal of Metals*, Vol. 6, No. 3, 1954.
16. E. S. Machlin and M. Cohen, "Habit Phenomenon in the Martensitic Transformation," *Transactions*, American Institute of Mining and Metallurgical Engineers, Vol. 191, 1951, p. 1019-1029.
17. R. E. Cech, "A High-Low Temperature Microscope Stage," *Review of Scientific Instruments*, Vol. 21, No. 8, August 1950, p. 747.

STRAIN HARDENING OF AUSTENITIC STAINLESS STEEL

By G. W. POWELL, E. R. MARSHALL AND W. A. BACKOFEN

Abstract

The strain-hardening characteristics of types 301 and 304 austenitic stainless steel have been studied as functions of temperature (20 to -263°C), strain rate (100-fold variation), and stress system (tension, torsion, and compression), and correlated with quantitative measurements of the progress of the martensitic transformation.

The stress-strain relationship is strongly dependent upon the stability of austenite with respect to transformation. Effects of the experimental variables are explained in terms of their influence upon austenite stability. At -263°C , tensile deformation is characterized by discontinuous yielding and multiple necking; such instability is attributed in large measure to localized softening caused by heat evolved in testing at temperatures where specific heat is low and flow stress is highly temperature-dependent. (ASM International Classification Q24M, LN8; SS-e)

INTRODUCTION

THE MECHANICAL behavior of austenitic stainless steel has long been the subject of extensive study. Much of the interest derives from the martensitic transformation of face-centered cubic austenite (γ) to body-centered cubic ferrite (α), or low-carbon martensite, that this material may undergo. Transformation tendencies have been shown to be influenced by a number of variables, including plastic strain (1-4)¹ and temperature of deformation (3,5-8) for steels of various analyses.

Fundamental relationships between the martensitic transformation and the nature of the applied stress have been investigated largely through studies concentrating on changes in the M_s temperature. Machlin and Cohen (9) demonstrated that the formation of a martensite plate in a 30 Ni-70 Fe alloy is associated with a shear strain of

¹ The figures appearing in parentheses pertain to the references appended to this paper.

A paper presented before the Thirty-Ninth Annual Convention of the Society, held in Chicago, November 4-8, 1957. Of the authors, G. W. Powell is associated with Nuclear Metals, Inc., Cambridge, Massachusetts, E. R. Marshall is Associate Professor of Civil Engineering, University of Vermont, Burlington, Vermont and W. A. Backofen is Assistant Professor of Metallurgy, Massachusetts Institute of Technology, Cambridge, Massachusetts. Manuscript received July 11, 1956.

0.2 in the habit plane and a simultaneous tensile strain of 0.05 normal to the habit plane. Subsequent experiments with a 0.5 C-20 Ni steel showed M_s to be raised by pure tension and compression in the elastic range, a tensile stress raising M_s more than a compressive stress of equal magnitude; triaxial and hydrostatic compression were found to lower M_s (10). Such findings were interpreted as showing that the formation of a martensite plate is aided by applied stress producing tensile strain normal to the habit plane in addition to shear strain in the habit plane.

Cina (11) has found that the nature of the applied stress can also exert considerable influence on the extent of martensite formation during plastic deformation. In a comparison of tensile and compressive deformation, it was found that for a given strain, tensile extension produces the greater amount of martensite.

Some investigations have also shown that strain rate can have a marked influence on the martensitic transformation. Specifically, less transformation has been observed to accompany higher strain rates (3,12,13), an effect attributed to the temperature rise in increasingly rapid deformation.

From the broad coverage of previous research, it is known that temperature, stress system, steel analysis, plastic strain, and strain rate have an influence on the γ to α transformation. With respect to the important variable of stress system, the more detailed body of information, well understood in terms of theory, applies to elastic behavior. It appears, however, that the attempt has not yet been made to relate the influence of such variables on the strength-producing martensitic transformation to the actual strain hardening characteristics described by stress-strain curves. Therefore, an exploration of this area, using austenitic stainless steels of the 18-8 variety as experimental materials, was made the objective of the present work.

MATERIALS AND PROCEDURES

Materials

Chemical analyses, lattice parameters of γ and α , M_s temperatures, grain size, and hardness values of the two steels in the annealed condition prior to testing are given in Table I. Type 301 was prepared as a 4-inch diameter vacuum-melted ingot which was then forged to $\frac{5}{8}$ -inch diameter rod. After a further 6-hour homogenizing anneal at 1065 °C (1950 °F), the rod was reduced by cold drawing to a diameter of 0.550 inch. Specimens were machined from the cold-drawn stock and then annealed for 7 minutes at 1065 °C (1950 °F). Type 304 was obtained from a commercial source as cold-finished $\frac{3}{4}$ -inch diameter rod from which specimens were machined and then annealed for 1 hour at 1065 °C (1950 °F).

Table I
Composition and Other Characteristics of the Steels

Steel	Composition, %					Lattice Parameters (Angstrom Units)		ASTM Grain Size	Measured M _s (°C)	Vickers Hardness
	C	Ni	Cr	Mn	P	Si	S			
301	0.053	7.91	18.11	—	—	—	—	3.590	2.872	150
304	0.055	10.62	18.05	1.86	0.02	0.52	0.013	3.591	2.872	160

Procedures

Tensile Testing: Standard ASTM specimens of 0.375-inch diameter were pulled at carefully controlled constant true-strain rates using an apparatus and technique that has been described elsewhere (14). Most tension tests were conducted at room temperature of approximately 20 °C (68 °F), -78 °C (-108 °F) (dry ice and acetone mixture), and -196 °C (-320 °F) (boiling liquid nitrogen). All room-temperature tests were made with the specimen immersed in water at 20 °C. The true-strain rates used were 6×10^{-3} , 60×10^{-3} , 180×10^{-3} , 300×10^{-3} , and 600×10^{-3} min.⁻¹. Some tests were made at -263 °C (-441 °F) employing low-temperature equipment, also described elsewhere (15).

To follow the progress of transformation, specimens were extended to different strains, all less than the necking strain, and sectioned to yield an approximately 1-inch long sample from the gage length of each. Then density was determined and the volume percentage of martensite calculated in the manner described below.

Torsion Testing: The maximum shear strain, γ , at the surface of a round bar of radius, a , is defined as $\gamma = a\theta$, where θ is the angle of twist in radians per unit length. The maximum shear stress, τ , corresponding to the maximum shear strain, γ , is obtained with the conventional graphical treatment of the plot relating torque and angle of twist per unit length (16).

Tests were made at shear-strain rates of 250×10^{-3} and 600×10^{-3} min.⁻¹. The maximum shear strain in uniaxial tension can be related at least approximately to the maximum tensile strain by (17)

$$\gamma = 3/2\epsilon \quad \text{Equation 1}$$

From Equation 1 the shear-strain rates given above are seen to be roughly equivalent to tensile strain rates of 167×10^{-3} and 400×10^{-3} min.⁻¹ and hence fall within the range of strain rates employed in the tension testing.

At 20 °C, both steels were twisted at the two strain rates. However, to avoid temperature changes in the strain-gage torque dynamometer, only the higher was used at -78 °C (-108 °F) and -196 °C (-320 °F). Specimens of 301 were twisted to various strains at 20 °C and sectioned to obtain samples for density determinations.

Compression Testing: The strain hardening of 301 in compression was studied with a 0.5-inch diameter specimen, 1-inch long, deformed at 20 °C and a true strain rate of approximately 60×10^{-3} min.⁻¹. The test was interrupted at a strain of 0.3 for remachining to prevent excessive barreling of the specimen. A colloidal suspension of molybdenum disulphide was used for lubrication in the specimen-platen interface. Additional specimens of 0.312-inch diameter and 0.75-inch

long were compressed to various strains for density determinations; approximately $\frac{1}{16}$ inch was turned from the ends of each after compression to remove any nonplastic cone that might have developed during the deformation.

Density Determinations for the Calculation of Percent Martensite:

Of the several techniques for determining volume fraction of martensite, that involving density measurements was chosen. The experimental procedure adopted was that described by Fletcher and Cohen (18), which was developed for essentially the same application that it found in the present work.

Assuming the lattice parameters required in the calculations to be known exactly, the accuracy of such a method for determining V_a , based on a reproducibility of the weighings of ± 0.1 milligram, is computed to be $\pm 1\%$ of martensite; by repeating the weighings after intervals of time, this was found to be a good estimate of accuracy. The error in the lattice parameters given in Table I is about 1 part in 3000. From the standpoint of comparison, however, only the weighing error is significant, as an error in lattice parameter is constant and common to all measurements, and therefore affects only the absolute value of V_a .

In specimens taken from the twisted bars, strain varied linearly from zero at the centerline to a maximum at the surface. Therefore, the volume fraction of martensite derived from the density of the entire sample, representing a wide range of strain and transformation, was only an average value, \bar{V}_a . A simple analysis of the data was carried out, however, which required only the assumption that, for given test conditions, the extent of transformation is a function of shear strain alone. By this analysis, V_a could be computed as a function of γ from the experimentally determined \bar{V}_a versus γ relationship.

EXPERIMENTAL RESULTS

Tensile Testing

True stress-strain curves of 304 and 301 at various constant true-strain rates and temperatures are shown in Figs. 1 and 2. Fig. 3 illustrates the variation of the uniform or necking strain, determined by Considere's construction (19), with test temperature for a strain rate of $60 \times 10^{-3} \text{ min.}^{-1}$. V_a as a function of strain for 304 at -196°C (-320°F) and 301 at 20°C and -196°C (-320°F) is presented in Fig. 4.

At -263°C (-441°F , 10°K) there is a radical change in the strain-hardening characteristics of both 301 and 304. Fig. 5 is a detailed plot with a considerably magnified strain scale of results obtained with annealed 301 which contained 28 volume percent of martensite directly after quenching to this temperature. The specimen after frac-

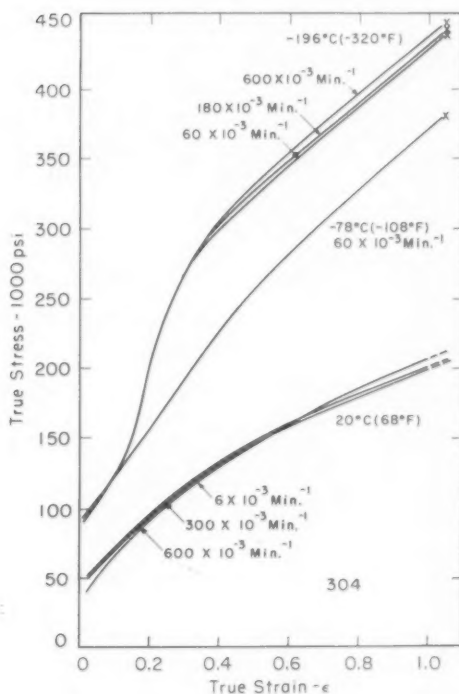


Fig. 1—True Stress-Strain Curves for Type 304 at 20°, -78°, and -196°C and Various Constant True-Strain Rates.

ture is shown in Fig. 6. Four shallow necks are found along the gage length with a true-strain difference between "peaks" and "valleys" of approximately 0.09. Such discontinuous and localized deformation has also been observed by Collins (20) in experiments with type 303 stainless steel over a range of very low temperatures. A tensile load-elongation plot of Uzhik (21) from a test at -253°C (-423°F) on a steel comparable to type 321 likewise shows some serrations. A tendency towards localized deformation at more than one section of the gage length in tests on types 302 and 347 stainless steel at liquid nitrogen temperature is indicated in data presented by Krivobok and Talbot (22).

Only the envelope of the stress maxima and minima at -263°C (-441°F) is given in Fig. 7 for annealed 304, and for 304 prestrained to $\epsilon = 0.4$ at room temperature; also included is a plot of V_a as a function of strain for the prestrained steel. No martensite is produced by cooling either the annealed or prestrained 304 to this temper-

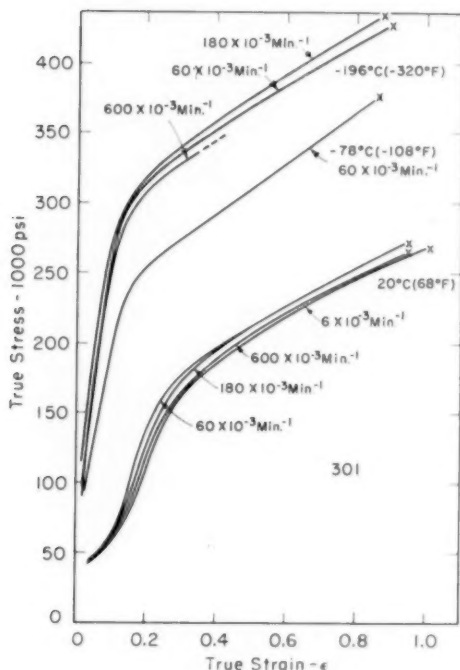


Fig. 2—True Stress-Strain Curves for Type 301 at 20°, -78°, and -196°C and Various Constant True-Strain Rates.

ature. The internal character of each envelope has all the features of the curve of 301 plotted in Fig. 5, and each steel exhibited the multiple necking.

Torsion Testing

Shear stress-strain curves of 304 and 301 tested in torsion at the different temperatures and rates are plotted with the continuous lines in Figs. 8 and 9. Also plotted in these figures with the broken lines are shear stress-strain curves derived from the true stress-strain tension curves of Figs. 1 and 2, established at the same temperatures and with roughly equivalent strain rates.

The primary purpose of this comparison was to illustrate any effect of stress system on the strain-hardening characteristics of 304 and 301. It was necessary, therefore, to select stress and strain terms fundamental to strain hardening in both tension and torsion. In austenitic stainless steel, structural instability in the form of the martensitic transformation is a major consideration in strain-hardening studies.

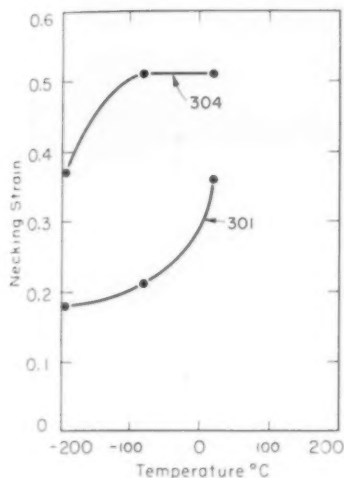


Fig. 3—Necking Strain as a Function of Test Temperature. $\dot{\epsilon} = 60 \times 10^{-4}$ minute $^{-1}$.

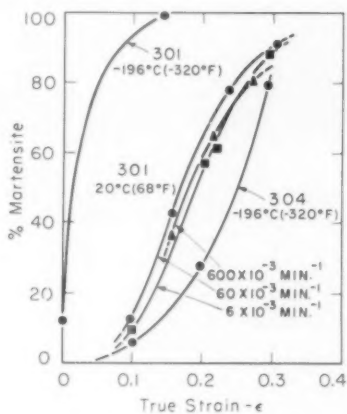


Fig. 4—Volume Percent Martensite Produced by Tensile Deformation. $\dot{\epsilon} = 60 \times 10^{-3}$ min. $^{-1}$ for 304 and 301 at -196°C .

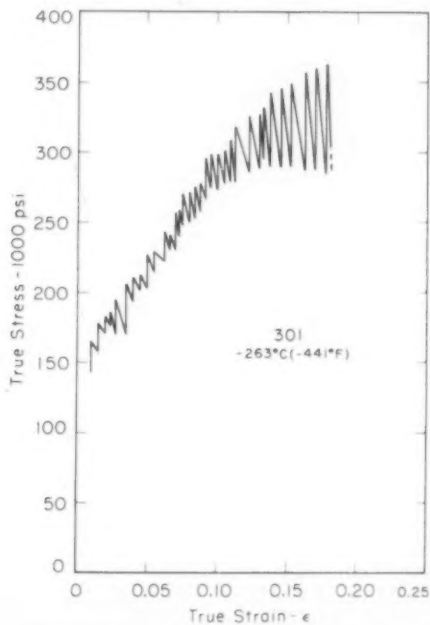


Fig. 5—True Stress-Strain Curve for 301 at -263°C . Approximately constant head-speed test.



Fig. 6—Tensile Specimen of 301 Fractured at -263°C After Multiple Necking. True strain difference between "peaks" and "valleys" of necks distant from fracture ≈ 0.09 .

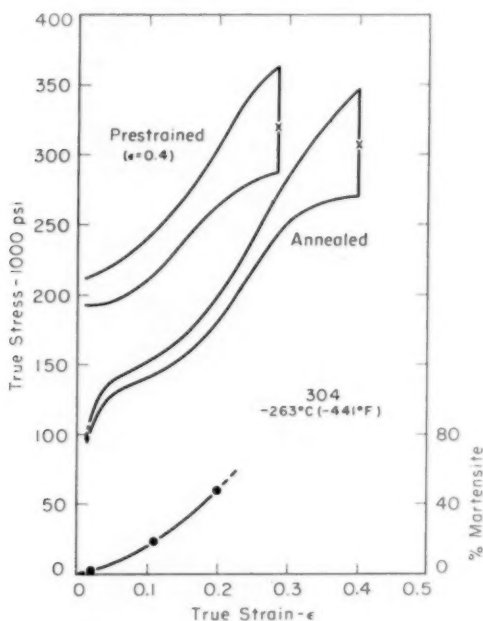


Fig. 7—True Stress-Strain Curves for Annealed and Prestrained 304 at -263°C ; Also Volume Percent Martensite as a Function of Strain for the Prestrained 304. Approximately constant head-speed tests.

Accordingly, there is an unusually important need for stress-strain terms that yield an essentially single-valued relationship under different stress systems in the absence of this instability.

A recent study (23) has shown that particularly good agreement between strain hardening in tension and torsion may be obtained with stable metals and alloys when maximum shear stress is plotted against

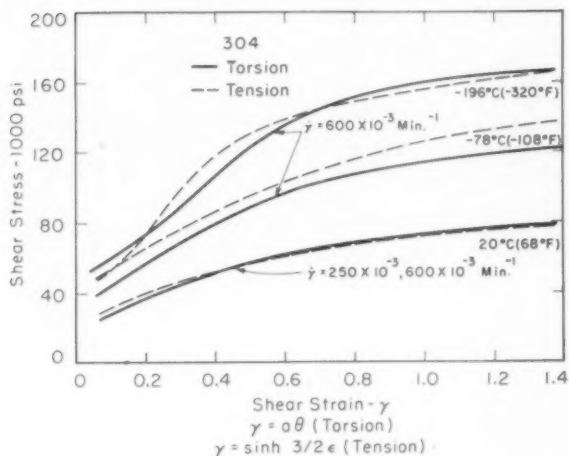


Fig. 8—Comparison of Strain Hardening in Torsion and Tension for 304 at Approximately Equivalent Strain Rates.

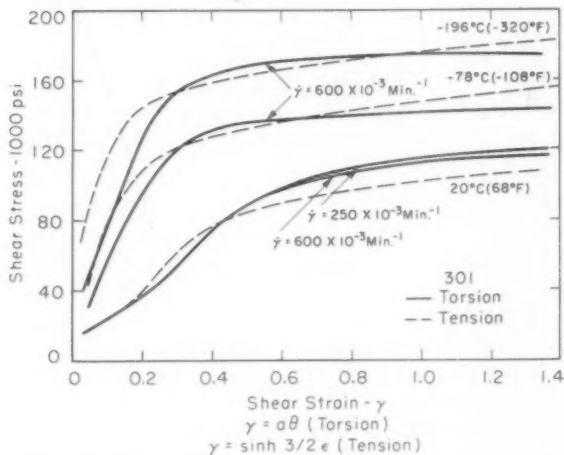


Fig. 9—Comparison of Strain Hardening in Torsion and Tension for 301 at Approximately Equivalent Strain Rates.

maximum finite shear strain. For torsion, the maximum shear stress and finite shear strain are the quantities determined in constructing a shear stress-strain curve. In tension, the maximum shear stress is simply one-half the conventionally determined, maximum true tensile

stress, while the rigorous definition of maximum finite shear strain in tension can be shown to be (23)

$$\gamma = \sinh 3/2\epsilon \quad (\text{tension}) \quad \text{Equation 2}$$

where ϵ is the conventionally determined maximum true tensile strain.

Before the tension-test data were replotted in Figs. 8 and 9, all stress values after necking were adjusted downward slightly with the Bridgman correction (24,25) to remove the strengthening effect of the

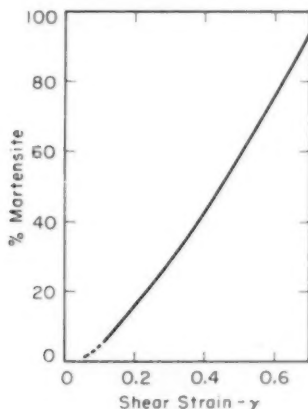


Fig. 10—Volume Percent Martensite Produced by Torsional Deformation of 301 at 20 °C. $\dot{\gamma} = 400 \times 10^{-3}$ minute⁻¹.

hydrostatic tension generated in the neck of a deforming test specimen. To apply the Bridgman stress-triaxiality correction, it is necessary to know the neck-profile radius. Such data were not obtained, however, so as a reasonable substitute, use was made of an empirical relationship between strain and the ratio of the radius at the minimum section to the neck-profile radius, established experimentally with many materials by Bridgman (24). The close agreement between shear stress-strain curves in tension (Bridgman-corrected) and torsion, for a structurally stable alloy, is illustrated in Fig. 8 by 304 at 20 °C.

Fig. 10 gives the V_a as a function of shear strain for the torsional deformation of 301 at 20 °C. No experimental points are shown as the curve was established with an empirical equation fitting the original plot of \bar{V}_a versus maximum (surface) shear strain, γ .

Compression Testing

Fig. 11 contains the true stress-strain curve in compression of 301 tested at 20 °C; for purposes of comparison, the tension curve at the

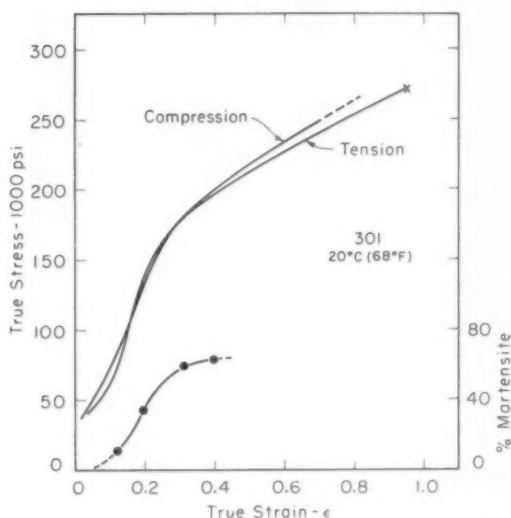


Fig. 11—Comparison of Strain Hardening in Compression and Tension for Type 301 at 20 °C and $\dot{\epsilon} = 60 \times 10^{-3}$ minute⁻¹; Also Volume Percent Martensite as a Function of Compressive Strain.

same temperature at $\dot{\epsilon} = 60 \times 10^{-3}$ min.⁻¹ is also included. The third plot relates V_a to true compressive strain.

DISCUSSION OF RESULTS

The strain-hardening characteristics of 304 and 301 described in detail by the various stress-strain curves are strongly dependent upon the stability of the austenite. The parabolic curve of 304 at 20 °C, when no martensite is formed, is characteristic of structurally stable ductile metals. Small amounts of martensite form in 304 at -78 °C (-108 °F) and are reflected by some departure from the parabolic course. As instability becomes pronounced, a concave-upward trend appears in the stress-strain curve following yielding. This is a prominent feature of the curves of 304 at -196 °C (-320 °F) and those of 301 at 20 °C, and should be compared with the corresponding percent martensite versus strain curves of Fig. 4. Angel (26) has fitted empirical equations to similar martensite versus strain curves and found the appropriate equations to be of the log-autocatalytic type. The stimulating effect which is evident in these curves at small strains probably has its origin in two phenomena: the autocatalytic nature of the martensitic transformation (27); and the increased rate of strain hardening due to prior martensite formation which has an indirect

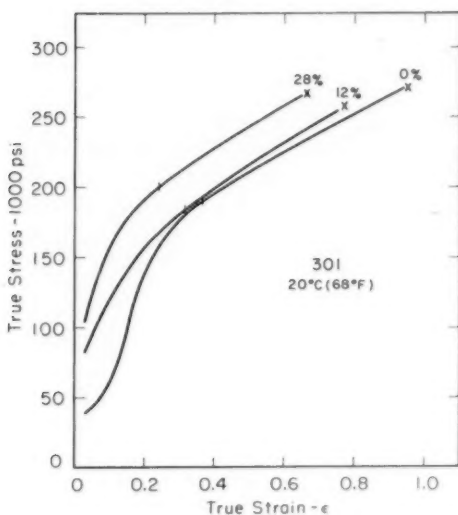


Fig. 12—Effect of Initial Martensite Contents of 0, 12, and 28 Volume Percent on the Strain Hardening of 301 at 20 °C. $\dot{\epsilon} = 60 \times 10^{-3}$ minute⁻¹. σ_0 of 12 and 28% produced by quenching in liquid nitrogen and liquid helium, respectively.

autocatalytic effect, serving to increase elastic strain about potential habit planes in the way which promotes martensite formation.

An important contribution to the initially rapid rise of stress with strain shown in Figs. 2 and 9 for 301 at -78°C (-108°F) and -196°C (-320°F) is considered to result from the martensite formed on cooling to test temperature. The effect of different initial amounts of martensite on strain hardening in 301 is illustrated in Fig. 12 which shows the flow stress to be greater for a given strain as the initial martensite content is increased. The contribution of martensite formation to strain hardening in general may be attributed to (a) a greater hardness of the transformation product (28) and (b) a subdivision of the microstructure by martensite plates which must be comparable in some measure to a decrease in grain size.

Data presented above also bring out the relationship between the onset of instability in a tension test specimen, or necking, and the progress of the martensitic transformation. At some strain, all curves but those for 304 at 20°C and -78°C (-108°F) exhibit a rather abrupt decrease in slope, which Figs. 3 and 4 show to correspond approximately to the necking strain and the strain at which the conversion to martensite is essentially completed.

Work by Geil and Carwile (29) established that the uniform elongation

gation or necking strain of copper, nickel, and two copper-nickel alloys increased with temperature down to -196°C (-320°F). Now, when lower temperatures lead to greater uniform elongation, the increase is explained by the higher, more persistent rate of strain hardening ($d\sigma/d\epsilon$) at the lower temperatures. As Fig. 3 illustrates, however, in the present work, uniform elongation was found to decrease with temperature of deformation. Although the introduction of martensite into the microstructure did act to maintain high levels of $d\sigma/d\epsilon$ during transformation, the saturation strain became less with lower temperatures, and accompanying saturation, the rate of strain hardening fell and necking began. If the austenitic steel could be extended in tension at progressively lower temperatures without the formation of martensite, uniform elongation could be expected to increase; data of Krivobok and Talbot (22) on several austenitic steels indicate such a trend. Consequently, it appears that martensite is responsible for the earlier onset of necking at lower temperatures. The different crystal structure of the martensite may be an explanation, as Geil and Carwile (30) and Smith, Spangler, and Brick (31) have observed the uniform elongation of ferrite to decrease with decreasing temperature.

As Figs. 1 and 8 show, the resistance to deformation of stable 304 at 20°C is only slightly affected by a hundredfold variation in strain rate. Strain-rate effects in an unstable austenitic stainless steel are illustrated in most detail by the data in Fig. 2 for 301 tested in tension at 20°C . An increase in strain rate from 6×10^{-3} to 60×10^{-3} min.^{-1} elevates the curve, and the percentage-wise elevation at small strains is rather large for a tenfold increase in rate; at a strain of 0.35, for example, the stress increase is 8% of the level corresponding to $\epsilon = 6 \times 10^{-3}$ min.^{-1} . The elevation is considered to result not only from the usual strain-rate effect, but also from an apparent stimulating effect of strain rate on the martensite transformation as shown in Fig. 4. The origin of the latter effect is likely the higher stresses and strain energy accompanying higher strain rates. Further increases in rate to 180×10^{-3} and 600×10^{-3} min.^{-1} reverse the trend, and the corresponding curves are displaced downward. A depression in the shear stress-strain curve of 301 at 20°C is also shown in Fig. 9 for the higher strain rate beyond $\gamma = 0.55$. Temperature rises with higher values of strain rate appear to be the logical explanation, for, even though room temperature tests were conducted with specimens immersed in water, temperature rises in the higher strain-rate tests were unavoidable; temperature measurements in a tension specimen tested at room temperature and $\epsilon = 180 \times 10^{-3}$ min.^{-1} showed a maximum rise of approximately 10°C . The effect of the temperature rise on the martensitic transformation is considered to be the principal cause of the depressed stress-strain curve, as such a temperature rise would be expected to have a relatively small effect on austenite flow stress. Fig. 4

shows that less martensite is formed at a given strain in the higher strain-rate tests when temperature rises must occur. At -196°C (-320°F), the curves of 304 are displaced in keeping with the common trend, and only the curve for 301 and $\dot{\epsilon} = 600 \times 10^{-3} \text{ min.}^{-1}$ is not consistent with that trend. The different strain-rate effect at -196°C (-320°F) would seem to be the result of superior heat transfer when a specimen is surrounded by boiling liquid nitrogen.

It is clear from Figs. 5 and 7 that at -263°C (-441°F) austenite instability is the most pronounced. Three specimens of 304, strained at this temperature and subsequently sectioned for density determinations, revealed the deformation pattern. After stretching $\frac{1}{16}$ inch, a region appeared at each end of the gage length, next to the shoulders, that was strained to $\epsilon = 0.10$, while the remainder of the gage length, from which the density sample was taken, was strained only to $\epsilon = 0.02$. With martensite formation contributing to the deformation, the localized strain adjacent to the shoulders is understandable as a consequence of a transformation-promoting hydrostatic tension imposed at that location by restraint from the larger shoulders. Upon stretching $\frac{1}{8}$ inch, the strain at the end of the gage length increased to $\epsilon = 0.16$ and diminished towards the center to a minimum again of 0.02 which now extended over only a very short distance. Deformation eventually became uniform after stretching $\frac{1}{4}$ inch, with regions of $\epsilon = 0.21$ alternating with those of $\epsilon = 0.18$. The final strain variation, $\Delta\epsilon$, along the fractured specimen, associated with the multiple necking, was approximately 0.06. Now, while approaching fracture, each sudden extension of the specimen resulted in a length increase, Δl , of about $\frac{1}{64}$ in. Therefore, by setting $\Delta\epsilon = \Delta l/l$, or $0.06 = 1/64l$, a value of $\frac{1}{4}$ inch is obtained for the length l over which an extension of $\frac{1}{64}$ inch would yield the strain of 0.06. Such a calculated gage length is found to be the average length (peak-to-peak) of the shallow necks as measured on the fractured specimen. Similar agreement was also obtained for the fractured 301 specimen. Therefore, each sudden length increase, at least nearing fracture, appears to be accompanied by the formation of a shallow neck.

A stress-strain curve containing some serrated regions resulting from the martensitic transformation in a 1.5C-12Cr steel tested in tension at room temperature has been published by Cohen (32). In the present work also, the martensitic transformation may well have contributed to the discontinuous extension. However, it is felt that another, and perhaps even more important, reason for the behavior at -263°C (-441°F) is a relatively strong temperature dependence of flow stress at the low temperature of testing. Such temperature dependence is indicated, for the case of aluminum, in work of Cottrell and Stokes (33) at temperatures down to that of liquid nitrogen. It is clearly illustrated in a forthcoming paper treating this low-temperature,

discontinuous yielding phenomenon in a variety of metals and alloys (34). At some point in the test specimen, the discrete nature of slip accompanied by martensite formation, coupled with a very low specific heat, results in a temperature rise. Since flow stress is highly temperature-dependent, load-carrying ability falls with localized deformation. The effect is transient, as elastic strain energy is drained out of the system under falling load, the temperature gradient disappears, and the resultant stress becomes less than the flow stress. Load must now build up until the next instability sets in. Since an over-all strengthening occurs with extension, load for subsequent yielding increases, the amount of elastic strain energy released becomes larger, the temperature rise proves greater, and the load drop grows as shown in Figs. 5 and 7. Such an explanation predicts that even structurally stable austenite, at low testing temperatures, will exhibit the behavior reported here for types 304 and 301.

That stress system influences the course of martensite formation during plastic straining is established by the curves of Fig. 13. The relationship between the curves, however, is not entirely what might be expected from previous work. Cina (11) obtained curves for tension and compression similar to these, although less widely separated. But there is no study involving torsional deformation for reference. Results of previous work have been generally interpreted in terms of strain rather than stress system, for it is the inter-relationship between strain associated with martensite formation and strain from applied loads that leads to the stress-system effect. These earlier studies have shown that the system of strain most tensile in character leads to most extensive transformation. Applied to the present work, such a finding suggests that the tension curve in Fig. 13 should be uppermost, as it is, with the torsion curve located between those for tension and compression. The latter arrangement is indicated at very small strains and is well defined after a strain of 0.34: in between, however, compression caused more transformation than torsion. Possibly some barrelling of the compression specimens, resulting in so-called secondary tensile stresses girdling the specimen, contributed to this situation.

It is now well established that over a wide range of plastic strain, tension stimulates the martensitic transformation to a greater extent than either torsion or compression. Therefore, when austenite is transforming, a comparison of stress-strain curves for tension and torsion, as in Figs. 8 and 9, should find the tension curve at a higher level, at least at small strains, because of the more extensive formation of the strength-producing martensite. As the microstructure approaches saturation with respect to martensite, they might then be expected to converge. On the whole, all 301 data and that for 304 at -196°C (-320°F) are consistent with such predictions. Furthermore, as the instability of the austenite increases with lower testing temperature

and complete conversion is approached at smaller strains, the range of strain over which the tension curve lies at a definitely higher level should decrease; and again this trend is found in the data. The curves for 304 at -78°C (-108°F) are difficult to explain without information like that in Figs. 4 and 10 for this particular temperature. At large strains, discussion of curve correlation is involved for several reasons. One is that the stress-correction for necking in tension was made with Bridgman's experimental curve, and this introduces some

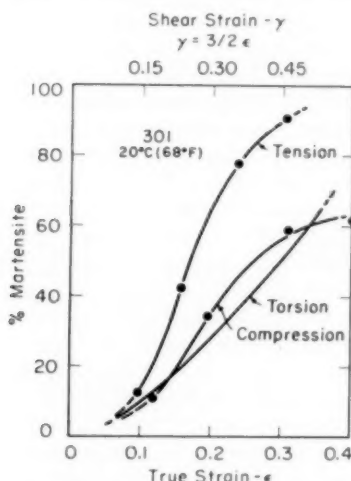


Fig. 13.—Volume Percent Martensite in Type 301 Produced by Tension, Torsion, and Compression at 20°C . Curves taken from Figs. 4, 10, and 11.

uncertainty. For another, the microstructures are approaching saturation, and transformation is occurring in rather heavily deformed austenite.

As an approximation, only elastic strains and attendant lattice distortion might be regarded as important to the production of martensite, even in plastically deformed austenite. However, deformation prior to transformation must also be considered since it has resulted in a small amount of the energy expended being stored up in the lattice to influence the activation energy for martensite formation. Also, and of special importance, the operating micromechanisms in untransformed but plastically deforming austenite result in partitioning and lattice disturbances which can impede transformation, reduce plate size, and influence the distribution of martensite that is eventually produced. These characteristics of the transformation product should influence strain-hardening characteristics, and to different extents depending

upon the degree of partitioning before transformation. Therefore when greater strain must be introduced by torsion to effect the same amount of transformation as in tension, the stress-strain curves as saturation is approached can still be expected to differ, as they do in Figs. 8 and 9.

The difficult comparison to rationalize is that involving tension and compression in Fig. 11. Little can be offered in way of explanation, considering the different transformation tendencies, except to note that specimen-platen interface friction can raise the compression curve artificially, and that many such comparisons in the past with stable materials have shown the compression curve to be the higher of the two.

It would, of course, be unwarranted to attempt an explanation of all curve details in terms of the transformation, for even though unstable austenitic steel is outstanding in the lack of correlation, similar correlations with stable materials are never exact.

SUMMARY AND CONCLUSIONS

The strain-hardening characteristics of types 301 and 304 austenitic stainless steel have been studied as functions of temperature, strain rate, and stress system, and correlated with the progress of the martensitic transformation. Relationships between extent of transformation and plastic strain under a number of test conditions were determined quantitatively through measurements of the density of deformed specimens.

It has been established that the shape of the stress-strain curve is strongly dependent upon the stability of the austenite. In the absence of any transformation, as in 304 deformed at room temperature, the stress-strain curve is of parabolic form. With increasing instability, marked decreases in the rate of strain hardening occur after some plastic strain. In general, the abrupt change in slope (a) occurred at smaller strains as austenite instability increased; (b) was accompanied by the terminal stage of transformation; and (c) corresponded approximately to the onset of necking in tension. Upon tension testing at -263°C (-441°F), both 301 and 304 exhibited multiple necking and discontinuous extension with serrated stress-strain curves from yielding to fracture. As an explanation, it is suggested that such instability is caused in large measure by localized softening from heat evolved in testing at a temperature where specific heat is low and flow stress is strongly temperature-dependent.

The effect of strain rate on the martensitic transformation was found to depend upon the magnitude of the rate. At 20°C , increasing strain rate from 6×10^{-3} to $60 \times 10^{-3} \text{ min.}^{-1}$ stimulated martensite formation, whereas further increases resulted in less transformation. The cause of the former effect is held to be the higher levels of stress and strain energy accompanying the higher rate, while the cause of the latter is regarded as a temperature rise in testing.

Mode of deformation has been shown to influence the progress of transformation in the plastic range. Uniaxial tension was found to promote martensite formation more than either compression or torsion. This finding correlated reasonably well with a comparison of strain hardening in tension and torsion based on the relationship between maximum shear stress and maximum finite shear strain.

ACKNOWLEDGMENTS

The authors are indebted to the Office of Naval Research for its support of this work and to Professor Samuel C. Collins and Dr. Z. Bazinski for their assistance and the loan of equipment for conducting some of the low-temperature tests.

References

1. E. C. Bain and W. E. Griffiths, "An Introduction to the Fe-Cr-Ni Alloys," *Transactions, American Institute of Mining and Metallurgical Engineers*, Vol. 75, 1927, p. 166.
2. V. N. Krivobok and R. A. Lincoln, "Austenitic Stainless Steels," *TRANSACTIONS, American Society for Metals*, Vol. 25, 1937, p. 637.
3. K. Mathieu, "Einfluss von Legierungsgehalt und Versuchsbedingungen auf die $\gamma \rightarrow \alpha$ Umwandlung bei der Kaltverformung austenitischer Stähle," *Archiv für das Eisenhüttenwesen*, Vol. 16, 1942, p. 215.
4. K. Mathieu, "Mesures de Saturation Magnétique et Leur Application en Contrôle Siderurgie," *Revue de métallurgie*, Vol. 41, 1944, p. 28.
5. K. Bungardt, R. Oppenheim, and R. Scherer, "Einfluss der Verformung bei tiefer Temperatur auf die Eigenschaften nichtrostender austenitischer Stähle," *Archiv für das Eisenhüttenwesen*, No. 9/10, 1953, p. 423.
6. N. A. Zeigler and P. H. Brace, "Hardening of Austenitic Stainless Steels by Mechanical Working at Sub-zero Temperatures," *Proceedings, American Society for Testing Materials*, Vol. 50, 1950, p. 861.
7. C. D. Starr, "Notes on the Plastic Critical Temperature in Strain-Induced Martensite Reactions," *Transactions, American Institute of Mining and Metallurgical Engineers*, Vol. 197, 1952, p. 654.
8. H. C. Doepken, "Tensile Properties of Wrought Austenitic Manganese Steel in the Temperature Range +100 to -196 °C," *Transactions, American Institute of Mining and Metallurgical Engineers*, Vol. 194, 1952, p. 166.
9. E. S. Machlin and M. Cohen, "Habit Phenomenon in the Martensitic Transformation," *Transactions, American Institute of Mining and Metallurgical Engineers*, Vol. 191, 1951, p. 1019.
10. S. A. Kulin, M. Cohen, and B. L. Averbach, "Effect of Applied Stress on the Martensitic Transformation," *Transactions, American Institute of Mining and Metallurgical Engineers*, Vol. 194, 1952, p. 661.
11. B. Cina, "Effect of Cold Work on the $\gamma \rightarrow \alpha$ Transformation in Some Fe-Ni-Cr Alloys," *Journal, Iron and Steel Institute*, Vol. 177, No. 4, 1954, p. 406.
12. A. W. McReynolds, "Effects of Stress and Deformation on the Martensite Transformation," *Journal of Applied Physics*, Vol. 20, 1949, p. 896.
13. G. W. Form and W. N. Baldwin, Jr., "The Influence of Strain Rate and Temperature on the Ductility of Austenitic Stainless Steels," *ONR Contract N6-ONR-273/1, Project NR-031-049, Tech. Report No. 30, Sept. 1954*.
14. G. W. Powell, E. R. Marshall, and W. A. Backofen, "A Diameter Gage and Dynamometer for True Stress-Strain Tension Tests at Constant True Strain Rate," *American Society for Testing Materials Preprint No. 88, 1955*.
15. A. S. Eldin and S. C. Collins, "Fracture and Yield Strength of 1020 Steel at Low Temperatures," *Journal of Applied Physics*, Vol. 22, 1951, p. 1296.
16. A. Nadai, "Theory of Flow and Fracture of Solids," McGraw-Hill Book Co., Inc., New York, 1950, p. 348-349.
17. A. Nadai, "Plasticity," McGraw-Hill Book Co., Inc., New York, 1931, p. 75-78.

18. S. G. Fletcher and M. Cohen, "The Effect of Carbon on the Tempering of Steel," *TRANSACTIONS, American Society for Metals*, Vol. 32, 1944, p. 333.
19. A. Nadai, "Theory of Flow and Fracture of Solids," McGraw-Hill Book Co., Inc., New York, 1950, p. 70-71.
20. S. C. Collins, F. D. Ezekiel, O. W. Sepp, and J. W. Rizika, "The Strength of Certain Stainless and Carbon Steels at Low Temperatures," *American Society for Testing Materials Preprint No. 74*, 1956.
21. G. V. Uzhik, "Strength and Ductility of Metals at Low and Extremely Low Temperatures," *Izvestiya Akademi Nauk, USSR*, OTN, No. 1, 1955, p. 56-57 (Henry Bratcher Translation No. 3537).
22. V. N. Krivobok and A. M. Talbot, "Effect of Temperature on the Mechanical Properties, Characteristics, and Processing of Austenitic Stainless Steels," *Proceedings, American Society for Testing Materials*, Vol. 50, 1950, p. 895.
23. E. R. Marshall, "Strain Hardening of Metals," Sc.D. Thesis, Massachusetts Institute of Technology, June 1953.
24. P. W. Bridgman, "The Stress Distribution at the Neck of a Tension Specimen," *TRANSACTIONS, American Society for Metals*, Vol. 32, 1944, p. 553.
25. E. R. Marshall and M. C. Shaw, "The Determination of Flow Stress from a Tensile Specimen," *TRANSACTIONS, American Society for Metals*, Vol. 44, 1952, p. 705.
26. T. Angel, "Martensite in Austenitic Stainless Steels," *Journal, Iron and Steel Institute*, Vol. 177, No. 1, 1954, p. 165.
27. E. S. Machlin and M. Cohen, "Burst Phenomenon in the Martensitic Transformation," *Transactions, American Institute of Mining and Metallurgical Engineers*, Vol. 191, 1951, p. 746.
28. A. E. Nehrenberg, P. Payson, and P. Lillys, "Effect of Carbon and Nitrogen on the Attainable Hardness of Martensitic Steels," *American Society for Metals, Preprint No. 16*, 1954.
29. G. W. Geil and N. L. Carwile, "Tensile Properties of Cu, Ni, and Some Cu-Ni Alloys at Low Temperatures," *NBS Circular No. 520*, p. 67.
30. G. W. Geil and N. L. Carwile, "Tensile Properties of Ingot Iron at Low Temperatures," *Journal of Research, NBS*, Vol. 45, 1950.
31. R. L. Smith, G. Spangler, and R. M. Brick, "Effect of Grain Size and Carbon Content on the Low Temperature Properties of High Purity Fe-C Alloys," *TRANSACTIONS, American Society for Metals*, Vol. 46, 1954, p. 973.
32. M. Cohen, "Retained Austenite," *TRANSACTIONS, American Society for Metals*, Vol. 41, 1949, p. 35.
33. A. H. Cottrell and R. J. Stokes, "Effects of temperature on the plastic properties of aluminum crystals," *Proceedings, Royal Society*, Vol. 233A, Dec. 1955, p. 17.
34. Z. Bazinski, private communication.

THE EFFECT OF RATE OF STRESS APPLICATION AND TEMPERATURE ON THE UPPER YIELD STRESS OF ANNEALED MILD STEEL

BY J. A. HENDRICKSON AND D. S. WOOD

Abstract

The upper yield stress of an annealed low carbon steel has been determined experimentally under various constant rates of stress application ranging from about 10^2 to 10^3 psi per second at temperatures of -110 and -200°F (-79 and -129°C). These data are compared with two expressions derived in different ways from the dislocation theory of the distinct yield point. The three undetermined constants appearing in each of the theoretical expressions are evaluated by means of previous data on the delay time for yielding under constant stress. Both theoretical expressions are found to be in good agreement with the experimental results. This indicates that the dislocation theory provides a means for accurate prediction of the upper yield stress and the time for yielding when the applied stress varies with time in any manner. (ASM International Classification: Q23b, 2-11, 3-17; CN)

INTRODUCTION

PREVIOUS INVESTIGATIONS (1,2,3,4)¹ have shown that mild steel exhibits a distinct delay time for the initiation of yielding when subjected to rapidly applied constant tensile stresses in excess of the static upper yield stress. The delay time has been determined for a particular annealed low carbon steel at temperatures ranging from -320 to 250°F (-196 to 121°C) and stresses from about 40,000 psi to about 125,000 psi. Within these ranges of temperature and stress the delay time varies from about 5×10^{-5} seconds to about 10^3 seconds. Krafft (5) has extended the data at room temperature to delay times as small as about 2×10^{-6} seconds. Cottrell (6,7), and Cottrell and Bilby (8) have developed the basic concepts of a dislocation theory of yield point phenomena. These concepts have been elaborated and compared with delayed yield data by Vreeland, Wood, and Clark, (9,10), Fisher (11), and Campbell (12). Such comparisons

¹ The figures appearing in parentheses pertain to the references appended to this paper.

A paper presented before the Thirty-Ninth Annual Convention of the Society, held in Chicago, November 4-8, 1957. Of the authors, J. A. Hendrickson is Research Assistant, and D. S. Wood is Associate Professor of Mechanical Engineering, The California Institute of Technology, Pasadena, California. Manuscript received May 15, 1957.

between theory and experiment serve to provide numerical values for the undetermined constants which appear in the theories. The various theories differ in the details of the dislocation models employed in their derivation and in the simplifying assumptions and approximations which they entail.

The dislocation theories may also be employed to derive expressions for the upper yield stress and the time for yielding as functions of temperature under types of loading other than rapidly applied constant stress. Campbell (12) has derived such expressions for the case of constant rate of stress application and the case in which the stress varies sinusoidally with time. The theoretical expressions for these cases contain the same numerical constants which appear in the expressions for the delay time for yielding under constant stress. Thus, if the numerical constants applicable to a given steel have been determined from delay time data it is possible to predict quantitatively the upper yield stress of the same steel for cases in which the applied stress varies continuously with time in some prescribed manner.

The procedure of correlating theory and experiment may be reversed. For example, the constants of the theory may be evaluated by fitting to data obtained under constant rates of stress application at different temperatures. Then the delay time for yielding under constant stress may be predicted as a function of temperature and the magnitude of the applied stress.

Theoretical predictions of the upper yield stress or the delay time for yielding of the type just discussed have not been compared with experimental data to test their validity. The reason for this is that the necessary data for a single steel subjected to two different types of load vs. time relations at different temperatures has not been available. The object of this paper is to present data of this type and make the comparison between theory and experiment. The quantitative evaluation of the undetermined constants of the theory is accomplished by fitting the theory to values of the delay time for yielding as a function of stress and temperature determined in previous investigations, (2,3,4), for a particular annealed low carbon steel. The experimental measurements required for comparison with the theory consist of tensile tests on the same steel at various constant rates of application of stress at two temperatures.

THEORETICAL CONSIDERATIONS

Two different dislocation theories of the yield point in mild steel will be presented and compared with experiment. The first is based upon a dislocation model of a yield nucleus which has been discussed previously, (9,10). Briefly, this model consists of a Frank-Read source, which is a dislocation segment with fixed end points, lying on a slip surface bounded by a grain boundary. The dislocation segment is

bound along its length by a Cottrell "atmosphere" of interstitial solute atoms such as carbon and nitrogen. This Frank-Read dislocation source may generate dislocation loops under the action of an applied stress and thermal fluctuations. A generated dislocation loop will then expand causing a very small amount of plastic deformation, until an obstacle, such as the grain boundary or a previously generated dislocation loop, prevents the loop from expanding further. The piling up of these loops at the grain boundary concentrates the stress acting on that boundary to a much higher value than the stress that acts on the dislocation source. The assumption is made that general yielding occurs when the concentrated stress acting on the grain boundary reaches a critical value.

The rate of generation of dislocation loops at the Frank-Read source is assumed to be controlled by the thermally activated release of the source dislocation from its "atmosphere." The expression for the rate of generation of dislocation loops at a given source is

$$\begin{aligned} \frac{dn}{dt} = \dot{n} &= \nu \exp(-W/kT), \quad \tau_s \geq Gb/l, \\ \dot{n} &= 0, \quad \tau_s < Gb/l, \end{aligned} \quad \text{Equation 1}$$

where n is the number of dislocations generated,
 t is the time,
 ν is the frequency of the appropriate form of thermal fluctuations,
 τ_s is the resolved shear stress at the Frank-Read source,
 k is Boltzman's constant,
 T is the absolute temperature,
 W is the thermal activation energy required for the release of a dislocation from an "atmosphere" of solute atoms,
 G is the shear modulus,
 b is the atomic slip distance or Burger's vector, and
 l is the distance between the end points of the Frank-Read source.

The thermal activation energy, W , required for the release of a dislocation from an atmosphere of interstitial solute atoms (carbon and nitrogen in iron) is a function of the stress acting on the dislocation. Cottrell and Bilby (8) derived an expression for W as a function of the stress which is rather complex. Fisher (11) has derived a simpler though probably less accurate expression which is

where

$$\begin{aligned} W &= \gamma_0^2 / b \tau_s \times f(\gamma/\gamma_0), \\ f(\gamma/\gamma_0) &= \cos^{-1}(\gamma/\gamma_0) - \gamma/\gamma_0 [1 - (\gamma/\gamma_0)^2]^{1/2}, \end{aligned} \quad \text{Equation 2}$$

γ_0 is the energy per atomic distance of a dislocation without an "atmosphere,"
 and γ is the energy per atomic distance of a dislocation with an "atmosphere."

Equation 1 may be put in the following form through the use of Equation 2:

$$\begin{aligned} \dot{n} &= \nu \exp(-B/2 \tau_s T), \\ B &= 2 \gamma_0^2 f(\gamma/\gamma_0) / b k. \end{aligned}$$

where

Further, if the applied shear stress at the source, τ_s , is assumed to be independent of the number of loops generated, and equal to one half the applied tensile stress, σ , then the rate of generation of dislocation loops is given by the expression

$$\dot{n} = \nu \exp(-B/\sigma T). \quad \text{Equation 3}$$

The local shear stress at the grain boundary or other obstacle after n dislocations have accumulated in the slip plane is $n\sigma/2$, where again the average shear stress on the slip plane is assumed to be equal to one half the applied tensile stress. The critical local stress at the obstacle which must be reached before macroscopic yielding begins is assumed to be equal to the theoretical strength of a perfect crystal, namely, aG , where a is a constant of the order of one tenth. Thus the number of dislocations, n^* , which must be generated to initiate yielding is given by the expression

$$n^* = 2aG/\sigma. \quad \text{Equation 4}$$

Equations 3 and 4 are the basic relations for this dislocation theory of yielding. They contain the three undetermined constants ν , B , and a which are to be evaluated by fitting specific results of the theory to experimental data. An expression for the delay time for yielding, t_d , under rapidly applied constant stress is readily derived from Equations 3 and 4. Thus

$$n^* = 2aG/\sigma = \int_0^{t_d} \nu \exp(-B/\sigma T) dt, \quad \text{and hence} \quad t_d = 2aG/\nu \sigma \exp(B/\sigma T). \quad \text{Equation 5}$$

For tests at constant rates of stress rise, $\sigma = \dot{\sigma}t$ where $\dot{\sigma}$ is the constant applied stress rate. The number of dislocation loops present at any instant is obtained by using this relation in Equation 3 and integrating with respect to time. The result is

$$n = \nu t \exp(-B/\dot{\sigma}tT) + B\nu/\dot{\sigma}T [Ei(-B/\dot{\sigma}tT)], \quad \text{Equation 6}$$

where $Ei(-B/\dot{\sigma}tT)$ is the exponential integral of the indicated argument. At the instant of the initiation of yielding $n = n^*$, and $\sigma t = \sigma_{yd}$, where σ_{yd} is the upper yield stress. Therefore Equations 4 and 6 combine to give the following relationship between upper yield stress, σ_{yd} , stress rate, $\dot{\sigma}$, and temperature, T ,

$$2aG = \nu/\dot{\sigma} \{ (\sigma_{yd})^2 \exp(-B/\sigma_{yd}T) + B\sigma_{yd}/T [Ei(-B/\sigma_{yd}T)] \} \quad \text{Equation 7}$$

Thus this first dislocation theory of yielding leads to expressions for the delay time for yielding under constant stress and for the upper yield stress as a function of applied stress rate given by Equations 5 and 7 respectively. Both expressions contain the temperature dependence of the yield point.

The second dislocation theory of the yield point which will be employed is due to Campbell (12). Campbell's derivations are based upon a slightly different dislocation model of yielding than that employed above. Campbell assumes that macroscopic yielding is initiated when a critical number of dislocations have been generated and that this number is independent of the applied stress. Also Campbell employs an approximate expression for the activation energy, W , proposed by Yokobori (13), namely,

$$W = -E_0 \ln(\sigma/\sigma_0), \quad \text{Equation 8}$$

where E_0 is an undetermined constant, and σ_0 is the upper yield stress at absolute zero temperature. Campbell's results are

$$t_d = C \dot{\epsilon} (\sigma/\sigma_0)^{-E_0/kT}, \quad \text{Equation 9}$$

and

$$\sigma_{yd} = \sigma_0 \left[(1 + E_0/kT) C \dot{\epsilon} \sigma/\sigma_0 \right]^{1/(1 + E_0/kT)}, \quad \text{Equation 10}$$

where C is an undetermined constant. Equation 9 gives the yield delay time as a function of constant applied stress and temperature, while Equation 10 expresses the upper yield stress as a function of the rate of stress application and temperature. The three undetermined constants of Campbell's theory are the quantities E_0 , σ_0 , and C .

The undetermined constants of both theories have been evaluated by fitting Equations 5 and 9 to the experimentally measured values of the delay time for yielding under rapidly applied constant stress. The values of the constants in Equation 5 are found to be

$$\begin{aligned} a &= 0.159 \\ B &= 1.67 \times 10^{-8} \text{ G}^2, \text{ psi } ^\circ\text{K}, \\ \text{and } r &= 6.77 \times 10^{10} \text{ sec}^{-1}. \end{aligned}$$

The shear modulus, G , has been taken to be the following function of temperature as obtained from Köster's (14) measurements of Young's modulus and the assumption that Poisson's ratio is independent of temperature:

$$G = (13.30 - 0.003T) \times 10^6 \text{ psi.}$$

The values of the constants in Equation 9 are found to be

$$\begin{aligned} E_0 &= 0.425 \text{ electron volts,} \\ \sigma_0 &= 168 \times 10^3 \text{ psi,} \\ \text{and } C &= 1.02 \times 10^{-10} \text{ sec.} \end{aligned}$$

The fits between theory and experiment obtained using these sets of constants are shown in Fig. 1. The dash-dot curves represent Equation 5 while the dashed curves represent Equation 9. Both theories fit the experimental data quite well for temperatures of -75°F and higher. However, they both deviate somewhat from experiment at the two lowest temperatures, -205 and -320°F . The numerical

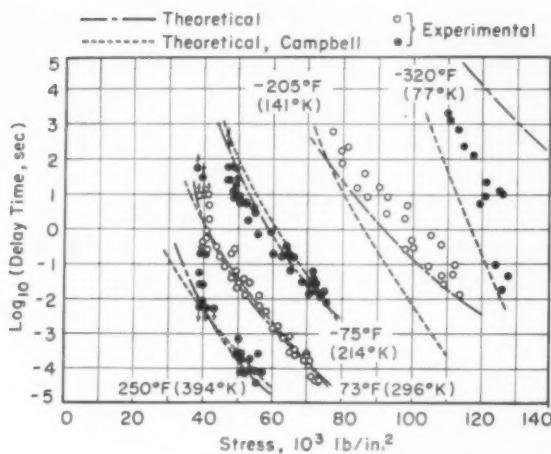


Fig. 1—Logarithm Delay Time versus Rapidly Applied Constant Tensile Stress for Annealed 0.17% Carbon Steel.

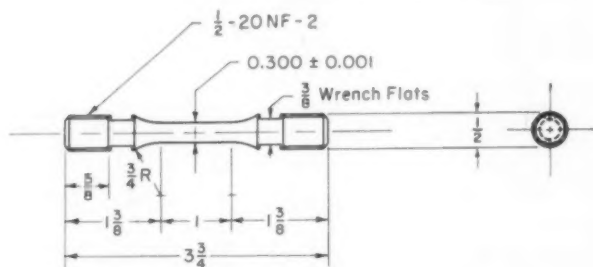


Fig. 2—Tensile Test Specimen.

values of the constants given above may be substituted into Equations 7 and 10 to provide the desired predictions of the upper yield stress as a function of applied constant stress rate and temperature.

EXPERIMENTAL MEASUREMENTS

The material used in this investigation is the same 0.17% carbon steel employed in previous studies (2,3,4), of delayed yielding. This steel was obtained from the Columbia Steel Company, Torrance, California Works. The steel was hot-rolled to $\frac{5}{8}$ inch diameter bars from one billet of heat number 32882. The analysis as given by the mill is as follows:

Carbon	0.17 %
Manganese	0.39 %
Phosphorus	0.017%
Sulphur	0.040%

The material was tested in the same annealed condition employed previously namely, the specimens were annealed by heating at 1600 °F for 50 minutes followed by slow cooling in the furnace. The entire annealing treatment was done in an atmosphere of dry hydrogen after all machining operations on the specimens had been completed. The average grain size of the material is ASTM number 6.5. The design of the specimens is shown in Fig. 2.

Tensile tests at constant rates of stress application were performed by means of a hydro-pneumatically operated rapid load tensile testing machine described previously (1). This machine is capable of rates of load application up to about 10^6 pounds per second. The diameter of

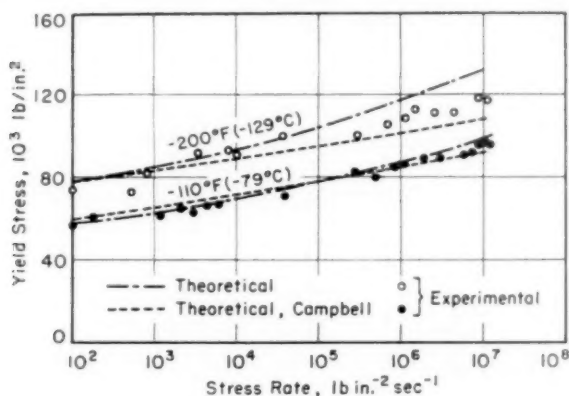


Fig. 3—Upper Yield Point versus Stress Rate for Annealed 0.17% Carbon Steel.

the gage section of the test specimen is 0.300 inch. Hence the maximum rate of stress application attainable is about 10^7 psi per second.

The applied load was determined as a function of time during each test by means of a calibrated dynamometer employing type AB-14, SR-4 wire strain gages. The signal from the dynamometer was amplified and recorded by means of a carrier bridge amplification system and galvanometer type of oscillograph, manufactured by the Consolidated Electrodynamics Corporation, Pasadena, California. The time resolution of the recording system is about ± 1 millisecc at the maximum recording rate. The load acting on the specimen at any time could be determined to within an estimated overall error of about 4%. The onset of macroscopic yielding is characterized by a sudden decrease of load which is readily detectable on the test records.

The specimens were tested at temperatures of -110 and -200°F (-79 and -129°C). These temperatures were obtained by means of a bath of Freon 12 held in a suitable container surrounding the speci-

men and portions of the grips. The temperature of -110°F (-79°C) was secured by using dry ice in the Freon bath. The temperature of -200°F (-129°C) was obtained by placing liquid nitrogen in a concentric container surrounding the Freon bath. A controlled electrical heater in the Freon bath provided the means for regulating the temperature of the specimen.

The temperatures were measured with three copper-constantan thermocouples. A thermocouple was attached to each of the specimen fillets and one was attached to the center of the specimen gage length. Temperature measurements made during the tests indicated that the total temperature difference along the specimen gage length was less than $\pm 5^{\circ}\text{F}$ for the tests at a temperature of -200°F (-129°C) and less than $\pm 1^{\circ}\text{F}$ during the tests at a temperature of -110°F (-79°C). The temperature variation was $\pm 10^{\circ}\text{F}$ or less during the tests at a temperature of -200°F (-129°C) and less than $\pm 1^{\circ}\text{F}$ during the tests at a temperature of -110°F (-79°C).

Tests were conducted at constant rates of stress application ranging from 10^2 to 10^7 psi per second. The values of the upper yield stress obtained in these tests are given by the plotted points shown in Fig. 3.

DISCUSSION

The theoretical predictions of the upper yield stress as a function of applied stress rate for the two test temperatures are shown by the curves in Fig. 3. The dash-dot curve represents the results of the first theory presented (Equation 7), while the dashed curve represents Campbell's theory (Equation 10). This comparison between theory and experiment shows that either of the two theories gives a reasonably accurate prediction of the upper yield stress.

The only significant differences between the theoretical predictions and the experimental results occurs for the tests at -200°F (-129°C) and stress rates exceeding about 10^5 psi per second. This is not surprising since at this temperature the dislocation theories do not fit the delay time data very accurately, as shown in Fig. 1. The reason for this discrepancy, which appears to be common to the two theories, is not clear. However, several suggestions have been made for its explanation. A portion of the discrepancy may be due to an error in the value of the shear modulus, G , at this temperature (9). Fisher (11), points out that the expression for the activation energy, W , employed in the first theory is probably appreciably in error when the stress exceeds about 120,000 psi. This may also be true of Yokobori's expression which is employed in Campbell's theory. The theories might be improved in the high stress range by employing the more exact expression for the activation energy derived by Cottrell and Bilby (8). Finally, the theories may be in error at the lower temperatures due to a change in the mechanism of yielding in that range. This

is indicated by the fact that in this temperature range brittle fracture is often observed in unnotched tensile specimens of mild steel.

The agreement between predicted and experimental values of the yield stress as a function of stress rate at a temperature of -110°F (-79°C) is very good. This may also be expected to be the case at higher temperatures up to at least 250°F since the dislocation theories fit the delay time data very well in that range, provided the stress exceeds the static upper yield stress.

Neither of the two dislocation theories of yielding presented in this paper account for the fact that the delay time for yielding is essentially infinite at a lower limiting stress (static upper yield stress). This is due to the approximation, made in both theories, that the shear stress at the Frank-Read source is independent of the number of dislocations which have been generated. Actually the stress at the source is reduced by the dislocations which have been generated and held up by the grain boundary or other obstacles (10). When the applied stress is less than the static upper yield stress, this effect is sufficient to reduce the local shear stress at the source to the value $\tau_s = Gb/l$. Hence the generation of dislocations ceases and yielding does not take place. The inclusion of this effect in the theoretical derivations presented in this paper would lead to expressions of considerably greater complexity.

The experimental data presented in this paper do not serve to evaluate the relative merits of the two theories. This is not surprising since the dislocation models upon which the two theories are based are similar. Other similar theories could be constructed by employing different forms of expressions for the activation energy for release of a dislocation from an "atmosphere." Somewhat different criteria for the onset of macroscopic yielding in terms of the applied stress and the number of dislocations released from atmospheres might also be used with success.

SUMMARY AND CONCLUSIONS

Two theoretical predictions of the upper yield stress of an annealed low carbon steel as a function of rate of stress application and temperature have been presented. Both predictions are based upon the basic concepts of the dislocation theory of the yield point in body-centered cubic metals containing interstitial solutes. The differences between the two predictions arise from differences in the various assumptions and approximations which are made in the derivations. Quantitative predictions of the upper yield stress are obtained by evaluating the undetermined constants of the two forms of the theory by means of experimentally determined values of the delay time for yielding under constant stress.

Experimental measurements of the upper yield stress as a function of the applied stress rate have been made at two temperatures. The

results obtained are in good agreement with the predictions of both forms of the theory. This indicates that the general aspects of the dislocation theory of yielding are correct. The experimental data available at the present time are not sufficient to evaluate the relative merits of the several specific theories which may be constructed by employing different detailed dislocation models. However, these theories are capable of predicting the upper yield stress of a mild steel subjected to various constant rates of stress application and temperatures.

The theory may also be employed to predict the upper yield stress under more complex stress versus time conditions. Furthermore, the experimental data required for quantitative evaluation of the theory could be obtained from tests at constant rates of stress application, rather than from delay time measurements. In this case the delay time could be predicted as a function of applied stress and temperature.

ACKNOWLEDGMENT

Appreciation is expressed to the Office of Ordnance Research, United States Army, who sponsored the work on which this paper is based. Mr. Wilfred Iwan assisted in the experimental work of this investigation. The support and encouragement of Professor Donald S. Clark is greatly appreciated.

References

1. D. S. Clark and D. S. Wood, "The Time Delay for the Initiation of Plastic Deformation at Rapidly Applied Constant Stress," *Proceedings, American Society for Testing Materials*, Vol. 49, 1949, p. 717.
2. D. S. Wood and D. S. Clark, "The Influence of Temperature Upon the Time Delay for Yielding in Annealed Mild Steel," *TRANSACTIONS, American Society for Metals*, Vol. 43, 1951, p. 571.
3. J. E. Johnson, D. S. Wood and D. S. Clark, "Delayed Yielding in Annealed Low-Carbon Steel under Compression Impact," *Proceedings, American Society for Metals*, Vol. 53, 1953, p. 755.
4. D. S. Clark, "The Behavior of Metals Under Dynamic Loading," Twenty-Eighth Edward de Mille Campbell Memorial Lecture, *TRANSACTIONS, American Society for Metals*, Vol. 46, 1954, p. 34.
5. J. M. Krafft, "Effect of Temperature on Delayed Yielding of Mild Steel for Short Loading Duration," *TRANSACTIONS, American Society for Metals*, Vol. 48, 1956, p. 249.
6. A. H. Cottrell, "Effect of Solute Atoms on the Behavior of Dislocations," Report of the Bristol Conference on Strength of Solids, *The Physical Society*, London, 1948, p. 30.
7. A. H. Cottrell, "The Yield Point in Single Crystals and Polycrystalline Metals," Symposium on the Plastic Deformation of Crystalline Solids, Mellon Institute, 1950, p. 60.
8. A. H. Cottrell and B. A. Bilby, "Dislocation Theory of Yielding and Strain Aging of Iron," *Proceedings, The Physical Society*, London, Vol. 62, Part A, 1949, p. 49.
9. T. Vreeland, Jr. and D. S. Wood, "A Comparison Between Dislocation Theory and Experimental Measurements of Delayed Yield in Steel," Eighth Technical Report under Office of Naval Research, Contract N6onr-24418, California Institute of Technology, April 1954.
10. T. Vreeland, Jr., D. S. Wood and D. S. Clark, "Pre-Yield Plastic and Anelastic Microstrain in Low-Carbon Steel," *Acta Metallurgica*, Vol. 1, July 1953, p. 414.

11. J. C. Fisher, "Application of Cottrell's Theory of Yielding to Delayed Yielding in Steel," *TRANSACTIONS, American Society for Metals*, Vol. 47, 1955, p. 451.
12. J. D. Campbell, "Dynamic Yielding of Mild Steel," *Acta Metallurgica*, Vol. 1, November 1953, p. 706.
13. T. Yokobori, "The Cottrell-Bilby Theory of Yielding in Iron," *Physical Review*, Vol. 88, Series 2, 1952, p. 1423.
14. W. Köster, "Die Temperaturabhängigkeit des Elastizitätsmoduls Reiner Metalle," *Zeitschrift für Metallkunde*, Vol. 39, 1948, p. 1.

DISCUSSION

Written Discussion: By Dr. J. D. Campbell, Department of Engineering Science, University of Oxford, Oxford, England.

The authors have presented some interesting experimental data concerning the relationship between yield stress, rate of loading and temperature in mild steel. In spite of the considerable difficulties inherent in rapid-loading tests, the results obtained by the authors are consistent enough to permit a comparison with theoretical relations derived from dislocation theory; it is encouraging that the agreement is in general good.

The authors' theory of yielding differs in two respects from that put forward by the writer: In the expression used for the activation energy of dislocation release, as a function of the applied stress; and in the assumption concerning the number of dislocation releases necessary to initiate macroscopic yielding.

The activation energy expression used by the authors is that due to Fisher, who assumed that the interaction energy of a dislocation with its atmosphere jumps discontinuously from one value to another at a loop. This is a somewhat crude assumption, since the width of the loop at release is only a few atomic distances. The resulting expression for the activation energy implies that this energy is finite however large the applied stress, a physically improbable result.

The authors assume that macroscopic yielding takes place when each active Frank-Read source has generated a certain number of dislocation rings, this number being inversely proportional to the applied stress at yield. It is further assumed that the generation of each ring is a thermally activated process, the activation energy being independent of the number of rings formed. This latter assumption seems open to question, since after the first loop is formed the source dislocation has kinetic energy associated with it, which may well enable it to continue to generate loops with little or no assistance from thermal fluctuations.

The assumption that the critical number of dislocations varies inversely with the applied stress can easily be incorporated with the writer's theory. It is merely necessary to take $C \propto 1/\sigma_{yd}$, where σ_{yd} is the dynamic yield stress. If we write $C = C'\sigma_0/\sigma_{yd}$, where C' is a constant, Equation 9 becomes

$$t_d = C'(\sigma/\sigma_0)^{-(1+E_0/kT)}$$

and Equation 10 becomes

$$\sigma_{yd} = \sigma_0 [(1 + E_0/kT) C' \dot{\sigma}/\sigma_0]^{\frac{1}{2+E_0/kT}}$$

Since E_0/kT is of order 15 at room temperature, the change in the exponents is not great. It is, therefore, difficult to discriminate between these two criteria by a comparison with experimental results.

The writer is unable to understand how the authors have obtained numerical values for the constants α and ν in their theory. These constants appear in Equation 5 only in the form α/ν ; it would seem, therefore, that it is not possible to obtain their absolute values by fitting Equation 5 to the experimental results.

The authors conclude that the fact that there is a static yield stress at which the delay time becomes very large is due to back stresses acting on the Frank-Read sources. However, another possibility which has been suggested by several writers is that, when the time of yielding is sufficiently great, relocking of dislocations occurs by rapid diffusion of carbon atoms. Campbell and Duby² have developed a modified criterion of yielding on this assumption. According to this criterion, the relation between delay time t_d and constant applied stress σ is

$$\sigma = \sigma_0 [bC/1 - \exp(-btd)]^{kT/E_0}$$

where b is a constant proportional to the rate of relocking of dislocations. This equation reduces to Equation 9 when t_d is small compared with $1/b$. When t is large compared with $1/b$ the equation indicates that $\sigma \rightarrow \sigma_0 (bC)^{kT/E_0}$; this expression, therefore, gives the 'static' yield stress. The available constant-stress test results are, unfortunately, not accurate enough to permit comparison with this theory.

Written Discussion: By Frederick Forscher, Nuclear Materials and Equipment Corporation, Apollo, Pa.

The authors are to be congratulated on the effort to obtain experimental results that would test the validity of two theories proposed to explain the rate and temperature dependence of the yield phenomenon. In recent years considerable attention has been given to this problem because of its importance not only to mild steel but also to other body-centered cubic metals and in some cases to metals of other crystallographic structure. California Institute of Technology has been one of the leaders in the renaissance of the study of the yield phenomenon.

Some time ago the discussor reported some experiments which may, it is suggested, have some bearing on this problem. (The Yield Rate of Mild Steel, ASTM Bulletin No. 205, 63, April 1955.) In these experiments, round specimens of mild steel were subjected to a constant tensile load and the rate of yielding was measured for a series of temperatures and stress levels. The experimental set-up was such that the yield stress was imposed and the yield rate was the dependent variable. In a conventional tensile experiment, on the other hand, the deformation rate (yield rate) is imposed and the lower yield stress is the dependent variable. The lower yield stress can be thought of as a parameter affecting the dynamic equilibrium of the specimen during yielding. Other parameters are the resulting deformation rate and the temperature. The material at the interface between the virgin region and the progressing Lüders' band is in effect experiencing an *upper* yield stress at the same time as the specimen is yielding at the *lower* yield stress. It follows that, the slower the transformation from the virgin to the yielded state, the slower will be the extension of the macrospecimen and, of course, the slower will Lüders' bands "eat up" the virgin material. This transformation from the virgin to the yielded state is controlled by atomistic processes, two of which are represented by the theories which the authors have chosen to compare.

It appears that the yield rate is, in fact, another measure of the delay time.

² J. D. Campbell and J. Duby, "Delayed Yield and Other Dynamic Loading Phenomena in a Medium-Carbon Steel," *Proceedings, Conference on the Properties of Materials at High Rates of Strain*, Institute of Mechanical Engineers, London, 1957. (In the press.)

Hence, one would expect to find that the yield rate depends on stress and temperature in the same manner as the delay time measured by the authors. This expectation has been verified. The yield rate experiments gave rise to the schematic relationships shown in the attached figure. It should be noted that the sigmoidal shape of the curves in the schematic diagram (top) can also be seen in the authors' experimental data. One has only to substitute the logarithm of yield rate for the logarithm of delay time to find a striking agreement between the authors' Fig. 1 and Fig. 4a. The mechanistic justification for such a substitution has been outlined above and constitutes the major point of this discussion.

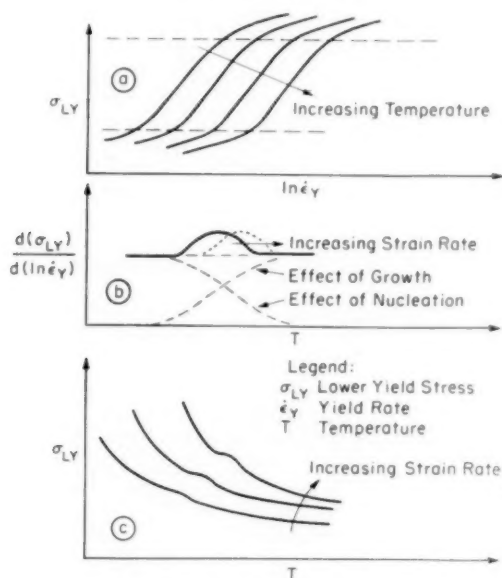


Fig. 4—Schematic Relationships.

If we now assume that the sigmoidal shape of these curves is real and actually represents the behavior of these materials we must conclude that the proposed atomistic theories can, at best, be used to explain the steady state (dynamic) condition but not the whole phenomenon. Thus, the application of these theories should be restricted to the portion between the two dashed lines in Fig. 4a.

Parenthetically it should be mentioned that yielding can also be considered from a nucleation and growth point of view and that this concept may possibly explain the sigmoidal shape of the basic curves (Fig. 4b). However, the concept of nucleation and growth of yielded regions is less pertinent in a study of the *upper* yield stress which is after all, the subject of the authors' paper and therefore should not be further pursued here except for one additional thought.

The experimental study of the yield phenomenon must always be cognizant of the importance of the machine-specimen interaction. Now, if the concept of nucleation and growth is pertinent to the yield phenomenon, its effect on the machine-

specimen interaction should be carefully analyzed. I can visualize the case, where nucleation is the predominant mechanism, when the machine-specimen interaction is greatly delayed. In that case the criterion for yielding, which is the key-stone in any theory, cannot be experimentally verified.

It is hoped that the authors will continue their excellent work in the field of the yield point phenomenon.

Written Discussion: By J. M. Krafft, U. S. Naval Research Laboratory, Washington, D. C.

The authors are to be complimented on their interesting treatment of this difficult problem. Workers at the U. S. Naval Research Laboratory³ have attempted a more empirical comparison of the effects of different loading patterns on the yield point which it might be appropriate to mention here. Our experiments provided, in addition to the presently discussed suddenly applied constant-stress and rapid constant-rate of stress application, a third pattern in which an oscillatory stress was superposed upon a static tensile bias stress near the lower yield stress. It was found that the onset of yielding could be predicted if one assumed that the damage to the material, which eventually culminates in rapid yielding, accumulates at a rate inversely proportional to the constant stress delay time for a given stress. Thus, we were able to empirically predict yielding for an arbitrary load pattern by the following steps: (a) fitting a curve through the constant stress versus delay time data, (similar to the authors' Fig. 1), (b) approximating the applied-load versus time pattern with finite steps, and (c) tabulating and cumulatively summing the ratios of the time at each step to the constant stress delay time for the applicable stress level (damage fraction by our nomenclature). When the sum of the damage fractions of step 3 reached unity, we found, within the experimental uncertainty, that yield would occur.

This empirical procedure appears to be basically similar to that applied theoretically in the present paper. The principal difference is that an analytic expression for constant stress delay time as a function of applied stress has been derived and fitted to the data, so that using another analytic expression for the constant-rate-of-load pattern, the integration of our step three can be performed directly rather than by numerical summations. But the basic assumption, that damage, or in the authors' terms the number of dislocations generated, is simply additive, is identical. It is inherent in the authors' Equation 3 giving the rate of generation of dislocation loops as combined with the assumption that a certain number are required to produce yield (at a given stress), and with the integration of Equation 3 to a time which will cause the integral to equal this limiting number. The empirical procedure of damage summation can be applied to the theoretical constant stress delay time curves of Fig. 1, to compute the curves yield stress versus stress rate shown in Fig. 3; this can be demonstrated for the case at which the test temperatures are nearly the same (-200°F). Thus we might consider the present theory as consisting of two essential parts, first the theory by which curves fitting the constant stress delay time data are obtained; and second, the hypothesis of additive damage accumulation.

It is noted that at the lower temperature (-200°F) the theoretical curves of Fig. 3 do not fit the data as well as could be desired. The authors suggest that

³ I. Vigness, J. M. Krafft and R. C. Smith, "Effect of Loading History Upon the Yield Strength of a Plain Carbon Steel," Conference on Properties of Materials at High Rates of Strain, London, British Institute of Mechanical Engineers, May 1, 1957.

this discrepancy may be attributable to failure of dislocation theory to fit the data of Fig. 1. I would like to suggest that it may be also the additive damage hypothesis which fails at low temperature. For if we fit a curve through the constant stress data of Fig. 1 (-205°C), and then transpose it to Fig. 3 using the cumulative damage (or additive number of dislocation) hypothesis, the resulting curve lies still further above the experimentally determined points than does that calculated from the authors' theory.

In questions of this kind, the role of pre-yield anelastic microstrain suggests itself as a factor. Would the authors have any estimate of how total microstrain might vary for yielding under these two loading patterns?

Written Discussion: By Professor Takeo Yokobori, Tohoku University, Department of Mechanical Engineering, Sendai, Japan.

May I express the following three comments on the authors' interesting work.

I treated the related phenomena¹⁻³ as a stochastic process or kinetic statistical phenomena on the basis of the dislocation theory, and have given the following formula independently from Campbell.⁷

$$t = t_0 (\sigma / \sigma_0)^{-(1/nkT)} \quad (1)^{2,8}$$

$$\sigma_{yd} = \sigma_0 (\dot{\sigma} t_0 / nkT \sigma_0)^{nkT} \quad (2)^{4,5}$$

where

t = the delay time for yielding under constant applied tensile stress σ .

$t_0 = 1/Z\nu n_0$.

n_0 = a critical number of dislocations required for macroscopic yielding.

$1/n$ = the constant with the dimension of energy.⁶

ν = the vibration frequency of a dislocation.

Z = the number of dislocations anchored in the region of stress concentration such as shoulders of a specimen.

σ_{yd} = the upper yield stress under constant applied stress rate $\dot{\sigma}$.

k = the Boltzmann's constant.

T = absolute temperature, and σ_0 = tensile yield stress at absolute zero temperature.

Equations 1 and 2 are quite the same form as the Campbell's Equations 9 and 10 of the article, and the assumption of critical number of dislocations for macroscopic yield is the same. The standpoint, however, is different. On the other hand, it seems unlikely that at lower stress level the phenomena are kinetic statistical phenomena. The aspect can also be inferred from the fact that below some limiting stress the stress for initiation of yielding does not appear to be temperature and time dependent sensitively. Hence the model was modified taking⁹ account of internal stress σ_1 arising from the presence of other near-by dislocations assembled at a grain boundary as an array of dislocations. Thus the following formulas were given:

$$t = t_0 (\sigma - \sigma_1 / \sigma_0 - \sigma_1)^{-(1/nkT)} \quad (3)$$

$$\sigma - \sigma_1 = (\sigma_0 - \sigma_1) (\dot{\sigma} t_0 / nkT \sigma_0)^{nkT} \quad (4)$$

In Equations 3 and 4 the assumption is made conveniently that general yielding occurs when one dislocation loop is released at the grain boundary. The result,

however, may formally be the same when a critical number of dislocations n_0 is assumed as required for macroscopic yielding. For that case t_0 in Equations 3 and 4 may assume $1/Zm_0$ instead of $1/Z\nu$. Using the same constants (four undetermined constants), the results calculated are roughly in good agreement with the data of the delay time and a few data of the temperature dependence of upper yield stress under constant stress rate on the same mild steel in the authors' literature.* The present data are more efficient in checking the formula of (3) and (4) with experiments.

Secondly, the value of stress concentration factor $q = \sigma/\sigma_0$ obtained fitting to the experimental data ranges from 1.5 to 3.0. From this value it seems that the stress concentration factor by piling-up dislocations, hence, a critical number of dislocations n^* in Equation 4 of the article or n_0 in Equations 1, 2, 3 and 4 are not so large. Then it is hoped that the experiments will be made on the dependence of upper yield stress upon a ferrite path, such as grain diameter. No definite conclusion on grain size dependence seems to be derived from available experiments by Sylwestrowicz and Hall,⁹ because of large scatter and excluding of the lower stress value among the data obtained.

Finally, concerning the fact that the delay time for yielding is essentially infinite at a lower limiting stress, the authors' opinion may be possible. Another interpretation may also be suggested. It has been pointed out by Ramberg and Irwin¹⁰ that the time delay of high strength steel obeys Equation 3 assuming the constant σ_1 as the static yield stress. Also a third probable explanation may be as follows: When applied stress falls below some limiting value, the mechanism of yielding is expected to change from Cottrell type¹¹ (temperature-and-time dependent) to Mott-Nabarro type¹² (temperature-and-time independent) in the presence of internal stress, or to Frank-Read type. It seems to be related to this transition that in the experiments of Kramer and Maddin¹³ with brass, the stress for initiation for yielding does not appear to be temperature and time dependent in the range of small applied stress.

Authors' Reply

The authors are gratified by the searching and stimulating discussion of this paper. Several alternative hypotheses regarding the mechanism of the initiation of yielding in body-centered cubic metals have been presented by the discussions. These, as well as those presented in the paper, may be successfully employed to

* T. Yokobori, "The Cottrell-Bilby Theory of Yielding of Iron," *Physical Review*, Vol. 88, Ser. 2, Dec. 1952, p. 1423.

² T. Yokobori, Paper presented at a meeting of the Physical Society of Japan, May 1953.

³ T. Yokobori, "Delayed Yield and Strain Rate and Temperature Dependence of Yield Point of Iron," *Journal of Applied Physics*, Vol. 25, May 1954, p. 593.

⁴ J. D. Campbell, "The Dynamic Yielding of Mild Steel," *Acta Metallurgica*, Vol. 1, Nov. 1953, p. 706.

⁵ D. S. Wood and D. S. Clark, "The Influence of Temperature Upon the Time Delay for Yielding in Annealed Mild Steel," *Transactions, American Society for Metals*, Vol. 43, 1951, p. 571.

⁶ W. Sylwestrowicz and E. O. Hall, "The Deformation and Aging of Mild Steel," *Proceedings of the Physical Society*, Vol. 64, Sec. B, June 1951, p. 495.

⁷ W. Ramberg and L. K. Irwin, *American Society for Testing Materials*, Special Technical Publication No. 176, 1956, p. 111.

⁸ A. H. Cottrell and B. A. Bilby, "Dislocation Theory of Yielding and Strain Aging of Iron," *Proceedings of the Physical Society*, Vol. 62, Jan. 1949, p. 49.

⁹ N. F. Mott and F. R. N. Nabarro, Report of a Conference on the Strength of Solids, Physical Society, London, 1948, p. 1.

¹⁰ I. R. Kramer and R. Maddin, "Delay Time for the Initiation of Slip in Metal Single Crystals," *Journal of Metals*, Vol. 4, Feb. 1952; *Transactions, American Institute of Mining and Metallurgical Engineers*, Vol. 194, 1952, p. 197.

correlate the data presented. Additional data obtained from diversified experimental measurements are needed to discriminate between the various hypotheses. Experiments in which direct observations of dislocations are made during the process of initiation of yielding would probably be most useful in this respect.

The authors agree with Dr. Campbell that Fisher's approximate activation energy expression does not exhibit a proper limit as the stress becomes large. This may be a partial explanation for the discrepancy between the delay time data at 77 °K and Equation 5 seen in Fig. 1. Nevertheless, Fisher's expression appears to be a sufficiently close approximation at lower stresses. Dr. Yokobori's expression for the activation energy is also an approximation of the complex relation originally derived by Cottrell and Bilby (8). In either case, the approximate expressions are employed in order to simplify the mathematics and obtain expressions for the delay time and upper yield stress in closed form.

Dr. Campbell points out that once an anchored Frank-Read source has been activated it may continue to generate dislocation loops with little or no assistance from thermal fluctuations. However, the existence of a delay time for yielding is difficult to understand if it is assumed that a large number of dislocations are generated from a given source after a single thermally activated process. One of the many sources within a specimen will be thermally activated immediately upon stress application. The large number of dislocations which would then be released within a few microseconds would produce a concentrated stress at the grain boundary sufficient to initiate the generation of dislocations in adjacent grains. Thus delay times of one second and longer could not be explained.

The alternative assumption may be made that on the average the kinetic energy of the source dislocation reduces the magnitude of the thermal activation energy required for release of dislocations from the Frank-Read source, but does not reduce the mean activation energy to zero. This assumption is consistent with the fact pointed out by Fisher (11), that the activation energy obtained by fitting the theory to measured values of the delay time is considerably less than the value predicted by the Cottrell-Bilby theory for the initial dislocation release.

The values of the constants α and ν cannot be determined individually by fitting Equation 5 to the delay time data, as Dr. Campbell has noted. Only the ratio, α/ν may be determined in this manner. Thus the theory given in the paper actually contains only two adjustable constants rather than three.

The value of α given in the paper was determined from the concept of the strength of a perfect crystal. The value $\alpha = 0.159$ gives a theoretical strength in tension of $2\alpha G = 1.9 \times 10^9 \text{ lb/in}^2$. This is equal to the maximum value of the measured tensile strength of iron whiskers reported by Sears and Brenner.* Thus this value is presumed to be equal to the strength of a perfect crystal.

Having chosen the value of α in the above manner, the value of ν may be determined by fitting Equation 5 to the delay time data. The value $\nu = 6.77 \times 10^{10} \text{ sec}^{-1}$ represents the frequency of those thermal fluctuations which are effective in aiding the release of the source dislocation from its "atmosphere". This value of ν appears to be of the correct order of magnitude from the following considerations. The length of the activated portion of the source dislocation at the time of its release from the "atmosphere" may be estimated as follows. The radius of curvature of the activated section of dislocation is given approximately by the relation $2\gamma_0/\sigma b$. A value of $\sigma = 50,000 \text{ lb/in}^2$ gives a radius of curvature of about 250 b.

* G. W. Sears and S. S. Brenner, "Metal Whiskers," *METAL PROGRESS*, Vol. 70, No. 5, 1956, p. 85.

From the work of Cottrell and Bilby (8) it appears reasonable to assume that the center of the activated dislocation segment moves a distance of about $4b$ away from the center of the "atmosphere" during the activation process. These values lead to an estimated length of the activated dislocation segment of about 0.9×10^{-6} in. The wave length of a thermal fluctuation which would cause such a segment to be activated is 1.8×10^{-6} in. Since the velocity of shear waves in iron is about 1.3×10^6 in/sec, the above wave length corresponds to a frequency of about 7.2×10^{10} cycles per sec. This value agrees well with the value of ν selected by fitting Equation 5 to the delay time data.

Dr. Campbell and Dr. Yokobori have suggested that the existence of a lower limiting stress (static upper yield stress) in the stress vs. delay time relation may have explanations other than the influence of back stresses acting on the Frank-Read source. However, the explanation in terms of the back stress appears to be in agreement with a wider range of experimental data (including data given elsewhere than in the present paper) than the other explanations suggested. For example, it has been observed (10) that the microstrains which precede macroscopic yielding proceed at a rate which decreases with time under constant applied stress. This may be interpreted as a decrease with time of the rate at which dislocations are released from anchored Frank-Read sources. The back stress hypothesis explains this observation very simply. The back stress increases as the number of dislocations released from a given source increases. This action decreases the total shear stress at the source which decreases the rate of release of dislocations.

Another experiment** indicates that relocking of dislocations by diffusion of carbon (or nitrogen) atoms is too slow to account for the static upper yield stress. Stress pulses were applied at room temperature in which the time under stress was less than the delay time for the particular stress employed. Repeated pulses, with intervening unloaded periods of several minutes at room temperature, produced yielding when the accumulated time under stress was equal to the normal delay time. Yielding under repeated stress pulses applied at room temperature could be prevented by aging for a critical time at a given temperature during the unstressed periods between load applications. An aging time of 12 minutes at a temperature of 200 °F was required to prevent yielding under repeated stress pulses. The critical aging time was 100 minutes at a temperature of 150 °F. Thus dislocations released during a stress pulse cannot be relocked during a period of a few seconds at room temperature. Such relocking in a few seconds at room temperature would be required to account for the fact that delay times as short as a few seconds are observed at the static upper yield stress.

Experimental measurements (1) have also shown that pre-yield microstrain takes place when a constant stress less than the static upper yield stress is applied. Thus some dislocations are apparently released from atmospheres at stresses below the static upper yield stress. This result indicates that the back stress hypothesis is preferable to those proposed by Dr. Yokobori in his discussion.

Dr. Yokobori has commented that the stress concentration factor associated with a "pile-up" of dislocations is only of the order of 1.5 to 3.0 since the ratio of the yield stress at absolute zero to the applied stress lies in this range. However, according to the dislocation model employed in the paper, this stress ratio is not indicative of the stress concentration produced by an array of like disloca-

** T. Vreeland, Jr., D. S. Wood and D. S. Clark, "A Study of the Mechanism of the Delayed Yield Phenomenon," *TRANSACTIONS, American Society for Metals*, Vol. 45, 1953, p. 620.

tions in the slip plane (i.e., a "pile-up"). The stress concentration factor, according to the present model, is the ratio of the theoretical strength of a perfect crystal to the applied stress, i.e., $2\alpha G/\sigma$. This gives values ranging from about 30 for the highest applied stress employed to about 100 for the lowest applied stress. These values are interpreted to be the number of dislocations which must be accumulated in the slip plane before macroscopic yielding occurs.

The authors agree with Dr. Krafft that the "cumulative damage" hypothesis advanced by Vigness, Krafft and Smith is in effect equivalent to the concept of accumulating dislocations in the slip plane as employed in the present paper. The employment of a physical (dislocation) model, as in this paper, has the advantage that a unified relationship may be obtained which expresses the influence of additional variables upon the initiation of yielding. For example, the expressions for delay time and upper yield stress given in the paper, give the temperature dependence of the phenomenon as well as the influence of time under stress and stress-time history.

The authors also agree with Dr. Krafft that the pre-yield microstrain is of importance in the mechanism of the initiation of yielding in steel. In fact, as the above discussion indicates, the dislocation model employed in the paper is largely based upon observations of pre-yield microstrains. Such observations provide a more direct indication of dislocation mechanisms than observations of yield stress and delay time alone. Measurements have not been made of the pre-yield microstrain under loading conditions other than at a constant applied stress. According to the dislocation model employed, the total pre-yield microstrain is only a function of the stress at which macroscopic yielding occurs. Thus in two tests, employing different stress-time histories, the microstrain is the same if macroscopic yielding occurs at the same stress in the two tests.

Dr. Forscher has advanced the concept that the rate at which Lüders' bands propagate (yield rate) is governed by the same underlying mechanism as that responsible for the delayed yield phenomenon. This is to be expected in the sense that both phenomena involve the release of dislocations from Cottrell "atmospheres", the generation of new dislocations, and the motion of dislocations through the crystal lattice. The quantitative aspects of the propagation of a Lüders' band must involve the stress conditions in the local region containing the boundary of the Lüders' band. However, these stress conditions may be somewhat different than those pertaining to the original initiation of yielding. Thus it is not expected that the formulae given in the paper can be applied in a straightforward manner to the problem of Lüders' band propagation.

SOME ASPECTS OF PREYIELD PHENOMENA IN MILD STEEL AT LOW TEMPERATURES

BY W. S. OWEN, M. COHEN AND B. L. AVERBACH

Abstract

In annealed mild steel tested at room temperature, discontinuous gross yielding occurs at, or above, the static upper yield stress only after a time delay during which the specimen undergoes a small nonelastic strain. A permanent microstrain also occurs at lower stresses, the elastic limit being defined as the lowest stress at which nonelastic strain can be detected. At subzero temperatures, the yield point is less well defined, and at -196°C (-320°F) the static yield stress has proved difficult to determine from the usual load-extension data because of the large nonelastic preyield strain and the long delay times. In this investigation the sequence of events leading to gross yielding at -196°C (-320°F) has been explored by metallographic techniques, by the observation of strain patterns on long thin prepolished specimens, and by precise strain measurements as a function of stress and time. It is found that the transition from the microstrain to Lüders' strain is not abrupt, as it is at room temperature, but occurs by a slowly accelerating creep process which, at certain stress levels, can occupy an appreciable time interval.

The influence of ferrite grain size, austenitizing temperature and cooling rate on the elastic limit and preyield phenomena has been surveyed. The total nonelastic strain at the static yield stress, unlike the yield stress itself, is dependent upon the austenitizing temperature and cooling rate rather than the grain size. The elastic limit at -196°C (-320°F) varies relatively little with grain size, but the elastic limit at room temperature shows a pronounced grain-size dependence. The implications of these data are briefly discussed in qualitative terms by reference to the Clark-Wood dislocation model. (ASM International Classification Q 21, Q 25 n; C N.)

INTRODUCTION

THE NONELASTIC strain which precedes the gross plastic strain (generation of Lüders' bands) in annealed mild steel is an impor-

A paper presented before the Thirty-Ninth Annual Convention of the Society, held in Chicago, November 4-8, 1957. Of the authors, M. Cohen and B. L. Averbach are associated with the Department of Metallurgy, Massachusetts Institute of Technology, Cambridge, Massachusetts and W. S. Owen is presently at the University of Liverpool, Great Britain. Manuscript received November 12, 1956.

tant consideration in recent theories of discontinuous yielding (1-4).¹ Various aspects of the phenomenon have been studied experimentally by Clark, Wood, et al (2,5,6,7,8) using a constant rapidly-applied tension load, by Krafft (9) using compressive wave loading, and by Averbach et al (10,11) using a tension step-load technique. The findings

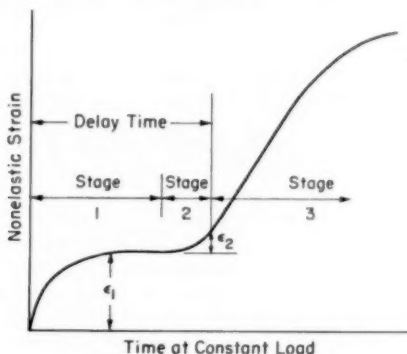


Fig. 1—Diagrammatical Representation of the Three Stages of Nonelastic Strain Leading to Gross Yielding at Constant Load.

may be summarized by reference to the generalized constant-load strain/time curve in Fig. 1. The strain can be separated into three stages:

1. *Microstrain*. Initially this strain increases rapidly but levels off at some constant value which is not more than about 50×10^{-6} .

2. *Microcreep*. This is a time-dependent strain which precedes the gross yielding. In all the work on annealed mild steel reported to date, the onset of gross yielding has been found to occur abruptly, with stage 2 occupying only a very short time interval.

3. *Lüders' strain*. The start of this stage is usually taken as the beginning of gross yielding.

The strain/time curve is influenced by the stress level applied. Below the elastic limit (σ_{EL}), only elastic strain is observed. Between the elastic limit and the "static" upper yield stress (σ_{YS}) the strain increases to the stage 1 plateau and remains constant for an indefinite time. The plateau ϵ_1 increases with applied stress and is somewhat recoverable (anelastic) on releasing the load. At higher stresses, the microcreep stage 2 is reached, but is rapidly followed by stage 3. This pronounced change in behavior occurs at a well defined stress (σ_{YS}). However, even above σ_{YS} the first stage (and possibly the second) can be detected. It occupies a time interval (the delay time) which has been measured systematically by Clark and Wood, (5,6) and by Krafft (9).

¹ The figures appearing in parentheses pertain to the references appended to this paper.

A model, which incorporates the Cottrell-Bilby locking concept and the Frank-Read dislocation mill, has been used by Vreeland and Wood (1,2) in discussions of the above observations. Good quantitative agreement is obtained between the theoretical predictions and the stress/delay-time data, the temperature dependence of σ_{YS} , and the shape of the microstrain/time curve at constant stress provided attention is confined to a temperature range of approximately 23 °C to -130 °C (73 to -202 °F). A somewhat simpler analysis by Fisher (12) also gives good agreement with the experimental data in this temperature range.

At lower temperatures, the only published measurements relate the delay time for some unspecified plastic strain to the applied stress at -196 °C (-320 °F). Existing theories are not even approximately compatible with the experimental data at this temperature (12). In the Clark-Wood experiments (13) at -196 °C (-320 °F) an unusually long time delay before yielding was observed, i.e., of the order of minutes compared with fractions of a second at higher temperatures, and no well defined stress level corresponding to the static yield stress (σ_{YS}) was found. However, precise strain measurements were not made and so the sequence of events leading to gross yielding was not revealed. Accordingly, one of the objects of the present investigation was to examine the constant load/strain-time relations at -196 °C (-320 °F).

The dependence of σ_{YS} on the ferrite grain size is well known from the experiments of Hall (14) at room temperature and Low (16) and Petch (15) at liquid nitrogen temperature. However, the influence of grain size and other metallurgical variables on the elastic limit and on the preyield strains has not been reported previously.

EXPERIMENTAL METHODS

Parallel experiments were carried out on two ship steels: one a semi-killed steel acceptable under American Bureau of Shipping Class B, and the other a rimmed steel with pronounced brittle tendencies. The steels were received in the form of 3/4-inch hot-rolled plate and had the following compositions respectively:

Steel	C	Mn	P	S	Si	Cu	Ni	Cr	V	Mo
B	0.16	0.69	0.014	0.028	0.022	0.028	0.015	0.01	0.005	0.01
E	0.22	0.36	0.016	0.031	0.002	0.17	0.13	0.08	0.005	0.025
	Al	Sn	As	H	N	O				
B	0.027	0.010	0.001	0.0001	0.0023	0.017				
E	0.009	0.012	0.001	0.0001	0.0021	0.006				

Standard 0.252 inch diameter tensile specimens were prepared by heat treating oversized blanks. One set of specimens was allowed to cool freely in air and the other was cooled slowly in the furnace. The austenitizing temperatures were in the range 850-1300 °C (1560-

2370 °F); at higher temperatures severe pearlite divorcement occurred. All the annealed specimens and those normalized in the lower part of the temperature range had approximately equiaxed ferrite grains. Specimens normalized above 950 °C (1740 °F) had pronounced Widmanstätten structures. Some of the specimens were banded; this feature was particularly evident after annealing in the temperature range 850–1050 °C (1560–1920 °F), being more severe in the B steel. A mean ferrite path, a_1 , (the average linear intercept between ferrite-ferrite and ferrite-pearlite boundaries) was measured by lineal analysis using a Hurlbut counter (17). For specimens with equiaxed ferrite, a_1 was converted to the average ferrite grain diameter d ; $d = 1.65a_1$.

Tensile tests on standard round bars were carried out on a hydraulic machine, eccentricity being minimized by loading through long high-carbon steel chains. When electrical resistance strain gages were used, each specimen was fitted with two parallel gages on diametrically opposite sides. These were connected in series to average small effects due to bending; tests in which the strain from each gage was observed separately revealed negligible differences. The gages were isolated from the liquid nitrogen by loose fitting plastic envelopes.

Constant-load experiments were conducted with a cantilever-type dead-load machine. A modified Hounsfield tensometer was used for those Lüders'-band experiments which required exact control and measurement of the strain rate. Some longer specimens with three or more strain gages attached were tested in the hydraulic machine.

EXPERIMENTAL RESULTS

Nature of the Yielding at -196 °C (-320 °F)

The E steel in the "as-received" condition was used in all the experiments to be discussed in this section.

In the first experiments, the standard load-unload procedure for determining the elastic limit and the preyield nonelastic strain was employed (11). The load was applied as quickly as possible (~ 30 seconds), held for a prearranged time and then reduced to zero. The strain both at load and on unloading was measured with a sensitivity of about 2×10^{-6} , by means of SR-4 type electrical resistance gages. The cycle was then repeated at successively higher loads. At -196 °C (-320 °F) it was found that the elastic limit, σ_{EL} , (the smallest stress at which a permanent strain of 2×10^{-6} could be detected on unloading) was not affected by the time that the specimen was held under load. However, this was not true of the strain measured at higher stresses. A comparison between the results obtained with two different loading schedules is afforded by Fig. 2 in which the total strain at load is plotted against the applied stress. At some stress between the elastic limit and the yield point, σ_{YS} , (in this case defined as the lowest stress

at which rapid plastic yielding occurred) the strain was found to increase with time at a constant stress. The additional strain was not recoverable when the load was removed. This microcreep phenomenon is more clearly evident in the strain/time curves of Fig. 3 which are replots of the data relating to curve 2 of Fig. 2.

Later, it was found convenient to define a stress σ_2 as the lowest stress at which creep greater than 10^{-6} per minute could be detected. In these and subsequent experiments of this type, the stress was in-

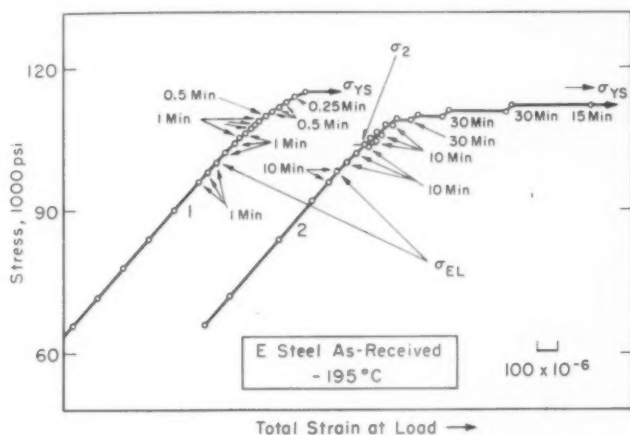


Fig. 2—Influence of Loading Time on Stress-Strain Curve at -196°C (-320°F). E steel as received.

creased in 1000 psi steps. Clearly, the value of σ_2 depends upon the time for which the load is maintained at each stress level. Although a time of 4 minutes was arbitrarily adopted, σ_2 so determined would not differ appreciably from that obtained if time intervals of 30 minutes had been used.

At stress levels between σ_{EL} and σ_2 , a small (less than 30×10^{-6}) nonelastic strain, increasing with increase in stress, was measured on unloading. This appeared very quickly and did not increase with time. Thus, it had all of the characteristics of the microstrain which has been measured previously at higher temperatures.

The yield point was well defined in the step-loading tests; that is, a stress was reached at which an increase of 1000 psi produced a marked increase in the plastic strain rate.

From these experiments, it is evident that all three modes of non-elastic deformation (microstrain, slow creep, and rapid gross yielding) are important at -196°C (-320°F). In the tests just described, these modes were observed at different stress levels. However, the

following experiments showed that they can occur in sequence at a constant stress.

A constant load was applied rapidly by means of a dead-load machine. The strain was measured as a function of time by SR-4 gages and a dial gage indicating cross-head motion. Typical results are shown in Figs. 4 and 5. Fig. 4 illustrates the strain sequence, as denoted by the dial gage, at a stress about 4500 psi below the static yield point.

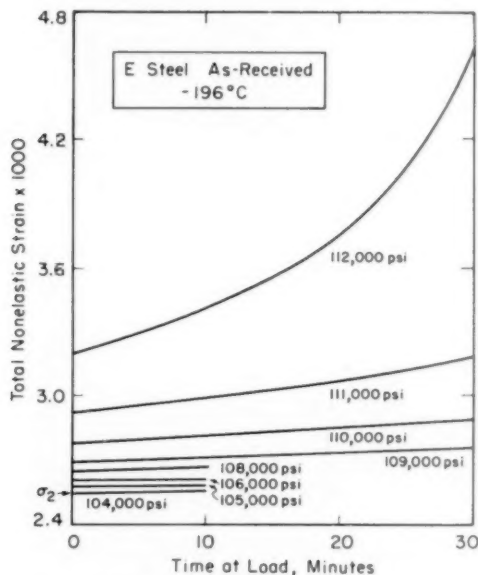


Fig. 3—Creep Strain at Constant Load, with Load Increased in Steps on the Same Specimen at -196°C (-320°F).

The elastic strain and the microstrain (stage 1) have been subtracted. The strain rate first increased (stage 2) until, in this case after about 120 minutes, the rate became constant and rapid (stage 3). After a further period (about 160 minutes in Fig. 4) increased strain hardening set in and the strain rate decreased. Soon afterwards, this particular specimen broke with a cleavage fracture.

The creep strain in stage 2 was revealed more accurately by the SR-4 strain gage readings. The data for three different loads at -196°C (-320°F) and two at -150°C (-238°F) are plotted in Fig. 5. Again the elastic strain and microstrain have been subtracted.

These experiments demonstrate that, if sufficient time is allowed, the stage 2 strain will accelerate to gross yielding (stage 3) at a stress

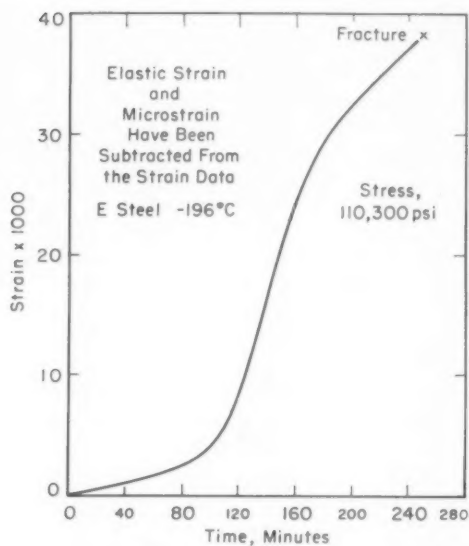


Fig. 4—Strain-Time Curve at Constant Load for E Steel, as Received, Tested at -196°C (-320°F). Strain from dial gage measuring cross-head motion. The upper yield stress in step-load experiments is 115,000 psi.

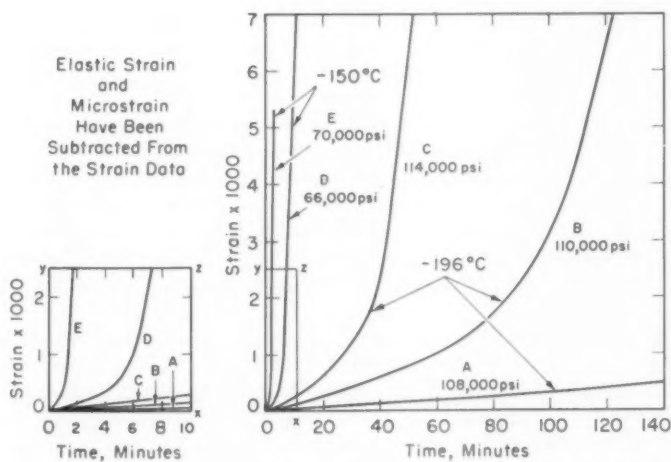


Fig. 5—Strain-Time Curves at Constant Load for E Steel, as Received, Tested at -196°C and -150°C (-320 and -238°F). Strain from SR-4 gages on the specimen.

appreciably below the usually measured static yield stress. Fig. 5 shows that the microcreep stage can also be measured at -150°C (-238°F), although it is less extensive at this higher temperature.

In room temperature tests, no clear evidence of the creep strain was obtained. On loading above the elastic limit, apparently instantaneous microstrain, increasing with the stress, was found until at some well defined stress, σ_{YS} , rapid yielding occurred. However, the yield stress was less well defined for coarse grained specimens, which may be the result of a narrow stress range in which the creep rate is slow enough to be classified as the stage 2 strain. When high speed loading and precise time measurements are employed, a creep stage can be detected at room temperature. Evidence of its existence can be found in data published by Clark and Wood (7) and by Krafft (9).

Curves such as that in Fig. 4 show no discontinuity on a time scale between the second and third stages. However, it is well known that the yield deformation in a tensile specimen is not homogeneous. Thus, it seemed necessary to inquire whether the three stages of strain are sequential or competitive processes. To this end, tests were carried out with specimens 5 inches long at the reduced section, 0.25 inches wide and 0.030 inches thick.

In the first series, one side of these thin-strip specimens was electro-polished and the other had a fine grid ruled with 1-millimeter intervals. The load was applied continuously at a controlled rate, and observations were made on the spread of Lüders' bands, as illustrated in Fig. 6. (The photographs are of comparable specimens unloaded after successively longer yielding times.) A region of deformation extending across the width of the specimen and about 1 millimeter wide first appeared at the shoulders. This initial Lüders' band was oriented at an angle of about 45 degrees with the tension axis (Fig. 6a). Attempts to stop the test before the band had propagated across the specimen width were unsuccessful: evidently, once a band was nucleated, it grew very rapidly. Further deformation occurred by the first band nucleating a second band in criss-cross fashion so that the deformed area enclosed small triangles (Fig. 6b). Subsequently, the crossed bands spread along the specimen (Fig. 6c). In some cases the band fronts appeared sharp, but frequently separate crossed bands were distinctly seen at the moving front (Fig. 6d), suggesting that the nucleation mechanism is perpetuated.

On slow loading, many fine strain markings (also with a criss-cross pattern) were observed on the surface between the Lüders' bands generated from both ends. When the load was applied rapidly the specimens were at maximum load only a short time and the fine markings were either much less distinct or absent. Similar markings have been observed by Paxton (21) on single crystals of iron tested at -196°C (-320°F).

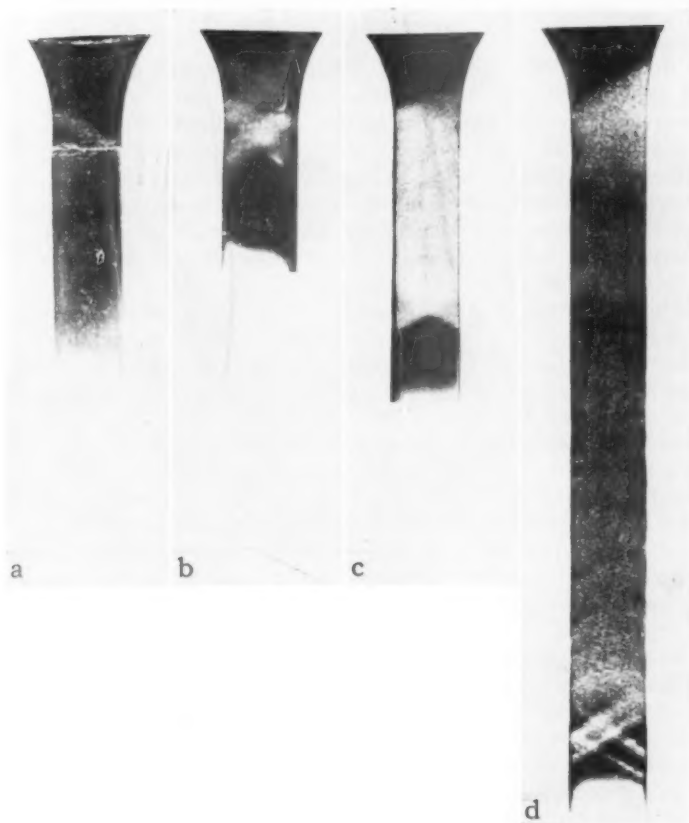


Fig. 6—Stages in the Spread of Lüders' Bands Along the Specimen.

The fine markings between the Lüders' bands were due to stage 2 strain, as shown by the second series of thin-strip tests in which strain gages (with $\frac{1}{2}$ -inch gage length) were placed at both ends and at the center of the specimen. The load was applied in steps and held for 10 minutes at each 1000 psi increment. The elastic limit was reached first at the ends of the specimen. Then, when the center gage indicated that the elastic limit had been attained there, the end gages revealed the second stage behavior. When rapid yielding started at the ends, the center was yielding slowly with time. On unloading, well-defined Lüders' bands were found at the ends and fine slip markings at the center. Thus, it appears that, as the stress is increased above σ_{EL} , the stages of nonelastic strain occur in sequence at any fixed location in the specimen. In the volume affected by the stress concentration at the shoul-

ders, successive stages are reached sooner than in the remainder of the specimen.

In contrast, once the Lüders' bands are nucleated, stages 2 and 3 become competitive; stage 2 creep continues in the central portion of the specimen at the same time as the Lüders' bands spread from the shoulders. With the geometry used in these experiments, the creep in the center did not progress sufficiently to nucleate new Lüders' bands even at the slowest extension rate it was practical to employ (0.0009 inches per minute on a 5-inch gage length). Thus, if fracture did not intervene, the central region was eventually "swept out" by the deformation bands propagating along from either end.

The total strain in stages 1 and 2 measured by a small gage located at the center of the reduced section length depends, in part, upon the time required for the primary Lüders' bands to spread from the shoulders to the gage and, accordingly, upon the length of the specimen and the loading rate. In the standard round-bar specimens, it is reasonable to assume that, although the Lüders' pattern is more complex (22), the general situation is similar. Hence, comparison of the effects of different metallurgical variables is proper only when the loading rate, the specimen dimensions and the gage length are standardized.

All the prepolished thin-strip specimens were examined metallographically. Specimens in the microstrain range (at a stress between σ_{EL} and σ_2) exhibited no change under the microscope, i.e., no evidence of slip was visible. After straining 200×10^{-6} at a stress in the micro-creep range, fine wavy slip was clearly seen in some ferrite grains. Similar slip was found between the Lüders' fronts in specimens loaded for some time at the yield stress. Within the Lüders' bands, the slip markings differed only in the height of the steps and the density of markings in certain grains.

In all specimens, except those with grain size larger than ASTM 4, mechanical twins were detected only in the Lüders' bands and then only a very small fraction of the ferrite grains contained twins. The contribution of twinning to the total strain was minor. In the large-grained specimens, twins were observed both in round bar specimens at stresses below σ_{YS} , and in the portion of the flat specimens unaffected by the Lüders' deformation. However, in all cases the stresses were appreciably above the elastic limit and some slip had occurred in grains remote from the twins. Thus, the elastic limit was not induced by twin formation.

Effects Produced by Some Metallurgical Variables

The step-load technique with round bars and a standardized loading schedule (4 minutes at each 1000 psi step) was used here since this procedure gives much information from relatively few specimens and is well suited to survey work. The values of σ_{EL} , σ_2 , σ_{YS} , ϵ_1 and the non-

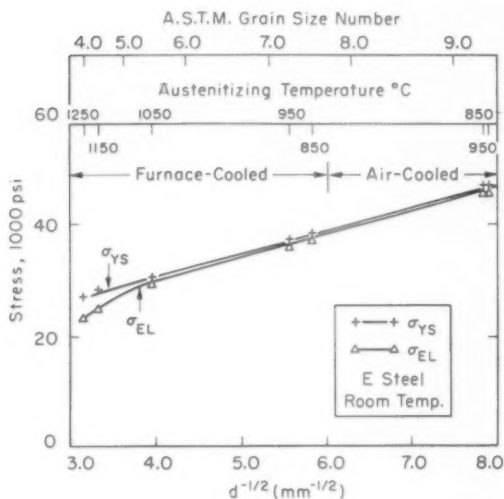


Fig. 7a—Critical Stresses as a Function of Ferrite Grain Size. E steel tested at room temperature.

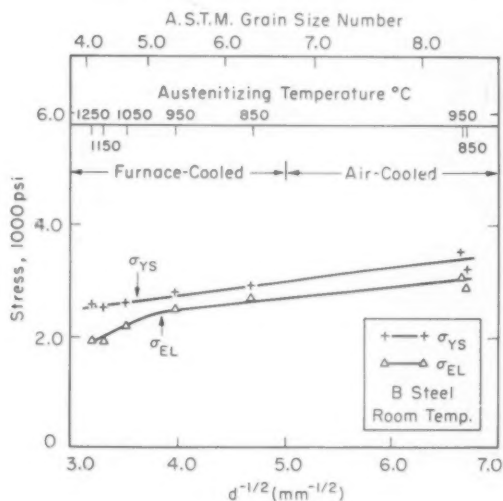


Fig. 7b—Critical Stresses as a Function of Ferrite Grain Size. B steel tested at room temperature.

elastic strain at the start of the third stage ($\epsilon_1 + \epsilon_2$) (see Fig. 1) were obtained, but the method cannot be used to determine delay times.

The room temperature critical stress values (σ_{EL} and σ_{YS}) are plotted

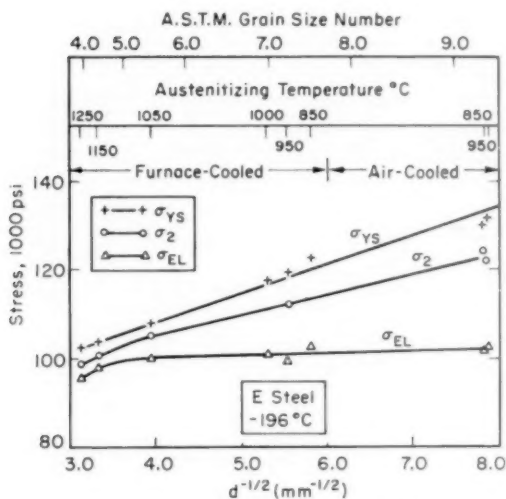


Fig. 8a—Critical Stresses as a Function of Ferrite Grain Size. E steel tested at -196°C (-320°F).

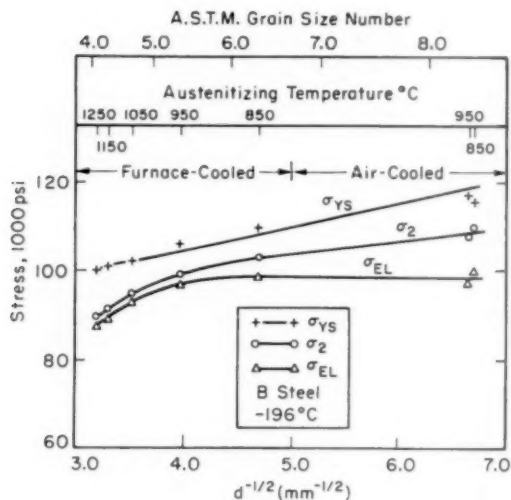


Fig. 8b—Critical Stresses as a Function of Ferrite Grain Size. B steel tested at -196°C (-320°F).

as a function of the reciprocal square root of the mean ferrite grain diameter in Figs. 7a and 7b. Only data from specimens with equiaxed ferrite (not Widmanstätten) are included. The yield points show the

expected linear relationship. σ_{EL} nearly follows along with σ_{YS} at small grain diameters (d) but there is considerable divergence as d is increased. Since the data from air-cooled and furnace-cooled specimens plot on the same curves, it may be deduced that cooling rate has no effect at least within these limits. However, as can be seen by comparing Figs. 7a and 7b, the properties depend on the composition of the steel.

Accurate measurements of ϵ_1 at σ_{YS} were not possible at room temperature due to the rapid variation of strain produced by a small stress change near this point, and so the value of ϵ_1 at 1000 psi below σ_{YS} was recorded. In both the furnace and air-cooled specimens, this strain increased with austenitizing temperature. In the furnace-cooled series, d also increased with austenitizing temperature, but in the air-cooled series (some specimens of which had a Widmanstätten structure) the mean ferrite path and the yield stress remained essentially constant. Thus, the microstrain seems to depend on the austenitizing temperature *per se* rather than on the ferrite grain size.

The data relating σ_{EL} , σ_2 and σ_{YS} at liquid nitrogen temperature with $d^{-1/2}$ for specimens with equiaxed structures are plotted in Figs. 8a and 8b. σ_{YS} is a linear function of $d^{-1/2}$. For σ_2 , the relationship holds approximately but there is some deviation from linearity at large grain sizes. The variation of σ_{EL} in all the specimens tested, furnace-cooled and air-cooled, was relatively small (compare Figs. 8a, 8b, 9b and 10b), although some decrease was detected at the largest grain sizes of the furnace-cooled series (Figs. 8a and 8b). In the air-cooled specimens with Widmanstätten structures and approximately constant mean ferrite path, neither σ_{YS} , σ_2 or σ_{EL} was affected by a change in austenitizing temperature (Figs. 9b and 10b).

The total nonelastic strain ($\epsilon_1 + \epsilon_2$) at 2000 psi below the upper yield stress is shown in Figs. 9a and 10a. In each series the strain increased with austenitizing temperature even though the mean ferrite path did not change significantly in the air-cooled specimens.

The foregoing comparisons show that in both the air-cooled and furnace-cooled specimens, the stresses σ_{YS} , σ_2 and σ_{EL} are changed only by heat treatments which produce a change in d or a_1 and, thus, it is concluded that the mean ferrite path is a primary variable; that is, the critical stresses are grain-size dependent. On the other hand, the pre-yield nonelastic strains ($\epsilon_1 + \epsilon_2$) close to the yield stress are sensitive to cooling rate and to changes in the austenitizing temperature which do not produce a change in the mean ferrite path. Therefore, it seems reasonable to conclude that a change in ferrite grain size is not the primary cause of changes in these properties.

In the Widmanstätten structures there was some increase in length of the ferrite plates with austenitizing temperature, but the breadth did not change materially. Because the mean ferrite path depends mainly

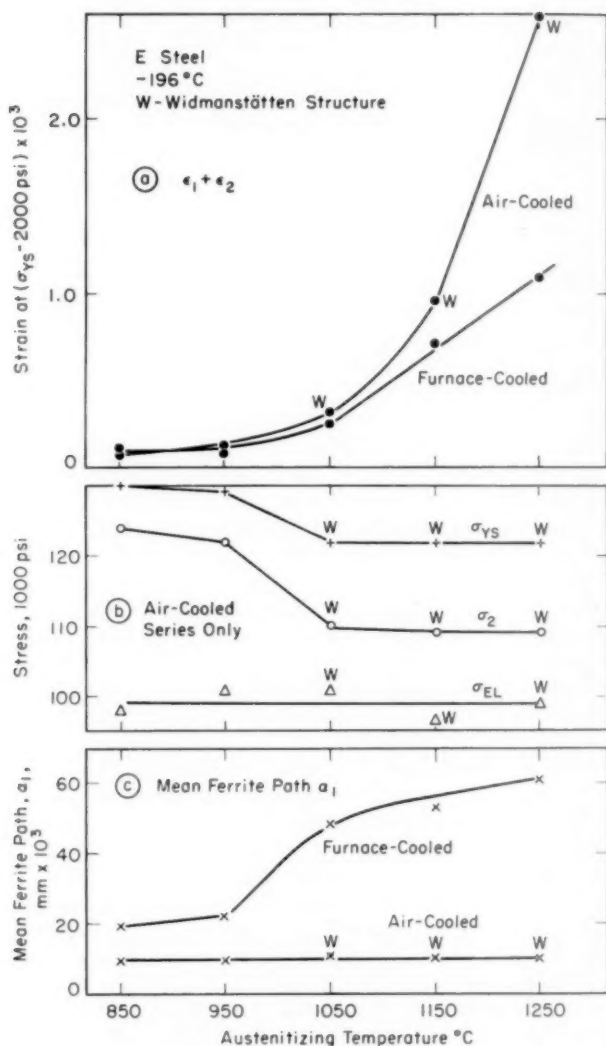


Fig. 9—Properties of E Steel at -196°C (-320°F) as a Function of Austenitizing Temperature. a. Nonelastic preyield strain ($\epsilon_1 + \epsilon_2$) at 2000 psi below δ_{ys} . b. δ_{ys} , σ_2 and σ_{EL} for air-cooled series. c. Mean ferrite path a_1 .

on the latter dimensions, a_1 was insensitive to the austenitizing temperature, but it is thought that the preceding argument remains valid.

In addition to the factors discussed, σ_{EL} and ϵ_1 at room temperature,

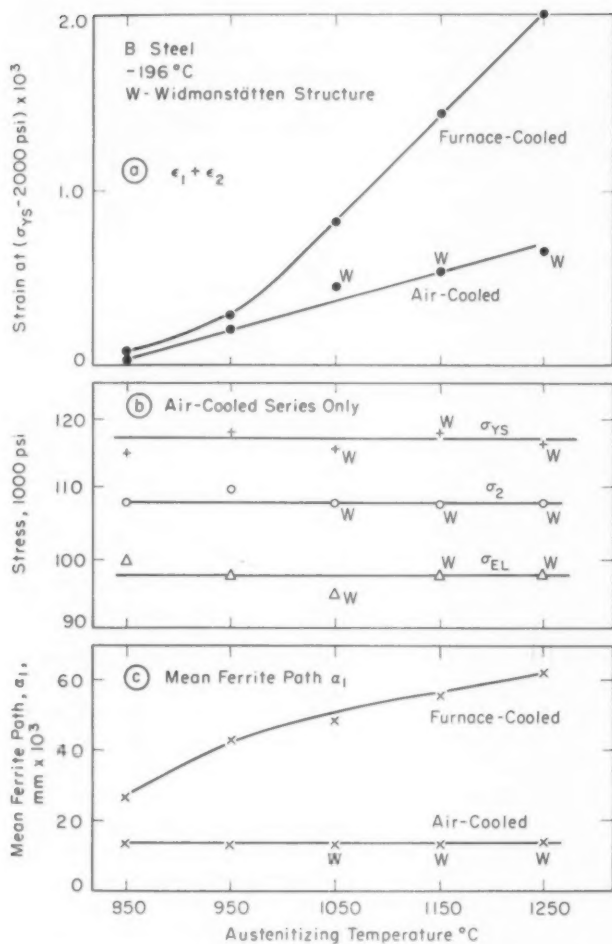


Fig. 10—Properties of B Steel at -196°C (-320°F) as a Function of Austenitizing Temperature. a. Nonelastic preyield strain ($\epsilon_1 + \epsilon_2$) at 2000 psi below δY_S . b. δY_S , $\delta \sigma_2$ and $\delta \epsilon_L$ for air-cooled series. c. Mean ferrite path a_1 .

σ_2 and ($\epsilon_1 + \epsilon_2$) at -196°C and σ_{YS} at both temperatures are different in the two steels. Evidently steel chemistry is an important factor.

GENERAL DISCUSSION

The most striking difference between the room temperature and liquid nitrogen temperature results is the slow transition from stage 1 microstrain to stage 3 Lüders' strain at the lower temperature. The

stage 2 microcreep, indicated by small gages which do not cover the total length of the reduced section of the specimen, occurs between the start of the time-dependent deformation and the arrival of Lüders' bands initiated earlier at the shoulders. Hence, in part, the prominence of the stage 2 creep in the low temperature experiments is due to the long delay in initiating the Lüders' strain at the shoulders and the slow spread of the bands along the specimen. Since transition creep assumes a conspicuous role at -196°C (-320°F) it is important that some criterion of "gross" yielding be adopted when measuring delay times at this temperature.

The prominence of microcreep at -196°C (-320°F) causes σ_{YS} to be strongly dependent upon the loading rate in the usual continuous-loading engineering test. Further, at slow loading rates the upper yield point jog in the stress-strain curve is less clearly defined at -196°C (-320°F) than at room temperature and appreciable deviations from elastic behavior can be detected in autographic load-extension plots before the upper yield is reached. This type of behavior has been found previously at room temperature in very low carbon steels (6) and in molybdenum containing traces of carbon (20). In these cases the blurring of the yield-point jog has been ascribed to incomplete dislocation locking due to the shortage of carbon or nitrogen atoms. This explanation does not appear to be tenable in the present case since the sharp yield point at room temperature can be taken as evidence of efficient locking and there is no reason to suppose that condensed carbon atmospheres formed above room temperature can be dispersed by lowering the temperature.

Wood et al (1,2,18,19) have given a detailed treatment of the yield phenomena in polycrystalline mild steel in terms of well-known dislocation concepts. Briefly, this model assumes that in annealed steel, Frank-Read sources on potential slip planes are locked by carbon atoms. When a local shear stress, sufficient to activate a source is applied, a dislocation loop is generated which spreads rapidly until it is blocked at a grain boundary. Successive loops are released provided the local stress remains large enough to separate the dislocation from the carbon atmosphere. The resulting concentric dislocation rings pile up against the grain boundary producing two effects: a back stress acting on the source, which will slow down and eventually stop the generation of dislocations, and a stress concentration in the neighboring crystal. If the source stops before the stress concentration induces slip in the next crystal only a microstrain is observed (ϵ_1). Gross yielding is assumed to occur when the stress concentration in adjacent grains is sufficient to activate dislocation sources in these crystals.

The present data are not suitable for comparison with the quantitative developments of the theory. However, they do provide a basis for discussion of certain qualitative aspects of the model. Ideally, the elastic limit should be defined as the lowest stress at which a dislocation

loop is released from a source. In practice such small strains cannot be detected and the elastic limit is defined as the stress to produce a certain nonelastic strain: in the present case, this strain is taken as 2×10^{-6} . Consequently, the first nonelastic strain detected experimentally is a microstrain at a stress somewhat greater than the minimum stress required to activate the first source. Vreeland and Wood (2) have predicted that ϵ_1 is dependent upon the distance between the source and the boundary and thus, upon the grain size, since it is reasonable to assume that the sources which contribute most to the microstrain are those located near the center of the grain. When, as in the present experiments, the nonelastic strain is measured after removing the load there is a further complication. Without the restraint of the applied resolved shear stress, the dislocation rings relax to some extent and the nonelastic strain decreases. Thus, the model predicts that small microstrains, and therefore the experimental elastic limit, are dependent upon grain size, although simple relations between these factors are not anticipated. The present data show that, in fact, the experimental elastic limit is influenced by the ferrite grain size. However, the diminution of this influence at low temperatures is apparently not predicted by the Clark-Wood model.

The theory indicates that the microstrain ϵ_1 at σ_{YS} should increase with grain size, and in the furnace-cooled specimens at room temperature this phenomenon was observed. However, in the air-cooled series, where there was little change in the mean ferrite path, the change of ϵ_1 at σ_{YS} as a function of austenitizing temperature was unexpected. Two possible contributing factors can be suggested. The change in the length of the Widmanstätten ferrite plates, which was not reflected in a_1 , may influence the microstrain in a similar manner to that produced by a change in grain diameter of equiaxed ferrite. In addition, the austenitizing may influence the extent or distribution of submicroscopic impediments to the movement of dislocations within the ferrite.

The appearance of microcreep at low temperatures seems to dictate some revision of that part of the theory concerned with the genesis of Lüders' strain. It has been assumed that gross yielding ensues as soon as the necessary internal stress concentration has been achieved. The present experiments have shown that this is not so at low temperatures. The measured preyield nonelastic strains are the result of observable slip and are much larger than the small microstrains considered in the model. The present observations can be taken as substantial support for the view that plastic strain on a macroscale is a prerequisite of Lüders' band generation (14).

CONCLUSIONS

At liquid nitrogen temperature, appreciable nonelastic strains precede gross yielding in annealed mild steel. In addition to microstrain (of the same nature as that found at room temperature) there is an

appreciable creep strain which increases with time at a constant load. There is also a well-defined elastic limit (σ_{EL}), a stress (σ_2) at which the creep strain first appears in fairly short time tests, and a yield stress, (σ_{YS}) which is much more sensitive to loading rate than in room temperature tests. At both temperatures, changes in the metallurgical condition of the steel produce appreciable effects:

1. At room temperature, the elastic limit is grain-size dependent and is sensitive to a change in steel chemistry. At -196°C , (-320°F), it is relatively unaffected by metallurgical factors except when the ferrite grain-size is large.

2. At room temperature, σ_2 so nearly coincides with the yield stress that it could not be detected in these experiments. At -196°C (-320°F), σ_2 lies between σ_{EL} and σ_{YS} , and is grain-size dependent.

3. At both temperatures, σ_{YS} is a linear function of the reciprocal square root of the mean ferrite grain diameter.

4. The room temperature microstrain (ϵ_1) at the yield stress is dependent upon the austenitizing temperature, the cooling rate, and the steel chemistry; grain-size being a secondary effect. The total preyield nonelastic strain ($\epsilon_1 + \epsilon_2$) at liquid nitrogen temperature shows similar trends.

Mechanical twinning plays no part in the yield phenomena at room temperature. However, at -196°C (-320°F) a few twins are found in all the specimens after gross yielding has occurred. In coarse-grained steels some twins are formed during the microcreep stage, but in all cases twinning is preceded by slip. None of the critical stress levels (σ_{EL} , σ_2 and σ_{YS}) can be associated with the first appearance of mechanical twins and, in general, twinning is not a significant factor in the preyield deformation of mild steel at liquid nitrogen temperature.

ACKNOWLEDGMENTS

The work was supported by the Ship Steel Subcommittee of the Ship Structure Committee under Contract No. Nobs-65918. The assistance of R. Asimov, who performed the constant load experiments, and R. C. Whittemore, E. Howell and E. Keplin is gratefully acknowledged.

References

1. T. Vreeland and D. S. Wood, *ONR Report*, California Institute of Technology, April 1954.
2. T. Vreeland, Jr., D. S. Wood and D. S. Clark, "Preyield Plastic and Anelastic Microstrain in Low-Carbon Steel," *Acta Metallurgica*, No. 4, Vol. 1, July 1953, p. 414.
3. A. N. Holden, "Dislocation Collision and the Yield Point of Iron," *Journal of Metals*, Vol. 4, Feb. 1952; *Transactions*, American Institute of Mining and Metallurgical Engineers, Vol. 194, 1952, p. 182.
4. E. Orowan, *Dislocations in Metals*, 1954. American Institute of Mining and Metallurgical Engineers, New York.

5. D. S. Wood and D. S. Clark, "The Influence of Temperature Upon the Time Delay for Yielding in Annealed Mild Steel," *TRANSACTIONS, American Society for Metals*, Vol. 43, 1951, p. 571.
6. D. S. Wood and D. S. Clark, "Delayed Yield in Annealed Steels of Very Low Carbon and Nitrogen Content," *TRANSACTIONS, American Society for Metals*, Vol. 44, 1952, p. 726.
7. T. Vreeland, Jr., D. S. Wood and D. S. Clark, "A Study of the Mechanism of the Delayed Yield Phenomenon," *TRANSACTIONS, American Society for Metals*, Vol. 45, 1953, p. 620.
8. D. S. Clark, "The Behavior of Metals Under Dynamic Loading," *TRANSACTIONS, American Society for Metals*, Vol. 46, 1954, p. 49.
9. J. M. Krafft, "Effect of Temperature on Delayed Yielding of Mild Steel for Short Loading Duration," *TRANSACTIONS, American Society for Metals*, Vol. 48, 1956, p. 249.
10. C. S. Roberts, R. C. Carruthers and B. L. Averbach, "The Initiation of Plastic Strain in Plain Carbon Steels," *TRANSACTIONS, American Society for Metals*, Vol. 44, 1952, p. 1150.
11. H. Muir, B. L. Averbach and M. Cohen, "The Elastic Limit and Yield Behavior of Hardened Steels," *TRANSACTIONS, American Society for Metals*, Vol. 47, 1955, p. 380.
12. J. C. Fisher, "Application of Cottrell's Theory of Yielding to Delayed Yield in Steel," *TRANSACTIONS, American Society for Metals*, Vol. 47, 1955, p. 451.
13. D. S. Wood, and D. S. Clark, *ONR Report*, California Institute of Technology, December 1951.
14. W. Sylwestrowicz and E. O. Hall, "The Deformation and Aging of Mild Steel," *Proceedings of the Physical Society*, Section B, Vol. 64, June 1951, p. 495.
15. N. J. Petch, "The Cleavage Strength of Polycrystals," *Journal, Iron and Steel Institute*, Vol. 174, May 1953, p. 25.
16. J. R. Low, Jr., "The Relation of Microstructure to Brittle Fracture," Paper from American Society for Metals Seminar, *Relation of Properties to Microstructure*, Vol. 46A, 1954, p. 163.
17. R. T. Howard and Morris Cohen, "Quantitative Metallography by Point-Counting and Lineal Analysis," *Transactions, American Institute of Mining and Metallurgical Engineers*, Vol. 172, 1947, p. 413.
18. T. Vreeland, D. S. Wood, and D. S. Clark, *ONR Report*, California Institute of Technology, September 1952.
19. J. A. Hendrickson, D. S. Wood, and D. S. Clark, *ONR Report*, June 1955.
20. J. A. Hendrickson, D. S. Wood and D. S. Clark, "The Initiation of Discontinuous Yielding in Ductile Molybdenum," *TRANSACTIONS, American Society for Metals*, Vol. 48, 1956, p. 540.
21. H. W. Paxton and A. T. Churchman, "The Effect of Temperature and Composition on the Deformation of Single Crystals of Iron," *Acta Metallurgica*, Vol. 1, Sept. 1953, p. 473.
22. H. W. Paxton and I. J. Bear, "Further Observations on Yield in Single Crystals of Iron," *Journal of Metals*, Vol. 7; *Transactions, American Institute of Mining and Metallurgical Engineers*, Vol. 203, Sept. 1955, p. 989.
23. W. M. Lomer, "The Yield Phenomenon in Polycrystalline Mild Steel," *Journal of the Mechanics and Physics of Solids*, Vol. 1, Oct. 1952, p. 64.

DISCUSSION

Written Discussion: By E. T. Wessel, Metallurgy Department, Westinghouse Electric Corporation, Research Laboratories, Pittsburgh.

The authors are to be complimented for their enlightening investigation of the sequence of events which occur during the early stages of plastic flow in mild steel. While the existence of small amounts ($\sim 10^{-4}$) of nonelastic strain prior to abrupt yielding had been recognized and studied previously (see authors' refer-

ences), many of the aspects were not well defined or understood. In the past most of the work was primarily concerned with measurements of the delay time for yielding as a function of the applied stress and temperature. The present investigation included the additional desirable features of precise strain measurements, metallographic observations and studies of the influence of metallurgical variables. In the discussor's opinion these additional observations have contributed substantially to a more detailed understanding of the phases of the early stages of plastic flow.

It seems appropriate at this time to relate the findings of this paper to other similar observations of the preyield phenomena which have been reported² for several body-centered cubic metals including mild steel (Fig. 11). These data were obtained in a different manner from that described in the present paper. The authors' results were obtained with stepwise and constant loading techniques,

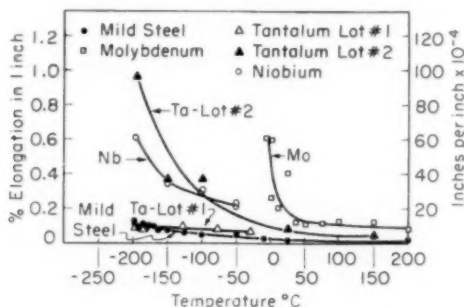


Fig. 11—Plastic Strain Preceding Abrupt Yielding.

whereas the data of Fig. 11 were obtained from tension tests where the load was continuously applied at a constant rate of crosshead movement ($\sim 1 \times 10^{-3}$ sec.⁻¹). As a result of the difference in test techniques, a direct comparison of the results is not possible. However, some qualitative comparisons can be described.

The plastic strain shown in Fig. 11 for the constant crosshead movement tests is the total amount which was observed prior to abrupt yielding (pronounced drop in load or formation of a Lüders' band). Although no exact distinction between different phases of preyield plastic flow could be specified for these tests, an examination of the stress-strain curves suggests a possible correspondence with the three stages of plastic flow described by the authors. These stress-strain curves (up to the onset of abrupt yielding) are shown in Figs. 12 to 15 for different body-centered cubic metals including a mild steel quite similar to that used in the current experiments. Unfortunately, plastic strains smaller than 0.01 percent (10^{-4}) could not be determined accurately with the strain measuring techniques that were used. Hence, the portions of the curves preceding 0.01 % (10^{-4}) plastic strain are not shown.

In the case of these four metals (Figs. 12 to 15) the plastic strain can be divided into three regions or categories. First there is a region (No. 1) where the stress rises rapidly with increasing strain. As the total amount of strain increases in this

² E. T. Wessel, "Abrupt Yielding and the Ductile-to-Brittle Transition in Body-Centered Cubic Metals," *Journal of Metals*, Vol. 9, July 1957, p. 930.

region, the rate of stress increase decreases. The observed behavior for this region is compatible with a dislocation pile-up type of explanation. It is visualized that dislocations are originally pinned by a Cottrell³ atmosphere, but some start to tear away at stresses which are considerably lower than currently measurable elastic limits. As the stress rises, increasing numbers of dislocations are torn loose and move through the lattice. These dislocations then propagate until they are piled-up at barriers which forestall further propagation, i.e., grain or subgrain boundaries, hard particles or phases, other dislocation groups, etc. An appreciable amount of plastic strain is associated with the propagation of these many dislocation groups.

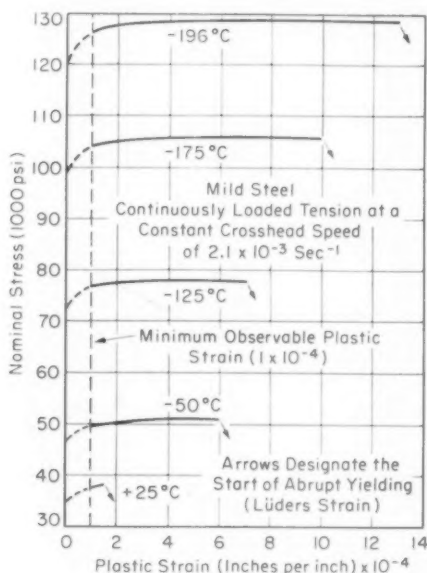


Fig. 12—Stress-Strain Relationship Prior to Abrupt Yielding in Mild Steel at Various Temperatures. (250 grains per sq. mm.)

This behavior leads into a second region (No. 2, Figs. 12 to 15) where considerable amounts of plastic strain occur at a relatively constant stress. This is believed to be indicative of a region where large numbers of the piled-up dislocation groups are able to break through or away from their barriers because of the high stress concentrations which develop in the vicinity of the pile-ups. This breakthrough can be accomplished by the activation of new dislocation sources in adjoining material and by the continued propagation of previously piled-up groups through adjacent material. As this process gains momentum more and more plastic strain can occur without any necessity for an increase in the applied (general) stress level. This breaking-through could be expected to occur generally throughout the gage length of the sample and to produce observable slip.

³A. H. Cottrell and B. A. Bilby, "Dislocation Theory of Yielding and Strain Aging of Iron," *Proceedings, Physical Society*, Vol. 62, Sec. A, Jan. 1949, p. 49.

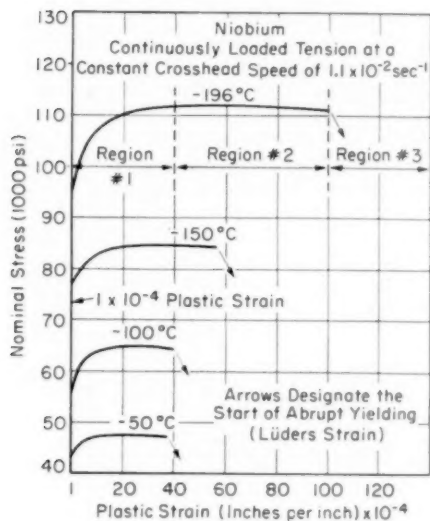


Fig. 13—Stress-Strain Relationship Prior to Abrupt Yielding in Niobium at Various Temperatures. (4 grains per sq. mm.)

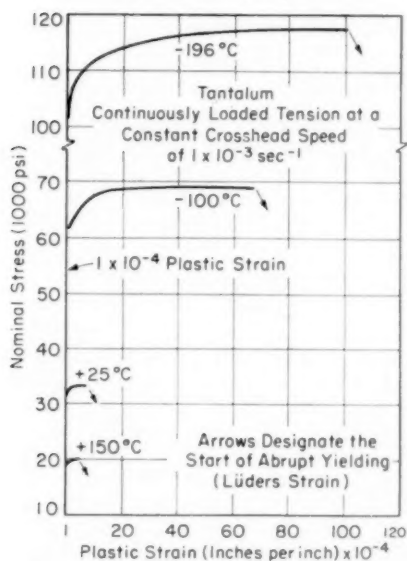


Fig. 14—Stress-Strain Relationship Prior to Abrupt Yielding in Tantalum at Various Temperatures. (500 grains per sq. mm.)

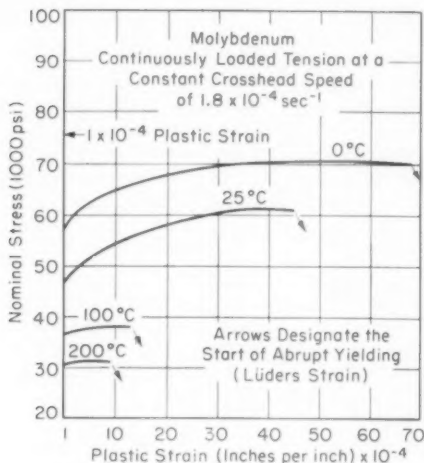


Fig. 15—Stress-Strain Relationship Prior to Abrupt Yielding in Molybdenum at Various Temperatures. (1000 grains per sq. mm.)

The abrupt gross yielding (formation of a Lüders' band, region No. 3) then takes place when sufficient breakthrough momentum develops in some localized region to cause the whole process to be greatly accelerated in this region. The resulting large amount of localized strain constitutes the Lüders' band. Any region of a specimen where there may be some general stress concentration would be the most logical area for the first occurrence of an accelerated breakthrough. Lüders' bands are nearly always first observed at the end of the gage length of a test specimen (shoulders) where such a general stress concentration exists.

All three of the regions of strain just described are most distinct for the case of niobium (Fig. 13) and tantalum (Fig. 14). In the case of the mild steel (Fig. 12), region No. 1 is not so well defined. Apparently in this case the amount of strain associated with the rapid rise in stress is relatively small and most of the region No. 1 behavior is, therefore, presumed to have occurred at plastic strains smaller than 10^{-4} . The stage No. 1 (microstrain) observed in the authors' steel was reported to also be relatively small (max. of $\sim 50 \times 10^{-6}$).

On the basis of the foregoing description of the stress-strain curves and the data reported by the authors, one might derive the following qualitative correlations:

Region No. 1 of the stress-strain curves where the stress increases rapidly with increasing strain may be likened unto stage No. 1 (microstrain).

Region No. 2 where straining occurs at a relatively constant stress would correspond to stage No. 2 (microcreep).

Region No. 3 where abrupt (gross) yielding occurs is comparable to stage No. 3 (Lüders' strain).

In order to establish a more positive correlation, it would be necessary to conduct

further experiments using the different types of tests on the same material and appropriate metallographic observations.

Some further substantiation of a correlation can be seen in terms of the relative amounts of preyield strain (ϵ_1 and ϵ_2) which occur at different temperature levels. The authors are apparently unable to report any specific differences in the amounts of microstrain (ϵ_1) between room temperature and -196°C (-320°F). However, it may be reasonable to expect larger amounts of ϵ_1 at the lower temperatures because of the higher stresses involved and the larger stress differences between the various yield criteria. In the case of the tensile data (Figs. 12 to 15) the magnitude of the strain which occurs in region No. 1 (ϵ_1) increases with decreasing temperature.

The authors do report that ϵ_2 (microcreep stage) increases considerably at lower temperatures, being essentially absent at room temperature and of the order of 10^{-3} at -196°C (-320°F). As seen in Figs. 12 to 15, the amount of strain which occurs in region No. 2 (ϵ_2) increases with decreasing temperature in all cases. Hence, the two investigations show good agreement in this respect. In fact, the values of ϵ_2 at -196°C (-320°F) for both mild steels are essentially equivalent ($\sim 10^{-3}$).

It is also apparent from Figs. 12 to 15 that ϵ_1 and ϵ_2 increase progressively with decreasing test temperature in all of the metals studied. Thus the behavior pattern is quite consistent. The magnitude of either ϵ_1 or ϵ_2 varies considerably between metals. Likewise the amount of this preyield plastic strain can vary considerably between lots of any one metal, i.e., the two lots of tantalum shown in Fig. 11. The authors also observe variations of ($\epsilon_1 + \epsilon_2$) between different lots of steel (E and B in Figs. 9 and 10), as well as in any one steel as a function of its heat treatment. The authors conclude that variations in steel chemistry, austenitization treatment and cooling rates influence the preyield behavior. It is suggested that these factors govern the extent or distribution of submicroscopic impediments, hence, influence the movement of dislocations within the ferrite. The same is thought to be true for the two lots of tantalum (Fig. 11) since no obvious difference in grain size or microstructure can be seen with the light microscope, yet a tenfold difference in preyield strain is observed at the lower temperatures. Further refined studies appear to be necessary before many of these details concerning the governing factors during the early stages of plastic flow can be understood.

In general the observations and discussion of these two independent investigations of the preyield phenomena are in very good agreement. The three regions of plastic strain observed in the continuously loaded, constant crosshead speed tests seemingly correspond quite well with the three stages of strain described by the authors for the stepwise and constant load tests. Both investigations provide a substantial amount of experimental evidence which indicates that plastic deformation on a macroscopic scale is a prerequisite of Lüders' band generation, particularly at low temperatures. These observations indicate that a modification of current concepts relative to abrupt yielding (onset of Lüders' strain) is necessary. A generalized concept which agrees quite well with the observations and discussion presented in the authors' paper has been suggested.⁹ Further detailed work of the quality and type described by the authors of the present paper will, undoubtedly, be of much value in providing further contributions to the understanding of the factors involved in the early stages of plastic flow.

THE ENERGY STORED IN INGOT IRON DEFORMED BY TORSION AT 25, -82 AND -185 °C

BY T. P. WANG AND NORMAN BROWN

Abstract

Stored energy of Armco ingot iron previously deformed at 25, -82 and -185 °C by torsion were measured during its release upon annealing. Energy from 0.3 to 1.1 cal./gm. was found to release in two stages. The first stage of energy release is attributed to recovery. The release of the major portion of the stored energy is concurrent with recrystallization. (ASM International Classification Q24, Q1, N5; Fe-a)

INTRODUCTION

EXPERIMENTAL evidences (1 to 13) as summarized in Table I indicate that stored energy introduced by plastic deformation of a metal can be measured. Most measurements were made upon the release of the stored energy during annealing of the deformed metal. Theoretical analyses (14 to 17) reveal that energy is stored through the increase in density of dislocations and vacancies; and its release is attributed to the annihilation of dislocations and vacancies.

Previous results on stored energy measurements were obtained on metals (mostly copper) deformed at room temperature. Different observations were reported on energy release in connection with recrystallization (6,8 to 11). It is the object of this investigation to construct an apparatus for the precision measurement of energy stored in ingot iron deformed at different temperatures.

EXPERIMENTAL PROCEDURE

General Principle

An experimental apparatus for measuring "temperature difference" during annealing was constructed based on Quinney and Taylor's method (4)¹ with modifications. This method was chosen because it

¹ The figures appearing in parentheses pertain to the references appended to this paper.

This paper is based on a thesis submitted by T. P. Wang as partial fulfillment for the Degree of Doctor of Philosophy in Metallurgy at the University of Pennsylvania.

A paper presented before the Thirty-Ninth Annual Convention of the Society, held in Chicago, November 4-8, 1957. Of the authors, T. P. Wang is Research Metallurgist of Wilbur B. Driver Co., Newark, New Jersey; Norman Brown is associate professor of Metallurgy at the University of Pennsylvania, Philadelphia. Manuscript received April 15, 1957.

Table I
Previous Work on Experimental Measurement of Stored Energy

Investigators	Material Used	Method of Deformation	Mechanical Energy Expended cal./gm.	Method of Measurement	Stored Energy cal./gm.	Temp. Range at Which Energy Was Released	Density of Dislocation per cm ²
Bever & Ticknor (1)	75:25 Au:Ag	Rolling	.5 to 12	Isothermal	.02 to .16		
Borelius (2)	Al	Tension					
Sato (3)	70:30 Cu:Ag	Rolling	4.2	Isothermal	8 cal./mole		
Quinney & Taylor (4)	Brass	Torsion	18.1	Temp. Diff.	.18	200° to 450 °C	
Welber (5)	Copper	Torsion	5.6	Temp.	.32	650° to 750 °C	
Suzuki (6)	Iron	Torsion	7.8	Diff.	.5	100° to 250 °C	
	Copper	Compression	11.9	Temp. Diff.	1.2	120° to 180 °C	
	Copper			Specific Heat	.41	180° to 300 °C	
Stansbury et al. (7)	Cu:Ag	Cold Swaging		Heat Specific	.8	375° to 400 °C	
Clarebrough et al. (8, 9, 10)	Copper	Torsion	3.84 to 34.30	Heat Power Diff.	.9	400 °C	
	Nickel				.1 to .33	290 °C	
	Copper	Fatigue			.33	50° to 370 °C	
Clarebrough et al. (11)	Copper	Compression			.05	530° to 650 °C	
	Copper	Tension		Power Diff.	.167	220° to 450 °C	
	Nickel	Torsion		Power Diff.	.075		1.2 x 10 ¹¹
	Arsenic	Torsion		Power Diff.	.30		5.6 x 10 ¹⁰
	Copper	Torsion		Power Diff.	.145		1.1 x 10 ¹¹
	Au:Ag	Torsion		Power Diff.	.05		1.6 x 10 ¹¹
		Filling		Power Diff.	.26		up to 3.7 x 10 ¹⁰
Greenfield & Bever (12)					.1 to .4		up to 1.9 x 10 ¹¹
Gordon (13)	Copper	Tension		Isothermal	2.52 to 6.21 cal./g. atom	160° to 200 °C	

enables one to obtain not only the magnitude of stored energy but also the temperature at which it releases during annealing. Modifications were introduced to improve accuracy and, at the same time, to make it possible for one person to obtain all measurements during experimental runs.

Quinney and Taylor's method consisted of heating a cold worked metal in vacuum to a temperature above its recrystallization range at a controlled heating rate. This was accomplished by use of a small heater inside the specimen. The whole assembly was placed in a radiation shield which was heated externally and manually controlled to the same temperature as that of the specimen. By comparing the temperature versus time curves (heating curves) of two successive runs, a temperature difference can be observed at the range where stored energy in form of heat is given off at the first run. This energy can be calculated from the product of observed temperature difference and the specific heat of the specimen at the temperature heat is given off.

In the present study, instead of twice annealing the cold worked specimen, two identical specimens, one cold-worked, one annealed, were heated together and the instantaneous temperature difference between them were measured. The stored energy liberated during annealing was similarly calculated.

Description of Apparatus

The principal apparatus in this study consisted of (a) equipment for the measurement of specific heat and (b) equipment for the measurement of temperature difference during annealing.

The specific heat of ingot iron in calories per grams per °C at different temperatures up to 800 °C (1470 °F) was measured in helium atmosphere with an apparatus based on Smith's design (18).

The schematic diagram of the assembly of the apparatus is shown in Fig. 1.

The cold-worked and the annealed specimens were heated internally by two identical heaters connected in series as shown in detail in Fig. 2. Fine nickel-chromium wire of 29 ohms in resistance was wound on each heater which was machined from No. 1 Lava. The total weight of each heater was 12 grams, about 5% of the weight of each test specimen. The specimens were supported by two thin pieces of Lava plates with minimum contact surfaces to eliminate heat exchange by conduction.

A current of 0.5 ampere was passed through the heaters during the runs. In order to obtain a constant power supplied to the heaters during the entire annealing cycle, a voltage stabilizer was used to eliminate line fluctuation. The electrical energy supplied by the heaters was used solely for heating up the specimens and the heaters themselves. This was made possible by enclosing the specimens and the heaters in a

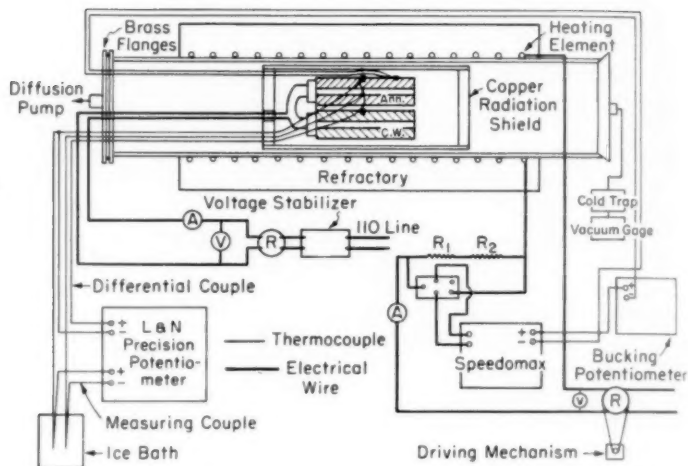


Fig. 1—Schematic Diagram of Experimental Setup for Measuring Temperature Difference During Annealing.

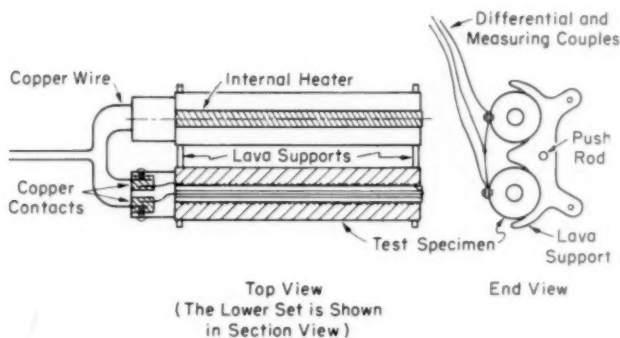


Fig. 2—Internal Heaters and Test Specimens Assembly.

radiation shield which was heated in a vacuum furnace and controlled to the same instantaneous temperature of the specimens throughout the course of annealing.

The radiation shield was a thin copper cylinder 2 inches in diameter and 6 inches long. One junction of a differential couple (made from calibrated iron-constantan thermocouple wire) was silver-soldered to the middle of the shield. The other junction was silver-soldered to a small copper washer which was fastened firmly to the annealed specimen by a set screw. This differential couple was connected through a potentiometer to a Leeds and Northrup Speedomax, the temperature

controlling device for the vacuum furnace. The function of the potentiometer was to supply bucking voltage to shift the zero of the temperature difference scale to the middle of the recording chart to improve sensitivity.

The instantaneous temperature differences between the cold-worked and the annealed specimens during annealing were measured by another differential couple as shown in Fig. 2. A constantan wire was welded into this differential couple such that it measured not only the temperature difference, but also the temperature of the annealed specimen. A precision Leeds and Northrup Potentiometer with a thermocouple switch was used for these temperature measurements.

In order to completely eliminate heat transfer by radiation between the specimens and the surrounding it was necessary that the latter be heated and controlled to the same instantaneous temperature of the

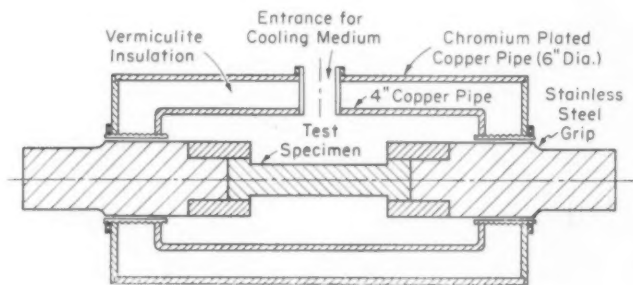


Fig. 3—Cold Chamber for Torsion Test at Low Temperature.

specimens. The control sensitivity of the Speedomax was improved by (a) changing from a off-and-on control into a 2-position control, (b) adding a driving mechanism which increases the power supplied to the vacuum furnace at a definite rate. As a result, the Speedomax was able to control the radiation shield to within $\pm 0.1^\circ\text{C}$ of the instantaneous temperature of the annealed specimen.

Calibration of Apparatus

The experimental setup for measuring the temperature difference was calibrated by heating two identical ingot iron specimens both in annealed condition (size, 0.800 by $3\frac{1}{2}$ inch, weights, 201.4 and 202.0 grams respectively) with a constant current of 0.500 ampere supplied to the internal heaters. The temperature difference curves and the heating curves of these three successive runs are shown in Fig. 4.

It was established from these annealing runs that:

- (a) The temperature difference curves of the two identical annealed

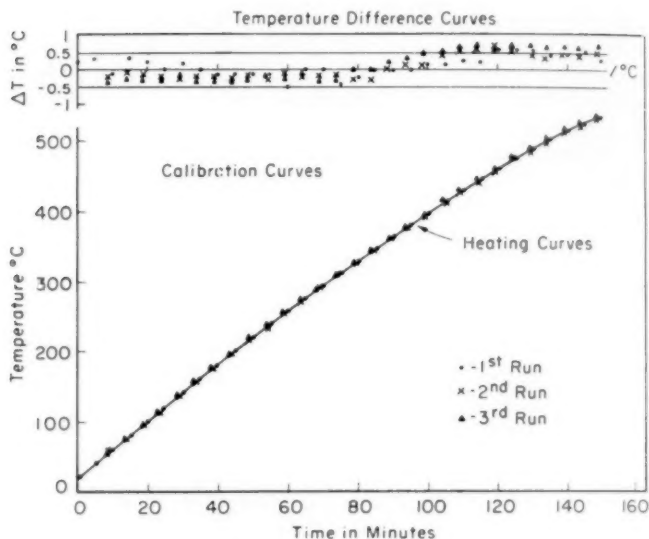


Fig. 4—Calibration Curves.

specimens during successive heating showed a characteristic pattern with a reproducibility of $\pm 0.2^\circ\text{C}$.

(b) Heating rates on successive runs were reproducible.

(c) The heat energy supplied by the two internal heaters at 29 volts and 0.500 amperes was 31,000 calories during the $2\frac{1}{2}$ -hour interval within which the specimens were heated to 525°C (975°F). The energy required to heat up the specimens and the heaters to 525°C (975°F), as calculated from the specific heat data of iron (Fig. 5) plus heaters was also 31,000 calories. This indicated that the heat transfer from the specimen to the surrounding, and vice versa, was negligible during the course of annealing.

The heat energy supplied by the two heaters was only 103 calories per minute. If the 200 gram cold-worked specimen liberated a stored energy of 0.5 cal./gm. at about 500°C (930°F), this would amount to a total of 100 calories which was in the same order of magnitude of the heat energy supplied per minute. Assuming no heat exchange, this 100 calories would cause a temperature increase in the cold-worked specimen of 3°C . This certainly should be detectable because the reproducibility of temperature difference was $\pm 0.2^\circ\text{C}$.

Preparation of Specimens

Armco iron rods 1-inch in diameter were annealed at 950°C

(1740 °F) for an hour in helium atmosphere and followed by furnace cooling to obtain a uniform No. 2 to 3 grain size and hardness of Rockwell B-36 to B-40.

The specimens to be deformed at room temperature were machined down to a gage section of 0.800 inch in diameter and 4 inches in length, with a fillet and shoulder section $1 \times 2\frac{1}{2}$ inches. The specimens to be deformed at low temperatures also had a gage section of 0.800 by 0.800 by $\frac{5}{8}$ inches such that they could be fitted into the stainless steel adapters in the cold chamber.

In order to permit the largest amount of work to be done in the speci-

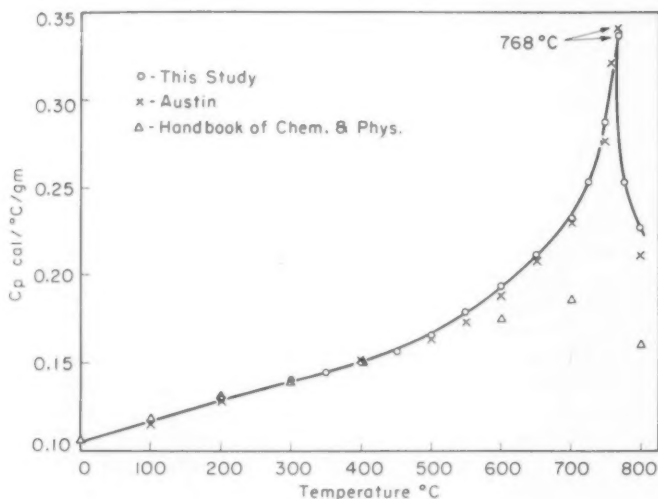


Fig. 5—Specific Heat Curve of Iron.

men before fracture takes place, torsion was used as the means of deformation. A Tinius Olsen torsion testing machine was used.

Torsional deformation at low temperatures was performed in a cold chamber as shown in Fig. 3. It consisted of a double wall brass cylinder with vermiculite as insulating material. The outer wall was chromium plated. Two 2-inch diameter stainless steel adapters with 0.800 by 0.800 by $\frac{5}{8}$ inch square holes were used to hold the specimens. The adapters were loosely fitted with the ends of the chamber so that they could turn freely during the process of twisting without moving the cylinders. A 1-inch diameter hole on the cylinders was provided for the entrance of the cooling medium.

Dry ice (-82°C) and liquid air (-185°C) were used as cooling media. In each case, the specimen was imbedded in the cooling medium

Table II
Specific Heat of Ingot Iron

Temp. in °C	cp in cal./gm./°C		
	This Study	Austin	Hdbk of Chem. & Phys.
0	0.131	—	0.1055
100	—	0.115	0.1168
200	0.131	0.128	0.1282
250	0.136	—	—
300	0.141	0.140	0.1396
350	0.144	—	—
400	0.150	0.151	0.1509
450	0.156	—	—
500	0.168	0.163	0.1623
550	0.179	—	—
600	0.193	0.188	0.1737
650	0.210	—	—
700	0.232	0.230	0.1850
725	0.252	—	—
750	0.287	—	—
768	0.336	0.340	—
(Curie point)	—	—	—
80	0.226	0.210	0.1592

and testing was not started until an equilibrium temperature was reached. A copper-constantan thermocouple was used for temperature measurement.

After the specimen was deformed to the desired number of turns, a $\frac{1}{4}$ inch section was cut from one end of the gage section. Rockwell B hardnesses were immediately taken and microstructures of the specimens were examined.

These specimens were saved for recrystallization studies.

The rest of the cold-worked specimen was machined with minimum delay down to 0.765 inches in diameter (or until the rough surface was removed) and a $3\frac{1}{2}$ -inch gage length obtained as shown in Fig. 2. The machining was done at low speed and lubricant was applied to minimize the heating of the specimen. A 0.257 inch diameter hole was drilled entirely through the specimen such that the $\frac{1}{4}$ inch diameter internal heater could be inserted. Two tapped holes were drilled as shown in Fig. 2 for fastening the thermocouples with the specimen.

The annealed sample used for comparison during annealing was obtained by cutting a $3\frac{1}{2}$ -inch section from the same bar and machined down to the same diameter (± 0.0005 inch) and length as that of the cold-worked specimen.

Measurement of Temperature Difference

The cold-worked and annealed specimens were put into the setup as shown in Fig. 1. Annealing was not started until the vacuum was down to 0.5 micron. The current supplied to the internal heaters was 0.5 ampere for every run. The radiation shield was controlled to the same temperature as the annealed specimen at all temperatures above 200 °C (390 °F). Measurements of temperature difference between the cold-worked and the annealed specimens and the temperature of the an-

nealed specimens were made almost simultaneously. The voltage and current of the internal heaters and the vacuum furnace were also measured in addition to recording the vacuum. Most first annealing runs consisted of heating to around 650 °C (1200 °F) and allowing to cool in vacuum overnight. The second and third runs were made on the next two days to a temperature a little lower than the first run.

Recrystallization Studies

After the annealing cycles, the cold-worked specimens were micro-examined on a plane tangential to the surface of the specimens.

The 1/4-inch disks of the deformed specimens were annealed to 650 °C (1200 °F) in a 50 °C interval at a heating rate close to that of the specimens used for temperature difference measurements. Rockwell B hardness were taken.

RESULTS AND DISCUSSION

Plastic Deformation by Torsion

Deformation by torsion produces a nonuniform strain across the radius of the specimen. All the specimens were almost plastically deformed all the way through. This was proven by calculation of the elastic zone (19) after deformation as shown in Table III. The elastic zones of the seven cold-worked specimens ranged from 0.0002 to 0.002 inches in radius for a specimen diameter of 0.800 inch. Therefore, all the test specimens were deformed almost completely plastically.

Micro examination of the specimens deformed at room temperature revealed a typical cold-worked structure with presence of strain lines and distorted grain structure. Mechanical twins were present in the cold-worked structure for specimens deformed at sub-zero temperatures.

Stored Energy Released During Annealing

The stored energy released during annealing was calculated from Equation 2, which is equivalent to Equation 3 when the temperature difference is small.

$$E = \int_{T_1}^{T_2} C_p dT \quad \text{Equation 2}$$

$$E = C_p (T_2 - T_1) \quad \text{Equation 3}$$

where E = Stored energy in cal. per gm.

C_p = Specific heat of the annealed specimen at the temperature at which heat is given off.

$T_2 - T_1$ = Temperature difference between the cold-worked and the annealed specimens.

In all tests, the temperature difference between the cold-worked and the annealed specimens showed a characteristic pattern which was

Table III
Radius of Elastic Zone of the Different Specimens

Spec. No.	Angle of Twist, Turns	Straining Temp., °C	Radius of Elastic Zone, inch
A20	3¼	- 25	0.0002
A15	4½	- 25	0.0002
A22	2½	- 82	0.0005
A24	3½	- 82	0.0004
A28	2½	-185	0.001
A31	2	-185	0.0015
A30	1½	-185	0.002

slightly different for different sets of specimens (Fig. 4). The characteristic pattern depends on the relative position between the specimens and the radiation shield for different sets of specimens. However, the reproducibility among the three successive runs in each set was within $\pm 0.2^\circ\text{C}$, when no heat was given off. Since the heating rates of the three successive runs in the same test were reproducible, then the temperature difference between the cold-worked and the annealed specimens measured at temperature T during the first run would be measured again at the same time (or temperature) as in the successive runs. This made it possible for the use of the second run as a base line in evaluating the temperature difference observed during the first run. The third run was conducted to double check the reproducibility of temperature difference and heating rate, and also assure that whether or not further energy was released.

Our specific heat data of ingot iron were shown in Fig. 5 with published results (20,21). Good agreement was found between ours and Austin's (20).

In Figs. 6 to 12, the differences in ΔT between the first and the second run, as well as between the third and the second run were plotted, where ΔT = instantaneous temperature difference between the cold-worked and the annealed specimens. This enabled direct reading from the graph of ΔT which was to be used for stored energy calculation. Although it was necessary to use three successive runs to obtain the temperature difference, yet this setup has the advantage over the annealing of a single specimen in that both the cold-worked and the annealed specimens received the same amount of small current fluctuation during annealing, thereby the true value of ΔT was not affected by this current fluctuation.

The calculated stored energy for different tests are shown in Table IV. Among these seven tests, the release of stored energy took place in two stages, with the major quantity released at a higher temperature range. This is in agreement with literature (11,13).

The major portion of the stored energy was released at a temperature range from 500 to 650°C (930 to 1200°F). The magnitude of this portion of energy ranged from 0.3 to 1.1 calories per gram representing 3 to 7% of the mechanical energy expended during deformation. It

Spec.

No.

A20

A15

A22

A24

A30*

A28

*Micro

Table IV
Stored Energy Released During Annealing

Spec. No.	Straining Temp. °C	Angle of Twist, Turns	Mech. Energy Expended Cal./gm.	Temp. at Which Energy Was Released		Energy Given off Cal./gm.		% Energy Released	
				1st	2nd	1st	2nd	1st	2nd
A20	-25	3½	9.75	370	600	0.12	0.3	1	3
A15	-25	4½	13.0	—	560	—	0.6	—	5
A22	-82	2½	7.7	480	618	0.15	0.3	2	4
A24	-82	3½	12.2	430	569	0.15	0.9	1	7
A30*	-185	1½	9.9	240	—	0.52	—	4	—
A31*	-185	2	13.4	150	515	0.12	0.43	1	3
A28	-185	2½	17.3	—	488	—	1.1	—	7

*Micrographic examination indicated that these two samples were only partially recrystallized.

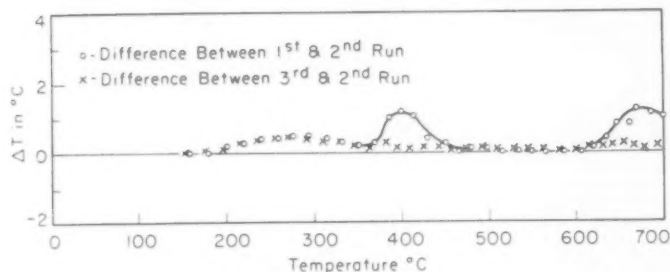


Fig. 6— ΔT versus T Curve of Specimen A 20, 3½ Turns at 25 °C.

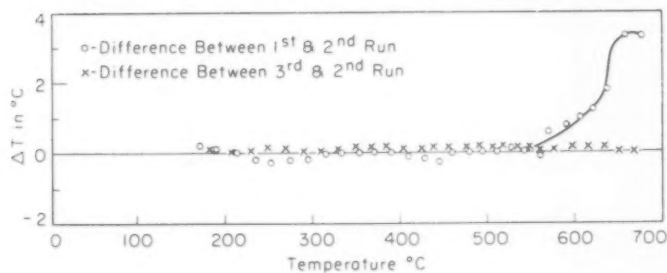


Fig. 7— ΔT versus T Curve of Specimen A 15, 4½ Turns at 25 °C.

can be observed that for all three straining temperatures, larger previous strain resulted in a higher stored energy which was released at a lower temperature upon annealing. Recrystallization temperature of a metal with higher strain is known to be lower than that of the same material deformed to a lower strain. Micro examination of the cold-worked specimens which had been annealed to about 650 °C (1200 °F) in the setup revealed that every specimen except A30 showed complete recrystallization at the surface. The original structure prior to torsion is shown in Fig. 13. The recrystallized structure of A20 is shown in Fig. 14, which is a typical example of the observed completely re-

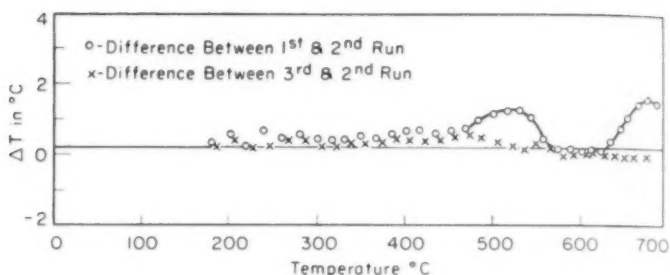


Fig. 8— ΔT versus T Curve of Specimen A 22, $2\frac{1}{2}$ Turns at -82°C .

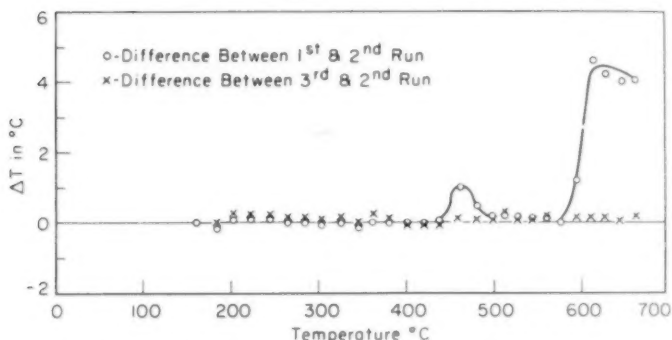


Fig. 9— ΔT versus T Curve of Specimen A 24, $3\frac{1}{2}$ Turns at -82°C .

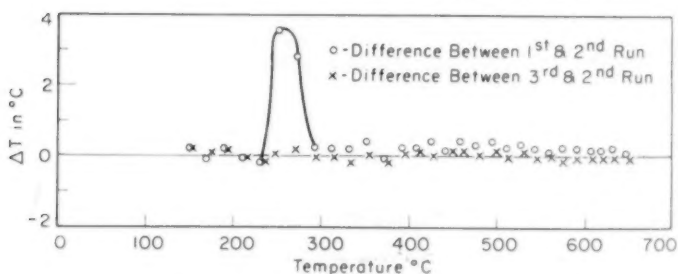


Fig. 10— ΔT versus T Curve of Specimen A 30, $1\frac{1}{4}$ Turns at -185°C .

crystallized structure. The above information indicated that stored energy was released before or concurrent with recrystallization.

This can be clarified by Fig. 15 which shows the hardness data of the deformed samples upon successive annealing at a 50°C interval with a rate similar to the annealing of the cold-worked specimens. It can be observed that a sharp drop in hardness, which usually accompanies recrystallization, was observed at the range where stored energy was

Table V
Calculated Density of Dislocations

Spec. No.	Deformation	Stored Energy cal./gm.	Calculated Density of Disloc./sq.cm.
A20	3¼, 25°C	0.4	2.5 x 10 ¹¹
A15	4½, 25°C	0.6	4 x 10 ¹¹
A22	2½, -82°C	0.4	2.5 x 10 ¹¹
A24	3½, -82°C	1.0	6.5 x 10 ¹¹
A30*	1½, -185°C	0.52	3 x 10 ¹¹
A31**	2, -185°C	0.55	3.5 x 10 ¹¹
A28	2½, -185°C	1.1	8 x 10 ¹¹

* Not recrystallized.

**Partially recrystallized.

*Micrographic examination indicated that these two samples were only partially recrystallized.

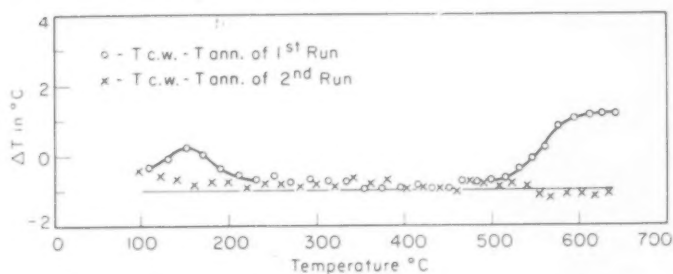


Fig. 11— ΔT versus T Curve of Specimen A 31, 2 Turns at -185°C .

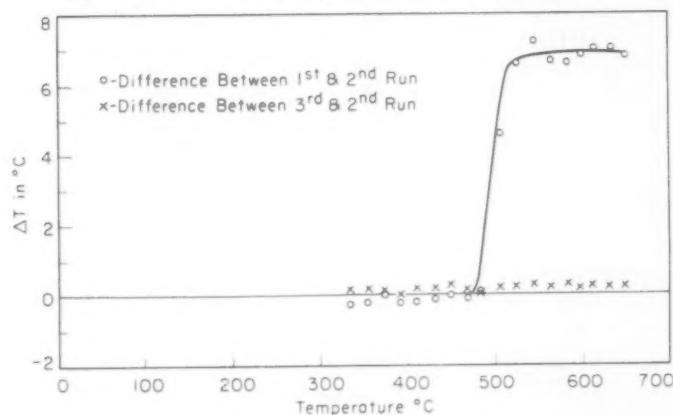


Fig. 12— ΔT versus T Curve of Specimen A 28, 2½ Turns at -185°C .

released. This observation was further confirmed by comparing the microstructures (Figs. 16 to 18) of A30, A31 and A28 deformed in liquid air for 1½, 2 and 2½ turns respectively and annealed to about 650°C (1200°F). Temperature difference curves indicated that no

measurable heat was given off by A30, 0.4 calories per gram by A31, and 1.1 calories per gram by A28. The surface of A30 was not recrystallized, A31 partially recrystallized and A28 completely recrystallized. Their corresponding hardness data at the surface of Rockwell B-62, B-51 and B-40 respectively versus the original hardness of 36 supported the micro examinations. From these evidences, it can be seen that the stored energy release was concurrent with recrystallization. Also, Figs. 16, 17 and 18 show that the recrystallization temperature is decreased as the amount of prior deformation is increased.

Calculation of Density of Dislocations of the Cold-Worked Metal

The measured values of the stored energy can be used to calculate the density of dislocations of the cold-worked metal with the following equation:

$$\text{where } E = \rho G b^2 \quad \text{Equation 4}$$

E = Stored energy per unit volume, ergs per cubic centimeter³
 G = Shear modulus
 $= 8 \times 10^{11}$ dynes per square centimeter for iron
 b = Distance of closest approach of atoms
 $= 2.48 \times 10^{-8}$ centimeter
 ρ = Density of dislocation, per square centimeter

The density of dislocations of the seven cold-worked specimens was thus calculated as shown in Table V. Literature shows that the density of dislocations in cold-worked metals ranges from 10^{11} to 10^{12} per square centimeter (9,11), while 10^{12} is considered to be the limiting number of dislocations which can be stored in a metal (22). The present experimental results are in agreement with previous estimates of density of dislocations in cold-worked metals.

First Stage Release of Stored Energy

The temperature difference curves indicated that energy of the magnitude corresponding to 1 °C temperature difference was first released at as low as 300 °C (570 °F). Since no recrystallization was observed at such a low temperature, this release might be associated either with recovery or strain aging. It is to be noted that two turns at -185 °C (-300 °F) produced an energy release at about 150 °C (300 °F). This is the lowest temperature at which the first stage of heat release was observed. Since Fig. 11 is based on two runs instead of the usual three, there is some uncertainty as to the reality of the energy release at 150 °C (300 °F).

Strain Aging: On account of the unavoidable time delay between deformation and annealing, the cold-worked specimens were susceptible to strain aging. Since the segregation of solute atoms is accompanied by the evolution of heat, strain aging could be a contributing factor to the initial stage of energy release. Therefore, the fraction of carbon atoms which had segregated within this time delay of 24 hours

Table VI
Micrographic Examination of Cold-Worked
Sample After Annealing

Specimen No.	RB Hardness in Cold-Worked State		Annealing Temp. °C	RB Hardness After Annealing		Micro Exam. on Surface
	Surface	$\frac{1}{8}$ " from Center		Surface	$\frac{1}{8}$ " from Center	
A20 ($3\frac{1}{2}$, 25°C)	95	88	690	39	50	Completely rex'l
A15 ($4\frac{1}{2}$, 25°C)	99	94	660	37	41	Completely rex'l
A22 ($2\frac{1}{2}$, -82°C)	91	86	675	42	54	Completely rex'l
A24 ($3\frac{1}{2}$, -82°C)	93	87	655	40	48	Completely rex'l
A30 ($1\frac{1}{2}$, -185°C)	82	78	650	62	64	Just begin to rex'l
A31 (2, -185°C)	86	82	645	51	53	Some rex'l grains
A28 ($2\frac{1}{2}$, -185°C)	90	85	655	40	46	Completely rex'l

[†]Hardness before cold working ranged from RB 36 to 40

*Hardness data shown here are averages of 3 or 4 readings

was calculated (22). It was found that for all the deformed specimens, over 90% of the solute atoms had been segregated to dislocations before annealing. Therefore, strain aging was not a contributing factor to the first stage energy release.

Recovery: The possible factors which contributed to the release of energy during the first stage may be pictured as follows: In the freshly cold-worked structure, the segregated solute atoms may be randomly distributed throughout the specimens as is shown schematically in Fig. 19. The curved lines represent bent dislocations. The dislocation density being in the neighborhood of 10^{11} to 10^{12} per sq.cm. After strain aging for 24 hours, the solute atoms may have segregated to the dislocations as shown in Fig. 20.

In order to determine whether the concentration of solute atoms around the dislocations changes appreciably at 300 °C (570 °F), one can utilize the following formula (22):

where $c = c_0 \exp(U/kT)$
 c = Concentration of solute atoms around dislocations
 c_0 = Average concentration
 U = Binding energy between carbon atoms and dislocation, 0.5 eV

Calculation shows that c/c_0 does not change. However, in this temperature range, the mobility of dislocations is increased through thermal fluctuation. Several processes could take place which would involve energy change:

(a) The Relief of the Strain Aging Effect: About 90% of the solute atoms were locked into the dislocations during the 24-hour period of strain aging. Hence, initially, energy must be supplied to separate the dislocations from their solute atom atmosphere.

(b) The Straightening of Bent Dislocations: Energy is released by

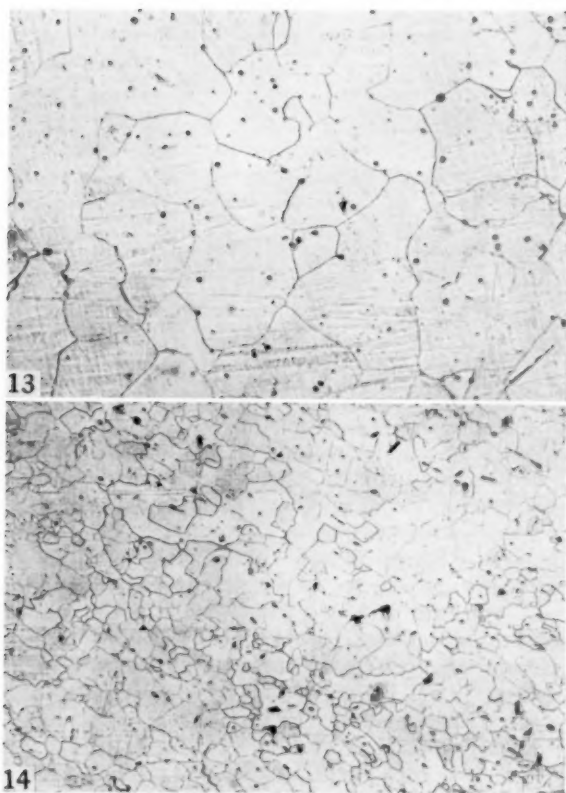


Fig. 13—Original Structure Prior to Torsion, Nital etch. $\times 100$.
Fig. 14—Recrystallized Structure of A 20 After Being Twisted $3\frac{1}{4}$ Turns at 25°C and Subsequently Heated to 690°C (1275°F), Nital etch. $\times 100$.

the shortening of the dislocation lines. This process can take place simultaneously with the first one.

Fig. 21 shows two possibilities that could exist after straightening of the dislocation lines and release of the carbon atoms. Case I. is a combination of processes (a) and (b) while Case II. is process (b) alone.

(c) The Annihilations of Dislocations of Opposite Signs Along the Same Slip Plane: This process produces a release of energy. It could safely be assumed, without introducing serious errors, that less than 25% of the total number of dislocations were annihilated in this stage. The magnitude of this energy is a function of the density of dislocations

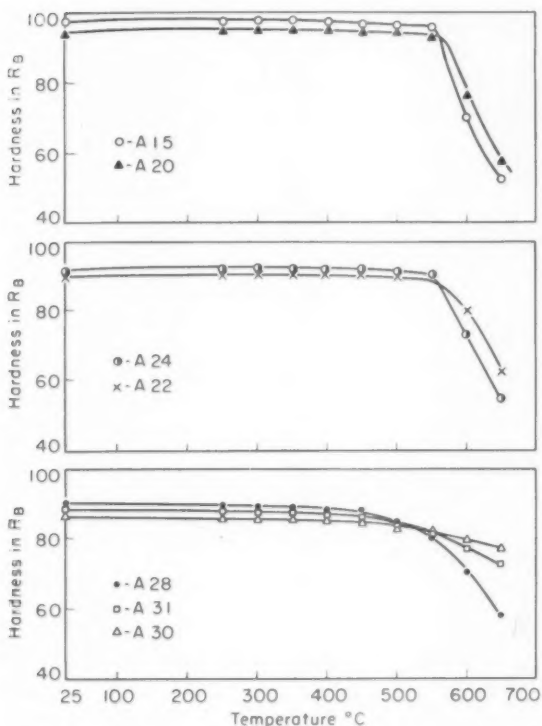


Fig. 15—Hardness Versus Annealing Temperature Curves.

in the structure. Processes (b) and (c) can be classified as recovery.

It is to be noted that the release of energy caused by the straightening of dislocation lines could contribute also towards the release of the solute atoms from the dislocations. Once the dislocations are free from the locking of solute atoms, they can move more readily. With the help of thermal fluctuations, the annihilation of the dislocations of the opposite signs along the same slip plane can take place, with the result of energy release.

(d) Vacancy Annihilation: It has been pointed out by Mott (23) that a plastic strain ϵ produces a concentration of vacancies by means of dislocations cutting dislocations where

$$c = 10^{-4} \epsilon$$

Taking $\epsilon = 1$ and assuming that the energy of annihilation of a vacancy in iron is about 0.5 e.v., the total energy released would be about 0.5 cal.

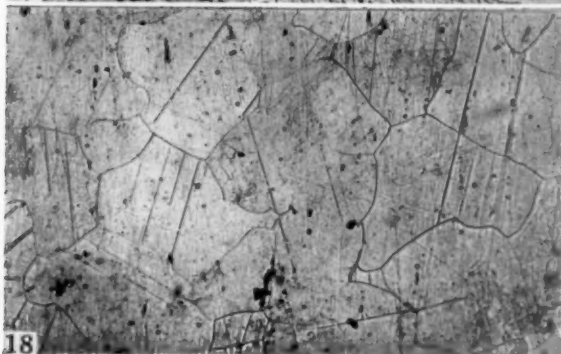
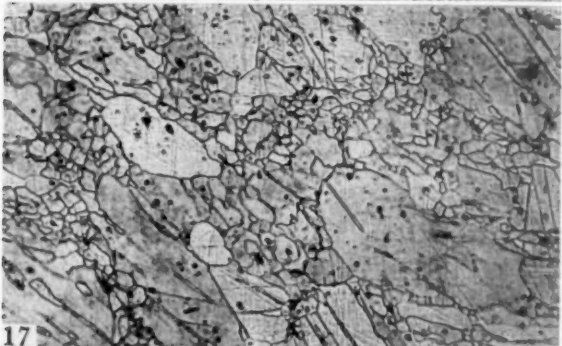
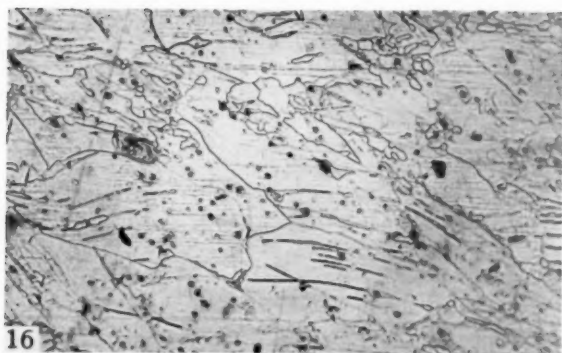


Fig. 16—Structure at the Beginning of Recrystallization After Being Twisted $1\frac{1}{2}$ Turns at -185°C (-301°F) and Subsequently Heated to 650°C (1200°F). Nital etch. $\times 100$.

Fig. 17—Partially Recrystallized Structure After Being Twisted 2 Turns at -185°C (-301°F) and Subsequently Heated to 645°C (1195°F). Nital etch. $\times 100$.

Fig. 18—Structure of A 28 After Being Twisted $2\frac{3}{4}$ Turns at -185°C and Subsequently Heated to 655°C (1210°F). Nital etch. $\times 100$.

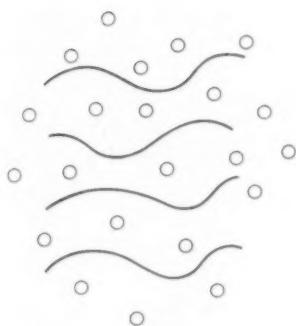


Fig. 19—Schematic Diagram of the Cold-Worked Structure Immediately After Deformation.

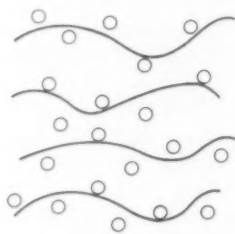
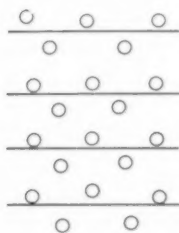
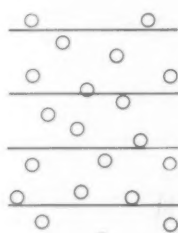


Fig. 20—Schematic Diagram of the Cold-Worked Structure After Being Strain Aged for 24 Hours.



Case I



Case II

Fig. 21—Schematic Diagram of the Cold-Worked Structure After Being Annealed to Around 300 °C (570 °F).

per gram. Thus, vacancy-annihilation would be detectable if it occurred over a sufficiently short temperature interval.

The Effect of Temperature of Deformation

As expected a given amount of twist required more energy the lower the twisting temperature. However, the fraction of input energy which is stored in the metal was roughly independent of the temperature of deformation. A given plastic strain produced at a low temperature will store more energy than the same plastic strain produced at a higher temperature. For example, $2\frac{1}{2}$ turns at -185°C stored 1.1 calories per gram against 0.45 calories per gram at -82°C , and $4\frac{1}{2}$ turns at 25°C stored 0.6 calories per gram against 1.05 calories per gram stored by only $3\frac{1}{2}$ turns at -82°C .

CONCLUSIONS

1. The energy stored in ingot iron specimens which were de-

formed in torsion at room temperature, dry ice and liquid air temperatures was found to range from 0.3 to 1.1 calories per gram.

2. The release of stored energy upon annealing takes place in two stages.
3. Recovery is responsible for the release of stored energy at the initial stage.
4. The major portion of stored energy is released at a temperature range concurrent with recrystallization.
5. Stored energy increases with increasing strain when straining temperature is the same.
6. Calculation of density of dislocations based on the measured stored energy data indicated that the specimens in cold worked state had a density of dislocations around $1 \text{ to } 8 \times 10^{11}$ per square centimeter.
7. For a given amount of strain more energy is stored the lower the temperature of deformation.

ACKNOWLEDGMENTS

This work was supported by the Office of Ordnance Research under Contract DA 36-034-ORD-491RD from June 1953 to August 1954.

The authors are indebted to the staff and graduate students of the School of Metallurgical Engineering of the University of Pennsylvania, especially to Dr. R. M. Brick for his initial guidance and suggestions. The authors wish to express their appreciations to Dr. R. L. Smith of Franklin Institute and Dr. F. Jaumot of General Motors for revision of the original manuscript and M. Herman of Franklin Institute for his suggestions. Gratitude is extended to E. Horn, L. Hudson, H. Pierce and L. Halley for construction of the equipments and machining of test specimens.

Appreciations are extended to Dr. C. D. Starr of Wilbur B. Driver Co. for reviewing the manuscript, to P. Asnis and W. Groninger, also of the above Company, for their aid in metallographic work.

References

1. M. B. Bever and L. B. Ticknor, "The Energy Stored During the Cold-Working of a Gold-Silver Alloy," *Acta Metallurgica*, Vol. 1, 1953, p. 116.
2. G. Borelius and S. Sjöberg, "Measurements on the Evolution of Heat During the Recovery of Cold-Worked Metals," *Arkiv Fysik*, Vol. 6, No. 2, 1953, p. 143.
3. S. Sato, *Scientific Reports*, Tohoku Imperial University, Vol. 20, 1931, p. 140.
4. H. Quinney and G. I. Taylor, "The Emission of the Latent Energy Due to Previous Cold-Working When a Metal is Heated," *Proceedings*, Royal Society, (London), Vol. 163, 1937, p. 157.
5. B. Welber, "Measurement of the Internal Energy in Copper Introduced by Cold-Work," *Journal of Applied Physics*, Vol. 23, 1952, p. 876.

6. T. Suzuki, "The Release of Energy Associated with Crystal Restoration Process in Cold-Worked Polycrystalline Copper," *Scientific Reports Research Institute*, Tohoku Imperial University, Vol. 1A, 1949, p. 193.
7. E. E. Stansbury, G. E. Elder, and M. L. Picklesimer, "Calorimetric Studies of Plastic Deformation and Phase Transformation for Period Ending December 1, 1952," *U.S. A.E.C.*, Public Document, 1953, (ORO-86).
8. L. M. Clarebrough, D. Mitchell, M. E. Hargreaves, A. K. Head, and G. W. West, "The Determination of the Energy Stored in a Metal During Plastic Deformation," *Proceedings*, Royal Society, (London), Vol. 215A, p. 507.
9. L. M. Clarebrough, M. E. Hargreaves, and G. W. West, "The Release of The Energy Stored in Deformed Nickel," *Philosophical Magazine*, Vol. 44, 1953, p. 913.
10. L. M. Clarebrough, M. E. Hargreaves, A. K. Head, and G. W. West, "Energy Stored During Fatigue of Copper," *Journal of Metals, Transactions American Institute of Mining and Metallurgical Engineers*, Vol. 7, No. 1, 1955, p. 99.
11. L. M. Clarebrough, M. E. Hargreaves, A. K. Head, and G. W. West, "The Release of Energy During Annealing of Deformed Metals," *Proceedings*, Royal Society, (London), Vol. 232, 1955, p. 252.
12. P. Greenfield and M. Bever, "The Evolution of the Energy Stored By A Gold-Silver Alloy Cold-Worked at -195°C and At Room Temperature," *Acta Metallurgica*, Vol. 4, 1956, p. 433.
13. P. Gordon, "Microcalorimetric Investigation of Recrystallization of Copper," *Journal of Metals, Transactions American Institute of Mining and Metallurgical Engineers*, Vol. 7, Sept. 1955, p. 1043.
14. J. S. Koehler, "On The Dislocation Theory of Plastic Deformation," *Physical Review*, American Institute of Physics, Inc., Vol. 60, No. 5, 1941, p. 397.
15. A. N. Stroh, "A Theoretical Calculation of the Stored Energy in a Work-Hardened Material," *Proceedings*, Royal Society, Vol. 218, No. 1134, p. 391.
16. N. S. Fastov, "Vydelenie Tepla Pri Plasticheskom Deformirovani," *Doklady Akad. Nauk.*, U.S.S.R., Vol. 83, (6), 1952, p. 851.
17. W. G. Burgers, *Proceedings*, Royal Academy of Science, Amsterdam, Vol. 50, 1947, p. 452, 595, 719, 858.
18. C. S. Smith, "A Simple Method of Thermal Analysis Permitting Quantitative Measurements of Specific and Latent Heats," *Transactions*, American Institute of Mining and Metallurgical Engineers, Institute of Metals Division, Vol. 137, 1940, p. 236.
19. O. Hoffman and G. Sachs, *Introduction to the Theory of Plasticity for Engineers*, 1953, p. 107. McGraw-Hill Book Co., Inc.
20. J. B. Austin, *Industrial and Engineering Chemistry*, Nov. 1932, p. 1225.
21. Wust, Meuthen and Durrer, "Specific Heat," *Handbook of Chemistry and Physics*, 34 ed., 1952-53, p. 1944. Chemical Rubber Pub. Co.
22. A. H. Cottrell, *Dislocations and Plastic Flow in Crystals*, 1953. Oxford Press.
23. N. F. Mott, "Note on The Electronic Structure of the Transition Metals," *Philosophical Magazine*, Vol. 44, 1953, p. 187.

CLASSIFICATION OF PRECIPITATION SYSTEMS

BY R. O. WILLIAMS

Abstract

It is proposed that all precipitation systems be classified according to three structural characteristics: degree of complexity of nucleation, the shape of the particles formed and the degree of order in the matrix and precipitate. It is expected that these characteristics are most intimately associated with the kinetics and physical properties. (ASM International Classification N7b)

THE PHENOMENON of precipitation or age hardening of metal alloy systems has been known for forty years and during this time a large body of information has been accumulated on at least a hundred systems. It has been found that a great variety of structures and properties can result as a consequence of the separation of a new phase from a supersaturated solid solution. Yet, at this time there is no satisfactory scheme by which the many systems can be classified in order to implement comparison. Too often attempts have been made to characterize the entire field by the behavior of one or two systems with a notable lack of success. The purpose of this paper is to present a method which will, at least in part, permit a classification of the different systems. For this purpose one chooses those structural features which seem most strongly related to the kinetics and properties.

At the present time there are three methods which have been proposed but none are adequate for the present purpose. The first of these describes the nature of the supersaturated solid solution and the precipitate in terms of terminal solid solutions, intermediate phases, and intermetallic compounds. This system has been presented in exhaustive form by Mehl and Jetter (1)¹ and more briefly by Geisler (2). A second system distinguishes between aging behavior at relatively low and high temperatures which for some systems are markedly different. The aging at the lower temperature (cold aging) is often considered the formation of Guinier-Preston zones although there is no generally accepted definition of these zones. Such a classification is, of course, only recognition of the fact that some systems' behavior is temperature dependent, not a description of the processes. A third suggestion as

¹ The figures appearing in parentheses pertain to the references appended to this paper.

A paper presented before the Thirty-Ninth Annual Convention of the Society, held in Chicago, November 4-8, 1957. The author, R. O. Williams, was formerly associated with General Electric Research Laboratory, Schenectady, New York, and is now with Cincinnati Milling Machine Company, Cincinnati, Ohio. Manuscript received August 13, 1956.

Table I
Classification of Precipitation Systems

Characteristics	Distinguishable Classes		
	Simple (α)	Complex (β)	Discontinuous (γ)
Nucleation			
Particle Shape	Needles (N) Polyhedra (R)	Spheres (S)	Plates (P)
State of Ordering	Four combinations of ordered or disordered matrix and precipitate		

Presentation convention: A given system is designated by three or four symbols as follows:

Nucleation Matrix order Particle shape Particle order.
If the matrix is ordered then a subscript 'o' is used, otherwise—
nothing; particle order is represented by 'o', disorder as 'd'.
Examples of possible systems are as follows: βPd , αSo and $\gamma_o\text{Pd}$.

to classification of precipitation systems is due to Guinier (3) and depends on the relative size of the different atoms. While there is no doubt that this size is important, it is by no means the only important aspect which determines the structures on precipitation.

THE SYSTEM

It is proposed that precipitation systems be classified according to three structural characteristics: 1) the nature or degree of complexity of the nucleation, 2) the predominate shape of the particles of the new phase, and 3) the degree of order which exists within the matrix and precipitate. As seen in Table I, it is proposed to distinguish among three kinds of nucleation and four kinds of particle shapes. Since there are four possible combinations of order-disorder, there will be a total of 48 classes. However, it is likely that many will be found to be unimportant. In particular, the matrix will probably be ordered so infrequently that its designation in the symbol will be included only for the ordered state.

By simple nucleation is meant the process by which a new phase is formed by the simple rearrangement of atoms on the lattice sites of the matrix accompanied perhaps, but not necessarily, by changes in lattice dimensions in one or more directions so as to reduce the total strain energy. Any such relaxation process would be controlled by the coherency between the matrix and precipitate as well as the restraints of the surrounding matrix and would be dependent upon particle shape. Small shears might also occur provided they were uniform with respect to all atoms in the new phase and were limited in magnitude to perhaps 0.01 maximum. An example of such a nucleation process would be that of a face-centered cubic precipitate in a face-centered cubic matrix which was coherent on one or more principal planes and which, necessarily, had the same crystallographic orientation as the matrix. Because of its simple nature this type of nucleation may often be homogeneous in the strictest sense of the word.

By complex nucleation is meant the process by which a phase is

formed which contains atomic positions markedly different from the matrix where it is now necessary to consider detailed steps by which it is possible to get from the matrix structure to that of the precipitate. It is possible that such a process could be accomplished by simple nucleation of a third structure which grows to a size appreciably greater than critical and then shears over into the new, complex structure. This matter will be discussed more later, but it is evident that this type of nucleation would normally be favored by singularities in the starting material. A good example of this type of nucleation might be the formation of a body-centered cubic precipitate from a face-centered cubic matrix.

Discontinuous precipitation occurs at or in the immediate vicinity of high-angle grain boundaries which sweep through the grains leaving behind a matrix of new crystallographic orientation and the precipitate. It is believed that most often existing grain boundaries began to move, often in both directions at different locations, and thus there would be no fixed crystallographic relation between the old grain and the new (4). It has been believed that the driving force for this type of precipitation arose from the straining of the matrix by general precipitation prior to the discontinuous precipitation (which in this case normally causes only a coarsening of the precipitate particles) and has been called 'recrystallization' precipitation because of the similarity (2). However, some systems are known which seem to give only discontinuous precipitation and hence, the above analogy is not entirely correct. The process has also been called cellular since the second phase is left behind in the form of cells (5). Most often the new phase ends up as plates normal to the moving boundary and looks much like pearlite.

The classes of particle shapes are essentially self-explanatory with the possible exception of the last. By 'polyhedra' is meant those particles whose surface energies are markedly dependent upon crystallography and hence, are multi-sided figures with essentially plane faces. While such particles exist in a great variety of shapes the point which seems most important is only the dependence of surface energy on crystallography and, hence, all are lumped into one class.

The last characteristic is that of ordering since one can certainly expect this to be important in the kinetics and properties of the precipitated system. (Note that normal ordering is not considered complex nucleation since it is accomplished by simple atom rearrangements.) A possible way in which ordering could give rise to complex kinetics would be for the new phase to nucleate as a disordered structure and perhaps order during growth.

It is evident that one can pass more or less continuously from class to class for each of the characteristics. This is unfortunate, but inevitable. However, this is not the problem which it might appear since it seems that most systems will fall clearly into only a single classification.

DISCUSSION

The purpose of any classification is to allow a systematic arrangement of items for the sake of simplifying, understanding, describing and predicting. In particular, for precipitation systems one is interested in knowing what aspects of the many systems can be compared, how the physical properties depend upon structure, how best to obtain optimum structures and the prediction of new, useful systems. For this classification, structural aspects have been chosen for the following reasons. There is considerably greater hope of transforming structural information into either kinetics or physical properties. The reverse transformation is normally not possible. In addition it is possible to

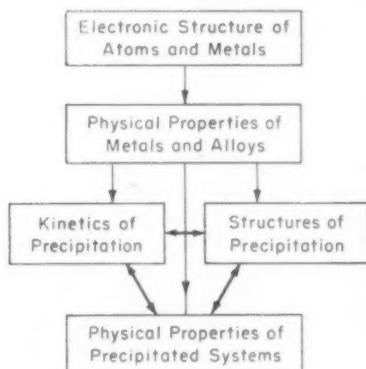


Fig. 1—Inter-Relationship of Aspects of the Precipitation Process.

consider structural information with greater concreteness than either kinetics or physical properties. However, for practical utilization it is primarily only kinetics and physical properties which are of interest.

There are more fundamental aspects of this problem. These include those properties of the system which cause the structures in the first place. In this class there are such things as the thermodynamics of all phases, the interfacial energies, kinetics of diffusion and strain energies. The entire problem, from the basic properties of atoms to the properties of precipitated systems, is outlined in Fig. 1. The properties which are responsible for the kinetics, structures and physical properties of precipitating systems are a direct result of the electronic structure of atoms and metals. As shown, the kinetics, structures and physical properties of precipitated systems are all interdependent. It would be desirable, of course, to go back a step or so, such that a really basic understanding for the phenomenon could be obtained. This is, how-

ever, not presently possible—one cannot calculate the necessary physical properties of the metals and alloys from the electronic structure. This is a problem considerably more extensive than say the calculation of phase diagrams from the number of electrons in the constituent metals. Experimental determinations of the properties are few and certain aspects are essentially impossible to measure. In addition, many of the steps needed to transform such data into kinetics, structures and properties are presently unknown. Thus it seems that the best compromise is that of structures.

It is evident that an attempt has been made to separate nucleation into three groups: The case where strain energy is of little or no importance, the case where it is very important and the case where presumably strain (or other factors), interfacial energy and diffusion rates are responsible for precipitation (or conglomeration) only at grain boundaries. While all three types may present problems in nucleation, it is complex nucleation which seems the most difficult because of the large strain energies. One of the earliest considerations of this problem was by Mehl and Jetter (1) where they believed the process occurred in essentially the following fashion. A region approaching the precipitate composition due to chance fluctuations accentuated by nonrandomizing forces simultaneously sheared, and enriched itself in the solute and perhaps grew until it was a stable particle of the new phase, although probably still in a coherent state. Barrett and Bowles (6) more recently proposed essentially the same mechanism except that they supposed that the shearing part would be rapid and thus qualify as a martensitic transformation on a very limited scale. If this proposal is correct there could be no diffusion during the martensitic shearing because of the extreme rapidity and hence, the particle would be the same size as the original fluctuation. Still a third modification of this idea is possible. Suppose that an intermediate structure were formed by simple nucleation which was metastable with respect to the latter precipitate, but thermodynamically stable with respect to the supersaturated solid solution. Such particles could grow to comparatively large sizes, then shear over to the final precipitate structure. Whether this shearing is fast or slow would certainly depend on how it started and what readjustments in atom positions are required.

There are, however, several methods in which complex nucleation could occur which essentially circumvent the necessity of the large strain energies. The most obvious is that of the role of dislocations. It seems safe to believe that dislocations could assist nucleation regardless of what kinds of atom rearrangements might be required. A particularly elegant example is the separation of the dislocations in the face-centered cubic systems to produce partial dislocations separated by a stacking fault. Such a stacking fault corresponds to four planes of the same sequence as close-packed hexagonal and can be considered a

nucleus for a close-packed hexagonal precipitate. This mode has been proposed in the case of the silver-lead system (7). Another system in which the same mechanism would work is that of aluminum-silver. It seems, however, that the role of dislocations is rather limited since one expects about 10^6 dislocations per square centimeter which would not normally be considered a very high particle density. Naturally, if they could move this would remove this limitation in part, but one normally expects that a particle would pin the dislocation for the same reasons which allowed the dislocation to assist nucleation in the first place.

It seems likely that vacancies provide some of the answers to this problem. Alloys which are to be strengthened by precipitation are almost invariably quenched and hence would have, during quenching and for a short time afterwards, a rather high supersaturation of vacancies. It seems likely that some of these cannot reach normal sinks (dislocations, etc.) and would nucleate some kind of defect as a disk or void. It is not unreasonable to believe that there can be enough of these defects to make a significant contribution to nucleation. The way in which such singularities would effect nucleation depends upon the system, but consider the example of the aluminum-silver system again. If the defects resulting from vacancy condensation were disks resulting from the removal of a single plane of atoms (giving a ring dislocation), it is evident that stacking through this disk is disrupted and again corresponds to the four planes of close-packed hexagonal structure, i.e., a nucleus. It is obvious that there are other ways in which this nucleation could have been effected.

In fact, vacancies are a very flexible constituent in precipitation. Besides the above possibilities the vacancies might simultaneously group with atoms and effect what would otherwise appear as a difficult nucleation problem. One kind of process which might occur would be the 'ordering' of vacancies and solute atoms to form a relatively open structure. The possibilities seem almost unlimited. It is unfortunate that the role of vacancies in any given system could not be simply elucidated. Along somewhat similar lines it has already been suggested that vacancies can be a convenient method by which the coherency strains can be eliminated (8).

It is reasonable to suppose that the shape of the precipitate particles is controlled by the nuclei shape, interfacial energy, strain energy and diffusion. There may also be an effect caused by the difficulty of atom transfer across the interface. At this time there does not seem to have been an extensive treatment of this problem. Note, however, that nucleation, as considered above, might determine to a large extent the particle shape. It has also become customary to expect plates when there is a good plane of similar atomic configuration for both the matrix and precipitate, especially so if this is a high density plane. Then in

some cases the strain energies will be appreciably less for a plate structure than more equiaxed spherical particles assuming coherency. Zener (9) has given the rates of growth for plates, rods and spheres where this is diffusion controlled. This is not the complete solution since one needs to know the rates of growth of edges of plates and ends of rods. This is the old problem, the so-called pointing effect of diffusion, which has never been solved.

It is immediately apparent that the presence of order in either the matrix or precipitate is a restrictive condition on the precipitation process and the recognition of its presence is important for several reasons. In the first place, the ordering is a kinetic process itself which may have the capacity in some systems to occur more or less independently of the precipitation process and would for such a case give complex kinetics. If the degrees of order were markedly dependent upon the temperature within the normal aging range then the driving force might change more rapidly than otherwise expected and the changes which one might observe might not otherwise be understood. One naturally expects physical properties to be dependent on the degree of order.

There are two other characteristics which are certainly important aspects of the precipitation process. These are the particle size and the coherency. The particle size is not a constant in that it starts at some small size, that of the critical nuclei, and increases. Thus, very roughly, the particles of all systems pass through the same size range. As for coherency, it is assumed that all systems start out with coherent particles in that no system is known in which there is not a definite crystallographic relationship between the matrix and the precipitate. It is believed that this can come about only through coherency during and following nucleation. Systems will, however, vary greatly as to the particle size which loses coherency. It seems likely that the process through which the coherency is lost is completed relatively quickly for any given particle. The main reason for believing this is that it seems that the process has to be nucleated and that once started can proceed rapidly. For those cases where the process is actually a dislocation running down the particle it seems very likely that after the first one, all the rest will follow in a fraction of a second.

As previously mentioned, what is ultimately desired is to correlate the structural aspects with the kinetics and physical properties. At the present, there are very few quantitative correlations worked out. However, Table II has been prepared to give some rough idea of what is known and what can be surmised. The listing is of questionable usefulness because of its qualitative nature. It does, however, point out deficiency of our knowledge.

As already mentioned, it has become customary to speak of the formation of G-P zones and the low-temperature aging, the two often

Table II
Dependence of Physical Properties on Characteristics of Precipitation Systems

Characteristics of Ppt. System	Crystal Structure Changes	Particle Shape	State of Ordering	Particle Size	Presence of Coherency
Physical Properties					
Yield Strength	Strong	?	Probable	Strong	Strong
Rate of Strain Hardening	?	?	Probable	?	?
Mechanical Properties					
Ultimate Strength	?	?	?	?	?
Elongation	?	?	?	?	?
Reduction of Area	?	?	?	?	?
Brittleness	?	?	?	?	?
Damping	?	?	?	?	?
Electrical Properties					
Electrical Resis.	Variable	Moderate	Probable	Probable	Probable
Thermal e.m.f.	?	?	?	?	?
Hall Effect	?	?	?	?	?
Magnetism					
Saturation Moment	Variable	Weak	Variable	Weak	Weak
Coercive Force	Strong	Strong	?	Strong	Strong
Remanence	Strong	Strong	?	Strong	Strong
Susceptibility	Strong	Weak	?	Weak	Weak
Magneto-Mechanical Effects	?	?	?	Weak	Weak
X-ray					
Diffuse Effects	Strong	Strong	Variable	Strong	Strong
Line Shift	Variable	Weak	Weak	Weak	Weak
New Lines	Strong	Weak	Strong	Strong	Weak
Kinetics					
Nucleation	Strong	Shape Dependent on Nucleation	?	*	Assumed
Growth	Moderate to Strong	Moderate	?	—	?
Conglomeration	?	?	?	—	?
Chemical Energy	Strong	Weak	Strong	Weak	Weak
Strain Energy	Weak	Strong	Weak	Weak	Strong
Misc.					
Specific Heat	Weak	Weak	Weak	Weak	Weak
Thermal Expansion	Variable	Weak	Medium	Weak	Weak
Volume Changes	Variable	Weak	Medium	Weak	Weak
Coherency	Strong	Strong	Weak	Strong	—
Thermal Conductivity	Similar to Strong	to Elec. Cond.	Weak	Strong	?
Microstructure	Strong	Strong	Weak	Strong	?

* Nucleation characterized by a critical size particle, this size is dependent on free energy, interfacial energy and strain energies.

being considered synonymous. Either or both of these could be one of three things; the change in atomic configuration in the absence of actual precipitation, as for example, the change in short range order, the precipitation of the equilibrium phase in a new fashion, or the precipitation of a metastable phase. It is well established, and expected from theory, that the atomic configuration should be temperature dependent, but it is believed that for most or all presently known systems which show distinct double aging characteristics, this is not the cause. Likewise, the changes observed seem to rule out the second explanation normally. It is thus believed that most systems which give the so-called low-temperature aging do so because of the precipitation of a metastable phase, a matter discussed at length by Hardy and Heal (10). The explanation in part lies in the structural considerations discussed here. First, one must obviously have a free energy decrease for

the structure or structures in question. The phase which appears first will be the one which can nucleate most rapidly and grow most rapidly. This means that most often the low-temperature phase will exhibit simple nucleation and presumably a phase of less compositional change would be favored. Predictions in any given system are not possible since it is not possible to calculate energies of conceivable metastable structures. There is also the possibility that in some systems the new phase may become stable with respect to the high-temperature phase at some lower temperature. Below this temperature the high-temperature phase would never be found to precipitate provided the low-temperature phase could nucleate and grow appreciably more rapidly. For those systems in which more than one mode or type of precipitation occurred it would be proper to state the classification of each and perhaps specify the sequence and temperature ranges. Since the structure of the metastable low-temperature phase is unrelated to the subsequent stable phase, its presence need have little, if any, affect upon the nucleation of the later structures. The presence of the metastable phase will then have no effect other than to reduce the driving force for the stable phase, although in practice it seems this effect is too small to be noticed.

It is not feasible at this time to attempt to classify all the known systems according to the above scheme because the data are too limited. However, some of the more common systems can be classified.

The best known system of all, the Al-Cu system, cannot be classified completely. At high temperatures, above about 200 °C (390 °F) the system is of the type βP_o and at low temperatures a new type, probably αP_a , precedes the first type. There are some data which suggest there is a second low-temperature form which is perhaps ordering in the particles of the low-temperature form to make it of the type αP_o . The data are not detailed enough, nor sufficiently well understood, to be able to describe this system well (10,11).

The Al-Ag system seems to be probably the most complex system known which is reasonably well understood. Above about 190 °C (375 °F) this system exhibits first the βP_a type of precipitation to be followed by the αP_a type (12). However, below 190 °C (375 °F) there is an additional type of precipitation, αS_o (13), which precedes the above types. For this low-temperature aging the ideal precipitate composition appears to be Ag_3Al , which is structurally the same as the aluminum-rich matrix except that it is ordered.

Some of the newer permanent magnets are interesting precipitation systems. The most important is the Alnico's, based upon the Al-Ni-Fe system where the precipitation is of the type $\alpha_o P_a$ or αP_o depending on whether the ordered Ni-Al phase is considered the matrix or the precipitate. Two other systems, Cu-Ni-Co and Cu-Ni-Fe are of the type αP_a , although the Cu-Ni-Co system exhibits also the γP_a type after longer times (15).

The isomorphous system Ag-Cu exhibits first the αP_d type and later the γP_d type at both ends (16). There may be, however, some complications and perhaps it is not this simple. The system Au-Ni, precipitating as a result of a miscibility gap, exhibits only the γP_d type it seems (17).

In conclusion it seems that it is possible to classify precipitation systems according to certain structural aspects which would appear to be closely related to the kinetics of the systems and, likewise, are of prime importance in determining the physical properties. It is to be hoped that the use of such a system will aid materially in the further understanding of this phenomenon. Some of the kinetic aspects, as associated with the structural aspects, have also been discussed.

References

1. R. F. Mehl and L. K. Jetter, "The Mechanism of Precipitation from Solid Solution. The Theory of Age Hardening," *AGE HARDENING OF METALS*, American Society for Metals, Cleveland, 1940, p. 342.
2. A. H. Geisler, "Precipitation from Solid Solutions of Metals," *Phase Transformation in Solids*, 1951, p. 387, Wiley, New York.
3. A. Guinier, "Precipitation dans les Alliages. (Precipitation in Alloys)," *Physica*, Vol. 15, 1949, p. 148; (See also reference 10).
4. C. S. Smith, "Microstructure," *TRANSACTIONS*, American Society for Metals, Vol. 45, 1953, p. 533.
5. D. Turnbull, "Theory of Cellular Precipitation," *Acta Metallurgica*, Vol. 3, 1955, p. 55.
6. J. S. Bowles and C. S. Barrett, "Crystallography of Transformations," *Progress in Metal Physics*, Vol. 3, 1952, p. 1, Interscience Publishers, New York.
7. R. D. Heidenreich, "Transition Structure in Lead-Silver Alloys and A Dislocation Mechanism," *Acta Metallurgica*, Vol. 3, 1955, p. 79.
8. R. O. Williams, "Diffusion of Vacancies under a Stress Gradient," Letter to the Editor, *Acta Metallurgica*, Vol. 5, 1957, p. 55.
9. C. Zener, "Theory of Growth of Spherical Precipitates from Solid Solutions," *Journal of Applied Physics*, Vol. 20, 1949, p. 950.
10. H. K. Hardy and T. J. Heal, "Report on Precipitation," *Progress in Metal Physics*, 1954, p. 143, Interscience Publishers, New York.
11. J. M. Silcock, T. J. Heal and H. K. Hardy, "Structural Aging Characteristics of Binary Aluminum-Copper Alloys," *Journal*, Institute of Metals, Vol. 82, 1954, p. 239.
12. A. H. Geisler and J. K. Hill, "Analysis and Interpretation of X-Ray Diffraction Effects of Aged Alloys," *Acta Crystallographica*, Vol. 1, 1948, p. 238.
13. C. B. Walker and A. Guinier, "An X-Ray Investigation of Age Hardening in AlAg," *Acta Metallurgica*, Vol. 1, 1953, p. 505.
B. Belbeoch and A. Guinier, "Relation Entre Les Structures Et Les Proprietes Des Alliages Aluminium-Argent Pendant Le Durcissement Structural," *Acta Metallurgica*, Vol. 3, 1955, p. 373.
14. A. Guinier, "Mechanism of Precipitation in a Crystal of a Metallic Solid Solution," *Journal of Physical Radium*, Vol. 3, 1942, p. 124.
B. L. Averbach, Mats Hillert and M. Cohen, "Thermodynamic Properties of Solid Aluminum-Silver Alloys," *Acta Metallurgica*, Vol. 4, No. 1, Jan. 1956, p. 31.
15. A. H. Geisler, "Structure of Permanent Magnet Alloys," *TRANSACTIONS*, American Society for Metals, Vol. 43, 1951, p. 70.
16. C. S. Barrett, H. F. Kaiser and R. F. Mehl, "Studies upon Widmanstatten Structure VII-Copper-Silver System," *Transactions*, American Institute of Mining and Metallurgical Engineers, Vol. 117, 1935, p. 39. (See also discussion by C. S. Barrett to reference 2).
17. W. Koster and W. Dammoh, "Hardening of Gold-Nickel Alloys," *Zeitschrift fur Metallkunde*, Vol. 28, 1936, p. 248.

A METHOD FOR THE ETCHING OF METALS BY GAS ION BOMBARDMENT

BY J. B. NEWKIRK AND W. G. MARTIN

Abstract

An improved method for the etching of metal surfaces by bombardment with gas ions is described. Novel features, including the use of krypton as the etching agent and the application of a magnetic field in the ionization chamber, have made it possible to etch metallographic specimens more rapidly and with less heating of the specimen than has been reported here-to-fore. (ASM International Classification M20r.)

INTRODUCTION

CATHODE ion bombardment is becoming an increasingly useful method for revealing the microstructure of polished metallographic specimens. In 1954 Padden and Cain (1)¹ published a brief review of the literature concerning this etching method and proposed an apparatus design which they stated made possible a technique that was rapid and flexible, therefore suitable for routine metallography. A cathodic etching unit, which is similar in appearance to that of Padden and Cain and which is said to take advantage of their coolant system, was made commercially available soon thereafter.

One of the commercial units was used by the authors during a study of cathodic etching phenomena. During the course of this study several deficiencies of the unit became apparent. The most serious of these were the air leaks that repeatedly developed at the joint between the copper cathode and the top of the bell jar etching chamber. The leaks made it impossible to control the etching atmosphere. Attempts to seal this joint permanently were unsuccessful. Another trouble was the long time required to produce a satisfactory etch on the specimen. A copper-base alloy, for example, required about a half hour to become etched. Also there always seemed to be numerous pits of mysterious origin and irregular shape and distribution over the surface of the etched specimen. These pits did not appear when the specimen was etched chemically.

¹ The figures appearing in parentheses pertain to the references appended to this paper.

A paper presented before the Thirty-Ninth Annual Convention of the Society, held in Chicago, November 4-8, 1957. The authors, J. B. Newkirk and W. G. Martin are associated with the Research Laboratory, General Electric Company, Schenectady, New York. Manuscript received May 25, 1956.

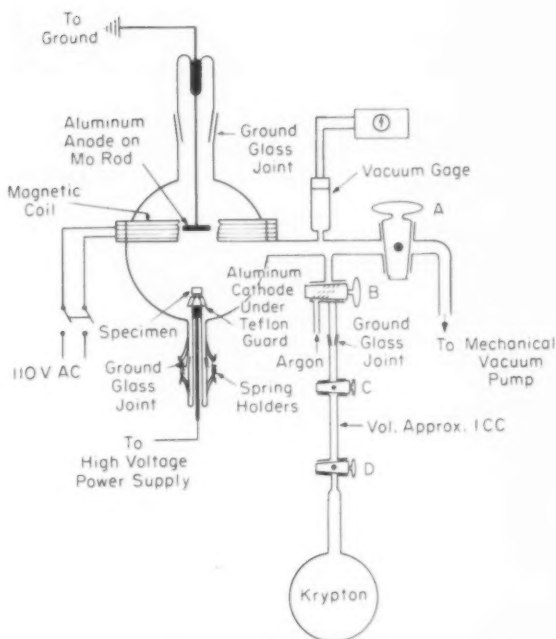


Fig. 1—Diagram of Etching Chamber and Vacuum System for Cathodic Etching.

In the present report a technique is described which is based on the Padden and Cain method but which avoids the troubles mentioned above. The new method features the use of krypton gas, as suggested by Fisher and Weber (2), and the application of a magnetic field to increase ionization efficiency. The method is now available for routine metallographic applications in this laboratory.

THE APPARATUS

The vacuum apparatus for cathodic etching is sketched in Fig. 1. The main etching chamber consists of a glass bulb 8.5 inches in diameter which is strong enough to withstand evacuation safely. The anode consists of an aluminum disk 1.5 inches in diameter and 0.25 inch thick on the end of a 0.125 inch diameter molybdenum shaft. This shaft is sealed to a ground glass joint, as shown in the sketch, for easy disassembly when the bulb is to be cleaned of sputtered metal. The cathode is in the form of a pedestal upon which is placed the specimen to be etched. The cathode is also sealed to a ground glass joint so that the cathode assembly may be easily removed. A detailed drawing (Fig. 2)

of the cathode pedestal shows the Teflon shield which is designed to minimize the ion bombardment damage to the cathode pedestal itself. The exposed metallic part of the pedestal may be easily replaced when needed.

Any mechanical vacuum pump which will reach 1 micron pressure in a reasonable time will serve as a suitable vacuum source. There should be a valve (A in Fig. 1) between the vacuum source and the etching

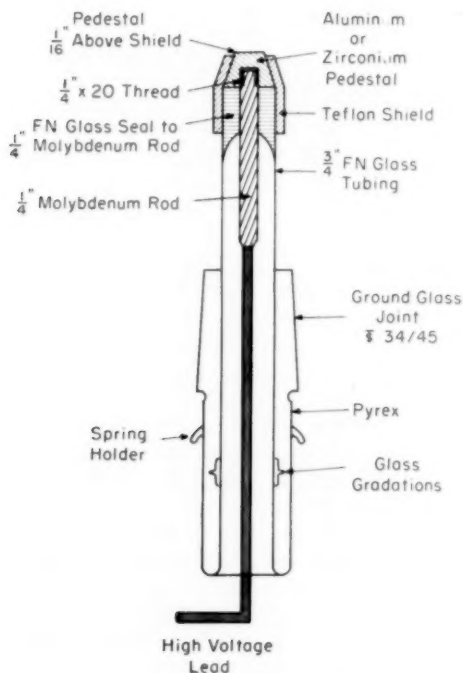


Fig. 2—Detail of Cathode Assembly.

assembly. The vacuum gage should permit the reading of pressure to within 5μ in the range 5 to 100 microns. A standard vacuum tube thermocouple gage has been found to be convenient.

Close to the etching chamber is the entry port for admitting the bombarding gas. The gas to be admitted is selected by valve B. (The system is first flushed with argon and then is filled with a small amount of the heavier and more efficient krypton for the actual etching process.) A coil having 380 turns of 0.086×0.040 F copper wire is placed horizontally around the bulb just above the equator to increase the etching efficiency. This coil, having a D.C. resistance of about 2 ohms, is op-

erated directly on 110 V AC. The magnetic field produced at the center of the coil is approximately 130 gauss R.M.S. value.

The power supply, sketched in Fig. 3, is a modification of that used in the Padden and Cain method. A timing device has been added to protect the transformer and electron tubes from surges of current be-

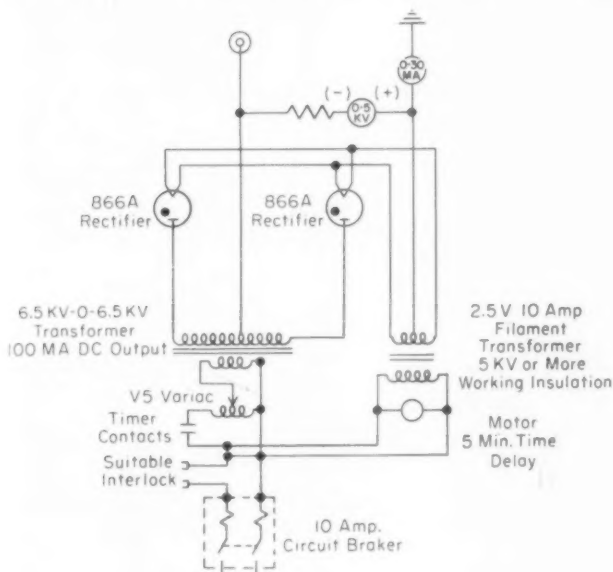


Fig. 3—Diagram of Power Supply.

fore the tubes have warmed up. The cathodic etching assembly is shown in Fig. 4.

SAFETY PRECAUTIONS

The high voltage lead should be carefully isolated to avoid accidental contact. Other metal parts should be well grounded. Also a guard cage with a clear window should be placed about the vacuum apparatus. This cage should be designed to permit freedom of manipulation and observation but provide adequate protection against the high voltage and the possibility of injury attending accidental globe implosion.

OPERATION PROCEDURE

The following procedure, with minor variations for different alloys, has been found to give a satisfactory etch in a reasonable time (See Table I).

A specimen, which has been metallographically polished, is placed

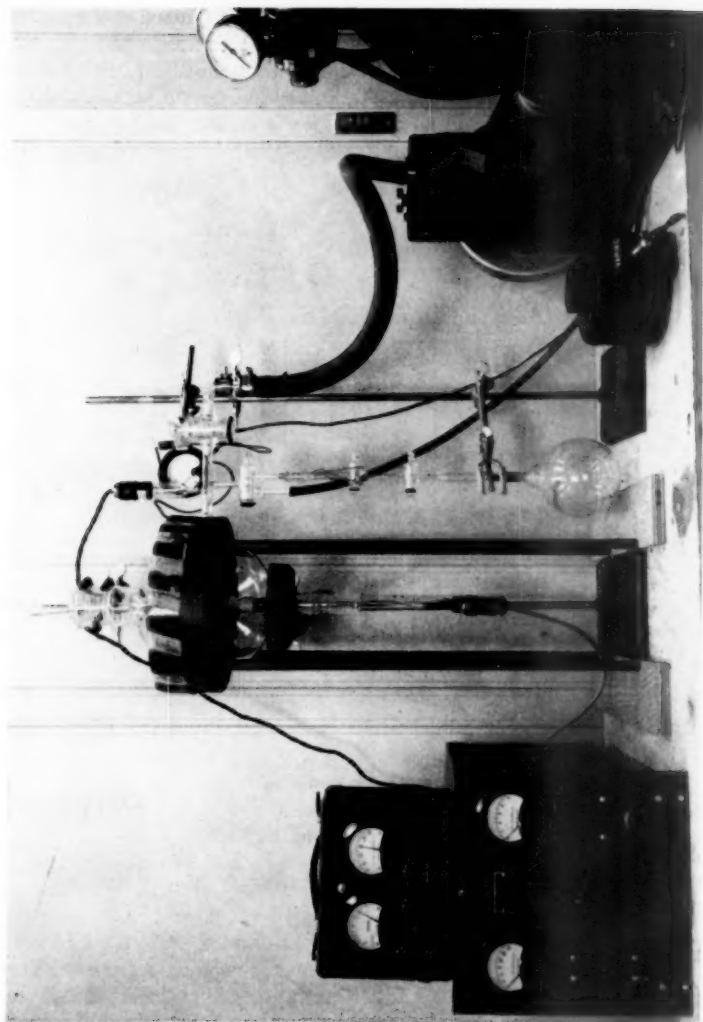


Fig. 4—The Cathodic Etching Apparatus.

on the cathode pedestal, polished side up, and the cathode assembly is fitted in its place within the etching chamber. The pressure in the chamber is then reduced to 1 micron using stopcock A. Using stopcocks A and B, argon is then admitted until the pressure is slightly above atmospheric. The pressure is again reduced to one micron and a small amount of krypton is admitted using stopcocks (B) (C) and (D). The

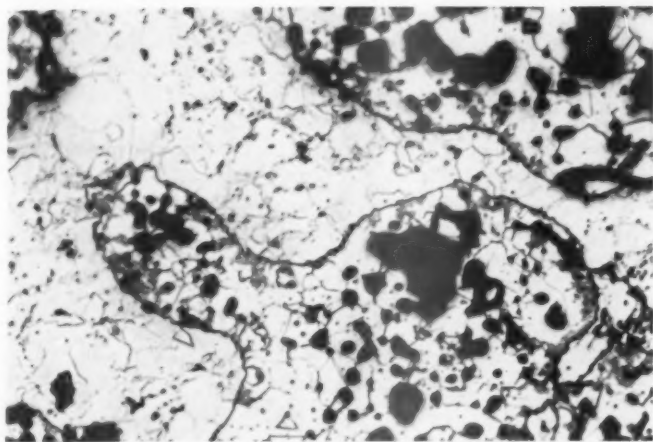


Fig. 5—Sintered Compact of Au-Ni, Cathodically Etched. $\times 250$.

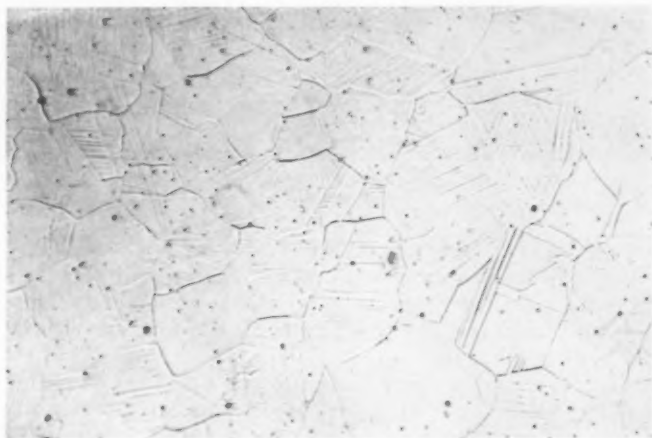


Fig. 6—Stainless Steel (18-8), Cathodically Etched. $\times 250$.

pressure is then reduced to 15μ and, with all stopcocks closed, the power is turned on and the etching potential is raised to about 4000 volts. This induces a current of approximately 1.5 ma to flow. The gas pressure, which will begin to rise when the current flows, should be kept to about 15μ by opening stopcock (A). A few seconds after the power is turned on a rise in current and a drop in potential will occur. Presumably this marks the removal of an insulating layer on the specimen surface and the beginning of the process of metal removal. Etching then follows.

The etching process can be accelerated by the presence of a suitable magnetic field within the etching chamber. The principle by which this occurs is described by Wehner (3) and depends upon the fact that charged particles are deflected by a magnetic field. Thus electrons, traveling in a curved instead of straight path from cathode to anode, have a greater chance of colliding with a gas atom, causing the atom to become ionized and able to bombard the specimen. Etching efficiency is

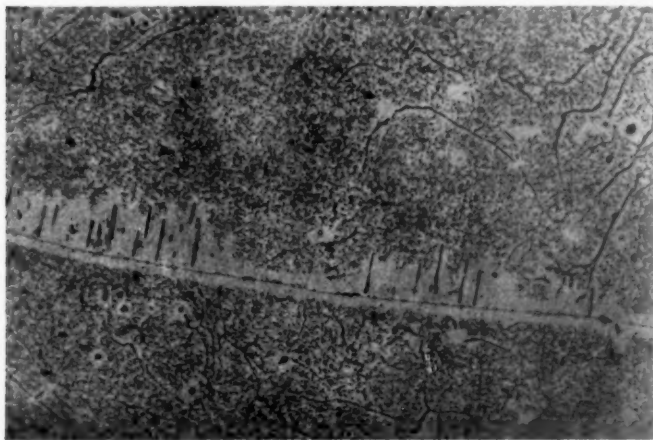


Fig. 7—Copper + 2.5% Iron, 1060 °C. W.Q., aged at 700 °C, cathodically etched. $\times 250$.

thereby improved. Using the coil described above, the etching time can be reduced by a factor of about three. For example, without the magnetic field, a satisfactory etch can be produced on a specimen of medium carbon steel in 10 minutes. With the field, a comparable etch is produced in three minutes.

In general, the lower the pressure at which a glow can be maintained at a given voltage, the less the specimen is heated. The presence of the magnetic field helps to maintain the glow and therefore permits etching at a lower gas pressure. Overheating has not been a problem in the present method since most metals do not reach a temperature above 300 °F by the time a satisfactory etch is obtained. This has been checked by having a small amount of low melting material on the specimen surface during the etching process. If extra cooling is desired, one may withdraw heat from the sample by cooling the external cathode rod with cold air.

EXAMPLES

The above method has been applied successfully to alloys which are

Table I
Etching Conditions for Several Alloys

Sample	Without Magnetic Field			With Magnetic Field (Approx. 100 Gauss)			
	Power Supply Voltage	ma/cm ²	Etching Time Min.	Pressure In Microns	Power Supply Voltage	ma/cm ²	Etching Time Min.
Cu +2.5% Fe	4500	2	4	20	3500	2	1
Brass	4000	2½	4	20	3500	1½	1
304 Stainless Steel	4500	2½	11	15	4500	1½	3
Uranium	4500	1	>45	15	4000	2	25
Duralumin	4500	2	>45	15	4000	2	20
Fe +7% Si	4500	1½	10	10	4000	1½	3
Medium Carbon Steel	4500	1½	10	10	4000	1½	3
Ti +3Al +5Cr	4000	2	15	10	4500	2	5

difficult to etch by the more conventional wet methods. For instance, porous specimens such as sintered compacts tend to hold liquids in the voids. This liquid oozes out and stains the specimen after it has been superficially dried. Since no liquid is used in the cathodic method, there is none to creep out and stain the surface. Fig. 5 shows a porous specimen of AuNi which has been cathodically etched. Alloys containing metals which are far apart in the electrochemical series are difficult to etch chemically because the more noble metal tends to redeposit upon the specimen surface. In cathodic etching this does not occur. Fig. 5 also illustrates this application. Several wet etching methods were unsuccessful in showing the true structure of this alloy.

Figs. 5 through 7 shows the microstructure of different types of alloys as revealed by this method of cathodic etching. Table I summarizes the conditions under which specimens of various types have been satisfactorily etched with and without the application of a magnetic field.

SUMMARY

The vacuum cathodic etching method described here avoids the problems attending poor atmosphere control within the etching chamber which were sometimes present when a commercial cathodic etching unit was used. As a consequence of the refinements proposed here, more reproducible results are obtained in less time than was previously required. The new features are:

1. More vacuum-tight etching chamber.
2. Rearrangement of the electrodes.
3. Radiation cooling.
4. Use of argon for flushing and krypton for etching.
5. Use of magnetic field to improve etching efficiency and reduce etching time.

References

1. T. R. Padden and F. M. Cain, Jr., "Cathodic Vacuum Etching," METAL PROGRESS, American Society for Metals, Vol. 66, No. 1, 1954, p. 108.

2. F. Fisher and C. E. Weber, "Cathodic Sputtering for Micro-Diffusion Studies," *Journal of Applied Physics*, American Institute of Physics, Vol. 23, 1952, p. 181.
3. G. K. Wehner, "Sputtering of Metal Single Crystals by Ion Bombardment," *Journal of Applied Physics*, American Institute of Physics, Vol. 26, 1955, p. 1056, and preceding publications.

DISCUSSION

Written Discussion: By Per M. Carlberg (Surahammars Bruks AB, Surahammar, Sweden), and Börje Löfblad (Sandvikens Jernverks AB, Sandviken, Sweden).

One of the difficulties with this etching method is to obtain a uniform attack on the specimen surface. Padden and Cain and others^{2,3} expose only a part of it through a hole in the cathode holder. The current density is then easily controlled, and the geometry of the chamber remains unchanged. The authors have instead chosen a solid pedestal, on which the specimen is placed. In this case, the edges of the specimen may be subjected to an intense etching.

At the Division of Metallography, Royal Institute of Technology in Stockholm, we have made some experiments⁴ with a cylindrical etching tube (Fig. 8). It is of the same basic lay-out as the present one, but it was operated with a negative-earth bridge rectifier. The cathode could be cooled externally by a cooling mixture. By using a hollow pedestal and shaft, direct water cooling is also possible. Without any shielding of the cathode, the major part of the discharge concentrated on the pedestal and the sides of the object. As pointed out by the authors, this results in severe sputtering, and unnecessary heating of the cathode. To design a suitable shield, the potential field around the cathode in a discharge-free chamber was studied on a two-dimensional blotting-paper model, soaked with sodium chloride solution. The model electrodes were fed with a small A.C. voltage, and the equipotential lines determined with a vacuum tube voltmeter. Cut-outs in the paper represented insulating parts. The result is shown in Fig. 9 a-d. Shielding the pedestal only (as used here by the authors) still leaves the sides of the specimen open to the discharge. Better results are obtained with cylindrical shields, where the equipotential lines are almost parallel with the surface. In the tube, the best results were obtained with a glass cylinder, placed around the cathode, and extending about 5 mm (3/16 in.) above the surface. A uniform etching was obtained, and the cathodic dark space was flattened in agreement with the model results.

The authors are to be congratulated for the results obtained with the magnetic field. It is a major improvement of this technique, as it reduces the current density, and thus the temperature of the specimen. In the Russian⁵ production model OIT-1, an elaborate cathode construction is used to place the small specimen (up to diameter 30×2 mm) in almost direct contact with a mixture of alcohol and dry ice. The current density is about 15 mA/cm² to give etching times comparable with the present ones. Is the use of krypton instead of argon of similar importance?

² H. Tsuchikura, *Hitachi Review*, Vol. 35, 1953, p. 491.

³ G. V. Spivak, V. E. Jurasova, F. F. Kushnir and I. N. Prilezhaeva, *Zhurnal Priboi i tekhnika eksperimenta*, 1957, No. 2, p. 106.

⁴ P. M. Carlberg and B. Löfblad, Metallurgical Engineering Thesis, Royal Institute of Technology, Stockholm, 1955.

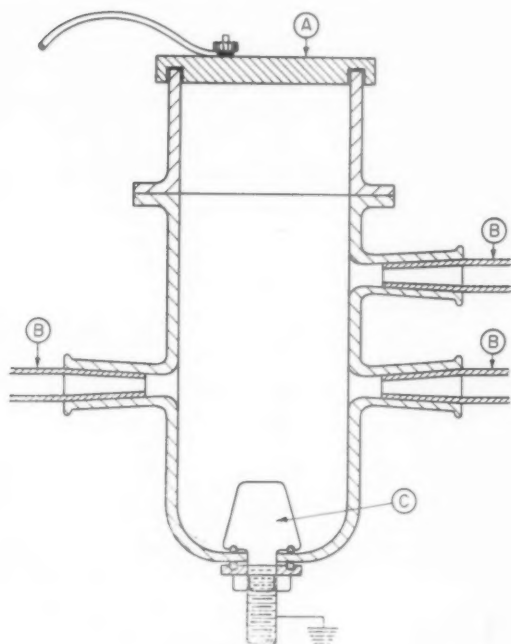


Fig. 8—Cylindrical Etching Tube. A—aluminum anode, B—
inlets for argon, pump, and vacuum gage, C—cathode pedestal
of stainless 18-8-steel.

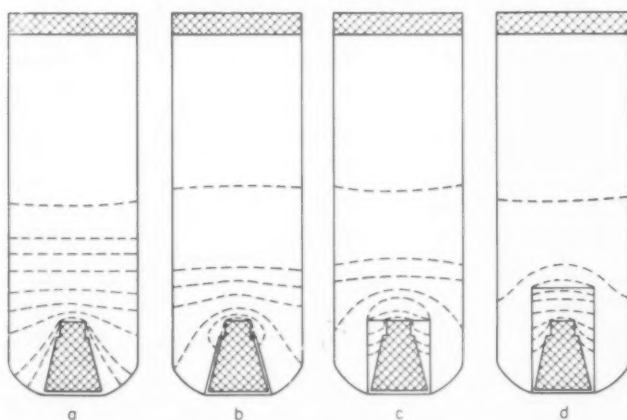


Fig. 9—Equipotential Lines in Discharge-Free Model. a—without shield,
b—shielding of pedestal only, c—cylindrical shield at level with object, d—cylindrical shield, extending 20 mm ($\frac{3}{4}$ in.) above surface of specimen.

Written Discussion: By W. L. Grube, Research Staff, General Motors Corporation, Detroit.

Since the introduction of gas ion bombardment etching to the field of metallography a few years ago, it has found an ever increasing application in the preparation of specimens that are difficult to etch otherwise. The advantages of the method have already been adequately demonstrated not only by the present authors but also by Padden,⁶ Bierlein^{6,7} and others. However, the long etching times required and the consequent excessive heating of the specimen have often been serious obstacles to its use. Further study of the ion bombardment etching

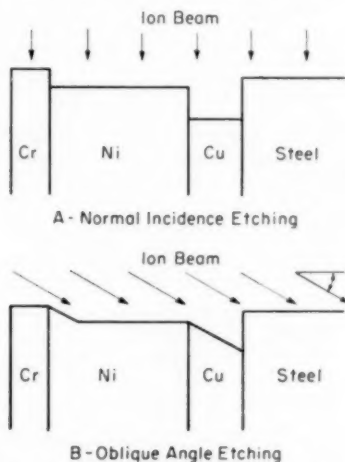


Fig. 10—Schematic of the Contours Developed for Normal and Oblique Incidence.

process has, therefore, been needed and the authors are to be commended for this serious effort to devise methods whereby etching conditions can be made more favorable so that etching time can be reduced. Any new methods and novel approaches which tend to make ion etching more universally applicable are certainly most welcome, and, therefore, the comments which I have to make are not to criticize that which has been said but rather to indicate those things which come to mind that have been omitted.

Although, as the authors have indicated, etching time is substantially reduced when a krypton atmosphere and a magnetic field are employed some heating of the specimen still must occur. The advisability of incorporating a method for cooling the cathode pedestal in the presently proposed method might, therefore, be considered. Padden and Cain⁶ and Bierlein, et al.⁷ have suggested methods for either

⁶ T. R. Padden and F. M. Cain, Jr., "Cathodic Vacuum Etching," *METAL PROGRESS*, Vol. 66, No. 1, 1954, p. 108.

⁷ T. K. Bierlein and B. Mastel, "Techniques for the Metallography of Irradiated Uranium," Paper No. B7, Annual Meeting, Electron Microscope Society of America, Sept. 10-12, 1956, Madison, Wisconsin.

⁷ T. K. Bierlein and B. Mastel, "Technique for Studying the Identical Area in Pre- and Post-Irradiated Uranium," Paper No. A5, Annual Meeting, Electron Microscope Society of America, Sept. 9-11, 1957, Cambridge, Mass.

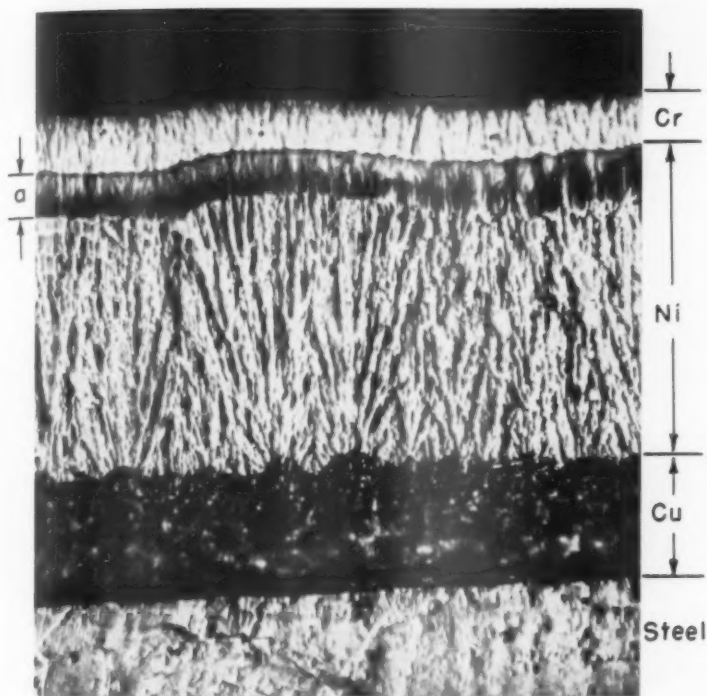


Fig. 11—Composite Electrodeposit Ion Etched at Angle of 30 Degrees. $\times 750$. L-1631. Etching conditions: 4 Kv, 10 ma, 25 microns argon, 1 hour. "a" is the sloping portion of the nickel deposit.

continuous or intermittent cooling that could be incorporated very easily into the equipment proposed by the authors. If through the combined use of krypton, magnetic fields, and specimen cooling the ambient temperature of the specimen could be reduced well below 100 degrees Centigrade, the method might then become suitable for etching quenched structures containing metastable phases.

An advantage of ion bombardment etching, already mentioned by the authors, is that it may be used to etch specimens containing two or more elements which are widely separated in the electrochemical series. Although the difference in etching rate between the various elements or phases may not be as great with ion etching as it is with chemical etching, the problem, nevertheless, still exists.

Consider for example, a composite electrodeposited coating consisting of successive layers of copper, nickel, and chromium with steel as a base material. A cross section of such a composite specimen is shown schematically at "A" in Fig. 10. When a specimen of this type is etched chemically the rate of attack on the various metals is so radically different that it is nearly impossible to develop and preserve the structure at the interfaces between the layers. Although not quite so pronounced, somewhat the same situation is encountered when ion bombardment etching is employed in the conventional manner. When the bombarding ions im-



Fig. 12—Ion Etched High Temperature Alloy (GMR 235) at Incident Angle of 30 Degrees.
× 750. L-1633.

pinge upon the surface at normal incidence, the nickel etches more rapidly than the chromium and the copper etches more rapidly than either the nickel or the steel base. This makes it difficult to observe any of the interface structure. If, on the other hand, the ions are made to impinge upon the surface at an angle, as shown at "B", certain interfaces can be preserved due to the shading effect of the more etch-resistant metals. For the angle of attack shown, both the chromium-nickel and the nickel-copper boundaries can be retained.

Control of the angle of incidence of the impinging ions cannot be accomplished simply by rotation of the specimen with respect to the plane of the anode. Since the lines of electric force still approach the specimen surface normally, so will the ions—or nearly so. If, however, the specimen is placed behind a screen or grid, held at cathode potential, the ions after passing through the screen will be, essentially, coasting in a field-free space. Since the ions do not change direction appreciably after passing the screen it then becomes possible to control the angle of incidence of the ions by simple rotation of the plane of the specimen surface. Fig. 11 shows a photomicrograph at × 750 of a composite electrodeposit of copper-nickel-chromium on steel ion etched in this manner. It can be seen that detail

can be observed on either side of both the chromium-nickel and the nickel-copper boundaries. The dark region in the nickel adjacent to the chromium is the sloping portion of the nickel deposit shown schematically at "B" in Fig. 10. The presence of this shaded area emphasizes the fact that caution must be exercised when interpreting detail seen in specimens that have been ion etched at oblique incidence. When specimens containing distributed phases are etched at an oblique angle, and when the distributed phase particles are more resistant than the matrix, a shaded area will appear in the matrix behind each particle. Such shaded areas are illustrated in Fig. 12 (see arrows). These areas can easily be mistaken for a part of the distributed phase or may even suggest a gradient within the matrix structure. Hence, the nature of their origin must always be kept in mind when interpreting the detail observed.

The authors of the paper have aptly illustrated how ion bombardment etching can be made more useful by proper manipulation of various factors involved in the process and the variation described in this discussion has been presented to further illustrate how control of another of these factors can be used to enhance the versatility, and thereby the usefulness, of this promising new metallographic tool. It should be remembered, however, that with any new method of etching the appearance of structures may be appreciably different than that obtained with conventional methods and, therefore, caution must be exercised in interpreting detail.

Written Discussion: By L. S. Birks, Electron Optics Branch, Optics Division, U. S. Naval Research Laboratory, Washington, D. C.

1. Have any measurements been made to determine the specimen surface temperature under the fast etching procedure using a magnetic field? 2. Is the present technique more suitable than previous ion bombardment methods for studying structures such as martensite that transform slightly above room temperature?

Written Discussion: By T. K. Bierlein, physical metallurgist, Hanford Laboratories Operation, General Electric Co., Richland, Washington.

The method of etching metals by ion bombardment, although described in many technical journals and publications, has not for some unknown reason provoked general attention. This is indeed unfortunate, since ion bombardment approaches a "universal" etching method for not only metallic specimens, but cermets and refractories as well.

The apparatus described by the authors, similar in many respects to apparatus designed at Hanford in 1953 for developing the microstructure of nonradioactive and radioactive materials, incorporates a magnetic field for increasing etching efficiency. The utility of the magnetic field undoubtedly stems from the fact that a lower krypton pressure can be used during the etching. The redeposition rate of sputtered material onto the specimen, an inverse function of mean free path, is therefore reduced. This consequence is far more important than a two to three fold reduction in etching time. In general, the actual etching time is small in comparison to the total time associated with assembling the apparatus, obtaining the vacuum, adjusting to correct krypton pressure, outgassing and removing surface films, etching the specimen, permitting the specimen to cool, removing the specimen from the chamber, and cleaning the apparatus.

The authors state that the static pressure in the chamber rises when current flows through the chamber, and that the pressure should be readjusted to the initial value by pumping. Unless krypton is allowed to flow continuously into the chamber, the inert gas atmosphere will become contaminated. Chemical reaction concurrent with the inert bombardment will occur. For example, if a continuous flow

of krypton is used in the etching of uranium specimens, it is possible to achieve an etch satisfactory for both optical and electron microscopy in a time of only 10 minutes without the aid of a magnetic field. In cases of chemically reactive, porous sintered specimens the time required for a satisfactory etch may be as long as 1 hour as a consequence of gas contamination.

Table I of the authors' paper lists various etching conditions applied to particular metallic specimens. At first glance it might appear that particular values of applied voltage, current density, and gas pressure are required. Our experience indicates a relatively wide latitude in etching conditions. If the specimen area is small compared to the area of the cathode plate, the total current through the chamber is determined almost completely by the applied voltage and the gas pressure. It is therefore possible to etch a variety of materials under exactly identical conditions of voltage, pressure, and current density. Etching can therefore be applied to almost any material in a routine fashion. A low pressure, of course, is advisable for reducing redeposition.

Written Discussion: By F. M. Cain, Jr., manager, Metallurgical Services, Nuclear Materials and Equipment Corporation, Apollo, Pa.

The authors center considerable attention on their reference (1) which is the work reported by Padden and Cain in the July 1, 1954 issue of *METAL PROGRESS*. In fact, one could readily conclude after reading the subject paper that the instrument design and etching method of reference (1) were unsuitable for routine metallography and that Messrs. Newkirk and Martin had improved measurably on both the instrument design and the etching technique. However, when comparing the results reported in the subject paper with those reported in reference (1) there are few, if any, apparent improvements.

As a result of their new design and technique the authors claim: to have eliminated troublesome air leaks, to have established shorter etching time, to obtain more reproducible results, etc.

Air leaks were not a problem in the Padden and Cain etcher, and etching times for a variety of different materials were from one to three minutes without the use of expensive krypton or a magnetic field. Also, uranium was etched in three minutes as compared to 25 minutes for the new design. As for reproducible results, the illustrative photomicrographs of typical results in the Padden and Cain paper speak for themselves.

This error on the part of the authors is understandable since their reported work was performed with a commercial cathodic etcher designed by the Optical Film Engineering Company. This unit was patterned in some respects after the published design of Padden and Cain, but the manufacturer's implied claim of similarity was entirely unjustified.

Authors' Reply

Several significant refinements of the vacuum cathodic etching technique are contained in these stimulating comments. The evident interest in our paper is very gratifying and we wish to thank all of the discussors for their contributions.

We are especially indebted to Messrs. Carlberg and Löfblad for pointing out the very recent development of this technique by Spivak et al. and for describing their own study of the effect of electrical shielding of the specimen itself. In reply to their concluding question, we have found that better results in general are obtained when krypton is used instead of argon. We owe this to the higher efficiency

of momentum exchange due to the greater mass of the krypton atoms. Only a very small (<0.5 cc at one atmosphere) amount of Kr need be used per specimen so the extra cost is relatively small.

We see no reason why additional cooling could not be provided as suggested by Dr. Grube, although we have not found it to be necessary for our work. His idea of bombarding at an angle oblique to the specimen surface is intriguing and should find useful application. A further refinement of the technique might be to bombard the specimen with ions of uniform energy from an ion gun. This would allow close control of the etching intensity and permit highly selective removal of surface atoms.

We offer the following replies to Mr. Birks' questions:

1. We have not measured the actual surface temperature during etching. However, we know it does not rise above 232°C (450°F) because a small piece of tin resting on the specimen surface during bombardment does not melt. A pellet of Wood's metal, however, does melt. Therefore, the surface temperature probably exceeds 70°C (158°F).
2. Specimen heating seems to be less with this etching method than with other ionic bombardment techniques we have tried. It follows, therefore, that the method we describe should be more suitable for etching specimens whose microstructure would be altered by a temperature rise of more than a hundred or so degrees.

Dr. Bierlein has properly emphasized the importance of minimizing the redeposition of sputtered material upon the specimen surface by etching at the lowest possible gas pressure. Since this phenomenon is discussed in our references (1) and (3) we did not elaborate upon it. We feel that the magnetic field provides two significant improvements:

1. In the presence of the field the glow can be maintained at a lower gas pressure and redeposition is, therefore, less.
2. Ionization efficiency is improved due to the helical motion of electrons as they travel from cathode to anode. A larger proportion of the current is, therefore, carried by working ions instead of electrons. The result is less heating for a given amount of surface metal removed.

We agree that reductions of temperature and redeposition are more important factors than is a saving of time. However, if many specimens are to be etched the time saving could also become significant. The procedure steps listed by Bierlein need not be lengthy. If the apparatus is kept evacuated the chamber itself need not be outgassed each time. Inserting and removing the specimen requires only a few seconds: the pressure in the chamber of our apparatus reaches 30 microns after three and a half minutes pumping at which time the chamber is flushed with argon or krypton and is then pumped in three more minutes to about 20 microns operating pressure; since the specimen is not appreciably heated we need not wait for it to cool; the chamber needs to be cleaned only rarely.

A continuous flow system is no doubt satisfactory if the atmosphere is controlled properly during etching. We prefer the static atmosphere method because it gives satisfactory results with less tinkering.

We regret that Mr. Cain has read into the paper a criticism of his design which we have not expressed. Our second paragraph specifically states that our criticism

is of a commercial cathodic etching unit which we tested. The Padden and Cain apparatus is evidently similar in many respects to this commercial unit and in fact is specifically cited by the manufacturer in his sales literature. As in all scientific endeavor our work does not necessarily negate but rather extends the work of previous authors. We maintain that our electrode arrangement and the use of a magnetic field are distinct improvements upon the commercial unit as well as upon the Padden and Cain apparatus.

THE RELATION BETWEEN CONSTITUTION AND ULTIMATE GRAIN SIZE IN ALUMINUM—1.25% MANGANESE ALLOY 3003

BY PHILIP R. SPERRY

Abstract

The ultimate grain size of annealed 3003 aluminum alloy sheet rolled from semi-continuous direct chill cast ingot is affected by the application or omission of an initial thermal treatment of the ingot for reasons which had not hitherto been explained. Comparison of sheet from ingot which had previously been homogenized and that which had not, showed that in the latter there could be a correlation between a fine, highly concentrated precipitate and an abnormal recrystallization behavior which led to a coarse grain structure. A further experiment in which other external variables were eliminated confirmed that the fine precipitate was responsible for the coarse grain size. The precipitate caused an extension of the recrystallization temperature range and strengthened the alloy. Solid solution differences were minor and without substantial effect on grain size. (ASM International Classification M27c, N5; Al, 4-3)

INTRODUCTION

THE GRAIN SIZE of annealed sheet of the aluminum alloy containing 1.25% manganese (3003) is distinctly related to the prior thermal history of the material. If ingot produced by the semi-continuous direct chill method is given a high temperature homogenization heating, known as a "preheat," before hot rolling, it is not difficult to obtain a fine grain size with normal production control. Omission of the homogenization treatment leads to an undesirably coarse ultimate grain size. It was considered important to the fundamental understanding of grain size control to investigate the manner in which the constitution of the alloy was related to grain size.

It is generally acknowledged that additions of manganese raise the recrystallization temperature of aluminum and favor a coarse grain size when relatively small amounts are exceeded (1)¹. Marchand (2) has shown both of these effects in high purity alloys and suggested that

¹ The figures appearing in parentheses pertain to the references appended to this paper.

A paper presented before the Thirty-Ninth Annual Convention of the Society, held in Chicago, November 4-8, 1957. The author, Philip R. Sperry, is research metallurgist, Dept. of Metallurgical Research, Kaiser Aluminum and Chemical Corporation, Spokane, Washington. Manuscript received April 15, 1957.

the manganese content of the solid solution should be kept to less than 0.30 to 0.40% in the commercial 1.25% alloy for minimum grain size. Marchand pointed out the need of thermal treatment before rolling, inferring that it produced the desired solid solution composition. Rosenkranz (3), referring to a commercial 1.5% manganese alloy, linked the restraint of recrystallization by the omission of the preheating treatment to the absence of equilibrium, indicating that a supersaturated solid solution existed in this instance. Hug (4), in a study of a similar alloy (Aluman), concluded that a high temperature homogenization treatment of the ingot was indispensable to a fine grain size. Hug did not attempt to give reasons for this behavior, but he presented data showing that unhomogenized material not only recrystallized at higher temperatures but that it had higher strength in the annealed condition. The fact that coarse grain size is associated with higher recrystallization temperatures and higher strength is suggestive of a solid solution effect. However, a tendency has been noted for aluminum alloys containing manganese to precipitate a constituent at fairly high temperatures, and a relationship between this so-called "fine dispersoid" and the inhibition of recrystallization had been proposed (14,15).

Some means had to be found to distinguish between the effects of the constitutional factors, solid solution and precipitate, and to control the many external variables in deformation and annealing practices which also influence grain size. This was accomplished by two approaches: (a) a detailed step-by-step comparison throughout simulated normal processing from ingot to sheet of homogenized and unhomogenized material; (b) a comparison of various combinations of solid solution and precipitate concentration, keeping initial grain size, and amount of cold reduction constant. By these two methods, it was established that the precipitate was responsible for the increased strength, recrystallization temperature and grain size in unhomogenized material.

COMPARISON WITH NORMAL PROCESSING

Procedure

Two blocks were cut from a location midway between the surface and central planes of a direct chill 3003 aluminum alloy sheet ingot with the following chemical analysis:

	Mn	Fe	Si	Cu	Mg	Zn	Ti
Weight %	1.14	0.57	0.18	0.12	0.01	0.02	0.01

The processing of the blocks is included as part of Table I. The homogenizing heat treatment at 1130 °F (610 °C) was preceded by a slow heating and followed by slow cooling to 1000 °F (540 °C). The unhomogenized material was heated directly to the latter temperature, at which both were held 4 hours before rolling. The simulated coil anneal

Table I
Hardness* Changes During Processing from Ingot to Annealed Sheet

Processing Stage	Unhomogenized		Homogenized	
	Chill Side	Interior	Chill Side	Interior
As cast			74	
1130°F (610°C) 10 hours, quenched				64.5
1000°F (540°C) 4 hours, quenched		71.5		61.5
Hot rolled at 1000°F (540°C) from 3 to 1 inch	75.5	70	68	65
Hot rolled at 725°F (385°C) to 0.255 inch	91	88.5	87	85
Hot rolled at 400°F (205°C) to 0.175 inch	96	93	93	91
Cold rolled to 0.130 inch	98	97	95	94.5
Annealed 2 hours at 700°F (370°C)	72	66	58	59
Cold rolled to 0.040 inch	97**		95**	
Coil annealed 6 hours at 775°F (410°C)	66**		57**	

*Rockwell H (60-kilogram load, $\frac{1}{16}$ inch ball)

**Converted from Rockwell superficial 15T (15 kg. load, $\frac{1}{16}$ inch ball).

of the 0.040 inch sheet included a 75 °F (42 °C) per hour heating period.

At each stage of the processing, samples were removed for metallographic examination and other tests which are described below. Samples from elevated temperature stages were water quenched. Some supplementary experiments were also conducted.

Hardness Tests

The hardness test results are listed in Table I. One surface of each original block corresponded to the ingot chill surface while the other side corresponded to the interior of the ingot. These differences are included in the tabulation for the intermediate rolling stages. Table I indicates consistently higher hardness values for the unhomogenized material at all stages. There is also a consistently greater hardness on the chill side of the samples, the difference being somewhat greater in the unhomogenized material. The hardness differences between homogenized and unhomogenized material are consistent with the tensile strength differences reported by Hug for the alloy, Aluman (4). Tensile test values from some additional lots of 3003 sheet are listed in Table II, and give further confirmation to these observations.

Table II
Some Properties of Annealed 3003 Sheet from Unhomogenized and Homogenized Direct Chill Ingot

Ingot Description	Grains per sq. mm.	Longitudinal Tensile Properties				Equivalent Mn content of solid solution (%) (Ref. 2)
		Ultimate (psi)	Yield at 0.2% offset (psi)	Elongation (% in 2 in.)	Resistivity (microhm-cm at 20°C)	
Laboratory cast						
Unhomogenized	85	17,550	7,350	31.5	3.48	0.15
Homogenized	640-1540	16,600	6,600	34.0	3.60	0.19
Production plant cast						
Unhomogenized	95	17,850	7,900	30.5	3.45	0.14
Homogenized	855	16,800	7,500	31.5	3.56	0.17

Table III
Solid Solution Composition as Affected by Prior Treatment

No.	Treatment	Resistivity (microhm-cm at 20 °C)	Equivalent Mn content of solid solution (%) (Ref. 2)
1H	1130 °F (610 °C) for 10 hours plus 1000 °F (540 °C) for 4 hours	4.52	0.54
1U	1000 °F (540 °C) for 4 hours	4.54	0.54
2H	1130 °F (610 °C) for 10 hours plus 1000 °F (540 °C) for 26 hours	4.32	0.46
2U	1000 °F (540 °C) for 26 hours	4.38	0.48
3H	Same as No. 1H, hot-rolled from 1½ in. square to ¾ inch round	4.19	0.41
3U	Same as No. 1U, hot-rolled same as No. 3H	4.00	0.33

Microstructure and Constitution

Upon heating of alloy 3003 ingot to the initial hot rolling temperature, with or without a homogenization heat treatment, a fine precipitate appeared in the microstructure. The precipitate was most heavily concentrated in the primary aluminum dendrites. The secondary aluminum associated with the eutectic structure in the dendrite interstices remained relatively clear. The precipitate particles in the unhomogenized material were much finer and more densely concentrated than in the homogenized material. In Fig. 7, Sample No. 2 shows an ingot heated at 1000 °F (540 °C) following a preheat at 1130 °F (610 °C), while Sample No. 6 shows one heated at 1000 °F (540 °C) without the preheat. A heavy etch has intensified the precipitate by exaggerating the particle sizes, but the differences are typical. These differences in precipitate density were maintained throughout the subsequent normal processing, and they are typified by the final annealed sheet of Samples Nos. 2 and 6 in Fig. 8. It is difficult to compare the total volume of precipitated phase directly, but it is certain that the lack of homogenization resulted in a significantly greater total number of precipitate particles.

The composition of the solid solution was assessed by means of electrical resistivity measurements, using Marchand's data for estimating the manganese content (2). The treatments employed, the resistivity, and the equivalent manganese content of the solid solutions are given in Table III. The mean composition of the solid solution just prior to hot rolling was the same regardless of whether or not a homogenization heat treatment had been used (Nos. 1H and 1U). A stable condition was not attained in four hours at 1000 °F (540 °C), as shown by the fact that the solid solution content had further decreased with continued heating up to 26 hours (Nos. 2H and 2U). Hot working accelerated the breakdown of the solid solution to a greater extent in unhomogenized than in homogenized material (Nos. 3H and 3U). Table II shows that a relationship similar to that in hot-rolled material exists in annealed sheet.

Referring back to the hardness and strength differences previously

mentioned, it seems that the high hardness of the unhomogenized 3003 alloy at all stages of processing must be attributed to the fine, densely concentrated precipitate. The hardening effect is probably due to the microscopically visible dispersion and not to any submicroscopic phenomena such as are associated with alloys of the precipitation hardening type. On the other hand, the as-cast ingot obtained its hardness from the high manganese content of the solid solution matrix. Since the homogenized sample had its solid solution content reduced as much as the unhomogenized, the precipitate in the former must have had a minor hardening effect.

Another feature of the alloy constitution which had a bearing on the potential quantity of precipitate was the relative proportion of the two intermetallic phases $(\text{Mn,Fe})\text{Al}_6$ and $\alpha\text{Al}(\text{Mn,Fe})\text{Si}$ in the interdendritic regions. In a previous publication (5), the author had shown that the principal constituent in direct chill cast 3003 alloy ingot is $(\text{Mn,Fe})\text{Al}_6$, which forms as a binary eutectic. Slower rates of cooling than those which normally apply for direct chill ingot allow two additional solidification reactions to proceed to a much greater extent. These are:

(Peritectic) $\text{Liquid} + (\text{Mn,Fe})\text{Al}_6 \rightarrow \alpha\text{Al}(\text{Mn,Fe})\text{Si} + \text{Al solid solution.}$

(Eutectic) $\text{Liquid} \rightarrow \alpha\text{Al}(\text{Mn,Fe})\text{Si} + \text{Al solid solution.}$

Subsequent heating of the solidified alloy leads to a continuation of the peritectic reaction to obtain the equilibrium proportions of the two intermetallic constituents as demanded by the phase diagram. The liquid reactant, of course, is replaced by the aluminum solid solution which is in contact with $(\text{Mn,Fe})\text{Al}_6$.

In order to compare the extent to which equilibrium was restored to cast direct chill ingot just prior to hot rolling, a microscopic lineal analysis was made of three samples—as-cast, unhomogenized and homogenized. The latter two samples were held for four hours at 1000 °F (540 °C) and quenched. Measurements were made of only those particles which were in the dendrite interstices and, therefore, had originally been in the cast structure. The volume fractions of each constituent were taken as the ratio of total intercepts for that constituent to the total traverse. The volume fractions were converted to weight fractions with the aid of published density values (8,11). The quantity of alloying element in each phase was calculated by published composition data (6,7,8,9,10), using values of 25.4% Mn + Fe for $(\text{Mn,Fe})\text{Al}_6$, and 25.5% Mn + Fe and 5.5% Si for $\alpha\text{Al}(\text{Mn,Fe})\text{Si}$. The results are given in Table IV. The manganese and silicon available to the aluminum matrix were calculated by the difference between the overall composition and the quantities of alloying elements tied up in the intermetallic phases. The aluminum matrix includes the solid solution and the fine precipitate.

Table IV
Distribution of Alloying Element Computed
from Lineal Analysis

	As-cast	Unhomogenized	Homogenized
No. particles intercepted in 6 mm.	134	137	131
Average particle diameter (microns)			
(Mn,Fe)Al ₆	1.4	1.2	1.2
αAl(Mn,Fe)Si	1.0	1.4	1.6
Weight % of constituent (computed from volume %)			
(Mn,Fe)Al ₆	3.39	2.06	1.26
αAl(Mn,Fe)Si	0.45	1.93	3.12
Calculated composition (weight %)			
Total Mn + Fe in alloy	1.71	1.71	1.71
Mn + Fe in (Mn,Fe)Al ₆	0.86	0.52	0.32
Mn + Fe in αAl(Mn,Fe)Si	0.11	0.49	0.80
Total Mn + Fe in constituents	0.97	1.01	1.12
Balance-Mn available in Al matrix*	0.74	0.70	0.59
Total Si in alloy	0.18	0.18	0.18
Si in αAl(Mn,Fe)Si	0.02	0.10	0.17
Balance-Si available in Al matrix	0.16	0.08	0.01

*The solubility of iron in aluminum is so low that it can be assumed that it is all associated with the intermetallic phases.

Admittedly, the calculated composition values in Table IV are only a first approximation because of much uncertainty about the data on which they were based. However, the relative values were significant. Homogenization caused most of the silicon in solid solution to react with eutectic (Mn,Fe)Al₆ to form αAl(Mn,Fe)Si. The manganese content of the matrix was simultaneously reduced. Lack of homogenization left a greater proportion of manganese and silicon in the matrix. If the estimated percentage of manganese in solid solution (Table III, Nos. 1H and 1U) is subtracted from the total manganese available in the matrix (Table IV), one arrives at a figure of $0.70 - 0.54 = 0.16\%$ manganese tied up as precipitate in unhomogenized material as against $0.59 - 0.54 = 0.05\%$ in homogenized material. Thus it is indicated that there is a much greater total volume of fine precipitate in unhomogenized than in homogenized material even before hot rolling commences. This relationship would continue as the solid solution decomposed further during hot rolling and annealing, since it was found that lack of homogenization accelerated the decomposition.

Recrystallization Behavior and Grain Size

Table V gives a qualitative description of recrystallization and grain size differences between homogenized and unhomogenized material through part of its processing. The differences between the sides of the starting block corresponding to the ingot chill face and the ingot interior are also included. Unhomogenized material showed great reluctance to recrystallize, especially at the chill side of the ingot, recrystallized grains were coarse and elongated after the intermediate anneal at 0.130 inches, and recrystallization was not complete. Homogenized material began to recrystallize at an early stage of hot rolling and the

Table V
Extent of Recrystallization and Relative Grain Sizes

Processing Stage	Unhomogenized		Homogenized	
	Chill Side	Interior	Chill Side	Interior
Hot rolled at 1000 °F (540 °C) to 1 inch	No recrystallization	Partial recrystallization on surface only	Shallow recrystallized layer, medium coarse grains	Deep recrystallized layer, medium fine grains
Hot rolled at 725 °F (385 °C) to 0.255 inches	No distinct recrystallization	No distinct recrystallization	Partial recrystallization, medium coarse grains	Partial recrystallization, medium fine grains
Cold rolled to 0.130 inches and annealed at 700 °F (370 °C) for 2 hrs.	Partial recrystallization, very coarse elongated grains	Nearly complete recrystallization, coarse elongated grains	Complete recrystallization, uniform fine grains, nearly equiaxed	

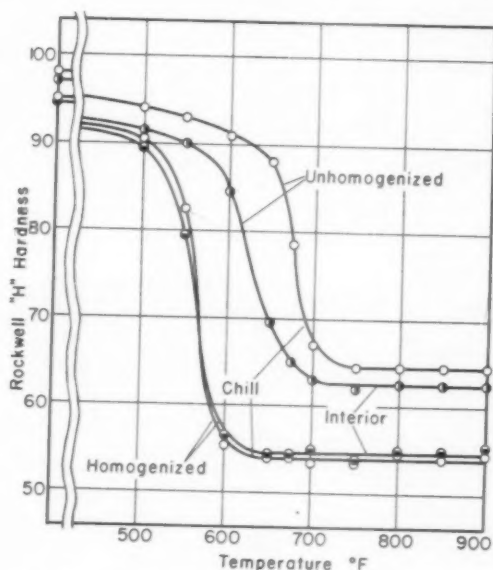


Fig. 1—Hardness versus Temperature Curves for 0.130 Inch Cold-Rolled Sheet Heated for 2 Hours and Quenched.

intermediate anneal caused complete recrystallization with a fine grain size.

Some of the cold-rolled 0.130-inch material was heated for 2 hours at various temperatures and quenched. Hardness measurements of both sides of the sheet were plotted against temperature in Fig. 1. Recrystallization was complete in homogenized material at 650 °F (345 °C), while in unhomogenized material it was complete at 700 °F (370 °C) on the side corresponding to the ingot interior and at 750 °F

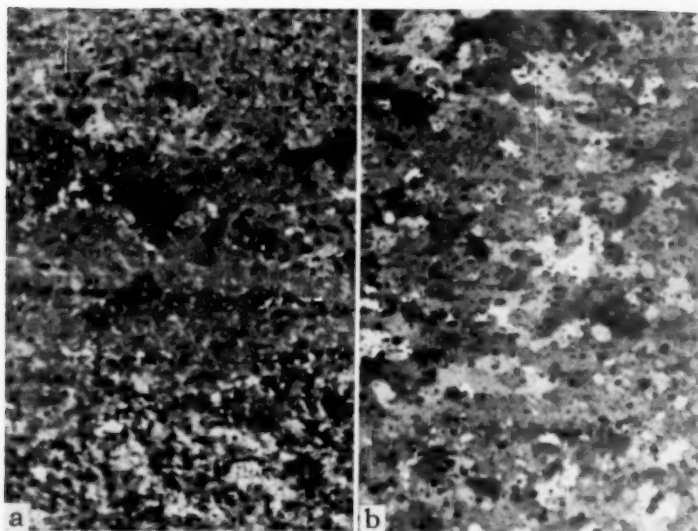


Fig. 2—Cold-Rolled 0.130 Inch Sheet from Homogenized Ingot Heated for 2 Hours at (a) 550 °F (290 °C) and (b) 600 °F (315 °C), Showing Normal Recrystallization. Anodized, crossed polarizers, sensitive tint. Sections parallel to sheet surface. $\times 100$.

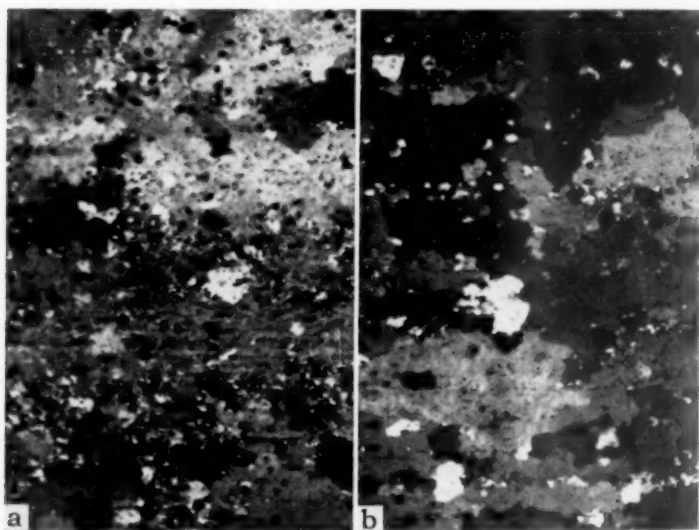


Fig. 3—Cold-Rolled 0.130 Inch Sheet from Unhomogenized Ingot, Chill Surface, Heated for 2 Hours at (a) 675 °F (355 °C) and (b) 750 °F (400 °C). Note the extremes of fine and coarse grains. Anodized, crossed polarizers, sensitive tint. Sections parallel to sheet surface. $\times 100$.

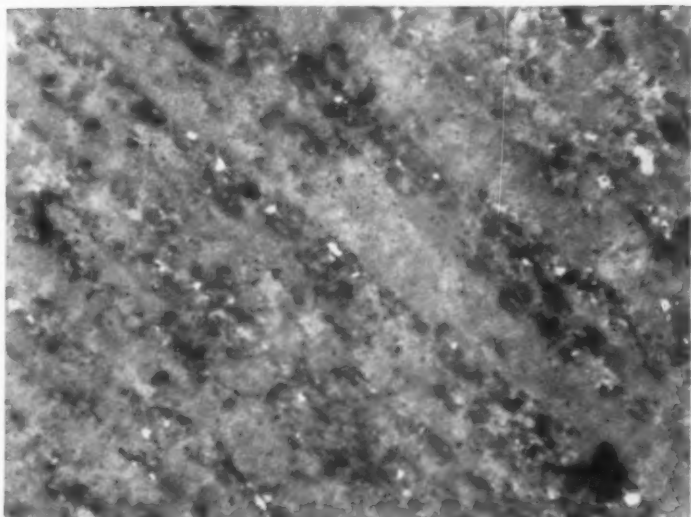


Fig. 4—Another Area of Same Specimen as Fig. 3a, Where Recrystallization Was Not as Advanced. Fine recrystallized grains are concentrated in bands which comprise original dendrite interstices. Dark grain in lower right is just starting to coarsen. Anodized, crossed polarizers, sensitive tint. $\times 250$.

(400 °C) on the side corresponding to the ingot chill surface. This confirms the higher recrystallization temperature for unhomogenized aluminum-manganese alloy as reported by Hug (4).

Microscopic examination of the hardness test specimens revealed a difference in the mode of recrystallization which is illustrated by Figs. 2a and 2b and 3a and 3b. In homogenized material, recrystallization was conventional, showing gradual appearance and growth of new grains until deformed crystals had entirely disappeared. In unhomogenized material, numerous fine recrystallized grains formed at early stages of recrystallization, but relatively few of these new grains grew and these attained considerable size. A duplex structure existed when recrystallization was just complete, and the effect of further annealing was to absorb many of the remaining fine grains. The fine grains which appeared initially were found most frequently within bands coinciding with the original dendrite interstices where precipitation was relatively light (see Fig. 4).

The recrystallization behavior of cold rolled 0.040-inch material was investigated by heating samples at 75 °F (42 °C) per hour and quenching them from various temperatures. This heating cycle was representative of a batch coil annealing practice. Fig. 5 shows that the recrystallization relationships with this type of heating were similar in form to

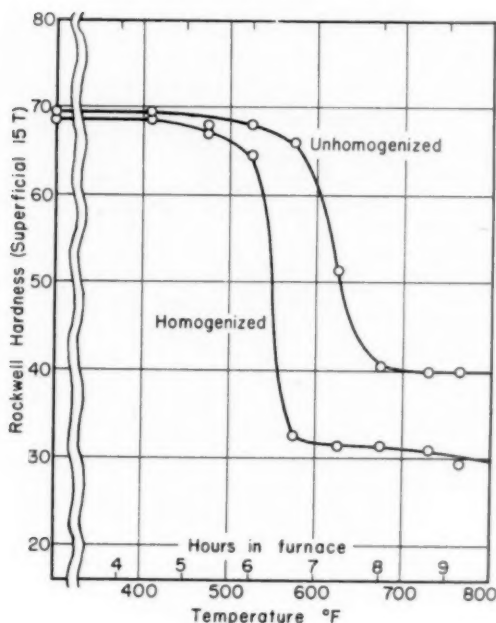


Fig. 5—Hardness versus Temperature Curves for 0.040 Inch Cold-Rolled Sheet Heated at 75 °F (42 °C) per Hour.

Table VI
Grain Size Estimates in Longitudinal Sections
of 0.040 Inch Sheet

	Grains/sq. mm.*	Length: thickness
Coil annealed at 775 °F (410 °C) for 6 hours		
Unhomogenized—chill side	75	8:1
—inner side	422	4:1
Homogenized —both sides	1780-2370	2:1
Rapidly heated in salt bath		
775 °F (410 °C) for either 15 min. or 24 hours		
Unhomogenized—chill side	1330	2:1
—inner side	1780	2:1
Homogenized —both sides	5620	1:1
930 °F (500 °C) for 70 hours		
Unhomogenized—chill side	1330	2:1
—inner side	2370	2:1
Homogenized —both sides	4220	1:1

*Successive grain size values are related to each other by a constant ratio of 1.333.

those with isochronal heating (Fig. 1). The microstructural evolution of recrystallization was also the same as that described for the 0.130-inch material. The final grain sizes and shapes are pictured in Figs. 6a and 6b.

Table VI lists some grain sizes and shapes estimated by the Kostrom method (12) on slowly and rapidly heated 0.040-inch sheet. These figures demonstrate the well-known grain refining effect of high rates of

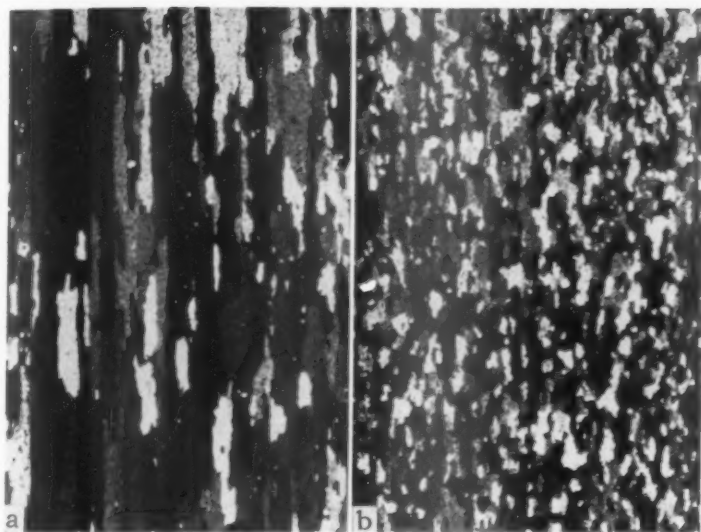


Fig. 6—Longitudinal Cross Sections of 0.040 Inch Coil Annealed Sheet from (a) Unhomogenized and (b) Homogenized Ingot. The original chill surface of the ingot lies to the left of each section. Anodized, crossed polarizers. $\times 50$.

heating in 3003 aluminum alloy, and also show that the amount of grain growth which follows recrystallization is negligible. It is clear that coarser grain sizes tend toward greater flattening of the grain shape.

Significance of Results

The foregoing experimental results have revealed that there are constitutional differences accompanied by differences in recrystallization behavior between 3003 alloy sheet rolled from homogenized and unhomogenized ingot. Contrary to expectations, the unhomogenized material retains less manganese in solid solution after hot rolling and annealing operations than the homogenized, and the difference does not appear to be great enough to explain the abnormality in recrystallization behavior and grain size. It seems more likely that the explanation might lie in the heavily concentrated fine precipitate in the unhomogenized material.

The comparisons of recrystallization behavior of the 0.130 inch and 0.040 inch sheet were of such a nature that the constitutional factors could not be evaluated without some question as to the auxiliary effects of prior amount of cold work and prior grain size. Hence, another experiment was conducted to compare several different combinations of solid solution composition and precipitate distribution for their effects on the recrystallization process, eliminating all other processing variables.

Table VII
Solid Solution Composition and Hardness before Rolling and
after Rolling and Annealing at 800 °F (425 °C) for One Hour

	As-Cast	HT No. 1	HT No. 2	HT No. 3	HT No. 4	HT No. 5	HT No. 6	HT No. 7
Resistivity (microhm-cm. at 20°C)								
Before rolling	5.92	4.94	4.62	4.41	4.58	4.39	4.59	4.42
After annealing	—	3.88	4.12	4.00	4.08	3.96	3.83	3.80
Equivalent Mn content of solid solution(%)								
Before rolling	~1.0	0.71	0.58	0.50	0.57	0.49	0.57	0.50
After annealing	—	0.29	0.38	0.33	0.37	0.32	0.27	0.26
Rockwell H Hardness								
Before rolling	74	68.5	64.5	62.5	65.5	62	74.5	72.5
After annealing	—	67.5	63.5	62.5	64.5	62.5	70.5	68

EFFECTS OF SOLID SOLUTION AND PRECIPITATE ON RECRYSTALLIZATION

Procedure

Seven blocks, 1.4 inches thick, were cut from the central portion of a direct chill cast 3003 aluminum alloy sheet ingot having the following chemical analysis:

	Mn	Fe	Si	Cu	Mg	Zn	Ti
Weight %	1.18	0.64	0.20	0.16	0.01	0.01	0.03

Each block was given a different initial heat treatment as follows:

- HT No. 1 Heated at 1130 °F (610 °C) for 16 hours, water-quenched.
- HT No. 2 Heated at 1130 °F (610 °C) for 16 hours, cooled at 100 °F (55 °C) per hour to 1000 °F (540 °C), held 4 hours, water-quenched.
- HT No. 3 Same as HT No. 2 but held 24 hours at 1000 °F (540 °C).
- HT No. 4 Heated at 1130 °F (610 °C) for 16 hours, water-quenched, reheated at 1000 °F (540 °C) for 4 hours, water-quenched.
- HT No. 5 Same as HT No. 4 but held 24 hours at 1000 °F (540 °C).
- HT No. 6 Heated at 1000 °F (540 °C) for 4 hours, water-quenched.
- HT No. 7 Same as HT No. 6 but held 2 hours at 1000 °F (540 °C).

A duplicate set of samples was prepared for resistivity measurements.

Each heat treated block was cold rolled in one rolling direction to a thickness of 0.070 inches, a 95% reduction. Samples of the cold-rolled sheet were heated to various temperatures and quenched. Two methods of heating were used:

Method A—One hour heating in a small electric muffle furnace (five to ten minutes to reach temperature).

Method B—Heating in a circulating air furnace at 75 °F (42 °C) per hour.

A duplicate set of rolled strips for resistivity measurements was annealed in an air furnace at 800 °F (425 °C) for 1 hour and air-cooled.

Hardness, Microstructure, and Constitution

The hardness test results, electrical resistivities and equivalent manganese contents of the aluminum solid solutions are listed in Table VII.

These data cover heat treated ingot blocks before rolling and the same materials after cold rolling 95% and annealing at 800 °F (425 °C) for 1 hour.

The hardness and solid solution composition variations were consistent with the previous findings. Before rolling, the highest hardness was obtained in those materials which did not receive any treatment at 1130 °F (610 °C), HT Nos. 6 and 7. The solid solution composition of HT No. 6 was just about identical with those of HT Nos. 2 and 4, all three of which had been heated 4 hours at 1000 °F (540 °C). The same was true for HT Nos. 3, 5, and 7 which had been held 24 hours at 1000 °F (540 °C). Therefore, the higher hardness of HT Nos. 6 and 7 was unquestionably due to the precipitate. The strengthening effect of the precipitate in the other five materials was very minor and the solid solution composition differences became predominant. Thus, HT No. 1 had the highest hardness of the group which had been heated at 1130 °F (610 °C). The as-cast material, which is included for comparison, illustrates the supersaturation of the solid solution which is characteristic of aluminum-manganese alloys with cooling rates representative of production practice.

After rolling and annealing, most of the hardness values showed little change. This was rather surprising because of the relatively large change in solid solution composition, especially in HT No. 1. It can be concluded that the strengthening effect of the precipitate dispersion formed during the final anneal compensated for the loss in hardness due to depletion of the solid solution. Grain refinement also may have caused some increase in hardness. HT Nos. 6 and 7 apparently had passed beyond the optimum combination of solid solution composition and precipitate distribution and were softened somewhat.

The precipitate distributions before and after rolling can be compared by the photomicrographs, Figs. 7 and 8. As expected, HT Nos. 6 and 7 displayed the greatest concentrations of precipitate, but the precipitate density—i.e., the number of particles per unit volume—was lower in HT No. 7 because of coalescence achieved during the 24-hour heating at 1000 °F (540 °C). Of the other five samples, HT No. 1 had the least precipitate before rolling and the most after annealing, which lends support to the interpretation of the hardness data. The homogenizing heat treatment at 1130 °F (610 °C) which the first five samples received did not permit a precipitate density as great as that in the last two.

Recrystallization Behavior and Grain Size

The recrystallization curves obtained by hardness measurements and the grain sizes after heating to 800 °F (425 °C) by Methods A and B were almost identical for a given preheat treatment. Although this was contrary to expectations, in view of the normal sensitivity of

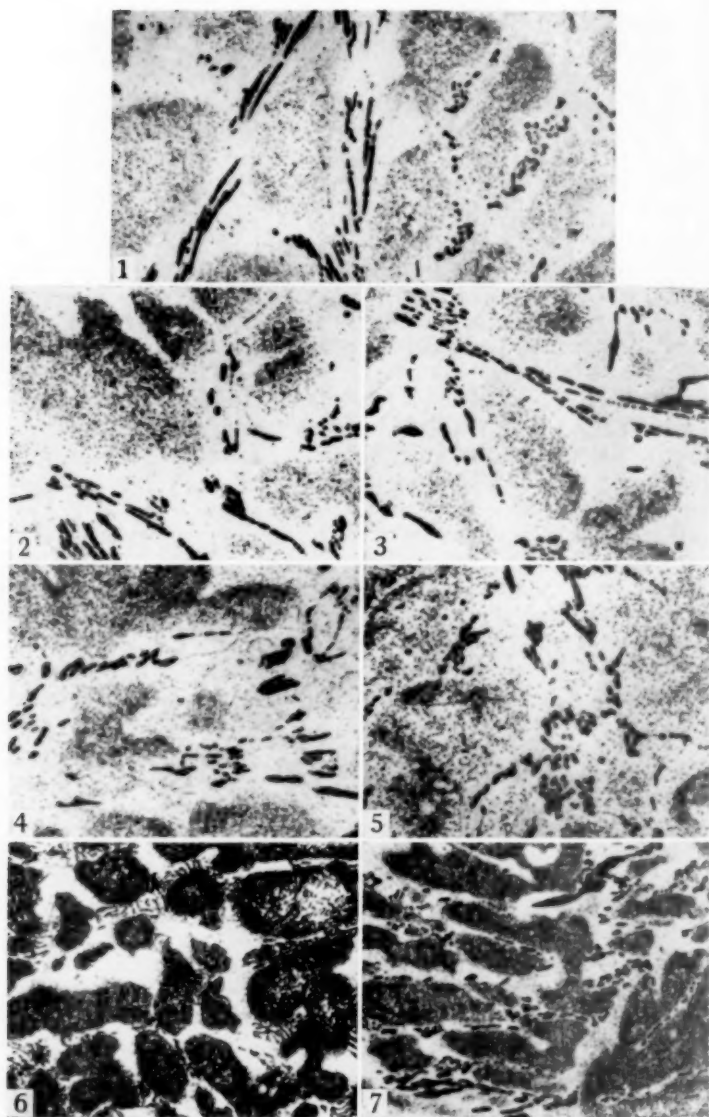


Fig. 7—Relative Precipitate Concentrations of Ingot After Initial Heat Treatments, HT No. 1 to HT No. 7. $\frac{1}{4}\%$ HF etch, 1 minute. $\times 250$.

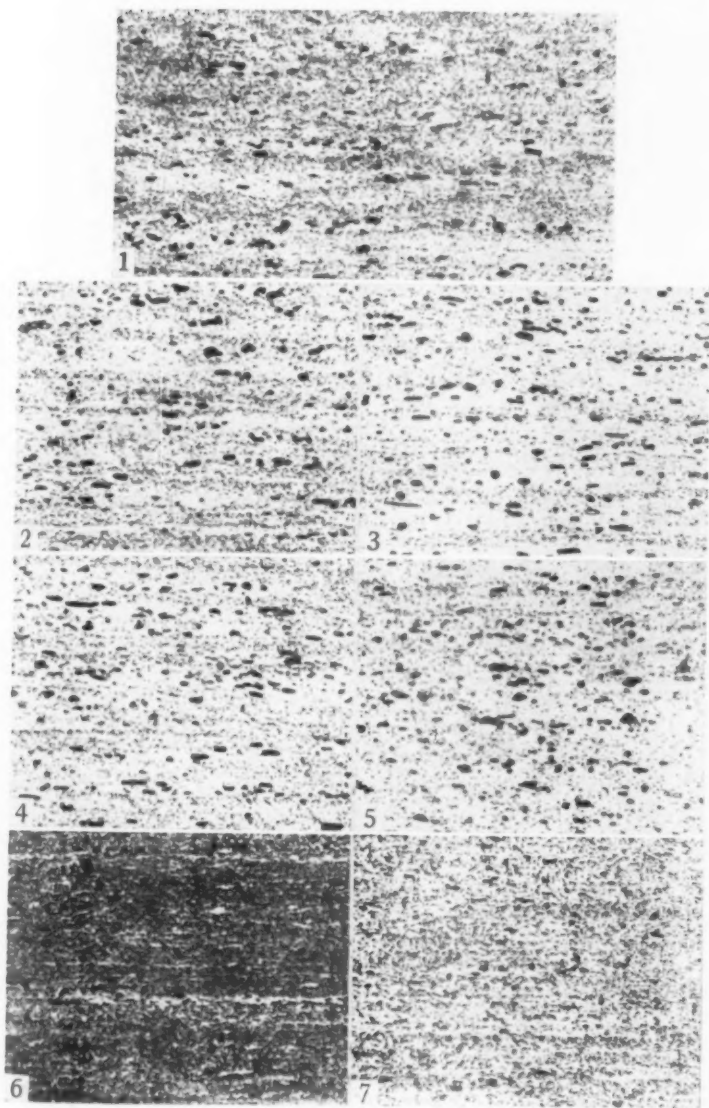


Fig. 8—Relative Precipitate Concentrations of Annealed Sheet Rolled from the Heat Treated Ingots of Fig. 7. $\frac{1}{4}\%$ HF etch, 1 minute. $\times 250$.

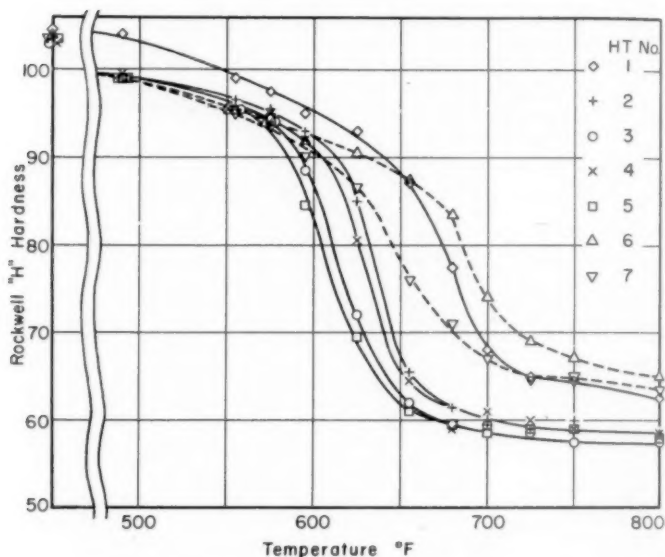


Fig. 9—Hardness versus Temperature Curves for 3003 Alloy with Seven Different Initial Heat Treatments After Cold Rolling 95% and Heating for 1 Hour.

3003 aluminum alloy to heating rate, the discrepancy was assumed to be due to the unusual experimental conditions—i.e., omission of hot rolling and intermediate anneals. At any rate, only the results of Method A are presented herein.

Fig. 9 shows the recrystallization curves based on hardness test results. HT Nos. 2, 3, 4, and 5 formed a group whose recrystallization temperatures varied within a range of 25 °F. The curve for HT No. 1 was displaced toward higher temperatures and higher hardnesses due to the higher initial solid solution content. The curves of HT Nos. 6 and 7, however, were of a totally different type. At the beginning stages of recrystallization, they showed softening similar to that of HT Nos. 2, 3, 4, and 5, but the rate of softening did not increase appreciably until much higher temperatures were reached. The end points of recrystallization were indistinct, and that for HT No. 6 was indicated to be at a higher temperature than that for HT No. 1. In view of the fact that the initial solid solution compositions of HT Nos. 2, 4, and 6 and of HT Nos. 3, 5, and 7 were about the same, it was confirmed that the precipitate concentration was the factor causing the abnormal recrystallization in the case of HT Nos. 6 and 7.

Microscopic checks of numerous samples within the recrystallization range showed that the recrystallization process in HT Nos. 1, 2, 3, 4, and 5 was similar to that of 3003 aluminum alloy sheet normally proc-

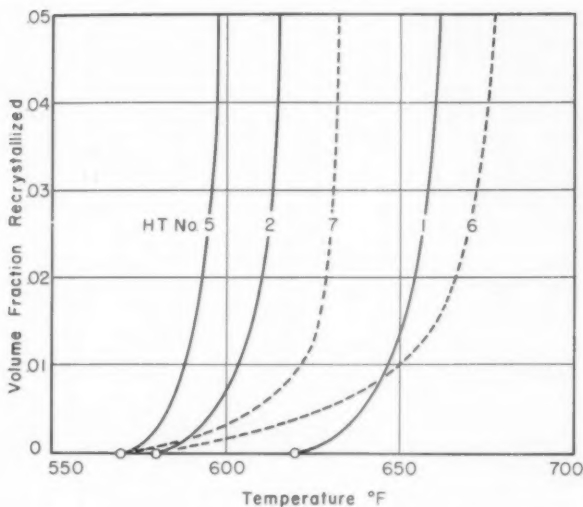


Fig. 10—Temperature Dependence of Recrystallization at its Early Stages Based on Microscopic Estimates.

essed from homogenized ingot. The recrystallization process in HT Nos. 6 and 7 was similar to that of unhomogenized 3003 aluminum alloy. Small recrystallized grains were detected at temperatures below 600 °F (315 °C), but they did not increase greatly in number or size until 650 °F (345 °C) was exceeded in HT No. 6 or 625 °F (330 °C) in HT No. 7. Then, coarse grains began to form in the manner previously described. The fundamental differences in the temperature dependence of recrystallization at its early stages are illustrated semi-quantitatively by Fig. 10. The solid solution effect, shown by HT Nos. 5, 2, and 1, is to displace the curves in the direction of the temperature coordinate. The precipitate effect, shown by HT Nos. 6 and 7, is to extend the temperature range over which only the mere beginnings of recrystallization are observable. These characteristics were just as applicable for the continuous 75 °F (42 °C) per hour heating as they were for the isochronal heating illustrated by Fig. 10.

The relative grain sizes of the samples heated to 800 °F (425 °C) for 1 hour are shown by Fig. 11. A considerable variation in any given sample could be traced to the original cast grains. These variations made grain size measurements rather meaningless. However, the grain sizes of all samples except HT No. 6 fell within a similar order of magnitude while HT No. 6 was eminently coarser. The grains of HT Nos. 1 to 5 had fairly smooth boundaries and a normal distribution of sizes while those of HT Nos. 6 and 7 had very irregular boundaries and consisted of mixed fine and coarse sizes, similar to Fig. 3b.

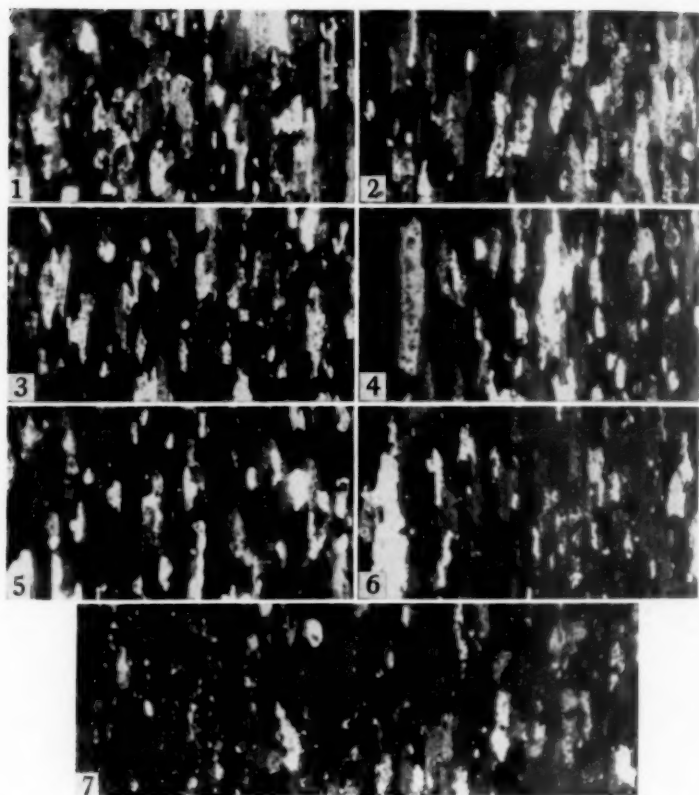


Fig. 11—Relative Grain Sizes and Shapes in Longitudinal Cross Sections of Sheet Annealed for 1 Hour at 800 °F (425 °C) After Cold Rolling from Ingots with Seven Different Heat Treatments. Anodized, crossed polarizers. $\times 100$.

DISCUSSION

The foregoing evidence indicates that when 3003 aluminum alloy ingot receives a suitable homogenizing heat treatment it recrystallizes and achieves a degree of grain refinement consistent with what can be considered as "normal." When the homogenization treatment is omitted, an abnormality in the recrystallization process is encountered. This discussion concerns the possible cause of this abnormality.

The solid solution composition differences, although affecting the recrystallization temperature range, have been eliminated as the cause of the coarse grain size. The tendency to form large recrystallized grains in unhomogenized material exists over a wide range of solid solution

compositions. The same wide range of compositions is encountered in homogenized materials without the corresponding formation of coarse recrystallized grains. The evidence points to the second phase dispersion as being responsible for an abnormal recrystallization behavior and a concomitant large grain size.

In considering the second phase distribution, one must distinguish between the larger particles which are already present in the cast structure and the finer particles which precipitate from solid solution during subsequent heating. The former are common to homogenized and unhomogenized material. Table IV shows that their number remains essentially constant, but that the $\alpha\text{Al}(\text{Mn,Fe})\text{Si}$ particles increase in size as they replace $(\text{Mn,Fe})\text{Al}_6$. Constituent particles of this magnitude are known to restrain normal grain growth by blocking the movement of grain boundaries (13). This undoubtedly accounts for the lack of grain growth following recrystallization. It is probably also a factor in the refinement of recrystallized grains in commercial purity aluminum as compared with high purity aluminum. In the case of unhomogenized 3003 alloy, the refining effect of these larger particles is apparently counteracted by some other influence.

The evidence that a fine, heavily concentrated precipitate can inhibit recrystallization offers a possible explanation of the grain coarsening phenomenon. It was shown in Fig. 10 that this inhibition does not act in the same sense that a high content of manganese in solid solution does. The precipitate apparently does not prevent the initial formation of nuclei at temperatures which are characteristic for the beginning of recrystallization in a precipitate-free alloy with an equivalent solid solution composition. As the temperature is increased, however, these initial nuclei fail to grow at a normal rate. It could not be determined how the rate of nucleation was affected, but it appeared that there was preferential nucleation in zones which were deficient in precipitate. At the higher temperatures where growth did begin, it was very selective and occurred at a rapid rate. It is this selective growth which is responsible for the large recrystallized grains. In turn, it is the precipitate which obstructs normal growth of nuclei and creates a sort of "discontinuous recrystallization," somewhat analogous to "discontinuous grain growth" where normal growth is inhibited by a second phase dispersion (13).

The precipitate in unhomogenized 3003 must have some characteristic to distinguish it from most other precipitates which do not affect recrystallization in such a distinct manner. This uniqueness is probably its stability at temperatures within the hot rolling and annealing range. Whereas other precipitates might be in the process of dissolving or coalescing in this temperature range the manganese precipitate continues to form and has extremely little tendency to coalesce. Three factors influence this behavior:

1. The tendency of manganese to saturate or even supersaturate the solid solution during solidification.
2. The low solubility of manganese at the temperatures concerned, especially with iron and silicon impurities present.
3. The extreme sluggishness of manganese due to its low rate of diffusion in aluminum.

It is very likely that there is a critical maximum particle size or minimum concentration which must exist before the inhibition of recrystallization becomes observable.

It is of interest to note the work of Gregory and Smith (16) on internally oxidized silver alloy single crystals. These authors found that the recrystallization temperature was definitely raised by the presence of a finely dispersed oxide. Some of the fundamental aspects of the inhibition of recrystallization by a dispersion of fine particles might well be studied in alloys of the type used by Gregory and Smith.

It was observed consistently that the solid solution decomposed to a greater extent in unhomogenized than in homogenized 3003 alloy (see Tables II, III, and VII). This fact seems at variance with the supposition that equilibrium is less readily obtained in unhomogenized material and, therefore, the solid solution should be more, rather than less saturated. The explanation for this anomaly may rest with the residual silicon content of the matrix, as indicated by Table IV. The equilibrium diagram for the aluminum-manganese-silicon system (9) shows that small silicon contents produce a marked decrease in solid solubility of manganese. Assuming that the actual matrix composition, and not the overall alloy composition, governs the solid solution of a major portion of the alloy at temperatures in the hot working and annealing range, it is conceivable that small differences in residual silicon can have a significant effect. This factor can likewise explain the fact that ingots such as those produced by the tilt mold process do not particularly require a high temperature homogenization heat treatment for grain size control (4). Tilt mold ingots are solidified more slowly and show a much larger proportion of $\alpha\text{Al}(\text{Mn,Fe})\text{Si}$ to $(\text{Mn,Fe})\text{Al}_6$ in the cast structure. This signifies that much of the silicon has already been withdrawn from the matrix. Lesser differences in solidification rate from surface to center of direct chill ingots also seem to be reflected in the differences in hardness, recrystallization temperature, and grain size shown in Tables I, V, and VI and in Fig. 1.

CONCLUSIONS

The major microstructural difference between wrought products from 3003 aluminum alloy ingot which has or has not been given a high temperature homogenization heat treatment lies in the greater quantity of fine precipitate particles in the latter. This high concentra-

tion of constituent particles leads to a modification of the normal recrystallization process in a manner which favors the formation of coarse recrystallized grains. The grain size in either case is a function of the recrystallization process only, subsequent grain growth being negligible. The highly concentrated precipitate imparts slightly higher strength, in addition to its effect on recrystallization behavior and grain size.

ACKNOWLEDGMENTS

The author expresses his appreciation to the numerous members of the staff of the Department of Metallurgical Research of Kaiser Aluminum and Chemical Corporation who have aided with the experimental work or have supplied helpful criticism in the interpretation of the results. He is especially grateful to F. M. Krill for his constructive review of the manuscript, and to Paul P. Zeigler, Director, for permission to publish these results.

References

1. H. W. L. Phillips, "Grain Size of Rolled Aluminum," *Journal, Institute of Metals*, Vol. 68, 1942, p. 47.
2. G. Marchand, "The Influence of Manganese in Solid Solution on the Recrystallization Temperature and Grain Size of Pure Aluminum Sheet," *Canadian Journal of Technology*, Vol. 31, 1952, p. 15.
3. W. Rosenkranz, "Investigation Concerning the Recrystallization Behavior of Aluminum Alloys After Hot and Cold Working," *Aluminum*, Vol. 31, 1955, p. 328.
4. H. Hug, "The Influence of High Temperature Heating of Ingots on the Microstructure and Properties of AlMn Alloy (Aluman)," *Metall*, Vol. 9, 1955, p. 176.
5. Philip R. Sperry, "Metallographic Study of Equilibrium Relationships in 3S (3003) Aluminum Alloy," *Transactions, American Institute of Mining and Metallurgical Engineers*, Vol. 203, 1955, p. 145.
6. G. V. Raynor, "The Effect on the Compound $MnAl_6$ of Iron, Cobalt, and Copper," *Journal, Institute of Metals*, Vol. 70, 1944, p. 531.
7. J. N. Pratt and G. V. Raynor, "The Intermetallic Compounds in the Alloys of Aluminum and Silicon with Chromium, Manganese, Iron, Cobalt, and Nickel," *Journal, Institute of Metals*, Vol. 79, 1951, p. 211.
8. Gösta Phragmen, "On the Phases Occurring in Alloys of Aluminum with Copper, Magnesium, Manganese, Iron, and Silicon," *Journal, Institute of Metals*, Vol. 77, 1950, p. 489.
9. H. Hanemann and A. Schrader, *Atlas Metallographicus*, Vol. III, Part 2, Verlag Stahleisen M.G.H., Düsseldorf, 1952.
10. M. Armand, "Liquation and Equilibrium Diagrams as Applied to the Al-Fe-Si Diagram," *Rapports Presentes au Congres International de L'Aluminium*, 1954, p. 305.
11. A. D. I. Nicol, "The Structure of $MnAl_6$," *Acta Crystallographica*, Vol. 6, 1953, p. 285.
12. H. Kostron, "Contribution to Metallographic Grain Size Measurement: II—Two New Rapid Processes for Cross Section Determinations," *Archiv für Metallkunde*, Vol. 3, 1949, p. 229.
13. Paul A. Beck, M. L. Holzworth and Philip R. Sperry, "Effect of a Dispersed Phase on Grain Growth in Aluminum Manganese Alloys," *Transactions, American Institute of Mining and Metallurgical Engineers*, Vol. 180, 1949, p. 163.
14. J. T. Hobbs, Jr., "Grain Control in Wrought Aluminum and Magnesium Products," *Grain Control in Industrial Metallurgy*, 1949, p. 209, American Society for Metals, Cleveland.

15. K. L. Dreyer and M. Dudek, "Structure and Property Anomalies in Manganese Containing Aluminum Alloys as a Result of Undercooling," *Metal*, Vol. 3, 1949, p. 219.
16. E. Gregory and G. C. Smith, "The Effects of Internal Oxidation on the Tensile Properties of Some Silver Alloys at Room and Elevated Temperatures," *Journal, Institute of Metals*, Vol. 85, 1956-57, p. 81.

DISCUSSION

Written Discussion: By E. C. W. Perryman, Head, Research Metallurgy, Atomic Energy of Canada Limited, Chalk River Project, Chalk River, Ontario.

First I would like to congratulate the author in attempting to solve a very difficult problem, namely that of the effect of a second phase on the recrystallization process. The most interesting result from the author's work is that recrystallization of the homogenized alloy leads to a fine equiaxed grain structure while unhomogenized material gives a coarse grain size, see Fig. 3a and 3b, which is similar to that produced by discontinuous grain growth. This difference was much more apparent with the 0.130 inch sheet than with the 0.070 inch sheet which had been rolled to 95% reduction. Since the hardness of the former was less than that of the latter in the as-rolled condition, it would appear that increasing amounts of cold work may be decreasing the grain size differences between homogenized and unhomogenized material after recrystallization. These results are quite similar to the results G. Marchand and myself obtained a few years ago in aluminum-5% magnesium alloys. In this work it was found that secondary recrystallization occurred in the commercial alloy (5% Mg, 0.25% Fe, 0.13% Si, 0.27% Mn) but that this was very dependent on the amount of cold work and on the annealing temperature and annealing time, see Fig. 12. Subsequent work showed that this phenomenon was associated with the manganese content. For a given annealing temperature and amount of cold work, secondary recrystallization was found to increase with manganese content up to a certain level and then decrease with further increase in manganese. Similar effects could also be produced by a chromium addition, the only difference being that smaller amounts of chromium were necessary to produce the same effects. These effects of manganese and chromium are illustrated for a 5% Mg, 0.1% Fe, 0.1% Si alloy in Fig. 13. Electrical resistivity and metallographic examination showed that during recrystallization a manganese or chromium-rich phase was being precipitated and that this was responsible for the discontinuous grain growth. This was confirmed by preheating to precipitate the second phase followed by cold rolling and annealing. In this case, it was found that preheating prevented the formation of large secondary grains, see Fig. 13. It would seem, therefore, that discontinuous grain growth can be produced if the rate of precipitation of a second phase is of the correct magnitude just as it can be if the rate of solution of a second phase is correct.

The results given by the author in Table VII show that precipitation of the manganese-rich phase is occurring during annealing at 425 °C (795 °F) and that there is more precipitate being formed in unit annealing time with unhomogenized material than with homogenized material, cf HT No. 4, 5, 6 and 7 in Table VII. I would suggest, therefore, that in homogenized material the precipitate is not being produced sufficiently fast to produce discontinuous grain growth. If this ex-

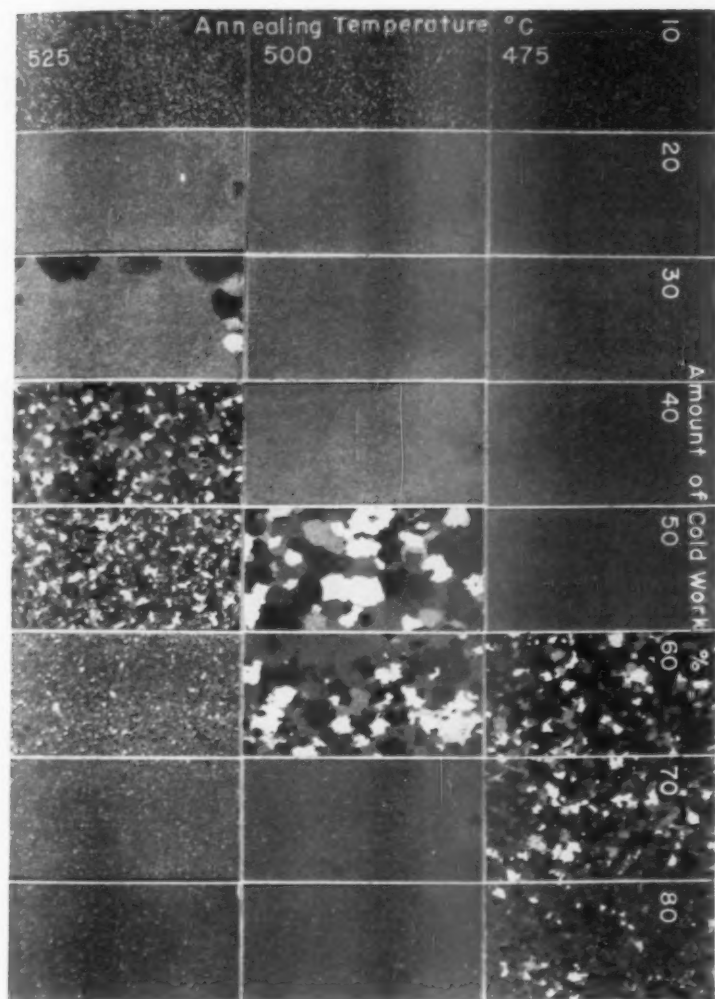


Fig. 12—Annealed 1 Hour in Air Furnace.

planation is correct, one would expect the recrystallization textures of the homogenized and unhomogenized material to be quite different. In fact, extrapolating from our own results with aluminum-magnesium alloys, I would expect the recrystallization texture of the unhomogenized material to be similar to that of the cold-worked texture. I would be interested to know if the authors have any results which would indicate that this is so.

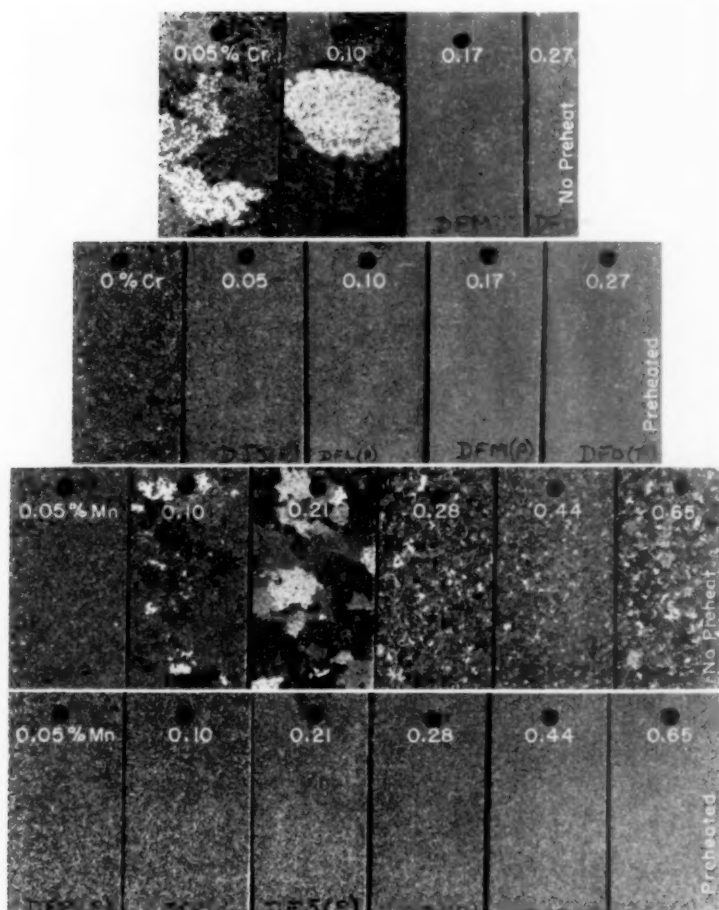


Fig. 13—60% Cold Work—Annealed 18 Hours at 975 °F.

The fact that precipitation is taking place during annealing may also serve to explain the apparent difference in the rate of recrystallization between homogenized and unhomogenized material in the early stages as shown in Fig. 10 of the author's paper. It is difficult to see why a precipitate which is being formed at the same time as new recrystallized grains should influence the rate of nucleation. However, it will decrease the rate of growth of these new grains and so show up the recrystallization process.

Written Discussion: By Gilles Marchand, Physical Metallurgy Division, Aluminum Laboratories Ltd., Kingston, Ontario, Canada.

The author is to be congratulated on a very good piece of metallographic work. Some observations we have made on the behaviour of Alcan 3S (Alloy 3003 without Cu) agree with his results but there is one which is an apparent disagreement with his data, that is: a slow furnace cool after "homogenizing" at temperatures in the vicinity of 600 °C (1110 °F) generally results in a finer grain size. It would be expected therefore that heat treatment No. 2 in the author's second experiment would give finer grain size than treatment No. 1 but this does not appear to be the case. In fact, in the light of the explanation given by the author regarding the influence of fine precipitate on the recrystallization process it is surprising that a greater variation in grain sizes was not noted corresponding to the range of microstructures shown in Figs. 7 and 8 of this paper.

A second point of interest concerning Alloy 3003 is the sensitivity of the grain size to the rate of heating to the annealing temperature; this alloy is considered to be more sensitive in this respect than the base metal from which it is prepared. Although this point is not specifically relevant to the paper, the author may have made similar observations and may care to comment on these points in terms of his theory.

It is mentioned that the manganese-rich precipitate must attain a certain size before it interferes with the recrystallization process. It can also be inferred from this work that once it grows to a large enough size it no longer impedes recrystallization. Would the author have made any measurements of the range of size which could be considered as critical?

The initial "homogenizing" treatment mentioned by the author may be regarded, especially in industrial practice where no water quenching would be used, primarily as a precipitation treatment. A second function of this treatment may be to allow the precipitate to coalesce and to grow to a noncritical size. The effect of this treatment on the subsequent rate of decomposition of the matrix and the final microstructure and grain size could be interpreted mainly in terms of precipitation if it is assumed that further precipitation during the fabrication process will occur preferentially on the particles formed during "homogenizing". (A comparison of Figs. 7 and 8 in the paper, shows that this assumption is reasonable.) It is granted that homogenizing probably occurs in the process and that its effect is not negligible. It is not without interest, however, to determine which mechanism has the most influence on the course of recrystallization for, if it is the latter, "homogenizing" for optimum results should be carried out at as high a temperature as possible; if precipitation and coalescence are more important then some intermediate temperatures should be desirable.

Written Discussion: By R. S. Mapes, Chief, Physical Metallurgy Section, Reynolds Metals Company, Metallurgical Research Laboratories, Richmond, Virginia.

Mr. Sperry has investigated the effects of homogenization treatment of DC cast ingots of 3003 alloy in relation to ultimate grain size. This paper is a natural sequel to a previous paper, entitled "Metallographic Study of Equilibrium Relationships in 3S (3003) Aluminum Alloy", in which he has shown that the homogenization treatment results in the formation of $AlFeMnSi$ by reaction between $FeMnAl_3$ and the $AlMn$ solid solution matrix which contains silicon in solid solution.

He has shown in this paper that the ultimate grain size of wrought sheet is related to the finely dispersed precipitate in the matrix rather than to the varying amounts of manganese in solid solution which had been previously suggested. He has shown that this finely dispersed constituent also is related to the higher

temperatures required for recrystallization of unhomogenized sheet and the accompanying higher mechanical properties.

Mr. Sperry is to be congratulated on a very worthwhile paper. It would be worthwhile to further determine the effects of the actual particle size of the constituent or dispersoid upon the recrystallization behavior of the alloy.

Written Discussion: By D. N. Williams, Battelle Memorial Institute, Columbus, Ohio.

This is the second paper which Mr. Sperry has published describing his very interesting studies of the metallurgical reactions occurring in 3003 alloy. My comments regarding the present paper are not related to the data given, which would appear to be most carefully obtained, but rather to the interpretation of the data.

The author has shown the existence of a relationship between coarse ultimate grain size in 3003 alloy and the presence of a very fine precipitate. This relationship is contrary to that normally observed. Studies underway at a number of laboratories aimed at improving the creep resistance by alloying to produce an insoluble dispersion illustrate this quite clearly. It has been observed that the dispersed phase when present in small amounts (1-3% by volume) decreases rather than increases creep resistance. This effect has been traced to the marked grain refining action of the dispersion, the loss in creep resistance due to grain refinement more than offsetting the gain due to the presence of the dispersion. Therefore, the author's conclusion that coarse grain size is caused by the presence of a very fine precipitate is somewhat difficult to accept. An alternate explanation would seem preferable.

Both in this paper and its predecessor, Mr. Sperry has pointed out that the principal reaction occurring during homogenization is the conversion of $(\text{Mn,Fe})\text{Al}_6$ to $\alpha\text{Al}(\text{Mn,Fe})\text{Si}$ which is accompanied by a noticeable reduction in the silicon content of the matrix. It has also been pointed out that the presence of silicon in solid solution reduces the solubility of manganese. Therefore, I wonder whether the correlation between amount of fine precipitate and grain size may not be of secondary origin and may not be confusing the true cause of the effect, the amount of silicon remaining in solid solution. It seems reasonable that precipitation will be much greater in a high silicon alloy than in a low silicon alloy due to the differences in manganese solubility. Relating grain size to silicon content would require the assumption that silicon can exert such a strong influence on the recrystallization process in an Al-Mn solid solution that even the presence of a fine dispersed phase is not able to suppress its action. The data given in the present paper does not appear in any manner to contradict this explanation. However, there may be objections to this explanation which are not apparent to me which are even more significant than those which I have raised regarding the original explanation of the data.

I wish that the author would comment on this alternate explanation of his data and also indicate, on the basis of his considerable familiarity with this alloy system, whether there is any reason to suspect that silicon might affect recrystallization behavior in the manner suggested.

Author's Reply

In reply to Dr. Williams' question concerning the effect of silicon, there is no evidence that the silicon itself substantially influences the recrystallization process.

In the absence of manganese, silicon in any amount up to its saturation limit has a very minor effect on recrystallization temperature of aluminum, and, to my knowledge, has never resulted in abnormally large grain sizes. However, it is believed that the presence of silicon contributes greatly to the coarsening effect by increasing the potential quantity of precipitate and—what is probably more important—accelerating the rate of formation of the fine precipitate. This latter effect has been shown very nicely in a Japanese article which appeared too recently to have been referred to in my paper.*

As Dr. Williams states, it is difficult to associate a precipitate dispersion with a coarsening of the grain when normal experience dictates that the opposite is generally true. That is why I state that there is undoubtedly a critical concentration and particle size necessary to produce this effect. This leads to Mr. Marchand's question regarding the probable dimensions involved. No measurements have been made as yet, but numerous observations indicate that the particles of importance lie just at or beyond the resolving power of the optical microscope ($\sim 0.2\mu$). The critical spacing may be in the same order of magnitude as the fine substructures which appear in aluminum preceding recrystallization. The crux of the argument for coarsening is that the precipitate dispersion is not uniform—therefore, the extent of inhibition is not uniform. This leads to a situation in which small recrystallized grains lie in contact with large unrecrystallized regions and, as higher temperatures are attained, some grains are favorably disposed to overcome the inhibition and grow at a rapid rate (Fig. 4 of paper). In the hypothetical case that the critical precipitate was absolutely uniformly distributed throughout the alloy, I would hesitate to predict whether such an alloy would be fine or coarse grained upon recrystallization. However, when the precipitate has coarsened or coalesced beyond the critical point, the recrystallized grains are refined, in accordance with normal experience.

The answer to Mr. Marchand's question on the lack of difference in final grain size between samples with treatment Nos. 1 and 2 is difficult to find. Again, it is pointed out that when the critical dispersion is absent, other constitutional variables become predominant. One factor in apparent lack of grain refinement was the large initial grain size of the cast material, which limited the extent of refinement possible. (A greater initial grain size leads to a greater final grain size.) Another factor was mentioned in Dr. Perryman's comment upon a variable which I have only touched upon briefly—that is the effect of a precipitation process occurring concurrently with recrystallization. This effect, indeed, may account for some of the lack of marked difference in grain size in the seven heat treated ingot blocks after final annealing. However, contrary to Dr. Perryman's suggestion, I am certain that no secondary recrystallization—or discontinuous grain growth—occurred in these materials. This was established by the detailed examinations of recrystallizing specimens. Therefore, we are concerned only with primary recrystallization. Furthermore, if the rate of precipitation were a major factor in grain coarsening, then the material with H. T. No. 1 would be expected to show the most pronounced effect, which was not the case. Another reason for believing that the precipitation taking place during annealing has a minor effect, is that the recrystallization characteristics of homogenized and unhomogenized materials remain the same after a second cold working and annealing, when there is much less further decomposition of the solid solution.

* K. Shimizu, Y. Nakatani and M. Yoshizaki, *Light Metals* (Japan), Vol. 7, March 1957, p. 23-26 (*Metals Review*, August 1957, Item 216N).

In answer to Dr. Perryman's question, differences in type of preferred orientation after recrystallization were sought without success. All materials had a weak deformation type of texture after recrystallization.

Mr. Marchand's observation on the terminology used is well-taken. To obtain a fine grained material, the homogenization which is achieved is incidental to the principal purpose of heating the ingot, which is to cause both precipitation and coalescence. The conditions of heating should be such as to obtain maximum precipitation and coalescence in a minimum time. Heating first to a high temperature and then cooling to the hot rolling temperature meets these requirements. Analogous heating cycles are used on many other aluminum alloys, with the main purpose of homogenizing—hence, the use of that term.

The effect of heating rate on grain size mentioned by Mr. Marchand is a very interesting subject, but one which would require too much room to include in this discussion.

In closing, I would like to emphasize the importance of a thorough and complete correlation between microstructural changes in alloy constitution and accompanying changes in grain structure for all studies of recrystallization and grain growth. I believe that much valuable work has been wasted or minimized in value by a lack of such correlations.

I wish to thank the discussers for their interest in this paper.

THE OCCURRENCE OF LAVES-TYPE PHASES AMONG TRANSITION ELEMENTS

BY R. P. ELLIOTT AND W. ROSTOKER

Abstract

The periodic variation of the crystal structure type of the Laves phases of titanium, zirconium, hafnium, niobium and tantalum may be correlated with electronic variations. Allotropy is the exception rather than the rule and occurs only for those binary phases that have electron:atom ratios near a critical value.

Consideration of ternary Laves-type phases indicates that there are two Brillouin Zone overlaps governing the structure type. On the assumption that the valency of titanium is near four, it has been possible to calculate the valencies of the first transition elements as follows: titanium, 3.92; zirconium, 3.25; vanadium, 2.19; chromium, 1.69; manganese, 1.35; iron, 0.92; and cobalt, 0.72. Valencies of 0.25 and 0.00 for nickel and copper, respectively, are consistent with the foregoing valencies. (ASM International Classification: M26; Ti, Zr, Hf, Cb, Ta)

ISOMORPHS of MgCu_2 , MgZn_2 and MgNi_2 , commonly referred to as Laves-type phases, occur frequently in alloy systems among the metals of the first, second and third transition series. A detailed study of the occurrence, miscibility ranges and nonoccurrence of these intermediate phases can serve as a basis for understanding the factors which govern their existence. Such a study could yield other useful by-products. In the work (1)¹ on pseudo-binary and pseudo-ternary systems of the three prototype Laves phases among themselves and with aluminum, silver and silicon, there was convincing evidence that electronic concentration was an operative factor governing the range of miscibility of single-phase fields. One might hope that a similar correlation would exist in Laves phases among the transition elements and, accordingly, a basis provided for estimating at least their relative valencies.

¹ The figures appearing in parentheses pertain to the references appended to this paper.

This paper represents, in part, a thesis submitted by R. P. Elliott to the Graduate School of the Illinois Institute of Technology in partial fulfillment of the requirements of the degree Doctor of Philosophy in Metallurgical Engineering.

A paper presented before the Thirty-Ninth Annual Convention of the Society, held in Chicago, November 4-8, 1957. Of the authors, R. P. Elliott is Research Metallurgist, and W. Rostoker is Assistant Manager, Metals Research, Armour Research Foundation of Illinois Institute of Technology, Chicago. Manuscript received January 7, 1957.

The effective valencies of the transition elements in alloy formation have been a subject of question and controversy for many years. So far there has not been convincing evidence that Brillouin Zone effects have any bearing on alloy formation among transition metals. The possibility also exists that their valency characteristics with nontransition elements are not the same as with members of the three transition series. The present study has undertaken to systematize and complete the state of knowledge on the existence of Laves phases in binary systems and selected ternary systems with transition elements and to deduce therefrom whether a self-consistent valency assignment to the individual elements can be correlated with the information so derived and the estimated Brillouin Zones for the crystallographic structures.

"Laves Phases" are compounds of the general formula AB_2 . The three crystal types which are characteristic of this group of phases are:

- (a) $MgCu_2$, cubic C15 type, 24 atoms per unit cell, $a = 7.03 \text{ kX}$
- (b) $MgZn_2$, hexagonal C14 type, 12 atoms per unit cell,
 $a = 5.15 \text{ kX}$, $c/a = 1.65$
- (c) $MgNi_2$, hexagonal C36 type, 24 atoms per unit cell,
 $a = 4.81 \text{ kX}$, $c/a = 3.28$

There is marked similarity among the structures of the three compounds. These consist of double layers of hexagonal arrays of magnesium atoms surrounded by tetrahedra of the B elements. The $MgCu_2$ structure consists of such layers stacked ABCABC, while $MgZn_2$ consists of such layers stacked ABABABAB. $MgNi_2$ may be regarded as a transitional phase between the $MgCu_2$ structure and the $MgZn_2$ structure with a stacking of these layers ABACABAC.

The existence of the Laves phases appears to correlate with the ratio of the diameters of the atomic species. Space can be filled most conveniently with spheres in which the ratio of the atomic diameters is $d_A/d_B = \sqrt{3}/2$, or 1.225, where d_A and d_B are the atomic diameters of the A and B atoms. Such a closely packed structure has an average coordination number of 13.33, which is indicative of the metallic nature of these phases.

Elements selected for investigation are shown in Table I with their Goldschmidt atomic diameters. Combinations of the selected elements with a diameter ratio greater than unity were selected for study. Existing literature was consulted. Alloys were made of all known Laves phases and for those compositions in which the known phase equilibria were questionable.

BINARY INVESTIGATIONS

Since the transition elements have melting temperatures in excess of 1000°C (1830°F), specialized techniques as have been employed in the melting of refractory elements (2) were necessary. The melting

Table I
Elements Investigated for Laves-Type Phases

Element	Goldschmidt's Atomic Diameter, kX
Period 4	
Ti	2.918
V	2.706
Cr	2.568
Mn	2.611*
Fe	2.521
Co	2.501
Ni	2.486
Cu	2.551
Period 5	
Zr	3.195
Nb (Cb)	2.939
Mo	2.802
Period 6	
Hf	3.169
Ta	2.940
W	2.816

*Calculated from γ -Mn structure, a face-centered tetragonal.

operation was done by the use of a nonconsumable electrode arc furnace and inert atmosphere protection using a water-cooled copper crucible. Ten and twenty-five gram melts were adequate. The best quality materials obtainable were used as melting stock. All, with the exception of hafnium, had purities in excess of 99.5%. Alloys containing tungsten were difficult to prepare because of the very high melting temperature of tungsten. Powder metallurgical techniques were resorted to in these instances.

X-ray diffraction is the standard technique for determining the crystal structure. Diffraction patterns were made with nickel-filtered copper radiation using a Straumanis camera of 14.324 centimeters in diameter. If the as-cast ingot was brittle, powder was prepared by crushing to -200 , $+325$ mesh. Ductile ingots were filed and the powder subsequently annealed.

For those compositions which proved to have a crystal structure isomorphous with one of the Laves-type phases, the melting temperature was determined by incipient melting techniques (2) if it had not been previously established. Pieces of ingot were then annealed at 200°C (390°F) intervals from 600°C (1110°F) to the melting temperature. Annealing times varied from 312 hours at 600°C (1110°F) to 0.1 hour at 2000°C (3630°F). High temperature anneals were done by suspending samples on tungsten wires in a vacuum resistance furnace (3).

The very close similarity between the powder patterns of the three types of Laves phases makes identification of allotropic types difficult. There is an equivalence of reflections of similar interplanar spacing in the three structures. The MgCu_2 pattern can be identified very easily, since it has relatively few reflections. The difference between the MgZn_2 and MgNi_2 structures is much more difficult to detect. The

Table II
Equivalence of Indices
of Interplanar Spacings of Laves-Type Phases

MgCu ₂	MgZn ₂	MgNi ₂
220	11.0	11.0
311	11.2	11.4
222	00.4	00.8
422	30.0	30.0
511/333	30.2	30.4
440	22.0	22.0
620	10.7	10.14

Table III
Summary of Data for Binary Laves Phases

AB ₂	Crystal Type	Parameters, kX		d _A /d _B	Melting Temp.
		a	c		
HfCo ₂	MgCu ₂	6.908		1.267	1570
HfCr ₂	MgZn ₂	5.064	8.210	1.234	1480
HfFe ₂	MgCu ₂	7.011		1.257	1650
HfFe ₂	MgZn ₂	4.970	8.109	1.257	1650
HfMn ₂	MgNi ₂ (?)	5.006	16.334	1.214	1585
HfMo ₂	MgNi ₂ (?)	5.330	17.312	1.131	>2300
HfMo ₂	MgCu ₂	7.562		1.131	>2300
HfV ₂	MgCu ₂	7.397		1.171	1500
HfW ₂	MgCu ₂	7.556		1.125	>2000
NbCo ₂	MgCu ₂	6.755		1.175	1570
NbCr ₂	MgCu ₂	6.971		1.144	1710
NbFe ₂	MgZn ₂	4.824	7.864	1.166	1625
NbMn ₂	MgZn ₂	4.869	7.866	1.126	1480
TaCo ₂	MgCu ₂	6.745		1.176	1610
TaCr ₂	MgZn ₂	4.922	8.066	1.145	2015
TaFe ₂	MgZn ₂	4.817	7.822	1.165	1775
TaMn ₂	MgZn ₂	4.854	7.931	1.126	—
TiCo ₂	MgCu ₂	6.692		1.167	1250*
TiCr ₂	MgCu ₂	6.926		1.136	(1350)†
TiCr ₂	MgZn ₂	4.890	7.911	1.136	(1350)†
TiFe ₂	MgZn ₂	4.750	7.815	1.157	1530
TiMn ₂	MgZn ₂	4.807	7.869	1.118	1330
WFe ₂	MgZn ₂	4.735	7.706	1.117	—
ZrCo ₂	MgCu ₂	6.940		1.277	1560
ZrCr ₂	MgCu ₂	7.193		1.244	1700
ZrCr ₂	MgZn ₂	5.092	8.222	1.244	1700
ZrFe ₂	MgCu ₂	7.056		1.267	1645
ZrMn ₂	MgZn ₂	5.099	8.233	1.224	1340
ZrMo ₂	MgCu ₂	7.581		1.140	1880*
ZrV ₂	MgCu ₂	7.43		1.181	1740*
ZrW ₂	MgCu ₂	7.600		1.135	2175*

*Peritectic

†Decomposes into solid

MgNi₂ structure produces all the reflections of the MgZn₂ structure, but with doubled *l* indices since it is based on a cell of double the *c* parameter. On the other hand, (*hkl*) planes with *l* odd in the MgNi₂ structure have no equivalence in the MgZn₂ structure. The X-ray powder pattern of the MgNi₂ structure is, therefore, the same as MgZn₂ pattern but with extra lines. Such a similarity arises because of the stacking configurations in the two structures. Table II shows the equivalence of reflections occurring in the three structures.

The lattice parameter of the cubic MgCu₂ type was determined most exactly by extrapolating against the function of Nelson and Riley (4) to $\theta = 90^\circ$. The parameters of the hexagonal MgZn₂ and MgNi₂ types were calculated by least squares solutions of the back reflec-

tion lines. The accuracy for such a solution is not as good as the extrapolation, since diffraction lines could be indexed only to interplanar spacings of about one kX unit.

The experimental data are summarized in Table III. Some of the findings of the present investigation differ with previously published data by various authors and hence should be discussed. Such discussions are included in the appendix.

The three Laves structures were shown to exist primarily on the basis of geometrical considerations. Each of the three structure types was on this basis equally probable. Other factors, obviously then, must

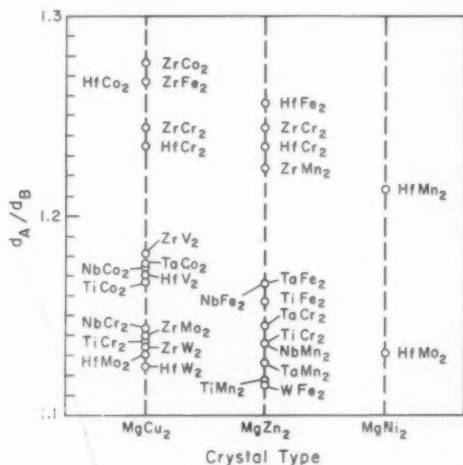


Fig. 1—Occurrence of Laves Phases as a Function of the Diameter Ratio.

determine which structure is stable. Experiments of Laves and Witte (1) showed that the MgCu_2 structure could dissolve elements of higher valency until an electron: atom ratio of approximately 1.8 was reached. The MgZn_2 structure similarly could dissolve elements of lower valency replacing zinc. These experiments indicated that the structure choice was a function of the electron: atom ratio. Recently, Berry and Raynor (5), in their examination of the existing literature, concluded that the MgZn_2 structure types exist at atom diameter ratios near the ideal of 1.225, while the MgCu_2 structure type occurs at values other than the ideal. This latter hypothesis may be tested by examination of the data of Table III. For convenience, these data are plotted in Fig. 1. It is obvious that such a simple factor as deviation from the ideal diameter ratio does not control occurrence of the structure type.

If the size factor were the only requirement governing the existence

Table IV
Crystal Structures of Laves Phases
in Transition Elements

A Element	V	Cr	B Element Mn	Fe	Co
Ti	—	MgZn ₂ † MgCu ₂ ††	MgZn ₂	MgZn ₂	MgCu ₂
Zr	MgCu ₂	MgCu ₂ † MgZn ₂ ††	MgZn ₂	MgCu ₂	MgCu ₂
Hf	MgCu ₂	MgCu ₂ † MgZn ₂ ††	MgNi ₂ (?)	MgZn ₂	MgCu ₂
Nb	—	MgCu ₂	MgZn ₂	MgZn ₂	MgCu ₂
Ta	—	MgZn ₂	MgZn ₂	MgZn ₂	MgCu ₂

†High Temperature

††Low Temperature

of Laves phases, such phases would be expected for the stoichiometric compositions HfCu₂, HfNi₂, MoCo₂, MoNi₂, NbNi₂, TaCu₂, TaNi₂, TiCu₂, TiNi₂, WCo₂, WCu₂, WNi₂, ZrCu₂ and ZnNi₂, all of which have a diameter ratio within the prescribed range. The nonexistence of Laves phases at such compositions is further indication that something else such as electronic concentration is important.

If the Laves-type structure for a given A element is plotted for increasing atomic numbers for the first transition series, as in Table IV, it is observed that there is a trend for the alloys with cobalt to be of the MgCu₂ type, while the alloys with iron and manganese are usually of the MgZn₂ type. In terms of the work of Laves and Witte, this trend indicates that there is a progressive decrease in valency in the progression from manganese to cobalt. Similarly, intermediate phases with chromium and vanadium show a high frequency of occurrence of the MgCu₂ type of structure. Thus, it might seem that as the first transition series is traversed from chromium to cobalt there is an increase and subsequent decrease in the electronic valency. The electron:atom ratios would be interpreted to increase from a value in which the MgCu₂ type is stable to a value in which the MgZn₂ type is stable, and subsequently to fall again to a value in which the MgCu₂ structure is stable. Fig. 2 shows hypothetical electron:atom ratios for Laves phases of the first transition series with titanium assuming such a variation in valency as the transition series is traversed. It will be noted that the electron:atom ratio of TiCr₂ is indicated at the critical value of 1.83. A variation in electronic valency or specific heat as a function of temperature will cause this phase to undergo the allotropic change.

The transition from the MgCu₂ type to MgZn₂ and back to MgCu₂ could also be interpreted with a continuous decreasing (or increasing) valency, but with a density of states curve containing two maxima for the MgCu₂ structure with a single maximum for the MgZn₂ structure at an intermediate electron:atom ratio. Witte (6) has calculated the electron:atom volumes of Brillouin Zones for the Laves-type compounds and has shown the discontinuity for the MgCu₂ type to be at

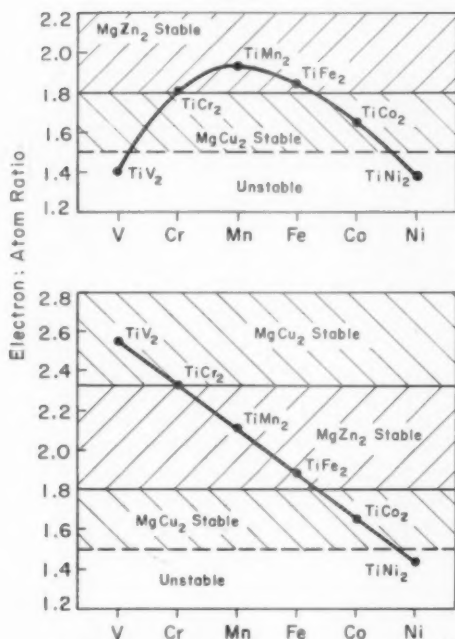


Fig. 2—Schematic Rationalization of Variation of Crystal Type for the Laves Phases of Titanium.

an electron:atom ratio of 1.83, and the discontinuities for MgZn_2 to be at 1.93 and 2.32 electrons:atom. There is no indication in these calculations that at higher electron:atom ratios there should be a reversion to the MgCu_2 type structure. This second explanation for the variation of crystal structure is also shown schematically in Fig. 2. The non-existence of TiV_2 as a Laves phase is justified by an unfavorable size factor.

TERNARY INVESTIGATIONS

The systematic variation of crystal structure type with the position in the periodic table of the B element for a constant A element suggests that an approach similar to that of Laves and Witte would yield data that can be interpreted on the basis of electron:atom ratios. A series of quasi-binary phase diagrams was therefore investigated. The alloy systems studied are shown in Fig. 3.

Ten gram alloys were prepared at ten atomic per cent intervals. These alloys were arc melted and then heat treated. With the exception of the alloy system $\text{Zr}(\text{V}, \text{Co})_2$, the zirconium systems were annealed for 24 hours at 1200 and 800 °C (2190 and 1470 °F). The system Zr

the MgCu_2 structure is stable at electron : atom ratios greater than 2.32. The upper critical electron : atom ratio of 2.32 was selected in preference to 1.93 for two reasons:

- (a) The higher electron : atom ratio has a greater energy gap (6).
- (b) The prototype quasi-binary systems showed no change in structure at the electron : atom ratio of 1.93 (1).

The line of reasoning in calculating the valencies of the transition elements is as follows:

(a) It is seen in Table II that TiFe_2 is isomorphous with the MgZn_2 structure, while ZrFe_2 is isomorphous with the MgCu_2 structure. Since the crystal structures of the Laves phases differ only in stacking configurations and since the elements are very similar, it is assumed that the valencies of the elements do not change. Hence, for a constant valency for iron, titanium must have a greater valency than zirconium in order that the electron : atom ratio of ZrFe_2 be below 1.80 while that of TiFe_2 is greater than this value.

It has been assumed here that only those binary alloys with electron : atom ratios near the critical values exhibit allotropy. Thus, at a first approximation, it would appear that the electron : atom ratio of ZrCr_2 and TiCr_2 is 2.32. Since titanium and zirconium have different valencies, this, of course, cannot be. On close examination, it may be seen that ZrCr_2 and TiCr_2 do not behave identically. The allotropic modifications of these two phases are reversed; the low temperature structure of TiCr_2 is MgZn_2 , while that of ZrCr_2 is MgCu_2 . This is easy to rationalize. Since titanium has a higher valency than zirconium, it would be expected that at low temperatures where specific heat and free energy curve effects are minimized that TiCr_2 , having a higher electron : atom ratio than ZrCr_2 , would be of the MgCu_2 type while the latter is of the MgZn_2 type. Apparently the effect of temperature on the allotropy is important for those compounds near a critical electron : atom ratio.

The low temperature quasi-binary sections are used in all instances for calculation in order to divorce the electronic effects from the temperature effects as much as possible.

(b) On the assumption that the critical electron : atom ratios of 1.80 and 2.32 govern the ranges of stability of the MgCu_2 and MgZn_2 structures, equations may be written for the valencies of the elements at the composition limits of these structures in the quasi-binary systems shown in Fig. 3. The systems $\text{Zr}(\text{V}, \text{Co})_2$ and $\text{Zr}(\text{V}, \text{Fe})_2$ permit a pair of equations to be written. When these equations are solved simultaneously, the electron : atom ratios of the binary structures are determined. Adjustment of the compositions substituted in the simultaneous equations for the quasi-binary systems containing vanadium was made within the experimental limits of data such that the calculated electron :

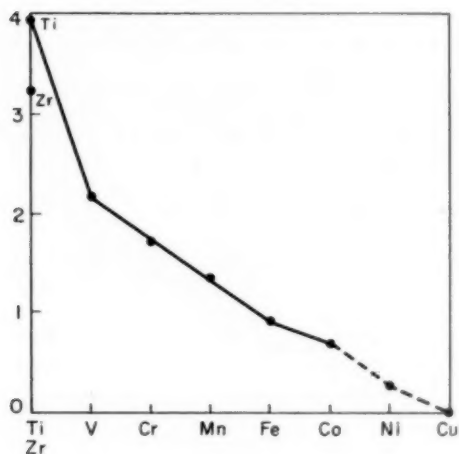


Fig. 4—Electronic Valencies of the Transition Elements.

atom ratio of ZrV_2 was very nearly the same when solved from the two systems Zr(V, Co)_2 and Zr(V, Fe)_2 . For an assumed valency of zirconium, the valencies of vanadium, cobalt and iron can be made. The electron:atom ratios of ZrV_2 , ZrFe_2 and ZrCo_2 used for calculation are, respectively, 2.54, 1.70, and 1.56.

(c) Equations for the valencies of chromium and manganese may be written from the quasi-binary sections Zr(V, Mn)_2 and Zr(Cr, Co)_2 . The electron:atom ratio of this composition-dependent change of structure is 2.32. The valencies of vanadium and cobalt must first be determined by the method outlined in (b).

(d) The valency of titanium may be calculated in terms of the valencies of the elements of the first transition series for an assumed valency of zirconium. This is done by considering the composition at which the MgCu_2 structure changes to the MgZn_2 structure at an electron:atom ratio of 1.80 in the quasi-binary system Ti(Fe, Co)_2 .

Independent investigators have shown that titanium may be considered to be tetravalent. Rostoker (7) has shown experimentally that a discontinuity of lattice parameters of α -titanium-aluminum occurs at the predicted electron:atom ratio if titanium is considered to be tetravalent in the presence of trivalent aluminum. Hume-Rothery and Raynor (8) consider experimental evidence of the linearity of interatomic distances, compressibilities, coefficients of linear expansion, and the melting temperatures of the elements potassium, calcium, scandium, and titanium as indicative that titanium is tetravalent. In the titanium-copper system, there exists the intermetallic compound TiCu_3 , which has a deformed hexagonal close-packed structure. This may be con-

sidered to be a $7/4$ electron compound if titanium is considered to be tetravalent.

Solutions of the valencies of the transition elements were made for various assumed valencies of zirconium. For an assumed valency of 3.25 for zirconium, the valency of 3.92 is calculated for titanium, which is near the desired value of four. Using 3.25 as the assumed valency of zirconium, the following valencies are calculated:

Ti	3.92
Zr	3.25
V	2.19
Cr	1.69
Mn	1.35
Fe	0.92
Co	0.72

These are plotted in Fig. 4.

As a check, the electron:atom ratios for the binary alloys and compositionally dependent structure changes are compared with the theoretical values.

Structure	Electron:Atom Ratio	
	Calculated	Theoretical
TiCr ₂	2.43	>2.32
TiMn ₂	2.21	<2.32, >1.80
TiFe ₂	1.92	<2.32, >1.80
TiCo ₂	1.79	<1.80
ZrV ₂	2.54	>2.32
ZrCr ₂	2.21	<2.32, >1.80
ZrMn ₂	1.98	<2.32, >1.80
ZrFe ₂	1.70	<1.80
ZrCo ₂	1.56	<1.80
Zr + 0.6 Fe + 1.4 V	2.29	2.32
Zr + 1.8 Fe + 0.2 V	1.77	1.80
Zr + 0.4 Co + 1.6 V	2.35	2.32
Zr + 1.5 Co + 0.5 V	1.81	1.80
Zr + 0.8 Mn + 1.2 V	2.32	2.32
Zr + 0.6 Cr + 1.4 Co	1.76	1.80
Ti + 1.8 Co + 0.2 Fe	1.80	1.80
Zr + 1.8 Cr + 0.2 V	2.24	2.32
Ti + 1.8 Cr + 0.2 Fe*	2.38	2.32

* Data taken from Reference 9.

The synthesized valencies presented above permit an agreement between calculated and theoretical electron:atom ratios which is exceptionally good. The stability ranges of the binary Laves phases with titanium and zirconium are shown graphically in Fig. 5. This graph replaces the hypothesized diagram shown in Fig. 2.

There are no Laves compounds composed of titanium, zirconium, hafnium, tantalum or niobium as the A element with nickel or copper as the B element, although the diameter ratio is favorable. In these instances the nonexistence of Laves type structures must therefore be rationalized as a result of an unfavorable electron:atom ratio. The valency of one for copper, as is the usual case in electronic concentra-

tion rationalizations of the alloy systems with nontransition elements, cannot be valid in the alloy systems of Laves phases with transition elements. If copper were monovalent, the existence of TiCu_2 as a Laves phase would be predicted on the basis of a favorable diameter ratio and a favorable electron:atom ratio.

If the trend in valencies as calculated is extrapolated, valencies of about 0.25 for nickel and 0.0 for copper are deduced.

Transition Laves phases can dissolve appreciable amounts of both nickel and copper as is shown in Fig. 3. If nickel or copper is added to a MgZn_2 structure, on a consideration of electron:atom ratios, a range of existence of the MgCu_2 structure would be expected. Experimental data do not show this to be the case. Ranges of miscibility of nickel and copper in Laves phases of titanium and zirconium, and vanadium in Laves phases of titanium can be rationalized on an electron:atom consideration, however.

The data for vanadium, copper and nickel seem to indicate that, when added to a particular binary Laves phase, the miscibility range of that particular structure is controlled by electronic concentration, but reversions to other Laves phases are inexplicably forbidden. Thus, vanadium can be added to a MgZn_2 structure until the electron:atom ratio reaches 2.32 but can be added to the lower MgCu_2 structures only until the electron:atom ratio reaches 1.80.

Additions of copper or nickel to the lower electronic range MgCu_2 structures indicate a lower electron:atom limit of about 1.4. This could correspond to the energy of a tangency of the Fermi sphere to one of the faces of the Brillouin Zone as predicted by Schubert (10).

	Electron:Atom Ratio	
	Calculated	Theoretical
Vanadium added to MgZn_2		
Ti + Fe + V	2.34	2.32
Ti + 1.2 Mn + 0.8 V	2.43	2.32
Vanadium added to MgCu_2		
Ti + 1.9 Co + 0.1 V	1.83	1.80
Copper or Nickel added to MgZn_2		
Ti + 1.6 Fe + 0.4 Cu	1.80	1.80
Ti + 1.2 Fe + 0.8 Ni	1.74	1.80
Copper or Nickel added to MgCu_2		
Zr + 0.4 Fe + 1.6 Ni	1.33	<1.5
Zr + 0.8 Co + 1.2 Ni	1.37	<1.5

The upper limit of the Laves phase miscibility in the system Ti(V, Cr)_2 probably corresponds to a point where the size factor becomes unfavorable. The systems Ti(Mn,Co)_2 , Ti(Mn,Ni)_2 and Ti(Mn, Cu)_2 were also studied. The electron:atom ratio of the limits of the MgZn_2 structure in these systems are 2.00, 2.06, and 2.12, respectively. These values are higher than the predicted 1.80. A systematic analysis in these systems is difficult because the Laves phase comes into equilib-

rium with a body-centered cubic phase based on a solid solution of the elements in beta-titanium. It is entirely possible that the phase boundary is being restricted by free energy consideration of the intermediate beta-titanium phase.

There are no Laves-type phases in the quasi-binary system Ti(V, Ni)_2 although over a range of compositions both the electron:atom and diameter ratios are favorable.

VALENCIES OF THE TRANSITION ELEMENTS

The numerous attempts to develop the systematic valency behavior of the elements of the first transition series fall into two general categories. In the first of these, correlations have been made with electron

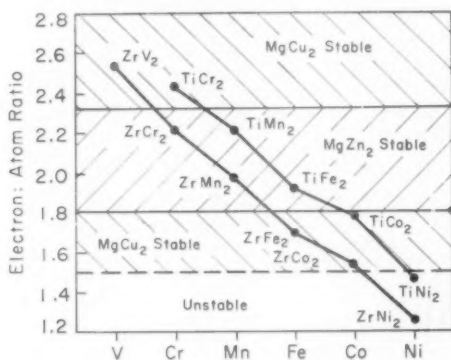


Fig. 5—Stability Ranges of Binary Laves Phases.

vacancies or "bonding" electrons based on the atomic structure concept set forth by Pauling (11) to account for the magnetic behavior of the elements and their alloys. Papers by Rideout, et al. (12), Sully (13), and Greenfield and Beck (14,15) on the occurrence of sigma phases are in this vein. These approaches must be criticized because in the Brillouin Zone concept of phase stability, the electronic concentration and the distribution of permissible electronic states are unseparable. Accordingly, any critical derived electronic concentrations must correlate with the occurrence of zones for the particular structure under consideration. Without this correlation, a truly electronic concentration dependent effect may be analyzed by a wide variety of numerical systems. In the particular case of sigma phases, Bloom and Grant (16) arrived at this conclusion.

Other groups, notably, Hume-Rothery, et al. (17), Geach and Summers-Smith (18,19), and Hume-Rothery and Haworth (20) have used the phase limits imposed by transition elements on terminal solid solutions and $3/2$ electron compounds to interpret their valency char-

Table V
Valencies of the Transition Elements As Used
by Various Investigators in Alloy Formation

	Ekman (21)	Raynor (22,23)	Rideout et al. (12)	Sully (13)	Bloom and Grant (16)	Greenfield and Beck (14,15)	Geach and Summers-Smith (18,19)	Haworth and Hume-Rothery (20)	This Investigation
Titanium							4		3.92
Vanadium				0.12	5	5.66, 4.88	3		2.19
Chromium		-4.66	4.66	0.46	6	4.66	2		1.69
Manganese		-3.66	3.66	2.12	7	3.3	2	1.9	1.35
Iron	0	-2.66	2.66	2.46	8	2.66	1	1.0	0.92
Cobalt		-1.71	1.71	3.46	9	1.71	2	0.8	0.72
Nickel	0	-0.61	0.61	4.46	10	0.61	1	0.6	0.25

acteristics. Ekman (21) showed that intermediate phases of iron and nickel with zinc could be rationalized as electron compounds if the transition elements are considered zero-valent. Raynor (22,23) and subsequent investigators correlated proposed systems of electronic concentration with the structure and ternary equilibrium behavior of Al-rich intermediate phases with transition metals. These treatments are basically correct within the framework of the zone theory but are based on the premise that the ionization behavior of transition elements in association with nontransition elements is the same as that with their own kind. In the particular case of the work of Geach and Summers-Smith (18,19) on the terminal solid solubility of transition elements in gold, there is always the question of whether the determined solubility limits were not influenced unduly by the relative free energies of the first intermediate phases. In early work on alloy theory, this was termed the electrochemical effect, but its implications are broader in present perspective. A summary of the results of these various authors is given for easy visual comparison in Table V.

By concentrating on the compositional correlations of the structurally similar Laves phases in all-transition metal systems, it is hoped that this investigation has avoided the uncertainties implicit in prior work. There is, however, a reasonable comparison with the results of Geach and Summers-Smith (18,19) in the Ti, V, Cr sequence and of Haworth and Hume-Rothery (20) in the Mn, Fe, Co, Ni sequence.

ACKNOWLEDGMENT

This research was sponsored by the United States Air Force through the Office of Scientific Research of the Air Research and Development Command, Baltimore, Maryland, under Contract Nos. AF 18(600)-642 and AF 18(600)-1399. The sponsorship and permission to publish are gratefully acknowledged.

Appendix

In several instances the data reported in this paper are in contradiction to previously published work or have never been previously

reported. The disputed compounds in all instances are those which have an electron:atom ratio near one of the critical values. Contamination of melting stock and the similarity of diffraction patterns can account for these discrepancies.

HfCo₂, HfCr₂, HfFe₂, HfMn₂, HfMo₂, HfV₂, and HfW₂—There are no published data on the alloy systems in which these compounds occur. A separate publication is planned in which these data will be discussed.

TaCr₂—Duwez and Martens (24) have shown this phase to have an allotropic change with the MgCu₂ type at low temperatures and the MgZn₂ type at high temperatures. In contradiction to the above authors, it was found that TaCr₂ was isomorphous with MgZn₂ at all temperatures from 600° to 2000°C.

TiCo₂—Wallbaum (25) and later Duwez and Taylor (26) report that TiCo₂ occurs only in the MgNi₂ structure. The present work indicates TiCo₂ is the cubic MgCu₂ type with no allotropy in the temperature range 600° to 1200°C.

ZrV₂—Wallbaum (27) had shown this phase to be isomorphous with MgZn₂. ZrV₂ was found to be of the MgCu₂ structure from 600° to 1500°C, the temperature of decomposition by peritectic reaction.

References

1. F. Laves and H. Witte, "The Influence of Valency Electrons on the Crystal Structure of Ternary Magnesium Alloys," *Metallwirtschaft*, Vol. 15, 1936, p. 840.
2. M. Hansen, H. D. Kessler and D. J. McPherson, "The Titanium-Silicon System," *TRANSACTIONS, American Society for Metals*, Vol. 44, 1952, p. 578.
3. R. F. Domagala and D. J. McPherson, "System Zirconium-Oxygen," *Transactions, American Institute of Mining and Metallurgical Engineers*, Vol. 200, 1954, p. 238.
4. J. B. Nelson and D. P. Riley, "An Experimental Investigation of Extrapolation Methods in the Derivation of Accurate Unit-Cell Dimensions of Crystal," *Proceedings of the Physical Society*, Vol. 57, 1945, p. 160.
5. R. L. Berry and G. V. Raynor, "The Crystal Chemistry of the Laves Phase," *Acta Crystallographica*, Vol. 6, 1953, p. 178.
6. H. Witte, *Zur Struktur und Materie der Festkörper*, 1952, p. 272-304, Springer, Berlin.
7. W. Rostoker, "Observations on the Lattice Parameters of the Alpha Solid Solution in the Titanium-Aluminum System," *Transactions, American Institute of Mining and Metallurgical Engineers*, Vol. 194, 1952, p. 212.
8. W. Hume-Rothery and G. V. Raynor, *The Structure of Metals and Alloys*, 3rd edition, Institute of Metals, 1954, London.
9. R. J. Van Thyne, H. D. Kessler and M. Hansen, "System Titanium-Chromium-Iron," *Transactions, American Institute of Mining and Metallurgical Engineers*, Vol. 197, 1953, p. 1209.
10. K. Schubert, discussion to Reference 6.
11. L. Pauling, "The Nature of Interatomic Forces in Metals," *Physical Review*, Vol. 54, Series 2, 1938, p. 899.
12. S. Rideout, W. D. Manley, E. L. Kamen, B. S. Lemont and P. A. Beck, "Intermediate Phases in Ternary Alloy Systems of Transition Elements," *Transactions, American Institute of Mining and Metallurgical Engineers*, Vol. 191, 1951, p. 872.
13. A. H. Sully, "The Sigma Phase in Binary Alloys of the Transition Elements," *Journal, Institute of Metals*, Vol. 80, December 1951, p. 173.

14. P. Greenfield and P. A. Beck, "The Sigma Phase in Binary Alloys," *Transactions*, American Institute of Mining and Metallurgical Engineers, Vol. 200, 1954, p. 253.
15. P. Greenfield and P. A. Beck, "A Correction to 'The Sigma Phase in Binary Alloys,'" *Transactions*, American Institute of Mining and Metallurgical Engineers, Vol. 200, 1954, p. 758.
16. D. S. Bloom and N. J. Grant, "Regarding Sigma Phase Formation," *Transactions*, American Institute of Mining and Metallurgical Engineers, Vol. 197, 1953, p. 88.
17. W. Hume-Rothery, G. W. Mabbott and K. M. Channel-Evans, "The Freezing Points, Melting Points, and Solid Solubility Limits of Alloys of Silver and Copper with the Elements of the B-Sub-Groups," *Philosophical Transactions of the Royal Society*, Vol. 233, 1934-A, p. 1-97.
18. G. A. Geach and D. Summers-Smith, "The Constitution of Gold-Molybdenum Alloys, with Particular Reference to the Solubility of Molybdenum in Gold," *Journal*, Institute of Metals, Vol. 82, June 1954, p. 471.
19. D. Summers-Smith, "The Solubility of Vanadium in Gold," *Journal*, Institute of Metals, Vol. 83, 1954-55, p. 189.
20. J. B. Haworth and W. Hume-Rothery, "The Effect of Four Transition Metals on the α/β Brass Type of Equilibrium," *The Philosophical Magazine*, Vol. 43, Series 7, 1952, p. 613.
21. W. Ekman, "Structural Analogies of Binary Alloys of Transition Elements and Zinc, Cadmium and Aluminum," *Zeitschrift für Physikalische Chemie*, Vol. 12, 1931-B, p. 57.
22. G. V. Raynor and P. C. L. Pfeil, "The Constitution of the Aluminum-Rich Aluminum-Iron-Nickel Alloys," *Journal*, Institute of Metals, Vol. 73, 1947, p. 397.
23. G. V. Raynor and M. B. Waldron, "The Constitution of the Aluminum-Rich Aluminum-Cobalt-Iron Alloys, with Reference to the Role of Transitional Elements in Alloy Formation," *Proceedings of the Royal Society*, Vol. 194, Series A, 1948, p. 362.
24. P. Duwez and H. Martens, "Crystal Structure of $TaCr_2$ and $CbCr_2$," *Transactions*, American Institute of Mining and Metallurgical Engineers, Vol. 194, 1952, p. 72.
25. H. J. Wallbaum, "Results of the X-Ray Structure Investigations of Alloys with the Composition AB_2 of the Iron Metals with Titanium, Zirconium, Niobium and Tantalum," *Zeitschrift für Kristallographie*, Vol. 103, 1941, p. 391.
26. P. Duwez and J. L. Taylor, "The Structure of Intermediate Phases in Alloys of Titanium with Iron, Cobalt, and Nickel," *Transactions*, American Institute of Mining and Metallurgical Engineers, Vol. 188, 1950, p. 1173.
27. H. J. Wallbaum, "Some New Zirconium Compounds with Transition Elements," *Naturwissenschaften*, Vol. 30, 1942, p. 149.

DISCUSSION

Written Discussion: By A. E. Dwight, Argonne National Laboratory, Lemont, Illinois.

This discussion is concerned primarily with the structure of the $TiCo_2$ composition. Two alloys were prepared having the nominal compositions 64 and 69 a/o cobalt. Crystal bar titanium and electrolytic cobalt were used, and the alloys were prepared by arc melting in a water cooled copper crucible under argon gas. Diffraction patterns were taken with cobalt radiation both in the as-cast condition and after annealing for 23 hours in vacuo at 1200 °C (2190 °F).

The $Ti + 64$ a/o Co alloy after annealing at 1200 °C (2190 °F) gave a pattern containing 21 lines, 6 of which were indexed as the CsCl-type $TiCo$ phase and 15

of which were indexed as the MgCu_2 -Type TiCo_2 phase. The a_0 of the latter phase is 6.706 Å or 6.693 KX, which is in good agreement with the results obtained in the paper under discussion.

The Ti + 69 a/o Co alloy after annealing at 1200 °C gave all the lines of the MgCu_2 -type phase plus 13 more lines, yet metallographically the alloy appeared to be a single phase. However, 27 of the 28 lines could also be indexed as a MgNi_2 -type TiCo_2 phase, with $a_0 = 4.719$ Å, $c_0 = 15.452$ Å and $c/a = 3.274$. The lattice parameter values were obtained by the method of successive approximations.

Our data confirm the phase relations originally reported by Wallbaum and Witte² in that the MgCu_2 and MgNi_2 -type phases both appear to be stable and to be dependent on the cobalt content for their existence.

Authors' Reply

The data presented in this paper were for stoichiometric compositions only. It is interesting to note that these anomalous composition-dependent structures in binary systems have been reported for TiCo_2 , NbCo_2 , TaCo_2 , and ZrFe_2 . On pseudobinary sections it is observed that these compositions have electronic concentrations such that slight contamination can cause other structures to become stable.

The most expeditious means of answering the discussion was by duplicating the alloys of Mr. Dwight. Ten-gram ingots of Ti + 64 atomic % Co and Ti + 69 atomic % Co were arc melted. Iodide titanium and electrolytic cobalt were used (the latter obtained from Mr. Dwight). Two additional melts were prepared in which the alloys were purposely contaminated with oxygen to an extent of one per cent of the titanium. (Mr. Westbrook of General Electric Research Laboratory, Schenectady, N.Y. in an oral discussion had suggested that oxygen contamination could be the source of these crystal structure anomalies.)

Powder patterns were prepared of material in the as-cast condition only since time limitations precluded annealing. Filtered copper radiation was used. No evidence was observed to indicate that the MgNi_2 structure existed. The Ti + 64 atomic % Co alloy had additional lines of the BCC TiCo phase.

Powder patterns were then prepared using iron radiation. The Ti + 69 atomic % Co had additional lines which could be indexed as MgNi_2 although the principal pattern was of the MgCu_2 structure. The Ti + 64 atomic % Co alloy containing the oxygen as a contaminant was MgCu_2 type with a pattern of TiCo . The authors must therefore concur with Mr. Dwight that the MgNi_2 structure does exist in the binary titanium-cobalt system. The presence of oxygen does not appear to influence the formation of the MgNi_2 structure.

The existence of the MgNi_2 structure at the nonstoichiometric composition in no way negates the theory presented in the paper. It does, however, pose the additional problem of rationalizing the factors influencing the stability of the MgNi_2 structure in binary alloys.

² H. J. Wallbaum and H. Witte, *Zeitschrift für Metallkunde*, Vol. 31, 1939, p. 185.

BRITTLE FRACTURE OF MILD STEEL IN TENSION AT -196°C

BY W. S. OWEN, B. L. AVERBACH AND M. COHEN

Abstract

The tensile fracture behavior of a mild steel at -196°C (-320°F) has been studied in some detail. With the aid of long thin strip specimens loaded at controlled crosshead speeds between 8.9×10^{-4} and 1.6×10^{-1} inch per minute, the strain pattern and microscopic changes preceding fracture were observed, and the local strain situation was measured. Specimens heat treated to alter the tendency toward brittle behavior, but maintaining ferrite-pearlite structures, were also examined.

Under these conditions, all the Lüders' bands display microcracks in some ferrite grains. However, the as-received and normalized specimens do not fracture at low yield stresses (slow loading speeds) during the spread of the Lüders' bands. By raising the loading speed, a critical stress is reached when fracture occurs after a delay time, the formation of microcracks and fracture always being preceded by gross yielding. On further increasing the loading rate, the fracture stress rises along with the yield stress.

Deductions from the dislocation pile-up theory of fracture in polycrystalline metals are not compatible with the experimental data. It is concluded that the microcrack model suggested by Low is more appropriate.

Some observations are included on the creep occurring in Lüders' bands during their propagation at -196°C . (ASM International Classification Q26s, 1-13; CN)

INTRODUCTION

MOST RECENT discussions of brittle fracture in polycrystalline metals (1-7)¹ have utilized a model elaborated by Stroh (1,2) and applied by Petch (3,4), in which it is assumed that the local stress concentration necessary to cleave a crystal is produced by an extensive defect in the form of piled-up dislocations against a grain boundary. It has been implied (2,7) that this is, in effect, a restatement of the

¹ The figures appearing in parentheses pertain to the references appended to this paper.

A paper presented before the Thirty-Ninth Annual Convention of the Society, held in Chicago, November 4-8, 1957. Of the authors, B. L. Averbach and M. Cohen, are associated with the Department of Metallurgy, Massachusetts Institute of Technology, Cambridge, Massachusetts, and W. S. Owen is presently at the University of Liverpool, Great Britain. Manuscript received March 20, 1957.

Griffith (8) concept of fracture in terms of dislocation theory. However, Low (9,10) maintains that, at least in mild steel, real cracks of subcritical size are actually formed before the main fracture occurs and, thus, a more direct application of the Griffith model (as modified by Orowan (11)) is appropriate.

The experimental evidence supporting these theories is not extensive. Stroh and Petch rely principally upon two related experimental observations: that the fracture stress (σ_F) at -196°C (-320°F) is linearly related to the reciprocal of the square root of the mean grain diameter (d), and that the proportionality constant so determined is of the expected magnitude (2). However, Low (9) demonstrated the existence of subcritical cracks in iron deformed by slow bending at -196°C (-320°F); he also found a linear σ_F versus $d^{-1/2}$ relationship by tension tests, and deduced a value of the proportionality constant which is compatible with the Griffith-Orowan theory. Clearly, comparisons over a wider range of experimental data are required to assess the applicability of these theories to the low temperature fracture of mild steel. In the present work, the search for subcritical microcracks is extended to specimens tested in tension, and the predictions of the two theories are compared with the experimental fracture stress and strain as a function of the loading rate.

As the stress is increased slowly in a simple tensile test at -196°C (-320°F), four stages of nonelastic strain are identifiable. First, there is a preyield microstrain which is less than about 50×10^{-6} . This is followed by a microcreep strain, occupying an appreciable time interval before it is replaced by a third stage, the generation of Lüders' bands (12). The -196°C (-320°F) microcreep strain may be as large as 10^{-3} , and is accompanied by the appearance of fine slip markings. During the propagation of the Lüders' bands, the stress is reasonably constant, but it increases again in the fourth stage (strain hardening) after bands have covered the whole specimen. Subsequent fracture is still predominantly by cleavage, and it was in this range that Low (10), using a slow-bend technique, observed microcracks which did not propagate until the stress was further increased. Petch (4) also obtained much experimental data in this range. Considering that such specimens exhibit appreciable ductility before final rupture, it would seem more appropriate to examine the theories of brittle fracture in relation to data where the plastic strain preceding fracture is a minimum.

Mild steel specimens which fracture at -196°C (-320°F) with very small overall ductility are readily obtained by suitable heat treatment, but relatively few accurate measurements of the nonelastic strain have been reported. During the spread of a Lüders' band, the deformation is heterogeneous on a macroscale as well as on a microscale, and observations over a 1 or 2-inch gage length give no indication of the

strain in the vicinity of the fracture. Furthermore, the recorded strain is dependent upon the geometry of the specimen. In the present experiments, a technique was employed by which the local strain pattern could be observed both in the vicinity of the fracture and in similar locations where no fracture occurred.

EXPERIMENTAL METHODS

The mild steel² investigated here was of the rimmed type, and was received in the form of a hot-rolled $\frac{3}{4}$ -inch plate. The effects of a wide variety of heat treatments on this material have been studied in detail using Charpy V-notch and low temperature standard tensile tests (13). It has been found that the -196°C (-320°F) properties can be varied from extreme brittleness (950 $^{\circ}\text{C}$ furnace-cooled) to excellent ductility (950 $^{\circ}\text{C}$ air cooled), all with normal equiaxed ferrite plus pearlite microstructures. Specimens treated in this way and some in the as-received condition were used in the present series of tests. The standard-test data are shown in Table I.

Table I
Standard Test Data for Mild Steel*

Heat Treatment	Charpy V-notch Transition Temp. $^{\circ}\text{C}$	Yield Stress at -196°C (-320°F) Round Bar Tensile Test, 10^3psi	Fracture Stress at -196°C (-320°F) Round Bar Tensile Test, 10^3psi	Reduction in Area at -196°C (-320°F) Round Bar Tensile Test, %	Ferrite Grain Size ASTM No.
950 $^{\circ}\text{C}$. Furnace- Cooled	22.4	119	122	0.3	7.3
As-Received	15.7	117	122	2.6	7.2
950 $^{\circ}\text{C}$. Air- Cooled	-23.1	140	186	30.0	8.9

*See footnote at bottom of page for composition of steel.

The heat treatments were carried out in a helium atmosphere on full-plate thickness blanks. The specimens, flat strips 0.035–0.040 inches thick with a parallel-sided gage section of 5 inches long and 0.25 inches wide, were machined from the center, the last 0.010 inches being removed by slow grinding with a well lubricated porous wheel. Deep etching revealed no evidence of overheating. The specimen and plate surfaces were mutually parallel, the specimen axis coinciding with the rolling direction. One surface of each specimen had a ground finish with all the scratches (corresponding to about 0 emery paper) running longitudinally. The other was taken down to 000 paper before being polished with diamond paste. An accurate scribing machine was used to mark a scale with 1-millimeter intervals on the ground side along the whole length of the specimen, the short transverse scratches being hardly deeper than the longitudinal grinding marks.

The tests were conducted with a modified Hounsfield tensile ma-

² Analysis:

C 0.22, Mn 0.36, P 0.016, S 0.031, Si 0.002, Cu 0.17, Ni 0.13, Cr 0.08, V 0.005, Mo 0.025, Al 0.009, Sn 0.012, As 0.001, O 0.006.

chine. The load was applied through an electrically driven screw and gear train, and measured by the deflection of a stiff spring. The overall rate of strain was the independent variable, the range of crosshead speeds lying between 8.9×10^{-4} and 1.6×10^{-1} inch per minute. The resulting yield stress was indicated on a semi-automatic load-extension recorder.

If the specimen did not break, the test was discontinued when the Lüders' bands covered almost the whole gage section (yielding time

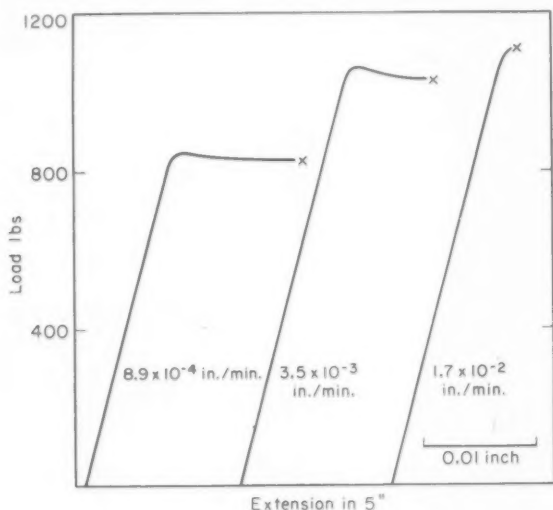


Fig. 1—Typical Load-Extension Curves at -196°C (-320°F) with Different Crosshead Speeds. Steel as received. X—cleavage fracture.

40–60 minutes). After each run the specimen was removed from the liquid nitrogen bath, warmed to room temperature in cold water, and dried with alcohol and a warm air blast. The strain pattern was easily observed on the prepolished surface, and was examined subsequently by optical microscopy. The plastic strain along the length of the specimen was determined by measuring the inscribed millimeter scale under a low power microscope with a Hurlbut counter.

EXPERIMENTAL RESULTS

The Stress-Strain Conditions

The preyield nonelastic phenomena and the initiation of Lüders' strain at -196°C (-320°F) in these specimens have been described elsewhere (12). Typical load-extension curves are shown in Fig. 1. As

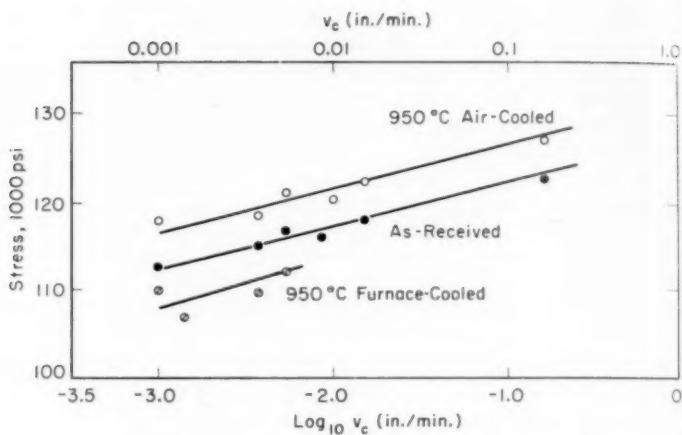


Fig. 2—Dependence of Upper Yield Stress on Crosshead Speed (v_c). Tested at -196°C (-320°F).

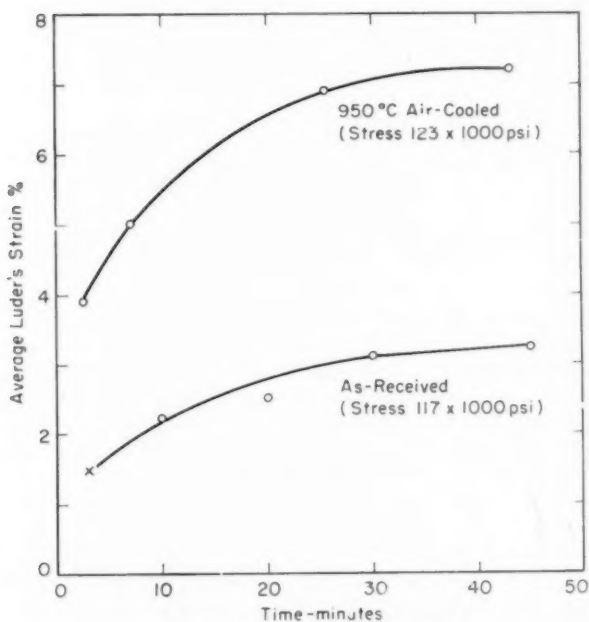


Fig. 3—Average Lüders' Strain as a Function of Time of Yielding. Steel tested at -196°C (-320°F) with a crosshead speed of 3.6×10^{-4} inches per minute.

anticipated (21), the yield stress was found proportional to the logarithm of the crosshead speed (v_c) (Fig. 2). The maximum drop in load during yielding in any specimen corresponded to a decrease of only 3500 psi, based on the original cross section. Contrary to the classical model of Lüders' band propagation, the average strain over the length of the bands increased with the time of loading (Fig. 3). In addition, the local strain within a well developed Lüders' band was not uniform (Fig. 4), being a little greater near the point of initiation at the shoulder of the specimen. An average "true" stress was calculated from the measured load and the corresponding average Lüders' strain at selected times. Although the load decreased somewhat as the Lüders' strain increased during the time-dependent yielding, the stress remained constant to within about 500 psi, which is an appreciably smaller variation than the experimental reproducibility of the yield stress (about 2000 psi).

Fisher and Rogers (14) have demonstrated the existence of creep at -78°C (-108°F) in mild steel wires after the whole specimen is covered by Lüders' bands. The time-dependent Lüders' strain at -196°C (-320°F) observed in the present experiments appears to be a related effect. According to Fisher and Rogers (14), the Lüders' strain depends upon the applied stress and is not directly affected by the testing temperature. Unfortunately, the Lüders' strain is also influenced by the stiffness of the testing machine and the geometry of the specimen (15), so that it is not feasible to compare data obtained by different techniques. After normalizing at 950°C (1740°F), there was a striking increase both in the creep rate and in the maximum strain (Fig. 3.) At the same loading rate, the normalized specimen had a yield stress 6000 psi greater than the as-received specimen, but it seems improbable that this 5.1% increase in stress is sufficient to account for the 130% difference in Lüders' strain. Thus, it appears that at -196°C (-320°F) the Lüders' strain is sensitive to changes in heat treatment.

Lüders' bands started at both ends and moved slowly towards each other. Between the bands, the steel was stressed above the elastic limit and contained a small nonelastic microstrain (stage 1) which then increased slowly with time (stage 2) (12). At very slow crosshead speeds, the maximum load could be applied for several hours before the Lüders' bands traversed the whole specimen, and during this time, fine slip lines could be observed between the bands. However, no new Lüders' bands were initiated although it seems probable that, with longer specimens or still slower loading rates, this could occur.

Influence of Loading Rate on Cleavage Fracture

At constant stress, the time to fracture or, if no break occurred, to the termination of the test was measured from the onset of gross yield-

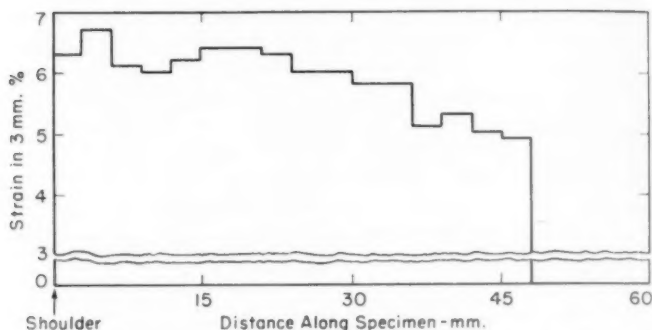


Fig. 4—Example of Distribution of Strain in a Lüders' Band When Measured Over 3 Millimeters Gage Lengths. Steel air-cooled from 950 °C (1740 °F). Tested at -196 °C with a crosshead speed of 3.6×10^{-3} in./min.

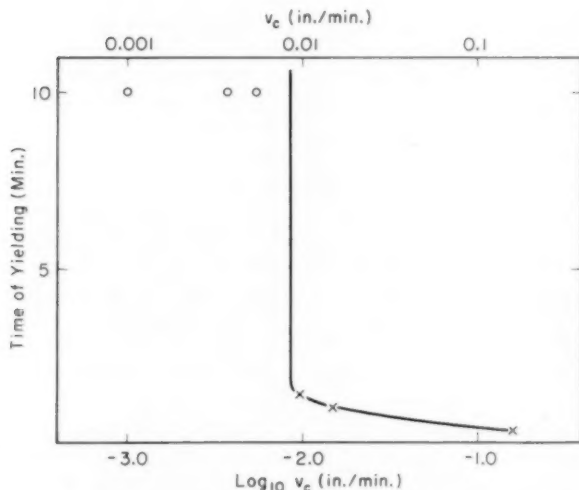


Fig. 5—Time of Yielding Before Fracture as a Function of the Crosshead Speed (v_c). Steel air-cooled from 950 °C (1740 °F) and tested at -196 °C (-320 °F). X—specimen broke. O—no fracture.

ing as indicated by the load extension curve. There was always a time delay before fracture which, as an example, is plotted as a function of the crosshead speed for the air-cooled specimens in Fig. 5. In this case, there was a well defined crosshead speed (8.5×10^{-3} inch per minute) above which the specimens fractured quickly and below which they were ductile. All the specimens furnace-cooled from 950 °C (1740 °F) broke in a short time, but showed a decrease in time-to-fracture with

increase in crosshead speed, corresponding to the right-hand branch of Fig. 5. The slowest loading rate for brittle fracture of the as-received specimens lay between those for the other two series. At crosshead speeds greater than 3.6×10^{-3} inch per minute, all the as-received specimens broke after some delay. However, in seven tests at this borderline speed, three specimens broke quickly while the remaining four did not fracture in long-time tests.

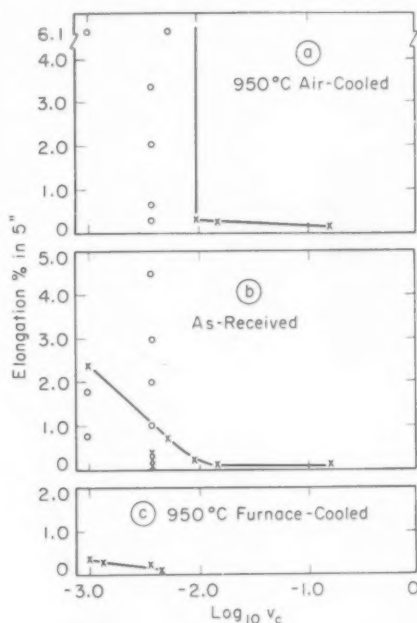


Fig. 6—Elongation in 5-inch Gage Length as a Function of Crosshead Speed (v_c). Temperature -196°C (-320°F). X—specimen broke. O—no fracture.

The overall elongation (in 5 inches) was governed by the extent of Lüders' strain and the distance covered by the bands during the time of the test. The measured elongation is shown as a function of the crosshead speed in Fig. 6.

When the overall elongation is plotted against the average "true" stress in the Lüders' bands at the end of each test, the curves shown in Fig. 7 are obtained. These suggest that in each series there is a stress above which the steel is brittle. In the normalized series, the demarcation was well defined, but in the furnace-cooled specimens, a sufficiently low stress to permit ductile behavior was not attained. The lowest stress achieved experimentally for the as-received specimens was very

close to the transition stress, and the scatter in the ductility data probably resulted from small differences in specimen dimensions or heterogeneity in the steel.

As the crosshead speed was increased in the brittle range, the yield and fracture stresses increased (Figs. 2 and 7) and the time to fracture decreased (Fig. 5). However, no fracture occurred without prior gross deformation. The average Lüders' strain in fractured specimens was

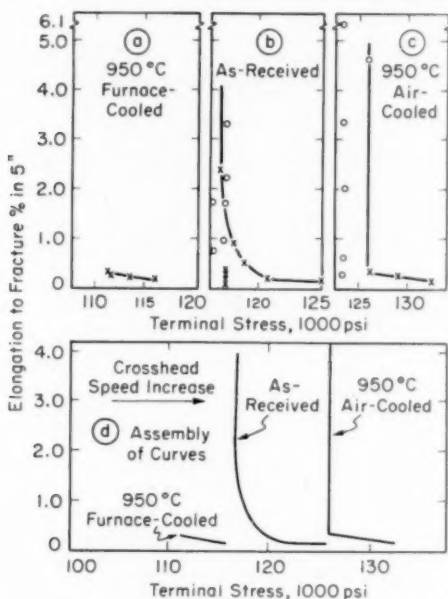


Fig. 7—Elongation in 5-inch Gage Length as a Function of the True Stress at the End of the Test. Temperature -196°C (-320°F). X—specimen broke. O—no fracture.

between 2.1 and 5.2%, while the maximum strains in 3 millimeters were between 3.2 and 6%. Larger average strains were found in many of the ductile specimens. For example, average strains greater than 7% (with a maximum in 3 millimeters of 10.1%) were observed in normalized specimens tested at slow speeds such that no fracture occurred during the run (Fig. 3).

Metallographic Observations

By visual examination of the polished surface it was noted that each fracture was located within a Lüders' band. This was true even at the fastest crosshead-speeds where the Lüders' bands spread only about 1 millimeter before fracture. Although the fracture was often fairly

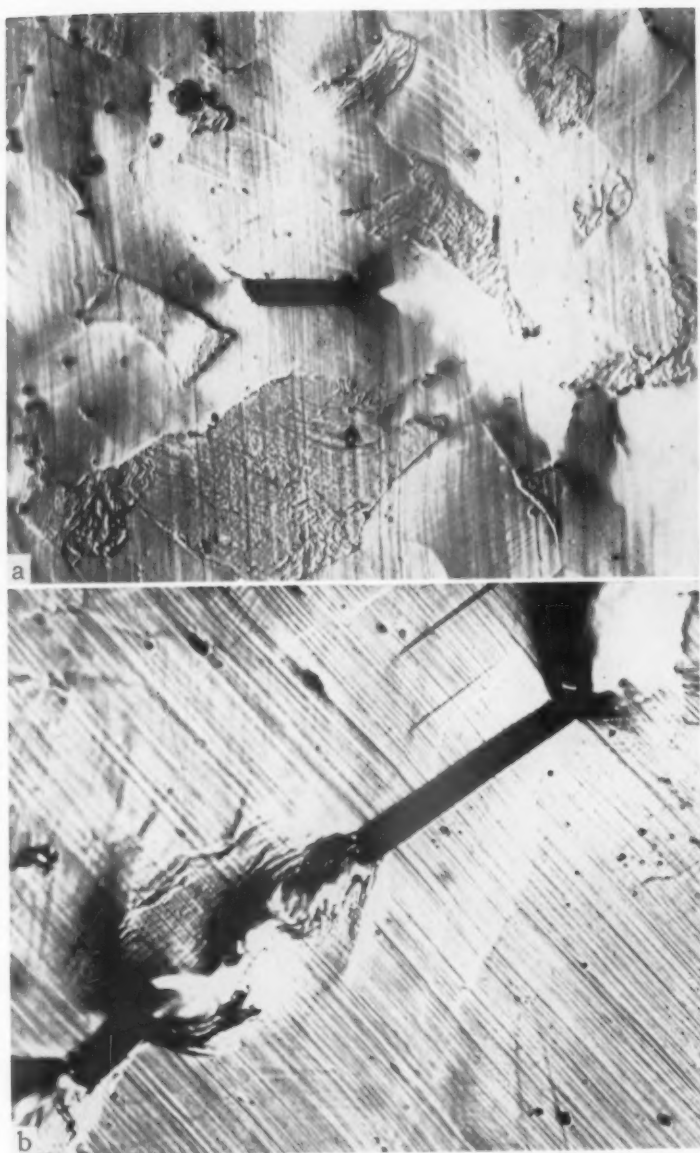


Fig. 8—Examples of Microcracks formed at -196°C (-320°F) in Ductile Specimens.
 $\times 1000$.



Fig. 9—Assembly of Microcracks in Specimen Without a Complete Fracture. (a) and (b) the same area. (a) $\times 1000$, (b) $\times 150$.

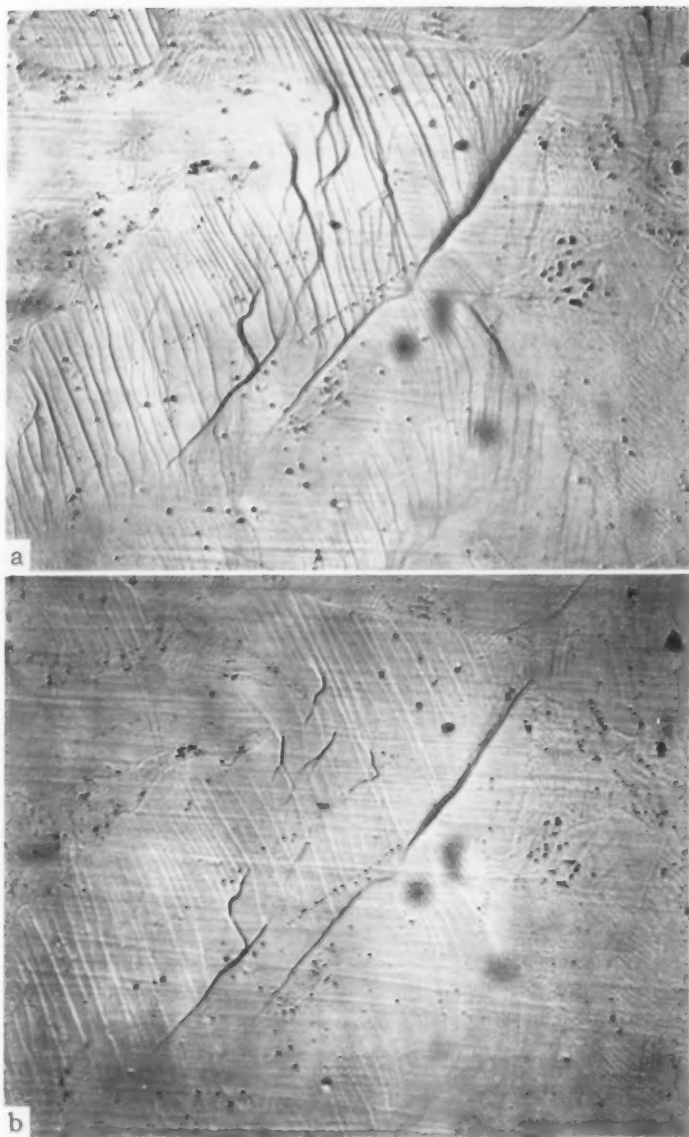


Fig. 10—Unusual Slip Markings Observed After Deformation at -196°C (-320°F). (a) and (b) are the same area with different position of the oblique illumination. $\times 1000$.

close to the leading edge of a band, it never coincided with the interface and in some instances was more than $\frac{1}{4}$ -inch behind the front.

Microcracks were observed in the Lüders' bands of all the specimens, even those which behaved in a ductile manner. Usually the cracks traversed only one or two ferrite grains (Fig. 8) although there were instances of several microcracks joined by very severe local deformation, the whole assembly extending across five or more grains (Fig. 9). The longest strings of cracks were found in specimens subjected to the slowest loading rate and lowest stress. It appears that some single grain microcracks spread slowly by inducing cleavage in neighboring grains, and at low stresses this process is able to continue for some time before fracture results.

A few twins were seen in the Lüders' bands, but these were easily distinguished from the microcracks both by their general appearance in rotated oblique illumination and by repolishing and re-examining the unetched surface when the cracks, unlike the twins, persisted. The twins were not associated with the microcracks. In the area between the Lüders' bands, no microcracks were noted in any of the specimens.

The genesis of the microcracks proved elusive. None smaller than a grain diameter was found, and all produced secondary deformation at their ends tending to obliterate the original slip traces. In addition to the microcracks, numerous markings indicating slip at variance with the predominant slip orientation and with exceptional step heights were observed (Fig. 10). However, no direct evidence connecting these with the subsequent formation of microcracks was obtained.

DISCUSSION

Comparison of the Stroh and Low Theories

Stroh (1,2) has postulated that a cleavage crack can form when n dislocations, piled up under the action of a shear stress, σ_s , satisfy the condition

$$n b \sigma_s = 12 \gamma \quad \text{Equation 1}$$

where b is the Burger's vector and γ the surface energy of the cleaved faces of a single crystal. Assuming the blockage is provided by a grain boundary, the piled-up dislocations are pictured to occupy a length equal to half the grain diameter, d , and the fracture stress, σ_F , is then

$$\sigma_F = 4 [6\gamma G/\pi (1 - \nu)]^{1/2} d^{-1/2} \quad \text{Equation 2}$$

where G is the shear modulus and ν is Poisson's ratio. At a given temperature,

$$\sigma_F = k d^{-1/2} \quad \text{Equation 3}$$

which has been verified experimentally for polycrystalline zinc by

Greenwood and Quarrell (5). To fit the experimental data for iron and steel at -196°C (-320°F) Petch (3,4) found it necessary to introduce a second constant σ_0 , the yield stress of a single crystal at the testing temperature, so that

$$\sigma_F = \sigma_0 + kd^{-1/2} \quad \text{Equation 4}$$

Low (10) also observed a linear relationship between σ_F and $d^{-1/2}$ for low carbon iron at -196°C (-320°F), but explained the result in terms of the Griffith-Orowan concept:

$$\sigma_F = [4 E p / \pi]^{1/2} d^{-1/2} \quad \text{Equation 5}$$

where E is Young's modulus and p is an energy term which includes the surface energy and the plastic work done during fracture.

According to Stroh (2), the proportionality constant k in equation (3), (which does not include a plastic work term) agrees with experimental values deduced from the Petch (3,4) and the Greenwood-Quarrell data (5). On the other hand, Low (10) maintains that the plastic work term far outweighs the surface energy term since the experimental value found for p in Equation 5 is at least two orders of magnitude greater than the known surface energies of metals.

An important stimulus to the development of the dislocation theory has been the belief that subcritical Griffiths cracks do not exist in a real metal prior to brittle fracture. The present work has shown clearly that this belief is unfounded in the case of mild steel since microcracks are formed before fracture.

The dislocation pile-up theory does not account for either the location of the fracture or the effects of loading rate observed in the present experiments. In this view (2), fracture and yielding are taken to be competitive processes, cleavage resulting from the normal stresses and yielding from the shear stresses around a queue of dislocations. The shear stress required to activate a dislocation source in a neighboring crystal increases as the temperature is decreased, so that at some temperature the necessary normal stress for cleavage is achieved before the shear stress to induce further slip is reached. The present experiments were carried out well below Stroh's estimated temperature (2) of transition from slip to cleavage behavior, and also below the measured tensile transition temperature (16). Consequently, the strain preceding fracture should be only that resulting from the pile-up of dislocations, its magnitude being about the same as that of the first-stage microstrain. In other words, brittle fracture should occur either before gross yielding in the vicinity of the stress concentration near the specimen ends or, subsequently, at the front of the Lüders' bands. In none of the experiments did fracture occur in either of these situations.

The time required to build up a dislocation queue at a constant ap-

plied stress should be that necessary to establish the microstrain (stage 1). These times for mild steel, at different stresses and temperatures, have been measured by Clark and Wood (17-19). At the static yield stress, they are very small compared with the delay time for yielding. Thus, since there is no term in Equation 2 suggesting a built-in time dependence for cleavage, the Stroh theory predicts that the fracture stress should be less sensitive than the yield stress to an increase in the loading rate, and that the probability of fracture without prior gross yielding should be greater when the crosshead speed is increased. In the present experiments, fracture was always preceded by gross yielding and the fracture stress increased with the yield stress.

The Low concept of brittle fracture in iron at -196°C (-320°F) rests on two propositions:

1. Fracture is preceded by yielding and the formation of microcracks of a size related to the grain diameter.
2. The fracture stress is that stress which causes the microcracks to propagate to complete failure, the critical conditions being defined by Equation 5.

The relation between yielding and fracture was demonstrated experimentally by showing that in coarse-grained iron the fracture stress in tension coincides with the yield stress in compression when both tests are conducted at -196°C (-320°F) and at the same strain rate. A separate slow-bend test was used to demonstrate the presence of subcritical microcracks. These were caused to propagate to complete failure by increasing the applied stress. Thus, the conditions were comparable with those in the fourth stage of the nonelastic strain in a tension test, that is, after the Lüders' bands have covered the specimen. The present experimental data, which show this behavior even in the situation of minimum ductility in tension at -196°C (-320°F), provide substantial support for Low's viewpoint over a range of testing speeds. At all stresses which produced gross yielding at -196°C (-320°F), microcracks were found in the Lüders' bands. In the air-cooled and as-received specimens, these did not propagate to failure within the time of testing (about 40 minutes) unless the stress was greater than a certain minimum (Fig. 7D). It is reasonable to assume that in the more brittle furnace-cooled specimens, the yield stress was always greater than the minimum stress required to cause the microcracks to spread rapidly.

General Discussion

To form a microcrack it is necessary to cause appreciable plastic deformation and to reach a sufficiently high stress. The minimum stress necessary at -196°C (-320°F) could not be ascertained since microcracks were produced at the lowest yield stress attainable. Nor

was it possible to obtain any direct information about the mechanism by which the microcracks are generated. Single crystal techniques appear to be more appropriate for studying this problem.

At a constant applied stress, there is a time delay before cleavage fracture (Fig. 5). This has three components: the delay time for the initiation of Lüders' bands, the time for formation of microcracks, and the interval between their formation and propagation to complete fracture. The first component is not significant in the present data since the times were measured from the start of gross yielding. In the slow-speed tests on air-cooled specimens, microcracks were found in less than 30 seconds after the initiation of Lüders' strain, although the bands continued to spread for an additional 40 minutes without fracture. Evidently, the propagation of the cracks is the major time-deciding factor.

The delay in propagation cannot be understood in terms of Equation 5 which does not contain any time-dependent factors. The average plastic strain (although time dependent) is not a criterion for fracture since the slowly-loaded specimens which did not break contained a much larger Lüders' strain than the specimens which fractured at higher stresses. As explained earlier, the average stress on a Lüders' band did not fluctuate more than about 0.4%. While it is possible that this fluctuation could account for the delay in fracture, it seems more probable that the important changes occur on a much smaller scale.

The delayed fracture is thought to be a consequence of the time dependence of the Lüders' strain at low temperatures (Fig. 3). As measured on the millimeter grid, the strain along a band is not uniform (Fig. 4) and frequently fractures are not located near the maximum strain even on this scale. Microscopically the deformation is very heterogeneous. The stress-strain pattern in the vicinity of any one grain is not accurately reflected by the average measurements, and it changes continuously as creep progresses. Under these conditions the development of microcracks is complex. The material surrounding a crack is not isotropic, as assumed by Equation 5. Further the relative grain orientations must be a factor in determining the probability that one of the original microcracks will induce cleavage in a neighboring grain. When cracks have formed in several connected grains, d in Equation 5 should be replaced by the length of the crack assembly, and the same applied stress can now drive the fracture through more unfavorable environments. There is some critical size such that fracture can progress through any surroundings it encounters, and then catastrophic failure ensues.

A sequence of cracks extending through a number of grains, N , (Fig. 9) was observed in several of the specimens which had yielded extensively at stresses below the minimum stress for failure. Similar, but less extensive, arrays of cracks were observed in some of the frac-

tured specimens in locations remote from the main fracture. It is evident that at stresses close to and below the minimum fracture stress, the critical size for final failure is appreciably greater than that for the first-formed microcrack. If Equation 5 is used to compute the minimum fracture stress, d must be replaced by N^*d , N^* being the number of single-grain microcracks in the assembly of critical size. Then,

$$\sigma_F = \text{Const. } (P/N^*d)^{1/2} \quad \text{Equation 6}$$

The present experimental conditions approximate the situation where the applied stress, σ , is held constant while N increases with time.

Fracture occurs if the total crack length (Nd) reaches a critical value in the time available. It may be that the growth rate of a sub-critical crack is affected by the grain size and heat treatment, but no information on this point is available. However, it is clear that the critical crack length is determined by the value of P . Grain size is an important factor in fracture behavior and, thus P must be a function of d . This is readily understood if the contributions to the plastic work term are considered. The two major sources of energy absorption are the deformation which occurs at cleavage steps within the grains (E_{step}) and the shear deformation required to join adjacent cleavages (E_{tear}). The lattice affects a large volume of metal (Figs. 8 and 9) and certainly appears to be the major contribution. Since the number of discontinuities in the cleavage, and therefore the number of sheared volumes, must increase with a decrease in grain size, it seems likely that the grain size effect operates by virtue of its influence on E_{tear} , and thus on p .

It has been suggested that σ_F is proportional to $d^{-1/2}$ (3,4,9,10) (thus, if the preceding argument is correct, P is proportional to d^{-1}), but the minimum fracture stress as revealed by the present experiments conforms only very approximately to this relation (Table II). The range of d investigated was small but appreciable effects were pro-

Table II
Variation of $\sigma_F d^{1/2}$ with Heat Treatment

Heat Treatment	min. value of $\sigma_F d^{1/2}$ (lb/in ^{3/2})
950 °C (1740 °F), Furnace-Cooled	<3.97
As-Received	4.18
950 °C (1740 °F), Air-Cooled	3.22

duced by changes in heat treatment. For example, at 125×10^3 psi the furnace-cooled and as-received specimens fractured in a short time while the air-cooled specimen was ductile (Fig. 7d), thus reinforcing a previous conclusion (13) from work on these steels that changing the cooling rate produces greater effects than can be accounted for on the basis of grain size alone.

Low (10) and Petch (4) employed short tensile bars of circular cross section and probably loading rates* approaching the most rapid used in the present experiments. Under their conditions, the creep and delayed fracture phenomena are not significant because the specimen is at the constant lower yield for only a short time. As stated by Low (10), in coarse-grained steel microcracks form and propagate to failure at the yield stress, but when the grains are small they do not propagate until the continuously increasing applied stress reaches some higher value. In the former case, σ_F closely corresponds with σ_{YS} and both are the same linear function of $d^{-1/2}$. The second situation, when the specimens show some ductility, is complex. Then the first-formed microcrack (about one grain diameter) is smaller than the critical size ($N*d$) and, consequently, it is expected that the effective crack size (Nd) increases as the stress (σ) is increased. P also is expected to increase with σ since further plastic deformation occurs. Low found experimentally that the additional stress required to cause crack propagation to failure was proportional to $d^{-1/2}$ although the data indicated appreciable scatter, and subsequent investigations have shown that grain size is not the only heat treatment sensitive variable in this situation (13,22).

CONCLUSIONS

The following refers only to mild steel, long-strip specimens, tested in tension at -196°C with testing speeds between 8.9×10^{-4} and 1.6×10^{-1} inch per minute.

1. Fracture is always preceded by gross yielding; thus, when the testing speed is increased, the fracture stress increases with the yield stress. Microcracks and complete fractures are located only in the Lüders' bands, usually some distance behind the moving front.

2. Although microcracks are formed at all loading rates within the stated range, there is a minimum stress required for complete fracture, this minimum stress is materially affected by heat treatment.

3. The magnitude of the Lüders' strain is time dependent and sensitive to changes in heat treatment.

4. Fracture occurs in stages: first microcracks, about one grain diameter, are formed. By inducing cleavage in neighboring grains, these microcracks spread subsequently across a number of grains, the individual cleavages being connected by regions of very severe deformation. Finally, the assembly of cracks reaches a critical size and propagates rapidly to failure.

5. At a constant stress during yielding, there is a time delay to fracture. This appears to be a result of the creep which occurs in the Lüders' strain.

In general terms, these observations are compatible with Low's ap-

* Their loading rates are not given.

plication of the Griffith-Orowan concepts rather than with the dislocation pile-up theory which does not appear applicable to the brittle fracture of mild steel.

ACKNOWLEDGMENTS

The work was supported financially by the Ship Steel Committee of the Ship Structure Committee under Contract NObs 65918. E. Howell and R. C. Whittemore assisted in the experimental work.

References

1. A. N. Stroh, "The Formation of Cracks as a Result of Plastic Flow," *Proceedings of the Royal Society*, Vol. 223, Series A, 1954, p. 404.
2. A. N. Stroh, "Brittle Fracture and Yielding," *Philosophical Magazine*, Vol. 46, 1955, p. 968.
3. N. J. Petch, "The Fracture of Metals," *Progress in Metal Physics*, Vol. 5, 1954, p. 1, Pergamon Press Ltd., London.
4. N. J. Petch, "The Cleavage Strength of Polycrystals," *Journal of the Iron and Steel Institute*, Vol. 174, 1953, p. 25.
5. G. W. Greenwood and A. G. Quarrell, "The Cleavage Fracture of Pure Polycrystalline Zinc in Tension," *Journal, Institute of Metals*, Vol. 82, 1953-54, p. 551.
6. N. F. Mott, "Theories of Fracture in Metals," *International Union of Theoretical and Applied Mechanics Colloquium*, Madrid, September 1955.
7. N. F. Mott, "Fracture in Metals," *Journal, Iron and Steel Institute*, Vol. 183, 1956, p. 233.
8. A. A. Griffith, "Theory of Rupture," *Proceedings, First International Congress of Applied Mechanics*, Delft, 1924, p. 55.
9. J. R. Low, "Dislocations and Brittle Fracture in Metals," *International Union of Theoretical and Applied Mechanics Colloquium*, Madrid, September 1955.
10. J. R. Low, "The Relation of Microstructure to Brittle Fracture," *Relation of Properties to Microstructure*, 1954, p. 163, American Society for Metals.
11. E. Orowan, "Fundamentals of Brittle Behavior in Metals," *Fatigue and Fracture of Metals*, 1952, p. 139, John Wiley and Sons, New York.
12. W. S. Owen, M. Cohen and B. L. Averbach, "Some Aspects of Preyield Phenomena in Mild Steel at Low Temperatures," *TRANSACTIONS, American Society for Metals*, This Volume, 1958, p. 517.
13. W. S. Owen, D. H. Whittemore, C. P. Sullivan, B. L. Averbach and M. Cohen, "The Relation of Charpy Impact and Low-Temperature Tensile Properties to the Microstructure of Two Ship Steels," *Ship Structure Committee, Report No. 102*, 1956.
14. J. C. Fisher and H. C. Rogers, "Propagation of Lüders' Bands in Steel Wires," *Acta Metallurgica*, Vol. 4, 1956, p. 180.
15. J. Miklowitz, "The Initiation and Propagation of the Plastic Zone in a Tension Bar of Mild Steel as Influenced by the Speed of Stretching and Rigidity of Testing Machine," *Journal of Applied Mechanics*, Vol. 14, No. 1, 1947, p. A-31.
16. G. Hahn, unpublished work.
17. D. S. Clark and D. S. Wood, "The Time Delay for the Initiation of Plastic Deformation at Rapidly Applied Constant Stress," *Proceedings, American Society for Testing Materials*, Vol. 49, 1949, p. 717.
18. D. S. Clark and D. S. Wood, "The Influence of Temperature Upon the Time Delay for Yielding in Annealed Mild Steel," *TRANSACTIONS, American Society for Metals*, Vol. 43, 1951, p. 571.
19. T. Vreeland, Jr., D. S. Wood and D. S. Clark, "Preyield Plastic and Anelastic Microstrain in Low-Carbon Steel," *Acta Metallurgica*, Vol. 1, 1953, p. 414.
20. J. J. Gilman, "Cleavage Steps on Zinc Monocrystals: Their Origins and Patterns," *Transactions, American Institute of Mining and Metallurgical Engineering*, Vol. 203, 1955, p. 1252.

21. A. H. Cottrell and B. A. Bilby, "Dislocation Theory of Yielding and Strain Aging of Iron," *Proceedings, The Physical Society*, Vol. A62, 1949, p. 49.
22. W. P. Rees, Discussion of Reference No. 4, *Journal, Iron and Steel Institute*, Vol. 177, 1954, p. 342.

DISCUSSION

Written Discussion: By G. Schoeck and E. T. Wessel, Westinghouse Electric Corporation, Research Laboratories, Pittsburgh.

The authors made a valuable contribution to the investigation of brittle fracture in steel. They show that for mild steel at -196°C (-320°F) fracture occurs only after a Lüders' band has been formed, and that before fracture many stable microcracks are formed within a Lüders' band. Under the conditions of these tests therefore the fracture stress is not the stress necessary to initiate cracks but is the stress that is required to propagate existing cracks.

From their observations the authors conclude that the dislocation pile-up theory of fracture is not compatible with the experimental results. A critical examination of the arguments shows, however, that this conclusion seems not to be justified. The authors imply that the pile-up theory predicts:

- (a) There exist no cracks prior to brittle fracture.
- (b) At the temperature of the experiments the strain prior to brittle fracture should be only of the first stage micro-strain i.e. of the order of $\epsilon \approx 5 \cdot 10^{-8}$.
- (c) Fracture should occur prior to gross yielding and dislocation theory is not able to account for the delay time for fracture.

The pile-up theory of brittle fracture³, however, makes at least in its later developments^{4,5} a distinction between crack formation and crack propagation. Stroh's³ criterium for fracture

$$n\tau b = 12\gamma$$

(n = number of dislocations in pile-up, τ = shear stress, b = Burgers vector, γ = surface energy) is the condition for nucleation of a crack. In order to obtain a large enough pile-up always some deformation has to proceed the crack formation.

Let us consider the conditions quantitatively. Since the maximum shear stress is equal to $\frac{1}{2}\sigma_F$ the number of dislocations necessary to form a crack is from Stroh's calculation

$$n_F = 24\gamma/b\sigma_F$$

In using the value of $\gamma \approx 2000 \text{ erg cm}^{-2}$ for the surface energy of iron and the value of $\sigma_F = 120 \cdot 10^8 \text{ psi}$ for the fracture stress we obtain

$$n_F \approx 230$$

³ A. N. Stroh, *Proceedings, Royal Society*, Vol. 223, 1954, p. 404.

⁴ A. N. Stroh, *Philosophical Magazine*, Vol. 46, 1955, p. 968.

⁵ N. F. Mott, *Journal, Iron and Steel Institute*, Vol. 174, 1956, p. 25.

On the other hand we can correlate the number n of dislocations per grain which have moved over the grain diameter d , with the plastic strain ϵ by the relation

$$\epsilon \approx nb/d$$

Since the grain diameter in these tests was of the order of $d \approx 4 \cdot 10^{-3}$ cm the number of dislocations n_1 per grain to produce the microstrain of $\epsilon \approx 5 \cdot 10^{-3}$ would be

$$n_1 \approx 8$$

This number is obviously too small to produce a crack. If we consider, however, a Lüders' band where the strain is of the order of $4 \cdot 10^{-2}$ we obtain as the number of dislocations per grain

$$n_2 \approx 6400$$

These dislocations will be produced, of course, by different Frank-Read sources and if about 30 sources are present each of them would produce enough dislocations to initiate a crack.

The crack which is formed by a pile-up, however, can be stable and it will only propagate if there exists a large enough tensile stress to make it spread and if it is not damped out by plastic flow around its apex. In order to prevent plastic flow the Frank-Read sources have to be locked effectively and this itself depends on the temperature and on the velocity of crack propagation. A theoretical analysis is rather complex. The delay time for fracture, however, could well be interpreted that by the increase in Lüders' strain with time finally the condition for crack propagation is reached either by accumulating of more dislocations until a critical crack size or stress concentration is reached or by joining up of several individual cracks.

It has to be emphasized here that the occurrence of fracture changes with temperature and it is interesting to compare the present results with similar investigations. Wessel⁶ has studied fracture of the same kind of material (rimmed

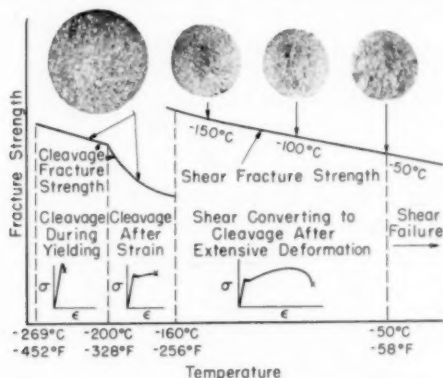


Fig. 11—Comparison of Fracture Appearance and Type of Stress-Strain Curves for Various Test Temperatures (6).

⁶ E. T. Wessel, *Proceedings, American Society for Testing Materials*, Vol. 56, 1956, p. 540.

mild steel) over a wide temperature range from -269°C to -50°C (-452 to -58°F). An extensive discussion of these experiments has been given elsewhere,^{6,7} but the important result is shown in Fig. 11. The tests were made at a constant strain rate of about $2 \cdot 10^{-3} \text{ sec}^{-1}$. It is possible to distinguish between 3 different regions:

- I) from -269 to -200°C (-452 to -328°F) cleavage fracture occurs during the drop in load usually associated with yielding.
- II) from -200 to -160°C (-328 to -256°F) cleavage fracture occurs after the yield drop, usually during the lower yield point elongation (propagation of Lüders' band).
- III) above -160°C (-256°F) fracture occurs during deformation following the Lüders' strain. Rupture starts after necking as shear fracture which converts later to cleavage.

It is important to notice that in these tests the deformation before the yield drop was of the order of 10^{-3} . This corresponds to about 300 dislocations per grain which is of the order of magnitude necessary to initiate microcracks.

The authors' tests were made in region II slightly above the transition temperature from region I. The present experiments show that in region II the fracture stress is that for crack propagation. In region I the situation is different. There is no evidence that cracks are formed before the "yield drop". Hence here the "yield drop" may actually be caused by crack formation and a crack once started is able to propagate and lead to gross failure. Therefore in region I it is likely that crack formation occurs before the formation of a Lüders' band, although further studies will be necessary to confirm this point.

Authors' Reply

The discussion by Schoeck and Wessel highlights some of the main issues in the dislocation pile-up hypothesis for brittle fracture. It is now clear that, at least in the present tests, a distinction must be made between the conditions leading to the formation of microcracks and their subsequent propagation to fracture. Stroh's equations deal with the problem of nucleating a crack, but the predictions have been compared with the experimental fracture stress rather than with the local stress required to nucleate a microcrack.

Once it is granted that the microcracks do not form until after gross deformation has occurred, as is the case at hand, there is no longer a competitive situation between plastic deformation and cleavage fracture during the early stages of loading. The theory requires that one or the other should take place, but since gross plastic deformation intervenes, we do not have the neat dislocation queues to explain the subsequent microcracks.

According to the analysis given by the discussors, enormous dislocation pile-ups would be needed to account for the origin of the microcracks. But inasmuch as inhomogeneous yielding has already occurred before the microcracks are observed, these dislocations have clearly broken through the grain boundaries and the specimen surface in the gross deformation and they can no longer furnish the pile-ups demanded by the theory.

It appears that the resolution of this dilemma must await a clearer picture of the conditions under which the microcracks in steel are generated.

⁷ E. T. Wessel, *Transactions, American Institute of Mining and Metallurgical Engineers*, Vol. 212, 1957, p. 930.

THE INITIATION OF BRITTLE FRACTURE IN MILD STEEL

BY J. A. HENDRICKSON, D. S. WOOD, AND D. S. CLARK

Abstract

This paper presents the results of a study of the conditions underlying the initiation of brittle fracture in an annealed low-carbon steel. Notched tensile specimens have been tested at temperatures of -23 , -110 , and -200 °F (-30 , -79 and -129 °C) at rates of application of nominal stress ranging from 10^3 to 10^7 psi per second.

The magnitude of the maximum nominal stress (fracture stress) has been determined for those tests in which brittle fracture occurred. The distribution of stress on the cross section at the root of the notch at the instant of brittle fracture has been determined analytically. The effect of local plastic deformation at the root of the notch has been taken into account by employing an elastic-plastic stress analysis. The analysis makes use of values of the upper yield stress of the material determined in a previous investigation as a function of temperature and rate of stress application.

The maximum tensile stress within the specimen occurs at the boundary of the region of local plastic deformation directly beneath the root of the notch. The magnitude of this stress at the instant of brittle fracture is found to be independent of both the temperature and rate of stress application. This critical tensile stress is not attained in the specimens when the conditions of temperature and rate of stress application are such that ductile behavior occurs. These results indicate that the initiation of brittle fracture in mild steel is governed by a critical tensile stress which is independent of temperature and rate of loading. The influence of temperature and rate of loading upon brittle fracture arises entirely from the influence of these variables upon the yield stress. (ASM International Classification: Q26s; CN)

INTRODUCTION

THE PROBLEM of brittle fracture in steel has been of ever increasing interest. Extensive research has been devoted to this subject in an attempt to understand the underlying principles. Certain conditions such as low temperature, a triaxial stress state as prevails

A paper presented before the Thirty-ninth Annual Convention of the Society, held in Chicago, November 4 to 8, 1957. Of the authors, J. A. Hendrickson is research assistant, D. S. Wood is Associate Professor of Mechanical Engineering, and D. S. Clark is Professor of Mechanical Engineering, California Institute of Technology, Pasadena, California. Manuscript received April 6, 1957.

beneath a notch, and a high rate of stress rise are known to be conducive to brittle fracture. However, the particular combinations of these parameters which will cause the initiation of brittle fracture are not well understood.

An understanding of the interdependence of these parameters is of importance from two points of view. First, such an understanding is necessary for the establishment of quantitative methods by which the susceptibility of structures to brittle fracture in service may be predicted from the results of laboratory fracture tests. Second, quantitative knowledge and control of these macroscopic parameters is a prerequisite to the planning and interpretation of experimental investigations concerning the microscopic or atomistic mechanism of the initiation of brittle fracture. Investigations of the latter type are the means by which a fundamental understanding of the influence of metallurgical variables, such as grain size, chemical composition, heat treatment, etc. upon the initiation of brittle fracture may be obtained. An understanding of the mechanism by which brittle fracture is initiated may require new rather than traditional avenues of approach as has been indicated by Shank (1)¹ in an excellent summary of progress in the field of brittle fracture.

Brittle fracture of the type associated with a transition temperature in conventional notched bar impact tests has been found to occur in many, if not all, of the metals which exhibit the body-centered cubic crystal structure. While some of the hexagonal close-packed metals also exhibit this transition temperature, the face-centered cubic metals do not (1). It is significant that the classification of metals on the basis of their crystal structure also differentiates those which do and do not exhibit distinct yield points or discontinuous yielding in their conventional stress-strain relations. The metals that crystallize in the body-centered cubic structure and some of those that have the hexagonal structure exhibit distinct yield points while the face-centered cubic metals do not. Those metals that exhibit a transition temperature and distinct yield points, also exhibit delayed yielding (2,3,4,5,6). The probability is thus strong that the existence of a ductile to brittle transition temperature and delayed yielding are closely related.

This paper presents the results of an investigation of the behavior of notched tensile specimens of annealed mild steel subjected to different constant rates of loading at different temperatures. The purpose of this investigation is to determine quantitatively the inter-relationship between temperature, loading rate, and stress state beneath a notch which governs the initiation of brittle fracture.

THEORETICAL CONSIDERATIONS

The stress condition beneath a notch, in a tensile specimen, includes triaxial tensile stresses. Such a stress condition suppresses general

¹ The figures appearing in parentheses pertain to the references appended to this paper.

yielding of the material and hence is conducive to fracture with greatly reduced plastic flow or brittle fracture. The fact that some plastic deformation in a local region near the notch root precedes brittle fracture, even in the case of extremely sharp notches, is rather well established (7). Brittle fracture appears to be initiated at some distance beneath the notch surface (8), presumably at some point near the boundary be-

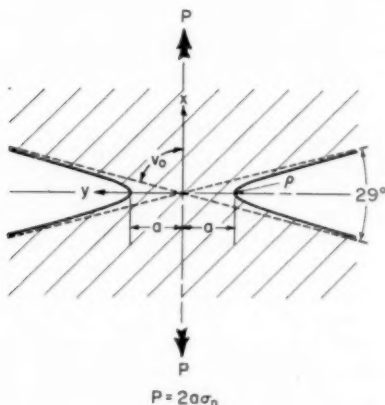


Fig. 1—Elastic-Plastic Solid with Hyperbolic Notches.

tween the region of elastic behavior and the plastically deformed region. Since plastic deformation occurs prior to the initiation of brittle fracture, the stress distribution beneath the notch at the instant of initiation of fracture cannot be determined solely by means of the theory of elasticity. Thus a suitable form of the theory of plastic deformation must be employed in the region of plastic flow, while the theory of elasticity is employed for the remainder of the specimen.

An elastic-plastic stress analysis appropriate for application to the experimental results obtained in this investigation has been derived. The stress analysis has been made for a solid body having the cross section shown in Fig. 1. The notch surfaces are formed by the two sheets of an hyperbola having an included angle of 29° between the asymptotes. The ratio of the half width at the minimum cross-section, a , to the radius of curvature at the root of the notch, ρ , is $a/\rho = 15$. The body is of infinite extent in the plane of Fig. 1 and in the direction normal to that plane. All cross sections parallel to the plane of the figure are the same. Thus the problem is one of plane strain.

The tensile load, P , per unit thickness normal to the plane of the figure acts in the direction perpendicular to the plane of the minimum

cross section. This load is assumed to be applied by suitably distributed surface forces acting on the body at an infinite distance from the minimum cross section. The load may be expressed in terms of the nominal stress, σ_n , acting on the minimum cross section by the relation $P = 2a\sigma_n$.

This elastic-plastic body does not coincide with the actual specimen shape employed in the experimental portion of this investigation. The specimen shape is axially symmetric with the notch surface in the form of an hyperboloid of revolution. However, the results of the stress analysis are believed to provide a close approximation to the stress state in the test specimen, as will be discussed later. The plane strain approximation is employed in the analysis because a method of solution for this problem is available while a method applicable to the axially symmetric case is not.

The stress analysis for the elastic-plastic body in plane strain is based upon the following assumptions:

(a) The material (mild steel) is assumed to be homogeneous and isotropic in both the elastic and plastic regions. This assumption means, in effect, that the stresses and strains are only considered as average values over regions larger than the grain size of the material.

(b) Hooke's Law, implying a linear relation between stress and strain, is assumed to apply at any point in the elastic region.

(c) Plastic deformation occurs when the maximum shear stress, τ_{max} , reaches a critical value, τ_c . This is the commonly used Tresca Yield condition and holds quite well for steel which exhibits a distinct yield point.

(d) The material is non-strain hardening. This assumption holds true in mild steel for small plastic strain. The inclusion of strain hardening considerations in this investigation would require a modification of the yield condition with an attendant increase in mathematical complexity.

(e) The direction of the maximum shear stress, τ_{max} , is assumed to always lie in the plane of Fig. 1. Hence the component of plastic strain in the direction normal to the plane of Fig. 1 is always zero. When plastic deformation is first initiated at the root of the notch, this condition is satisfied. Thus it may also be expected to hold true for a small penetration of the plastic region beneath the notch.

(f) The displacements at the free (notch) surface are small enough that the change in shape of the notch contour during plastic deformation need not be taken into account. The justification of this assumption comes from the solution of the problem. Namely,

the plastic region existing at the instant of initiation of brittle fracture is always small and confined to the immediate vicinity of the notch root. Thus the plastic strains are small (of the order of elastic strains), and therefore the displacements of the free surface are negligible.

(g) The load is applied in a monotonically increasing manner and the strain in any element of the body increases monotonically. This corresponds with the type of loading employed in the experimental work.

The origin of the coordinate system employed in the stress analysis is at the center of symmetry of the body as shown in Fig. 1. The z coordinate is normal to the plane of the figure. The x axis is in the direction of the applied load and the y axis passes through the notch root.

The deformation is entirely elastic for small values of the applied nominal stress, σ_n . The stresses for this case have been determined analytically by Neuber (9). The maximum stress is 4.96 times the nominal stress, for the particular notch employed in this investigation. This maximum stress occurs at the root of the notch in the direction of the applied load. When the nominal stress is increased to the value $\sigma_n = 1/4.96 \sigma_{yd}$, where σ_{yd} is the yield stress of the material in simple tension, plastic deformation begins at the root of the notch.

There is no known method for obtaining analytical expressions for the stress once plastic deformation begins. However, solutions may be obtained by a technique of step by step numerical calculations known as the relaxation method (10). This method has been employed by Allen and Southwell (11) to obtain the solutions of problems of elastic-plastic deformation similar to that of this investigation. The calculations have been performed for four values of the ratio between the nominal stress and the yield stress, namely, $\sigma_n/\sigma_{yd} = 0.70, 0.81, 1.12, \text{ and } 1.35$.

The principal stresses at the minimum cross-section are shown as a function of position, $(a - y)/\rho$, near the root of the notch in Fig. 2 for the case $\sigma_n/\sigma_{yd} = 0.81$. The full lines represent the stresses for elastic-plastic deformation and the dashed lines show the stresses for purely elastic deformation. The maximum stress, $(\sigma_n)_{\max}$ in the case of elastic-plastic deformation is the stress in the x direction at the elastic-plastic boundary. The value of this maximum tensile stress in the notched bar has been determined for several values of nominal stress for which the elastic-plastic stress analysis has been made. The relationship between $(\sigma_n)_{\max}/\sigma_{yd}$ and σ_n/σ_{yd} for the notch considered in this investigation is shown in Fig. 3.

The position and shape of the elastic-plastic boundary within the body are also obtained from the stress analysis calculations. These are shown later. The regions of plastic deformation which occur for the cases in which $1/4.96 < \sigma_n/\sigma_{yd} < 1.35$ are confined to the immediate

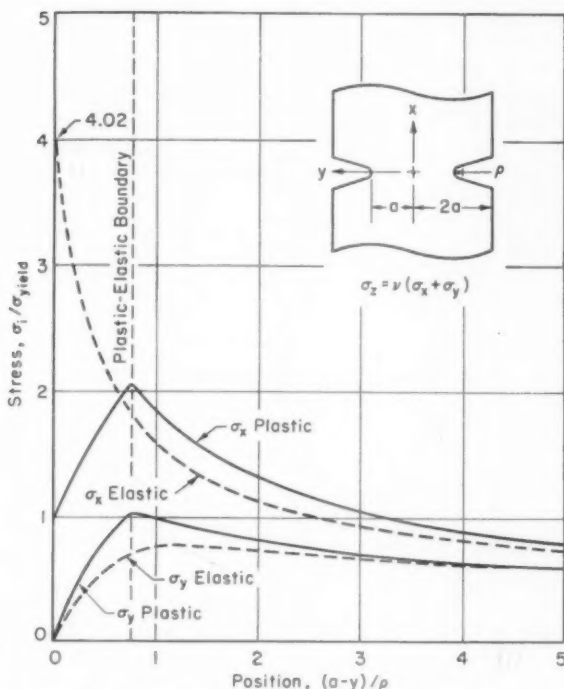


Fig. 2—Stresses on Minimum Cross Section of a Plane Hyperbolic Notch with $a/\rho = 15$ and $\sigma_a/\sigma_{yd} = D.B.I$ under Tension.

vicinity of the root of the notch. However, when σ_n/σ_{yd} exceeds about 1.35, narrow regions of plastic deformation extend toward the axis of the specimen but away from the minimum cross-section. This mode of plastic deformation is very similar to that found by Allen and Southwell (11) for "v" notched specimens when a critical load is exceeded. The extended regions of plastic deformation join with small isolated plastically deformed regions which form on the axis of the specimen away from the center of symmetry. Thus for the notch considered in this investigation the confined plastic regions at the root of the notch become unstable at a nominal stress of $\sigma_n = 1.35 \sigma_{yd}$, and plastic deformation extends completely across the body with very little further increase in the applied load. As Hill (12) has pointed out, the present method of solution is no longer strictly valid for loads which exceed this critical value. For this reason the relation between $(\sigma_n)_{max}/\sigma_{yd}$ and σ_n/σ_{yd} shown in Fig. 3 is terminated at the value $\sigma_n/\sigma_{yd} = 1.35$.

A consistent definition of "brittle" as opposed to "ductile" fracture in notched specimens may be made on the basis of the foregoing results.

Namely, "brittle" fracture is a fracture which takes place while the plastically deformed regions are confined to the vicinity of the notch root. Thus any fracture which occurs in the particular notched specimen employed in this investigation, at a nominal stress $\sigma_n/\sigma_{yd} < 1.35$ is a "brittle" fracture. Conversely any fracture which occurs after plastic deformation has progressed to the axis of the specimen, i.e., when $\sigma_n/\sigma_{yd} > 1.35$, is a "ductile" fracture. This definition of the distinction between brittle and ductile fractures should correlate well with the transition in the amount of energy absorbed by the notched specimen,

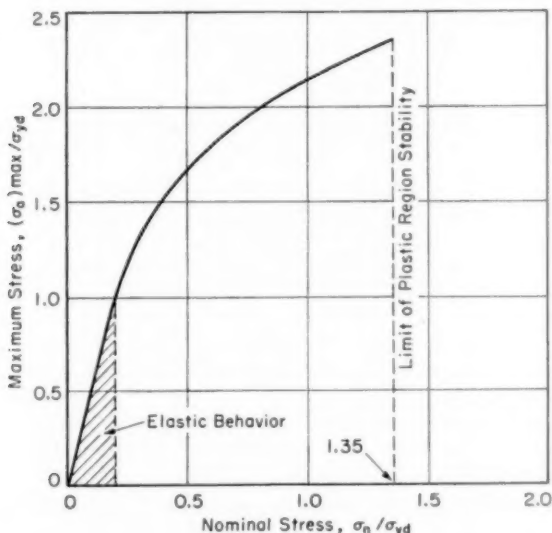


Fig. 3—Maximum Stress Ratio, $(\sigma_n)_{max}/\sigma_{yd}$ vs. Nominal Stress Ratio, σ_n/σ_{yd} , for a Plane Hyperbolic Notch with $a/\rho = 15$ under Tension.

since the total energy absorbed will increase markedly when the plastically deformed region extends to the specimen axis.

The results of the theoretical investigation provide a means for computing the maximum stress beneath the root of the notch at the instant of initiation of brittle fracture. These calculations can be made provided the values of the nominal fracture stress, σ_{nf} , and the yield stress, σ_{yd} , are determined experimentally.

MATERIAL TESTED AND TEST SPECIMENS

The material used in this investigation is the same 0.17% carbon steel employed in previous studies (2,3). Thus its delayed yield behavior under rapidly applied constant stress in the absence of notches

men at the minimum cross section and the radius of curvature of the root of the notch is $a/\rho = 15$, with $a = 0.150$ inch and $\rho = 0.010$ inch. The notches are cut in a cylindrical specimen of 0.600 inch diameter. Thus the stress analyses for an infinitely deep notch does not strictly apply. However, since the notch root radius is small compared with the notch depth, the errors introduced in this way are negligible. The specimen design is shown in Fig. 4. The notch was ground with a gen-

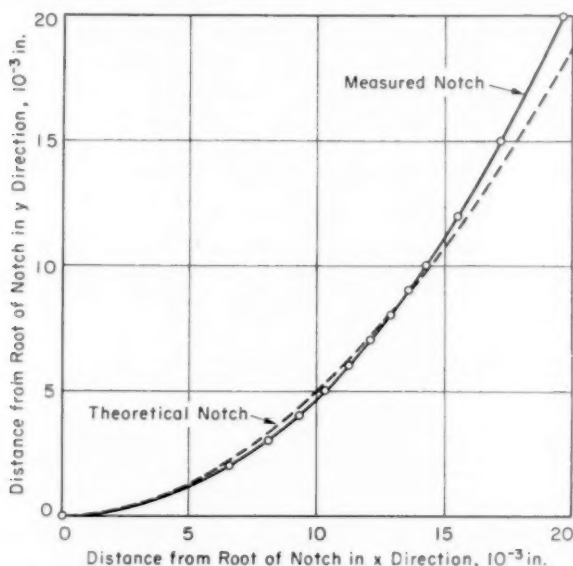


Fig. 5—Comparison of Shape of Actual Notch with Theoretical Hyperbolic Notch, $a/\rho = 15$.

erating type of operation. The principle involved in this grinding operation is based on the fact that a hyperboloid of revolution can be generated by straight lines.

The dimensions of the notches produced were determined by means of an optical comparator. The measurements show that the notches correspond quite well to the theoretical shape as indicated in Fig. 5. The radius of curvature at the root of the notch is reproducible to within 10% from specimen to specimen.

EQUIPMENT AND TEST PROCEDURE

Rapid Load Tests on Notched Specimens

The load was applied to the specimens at the desired constant rates, by means of a hydro-pneumatically operated rapid load tensile testing

machine described previously (2). This machine is capable of rates of load application up to about 10^6 pounds per second. The extension of the specimen is limited to a maximum of about 0.05 inch. Therefore specimens which exhibited a substantial degree of ductility were not fractured in the tests.

The applied load was determined as a function of time during each test by means of a dynamometer, described previously (13), employing type AB-14, SR-4 wire strain gages. The signal from the dynamometer was recorded on photographic paper by means of a recording oscillograph and associated amplifying equipment. The time resolution of the recording system is about one millisecond. The load acting on the specimen at any time could be determined to within an estimated overall error of about 4%. The rate of loading and the load at fracture (when fracture occurred), could be easily determined from the oscillograph records. Fracture was always very abrupt so that the load trace on the record exhibited a discontinuous change in direction at the fracture load.

The notched mild steel specimens were tested at temperatures of -23 , -110 and -200 °F (-30 , -79 and -129 °C). These specimen temperatures were obtained by means of a thermostatic bath of Freon 12 held in a suitable container surrounding the specimen and portions of the grips. The temperature of -23 °F (-30 °C) was obtained by allowing the Freon to boil. The use of dry ice in the bath provided the temperature of -110 °F (-79 °C). The temperature of -200 °F (-129 °C) was obtained by placing liquid nitrogen in a concentric container surrounding the inner container of Freon. A controlled electric heater in the Freon bath then permitted the desired temperature to be maintained.

The temperature of the notched specimens was determined by means of copper constantan thermocouples secured to the specimen by "Scotch" electrical tape. A thermocouple was secured to the specimen at each of two positions about $\frac{1}{4}$ inch on each side of the notch. Readings during tests indicated that the total temperature difference across the notch was less than ± 4 °F for the tests at a temperature of -200 °F (-129 °C), and negligible for the other two test temperatures. The temperature variation during a test and from test to test was about ± 3 °F at -200 °F (-129 °C) and negligible at temperatures of -110 and -23 °F (-79 and -30 °C).

Location of the Elastic-Plastic Boundary

The position of the elastic-plastic boundary was determined experimentally for several of the notched specimens that fractured at test temperatures of -110 and -200 °F (-79 and -129 °C). The fractured specimens were sectioned longitudinally along the axis of symmetry and mounted in lucite. The specimens were then alternately

Table I
Experimental Results and Computed Values of the Maximum
Tensile Stress, $(\sigma_n)_{\max}$

Specimen Number	Nominal Fracture Stress σ_{nf} lb/in. ²	Nominal Stress Rate $\dot{\sigma}_n$ lb/in. ² sec	$\frac{\sigma_{nf}}{\sigma_{yd}}$	Temperature (σ_n) °F	$\max.$ 10 ³ lb/in. ²
58	128.0 x 10 ³	1.03 x 10 ³	1.64	-200 (1)	—
54	135.5 x 10 ³	4.91 x 10 ²	1.62	-200 (1)	—
57	133.8 x 10 ³	9.97 x 10 ²	1.54	-200	206
6	122.1 x 10 ³	2.59 x 10 ³	1.34	-200	207
3	105.6 x 10 ³	3.27 x 10 ³	1.04	-200	213
9	102.2 x 10 ³	4.08 x 10 ³	1.00	-200	211
27	98.35 x 10 ³	3.41 x 10 ³	0.89	-200	219
1	89.32 x 10 ³	6.57 x 10 ³	0.79	-200	215
7	89.27 x 10 ³	1.41 x 10 ⁴	0.77	-200	218
37	94.70 x 10 ³	3.19 x 10 ³	0.80	-200	226
29	90.60 x 10 ³	5.50 x 10 ³	(2) —	-200	—
38	90.22 x 10 ³	7.35 x 10 ³	(2) —	-200	—
4	85.30 x 10 ³	8.84 x 10 ³	(2) —	-200	—
18	95.67 x 10 ³	1.57 x 10 ⁴	(2) —	-200	—
44	No fracture	7.74 x 10 ³	—	-110	—
33	No fracture	9.80 x 10 ³	—	-110	—
10	No fracture	1.22 x 10 ⁴	—	-110	—
52	No fracture	1.70 x 10 ⁴	—	-110	—
26	113.0 x 10 ³	2.88 x 10 ³	1.17	-110	210
17	106.0 x 10 ³	5.24 x 10 ³	(3) 1.07	-110	209
28	106.0 x 10 ³	6.46 x 10 ³	(3) 1.06	-110	210
D1	88.59 x 10 ³	1.45 x 10 ⁴	(3) 0.86	-110	202
36	92.20 x 10 ³	1.56 x 10 ⁴	(3) 0.90	-110	206
D11	83.23 x 10 ³	1.69 x 10 ⁴	(3) 0.81	-110	200
34	85.90 x 10 ³	2.20 x 10 ⁴	(3) 0.82	-110	203
22	No fracture	3.62 x 10 ³	—	-23	—
32	No fracture	4.35 x 10 ³	—	-23	—
13	No fracture	5.70 x 10 ³	—	-23	—
53	No fracture	1.49 x 10 ⁴	—	-23	—

(1) Not obtainable since $\sigma_n / \sigma_{yd} > 1.5$. (Not brittle fracture)

(2) Not obtainable since yield stress not established for these rates.

(3) Based on extrapolation of yield stress vs. stress rate curves to higher rates than experimentally established.

polished and etched to remove the cold-worked surface layer. A micro-hardness survey was then made in the vicinity of the root of the notch. The hardness determinations were made with a Tukon Hardness Tester using a 136-degree diamond penetrator and a 0.2 kilogram load. Hardness readings were taken at a sufficient number of points to establish the position of the elastic-plastic boundary. All hardness readings were taken in regions of ferrite grains since the pearlite is harder than the ferrite and any overlap of the penetrator between the two structures would give a misleading hardness indication.

EXPERIMENTAL RESULTS

Rapid Load Tests on Notched Specimens

The results of the tests on notched specimens are shown in Fig. 6 for temperatures of -110 and -200 °F (-79 and -129 °C). These results are also listed in Table I together with the results obtained at a temperature of -23 °F (-30 °C). Fig. 6 shows the relation between the nominal fracture stress (σ_{nf}) and the logarithm of the rate of nominal stress application (nominal stress rate). The trend of the test points is represented by straight lines for both test temperatures. The specimens tested at a temperature of -110 °F (-79 °C) fractured

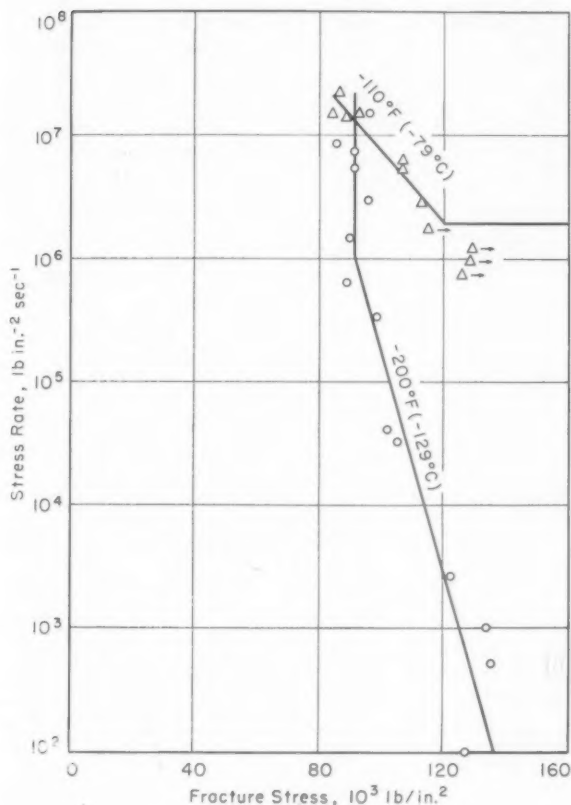


Fig. 6—Stress Rate versus Nominal Fracture Stress for Hyperbolic Notch $a/p = 15$ Annealed 0.17% Carbon Steel.

when the nominal stress rate at the minimum section was greater than about 2×10^6 psi per second. Nominal stress rates of less than about 2×10^6 psi per second did not produce fractures at a temperature of -110°F (-79°C) within the range of maximum obtainable nominal stress (140,000 psi) and maximum attainable specimen extension (0.05 inch). The results of tests at a temperature of -110°F (-79°C) in which fracture did not occur are shown with arrows in Fig. 6, indicating that fracture would eventually occur if there were no restrictions on specimen extension or applied load.

Fractures occurred in the notched specimens tested at a temperature of -200°F (-129°C) within the entire range of applied nominal stress rates (1.4×10^2 to 1.4×10^7 psi per second). Fractures did not

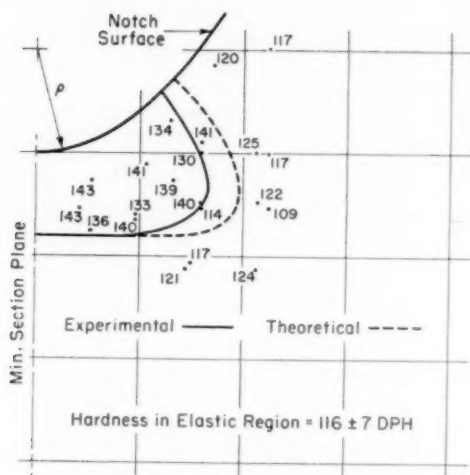


Fig. 7—Hardness Numbers (DPH) Below Notch of Fractured Specimen Showing Elastic-Plastic Boundary, For $\sigma_{ut}/\sigma_{yd} = 0.90$, Temp. -110°F (-79°C), Annealed 0.17% Carbon Steel.

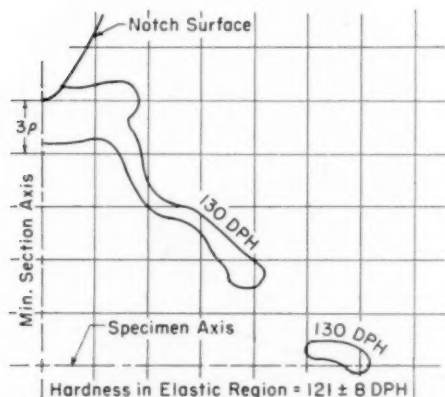


Fig. 8—Hardness Numbers (DPH) Below Notch of Fractured Specimen Showing Elastic-Plastic Boundary, For $\sigma_{ut}/\sigma_{yd} = 1.64$, Temp. -200°F (-129°C), Annealed 0.17% Carbon Steel.

occur in any of the four tests at a temperature of -23°F (-30°C) which included the range of stress rates from 5.7×10^6 to 1.49×10^7 psi per second.

Location of the Elastic-Plastic Boundary

Examples of the results of the surveys of micro-hardness on the

cross-sections of notched specimens that fractured are shown in Figs. 7 and 8 for the tests in which the values of σ_{nt}/σ_{yd} were 0.90 and 1.64 respectively. Surveys were also made on specimens for which the values of σ_{nt}/σ_{yd} were 0.79 and 1.25. The means of obtaining the ratio σ_{nt}/σ_{yd} will be explained later. The values of the hardness in the region of elastic behavior obtained in these surveys were determined by 10 measurements taken at positions remote from the notch root. The

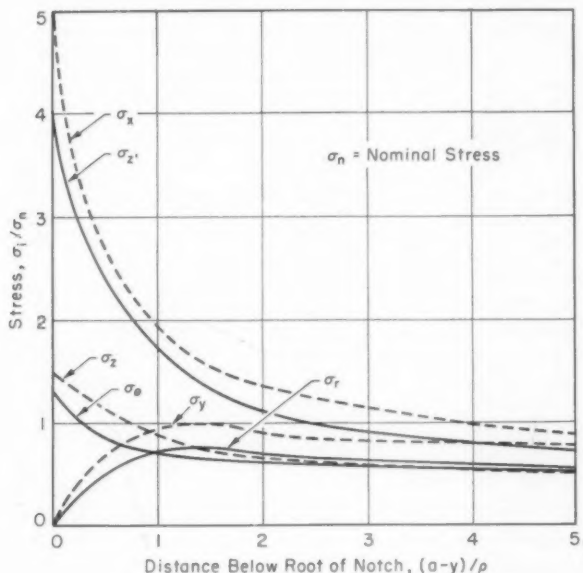


Fig. 9—Comparison of Elastic Stresses at the Minimum Cross Section of Axially Symmetric (σ_z , σ_r , σ_θ) and Plane (σ_x , σ_y , σ_z) Bars with Hyperbolic Notches ($a/\rho = 15$) in Tension.

elastic-plastic boundary, shown by the solid lines in Figs. 7 and 8, bounds the region within which the hardness is greater than the maximum hardness obtained in the elastic region. The dashed boundary shown in Fig. 7 is the elastic-plastic boundary as predicted by theory. The theory is not applicable to values of $\sigma_{nt}/\sigma_{yd} > 1.5$, hence there is no theoretical elastic-plastic boundary shown in Fig. 8. The experimental elastic-plastic boundary shown in Fig. 8, is based on the results of about 140 hardness readings.

DISCUSSION

The maximum stress within the notched test specimens at the instant of initiation of brittle fracture may be determined by application of the

elastic-plastic stress analysis to the experimental results. However, it is necessary to consider the fact that the stress analysis is made for plane strain deformation whereas the experiments were performed on axially symmetric specimens. An exact comparison between the stresses in axially symmetric and plane bodies of the shape considered in this report may be made in the case of purely elastic deformation. This is possible since Neuber (9) has obtained analytical solutions for both of these problems. This comparison is shown in Fig. 9. This shows that in the region extending a distance of about one root radius, ρ , below the root of the notch, the elastic stresses, σ_x , σ_r , and σ_θ in the axial, radial, and circumferential directions respectively, are smaller in the axially symmetric body than the corresponding stresses, σ_x , σ_y , and σ_z in the plane body under the same nominal stress, σ_n .

The region extending for a distance of about one root radius of curvature below the root of the notch is the region of primary interest for this investigation. This is true because the depth of penetration of the plastic deformation which occurs prior to the initiation of brittle fracture is limited to this region, as shown in Fig. 7. The elastic stresses in this region in the axially symmetric bar are nearly equal to those in the plane bar when the nominal stress in the axially symmetric bar is ten per cent greater than the nominal stress in the plane bar. This should also be the case when small plastic strains take place in the immediate vicinity of the notch root. Therefore in the application of the elastic-plastic stress analysis to the experimental results it will be assumed that the nominal stress acting on the test specimen for a given state of stress is ten per cent greater than the nominal stress which is required to produce the same state of stress in the plane bar. Thus the value of the nominal stress ratio, σ_n/σ_{yd} , which produces a given maximum axial stress ratio, $(\sigma_a)_{\max}/\sigma_{yd}$, in the test specimen is taken to be ten per cent greater than the value shown by the curve in Fig. 2. For example the critical nominal stress ratio which produces instability of the region of plastic deformation in the test specimens will be taken as $(\sigma_n/\sigma_{yd})_{\text{crit}} = 1.5$ rather than the value 1.35 shown in Fig. 2.

The application of the elastic-plastic stress analysis to the experimental results requires that the value of the yield stress, σ_{yd} , be known as a function of the rate of load application and temperature. The yield stress versus stress rate has been established for the steel employed in this investigation (15) and is presented in Fig. 10.

The relationship between the yield stress in unnotched specimens and the yield stress in notched specimens is now required. This relationship may be obtained as follows: the rate of increase of the axial stress at the root of the notch during the period of purely elastic deformation, σ_a , in the notched specimen is equal to the product of the nominal rate of stress application, $\dot{\sigma}_n$, and the axial stress concentration

factor, $k=4.03$. Thus yielding in the notched specimen will begin when the axial stress at the root of the notch is equal to the yield stress as determined from tests on unnotched specimens for the same temperature but for a rate of stress application in the unnotched specimen equal to k times the nominal stress rate, $\dot{\sigma}_n$, for the notched specimen. The yield stress actually varies as yielding spreads from the root of the notch toward the axis of the specimen since the rate of stress rise at the elastic-plastic boundary varies as the boundary moves inward. However, the assumption will be made that the yield stress remains

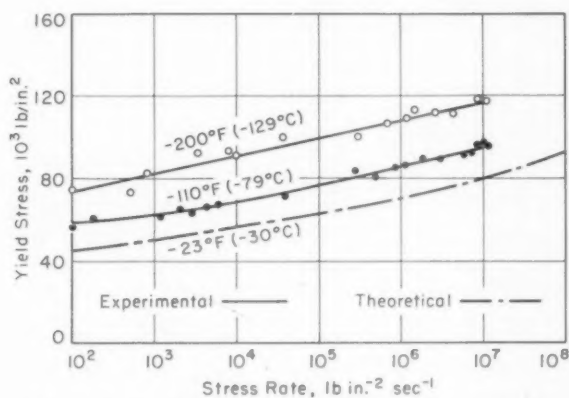


Fig. 10—Upper Yield Stress versus Stress Rate for Unnotched Specimens Annealed 0.17% Carbon Steel.

constant and equal to the initial value. The error introduced by this assumption is expected to be small in the case of brittle fracture since the plastic strain is confined to a small depth of penetration beneath the root of the notch. Thus the ratio of the measured nominal fracture stress to the yield stress, σ_{nt}/σ_{yd} , may be computed for each test on notched specimens in which brittle fracture occurred. These values are given in Table I. A knowledge of the value of σ_{nt}/σ_{yd} for a particular fracture test allows the results of that test to be compared with theoretical predictions.

The validity of the application of the elastic-plastic stress analysis to the experimental results may be checked by means of the hardness surveys. The position of the elastic-plastic boundary determined from micro-hardness measurements may be compared with the position calculated by the analysis for different values of $\sigma_{nt}/\sigma_{yd} < 1.5$. This comparison is shown in Fig. 7, and substantiates the validity of the assumptions and the accuracy of the relaxation calculations made in the elastic-plastic stress-analysis.

The elastic-plastic stress analysis shows that the axial tensile stress

is a maximum at the elastic-plastic boundary on the minimum section of the notched specimens. The value that the maximum axial stress attains at the instant of brittle fracture may be computed by applying the analysis to the experimental results obtained in this investigation. The method of determining this stress may best be illustrated by reference to Fig. 11, Figs. 11a and 11b are schematic representations of Figs. 6 and 10 respectively. Fig. 11c is a schematic representation of Fig. 3. The latter represents the theoretical relation between the maximum axial stress

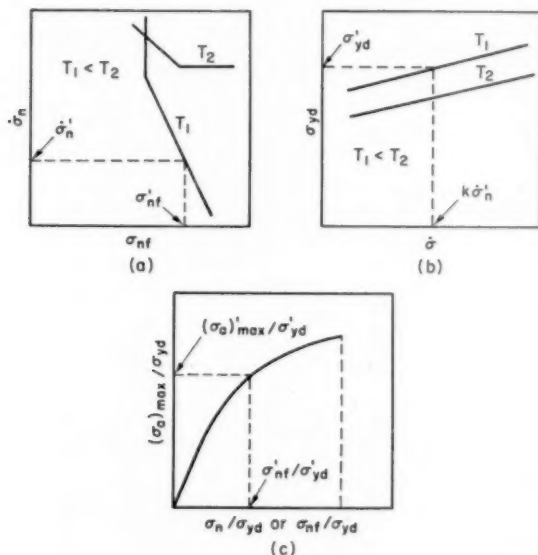


Fig. 11—Graphical Representation of Method of Determining the Maximum Axial Stress at the Instant of Brittle Fracture.

ratio, $(\sigma_a)_{max} / \sigma'_{yd}$, and the nominal stress ratio, σ_n / σ'_{yd} . The values of σ_n / σ'_{yd} in Fig. 11c are considered to be the values in Fig. 3 plus ten per cent, as discussed previously.

Fracture occurs at a nominal stress of σ'_{nf} when a nominal rate of stress rise $\dot{\sigma}_n$ is applied to the notched specimen at a temperature T_1 , as shown in Fig. 11a. The yield stress, σ'_{yd} , is obtained from Fig. 11b for a stress rate of $k\dot{\sigma}_n$ and the temperature T_1 . Now the ratio $\sigma'_{nf} / \sigma'_{yd}$ may be obtained and if this ratio is less than 1.5 the ratio of $(\sigma_a)_{max} / \sigma'_{yd}$ can be determined as indicated in Fig. 11c. Hence the value of the maximum axial stress beneath the notch at the instant of brittle fracture, $(\sigma_a)_{max}$ may be obtained.

Table I shows the value of $(\sigma_a)_{max}$ computed for each brittle frac-

ture observed at temperatures of -110°F (-79°C) and -200°F (-129°C) in all cases where the necessary information is available. The values of $(\sigma_n)_{\max}$ presented in Table I are constant within the probable experimental and theoretical errors, namely within the range from 200,000 to 226,000 psi with an average value of 210,000 psi. Thus the results of this investigation show that brittle fracture is initiated at a point in the material when the stress at that point attains a critical value (210,000 psi). The results also show that this critical stress is independent of temperature and rate of loading.

The evidence obtained thus far indicates that a necessary and sufficient condition for the occurrence of brittle fracture in the notched steel specimens of this investigation is that a critical value of the tensile stress of about 210,000 psi is reached before plastic deformation extends to the axis of the specimen.

The critical value of tensile stress is never reached in some tests on notched specimens before plastic deformation progresses to the axis of the specimen ($\sigma_n/\sigma_{yd} > 1.5$). The fracture which ultimately occurs in such tests is ductile rather than brittle. This is the case for those tests at -110°F (-79°C) in which the nominal stress rate was less than 2×10^6 psi per second and all the tests performed at -23°F (-30°C). Thus transition from brittle to ductile behavior, for the particular notch investigated, occurs when $\sigma_n/\sigma_{yd} = 1.5$ at the instant $(\sigma_n)_{\max} = 210,000$ psi. Fig. 3 shows that the transition from brittle to ductile behavior for the notch employed in this investigation occurs when $(\sigma_n)_{\max}/\sigma_{yd} = 2.34$ or for $\sigma_{yd} = 210,000/2.34 \approx 90,000$ psi. Hence these notched specimens behave in a ductile fashion when the yield stress is less than 90,000 psi. Fig. 10 shows that a yield stress of 90,000 psi occurs in unnotched specimens at temperatures of -110°F (-79°C) and -200°F (-129°C) when the rate of stress application is about 4×10^6 and 10^4 psi per second respectively. Hence the transition from ductile to brittle behavior in notched specimens should occur at nominal stress rates of about 10^6 and 2×10^3 psi per second ($\dot{\sigma}_n = k\dot{\sigma}_n$) for temperatures of -110 and -200°F (-79 and -129°C) respectively (rates greater than these correspond to brittle behavior). Fig. 6 shows that a discontinuous change occurs in the relationship between the nominal fracture stress and the nominal stress rate at a rate of 10^6 psi per second for the tests at -110°F (-79°C). This is in agreement with the prediction. However the results obtained at -200°F (-129°C) do not exhibit a discontinuity at a nominal stress rate of 2×10^3 psi per second. Nevertheless the hardness surveys of specimens tested at -200°F (-129°C) at nominal stress rates less than 2×10^3 psi per second show that these specimens exhibit greater ductility than those tested at rates greater than 2×10^3 psi per second.

An example is given by the results of the hardness survey of the specimen tested at a rate of 1.03×10^2 psi per second shown in Fig. 8.

This shows that plastic deformation has progressed very nearly to the axis of the specimen as expected.

Fig. 6 indicates that at a temperature of -200°F (-129°C) there may be a change in the fracture behavior for nominal stress rates greater than about 10^6 psi per second. The fractures occurring in this range are of the brittle type since $\sigma_{nt}/\sigma_{yd} < 1.5$. However, Fig. 6 indicates that at a temperature of -200°F (-129°C) the nominal fracture stress is constant for nominal stress rates exceeding 10^6 psi per second. This behavior is probably attributable to an independence of the yield stress upon stress rate in this range. This range in notched specimens corresponds to stress rates greater than 4×10^6 psi per second in unnotched specimens.

Fig. 10 indicates that if the yield stress is constant for rates of stress application greater than about 10^7 psi per second at a temperature of -200°F (-129°C) the maximum value of the yield stress would be about 120,000 psi. A stress of 120,000 psi corresponds approximately to the upper limiting stress in the stress vs. log delay time relationship for this material at a temperature of -320°F (-196°C) (3). An upper limiting stress was not observed in the stress vs. log delay time relationship at a temperature of -200°F (-129°C) at the shortest delay time investigated, namely 10^{-2} second. However, it is not unreasonable to expect that such an upper limiting stress exists at delay time shorter than 10^{-2} second. Therefore the constancy of nominal fracture stress with respect to nominal stress rate for rates exceeding 10^6 psi per second at a temperature of -200°F (-129°C) may be attributable to this upper limiting yield stress.

Brittle fractures were not observed in the tests at a temperature of -23°F (-30°C), within the range of stress rates investigated. This behavior is consistent with the criterion for the occurrence of brittle fracture deduced from the results obtained at lower temperatures. This consistency may be shown by considering the conditions existing at the maximum nominal stress rate, 10^7 psi per second, for tests on notched specimens. Lower stress rates are less conducive to brittle fracture. This nominal stress rate in a notched specimen corresponds to a stress rate of 4×10^7 psi per second in unnotched specimens ($\dot{\sigma}_n = k\sigma_n^m$). A theoretically derived relation (15) between upper yield stress and stress rate for a temperature of -23°F (-30°C) is shown in Fig. 10. The yield stress corresponding to a stress rate of 4×10^7 psi per second is about 85,000 psi. Ductile behavior of the material is expected since this yield stress is less than 90,000 psi (σ^*_{yd}).

SUMMARY AND CONCLUSIONS

The true distribution of stress on the minimum cross section of a notched specimen subjected to tensile loading has been determined by means of an elastic-plastic stress analysis. This analysis takes into

account plastic deformation which is limited to the immediate vicinity of the root of the notch. The analysis provides a theoretical prediction of the position of the boundary between the regions of plastic and elastic deformation.

An experimental investigation has been conducted on notched specimens subjected to tensile loading at different temperatures and rates of loading. The position of the elastic-plastic boundary determined experimentally is found to be in agreement with the position predicted by the stress analysis.

The nominal stress at the instant of fracture in notched specimens as a function of nominal stress rate has been determined experimentally at two temperatures -110 and -200°F (-79 and -129°C). The true tensile stress at the position and at the instant of initiation of brittle fracture has been determined from the experimental results by the application of the stress analysis. The results show that brittle fracture is initiated in the material employed in this investigation when a critical tensile stress of about 210,000 psi is attained. This value is found to be independent of stress rate and temperature.

Brittle fracture in notched specimens depends on the notch acuity, the stress rate, and the temperature. This investigation shows that the influence of temperature and stress rate on the initiation of brittle fracture is associated entirely with the dependence of the yield stress on temperature and stress rate.

The results of this investigation indicate that it should be possible to predict the conditions under which brittle fracture will occur in specimens of mild steel having any notch geometry. This is possible provided the influence of stress rate and temperature on the yield stress and the true fracture stress for the material under consideration are known.

ACKNOWLEDGMENTS

This investigation was conducted under the sponsorship of the Office of Ordnance Research, United States Army. Appreciation is expressed to this agency for support of this work.

Appreciation is extended to Professor T. Vreeland, Jr., and Professor G. W. Housner for their many valuable comments and suggestions made throughout the course of the research. Acknowledgement is also made to Mr. Wilfred Iwan for his assistance in certain phases of the experimental work.

References

1. M. E. Shank, "Brittle Failure of Steel Structures," *METAL PROGRESS*, American Society for Metals, Vol. 66, September 1954, p. 83; Vol. 66, October 1954, p. 120; Vol. 67, June 1955, p. 111.
2. D. S. Wood and D. S. Clark, "The Influence of Temperature Upon the Time Delay for Yielding in Annealed Mild Steel," *TRANSACTIONS, American Society for Metals*, Vol. 43, 1951, p. 571.

3. D. S. Wood and D. S. Clark, "Delayed Yielding in Annealed Mild Steel with Special Reference to Yielding at Low Temperature," Fourth Technical Report submitted to Office of Naval Research, Contract N6onr-24418, December 1951.
4. J. A. Hendrickson, D. S. Wood and D. S. Clark, "The Initiation of Discontinuous Yielding in Ductile Molybdenum," *TRANSACTIONS, American Society for Metals*, Vol. 48, 1956, p. 540.
5. I. R. Kramer and R. Maddin, "Delay Time for the Initiation of Slip in Metal Single Crystals," *Journal of Metals*, Vol. 4, 1952, p. 197.
6. Tien-Shih Liu, I. R. Kramer and M. A. Steinberg, "The Delay-Time Phenomenon in Metal Single Crystals," *Acta Metallurgica*, Vol. 4, No. 4, July 1956, p. 364.
7. D. K. Felbeck and E. Orowan, "Experiments on Brittle Fracture of Steel Plates," *Welding Journal Research Supplement*, Vol. 34, No. 11, November 1955, p. 570-s.
8. C. Crussard, et al., "A Study of Impact Test and the Mechanics of Brittle Fracture," *Journal, Iron and Steel Institute*, Vol. 183, Part 2, June 1956, p. 146.
9. H. Neuber, *Theory of Notch Stresses: Principles for Exact Stress Calculations*, David Taylor Model Basin Translation No. 74, 1937, Julius Springer, Berlin.
10. R. V. Southwell, "Relaxation Methods in Theoretical Physics," 1946, Oxford at the Clarendon Press, England.
11. D. N. de G. Allen and Sir Richard Southwell, "Relaxation Methods Applied to Engineering Problems' XIV. Plastic Straining in Two Dimensional Stress-Systems," Royal Society, London, *Philosophical Transactions*, Vol. 242, Series A, 1949, p. 379.
12. R. Hill, "The Mathematical Theory of Plasticity," 1950, p. 245, Oxford University Press, London.
13. T. Vreeland, Jr., D. S. Wood, and D. S. Clark, "A Study of the Mechanism of the Delayed Yield Phenomenon," *TRANSACTIONS, American Society for Metals*, Vol. 45, 1953, p. 620.
14. J. A. Hendrickson, D. S. Wood and D. S. Clark, "The Influence of Temperature on Pre-Yield Plastic and Anelastic Microstrain in Low-Carbon Steel," *Acta Metallurgica*, Vol. 4, November 1956, p. 593.
15. J. A. Hendrickson and D. S. Wood, "The Effect of Rate of Stress Application and Temperature on the Upper Yield Stress of Annealed Mild Steel," *TRANSACTIONS, American Society for Metals*, This Volume, 1958.

DISCUSSION

Written Discussion: By J. R. Low, Jr., General Electric Company, Research Laboratory, Schenectady, New York.

The authors' finding that a substantially constant fracture stress is observed for two different temperatures and a wide variation in rates of loading is very interesting, particularly since the yield strength of their material is markedly affected by these two variables. Their analysis suggests that the fracture should be nucleated below the surface of the notch in their specimens and at a specific zone in the cross section. I would like to ask if they have any evidence, either from the examination of fracture surfaces or from their metallographic work, that their fractures did in fact start below the surface of the notch.

The fracture stress value of approximately 210,000 psi is presumably characteristic of the particular structure existing in their specimens. Do the authors have any information on the effect of varying the dimensions of the microstructure, e.g., ferrite grain size or pearlite spacing, on the value of the fracture stress determined in this manner?

Finally, did the authors examine their specimens for decarburization after the heat treatment described? Since the finish-machined specimens were heat treated in hydrogen the critical region at the notch root may have been affected.

Written Discussion: By C. Crussard, J. B. Lean, J. Plateau, and Y. Morillon, Institut de Recherches de la Siderurgie, 185 Rue President-Roosevelt, St-Germain-En-Laye, France.

The authors are to be congratulated on the considerable experimental ingenuity displayed in their investigation; the development of a generating method of grinding hyperbolic notches should greatly facilitate the practical application of Neuber's stress-analysis in researches of this nature.

We note the similarity between the results obtained in the authors' theoretical "elastic-plastic" analysis and in our practical investigations (Ref. 8 of the text), the value of 1.31 in Ref. 8 and 1.35 in the authors' paper for the ratio σ_n/σ_y d when complete plastification of the notched section takes place, are in good agreement considering the different notch geometrics and steels employed in the two cases.

We would like to re-direct the authors' attention to the use of Fry's reagent for the experimental mapping of the elastic plastic boundary surface. We have used microhardness tests in conjunction with Fry's reagent with very good accord between the two results for slowly deformed notches. However, we consider the use of microhardness tests insufficiently sensitive in the case of dynamic loading; comparison of Fig. 33 with Fig. 39 of Ref. 8, and of Figs. 14 and 15 of Green and Hundy's paper (*Journal of the Mechanics and Physics of Solids*, Vol. 4, 1956, p. 128 to 144), shows that the authors' microhardness tests must have been carried out in areas where the deformation bands have been fragmented into discrete lines following directions of maximum shear stress, this combined with the presence of pearlite would render the mapping of the boundary between the plastic and the elastic zone somewhat difficult.

While we are in complete accord with the authors' thesis that there is some critical strength for brittle fracture, we cannot agree that the experimental figures reported in Table I support their statement that this critical strength is independent of temperature. Recent tests carried out at IRSID, as yet unpublished, have established (for a range of three low temperatures, three speeds in the brittle range, in tension tests of unnotched specimens, breaking a mean of five test pieces at each temperature) an average variation of σ_c with temperature of the order of $0.10 \text{ Kg/mm}^2/^\circ\text{C}$. A. S. Eldin and S. C. Collins (*Journal of Applied Physics*, Vol. 22, 1951, p. 1296) over a wide range of low temperatures give figures from which a variation of approximately $0.17 \text{ Kg/mm}^2/^\circ\text{C}$ may be deduced.

Accepting the fact that the authors' experimental variation is almost as great as that due to the effect sought, we find, however, that a simple statistical analysis, adjusted for small samples, of the 15 figures for (σ_a) max given in the paper reveals that the difference between the means of the -200°F and -110°F tests is significant at between the 5% and 1% levels for 13 degrees of freedom. The calculated variation of (σ_a) max with temperature is then $0.11 \text{ Kg/mm}^2/^\circ\text{C}$ and therefore, although the authors' prudence in not drawing conclusions from these figures is justified considering the possible systematic errors involved in their theoretical approach to the measurement of (σ_a) max, their results are in excellent agreement with other estimates of the effect of temperature on the critical strength.

Finally we would like to ask the authors whether complete plastification of the

cross section is, in their experience, a *sufficient* as well as a *necessary* condition for ductile fracture? Have they been able to establish from the broken surfaces a change in the appearance of the fracture, or a change in the position of the initiation of fracture accompanying this plastification. We are investigating this problem in tensile tests and would be most interested in the authors opinion.

Written Discussion: By Dr. C. J. Tipper, Cambridge University Engineering Department, Cambridge, England.

The outstanding conclusion of this investigation is that a critical tensile stress must be reached before a brittle fracture is initiated and that the value is independent of stress rate and temperature. It is not quite clear from the definition of "ductile" and "brittle" given in the paper, that "brittle" is synonymous with cleavage, but it may be inferred that it is so. Hence, it must also be inferred that there is a true brittle fracture strength for a given material, a contention that was put forward first by Ludwik and by numbers of subsequent investigators. Before the conclusions in this paper can be accepted fully, another material should be submitted to a similar investigation, or the same material tested with a different test-piece geometry.

The writer considers that further useful information could have been derived from a study of the microstructure of the broken test pieces. For example, the break in the curve in Fig. 6 showing the relation between stress rate and fracture stress at -200°F (-129°C) might be due to a change in the mechanism of yielding. Moreover, the connection between the yielded zone and the path of fracture has not been stated. It is to be hoped that the authors will supplement their valuable results by giving this information.

Written Discussion: By Marian Szczepanski, Director of Research, Abrasive Dressing Tool Company, Detroit.

Opinion on the subject whether resistance to initiation or resistance to propagation is more important, is divided. Obviously fracture cannot be propagated if it is not initiated. This probably is the reason why some authors suggest that resistance to the initiation of a fracture is of greater practical importance than the resistance to its propagation.

In view of this it is interesting to examine if fracture can be prevented from starting.

Notches of one sort or another are always liable to be present, although good design and workmanship can minimize their effect and severity. Cracks due to fatigue, stress corrosion or welding are practically impossible to avoid. It must then be accepted that even with the best of material, workmanship and design, it is impossible to eliminate completely small cracks or notches which can be regarded as incipient fracture of varying degrees of sharpness.

If then it is impossible to avoid initiation of fracture, the resistance to its propagation becomes of prime importance.

Some investigators express the view that once the fracture begins it progresses in a brittle manner. This is not always true. It was shown experimentally, that some artificially initiated fractures progressed under the influence of tensile stress in a ductile manner, provided the temperature of the steel was above the transition temperature of the material as found by notch tensile or impact test.

To give a more definite answer to the question discussed, it would be advantageous;

- (a) to separate and measure energy of initiation and propagation.
- (b) to find out the influence of temperature on the initiation and propagation respectively.

The two energies cannot be separated by normal (without special equipment) impact test. This can be done, however, by notch bend testing.

It would be interesting to find out how temperature affects each energy respectively. This could be a good clue to decide which energy determines whether fracture is brittle or not.

If, for example, it was found that resistance to initiation does not depend to a large extent on temperature, it could not be accepted as a criterion, because it is known that service behavior of the material is a function of temperature.

Sharpness of the notch and the speed of loading are other factors which probably influence each energy in a different manner.

Jaffe, Reed and Mann proved that brittle transgranular fracture of polycrystalline metals does not originate at a point and propagate continuously across the material, but rather develops at numerous related points, leading to a series of microcracks which subsequently link up.

In the regions close to a brittle transgranular fracture a number of discontinuous microcracks have been observed. This observation has been made in fatigue specimens, impact specimens and failed parts made from steel forgings and castings.

The presence of the series of microcracks can be explained in the light of the theory of discontinuous crack propagation. This theory suggests that a crack propagates along a crystallographic plane, in a brittle fashion, until it is stopped by a grain boundary or by a particle of a second phase. New cracks are likely to start in the zone of stress concentration at the end of the arrested crack. The process then repeats itself, leading to discontinuous branching chains of microcracks. The cracks may also stop because the elastic energy released by their further spread would not be sufficient to propagate the cracks (to form the new surfaces). In this last case, new cracks would have to be at orientations which would provide greater energy release.

Gilbert, using nodular cast iron has shown that the unnotched Charpy impact test gives the energy required for the initiation of fracture, whereas V-notched Charpy test measures primarily the energy required for the propagation of fracture. It seems, therefore, that the transition in unnotched Charpy specimens represents a transition in energy required for crack initiation whereas in V-notched Charpy specimen it corresponds to transition in crack propagation energy.

Both transitions occur in either test piece but each of them is particularly suitable for detection of one transition only from the impact properties point of view. Both transitions can be detected with the use of a keyhole notch.

Other criteria can also be used to distinguish initiation and propagation energies. In ordinary tensile testing for example, the elongation corresponding to the maximum force acting on the specimen is an approximate measure of the energy required for crack initiation and the elongation which occurs during "necking" indicates the amount of energy required for crack propagation.

Authors' Reply

The authors wish to thank those who have discussed this paper for their interesting and stimulating comments. Dr. Crussard and his associates, Dr. Low and Dr. Tipper have all asked whether microscopic observations of the fracture surfaces were made in connection with this investigation. This was not done. However, cross sections through the fracture surface containing the specimen axis were polished and etched in connection with the microhardness surveys. These showed that the ferrite and fine pearlite structure, normal for an annealed low-carbon steel, existed in all regions including the region at the root of the

notch. Thus no decarburization of the critical region at the root of the notch was evident, which was of concern to Dr. Low. The dew point of the hydrogen employed in the annealing treatment was reduced to -196°C or lower and the time at the annealing temperature was relatively short compared with the time usually employed in wet hydrogen decarburizing treatments. Hence no detectable decarburization was expected.

Microscopic examination of the cross sections containing the fracture surface also showed that a few twins (Neumann bands) had been produced adjacent to the fracture surface. Previous investigators have indicated that this is commonly observed in brittle fractures.

Attempts were made to delineate the plastically deformed regions by means of Fry's reagent, as suggested by Dr. Crussard. However, this was not found to be effective for the particular steel investigated. Probably this is characteristic of a killed steel such as that employed in the present investigation, as opposed to a rimmed steel. The authors agree that the microhardness method for determining the position of the elastic-plastic boundary leaves something to be desired in the matter of accuracy.

No direct evidence for the position of the initiation of fracture was obtained, as asked by Dr. Low. However, the micro-fractographs obtained by Dr. Crussard and his collaborators using electron microscopy (8) show that brittle fracture in notched specimens is initiated at or near the boundary of the plastic zone, as suggested by the stress analysis given in the present paper.

Dr. Tipper has inquired about the relationship between the path of fracture and the yielded zone. The fracture surface remained quite close to the minimum cross section of the specimen in both the yielded and unyielded zones. Thus the fracture passed essentially through the middle of the yielded region. A very small shear lip was observed at the root of the notch in a few specimens. However, this deviation of the fracture surface from the plane of the minimum cross section was small compared with the size of the yielded region.

Dr. Tipper and Dr. Crussard have both inquired regarding the definitions of the terms "brittle" and "ductile" as applied to the fractures reported in the paper. The definitions adopted for the present paper are based upon the relative amounts of energy absorbed prior to fracture rather than upon the appearance of the fracture surface. Thus, if the region of plastic deformation extends completely across the specimen, the fracture is considered to be ductile since a relatively large volume of material has been plastically deformed and hence a relatively large amount of energy absorbed. Conversely, fractures which occur while plastic deformation is confined to a localized region at the root of the notch are defined in the paper as "brittle".

Dr. Crussard and his associates have pointed out that the results given in the paper may be interpreted in such a manner as to indicate that the brittle fracture stress, $(\sigma\alpha)_{\text{max}}$, depends slightly upon temperature. Namely that this stress may increase by about 5% when the temperature is decreased from -110°F to -200°F . This interpretation depends upon a statistical analysis of the experimental results. The assumption is made that the sum of all systematic errors which may exist in the experimental measurements and stress analysis calculations are substantially less than 5%. The authors are not satisfied that the experimental results and the associated calculations are free from systematic errors to this degree of accuracy. Thus the results presented in the paper are inadequate to either prove or disprove this suggestion of Dr. Crussard, et al.

The authors agree with Dr. Low and Dr. Tipper that further experimental work on different materials, using the techniques presented in the paper, is needed. The fracture stress value of 210,000 psi is expected to be a function of the metallurgical variables, such as grain size, as Dr. Low has suggested, although their effects have not been determined.

Some additional experiments, using a different specimen geometry, as suggested by Dr. Tipper, have recently been completed and will be reported in the near future. This work employed the standard Izod impact specimen and method of testing. The results substantiate those given in the present paper within experimental and computational accuracies. Further improvement of these accuracies are needed and remain to be accomplished.

The problem of the propagation of a brittle fracture, which Mrs. Szczepanski has discussed, is not mentioned in the paper. However, this omission is not intended to imply that the problem of fracture propagation is less important than the problem of fracture initiation. Further understanding of both of these aspects of brittle fracture is needed.

Mrs. Szczepanski also points out the fact that both the initiation and propagation of a brittle fracture proceed by the generation and subsequent joining of individual microcracks, rather than by initiation at one submicroscopic point and continuous growth of a single crack from that point. The point of view adopted in the paper and the results obtained are not inconsistent with this microscopic mechanism of brittle fracture. The paper is limited to a consideration of the macroscopic parameters which influence the initiation of brittle fracture. For example, the brittle fracture stress discussed in the paper cannot be considered to be the true stress acting on areas within the specimen corresponding to a single grain or less. This fracture stress is an average value pertaining to regions no smaller than that occupied by several grains. Nevertheless it is a stress which may be considered to be localized with respect to the macroscopic dimensions of the specimen. Thus the local fracture stress defined in the paper has more physical significance than the nominal fracture stress given by the ratio of the load at fracture to the area of the minimum cross section of the specimen.

A STUDY OF THE ROLE OF CARBON IN TEMPER EMBRITTLEMENT

By E. B. MIKUS AND C. A. SIEBERT

Abstract

Electron microscopy and autoradiography using carbon-14 were used to study the distribution of carbon in tough and temper-embrittled structures of a SAE 3140 steel. Isothermal heat treatments up to 500 hours were investigated. In light of these studies a number of theories on the mechanism of temper-embrittlement were evaluated and a new mechanism was proposed based on the development of strained prior austenite boundaries during the embrittling heat treatment. (ASM International Classification Q26S, 2-14; AY)

INTRODUCTION

THE TERM temper embrittlement has been used to describe the adverse effect on the impact properties of a tempered low alloy steel when the material has been either slowly cooled through a temperature region of 1250–700 °F or isothermally held in this temperature range for an extended period of time. This phenomenon leads to a brittle fracture which occurs along prior austenite grain boundaries. In most of the recent work in this field the degree of embrittlement was determined by using the shift in transition temperature as a criterion.

In spite of a large number of investigations and the accumulation of experimental data, there has evolved no consistent mechanism for explaining temper embrittlement. In many of these suggested mechanisms carbon atoms or carbide particles were considered to be a dominant factor in promoting temper embrittlement. The object of this investigation was to study the influence of carbon on the temper embrittlement of a susceptible steel. For this purpose a severely temper embrittled condition was used to compare with the tough condition. The role of carbon in this phenomenon was studied from the point of view of how these atoms were distributed in the two conditions of heat treatment.

This paper is based on part of a thesis by E. B. Mikus, submitted in partial fulfillment of the requirements for the degree of Doctor of Philosophy to the Department of Chemical and Metallurgical Engineering, University of Michigan, Ann Arbor, Michigan.

A paper presented before the Thirty-Ninth Annual Convention of the Society, held in Chicago, November 4–8, 1957. Of the authors, E. B. Mikus is Research Engineer, General Motors Corporation, Research Staff, Detroit, Michigan, and C. A. Siebert is Professor of Metallurgical Engineering, University of Michigan, Ann Arbor, Michigan. Manuscript received April 16, 1957.

Electron microscopy was used to study the size, shape, and distribution of the carbide particles as well as a stripping film autoradiographic technique using carbon —14.

Influence of Alloying Elements

In considering the substitutional alloying elements it seems that these can be classified into two categories: those that retard or play passive roles and those that actively contribute to the development of temper embrittlement. In the former group are found nickel, molybdenum, tungsten, and columbium. In the latter group, the common elements that are associated with low alloy steels and temper embrittlement, are found manganese, chromium, phosphorus, and vanadium. In general, there is fair agreement among investigators on the effects of substitutional elements on temper embrittlement. This has not been the case for carbon.

Opinions as to the role of carbon have varied from a positive to a completely negative contribution. Jaffe and Buffum (1)¹ and Libsch, Powers, and Bhat (2) have suggested that plain carbon steels are very susceptible to temper embrittlement, so much so, that they become embrittled during the quench from the tempering temperature. However, Woodfine (3) has pointed out that factors other than the presence of carbon were present which accounted for the observed changes in impact strength. Woodfine states that plain carbon steels with manganese contents less than 0.5% are not susceptible to temper embrittlement.

Jolivet and Vidal (4) have shown that when the carbon content of a chromium steel was reduced from 0.22 to 0.073%, the temper embrittlement was reduced but not removed. Jaffe (5) has reported that a vacuum-melted nickel-chromium steel with 0.016% carbon was susceptible to temper embrittlement. Buffum, Jaffe, and Clancy (6) claimed to have found no temper embrittlement in an alloy containing 1.5% nickel, 0.6% chromium, and 0.003% carbon. Preece and Carter (7) also found no embrittlement in a series of synthetic chromium, phosphorus, iron, and manganese, phosphorus, iron alloys where the carbon was at a level of 0.003%. On the other hand Hultgren and Chang (8) reported that a series of synthetic SAE 3300 steels prepared by melting under helium and free from carbon were susceptible to temper embrittlement as measured by the transition temperature criterion on specimens slowly cooled through the susceptible temperature region.

Theories of Temper Embrittlement

A number of theories have been advanced in attempts to explain the temper embrittling mechanism. However, many of these theories have

¹ The figures appearing in parentheses pertain to the references appended to this paper.

been shown to be in error in light of recent work. In this discussion the theories which seem to be most promising will be considered.

In general these attempts to explain temper embrittlement can be cataloged into three groups: 1) those that consider a precipitate of carbide, nitride, or phosphide (3,9) occurring at the prior austenite grain boundaries during the embrittling treatment; 2) those that consider a diffusion of some alloying element or elements to the prior austenite grain boundaries on a submicroscopic scale during exposure to the embrittling temperature (3,10,11); and 3) those that consider a carbide modification and dispersion reaction as being responsible (12,13).

The difficulty with the precipitation theories is that as yet, no precipitate has been detected in temper-embrittled steels which can be established as being responsible for the phenomenon. Micrographs showing the effects of special etches on temper-embrittled material do not reveal a boundary phase, but merely a grain boundary attack.

This discrepancy between observation and theory has been circumvented in the theories suggesting a diffusion of elements to the prior austenite grain boundaries on a submicroscopic scale. Both interstitial as well as substitutional alloying elements have been suggested as being responsible.

In the third group a carbide modification or carbide dispersion in the matrix has been suggested, but how this modification can account for several important experimental observations on the characteristics of a temper-embrittled material has not been elucidated. As an example, how does a carbide modification account for 1) brittle failure occurring at prior austenite grain boundaries, 2) delineation of the prior austenite grain boundaries by special etchants, 3) the reversibility of the temper embrittling phenomenon with temperature as well as time, and 4) the apparent absence of temper embrittlement in plain carbon steels?

EXPERIMENTAL PROCEDURES

A commercial heat of SAE 3140 steel was used in this investigation. The steel had a No. 8 grain size with the following composition:

C	Mn	Si	P	S	Cr	Ni	Mo
0.39	0.78	0.28	0.010	0.019	0.61	1.26	0.04

Samples used for electron microscope examination were obtained from fractured impact bars representing tough and severely temper-embrittled conditions. The tough condition was obtained by tempering, after hardening, for 1 hour at 1250 °F in a salt bath. To obtain the severely temper-embrittled condition some of the tempered tough specimens were given an additional treatment consisting of 500 hours at 850 °F in a vertical muffle furnace. The shift in the impact transition

temperature produced by this embrittling treatment using a criterion of 50 ft-lbs fracture energy amounted to 181 °F, from -162 °F for the tough condition to 19 °F for the temper-embrittled condition. These samples were electrolytically polished in 20% perchloric acid-alcohol solution and etched with an ethereal picric acid solution for 10 seconds. After etching, collodion replicas were prepared. Polystyrene-latex particles of a known size were placed on the replicas prior to shadowing with palladium to facilitate an easier interpretation of the electron micrographs.

Specimens used for autoradiography studies were prepared in the following manner: the carbon in the original SAE 3140 steel was removed by decarburizing in moist hydrogen; then, recarburized with specific amounts of radioactive carbon -14. This was carried out in a copper-plated capsule which contained charcoal and BaCO_3 . A portion of the carbon in the BaCO_3 consisted of C-14 which produced an activity of 0.0282 millicuries per milligram of BaCO_3 . The sealed capsule was then heated for 72 hours at 1700 °F for the carburizing treatment. All samples were examined microscopically to determine the extent and homogeneity of carburization. Table I lists the various charges used in this investigation and the estimated carbon transfer into the metal as a result of carburization.

After carburization the samples were sealed in vycor tubing under a vacuum, heated to 2000 °F for 1 hour, and quenched into oil to produce martensite. All of the samples were sealed again in an evacuated vycor tube and tempered 1 hour at 1250 °F in salt to produce a tough condition in the steel. The embrittled condition was produced in a number of samples utilizing additional tempering cycles of 100 and 500 hours at 850 °F. All samples were water-quenched after all tempering operations.

After heat treatment the radioactive specimens were mechanically polished and etched with ethereal picric acid solution. Autoradiographs were then made using exposures ranging from 1 to 12 days. These were examined at magnifications up to $\times 1000$. The specific activity of each sample was not determined but various levels of specific activity were studied on the basis of the amount of active BaCO_3 charged into the carburizing capsule as indicated in Table I.

The stripping film used in this investigation was obtained from Eastman Kodak, known as Experimental Permeable Base Autoradiographic Stripping Film. The film consisted of a beta-ray sensitive emulsion layer of about 5 microns thick supported by a pure gelatin layer of equal thickness. These layers were further supported on a cellulose acetate base. The film was applied to the specimen after the gelatin emulsion base was stripped from the cellulose acetate backing with the emulsion side towards the specimen.

Table I
Charge Distribution for Carbon-14 Carburizing Runs

Carbon-14 Carburizing Run No.	Active* BaCO ₃ , Milligrams	Inactive BaCO ₃ , Milligrams	Charcoal Milligrams	Weight of Metal, Milligrams	Estimated Carbon Content After Carburizing, %
1	10.0	220.0	15.0	1405.8	0.4
2	4.8	224.5	15.0	1450.3	0.4
3	11.1	220.3	15.0	1410.2	0.4
4	10.2	220.6	15.4	1390.7	0.4
5	20.1	210.0	15.0	1435.1	0.4
6	3.1	113.2	7.1	1769.8	0.4
7	2.9	13.1	1.0	2024.2	0.1
8	4.7	31.2	2.2	2155.6	0.2
9	5.1	47.6	3.2	1589.1	0.3

*Specific Activity of BaCO₃—0.0282 millicuries per milligram of BaCO₃.

The procedure for preparing a specimen for autoradiographic examination has been adequately described by Yukawa (14). However, in the actual examination of the emulsion and microstructure after development of the film, a somewhat modified procedure was adopted. In examining the microstructure of an autoradiographic sample one actually looks through the developed photographic emulsion which is in intimate contact with the specimen. Since the microstructure of tempered martensite appeared as a distribution of carbide particles, which appear as black spots in a white ferrite matrix, difficulty was encountered in distinguishing these carbide particles from the black, developed silver grains of the photographic emulsion. By focusing on the metal structure and then focusing on the emulsion this difficulty was circumvented but required two photomicrographs of the same area. By this means the distribution of the active carbon atoms in the material could be traced without confusing these activity centers with normal carbon carbides. At a magnification of $\times 1000$ this method could be applied successfully because of the small depth of field characteristic of the lens.

Autoradiographic studies were performed on samples in the tough condition and the 100-hour and 500-hour temper-embrittled conditions. Various etching times, exposure times, and specific activity levels were used in an attempt to maximize the conditions for observing any segregation of the carbide particles or carbon atoms that might take place.

RESULTS

Electron Microscopy

It has been shown by several investigators (15-18) that temper-embrittled steels are selectively etched by certain etching reagents at prior austenite grain boundaries; whereas, the same steel in the tough condition is not susceptible to this type of attack.

Fig. 1 is a typical electron micrograph of a tough structure obtained by 1 hour at 1250 °F after hardening. The black ball appearing in the

micrograph is a polystyrene-latex particle of a given size such that its diameter in millimeters times 4000 gives the magnification. The presence of these polystyrene-latex particles is also helpful in interpreting the micrographs properly. It must be remembered that these particles were placed on the stripped replica prior to shadowing with palladium. Therefore, these particles were actually above the surface of the replica causing the white rim that is found near them in the electron micrographs. The side on which the white rim exists was the side that "saw" less palladium atoms during shadowing. Therefore, any particle having a white rim on a side opposite that of the polystyrene-latex ball is a depression in the replica and consequently a particle in relief on the original metal surface. A white rim on the same side of a particle or impression as that which exists near the polystyrene-latex ball means that, on the replica, this particle or impression was in relief above the surface of the replica, and consequently, below the surface of the original metal.

Even though with the light microscope no grain boundary attack was evident in a tough structure when etched with ethereal picric solution, a slight indication of such an attack is revealed in the electron micrograph of Fig. 1. This attack seems to follow the outline made by the larger carbide particles found in the structure. Figs. 2 to 6 are electron micrographs of temper-embrittled structures with increasing degrees of embrittlement. As the severity of embrittlement increases at 850 °F due to holding times of 1, 10, 50, 100, and 500 hours, the boundary attack becomes more severe. In Figs. 5 and 6 the outlines of the larger grains, which are believed to be the prior austenite grain boundaries, are very well delineated from the matrix. In most cases the prior austenite grain boundaries follow the larger carbide particles found in the structure. However, no change in size or distribution of these carbide particles can be discerned between the tough and temper-embrittled structures. Furthermore, no evidence of a continuous film around the prior austenite grain boundaries is evident. It is apparent that the outlines of these prior austenite grains are grooves in the original metal surface and not an etching stain. It can also be observed that the particles appearing in the boundaries and matrix are in relief on the metal surface and not holes created by an etching reaction which eats away the particles, leaving the matrix behind.

Autoradiography

Figs. 7 and 8 show typical autoradiographs obtained on tough and temper-embrittled samples of Carburizing Run Number 5 illustrating the effect of etching time on the amount and distribution of carbon in the steel. Both sets of autoradiographs were obtained with 6-day exposures. Fig. 7 compares the tough and temper-embrittled structures as revealed by a 10-second ethereal picric immersion etch. The tough sample shows no grain boundary attack; whereas, the temper-embrittled

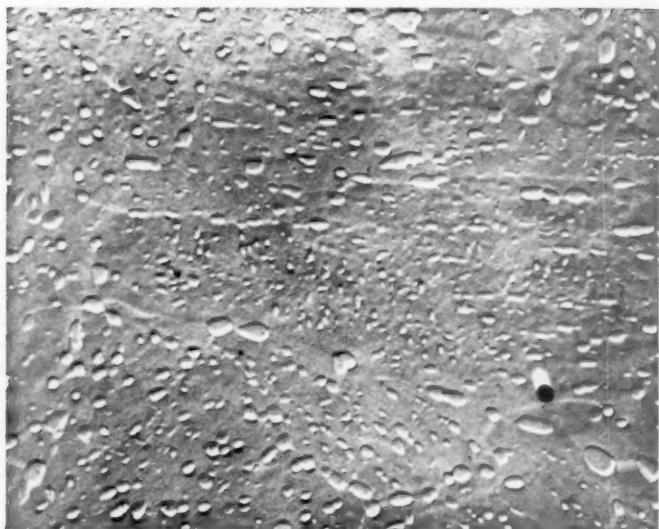


Fig. 1—Electron Micrograph of Structure Produced by Tempering 1 Hour at 1250 °F, Water-quenched, Tough Condition. Electrolytic polish. Ethereal picric immersion etch—10 seconds. $\times 10,000$.

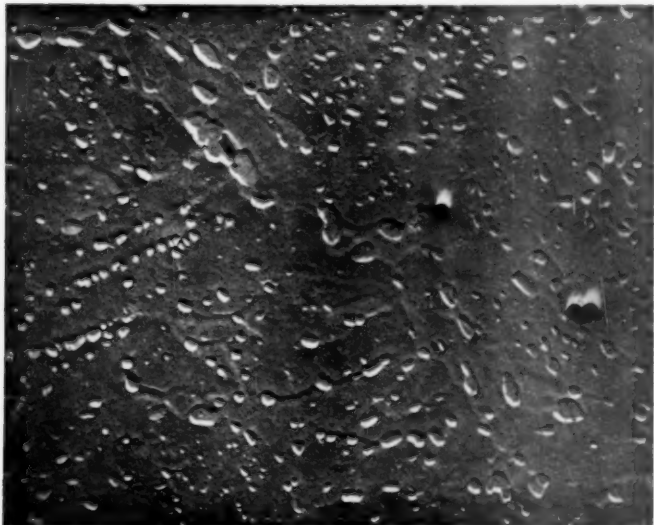


Fig. 2—Electron Micrograph of Structure Produced by Embrittling Cycle of 1 Hour, 850 °F, Water-quenched, Preceded by 1 Hour, 1250 °F, Water-quenched, Electrolytic Polish. Ethereal picric immersion etch—10 seconds. $\times 10,000$.

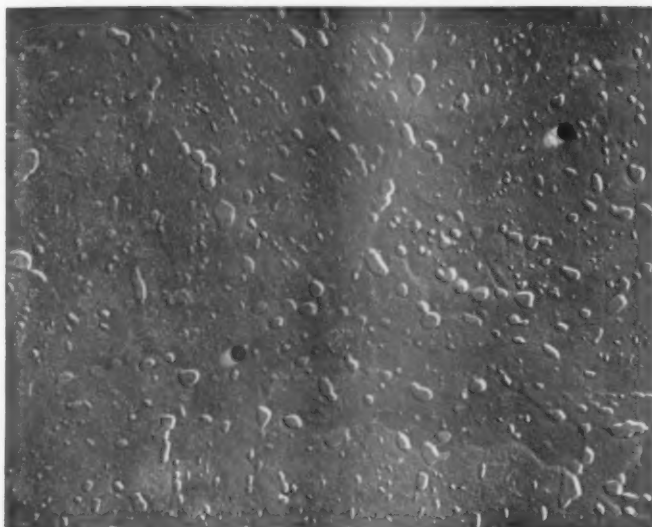


Fig. 3—Electron Micrograph of Structure Produced by Embrittling Cycle of 10 Hours, 850 °F, Water-quenched, Preceded by 1 Hour, 1250 °F, Water-quenched, Electrolytic Polish. Ethereal picric immersion etch—10 seconds. $\times 10,000$.

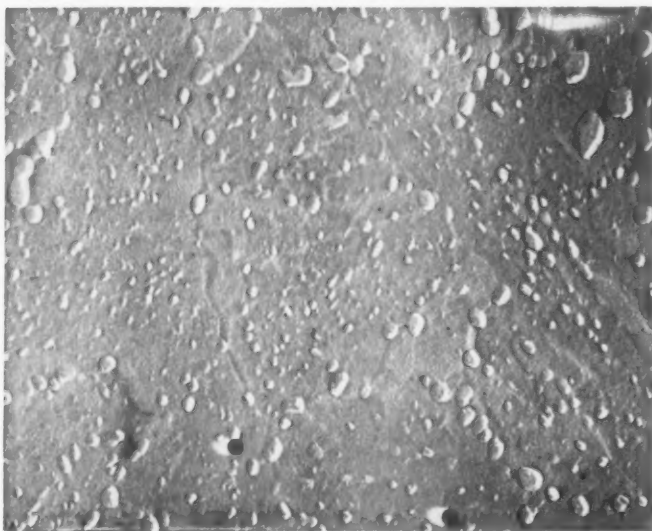


Fig. 4—Electron Micrograph of Structure Produced by Embrittling Cycle of 50 Hours, 850 °F, Water-quenched, Preceded by 1 Hour 1250 °F, Water-quenched, Electrolytic Polish. Ethereal picric immersion etch—10 seconds. $\times 10,000$.

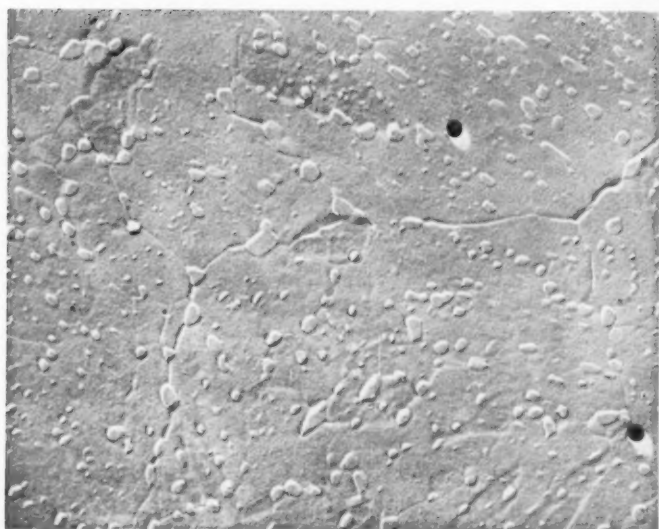


Fig. 5—Electron Micrograph of Structure Produced by Embrittling Cycle of 100 Hours, 850 °F, Water-quenched, Preceded by 1 Hour, 1250 °F, Water-quenched, Electrolytic Polish. Ethereal picric immersion etch—10 seconds. $\times 10,000$.



Fig. 6—Electron Micrograph of Structure Produced by Embrittling Cycle of 500 Hours, 850 °F, Water-quenched, Preceded by 1 Hour, 1250 °F, Water-quenched, Electrolytic Polish. Ethereal picric immersion etch—10 seconds. $\times 10,000$.

structure shows a slight grain boundary attack even with this light etch. The black specks appearing above the grain boundaries in the embrittled structure are the result of C-14 atoms emitting beta radiation which have exposed the film emulsion in intimate contact with the metallic surface. Fig. 8 shows the sample etched for $2\frac{1}{2}$ minutes in ethereal picric solution. In this case the etchant has attacked the grain boundaries of the embrittled steel to a great extent. Again, there are activity centers directly above the delineated grain boundaries in the embrittled structure. Fig. 9 shows another set of autoradiographs obtained on tough and severely temper-embrittled structures containing less specific activity than the previous structures shown in Figs. 7 and 8.

An examination of the presented autoradiographs shows that although some carbon is found in the prior austenite grain boundaries of a temper-embrittled steel, it is by no means extensive. The presence of some activity centers in the prior austenite grain boundaries is expected since inspection of microstructures with light and electron microscopes reveal their presence. However, no significant segregation of carbon or carbides to the prior austenite grain boundaries appears evident. Nor can a continuous film of carbon or carbide be detected by the autoradiographs obtained in this investigation. Although, in some cases, a line-up of activity centers can be observed in the autoradiographs of the embrittled structures, it is not believed that these are responsible for temper embrittlement since similar line-ups can be seen in the tough structures, also.

DISCUSSION

Bush (18) has proposed that interstitial elements are responsible for the early stages of embrittlement; whereas, the substitutional elements come into play at a more advanced stage of embrittlement by diffusing to prior austenite grain boundaries. An analysis of the transition shifts reported by Bush and Siebert (10) using a reaction rate type plot of log embrittling rate versus reciprocal temperature leads to an activation energy for temper embrittlement of about 39,000 calories per mole. Since the activation energy for carbon diffusion in alpha iron is in the order of 20,000 calories per mole, whereas, for substitutional elements the value is closer to 80,000 calories per mole, evidence lends support to the claim that carbon is contributing to the early stages of temper embrittlement. Further evidence of carbon contributing to the embrittling reaction has been noted in studies indicated previously. Evidence of a contribution to embrittlement by substitutional elements, phosphorus, chromium, manganese, etc. is well founded. Although this theory does not recognize the existence of a precipitated phase or film existing about the prior austenite grain boundaries, it does postulate the existence of segregation of interstitial and substitutional elements to these regions. However, the results of the autoradiographic

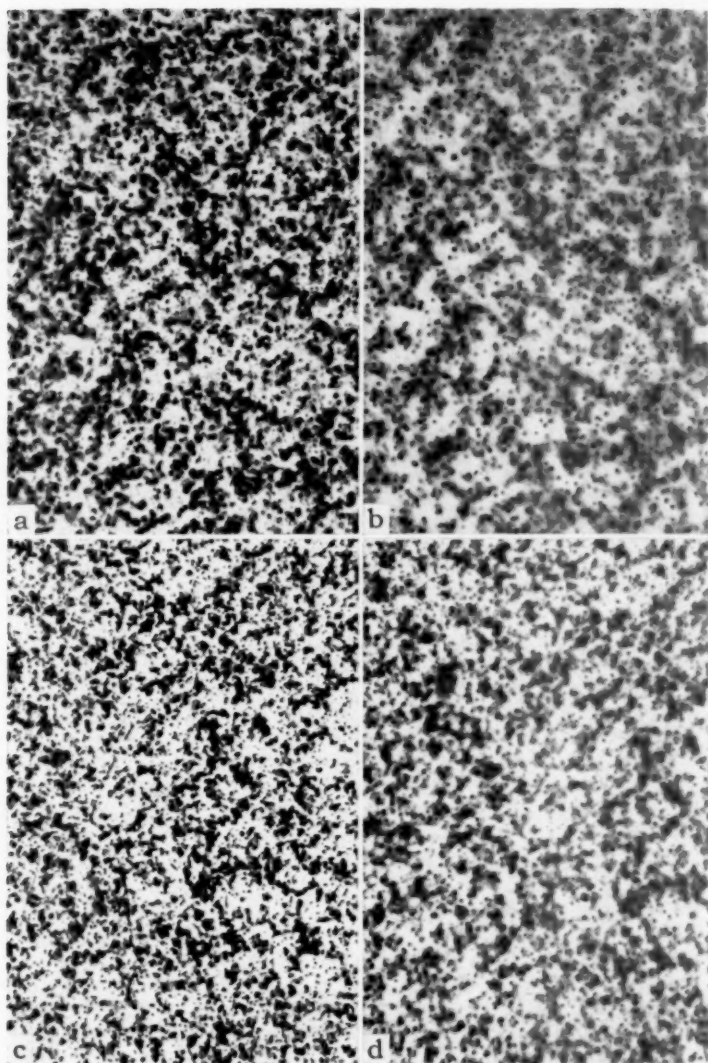


Fig. 7—Six Day Exposure Autoradiograph on Samples of Carburizing Run Number 5. Carburized with 20.1 milligrams of active barium carbonate. Hand polished. Ethereal picric immersion etch—10 seconds. $\times 1000$. (a) 1 Hour, 1250 °F, water-quenched, tough condition. Focus on metal; (b) 1 Hour, 1250 °F, water-quenched, tough condition. Focus on film; (c) Tough condition + 100 Hours, 850 °F, water-quenched. Focus on metal; (d) Tough condition + 100 Hours, 850 °F, water-quenched. Focus on film.

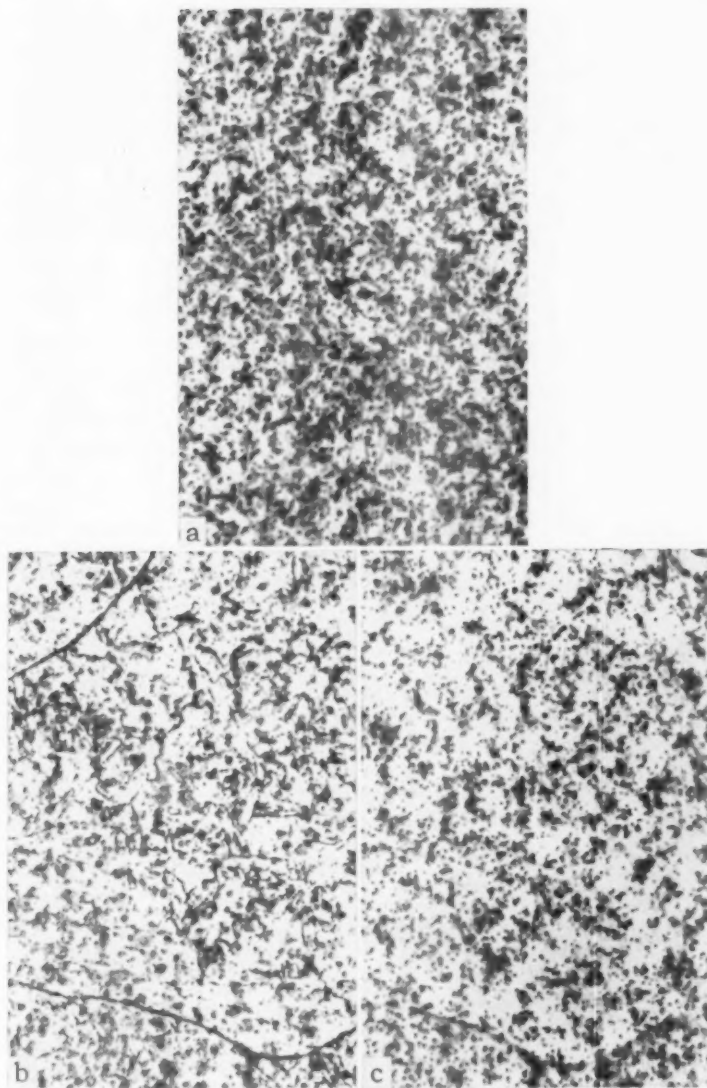


Fig. 8—Six Day Exposure Autoradiograph on Samples of Carburizing Run Number 5. Carburized with 20.1 milligrams of active barium carbonate. Hand polished. Ethereal picric immersion etch—2.5 minutes. $\times 1000$. (a) 1 Hour, 1250 °F. water-quenched, tough condition. Focus on film; (b) Tough condition + embrittled 100 hours, 850 °F. water-quenched. Focus on metal; (c) Tough condition + embrittled 100 hours, 850 °F. water-quenched. Focus on film.

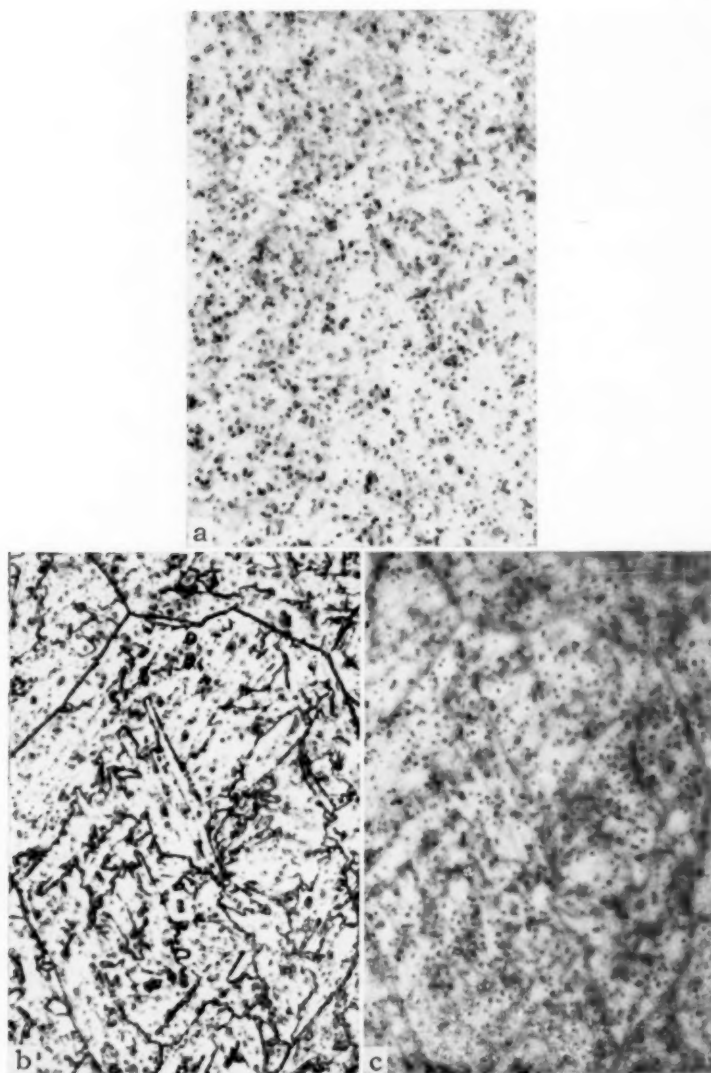


Fig. 9—Six Day Exposure Autoradiograph on Samples of Carburizing Run Number 3. Carburized with 11.1 milligrams of active barium carbonate. Hand polished. Ethereal picric immersion etch—2.5 minutes. $\times 1000$. (a) 1 Hour, 1250 °F, water-quenched, tough condition. Focus on film; (b) Tough condition + embrittled 500 hours, 850 °F, water-quenched. Focus on metal; (c) Tough condition + embrittled 500 hours, 850 °F, water-quenched. Focus on film.

studies in this investigation do not indicate the presence of carbon segregated to the prior austenite grain boundaries in any form. Therefore, the idea of carbon segregating to the prior austenite grain boundaries contributing to temper embrittlement is not substantiated.

Other mechanisms of temper embrittlement have been proposed which involve only a diffusion of substitutional elements to the prior austenite grain boundaries (11,15). In the hypothesis advanced by Woodfine (15) substitutional elements are believed to diffuse to the prior austenite grain boundaries on a submicroscopic scale from the ferrite matrix at the embrittling temperature as well as from the austenite matrix existing during the initial hardening of the steel. Woodfine's theory is not consistent with the activation energy for temper embrittlement obtained from the data of Bush and Siebert (10). This calculation gave a result which was closer to that of an interstitial element than any of the substitutional elements that contribute to temper embrittlement. Nor is it easy to understand how a reaction occurring in the austenite can influence temper embrittlement when the embrittlement can be completely removed by a retempering operation below the lower critical temperature where the material is completely ferritic. Furthermore, carbon additions to a susceptible steel will increase the degree of embrittlement attainable by a given heat treatment. Additional evidence against the theory of substitutional elements diffusing to the prior austenite grain boundaries leading to embrittlement is the fact that plain nickel steels are not susceptible to temper embrittlement. It appears that this theory is not adequate to explain the complexity of the temper embrittlement in its entirety.

The fact that the prior austenite grain boundaries during etching are preferentially attacked in a brittle structure and that this attack progressively increases with increasing embrittlement suggests two alternatives. Either the chemical composition of the boundary regions is altered during embrittlement so that they are selectively etched or a severe stress concentration is present in these regions which leads to a stress-corrosion type of attack. Since in the preceding discussion the idea of segregation to the prior austenite boundaries of interstitial and/or substitutional elements was shown to be unsupported by existing experimental evidence, the strain mechanism for temper embrittlement needs to be examined as a possible explanation.

The enrichment of cementite in alloy content in an embrittled steel has been reported by Maloof (13). If it is assumed that during the embrittling process a modification of carbides in the matrix comes about through a reaction between the existing carbides and the alloying elements dissolved in the matrix, then a strain could be developed across the prior austenite grain boundaries by virtue of the contracting ferrite grains. It is known that the lattice parameter of a temper-embrittled steel is smaller than a corresponding tough steel (10,13). This may

mean that carbon and some of the carbide forming elements have come out of solution from the ferrite matrix. Since these elements are not believed to diffuse to the prior austenite grain boundaries, the remaining likely positions that are available are associated with the existing carbide phases. In this manner carbon could still be responsible for the initial rapid rate of embrittlement and the substitutional elements with the latter stages of embrittlement. The return of toughness by reheating a temper-embrittled structure below the lower critical temperature would be brought about by a relief of strain at the higher temperature and a re-solution of some elements into the ferrite matrix.

CONCLUSIONS

1. No continuous film of any kind is observed in the prior austenite grain boundaries of a temper-embrittled structure developed in a SAE 3140 steel.
2. Although carbides are observed in the prior austenite grain boundaries of an embrittled structure, it is unlikely that these have any effect on temper embrittlement since carbides are also observed in similar positions in the tough condition.
3. The prior austenite grain boundaries as revealed by an ethereal picric etch are actual grooves between the grains which increase with etching time and degree of embrittlement and are not a staining effect of the etchant.
4. Autoradiographic studies using carbon-14 and electron microscope observations of embrittled structures of a SAE 3140 steel do not reveal that carbon atoms or carbides have segregated to the prior austenite grain boundaries.
5. Temper embrittlement is brought about by a strain developed across prior austenite grain boundaries at the embrittling temperature as a result of a contraction of the ferrite lattice when dissolved alloying elements are removed from solution in the ferrite by a reaction with the existing minor carbide phases.

References

1. L. D. Jaffe and D. C. Buffum, "Temper Brittleness of Plain Carbon Steels," *Transactions, American Institute of Mining and Metallurgical Engineers*, Vol. 180, 1948, p. 513.
2. J. F. Libsch, A. E. Powers and G. Bhat, "Temper Embrittlement of Plain Carbon Steels," *TRANSACTIONS, American Society for Metals*, Vol. 44, 1952, p. 1058.
3. B. C. Woodfine, "Temper Brittleness: A Critical Review of the Literature," *Journal, Iron and Steel Institute*, Vol. 173, No. 3, 1953, p. 229.
4. H. Jolivet and G. Vidal, "Value of Impact Testing for the Study of Temper Brittleness," *Revue de metallurgie*, November and December 1944, p. 378.
5. L. D. Jaffe, "Temper Brittleness of Some Fe-Ni-Cr Alloys," *Journal of Metals*, Vol. 7, No. 2, February 1955, p. 412.
6. D. C. Buffum, L. D. Jaffe and W. P. Clancy, "Effect of Carbon and Nitrogen on Temper Brittleness," *Transactions, American Institute of Mining and Metallurgical Engineers*, Vol. 185, 1949, p. 499.

7. A. Preece and R. D. Carter, "Temper Brittleness in High-Purity Iron-Base Alloys," *Journal, Iron and Steel Institute*, Vol. 173, April 1953, p. 387.
8. R. R. Hultgren and C. Chang, "Investigation of the Temper Brittleness of Steels," Final Report—Effect of Chemical Composition. University of California, ONR, 1951, p. 1-62 plus Appendix.
9. J. H. Hollomon, "Temper Brittleness," *TRANSACTIONS, American Society for Metals*, Vol. 36, 1946, p. 473.
10. S. H. Bush and C. A. Siebert, "Temper Embrittlement of a 5140 Steel," *Transactions, American Institute of Mining and Metallurgical Engineers*, Vol. 200, 1954, p. 1269.
11. D. McLean and L. Northcott, "Micro-Examination and Electrode—Potential Measurements of Temper Brittle Steels," *Journal, Iron and Steel Institute*, Vol. 158, February 1948, p. 169.
12. E. Maurer, O. H. Wilms and H. Kiessler, "Einfluss des Phosphors und Verschiedener Legierungsmetalle auf die Anlasszprodigkeit und Warmversprodnung von Baustahl," *Stahl und Eisen*, Vol. 62, 1942, p. 81.
13. S. R. Maloof, "Some X-Ray Diffraction and Electron Microscope Observations on Temper Brittle Steels," *TRANSACTIONS, American Society for Metals*, Vol. 44, 1952, p. 264.
14. S. Yukawa, "Grain Boundary Diffusion in the Copper-Bismuth and Copper-Nickel Systems," Doctoral Thesis, University of Michigan, 1954.
15. B. C. Woodfine, "Some Aspects of Temper Brittleness," *Journal, Iron and Steel Institute*, Vol. 173, 1953, p. 240.
16. J. B. Cohen, A. Hurlich and M. Jacobson, "A Metallographic Etchant to Reveal Temper Brittleness in Steel," *TRANSACTIONS, American Society for Metals*, Vol. 39, 1947, p. 109.
17. P. A. Jaquet, "Confirmation Micrographique de la Reversibilite de la Transformation Conferant la Fragilite de Revenu aux Aciers a Basses Teneurs en Nickel et en Chrome," *Comptes Rendus*, Vol. 230, February 13, 1950, p. 650.
18. S. H. Bush, "An Investigation of the Isothermal Temper-Embrittlement of a 5140 Steel," Doctoral Thesis, University of Michigan, 1953.

DISCUSSION

Written Discussion: By Dr. A. E. Powers, General Electric Company, Power Tube Department, Schenectady, New York.

The authors have dismissed the theory that temper brittleness may be due to the grain boundary segregation of substitutional alloying elements. They cite a measured activation energy for temper embrittlement of around 39,000 cal. per mole as being too far removed from the activation energy of 80,000 cal. per mole for the diffusion of substitutional elements in alpha iron. The figure of 80,000 cal. per mole seems to be too high when one considers such measured values as 73,000 and 59,800 cal. per mole for the self diffusion of iron^{2,3} and 57,700 cal. per mole for the diffusion of molybdenum in alpha iron.⁴ A while ago, I attempted to find the activation energy for embrittlement from the slopes of isoembrittlement curves for SAE 3140 constructed by Carr, Goldman, Jaffe, and Buffum.⁵ Their diagram is one of the most detailed and precise embrittlement diagrams available.⁶ The

² C. E. Birchanall and R. F. Mehl, "Self Diffusion in Alpha and Gamma Iron," *Transactions, American Institute of Mining and Metallurgical Engineers*, Vol. 188, 1950, p. 144-149.

³ F. S. Buffington, J. D. Bakalar, and M. Cohen, Chapter 6, *The Physics of Metals*, W. E. Kingston, editor, McGraw-Hill Book Company, 1951.

⁴ J. L. Ham, "The Rate of Diffusion of Molybdenum in Austenite and in Ferrite," *TRANSACTIONS, American Society for Metals*, Vol. 35, 1945, p. 331-361.

⁵ F. L. Carr, M. Goldman, L. D. Jaffe, and D. C. Buffum, "Isothermal Temper Embrittlement of SAE 3140 Steel," *Transactions, American Institute of Mining and Metallurgical Engineers*, Vol. 197, 1953, p. 998.

⁶ A. E. Powers, "A Study of Temper Brittleness in Cr-Mn Steel Containing Large Amounts

derived activation energy for embrittlement was between 46,000 and 60,000 cal. per mole. This is so far removed from the activation energy for diffusion of carbon that it is difficult to understand how the diffusion of carbon can have anything to do with temper brittleness.

Modification of the carbides during embrittlement is difficult to understand, since embrittlement is known to develop without any significant tempering of the steel. Whether or not any significant tempering has occurred during embrittling can be estimated from Holloman and Jaffe's tempering parameter, $T(C + \log t)$. Any strain that is developed across grain boundaries should be relieved by creep during aging, even at temperatures below 1000 °F. The authors' theory of grain-boundary strain suggests that temper brittleness should lead to stress-corrosion cracking. Such cracking has never been observed to be a consequence of temper embrittlement. In fact, the nature of the grain-boundary attack has lead Perryman to suggest that the embrittled grain boundaries are cathodic to the matrix rather than anodic.⁷

In speaking of the contraction of the ferrite lattice during embrittling, the authors have not provided any distinction between lattice contraction as a consequence of embrittling treatments and as a consequence of normal tempering processes. It is probable that in all cases where lattice contraction has been noticed, the state of tempering was advanced slightly, as measured by the growth of carbides or changes in hardness or calculated precisely by the tempering parameter.

In 1955, I attempted to detect intergranular microsegregation of radioactive phosphorus in temper-embrittled steel, using the same autoradiographic stripping-film method as used by the authors. The results were negative presumably because of insufficient resolution conferred by the beta rays. I came to the conclusion that the only chance for detecting intergranular segregation by autoradiographic techniques would be with the utilization of an alpha-emitting element.

Written Discussion: By G. K. Bhat, Staff Metallurgist, Research and Development Laboratory, Crucible Steel Company of America, Pittsburgh.

The authors have presented some interesting results on the role of carbon in temper embrittlement. The writer is in agreement with authors' general conclusion that carbon does not seem to segregate to prior austenite grain boundaries. Therefore, carbon might not play a significant role in causing 900 °F embrittlement.

However, the attention of the authors is directed to a few misquotations and unwarranted conclusions which they have drawn from earlier work.

The temper embrittlement phenomenon leads to brittle fracture not only along prior austenite grain boundaries but also along ferrite grain boundaries. Brittle fracture along prior austenite grain boundaries has been seen in specimens embrittled at 800 to 975 °F. In specimens embrittled at 1100 to 1250 °F, fracture occurs predominantly along ferrite grain boundaries. Specimens embrittled in the range 975 to 1100 °F tend to show mixed fractures.^{8, 9, 10}

of Molybdenum, Tungsten, and Vanadium", *Journal of the Iron and Steel Institute*, Vol. 186, July 1957, p. 323-328.

⁷ E. C. W. Perryman, "Grain Boundary Attack on Aluminum in Hydrochloric Acid and Sodium Hydroxide," *Transactions, American Institute of Mining and Metallurgical Engineers*, Vol. 197, 1953, p. 911-917.

⁸ G. K. Bhat, "Embrittlement During Tempering Engineering Alloy Steels and Its Causes," Ph.D. Dissertation, Lehigh University, 1955.

⁹ G. K. Bhat and J. F. Libsch, "Studies of the Development and Causes of Embrittlement in Alloy Steels," First Partial Report on Contract DA 36-034-ORD-1583 WAL 801/6-26, Lehigh Institute of Research, December 1954.

¹⁰ L. D. Jaffe and D. C. Buffum, "Upper-Nose Temper Embrittlement of a Nickel-Chromium Steel," *Journal of Metals*, Transactions Section, January 1957, p. 8.

Isoembrittlement diagrams for nickel alloy steels are now available. It has been clearly shown that nickel alloy steels of the type AISI 2340 are susceptible to temper embrittlement. A definite opinion concerning the influence of nickel per se on the development of embrittlement cannot be found in the references cited by the authors. Yet, the authors without presenting any evidence, claim that plain nickel steels are not susceptible to temper embrittlement.

Libsch, Powers and Bhat¹¹ have not stated that plain carbon steels become embrittled during the quench from the tempering temperature. These authors have clearly pointed out that in plain carbon steel embrittlement develops so rapidly that it could be prevented only by restricting the time at tempering temperature. It is to be noted, that in plain carbon steel maximum embrittlement develops at temperatures much higher than 900 °F. Woodfine¹² does not consider embrittlement occurring at temperatures above 900 to 975 °F as temper-embrittlement. Since the present authors consider that temper embrittlement occurs in steels tempered in the range 700 to 1250 °F, it is difficult to accept their statement that plain carbon steels are not susceptible to temper-embrittlement.

The present authors have quenched their carburized steel from 2000 °F. Quenching an AISI 3140 steel from temperatures above 1750 °F increases the tendency of austenite retention. Retained austenite is known to retard the development of embrittlement.⁸ In view of this, have the authors noticed any retained austenite in their specimens quenched from 2000 °F?

The authors have stated that "in most cases the prior austenite grain boundaries follow the larger carbide particles". In studies made by the writer, larger carbide particles seemed to form at prior austenite and also at ferrite grain boundaries, depending upon the embrittling temperature and times used and the alloy content of the steel.

For a clearer understanding of the mechanism of embrittlement in constructional steels, a study of the kinetics of the embrittlement in the temperature range 750 °F up to the lower critical temperature of the steel is very necessary.

An inspection of isoembrittlement diagram available for several steels^{8, 10, 12} shows that embrittlement in alloy steels proceeds according to at least two modes: a high temperature mode and a low temperature mode. Without going further into these two modes of embrittlement, the cause of embrittlement appears to be different, for the embrittlement developed in the high and low temperature regions. The reaction itself is very complex and values of the activation energy of the reaction at any temperature do not help one to pin down the element responsible for embrittlement. Arguments presented in this paper on the basis of activation energy values are largely open to question.

For an explanation of the mechanism of embrittlement, it is desirable to follow changes occurring in the steel from the austenitizing stage. The iron lattice is in a distorted state at the grain boundaries. Consequently, atoms nearer to the grain boundary could be in a state of tension or compression. The distortion of the system as a whole would be reduced if alloy atoms, during austenitizing, occupy the grain boundary sites. The austenite-martensite transformation may be considered a diffusionless process. When the quenched steel is tempered, the first ele-

¹¹ J. F. Libsch, A. E. Powers and G. Bhat, "Temper Embrittlement of Plain Carbon Steels," *TRANSACTIONS, American Society for Metals*, Vol. 44, 1952, p. 1058.

¹² B. C. Woodfine, "Temper Brittleness: A Critical Review of the Literature," *Journal, Iron and Steel Institute*, Vol. 173, No. 3, 1953, p. 229.

¹³ A. E. Powers and R. G. Carlson, "The Effect of Boron on Notch Toughness and Temper Embrittlement," *TRANSACTIONS, American Society for Metals*, Vol. 46, 1954, p. 483.

ment that diffuses appreciably is carbon, other interstitials would be expected to behave similarly to carbon. An element which diffuses rapidly is least likely to segregate. The present authors' results tend to confirm this view.

During the early stages of tempering there may be a residual concentration of certain types of atoms at the grain boundaries since substitutional alloy atoms are slow to diffuse at low temperatures (800 to 1000 °F). This might cause a temporary change in the behavior of the grain boundary material. This situation might be responsible for low temperature embrittlement.

The authors' suggestion that strain developed across prior austenite grain boundaries is the cause of embrittlement remains unsupported. Tempering strains are normally considered insignificant when tempering is done above 600 °F—and especially so for medium carbon, low alloy steel.

The removal of low temperature embrittlement by heating embrittled specimens to higher temperatures might be due to a homogenization of composition between grain interior and the grain boundary material by diffusion of alloy atoms. Some of the alloy atoms may also combine with carbon to form stable carbides.

At temperatures above 1100 °F, increasing amount of carbon and probably other interstitial elements having low solubility in ferrite separate and these seem to precipitate¹⁴ in some form along ferrite grain boundaries. This could also be the cause of embrittlement in plain carbon steels in which maximum embrittlement develops at about 1250 °F.

Written Discussion: By A. S. Keh, Edgar C. Bain Laboratory For Fundamental Research, United States Steel Corporation, Research Center, Monroeville, Pa.

This new addition to the literature of temper embrittlement is very welcome. The strain theory as proposed by the authors is very enlightening, and the writer would like to see more experimental evidence in the future.

The autoradiographic technique is a very useful research tool in the field of metallurgy. However, in the opinion of the writer, it is not sensitive enough in the present case. The resolution of an autoradiograph is about 2 microns; however, the mean carbide spacing as shown in the electron-micrographs (Figs. 1-6) is much smaller than 2 microns. That means each localized black spot on the autoradiograph actually represents a cluster of carbide particles. It is known that the layer of grain boundary segregation of any solute atom is not more than 10 Å thick. If there is carbon segregation at the grain boundaries, its contribution to the intensity of the autoradiographic film is but a very small fraction of that due to the carbide particles. Therefore, the autoradiographic results shown in this paper do not necessarily prove that carbon is not segregated to the grain boundaries of iron.

Written Discussion: By S. R. Maloof, Nuclear Metals, Inc., Cambridge, Massachusetts.

The possibility that strain may contribute to temper embrittlement should not be overlooked. In an earlier publication,¹⁵ it was shown that the back-reflection lines of the (310) reflection from the ferrite matrix were more diffuse for the

¹⁴ G. K. Bhat, "A New Look at Temper Brittleness," *Iron Age*, January 24, 1957, p. 73.

¹⁵ S. R. Maloof, "Some X-Ray Diffraction and Electron Microscope Observations on Temper Brittle Steels," *TRANSACTIONS, American Society for Metals*, Vol. 44, 1952. See Fig. 13 on page 281.

embrittled samples (slowly cooled from the tempering temperature of 1200 °F) than for the tough samples (water-quenched from 1200 °F). This is contrary to what one might have anticipated, and it appears that internal strains are generated in the ferrite lattice during the diffusion of alloying elements from the ferrite matrix into the existing carbide phase (cementite) and/or during the precipitation of carbide from solid solution.

The authors' disclosure that the larger carbide particles outline the prior austenite grain boundaries is in agreement with the earlier observations of the writer. These larger carbide particles presumably form at the high tempering temperature (1250 °F). During the embrittling treatment, enriched cementite ($[\text{Fe,Cr}]_s\text{C}$) particles form in situ and appear to stand in relief from particles of the more massive and irregular-shaped cementite (Fe_3C). These findings are not evident in this study, in spite of the fact that the steel used by the authors is very similar in composition to that investigated by the writer. Furthermore, the extent of grain boundary attack is not as marked as that shown in the writer's samples. It is believed that this difference is due to the fact that the authors used an ethereal picric acid solution to etch their specimens, whereas a Zephiran chloride etch was used by the writer. Earlier work on both of these etchants disclosed a definite difference in their etching behavior. The Zephiran chloride etch appeared to attack the grain boundaries more markedly than did the ethereal picric acid solution. Possibly the authors have investigated this point?

As the authors point out, a change in chemical composition in the immediate vicinity of a prior austenite grain boundary could also explain the increased preferential attack in embrittled samples. Enriched cementite ($[\text{Fe,Cr}]_s\text{C}$) particles formed in situ would drain the surrounding matrix of its chromium content and hence accelerate the grain boundary attack. Possibly a micro x-ray spectrographic technique could shed some light on this proposed mechanism?

The authors are to be congratulated for their continued interest in such a difficult problem. More research of this type would indeed be welcome.

Written Discussion: By Spencer H. Bush, Hanford Laboratories Operation, General Electric Company, Richland, Washington.

The authors are to be complimented on their approach to the problem of temper embrittlement. It is only through such studies that the true mechanism of such embrittlement will be ascertained.

Unfortunately, there are still several questions left unanswered by this study. The autoradiographic results when analyzed do not indicate a gross movement of carbon to the prior austenite grain boundaries. This in itself is significant, but there is no assurance that more than a limited change in carbon content is required which is below the threshold of detection of the autoradiographic technique. Compositional changes of a few parts per million are known to cause marked changes in several metallic systems. Conceivably the same may be true here.

The authors propose a mechanism based on a straining of the prior austenite grain boundaries. Certainly some etchants attack these boundaries selectively, indicating the existence of foreign atoms or strains. Even so their statement that a contraction of the ferrite grains results in such strain requires clarification. The contraction which has been observed in x-ray diffraction studies^{16, 17} could strain

¹⁶ S. H. Bush, "An Investigation of the Isothermal Temper-Embrittlement of a 5140 Steel," Doctoral Thesis, University of Michigan (1953).

¹⁷ S. R. Maloof, "Some X-ray Diffraction and Electron Microscope Observations on Temper Brittle Steels," *TRANSACTIONS, American Society for Metals*, Vol. 44, 1952, p. 264.

**Correlation of Transition Temperature and Lattice Parameter
For 5140 Steel After Various Heat and Embrittling Treatments**

Heat Treatment	50 ft-lb Impact Energy *E	50 Per cent Brittle Fracture	Lattice Parameter
1600 °F, 1275 °F, 5 hours *	—103	—103	2.8620
1050 °F, 1 hour	—81	—81	2.8614
1050 °F, 10 hours	—51	—53	2.8614
1050 °F, 24 hours	—63	—49	2.8610
1050 °F, 100 hours	—74	—67	2.8614
1050 °F, 1000 hours	—56	—56	2.8611
1050 °F, 3000 hours	—67	—58	2.8614

* Base condition, all other specimens have this initial heat treatment unless otherwise noted.

the ferrite boundaries equally well yet most evidence points to a failure through the austenite rather than the ferrite boundaries in an embrittled steel.

Another point requiring clarification or amplification in their grain boundary strain theory is the reversal in transition temperature and lattice parameter observed in extended tempering as shown in the accompanying Table.¹⁸

Such reversals of embrittlement with time as shown in the table would indicate a variation in grain boundary strain, but the authors' mechanism requires some additional explanation if such changes are to be explained.

Authors' Reply

The authors appreciate the comments received on this paper. The lively response indicates the controversial nature of this interesting subject.

Controversial as the subject may be, some workers confuse the issue further by attributing all phenomenon which leads to an increase in transition temperature obtained by impact testing as temper embrittlement. Apparently, Dr. Bhat holds this viewpoint when he claims that his work shows that plain carbon steels are susceptible to temper embrittlement. It has been clearly and irrevocably pointed out by Woodfine¹⁸ in his review of the paper by Bhat and co-workers that the transition shifts observed by them were not due to temper embrittlement but to an increase in ferrite grain size as tempering progressed. A further analysis by Queneau¹⁹ substantiates this conclusion.

While Jaffe, Buffum, Bhat and co-workers all have indicated that plain carbon steels are very susceptible to temper embrittlement, only the former authors have suggested that they become embrittled during the quench from the tempering temperature. We intended no misrepresentation and thank Dr. Bhat for clarifying this point.

References (3) and (11) in the paper and footnote (19) in this discussion cite examples which indicate the nonsusceptibility of plain nickel steels. The general opinion concerning nickel in its relation to the temper embrittlement is that alone nickel has little or no effect but in the presence of other elements that promote embrittlement nickel will increase the susceptibility.

Only the carburized steel samples used for autoradiographic studies were austenitized at 2000 °F. The criterion used to establish embrittlement was the response of the ductile and brittle samples to the ethereal picric etch. In all cases the ductile samples exhibited no prior austenite grain boundary attack; whereas, the samples heat treated to give a brittle structure exhibited an attack comparable to that

¹⁸ B. C. Woodfine, "Temper-Brittleness: A Critical Review of the Literature," *Journal, Iron and Steel Institute*, Vol. 173, No. 1, 1953, p. 234.

¹⁹ B. R. Queneau, *The Embrittlement of Metals*, American Society for Metals, Cleveland, Ohio, 1955, p. 35.

obtained on the virgin 3140 steel samples temper embrittled by an identical tempering treatment.

This investigation was concerned only with the embrittled structure obtained in 3140 steel at 850 °F. At this temperature the larger carbide particles were observed in the prior austenite grain boundaries. Tempering at a higher temperature results in a general carbide conglomeration in which case the ferrite boundaries may become populated with these larger particles as well, as Dr. Bhat has observed.

In regard to Dr. Bush's remarks it is true that the segregation assumed to take place may be below the limit of detection of the autoradiographic technique employed. However, as will be pointed out in answer to Dr. Keh's comments, the technique employed is highly sensitive. In our investigation it was observed that when a severely embrittled structure was etched long enough with ethereal picric solution some ferrite boundaries began to appear along with the prior austenite grain boundaries. This would indicate a degree of strain at the ferrite boundaries but somewhat less than that existing at the prior austenite boundaries. Ferrite boundaries are rather mobile and at the embrittling temperature they move about and thereby reduce the strain in these regions. On the other hand prior austenite grain boundaries do not tend to move at the embrittling temperature. Therefore, they lack the opportunity to relax the strain by diffusion.

In the reversal in transition temperature observed by Dr. Bush it should be noted that in no case was complete recovery achieved at long times at the embrittling temperature. Since the temper embrittling reaction is complex in nature, involving many elements with significant differences in diffusion rates, the partial reversals observed can be explained on the basis of the different times at which various elements come into play in the embrittling reaction. The interstitials such as C and N₂ operate first and the substitutional elements later. Therefore, a partial balance between the strain set up in the prior austenite grain boundaries by a given element taking place in the reaction with existing carbides and the relaxation afforded by the tempering temperature could be observed before another element having a lower diffusion rate becomes predominating.

Concerning Dr. Keh's comments, the authors would like to point out that in this investigation the question of resolution of the autoradiographic technique is not critical. The important factor in this type of autoradiography is the level of specific activity available. Calculations on the specific activity available in these experiments using the data of Towe and co-workers²⁰ indicate that a segregation as small as 10 Å on each side of a prior austenite grain boundary containing carbon in the amount present in Fe₃C would be readily detectable.

The authors agree with Dr. Maloof that a micro probe technique might shed some light on the mechanism of temper embrittlement. In addition, we believe valuable information could be obtained through internal friction as well as further autoradiographic studies.

As pointed out in the discussion above, resolution is not an important factor in these particular autoradiographs. May we suggest to Dr. Powers that his results were negative not because the resolution was poor but perhaps because temper embrittlement does not occur by this mechanism.

In considering the segregation theories of temper embrittlement, it is difficult to reconcile a formation of a submicroscopic layer of foreign atoms about the prior

²⁰ G. C. Towe, H. J. Gombert, and J. W. Freeman, *High Resolution Autoradiography*, NACA Tech Note 3209, July 1954, p. 14.

austenite grain boundaries with the gradual increase in transition temperature as embrittlement becomes more severe at a given temperature. It would seem logical to assume that once a layer of foreign atoms has been established about the prior austenite grain boundaries, the structure would have achieved maximum brittleness. Further segregation which would take place on continued tempering would not be expected to affect the susceptibility of the structure to brittle fracture. On the other hand a strain concept as proposed by the authors would explain the observed fact that the transition temperature increases with the severity of embrittlement.

BRITTLE TO DUCTILE TRANSITION TEMPERATURES OF BINARY CHROMIUM-BASE ALLOYS

BY E. P. ABRAHAMSON, II, AND N. J. GRANT

Abstract

A study has been made of the transition temperature for brittle fracture of chromium alloys with up to 30 weight percent of twenty-one different elements in binary combinations.

A correlation between the rate of transition temperature change and the electron configuration of the solute element is shown and a tentative explanation of transition temperatures is put forward. (ASM International Classification Q23r; Cr)

INTRODUCTION

ALTHOUGH chromium-base alloys are attractive high temperature materials from an oxidation standpoint, the lack of room temperature ductility exhibited by these alloys presents a major development problem. Considerable progress has been made in producing chromium, in small amounts, that is ductile at room temperature. However, all work to date has shown that the addition of a second element to chromium raises the brittle to ductile transition temperature. Sully, Brandes and Mitchell (1)¹ have found this to be true for binary additions of aluminum, copper, nickel, manganese, iron, silicon and tungsten to chromium. Wain, Henderson and Johnstone (2) and Smith and Seybolt (3) have shown that nitrogen, in the absence of other elements, markedly increases the transition temperature. On the other hand, very little effect was noted for oxygen up to 0.34 weight % and for carbon and sulphur up to 0.02 and 0.1 weight %, respectively (3).

The purpose of this work, then, was to examine more broadly the investigations mentioned above, and to expand the investigation to include other alloying elements. It was felt that additions of ten or

¹ The figures appearing in parentheses pertain to the references appended to this paper.

Based on a thesis submitted in partial fulfillment of the requirements for the degree of Doctor of Science, Department of Metallurgy, Massachusetts Institute of Technology, Cambridge, Massachusetts.

A paper presented before the Thirty-Ninth Annual Convention of the Society, held in Chicago, November 4-8, 1957. Of the authors, E. P. Abrahamson, II, is Research Associate, and N. J. Grant is Professor, Department of Metallurgy, Massachusetts Institute of Technology, Cambridge, Massachusetts. Manuscript received May 6, 1957.

more weight percent of a second element might have an effect which corrects for the initial increase in transition temperatures noted.

MATERIALS AND EXPERIMENTAL TECHNIQUES

Chromium of several grades of purity was alloyed with elements in Groups IV_B, V_B, VI_B, VII_B, and VIII in the periodic table. These elements, listed in Table I, were of the highest available purity. In addition, the effect of small individual additions of beryllium, aluminum, boron, carbon and silicon was investigated. Hydrogen purified electrolytic chromium was used; it contained, in weight percent, 0.012 to 0.02 oxygen, 0.008 to 0.015 nitrogen, 0.006 to 0.010 carbon, and 0.0004 to 0.0006 hydrogen.

All alloys were melted under purified argon in a water-cooled copper crucible, tungsten electrode arc furnace. The 100-gram buttons were inverted at least three times before a sample was sucked up in a 1/8-inch inside diameter quartz tube. This method of casting gave a relatively fine grain size that was essentially constant for all of the alloys. The rods were then electro-polished to remove the thin outer layer of silicon contamination. This layer was found to raise the transition temperature by several hundred degrees Fahrenheit, although part of this increase was probably ascribable to micronotches on the surface of the casting. All specimens were tested in the as-cast condition, the most unfavorable condition from the standpoint of transition temperature.

The brittle to ductile transition temperature was measured by means of a bend test. The test apparatus consisted of a double specimen support giving a span of one inch and a load rod, both enclosed in a furnace capable of attaining 2200 °F. The testing temperature was measured at the specimen. All specimens were held at the testing temperature for five minutes prior to bending. Vacuum fusion analyses of the total sample showed no nitrogen pick-up during this time. A strain rate of from

Table I
Composition of Elements Used for Alloying with Chromium

Element	% Element Minimum	Weight Percent Impurity								
		O	N	H	C	Fe	Ta	Cu	Si	Ni
Nb	99.5	0.11	0.039	0.002	0.2	0.01	0.16	0.1	0.05	0.1
Co	98.8	0.007	0.001	—	—	—	—	—	—	1.10
Fe	99.9	0.08	—	—	0.01	—	—	—	—	—
Ir	99.95	—	—	—	—	0.001	—	—	—	—
Mn	99.9	—	—	—	0.004	—	—	—	—	—
Mo	99.98	—	—	—	0.004	—	—	—	—	—
Ni	99.9	0.005	0.004	—	—	—	—	—	—	—
Pd	99.98 +	—	—	—	—	—	—	—	—	—
Pt	99.98 +	—	—	—	—	—	—	—	—	—
Re	99.9	—	—	—	—	—	—	—	—	—
Rh	99.8	—	—	—	—	—	—	—	—	—
Ru	99.97	—	—	—	—	0.003	—	—	—	—
Ta	99.9	—	—	—	0.03	0.03	—	—	—	—
Ti	99.9	0.018	0.006	0.011	0.037	0.013	—	—	—	—
V	99.7	0.049	0.092	0.001	0.085	—	—	—	—	—
Zr (in ppm)	99.8	—	—	—	—	500	—	—	—	13

0.1 to 0.01 inch per minute was applied manually by means of a lever arm. More exact control was not warranted since Sully's data (4) showed that a strain rate change from 0.003 to 0.77 inch per minute raised the transition temperature only 50 °C.

The bend test results were plotted as a graph of the angle of bend, measured after fracture, versus test temperature; see Fig. 1. This figure shows a change in transition temperature with a change in nitrogen, while the slopes are essentially equal. The maximum bend attainable was 130 degrees. As can be seen, the values of transition temperature for brittle to ductile behavior can be approximated by a straight line. A 65-degree bend was chosen as the arbitrary transition temperature. The temperature at which this amount of ductility was observed was plotted against the atomic percentage of solute element as shown in Fig. 2.

The alloy content was checked occasionally by chemical analysis. The

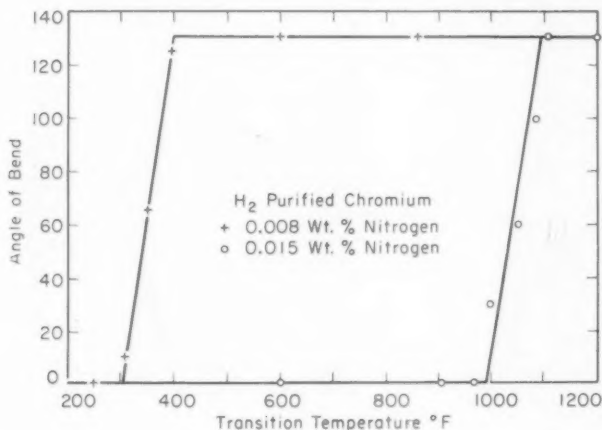


Fig. 1—Typical Bend Test Data.

deviation from the nominal content of alloying element was never greater than about two percent of the quantity added.

RESULTS

Figs. 2, 3A and 3B show that with the exception of ruthenium and beryllium, the addition of all other solute atoms investigated initially increased the transition temperature. Fig. 2 indicates that with additions of some elements, a composition is reached beyond which the transition temperature is no longer increased with increasing additions. At this composition a decrease in transition temperature was noted. This decrease occurred in both single and two-phase alloys, provided that a

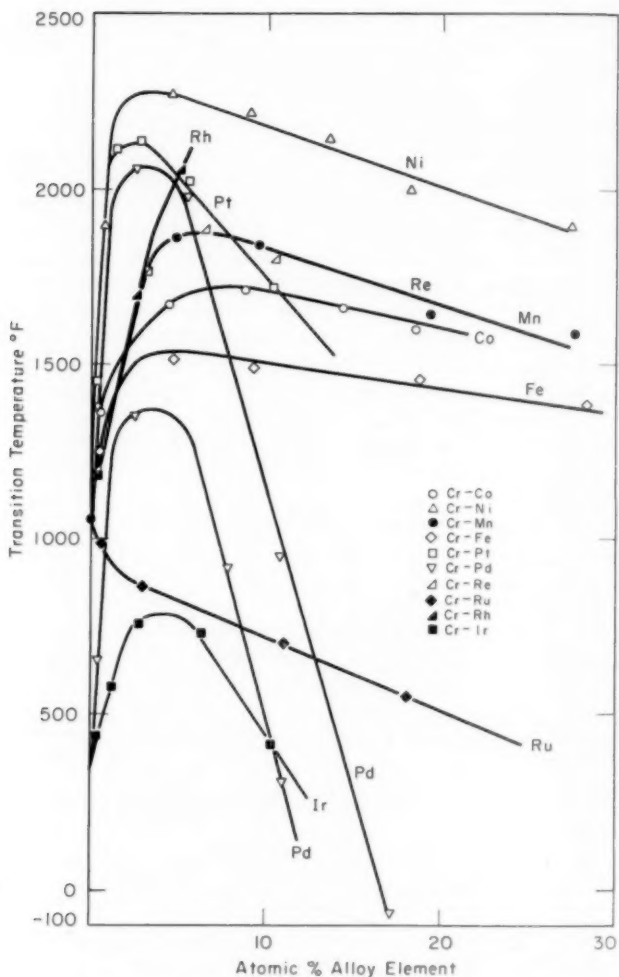


Fig. 2—Transition Temperature for 65 Degree Bend Versus Atomic Percent Alloy Addition. Curves are for two grades of chromium.

continuous brittle phase was not formed. The elements palladium, iridium, ruthenium and platinum brought about the greatest decrease in transition temperature.

DISCUSSION

As can be seen in Fig. 3A and Table II, the initial change in transition temperature is not a function of the atomic size. Elements having

Table II
Summary Data for Chromium Alloy Systems Investigated

System	Sol. in Cr at 900° C at. %	Compound	Intermetallic	Type	At. % for Max. T, T	Goldsch. At. rad.	Initial slope of transition Temperature per at. %	
							Initial	Final
Cr-Ti	16.05 (13)	TiCr ₃ (13)		MgCu ₃	*	1.47	4,100	**
Cr-V	69 (4)	—		σ	*	1.36	2,050 (est.)	**
Cr-Mn	100	CrMn ₃		σ (V ₃ Ni ₂)	6	1.18	510	16
Cr-Fe	10.75 (8)	—		σ	4	1.28	540	17
Cr-Co	13.5 (9)	Cr ₃ Co		σ	7	1.23	550	17
Cr-Ni	1.73 (12)	ZrCr ₃ (12)		MgCu ₃ , MgZr ₃	3	1.23	1,000	**
Cr-Zr	107.9 (4)	NbCr ₃ (11)		MgCu ₃	*	1.60	4,500	**
Cr-Nb	18 (10)	RuCr ₃		σW type	*	1.47	1,600	**
Cr-Ru	5.5 (10)	57-86 wt. % Rh		h.c.p.	2	1.40	770	**
Cr-Rh	1.5 (7)	PdCr (570° C)		i.c.c.	*	1.34	280	**
Cr-Pd	1.5 (4)	TaCr ₃ (11)		MgCu ₃ , MgZr ₃	2	1.37	525	150
Cr-Ta	—	Cr ₃ Re ₃		σ	*	1.47	2,200	**
Cr-Re	2.5 (10)	IrCr ₃		σW type	6	1.38	560	16
Cr-Ir	2.5 (10)	PrCr ₃		NiMn	4	1.35	270	94
Cr-Pt	4 (4)	Miscibility gap			3	1.38	790	**
Cr-W	—				*	1.36	1,100	**

*Temperature for maximum transition temperature above 2200°F

**Not noted in this investigation

Numbers in parentheses are references

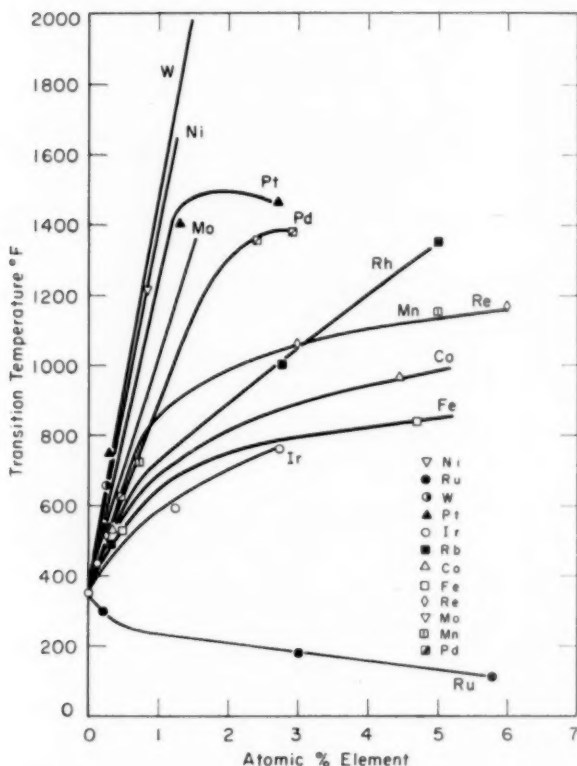


Fig. 3A—Initial Transition Temperature for 65 Degree Bend Versus Atomic Percent Alloy Addition.

approximately the same atomic size as chromium, such as iron, cobalt, and nickel, exhibited marked differences in their effects. An even greater contrast between the effects of elements with the same size was noted between ruthenium and rhodium. The former element decreased and the latter increased the transition temperature.

Fig. 3B shows similar lack of atomic size effect. Incidentally, the different transition temperature values listed for pure chromium are due to differences in initial content of oxygen, carbon and nitrogen. In Fig. 3B it will be noted that the slopes of the curves for carbon and silicon additions on the one hand, and boron and aluminum on the other hand, are approximately the same. This is especially interesting when one considers that carbon and boron are interstitial alloying elements and aluminum and silicon are substitutional.

Ruthenium was the only metal investigated which decreased the

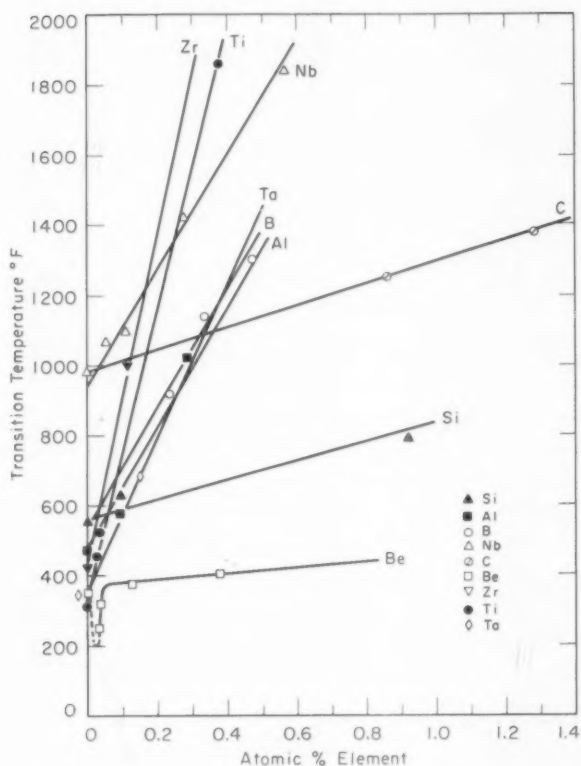


Fig. 3B—Initial Transition Temperature for 65 Degree Bend Versus Atomic Percent Alloy Addition. Variety of chromium grades used as addition base.

transition temperature of chromium with the very first small additions. The decrease shown for beryllium additions was due to the scavenging effect on oxygen and nitrogen. Similar initial decreases in transition temperature were observed due to additions of titanium, aluminum, zirconium, and other strong deoxidizing and denitrifying elements to chromium of high transition temperature (about 1000 °F) (5).

The chromium-palladium alloys in Fig. 2 indicate that the transition temperature of a binary alloy is dependent on the transition temperature of the original chromium as well as on the particular alloying element. The slope of the curve was retained from one grade of chromium to another, but was transposed by an amount equal to the difference in the transition temperatures of the chromium grades. This result places added importance upon the further purification of chromium

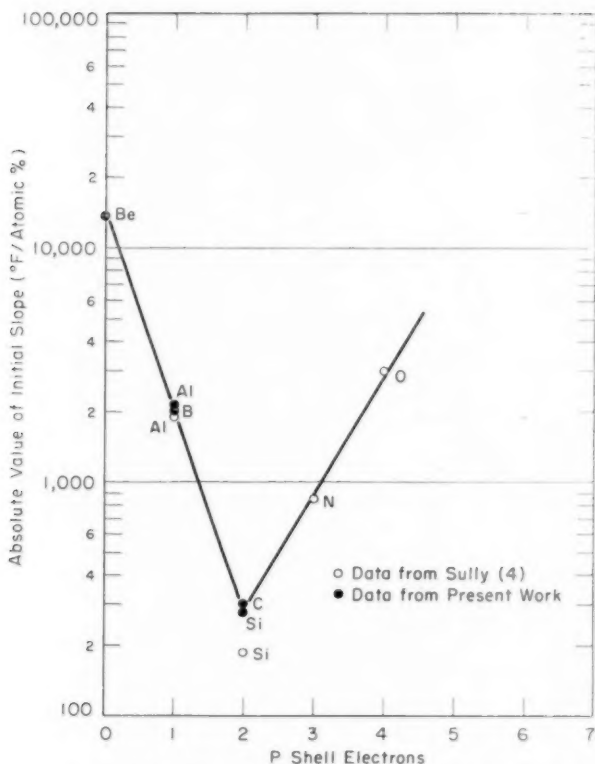


Fig. 4—Initial Change in Transition Temperature with the Addition of Elements with Unfilled P Shells.

to lower the transition temperature as low as possible and thus lower the alloy transition temperature.

The rate of transition temperature increase is periodic in nature, depending upon the outer electron configuration of the solvent and solute atoms. This is seen in Figs. 4 and 5. The smallest effect on the 65-degree bend transition temperature occurred for metals in the transition series having an outer configuration of 8 electrons. For example ruthenium (d^7s^1) has the smallest effect, and iron (d^6s^2) has a slightly larger effect; (see Fig. 5). In the case of materials with unfilled S and P shells, the smallest effect on transition temperature is noted for a configuration of 4 electrons, carbon and silicon both having p^2s^2 ; (see Fig. 4). A similar effect was noted when this approach was applied to data obtained on molybdenum (6).

Of interest is the effect of the change of one electron from the S shell

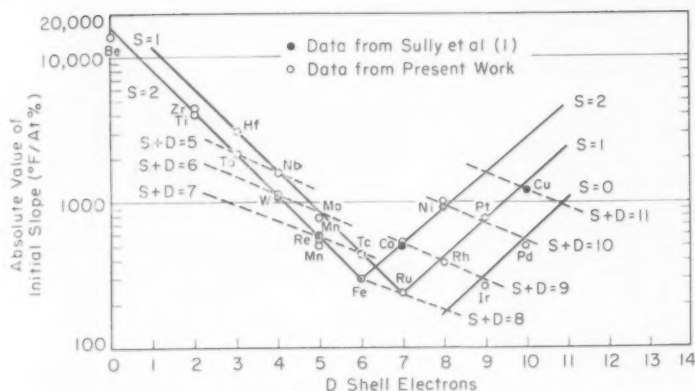


Fig. 5—Initial Change in Transition Temperature with the Addition of Elements with Unfilled D Shells.

to the D shell as in the case of iron and ruthenium. Iron raised the transition temperature while ruthenium lowered it. Fig. 5 is especially clear in showing the additive effect of S and D electrons on transition temperature.

A correlation was found among the data for elements with unfilled D shells and unfilled P shells with the initial rate of change in transition temperature. This is shown by comparing Figs. 4 and 5. It would be expected that an extrapolation to zero P shell electrons would be the same as an extrapolation to zero D shell electrons; the element concerned is beryllium. The figures show that, within experimental error, the agreement is quite good.

It can easily be seen that, similar to the initial change in transition temperature, the maximum transition temperature is not a function of the atomic size of the added element. Furthermore, an examination of the data in Table I makes it doubtful that the extent of solubility of the second element in chromium is a primary factor. Although the maximum temperature occurred near the solubility limit for Cr-Pt and Cr-Ir, a maximum was also found in the region of solid solubility in the Cr-Fe and Cr-Ru systems, and beyond the solubility limit in the Cr-Pd alloys.

From Fig. 6 it would appear that the best relationship that can be found among the transition metals is between the maximum transition temperature and the initial slope of transition temperature versus atomic percent solute. The particular curve shown in Fig. 6 will maintain the same slope but will change its intercept depending on the transition temperature of the chromium used to make the binary alloy.

The decrease in transition temperature following the maximum does not appear to be affected by intermetallic compound formation,

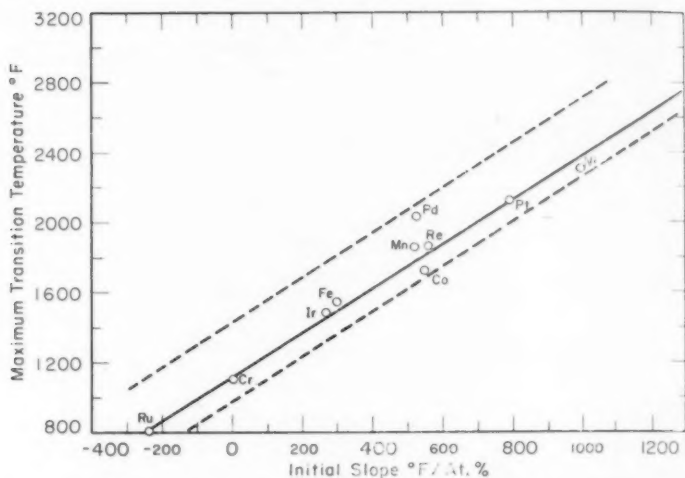


Fig. 6—Initial Slope (From Figs. 2 and 3) Versus Maximum Transition Temperature Achieved. Curve based on the use of chromium with a transition temperature of 1050 °F.

or lack of its formation, provided the compound does not form a continuous phase. The alloys of Cr-Fe and Cr-Mn investigated are solid solutions and show a gradually decreasing transition temperature slope. On the other hand Cr-Pt, which contained an intermetallic compound, had a much greater slope. Finally, Cr-Rh, which forms a continuous intermetallic phase in the microstructure, does not exhibit a maximum transition temperature or a decreasing transition temperature slope. (The point for rhodium in Fig. 7 represents its probable position on the assumption of a noncontinuous second phase in the structure).

The formation of a second ductile phase is not necessary for lowering the transition temperature. If, however, the second phase is the continuous phase, there may be no discontinuity in the transition temperature slope (note Cr-Pd). In comparing Cr-Ni and Cr-Pd, it was found that there was a very large difference in their slopes, although both systems form ductile second phases.

It is not to be construed that the slope of the decreasing transition temperature as a function of atomic percent solute can be extrapolated to 100% of solute. Extrapolation becomes impossible when a continuous intermetallic network is involved or when a large amount of a second phase is present (that amount and its distribution cannot as yet be accurately defined or predicted).

The effect of an abundance of solute atoms on the brittle to ductile transition temperature is opposite to the effect of a few solute atoms. In the latter case an increase in transition temperature with increasing

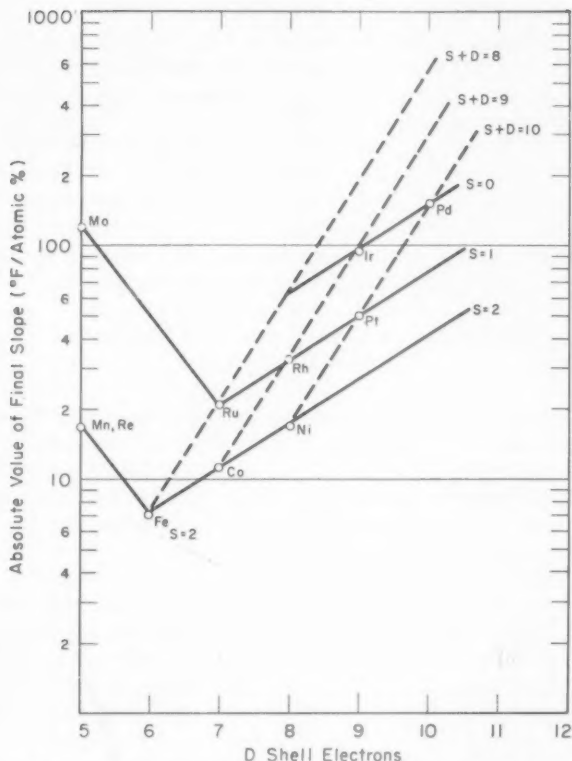


Fig. 7—Final Change in Transition Temperature with the Addition of Elements in the Transition Series.

solute content was noted; in the former case a decrease is noted. Both cases exhibit a periodicity which is dependent upon the configuration of outer electrons of the solute atoms as shown in Figs. 5 and 7. It will be seen that the curves representing various values for D shell electrons at constant S shell levels plot as straight line segments. The angles formed by these segments remain constant for both increasing and decreasing slope. These plots differ in two respects: first, in the magnitude of absolute value of slope and, second, in the relative positions of the elements in Group VIII. The latter difference can be seen by close comparison of Figs. 5 and 7. It will be seen that whereas nickel, platinum and cobalt additions to chromium cause the greatest initial change in transition temperature, palladium and iridium cause the greatest final change. This difference is roughly equivalent to a rotation of 180-degrees about an axis passing through the elements iron, ruthenium and palladium.

The data of Sully et al. (1) were of considerable support in establishing confidence in the curves used in Figs. 4 and 5. It will be noted that there is excellent agreement between their data and the present results. Sully et al. unfortunately did not extend their alloying investigation to higher compositions.

THEORY

A definition of the brittle to ductile transition temperature is that temperature at which some degree of ductile behavior (arbitrarily selected) is first noted. At a given strain rate for a given alloy, the temperature is variable depending upon whether the specimen is as-cast, worked or annealed. Past experience has shown that the as-cast condition invariably exhibits the highest transition temperature.

The phenomenon of transition temperature has been noted in all body-centered cubic metals, and occasionally in face-centered cubic metal alloys. The former metals are particularly interesting due to their 48 slip systems which necessitates cooperative slip for deformation.

Body-centered cubic metals of very high purity have exhibited transition temperatures approaching absolute zero. From this it must be deduced that their usual high transition temperatures are due to certain solute elements which are normally present.

In a body-centered cubic metal, any solute atom present interacts with its nearest neighbors, all of which lie in planes of slip. Slip may be inhibited on several planes directly, and on many more indirectly due to the need for co-operative slip. The data presented would indicate that there is an interaction of the bonding electrons of the solute and solvent which in some manner contributes to an increase in transition temperature for brittle fracture. The effect on the transition temperature is not a major function of the total number of electrons per atom, atomic size or position of the atom in the lattice. The solute-solute and solvent-solvent force fields are generally weaker than the solute-solvent force field. The interaction strength is a prime function of the number and position of the outer electrons in both elements.

With the foregoing postulations, we may then picture the transition temperature as that temperature at which the interaction force field is sufficiently weakened to allow deformation to take place. As the number of solute atoms is increased, an increase in thermal energy is needed to weaken the additional force fields. This therefore results in a higher transition temperature.

As the number of solute atoms increases, there is a higher probability of several solute atoms becoming nearest neighbors. This decreases the number of interactions between solute and solvent and hence the temperature will not rise as rapidly with solute atom additions or will start to decrease. The generally weaker solute-solute interaction may further decrease the transition temperature. In cases where two different solute

atoms are present in small amounts, their effect on the transition temperature of the alloy will be additive, provided there is no compound formed between the two solute elements.

CONCLUSIONS

Based on studies of as-cast chromium binary alloys with an arbitrary 65° bend angle as a measure of transition temperature, the following conclusions are drawn:

1. A characteristic transition temperature for brittle to ductile fracture has been noted for binary alloys of chromium with elements having unfilled S and D shells and unfilled S and P shells. There is a rapid increase in transition temperature with increasing alloy content to a maximum, after which there is a decrease in transition temperature with further additions.

2. An exception to the above is the case of Cr-Ru in which an immediate decrease in transition temperature is observed.

3. Another exception is the lack of a maximum or decreasing transition temperature when a continuous brittle intermetallic phase forms.

4. The transition temperature versus percent alloying content curves shift up or down as the transition temperature of the chromium is varied, however the curves appear to stay parallel.

5. A relationship has been observed between the rate of increase of transition temperature or the rate of decrease of transition temperature with the configuration of the bonding electron of the solute element.

6. Evidence is shown that room temperature ductile alloys based on chromium can be achieved if the transition temperature of the starting chromium is sufficiently low. Such alloys will fall in the 60 to 90% chromium range.

References

1. A. H. Sully, E. A. Brandes and K. W. Mitchell, "The Effect of Temperature and Purity on the Ductility and Other Properties of Chromium," *Journal, Institute of Metals*, Vol. 81, 1953, p. 585.
2. H. L. Wain, F. Henderson and S. T. M. Johnstone, "A Study of the Room Temperature Ductility of Chromium," *Journal, Institute of Metals*, Vol. 83, 1954, p. 133.
3. W. H. Smith and A. U. Seybolt, "Ductile Chromium," *Journal of the Electrochemical Society*, Vol. 103, 1956, p. 347.
4. A. H. Sully, *Chromium*, 1954, Academic Press, Inc., New York.
5. E. P. Abrahamson, II and N. J. Grant, "Transition Temperatures of Chromium and Chromium Base Alloys," to be published.
6. J. Wulff, Private communication.
7. E. Raub and W. Mahler, "Die Palladium-Chrom-Legierungen," *Zeitschrift für Metallkunde*, Vol. 45, Part II, 1954, p. 468.
8. E. P. Abrahamson, II and N. J. Grant, Unpublished data.
9. C. Stein and N. J. Grant, "Chromium-Rich Portion of the Chromium-Nickel Phase Diagram," *Transactions, American Institute of Mining and Metallurgical Engineers*, Vol. 203, 1955, p. 127.
10. E. Raub and W. Mahler, "Chromium Alloys with Platinum, Iridium, Rhodium, and Ruthenium," *Zeitschrift für Metallkunde*, Vol. 46, No. 3, 1955, p. 210.

11. P. Duwez and H. Martens, "Crystal Structure of $TaCr_2$ and $CbCr_2$," *Transactions, American Institute of Mining and Metallurgical Engineers*, Vol. 194, 1952, p. 77.
12. D. J. McPherson and M. Hansen, "System Zirconium-Chromium," *Journal of Metals; Transactions, American Institute of Mining and Metallurgical Engineers*, Vol. 197, 1953, p. 279.
13. F. B. Cuff, Jr., N. J. Grant and C. E. Floe, "Titanium-Chromium Phase Diagram," *Transactions, American Institute of Mining and Metallurgical Engineers*, Vol. 194, 1952, p. 848.

DISCUSSION

Written Discussion: By Daniel Maykuth and R. I. Jaffee, Battelle Memorial Institute, Columbus, Ohio.

In view of the exceptional correlation between mechanical behavior and electronic structure of chromium-base alloys noted by the authors, as shown by Fig. 5, it is appropriate to examine the methods and materials used. It is rare that such a remarkable correlation is achieved in experimental metallurgical studies.

Fig. 1, which was inserted in the paper with no explanatory notes, shows that increasing the nitrogen content of chromium from 0.008 to 0.015% lowers its ductile-to-brittle bend transition temperature. These data, if correctly presented, are in direct conflict with the separate works of Wain, Smith, and Seybolt in which the embrittling effect of nitrogen in chromium was clearly established.

The authors determined bend ductility using a hand brake with no control over strain rate except that of the operator's judgment. Also, the radius of the load rod contacting the specimen was not mentioned, nor were the specimen dimensions mentioned.

The authors justify the use of variable strain rates in bend testing on the basis of Sully's work which was carried out with a selected lot of chromium that had a much lower transition temperature (122 °F) than that of any of the material used in the present work. The authors, thus, assume that the strain rate sensitivity of chromium is independent of the metal's purity as well as alloy composition. We question the validity of this assumption, particularly in view of current work by the Armour Research Foundation for the Air Force which has shown that the ductility of chromium, with a tensile transition temperature of 690 °F, is very sensitive to strain rate.

The authors state that, while the transition temperature versus per cent alloy content curves shift up or down as the transition temperature of chromium is varied, the curves appear to stay parallel. However, the only evidence furnished to support this conclusion are the curves for the Cr-Pd alloys. On the other hand, visual comparison of the slopes of the curves presented in Figs. 2 and 3a for palladium, cobalt, iron, rhodium, rhenium, and manganese shows that the relative effects of these metals are not the same in two of the different chromium bases used. Further, the relative order of these metals, arranged in the order of decreasing slopes using the values in Table II is not consistent with the slopes indicated for these metals in either Fig. 2 or Fig. 3a. In view of these inconsistencies, it is not at all clear as to how the slope values listed in Table II were obtained.

The authors state that good agreement was obtained in comparing their data with those obtained by Sully. However, a spot check of Sully's data fails to support this statement. For example, the calculated initial slope value for the Cr-W

system (based on the curve presented in "Chromium," A. H. Sully, Academic Press, Inc., Fig. 63, p. 136, 1954) is 950 °F per atom %. This value indicates that the plotted points for tungsten in Figs. 3a and 5 should fall below the points for nickel instead of above them as indicated in these figures.

Additional errors in plotting the data of Fig. 5 include the erroneous representation of both iridium and platinum as having 9 d shell electrons since these metals have, in fact, 7 and 8 d shell electrons, respectively. Also, the rhodium data point is plotted for a slope value of about 400 °F per atom % while Table II indicates this value should be 280 °F per atom %. Further, the graphic representation of slope for the Cr-Ru system in Fig. 5 fails to take the negative value of this slope into consideration. The significance of absolute slopes covering positive or negative values is not clear.

There appear to be serious questions concerning the accuracy of the transition temperatures reported. It would follow that the slopes of the curves of transition temperature versus alloy content would be further in error, particularly since many curves were based on only two data points.

Considering only these errors and inconsistencies, it is apparent that the correlations of electronic configuration and bend transition temperature are not nearly so concise as indicated by the authors in Figs. 4 through 7, inclusive. Indeed, it is questionable whether any firm correlation between these parameters can be proven on the basis of the data presented in this paper.

Written Discussion: By Peter R. Kesting, director, Metallurgical and Engineering Sciences Division, Office of Ordnance Research, U. S. Army, Duke University, Durham, North Carolina.

This paper by Messrs. Abrahamson and Grant is considered to be very stimulating. It suggests that the actual electron configuration of the solvent and solute atoms affect the ability for deformation to take place. When the paper is studied with the help of a periodic table of the elements, such as that given in the ASM Handbook, the need for further careful study of this sort is immediately apparent.

Early in the paper, the statement was made that the addition of a second element to chromium raised the brittle to ductile transition (b-d-t) temperature. The experimental evidence negates this statement somewhat because, first, there was one element which caused a decrease with the very first small additions and, second, there was another element and, perhaps, there were at least three more which caused a decrease when added to chromium of high b-d-t temperature before the usual effect of increase was noted. The development metallurgist has been interested in the latter aspect and has frequently demonstrated that the addition of small amounts of a third element to a commercially pure chromium-base binary alloy was beneficial. As indicated in the paper, the reasons for this benefit are different from the effect being studied by the authors.

The indications in the paper are that the best as-cast chromium had a b-d-t temperature when measured by bending to an angle of 65 degrees, of 350 °F. Data were used from chromium having b-d-t temperatures as high as 1050 °F. The ability of the authors to bring order out of this vast variation is noteworthy.

In Fig. 2, ruthenium is shown to cause a decrease in b-d-t temperature, which decrease is continuous with increasing alloy addition up to 15%. The slope of the curve should be negative at all times. The data in Fig. 3a indicates the same is so using chromium of another purity and additions up to about 6%. This is in conflict with the information in Table II, which indicates a positive final slope like the

initial slopes of all of the other elements. Table II also indicates that the final slope of the curves for such elements as Pd, Ir, Fe, Co, Mn, Ni are positive, whereas they are negative in Fig. 2. It is unfortunate that there is no full explanation of the data listed in Table II.

Authors' Reply

As noted by Maykuth and Jaffee, Fig. 1 contained a typographical error which has been corrected. These data are in agreement with that of Wain, Smith and Seybolt. However, this plot was included not so much to indicate the effect of nitrogen as to show typical bend test data.

Though there was no exact control over strain rate, except the operator's judgment, retrials of many heats showed the data to be in good agreement with the original data ($\pm 30^\circ\text{F}$). The specimen size was one-eighth inch O. D. while the rod contact radius was one-eighth of an inch.

In regard to the findings of Armour Research Foundation on the effect of strain rate upon transition temperature, there appears to be an effect of the type of test. . . . "The transition temperature of this grade of chromium thus appears to be dependent upon the type of stress system to which it is subjected, and in the case of torsion, to the grain size of the material."²

The experiment with two series of Cr-Pd alloys was considered a critical experiment based in part upon the retention of initial slope upon changing the type of chromium. Unfortunately, the difference in scales and the reduction in size from the originals of Figs. 2 and 3 may make these appear to be a difference. A check with the experimental data, however, has not shown this to be so.

The authors appreciate the discovery of the misprint in Table II. The initial slope for Cr-Rh should read 450. In checking the original graphs, it was found that there is complete agreement with Table II, other than the correction noted.

In comparing this work with that of Sully, Brandes and Mitchell,³ the authors did not derive the values used in Figs. 4 and 5 from the curves, but rather by changing Sully, et al's data in Table II to degree Fahrenheit and atomic % addition. This data was then plotted in a manner similar to Figs. 3a and 3b. A check of this data has been found to agree with Fig. 5.

As to configurations in the ground state of the free atom used in this work, the values used were obtained from the latest source available.⁴

The term "absolute slope" used in this paper is in keeping with mathematical terminology, i.e., the values shown may be either positive or negative. In a plot of the type of Fig. 5, it would be impossible to show both positive and negative values in any other way.

We thank Dr. Kosting for having brought to light the oversight concerning final slopes. Listed in Table II, all values shown should be negative.

The data in Table II are a compilation of the results of this work plus information concerning the atomic size, solubility and structures of any second phase concerned. All three of these subjects are discussed generally in the paper and the data has been noted for the reader's comparison.

The statement that the addition of a second element to chromium raises the

² A. G. Metcalfe and S. A. Spachner, Armour Research Foundation, Project No. B082, "Mechanical Properties of Unalloyed Chromium," Quarter Report No. 9, p. 8.

³ A. H. Sully, E. A. Brandes, and K. W. Mitchell, Institute of Metals, *Journal*, Vol. 81, 1953, p. 585.

⁴ C. Kittel, "Introduction to Solid State Physics," John Wiley & Sons, Inc., 2nd Ed., New York, 1956, p. 66.

b-d-t temperature was made in regard to the conclusions of Sully, Brandes, and Mitchell⁴ in the introduction. In our work, however, we have stated "that with the exception of ruthenium and beryllium, the addition of all other solute atoms investigated initially raised the transition temperature". The initial effect of beryllium was later explained to be that of scavenging the oxygen and nitrogen from the chromium.

EFFECT OF MICROSTRUCTURE AND HEAT-TREATMENT ON THE MECHANICAL PROPERTIES OF AISI TYPE 431 STAINLESS STEEL

BY G. E. DIETER

Abstract

Transverse tensile tests on commercial forgings of AISI Type 431 stainless steel show that the transverse ductility is considerably improved when the steel does not contain delta-ferrite stringers. Ordinary Type 431 steel with ferrite stringers does not possess adequate transverse ductility when heat treated to a tensile strength of 200,000 psi. Examination of the deformation process indicates that the low ductility is the result of localized cracking in the ferrite stringers. The ductility of a ferrite-free steel may also be affected by carbide precipitation at grain boundaries. The yield strength depends on the amount of retained austenite present in the microstructure. (ASM International Classification: Q27a, 2-14, 3-21; SS)

INTRODUCTION

MANY CRITICAL applications in chemical equipment, aircraft, and ordnance require a material of construction with high strength and good corrosion resistance. Frequently the strength requirement exceeds that obtainable with austenitic or ferritic stainless steel and it is necessary to use one of the martensitic stainless steels. AISI Type 431 (16% Cr, 2% Ni), the British-developed "two-score" alloy (1),¹ is one of the most potentially attractive steels in this class because it provides the highest corrosion resistance of this series of alloys (2) and is capable of providing mechanical properties equivalent to those of low alloy steels with about the same carbon content.

However, there are a number of factors which have restricted the widespread use of this material. The tempering behavior of Type 431 stainless steel is shown in Fig. 1. These curves are typical of those published in the literature. The rapid drop in hardness over a narrow temperature range makes it very difficult to control the hardness by heat treatment. In effect, this steel has two heat treated conditions, a

¹ The figures appearing in parentheses pertain to the references appended to this paper.

A paper presented before the Thirty-Ninth Annual Convention of the Society, held in Chicago, November 4-8, 1957. The author, G. E. Dieter, is Research Engineer, Engineering Research Laboratory, E. I. duPont de Nemours & Co., Inc., Experimental Station, Wilmington, Delaware. Manuscript received March 18, 1957.

Table I
Compositions of AISI Type 431 Steels Investigated—Weight Per Cent

Steel	Approx. Per Cent Ferrite	C	Mn	P	S	Si	Ni	Cr	N
A	10%	0.15	0.88	0.014	0.012	0.43	2.12	16.82	0.008
B	1%	0.16	0.51	0.014	0.015	0.42	2.16	16.22	0.011
C	Variable	0.16	0.46	0.015	0.010	0.49	2.23	16.15	0.011
D	<1%	0.15	0.68	0.017	0.013	0.37	2.17	15.87	0.075

high hardness condition resulting from a low temperature tempering treatment or stress relief at 400–800 °F and a low hardness state resulting from tempering above 1100 °F. In the low hardness condition the strength properties are not particularly attractive, while in the high hardness condition the ductility is apt to be low. The ductility in the transverse direction of forgings is particularly poor at high strength levels. This limits the use of this material in many applications where the principal tensile stresses occur in the transverse direction.

Most commercially produced Type 431 stainless steel contains an appreciable amount of delta ferrite as a microconstituent. These ferrite regions become elongated during hot working and produce a highly anisotropic structure. The high alloying additions in this steel result in a low M_s temperature and a relatively stable austenite phase, so that appreciable amounts of austenite are retained after quenching and tempering. Both delta ferrite and retained austenite can have appreciable effects on mechanical properties.

The transverse tensile properties of a number of commercial forgings of Type 431 stainless steel, which were heat treated to a tensile strength of over 200,000 psi, were determined. The steels contained different amounts of delta ferrite, and the transverse ductility was correlated with the amount of this microconstituent. The mechanism of deformation in this multiphase structure was studied as further confirmation of the importance of ferrite stringers in controlling the transverse ductility. The effect of retained austenite on the tensile properties and heat treatments for minimizing retained austenite were studied.

EXPERIMENTAL PROCEDURE

Commercial forgings of Type 431 stainless steel were obtained from three suppliers. The chemical compositions and approximate percentage of delta ferrite in these steels are given in Table I. Steels A and D were obtained in the form of 5-inch diameter bars. Steel B was a forged slab with a cross section of 1.5 by 4.5 inch, while steel C was a 4-inch square forged billet. Steels A and C were reduced approximately 5:1 by forging. The forging reduction was approximately 12:1 for steels B and D.

Longitudinal and transverse tensile tests were made on steel A to determine the properties of a large forging of Type 431 stainless steel

Table II
Tensile Properties for Steel A As Function of Tempering Temperature

Tempering Temperature, °F.	Specimen Orientation	Yield Strength (0.2% Offset), p.s.i.	Tensile Strength, p.s.i.	Elongation in 1 in., %	Reduction of Area, %
A. Data for Specimens Austenitized at 1800 °F.					
500	Trans.	151,000	203,500	10	12.4; 17.5
700	Trans.	171,000	210,200	6	9.4; 11.7
	Long.	171,500	211,000	9	15
800	Trans.	164,000	207,000	11	27; 37
900	Trans.	171,200	215,500	—	2
	Long.	175,000	218,000	8	10.2
1100	Trans.	112,200	142,700	15	43; 44
	Long.	115,000	144,500	17	50
B. Data for Specimens Austenitized at 1900 °F.					
500	Trans.	128,000	210,000	9	12.4; 13.1
700	Trans.	133,600	192,700	8	10.9; 11.5
800	Trans.	137,000	200,000	12	18.9
900	Trans.	112,000	193,000	—	3.9; 6.3
	Long.	119,000	202,500	9	10.2
1100	Trans.	117,000	152,000	10	14.6; 22
	Long.	115,200	156,500	12	32

containing an appreciable amount of delta ferrite. Steel B represents the first ferrite-free Type 431 steel which was obtained, while the tests on steel D may be considered representative of properties attainable on such a steel in a large section size. In addition, tensile tests were made on other steels for the purpose of illustrating the effect of ferrite stringers on transverse ductility.

Standard 0.252-inch diameter tensile specimens were machined from the bars at half-radius position and from the slab at positions corresponding to one-quarter of the thickness. All specimens were heat treated after machining in a gas-fired muffle furnace with a slightly reducing atmosphere. The specimens were polished before testing to remove oxidation products. Metallographic examination of the cross section of tensile specimens showed no evidence of reaction between the steel and the furnace atmosphere. In view of the known (3) susceptibility of martensitic stainless steels to hydrogen embrittlement, a check was made to see if there was any evidence of embrittlement. No difference could be found between the ductility of specimens heat treated as described above and heat treated in an argon atmosphere. Tensile tests were made with a hydraulic testing machine at a cross-head speed of 0.02 inch per minute. A differential transformer extensometer was used to measure the initial portion of the stress-strain curve. Transverse tensile values are based, in general, on the average of two specimens. Individual values are given for transverse reduction of area (RAT) because of the known scatter in this property.

EXPERIMENTAL RESULTS

Tensile Properties

The tensile properties for steel A, which contained a relatively high percentage of ferrite stringers, are given in Table II. Values are given

for specimens austenitized for 0.5 hour at 1800 and 1900 °F, oil-quenched, and tempered 3 hours at 500, 700, 800, 900, and 1100 °F. The transverse reduction of area is quite low for tempering temperatures below 1100 °F. In fact, the longitudinal ductility is also below the average values to be expected in small section sizes, Fig. 1. The

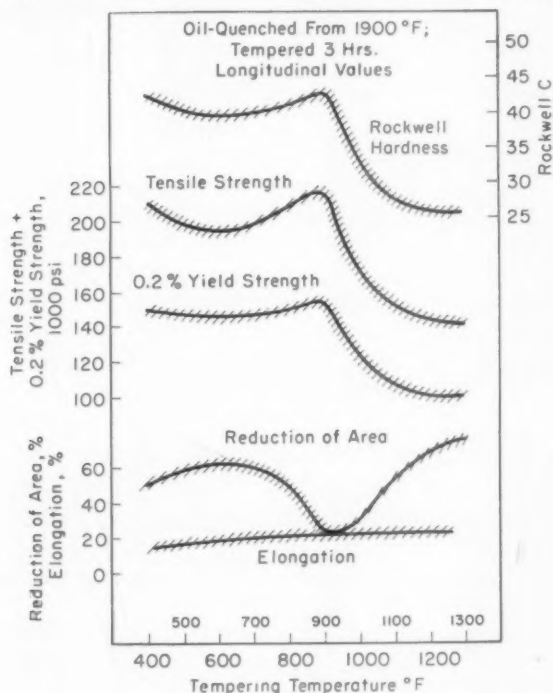


Fig. 1—Typical Trends for Variation of Mechanical Properties of Type 431 Stainless Steel with Tempering Temperature.

yield strength is lower for specimens quenched from 1900 °F than those quenched from 1800 °F. This point will be discussed in more detail later.

Tensile specimens cut from steel B, with the low ferrite content, showed much more encouraging results. Specimens were oil-quenched after 0.5 hour at 1900 °F, and tempered for 3 hours at the temperatures given in Table III. As can be seen from the table, there is still considerable anisotropy in reduction of area values, but the transverse ductility is quite acceptable for the high strength level. Fig. 2 shows that the transverse reduction of area for this material is superior to that of SAE 4340 at high strength levels. The data for SAE 4340 are

Table III
Tensile Properties for Steel B As Function of Tempering Temperature
 (Austenitized $\frac{1}{2}$ Hr. at 1900°F.; Tempered 3 Hrs.)

Tempering Temperature, °F.	Specimen Orientation	Yield Strength (0.2% Offset), psi	Tensile Strength, psi	Elongation in 1 inch, %	Reduction of Area, %
500	Trans.	143,800	212,000	15	32.8; 37.2
	Long.	143,500	214,000	20	61.1
700	Trans.	161,700	212,500	15	36.6; 40.8
	Long.	159,500	213,000	21	60.5
1100	Trans.	111,700	147,500	13	33.4; 34.0
	Long.	111,000	146,000	18	51.3

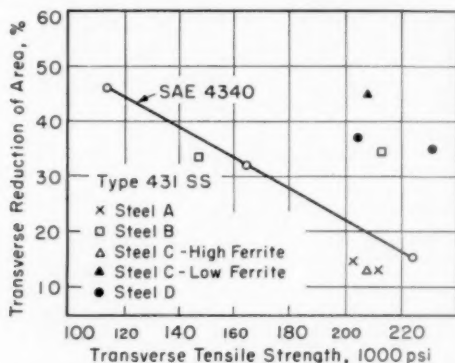


Fig. 2—Relationship of Transverse Reduction of Area to Transverse Tensile Strength.

the average of four values for subsize tensile specimens cut from 5-inch diameter forgings.

A comparison of the data for steels A and B suggests that the poor transverse ductility of Type 431 stainless steel is due to the pressure of ferrite stringers. However, these data do not by themselves present a clear-cut demonstration of the effect of ferrite on ductility, since the two steels had been given quite different forging reductions and the nonmetallic inclusion contents were not the same in the two steels. The inclusion content was appreciably higher in steel B, which had the higher ductility and an almost complete absence of ferrite. Additional evidence for the effect of ferrite on transverse ductility will be given in the next section.

EFFECT OF FERRITE STRINGERS ON TRANSVERSE DUCTILITY

Steel C presented an excellent opportunity for studying the effect of ferrite stringers on transverse reduction of area. A macro-etched disk from this steel showed a rectangular macroscopic segregation pattern of the original ingot. Metallographic examination showed that the segregated region was high in ferrite (Fig. 3a) while the nonsegregated

Table IV
Transverse Tensile Properties for Steel C
(Austenitized $\frac{1}{2}$ Hr. at 1900°F.; Oil-Quench and 3-Hr. Temper at 700°F.)

Position in Billet	Yield Strength (0.2% Offset), psi	Tensile Strength, psi	Elongation in 1 inch, %	Reduction of Area, %
Center Segregated Region-High Ferrite	152,000	206,000	7	13.1; 14.5
Edges-Low Ferrite	153,000	209,000	18	43.5; 48.1

Table V
Tensile Properties of Am 350 Stainless Steel

Heat Treatment	Specimen Orientation	Yield Strength (0.2% Offset), psi	Tensile Strength, psi	Elongation in 1 inch, %	Reduction of Area %
1	Trans.	130,000	164,500	4	2.3; 6.3
	Long.	135,500	174,500	26	56.2
2	Trans.	112,000	141,000	3	2.3
	Long.	128,000	155,000	20	46.8
3	Trans.	113,000	170,000	10	11.3
	Long.	125,500	176,500	22	54.3

Heat Treatments

1. Oil-quenched from 1750 °F, refrigerated at -100 °F for 2 hours; tempered at 880 °F for 2.5 hours.
2. Oil-quenched from 1750 °F, aged at 1350 °F for 1 hour and air cooled; aged at 750 °F for 2.5 hours and air-cooled.
3. Oil-quenched from 1800 °F, refrigerated at -100 °F for 2 hours; tempered 2.5 hours at 750 °F.

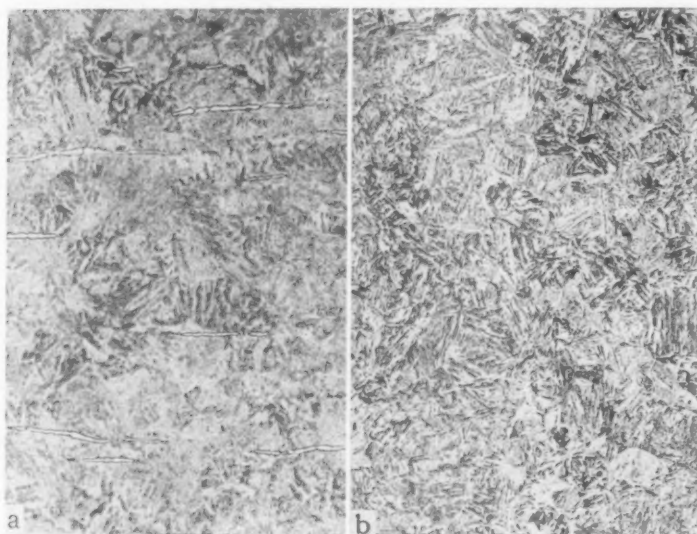


Fig. 3a—Longitudinal Section from Segregated Region of Steel C.

Fig. 3b—Longitudinal Section from Ferrite-Free Region of Steel C. Picral-HC1 etch, $\times 100$.

case was almost completely ferrite-free (Fig. 3b). Transverse tensile specimens were cut from these two regions. The results, after an oil-quench from 1900 °F and a 3-hour temper at 700 °F, are given in Table IV. It can be seen that, for the same steel, there is a considerable improvement in transverse ductility when the steel does not contain ferrite stringers.

An extreme effect of ferrite stringers on transverse ductility was ob-

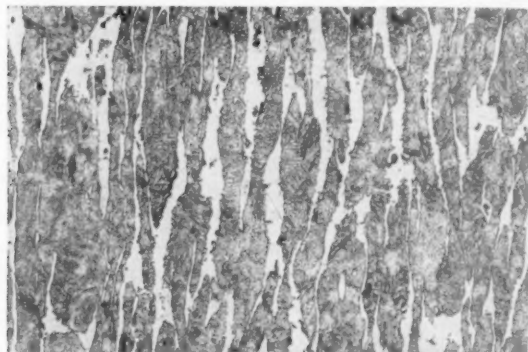


Fig. 4—Longitudinal Section of AM 350 Stainless Steel. Picral-HCl etch, $\times 100$.

served on a 4-inch square forging of AM 350. This alloy does not conform strictly to the Type 431 stainless steel composition*; but, since the microstructure consists of ferrite and tempered martensite, it is felt that the results obtained are pertinent to this study. The microstructure of a longitudinal section through this material is shown in Fig. 4. The structure contains about 20% ferrite. The tensile properties resulting from certain heat treatments are listed in Table V. There is a pronounced anisotropy in ductility, which must be due to the pronounced fibering of the ferrite phase. This material was an experimental forging and may not be typical of the properties of AM 350. In fact, AM 350 in sheet form is reported (4) to be practically isotropic with respect to ductility values. Nevertheless, the data reported above are believed to substantiate the principle that elongated ferrite stringers will seriously decrease tensile ductility in a direction perpendicular to the length of the stringers.

Some idea of the mechanism by which ferrite stringers affect ductility was obtained by tests on flat bend specimens. Specimens were cut from the segregated region of steel C and were oriented so that the ferrite stringers ran either parallel or perpendicular to the direction of

* AM 350 has the following nominal chemical composition: 0.08% C, 0.60% Mn, 0.40% Si, 17% Cr, 4.2% Ni, 2.75% Mo.

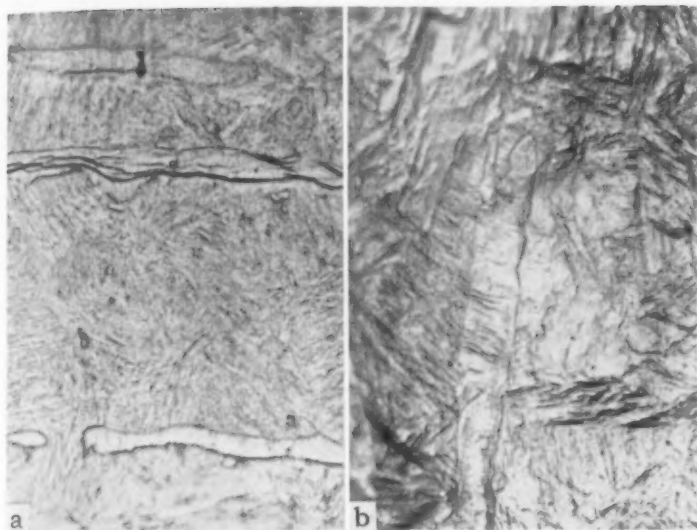


Fig. 5a—Localized Cracking in Ferrite-Stringer in Transverse Bend Specimen. Tensile stress in vertical direction, $\times 750$.

Fig. 5b—Localized Cracking in Ferrite-Stringer in Longitudinal Bend Specimen. Tensile stress in vertical direction, $\times 750$.

the tensile stress. The specimens were supported as simple beams and slowly bent in a testing machine until a crack was observed. Microscopic observations were then made of the deformation on the tension surface of the specimen. Figs. 5a and 5b show that cracks form in the ferrite stringers in a direction roughly perpendicular to the tensile stress and at the interface between the ferrite and the matrix. Slip occurs in the ferrite at a low stress, but it is localized in these regions, and soon develops into fine cracks at strains which are well below those required for extensive deformation of the tempered-martensitic matrix.

It is hypothesized that since the elastic moduli of the stringers and matrix are nearly equal, the transverse stringers do not constitute regions of high stress concentration until the ferrite regions start to deform. Deformation is restricted initially to the ferrite regions, and cracks soon open up. When the fracture stress of the ferrite is exceeded, all of the load is transferred to the matrix, continuity is disrupted, and the matrix experiences a stress concentration approaching that which would result if the ferrite regions were replaced by cavities. At a given strain, the stress in the matrix is greater for a specimen with transverse stringers than for one with longitudinal stringers, so that the transverse specimen reaches its fracture stress at a smaller average strain. Thus, there is a very considerable anisotropy of ductility for a steel with ferrite stringers. When the steel is ferrite-free, this anisotropy

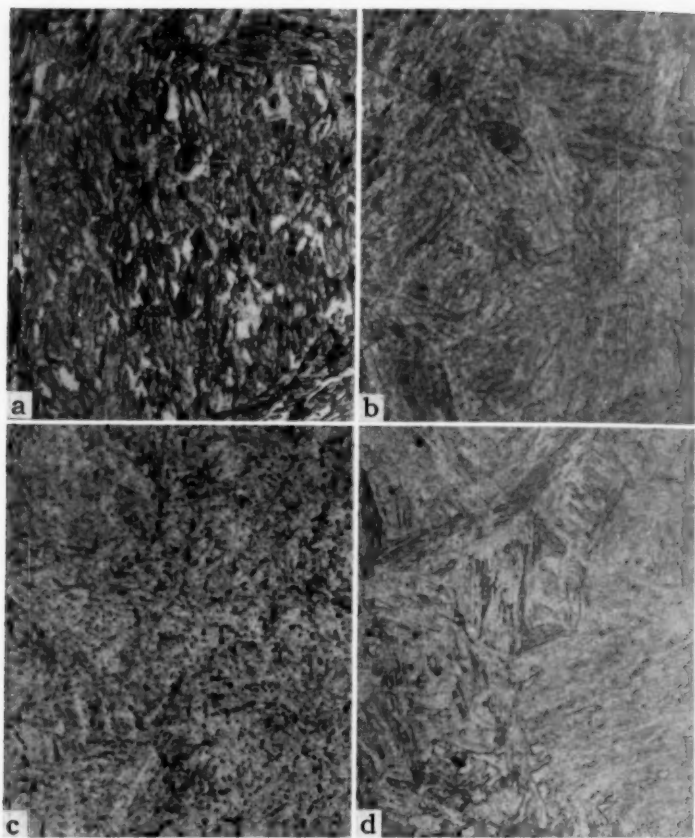


Fig. 6a—Oil Quench from 1900 °F, Tempered 3 Hours at 700 °F.

Fig. 6b—Refrigerated in Liquid N₂ for 2 Hours Between Quench and Temper.

Fig. 6c—Oil Quench from 1800 °F, Tempered 3 Hours at 700 °F.

Fig. 6d—Oil Quench from 1900 °F, Tempered 3 Hours at 700 °F.

is much less, and is due to other factors such as fibering, alignment of inclusions, and preferred orientation, which are not as readily defined.

RETAINED AUSTENITE

The high alloy content of Type 431 stainless steel results in a stable austenite and a fairly low M_s temperature, so that it is not surprising that retained austenite is found after ordinary quench and tempering heat treatments. Fig. 6a shows the microstructure after an oil-quench

Table VI
Transverse Tensile Properties of Steel D

Heat Treatment	Yield Strength (0.01% Offset) psi	Yield Strength (0.2% Offset) psi	Tensile Strength, psi	Elongation in 1 inch, %	Reduction of Area, %
1	105,000	144,300	203,000	16	35.4; 41.7
2	111,500	153,000	207,400	13	24.4; 37.0
3	130,000	173,500	234,000	12	31.8; 39.5
4	123,000	162,000	216,000	8	12.4; 18.2

Heat Treatments

1. Oil-quenched from 1900 °F tempered 3 hours at 700 °F.
2. Oil-quenched from 1900 °F double tempered at 700 °F.—3 hours.
3. Oil-quenched from 1900 °F refrigerated at -100 °F for 2 hours, tempered 3 hours at 700 °F.
4. Oil-quenched from 1800 °F tempered 3 hours at 700 °F.

from 1900 °F and a 3-hour tempering treatment at 700 °F. Austenite regions are readily visible and x-ray diffraction measurements indicate that there is about 30% retained austenite. When refrigeration in liquid nitrogen is used after the quench, the retained austenite is reduced to a low level (Fig. 6b).

It has been shown (5) that retained austenite decreases the yield strength in tension for heat treated low alloy steel. A similar effect was noticed with these steels. Quenching from 1900 °F results in a greater amount of retained austenite than quenching from 1800 °F because of the increased solution of carbon and nitrogen at the higher temperature. The increased amounts of retained austenite have been reported (2) to give higher impact strength when the steel is tempered at low temperatures, but as can be seen in Table VI, the yield strength is lowered when retained austenite is present. Table VI gives the tensile properties of steel D after various heat treatments which would be expected to affect the amount of retained austenite. Double tempering (treatment 2) results in some transformation of retained austenite, but it is not as effective as refrigeration after quenching (treatment 3). The yield-strength values increase with decreased amounts of retained austenite and the ductility is not appreciably affected. Retained austenite can be minimized by austenitizing at 1800 °F, but the ductility is decreased by a carbide precipitation at the grain boundaries (Fig. 6c).

DISCUSSION

These tests have shown that the elimination of delta-ferrite stringers from Type 431 stainless steel (16% Cr, 2% Ni) results in a significant increase in the transverse tensile elongation and reduction of area when the steel is heat treated to a tensile strength of around 200,000 psi. The same situation should exist for other hardenable stainless steels, such as Type 410 and 414, and for precipitation-hardening stainless steels such as 17-4 PH and AM 350 which contain delta ferrite. Because of the nature of the tempering behavior of the 400-series of hardenable stainless steels, it is frequently only possible to use these steels at two levels

of strength. They usually possess adequate ductility in the longitudinal or forging direction of a bar at high strength levels, but, as has been shown in this paper, the transverse ductility is poor when the steel contains ferrite stringers. Elimination of ferrite stringers by the proper balance of composition and careful mill processing results in a steel with good transverse ductility which can be used at a high strength level. This can be quite important in the design of a part, such as a pressure vessel, where the principal tensile stresses act in the transverse direction. As an example, for a pressure vessel with a 2-inch I.D. and an 8-inch O.D., the design equations (6) indicate that the yielding pressure would be increased 25% and the bursting pressure increased 40% when Type 431 stainless steel is used in the high strength rather than the low strength condition. However, good design practice would only permit this steel to be used in the high strength condition if it possessed some usable transverse ductility—and this requires a ferrite-free steel.

It would also be expected that the elimination of ferrite stringers would result in improved transverse fatigue properties. There are some fatigue data for Types 414 and 416 to substantiate this (7), and further work is in progress at this Laboratory.

There are several problems which may be encountered in using ferrite-free Type 431 stainless steel. Retained austenite can be troublesome, particularly when it is necessary to get the highest possible yield strength. Refrigeration may not always be practical as a means of minimizing retained austenite, particularly in large sections where the tendency for quench-cracking is accentuated. There is also some indication that this material may be more notch-sensitive than low alloy steels at a tensile strength of 200,000 psi. Further work on this is needed, particularly to determine the role played by retained austenite.

CONCLUSIONS

1. The transverse reduction of area of Type 431 stainless steel is considerably improved at high strength levels when the steel does not contain ferrite stringers. This should also apply to other hardenable stainless steels.
2. Fracture occurs in the ferrite stringers and results in high stress concentrations in the tempered-martensitic matrix.
3. The transverse ductility is also somewhat sensitive to the quenching temperature, reaching a low value in ferrite-free steel when the austenitizing temperature is one at which a grain boundary precipitation of carbide occurs.
4. Retained austenite reduces the yield strength of this steel. This effect can be minimized by a refrigeration treatment.

References

1. S. P. Watkins, "16-2 Stainless Steel," *METAL PROGRESS*, American Society for Metals, Vol. 44, 1943, p. 99-103.

2. F. K. Bloom, "Effect of Heat Treatment and Related Factors on Straight-Chromium Stainless Steels," *Corrosion*, Vol. 9, No. 2, 1953, p. 56-65.
3. Peter Lillys and A. E. Nehrenberg, "Effect of Tempering Temperature on Stress-Corrosion Cracking and Hydrogen Embrittlement of Martensitic Stainless Steels," *TRANSACTIONS, American Society for Metals*, Vol. 48, 1956, p. 327-367.
4. "Engineering Properties of Precipitation Hardening Alloy-AM 350," Allegheny Ludlum Steel Corporation, Pittsburgh.
5. L. S. Castleman, B. L. Averbach and Morris Cohen, "Effect of Retained Austenite Upon Mechanical Properties," *TRANSACTIONS, American Society for Metals*, Vol. 44, 1952, p. 240-263.
6. J. H. Faupel, "Yield and Bursting Characteristics of Heavy-Wall Cylinders," *Transactions, American Society of Mechanical Engineers*, Vol. 78, No. 5, 1956, p. 1031-1064.
7. H. J. Noble and W. H. Sharp, "Steels and Protective Treatment for Use up to 1000 °F," *Transactions, Society of Automotive Engineers*, Vol. 64, 1956, p. 59-75.

DISCUSSION

Written Discussion: By R. H. Gassner, Chief Metallurgist, Douglas Aircraft Co., Inc., El Segundo, Calif.

The author is to be commended for pointing out the importance of control of microstructure in 431 stainless steel when transverse ductility is required. However, it should not be assumed that elimination of banded ferrite fully guarantees transverse ductility. Our experience indicates a tendency towards overcorrection when producers attempt to eliminate ferrite by rectification of chemical analysis. When this occurs, the resultant banded retained austenite affects transverse mechanical properties similarly.

Material containing banded austenite can be used effectively providing that the banding is detected and eliminated before final heat treatment. The mechanical properties obtained when these precautions are taken (and heat treatment includes refrigeration plus double tempering at 550 °F) are compared in the following table with those for ferrite containing material:

Typical Mechanical Properties of 431 Stainless Steel

% Banded ferrite in tempered martensite	<1		8-10	
	Longitudinal	Transverse	Longitudinal	Transverse
Ultimate tensile strength (ksi)	210	210	185	184
Notched ultimate tensile strength (ksi)	257	256	227	166
0.2% Yield strength (ksi)	154	153	135	123
% Elongation in 2 inches	19	15	20	7
% Reduction of area	60	40	60	13
Izod impact (ft-lbs)	52	23	63	10

Because the austenite banding is a consequence of carbon segregation, alternate bands of high carbon and low carbon martensite result when refrigeration and double tempering are used to ensure complete transformation; satisfactory transverse mechanical properties are not obtained from this structure, probably because

of its heterogeneity. Carbon segregation can be removed from 431 stainless steel before heat treatment by soaking at 2200 °F for three 1-hour periods, cooling in air to room temperature after each soaking period. (The three steps are necessary in order to take advantage of the acceleration resulting from precipitation of $M_{23}C_6$ carbides at the grain boundaries during cooling through the 1250-850 °F critical range.) The resultant large grained structure can be refined, and machinability restored, by soaking at 1550 °F for 30 minutes, air cooling to room temperature, and heat treating to 125-145 ksi.

In order to assure detection of borderline conditions, specimens should always be heat treated prior to microscopic examination; a high tempering temperature should be used and refrigeration and double tempering should be avoided. Of course, final heat treatment should include refrigeration and double tempering to achieve optimum properties.

The author states that *transverse* ductility is lowered by the presence of grain boundary carbides in ferrite-free material. Can it be assumed that longitudinal ductility was not similarly lowered by this condition? Our tests have shown that grain boundary carbides precipitated during slow quenching of ferrite-free material affect longitudinal and transverse ductility approximately equally. Conversely, they do not affect longitudinal ductility of ferrite containing material, but produce more severe transverse brittleness than in ferrite-free steel. This difference is readily explained by the fact that precipitation in ferrite containing material occurs preferentially at the boundaries between the ferrite bands and the matrix while in the ferrite-free material, it occurs at the prior austenite grain boundaries.

Written Discussion: By Edward A. Loria, staff metallurgist, Crucible Steel Company of America, Pittsburgh.

This is one of the first papers to show the transverse tensile properties of a hardenable stainless steel and it will stimulate further study in this important area. Questions have been asked concerning the effect of ferrite on the impact strength, fatigue strength, stress rupture and other properties of the 12 to 16% chromium steels heat treated to high hardness or tensile strength levels. Type 431 appears to be a good candidate in this category of steels, provided that its ferrite content can be removed by controlled nitrogen additions and proper mill processing.

Ferrite formation in type 431 is a function of the austenitizing temperature as well as the composition balance between the ferrite forming elements and the austenite forming elements in its composition. It is surprising that the author has not shown any difference in the % ferrite when the austenitizing temperature is raised. For example, how much was the free ferrite lowered in steel A in the results shown in Table II? In 6 heats of a 12% Cr-Mo-W-V steel containing 15-17% ferrite, when austenitized at 1800 °F, had only 4-12% when austenitized at 1900 °F. In Fig. 2, it is unusual to note that the 1% ferrite steel B had the same RAT value at both the 140,000 psi and 210,000 psi tensile levels.

The addition of nitrogen, coupled with other variations in analysis, can actually produce banded retained austenite in place of banded free ferrite in type 431. Such retained austenite bands are difficult to remove by several annealing treatments and can create analogous problems. Refrigeration will not be practical as a means of minimizing retained austenite in large bars and billets. Would the author comment on the percent retained austenite in steel D, or any other heat containing around 0.10% nitrogen? The retained austenite in Fig. 6a does not appear to be in the form of bands which indicates that this particular material was not severely

worked. Does the author feel that refrigeration will remove banded retained austenite as easily as the uniformly dispersed areas shown in Fig. 6a?

It should be noted that though delta ferrite may be designated as the culprit in lowering certain mechanical properties, it may actually be that segregation, or the partition of the composition in such a way that a duplex structure is produced, may be the important factor and not delta ferrite per se. For example, when delta ferrite is observed, grain boundary carbides, carbide precipitate around ferrite and nonmetallic inclusions are also quite in evidence. The effect of carbide distribution is well known in that the best properties (for example, impact strength) are obtained when the carbides are dispersed randomly rather than along grain boundaries.

Grain size and ductility will bear a close relationship. The presence of some delta ferrite will actually be beneficial in regard to grain coarsening. For example, a martensitic stainless grade containing 15% ferrite avoided grain coarsening even after 4 hours at 2200 °F, whereas severe grain coarsening with decreased reduction of area occurs in ferrite free material when exposed to high temperatures for long periods of time. Could the author comment on the grain size differences between the low ferrite and high ferrite areas which produced the differences in tensile test results of Table IV?

It is surprising that the author did not include any impact test data. The relation of notch ductility to microstructure is supposed to be very good. Free ferrite is not deleterious, for example, to the notch ductility of type 410 for ferrite contents as high as 10%. However, this amount in bands might be lower in transverse tests. Also, it could be noted that notched bar tensile test results might be lower than the smooth bar results plotted in Fig. 1 in the 800-900 °F tempering range and would be the design limit. The author could elaborate on the decrease in impact strength in type 431 (with and without ferrite) within certain tempering ranges. Has he tried slow cooling (furnace) martensitic stainless through the M_s - M_r region, and thereby tempering the martensite as it forms. After a second temper, this procedure may produce better impact properties than a fast cool through the M_s and then reheating for the first tempering treatment.

In all of the test data reported, it would be well for the author to state if the heat treatments were made on tensile test bar coupons cut out of the 4-inch cross sections or were the heat treatments made on the full cross sections? Also, this same question applies to the cases where a refrigeration treatment was employed. The matter of a balanced composition to lower or even eliminate ferrite has been shown to be possible in sections up to 5 inches. The question of being able to do this in larger sections for forging remains to be answered. Since a certain small amount of ferrite can be tolerated, is the author prepared to go so far as to set up a classification chart showing the microstructural limit of banded free ferrite which would be acceptable versus the rejectable amounts of banded free ferrite?

Notched bar fatigue tests would be another good way of showing the detrimental effect of ferrite percentages around 15-20%. Martensitic stainless steels with high per cent free ferrite are particularly notch sensitive in fatigue. In ferrite-free martensitic stainless, the notched bar rupture strength is higher than the smooth bar rupture strength indicating that such steel is not notch sensitive for long holding periods. There are no conclusive data which indicate that ferrite percentages have any effect on the stress rupture properties of longitudinal test bars.

The author shows that a second steel, AM-350, contains 20% ferrite in a 4-inch forging, Fig. 2, and that, consequently, the transverse tensile test ductility is very poor, Table VI. He states that AM-350 in sheet form is reported to be practically isotropic and infers that the sheet product is free of ferrite. Actually, AM-350 sheet still contains 15-20% ferrite and it is claimed that this high amount of ferrite does not lower the transverse properties of continuous mill sheet. Would the author care to comment on this apparent anomaly in line with his localized cracking theory?

Author's Reply

It is encouraging to receive discussion which supplements so well the data presented in this paper. It is hoped that this degree of interest indicates that additional research is in progress to answer some of the problems which limit the use of Type 431 stainless steel in the high-strength condition.

Banded retained austenite can be a problem with ferrite-free 431 steel. Fortunately this was not encountered to any great extent in any of the steels which we studied, although steel D, with the high nitrogen, was the worst in this respect. Mr. Gassner has ably discussed this problem and points out methods for its control. We agree with him that grain boundary carbides would decrease longitudinal as well as transverse ductility.

Mr. Loria has presented a number of specific questions which will be answered in the same order in which they appear in his discussion. No obvious difference was observed in the amount of ferrite in specimens austenitized at 1800 and 1900 °F. The author agrees with the discussor that it is unusual for steel B to have the same transverse reduction of area at 140,000 psi as at 200,000 psi. Only limited data are available at the lower tensile strength, so that it was not possible to check on this point. Questions regarding retained austenite have been partly answered in Mr. Gassner's discussion. The author agrees with Mr. Loria that refrigeration may not be a practical means of minimizing retained austenite in large size sections. We have experienced cracking when bars over 2 in. in diameter containing geometrical irregularities were refrigerated. On the other hand, Mr. Gassner reports what appears to be a successful use of a refrigeration treatment. It would be interesting to know what sizes he is considering.

The grain size in the steels tested varied from ASTM No. 6 or 7 for a ½-hour austenitization at 1800 °F to ASTM No. 5 when austenitized at 1900 °F. No difference in grain size was found between the low and high ferrite areas which produced the differences in tensile ductility shown in Table IV. All of the tensile data are for specimens heat-treated in the form of tensile bar coupons. We do not feel that our tests are extensive enough to establish acceptance limits based on the amount of ferrite stringers. However, we do feel that our results show that a substantial reduction in the amount of ferrite results in optimum transverse tensile properties. Mr. Gassner's data also support this statement.

A limited amount of room temperature impact testing showed that the ferrite-free steels had somewhat higher impact resistance for the same tempering treatment. Again, Mr. Gassner's data illustrate this point. We agree that further tests to establish the effect of heat treatment and microstructure on notch sensitivity are required with this steel.

The author did not mean to infer that AM-350 steel in sheet form does not contain free ferrite. The reason that this sheet material yields isotropic elongation

values in tension is not particularly evident. This behavior is most likely related to the lower restraint to plastic flow of a sheet specimen compared with a cylindrical specimen which permits a more favorable redistribution of stress in the region of the second phase particles. It is also possible that the processing of the sheet results in ferrite particles which are less elongated than in forgings.

EFFECT OF AGING CYCLE ON THE PROPERTIES OF AN IRON-BASE ALLOY HARDENED WITH TITANIUM

BY T. W. EICHELBERGER

Abstract

A study has been made of the effect of various aging cycles on the physical properties of an iron-base alloy hardened with titanium. It has been possible through this work to develop an aging treatment that increases the creep-rupture time for both plain and notch bar specimens. The notch sensitivity of the material in creep has been greatly reduced by this new aging treatment; however, no change has been produced in the room temperature or 1200 °F tensile properties. (ASM International Classification: N7a, J27d, Q3m, Q23s; Fe, Ti)

INTRODUCTION

DURING the past decade the use of age hardening materials in engineering applications has been expanding very rapidly. Several Fe-Ni-Cr precipitation hardening alloys developed during this period for application at elevated temperatures, have been found to be very useful in the manufacture of rotors for jet engines and for bolts in both gas and steam turbines. In an effort to improve the properties of these materials, considerable work has been directed toward the processing variables such as solution treatment time and temperature, and aging time, temperature and cycle. This paper covers the findings of the study involving the aging cycle and the development of a new and improved type of aging cycle.

Several types of aging cycles are in common use in the commercial heat treatment of age hardenable "superalloys" intended for high temperature applications. The first and simplest is aging at a single temperature for a given time. This temperature is usually selected to give substantial hardening in a reasonable period of time, e.g., 20-40 hours (1)¹. A second type of aging is called a "double age". It is characterized by a high initial aging temperature and a lower final aging temperature. The material may be cooled to room temperature between ages or it may be slowly cooled in the furnace in a period of about 1-10

¹ The figures appearing in parentheses pertain to the references appended to this paper.

A paper presented before the Thirty-Ninth Annual Convention of the Society, held in Chicago, November 4-8, 1957. The author, T. W. Eichelberger, is associated with the Metallurgy Department, Westinghouse Research Laboratories, Pittsburgh. Manuscript received May 14, 1957.

hours to the lower temperature (2). The advantages of the double age are more stable hardness and dimensions of the piece in service, a higher aged hardness for a given hardener content, and less effect of hardener content on aged hardness (2). A third type of aging cycle is called a "reversed age." The name was derived from the fact that aging is done first at a low temperature and then at a higher temperature, i.e., the reverse of a "double age". Present commercial practice is to air cool to room temperature between ages.

These aging cycles have been adopted by various companies for a variety of reasons. However, there has not been a clear theoretical or experimental demonstration of the advantages or disadvantages of different cycles. With this in mind, a theoretical approach to the design of an optimum aging cycle was attempted. As a result of these considerations, a new aging cycle has been developed that produces marked improvements in creep and notched-bar rupture properties at elevated temperatures. This cycle will be referred to as the "genuine" * treatment and consists of a reversed age with a controlled rate of heating from the lower to the higher temperature.

Theoretical Considerations

The use of precipitation hardening is not confined to any alloy system or any particular type of alloy but could be used in almost every conceivable alloy base. The only requirement of an alloy to exhibit the precipitation phenomenon is to have a phase which has a decreasing solubility in the matrix with decreasing temperature. The extent of the hardening obtained on aging depends on the following factors:

1. The degree of supersaturation,
2. The lattice parameters of the precipitate and the matrix,
3. The size and shape of the precipitate,
4. The type of lattice of the matrix and of the precipitate,
5. Relative sizes of the solute and solvent atoms.

During precipitation many of the physical, chemical and mechanical properties of the alloy undergo rather marked changes. These changes are too numerous and varied for discussion here, however, there are several excellent references on this subject (3,4,5).

The precipitation reaction is a temperature and time dependent reaction and is controlled by the rates of diffusion, nucleation and growth. The classical theory of this reaction suggests that nucleation occurs when groups of atoms of a size larger than a critical size grow with a decrease in the free energy of the atom group. The use of the term "critical size nucleus" is actually somewhat ambiguous since the critical size is dependent on such factors as: the perfection of the matrix lattice, grain boundaries, inclusion boundaries, slip bands and twins, and prior

* Derived from the descriptive phrase: *General Nucleation, Accelerated Growth*.

precipitations. From visual observations of the growth of nuclei, the critical nucleus size is apparently smallest along grain boundaries and slip bands, and largest inside of the grains. Twin bands appear to be an intermediate case and the relative orientation of grains apparently influences the critical nucleus size along their boundary, with the critical size increasing as the grain orientation relationship approaches that of a twin relationship. It is felt that dislocations and other atomic scale imperfections probably serve as sites for general nucleation within the grain. The term "critical size nucleus" will, therefore, be used to indicate the critical size under each of the above stated lattice conditions.

As the state of supersaturation of the system increases, the size of the critical nucleus decreases. This increase in supersaturation may be accomplished by either a decrease in aging temperature or an increase in solute concentration. A decrease in temperature decreases the amount of free energy required to form a new phase and, therefore, the critical size of the nucleus is reduced. The equations which have been set forth by various investigators to predict the rate of nucleation from a solid solution are not very satisfactory in that one is not able to determine the following information needed for a complete solution:

1. The exact composition of the precipitating particle,
2. The state of strain in the matrix and precipitating particle,
3. The interfacial energy between the matrix and the precipitating particle, and
4. The shape of the precipitating particle.

However, it is known in a qualitative way what results may be obtained by changes in temperature of precipitation for a given solute concentration. The rate of nucleation just below the equilibrium temperature for the solid solution will be very low. This is caused by the large size of the critical nucleus and the small probability that such a large nucleus will form. Precipitation will be localized and the particles will tend to be very large because of the high rate of growth. As the temperature is lowered, the rate of nucleation will first increase because of a decrease in the size of the critical nucleus, but the rate of growth will decrease due to a decrease in the rate of diffusion. The rate of nucleation will continue to increase with decreasing temperature until the rate of nucleation becomes controlled by the rate of diffusion and not by the decreasing of the size of the critical nucleus. The rate of nucleation will then decrease with temperature until the rate of diffusion is so low that the reaction no longer occurs. The rate of growth is controlled by the rate of diffusion at all temperatures and, therefore, always decreases with decreasing temperature.

By the use of this present knowledge of what takes place during precipitation reactions and the understanding of the mode of fracture in

Table I
Chemical Composition

Heat No.	Ti	Mo	Ni	Cr	Mn	Si	C	Al	V	Fe
6929	1.62	3.33	24.8	14.2	1.38	0.76	0.036	0.11	0.068	Balance
6931	2.04	3.33	24.8	14.1	1.38	0.82	0.032	0.12	0.078	Balance
6932	1.72	2.28	24.9	14.1	1.41	0.87	0.032	0.11	0.078	Balance
6966	2.41	3.22	25.2	14.4	1.28	0.74	0.024	0.10	—	Balance
6968	2.63	1.23	25.5	14.2	1.28	0.74	0.02	0.19	—	Balance
6969	1.48	3.40	25.2	14.5	1.17	0.88	0.038	0.06	—	Balance
7040	1.69	3.03	26.4	13.7	1.60	0.71	0.04	0.15	—	Balance

creep, it was felt to be possible to design a new aging heat treatment to improve the creep-rupture properties of some alloys operating at elevated temperatures. The normal mode of fracture at high temperatures during creep is by failure along the grain boundaries or in the material immediately adjacent to the grain boundary. If precipitation takes place at high aging temperatures a continuous hard, brittle phase is formed in the grain boundary with a soft phase immediately adjacent to it in the grain, this soft phase being caused by the diffusion of the hardener content from this area into the grain boundary. The presence of the continuous hard phase at the grain boundary and the adjacent soft phase in the grains makes it very easy for a crack to propagate in this area. Therefore, if this continuous path could be eliminated it should be possible to increase the creep strength of the material.

EXPERIMENTAL PROCEDURE

All of the material used in this work was prepared in the following manner at the Research Laboratories. The virgin metal charge was melted in a 25-pound induction furnace in air and poured into a 2 $\frac{7}{8}$ inches square mold made of 0.038-inch thick sheet metal. The shell is surrounded by sand, rests on a water-cooled copper stool, and is covered with a gas fired hot top. The ingots were all sound and had no porosity or pipe extending below the hot top. After removing the hot tops, the ingots were soaked for 4 hours at 2100 °F (1150 °C) before the first rolling step. The ingots were reduced 30 to 35% during each of four rolling steps from 2100 °F. The ingots were reheated to 2100 °F between steps for periods of 1 $\frac{1}{3}$ to 2 $\frac{2}{3}$ hours to insure complete recrystallization. The next two reductions were made from 1900 °F after 1 hour at that temperature. The reductions were again kept between 30 and 35%. The two final rolling steps were made after the bars had been at 1800 °F for 1 hour. The reductions were 30 and 40% respectively. The final bar size was 5 $\frac{1}{8}$ inch diameter.

Table I gives the chemical analysis of all of the heats used in this study. The basic composition of these heats is very much the same and the only important variables are in the titanium and molybdenum contents. The titanium is varied purposely in this study to show its effect on the heat treatment and properties. The molybdenum content was

varied only because these heats were available for study and some data had already been collected on them for other studies. The only heats in which the molybdenum varies greatly from $3\frac{1}{4}\%$ are 6932 and 6968, and as long as the data from these heats are only compared with data from the same heat no serious difficulties should arise.

The test specimens used in this study are shown in Fig. 1. The specimen shown in Fig. 1a was used for room temperature tensile tests, in Fig. 1b for 1200 °F (650 °C) tensile tests and 1200 °F (650 °C)

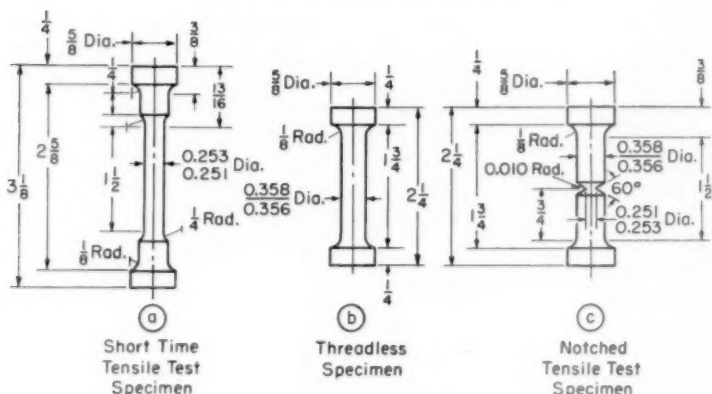


Fig. 1—Test Specimens.

creep-rupture tests, and in 1c for notched creep-rupture tests. The elastic stress concentration factor, K_t , for specimen 1c was 3.35. The specimens were cut and solution treated prior to machining, grinding, and polishing. After polishing the specimens were aged as described.

EXPERIMENTAL RESULTS

In a preliminary program in which the aging reaction was being studied, using heat No. 6932, it was observed that a specimen aged 400 hours at 1200 °F (650 °C) had much better overall creep-rupture properties than specimens given other single and double aging treatments (See Fig. 2). The notch-bar properties given in Table II did not indicate any serious adverse effect of this treatment on the notch sensitivity of the material. It should be noted that as the top aging temperature was lowered, the creep-rupture properties in general improved for both plain and notched-bar tests, with the exception of a slight decrease in notched-bar rupture time for the 400 hours, 1200 °F single age. The band shown by the dashed lines in Fig. 2 and subsequent figures indicates the quality limits of other heats produced at the Research Laboratories and processed in a similar manner with an aging

Table II
Effect of Various Aging Treatments on the Notched-Bar Creep-Rupture Properties of
Heat No. 6932 at 1200°F
All Specimens Solution Treated 1 Hour at 1950°F

Specimen Number	Aging Treatment	Hardness		Load PSI	Rupture Time Hours
		As Aged DPH	After Testing DPH		
3	1	274	295	70,000	83
4	1	299	300	70,000	52
13	1	255	274	65,000	131
14	2	266	278	65,000	290
15	5	262	276	65,000	86
16	6	279	286	65,000	225
17	4	266	272	65,000	126
18	3	258	280	65,000	310
19	1	258	280	65,000	212
20	2	266	283	65,000	276
21	4	269	284	65,000	260
22	3	248	282	65,000	374

Aging Treatment

- 1—20 hours at 1350°F, cool to 1200°F in 4 hours, hold at 1200°F for 20 hours and air cool.
- 2—20 hours at 1300°F, cool to 1200°F in 4 hours, hold at 1200°F for 20 hours and air cool.
- 3—20 hours at 1300°F and air cool.
- 4—16 hours at 1325°F, cool to 1200°F in 3 hours, hold at 1200°F for 24 hours and air cool.
- 5—4 hours at 1400°F, cool to 1200°F in 20 hours, hold at 1200°F for 20 hours and air cool.
- 6—400 hours at 1200°F and air cool.

treatment of 20 hours at 1350 °F (730 °C) cooling to 1200 °F (650 °C) and holding at 1200 °F (650 °C) for 20 hours followed by an air cool. It will be noted that the "quality" of the specimen given the 400-hour age at 1200 °F (650 °C) falls above the previous limits. This type of quality plot has the advantage that the factors of strength and rupture ductility are both considered and the possible exchange of one for the other by processing and composition variables can be evaluated. These results also agree very well with results obtained by Frey, Freeman and White on Inconel X (6), and those by Clauss and Weeton on Stellite 21 (7,8). These data indicated that a finer more evenly distributed precipitate produces a more creep resistant material at elevated temperatures than does a coarse precipitate.

This heat treatment of 400 hours at 1200 °F (650 °C), however, is not commercially practical and, therefore, a way was sought to produce the same results in a shorter length of time. From the previous discussed knowledge of precipitation reactions, it was deduced that it should be possible to use the lower temperatures of 1200 °F (650 °C) to produce a large number of small generally distributed precipitate particles and then by slowly increasing the temperature of aging to allow these precipitated particles to grow more rapidly at an elevated temperature. The heating rate from the nucleating temperature is very critical; if it is too rapid many of the small nucleated particles will become unstable and will redissolve. This has been shown by the occurrence of retrogression in many of the property changes of alloys during rapid heating from a lower to a higher aging temperature.

In line with this reasoning, a series of preliminary experiments was conducted to determine the proper heating cycle. These tests were

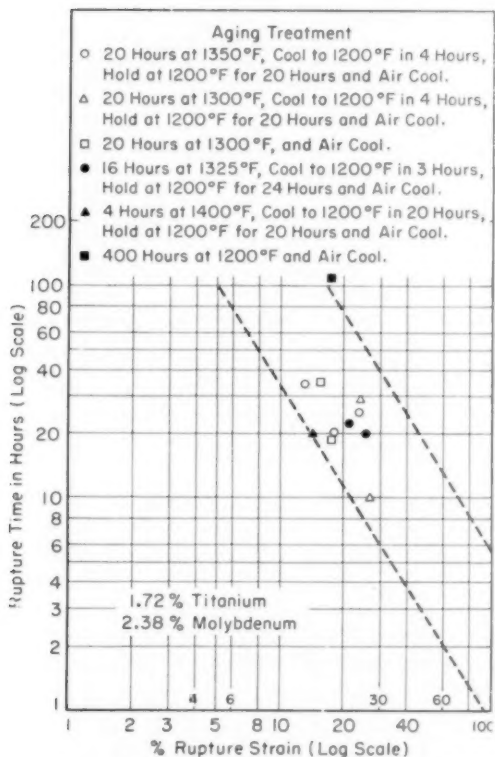


Fig. 2—Creep Rupture Properties of Heat No. 6932 at 60,000 PSI and 1200°F. All specimens solution treated 1 hour at 1950°F.

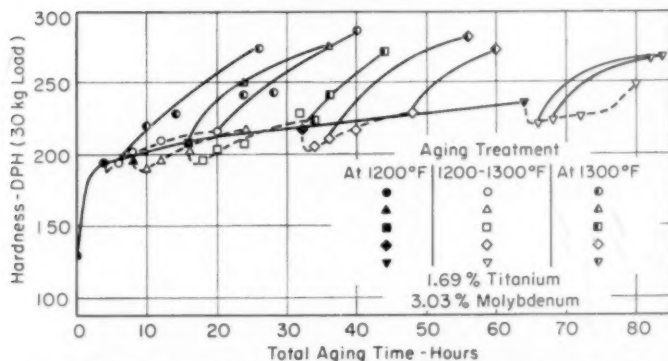


Fig. 3—The Effect of Various Aging Cycles on the Hardness of Heat. No. 7040. All specimens solution treated 1 hour at 1950°F and oil-quenched.

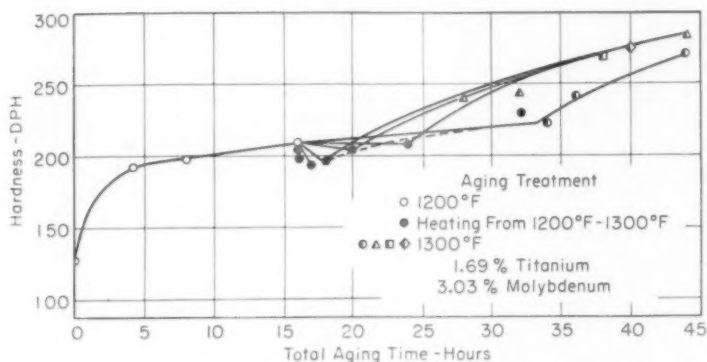


Fig. 4—The Effect of Rate of Heating from 1200 to 1300 °F on Hardness After Aging 16 Hours at 1200 °F. No. 7040. All specimens solution treated 1 hour at 1950 °F and oil-quenched.

based on the change of hardness with time at 1200 °F (650 °C), with heating rate from 1200 to 1300 °F (650–705 °C), and with time at 1300 °F (705 °C). These temperatures were based on previous aging data on these alloys, and may not be the optimum temperatures for best results, but are used here to demonstrate the features of this aging treatment.

The specimens were all solution treated 1 hour at 1950 °F (1065 °C). Four specimens were then aged at 1200 °F (650 °C) for the following times: 4, 8, 16, 32 and 64 hours and air-cooled. One specimen from each of the above groups was then heated at a constant rate from 1200 to 1300 °F (650–705 °C) in 2, 4, 8 and 16 hours and air-cooled again. As a result of hardness data taken at this point in the experiment, the specimens were heated various lengths of time at 1300 °F (705 °C) to obtain a desired hardness of 270–290 DPH (See Fig. 3). From Fig. 3 it can easily be seen that part of the hardness and, therefore, presumably some of the nuclei are lost by too rapid heating between 1200 and 1300 °F (650–705 °C). It appears within the limits of this experiment that the longer the holding time at 1200 °F (650 °C) the more slowly the material must be heated to avoid this retrogression effect. This is probably caused by the rapid rate of nucleation and the slow rate of growth which results in an increasing concentration of small nuclei which are dissolved by too rapid heating. Also, the supersaturation of the matrix is increasingly reduced the longer the holding time at 1200 °F (650 °C) which results in a decreased driving force for precipitation. A more detailed picture of the effect of the rate of heating between 1200 and 1300 °F (650–705 °C) is given, for the specimen held 16 hours at 1200 °F (650 °C), in Fig. 4. Three points have been added to this curve for heating in a salt pot (10 seconds), and a

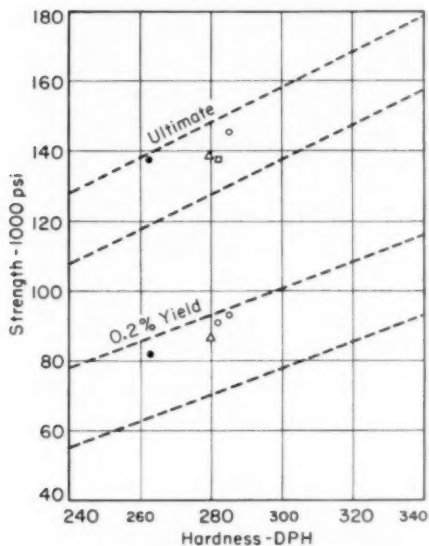


Fig. 5—Room Temperature Tensile Tests of Heat No. 7040 Tested at a Constant Strain Rate of 750% Per Hour. (See table III for code.)

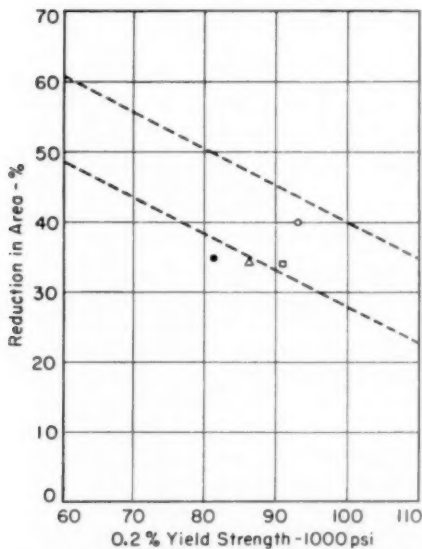


Fig. 6—Room Temperature Tensile Tests of Heat No. 7040 Tested at a Constant Strain Rate of 750% Per Hour. (See table III for code.)

furnace (10 minutes and 1 hour) to 1300 °F (705 °C). Here the effect of rapid heating on the hardness can be seen very easily. It was felt that the practical limit for aging time was about 44 hours as is now used for one of the present commercial aging treatments and, therefore, the selection of heat treatments for further investigations

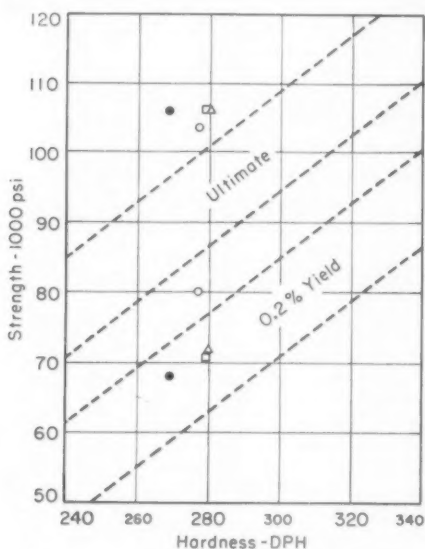


Fig. 7—1200 °F Tensile Properties of Heat No. 7040 at a Constant Strain Rate of 750% Per Hour. (See table III for code.)

was limited by this consideration. From these tests the following cycles were chosen for comparison with this standard aging cycle:

1. Age 4 hours at 1200 °F (650 °C), heat to 1300 °F (705 °C) in 2 hours, heat at 1300 °F (705 °C) for 20 hours and air cool.
2. Age 8 hours at 1200 °F (650 °C), heat to 1300 °F (705 °C) in 8 hours, heat at 1300 °F (705 °C) for 20 hours and air cool.
3. Age 16 hours at 1200 °F (650 °C), heat to 1300 °F (705 °C) in 16 hours, heat at 1300 °F (705 °C) for 12 hours and air cool.

Tests were conducted on these specimens as follows: Room temperature tensile tests, 1200 °F (650 °C) tensile test, notch-bar creep-rupture tests at 1200 °F (650 °C) and 70,000 psi stress, and plain-bar creep-rupture tests at 1200 °F (650 °C) and 60,000 psi stress. The results of these tests are compared with test results (9) on specimens

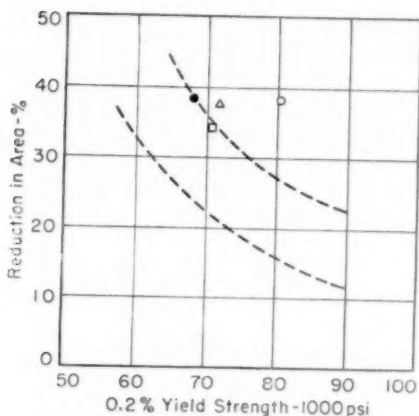


Fig. 8—1200 °F Tensile Tests of Heat No. 7040 at a Constant Strain Rate of 750% Per Hour. (See table III for code.)

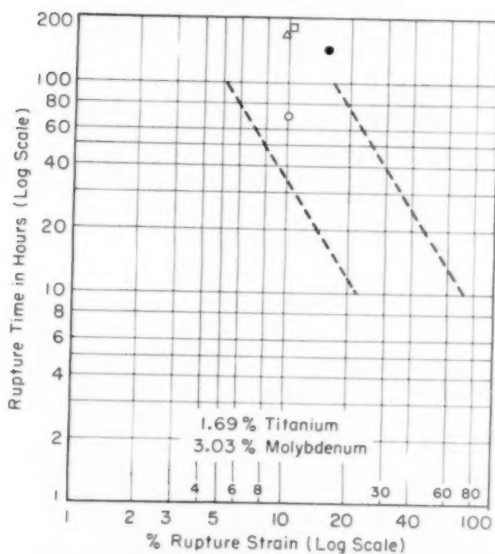


Fig. 9—Creep Rupture Properties of Heat No. 7040 at 60,000 PSI and 1200 °F. All specimens solution treated 1 hour at 1950 °F. (See table III for Code.)

given the previously mentioned double aging cycle in Figs. 5 through 9. The room temperature tensile tests show little or no change in the strength characteristics, however, some decrease is indicated in the rupture ductility as shown by the reduction in area. This same decrease is

Table III
Notch-Bar Creep-Rupture Tests of Heat No. 7040 at 1200°F
All Specimens Solution Treated 1 Hour at 1950°F

Specimen Number	Aging Treatment	Hardness		Load PSI	Rupture Time Hours
		As Aged DPH	After Testing DPH		
27	4	282	288	70,000	127
36	1	282	304	70,000	668
40	2	278	295	70,000	602
44	3	268	295	70,000	736
Aging Treatment	Symbols For Fig. 5-9				
1	△	4 hours at 1200°F, temperature increased to 1265°F in 1½ hours, held at 1265°F for 2 hours, raised to 1300°F in 10 minutes, held at 1300°F for 20 hours and air cooled.			
2	□	8 hours at 1200°F, temperature increased to 1300°F in 8 hours, held at 1300°F for 20 hours and air cooled.			
3	●	16 hours at 1200°F, heated to 1300°F in 16 hours, held at 1300°F for 12 hours and air cooled.			
4	○	20 hours at 1300°F cooled to 1200°F in 4 hours, held at 1200°F for 20 hours and air cooled.			

Table IV

Aging Treatments for Table V and Figures 10-12

1 20 hours at 1350°F, cool to 1200°F in 4 hours, held at 1200°F for 20 hours and air cool.

1* Same as 1 except cool to 1200°F in 3 hours.

1† Same as 1* except held at 1200°F for 17½ hours.

2 20 hours at 1300°F, cool to 1200°F in 4 hours, held at 1200°F for 20 hours and air cool.

3 20 hours at 1325°F.

4 16 hours at 1200°F, heated to 1300°F in 16 hours, held at 1300°F for 12 hours and air cool.

4* 16 hours at 1200°F, heated to 1250°F in 8 hours, held at 1250°F for 16 hours and air cool.

5 16 hours at 1325°F.

Aging Treatments	Symbols For Figs. 10-12				
	Heat Number				
	6929	6931	6966	6968	6969
1, 1*, 1†	○	△	□	◇	▽
2	●	▲	■	◆	▼
3	⊙	△	□	◇	▽
4, 4*	●	▲	■	◆	▼
5	⊙	△	□	◇	▽

noted in the 1200 °F (650 °C) tensile tests. The strength properties of the double aged tensile specimen at 1200 °F (650 °C) are higher than previous heats as given by the dashed zones in Figs. 7 and 8. The 0.2% yield strength has apparently been lowered by the genuage treatment at 1200 °F (650 °C), however, this difference was later proved to be due to the chance specimen selection.

The plain-bar creep tests in Fig. 9 indicate a general improvement in quality of the material given the genuage aging cycles over the material given the double aging cycle. The best combination of strength and ductility is shown by the specimen receiving treatment No. 3. However, all of the genuage specimens show similar improvement in creep properties.

Table V
The Effect of Various Aging Treatments on the
Notched-Bar Creep-Rupture Properties at 1200°F

Specimen Number	Aging Treatment Ø	As Aged DPH	After Test DPH	Load PSI	Rupture Time Hours
6929-6	1	297	299	70,000	180
-9	5	186	282	70,000	36
-10	1†	256	269	70,000	37
-14	1**	258	273	70,000	98
-16	1*	255	280	75,000	93
-18	2	274	283	65,000	32.5
-28	5	179	287	60,000	300
-29	2	258	320	60,000	363
-30	4	277	295	70,000	403
6931-3	1	328	326	70,000	54.5
-9	5	311	333	70,000	38
-10	1†	339	318	70,000	41
-14	1*	323	307	70,000	41
-16	1*	304	323	65,000	79
-18	3	284	311	65,000	144
-28	5	298	329	60,000	261
-29	2	308	320	60,000	317
-30	4	295	331	70,000	508
6966-4	1*	344	331	70,000	1.5
-6	1*	333	349	60,000	23
-8	3	308	341	65,000	33
-18	5	304	334	60,000	35.5
-19	2	336	355	60,000	49
-20	4	336	355	70,000	74
6968-18	5	320	347	60,000	153
-19	2	333	373	60,000	1.5
-20	4	336	355	70,000	123
6969-4	1*	253	269	70,000	33
-6	1*	246	268	65,000	199
-8	2	252	269	65,000	49
-18	5	144	278	60,000	914
-19	2	263	268	60,000	343
-20	4*	248	294	70,000	521

Ø—See Table IV for code.

The notch-bar creep properties given in Table III show a 4 to 5 fold increase in rupture time over the double aging procedure for all the genuage treatments, however, the specimen receiving treatment No. 3 is again the best. It is obvious from these results that by the use of the genuage treatment it has been possible to increase creep-rupture strength without reducing creep-rupture ductility.

In order to confirm these results on alloys of varying titanium (hardener) content, the notched-bar and plain-bar creep-rupture tests were repeated on alloys having five different titanium levels. (Heats Nos. 6929, 6931, 6966, 6968, and 6969.) The compositions are given in Table I, and the results of the tests are given in Table V and Figs. 10 through 12. The results of room temperature and 1200 °F (650 °C) tensile tests did not indicate any change in properties as a function of the aging treatment. It is, therefore, shown that the decrease in ductility noted on tests of heat No. 7040 was only caused by a chance specimen selection. All of the results fall in the area of the dashed lines given for tensile data in Figs. 5 through 8 so no actual test data is reported here.

The creep-rupture properties shown in Fig. 10 show that the time

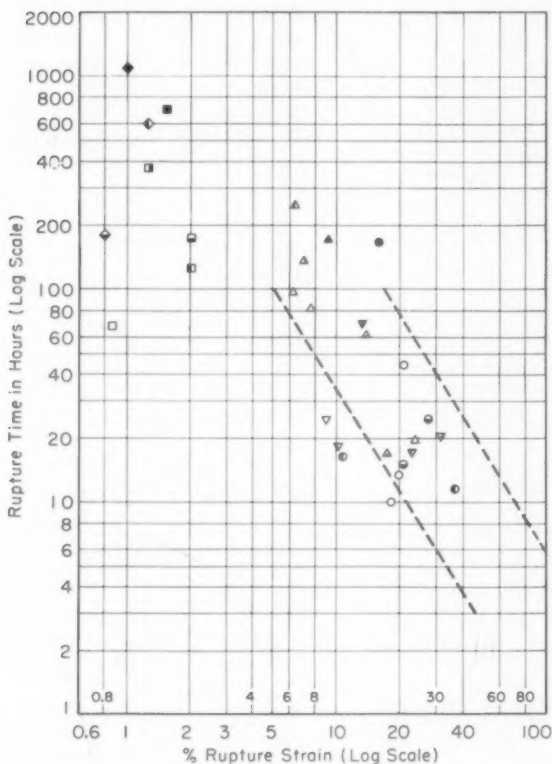


Fig. 10—Creep-Rupture Properties of Alloys with Several Different Aging Treatments Tested at 60,000 PSI and 1200 °F. (See table IV for code.)

to rupture has been increased in most cases by a factor of two to four by the genuage treatment, however, this has not resulted in the usual decrease in rupture strain. The aging treatment has not increased the rupture strain of the very high titanium heats, but it can be seen from the increase in the notched-bar creep-rupture times given in Fig. 11 that the material is no longer notch sensitive.

Fig. 12 compares the results of the tests using the genuage treatment and the best of the previously used double aging treatments. The notched-bar creep-rupture properties are better with the genuage treatment at a stress of 70,000 psi than the notched-bar specimens with the double age at 60,000 psi. The plain-bar creep-rupture time and time to 1% elongation have also been improved substantially by the genuage treatment as can easily be seen from the curve. With the

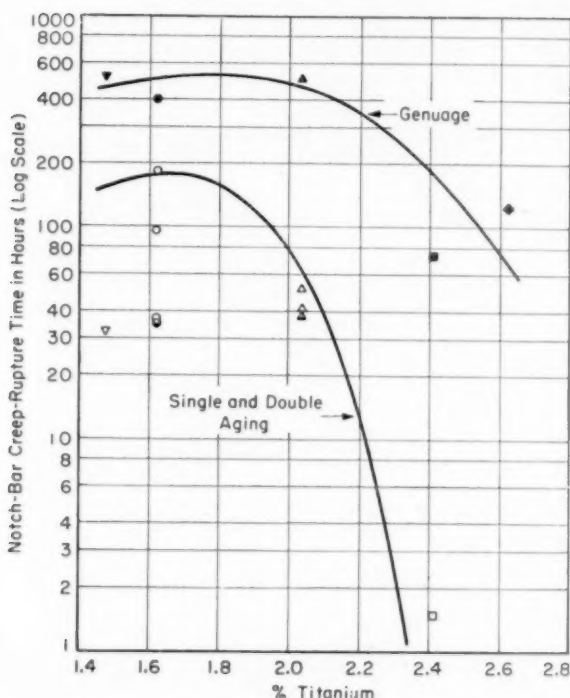


Fig. 11—Notch Creep Rupture Tests of Alloys, with Several Different Aging Treatments, Tested at 70,000 PSI and 1200 °F. (See table IV for code.)

double aging treatment used for this comparison, the material became notch sensitive at a titanium content of about 2.2%, however, none of the specimens tested with the genuage treatment are notch sensitive as judged by comparison with previous data.

Microstructural changes which occurred as a result of the aging treatments studied here are shown in Figs. 13 and 14. The specimens were etched for 50 seconds in a solution of 15 grams ferric chloride, 15cc.HCl, and 60 cc. alcohol. The electron microscope pictures in Fig. 13 are of specimens which received the three genuage treatments used in this work. The oval shaped spots in Fig. 13a are polystyrene spheres which were placed on the surface of the replica to determine the elevation of the constituents which appear in the structure. The structures of all three samples in Fig. 13 are relatively clear of distinct precipitate particles in the grain boundary area but in addition to this it will be noted that no precipitate particles are distinguishable in the grains themselves.

Fig. 14 shows a comparison of the structure resulting from two of

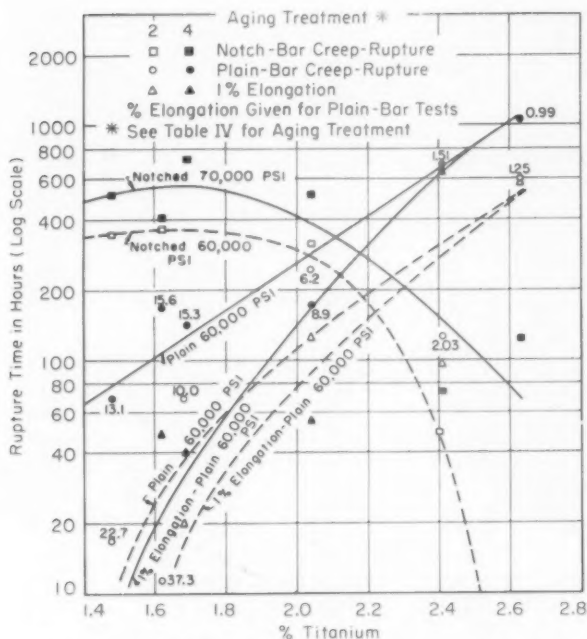


Fig. 12—1200 °F Creep-Rupture Tests on Alloys with Varying Titanium Contents.

the commonly used commercial aging treatments with that resulting from the gennage treatment. The structures which are developed by the commercial aging treatments show rather large and distinct particles in the grain boundary area. As might be expected the extent of this precipitation appears to be a function of relative grain orientations of the adjoining grains. It should also be noted that the grains themselves show very small but distinct precipitates in contrast to the specimens shown in Fig. 13 or as shown in Fig. 14c. Fig. 14c again shows the typical structure resulting from the gennage treatment.

SUMMARY

The data presented here shows that the room temperature tensile properties and the 1200 °F (650 °C) tensile properties are not affected by the type of aging treatment used. The hardness obtained on aging is apparently the determining factor for all tensile properties.

The creep-rupture properties, on the other hand, are greatly influenced by the aging treatment. It is shown that the long time (400 hours) low temperature (1200 °F) aging treatment produces excellent creep-rupture results, but this type of treatment is not economical on a commercial basis. These same results may be obtained by a new aging

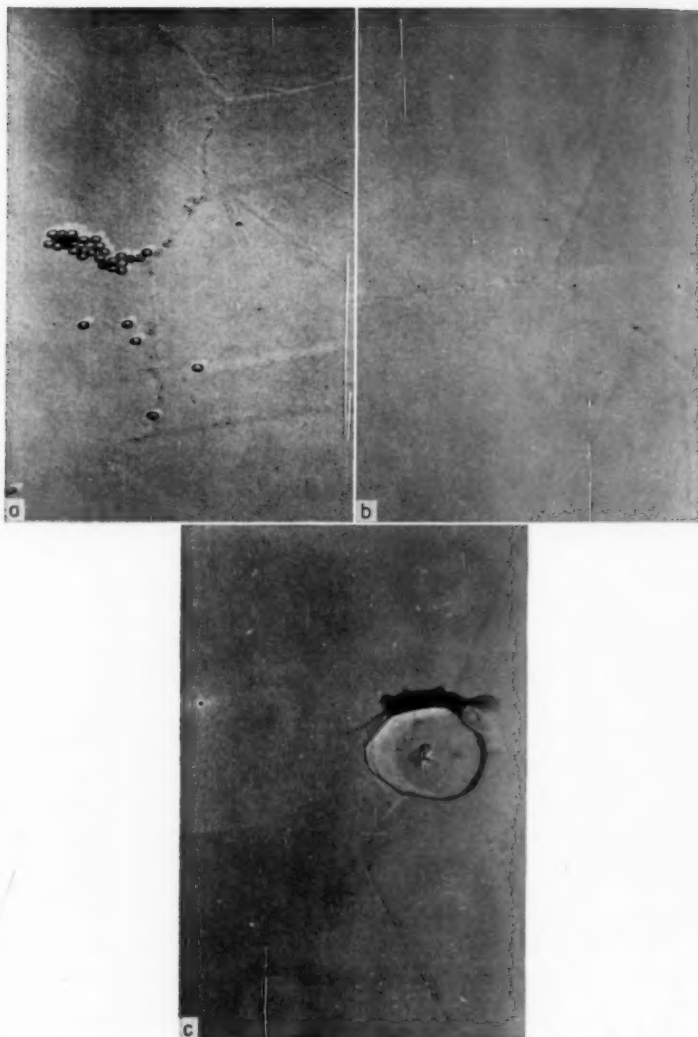


Fig. 13—Electron Micrographs of the Grain Boundary Area of Specimens from Heat No. 7040 Given Three Different Genuage Treatments. Specimens were solution treated 1 hour at 1950 °F and oil-quenched. X 4025. (a) Aged 4 hours at 1200 °F, raised to 1300 °F in 2 hours, held 20 hours at 1300 °F and air-cooled. (b) Aged 8 hours at 1200 °F, raised to 1300 °F in 8 hours, held 20 hours at 1300 °F and air-cooled. (c) Aged 16 hours at 1200 °F, raised to 1300 °F in 16 hours, held 12 hours at 1300 °F and air-cooled.

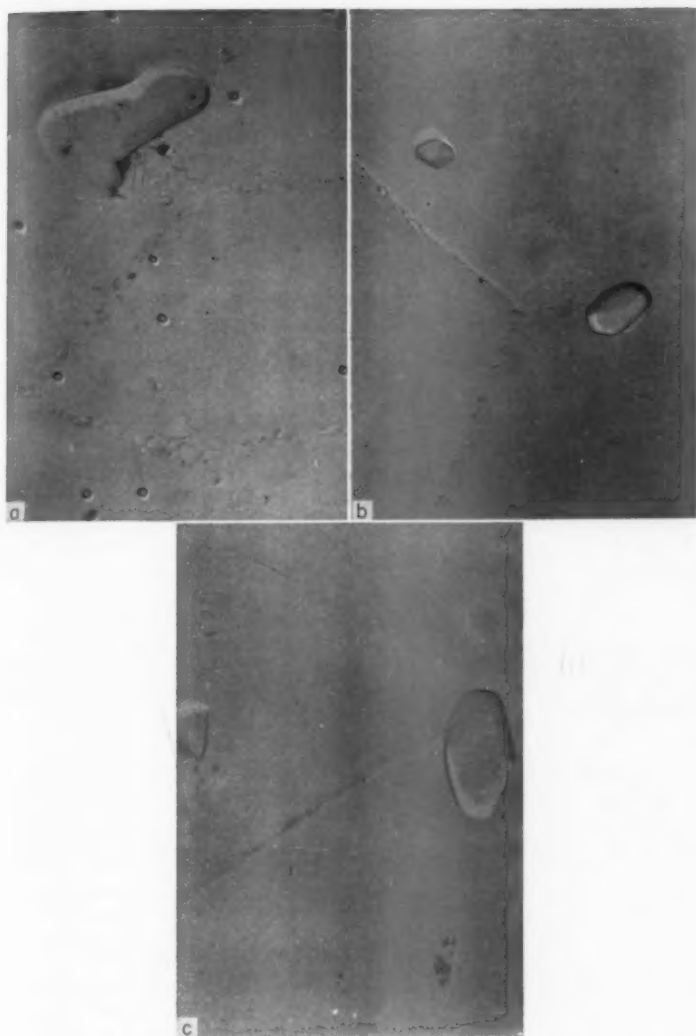


Fig. 14—Electron Micrographs of Specimens from Heat No. 6929, Comparing the Structure Resulting from Previous Standard Aging Cycles and the New Genuage Treatment. All specimens solution treated 1 hour at 1950 °F and oil-quenched. X 4025. (a) Aged 16 hours at 1325 °F and air-cooled. (b) Aged 20 hours at 1300 °F, cooled to 1200 °F in 4 hours, held 20 hours at 1200 °F and air-cooled. (c) Aged 16 hours at 1200 °F, raised to 1300 °F in 16 hours, held 12 hours at 1300 °F and air-cooled.

treatment called the "genuage treatment", which requires a much shorter time. This heat treatment consists of:

1. Starting the aging reaction at a low enough temperature to give rapid general nucleation and a minimum of diffusion of the hardener content to nuclei in the grain boundary.
2. The aging temperature is then raised slowly, to prevent retrogression, to a higher temperature where the precipitated particles will grow more rapidly.
3. The material is then held at this higher temperature until the desired hardness is obtained. The material may then be given a stabilizing age at a lower temperature but this is not considered to be necessary for most applications.

The temperatures used in this work for the first and second aging steps were 1200 and 1300 °F (650–705 °C), however, these are not necessarily the optimum temperatures for every application. It appears that other factors may be involved in obtaining the optimum heat treatment for a given part and a given application. Additional work is being done along the same line to seek answers to some of the problems which have limited the use of this type of alloy in the past. It is possible that the same approach used here may also be applied to other precipitation hardening alloy systems to improve the creep properties.

ACKNOWLEDGMENT

The author wishes to express his appreciation to Dr. C. Zener and Dr. F. C. Hull for their many helpful suggestions and their encouragement during the progress of this work.

References

1. H. Scott and R. B. Gordon, "Precipitation Hardened Alloys for Gas Turbine Service," *Transactions, American Society of Mechanical Engineers*, Vol. 69, 1947, p. 583.
2. H. Scott, R. B. Gordon and F. C. Hull, U. S. Patent 2,519,406 (Aug. 22, 1950).
3. American Society for Metals Symposium, *Age Hardening of Metals*, 1940, Tower Press.
4. A. H. Giesler, *Precipitation from Solid Solutions of Metals*, National Research Council Symposium on Phase Transformation in Solids, 1951, p. 387, John Wiley and Sons, Inc.
5. G. C. Smith, "Age Hardening of Metals," *Progress in Metal Physics*, Vol. I, 1949, p. 163, Interscience Publishers, Inc.
6. D. N. Frey, J. W. Freeman and A. E. White, "Fundamental Aging Effects Influencing High-Temperature Properties of Solution-Treated Inconel X," National Advisory Committee for Aeronautics Technical Note 2385, June 1951.
7. F. J. Clauss, and J. W. Weeton, "Effect of Heat Treatment Upon the Microstructure and Hardness of Wrought Cobalt-Base Alloy Stellite 21 (AMS 5385)," National Advisory Committee for Aeronautics Technical Note 3107, March 1954.
8. F. J. Clauss and J. W. Weeton, "Relation of Microstructure to High-Temperature Properties of a Wrought Cobalt-Base Alloy Stellite 21 (AMS 5385)," National Advisory Committee for Aeronautics Technical Note 3108, March 1954.
9. T. W. Eichelberger, unpublished data.

DISCUSSION

Written Discussion: By Francis J. Clauss, Aeronautical Research Scientist, National Advisory Committee for Aeronautics, Cleveland.

The strengthening action of a double-aging treatment, in which scattered nucleation sites are produced in solution-treated material by first aging at a low temperature and the precipitates are then developed in a reasonable period of time by a second aging at a higher temperature, was described by John Weeton and myself for the alloy HS-21, a cobalt-base superalloy, in an NACA report published in March 1954, cited as reference 8 in the preprint of the author's paper. We found that the stress-rupture life of HS-21 could be increased by a factor of slightly more than four-fold by aging first at 1200 °F (following solution treatment) and then at 1500 °F, as compared to the life obtained when the nucleation-age at 1200 °F was omitted. This was for stress-rupture tests at 1500 °F and stresses that gave lives on the order of 100 hours. The fine precipitates developed by double-aging HS-21 resulted in better stress-rupture strength than any of the single-aging treatments. Mr. Weeton and I suggested in our report that our conclusions for HS-21 should have general significance in the heat treatment of other high temperature alloys, and we have since obtained additional indications that this is true. We are glad to have the further confirmation provided by Mr. Eichelberger's results.

While there are undoubtedly many applications where the use of double-aging heat treatments of the type discussed should be beneficial, a few words of caution should be voiced. First, since fine particles are more unstable than coarse ones at elevated temperatures, overaging can occur more rapidly with fine particles and the strengthening action of double-aging can be lost at very high temperatures and/or long times of service. In other words, although the fine dispersion of precipitates should be strongest at low temperatures, a coarser structure is often stronger at higher temperatures or longer times.

Second, with many alloys the increase in strength due to a fine dispersion of precipitates is accompanied by a marked loss in ductility. This is not always the case, as indicated by the author's results.

Third, to be entirely successful, double-aging should be preceded by a very thorough solution treatment which dissolves all secondary phases and leaves no residual particles for spurious nucleation. This insures that the nucleation sites will be uniformly distributed by the first age at the low temperature. When some particles are undissolved after solution treatment, the double-aging treatment will be less successful, although large benefits can still accrue. As we have learned in several of our programs at the NACA on the heat treatment of turbine blades for gas turbojet engines and turbosuperchargers, attempts to obtain complete solution treatment can introduce practical difficulties during heat treatment, particularly when the secondary phases are difficult to dissolve and high temperatures of solution treatment are necessary. Cast HS-21 turbine blades, for example, often suffer pronounced interdendritic segregation in the areas around the primary carbides, and we have observed eutectic melting to occur in such blades when the solution treating temperature was too high, as was necessary to dissolve all of the carbides.² The loss in strength due to eutectic melting more than offset any gain that might

² Francis J. Clauss, Floyd B. Garrett, and John W. Weeton, "Effect of Some Selected Heat Treatments on the Operating Life of Cast HS-21 Turbine Blades," NACA TN 3512, July 1955.

have resulted from subsequent double-aging. When segregation was less, as in small castings, such as turbosupercharger blades of the same alloy, eutectic melting did not occur and heat treatments were more successful. Blades cast by different manufacturers were found to respond differently to heat treatment. This emphasizes that successful heat treatment of cast materials can depend upon the as-cast microstructure, as influenced by the metal casting temperature, mold temperature, and rates of solidification and cooling.

With forgings, we have found that certain areas sometimes contain critical amounts of deformation that lead to pronounced grain growth during solution treatment at high temperatures.⁸ Such grain growth in forged turbine blades is usually concentrated along the leading and trailing edges and can lead to early fatigue failures initiated in those areas. Although it is well known that the stress-rupture strength of many superalloys can be increased by raising the solution treating temperatures, such side effects as grain growth, loss in ductility, and lowered fatigue strength have in the past ruled out high temperatures for solution treatment.

Properly carried out to avoid these practical difficulties, we feel that the use of solution treatment and double-aging in the manner discussed can be very beneficial in those applications where the service times and temperatures do not cause marked overaging of the fine particles of precipitate.

Author's Reply

The author wishes to thank Mr. Clauss for adding some of the recent results of his own work to this presentation. The results which are reported agree very closely with later results by the author on other alloy systems. However, the remarks on the effect of finer precipitate particles may prove to be a little misleading. The following remarks pertain to precipitate particles which are sub-microscopic in size and coherent with the matrix, since these are the particles which contribute the most to mechanical strength. A small precipitate particle is certainly less stable than a larger particle. However, if the small particles are larger than a critical size nucleus, they will agglomerate and at some point during their growth pass through the size range of the larger particles. This means that smaller initial particles take longer to overage.

A very coarse precipitate is required in some instances because the material is overalloyed with hardening or precipitating elements. This over alloying produces a large quantity of precipitate in the grain boundary area which results in a weak material as indicated by the author in this paper. As the hardener content is increased, the material will finally become so notch-sensitive that it will show very poor results with the gennage type of heat treatment. If, however, the material is intentionally overaged so that the grain boundary precipitate is agglomerated, the brittle condition may be relieved enough to produce a usable material. It is very easy to observe such behavior in the microstructure and come to the conclusion that a coarse precipitate is desirable; however, this conclusion is not warranted when all factors are considered.

Mr. Clauss's comment on the desirability of complete solution treatment prior to aging is certainly in line with our experience, but as stated, it is not always possible to achieve because of other factors.

⁸ J. W. Weeton, F. J. Clauss, and J. R. Johnston, "Performance of As-Forged, Heat-Treated, and Overaged S-816 Blades in a Turbojet Engine," NACA RM E54K17, March 3, 1955 (Declassified Nov. 14, 1956).

INFLUENCE OF NICKEL ON INTERGRANULAR CORROSION OF 18% CHROMIUM STEELS

BY J. R. UPP, F. H. BECK AND M. G. FONTANA

Abstract

Type 304 (18-8) stainless steel is made susceptible to intergranular corrosion when heated in the temperature range of approximately 1200-1400 °F. This heat treatment imparts resistance to intergranular corrosion for Type 430 (18% Cr) steels. Quenching from 1900-2000 °F provides optimum resistance to Type 304 but makes Type 430 susceptible to intergranular corrosion. The major compositional difference in these steels is nickel (8% and 0%). Alloys containing intermediate nickel compositions were cast, rolled, heat treated, and tested to determine the influence of this element on corrosion behavior. It was found that the transition occurs at about 2.5 to 3% nickel. Steels with higher nickel should be heat treated like the austenitic steels and those below like the ferritic steels. An unexpected result was the good resistance to intergranular corrosion of all of these alloys when water quenched from 1400 °F. (ASM International Classification R2h, 2-10; SS, Cr, Ni)

INTRODUCTION

A GREAT DEAL of work has been performed during the past thirty years or so, on the mechanism and prevention of intergranular corrosion of the austenitic stainless steels such as Type 304 (18% Cr-8% Ni). Some work has been done in recent years, along these same lines, on the ferritic stainless steels such as Type 430 (16-18% Cr). The interest in the latter, or straight chromium steels seems to increase during periods when nickel is difficult to obtain.

Types 304 and 430 steels can be made relatively immune to intergranular attack or made susceptible (sensitized) through selected heat treatments. Of particular interest is the fact that a specific given heat treatment makes one steel immune and the other susceptible, and another specific heat treatment results in the reverse situation. In other words, a "good" heat treatment for Type 304 is "bad" for Type 430 and vice versa. The question naturally arises—at what nickel content

This paper is based on J. R. Upp's thesis in partial fulfillment of the requirements for a Master of Science degree.

A paper presented before the Thirty-Ninth Annual Convention of the Society, held in Chicago, November 4-8, 1957. Of the authors, Lt. J. R. Upp is project engineer, Wright Air Development Center, Wright-Patterson Air Force Base, Ohio. F. H. Beck is associate professor, Engineering Experiment Station, and M. G. Fontana is professor and chairman, Department of Metallurgical Engineering, The Ohio State University, Columbus, Ohio. Manuscript received April 1, 1957.

does the "switch" occur? The purpose of this investigation was to study 18% chromium steels with intermediate nickel contents to determine where the division or transition in the mechanisms of intergranular corrosion occurs and also the heat treatments required for optimum corrosion resistance.

SURVEY OF THE LITERATURE

Type 304 Stainless Steels

Much has been written on intergranular corrosion of austenitic (non-magnetic) stainless steels since the classic papers by Payson (1)¹ and by Bain, Aborn, and Rutherford (2). The phenomenon is well known. The chromium impoverishment theory is the commonly accepted explanation as summarized by Fontana (3). When 18-8 steels are heated in the temperature range approximately 900 to 1400 °F, chromium carbide precipitates at the grain boundaries. This precipitation "ties up" some of the chromium and lowers the chromium content in the surrounding areas adjacent to the grain boundaries, and this decreases the effective corrosion resistance of the metal. Immunity can be restored by heating the steels to a high temperature, such as 1950 °F, to dissolve the carbides and then quenching to pass rapidly through the sensitizing temperature zone. Payson (1) states that the presence of a ferrite phase decreases susceptibility to intergranular corrosion. Mahla and Nielsen (4) show the carbides as leaf-like structures exhibiting dendritic patterns. Intergranular corrosion can also be controlled or minimized (3) by adding strong carbide formers such as columbium (niobium) and titanium and also by reducing the carbon content below 0.03%.

Type 430 Stainless Steels

These are the ferritic steels that are not hardenable by heat treatment. Previous work (5,6) shows that Type 430 steels become susceptible to intergranular corrosion when cooled rapidly from above 1700 °F. Most authors agree that immunization may be imparted by short-time heating at approximately 1450 °F. Kiefer (6) proposes a mechanism for intergranular corrosion of welded Type 430 steel. He found that martensite corroded preferentially to the ferrite when both constituents are present. The martensite formed a sheath around the ferrite. Houdremont and Tofante (5) hold that it is the precipitation upon rapid cooling of nonresistant, easily attacked iron carbides, from austenite, at the grain boundaries of the ferrite grains that produces material susceptible to intergranular attack. Upon heating to 1450 °F, the iron carbide is changed to a chromium carbide, probably Cr_{23}C_6 , which restores immunity to intergranular attack.

¹ The figures appearing in parentheses pertain to the references appended to this paper.

The latest explanation comes from Lula, Lena, and Kiefer (7). They have shown that austenite was not necessary for intergranular corrosion, titanium stabilization does not prevent intergranular attack, the sensitizing temperature is independent of chromium content, and that intergranular corrosion was still present when the carbon content was 0.005%. The mechanism they proposed is that upon rapid cooling a carbide or nitride is precipitated in the grain boundary causing excess strain of the material. It is this stressed material that is attacked. Short-time annealing at 1450 °F relieves this stress next to the carbide or nitride.

Addition of increasing amounts of nickel to 18% chromium steel results in more and more retained austenite until a completely austenitic structure is retained at room temperature when about 8% or more nickel is present (Type 304). Intermediate amounts of nickel result in duplex structures of ferrite and austenite. The addition of nickel increases the general corrosion resistance of the alloy.

EXPERIMENTAL PROCEDURES

Preparation of Alloys

Twelve heats of 18% chromium stainless steels were prepared with nickel contents ranging from 0 to 8.3%. All alloys were made up as 3500-gram charges and melted in a high frequency induction furnace

Table I
Chemical Composition of Materials

Material	% Element		
	C	Ni	Cr
Commercial Alloys			
304*	0.08	10.39	18.34
430	0.05	0.18	16.02
Experimental Alloys			
X-1**	0.106	0.00	18.01
X-2	0.069	1.70	18.15
X-3	0.073	2.21	18.25
X-4	0.072	2.92	17.61
X-5	0.068	3.24	17.52
X-6	0.075	3.67	18.44
X-7	0.063	3.89	18.43
X-8	0.069	4.33	18.62
X-9	0.072	4.80	17.58
X-10	0.085	5.46	17.54
X-11	0.076	5.84	17.93
X-12	0.097	8.29	18.50

*0.56% Mn, 0.41 Si, 0.022% P and 0.010% S.

**All experimental heats charged with 0.75% Mn and 0.50% Si.

using magnesia crucibles. Each charge was prepared from ferro-alloys, Armco iron and electrolytic nickel. After melting, each heat was cast into a round bar. The results of wet chemical analyses of each heat are listed in Table I. The bars were rolled at 2000 °F into strips approximately $\frac{3}{16}$ inch thick and 2 to 3 inches wide, then air-cooled. Numerous $\frac{3}{4}$ inch by $\frac{3}{4}$ inch specimens were cut from the center of the strip for heat treatment and corrosion testing.

Heat Treatment

Heat treatment temperatures were selected from both the sensitizing and immunizing ranges of each steel. These were 2000 °F and 1400 °F. An intermediate temperature, 1650 °F, was also used. Heat treatments consisted of water quenching, air cooling, and furnace cooling (300 to 400 °F per hour) from each of the aforementioned temperatures, making a total of nine specimens for each alloy. Heat treating was done in a Globar tube furnace (air atmosphere) with temperature controlled at ± 10 °F. Heat treating was performed on the alloys in the as-rolled condition.

No preliminary heat treatment was performed because of the variance of composition and structures of each alloy. This allowed a direct comparison of results to be made. A check was made to see if prior heat treatment had any effect on the corrosion resistance of the alloy. The two process annealing treatments that are customarily used on Types 304 and 430 were first given the 8.3% and 0.0% nickel alloys before test heat treatments. These were water quenching from 2000 °F and furnace annealing from 1400 °F, respectively. After prior treating, these alloys were heat treated the same as the experimental specimens.

Corrosion Tests

In preparing the specimens for the corrosion tests, each was ground to a 120-grit finish on a belt grinder, measured, and the surface areas calculated. Then each specimen was degreased in acetone and weighed.

After weighing, each specimen was placed into individual glass cradles so as to provide a maximum surface area available to the acid. Each specimen was submitted to a standard 240-hour Huey corrosion test with boiling 65% HNO_3 acid. This consists of five 48-hour periods. At the end of the test, the corrosion rates for each specimen were calculated. The rate in mils penetration (thousandths of an inch) per year was calculated by means of the following formula (3):

$$\text{mils per year} = 534w/D A T$$

w = weight loss in milligrams

D = specific gravity or density—grams per cubic centimeter

A = area in square inches

T = time of test in hours.

Metallographic Examination

Because of the fact that intergranular corrosion cannot be detected entirely by the weight loss in the Huey test, each specimen was polished, etched electrolytically, and observed under a microscope. Both the structure and evidences of intergranular attack were noted. No photomicrographs are shown in this paper in order to save space and because they are not absolutely necessary.

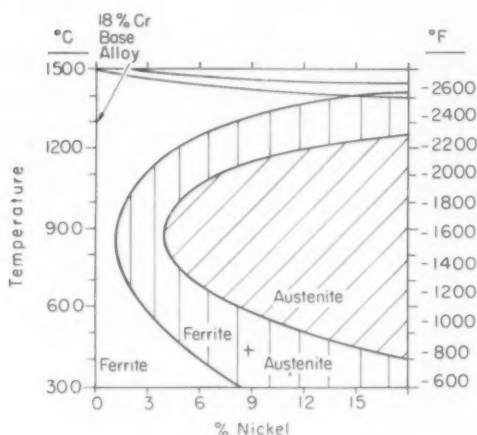


Fig. 1—Constitutional Diagram Showing the Effect of Nickel on 18% Cr-Fe Base Alloys with Negligible Carbon (8).

Table II
Corrosion of Alloy X-1 (0.00% Ni) by Boiling 65% Nitric Acid

Material Condition (a)	Corrosion Rate in Mills per Year			
	First Period (b)	Third Period	Fifth Period	Average
WQ 2000°F	26	190	330	185
AC 2000°F	55	430	470	320
FC 2000°F	40	75	115	75
WQ 1650°F	24	44	65	45
AC 1650°F	53	295	330	235
FC 1650°F	28	37	48	38
WQ 1400°F	18	21	22	21
AC 1400°F	20	25	27	25
FC 1400°F	24	24	26	25

(a) Specimens held at temperature 1 hr. before cooling. WQ—water-quenched; AC—air-cooled; FC—furnace-cooled (300 to 400°F per hr.).

(b) 48-hr. periods. Second and fourth periods omitted in all tables to save space. These two periods all "line-up" in good shape. Periods needed to show effect of time on corrosion.

RESULTS AND DISCUSSION

Corrosion data on the 12 experimental alloys and the two commercial alloys are shown in Tables II through XVII. Details of heat treatment are also included in these tables. Alloy X-1 (Table II) represents the 18% chromium steel without nickel (Type 430) and alloy X-12 (Table XIV) represents the 18-8 (Type 304). Alloy X-12 contains slightly higher carbon than normal Type 304 but this had no significant effect for this study. Alloys X-1 and X-12 form the basis for comparison for the alloys with intermediate nickel contents with regard to intergranular corrosion behavior.

Although nine heat treatments were used, only four of them provided valuable and pertinent information. Specimens treated at 1650 °F showed approximately the same corrosion resistance and structures as those heated at 2000 °F, with the exception of X-8 (4.33% Ni) and X-9 (4.80% Ni). This is because these two steels fell into the solid gamma field (Fig. 1, Reference 8) at 1650 °F, while at 2000 °F they

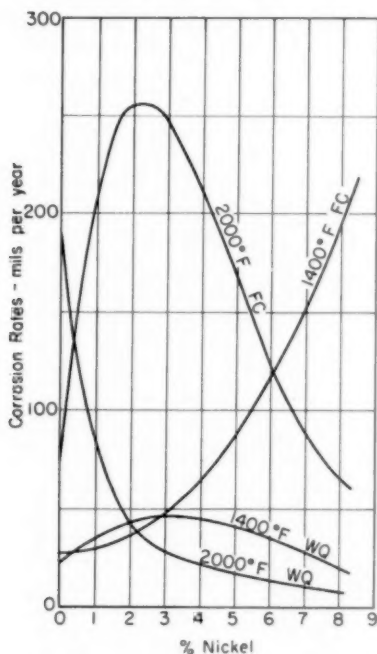


Fig. 2—Summary of the Effect of Nickel and Heat Treatment on Corrosion of 18% Chromium Stainless Steels. (Average corrosion rates for five 48-hr. periods.)

were in a two-phase region. Air cooling from all temperatures produced structures very similar to those structures exhibited by the solution quenched specimens. The major difference observed was that the air-cooled specimens were attacked more severely than the quenched specimens. A good example of this is X-1 quenched from 2000 °F. (Table II). Hence, the most valuable information was gained from four treatments, namely water quenched and furnace cooled from 2000 °F, and water-quenched and furnace cooled from 1400 °F.

These treatments are both sensitizing and immunizing, depending on the steel in question. Fig. 2 is a plot of these four heat treatments

Table III
Corrosion of Alloy X-1a (0.00% Ni) by Boiling 65% Nitric Acid
Specimens furnace annealed (cooled at 100°F per hr.) from 1450°F to 1100°F prior to further heat treatment. (a)

Material Condition (b)	Corrosion Rate in Mills per Year			Average
	First Period (c)	Third Period	Fifth Period	
WQ 2000°F	28	180	265	155
AC 2000°F	60	420	525	350
FC 2000°F	41	85	135	85
WQ 1650°F	22	43	75	45
AC 1650°F	45	310	381	260
FC 1650°F	31	51	75	50
WQ 1400°F	21	19	20	20
AC 1400°F	22	25	29	25
FC 1400°F	21	21	24	20

(a) Specimens held at 1450°F $\frac{1}{2}$ hr. before cooling.

(b) Specimens held at temperature 1 hr. before cooling. WQ—water-quenched; AC—air-cooled; FC—furnace-cooled (300 to 400°F per hr.).

(c) 48-hr. periods.

Table IV
Corrosion of Alloy X-2 (1.70% Ni) by Boiling 65% Nitric Acid

Material Condition (a)	Corrosion Rate in Mills per Year			Average
	First Period (b)	Third Period	Fifth Period	
WQ 2000°F	28	36	45	35
AC 2000°F	50	180	225	155
FC 2000°F	85	290	355	255
WQ 1650°F	30	33	35	33
AC 1650°F	34	39	41	40
FC 1650°F	42	75	86	70
WQ 1400°F	34	39	40	40
AC 1400°F	39	53	55	50
FC 1400°F	34	44	46	40

(a) Specimens held at temperature 1 hr. before cooling. WQ—water-quenched; AC—air-cooled; FC—furnace-cooled (300 to 400°F per hr.).

(b) 48-hr. periods.

Table V
Corrosion of Alloy X-3 (2.21% Ni) by Boiling 65% Nitric Acid

Material Condition (a)	Corrosion Rate in Mills per Year			Average
	First Period (b)	Third Period	Fifth Period	
WQ 2000°F	29	32	36	32
AC 2000°F	41	135	165	115
FC 2000°F	95	350	330	260
WQ 1650°F	32	36	38	35
AC 1650°F	36	52	57	49
FC 1650°F	47	80	90	75
WQ 1400°F	34	38	41	40
AC 1400°F	35	42	46	40
FC 1400°F	35	40	43	40

(a) Specimens held at temperature 1 hr. before cooling. WQ—water-quenched; AC—air-cooled; FC—furnace-cooled (300 to 400°F per hr.).

(b) 48-hr. periods.

as a function of nickel content. It can be seen that for all heat treatments involved, there is a rather sharp change in the shape of the curves in a range of 2.5 to 3.0% nickel. It might then be postulated that to the left of this zone the mechanism of intergranular corrosion would be that exhibited by ferritic steels, while to the right the austenitic type of mechanisms would be dominant.

Table VI
Corrosion of Alloy X-4 (2.92% Ni) by Boiling 65% Nitric Acid

Material Condition (a)	Corrosion Rate in Mils per Year			Average
	First Period (b)	Third Period	Fifth Period	
WQ 2000°F	30	31	34	32
AC 2000°F	32	36	39	35
FC 2000°F	100	300	310	255
WQ 1650°F	30	28	32	30
AC 1650°F	33	58	70	55
FC 1650°F	76	175	180	150
WQ 1400°F	40	45	48	45
AC 1400°F	48	62	62	59
FC 1400°F	46	60	62	57

(a) Specimens held at temperature 1 hr. before cooling. WQ—water-quenched; AC—air-cooled; FC—furnace-cooled (300 to 400°F per hr.).

(b) 48-hr. periods.

Table VII
Corrosion of Alloy X-5 (3.24% Ni) by Boiling 65% Nitric Acid

Material Condition (a)	Corrosion Rate in Mils per Year			Average
	First Period (b)	Third Period	Fourth Period	
WQ 2000°F	30	31	32	31
AC 2000°F	31	34	35	33
FC 2000°F	75	305	340	230
WQ 1650°F	32	36	37	35
AC 1650°F	36	48	52	45
FC 1650°F	90	200	200	165
WQ 1400°F	38	45	43	40
AC 1400°F	42	55	55	50
FC 1400°F	48	57	58	55

(a) Specimens held at temperature 1 hr. before cooling. WQ—water-quenched; AC—air-cooled; FC—furnace-cooled (300 to 400°F per hr.).

(b) 48-hr. periods.

Table VIII
Corrosion of Alloy X-6 (3.67% Ni) by Boiling 65% Nitric Acid

Material Condition (a)	Corrosion Rate in Mils per Year			Average
	First Period (b)	Third Period	Fifth Period	
WQ 2000°F	23	22	24	23
AC 2000°F	23	26	30	26
FC 2000°F	65	310	335	245
WQ 1650°F	23	23	26	24
AC 1650°F	23	26	28	26
FC 1650°F	49	140	162	125
WQ 1400°F	30	32	34	32
AC 1400°F	30	41	44	40
FC 1400°F	33	49	52	45

(a) Specimens held at temperature 1 hr. before cooling. WQ—water-quenched; AC—air-cooled; FC—furnace-cooled (300 to 400°F per hr.).

(b) 48-hr. periods.

This is further verified by an examination of the microstructures of those specimens from which data are plotted in Fig. 2. Specimens X-1 (0.00% Ni), X-2 (1.70% Ni), and X-3 (2.21% Ni) at 2000 °F showed a two-phase area, predominantly ferrite with from 10 to 40% martensite, while at 1400 °F the structure consisted of masses of dark

Table IX
Corrosion of Alloy X-7 (3.89% Ni) by Boiling 65% Nitric Acid

Material Condition (a)	Corrosion Rate in Mils per Year			Average
	First Period (b)	Third Period	Fifth Period	
WQ 2000°F	21	20	22	20
AC 2000°F	21	20	22	20
FC 2000°F	42	175	215	160
WQ 1650°F	20	20	22	20
AC 1650°F	21	22	24	22
FC 1650°F	51	180	205	150
WQ 1400°F	27	30	32	30
AC 1400°F	29	34	44	37
FC 1400°F	31	48	53	45

(a) Specimens held at temperature 1 hr. before cooling. WQ—water-quenched; AC—air-cooled; FC—furnace-cooled (300 to 400°F per hr.).

(b) 48-hr. periods.

Table X
Corrosion of Alloy X-8 (4.33% Ni) by Boiling 65% Nitric Acid

Material Condition (a)	Corrosion Rate in Mils per Year			Average
	First Period (b)	Third Period	Fifth Period	
WQ 2000°F	18	17	20	18
AC 2000°F	19	22	26	22
FC 2000°F	66	300	375	260
WQ 1650°F	22	24	26	24
AC 1650°F	23	32	38	30
FC 1650°F	41	120	135	102
WQ 1400°F	27	31	35	30
AC 1400°F	29	41	47	40
FC 1400°F	32	62	70	55

(a) Specimens held at temperature 1 hr. before cooling. WQ—water-quenched; AC—air cooled; FC—furnace-cooled (300 to 400°F per hr.).

(b) 48-hr. periods.

Table XI
Corrosion of Alloy X-9 (4.80% Ni) by Boiling 65% Nitric Acid

Material Condition (a)	Corrosion Rate in Mils per Year			Average
	First Period (b)	Third Period	Fifth Period	
WQ 2000°F	27	24	25	25
AC 2000°F	30	28	31	29
FC 2000°F	120	160	310	205
WQ 1650°F	28	28	30	28
AC 1650°F	37	43	49	43
FC 1650°F	75	210	200	170
WQ 1400°F	35	36	37	35
AC 1400°F	37	48	52	46
FC 1400°F	44	70	80	65

(a) Specimens held at temperature 1 hr. before cooling. WQ—water-quenched; AC—air-cooled; FC—furnace-cooled (300 to 400°F per hr.).

(b) 48-hr. periods.

carbide in an all-ferritic matrix. X-1 in an Fe-Cr system, might not be expected to have martensite present, but because of the carbon, the two-phase region of the gamma loop is moved toward the right, hence a two-phase structure with no nickel present in the alloy. The martensite and carbides were elongated due to the worked condition of the

Table XII
Corrosion of Alloy X-10 (5.46% Ni) by Boiling 65% Nitric Acid

Material Condition (a)	Corrosion Rate in Mils per Year			
	First Period (b)	Third Period	Fourth Period	Average
WQ 2000°F	24	16	17	18
AC 2000°F	24	20	21	21
FC 2000°F	28	55	80	60
WQ 1650°F	28	26	27	27
AC 1650°F	28	33	36	33
FC 1650°F	80	240	245	200
WQ 1400°F	32	31	33	30
AC 1400°F	34	46	50	45
FC 1400°F	55	110	115	100

(a) Specimens held at temperature 1 hr. before cooling. WQ—water-quenched; AC—air-cooled; FC—furnace-cooled (300 to 400°F per hr.).

(b) 48-hr. periods.

Table XIII
Corrosion of Alloy X-11 (5.84% Ni) by Boiling 65% Nitric Acid

Material Condition (a)	Corrosion Rate in Mils per Year			
	First Period (b)	Third Period	Fifth Period	Average
WQ 2000°F	14	11	11	12
AC 2000°F	14	13	13	13
FC 2000°F	20	125	290	145
WQ 1650°F	16	18	18	17
AC 1650°F	18	33	44	30
FC 1650°F	43	160	190	140
WQ 1400°F	24	35	35	30
AC 1400°F	26	47	50	42
FC 1400°F	70	120	110	100

(a) Specimens held at temperature 1 hr. before cooling. WQ—water-quenched; AC—air-cooled; FC—furnace-cooled (300 to 400°F per hr.).

(b) 48-hr. periods.

Table XIV
Corrosion of Alloy X-12 (8.29% Ni) by Boiling 65% Nitric Acid

Material Condition (a)	Corrosion Rate in Mils per Year			
	First Period (b)	Third Period (c)	Fifth Period	Average
WQ 2000°F	10	7	7	8
AC 2000°F	10	8	8	8
FC 2000°F	14	51	120	65
WQ 1650°F	10	8	8	8
AC 1650°F	9	11	13	11
FC 1650°F	23	75	125	70
WQ 1400°F	10	14	19	15
AC 1400°F	11	25	41	25
FC 1400°F	39	260	345	230

(a) Specimens held at temperature 1 hr. before cooling. WQ—water-quenched; AC—air-cooled; FC—furnace-cooled (300 to 400°F per hr.).

(b) 48-hr. periods.

(c) This period was only 36-hrs. in duration.

material. The attack in these specimens was primarily along the martensitic grain boundaries and at times in the martensite itself. X-4 (2.92% Ni) was somewhat of a borderline case, neither one side nor the other, but located approximately in the center of the transition zone. From Fig. 1 it can be seen that X-4 falls almost in the middle of the two-phase area. The structure was continuous martensite with

Table XV
Corrosion of Alloy X-12a (8.29% Ni) by Boiling 65% Nitric Acid
Specimens were water-quenched from 2000°F prior to further heat treatment. (a)

Material Condition (b)	Corrosion Rate in Mils per Year			
	First Period (c)	Third Period	Fifth Period	Average
WQ 2000°F	10	7	7	8
AC 2000°F	9	6	7	7
FC 2000°F	11	49	124	70
WQ 1650°F	9	8	8	8
AC 1650°F	9	9	12	10
FC 1650°F	11	32	70	35
WQ 1400°F	10	12	17	12
AC 1400°F	10	18	35	20
FC 1400°F	18	130	375	165

(a) Specimens held at 200°F ¼ hr. before quenching.

(b) Specimens held at temperature 1 hr. before cooling. WQ—water-quenched; AC—air-cooled; FC—furnace-cooled (300 to 400°F per hr.).

(c) 48-hr. periods.

Table XVI
Corrosion of Wrought Commercial Type 304 (0.08% C) by Boiling 65% Nitric Acid

Material Condition (a)	Corrosion Rate in Mils per Year			
	First Period (b)	Third Period	Fifth Period	Average
WQ 2000°F	9	6	6	7
AC 2000°F	9	5	5	6
FC 2000°F	9	54	185	75
WQ 1650°F	9	9	12	9
AC 1650°F	10	15	35	19
FC 1650°F	115	1090	1060	890
WQ 1400°F	10	36	220	70
AC 1400°F	11	105	345	150
FC 1400°F	230	1540	1200	1100

(a) Specimens held at temperature 1 hr. before cooling. WQ—water-quenched; AC—air-cooled; FC—furnace-cooled (300 to 400°F per hr.).

(b) 48-hr. periods.

Table XVII
Corrosion of Wrought Commercial Type 430 (0.05% C) by Boiling 65% Nitric Acid

Material Condition (a)	Corrosion Rate in Mils per Year			
	First Period (b)	Third Period	Fifth Period	Average
WQ 2000°F	46	290	370	245
AC 2000°F	65	410	445	320
FC 2000°F	74	165	240	153
WQ 1650°F	41	46	54	47
AC 1650°F	45	95	135	93
FC 1650°F	92	230	240	195
WQ 1400°F	30	30	33	30
AC 1400°F	32	40	42	38
FC 1400°F	34	41	52	43

(a) Specimens held at temperature 1 hr. before cooling. WQ—water-quenched; AC—air-cooled; FC—furnace-cooled (300 to 400°F per hr.).

(b) 48-hr. periods.

approximately 20–25% ferrite and was not typical to either mechanism. The attack was at heavy carbide precipitates in the grain boundaries next to the ferritic material.

At 2000 °F, specimens X-5 (3.24% Ni) to X-9 (4.80% Ni), contained approximately 10 to 15% ferrite with the continuous phase being

martensite. At 1400 °F, the structure was a tempered martensite with stringers of ferrite. These alloys still exhibited a two-phase structure as might be expected from Fig. 1. X-10 (5.46% Ni) and X-11 (5.84% Ni) just began to reach the solid austenitic field and some austenite was present in the structure at room temperature after treatment at 2000 °F. The furnace-cooled 1400 °F specimens were beginning to corrode rather severely in the grain boundary areas. The matrix was ferritic with large precipitated carbides. X-12 (8.29% Ni) was a wholly austenitic alloy and the furnace-cooled 1400 °F specimen exhibited very severe intergranular attack.

It might be mentioned here that the curve for specimens furnace cooled from 2000 °F in Fig. 2 shows increasing corrosion rates up to a maximum at the transition, then decreases with increased nickel. This might be due to one of two reasons, or both. One that in the condition of equal ferrite and austenite the material is more susceptible after a short heat treatment than if the specimen had been held at temperature for a longer time. These specimens were held at temperature for only 1 hour. Also, it was noted that, in this zone, a maximum amount of carbides were precipitated, which were severely attacked. As the nickel was increased, the amounts of carbide seemed to decrease slightly.

One unusual fact was noted. All specimens when water-quenched from 1400 °F did not exhibit any intergranular attack. To the left of the 2.5–3.0% nickel zone, this temperature is the immunization temperature for ferritic steels. Specimens with higher nickel, exhibit a martensitic or austenitic structure. The carbides present were scattered in and out of the grains. From Fig. 1 it can be seen that specimens X-10 (5.46% Ni) through X-12 (8.29% Ni) at 1400 °F are in the complete austenite area the same as at 2000 °F. Thus the carbides may be in solution to some degree, and when quenched it possibly has the same effect as quenching from 2000 °F. Without further investigation it would be difficult to explain completely this phenomenon.

When the proper heat treatment to impart immunity was applied (i.e., furnace annealing X-1 and solution quenching X-12), extremely good corrosion resistance was observed.

As mentioned above, there was some doubt as to the effect that a prior heat treatment might have on the validity of the results. Specimen X-1a (Table III) was furnace annealed and X-12a (Table XV) was solution quenched prior to test heat treatments, then corroded as were the other specimens. Tables II, III, XIV, and XV show that there is very little deviation in actual values, and a close agreement as to the rates of corrosion at each heat treatment. The microstructures were almost identical excepting some variation in grain size. This was a spot check and was not performed in all experimental alloys.

Huey tests were run on commercial Types 430 and 304 steels. It was

found that the correlation in susceptibility between commercial and experimental alloys was good, but in the susceptible conditions the commercial alloys corroded at rates much higher than those of the experimental alloys.

Thus from corrosion rates obtained from the Huey tests, plotted as a function of nickel content, and a microscopic examination, it is the authors' belief that 18% chromium steels containing from 0 to 2.5% nickel can be properly treated (insofar as intergranular corrosion is concerned) as ferritic steels, and those containing 3% or more nickel, fall into the category of austenitic steels and should be heat treated accordingly.

SUMMARY AND CONCLUSIONS

1. Alloyed nickel is the direct cause in the shift of the mechanism of intergranular corrosion of Type 430 to that of Type 304.
2. The transition from one mechanism to the other was found to occur at 2.5 to 3.0% nickel.
3. 18% Cr steels with less than 2.5% nickel should be heat treated as ferritic stainless steels and those above 3.0% nickel as austenitic stainless steels.
4. Prior heat treatment to the as-rolled material did not show any appreciable change in corrosion resistance.
5. Furnace cooling specimens in the transition range (2.0 to 3.5% nickel) from 2000 °F brought on extreme cases of intergranular attack.
6. None of the alloys exhibited intergranular corrosion when water quenched from 1400 °F.

ACKNOWLEDGMENT

The interest and support of the Office of Naval Research is greatly appreciated. This work was carried out under Contract N6ori-17 between the Office of Naval Research and The Ohio State University Research Foundation.

References

1. P. Payson, "Prevention of Intergranular Corrosion in Corrosion Resistant Chromium-Nickel Steels," *Transactions, American Institute of Mining and Metallurgical Engineers*, Vol. 100, 1932, p. 306.
2. E. C. Bain, R. H. Aborn and J. J. B. Rutherford, "The Nature and Prevention of Intergranular Corrosion in Austenitic Stainless Steels," *TRANSACTIONS, American Society for Steel Treating, (American Society for Metals)*, Vol. 21, 1933, p. 481.
3. M. G. Fontana, *Corrosion: A Compilation*, 1957, p. 29. Hollenback Press, Columbus, Ohio.
4. E. M. Mahla and N. A. Nielsen, "Carbide Precipitation in Type 304 Stainless Steel—An Electron Microscope Study," *TRANSACTIONS, American Society for Metals*, Vol. 43, 1950, p. 290.
5. E. Houdremont and W. Tofante, "Kornzerfallbesandigkeit Nichtrostenber Ferritizher und Martensitischer Chromstahle," *Stahl und Eisen*, Vol. 72, 1952, p. 539.

6. G. C. Kiefer, *Engineering Experiment Station News*, Vol. 22, June 1950, p. 21, The Ohio State University.
7. R. A. Lula, A. J. Lena and G. C. Kiefer, "Intergranular Corrosion of Ferritic Stainless Steels," *TRANSACTIONS, American Society for Metals*, Vol. 46, 1954, p. 197.
8. C. A. Zapffe, *Stainless Steels*, 1949, p. 136, American Society for Metals, Cleveland.

DISCUSSION

Written Discussion: By Stephen F. Urban, Director of Research, Titanium Alloy Manufacturing Division, National Lead Company, Niagara Falls, N. Y.

The data presented in the paper by Messrs. Upp, Beck, and Fontana again shows that inflection points on the corrosion curves in nitric acid probably correspond to changes in microstructure. It is regrettable that photomicrographs were not included but from the Society's viewpoint, this is understandable.

If another group were to attempt to duplicate results described in a general fashion, this goal will be attained. If one expected more precise checks, one would be disappointed and I believe mostly because melts from two sites would contain variable nitrogen contents. For example, if we select any arbitrary composition, say 14% chromium, depending upon the melting technique, one will obtain anywhere from 0.015 to about 0.08% nitrogen. This is extremely important because nitrogen is a very powerful austenite former and a fairly good stabilizer. Because of these circumstances, two pieces of metal made at two different sites would, with a given heat treatment, have different structures in correspondingly quite different corrosion rates. This would be true despite the fact that chromium, carbon and nickel contents were identical.

The authors conducted their work in nitric acid and it may be interesting to note that similar differences are sometimes obtained when hydrochloric acid is the medium.

Authors' Reply

The authors wish to thank Dr. S. F. Urban for his interesting discussion.

We believe that the effect of increasing nitrogen would be to shift the inflection point to the left, i.e., towards a lower nickel content. Both nickel and nitrogen are austenite formers.

The heats described in the paper were made with low nitrogen ferro-chrome so the nitrogen contents should be on the low side. Attempts to produce higher nitrogen heats resulted in "gassy" ingots so this portion of the work was discontinued.

The last paragraph in Dr. Urban's discussion also makes an interesting point. Other work is in progress here on the effects of microstructure differences on corrosion of "18-8" by other environments including hydrochloric acid, acetic acid, and calcium chloride. We expect to publish this work at a later date.

PHASE RELATIONSHIP IN AUSTENITIC Cr-Mn-C-N STAINLESS STEELS

BY CHI-MEI HSIAO AND E. J. DULIS

Abstract

The stable austenite region in the Cr-Mn-C-N steels containing 0.10/0.80% C, 10/28% Mn, 12/28% Cr, and 0.10/0.80% N has been determined. At 2100 °F, the minimum amount of carbon plus nitrogen required for a completely austenitic structure increases with increasing amount of chromium, and this relationship can be represented by the expression $C + N = 0.078 (Cr - 12.5\%)$. When the chromium is over 15%, about 12% manganese is required to stabilize the austenite; and when the chromium is between 12 and 15%, 12 to 18% manganese is required.

The microstructural changes associated with (a) the solution treatment at different temperatures (1900 to 2300 °F) and (b) the three solid-state reactions (precipitation, martensite transformation, and sigma phase formation) that could occur during or after aging in the range 1200 to 1600 °F for up to 100 hours have been extensively investigated and the results are presented. Also, the solution hardening and the hardening due to different aging reactions have been discussed. (ASM International Classification: N8, N7a; SS-e)

INTRODUCTION

ONE PHASE of a program aimed at the development of nickel-free austenitic stainless steels for elevated temperature applications was the establishment of the relationships among composition, heat treatment, and phase formation in iron-rich Cr-Mn-C-N alloys. A knowledge of these relationships is important in obtaining the comprehensive understanding of the characteristics of these steels that is required for a new steel development program.

Most of the early studies and developments on austenitic Cr-Mn steels were made in Germany and Russia, probably because of the shortage of nickel in those two countries. The low carbon (up to 0.10%) austenitic Cr-Mn steels were investigated by Becket (1),¹

¹ The figures appearing in parentheses pertain to the references appended to this paper.

This research was supported in part by the United States Air Force under Contract AF33 (616)-3318, monitored by the Materials Laboratory, Wright Air Development Center, Wright-Patterson Air Force Base, Ohio.

A paper presented before the Thirty-Ninth Annual Convention of the Society, held in Chicago, November 4-8, 1957. The authors are associated with the Research and Development Laboratory, Crucible Steel Company of America, Pittsburgh. Manuscript received April 11, 1957.

Köster (2), Gunzberg et al. (3), Schmidt and Legat (4,5), Burgess and Forgeng (6), Bruhl (7), and Borzdyka (8,9). One of the most interesting findings of these investigations was that the amount of austenite produced in a Cr-Mn steel at high temperatures is almost entirely a function of its chromium and carbon contents. That is, the addition of manganese does not increase the amount of austenite appreciably; however, manganese does increase very markedly the stability of the austenite at low temperatures.

The austenite-forming ability of nitrogen in high Cr steels was noted by Krivobok (10), Franks (11), and Colbeck and Garner (12). Also, some studies on nitrogen-bearing Cr-Mn steels were made by Krainer and Mirt (13), Rapatz (14), and Schaeben (15). However, in these latter studies, nitrogen contents were limited to a maximum of 0.25%. Recently, Franks et al. (16) determined the austenite regions for 0.10% carbon steels containing 12 to 18% chromium, 1 to 22% manganese, 0 to 14% nickel and 0.03 to 0.19% nitrogen. A similar investigation was made by Whittenberger et al. (17) on 0.12% carbon steels containing 15 to 21% chromium, 12 to 18% manganese, 0 to 3% nickel and 0.25 to 0.45% nitrogen. Both investigations were limited to low carbon steels, and the austenite was formed and stabilized by the addition of nitrogen and manganese. It is of interest to note that manganese in excess of about 10% tends to enlarge slightly the delta ferrite-austenite region when the chromium content is greater than 15% (16,17). Other investigations on Cr-Mn-C-N steels include those reported recently by Zackay et al. (18) and Carlson and Zackay (19).

A related investigation on the phase relationships in Cr-C-N steel has been made recently by Tisinai et al. (20). In these steels, the austenite formed by the addition of C and N was not sufficiently stable and could be retained at room temperature only by rapid cooling. The austenite decomposed either during moderately slow cooling from the austenitizing temperature, or when reheated to temperatures below the austenitizing temperature.

The primary purpose of the present investigation was to determine the base compositions of the Cr-Mn-C-N steels that contain no delta ferrite, and which do not transform to martensite after different heat treatments. Fully austenitic steels are more desirable than those with mixed structures because of their superior hot working characteristics and superior mechanical properties at temperatures over about 1200 °F. In this study, the following two factors were determined as a function of composition:

- (a) whether the steel was wholly austenitic after a solution treatment, and
- (b) whether the wholly austenitic steel was stable after an aging treatment.

MATERIALS AND PROCEDURES

The experimental steels of this investigation encompassed the following composition ranges: 0.10/0.80% carbon, 5/28% manganese, 12/28% chromium, and 0.10/0.80% nitrogen. The steels were prepared as 15-pound induction-melted heats, and the ingots from these heats were forged to $\frac{5}{8}$ -inch square bars. The compositions of these steels are given in Table I.

The heat treatments used in this investigation included solution treating and aging. The solution treating consisted of heating the specimens ($\frac{5}{8}$ -inch square by $\frac{1}{2}$ -inch high) for $\frac{1}{2}$ to 2 hours at temperatures in the range 1700 to 2300 °F and water quenching to room temperature. The aging treatments consisted of heating the solution-treated specimens at temperatures in the range 1200 to 1600 °F for various periods of time and water quenching.

The microstructures of all experimental steels in both the solution-treated and the solution-treated and aged conditions were examined to determine the following:

- (a) The presence of delta ferrite and martensite,
- (b) The amount of residual carbides and nitrides,
- (c) The grain size, and
- (d) The structural changes that occur during or after aging.

Delta ferrite was delineated from austenite by deeply etching the test samples in 20% hydrochloric acid in alcohol. The ferrite occurred as stringers of polygonal areas in the austenite matrix. The microscopic detection of the presence of delta ferrite was in general agreement with the Magne-Gage measurements. A calibration curve (Magne-Gage readings versus % of delta ferrite) was determined by using lineal analyses to establish the amount of ferrite present. Although the magnetic test is simpler and more sensitive, the direct observation by microscopic methods was also used because this method differentiates between the two magnetic phases, delta ferrite and martensite, which occur in some of the steels.

At each stage of heat treatment, magnetic tests (Magne-Gage) were made to detect the possible formation of the magnetic constituents ferrite and/or martensite. Also, room temperature Rockwell hardness tests were made on the specimens after each heat treatment in order to evaluate any aging reactions that might have occurred. To determine the solution-hardening attributable to the presence of the interstitial elements, carbon and nitrogen, the microhardness of the austenite of some specimens was measured by a Reichert microhardness tester.

To identify the phases present in the steels, x-ray diffraction tests supplemented by chemical analyses were made on selected specimens. For these tests, electrolytically extracted residues were studied by procedures which were described previously (21).

Table I
Composition of Steels

Steel No.	Chromium	Manganese	Carbon	Nitrogen	C + N
W96	12.41	13.72	0.062	0.11	0.17
W95	11.95	11.84	0.055	0.12	0.17
W27	12.04	10.35	0.103	0.19	0.29
W42	11.71	12.35	0.112	0.20	0.31
W43	12.48	14.15	0.097	0.23	0.33
W1a	12.03	9.96	0.30	0.06	0.36
W26	13.14	6.98	0.26	0.12	0.38
W1b	12.82	9.79	0.30	0.19	0.49
C1	11.59	10.56	0.25	0.16	0.41
W25	13.16	4.94	0.28	0.13	0.41
W5a	12.75	27.88	0.31	0.11	0.42
W5b	12.82	28.16	0.29	0.14	0.43
W3d	12.24	10.47	0.27	0.17	0.44
W88	12.25	12.45	0.189	0.28	0.47
W3a	12.03	10.50	0.30	0.17	0.47
C3	11.61	10.64	0.37	0.11	0.48
W3c	12.55	10.89	0.28	0.21	0.49
W3b	12.19	10.53	0.29	0.22	0.51
C4	11.90	10.53	0.40	0.18	0.58
W76	13.46	11.92	0.32	0.30	0.62
W20	12.42	26.19	0.51	0.13	0.64
W17	13.39	11.07	0.59	0.14	0.73
W13	11.72	28.27	0.79	0.09	0.88
W9	12.84	10.31	0.78	0.11	0.89
W10b	12.35	10.40	0.74	0.20	0.94
W10a	12.60	10.43	0.78	0.21	0.99
W8a	13.00	29.00	0.34	0.67	1.01
W8b	12.61	28.21	0.26	0.84	1.10
W14a	12.06	28.44	0.80	0.57	1.37
W14b	12.36	27.91	0.79	0.67	1.46
W98	15.04	13.52	0.102	0.13	0.23
W97	15.31	11.92	0.116	0.16	0.28
W44	15.44	12.24	0.110	0.22	0.33
W45	15.42	14.24	0.105	0.23	0.33
W30	15.51	10.60	0.092	0.31	0.40
W28	15.62	10.38	0.30	0.12	0.42
W29	15.68	10.52	0.28	0.22	0.50
W99	17.10	11.75	0.22	0.13	0.35
W100	17.18	11.78	0.30	0.15	0.45
C5	16.90	10.56	0.42	0.26	0.68
W46	18.16	12.19	0.29	0.28	0.57
C6	17.89	16.88	0.40	0.18	0.58
W47	17.91	11.83	0.41	0.19	0.60
C12	17.97	4.50	0.38	0.23	0.61
C7	17.79	16.88	0.41	0.26	0.67
W21	17.62	15.75	0.42	0.28	0.70
C8	17.51	16.27	0.41	0.32	0.73
C14	17.88	8.54	0.37	0.37	0.74
W55	18.42	12.47	0.40	0.39	0.79
C13	18.00	4.41	0.55	0.29	0.84
C15	17.79	8.56	0.60	0.27	0.87
W31	18.71	11.60	0.32	0.14	0.46
W33	18.82	12.54	0.132	0.45	0.58
W32	18.76	12.54	0.30	0.35	0.65
W48	20.15	12.61	0.094	0.63	0.72
W50	21.20	12.24	0.29	0.41	0.70
W51	21.29	11.52	0.50	0.26	0.76
W35	21.35	12.71	0.29	0.48	0.77
W37	21.35	12.16	0.76	0.17	0.93
W34	21.81	12.60	0.123	0.55	0.67
W49	22.41	12.88	0.177	0.56	0.74
W36	21.87	11.75	0.55	0.41	0.96
W82	21.62	12.26	0.48	0.54	1.02
W23	22.47	13.22	0.82	0.29	1.11
W24	23.50	13.46	0.073	0.62	0.69
W22	23.33	13.11	0.42	0.42	0.84
C10	23.05	13.60	0.71	0.15	0.86
C9	23.23	13.54	0.43	0.46	0.89
C11	23.38	13.05	0.71	0.26	0.97
C2	23.52	13.48	0.29	0.45	0.74
W38	24.38	13.37	0.30	0.58	0.88

Table I continued

Steel No.	Chromium	Manganese	Carbon	Nitrogen	C + N
W54	24.39	13.55	0.63	0.29	0.92
C28	24.30	11.39	0.57	0.39	0.96
C18	23.71	8.22	0.67	0.31	0.98
C16	23.87	4.74	0.62	0.44	1.06
C17	24.13	4.74	0.79	0.47	1.26
C19	24.00	8.53	0.80	0.49	1.29
W94	24.42	12.40	0.64	0.72	1.36
C31	24.93	14.35	0.40	0.43	0.83
C27	24.97	14.49	0.50	0.36	0.86
C32	24.99	14.49	0.47	0.43	0.90
W53	24.74	13.08	0.43	0.48	0.91
C29	25.16	11.50	0.65	0.34	0.99
C34	25.12	14.31	0.72	0.34	1.06
W52	24.54	14.52	0.31	0.78	1.09
C33	24.71	13.52	0.66	0.44	1.10
W39	24.59	10.60	0.69	0.44	1.13
W40	24.84	12.62	0.75	0.40	1.15
C30	24.97	11.69	0.79	0.40	1.19
W2b	28.43	10.10	0.30	0.22	0.52
W18	27.86	9.84	0.53	0.18	0.71
C22	27.32	16.86	0.60	0.44	1.04
W11	27.83	9.78	0.81	0.25	1.06
C21	27.58	14.59	0.59	0.50	1.09
C23	28.13	18.17	0.59	0.52	1.11
W19	28.33	10.45	0.55	0.69	1.24
W12	27.98	10.51	0.81	0.66	1.47
W41	27.43	14.51	0.87	0.75	1.62
W2a	28.74	10.05	0.25	0.25	0.50
W4	28.66	10.25	0.28	0.69	0.97
C25	30.03	16.25	0.62	0.51	1.13
C26	29.91	18.06	0.60	0.57	1.17
C24	29.77	14.40	0.60	0.58	1.18
C20	29.01	13.12	0.86	0.74	1.60

RESULTS AND DISCUSSION

Based on the results of microstructural studies, magnetic measurements, and hardness tests, the experimental steels were classified into the following three groups:

- Stable austenitic steels—These are austenitic after solution-treating, and after solution-treating and aging.
- Duplex steels—These contain austenite and ferrite after solution treating and austenite, sigma, and/or ferrite after aging.
- Unstable austenitic steels—These are austenitic at the solution-treating temperatures but transform into martensite (completely or partially) during cooling to room temperature or after subsequent aging.

AUSTENITE FORMATION

Austenite-Austenite plus Ferrite Boundary

The austenite-austenite plus delta ferrite phase boundary at 2100 °F was plotted as a function of chromium content versus carbon plus nitrogen content, Fig. 1. Also, the manganese content and the aforementioned classification of the individual steels is denoted on the graph.

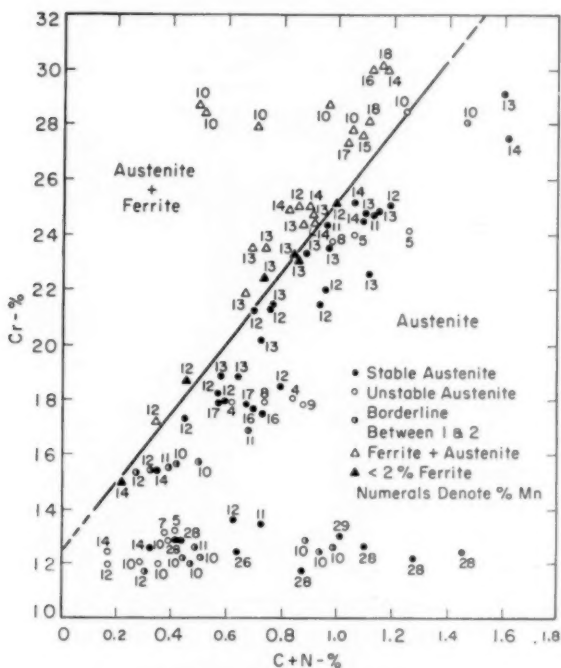


Fig. 1—Phase Relation in Fe-Cr-Mn-C-N System at 2100 °F.

The boundary line between the austenite and austenite plus ferrite fields, Fig. 1, indicates that the minimum amount of carbon plus nitrogen required for a completely austenitic structure increases with increasing amount of chromium, and this relationship can be represented by the following equation:

$$C + N = 0.078 (Cr - 12.5) \quad \text{Equation 1}$$

This equation is applicable for steels that contain from 5 to 14% manganese; no extensive work has been done for higher manganese steels.

The equivalence of carbon and nitrogen in their ability to form austenite has also been found recently by DeLong et al (22).

It should be noted that the boundary line in Fig. 1 is for the isothermal section at 2100 °F. At temperatures other than 2100 °F, this boundary line will be shifted.

The effect of solution-treating temperature on the amount of delta ferrite is shown in Table II. For the high carbon steels (W11, W19, and W54), the amount of delta ferrite decreased with increasing solution-treating temperature. This behavior in the high carbon steels

Table II
Effect of Solution-Treating Temperature on the Amounts of Delta Ferrite

Steel No.	Composition (Wt. %)					(C+N) (1)	% of Delta Ferrite at Indicated Temperature (°F) (g)					$\Delta/\Delta T$	Relationship Inflection Point (°F)	T Min. (°F)
	Cr	Mn	C	N	C+N		1900	2000	2100	2200	2300			
W11	27.8	9.8	.81	.25	1.06	1.19	29	26	23	19	14	(-)	—	2300
W19	28.3	10.4	.55	.69	1.24	1.23	20	5.6	1.0	0	0	(-)	—	2300
W31	18.7	11.6	.32	.14	0.46	0.48	2.4	1.0	2.4	4.7	7.5	*	2000	2300
W32	18.8	12.5	.30	.35	0.65	0.49	0	0	0	0	0	(-)	—	2025
W33	18.8	12.5	.13	.45	0.58	0.49	0	0	0	0	2.2	(+)	—	1800
W35	21.3	12.7	.29	.48	0.77	0.69	0	0	0	0	0	*	2100	2050
W38	24.3	13.4	.30	.58	0.88	0.92	12	8.5	0.4	0.2	10	*	—	2135
W46	17.2	12.8	.29	.18	0.47	0.44	0	0	0	0	0	(-)	—	2125
W49	22.4	12.9	.41	.19	0.60	0.42	0	0	0	0	0	*	2000	2050
W50	21.2	12.2	.29	.41	0.70	0.68	0	3.8	4.4	6.8	9.4	(+)	—	2225
W51	21.3	11.5	.50	.26	0.76	0.69	0	0	0	0	0	(-)	—	2150
W52	24.5	14.5	.31	.78	1.09	0.94	0	0	0	0	0	*	2200	2250
W53	24.7	13.1	.43	.48	0.91	0.95	8.8	6.8	4.4	2.8	4.4	(-)	—	2300
W54	24.4	13.5	.63	.29	0.92	0.93	13	11	7.4	3.5	1.8	(+)	—	1700
W97	15.3	11.9	.12	.16	0.28	0.22	0	0	0	1.8	9.6	(+)	—	1650
W98	15.0	13.5	.10	.13	0.23	0.20	0	0	0	3.2	10.0	(+)	—	1925
W99	17.1	11.8	.22	.13	0.35	0.36	0	1.0	3.5	7.4	12.1	(+)	—	2000
W100	17.2	11.8	.30	.13	0.43	0.37	0	0	0	0	0	(-)	—	2000

Note: (1) (C+N) min.—Minimum amount of carbon plus nitrogen required for a completely austenitic structure at 2100°F, calculated from Equation 1.

(2) Time at temperature: 1900 to 2100°F, 2 hours; 2200 to 2300°F, 1 hour

(3) T min.—Lowest temperature for complete solution of carbides and nitrides, Fig. 2.

* The amounts of delta ferrite are first decreased and then increased with increasing solution treating temperature, and the inflection points of the Δ -T curve are near the T min.

is attributable to the availability of residual carbides to go into solution at the high solution-treating temperatures, whereas in the low carbon steels all the carbides go into solution at low solution-treating temperatures. (The effect of composition and solution-treating temperature, T , on the solution of residual carbides and nitrides will be discussed later.) The effect of increasing the carbon and chromium in solution is such that the carbon increases the amount of austenite that forms despite the opposing tendency of chromium. For the low carbon steels (W33, W97, W98, and W99) the amount of delta ferrite increased with increasing solution-treating temperature. This behavior is in agreement with the well known effect of temperature on the formation of delta ferrite and is illustrated by the familiar loop phenomenon on the Fe-Cr equilibrium diagram. For the medium carbon, high chromium steels (W38, W49, and W53), the amount of delta ferrite first decreased and then increased with increasing solution-treating temperature. This is a combination of the aforementioned two cases and is related to the minimum temperature for complete solution of carbides. The presence of delta ferrite at very high temperatures, e.g., 2300 °F, could be prevented by a slight increase in the amount of carbon and/or nitrogen. This is evident by comparing the data for the following steels: W31, W33, and W32; W99 and W100, Table II.

Residual Carbides and Nitrides

The amounts of residual carbides and nitrides in the steels that had been solution-treated were found to decrease with increasing solution-treating temperature. The lowest temperature, T , for the complete solution of the residuals was determined by solution-treating selected steels in the temperature range 1600 to 2300 °F (in 50 °F intervals) and examining the microstructures of the steels after these heat treatments. The test results show that T increases with increasing amounts of chromium and carbon and decreases slightly with increasing amounts of manganese, Fig. 2. Also, T is independent of the amount of nitrogen present in the steels. The curve for the 18% chromium steels of this investigation agrees fairly well with the published results for 18-8 Cr-Ni stainless steels (23).

The dependence of T on the amounts of chromium and carbon indicates that, as expected, the solubility of chromium carbide in austenite increases with increasing temperature, and that in steels high in chromium and carbon, large amounts of chromium and carbon are available to form chromium carbide. The effect of nitrogen on T is probably masked by the pronounced effect of chromium and carbon. Also, the effect of manganese on T is small; for example, in the 28% manganese steels, T values are slightly lower than those of comparable 10% manganese steels, Fig. 2.

To indicate the compositions that contain residual carbides in the

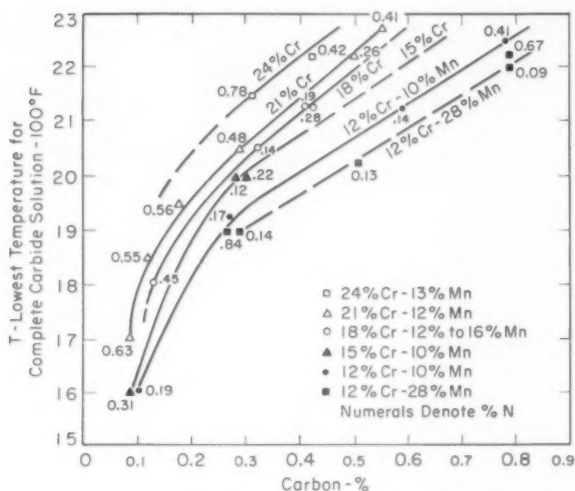


Fig. 2—Effect of Composition on the Lowest Temperatures for Complete Solution of Carbides and Nitrides.

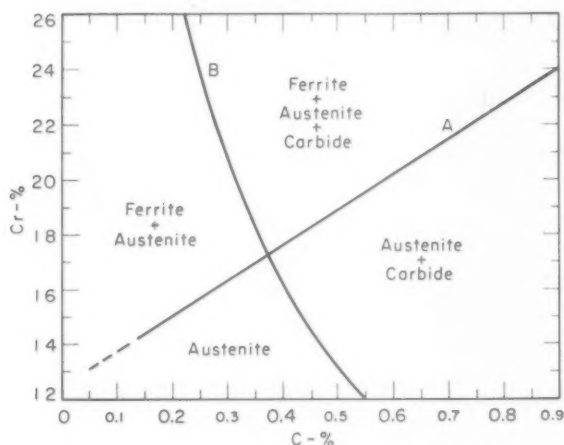


Fig. 3—Isothermal Section of Cr-Mn-C Steels at 2100 °F.

isothermal section at 2100 °F, Fig. 3 was prepared. In this figure, line A was plotted from Fig. 1 assuming no nitrogen is added, and line B, from Fig. 2. Fig. 3 can be used for designing austenitic Cr-Mn-C-N steels free from both delta ferrite and residual carbide. For example, a minimum amount of carbon and nitrogen required for a 21% chromium austenitic steel is 0.66% at 2100 °F (Fig. 1 and Line A, Fig. 3),

and the maximum amount of carbon which could be dissolved at this temperature is 0.30% (Line B, Fig. 3). Therefore, a steel which contains 0.30% carbon, 21% chromium, 0.36% nitrogen would remain austenitic and free from both delta ferrite and residual carbides by a 2100 °F solution treatment. As discussed previously, 12% manganese is required to stabilize this steel from martensite transformation.

Grain Size

As expected, the grain sizes of the experimental steels were found to increase with increasing solution-treating temperature. An example of this effect is shown in Fig. 4. The grain size varies from steel to steel

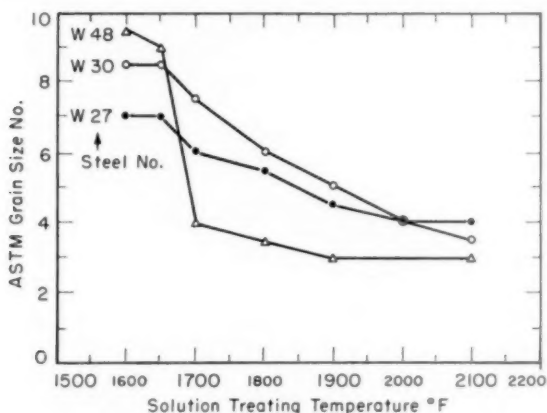


Fig. 4—Effect of Solution Treating Temperature on Grain Size.

and ranges from ASTM grain size No. 1 to No. 10. The effect of composition on the grain size appears to be related to the lowest solution-treating temperature for complete carbide solution, i.e., grain growth is retarded by the presence of residual carbides and nitrides.

AUSTENITE STABILITY

Martensite Transformation

Whether the austenite that formed at the solution-treating temperature or that existed at the aging temperature would resist transformation to martensite during cooling to room temperature depends on the composition of the austenite. The effect of composition on the M_s temperature of 18-8 type stainless steels has been determined by Eichelman and Hull (24) to have the following relationship:

$$M_s = 75(14.6 - Cr) + 110(8.9 - Ni) + 60(1.33 - Mn) + 50(0.47 - Si) + 3000 [0.068 - (C + N)] \quad \text{Equation 2}$$

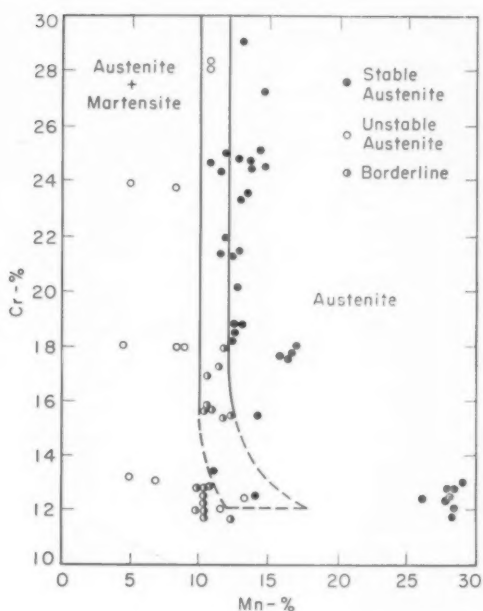


Fig. 5—Stabilizing Effect of Manganese on Austenite.

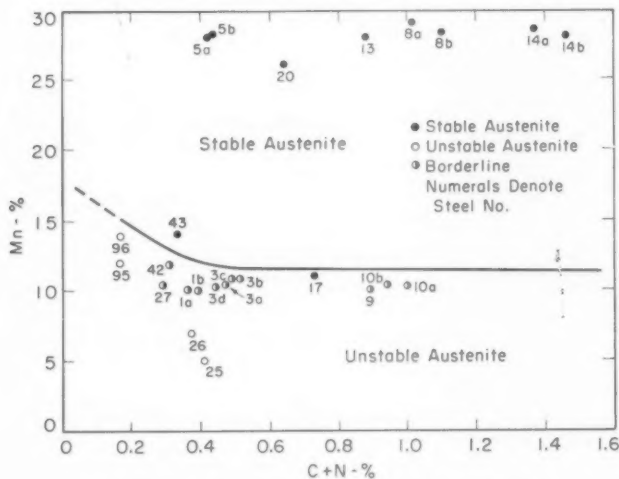


Fig. 6—Stabilizing Effect of Manganese and (C + N) on 12% Chromium Steels.

Although the compositions of the experimental steels in the present investigation are beyond the compositional range from which Equation 2 was derived, it is believed (based on the well known characteristics of the additive elements) that the relative effects of the alloying elements on M_s temperature are applicable. Also, it is of interest to note the effect of chromium in the equation, i.e., chromium retards the martensite transformation when it is over 14.6%. This effect has also been observed in other studies on the Fe-Cr-C-N system (20).

The following conclusions can be deduced from the experimental results shown in Figs. 1 and 5, and these conclusions are in agreement with the results of other published investigations in regard to the relative effects of chromium, manganese, carbon, and nitrogen in stabilizing the austenite from transforming to martensite.

(a) When the chromium is over 15%, about 12% manganese is required to stabilize the austenite to avoid a martensitic transformation. The excess amount of C + N over that required to form a completely austenitic structure at solution treating temperatures does not prevent the transformation of austenite to martensite during cooling to room temperature after aging. For example, at 18% chromium, the minimum amount of C + N required for a completely austenitic structure is 0.43%, however, a steel with 0.88% (C + N) and 9% manganese is unstable, whereas a steel with 0.60% (C + N) and 12% manganese is stable (Fig. 1).

(b) When the chromium is between 12 to 15%, the amount of manganese required to stabilize the austenite to avoid a martensite transformation varies from 12 to about 18% (extrapolated from Fig. 6). The variation depends upon the amounts of chromium and of (C + N) in the steel. For example, at the 12% chromium level, Steel W17 (0.73% carbon + nitrogen, 11% manganese) showed no martensitic transformation even after aging for 100 hours, whereas Steel W95 (0.17 C + N, 12% manganese) transformed to martensite during cooling from the solution-treating temperature. The strong effect of manganese in stabilizing the austenite is also evident by comparing the 12% chromium steels, W25, W26, W27, and W42 (Fig. 7), whose compositions are (0.41 C + N, 5% manganese), (0.38 C + N, 7% manganese), (0.29 C + N, 10% manganese), and (0.31 C + N, 12% manganese), respectively.

The relative effect of manganese, carbon, and nitrogen on stabilizing austenite after various aging treatments implies that little, if any, manganese would be present in the precipitated carbides and nitrides. This phenomenon has been observed previously (21) and is further confirmed by the new experimental data, Tables III and IV.

Some of the experimental steels, e.g., W25, were austenitic in the solution-treated condition, but became magnetic and showed a substantial increase in hardness after aging, Fig. 8. This behavior indicated

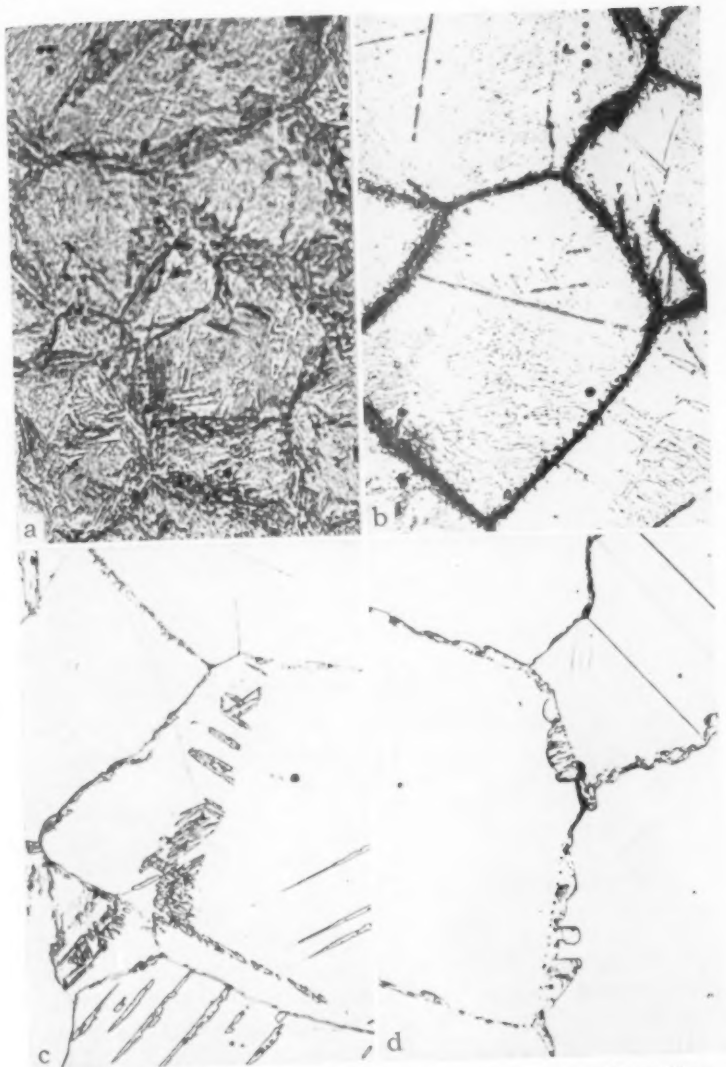


Fig. 7—Microstructures of 12 Cr Steels—Effect of Mn. Heat treatment: 2100 °F, Water-Quenched, Plus 1400 °F for 100 Hours. Etchant: 20% HCl in Alcohol $\times 500$. a. Steel W25 5Mn Rockwell C-43. b. Steel W26 7Mn Rockwell C-35. c. Steel W27 10Mn Rockwell C-23. d. Steel W42 12Mn Rockwell C-21.

Table III
Chemical Analyses of Residue and Matrix of Steel W48
Heat Treatment: Solution-treated 2100°F and aged 100 hours at 1400°F

	Weight (grams)	Iron	Chemical Composition (Weight %)		Carbon	Nitrogen
			Chromium	Manganese		
Sample Prior to Extraction	61.718	66.10	20.15	12.61	0.094	0.63
Extracted Residue	5.497	14.36	64.70	4.63	1.05	5.87
Remaining Matrix	56.221	71.17*	15.06	13.35	0.01*	0.12*

Note: *Calculated from the material balance

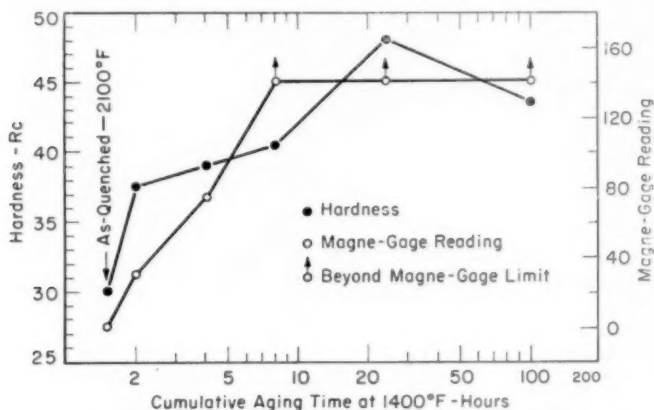


Fig. 8—Martensitic Hardening of Cr-Mn-C-N Steel (W25). Composition: 0.28% carbon—5% manganese—13% chromium—0.13% nitrogen.

that martensite formed during the aging treatment, and the microstructural studies have confirmed this explanation, Fig. 7a. Within the individual austenite grains, four different directions of martensite plates were observed, Fig. 9. This observation indicates that the habit plane of martensite is the (111) plane of the austenite (25).

This type of hardening has been utilized in some commercial stainless steels such as 17-7 PH, AM350, etc.

Precipitation Reactions

Metallographic studies were made on all the experimental steels after solution treating at 2100 °F and aging at different temperatures in the range 1200 to 1600 °F. Besides the carbide precipitation along the grain

Table IV
Distribution of Iron, Chromium, Manganese, Carbon, and Nitrogen between Precipitate and Matrix of Steel W48 (Wt. %)

	Heat Treatment: Solution-treated 2100°F and aged 100 hours at 1400°F					
	Total	Iron	Chromium	Manganese	Carbon	Nitrogen
Matrix	91.9	98.1	70.4	96.7	0.5	17.0
Precipitate	8.1	1.9	29.6	3.3	99.5	83.0

and twin boundaries, two other types of precipitation reactions, grain boundary reaction and general precipitation, occurred during the aging of austenitic Cr-Mn-C-N steels (21). The grain boundary reaction is characterized by the formation of lamellar nodules and occurs by a nucleation and growth process. General precipitation is characterized by a Widmanstätten pattern and is controlled by the crystallographic

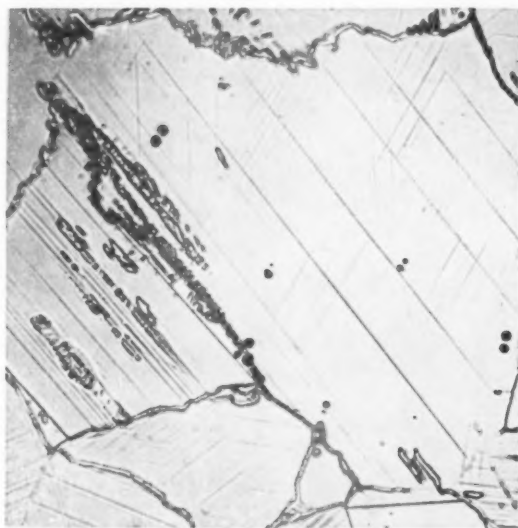


Fig. 9—Microstructures of Steel W27—Habit Plane of Martensite. Heat treatment: 2100 °F, water-quenched, plus 1400 °F for 100 hours. Etchant: 20% HCl in alcohol $\times 500$.

relationship between the precipitate and the matrix. The precipitates in the lamellar nodules were identified to be either Cr_{23}C_6 or Cr_2N depending upon the composition of the steel, whereas the general precipitate was identified to be Cr_{23}C_6 . The identifications were made by x-ray diffraction analyses supplemented by chemical analyses on the electrolytically extracted residues.

The predominance of one reaction over the other depends on the composition of the steel and on the aging temperature. During aging at 1400 °F, the grain boundary reaction product was found predominantly in the high nitrogen steels, and the general precipitation product was found predominantly in low nitrogen, high carbon steels. The relationship between carbon and nitrogen in controlling the type of precipitation reaction is shown in Fig. 10, and the illustrative microstructures are shown in Figs. 11 through 13.

It is expected that for aging temperatures other than 1400 °F, the

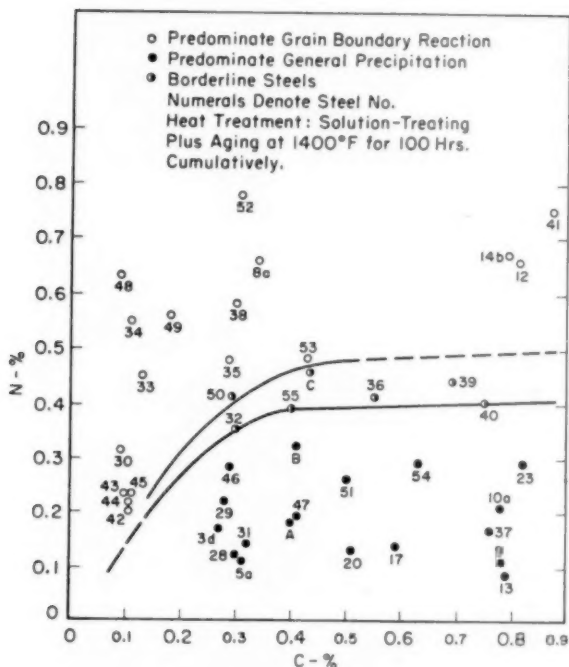


Fig. 10—Effect of Composition on the Solution-Treated and Aged Microstructure.

boundary line in Fig. 10 will shift downward for higher temperatures and upward for lower temperatures. The faster diffusion rate at higher aging temperatures favors the grain boundary reaction. These conclusions are based on the results of experiments carried out on fourteen selected steels by aging them at 1200, 1300, 1500, and 1600 °F for 100 hours. The results of the microstructural study on these specimens are summarized in Fig. 14. These curves indicate the effect of aging temperature in addition to the effects of carbon and nitrogen in controlling the types of precipitation reactions.

Formation of Sigma Phase

The increase in hardness with an accompanying decrease in magnetic response in the duplex steels (austenite plus ferrite) during aging, Fig. 15, is due to the transformation of the delta ferrite to sigma phase. Fig. 16a shows the partial transformation of ferrite to sigma around the clear large ferrite grains; and Fig. 16b shows large particles of sigma (black) and the partially transformed delta particles (duplex stringers).

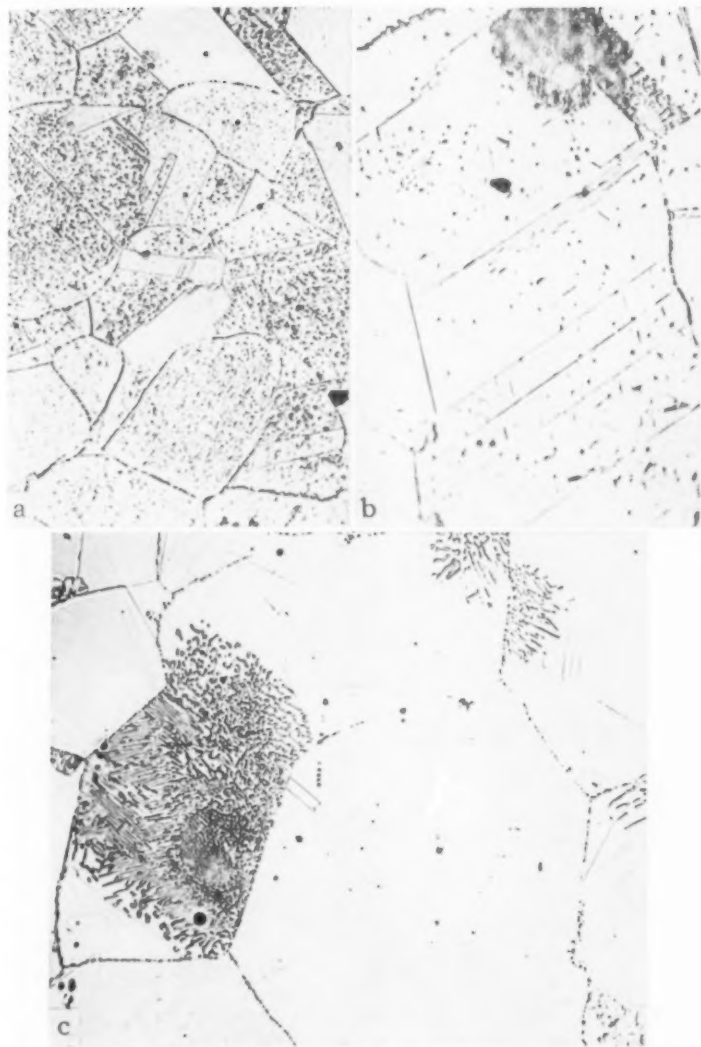


Fig. 11—Microstructures of 19Cr-12Mn Steels—Effect of C and N. Heat treatment: 2100 °F, water-quenched, plus 1400 °F for 100 hours. Etchant: 20% HCl in alcohol $\times 500$. a. Steel W31 .32C-.14N. b. Steel W32 .30C-.35N. c. Steel W33 .13C-.45N.

The formation of large sigma particles has also been observed in wholly austenitic steels, usually associated with the lamellar nodules of the grain boundary reaction product, Fig. 12d.

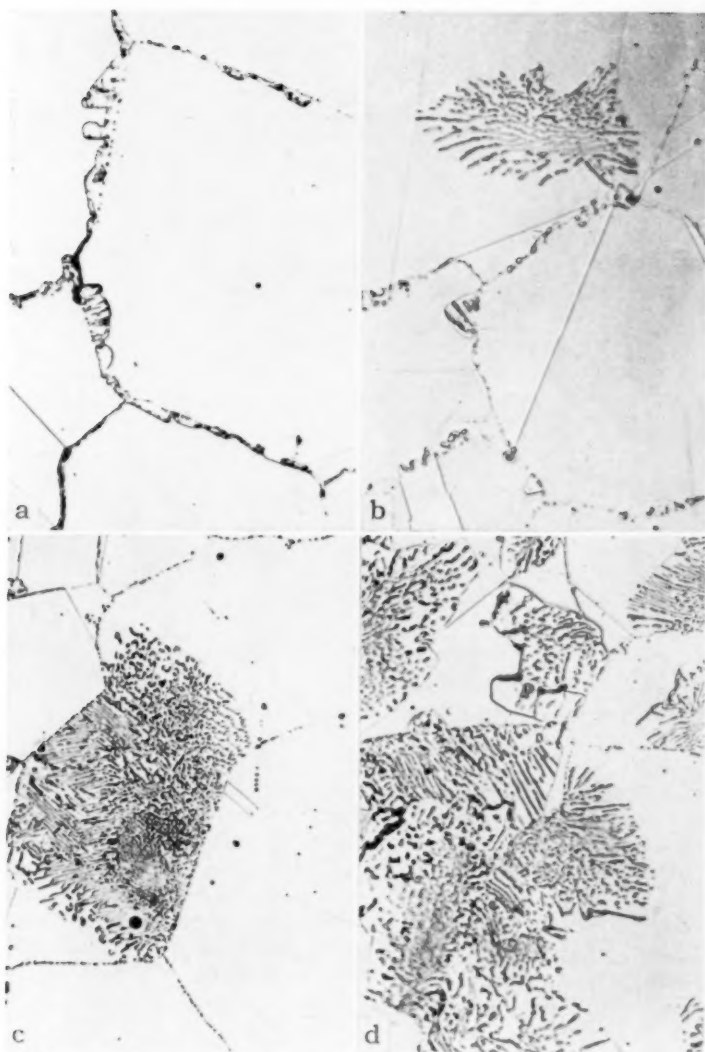


Fig. 12—Microstructures of 0.1C Steels—Effect of Nitrogen. Heat treatment: 2100 °F, water-quenched, plus 1400 °F for 100 hours. Etchant: 20% HCl in alcohol $\times 500$. a. Steel W42 12Mn-12Cr-.20N. b. Steel W30 11Mn-16Cr-.31N. c. Steel W33 12Mn-19Cr-.45N. d. Steel W48 13Mn-20Cr-.63N.

HARDNESS

Solution-Treated Condition

In general, the hardness of the ferrite-free austenitic steels in the

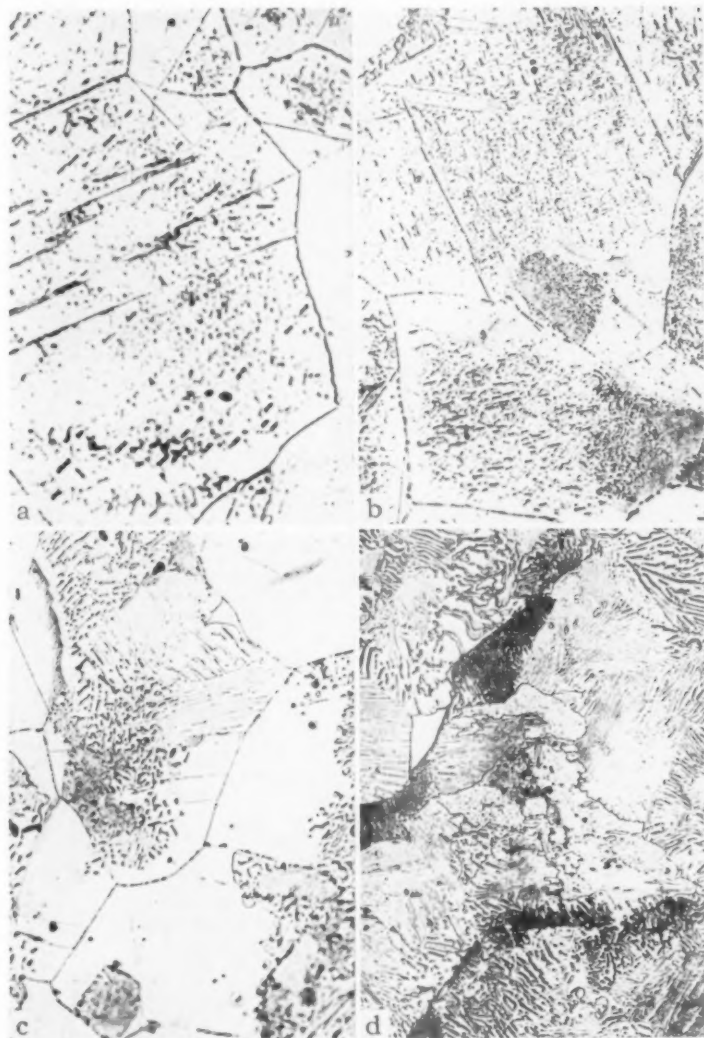


Fig. 13—Microstructures of 0.3C Steels—Effect of Nitrogen. Heat treatment: 2100 °F, water-quenched, plus 1400 °F for 100 hours. Etchant: 20% HCl in alcohol $\times 500$. a. Steel W46 12Mn-18Cr-.28N. b. Steel W50 12Mn-21Cr-.41N. c. Steel W35 13Mn-21Cr-.48N. d. Steel W8a 29Mn-13Cr-.67N.

solution-treated condition increases with increasing amounts of carbon and nitrogen and with lowering of the solution-treating temperatures. The compositions of the austenitic steels and the solution treatments

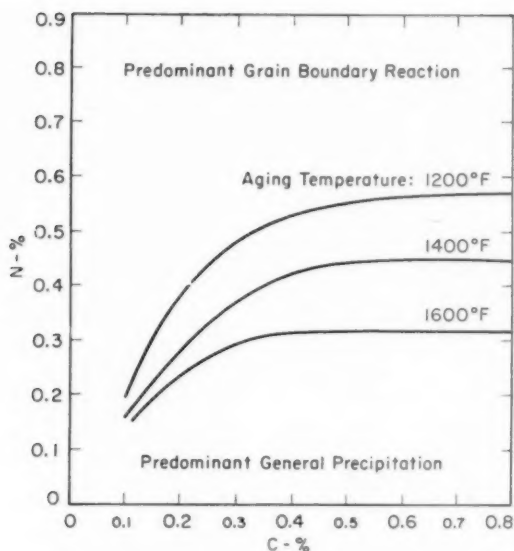


Fig. 14—Effect of Composition and Aging Temperature on the Solution-Treated and Aged Microstructure.

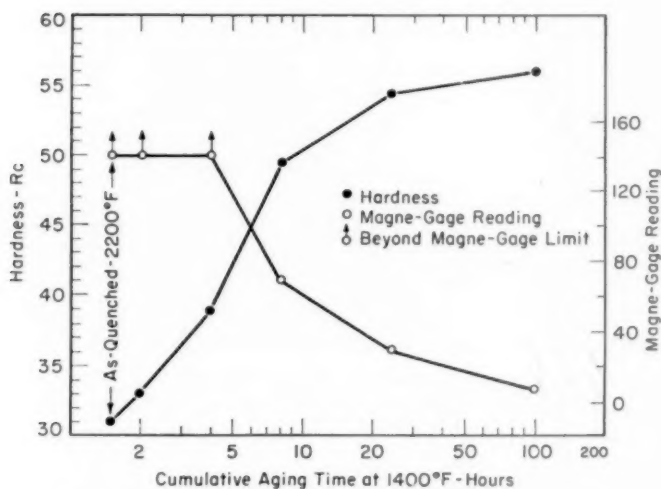


Fig. 15—Sigma Hardening of Cr-Mn-C-N Steel (W4). Composition: 0.28 C—10 Mn—29 Cr—0.69 N.

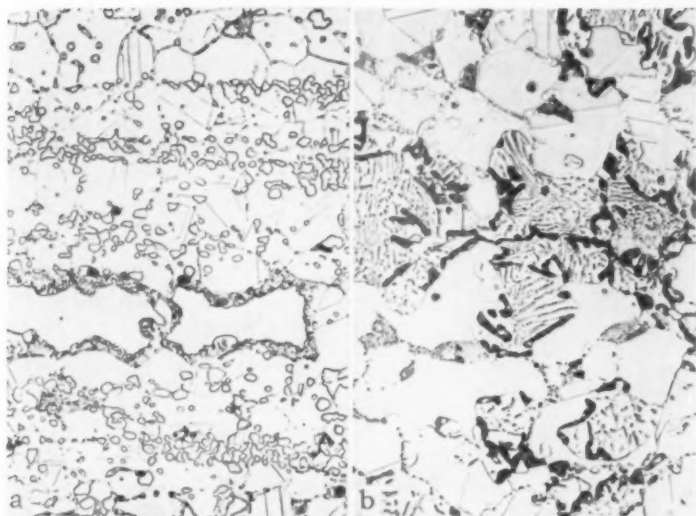


Fig. 16—Microstructures of Steels W11 and W34—Sigma Phase. Heat treatment: Solution treated plus 1400 °F for 100 hours. Etchant: 20% HCl in alcohol $\times 500$. a. Steel W11 .81C-10Mn-28Cr-25N. b. Steel W34 .12C-13Mn-22Cr-55N.

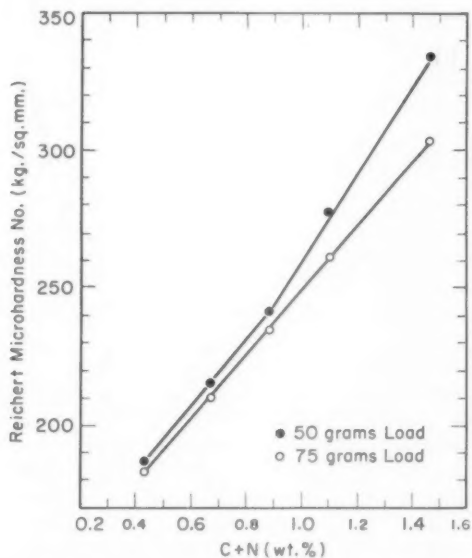


Fig. 17—Effect of Carbon and Nitrogen on the Microhardness of Austenite. Composition: 12 Cr—28 Mn heat treatment: 2200 °F, $\frac{1}{2}$ hour, water-quenched.

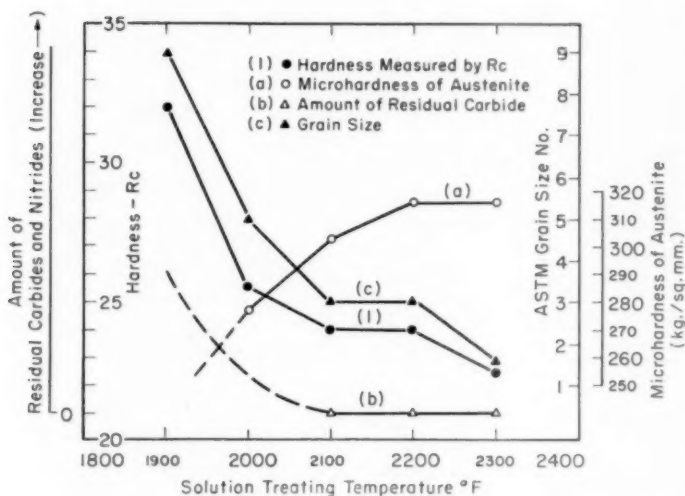


Fig. 18—The Effect of Solution-Treating Temperature on the Contributing Factors that Influence the Hardness of Steel W35. Composition: 0.29 C—12.7 Mn—21.3 Cr—0.48 N.

given to them could affect their hardnesses by changing the following items:

- (a) The amount of solutes in the austenite,
- (b) The amounts of residual carbides and nitrides, and
- (c) The grain size.

Inasmuch as the amounts of the interstitial elements that could be dissolved by the solution treatments at definite temperatures are limited, Fig. 2, the hardness of the austenite due to solution hardening should also be limited. Beyond this limit, the hardness of the steels is attributable to the residual carbides and their effect in retarding grain growth.

The effect of solution hardening is illustrated in Fig. 17, in which the microhardness of the austenite is plotted against a compositional variable ($C + N$), where carbon and nitrogen represent the amounts (wt. %) of carbon and nitrogen in the austenite, respectively. The linear relationship shown in Fig. 17 indicates that the effects of carbon and nitrogen in solution hardening of the austenite are about equal; this is expected, as both carbon and nitrogen are dissolved in the austenite interstitially, and their atomic radii are about the same (0.77 Å for carbon and 0.70 Å for nitrogen). The grain size of the five steels included in Fig. 17 varies from ASTM No. 1 to 2.

The effect of solution-treating temperature is illustrated in Fig. 18. The measured Rockwell C macro-hardness of the steel (Line 1) is the sum of the three contributing components: hardness of the austenite (Line a), amounts of residual carbides and/or nitride (Line b), and grain size (Line c).

Empirically, the hardness of the austenitic Cr-Mn-C-N steels (0.1/0.8% carbon, 10/14% manganese, 12/28% chromium, 0.1/0.8% nitrogen), after being solution treated at 2100 °F appears to increase linearly with the compositional variable $(1.5 C + N)$, Fig. 19, where

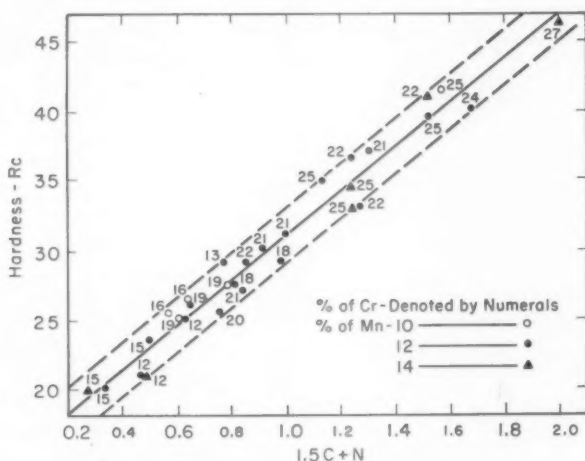


Fig. 19—Effect of Composition on Hardness of Stable Austenitic Steels. Heat treatment: 2100 °F, $\frac{1}{2}$ hour, water-quenched.

carbon and nitrogen are the weight % of carbon and nitrogen in the steel, respectively. The experimental data indicate that the amounts of chromium and manganese have either no effect or much smaller effect than those of carbon and nitrogen.

Solution-Treated and Aged Condition

Precipitation causes hardening of austenitic Cr-Mn-C-N steels (21). Inasmuch as composition controls the type and the amount of the precipitates, the maximum hardness (H_{max}) which could be developed for fixed solution and subsequent aging treatments depends on the composition of the steel. This relationship is shown in Fig. 20, in which iso-hardness contours for H_{max} are plotted as a function of the amounts of carbon and nitrogen. These are the maximum hardness values of the experimental steels that had been solution-treated at 2100 °F and subsequently aged at 1400 °F for 100 hours.

The effects of solution-treating temperature and of aging temperature on the response of the experimental steels to hardening are in agreement with the familiar age-hardening phenomenon.

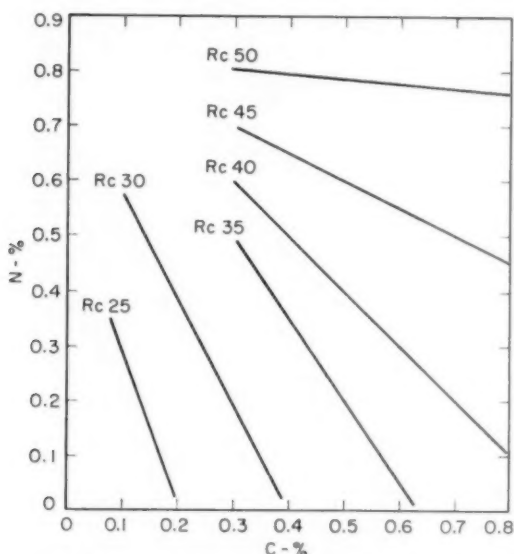


Fig. 20—Effect of Composition on the Maximum Hardness of Stable Austenitic Steels. Heat treatment: 2100 °F, water-quenched, + 1400 °F, 100 hours cumulatively.

The hardening due to martensitic transformation and sigma phase formation has been described in the previous sections.

SUMMARY AND CONCLUSIONS

The stable austenite region in the Cr-Mn-C-N steels containing 0.10/0.80% carbon, 5/28% manganese, 12/28% chromium, and 0.10/0.80% nitrogen has been determined.

At 2100 °F, the minimum amount of carbon plus nitrogen ($C + N$) required for a completely austenitic structure (delta-ferrite free) increases with increasing amount of chromium, and this relationship can be represented by the following equation:

$$C + N = 0.078 (\text{Cr} - 12.5\%)$$

This equation is applicable for steels that contain from 5 to 14% manganese; no extensive work has been done on higher manganese steels.

The effect of solution-treating temperatures in the range 1900 to 2300 °F on the amount of delta ferrite that forms has been discussed.

Whether the austenite that formed at the solution-treating temperature can be retained at room temperature and whether it is stable after being subjected to aging treatments depend on the composition of the austenite. When the chromium is over 15%, about 12% manganese is required to stabilize the austenite to avoid a martensite transformation. When the chromium is between 12 to 15%, the amount of manganese required to stabilize the austenite to avoid a martensite transformation varies from 12 to 18%. In addition to the effect of chromium, the variation in the amount of manganese that is required to stabilize the austenite also depends upon the amount of $(C + N)$ in the steel. That is, for lower chromium and $(C + N)$ contents, higher manganese contents are required for stabilization of the austenite.

The grain size is increased and the amounts of residual carbides and nitrides are decreased with increasing solution-treating temperature. The minimum temperature for the complete solution of the residual carbides increases as the amounts of carbon and chromium increase. Nitrogen and manganese contents have little influence on the solution temperature.

The solution hardening and the hardening due to different aging reactions have also been discussed.

Two types of precipitation reactions, grain boundary reaction and general precipitation, were found in the experimental steels that had been solution-treated and subsequently aged. The grain boundary reaction product was found predominantly in high nitrogen steels, and this reaction was favored at higher aging temperatures; whereas the general precipitation product was found predominantly in low nitrogen, high carbon steels. Also, sigma phase formation during aging has been discussed.

The results of this investigation are applicable (a) for designing compositions of stable austenitic Cr-Mn-C-N steels and (b) for understanding the various elevated temperature solid state reactions that occur in these steels. Thus, as a result of understanding the factors that control the different reactions, and, thereby, the structural characteristics of the steels, heat treatments can be developed that would result in optimum mechanical properties at both room and elevated temperatures.

ACKNOWLEDGMENT

The authors are grateful to the management of Crucible Steel Company and to Materials Laboratory, Wright Air Development Center, for granting permission to publish this paper (most of this work was done under WADC Contract No. AF33(616)-3318). The authors wish to thank Mr. P. Payson, Assistant Director of Research and De-

velopment, for his encouragement, assistance, and advice. Also, they are pleased to acknowledge their gratitude to Messrs. John Moll, Joseph Boelky, and other members of the staff of the Research and Development Laboratory who aided in various phases of the work leading to the publication of this paper.

References

1. F. M. Becket, "Chromium-Manganese Steel," *Yearbook*, American Iron and Steel Institute, 1930, p. 173.
2. W. Köster, "Iron End of the Iron-Manganese-Chromium System," *Archiv für das Eisenhüttenwesen*, Vol. 7, 1933-34, p. 687-688, Brucher Translation No. 651.
3. S. Gunzberg, N. A. Aleksandrova and L. S. Geldermann, "Properties of Chromium-Manganese and Chromium-Nickel-Manganese Stainless Steels," *Archiv für das Eisenhüttenwesen*, Vol. 8, 1933-34, p. 121-123, Brucher Translation No. 686.
4. M. Schmidt and H. Legat, "Heat-Resisting Chromium-Manganese Steels," *Archiv für das Eisenhüttenwesen*, Vol. 10, 1936-37, p. 297-303, Brucher Translation No. 494.
5. H. Legat, "Further Data on Austenitic Chromium-Manganese Steels," *Archiv für das Eisenhüttenwesen*, Vol. 11, 1937-38, p. 337-341, Brucher Translation No. 514.
6. C. O. Burgess and W. D. Forgeng, "Constitution of Iron-Chromium-Manganese Alloys," *Transactions*, American Institute of Mining and Metallurgical Engineers, Iron and Steel Division, Vol. 131, 1938, p. 277-298.
7. F. Bruhl, "Structure and Properties of Chromium-Manganese Steels with up to 1% C, 15% Mn, and 30% Cr," *Archiv für das Eisenhüttenwesen*, Vol. 10, 1936-37, p. 243-255, Brucher Translation No. 509.
8. A. Borzdyka, "Chromium-Molybdenum-Manganese Steels and Chromium-Tungsten-Manganese Steels," *Kachetvonnaga Stal*, Vol. 5, No. 8, 1937, p. 33-36, Brucher Translation No. 660.
9. A. Borzdyka, "Precipitation Hardening of High Alloy Chromium-Manganese-Titanium Steel," *Metallurg*, Vol. 15, No. 10, 1940, p. 31-35, Brucher Translation No. 1289.
10. V. N. Krivobok, "Alloys of Iron and Chromium," *TRANSACTIONS*, American Society for Metals, Vol. 23, 1935, p. 1.
11. R. Franks, "Chromium Steels of High Nitrogen Content," *TRANSACTIONS*, American Society for Metals, Vol. 23, 1935, p. 968.
12. E. W. Colbeck and R. P. Garner, "The Effect of Nitrogen Additions and Heat Treatment on the Properties of High Chromium Steels," *Journal*, Iron and Steel Institute, Vol. 193, p. 99.
13. H. Krainer and O. Mirt, "Constitution Diagram of Nitrogen Containing Chromium and Chromium-Manganese Steels," *Archiv für das Eisenhüttenwesen*, Vol. 15, 1941-42, p. 467-472, Brucher Translation No. 1321.
14. F. Rapatz, "Applications of Stainless and Heat-Resisting Steels Alloyed with Nitrogen," *Stahl und Eisen*, Vol. 61, 1941, p. 1071-1078, Brucher Translation No. 1255.
15. L. Schaeben, "Intergranular Corrosion of Chromium-Manganese Steels," *Korrosion Metallschutz*, Vol. 19, 1943, p. 44-46, Brucher Translation No. 1486.
16. R. Franks, W. O. Binder and J. Thompson, "Austenitic Chromium-Manganese-Nickel Steels Containing Nitrogen," *TRANSACTIONS*, American Society for Metals, Vol. 47, 1955, p. 231-266.
17. E. J. Whittenberger, E. R. Rosenow and D. J. Carney, "Elevated Temperature Phase Relationship in the Cr-Ni-Mn-N System," Presented at American Institute of Mining and Metallurgical Engineering Annual Meeting, Feb. 1957.
18. V. F. Zackay, J. F. Carlson, and P. L. Jackson, "High Nitrogen Austenitic Cr-Mn Steels," *TRANSACTIONS*, American Society for Metals, Vol. 48, 1956, p. 509-525.

19. J. F. Carlson and V. F. Zackay, "High Nitrogen Cast Austenitic Steels," *Transactions, American Institute of Mining and Metallurgical Engineering*, Vol. 203, 1955, p. 112-113.
20. G. F. Tisinal, J. K. Stanley and C. H. Samans, "Austenitic Fe-Cr-C-N Stainless Steels," *TRANSACTIONS, American Society for Metals*, Vol. 48, 1956, p. 356-367.
21. C. M. Hsiao and E. J. Dulis, "Precipitation Reactions in Austenitic Cr-Mn-C-N Stainless Steels," *TRANSACTIONS, American Society for Metals*, Vol. 49, 1957, Preprint No. 26.
22. W. T. DeLong, G. A. Ostrom and E. R. Szumachowski, "Measurement and Calculation of Ferrite in Stainless Steel Weld Metal," *Welding Research*, Vol. 21, November 1956, No. 11, p. 521s-528s.
23. R. H. Aborn and E. C. Bain, "Nature of the Nickel-Chromium Rustless Steels," *TRANSACTIONS, American Society of Steel Treating*, Vol. 18, 1930, p. 837-873.
24. G. H. Eichelman, Jr. and F. C. Hull, "The Effect of Composition on the Temperature of Spontaneous Transformation of Austenite to Martensite in 18-8 Type Stainless Steel," *TRANSACTIONS, American Society for Metals*, Vol. 45, 1953, p. 77-104.
25. R. F. Mehl and C. S. Barrett, "Studies Upon the Widmanstätten Structure," *Transactions, American Institute of Mining and Metallurgical Engineers*, Vol. 93, 1931, p. 78-110.

DISCUSSION

Written Discussion: By H. E. McCune, Allegheny Ludlum Steel Corporation, Research and Development Laboratories, Brackenridge, Pa.

The work of the authors has appreciably increased the available knowledge of austenitic chromium manganese steels. Equation 1, $C + N = 0.078$ (Cr-12.5) which relates the temperature of formation of delta ferrite to the chemical composition, is interesting in that it contains no factor for the effect of manganese. Work which was done by Allegheny Ludlum Steel Corporation and the United States Steel² shows that the manganese content will effect the maximum amount of chromium which can be tolerated. Fig. 21 shows the amount of chromium necessary to form delta ferrite over a range of manganese contents at a constant temperature and a constant nitrogen content. From the graph it can be seen that as the manganese content is increased the chromium content must be decreased in order to maintain a completely austenitic structure. There is also an indication that the negative slope of the plot increases as the nitrogen content is increased. It is believed that the relationship between the alloying elements could be more accurately expressed by the following equation:

$$C + f_1(N) = (K + f_2(Mn)) \text{ (Cr-12.5)}$$

$$f_1 \neq f_2$$

$$K = \text{Constant at the minimum manganese content}$$

We have also found that the hardness of the stable alloys will increase during aging. It is of interest to note that in the accompanying table the hardness increased from Rockwell C-25 to 29, but the strength was not increased. The yield strength decreased 13000 psi, the tensile strength remained essentially the same, and the elongation decreased 31%. Fig. 10 of the authors' paper predicts that the

² D. J. Carney, "High Nitrogen Steels: New Stainless Family," *Steel*, Vol. 137, November 7, 1955, p. 138-144.

	C	Mn	Si	Cr	N
	0.11	14.80	0.39	16.58	0.67
Treatment	Hardness	Yield Strength (0.2% Offset)	Tensile Strength	% Elong. (2")	
1900 °F	25 RC	86,860 PSI	134,770 PSI	44	
1900 °F + 1400 °F, 1 hour	26 RC	82,260 PSI	133,170 PSI	24	
1900 °F + 1400 °F, 4 hours	28 RC	75,520 PSI	133,420 PSI	14	
1900 °F + 1400 °F, 8 hours	29 RC	73,180 PSI	132,570 PSI	13	

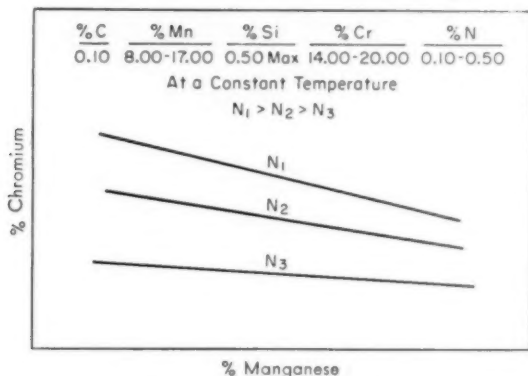


Fig. 21—Phase Relationship in Fe-Cr-Mn-N System.

reactions involved should be predominantly grain boundary reactions, and this was found to be true. With a heavy grain boundary precipitate the decrease in elongation could be expected.

Written Discussion: By F. K. Bloom, Research Metallurgist, Research Laboratories, Armco Steel Corporation, Baltimore.

We have studied this paper with more than usual interest and would like to congratulate the authors for their thorough study. The photomicrographs accompanying this paper are of unusually fine quality, bespeaking most careful work.

The writer's laboratory has been engaged for a number of years in the development of alloys falling in this same composition range and, in general, where comparable data were obtained on the effects of composition on structure, the agreement is excellent.

It may be of interest to the readers of this paper to know that the austenitic high-carbon, high-nitrogen, chromium-manganese alloys have been found to possess properties which make them particularly well suited for internal combustion engine exhaust valves. One such alloy, which has been described by P. A. Jennings in U.S. Patent 2,698,785 (January 4, 1955), was found to have a hot hardness at 1400 °F of 185 Brinell as measured by the cold ball method. Alloys of this type are characterized by excellent resistance to attack by the combustion products of leaded fuels and by good resistance to stretch under high stress.

Similar alloys containing small amounts of nickel are being widely used today in our modern high compression automobile engines. The typical analysis and

mechanical properties after solution treating at 2150 °F and aging at 1400 °F are given below.

Elong
(2")
44
24
14
13

	C	Mn	Cr	Ni	N
	0.55	8.50	20.50	3.50	.40
Short-Time Tensile Properties at Room and Elevated Temperatures					
	Room		Tested at 900 °F		1400 °F
Ultimate Tensile Strength, psi	162,000		114,000		62,000
0.2% Yield Strength, psi	102,000		58,000		37,000
Elongation in 2", %	9.0		20.0		18.0
Reduction of Area, %	9.0		21.0		25.0
Brinell Hardness	344		236		194

Fig. 1 from Hsiao and Dulis suggests that this composition should be free from delta ferrite when quenched from 2100 °F, and this is found to be the case. Their Fig. 5 suggests that the alloy might exhibit some austenite to martensite transformation. We have seen no evidence of this as the alloy is found to be stable even after prolonged heating at 1400 °F. No doubt, this is the result of the presence of 3.5% nickel, which depresses the M_s temperature more markedly than manganese.

Authors' Reply

We were pleased to have Mr. McCune's informative comments on the effect of manganese content and on the tensile properties of a steel that formed grain boundary reaction products during aging. We were well aware of the effect of manganese on the phase boundary relationships in low carbon chromium-manganese-nitrogen steels. Indeed, as early as 1936 Schmidt and Legat (Ref. 4) showed that as the manganese content increased the chromium content had to be decreased to maintain a completely austenitic structure in a 0.1% carbon steel. However, in this early work and in subsequent works, the reported effect of manganese was practically negligible. For example, Franks, Binder, and Thompson (Ref. 16) reported that in a 0.10 to 0.12% carbon 0.08 to 0.15% nitrogen chromium-manganese steel containing no nickel, the chromium content had to be lowered from about 15.2 to 14.8% when the manganese was increased from 8 to 22%. Therefore, for the relatively high carbon plus nitrogen steels of the present study, the effect of manganese could reasonably be considered negligible and the relationship given in Equation 1 of the paper is correct for all practical purposes.

The decrease in yield strength and elongation that was caused by the formation of grain boundary reaction products during aging at 1400 °F (Table I of discussion) is in agreement with our unpublished findings. However, it is important to point out that aging reactions per se do not necessarily cause a decrease in room-temperature tensile and yield strengths and ductility. When the composition and aging temperature are such that a general precipitation (rather than a grain boundary nucleated lamellar precipitate) occurs, an increase in strength with little sacrifice in ductility is found. An example of this behavior follows on next page.

We were pleased to learn of the agreement between our work and that of Armco Steel Company's Research Laboratory. Mr. Bloom's comments on the commercial application and the tensile properties of a chromium-manganese-carbon-nitrogen steel that contains 3.5% nickel were of considerable interest. Be-

Effect of Microstructure on Room Temperature Tensile Properties

Steel Composition: 0.40 C — 12.5 Mn — 18.4 Cr — 0.39 N							
Heat Treatment	Micro-structure	Hardness, Rc	Tensile Strength, psi	Yield Strength, psi		Elong., %	R.A., %
2100 °F, W.Q.	Austenite	27	141,700	0.02%	68,700	79,900	63 66
2100 °F, W.Q., + 1200 °F for 24 hours	Austenite + fine general ppt.	28	145,300	73,100	83,900	53	37
2100 °F, W.Q., + 1600 °F for 24 hours	Austenite + lamellar ppt.	35	143,100	59,100	75,900	17	16

cause of some of their unique properties, we believe that chromium-manganese-carbon-nitrogen austenitic steels might find expanded applications in the future.

In regard to the effect of 3.5% nickel in stabilizing the austenite of the 8.5% manganese steel against a martensitic transformation, we are wholly in agreement with Mr. Bloom. However, as can be noted from Fig. 5 of the paper, a 3.5% increase of manganese should accomplish the same effect.

CARBIDE PRECIPITATION AND BRITTLENESS IN AUSTENITIC STAINLESS STEEL

BY A. KRAMER AND W. M. BALDWIN, JR.

Abstract

The tensile ductility of three 18-8 austenitic stainless steels—AISI Types 304 ELC (extra low carbon, 0.024% carbon), 304 (0.060% carbon), and 302 (0.09% carbon) in both the annealed and the sensitized condition (carbide-precipitated condition)—was determined as a function of testing temperature (-321 to $+500$ °F) and strain rate (0.05 to 19,000 inch per inch per minute).

The ductility of all three steels in the annealed condition dropped as the strain rate was increased, the drop being greatest at room temperature. The ductility showed a maximum at about room temperature at low strain rates, but at high strain rates it increased steadily with temperature. Magnetic measurements of the martensite formed during deformation confirmed earlier results that the $\gamma \rightarrow \alpha$ transformation cannot account for all these behaviors. All these features were retained in the sensitized Type 304 ELC. Sensitization of Types 304 and, to a greater degree, 302 resulted in severe embrittlement in a critical range of low temperatures at low strain rates. Beyond this range, the ductility behavior of sensitized and annealed material was almost identical.

Thus, neither carbide precipitation nor the $\gamma \rightarrow \alpha$ transformation can explain the high speed embrittlement encountered in austenitic stainless steels as a class. (ASM International Classification Q23p, N8; SS-e)

INTRODUCTION

AUSTENITIC stainless steels lose ductility when deformed at high strain rates. For a number of years this has been observed in the laboratory (1-5)¹ and in industry (6,7,8). In most attempts to rationalize this phenomenon, it has been assumed that strain rate embrittlement is related to the martensite transformation which occurs

¹ The figures appearing in parentheses pertain to the references appended to this paper.

This paper is based upon a portion of a research program conducted in the Department of Metallurgical Engineering, Case Institute of Technology, in cooperation with the Office of Naval Research. The data were used as the basis of a thesis submitted by Mr. Kramer in partial fulfillment for the Degree of Master of Science.

A paper presented before the Thirty-Ninth Annual Convention of the Society, held in Chicago, November 4-8, 1957. Of the authors, A. Kramer is research assistant and W. M. Baldwin, Jr. is research professor, Case Institute of Technology, Cleveland. Manuscript received May 15, 1957.

during plastic deformation (9,10), but this has recently been discounted (11).

A search of the literature disclosed that little was known about the effect of carbide precipitation upon the ductility of austenitic stainless steels, except that in some general way they were embrittled.² Udy's results (12) indicate that the effects of sensitization upon the impact toughness of AISI Type 302 are much more critical at -300°F than at room temperature. In order to determine whether carbide precipitation is responsible for high speed embrittlement in stainless steels and to characterize completely the relationship of ductility with strain rate and temperature of deformation, tensile tests of both annealed and sensitized austenitic stainless steels of varying carbon content were conducted over a wide range of temperatures and strain rates.

MATERIAL AND PROCEDURE

Three commercial austenitic stainless steel grades differing in carbon content—AISI Types 304 ELC (extra low carbon), 304, and 302—were selected for this investigation. The compositions of these 18Cr-8Ni grades are listed in Table I.

Table I
Composition of Steels Studied

Type	C*	Si	S	P	Mn	Cr	Ni	Mo	Cu
304 ELC	0.024	0.49	0.018	0.024	1.33	19.00	10.12	0.09	0.14
304	0.060	0.55	0.030	0.029	1.38	18.49	9.47	0.20	0.21
302	0.09	0.69	0.010	0.040	0.88	18.70	9.27	0.24	0.13

* Check analyses for Types 304 ELC, 304 and 302 were 0.022, 0.054, and 0.099, respectively.

Tensile specimens, $1\frac{1}{2}$ inches long with a minimum diameter of 0.212 inch, were machined from $\frac{3}{4}$ -inch rod after annealing and after sensitizing. The annealing treatment consisted of heating to 1980°F for 5 hours and water quenching. The sensitizing treatment consisted of heating the annealed rod at 1200°F for 24 hours³ and cooling in air. The annealed material was single-phase, with Type 302 of a somewhat smaller grain size than the other two grades. Sensitizing resulted in a localized carbon precipitation at the grain boundaries and twin planes, with the amount of carbide precipitation increasing with carbon content. The microstructures of the sensitized Types 304 and 302 are shown in Figs. 1a and 1b.

Tensile tests were made at temperatures of -321 , -200 , -50 ,

² The effect of carbide precipitation on intergranular failure under corrosive conditions is, of course, well known. We are concerned here with purely mechanical effects.

³ Mahla and Nielsen (13) found that the size, shape, and distribution of the carbide precipitate changes progressively with time, and that the maximum rate of sensitization occurs at 1200°F . Although no systematic study was conducted, preliminary tests at this laboratory indicated that the sensitizing time has a small but progressive effect on the impact properties and tensile ductility. For example, reduction-in-area values of Type 304 dropped from an annealed value of 82%, at room temperature and low strain rate, to 74% after sensitizing of 1200°F for 168 hours. Effects of this order of magnitude were also noted for sensitizing temperatures of 1100° and 1300°F .

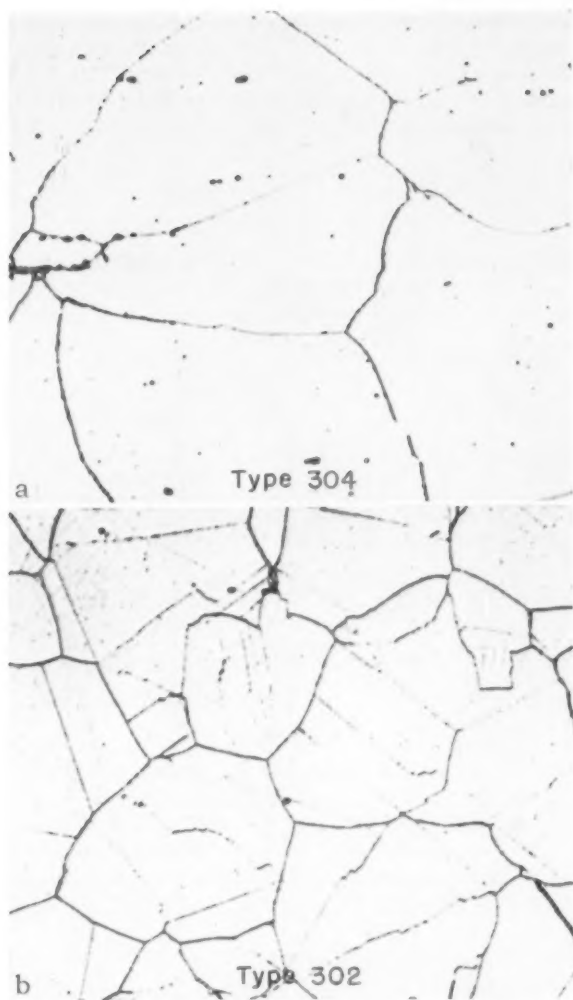


Fig. 1—Microstructures of Carbide—Embrittled Types 304 and 302 Stainless Steel. (a) Steel type 304; (b) Steel type 302. Oxalic acid etch. $\times 300$.

room temperature, 200, 350, and 500 °F, and at strain rates of 0.05, 10, 100 and 19,000 inch per inch per minute. Each ductility value, $\epsilon = 2 \ln d_o/d_f$, was obtained as an average of six measurements of the initial and final diameter on an optical comparator at 20 magnifications. Magnetic measurements were made at room temperature on broken tensile

specimens to detect the presence of any alpha-phase (martensite) which had formed during the tensile test. Oscilloscope readings gave a qualitative measure of the amount of martensite present. The details of the tensile testing and martensite-measuring procedures have been described in detail previously (11).

RESULTS AND DISCUSSION

Annealed Stainless Steels

The ductility of the three steels is plotted as a function of strain rate for various temperatures in Fig. 2. The ductility behavior of Types 304 ELC, 304, and 302 in the annealed condition is the same, and may

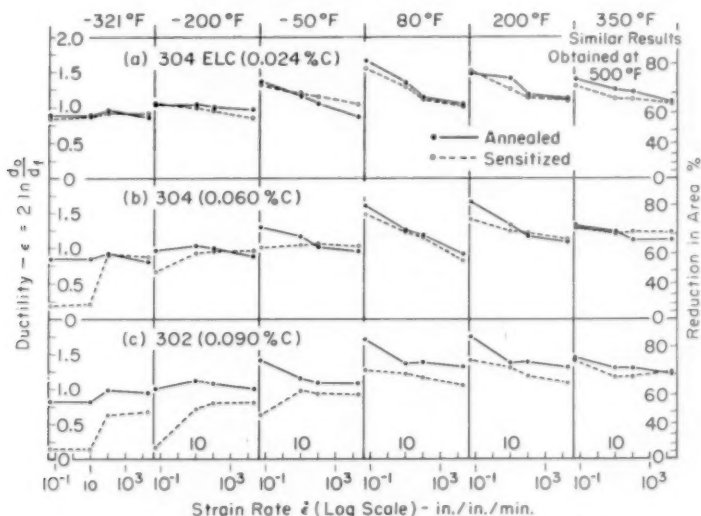


Fig. 2—Ductility of Three Austenitic Stainless Steels as a Function of Strain Rate at Various Test Temperatures. (a) Steel 304 ELC (0.024% Carbon); (b) Steel 304 (0.060% Carbon); (c) Steel 302 (0.090% Carbon).

be represented over the entire range of temperatures and strain rates by the three-dimensional graph of Fig. 3 (solid lines), using the data points for Type 304. This plot reveals three major characteristics of the ductility behavior, which are in complete agreement with the previously reported (11) behavior of annealed austenitic Type 303 (sulphurized 18 Cr-10 Ni, 0.045% C) and Type 310 (23 Cr-20 Ni, 0.044% C):

- (a) The strain rate sensitivity is most pronounced at room temperature, while it is relatively small at low temperatures and disappears at 500 °F.

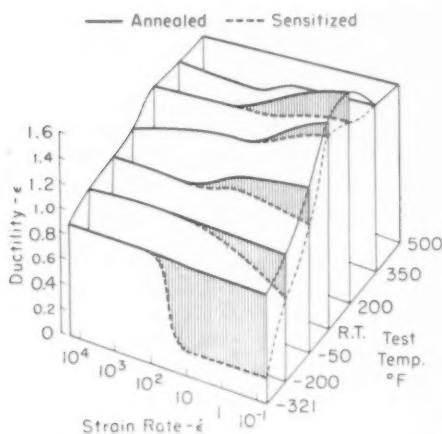


Fig. 3—Ductility as a Function of Strain Rate and Temperature for Type 304 Stainless Steel. Shaded regions indicate extent of embrittlement after sensitization.

- (b) At low strain rates the ductility shows a maximum at room temperature.
- (c) At high strain rates the ductility rises slowly, if irregularly, with temperature.

Thus, for a fairly wide range of carbon contents (the carbon present in solid solution) the annealed austenitic stainless steels behave as a class.

The relative amounts of martensite present, as measured by oscilloscope readings of broken test specimens, are plotted as a function of strain rate for various tensile test temperatures in Fig. 4. Parallel patterns are obtained for annealed Types 304 ELC, 304, and 302, which are in close agreement with those reported for annealed Type 303 (11)⁴. The major characteristics of these patterns are:

- (a) No martensite is detected in tensile testing above room temperature.
- (b) At a given temperature below room temperature, the amount of martensite drops with increasing strain rate.⁵
- (c) At a given strain rate the amount of martensite drops with increasing temperature.

A comparison of these curves with the ductility curves shows that the

⁴ No martensite was detected on straining Type 310 at temperatures as low as -321°F .

⁵ A. W. McReynolds (14) is of the opinion that the decrease of martensite with increased strain rate results from the fact that the process is adiabatic. The rapid deformation heats the specimen to a temperature above the M_s point (the temperature above which no martensite is formed) preventing further transformation. He further points out that the heating would be expected to be localized at the slip bands where transformation presumably occurs. The present results do not contradict his presumptions.

amount of martensite in annealed austenitic stainless steels cannot be correlated with the ductility. For example, in the range where martensite is found, a drop in temperature at a constant strain rate increases the amount of martensite and decreases the ductility; however, an increase in strain rate at constant temperature lowers both ductility and the amount of martensite. These findings are in agreement with those reported for Type 303 (11).

Sensitized Stainless Steels

The ductility behavior of sensitized Type 304 ELC is the same as that of the annealed material, Fig. 2a, indicating that the sensitizing treatment did not embrittle this steel. The resistance of Type 304 ELC to sensitization is not surprising since the carbon content is so low (0.022% carbon) that it precludes precipitation of significant amounts of carbides. (Carbon is soluble to the extent of 0.02% at the sensitizing temperature of 1200 °F.)

In contrast to Type 304 ELC, the ductility behavior of Types 304 and 302 is affected by the sensitizing treatment, differing from annealed material in one major respect:

Sensitizing results in severe embrittlement in the range of low temperatures at low strain rates (see Fig. 2, and compare the solid and dotted lines of Fig. 3). Beyond this range the effect of sensitization is minor, the ductility of the sensitized material paralleling that of the annealed material at a somewhat lower level.

The embrittlement of the higher carbon grade (Type 302) is more pronounced than that of Type 304.

An interesting feature of the ductility behavior of the sensitized Types 304 and 302 at low temperatures (—321 and —200 °F) is that the ductility level at high strain rates is greater than that at low strain rates. This ductility increase may be due to a rise in specimen temperature as a result of the greater heat of deformation at high testing speeds.⁶

Metallographically, sensitized specimens of Type 304 and 302 showed definite intergranular breaks for all test temperatures below room temperature at all strain rates, Fig. 5. Above this range, the mode of fracture could not be determined with any definiteness. All of the annealed steels and the sensitized Type 304 ELC appeared to fracture transgranularly under all test conditions.

A comparison of the ductility curves with the amount of martensite formed during deformation reveals a number of interesting features which serve as further evidence that the amount of martensite formed

⁶ The heat effect may explain the absence of strain rate embrittlement of annealed material at liquid nitrogen temperatures, the embrittlement being masked by a rise in specimen temperature.

during straining cannot be correlated with the ductility. For example, the amount of martensite in sensitized Type 304 ELC is somewhat less than that in the annealed material under identical tensile test conditions, Fig. 4a, but their ductilities are at the same level, Fig. 2a. Surprisingly enough, this is the reverse of the anticipated behavior. The sensitizing treatment is expected to result in a less stable austenite and therefore more martensite during deformation, since carbon, a strong austenite stabilizing element, is precipitated from solution (as chromium carbide).

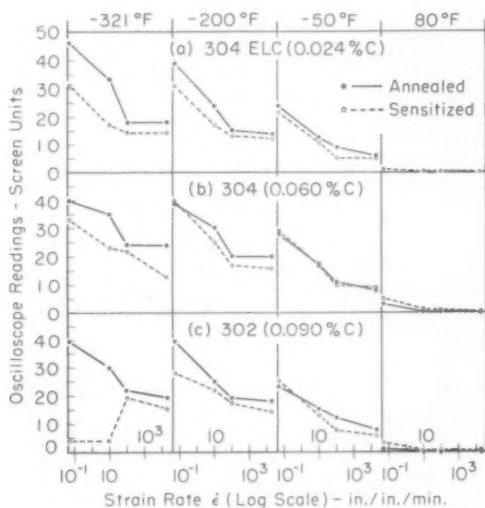


Fig. 4 (a-c)—Effect of Strain Rate on the Magnetic Behavior (Measured at 80 °F) of Three Austenitic Stainless Steels at Various Tensile Test Temperatures.

The formation of only a small amount of martensite in the sensitized Type 302 specimens broken at low strain rates in liquid nitrogen might be expected from the little deformation that occurred before fracture. Under the same test conditions the sensitized Type 304 displayed the same ductility but a higher martensite content which may be attributed to its lower carbon content since martensite formation is enhanced at low carbon concentrations (15). However, it is noted that this latter line of reasoning could not explain the difference in behavior between annealed and sensitized Type 304 ELC.

Lastly, it should not be construed from the ductility behavior of sensitized stainless steels, Fig. 3 (dotted lines), that the ductility-test temperature data at a low strain rate follows a typical ductile-brittle transition curve. This is unlikely for a number of reasons. The austen-

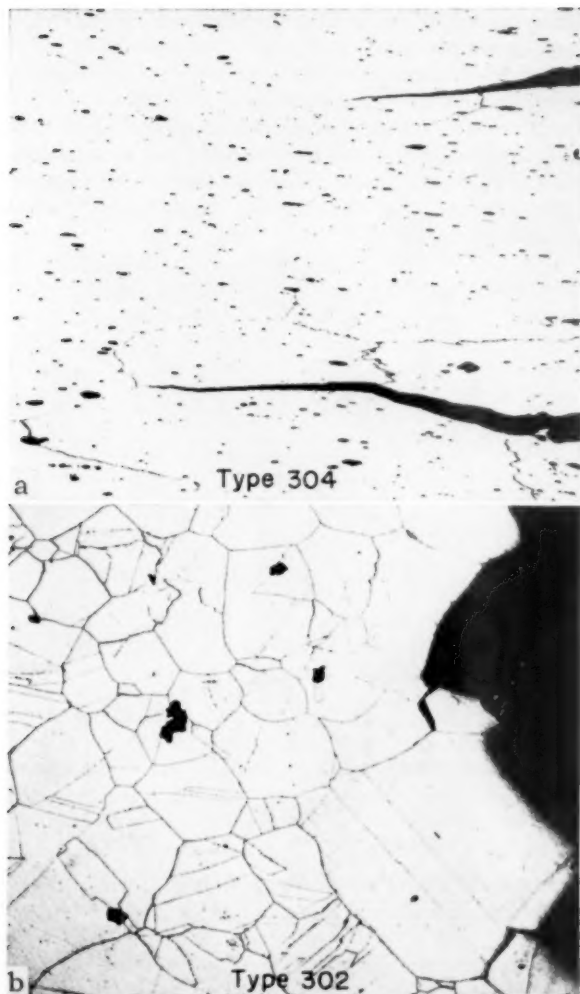


Fig. 5—Intergranular Fracture of Carbide-Embrittled Types 304 and 302 Stainless Steel. (a) Steel type 304 tested at 80 °F strain rate 0.05 in/in/min.; (b) Steel type 302 tested at -321 °F strain rate 0.05 in/in/min. Oxalic acid etch. $\times 150$.

itic stainless steels are face-centered cubic, and single-phase metals of this crystal system do not display a transition temperature,⁷ which is a

⁷ Single-phase, face-centered cubic alloys of copper-antimony (16,17) and antimony-bearing 70:30 brass (18) show a form of low temperature brittleness which is of a different species than that exhibited by body-centered cubic iron, chromium, etc. In Cu-Sb alloys for example the drop in ductility with decreasing temperature is moderate; occurs over a broad temperature range; and does not react to strain rate as does iron.

characteristic of many non face-centered cubic metals. It might be argued that the sharp drop in ductility experienced by the sensitized stainless steels below room temperature is due to the formation of martensite (body-centered tetragonal); however, the amount of martensite decreases as the test temperature is lowered, as shown in Fig. 4. These features, coupled with the fact that the apparent ductile-brittle curve does not shift to higher temperatures with increased strain rate, establishes conclusively that the embrittlement under consideration here is actually due to carbide precipitation.

CONCLUSIONS

The following conclusions are drawn from tensile tests of annealed and sensitized austenitic stainless steels of varying carbon content—Types 304 ELC (0.024% carbon), 304 (0.060% carbon), 302 (0.09% carbon)—tested over a wide range of temperatures and strain rates.

For the annealed material, the present findings are in complete agreement with those previously reported (11) for annealed Types 303 and 310:

1. At low strain rates, austenitic stainless steels exhibited a maximum in tensile ductility at room temperature as the test temperature was varied from -321 to 500°F .
2. At high strain rates, the steels gained steadily in ductility as the test temperature was increased.
3. At constant temperature, stainless steels lost ductility as the strain rate increased; the greatest loss occurred at room temperature.
4. The amount of martensite formed during deformation cannot be correlated with the ductility.

For the sensitized material:

5. The degree of sensitization was a function of the carbon level. Type 304 ELC (0.024% carbon) was not embrittled, whereas Type 304 (0.060% carbon) was embrittled but to a lesser extent than Type 302 (0.090% carbon).
6. Carbide embrittlement manifested itself primarily in the range of low temperatures at low strain rates.
7. The carbide-embrittled specimens fractured inter-granularly.
8. Carbide embrittlement cannot account for the high speed embrittlement which is characteristic of austenitic 18-8 stainless steels as a class.

References

1. D. S. Clark and G. Datwyler, "Stress-Strain Relation Under Tension Impact Loading," *Proceedings, American Society for Testing Materials*, Vol. 38, 1938, p. 98.
2. G. Jones and H. F. Moore, "An Investigation of the Effect of Rate of Strain on the Results of Tension Tests of Metals," *Transactions, American Society for Testing Materials*, Vol. 40, 1940, p. 610.

3. E. R. Parker and C. Ferguson, "The Effect of Strain Rate on the Tensile Impact Strength of Some Metals," *TRANSACTIONS, American Society for Metals*, Vol. 30, 1942, p. 68.
4. "Cooperative Study of the Effect of Strain on the Tensile Properties of Stainless Steel," Report of Subcommittee V on Mechanical Tests, *Proceedings, American Society for Testing Materials*, Vol. 44, 1944, p. 133.
5. D. S. Clark and D. S. Wood, "The Tensile Impact Properties of Some Metals and Alloys," *TRANSACTIONS, American Society for Metals*, Vol. 42, 1950, p. 45.
6. V. N. Krivobok and G. Sachs, "Forming of Austenitic Chromium-Nickel Stainless Steels," 1947, p. 13, International Nickel Company.
7. S. Storchheim, "How Draw Speed Affects Stainless Wire," *American Machinist*, Vol. 96, 1952, p. 124.
8. C. A. Beiser and W. M. Baldwin, "Why Stainless Is Hard to Cold Head," *Iron Age*, January 13, 1955, p. 82.
9. M. Cohen, "Principles of the Austenite-Martensite Reaction," *TRANSACTIONS, American Society for Metals*, Vol. 41, 1949, p. 35.
10. W. O. Binder, "Effect of Cold Work at Low Temperature on Austenitic 18-8 Stainless Steel," *METAL PROGRESS*, Vol. 58, August 1950, p. 201.
11. G. W. Form and W. M. Baldwin, Jr., "The Influence of Strain Rate and Temperature on the Ductility of Austenitic Stainless Steels," *TRANSACTIONS, American Society for Metals*, Vol. 47, 1955, p. 474.
12. M. J. Udy, *Metallurgy of Chromium and Its Alloys*, Vol. 2, 1956, p. 195, Reinhold Publishing Corporation, New York.
13. E. M. Mahla and N. A. Nielsen, "Carbide Precipitation in Type 304 Stainless Steel—An Electron Microscope Study," *TRANSACTIONS, American Society for Metals*, Vol. 43, 1951, p. 290.
14. A. W. Reynolds, "Effects of Stress and Deformation on the Martensite Transformation," *Journal of Applied Physics*, Vol. 20, 1949, p. 902.
15. H. C. Fiedler, B. L. Averbach and Morris Cohen, "The Effect of Deformation on the Martensitic Transformation in Austenite Stainless Steel," *TRANSACTIONS, American Society for Metals*, Vol. 47, 1955, p. 267.
16. A. Magnussen and W. M. Baldwin, Jr., "Low Temperature Brittleness," *Transactions, American Institute of Mining and Metallurgical Engineers*, 1957.
17. L. M. T. Hopkin, "The Intergranular Brittleness of Single-Phase Copper-Antimony Alloys," *Journal, Institute of Metals*, Vol. 84, 1955-1956, p. 102.
18. D. McLean and L. Northcott, "Antimonial 70:30 Brass," *Journal, Institute of Metals*, Vol. 72, 1946, p. 583.

DISCUSSION

Written Discussion: By H. F. Ebling, Metallurgical Research Department, A. O. Smith Corporation, Milwaukee.

The authors have made a valuable contribution to the study of brittleness in austenitic stainless steel. The fact that the loss of ductility at temperatures of -321°F and low strain rates was not revealed by the sensitized type 304 ELC material was of interest. The reason for this probably stems from the definition of sensitize. I believe originally sensitize was used in reference to a structural condition which caused the material to be susceptible to intergranular corrosion. This structural condition could be caused by heating the material over a range of temperatures and times.

To prove the material was sensitized required a corrosion test such as the nitric acid test or acidified copper sulphate test. With the regular types of materials, 0.06 to 0.10% carbon, apparently a standard sensitizing temperature of 1200°F was used with a soaking time of one or two hours. This treatment, as far

as I know, always made the material susceptible to intergranular attack. However, with the introduction of the 0.03% max. carbon type 304 material, this sensitizing temperature does not make the material susceptible to intergranular attack. Thus I would say that 1200 °F is *not* a sensitizing temperature for type 304 ELC. It is my opinion, without fact, that the embrittlement is a function of a grain boundary precipitate but not as to the quantity of the precipitate but more in its distribution and character.

If it is possible for continuing this investigation, I would suggest sensitizing some tests at a lower temperature for longer time periods. For the type 304 and 302 materials, a temperature of 900 °F for 100 to 500 hours, and type 304 ELC a temperature of 1000-1050 °F for 350 to 1000 hours are known to be far more devastating as far as intergranular corrosion resistance than the 1200 °F treatment. The embrittlement of the materials after these heat treatments may be likewise affected.

Written Discussion: By R. D. Wylie, Chief Metallurgist, The Babcock & Wilcox Company, Barberton Works, Barberton, Ohio.

We have reviewed with interest the data presented by the authors. The subject of the effects of strain rate on the mechanical properties of austenitic steels has received new emphasis recently because of the sharp temperature fluctuations which are anticipated in operating nuclear power equipment. It is surprising to find that there is little published data on the effect of strain rate changes on the tensile properties of these steels.

We, therefore, were somewhat disappointed that the authors in their paper did not report tensile strength and offset yield strength as a function of rate of strain. We wonder whether load deformation curves were obtained, and if so, whether additional valuable information might be derived from these test results.

Authors' Reply

Mr. Ebling's comments are well taken. We have no doubt that 304 ELC stainless steel can be sensitized by proper heat treatment—or should we say improper?—and that once sensitized it would be brittle at low temperatures and strain rates. Our original purpose, of course, was to determine whether the precipitation of carbides was the cause of high speed embrittlement in austenitic stainless steels and to this end we chose such steels and heat treatments that would produce precipitation and, for comparisons sake, would not produce precipitation.

We are very sorry that we cannot supply the data requested by Mr. Wylie, but this information is very difficult to obtain at high strain rates and requires special equipment which we do not possess.

EFFECTS OF TEMPERATURE-TIME HISTORIES ON THE TENSILE PROPERTIES OF AIRFRAME STRUCTURAL ALUMINUM ALLOYS

BY R. E. FORTNEY AND C. H. AVERY

Abstract

As a means of analyzing the effect of complex combinations of temperature-time exposures on the strengths of structural airframes, generalized expressions have been developed for the tensile properties of 7075-T6 and 2024-T3 clad sheet.

To obtain generalizations tensile tests were performed at room temperature, 200, 300 and 400 °F after single and sequential exposures sampling the temperature ranges of 300–600 °F (2024-T3) and 250–500 °F (7075-T6) and the time range of 0.1–1000 hours. Normalization and generalization procedures were applied to the yield and ultimate tensile strength data, using semi-empirical parameters based on the rate-process theory. Statistical calculations were made to determine the degree of conformance of test data and generalized equations.

The conclusion was reached that the yield and ultimate strength generalized equations are adequate for analyzing the effects of those service time-temperature exposure histories within the range room temperature to 500 °F and 1.0 to 1000 hours on the room temperature to 400 °F tensile strengths of subject airframe alloys. (ASM International Classification: Q27a, 2–11; Al, SGB-s)

INTRODUCTION

THE EXTENSION of airframe operating speeds into the aerodynamic heating region presents an extensive and important need for information relating the effects of service temperature-time-stress histories to the mechanical properties of metallic materials. The realization of this need caused instigation of an investigation being conducted by Northrop Aircraft, Inc. under contract with Wright Air Development Center (1)¹. This paper represents certain phases of the in-

¹ The figures appearing in parentheses pertain to the references appended to this paper.

A paper presented before the Thirty-Ninth Annual Convention of the Society, held in Chicago, November 4–8, 1957. Of the authors, R. E. Fortney is Senior Engineer, Structures Research Section, Structures Dept., and C. H. Avery is Senior Engineer, Metallurgical Section, Materials and Process Engineering, Northrop Aircraft, Inc., Hawthorne, California. Manuscript received April 17, 1957.

ON vestigation and deals with the effect of temperature-time exposure histories on the yield and ultimate tensile strengths of 2024-T3 and 7075-T6 alclad sheet for those exposure conditions considered most applicable to airframe design. Generalized equations applicable to complex temperature-time conditions are developed from relationships obtained under single and sequential exposure test conditions and conclusions made regarding limits for prediction of tensile strengths under complex temperature-time conditions.

MATERIALS, METHODS AND DATA

Reference 1 presents full details of the material, equipment and procedures used to obtain the data for this investigation. However, a summarized presentation of the materials and methods is necessary to fully weigh the results obtained.

Two full sheets each of 0.064 gage 2024-T3 and 7075-T6 alclad sheet were utilized. Each sheet was cut into panels, fourteen tensile specimens wide with the axis of each specimen transverse to the rolling direction of the sheet. Twelve elevated temperature exposure specimens were tested from each panel and the two center specimens were used to determine the original room temperature tensile properties of the panel. By expressing all other tensile properties in terms of "percent of room temperature properties" and by comparing the properties of those specimens of any one panel exposed to elevated temperatures with the room temperature specimens from the same panel, it was hoped to minimize the effect of inherent material variability on the tensile properties obtained. This was accomplished to the extent shown

	2024—T3 Alclad		7075—T6 Alclad	
	Yield Strength (psi)	Ultimate Strength (psi)	Yield Strength (psi)	Ultimate Strength (psi)
Typical Expected Properties	45,000	65,000	67,000	76,000
Minimum Expected Properties	40,000	62,000	62,000	72,000
Test Material Average Properties	44,300	68,000	67,100	78,200
Test Material Minimum Properties	42,700	66,600	64,300	75,700
Maximum Variation in Test Material Properties	2,900	2,600	5,000	4,600
Maximum Variation Between Adjacent Panel Properties	1,300	1,300	2,200	1,700

above. The variation in test material properties between the centers of adjacent panels was roughly one-half the total test material variation. Since the distance between the room temperature specimens of adjacent panels is the same as the length of a single panel, the maximum variation between adjacent panels is the same as the maximum variation within each panel. Also, as shown above, the test material has tensile properties close to those of typical material. Thus, the results of this paper should represent those of typical 2024-T3 and 7075-T6 alclad sheet.

Conventional air furnaces were utilized for all elevated temperature exposure and tensile testing. Temperature control of the tensile specimens was maintained to $\pm 5.5^\circ\text{F}$ or less of temperatures listed for 0.1 and 1.0 hour exposures and all tensile testing and to $\pm 8.0^\circ\text{F}$ or less for longer exposures. The time interval of elevated temperature exposures was controlled to a maximum variation of 1 minute for 100 and 1000 hour exposures and, by contact of the specimens with massive aluminum blocks, to a maximum variation of 20 seconds for 0.1, 1 and 10 hour exposures. Tensile testing equipment was of a conventional type with hydraulic or mechanical load application, hydraulic-pneumatic load measurement and differential transformer follower, electronic-mechanical recorder strain measurement. Load and strain measuring systems were checked and standardized twice during the investigation.

The testing sequence consisted of inserting a specimen in an air furnace, soaking at the exposure temperature for the required time, removing from exposure furnace and re-exposing in another furnace as many times as required (sequential exposure tests) or removing from the exposure furnace and inserting in the tensile test air furnace (end of single or sequential exposures), and finally tensile testing. Although the exposure times could be closely controlled it was not possible to control the time at temperature during tensile testing. Since the rate of straining was maintained near 0.005 inch per inch per minute throughout tensile testing, the time at temperature varied from about 3 to 33 minutes, depending on the total elongation of the specimens.

To initiate testing a series of single exposure tests were performed which served as a base with which to compare subsequent sequential exposure tests.

Temp., °F	Single Exposure Conditions		Temp., °F		
	2024—T3	Time, Hours		7075—T6	Time, Hours
300		0.1, 1.0, 10, 100, 1000	250		100, 1000
400		0.1, 1.0, 10, 100, 1000	300		0.1, 1.0, 10, 100, 1000
500		0.1, 1.0, 10, 100, 1000	400		0.1, 1.0, 10, 100, 1000
600		0.1, 1.0, 10	500		0.1, 1.0, 10, 100, 1000

Then a series of sequential exposure tests were performed. Those tests were selected so that each exposure of a sequence equally sampled the inclined portion of the Larson-Miller type curves obtained from the single exposure tests (Figs. 1, 2, 3 and 4).

After each single or sequential exposure condition triplicate tensile specimens were tested at each of the temperatures: R.T., 200°F , 300°F , 400°F . The average tensile properties for each group of three specimens, expressed nondimensionally as "percent of room temperature properties" as explained previously, are used for all subsequent

Sequence Number	Sequential Exposure Conditions							
	1st Exposure		2nd Exposure		3rd Exposure		4th Exposure	
	Temp. °F	Time, Hrs.	Temp. °F	Time, Hrs.	Temp. °F	Time, Hrs.	Temp. °F	Time, Hrs.
2024-T3 Alloy								
11	600	1.0	555	4.1	510	18.7	465	99.6
12	555	1.0	510	4.3	465	21.5	420	126.1
13	510	1.0	465	4.6	420	25.2	375	164.0
14	465	1.0	420	5.0	375	30.0	330	219.0
7075-T6 Alloy								
15	500	1.0	460	3.9	420	17.6	380	90.5
16	460	1.0	420	4.2	380	20.2	320	113.4
17	420	1.0	380	4.5	340	23.4	300	145.1
18	380	1.0	340	4.8	300	27.7	260	191.7

data generalization procedures. The test data for the tensile tests listed above are shown in reference 1.

DATA GENERALIZATION

In the first attempt to generalize the test data of the seventy-two single exposure test conditions for each of the materials, 2024-T3 and 7075-T6 alclad aluminum alloy sheet, the well-known Larson-Miller

$$\theta = T_{0R} (20 + \log_{10} t_{hr}) \quad \text{Equation 1}$$

(2) parameter was utilized. This parameter has previously been applied to various creep and other phenomena. In this paper the parameter is applied to the over-aging behavior and with certain modifications provides a means of predicting the tensile strengths of the above materials at room temperature through 400 °F after single exposures as severe as 1000 hours at 500 °F or after an equivalent spectrum of exposures.

Single Exposures

After slight modifications of the above parameter to achieve a better overall agreement among the various exposures, the single exposure test data for the 2024-T3 alclad sheet was found to show the least scatter when utilizing the modified parameter

$$\theta'' = T_{0R} (20 + 1.3 \log_{10} t_{hr}) \quad \text{Equation 2}$$

while for 7075-T6 alclad sheet the best concurrence of time and temperature was obtained with

$$\theta' = T_{0R} (20 + 1.46 \log_{10} t_{hr}) \quad \text{Equation 3}$$

At first glance the parameters 2 and 3 may seem unduly different from similar parameters appearing in the literature which have modified the constant 20 of Equation 1. However, mathematically they can be shown to be equivalent.

The results of the utilization of θ'' and θ' are shown in Figs. 1, 2, 3

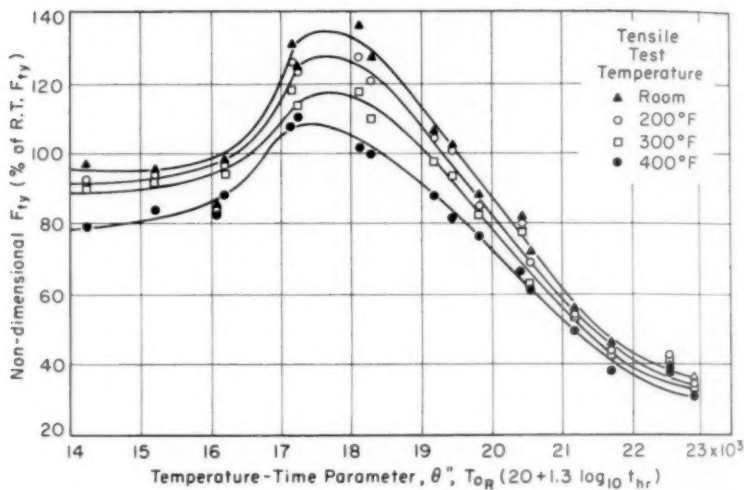


Fig. 1—Nondimensional Tensile Yield Strength of 2024-T3 Alclad Sheet versus Temperature-Time Parameter θ'' .

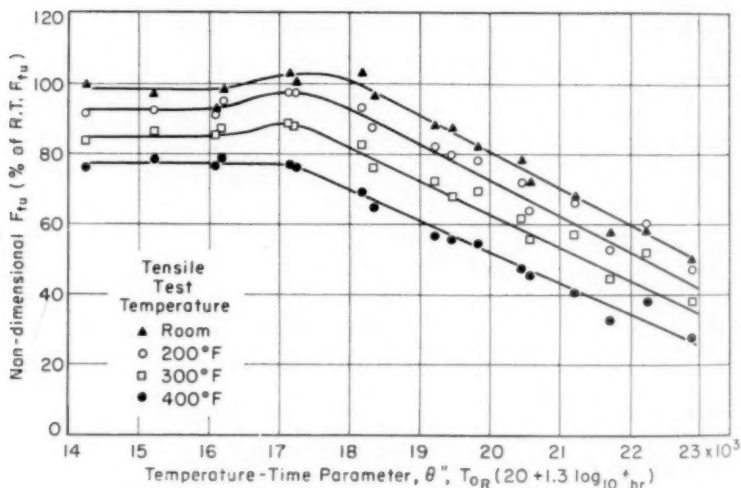


Fig. 2—Nondimensional Tensile Ultimate Strength of 2024-T3 Alclad Sheet versus Temperature-Time Parameter θ'' .

and 4. Statistical analyses have been made which show that over 95% of the test data points fit the curves within 8% of the respective non-dimensional tensile strength. By using these curves it is possible to

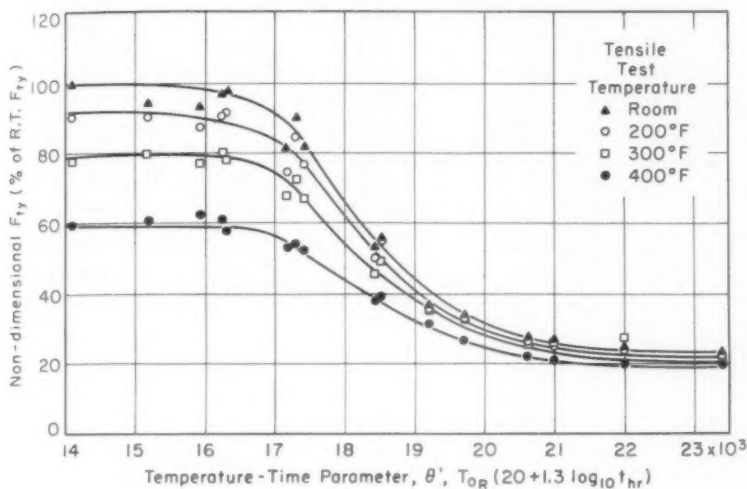


Fig. 3—Nondimensional Tensile Yield Strength of 7075-T6 Alclad Sheet versus Temperature-Time Parameter θ' .

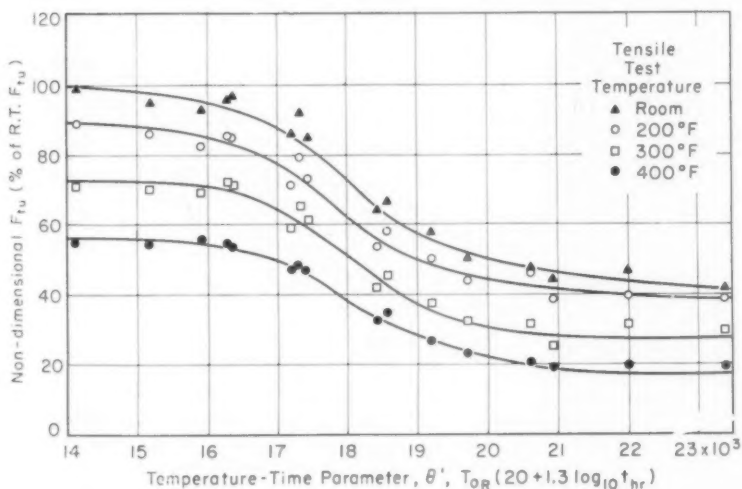


Fig. 4—Nondimensional Tensile Ultimate Strength of 7075-T6 Alclad Sheet versus Temperature-Time Parameter θ' .

predict the tensile yield or ultimate strength of either material at R.T., 200, 300 and 400 °F after almost any normal, single, service exposure to which these materials will be subjected. This generalized data presentation materially assists analysis of temperature-time exposures

but the analysis of tensile test temperatures is very restricted.

To remove this restriction the four curves in each of Figs. 1, 2, 3, and 4 were normalized with respect to the test temperature, i.e., mathematically reduced to a single curve. To do this the nondimensional tensile strength was replaced by a ratio of the general form

$$R = \frac{\text{Nondimensional Strength at Test Temperature After Exposure}}{\text{Nondimensional Strength at Test Temperature, No Exposure}} \quad \text{Equation 4}$$

Further degrees of complexity were required of Equation 4 in some cases to empirically minimize the scatter of the test results. The specific ratios utilized in the normalized curves, Figs. 5, 6, 7 and 8, are as shown below:

$$R_1 = \frac{\% \text{ R.T. } F_{1Y} (T, \theta'')}{\% \text{ R.T. } F_{1Y} (T) + [100 - \% \text{ R.T. } F_{1Y} (T)] \left[\frac{22940 - \theta''}{17,460} \right]} \quad \text{Equation 5}$$

$$R_2 = \frac{\% \text{ R.T. } F_{1U} (T, \theta'')}{\% \text{ R.T. } F_{1U} (T) + [100 - \% \text{ R.T. } F_{1U} (T)] \left[\frac{17200 - \theta''}{8730} \right]} \quad \text{Equation 6}$$

$$R_3 = \frac{\% \text{ R.T. } F_{1Y} (T, \theta')}{\% \text{ R.T. } F_{1Y} (T)' + [100 - \% \text{ R.T. } F_{1Y} (T)'] \left[\frac{\theta' - 14,090}{18,600} \right]} \quad \text{Equation 7}$$

$$R_4 = \frac{\% \text{ R.T. } F_{1U} (T, \theta')}{\% \text{ R.T. } F_{1Y} (T)} \quad \text{Equation 8}$$

where

$\% \text{ R.T. } F_{1Y} (T, \theta'')$ = Nondimensional yield strength at test temperature T after exposure θ'' ,

$\% \text{ R.T. } F_{1Y} (T)$ = Nondimensional yield strength at test temperature T , no prior exposure,

$\% \text{ R.T. } F_{1U} (T, \theta'')$ = Nondimensional ultimate strength at test temperature T after exposure θ'' ,

$\% \text{ R.T. } F_{1U} (T)$ = Nondimensional ultimate strength at test temperature T , no prior exposure,

$\% \text{ R.T. } F_{1Y} (T, \theta')$ = Nondimensional yield strength at test temperature T after exposure θ' ,

$\% \text{ R.T. } F_{1Y} (T)'$ = Nondimensional yield strength at test temperature T after 0.1 hr., 300 °F exposure.

$\% \text{ R.T. } F_{1U} (T, \theta')$ = Nondimensional ultimate strength at test temperature T after exposure θ' .

Statistical analyses have been made of the normalized data points in Figs. 5, 6, 7 and 8 and again it was shown that over 95% of the data points fit the curves within 8% of the respective nondimensional strength. Using these curves it is possible to predict the yield or ultimate tensile strength of either material at any temperature between room and 400 °F after almost any normal, single, service exposure to

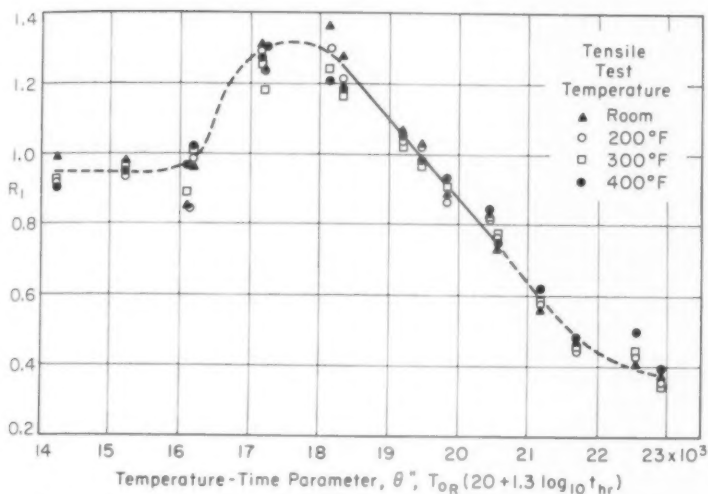


Fig. 5—Tensile Yield Strength Ratio, R_1 , for 2024-T3 Alclad Sheet Versus Temperature-Time Parameter θ'' .

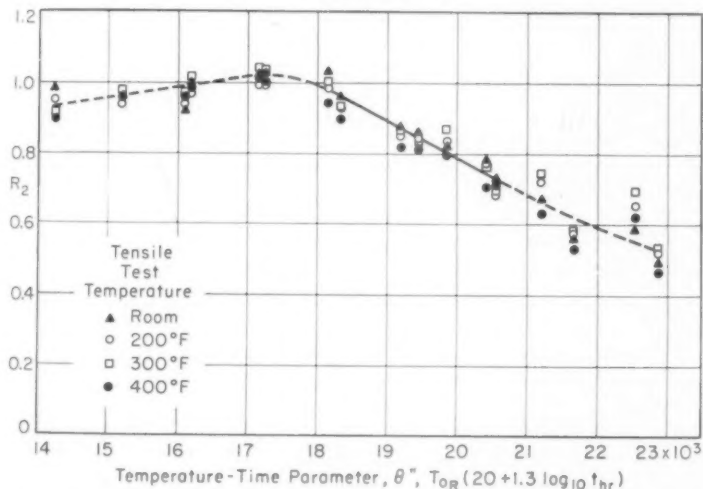


Fig. 6—Tensile Ultimate Strength Ratio, R_2 , for 2024-T3 Alclad Sheet versus Temperature-Time Parameter θ'' .

which subjected. Thus these normalization procedures have increased the usefulness of the data in that it is no longer necessary to approximate by interpolation test temperatures other than room, 200, 300 and 400 °F. However, use of the data is still restricted to single exposure environments.

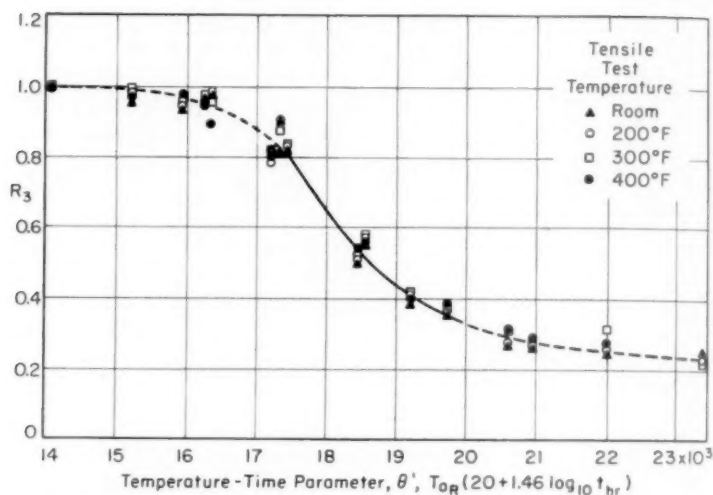


Fig. 7—Tensile Yield Strength Ratio, R_3 , for 7075-T6 Alclad Sheet versus Temperature-Time Parameter θ' .

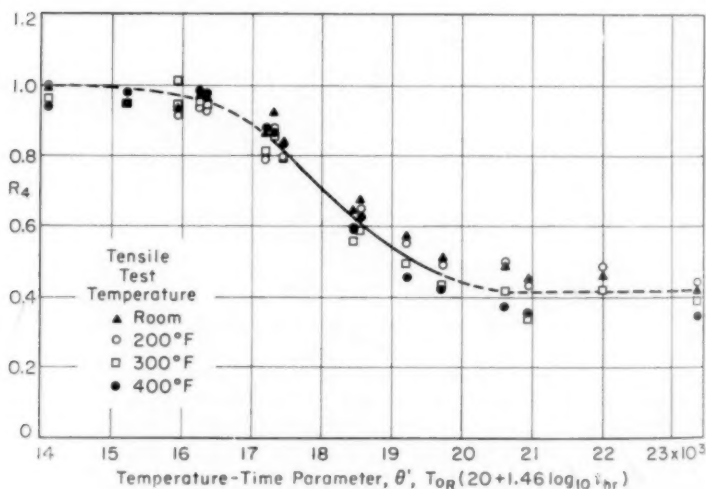


Fig. 8—Tensile Ultimate Strength Ratio, R_4 , for 7075-T6 Alclad Sheet versus Temperature-Time Parameter θ' .

Unfortunately service environments are seldom one of a single exposure, but usually one of a spectrum of exposure temperatures and times.

Sequential Exposures

Thus, the next very logical step is to determine an analytical method to calculate an effective θ'' or θ' for a spectrum exposure consisting of numerous single exposures. The method determined and utilized requires only simple calculations to determine the equivalent or effective θ_t'' or θ_t' for any sequence of exposures. The procedure for the calculation of θ_t' , for example, of any sequence of exposures at temperatures $T_1, T_2 \dots T_n$ for times $t_1, t_2, \dots t_n$ respectively, is outlined as follows:

1. Choose a reference temperature T_r
2. Calculate $\theta_1', \theta_2', \dots \theta_n'$ for each individual exposure of the sequence. $\theta_1' = T_{10R} (20 + 1.46 \log_{10} t_{1br})$
3. Determine $tr_1, tr_2 \dots tr_n$ the times at the reference temperature, T_r , which would give $\theta_1', \theta_2', \dots \theta_n'$ respectively. The general formula for t_r in the determination of θ_t' is

$$t_{r_1} = \text{anti log}_{10} \left[\frac{\theta_1'/T_r - 20}{1.46} \right] \quad \text{Equation 9}$$

Likewise, the general formula for t_{r1} in the determination of θ_t'' is

$$t_{r_1} = \text{anti log}_{10} \left[\frac{\theta_1''/T_r - 20}{1.3} \right] \quad \text{Equation 10}$$

4. Now that each individual exposure is represented by times at a reference or "common denominator" temperature, T_r , these times may be added to obtain the total effective time at T_r since $t_r = \sigma t_{r1}$.
5. Utilizing T_r and t_r the reference temperature and total effective time of the sequence respectively the exposure parameter, θ_t' , for the sequence can be calculated as

$$\theta_t' = T_{r_{on}} (20 + 1.46 \log_{10} t_{r_{br}})$$

The same value of θ_t' will be obtained regardless of the chosen reference temperature.

With the derivation of the analytical method above it is now possible to compare and determine whether the sequential exposure data is in agreement with that of the single exposure tests. The curves of Figs. 5, 6, 7 and 8 all approximate a horizontal portion followed by a steep negative slope and then another horizontal portion. Although the 2024 alloy curves have humps due to the strengthening occurring during artificial aging of the -T3 (naturally aged) temper of this alloy, the increase in strength cannot be generally utilized in structural analyses because maximum loads must be supported before the strengthening

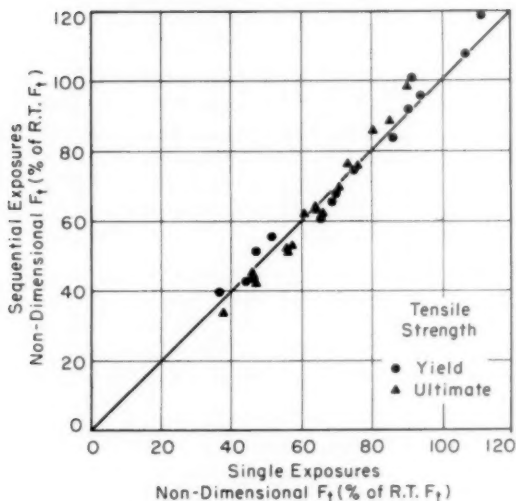


Fig. 9—Comparison of Sequential Exposure Data with Single Exposure Curves for 2024-T3 Alclad Sheet.

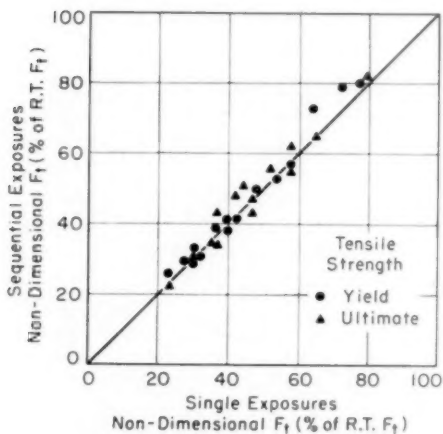


Fig. 10—Comparison of Sequential Exposure Data with Single Exposure Curves for 7075-T6 Alclad Sheet.

has occurred. No valid check of the above calculation procedure can be accomplished completely within the horizontal portions of the curves. Therefore, all sequential exposures were planned to provide θ'' and θ' values along the steep negative slope portion of the curves. To keep

Table I
7075-T6 Alclad Sheet—Sequential Exposure Comparison

θ	Sequential Exposure Time and Temperature			Tensile Test Temp., °F.	Yield Strength		Sequen. Dia., Non-Dim.	Ultimate Strength	
	First	Second	Third		Single Expos. R	Non-Dim. Strength		Single Expos. R	Non-Dim. Strength
17.540	1 hr. 380°F	4.8 hr. 340°F	27.6 hr. 300°F	191.7 hr. 260°F	R.T.	0.767	76.7	0.795	79.3
	380	340	300	260	200	0.767	72.0	0.795	71.3
	380	340	300	260	300	0.767	63.5	0.795	57.3
	380	340	300	260	400	0.767	51.8	0.795	43.7
18.370	1 hr. 420°F	4.5 hr. 380°F	23.4 hr. 340°F	145.1 hr. 300°F	R.T.	0.568	56.7	0.645	64.3
	420	380	340	300	200	0.568	53.3	0.645	57.8
	420	380	340	300	300	0.568	47.5	0.645	43.5
	420	380	340	300	400	0.568	39.5	0.645	35.5
19.210	1 hr. 460°F	4.2 hr. 420°F	20.2 hr. 380°F	113.4 hr. 300°F	R.T.	0.421	42.1	0.517	51.5
	460	420	380	300	200	0.421	39.7	0.517	46.4
	460	420	380	300	300	0.421	35.7	0.517	37.3
	460	420	380	300	400	0.421	30.1	0.517	28.4
20.040	1 hr. 500°F	4.0 hr. 460°F	17.5 hr. 420°F	90.5 hr. 380°F	R.T.	0.312	31.2	0.419	41.8
	500	460	420	380	200	0.312	29.5	0.419	37.6
	500	460	420	380	300	0.312	26.7	0.419	30.2
	500	460	420	380	400	0.312	22.9	0.419	23.0

Table II
2024-T3 Alclad Sheet—Sequential Exposure Comparison

Ø	Sequential Exposure Time and Temperature				Tensile Test Temp., °F.	Yield Strength		Sequence Data, Non-Dim.	Single Expos. R	Ultimate Strength	
	First	Second	Third	Fourth		Single Expos. R	Non-Dim. Strength			Single Expos. R	Non-Dim. Strength
18.880	1 hr. 465°F	5 hr. 420°F	30 hr. 375°F	219 hr. 330°F	R.T.	1.125	112.5	127.2	0.903	90.3	99.0
	465	420	375	330	200	1.125	111.5	118.8	0.903	85.2	88.9
	465	420	375	330	300	1.125	106.3	108.9	0.903	73.6	76.5
	465	420	375	330	400	1.125	93.1	95.9	0.903	64.3	64.2
19.810	1 hr. 510°F	4.6 hr. 465°F	25.2 hr. 420°F	164.0 hr. 375°F	R.T.	0.911	91.1	101.6	0.807	80.7	86.6
	510	465	420	375	200	0.911	90.2	92.0	0.807	75.7	75.6
	510	465	420	375	300	0.911	85.7	83.8	0.807	64.4	63.1
	510	465	420	375	400	0.911	74.4	74.6	0.807	55.3	52.1
20.750	1 hr. 555°F	4.3 hr. 510°F	21.5 hr. 465°F	126.1 hr. 420°F	R.T.	0.695	69.5	68.2	0.709	70.9	69.4
	555	510	465	420	200	0.695	68.3	68.3	0.709	66.1	65.1
	555	510	465	420	300	0.695	65.2	61.1	0.709	53.4	52.6
	555	510	465	420	400	0.695	56.0	55.6	0.709	46.7	42.7
21.760	1 hr. 600°F	6.0 hr. 555°F	16.6 hr. 510°F	99.6 hr. 465°F	R.T.	0.463	46.3	51.7	0.604	60.4	61.8
	600	555	510	465	200	0.463	45.8	43.3	0.604	56.0	52.2
	600	555	510	465	300	0.463	43.2	43.5	0.604	46.1	44.4
	600	555	510	465	400	0.463	36.7	39.2	0.604	38.0	33.8

the times from becoming excessive or the temperature difference from becoming too small, each sequence was made to consist of four single exposures. Four sequential exposures were used to check each property, yield and ultimate strengths, of each alloy, 2024 and 7075. The nondimensional strengths of these sequential exposures are tabulated in Tables I and II along with R values and derived nondimensional strengths for the same θ'' , θ' values but taken from the curves of Figures 5, 6, 7 and 8. A comparison of the sequential data with the derived single exposure curve nondimensional strengths in Tables I and II indicates close agreement. This is further verified by plotting the sequential data nondimensional strengths versus the derived single exposure nondimensional strengths as in Figs. 9 and 10. A statistical analysis indicates that over 95% of the sequential exposure data are within 10% of the nondimensional strengths of the single exposure curves. At the same time the greatest errors will cause conservative structural analyses. Thus the sequential exposure tensile ultimate strengths are predicted accurately and with no significant difference in divergence from that of the single exposure strengths. Whereas, the sequential exposure tensile yield strengths are predicted conservatively and with no significant difference in divergence from that of the single exposure strengths.

From the above it can now be concluded that four-step sequential exposures can be safely predicted. But how about more complex exposures?

CONCLUSIONS

Based upon the facts that the divergences are not significantly different between the single exposure and the four-step sequential data and that the means are not significantly different for the tensile ultimate strengths and significantly but conservatively different for the tensile yield strengths, it may be concluded that the data generalizations presented in this paper can be safely utilized for determining tensile strengths of 2024-T3 and 7075-T6 alclad sheet at temperatures from room through 400 °F after complex sequences of exposure in the range room temperature through 500 °F for times of 1.0 through 1000 hours, i.e., after complex exposures in the estimated usage range of times and temperatures indicated for airframes.

ACKNOWLEDGMENT

Data for this work was obtained during certain phases of an investigation conducted at Northrop Aircraft, Inc., under Wright Air Development Center Contract No. AF 33(616)-3028, Task No. 73605. Permission to publish these results is gratefully acknowledged. The assistance of Mr. A. Scow and Mr. T. Osa are acknowledged with thanks.

References

1. Robert E. Fortney and Charles H. Avery, "Effects of Temperature-Time-Stress Histories on the Mechanical Properties of Aircraft Structural Metallic Materials," WADC Technical Report 56-585 Part I, December 1956.
2. F. R. Larson and James Miller, "A Time-Temperature Relationship for Rupture and Creep Stresses," *TRANSACTIONS, American Society of Mechanical Engineers*, Vol. 52, July 1952, p. 765.

DISCUSSION

Written Discussion: By Wayne A. Reinsch, senior research engineer, North American Aviation, Inc., Los Angeles Division, Los Angeles, California.

The authors are to be congratulated for their contribution in an area which is frequently underemphasized—that of putting valuable data to their maximum use by thorough analysis and interpretation.

The selections of alloys, temperatures, and times for this study were well made, since they are applicable to airframes designed for speeds below Mach 3. At sustained speeds below Mach 3, aerodynamic heating will produce skin temperatures in the range selected, and 2024 and 7075 alloys will generally provide useful properties.

The analytical method of estimation described by the authors is obviously superior to some other methods previously used. One such method is to simplify the temperature-time functions to a single exposure of maximum severity, and base estimated material property reductions on it. A second is to use the summation of property losses for several exposures, all based on original properties. A third is the actual testing of strategically located coupons after certain periods of airplane operation, and extrapolating the data for longer times.

The accurate use of the data presented depends upon our ability to estimate the time-temperature cycles applicable to specific airplanes and missiles. We ask ourselves, "what is a typical mission or flight during the life of a vehicle?" I find such an estimate difficult to make with a high degree of confidence because most designs will be used under a wide spectrum of operational conditions. In this light, we consider that the degree of accuracy reported by the authors to be quite acceptable.

The conclusions state that sequential exposures in excess of four can be estimated safely. It is expected that most analyses of this type would be limited to three or four exposures.

The subject of this paper is considered both timely and valuable. It is presumed that similar analyses could be applied to the thermal resistant materials such as titanium or ferrous alloys which are of particular interest for future airframes.

Written Discussion: By Robert G. Hocker, Metallurgist, Douglas Aircraft Company, Inc., Santa Monica, California.

The information contained in this paper is particularly useful to the aircraft industry for analyzing the effects of service time-temperature exposure histories on the room temperature to 400 °F tensile strengths of 7075-T6 and 2024-T3 alclad sheet.

It is important to note that the test specimens and control specimens were well selected to minimize the effect of inherent material variability, and that the temperature-time control was well regulated throughout the investigation.

Utilizing limited available data, it was found that several short time exposure, room temperature tensile test points checked with the temperature-time parameter curves presented in this paper within 3%, or less than 2000 psi difference. However, a question arises concerning whether or not random sequential exposure conditions (instead of decreasing temperature increments and increasing time exposures used in this paper) would change the shape of the curve. Could it be possible that by starting with low temperatures there might result more accumulative damage than when starting with high temperatures.

Written Discussion: By J. R. Kattus, Head, Metallurgy, Southern Research Institute, Birmingham, Alabama.

There is very little that I can contribute in discussing this paper because the authors have so thoroughly accomplished what they set out to do, i.e., to develop a method for predicting tensile properties of 7075-T6 and 2024-T3 aluminum alloys after various exposures at elevated temperatures.

I would, however, like to ask three questions that occurred to me as I read the paper:

1. What were the heat-up and the cool-down times for the various exposures at elevated temperatures? Do you feel that these are important factors for those who may want to use your techniques for other alloys?

2. In your sequential exposures, you started with the highest temperature and the shortest time, and you then progressed to lower temperatures and longer times. Your determinations of θ' and θ'' are independent of this type of progression. Have you ever varied the time-temperature progression for sequential exposures to determine whether the progressive order of temperature levels and time levels has any effect on the resulting properties?

3. In order to establish, for other alloys over a comparable temperature range, general curves of the type shown in Figs. 5, 6, 7, and 8, do you feel that the amount of testing and checking should be about the same as you did for the 2024-T3 and 7075-T6 alloys, or do you feel that less effort would be necessary?

Authors' Reply

We are gratified by the favorable discussions presented and pleased to see the close agreement of data checked by Hocker with the data presented in this paper. The question concerning random sequential exposure conditions is well taken. We have not verified experimentally that a random sequence of exposures will or will not cause a change in shape of the curves presented. However, intuitively we believe there will be no change in the curves since only a single metallurgical phenomenon, i.e., overaging or coalescence of the precipitated particles of the hardening phase, is operative to cause a softening and rapid decrease in tensile strengths. Then it seems logical that only one rate of softening would occur for random sequences.

The heat-up and cool-down times during exposure as requested by Kattus were 10-20 seconds for 0.1, 1.0 and 10 hour exposures, and 30-60 seconds for the 100 and 1000 hour exposures as determined by actual temperature measurement. Heat-up and cool-down times are important if they become an appreciable part of the exposure time.

As to the amount of testing required to establish general curves of the type shown in this paper, but for other alloys, we believe that approximately the same amount of testing will be necessary with perhaps some reduction in the number of tests where approximate single exposure data already exist.

APPARATUS FOR DETERMINING THE HARDNESS OF METALS AT TEMPERATURES UP TO 3000 °F

Elevated Temperature Hardness of Iron, Molybdenum, Tungsten and S-816

BY M. SEMCHYSHEN AND C. S. TORGERSON

Abstract

An apparatus for determining the hardness of metals from room temperature to 3000 °F is described. The principles of the pyramid penetration method of hardness testing have been embodied in the apparatus by the use of synthetic sapphire for the penetrator. The hardness determinations are carried out in a purified argon atmosphere which protects the test specimen and heating element from oxidation.

The hardnesses of pure iron and of the S-816 alloy are reported from room temperature to 2300 °F. The sensitivity of the apparatus is demonstrated by the hardness values obtained for pure iron at the temperature of the α to γ transformations. Hardness values for molybdenum and tungsten are reported up to 3000 °F. (ASM International Classification Q29p, 1-3, 1-4; Fe- α , Mo, W, SS)

INTRODUCTION

THERE ARE numerous tests for evaluating the mechanical properties of materials at elevated temperatures. For the most part, the preparation of test specimens and the actual testing are time consuming. For the purpose of preliminary evaluation of strength of metals and alloys, a rapid, inexpensive test is desirable. A hardness test has been developed and used at the Research Laboratory of Climax Molybdenum Company for evaluation of molybdenum-base alloys at temperatures up to 3000 °F. Although it cannot be correlated directly with the long-time properties measured by creep tests, elevated-temperature hardness certainly gives an indication of potential high temperature strength and is useful for a preliminary classification of metals and alloys.

Several years ago, in research and development work at the same laboratory, a hot hardness test was devised for preliminary selection

A paper presented before the Thirty-Ninth Annual Convention of the Society, held in Chicago, November 4-8, 1957. The authors, M. Semchyshen and C. S. Torgerson are associated with the Climax Molybdenum Company of Michigan, Detroit. Manuscript received September 26, 1956.

of high strength alloys for gas turbine blades operating at temperatures up to 1600 °F. A paper by Bens (1)¹ describes the apparatus used for making the tests. In order to evaluate metals in general and molybdenum-base alloys in particular, at temperatures above 1600 °F, a new hot hardness apparatus was designed.

DESIGN OF APPARATUS

The hardness tester for use at temperatures up to 3000 °F differs from that described by Bens in that it employs an indenter more resistant to oxidation, a heating element capable of operating at high temperatures, and an atmosphere of argon rather than vacuum. Fig. 1 is a diagram of the new apparatus.

The standard diamond penetrator was rejected because of susceptibility to oxidation and the possibility of forming carbides and welding to the specimen. The use of synthetic sapphire, Al_2O_3 , as the penetrator 9 alleviates these difficulties, and although sapphire (9 Mohs) is softer than diamond (10 Mohs), the hardness of the metallic specimens at any given temperature is so much less than that of sapphire at the same temperature that sapphire does not deform. Furthermore, the orientation of the sapphire as it is mounted in the molybdenum indenter shaft 7 is such that under load the maximum resistance to glide and fracture is attained. The sapphire rods used as the penetrators are $\frac{1}{8}$ inch in diameter and about 1 inch long. They are mounted at the end of a molybdenum rod 7, and although a purely mechanical mounting is fairly successful, a small amount of platinum as binder aids greatly in holding the sapphire in place at the elevated temperatures. The working end of the sapphire rod is ground to the standard Vickers shape, that is, to a square-base pyramid having an angle of 136 degrees between opposite faces. The molybdenum indenter shaft 7 is screwed into the steel rod 5 which extends out of the furnace through a gas-tight, water-cooled bearing 3, and then through the soft rubber bellows 2. The load on the penetrator is applied by dead weight 1.

The specimens and penetrator are enclosed in a molybdenum-wound furnace 8 inside a water-cooled steel case 13, which is evacuated to about 5μ mercury and then filled with purified argon 4 to a pressure of 1 inch mercury above atmospheric pressure. The molybdenum heating element is wound on an alumina liner. Further insulation is provided by radiation shields. The furnace case 13 is water-cooled. The power supplied to the furnace is 220 volts AC through a Variac transformer. The argon is purified prior to and during the test by circulation through titanium chips at 1600 °F. Temperature of the specimen is measured by a Pt-Pt/Rh thermocouple 12 which is in contact with the base of the specimen.

Just before a hardness determination is made, the pressure of the

¹ The figures appearing in parentheses pertain to the references appended to this paper.

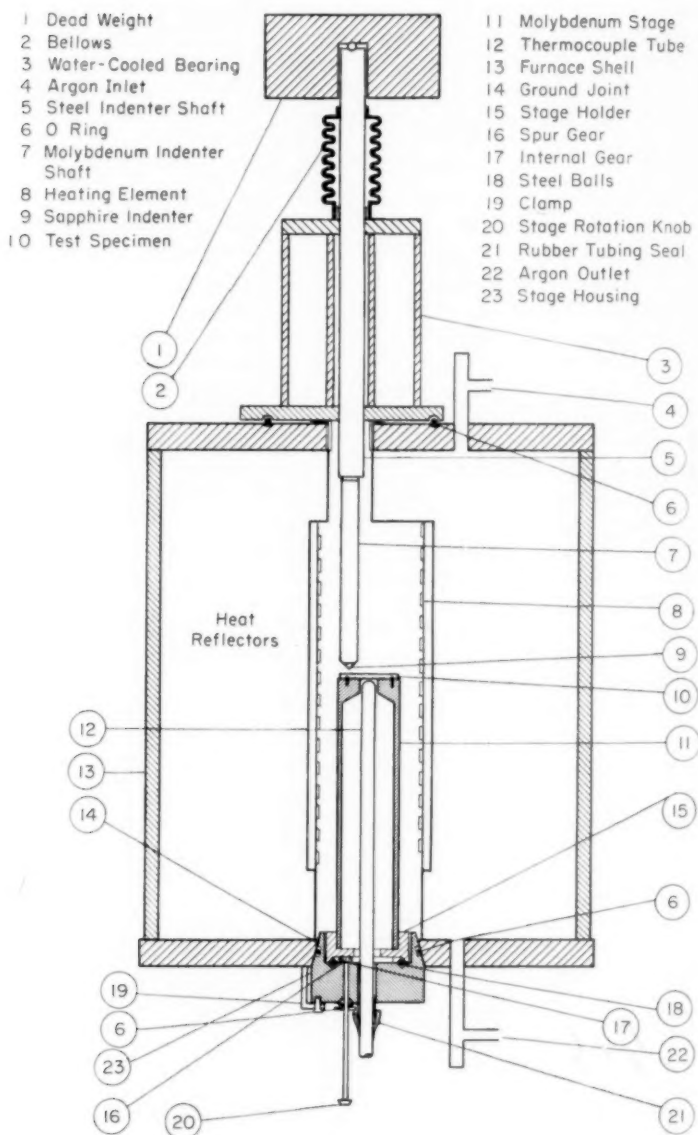


Fig. 1—Hot Hardness Tester For Tests To 3000 °F.

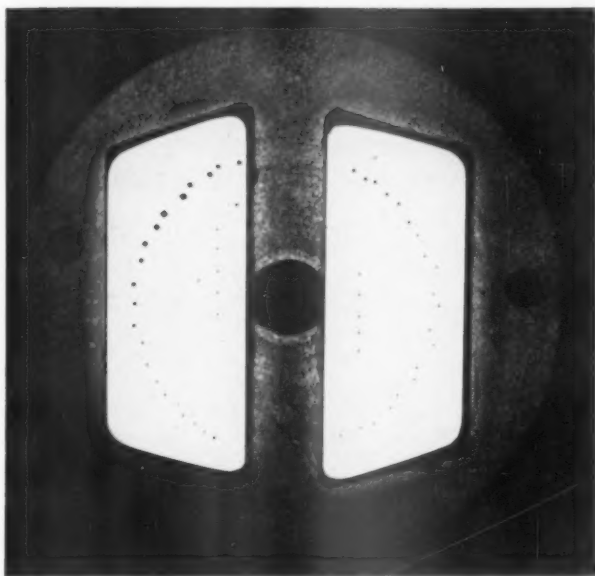


Fig. 2—Hot Hardness Samples In Holder, $\times 1\frac{1}{2}$.

system is reduced to atmospheric pressure 22, and the loaded penetrator, which at the start is about $\frac{1}{8}$ inch above the specimen 10, is gently lowered onto the specimen without impact. In the hardness data reported here, the total load on the indenter, 5 kilograms, was applied for ten seconds. Since the specimen and the penetrator are at the same temperature when the impression is made, there is no cooling of the specimen by the indenter. After the impression is made, the pressure of the system is again increased to 1 inch of mercury.

The specimen may be fastened to the stage by a molybdenum bolt. Bolting is not necessary, however, if the specimens are flat, in which case a pin through the specimen and stage suffices to hold the specimen in place and allows it to rotate with the stage. The axis of the indenter is displaced about $\frac{1}{2}$ inch from the axis of the specimen holder assembly. The stage is rotated and a series of impressions is made $\frac{1}{2}$ inch from the center of the specimen. The angle of rotation is 9 degrees between each impression; thus about 40 determinations may be accommodated on a single specimen. The rotation of the specimen and stage is accomplished without contamination of the atmosphere in the following manner.

The molybdenum stage 11 is attached to the stage holder 15, which rests upon steel balls 18. The stage holder 15 has an internal gear 17

soldered to its bottom, which engages the spur gear 16. The spur gear 16 is rotated by the stage rotation knob 20. The stage housing 23 does not rotate during the run and is held in place by clamps 19.

The preferred specimen size is $\frac{3}{16}$ to $\frac{3}{8}$ inch thick by $\frac{1}{4}$ to 2 inch in diameter. Smaller specimens may be inserted in an adapter, as shown in Fig. 2. The impressions made at intervals of 200 °F on heating to and cooling from 3000 °F are also shown in the photograph.

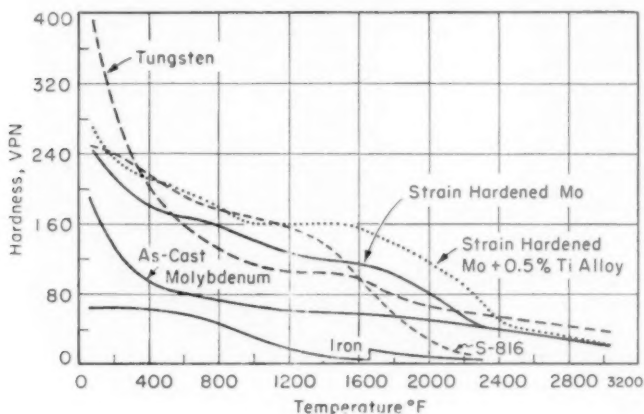


Fig. 3—Hardness of Some Metals and Alloys at Temperatures Up to 3000 °F.

The new apparatus was checked against the standard Vickers hardness machine at room temperature over the hardness range 20 VPN to 600 VPN, and the agreement was entirely satisfactory. Hardness values obtained in the apparatus described by Bens and those obtained in the new apparatus were compared in the range of room temperature to 1600 °F. Values obtained at a given temperature with the two machines varied insignificantly.

EXPERIMENTAL DATA AND DISCUSSION

Hardness values typical of those obtained by using the new hot hardness apparatus are presented in Fig. 3 as plots of hardness versus temperature. The specimens used for obtaining the data are described in Table I.

The hardness data presented for iron illustrate the sensitivity of the apparatus. The transformation from body-centered cubic to face-centered cubic structure for pure iron is reported at 1670 °F. The abrupt increase in hardness shown on the curve at 1665 °F for iron, which contained 0.003% carbon, is in excellent agreement with the transformation temperature reported for this carbon content (2).

Table I
Specimens Used for Hot Hardness Tests

Material	Source	Structural Condition
Iron	vacuum melted, 0.003% C	annealed
S-816	1½ in. dia bar stock	furnace cooled from 2200°F
Tungsten	½x½ in. bar stock prepared by powder metallurgy techniques	annealed 1 hr at 3000°F
Molybdenum	vacuum arc-cast, 0.025% C	as cast
	vacuum arc-cast, rolled to ½x½ in. bar, 0.025% C	strain hardened (as rolled)
Mo-0.50% Ti	vacuum arc-cast, rolled to ½x½ in. bar, 0.021% C, 0.46% Ti	strain hardened (as rolled)

The usefulness of the hot hardness tester in qualitative evaluation of materials according to strength at elevated temperatures is demonstrated in Fig. 3. Of the materials represented, iron is obviously the least attractive base metal for very high temperature applications. The hardness versus temperature plot for S-816, which was chosen as an example of the "superalloys," indicates that S-816 would have reasonable load-carrying ability at temperatures up to 1600 °F, as indeed it does. As the service temperature is increased above 1600 °F, however, cobalt-base alloys rapidly decrease in hardness and strength.

On the basis of the curve in Fig. 3, arc-melted unalloyed molybdenum in its softest conditions, that is, as-cast or fully recrystallized, would be expected to be stronger than the cobalt-base alloys at temperatures above 1800 °F. Further increase in hardness, and accordingly in strength, can be achieved by strain hardening and can be retained on heating to temperatures up to that at which recrystallization occurs. The hot hardness curves indicate that strain hardened molybdenum decreases in hardness at temperatures above 1800 °F more rapidly than molybdenum as cast—a reflection of the occurrence of recrystallization during hardness testing. The strain hardened 0.46% titanium alloy possesses greater hardness at temperatures up to about 2400 °F than any of the other materials tested; its superior stress-rupture strength at temperatures up to 2000 °F is recorded in Table II. Since, for all practical purposes, recrystallization is complete for both unalloyed molybdenum and the 0.50% titanium alloy at 2400 °F, no

Table II
Hardness and Stress-Rupture Strength of Strain Hardened
Unalloyed Molybdenum and Mo-0.5% Ti Alloy

Testing Temp, °F	Unalloyed Molybdenum		Mo-0.5% Ti Alloy	
	Hardness VPN	Stress to Produce Rupture in 100 Hr psi	Hardness VPN	Stress to Produce Rupture in 100 Hr psi
1600	112	31,000	156	68,000
1800	100	22,000	137	53,000
2000	80	13,000	118	34,000

The curve for tungsten shows the potential merit of this metal as an alloy base for high strength materials to serve at temperatures above 1600°F.

significant benefit is gained by strain hardening either unalloyed molybdenum or the 0.5% titanium alloy, although alloying produces minor solid solution hardening.

References

1. F. P. Bens, "Hardness Testing of Metals and Alloys at Elevated Temperatures," *TRANSACTIONS, American Society for Metals*, Vol. 38, 1947, p. 505.
2. L. S. Darken and R. W. Gurry, "Free Energy of Formation of Cementite and the Solubility of Cementite in Austenite," *Transactions, American Institute of Mining and Metallurgical Engineers*, Vol. 191, 1951, p. 1015.

DISCUSSION

Written Discussion: By T. K. Redden, Metallurgical Engineering, Applied Research Operation, General Electric Co., Aircraft Gas Turbine, Development Dept., Cincinnati.

The authors of this paper are to be congratulated for their design and description of a useful tool for probing the rather unknown field of test temperatures above 1600–1800 °F. In this era of missiles and rockets, knowledge of metal behavior at very high temperatures is of paramount interest.

Have the authors attempted any quantitative correlation between tensile and creep rupture properties and hardness? It would be of value to be able to extrapolate these parameters to higher temperatures based on hardness values. Admittedly, such a procedure would only give an approximation, but with the present lack of test apparatus at very high temperature an approximation would be welcome knowledge.

Could the authors comment on the reproducibility of the hardness data for a given material and temperature? Were the data of Fig. 3 obtained from one reading at each temperature or are they an average of several readings?

Authors' Reply

In making a hardness determination from room temperature to 3000 °F, we generally make two to three impressions per temperature. In the hardness range of 400 DPH and below the maximum variation in the size of the impressions made at a given temperature correspond to 5 DPH variation in hardness number. In hardness versus temperature plots, such as presented in Fig. 3, the average value of hardness obtained from two or three impressions per temperature are used. As to reproducibility of the hardness determinations, we find that for several tests on the same specimen at any given temperature the maximum variation from an average value of hardness is ± 5 DPH. We have noted in the determination of hardness of reactive metals, such as titanium and zirconium and their alloys, that greater variations can be obtained than those listed above. This greater variation in hardness is attributable to changes in the composition of the specimen surface due to reaction of the surface with the ambient atmosphere during the test. The change of composition of the surface is readily detected by comparing the room temperature hardness prior to the hot hardness test with the hardness obtained after the test. If these hardness values are different, a sample is cut to expose the cross section and a hardness determination is made at room temperature at the mid thickness position. If the mid thickness hardness is the

same as that prior to the hot hardness test, but both are different than the hardness after the hot hardness test, the change is obviously attributable to changes in the composition of the surface, and not to phase transformations in the test sample. To eliminate changes in surface composition of the test specimen, great care must be taken to remove impurities from the ambient atmosphere in the test chamber.

The correlation of hardness with other mechanical properties at a given temperature has been made, and the relationship yields useful qualitative results. One such example is presented in Table II of the paper which correlates hardness with creep-rupture tests. We also have found that for molybdenum-base alloys a qualitative value for the tensile strength at any given temperature can be obtained by multiplying by 400 the DPH hardness at that temperature.

The hot hardness data has been used as a first approximation of the limitations of present day hot working capacity for molybdenum-base alloys. It has been found that alloys not exceeding a hardness of 45 DPH at 2600 °F can be commercially extruded at 2600 °F. Alloys not exceeding a hardness of 55 DPH can be commercially extruded at 2300 °F. Alloys have already been produced in the cast state which exhibit hardnesses above those which can be successfully extruded. Extrapolating the hardness versus rupture strength relationship (Table II) to the known hardness range of the more highly alloyed systems indicates that 100,000 psi stress-rupture strength for 100 hour life at 2000 °F is not at all fantastic. Thus, the development of higher strength wrought molybdenum-base alloys is dependent upon further developments in the ability to work higher hardness materials.

THE MECHANICAL PROPERTIES OF FORGED CHROMIUM

BY S. A. SPACHNER AND W. ROSTOKER

Abstract

Procedures for melting, forging and machining chromium are described. The torsional mechanical properties of an electrolytic grade of chromium in the forged state have been studied in the testing range RT-1000 °C and 0.01-1 in./in./min. The transition temperature of chromium has been related to the amount and temperature of prestrain. Indications are cited that refinement of the recrystallized grain size can depress the transition temperature. (ASM International Classification Q23r, Q1a; Cr, 4-1)

IN RECENT YEARS there has been considerable interest in the development of wrought chromium as an engineering material, particularly for service applications at elevated temperatures. Small ingots have been hot-worked to wire (1)¹ and sheet (2). Under favorable conditions there is no doubt that chromium is ductile at elevated temperatures. The problem precluding immediate exploration of its usefulness is the lack of room temperature ductility because, as with other body-centered cubic metals, chromium shows a transition from ductile to brittle behavior on cooling. In the particular case of chromium, low in metallics, nitrogen and carbon, the transition occurs sharply at about 50 °C. The embrittlement is so complete for chromium below its transition temperature that it shows no ability to tolerate plastic deformation.

Most of the research to date has been devoted to the influence of contaminants on the transition temperature. Nitrogen and carbon, primarily the former, have a profound effect in raising the transition temperature (3). Of the metallic additions studied so far, many also seem to raise the transition temperature (4). Oxygen, on the other hand, appears to have no effect even in amounts greatly in excess of the solubility limit (5).

Apart from purification there are other recognized means for de-

¹ The figures appearing in parentheses pertain to the references appended to this paper.

Work performed under Contract No. AF33(616)-2978 to the Wright Air Development Center of the United States Air Force.

A paper presented before the Thirty-Ninth Annual Convention of the Society, held in Chicago, November 4-8, 1957. The authors, S. A. Spachner and W. Rostoker, are associated with the Metals Research Department, Armour Research Foundation of Illinois Institute of Technology, Chicago. Manuscript received March 28, 1957.

Table I
Typical Analyses of Three Grades of Chromium

	Commercial Grade Electrolytic	Laboratory Grade Electrolytic	High Purity Hydrogen Annealed
Oxygen	0.55%	0.56%	0.015%
Nitrogen	0.03	0.01	0.01
Carbon	0.02	0.01	0.01
Iron	0.17	0.007	—

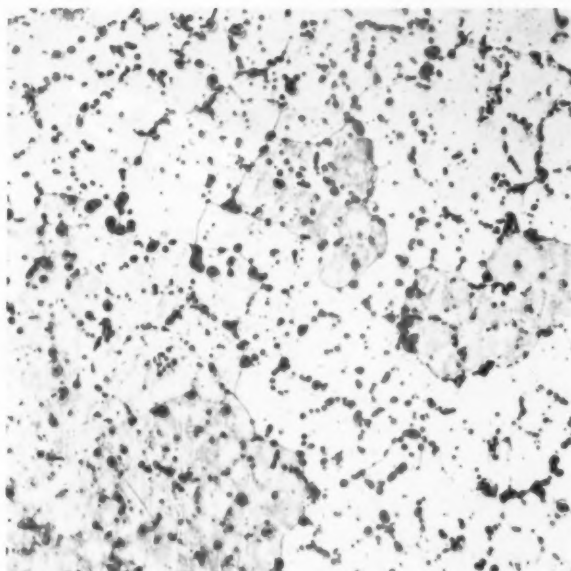


Fig. 1—Microstructure of Arc Melted Chromium Showing Oxide Inclusions.

pressing a transition temperature. These include rheotropic recovery, grain size reduction and appropriate alloy additions, usually in small amounts.

While an ultimate level of purification may provide an academic solution to the problem of producing room temperature ductile chromium, a pragmatic solution will probably have to be worked out in terms of available purities. The electrolytic refining process is capable of producing chromium metal very low in metallics, but somewhat higher in nitrogen than might be desirable. The chief impurity is oxygen of the order of 0.5%, present largely as oxides. Chromium melted from electrolytic charging stock is populated with oxide inclusions as shown in Fig. 1. The work presently reported has undertaken to evaluate the basic mechanical properties of forged chromium using available high

purity grades of metal. The results are sufficiently encouraging to indicate that a room temperature ductile chromium can be realized without resort to ultra-purification processes.

MATERIALS

The main body of this work was performed using a doubly electrolytically refined (laboratory grade) chromium supplied in flake form. As-received, the metal contains large amounts of hydrogen which must be removed by vacuum annealing at 600 °C (1110 °F) and 1.0 micron pressure to permit easier arc melting. For comparison, some limited work was done on a poorer grade of electrolytic chromium and on a special high purity metal low in oxygen, by virtue of a difficult, high temperature hydrogen annealing treatment. These materials were all procured from the Electro Metallurgical Company of Niagara Falls. A summary of typical chemistries is given in Table I.

MELTING PROCEDURES

The production of ingots for forging can be accomplished either by cold mold arc melting, or by vacuum induction melting in ceramic crucibles followed by pouring into appropriate molds. While pure chromium has a melting point of 1850 °C (3360 °F), the presence of 0.5% oxygen reduces the practical melting point by about 100 °C (210 °F). Nevertheless, the high melting temperatures and the strong reactivity of chromium at these temperatures makes for a limited selection of crucible materials. Some experience with stabilized zirconia crucibles² in vacuum melting indicates that these might be feasible although their lifetime is limited. Molten chromium wets the zirconia and permeates it. The chromium ingots so cast analyzed about 0.4% zirconium, most of which is probably as combined oxides supplanting the Cr₂O₃. Ingots produced by vacuum melting were as forgeable as those produced by arc melting.

The largest portion of the forged chromium used in the work was produced by nonconsumable, tungsten electrode, arc melting. Over 100 pounds of chromium in 5 to 10-pound ingot sizes were produced. Arc melting involved some difficulties, not all of which have been satisfactorily overcome. It is difficult to prevent some pickup of tungsten from the electrode. Particularly when grains of tungsten parted from the electrode fall into the melt pool and are entrapped as inclusions, problems arise later in machining. If the inclusions survive machining they invariably show up in fractured test pieces as the origin of premature failure.

If the melting current is too low, the ingot is riddled with cold shuts because of poor fluidity of the melt. If the melting current is too high, excessive boiling of the chromium and contamination from tungsten is

² Supplied by the Titanium Alloy Manufacturing Division of the National Lead Co.

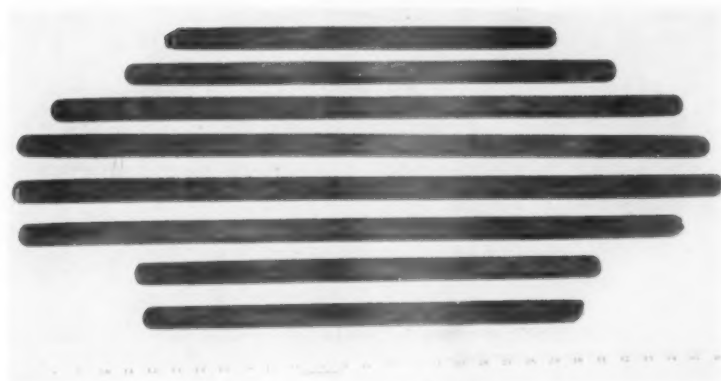


Fig. 2—Forged Bars of Chromium.

encountered. Another problem with excessive arc current is the mysterious appearance of long interconnecting holes which seem to bespeak a gas evolution.

Ingots were dressed for forging by cropping top and bottom and grinding or machining out surface cold shuts. There is a broad correlation between melting current, machinability and forgeability. Ingots produced with a low current arc were generally more difficult to machine and to forge.

FORGING

The key to the successful forging of cast chromium is strain rate. Ingots worked by drop hammer broke up immediately, whatever the pre-heat temperature. However, by careful press forging, ingots can be reduced to useful square and round bar. Using a 100-ton press, a 3-inch diameter \times 6 inch high ingot can be broken down in $\frac{1}{16}$ inch reductions progressing to $\frac{1}{8}$ inch reductions and finally by as much per pass as the press is capable. Initial pre-heat temperatures of as high as 1345 °C (2450 °F) are necessary although finishing temperatures of 1040 °C (1900 °F) are both permissible and, probably, desirable. The lower temperature limit is just above the recrystallization temperature. This is not a barrier, however, as chromium can be forged at much lower temperatures.

The strain rate dependency in forging applies as much to forged bar as to the ingot. One ingot was reduced more than 50% by press forging and cut into two lengths. The first length was hammer forged and broke up immediately. The second press forged readily to 1-inch square bar. Bars were generally forged to 1-inch squares as shown in Fig. 2. Although total soaking time in the furnace often amounted to 5 hours,

scaling was not excessive and could be removed by grit blasting. Undoubtedly, though, there was opportunity for some nitrogen pickup.

MACHINING

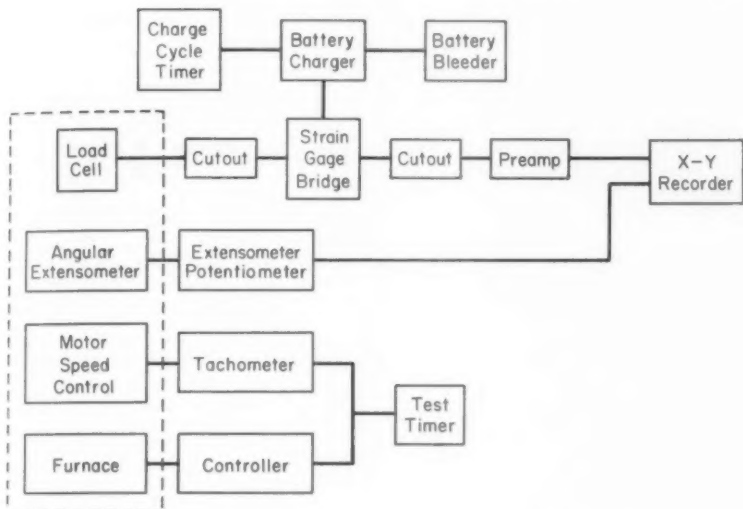
At various stages of production, cutting, grinding and turning operations were necessary. A number of pertinent observations may be usefully recorded since this is a relatively new metal. Superficial cold shuts in ingots may be ground out with a coarse grinding wheel without spalling. On occasions when over-all surface machining is desirable for conditioning, this may be accomplished on a lathe using a high speed tool bit with a positive rake angle and with or without lubricant. Forged bar may be cut without difficulty by an abrasive cutting wheel.

In turning of test specimens, a four-jaw chuck with a live tailstock was used to minimize deflection during machining. Since the specimens were usually brittle, extreme care was required in machining. Roughing cuts were made at 390 rpm, 0.015 inch of cut per pass with 0.005 inch feed per revolution. A sintered carbide tool bit (Carboloy 883) was used, pointed in shape, with a maximum 0.005 inch nose radius and a 6-7 degree relief angle. It was necessary to maintain a sharp edge on the tool at all times. A water soluble coolant produced a smoother finish and minimized galling.

A number of the test specimens were ground to shape. Grinding wheels of dimensions $7 \times 1\frac{1}{2} \times 1\frac{1}{4}$ inch (Sterling No. ZA60J16V2) were used at 3400 rpm. Hand feeding was necessary. Initial depths of cut were 0.003 inch and finishing depths were 0.001-0.0015 inch. Frequent wheel dressings were required.

TESTING PROCEDURES

Because of the apparent strain rate dependence of ductility during forging, it was felt that a full representation of the basic mechanical properties of chromium would require a spatial plot of property-temperature-strain rate. This was accomplished by the use of a specially designed torsion testing apparatus. Briefly, the capabilities of this testing machine include: controlled angular strain rates at any value between 0.002 and 2.3 rpm, controlled temperatures between 150 and 1000 °C (300 and 1830 °F) on a 3-inch constant temperature zone, and any torque delivery between 0.20 inch-pound and 6000 inch-pound. Through the use of a calibrated ring dynamometer with a built-in strain gage bridge for force measurement and calibrated high sensitivity potentiometers adequately amplified for twist measurement, torque-twist curves were autographically recorded by an X-Y recorder. By suitable adjustment the twist ranges for full-scale deflection could be set for any one of ten ranges between 0-6 degrees and 0-20 turns. The general arrangement of the device and measuring instruments is illustrated in Fig. 3.



Items enclosed by dashed line are mounted on torsion machine; other items are mounted on an enclosed relay rack.

Fig. 3—Pictorial View of the Autographic Recording, Torsion Testing Device.

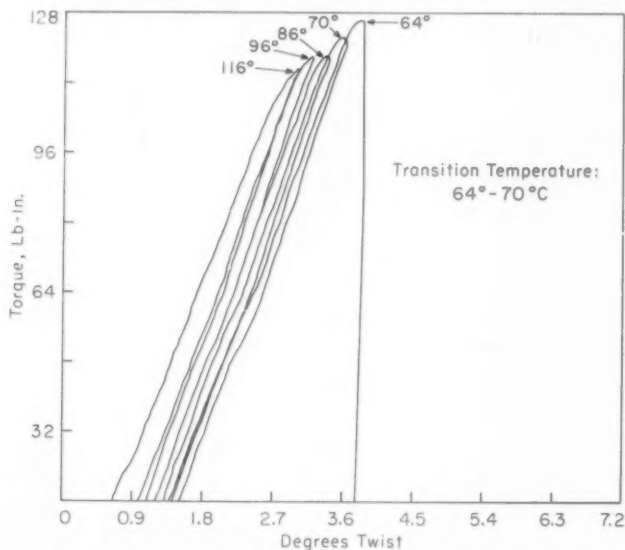


Fig. 4—An Example of the Successive Stress-Strain Tests Leading to Determination of the Transition Temperature of a Chromium Specimen.

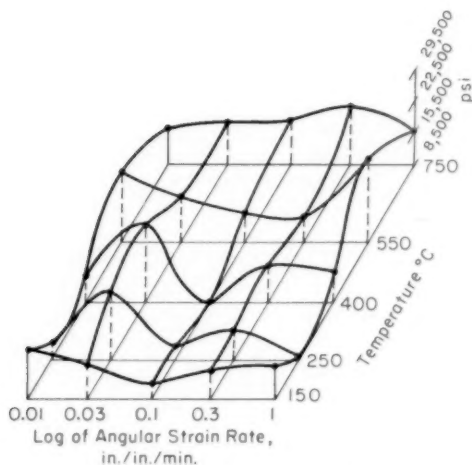


Fig. 5—Torsional Yield Strength-Temperature-Strain Rate Relationship for Forged Chromium.

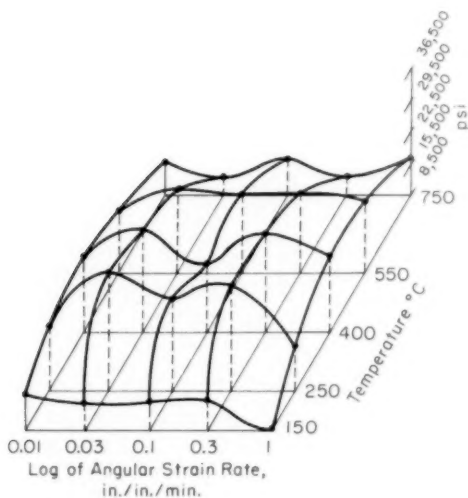


Fig. 6—Torsional Ultimate Strength-Temperature-Strain Rate Relationship for Forged Chromium.

Specimens for torsion testing were machined from 1-inch square forged chromium bar to dimensions 3 inches long by $\frac{1}{4}$ inch test diameter by 1.50 inch gage length with $\frac{3}{4}$ inch square shoulders which slide smoothly into the square recessed grips of the torsion test machine.

A few tensile test specimens were machined to $\frac{1}{4}$ inch diameter by 2 inches long test sections with threaded shoulders.

The determination of the transition temperature was accomplished with the use of only one specimen and usually to within an accuracy of $\pm 2^\circ\text{C}$. With the extensometer scale adjusted for the range 0–9 degrees of twist, the following procedure was developed. A test specimen set into the machine was heated to 120°C (250°F) (for instance) and twisted through the elastic range to 0.25–0.5 degrees into the plastic

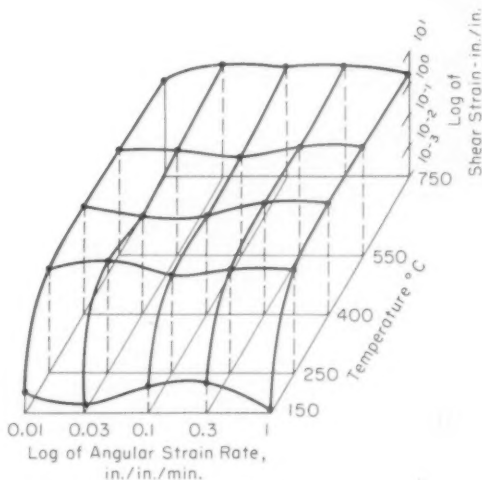


Fig. 7—Torsional Total Ductility-Temperature-Strain Rate Relationship for Forged Chromium.

range. If fracture had not occurred, the specimen was unloaded, the temperature lowered an arbitrary amount and the test repeated. When the ductile-brittle transition temperature was reached or exceeded, the specimen fractured at the elastic limit. Total plastic strain in any series of tests never exceeded 8 degrees twist, which by rechecking on several occasions with nonprestrained specimens was shown to have no effect on the transition temperature itself. The successive torque-twist curves for a single specimen are shown in Fig. 4.

THE TORSIONAL STRENGTH-DUCTILITY BEHAVIOR OF CHROMIUM

Thirty-nine specimens manufactured from laboratory grade electrolytic chromium were used to analyze strength and ductility over the temperature range R.T. to 1000°C (1830°F) and over the surface strain rate range of 0.01 to 1.0 inch per inch per minute. The behavior of yield point in shear, ultimate strength in shear and total ductility in shear are summarized graphically in Figs. 5, 6 and 7, respectively.

Table II
Torsional Stress-Strain Data for Chromium at 1000°C (1830°F)

Strain Rate inch per inch per minute)	Yield Stress (psi)	Ultimate Strength (psi)	Ductility (inch per inch) no fracture*
0.03	—	—	—
0.1	4700	5370	2.12
0.3	7300	3900	4.5
1.1	8475	9030	2.23

*Test was discontinued after specimen had twisted 10.7 revolutions without fracturing. An error in adjustment prevented the obtaining of a yield stress figure.

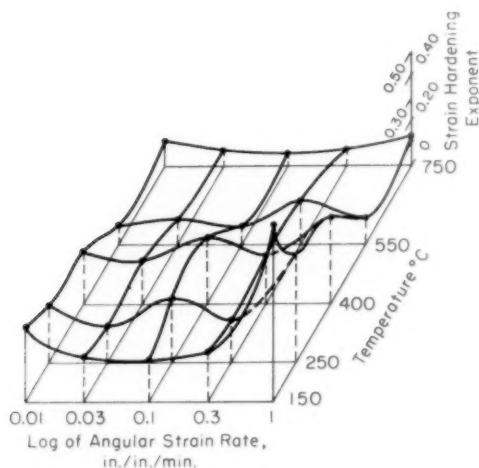


Fig. 8—Torsional Strain Hardening Exponent-Temperature-Strain Rate Relationship for Forged Chromium.

These plots have not included the 1000 °C (1830 °F) data because the very low strengths and very high ductilities could not be conveniently included in the scales used. The data are contained for comparison in Table II. As a rough guide to magnitudes of ductility, 1, 0.1, 0.01 inch per inch correspond to 1.9, 0.19, 0.019 revolutions of twist.

The salient features of these results are the excellent ductilities available at all temperatures above 250 °C (480 °F) and the maintenance of substantial strength up to 750 °C (1380 °F). In fact, there is a general gain in strength at 550 °C (1020 °F) as compared with 250 and 750 °C (480 and 1380 °F). This latter type of behavior usually reflects the action of the interstitial elements. There are indications of the same sort of effect in the hot tensile properties of vanadium and tantalum.

Ductilities drop sharply below 250 °C (480 °F) and by 150 °C (300 °F) are only marginal. There seems to be no indication of the strain rate sensitivity indicated by the experiences with forging. The

difference between hammer and press strain rates, however, may be much greater than the three magnitude range used in determining these surfaces. The significance of the convolutions of yield stress with strain rate is obscure, and these may only reflect the scatter consequent on the rather coarse grain size of many of the specimens.

The strain hardening exponent was derived from each of the torque-twist curves converted to effective stress-strain. These are summarized in Fig. 8. In general, values range between 0.1 and 0.45 with some

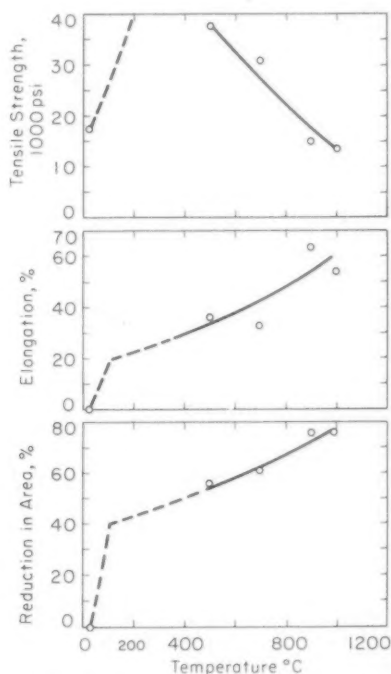


Fig. 9—Tensile Properties of Forged Chromium.

dependence on temperature and strain rate—maximizing at low temperatures and high strain rates.

By comparison, limited tensile data are shown in Fig. 9. These measurements were made at conventional strain rates and with the normal crosshead speed control available in hydraulic-type universal testing machines. The large ductilities at elevated temperatures are confirmed.

TORSIONAL STRENGTH-DUCTILITY AND PURITY

An ingot each of the very high purity chromium and the lowest purity

Table III
Torsional Ductility of Three Grades of Chromium at 750 °C (1380 °F)

Strain Rate (inch per inch per minute)	Total Ductility (inch per inch)		
	High Purity	Laboratory Grade	Commercial Grade
0.009	—	—	3.65
0.01	2.39	1.39	—
0.093	—	—	2.87
0.11	2.07	2.04	—
0.93	—	1.49	—
1.1	2.75	—	2.84

commercial grade of chromium was melted for comparative testing at 750 °C (1380 °F). There were no distinguishable differences in the forgeability of the three grades. The total ductility to fracture at these strain rates are summarized in Table III.

Paradoxically, the commercial grade material appears to exhibit slightly better ductility than the high purity material and considerably better ductility than the laboratory grade material. The principal differences between the laboratory and commercial grades lie in the amount of iron present. There is approximately twice as much iron (0.17%) in the commercial grade.

THE TRANSITION TEMPERATURE OF FORGED CHROMIUM

In the as-forged state, the transition temperature of the laboratory grade chromium was about 50 °C, which is in good agreement with the work of Sully (4). When small percentages of tungsten (~0.3%) were unwittingly dissolved into the chromium during the arc melting operation, the transition temperature rose a maximum of 20 °C. In another instance, when about 1.5% iron was picked up in the melt, the transition temperature was greater than 150 °C (300 °F). On occasions when incompletely dissolved tungsten appeared in the fracture, the transition temperature was invariably above 100 °C (210 °F).

The effect of strain rate on the transition temperature was investigated between the limits 0.001 and 0.05 inch per inch per minute. The results of these tests are summarized in Table IV. This material does not show the transition temperature dependency on strain rate reported by others.

The term "rheotropic recovery" is applied to the effect of increasing

Table IV
Effect of Strain Rate
on the Transition Temperature of Forged Chromium

Strain Rate (inch per inch per minute)	Transition Temperature (°C)
0.001	51
0.003	50
0.007	47
0.019	51
0.05	48

the ductility of a metal by prestraining plastically at a higher temperature which is below the recrystallization temperature. In the succeeding paragraphs, it will be shown that plastic prestrain of forged chromium above its transition temperature has the effect of both lowering and raising the transition temperature on subsequent testing, depending upon the amount of prestrain and the temperature at which it was carried out.

Prestrains were introduced in a specimen by twisting a predetermined amount at one of three temperatures. The temperature of the

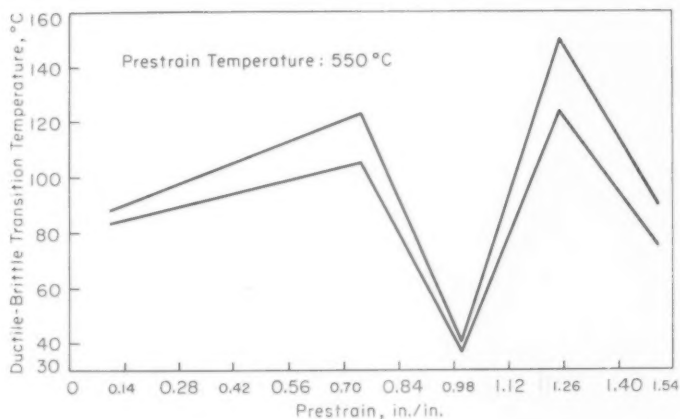


Fig. 10—Effect of Prestrain at 550 °C (1020 °F) on the Transition Temperature.

surrounding furnace was then lowered and at about 100–150 °C (210–300 °F) the previously described succession of tests was begun to determine the transition temperature. Prestrains were conducted at 550 °C (1020 °F) (0.3 inch per inch per minute), 400 °C (750 °F) (0.93 inch per inch per minute) and at 250 °C (480 °F) (0.03 inch per inch per minute). The strain rates were those which in prior testing gave the greatest ductility at the temperature designated.

Fig. 10 shows the effect of amount of prestrain at 550 °C (1020 °F) on the transition temperature. Except in the narrow range of 1.0 inch per inch of prestrain, the transition temperature was generally raised. On the other hand, prestrains at 250 and 400 °C (480 and 750 °F) lowered the transition to below room temperature. In these instances, instead of further lowering the temperature, the total ductility at room temperature was determined. The results for both temperatures are summarized in Fig. 11. The best result was provided by a prestrain of 0.75 inch per inch at 250 °C (480 °F), which gave a ductility at room temperature of 0.11 inch per inch (79.5 degrees of twist). There is a

clear trend of increased effectiveness of prestrain with the lower temperature at which the prestrain is done.

The prestrain can be introduced by pressing the original one-inch square bars between heated platens. At 250 °C (480 °F), 50% reductions in thickness were accomplished without evidence of cracking and with uninterrupted movement of the press. These specimens were then machined directly to standard torsion test pieces.

There are preliminary indications that refinement of the recrystal-

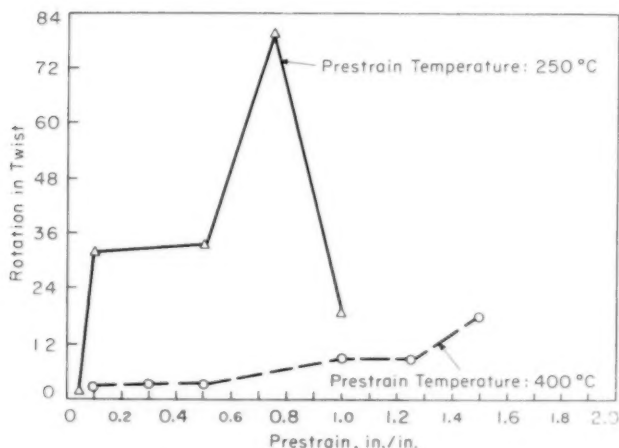


Fig. 11—Effect of Prestrain at 250 and 400 °C (480 and 750 °F) on the Total Ductility at Room Temperature.

lized grain size can bring about a depression of the transition to below room temperature. This has already proved effective in the case of molybdenum and tungsten. As remarked earlier, the grain size of the as-forged chromium, although equiaxed, was very coarse—of the order of 1 to 3 millimeters diameter. Control of grain size can be accomplished most simply through the minimum finishing forging temperature and with more control by strain hardening and recrystallization. A few specimens of both methods have shown room temperature ductility. Finish forging at 1065 °C (1950 °F) to an extent of 25–50% seems to work. The other procedure involved finish forging 50% at 1065 °C (1950 °F), followed by a 53% reduction at 250 °C (480 °F), and an anneal at 1000 °C (1830 °F) for 10 minutes. This latter specimen permitted 41 degrees of twist before fracture at room temperature. The grain size of these specimens was of the order of 0.03 millimeter diameter. The grain size is often heterogeneous; and subgrain boundaries are frequent, making size determinations difficult.

SUMMARY

An electrolytic grade of chromium containing 0.5% oxygen and 0.01% nitrogen (initially) can be arc melted, forged and machined into test specimens. Forging can only be accomplished by careful press forging.

Forged chromium shows substantial ductility above 250 °C (480 °F) and begins to lose strength only above 750 °C (1380 °F). The main body of test results derived by torsion tests have been qualitatively confirmed by tensile tests. Strain rate in the range 0.01 to 1.0 inch per inch per minute does not significantly affect strength or ductility in torsion at temperatures above 250 °C (480 °F).

The transition temperature of forged chromium is about 50 °C, in agreement with Sully's work (4). This temperature is not affected by strain rate in the range 0.001 to 0.05 inch per inch per minute, which is in disagreement with the same author's work.

The transition temperature of forged chromium can be depressed to below room temperature by prestraining at 250–400 °C (480–750 °F). Chromium with significant room temperature ductility can be produced in this way. Prestraining at higher temperatures does not produce the same magnitude of effect and can even cause an increase in the transition temperature. Prestraining can, of course, be erased by recrystallization at 900–1100 °C (1650–2010 °F) with a reversion of the transition to 50 °C.

Preliminary evidence indicates that a more permanent depression of the transition temperature can be effected by refinement of the recrystallized grain size. It is to be noted that these results have been obtained with a chromium which by virtue of its initial purity and subsequent prolonged exposure to air at 1345 °C (2450 °F) during forging must contain much more nitrogen than is considered dangerous and unworkable by the work of previous investigators (3,5).

ACKNOWLEDGMENT

This work was supported and encouraged by the Aeronautical Research Laboratory of the Wright Air Development Center. The sponsorship and permission to publish are gratefully acknowledged by the authors.

References

1. H. L. Gilbert, H. A. Johansen and R. G. Nelson, "Forging of Arc-Melted Chromium," *Transactions, American Institute of Mining and Metallurgical Engineers*, Vol. 197, 1953, p. 63.
2. W. J. Kroll, W. F. Hergert and L. A. Yerkes, "Ductile Chromium," *Transactions, Electrochemical Society*, Vol. 97, 1950, p. 258.
3. D. J. Maykuth, W. D. Klopp, R. I. Jaffee and H. B. Goodwin, "A Metallurgical Evaluation of Iodide Chromium," *Journal, Electrochemical Society*, Vol. 102, June 1955, p. 316.

4. A. H. Sully, E. A. Brandes and K. W. Mitchell, "The Effect of Temperature and Purity on the Ductility and Other Properties of Chromium," *Journal, Institute of Metals*, Vol. 81, 1953, p. 585.
5. H. L. Wain, F. Henderson and S. T. M. Johnstone, "A Study of the Room Temperature Ductility of Chromium," *Journal, Institute of Metals*, Vol. 83, 1954, p. 133.

DISCUSSION

Written Discussion: By A. H. Roberson, Supervising Metallurgist, U. S. Bureau of Mines, Region 1, Albany, Oregon.

The authors have presented some interesting information on the properties of chromium. The data developed for laboratory grade chromium agree remarkably well with those for high purity, room temperature, ductile metal prepared by the Bureau of Mines. It is surprising to learn that metal containing 0.4% zirconium as the oxide, 0.5 oxygen as Cr_2O_3 and appreciable amounts of tungsten should possess the reported ductility.

The authors have stated that room temperature ductility can be imparted to forged chromium by prestraining in the temperature range of 250–400 °C (480–750 °F). One test specimen in particular which was finish forged 50% at 1065 °C (1950 °F), followed by a 53% reduction at 250 °C (480 °F), and annealed at 1000 °C (1830 °F) for 10 minutes, was twisted 41 degrees at room temperature before fracture. This specimen must have been tested in the fully annealed or recrystallized state. It would appear then that some ductility also is evident in recrystallized structures.

Room temperature ductility being imparted to chromium by prestraining in the temperature range of 250–400 °C (480–750 °F) is in agreement with reported results by several investigators,^{3, 4, 5} who have obtained room temperature ductile chromium. Most of these other investigators have obtained considerable tensile ductility in small sections which had been prepared in such a manner that there was plastic deformation being imparted at an effective temperature range of 300–400 °C (570–750 °F). A good example of this was shown by Johansen³ who obtained room temperature ductile wire by drawing wire in the temperature range of 300–400 °C (570–750 °F), which is in effect no different than the "prestrained" material in this preprint. This ductile 0.05 inch diameter wire prepared by Johansen contained about 0.05% O_2 and about 0.005% N_2 and could be twisted from 10 to 20 revolutions per inch of gage length.

The questions which arise are:

- (1) Does the data plotted in figure 11 reflect tests on specimens which were not given this 1000 °C (1830 °F) anneal prior to testing?
- (2) Experience at the Bureau of Mines has indicated that wires drawn at 300–400 °C (570–750 °F), in effect prestrained at this temperature, showed increased ductility when 0.003–0.005 inch of metal was removed from the surface.

³ H. Johansen and G. Asai, "Room Temperature Ductile Chromium," *Journal, Electrochemical Society*, Vol. 101, Dec. 1954, p. 604.

⁴ W. Blum, *Transactions, Electrochemical Society*, Vol. 90, 1946, p. 87.

⁵ D. J. Maykuth and R. I. Jaffee, "The Mechanical Properties of Swaged Iodide-Basic Chromium and Chromium Alloys," *TRANSACTIONS, American Society for Metals*, Vol. 49, 1957, p. 948.

Was the effect of surface treatment of the subject specimens considered by the authors?

- (3) Nitrogen is said to be a potent factor in reducing the ductility of chromium. Your starting material contained 0.5% oxygen and 0.01% nitrogen. What was the nitrogen content of the test specimens which showed ductility at room temperature?
- (4) Were any efforts made to "prestrain" as-cast specimens at 250–400 °C (480–750 °F)?

Written Discussion: By C. W. Weaver, Defense Standards Laboratories, Melbourne, Victoria, Australia.

There are conflicting reports on the embrittling effect of nitrogen on chromium; for example, Wain, et al.⁶ found that ductility was critically dependent on very low nitrogen contents, whilst Brandes, et al.⁷ report that fully annealed chromium containing 0.09% nitrogen was ductile at room temperature. The chromium used by the present authors is fairly high in both nitrogen and oxygen, and yet it has a transition temperature of only 50 °C, which is far lower than that of the high purity chromium produced at D.S.L. and elsewhere. Our chromium contains about 0.001% nitrogen and 0.02% oxygen, and when annealed has a transition temperature of 300–350 °C (570–660 °F). These differences suggest that factors other than nitrogen may also influence ductility, such as the presence of other unidentified impurities, grain size and the effects of hot or cold working. Also

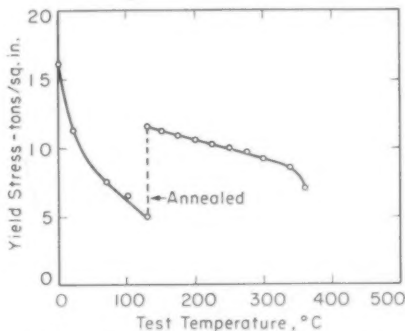


Fig. 12—Effect of Repeated Strainings on Yield Strength of Chromium.

they suggest that perhaps the nitrogen itself may be present in different forms in high and low nitrogen chromium.

It has been suggested^{8,9} that brittleness in chromium may be affected by two processes, namely Cottrell locking by interstitial solutes, and also by precipitation, and that small plastic strains may be effective in accelerating "over-aging". The authors' results on "rheotropic recovery" are a most interesting demonstration of this effect, and resemble closely some work carried out by D.S.L.

⁶ H. L. Wain, F. Henderson and S. T. M. Johnstone, *Journal, Institute of Metals*, Vol. 83, 1954, p. 133.

⁷ E. A. Brandes, H. T. Greenaway and H. E. N. Stone, *Nature*, Vol. 178, 1956, p. 582.

⁸ C. W. Weaver, *Nature* (to be published).

⁹ H. L. Wain, et al., *Journal, Institute of Metals* (to be published).

Repeated straining in tension to just beyond the yield point at successively lower temperatures, in a manner similar to that described by the authors, results in a marked lowering of this transition temperature, and other interesting features emerge as shown in Fig. 12. A tensile specimen annealed 1 hour 1250 °C (2280 °F) was strained to the yield point at 360 °C (680 °F), unloaded, cooled to 320 °C (610 °F) and restrained, and so on down to 130 °C (265 °F). At this stage the total plastic strain was 0.03 inch per inch. The specimen was reannealed for 1 hour at 1250 °C (2280 °F) and straining repeated at 130 °C (265 °F), the process of cooling and straining being continued down to 0 °C. The second plastic strain was 0.025 inch per inch. On reannealing for 1 hour at 1250 °C (2280 °F) and testing at 0 °C the specimen was brittle. The two most interesting features of these tests are first, that annealing after straining did not re-embrittle the chromium at 130 °C (265 °F) and second, that the yield strength at 130 °C (265 °F) was reduced to less than half by annealing. A softening of this order can hardly be ascribed to a change in grain size or to the removal of such a small amount of cold work. Subsequently it has been found that annealed chromium prestrained 3% at 400 °C (750 °F) has high ductility at room temperature (66% Elongation 76% Reduction of Area) and a brittle-to-ductile transition at -100 °C (-148 °F). The large effects of such small strains merits further study, since it is here that development of a ductile chromium shows promise.

So far as arc melting is concerned, we have found that tungsten pickup can be practically eliminated by using thoriated or zirconiated tungsten electrodes which are not wetted by condensed chromium.¹⁰ The "mysterious persistent holes" encountered under the arc are primarily due to hydrogen evolution, but can be eliminated by using an 80% helium 20% argon furnace atmosphere. Reasons for this have been partly worked out.¹⁰ Our experience also is that extrusion offers more promise for fabrication than forging, particularly when the stiffer alloys are being handled.

Authors' Reply

The authors wish to thank Mr. Roberson and Mr. Weaver for their comments and amplifying statements. The data plotted in Fig. 11 were obtained from forged specimens which were not annealed or recrystallized. The grain size in these specimens was large, about ASTM No. 1. All test specimens were obtained from forged stock to prevent any effects due to cast grain orientation or size. Although the as-received electrolytic chromium flake generally contained less than 0.02% nitrogen, the nitrogen content increased during heating and forging in all grades of material used. It was found that the nitrogen content of the forged specimens ranged from 0.03 to 0.04%. Effects of surface removal upon ductility were not considered in this investigation.

Recent work at the Armour Research Foundation has demonstrated that the ductile-brittle transition temperature of forged chromium does depend upon the type of stress system to which the specimen is subjected. Material which was grain-refined to an ASTM No. 5 size by warm working and recrystallization at 1000 °C (1830 °F) was subjected to tension, compression, and torsion tests. It was found that the ductile-brittle transition temperature in tension was 350-355 °C (660-670 °F), while the material could be deformed, in compression, to a 15% reduction in area at room temperature. In torsion, a ¼ inch diameter, 1.5 inch gage length specimen twisted 12 degrees in the plastic range before fracturing at room temperature. The nitrogen content ranged between 0.03 and 0.04%.

¹⁰ P. F. Weinrich, (to be published).

The electrolytic flake used in melting was indeed high in hydrogen. However, all melting stock was vacuum annealed at 600 °C (1110 °F) until a one-micron pressure in the vacuum cylinder could be maintained for a period of two minutes with the pumping system closed off from the vacuum cylinder. It appears unlikely that residual hydrogen would be evolved from material which was melted at 1500 amperes but would not be evolved from material which was melted at 1000 amperes. The similarity of results obtained on rheotropic recovery with those of the Defense Standards Laboratories is particularly interesting, in view of the great difference in the level of nitrogen content of the material used by us and that used by the Defense Standards Laboratories.

DEFORMATION AND FRACTURE OF ALPHA SOLID SOLUTIONS OF LITHIUM IN MAGNESIUM

BY F. E. HAUSER, P. R. LANDON AND J. E. DORN

Abstract

Whereas coarse polycrystalline aggregates of Mg are brittle at 78°K alpha solid solutions of lithium in magnesium are ductile. The improved ductility of the lithium alloys of magnesium is associated with the introduction of prismatic (1010) $\langle 2\bar{1}\bar{1}0 \rangle$ slip in addition to basal (0001) $\langle 2\bar{1}\bar{1}0 \rangle$ slip.

Evidently in the absence of prismatic slip, dislocation arrays pile up against the grain boundaries causing high localized tensile stresses that exceed the cohesive strength of the metal. But the introduction of prismatic slip permits deformation of the adjacent grains and thereby reduces the tendency toward formation of piled-up arrays of dislocations. The incidence of prismatic slip is unique for Mg-Li alloys since lithium is the only effective alloying element for reducing the axial ratio of magnesium. (ASM International Classification Q24, M26b; Mg, Li)

INTRODUCTION

TAYLOR (1)¹ demonstrated that plastic deformation cannot occur in polycrystalline aggregates unless each grain can undertake at least five independent mechanisms of deformation. This conclusion was obtained from the following type of analysis: In order to maintain the observed continuity across the boundaries of dissimilarly oriented adjacent grains throughout the course of deformation, each individual grain of the aggregate must be capable of undertaking a general deformation. Such a general deformation can be described in terms of the six components of the strain. But inasmuch as the volume remains substantially constant during plastic deformation, the sum of the three normal components of strain is zero and only five components of the strain need be independently variable. Consequently, at least five independent mechanisms of deformation must be invoked in order to account for the five independently variable strain components necessary for a general deformation.

¹ The figures appearing in parentheses pertain to the references appended to this paper.

A paper presented before the Thirty-Ninth Annual Convention of the Society, held in Chicago, November 4-8, 1957. The authors, F. E. Hauser, P. R. Landon and J. E. Dorn, are associated with the University of California, Department of Engineering, Institute of Engineering Research, Berkeley, California. Manuscript received December 21, 1956.

If each grain of the polycrystalline aggregate cannot undertake five mechanisms of deformation, slip in one grain will not be accommodated at the boundary by an appropriate combination of slip in adjacent dissimilarly oriented grains. Under these conditions arrays of dislocations will pile up against the boundary since they are unable to penetrate it. As shown by Nabarro, Eshelby and Frank (2) extremely high normal and shear stresses are introduced near the spur of a piled-up array of edge dislocations. Stroh (3) has shown that the localized normal stress arising from an array of edge dislocations can readily exceed the cohesive strength thereby initiating brittle fracturing. The brittle fracture strength (4) can be given by

$$\sigma_f = \sigma_1 + \sqrt{\alpha/d} \sigma_e \quad \text{Equation 1}$$

where

σ_f is the brittle fracture strength

σ_1 is a smeared back stress on the dislocation array due to interaction with other dislocations

σ_e is the theoretical cohesive strength

d is the mean grain diameter, and

α is a constant that depends on the average distance and orientation of the crack nucleus from the spur of the dislocation array.

Consequently if the individual grains of a polycrystalline aggregate cannot undertake at least five mechanisms of deformation, brittle fracturing should occur giving a fracture stress which increases linearly with the reciprocal of the square root of the grain diameter and is substantially independent of the temperature.

The well-known ductile behavior of polycrystalline aggregates of the face-centered cubic metals is readily rationalized in terms of the preceding discussion. Slip takes place on the (111) planes in the $\langle 1\bar{1}0 \rangle$ directions giving twelve possible mechanisms of deformation. In contrast, however, single crystals of such close-packed hexagonal metals as cadmium, zinc, and magnesium have been shown to exhibit only basal slip and twinning mechanisms of deformation at low temperatures. Since the three directions of slip of the form $\langle 2\bar{1}\bar{1}0 \rangle$ all lie in the single slip plane of the form (0001), only two independent mechanisms of slip are exhibited by these metals. Twinning occurs on the (10 $\bar{1}2$) plane and can account for six additional mechanisms. But the deformations that can be obtained by twinning are limited geometrically. For example, the maximum elongation that can be obtained upon complete twinning of a single grain of magnesium in the optimum orientation is only 7%. Inasmuch as the individual grains of a polycrystalline aggregate are more or less randomly oriented and inasmuch as each grain of the polycrystalline aggregate seldom exhibits complete

mechanical twinning, the total strain obtained as a result of twinning is considerably less than the maximum amount possible. Furthermore basal slip in the twinned portions of the grains must also be limited in view of the constraints at the twin boundaries. Consequently, twinning cannot assume the role of a major mechanism of deformation. Therefore, crystals of cadmium, zinc, and magnesium exhibit only two independent major mechanisms of deformation arising from the three coplanar mechanisms of basal slip. If at least three additional independent major mechanisms of deformation cannot be induced to take place, polycrystalline aggregates of these metals should exhibit brittle fracturing at low temperatures.

Partial confirmation of the preceding analyses has been obtained in two recent investigations: Greenwood and Quarrell (5) have shown that polycrystalline aggregates of zinc exhibit completely brittle fracturing over a wide range of low temperatures. More recently the present authors (4) have shown that polycrystalline aggregates of magnesium exhibit two uniquely different laws of fracturing. Over the high temperature range, where pyramidal as well as basal slip is believed to be operative, ductile fracturing occurs, the fracture stress being insensitive to grain size and decreasing with increasing temperature in a manner that parallels the effect of temperature on the flow stress; over the low temperature range, however, the fracture strength is insensitive to the temperature and increases with decreasing grain size in accord with the dictates for brittle fracturing given by Equation 1. Whereas σ_1 for zinc is zero and the strains at fracture are negligible, magnesium exhibits a few percent strain preceding fracturing. This results in internal stresses which give σ_1 a small value. Extensive metallographic examinations (6,7) of magnesium specimens that were deformed to fracture in the brittle range revealed that some localized grain boundary shearing had taken place at atmospheric temperatures, whereas minor amounts of prismatic slip on the $(10\bar{1}0)$ planes in the $\langle 2\bar{1}\bar{1}0 \rangle$ directions were observed locally near grain corners at the lower temperatures. It is reasonable to believe that these additional mechanisms coupled with twinning provided the necessary accommodation across grain boundaries to permit the small deformations which were observed to precede the brittle fracturing of magnesium. Two major objectives were initially outlined for this study. First it was thought possible that some alloying elements might increase the surface tension so as to cause a greater increase in the theoretical cohesive strength than in the flow strength. Such alloys would indeed be interesting because they would exhibit lower brittle to ductile transition temperatures than pure magnesium. Inasmuch as no theories are available on the effect of alpha solid solution alloying on surface tension it was recognized that an experimental survey of a host of alloys would be required to uncover interesting alloying elements for this objective.

The second objective concerned the possibility of introducing additional slip mechanisms by alpha solid solution alloying. If this could be done, the magnesium alloys exhibiting the additional facile slip mechanisms should exhibit more ductile fracturing over all temperature ranges where such mechanisms are operative. Two experimental observations suggested that this objective might be feasible. First, previous investigations (4,7) on the deformation of high purity magnesium at 78 °K have shown that in addition to basal slip, small amounts of localized prismatic slip were induced to take place in regions of high stress concentration adjacent to grain boundaries and in the vicinity of the junction of three grains. This suggested that the critical resolved shear stress for prismatic slip might be only slightly greater than that for basal slip in high purity magnesium. Secondly, the active slip planes in crystals are generally those which are most densely packed and the greatest distance apart from the next parallel plane. Consequently a reduction in the c/a ratio could well be effective in promoting more general prismatic slip, which coupled with basal slip, would furnish a greater number of independent slip mechanisms and might result in ductile behavior over all ranges of temperatures. Although Busk (8) has reviewed the effect of various alloying elements on the c/a ratio, it was considered advisable in this investigation to evaluate the plastic behavior of a large number of representative alpha solid solution alloys in order to detect the possible significance of such auxiliary factors as solid solution strengthening, Cottrell and Suzuki locking, and modifications of surface tension on the plastic deformation and fracture characteristics of magnesium alloys.

EXPERIMENTAL PROCEDURE

1. Materials and Specimen Preparation

High purity magnesium and the series of alpha solid solutions in magnesium given in Table I were selected for this investigation. The alloys used for a preliminary survey of their plastic properties, which are identified by an asterisk in Table I, were selected to have compositions in the alpha solid solution range near their solubility limit in the vicinity of room temperature.

This was done in preference to making this survey on alloys having the same atomic concentration of solute in the hope of obtaining the maximum possible effects of alpha solid solution alloying on the plastic properties. The alloying elements that were used for the preliminary survey were selected to have as wide a range of atomic radii, valencies and to induce as great changes in the c/a ratio as possible. As will be described later in the context of this report, the preliminary survey suggested that major emphasis should be placed on alpha solid solutions of lithium in magnesium. Consequently the plastic behavior of the series of lithium alloys whose composition is also reported in

Table II
Heat Treatments and Resulting
Grain Sizes of the Alloys

Atomic Percent	Temperature (°C)		Time (hours)	Average Grain Diameter (mm)
	°C	°F		
100.0 Mg	300	572	14	0.04
	300	572	14	0.04
2.6 Li	then 360	680	4	
	300	572	14	0.06
4.4 Li	then 360	680	4	(some duplex)
	300	572	14	0.06
7.6 Li	then 360	680	4	(some duplex)
	300	572	14	0.04
10.4 Li	then 330	626	4	
14.5 Li	300	572	14	0.05
0.29 Sn	370	698	3	0.15
12.7 Cd	300	572	6	0.10
0.17 Hg	370	698	3	0.13
0.33 Ag	370	698	3	0.09
4.83 Ti	370	698	3	0.09
10.6 In	370	698	3	0.15
0.20 Bi	370	698	3	0.03
1.8 Al	300	572	6	0.07

Table I were rather thoroughly studied. Parallel gage section tension specimens 0.250 inch wide and 0.10 inch thick, having a gage length of 3.75 inch were machined from the extruded strip. The surface of each specimen was hand polished through #600 grit paper to remove die markings and scratches. After polishing, the specimens were annealed in a specially built purified He atmosphere furnace to remove all cold work introduced by the machining operations and to develop a fairly uniform grain size throughout the alloy series.

The heat treatments necessary to produce the desired grain sizes are given in Table II.

The dual temperature treatments used on some of the alloys were necessary to avoid the formation of excessively duplexed grain sizes. Nevertheless a few large grains were present in the 4.4 and 7.6 atomic percent lithium alloy specimens.

In order to facilitate the identification of deformation mechanisms several coarse grained specimens of the Li alloys were prepared by the additional technique of annealing at 570 °C (1060 °F) for 3 hours. This yielded a grain size of approximately 0.5 millimeter which permitted orientation determination of individual grains by means of microbeam Laue x-ray examination.

All specimens were finished to a metallographic polish by dipping into 10% nitric acid following which they were etched with 10% citric acid to make the grain boundaries visible.

2. Tension Tests

The stress strain curves were autographically recorded, using a modified Foxboro SR-4 strain recorder in conjunction with a constant strain rate tensile testing machine. Strain gages on a calibrated proving

ring provided the load data as pen deflection on the recorder, while a rack and pinion driving a selsyn transmitter provided the crosshead movement data to a selsyn repeater geared to the strain recorder chart drive. The elastic strain of the pulling tab system was determined as a function of load by means of a calibration test using SR-4 strain gages attached to a dummy specimen. During actual tests the recorded crosshead movement was corrected for the elastic strain of the system to give the actual strain of the specimen. With a single exception, all tests were conducted at a constant strain rate of 1% per minute. The above method of determining the stress-strain relationship permitted an accuracy of ± 50 psi in stress and $\pm 0.01\%$ in strain over the entire range of temperatures tested.

During the tensile tests the whole specimen was submerged in a constant temperature bath. Constancy of temperature throughout the tests was assured by using boiling or freezing point temperatures wherever possible. The four primary test temperatures were:

- 4.2 °K boiling liquid helium
- 78 °K boiling liquid N₂
- 195 °K vaporizing solid CO₂ in isopentane
- 295 °K air

Several tests were performed at additional temperatures by using a cooled isopentane bath or a heated silicon oil bath. Upon completion of the tensile tests the specimens were brought to room temperature by immersion in alcohol.

3. Metallographic Examination

The fractured specimens and specimens which had been elongated to 2% were examined on the metallograph for identification of deformation and fracture mechanisms. The specially prepared coarse-grained specimens were examined microscopically before deformation and the orientations of certain grains were determined by a micro-beam Laue x-ray technique (6). After deformation, the active deformation mechanisms could be determined by trace analysis (6).

4. Determination of Lattice Parameters

The effect of temperature and alloying with lithium on the lattice constants of magnesium were measured to correlate changes in deformation mechanisms with changes in c/a ratio. Since the high lithium alloys oxidize rapidly when finely powdered, sheet samples of these alloys were prepared in the same manner as the tensile specimens and then mounted in a General Electric XRD-3 x-ray diffraction unit. For each sample the 2θ values for the (11 $\bar{2}$ 0) and (0004) planes were measured to an accuracy of 0.01°. Since no corrections were applied, the absolute values of the lattice constants obtained may not be precise;

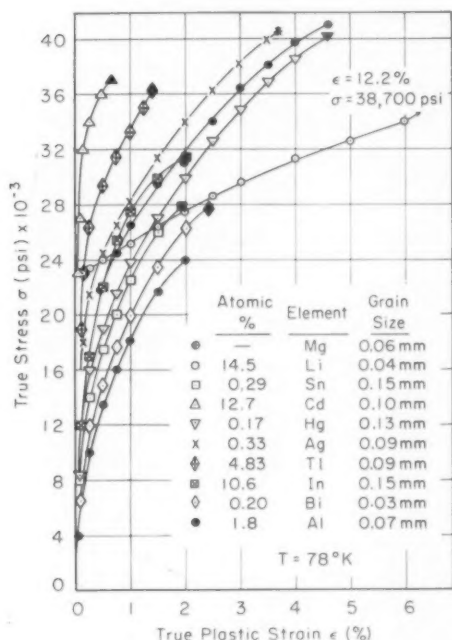


Fig. 1—Stress-Strain Curves of Solid Solutions in Mg at 78°K.

but comparative accuracy of constants among the samples is known to be better than 0.01%. The low temperature constants were determined by submerging most of each sample in liquid N₂ and grazing the x-ray beam over the surface of the bath. The beam struck the specimen at a point where the sample just protruded above the liquid, but where the temperature was very close to 78°K because all the vaporizing N₂ throughout the system was channeled along this surface of the sample. Also the formation of ice due to condensation of moisture was prevented by channeling the N₂ along the surface that was examined.

EXPERIMENTAL RESULTS

1. Survey of the Effect of Alpha Solid Solution Alloying on the Plastic Properties of Mg

The true stress-logarithmic strain curves given in Fig. 1 were obtained to permit a preliminary survey of the effect of alpha solid solution alloying on the plastic properties and fracturing characteristics of magnesium alloys. Since the percent strain preceding brittle frac-

turing of pure magnesium and Mg-Al alloys was previously shown to decrease with decreasing temperatures (4), at least down to the boiling temperature of liquid nitrogen, 78 °K was selected as the most readily accessible temperature that would be best suited for this survey.

All of the alloys, excepting the anomolous lithium alloy, fractured after a few percent strain in an essentially brittle manner. The greatest solid solution strengthenings were obtained in the cadmium and thallium alloys, and the highest fracture strengths and ductilities, again excepting the lithium solid solution alloys, were obtained in the mercury, aluminum, and silver alloys. The higher strains to brittle fracturing of the mercury, aluminum, and silver alloys and their relatively higher brittle fracture strengths suggest that alloying with these elements increases the theoretical cohesive strength of magnesium more rapidly than its flow strength. Very likely all of these alloys have a lower brittle to ductile transition temperature than pure magnesium. This expectation has been verified for the aluminum alloy as reported in a previous publication (4). Additional verification of this expectation for the mercury and silver alloys was postponed in favor of immediate pursuit of the more startling results obtained on the lithium alloy.

Whereas the remaining alloys of this survey exhibited the usual minor variations in plastic properties and fracturing that might be expected to result from solid solution alloying, the lithium alloy, in sharp contrast, behaved in such a uniquely different way that it appeared to be a member of an entirely different system. The stress-strain curve followed the general parabolic behavior of the other alloys up to a strain of slightly less than 0.2%, whereupon it changed rather abruptly into an almost linear curve which exhibited small rates of strain hardening. Ductile fracturing occurred following a minor amount of local necking at a stress of 38,700 psi and a strain of 12.2%. These results immediately suggested that some additional mechanism, perhaps prismatic slip, must also play a prominent role in the deformation of the lithium alpha solid solutions of magnesium. The following sections of this report are devoted to a partial resolution of several of the numerous facets concerning the unique effects of alpha solid solution alloying with lithium on the plastic behavior of magnesium.

2. The Plastic Properties of Alpha Solid Solutions of Lithium in Magnesium

Before any detailed examination of crystallographic mechanisms of deformation was attempted in the lithium alpha solid solutions, it was considered advisable to study their plastic properties over a series of temperatures.

The results of tensile tests at 295, 195, 78 and 4 °K and a strain rate of 1% per minute are shown as true stress versus true strain curves in Figs. 2 through 5. All stress-strain curves were smooth

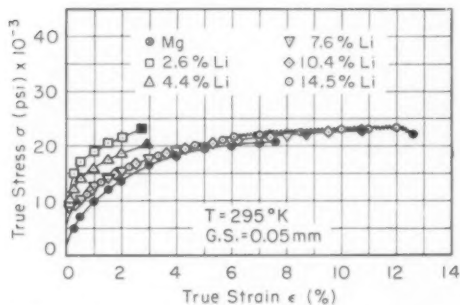


Fig. 2—Stress-Strain Relationship of Mg-Li Alloys at 295 °K.

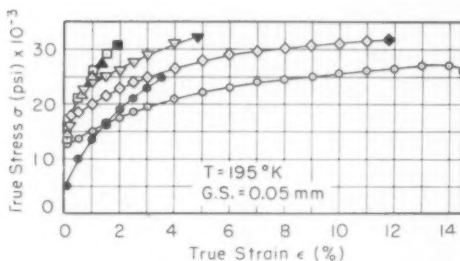


Fig. 3—Stress-Strain Relationship of Mg-Li Alloys at 195 °K.

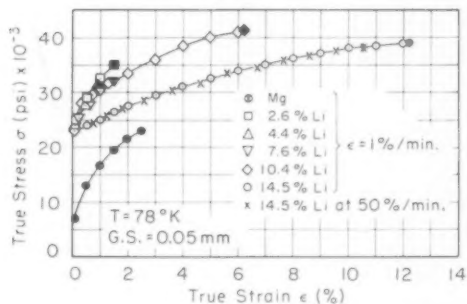


Fig. 4—Stress-Strain Relationship of Mg-Li Alloys at 78 °K.

excepting those for the 14.5 atomic percent lithium alloy at 295 °K and for all the alloys tested at 4 °K. During these tests, discontinuous jumps of strain accompanied by drops in stress were noted on the recorder. The serrations in the stress-strain curves of Figs. 2 and 5 are plotted schematically to illustrate the ranges of conditions where discontinuous deformation occurred during testing. In Fig. 4 an addi-

tional curve for 14.5 atomic percent lithium at 78 °K, performed at the higher strain rate of 50% per minute has been included for comparison. At that temperature, the strain rate seems to have little effect on the plastic properties of this alloy.

From the stress-strain curves it can be seen that the effect of adding small amounts of lithium to magnesium gives the usually observed increase in yield strength and rate of strain hardening that is known to accompany solid solution alloying. But as more lithium is added, a "knee" appears in the stress-strain curve separating the initial parabolic

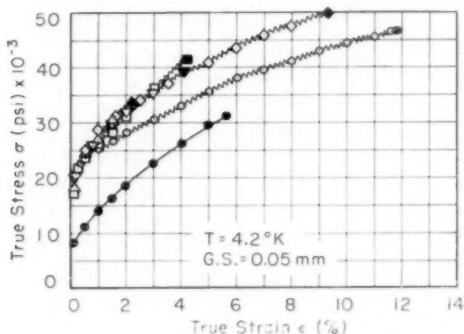


Fig. 5—Stress-Strain Relationship of Mg-Li Alloys at 4.2 °K.

portion from the more linear portion that exhibits a comparatively low rate of strain hardening. The stress level at which this knee appears decreases with increasing lithium content. For example in Fig. 3 at 195 °K the addition of 2.6 and 4.4 atomic percent lithium raises the yield strength and strain hardening rate in a manner usually expected in solid solutions. But when the lithium content is increased to 7.6 atomic percent, a sudden decrease in strain hardening rate occurs at about 22,000 psi. With further increases in lithium content, the change in slope of the stress-strain curve occurs at lower stresses. For the 14.5 atomic percent lithium alloy the lowering of the strain hardening rate occurs at so low a stress that the stress-strain curve of this alloy crosses the curve for pure magnesium. Although the final fracture stresses for these two materials are nearly the same, the elongation of the 14.5 atomic percent lithium is four times that for pure magnesium. Thus the Li-Mg alloys appear to provide an exception to one of the fundamental rules of alloying, namely, that solid solutions are invariably stronger than the pure parent metal. The existence of this apparent exception will be resolved later in this report.

In the introduction of this report it was shown that the limited ductility of polycrystalline magnesium could be ascribed to a deficiency in

the number of major deformation mechanisms that are available in magnesium at low temperatures. The sudden abnormal change in strain hardening rate and the associated increase in ductility in the lithium alloys indicated that additional deformation mechanisms must have been introduced by the alloying additions of lithium.

3. Metallographic Observations

A metallographic investigation into the active deformation mechanisms revealed that in all cases the sudden decrease in strain hardening rate of the lithium alloys at the knee in the stress-strain curve coincided with the appearance of general prismatic slip throughout some grains. Before the knee, at which a rather sharp change in the slope of the stress-strain curve is observed, prismatic slip was only observed locally at corners of grains and near grain boundaries as in pure magnesium at low temperatures (Fig. 6). In contrast the general prismatic slip traces after straining beyond the knee extended across an entire grain, and at high strains they formed a complete criss-cross pattern of slip traces similar to a deformed face-centered cubic metal under conditions of duplex slip (Fig. 7). Initially the appearance of the prismatic slip is fine and feathery and difficult to observe unless a small amount of corrosion helps to make the slip lines stand out as in Fig. 8. After large amounts of slip the identification of each active slip system becomes difficult because of the distortion of the surface. But in all cases where some straight traces were present and a trace analysis could be performed in conjunction with a microbeam Laue x-ray orientation determination, the active slip planes were found to be the basal $\{0001\}$ and prismatic $\{10\bar{1}0\}$ planes. The wavyness of the slip traces at large strains is probably due to cross slip from prismatic to basal planes (7). These traces are similar in appearance to slip traces in body-centered cubic metals where generally many slip systems are operative simultaneously.

The metallographic observations suggest that the lowering of the rate of strain hardening and the resulting knee in the stress-strain curve occurs when the stress reaches a transition value at which the deformation changes from primarily basal slip to prismatic slip plus basal slip.

The existence of such a transition stress can be rationalized in terms of the high rates of strain hardening in the initial portion of the stress-strain curve where basal slip predominates and the low rates of strain hardening that are observed after prismatic slip becomes active.

An investigation on a small cylindrical single crystal of 14.5% lithium alloy showed that the $\langle 11\bar{2}0 \rangle$ slip direction is active in both basal and prismatic slip. This fact is also confirmed by observations of cross slip in many grains.

The six mechanisms of slip on the $\{0001\}$ and the $\{10\bar{1}0\}$ planes in



Fig. 6—Primary Basal (0001) Slip with Local Secondary Prismatic (1010) Slip in Corner of Mg Grain at 78 °K. $\epsilon = 1\%$. ($\times 250$)

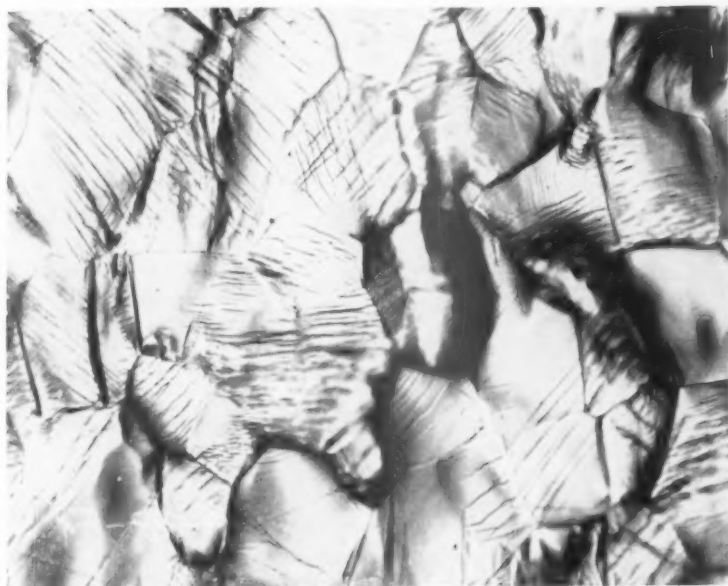


Fig. 7—Multiple Slip Traces in 14.5 Atomic % Li-Mg Alloy at 78 °K. $\epsilon = 12\%$. ($\times 500$)



Fig. 8—Slip Traces in 14.5 Atomic % Li-Mg Alloy at 195 °K. $\epsilon = 2\%$. ($\times 500$)

the $\langle 2\bar{1}\bar{1}0 \rangle$ directions lead to only four components rather than the required five components of strain that are necessary for a general deformation. This fact is most easily revealed by noting that the $\langle 2\bar{1}\bar{1}0 \rangle$ directions can never result in an elongation in the direction of the c axis of the crystal. Perhaps the incidence of twinning is helpful in permitting strains up to 12.2% in the 14.5 atomic percent lithium alloy. Obviously yet higher strains to fracture could be obtained if deformation could be induced to take place by some additional mechanism having any slip direction $[uvtw]$ where w is not zero.

Furthermore these same arguments suggest that brittle behavior should be obtained for conditions where close-packed hexagonal metals exhibit pure prismatic slip. Consequently, the good ductility obtained in the 14.5 atomic percent lithium alloys of magnesium at low temperatures is undoubtedly ascribable to the simultaneous action of both prismatic and basal slip.

The number of twins observed in the specimens after unloading or at fracture seemed to be independent of the lithium content but dependent on the maximum stress to which the specimen was subjected. Thus when comparing specimens at the same strain, the high lithium alloys seem to have fewer twins than the low lithium alloys because of the higher flow stress of the low lithium alloys at a given strain. Comparison of specimens pulled to approximately the same flow stress showed that the appearance and number of twins are apparently independent of lithium content. Therefore, contrary to popular opinion, the availability of additional deformation mechanisms does not seem to influence the occurrence of twinning in magnesium.

4. Yield and Transition Stresses

In Fig. 9 is shown a plot of σ_{TS} , the stress level at the knee of the stress-strain curve where prismatic slip first becomes prevalent, as a function of the atomic percent lithium in magnesium for four temperatures. The points with question marks are somewhat unreliable as the knees in the stress strain curves at these points were not well defined. At all temperatures below 295 °K an increase in lithium content lowered the stress for onset of general prismatic slip in an almost linear manner. At room temperature a low value of transition stress seemed to have been reached at about 8 atomic percent lithium and no further change was observed on increasing the lithium content.

The yield strength for 0.01% ϵ offset is roughly tripled by a small addition of lithium; but with further increases in lithium content the yield strength remained practically unchanged. In normal solid solution hardening the yield strength would have increased almost linearly with alloy content. To explain the insensitivity of the yield strength in magnesium to large lithium additions, one must consider that lithium not only solution hardens magnesium but also reduces the shear stress

necessary for local prismatic slip. This easier relief of local stress concentrations by prismatic slip seems to counteract the increased shear stress for basal slip due to solid solution hardening. Therefore, the yield strength of polycrystalline magnesium seems to be determined not only by the critical shear stress of the primary basal slip mechanisms, but also by the critical stress of the secondary prismatic mechanism.

The effect of lithium content on the ductility and fracture strength of magnesium is shown in Fig. 10. The 2.6% lithium alloy shows a marked decrease in ductility over pure magnesium and this trend continues to 4.4% lithium where the strain at fracture reaches a minimum value. Further additions of lithium increase the ductility again coincident with the onset of major amounts of prismatic slip. For the

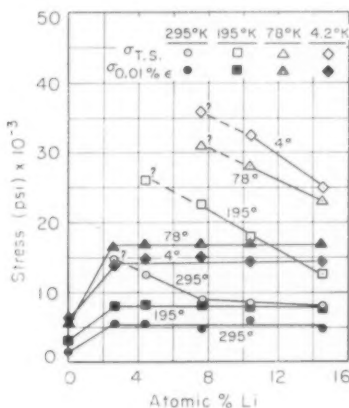


Fig. 9— $\sigma_{T.S.}$, The Stress Where Transition from Basal to Prismatic Slip Occurs, and $\sigma_{0.01\% \epsilon}$ the Flow Stress at $\epsilon = 0.01\%$ Versus % Lithium in Magnesium.

high lithium alloys where prismatic slip is active at all temperatures, the ductility is almost independent of temperature. It is interesting to note that the ductility at 4 °K for the pure magnesium and low lithium alloys is higher than that at 78 °K and at 195 °K. Metallographic examinations on pure magnesium show a greater amount of localized prismatic slip at this low temperature than at the higher temperature tested. It can also be seen from Fig. 5 that the initial strain hardening rate of magnesium is lower at 4 °K than at 78 °K and about equal to that at 195 °K, while the "prismatic slip strain hardening rate" at 4 °K is higher than at any other temperature.

Most of the 14.5 atomic percent lithium alloy specimens exhibited a sharp drop in load before fracturing, indicating the onset of necking in this alloy at all temperatures.

The drop in fracture strength in the 4 to 8% lithium range shown in Fig. 10 is probably due to the presence of duplexed grain sizes in these specimens. While the few large grains should not alter the shape of the stress-strain curve appreciably, the low brittle fracture strength of large grains (4) probably terminates the tensile tests prematurely. Several fracture stress values of tests performed on fine grained (0.025 mm) 4.4 and 7.6% lithium specimens are included in Fig. 10 to illustrate the possible significance of this point.

5. Effect of Grain Size

In Fig. 11 a comparison is shown of the effect of grain size on the flow and fracture stress of pure magnesium and a 14.5 atomic percent

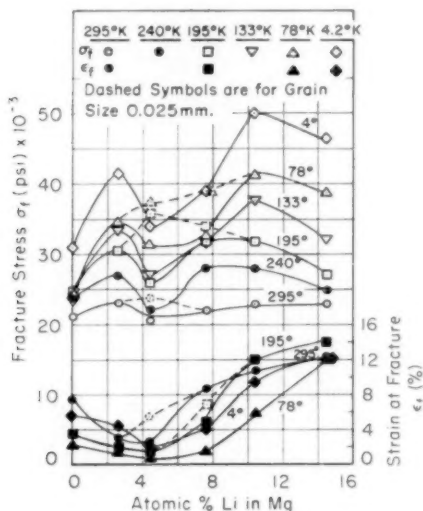


Fig. 10—Fracture Strength and Elongation Versus Atomic % Lithium in Magnesium. Grain size 0.05mm.

lithium alloy. The pure magnesium exhibits an independence of the brittle fracture stress on temperature. This behavior is also typical for the fracturing of such metals as zinc, iron and molybdenum. The only point that deviates significantly from the fracture stress line of the graph is that from a fine grain specimen at 295°K which failed in a ductile manner. In contrast the 14.5 atomic percent lithium alloy shows that the fracture strength and flow stress depend on grain size in a similar way. This behavior is typical of ductile fracturing. Therefore, the hexagonal close packed magnesium which exhibits brittle behavior at low temperatures has been changed into an apparently ductile mate-

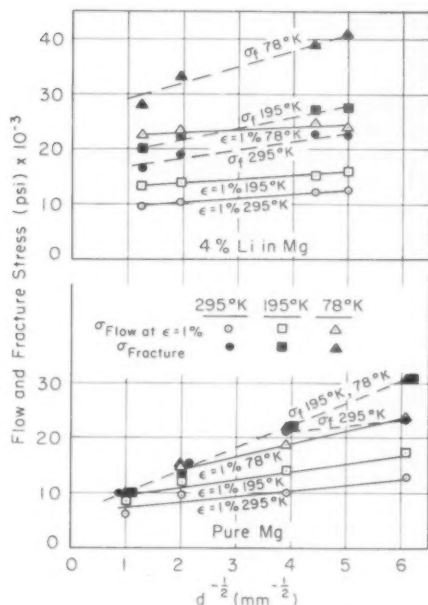


Fig. 11—Effect of Grain Size on Flow and Fracture Strength of 14.5% Lithium and Pure Magnesium.

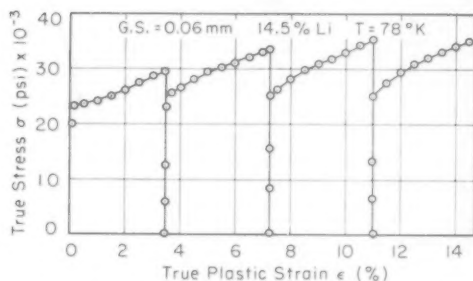


Fig. 12—Stress-Strain Curve of 14.5% Lithium Specimen at 78°K Periodically Unloaded and Recovered for 8 Minutes at 300°C. (No recrystallization.)

rial through alloying with lithium as a result of introduction of the additional prismatic slip mechanisms.

6. Recovery of Lithium Alloys

The strain hardening that takes place in the 14.5 atomic percent lithium alloy at 78°K is almost completely recoverable during a short anneal at elevated temperature. Fig. 12 shows the effect on the stress-

strain curve of such an alloy when it is recovered periodically for 8 minutes at 300 °C (570 °F). No recrystallization was visible metallographically after these recovery treatments. After the initial recovery following a 3.5% strain, the yield strength is raised about 3000 psi, but it then remains constant during subsequent cycles of stressing and recovery. The rate of strain hardening, however, is increased slightly in each consecutive cycle so that the stress-strain curves do not superimpose. While recovery in single crystals can eliminate the effects of cold work, in polycrystalline material usually very little softening oc-

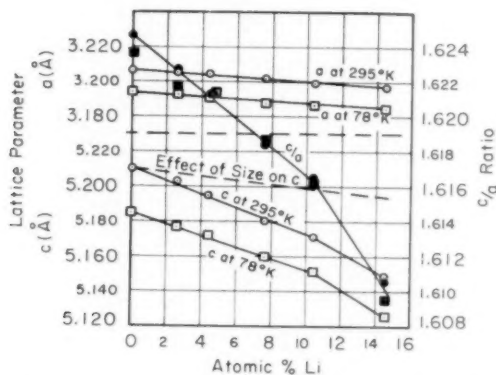


Fig. 13—Effect of Lithium on Lattice Parameters and c/a Ratio in Magnesium.

curs until the metal has recrystallized. The strain hardening which accompanies prismatic slip in the polycrystalline Li-Mg alloy, however, seems to be almost completely recoverable. This phenomenon is discussed further in a later section of this report.

7. Effect of Lithium on the Lattice Parameters of Magnesium

The change in lattice constants as a function of lithium content and temperature was studied in hope that it might reveal why lithium dissolved in solid magnesium introduces prismatic slip. From Fig. 13 it can be seen that the "a" lattice parameter decreases linearly with increase in lithium content. The decrease in "a" is exactly what one would expect from the difference in atomic radii between magnesium and the somewhat smaller lithium atom. The calculated effect of atomic radii on "c" is shown as a dashed line in Fig. 13 and if the "c" parameter followed this line the c/a ratio would have remained constant. The actual "c" value drops off much more steeply with lithium content and thus causes the c/a ratio to decrease with increase in lithium content. A temperature change from 295 to 78 °K seems to have little effect on the c/a ratio.

DISCUSSION

The most interesting facet of this investigation centers about the transition from brittle to ductile low temperature fracturing of polycrystalline magnesium upon alpha solid solution alloying with appropriate amounts of lithium. This transition is easily rationalized in terms of the introduction of facile prismatic as well as basal slip upon alloying magnesium with lithium. As shown by Taylor at least five independent mechanisms of slip are required for a general deformation which is necessary in order to provide for continuity at the boundaries of adjacent dissimilarly oriented grains. Pure magnesium exhibits primarily basal slip and twinning with minor amounts of grain boundary shearing and very localized prismatic slip. Twinning cannot account for such deformation since its action is limited geometrically. And the small amounts of grain boundary shearing and localized prismatic slip that occur during low temperature deformation of high purity polycrystalline magnesium suggest that extremely high shear stresses are required to initiate these deformation mechanisms. Furthermore, the three mechanisms of facile basal slip are coplanar and therefore provide only two independent deformation mechanisms. Under these conditions dislocations will pile up at the grain boundaries inasmuch as the adjacent dissimilarly oriented grains cannot deform in a sufficiently general manner to permit accommodation of the slip steps at the boundary. Localized tensile stresses at the spurs of such pile-up arrays of dislocations can easily exceed the theoretical cohesive strength of the metal, causing brittle fracturing.

Upon alpha solid solution alloying of magnesium with lithium, prismatic slip becomes more facile and at higher lithium contents, both prismatic $\{10\bar{1}0\} \langle 2\bar{1}\bar{1}0 \rangle$ and basal $\{0001\} \langle 2\bar{1}\bar{1}0 \rangle$ slip occur simultaneously. The two types of slip lead to four of the five independent mechanisms of slip necessary for completely general accommodation of deformation at the grain boundaries. Undoubtedly some additional accommodation of deformation at the grain boundaries is facilitated by twinning leading to ductile fracturing of the higher lithium content magnesium alloys.

Although the transition from brittle to ductile low temperature fracturing of magnesium upon solid solution alloying with lithium can be ascribed to the introduction of facile prismatic as well as basal slip, it is much more difficult to ascertain why lithium additions decrease the resistance to prismatic slip. Dislocations can move only under stresses that are sufficiently high to overcome the most difficult of the sequence of processes they must undertake during their motion. It is not known a priori for prismatic slip whether the most difficult process is (a) the activation of a Frank-Read source, (b) the motion of the dislocation or (c) the processes involved in the intersection of dislocations with

other dislocations threading the prismatic plane. A satisfactorily complete analysis of each possibility will not be attempted here. Nevertheless it will prove interesting to attempt a brief qualitative discussion of the potentialities of each process as the controlling mechanism for prismatic slip.

Extremely high energies are required to initiate slip at a Frank-Read source. The energies involved are so great that only rarely could a thermal fluctuation assist the applied stress in exciting a Frank-Read source. Consequently, this process should be athermal, giving a flow stress that is practically independent of the temperature. But the experimental results given in this report reveal that the flow stress for prismatic slip increases rather rapidly with decreasing temperature in a manner suggestive of a thermally activated process. For this reason the controlling mechanism for prismatic slip is not believed to be the initiation of slip at a Frank-Read source. Undoubtedly, as simple calculations will reveal, Frank-Read sources of appropriate length on prismatic planes will be easily activated under the applied stresses used in this investigation.

The jog energies resulting from intersection of a moving dislocation on the prismatic plane with a dislocation on the basal plane are the same as the jog energies resulting from the intersection of a moving dislocation on the basal plane with a dislocation on the prismatic plane. Consequently the absence of facile prismatic slip in high purity magnesium is not believed to be due to higher intersection energies for dislocations moving on the prismatic planes.

These arguments suggest that the limited prismatic slip in high purity magnesium might arise from a higher Peierls' force necessary to move a dislocation in the prismatic as contrasted to the basal plane. Unfortunately, the current theories for estimating the Peierls' force for slip have been made only on a simple tetragonal lattice and have neglected the possible effects of thermal fluctuations. Cottrell suggests that the stress necessary to move a dislocation through a simple tetragonal lattice at the absolute zero is given by

$$\sigma = 2G/(1 - \nu)e^{-2\pi ad/b(1-\nu)} \quad \text{Equation 2}$$

where G = shear modulus of elasticity

ν = Poisson's ratio

d = interplanar spacing

b = Burger's vector

For both basal and prismatic slip in magnesium the Burger's vectors were observed to be in the theoretically expected $\langle 2\bar{1}10 \rangle$ closest packed directions. Consequently, both basal and prismatic Burger's vectors are equal to the "a" lattice parameter. Whereas the basal plane dislocations can split into partials, simple geometric considerations

reveal that the prismatic plane dislocations must remain complete. Obviously screw components of dislocations on the prismatic planes could readily decompose into a pair of lower energy partials on the basal plane. This might in part account for the extensive prismatic-basal-cross-slip observed in this investigation.

Since the same Burger's vector, $b = a$, applies to both basal and prismatic slip, only G , ν and d control the active slip mechanism. If the possible roles of G and ν are relegated to a minor position, the operative slip mechanism should depend primarily on the interplanar spacing d . Obviously this factor is most significant because it appears in the exponential term of Equation 2. For the basal planes, d is equal to $c/2$, whereas for prismatic planes d equals $\sqrt{3}/2 a$. Consequently, neglecting other factors, basal slip should predominate when $c/a > 1.73$ whereas prismatic slip should predominate at $c/a < 1.73$. Actually prismatic slip does not become marked in Mg-Li alloy excepting for $c/a < 1.618$. Undoubtedly this discrepancy between theory and fact will be resolved by a more accurate calculation of the Peierls' force for the close-packed hexagonal system.

In spite of its quantitative inaccuracies, Equation 2 is yet believed to give correct qualitative trends. Thus a reduction in the c/a axial ratio for the close packed hexagonal systems should promote a transition from basal to prismatic slip. This general trend is verified by the experimental data from various sources assembled in Table III.

These data show that the axial ratio for pure magnesium is just slightly above that necessary to induce initiation of prismatic slip. Con-

Table III
Correlation of Slip Mechanisms with Axial Ratios

Metal	c/a	Active Slip Mechanisms at Room Temperature
Cd	1.89	(0001)
Zn	1.86	(0001)
Mg	1.624	(0001)
Mg + 14 at % Li	1.610	(0001) and (1010)
Ti	1.59	(0001) and (1010)
Zr	1.59	(0001) and (1010)
Be	1.57	(1010) and (0001)

sequently the conclusion appears justified that prismatic slip is introduced when magnesium is alloyed with sufficient amounts of lithium, because lithium reduces the c/a ratio.

Busk (8) found in an extensive survey that most solid solution alloying elements increased the axial ratio of magnesium. The few alloying elements that decreased the c/a ratio were lithium, silver, gold, cerium, and palladium. With the exception of lithium, however, these elements have such limited solubility that only minor decreases in c/a can be effected by them. Consequently, lithium assumes a rather unique posi-

tion among the alloying elements for magnesium because it alone appears to provide sufficient reduction in the c/a ratio to permit extensive prismatic slip.

The final question now concerns why lithium additions to magnesium cause a reduction in the c/a ratio. Hauser (9) has demonstrated that Brillouin zone theory suggests that lithium additions to magnesium should cause the c/a ratio to increase. Consequently the reasons for the reduction in c/a ratio of magnesium with lithium additions must be based on further advances in the theory of metallic bonding.

The discontinuous stress-strain curve at 295 °K for the 14.5% Li-Mg alloy is probably due to a strain aging phenomenon. Cottrell's widely accepted theory (10) assumes that strain aging is due to the pinning of dislocations by impurity atoms. The applied stress tears the dislocations free from their anchoring atmosphere, causing a yielding of the specimen. If the temperature and strain rate are appropriate, the impurities will diffuse at just the right rate to reanchor other dislocations causing a series of jerks in the stress-strain curve.

While strain aging can be visualized to occur at 295 °K, the diffusivity at 4 °K would be too low to permit strain aging. Many other metals show a discontinuous stress strain curve at 4 °K (11) and so the phenomenon seems to be associated with extremely low temperature and not with any particular alloy. While some observers have noted discontinuities in "pure" metals at low temperatures, the pure magnesium in the present investigation showed an almost smooth stress-strain curve while successively higher lithium contents caused systematic increases in the magnitude of the discontinuities. In each specimen the magnitude of the strain jumps and drops in stress increased as the stress increased. Near the maximum stress the strain per jump of the high lithium specimens was of the order of 0.2%. This large elongation would rule out the possibility of twins causing the discontinuities as has been suggested by Wessel (11). In addition, no unusual twins were observed metallographically after testing at 4 °K in the present investigation.

The thermal instability or thermal spike theory proposed by Zener and Hollomon (12) has also been presented to explain the low temperature jumps in the stress-strain curve. This theory assumes that during localized slip a large surrounding volume is heated up because of the low specific heat of metals at very low temperatures. The volume of heated metal would have a lower flow stress and deform. The resulting elongation of the specimen releases some of the elastic energy stored in the system and lowers the applied stress. This lowering of stress stops further deformation until the constant cross-head movement of the tensile machine builds up the stress to a level slightly higher than the previous strain hardened state and a new jump in strain occurs.

However, it is difficult to rationalize the smooth stress-strain curve

that was obtained on pure magnesium at 4°K, on the basis of this theory and simple calculations reveal that the increase in temperature is insufficient to be effective in causing the observed discontinuous yielding. It appears more probable that the 4°K discontinuous yielding arises from unleashing avalanches of dislocations through the action of the stress alone. Undoubtedly additional investigations will be required to completely rationalize the existence of serrated stress-strain curves at 4°K.

Many observers have shown that the rate of strain hardening of single crystals of magnesium deformed in simple shear is very low. The limited number of deformation mechanisms and the resulting inability to accommodate slip in adjacent grains seem to be the cause for the high strain hardening rate in polycrystalline magnesium. Thus it is not surprising that the addition of more slip mechanisms decreases the rate of strain hardening of the aggregate. The rate of strain hardening on prismatic slip planes could also be lower than that on basal planes, decreasing the total strain hardening rate observed still further. The fact that a large amount of cold working in the 14.5% lithium alloy can be removed by recovery (Fig. 12) indicates that the work hardening on prismatic slip planes differs from the usual work hardening in polycrystalline metals.

Multiple or turbulent slip, is usually associated with unrecoverable work hardening. During prismatic slip in hexagonal metals the Burgers vectors of two intersecting prismatic slip dislocations add up to form a dislocation with the Burgers vector in the third prismatic plane. Thus intersecting prismatic slip should not show the usual high rates of work hardening associated with turbulent slip. The ease with which the prismatic work hardening in the lithium alloys is recoverable seems to indicate that only a small amount of "entangling" takes place during prismatic slip. The unrecoverable portion of work hardening in Fig. 12 is probably due to intersections of basal and prismatic slip which would be true turbulent slip.

In a previous investigation, it was demonstrated that coarse-grained high purity magnesium fractured in a brittle manner over the temperature range from just below atmospheric temperature to 78°K. In the present investigation the same coarse-grained pure magnesium exhibited a ductile fracture following 5.7% elongation at 4°K. Metallographic examination reveals extensive prismatic slip as well as basal slip at 4°K whereas from 78°K to just below atmospheric temperatures slip occurred almost exclusively by means of the basal mechanism. Consequently the transition from brittle to ductile fracturing of polycrystalline magnesium upon lowering the test temperature from 78 to 4°K can be ascribed to the introduction of prismatic in addition to basal slip. The reason for the introduction of prismatic slip in this instance, however, is not known.

It is significant, however, to note that the ductile fracturing at 4 °K occurred at a stress of 32,000 psi which was well above the constant brittle fracture stress of 22,000 that applied over the range from 298 to 78 °K. The brittle fracturing of magnesium was completely rationalized in a previous report in terms of Stroh's analysis for the stresses at the spur of dislocation arrays piled up against the grain boundary, brittle fracturing being assumed to occur at the constant applied stress which promotes a localized stress at the spur of the dislocation array just in excess of the theoretical cohesive strength of the metal. It is therefore reasonable to believe that when the applied stress at 4 °K reaches the brittle fracture stress, local cohesive fracturing will occur because dislocation arrays similar to those which led to brittle fracturing at 78 °K will have been produced. Evidently such cracks do not grow catastrophically because of the high energy absorption due to the operation of prismatic as well as basal slip during the spreading of the crack. Under these conditions cracks introduced as a result of cohesive rupturing will grow slowly with additional straining until the Griffith-Orowan condition for fracturing is reached, whereupon catastrophic separation of the specimen will take place. The observation that the cracks in the near vicinity of the major fracture were not more than one or two grains in diameter following brittle fracturing at 78 °K, whereas the cracks were 8 to 10 grains long following ductile fracturing at 4 °K, lend partial support to this hypothesis. In general, however, the above observations suggest that Stroh's analysis for brittle fracturing is directly applicable only to those cases where the crack can propagate without excessive absorption of plastic strain energy.

CONCLUSIONS

1. When magnesium is alloyed with mercury, aluminum and silver, the transition temperature for ductile to brittle fracturing is decreased.
2. Solid solution additions of lithium increase the low temperature ductility of magnesium.
3. Large amounts of lithium in magnesium solid solutions decrease the rate of strain hardening in the alloy to such an extent that the higher lithium content alloys have lower stress strain curves than pure magnesium.
4. While pure magnesium fails in a brittle manner between 78 and 298 °K with fracture strengths that are independent of temperature, the high lithium content magnesium alloys fail in a ductile manner at all temperatures, exhibiting localized necking and a marked influence of temperature on the fracture strength.
5. The increase of ductility and decrease of strain hardening rate in the Li-Mg alloys seems to be associated with the introduction of prismatic slip $\{10\bar{1}0\} <11\bar{2}0>$ in addition to basal $\{0001\} <11\bar{2}0>$ slip.
6. The addition of lithium to magnesium decreases the c/a ratio in

the hexagonal lattice and this decrease in ratio seems to be associated with the introduction of the prismatic slip system.

ACKNOWLEDGMENT

The authors are indebted to the Office of Ordnance Research for their support of these investigations. They also wish to thank the Dow Chemical Company for their assistance in supplying the high purity alloys used in this investigation, and their personal thanks are extended to Mrs. G. Pelatowski for the preparation of the figures.

References

1. G. I. Taylor, "Plastic Strain in Metals," *Journal, Institute of Metals*, Vol. 62, 1938, p. 307-324.
2. J. D. Eshelby, F. C. Frank and F. R. N. Nabarro, "The Equilibrium of Linear Arrays of Dislocations," *Philosophical Magazine*, Vol. 42, 1951, p. 351.
3. A. N. Stroh, "The Formation of Cracks as a Result of Plastic Flow," *Proceedings, Royal Society, London*, Vol. 223, 1954, p. 404.
4. F. E. Hauser, P. R. Landon and J. E. Dorn, "Fracture of Magnesium Alloys at Low Temperatures," *Transactions, American Institute of Mining and Metallurgical Engineers*, Vol. 206, 1956, p. 589.
5. G. W. Greenwood and A. G. Quarrel, "The Cleavage of Pure Polycrystalline Zinc in Tension," *Journal of Metals*, Vol. 82, 1953-54, p. 551.
6. F. E. Hauser, L. D. Starr, L. S. Tietz and J. E. Dorn, "Deformation Mechanisms in Polycrystalline Aggregates of Magnesium," *TRANSACTIONS, American Society for Metals*, Vol. 47, 1955, p. 102.
7. F. E. Hauser, P. R. Landon and J. E. Dorn, "Deformation and Fracture Mechanisms of Polycrystalline Magnesium at Low Temperature," *TRANSACTIONS, American Society for Metals*, Vol. 48, 1956, p. 986.
8. R. S. Busk, "Lattice Parameters of Magnesium Alloys," *Transactions, American Institute of Mining and Metallurgical Engineers*, Vol. 188, 1950, p. 1460.
9. F. E. Hauser, Ph. D. Thesis, University of California, 1956, p. 35.
10. A. H. Cottrell, *Dislocations and Plastic Flow in Crystals*, 1953, p. 64, Oxford.
11. E. T. Wessel, "Some Exploratory Observations of the Tensile Properties of Metals at Very Low Temperatures," Westinghouse Research Laboratory Scientific Paper 8-0103-P1, 1956, p. 13.
12. C. Zener and J. H. Holloman, "Effect of Strain Rate Upon Plastic Flow of Steel," *Journal of Applied Physics*, Vol. 15, No. 1, Jan. 1944, p. 22.

DISCUSSION

Written Discussion: By G. W. Pearsall, Physical Metallurgy Section, Metallurgical Laboratory, The Dow Chemical Company, Midland, Michigan.

The authors have presented some interesting results concerning the deformation mechanisms operative in solid solutions of lithium in magnesium. The preferred orientation of an extruded binary magnesium alloy containing 14.8 atomic % lithium has been investigated in our laboratory, and the results correlate well with the authors' observations of the importance of nonbasal slip in such an alloy. Our material was extruded at 800 °F (425 °C) in the form of $1\frac{1}{4} \times \frac{1}{8}$ inch strip and its preferred orientation was determined using a Norelco x-ray spectrometer modified for use with the Schulz surface-reflection technique.* The basal pole

* L. G. Schulz, "A Direct Method of Determining Preferred Orientation of a Flat Reflection Sample Using a Geiger Counter X-ray Spectrometer," *Journal of Applied Physics*, Vol. 20, 1949, p. 1030.

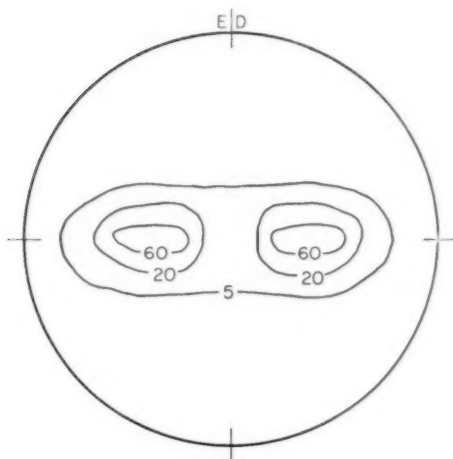


Fig. 14—(0002) Pole Figure for Mg-14.8 At% Li Alloy As-Extruded.

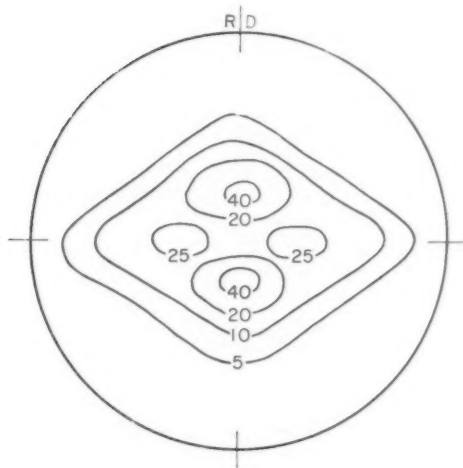


Fig. 15—(0002) Pole Figure for Extruded Mg-14.8 At% Li Alloy After Cold Rolling 70%.

figure of the extruded strip is shown in Fig. 14. It consists of two maximum basal pole densities rotated from the normal to the extrusion surface in the *transverse* direction; this is in contrast to the preferred orientation of most wrought magnesium alloys where the basal pole maxima are rotated in the longitudinal direction. The pole figure of the magnesium-lithium alloy resembles those observed for wrought

titanium, zirconium and beryllium in which nonbasal slip is known to be an important deformation mechanism. Williams and Eppelsheimer** have concluded that the simultaneous operation of nonbasal and basal slip during the rolling of titanium will rotate the basal poles into the transverse direction. Likewise, the authors' observations of pronounced prismatic slip together with basal slip in magnesium-lithium alloys may help explain the transverse spread of the basal pole maxima observed in our alloys. It is also interesting to note that after the extruded strip had been cold-rolled 70%, the preferred orientation changed to that shown in Fig. 15.

Written Discussion: By A. Moore and A. J. Martin, United Kingdom Atomic Energy Authority, Atomic Weapons Research Establishment, Aldermaston, Berkshire, England.

We should like to congratulate the authors on an extremely interesting and lucid paper. We observe that the theory is advanced that decreasing the c/a ratio in hexagonal close packed metals appears to favor prismatic slip. This is true in the case of the metals magnesium, magnesium/lithium, titanium and possibly zirconium; but, in contrast, beryllium, which has the smallest axial ratio of all, deforms preferentially by basal slip. In fact the critical resolved shear stress for slip on the prismatic plane is about five times that for basal slip at room temperature (G. L. Tuer and A. R. Kaufmann, "The Metal Beryllium," p. 383). Would the authors like to comment on this?

Authors' Reply

The authors were most pleased to receive Dr. Pearsall's observations agreeing with both their results and conclusions. It seems certain that prismatic slip contributes significantly to the deformation of the 14.8 atomic % lithium-magnesium alloy during high temperature extrusion as well as during the tensile deformation at lower temperatures investigated here.

The authors wish to thank Messrs. Moore and Martin for their comments on Be which appears to present somewhat of an exception to the usual rule that the transition from basal to prismatic is dependent on the c/a ratio. First, the authors should state that the theoretical justification for this rule is based on the hypothesis that deformation is controlled by the Peierls' mechanism. When other processes control slip this rule need not necessarily apply. Secondly, the crude rule neglects the effect of the anisotropy of the shear modulus of elasticity which enters Peierls' equation. Furthermore, other factors such as those dictated by changes in electronic energy states during the motion of a dislocation might prove significant. In this light the c/a rule can only be used as an important guide and should not be applied to the exclusion of other considerations.

** D. N. Williams and D. S. Eppelsheimer, "Origin of Deformation Textures of Titanium," *Nature*, Vol. 170, July 26, 1952, p. 146.

SOME PROPERTIES OF URANIUM-LOW TITANIUM ALLOYS

BY DANIEL J. MURPHY

Abstract

Titanium additions over the range 0.1 to 1.5 wt.% have been investigated for improvement in mechanical properties and corrosion resistance over those of unalloyed uranium. The effects on microstructure of various heat treatments and cooling rates have been correlated with mechanical properties. Observations show that increasing amounts of titanium increase strength, hardness, and resistance to corrosion but decrease ductility and impact strength. Heat treatment makes the trend more pronounced except in the case of the fast cooling rate of a water quench for which good impact strength and ductility, as well as improved tensile properties, are observed up to 1 wt.% titanium content. Corrosion tests in moist air show a 10 to 25 fold increase in corrosion resistance depending upon titanium content. (ASM International Classification Q general, R general, 2-14; U, Ti)

INTRODUCTION

THE INCREASING USE of uranium in the atomic energy field makes it important that there be made available uranium-base alloys having tensile, impact and corrosion properties superior to those of uranium itself. For maximum usefulness in such applications, these alloys should have minimum dilution of uranium by alloying elements, and the alloying elements used should, if possible, have appropriate neutron cross sections. Further, in addition to having superior mechanical and corrosion properties, it is desirable that these alloys be easily prepared and formed by melting, casting, mechanical methods, and standard machining operations, that their properties be controllable by metallurgical treatment, and that, in their final conditions, they be stable both in dimensions and in properties.

OBJECTIVE

The objective of this investigation was to explore the possibilities of

Work done under the auspices of the Atomic Energy Commission.

A paper presented before the Thirty-Ninth Annual Convention of the Society, held in Chicago, November 4-8, 1957. The author, Daniel J. Murphy, is professor, Department of Metallurgy, University of Arizona, Tucson; was formerly a staff member of Los Alamos Scientific Laboratory, Los Alamos, New Mexico. Manuscript received December 21, 1956.

improving the mechanical properties of uranium and its resistance to corrosion by small additions of titanium.

More specifically, its intent was to determine and evaluate the properties of such alloys which might have useful applications and in particular to establish the conditions of composition and metallurgical treatment which would give to them their optimum properties for such applications.

Previous Work

From the published results of a very limited amount of work done at other laboratories it appeared that desired requirements might be satisfied by certain binary uranium-titanium alloys having relatively low contents of titanium.

Investigations of phase relations in uranium-titanium alloys have led to the publication of constitutional diagrams by Battelle Memorial Institute (1)¹ and by the Research Laboratories of the Associated Electrical Industries Ltd, in England (2). These are reproduced in Figs. 1 and 2. While in general agreement, these diagrams differ in several respects in the low titanium region, and these differences will be referred to later in the paper.

Limited data concerning mechanical properties have shown that very small additions of titanium to uranium effected improvement in both its tensile strength and ductility. These improvements, while not spectacular, were significant, especially since they resulted from a very small alloying addition and a completely arbitrary heat treatment. They indicated that it may be reasonable to expect that the means for a substantial further improvement in properties might present itself when the general effects of alloy composition and heat treatment have been established by systematic investigation of these variables.

The results of corrosion test data on alloys made up of a wide assortment of alloying element additions to uranium have shown that relatively small titanium additions impart to uranium an appreciable degree of resistance to atmospheric corrosion.

With regard to castability, until recently there had been difficulty in preparing titanium alloys with predictable titanium contents and even a reasonable degree of homogeneity. This difficulty has been overcome, however, and the techniques now exist for making reasonably large castings of these alloys with excellent recovery of titanium and a remarkably high degree of homogeneity in the alloy content.

There appears to be little information available concerning the forming properties of uranium-low titanium alloys. No particular difficulty has been reported on forging and rolling these alloys except at compositions in the vicinity of the intermetallic compound U_2Ti (33 atomic % titanium) where the alloys were very brittle.

¹ The figures appearing in parentheses pertain to the references appended to this paper.

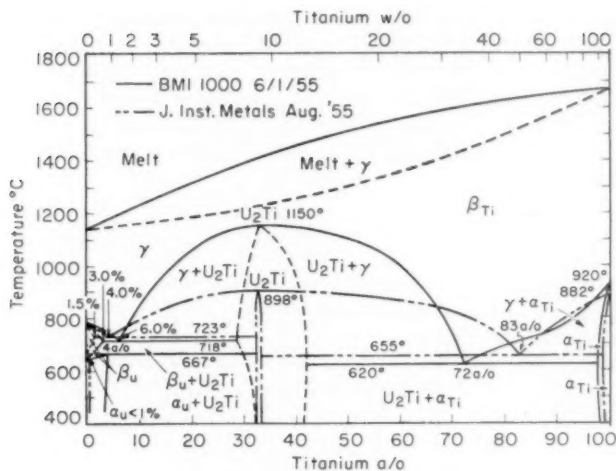


Fig. 1—Constitutional Diagram of U-Ti System.

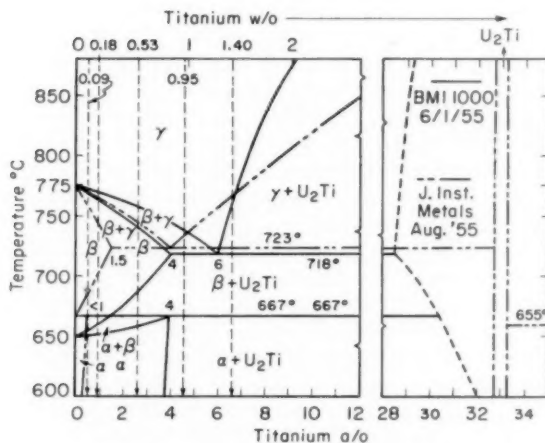


Fig. 2—U-Rich End of U-Ti Constitutional Diagram.

EXPERIMENTAL PROCEDURE

General—In the course of the investigation the following properties and characteristics were of interest:

a) Castability: While no foundry experimentation as such was contemplated, foundry procedures were observed in the preparation of

samples. All ingots were examined for titanium recovery, freedom from segregation, soundness and quality of surface.

b) **Tensile Properties:** A major aim of the program has been to determine the tensile properties of a series of uranium-low titanium alloys after a variety of heat treatments. Tensile properties measured were ultimate strength, yield strength, elongation, reduction of area, and elastic modulus. A minimum of three tensile bars was tested for each condition to insure that the data obtained were reasonably representative.

c) **Impact Properties:** Notched-bar impact resistance was determined for each alloy in each condition, using the standard Charpy v-notch specimen with a 60 ft-lbs load. A minimum of three Charpy bars was tested for each condition to insure that the data obtained were reasonably representative.

d) **Hardness:** Hardness measurements were made on all alloys in all conditions of heat treatment, as a rapid and convenient means for evaluating various heat- and precipitation-hardening treatments, and as a basis for correlating the properties of various alloys in various conditions.

e) **Microstructure:** Microstructures were examined throughout the investigation to determine the phases present and the phase distribution in each alloy after each treatment, and to correlate the structure of each alloy with its observed properties. Photomicrographs were made of representative or significant microstructures.

f) **Phase Identification:** Identifications of phases present were verified by x-ray diffraction methods where appropriate.

g) **Resistance to Corrosion:** Specimens from representative samples were submitted to an atmospheric corrosion test in an environment of 50% relative humidity air at 75 °C for periods up to 2000 hours.

Specific Handling of Material—Five castings, $1\frac{1}{8} \times 7\frac{1}{2} \times 10\frac{3}{8}$ inches in size and weighing approximately 33 kilograms each were made of high purity uranium containing the following nominal additions of titanium: 0.1, 0.2, 0.5, 1.0, 1.5 weight %. The corresponding specific analyses of these castings were respectively: 0.09, 0.18, 0.53, 0.95, and 1.40% titanium by weight, and these figures will be referred to frequently in the following sections. Impurity contents of the order of 65 ppm carbon, 70 ppm iron, 45 ppm aluminum, 50 ppm nickel, 85 ppm silicon, and much smaller amounts of other elements were also present. The size of the castings was determined by the amount of material required to provide sufficient tensile and impact test bars and other selected pieces for later investigations. Ingots were radiographed for soundness and chemically analyzed for homogeneity of composition.

Tensile, impact and hardness data were obtained for each of the five compositions in the as-cast condition. The broken segments of Charpy bars were sectioned into samples for observation of micro-

structure, x-ray analysis, and experimental heat treatment and precipitation hardening studies. Heat treatments were carried out in tube furnaces in vacua of the order of 0.1 micron. Precipitation hardening heat treatments of short duration were given in a lead bath and the longer duration treatments were conducted in evacuated tube furnaces.

RESULTS

Microstructure

a) *As-cast*: In the microstructures of the five alloys in their as-cast condition, as shown in Figs. 3 and 4, the presence of the titanium additions is increasingly apparent as the alloy composition increases.

In the photomicrograph of the 0.09 weight % titanium alloy, the structure is typical of that of unalloyed uranium—single-phase, duplex grains, twins, and the usual amount of inclusions. The small amount of titanium in the alloy appears to be completely dissolved in solid solution α -uranium.

The increased amount of titanium in the 0.18 weight % alloy is quite apparent in its microstructure as particles, believed to be the intermetallic compound U_2Ti , dispersed in an interdendritic pattern.

The further increase in titanium content to 0.30 weight % emphasizes this pattern in the microstructure.

At a level of 0.53 weight % titanium, the presence of titanium in the microstructure is still more pronounced, and more so at 0.95 weight % and 1.40 weight %, where, in the latter case the structure is strongly eutectoidal in character.

b) *After Heat Treatment*: The effects on the microstructure of heat treatments in the α , β , and γ regions of temperature are shown in Fig. 5.

Little if any effect is apparent from a long heating period at 625 °C (1155 °F) in the α -region of temperatures and the structure shows no change from that as cast.

The result of heating at 725 °C (1335 °F) in the β -region of temperature is a 2-phase structure in which an agglomeration of U_2Ti in spheroidal form is evident.

Treatment at 800 °C (1470 °F) in the γ -region of temperature results in the acicular structure typical of martensitic α -uranium. In this case, the white slivers are interpreted to be uranium supersaturated with titanium in a darker mottled matrix, unresolvable microscopically, though apparently two-phase.

c) *Upon Cooling at Different Rates*: The effects on the microstructure of cooling at various rates from the α -temperature range for a typical alloy composition containing 0.53 weight % titanium are shown in Fig. 6.

The furnace-cooled structure is similar to the as-cast structure, for which the original cooling rate in the casting furnace was about the same.

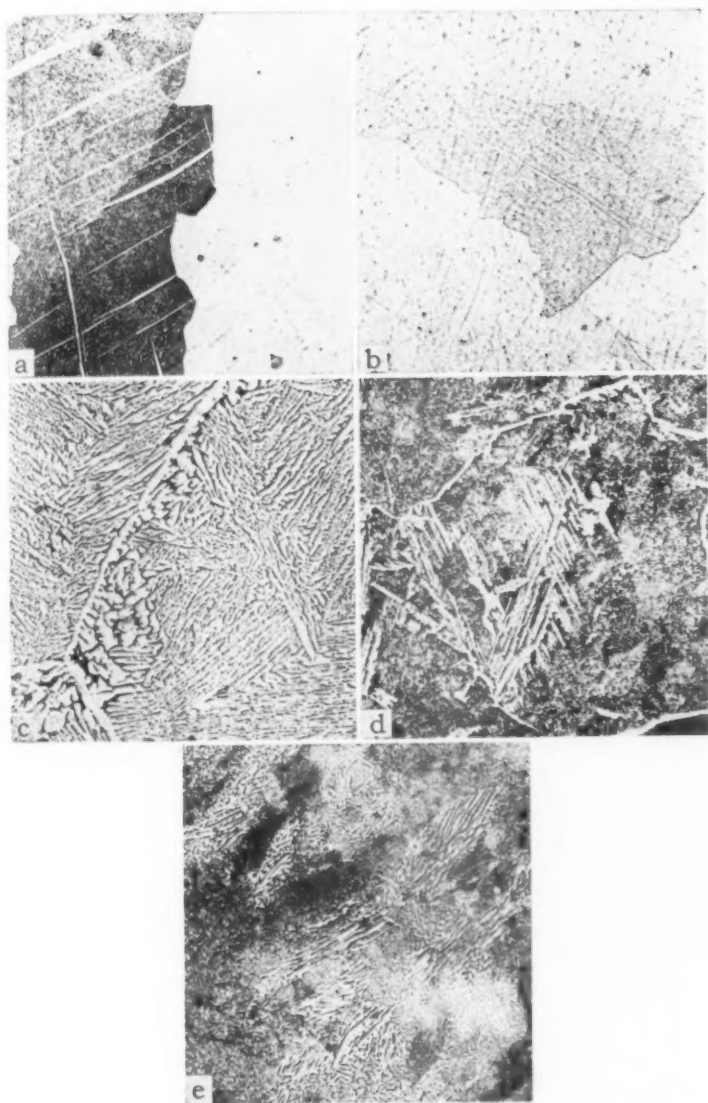


Fig. 3—Microstructures of U-Ti Alloys, As-cast. $\times 200$. (a) 0.09 weight %; (b) 0.18 weight %; (c) 0.53 weight %; (d) 0.95 weight %; (e) 1.40 weight %.

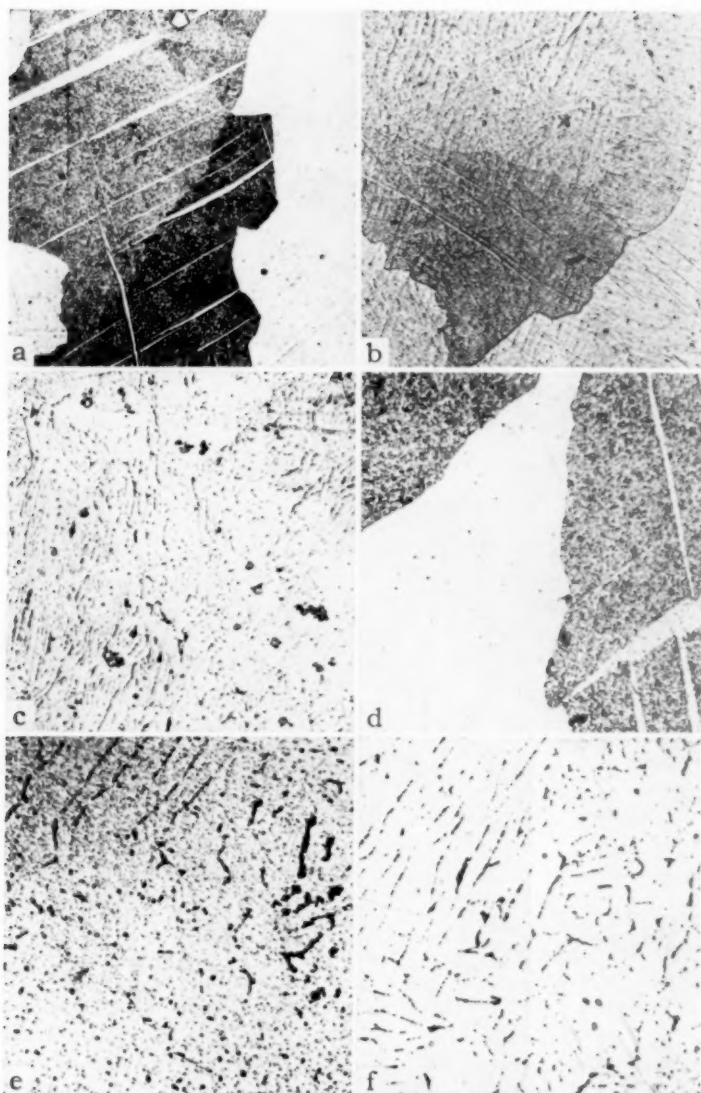


Fig. 4—Microstructures of 0.09, 0.18 and 0.30 weight % Ti Alloys, As-cast. Showing interlath structure above 0.09 weight % Ti. (a and d: 0.09 weight % at $\times 200$ and $\times 500$.) (b and e: 0.18 weight % at $\times 200$ and $\times 500$.) (c and f: 0.30 weight % at $\times 200$ and $\times 500$.)

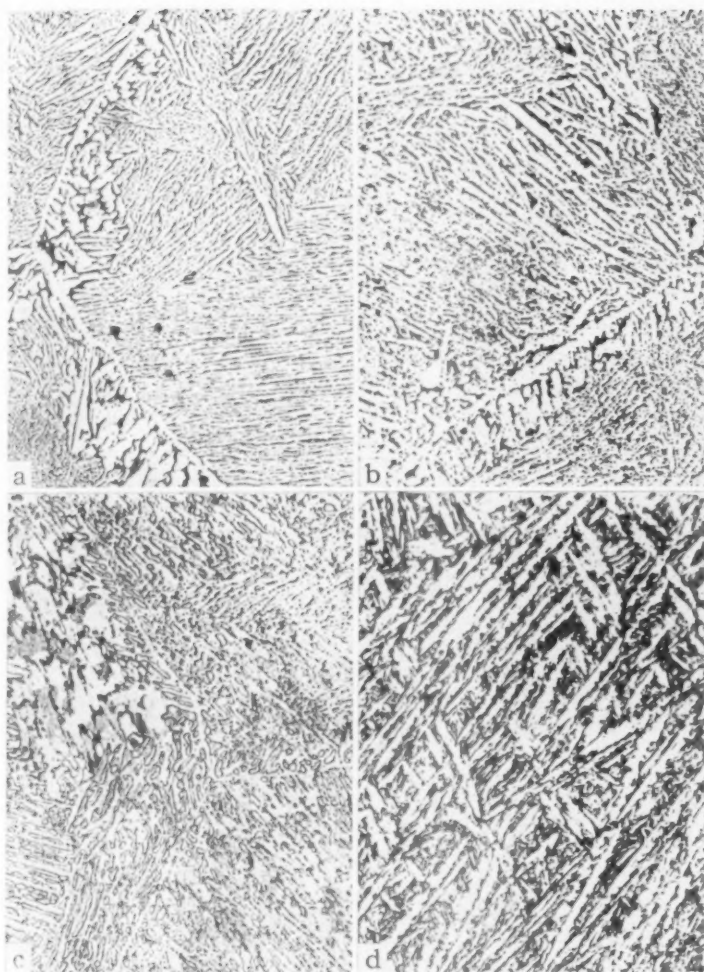


Fig. 5—Microstructures of 0.53 weight % Ti Alloy, Heat Treated at α , β , and γ -Temperatures. (a) As-cast; (b) after 72 hours at 625 °C, furnace cooled; (c) after 4 hours at 725 °C, water-quenched; (d) after 4 hours at 800 °C, water-quenched. $\times 200$.

The fast cooling rate of the water quench results in the acicular structure typical of martensitic α -uranium.

The slower cooling rates of the oil quench and air cool do not appear to be fast enough to entirely suppress the transformation of γ -uranium to other phases by the usual nucleation and growth type of phase trans-

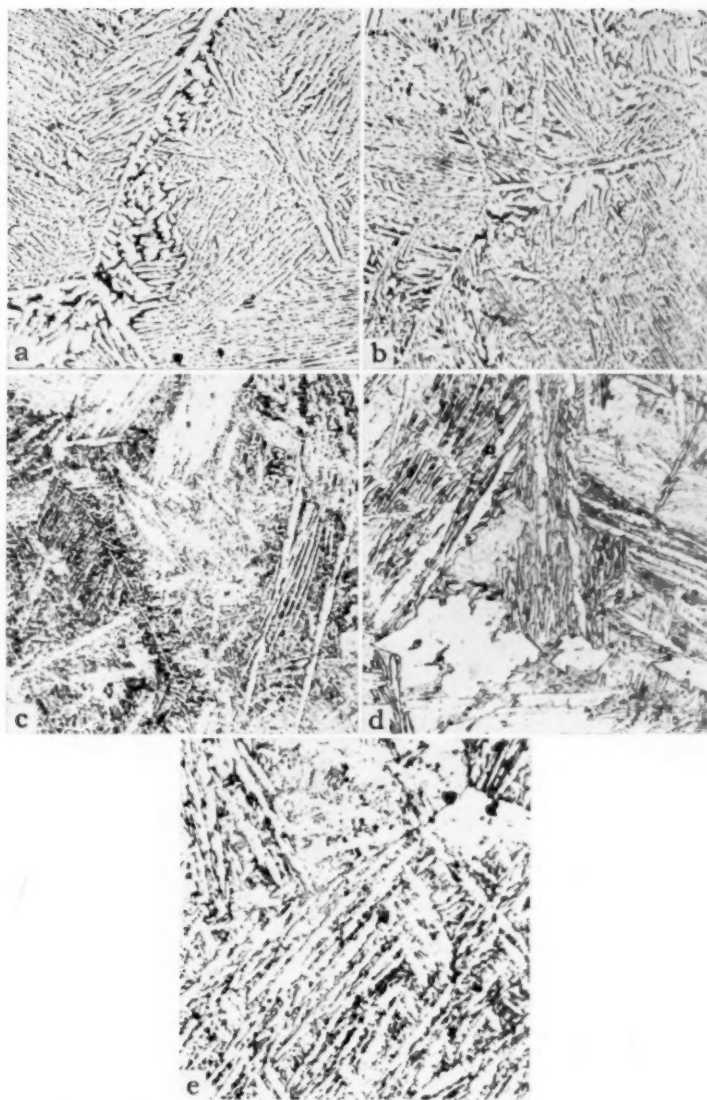


Fig. 6—Microstructures of 0.53 weight % Ti Alloy, Showing Effect of Cooling Rate. (a) As-cast; (b) furnace-cooled; (c) air-cooled; (d) oil-quenched; (e) water-quenched. $\times 200$.

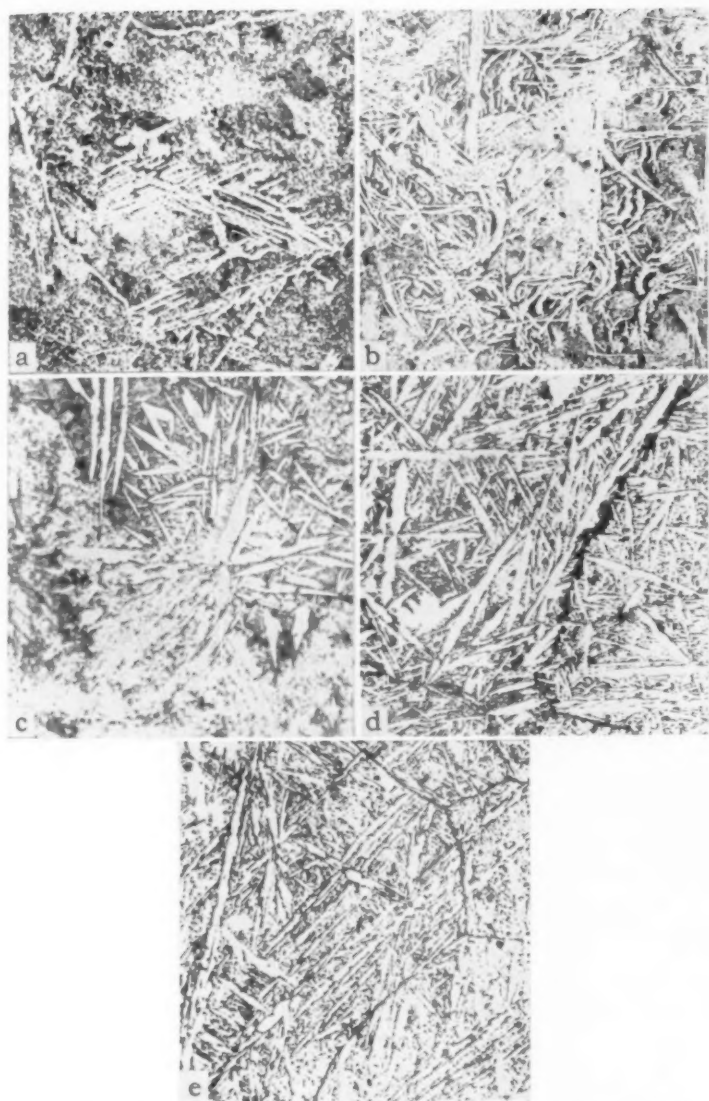


Fig. 7—Microstructures of 0.95 weight % Ti Alloy, Showing Effect of Cooling Rate. (a) As-cast; (b) furnace-cooled; (c) air-cooled; (d) oil-quenched; (e) water-quenched. $\times 200$.

formation mechanism. The acicular structure of martensitic α -uranium is still in evidence in the structures resulting from both oil quench and air cool, though in lesser proportion at the slower cooling rate.

Similar effects on the microstructure result in the case of the 0.95 weight % titanium alloy, for which a corresponding set of photomicrographs is shown in Fig. 7. The greater amount of the white slivers which appear in the microstructure, particularly after the oil quench, may be accounted for by the increased titanium content.

MECHANICAL PROPERTIES

Mechanical test results for each of the five compositions are shown in Fig. 8. The tests were conducted at room temperature on material which had been cooled at various rates from the γ -region of temperatures. Though the superposition of curves introduces several different scales on the ordinate axis, the composite plot affords a useful comparison of properties.

In the as-cast condition, it is evident that increasing amounts of titanium increase tensile strength, yield strength, and hardness, but decrease elongation and impact strength.

This trend becomes more pronounced upon heat treatment, evident in the increased upward slope of the tensile, yield, and hardness curves. The elongation and impact curves, however, show notable exceptions:

a) Elongation is increased by the heat treatment and the increase is sustained at the faster cooling rates up to at least 0.5 weight % titanium.

b) Impact strength is lost in every cooling rate except the water quench.

c) In the case of the water quench, a distinct plateau, extending out to 1.0 weight % titanium, shows up in the curves for elongation and impact strength at very promising values of 20% elongation and 20 ft-lbs of impact strength.

A different assortment of the curves shown in Fig. 8 is shown in Fig. 9. This arrangement accentuates the comparison of the preceding figure. It shows quite plainly that heat treatment improves these alloys, for the "as-cast" curve is in lowest position in almost every case. The greater benefit from the faster cooling rates is also very apparent, for these curves are in the uppermost position in every case. Particularly apparent in this plot is the sustained increase in elongation and impact strength produced by the water quench.

CORROSION RESISTANCE

An indication of the improvement in the resistance to corrosion of uranium which may be obtained by small additions of titanium is shown in Fig. 10. From these curves it appears that the greater the titanium content, the greater is the improvement obtained. However, an addition as low as 0.1 weight % results in a 10-fold improvement. A γ -quench

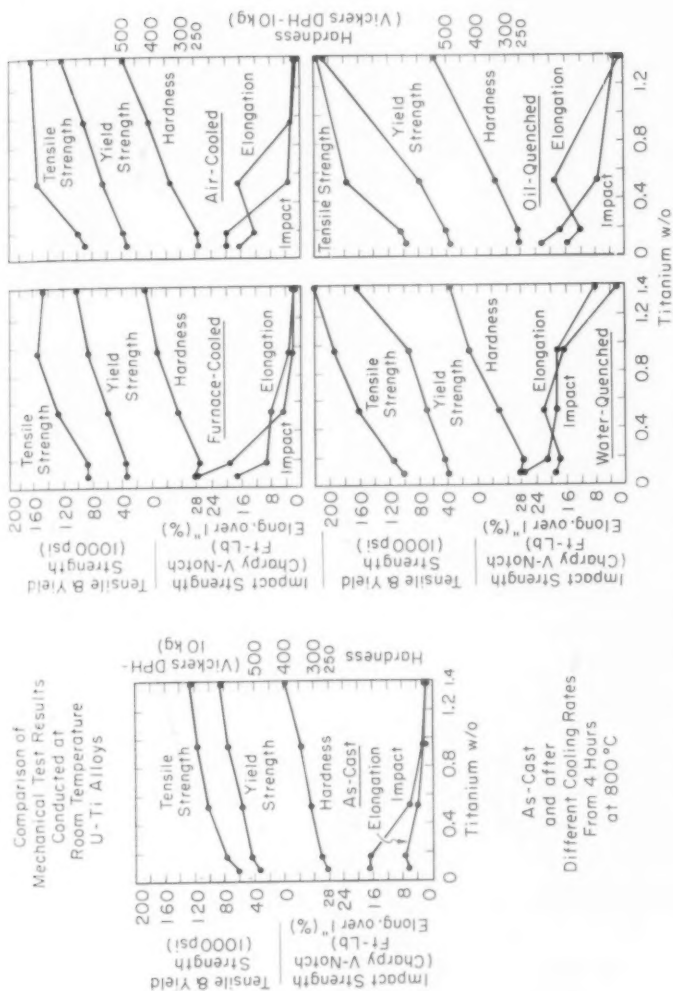


Fig. 8—Curves of Mechanical Test Values, Arranged According to Cooling Rate.

heat treatment gives evidence of improving the corrosion resistance still further over the as-cast condition.

PRECIPITATION HARDENING

The sustained retention of ductility in the γ water-quenched alloys indicated promise for increasing the tensile and yield strengths without sacrifice of ductility, particularly in the case of the 0.1 and 0.2 weight %

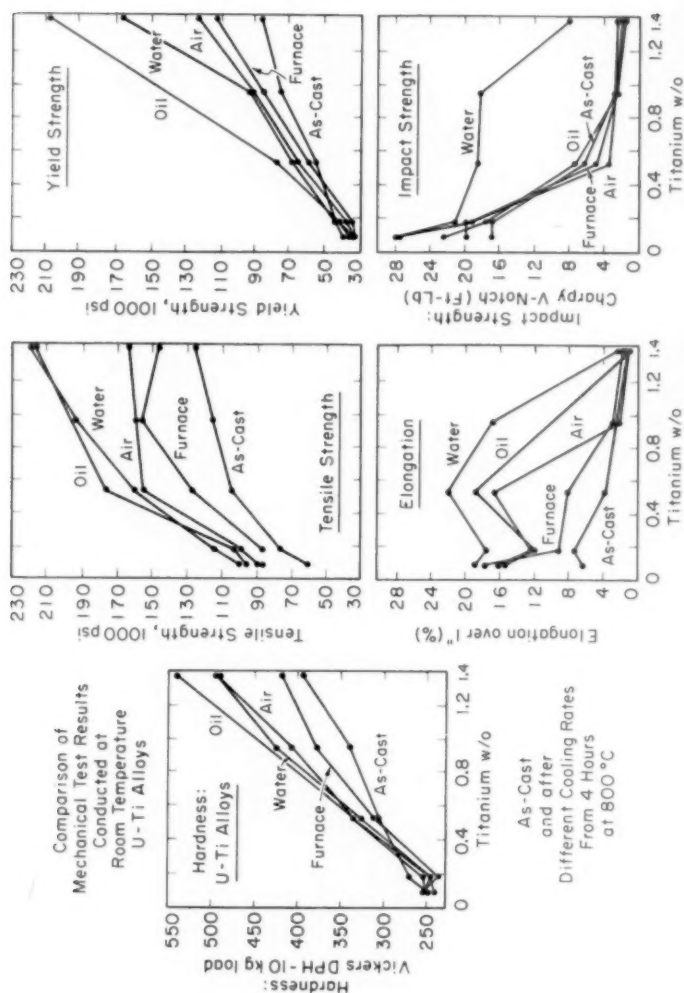


Fig. 9—Curve of Mechanical Test Values, Arranged According to Properties.

alloys which exhibited values not much above those of unalloyed uranium, by a precipitation hardening treatment.

In an early phase of the investigation observations had been made of the effect of a series of precipitation hardening treatments on an alloy containing 3.0 weight % titanium. This alloy showed typical precipitation hardening behavior over a range of temperatures. Very high peak hardness, of the order of 550 to 600 Vickers DPH, were obtained after

aging periods of less than 1 hour at moderate aging temperatures of the order of 450 to 500 °C (840-930 °F).

This very positive aging response in an alloy of relatively high titanium content suggested that a more useful response might be obtained in material containing less titanium. Precipitation hardening treatments carried out on alloys containing 0.1 and 0.2 weight % titanium, however, produced but very slight response to the treatment. Maximum

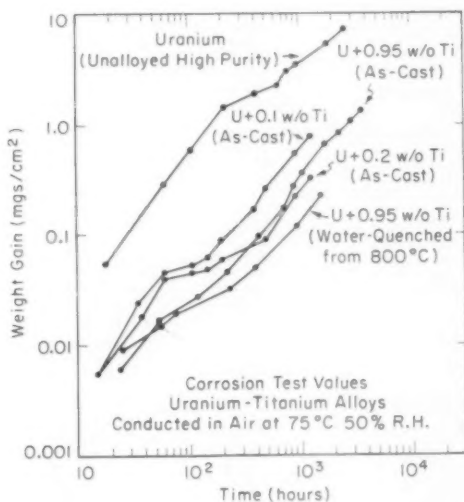


Fig. 10—Corrosion Resistance Curves of U-Ti Alloys.

hardnesses under 250 and 300 DPH, respectively, resulted after some 4 to 8 hours of aging at 500 °C (930 °F), representing an increase in hardness number of less than 50 in each case. More significant, however, was a distinct loss in ductility and impact strength accompanied by but a very small increase in tensile and yield strengths.

DISCUSSION OF RESULTS

Mechanical Properties and Corrosion Resistance. The results obtained indicate that the mechanical properties and corrosion resistance of uranium can be improved by small additions of titanium. From the test values obtained it appears that the optimum addition is about 0.5 weight % titanium, for this amount effects substantial all-around improvement in mechanical properties in the resulting alloy in the γ water-quenched condition, as shown in Fig. 9, and in the following tabulation which compares these properties with those of unalloyed uranium.

Tabulation

Property	Unalloyed Uranium As-Cast	U-0.53 wt% Ti after 4 hours at 800 °C-water- quenched *
Ultimate tensile strength (psi)	67,000	160,000
Yield Strength (psi)	26,000	69,000
Hardness, (DPH-10 Kg.)	218	327
Elongation in 1" (%)	12	22
Reduction in area (%)	12	24
Impact strength (Charpy V-notch) (ft-lbs)	18	18
Corrosion resistance in 50% R. H. air at 75 °C (Merit Ratio) **	1	25

* Average of three tests

$$** \text{ Merit Ratio (1000 hrs) } = \frac{\text{Wt gain (unalloyed)}}{\text{Wt gain (alloyed)}}$$

The above comparison of values shows a 2 to 3-fold improvement in tensile and yield strength over unalloyed uranium. Ductility is doubled and no reduction in impact strength is sustained. A 25-fold improvement in resistance to corrosion is indicated.

It is to be noted, however, that the mechanical tests were conducted at room temperature. The temperature dependence of mechanical properties which has been displayed by uranium containing small additions of other elements may very likely apply in the case of titanium. A systematic determination of mechanical properties over a useful range of temperatures below and above room temperature would therefore be necessary to afford a more complete picture of the behavior of this alloy composition.

The improved properties tabulated above are associated with the retention of distorted α -uranium containing a supersaturation of titanium in solid solution. Such a structure is not formed or retained at slower cooling rates and it may therefore be expected to appear only in relatively shallow sections upon quenching. Its retention in thick sections through suppression of the transformation to undistorted α -uranium, perhaps by means of additions of other elements, would serve a useful purpose if by this means the improved properties could be obtained at a slower cooling rate.

Constitutional Diagram

While it was not a purpose of this investigation to confirm values in the constitutional diagram, certain microstructural observations indicated:

- a. That the β -field may not extend to 4 atomic % titanium.
- b. That the solid solubility of α -uranium for titanium is not as great as 4 atomic %, but instead appears to be between 0.5 and 1.0 atomic % titanium.

Reference to the photomicrographs of Fig. 4 for 0.09 and 0.18 weight

% (0.5 and 1.0 atomic %) titanium shows that an addition of 0.09 weight % titanium is not perceptible in the microstructure and gives indication that this small amount of titanium is contained in solid solution in α -uranium. An addition of 0.18 weight % titanium, on the other hand, shows up in the form of particles, probably of the intermetallic compound U_2Ti , dispersed in an interdendritic pattern. Heat treatment and quench from 625 °C (1155 °F) in the α -temperature range produced similar structures, indicating that 0.5 atomic % titanium will dissolve but that 1.0 atomic % will not dissolve, and that the solubility of titanium lies between 0.5 and 1.0 atomic %, rather than 4.0 atomic % as shown in the constitutional diagram in Fig. 2.

Reference to the photomicrographs of Fig. 5, which show the result of heating a 0.53 weight % (2.5 atomic %) alloy at 725 °C (1335 °F) to be a 2-phase structure, indicates that the single phase β -field may not extend to as great a titanium content as 2.5%, whereas one of the constitutional diagrams of Fig. 2 shows it to extend to 4 atomic %.

Precipitation Hardening

Precipitation hardening, as a means for strengthening low titanium alloys of uranium without sacrifice of ductility or impact strength, does not appear to offer much promise. While the alloys respond to the aging process, the improvement in strength properties is accompanied by a falling off in ductility and impact strength to a considerable degree, neutralizing in effect the improvement sought.

CONCLUSIONS

This investigation has shown that:

- a. Small additions of titanium to uranium improve its mechanical properties and resistance to corrosion.
- b. The range in which useful improvement is obtained lies between 0.1 and 1.5 weight % titanium addition. Below this range, properties are essentially those of unalloyed uranium; above it, high strength is accompanied by brittleness, low ductility, and low impact strength.
- c. The mechanical properties of alloys of uranium containing small additions of titanium are very dependent upon the rate of cooling applied after a heat treatment in the γ -region of temperature.
- d. Optimum mechanical properties—tensile and yield strength, ductility, and impact strength—are obtained from additions of 0.5 to 1.0 weight % titanium, in γ water-quenched condition.
- e. The solid solubility of α -uranium for titanium is in the range of 0.5 to 1.0 atomic %, rather than 4 atomic % as reported in recent constitutional diagrams.
- f. The extent of the β -uranium phase field is less than 2.5 atomic % titanium, rather than 4 atomic % as reported in recent constitutional diagrams.

g. Precipitation hardening treatments improve tensile and yield strengths of uranium containing small additions of titanium but decrease sharply its ductility and impact strength.

ACKNOWLEDGMENTS

The writer is indebted to George E. Jaynes and Keith V. Davidson for their preparation of the castings on which this investigation was based; to John O'Rourke for x-ray diffraction phase determinations; to James T. Waber who made the corrosion studies; to Herman Rohr for careful specimen preparation; and to Morton C. Smith, who participated in the early stages of the investigation, for his interest, advice and counsel throughout the course of the work.

References

1. H. A. Saller and F. A. Rough, "Compilation of U. S. and U. K. Uranium and Thorium Constitutional Diagrams," Battelle Memorial Institute—1000, June 1, 1955.
2. A. G. Knapton, "The System Uranium-Titanium," *Journal, Institute of Metals*, Vol. 83, Part 12, August 1955, p. 497.

DISCUSSION

Written Discussion: By David L. Douglass, Battelle Memorial Institute, Columbus, Ohio.

It was very gratifying to see the results of Professor Murphy's research and to compare them with results obtained in similar research performed by this writer at Battelle. We agree that the published phase diagrams appear to be erroneous. Work has been in progress at Battelle on the uranium-rich end of the U-Ti system for some time, and the results of the study will probably be published within a few months.

Both hardness and tensile data have been obtained on quenched specimens that were similar in composition to the alloys used by Murphy. Murphy's data is compared with the Battelle data in Figs. 11 and 12. The Battelle specimens were both harder and stronger than the specimens reported by Murphy. In addition, the Battelle data displays a distinct plateau beyond about 0.4 weight % titanium in the case of both hardness and strength.

The writer can suggest two possible reasons for the apparent discrepancy in values. First, it has been observed that heating to as little as 150 °C (300 °F) will cause softening of martensitic specimens of this composition range.* For example, a uranium-0.94 weight % titanium alloy quenched from 800 °C (1470 °F) decreased in hardness from 470 to 425 DPH by mounting in Bakelite at 150 °C (300 °F). Therefore, hardness specimens should not be mounted in Bakelite. Were the author's hardness specimens mounted or unmounted; and if mounted, was a room temperature setting resin used? Second, the sample size affects the quenching rate. Large specimens may be soft and of low strength because the critical cooling velocity was not exceeded. The Battelle procedure was to quench

* D. L. Douglass and L. L. Marsh, Jr., "The Effect of Heat Treatment on the Hardness and Microstructure of Uranium-Titanium Alloys," to be published, *Journal of Metals*, 1957.

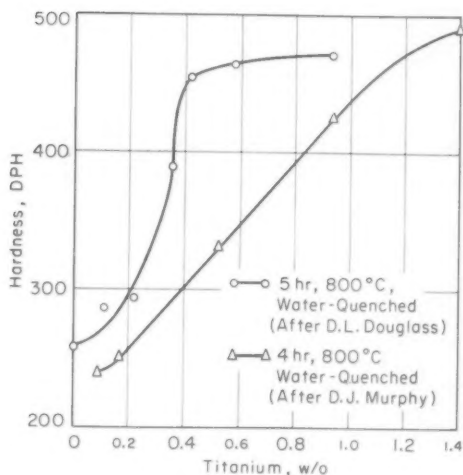


Fig. 11—Hardness of Quenched, Martensitic Uranium-Titanium Alloys.

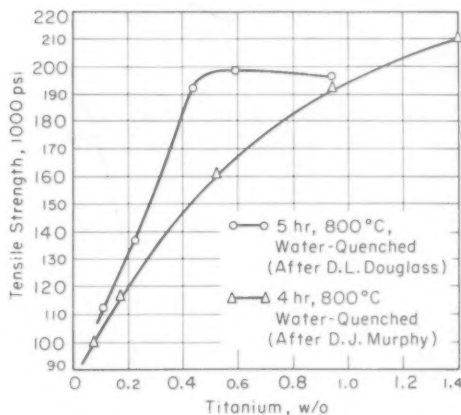


Fig. 12—Tensile Strength of Quenched, Martensitic Uranium-Titanium Alloys.

$\frac{1}{2}$ -inch diameter specimens in water after 5 hours at 800 °C (1470 °F). It appeared from subsequent metallographic examination that all the specimens were completely martensitic throughout the cross section. Was there something about the author's heat treatment that might have permitted some softer decomposition product to be present in the quenched specimens?

Professor Murphy showed the microstructure of an alloy containing 0.53 weight % titanium quenched from 725 °C (1335 °F) and stated that the structure con-

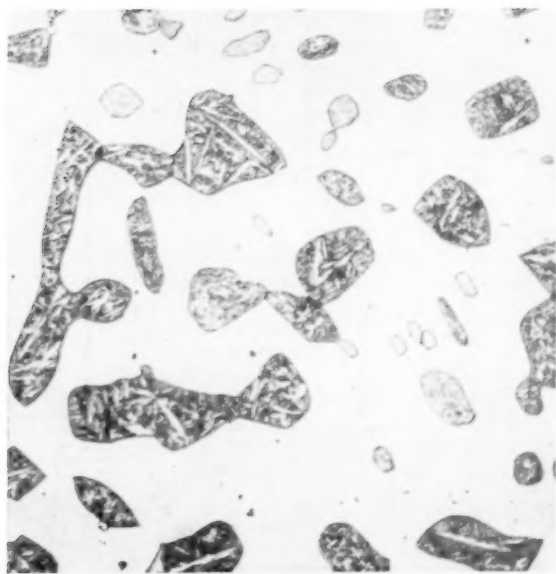


Fig. 13—Uranium 0.43 weight % (2.1 Atomic %) Titanium Alloy Quenched from 730 °C (1345 °F), Gamma Plus Beta Region. $\times 500$.

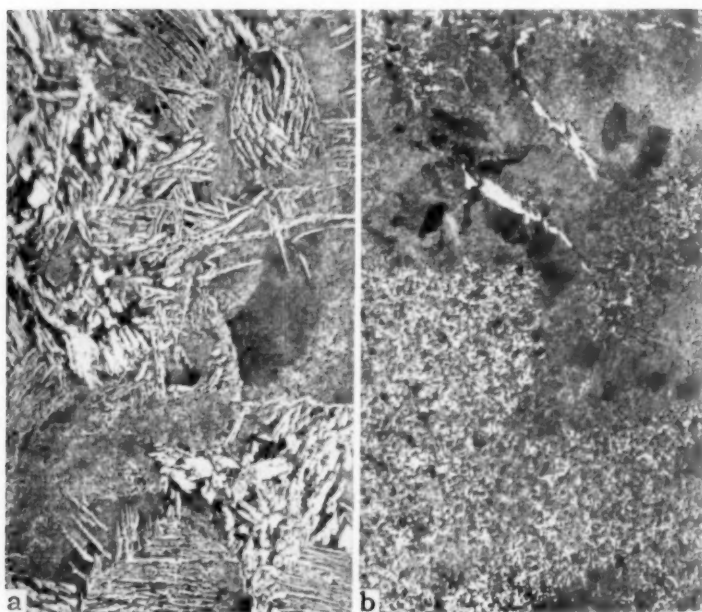


Fig. 14—Microstructures of "Slack-Quenched" Alloys, Showing Nodular Growth Products. $\times 500$. (a) 3.7 atomic % Ti, 0.76 weight %; (b) 5.7 atomic % Ti, 1.2 weight %.

sisted of dispersed U_2Ti in a matrix which had transformed during quenching. According to both phase diagrams this alloy was in the beta plus gamma region and should show a structure of martensite (formed from the gamma) and alpha (formed from the beta) as shown in Fig. 13. Any U_2Ti which formed would be very fine and hardly resolvable at $\times 500$. Can the author explain this?

The last point is the effect of cooling rate on the transformation of gamma. Professor Murphy observed lesser proportions of the acicular martensite with decreasing cooling rates. This writer has observed the presence of nodular colonies of a nucleation and growth product upon air cooling or furnace cooling. Examples of this structure are shown for "slack" quenched alloys in Fig. 14. A sharp distinction was apparent, as evidenced by the absence of acicular martensite, in alloys which were cooled less rapidly than by quenching. Was there any evidence of this behavior in some of the higher alloys, namely 0.95 or 1.40 weight % titanium?

Written Discussion: By Clayton O. Matthews, Head, Materials Research, Lockheed Missile Systems Division, Palo Alto, California.

It is gratifying to see this report on uranium alloy development which has been directed in the conventional and somewhat classical approach to making uranium metallurgically more satisfactory in its important end uses. To date, uranium research has emphasized the properties and behavior of the metal itself, fabrication techniques, and alloy equilibrium diagrams. The author's timely publication of this paper focuses attention to the fact that there has been altogether too little applied research directed toward the improvement of uranium properties by alloying.

Valuable contributions have been made on the mechanical and corrosion properties of low titanium alloys. Further work is needed on the interpretation of the microstructures and, as indicated by the author, on the phase diagrams in the region of the uranium terminal phases.

Metallographic research conducted by this reviewer on impurity phases in uranium metal would indicate the solubility of titanium is less than that which is reported in the published diagrams, as indicated by Dr. Murphy, with the data of Knapton apparently most nearly correct. Previous errors in this measurement can be explained, especially since it was shown several years ago in our investigations that the precipitated phase, U_2Ti in this case, occurs in a very fine form in a subgrain network. The particles are normally too small to be resolved by optical microscopy and are not evident in the conventional electropolished specimen. We uncovered this precipitate by developing the nitric acid electro-etching treatment: one volt anodically at 14 ma/cm² in 50% nitric acid, following the standard chromic-acetic electropolish. The dendritic pattern evident in many of Dr. Murphy's photomicrographs represents a similar structure as our high purity alloys with carbon. In this case, UC precipitated in the gamma substructure during cooling and at the transformation of gamma to beta uranium, where the solubility limit decreased abruptly.

The martensitic structure characterized in the titanium system was not obtained in alloys with carbon where the total solubility was much less (40 to 60 ppm). The microstructure of the titanium alloys is affected differently by heat treatment than low carbon alloys, not only because of the greater Ti solubility, but also because carbon diffuses (interstitially) much more rapidly than titanium in uranium.

In this low alloy range, the effect of carbon and other impurities which may combine with the titanium must also be taken into account.

The interpretation of the microstructure of the 0.53 weight % titanium alloy, quenched from 725 °C (1335 °F), is questionable. The two phase structure, equilibrated at 725 °C (1335 °F), might result from beta plus gamma rather than beta plus U_2Ti . Additional evidence such as microhardness measurements and x-ray diffractometry data would have contributed to an understanding of this region of the system in equilibrium.

Author's Reply

The comments of Mr. Matthews are particularly appreciated in the knowledge of the extensive work he has done on the metallography of uranium and in view of his familiarity with the character of microstructures similar to those encountered by the writer. Since his observations speak for themselves, no added comment will be made except with regard to his specific reference to the microstructure of the 0.53 weight % titanium alloy, which will be mentioned in the discussion which follows.

Mr. Douglass' comments are received with considerable interest in that they show a parallelism in individual observations of various aspects of the U-Ti system.

With reference to the deviation in hardness and tensile strength values in his Figs. 11 and 12, no obvious explanation suggests itself. The hardness specimens had not been mounted nor had they been subjected to heating. The tensile bars were of $\frac{1}{4}$ inch diameter size, machined from heat treated and quenched cylindrical blanks $\frac{1}{2}$ inch in diameter. No evidence of softer decomposition products were evident in the microstructure.

X-ray identification of the microstructures of the 0.53 weight % titanium alloy quenched from 725 °C (1335 °F) indicated it to be a two-phase structure of alpha uranium and U_2Ti . Though this heat treatment was originally performed to investigate a quench from the middle of the beta region of the Battelle diagram, it later turned out to be very close to the phase boundary at 723 °C between $\beta + \gamma$ and $\beta + U_2Ti$ of the later published Knapton diagram. Comparison with the excellent photomicrograph of Douglass in his Fig. 13 indicates that the 0.53 weight % alloy very likely was quenched from the $\beta + U_2Ti$ region, as evidenced by the agglomeration of U_2Ti particles, instead of from the region which provided Douglass with the interesting structure of martensitic α islands in an α -uranium matrix.

Mr. Douglass' microstructures of "slack" quenched alloys in his Fig. 14 show a close resemblance to several of the authors in Figs. 3 and 7 wherein the effects of slower cooling rates are evident. Further work done by the author on the effect of cooling rate on the transformation of gamma uranium has been submitted in a paper entitled "Transformation Characteristics of Low Ternary Alloys of Uranium". By the use of Jominy Bar heat treatments the decreasing proportions of acicular martensite with slower cooling rates were studied. The transformation rate was influenced by the type and quantity of the ternary addition to U-.50 weight % titanium alloys, though in general the acicular structure was observed to disappear entirely about one inch distant from the quenched end, giving way to a nucleation and growth product under slower cooling rates.

EFFECTS OF FABRICATION AND HEAT TREATMENT VARIABLES UPON THE THERMAL CYCLING BEHAVIOR OF URANIUM

BY S. T. ZEGLER, R. M. MAYFIELD AND M. H. MUELLER

Abstract

The growth of rolled uranium rod on thermal cycling is shown to depend upon the rolling temperature, the amount of rolling reduction, and the condition of the material prior to rolling. The growth of rod rolled at 300 °C is observed to be influenced by annealing above the recrystallization temperature.

Cycling variables, specifically heating and cooling rates, are shown to have a pronounced effect on the growth of beta-treated uranium. The temperature of beta-phase heat treatment influences growth only slightly. The time at temperature, cooling rate, and the fabrication history of the material prior to heat treating are shown to have no effect on the growth of beta treated material. The cooling rate on beta heat treatment is shown to be the major factor influencing surface wrinkling. (ASM International Classification P10d, P11, 3-18, 2-14; U)

INTRODUCTION

THE DIMENSIONAL instability of uranium upon thermal cycling in the alpha-phase temperature range (room temperature to 660 °C) has been studied by a number of investigators in AEC laboratories. The general features of the phenomenon have been summarized by Foote (1)¹ and Chiswik and Kelman (2). In wrought metal such as rolled rod, wire, or plate fabricated at alpha-phase temperatures the instability is generally characterized by substantial elongations in a direction parallel to that of working. The elongations, usually described as "growth", have been shown (3) to depend upon preferred orientation and grain size. The highest growth rates are shown to occur in material having a highly developed texture and fine grain size. In cast metal and metal heat treated at beta-phase (660 to 760 °C) and gamma-phase (760 to 1123 °C) temperatures the instability is manifested mainly in the form of surface roughening or wrinkling. Growth is re-

¹ The figures appearing in parentheses pertain to the references appended to this paper.

A paper presented before the Thirty-Ninth Annual Convention of the Society, held in Chicago, November 4-8, 1957. The authors, S. T. Zegler, R. M. Mayfield, and M. H. Mueller, are associated with Argonne National Laboratory, Lemont, Illinois. Manuscript received April 9, 1957.

stricted, due principally to essentially random orientation and coarse grain size.

This paper deals with an investigation of the effects upon growth and wrinkling of a number of fabrication and heat treatment variables, which, for some time, it has been felt may influence texture and grain size and hence cycling behavior. The chief fabrication variables dealt with are rolling temperature and the amount of rolling reduction; the heat treating variables are (a) temperature, (b) time at temperature, and (c) cooling rate.

MATERIALS AND EXPERIMENTAL PROCEDURE

The uranium used was 99.9+ weight % pure; the major impurity was carbon in concentrations ranging from 0.006 to 0.09 weight %. The materials were in the form of rolled rods fabricated as outlined in Fig. 1 from either vacuum melted castings or 1½-inch diameter billets received from Mallinckrodt Chemical Works. Presented below are significant details of fabrication, heat treatment, specimen preparation, and thermal cycling procedures followed in studies of individual variables.

Rolling Temperature

The effects of variable rolling temperature were studied with specimens prepared from two sets of rods rolled as in schedules T-1 and T-2. For both schedules the starting material was in the form of 3-inch square castings. These were rough rolled to 1½-inch rounds at 600 °C (1110 °F) on a 16-inch by 24-inch open square mill, then heat treated at 725 °C (1335 °F) and water-quenched. This heat treatment usually referred to as "beta treatment" was done to provide an essentially common texture and grain size prior to finish rolling. Finish rolling was performed on hand round (schedule T-1) and oval-edge-oval (schedule T-2) passes on a 9 by 16-inch mill, with the total reduction for both sets of rods about 75%. Heating for rolling was done in oil, lead, or carbonate salt baths (see Fig. 1). Bath temperatures ranged from 300 to 600 °C (1110 °F) at 100 °C intervals, and one bath at 640 °C (1185 °F). To control temperatures during rolling the rounds were returned to the baths between rolling passes and held for times sufficient to erase thermal gradients. Rolling temperatures were measured with a radiation pyrometer acting in conjunction with a high speed recorder. The maximum observed variations in rolling temperatures are given in Table I. After the final rolling pass the billets, ¾-inch diameter, were water-quenched, machine straightened, and then annealed at alpha phase temperatures as detailed in Table I. After annealing, the billets were machined and centerless ground to specimens ⅜-inch diameter by 1-inch long.

The specimens were thermally cycled in the vertical tube cyler described previously (4) between 50–550 °C (120–1020 °F), 2 minutes cold—5 minutes hot—5 seconds transfer times. Length measurements

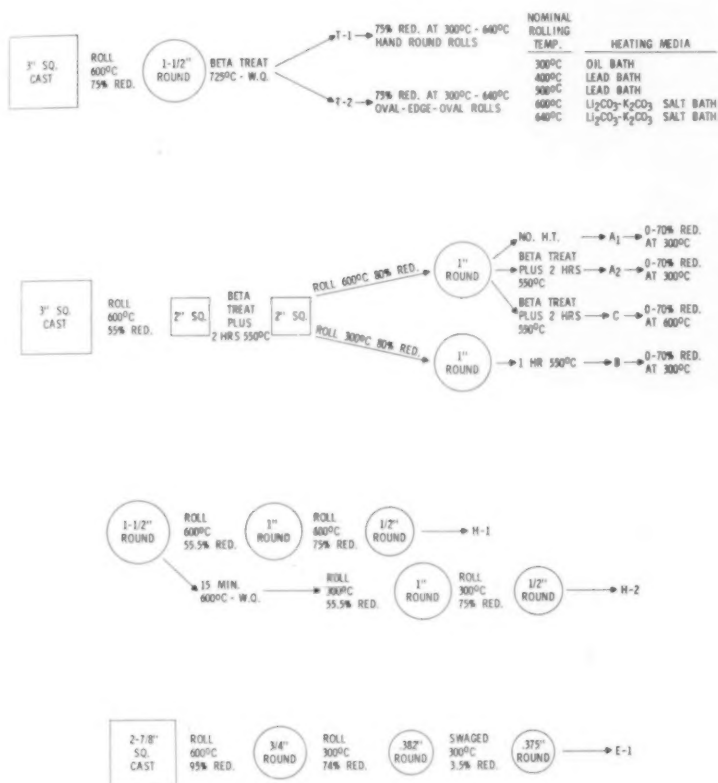


Fig. 1—Rolling Schedules Used for Uranium Rods.

were made with a hand micrometer to the nearest 0.0001 inch at the start of cycling and after N (number of cycles) = 200.

Alpha-Phase Annealing

The effects of annealing at high alpha-phase temperatures subsequent to rolling were studied with specimens prepared from a portion of the rods rolled to 75% reduction at 300 °C (570 °F) on hand round rolls in schedule T-1. The applied times and temperatures of the anneals and corresponding grain sizes obtained are given in Table II. The specimens were prepared and thermally cycled in the same manner described above.

Table I
Variation of Growth with Rolling Temperature

Rod Number	Preheat Bath Temperature (°C)		Rolling Temperature (°C)		Average	Annealing Schedule		Grain Size (mm average diameter)	Thermal Cycling Growth	
	Nominal	Actual	Min.	Max.		Temp. (°C)	Time (hours)		$\frac{L_{200}-L^0}{L^0} \times 100$	$G_A^{(1)}$ (microinches/inch/cycle)
34D-695-7	300	300±7	290	314	304	630	18	0.035	7.12	356
34D-708-7	400	399±3	352	417	389					
34D-708-8	500	500±3	434	469	454					
34D-706-2	600	604±3	551	570	560					
34D-695-2	640	638±3	571	618	590	575	2	0.03	7.72	379
						575	2	0.05-0.06	4.74	386
						575	2	0.055-0.06	4.94	237
44D-681-4	300	298±3	300	315	305	Oval-Edge-Oval Passes (T-2)		0.025-0.030	7.24	362
44D-680-2	400	400±3	378	415	402					
44D-680-6	500	500±3	441	472	459					
44D-677-3	600	596±3	518	542	535					
44D-677-6	640	638±3	545	601	588	575	2	0.025	8.94	447
						575	2	0.030	5.76	288
						575	2	0.053-0.065	3.44	172

(1) $G_A = \frac{1}{L} \cdot \left(\frac{dL}{dN} \right)$ calculated assuming that $\ln \left(\frac{LN}{L_0} \right)$ is a linear function of N between N=0 and N=200. Specimens cycled between 50-550 °C (120-1020 °F), 2 minutes cold, 5 minutes hot, 5 seconds transfer time.

Table II
Variation of Growth with Annealing Treatment

Rod (1) and Specimen Number	Annealing Treatment	Grain size (mm average diameter)	Thermal Cycling Growth	
			$\frac{L_{200}-L_0}{L_0} \times 100$	Gt ⁽²⁾ (microinches/inch/cycle)
34D-695-9 (9A)	2 hr. at 575 °C (1065 °F) in vacuum (0.05 micron)	0.012	9.18	459
34D-695-9 (1)	48 hr. at 635 °C (1175 °F) in vacuum (10-20 micron)	0.03	6.22	311
34D-695-9 (9B)	2 hr. at 575 °C (1065 °F) in argon	0.011	10.18	509
34D-695-7 (1)	18 hr. at 630 °C (1165 °F) in argon	0.035	7.12	356
34D-695-9 (2)	48 hr. at 635 °C (1165 °F) in argon	0.03	5.30	265
34D-695-9 (9C)	48 hr. at 655 °C (1210 °F) in argon	0.045	4.86	243

(1) All rods rolled to 75% reduction in schedule T-1.

(2) $Gt = \frac{1}{L} \cdot \left(\frac{dL}{dN} \right)$ calculated assuming that $\ln \left(\frac{LN}{L_0} \right)$ is a linear function of N between N = 0 and N = 200. Specimens cycled between 50-550 °C (120-1020 °F), 2 minutes cold, 5 minutes hot, 5 seconds transfer time.

Table III
Variation of Growth with Rolling Reduction

Specimen Number and Reduction	Treatment Prior to Final Rolling (see Fig. 1)	Finish Rolling Temp., °C	Thermal Cycling Growth	
			$\frac{L_{200}-L_0}{L_0} \times 100$	Gt ⁽¹⁾ (microinches/inch/cycle)
A1-0%	600 °C (1110 °F) Rolled-80%	300	1.18	59
A1-10%		300	0.44	22
A1-45%		300	1.15	57
A1-70%		300	1.86	92
B-0%	300 °C (570 °F) Rolled-80%	300	3.26	160
B-10%		300	2.20	108
B-45%		300	2.29	113
B-70%		300	2.54	125
A2-0%	600 °C (1110 °F) Rolled-80%	300	0.16	8
A2-10%		300	-0.07	-3.5
A2-45%		300	0.67	33
A2-70%		300	1.49	74
C-0%	600 °C (1110 °F) Rolled-80%	600	0.10	5
C-10%		600	0.09	5
C-45%		600	0.60	30
C-70%		600	1.24	61

(1) $Gt = \frac{1}{L} \cdot \left(\frac{dL}{dN} \right)$ calculated assuming that $\ln \left(\frac{LN}{L_0} \right)$ is a linear function of N between N = 0 and N = 200. Specimens cycled between 50-400 °C (120-750 °F), 2 minutes cold, 5 minutes hot, 5 seconds transfer time.

Rolling Reduction

The materials used to study the influence of rolling reduction were fabricated as in schedules A₁, A₂, B, and C (see Fig. 1). The starting materials in all cases were 3-inch square castings. These were rough rolled at 600 °C (1110 °F) to 2-inch squares and beta treated. A portion of the 2-inch squares was then rolled 80% at 600 °C (1110 °F) to 1-inch rounds. A part of the rounds was designated as A₁ and was used without any further treatment; another part, designated A₂, was beta treated and alpha annealed; a third part was treated the same as A₂, but designated C. These 1-inch rounds were then machined to a pre-calculated diameter so that 1/2-inch rounds would be obtained after

various final reductions were made. The A_1 and A_2 rounds were finish rolled at 300 °C (570 °F) to the following reductions: 0, 5, 10, 25, 45, 60, and 70%. The C rods were similarly reduced at 600 °C (1110 °F). Another portion of the 2-inch squares was rolled to 80% reduction at 300 °C (570 °F) to 1-inch rounds. This material, designated B, was annealed at 550 °C (1020 °F), machined to precalculated diameters and then given the same reductions as mentioned above at 300 °C (570 °F). The described rolling sequences produced three sets of rods rolled to varying reductions at 300 °C (570 °F) from three different starting conditions and one set rolled to similar reductions at 600 °C (1110 °F) after beta heat treating.

The four sets of rods were machined and centerless ground to specimens, $\frac{3}{8}$ -inch diameter, and thermally cycled 200 times in the vertical tube cyler between 50–400 °C, 2 minutes cold, 5 minutes hot, 5 second transfer times. It should be noted that cycling was conducted below the recrystallization temperature for uranium (450 °C). This was done to avoid possible effects of recrystallization which would be certain to occur at high temperatures during the early stages of cycling in materials rolled at 300 °C (570 °F).

Beta Heat Treatment Variables

The effects of temperature, time at temperature, and cooling rate during beta heat treatment were studied with specimens prepared from rods rolled in schedule H-2. The rods were rolled to 89% total reduction at 300 °C (570 °F) on two sets of hand round rolls. Heat treatments were made with as-rolled sections of the rods by either direct immersion in lead baths or with the sections enclosed in an argon atmosphere inside steel containers. The heat treatments applied for study of effects of temperature and time at temperature are detailed in Table IV. The heat treatments involved heating for times of from 2 seconds to 2 hours at 680, 700, and 750 °C (1255, 1290 and 1380 °F) and water quenching. On heat treatments for times up to 120 seconds the specimens were preheated in a lead bath for 5 minutes at 600 °C (1110 °F) (alpha phase) then transferred to the baths at the higher temperatures. The preheating was done solely to minimize the temperature drop of the lead baths at the beta-phase temperatures upon immersion of the specimens. The applied heat treatments for study of cooling rate effects are given in Table V. These involved heating to beta phase temperatures followed by (a) water quenching, (b) furnace cooling, and (c) air or bench cooling. After the applied heat treatments the sections were, except where otherwise noted, annealed for 2 hours at 575 °C (1065 °F) to relieve thermal stresses, then machined and centerless ground to specimens approximately $\frac{3}{8}$ -inch diameter. In all cases thermal cycling was done in the induction cycling unit previously described (4). The applied cycle was between 100–550 °C, 5–7

Table IV
Variation of Growth with Beta-Phase Heat Treating Temperature and Time

Thermal Cycling Growth					Beta-Phase Heat Treatment					Thermal Cycling Growth				
Specimen Number (4)	Pretreat-ment (°)	Temp. (°C)	Time (secs)	$\frac{L_{200} - L_0}{L_0} \pm 100$	Gt(3)(microinches)/inch/cycle		Specimen Number (4)	Pretreat-ment (°)	Temp. (°C)	Time (secs)	$\frac{L_{200} - L_0}{L_0} \pm 100$	Gt(3)(microinches)/inch/cycle		
					N = 0	N = 700						N = 0	N = 700	
6U-39	As Rolled and Annealed			18.7			6U-6	700			5.4	180	65	
							6U-7				6.1	210	75	
							6U-8				7.0	195	85	
							6U-9				6.9	132	20	
							6U-10				0.8	11	11	
							6U-11				1.1	19	5	
							6U-12				1.20	27	27	
							6U-50				1.9	32	5	
							6U-51				1.3	24	24	
											1.7			

(1) All specimens were prepared from rods rolled to 89% reduction at 300 °C in schedule H-2.

(2) Pre-treating was done by direct immersion of the specimens in lead baths.

(3) $Gt = \frac{L - L_0}{L_0}$ determined by graphical analysis of plots of $\ln \frac{L}{L_0}$ versus N in Figs. 4, 5, 6, 8. Specimens cycled between 100-550 °C (210-1020 °F), 5-7 minutes heating, 20-25 minutes cooling.

(4) All specimens were prepared from rods rolled to 89% reduction at 600 °C (1110 °F) in schedule H-1.

* Not Measured. (Warped)

Table V
Variation of Growth with Cooling Rate on Beta Heat Treatment

Specimen No.	Beta Heat Treatment	Anneal Temp. (°C)	Time (hrs)	Thermal Cycling Growth			
				% Growth $\left(\frac{L_N - L_0}{L_0} \times 100\right)$		Gt ⁽¹⁾ (Microinches/inch/cycle)	
				N = 300	N = 700	N = 0	N = 700
3U-30	2 hours at 720 °C (1330 °F); W.Q.	None		0.9	NC	30	—
3U-29	2 hours at 720 °C (1330 °F) furnace cooled ⁽²⁾ .	None		0.9	NC	30	—
3U-19 ⁽³⁾	120 secs. at 680 °C (1255 °F); W.Q.	575	2	0.56	1.3	18	18
3U-20 ⁽³⁾	120 secs. at 680 °C (1255 °F); air or bench cooled ⁽⁴⁾ .	575	2	0.29	0.9	12	12
3U-27 ⁽³⁾	120 secs. at 750 °C (1380 °F); W.Q.	575	2	0.36	0.7	10	10
3U-28 ⁽³⁾	120 secs. at 750 °C (1380 °F); air or bench cooled ⁽⁴⁾ .	575	2	0.41	0.9	12	12

- (1) $Gt = \frac{1}{L}$. (dL/dN) calculated assuming for Spec's Nos. 3U-30; 29 that $\ln(L_N/L_0)$ is a linear function of N between $N=0$ and $N=300$. For the remaining specimens $\ln(L_N/L_0)$ vs N is a straight line function between $N=0$ and $N=700$. Specimens cycled between 100 °C at 550 °C (1020 °F), 5-7 minutes heating, 20-25 minutes cooling.
- (2) Preheated five minutes at 600 °C (1110 °F) prior to immersion in lead baths at 680 and 750 °C (1255-1380 °F).
- (3) Furnace cooled in six hours to room temperature in an argon atmosphere.
- (4) Air cooled in three hours to room temperature.

minutes heating, 20-25 minutes cooling. Length measurements were made at N (number of cycles) = 0, 100, 300, and 700.

The influence of fabrication prior to beta heat treatment was studied with a set of specimens rolled as in H-1. These were heat treated (see Table IV) for variable times at 700 °C (1290 °F), water-quenched, and thermally cycled in the same manner as described above for the specimens rolled in H-2. In schedule H-1 rolling was done to 89% total reduction at 600 °C (1110 °F) on the same stands of hand round rolls as in H-2. The specimens prepared from H-1 and H-2 thus provided a comparison of materials rolled at 300 and 600 °C (570 and 1110 °F) prior to beta heat treatment at 700 °C (1290 °F).

Thermal Cycling Variables

A study was made of the effects of heating and cooling rates during

Table VI
Effects of Thermal Cycling Variables upon Growth of Beta Treated⁽¹⁾ Uranium

Specimen No.	Transfer Times ⁽²⁾		% Growth $\left(\frac{L_N - L_0}{L_0} \times 100\right)$			Gt ⁽³⁾ (Microinches/inch/cycle)	
	Heating	Cooling	N = 100	N = 200	N = 300	N = 0	N = 300
9	5 sec.	5 sec.	-0.29	-0.54	-0.65	-30	Nil
7-1	15 min.	5 sec.	0.30	0.80	1.54	27	76
8-1	5 sec.	15 min.	-0.33	-0.63	-0.65	-37	Nil
7	15 min.	15 min.	0.01	0.12	0.22	Nil	11

(1) Specimens simultaneously beta treated 2 hours at 725°C; (1335°F), water-quenched. Annealed 2 hours at 575°C (1065°F).

(2) Cycling was done between 50-550°C (120-1020 °F), 2 minutes cold, 5 minutes hot, transfer times varied as indicated.

(3) $Gt = \frac{1}{L}$. (dL/dN) determined by graphical analysis of plots of $\ln(L_N/L_0)$ versus N .

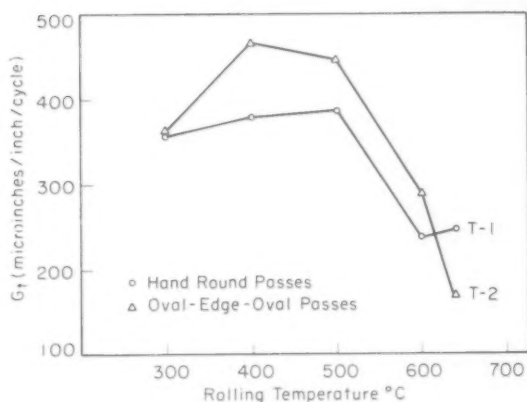


Fig. 2—Effect of Rolling Temperature on Growth Coefficient G_t at $N = 0$ to $N = 200$ (See table I).

cycling upon the dimensional behavior of beta heat treated material. The materials used were in the form of $\frac{3}{8}$ -inch diameter rods fabricated from $\frac{1}{2}$ -inch square castings as in schedule E-1 (see Fig. 1). Heat treatments were made with as rolled and machined sections, 0.36-inch diameter by 0.8-inch long. Heat treatment involved heating for 2 hours at 725 °C (1335 °F) in an argon atmosphere, water quenching, then annealing for 2 hours at 575 °C (1065 °F). The specimens were thermally cycled in the vertical tube cyler between 50–550 °C using variable heating and cooling transfer times with constant holding times at the high and low temperatures. The applied cycles are given in Table VI.

RESULTS

Effects of Rolling Temperature

The growth data of the specimens rolled to 75% reduction at variable alpha-phase temperatures are given in Table I. In Fig. 2 the rates of growth of the specimens in microinches per inch per cycle are plotted as a function of rolling temperature. The rates of growth are expressed as a coefficient defined as:

$$G_t = (1/L) (dL/dN) = (1/N) (\ln L_N/L_0) \text{ microinches/inch/cycle}$$

where L_0 = original length, L_N = length after N cycles. G_t is the slope of the plot $\ln L_N/L_0$ versus N .

The effects of rolling temperature upon growth are clearly evident from Fig. 2; with increasing rolling temperature from 300 to 500 °C (570 to 930 °F) growth increases slightly. For higher temperatures of 600 and 640 °C (1110 and 1185 °F) growth is substantially lower. The

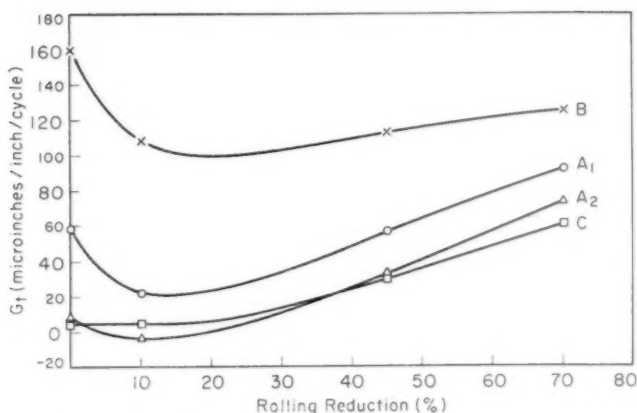


Fig. 3—Effect of Rolling Reduction on Growth Coefficient G_t at $N = 0$ to $N = 200$ (See Table III).

sharp drop in growth for the higher rolling temperatures (above the recrystallization temperature) is interpreted to be related to either the coarser grain size of the materials (see Table I) or to a difference in texture or both.

Effects of Alpha-Phase Annealing

In Table II are data showing the effects upon growth of alpha-phase annealing (above the recrystallization temperature) subsequent to rolling at 300 °C (570 °F). A direct relationship is apparent between the temperature and time of anneal, the grain size and the growth coefficient G_t . With increasing temperature and longer time of annealing, the grain size, as might be expected, is coarser and results upon thermal cycling in a significant decrease in the growth coefficient. The decrease in growth is not, however, attributed to solely grain coarsening. A change in the texture of the material upon annealing as shown by Mueller, et al. (5) is felt to be another likely contributing factor.

Effects of Varying Rolling Reduction

The growth data of the specimens rolled from 10 to 70% reduction at 300 and 600 °C (570 and 1110 °F) in schedules A₁, A₂, B, and C are given in Table III. In Fig. 3 the growth coefficients of the specimens are plotted as a function of rolling reduction. From Fig. 3 the following observations can be made:

1. For the specimens rolled at 300 °C (570 °F) coefficients of growth go through a minimum at 10% reduction and then increase progressively with still higher reductions up to 70%. This is evident from the curves for schedules A₁, A₂, and B. The cause of the mini-

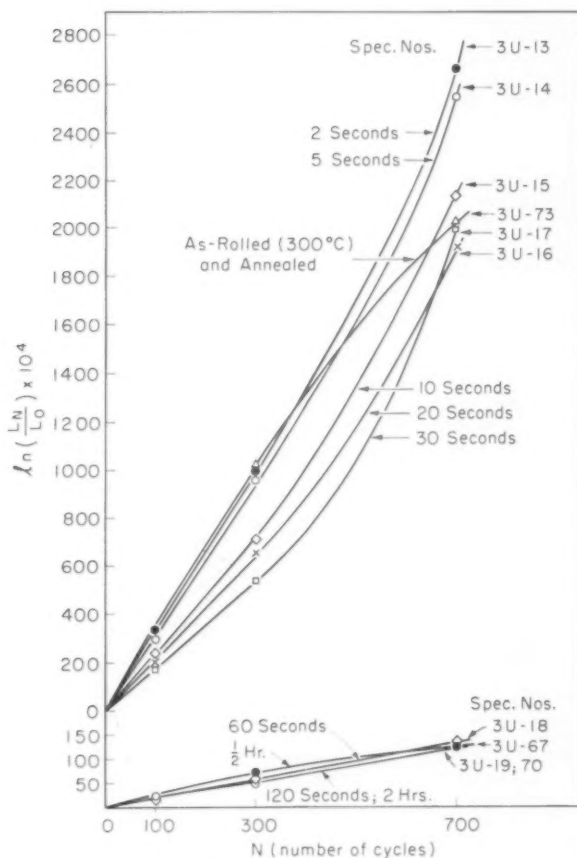


Fig. 4—Plot of $\ln(LN/L_0)$ Versus N for Specimens Heat Treated for Varying Times at 680°C and Water-Quenched. (Material initially rolled at 300°C in schedule H-2).

mums at 10% is unexplained. A change in the texture of the original starting material is held to be the most probable cause. The cause of the progressive increase in growth with higher reductions has been shown in another report (5) to be a sharpening in the degree of preferred orientation.

2. For the specimens rolled at 300°C (570°F) coefficients of growth are dependent upon the initial starting conditions of the materials. This can be seen from comparison of G_t values for specimens in schedule A_2 with those in A_1 and B. The lowest values are observed for A_2 wherein the initial material was beta heat treated; the highest values in B

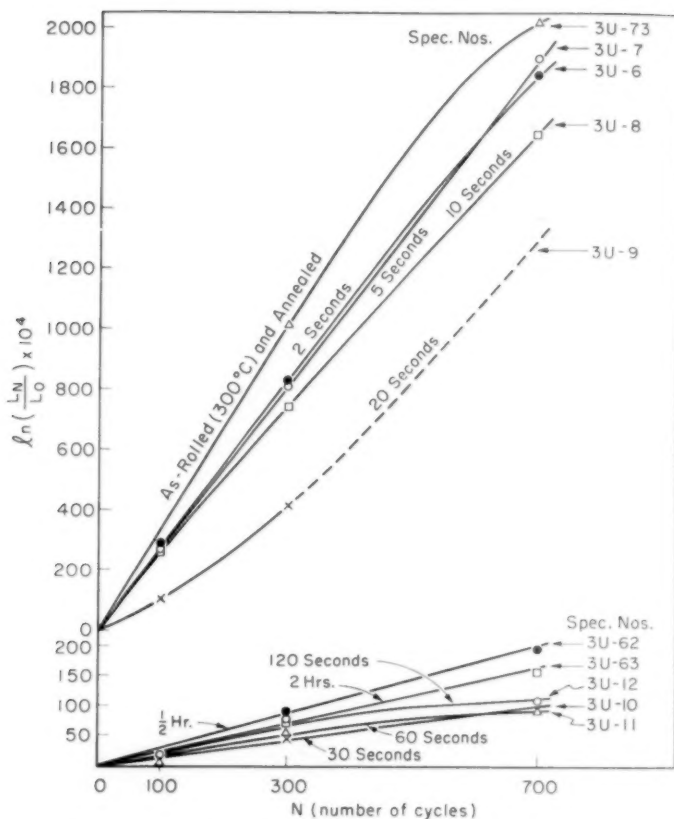


Fig. 5—Plot of $\ln(LN/L_0)$ vs. N for Specimens Heat Treated for Varying Times at 700 °C and Water-Quenched. (Material initially rolled at 300 °C in schedule H-2).

wherein the material was initially rolled 80% at 300 °C (570 °F) and alpha-phase annealed.

3. For the specimens rolled at 600 °C (1110 °F) in schedule C from a beta heat treated condition the coefficient is unchanged up to 10% reduction and then increases progressively with still higher reductions up to 70%. The cause of the increase in growth with higher reductions has also been shown (5) to be related to a sharpening in the degree of preferred orientation. From comparison of the curve for schedule C with that of schedule A₂ it can be seen that the temperature of rolling (600 °C versus 300 °C) has no gross effect on the growth coefficient for thermal cycling below the recrystallization temperature.

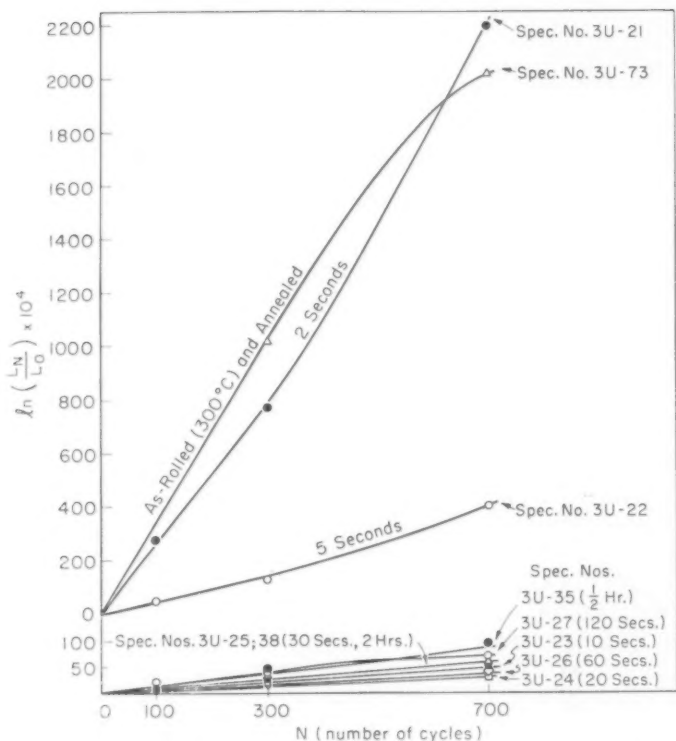


Fig. 6—Plot of $\ln (L_N/L_0)$ vs. N for Specimens Heat Treated for Varying Times at 750°C and Water-Quenched. (Material initially rolled at 300°C in schedule H-2).

Effects of Heat Treating Variables

Temperature and Time—The growth data of the specimens heat treated for varying times at beta-phase temperatures are given in Table IV and shown graphically in Figs. 4 to 6 by plotting the natural logarithm of the growth ratio L_N/L_0 versus N . The slopes of the plots permit as stated above a ready evaluation of rates of growth expressed as a coefficient G_U . For specimens heat treated for minimum times of and longer than 60 seconds at 680°C (1255°F), 30 seconds at 700°C (1290°F), and 10 seconds at 750°C (1380°F) the data between $N=0$ and $N=700$ in most cases fit straight lines indicating that coefficients are constant with N . The data for specimens heat treated for shorter times can be fitted to curves, which in most cases change in slope with N , indicating that coefficients vary; in some cases increasing with N , in others, decreasing. In Table IV are coefficients of the speci-

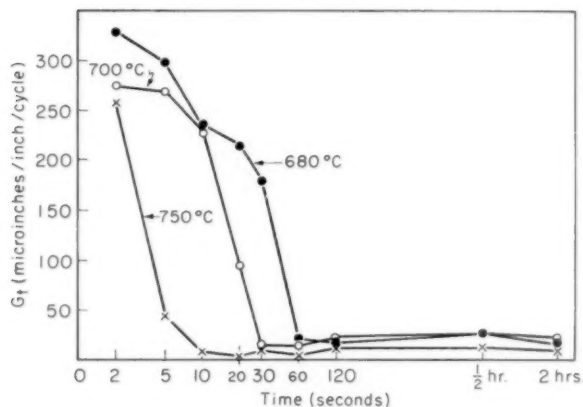


Fig. 7—Effect of Heat Treating Time and Temperature on Growth Coefficient G_t at $N=0$ (See Table IV). (Material initially rolled at 300 °C in schedule H-2).

mens determined by graphical analysis of the slopes of the curves at $N=0$ and $N=700$. In Fig. 7 the coefficients at $N=0$ are plotted as a function of temperature and holding time. From Fig. 7 the effects of the variables upon growth are clearly evident. With temperature constant, increasing time progressively decreases growth to a minimum. The minimum growth is reached after a definite time at temperature and is not influenced by longer time. With increasing temperature the minimum time required for minimum growth is decreased. From metallographic evidence the minimum time is that required to transform the entire section of the material from the alpha to the beta phase on heating. The magnitude of the minimum growth remains constant as the temperature varies from 680 to 700 °C. At 750 °C the magnitude of G_t is smaller by an amount that is small but significant.

The appearance of the specimens after $N=700$ is shown in Fig. 10. As may be seen all of the specimens that were effectively beta treated, i.e., heat treated for the minimum times or longer, evidence surface wrinkling. The extent of wrinkling is fairly consistent for all specimens, clearly indicating that both temperature and time at temperature have no gross effect on wrinkling.

Cooling Rate—The growth data of the specimens heated to beta-phase temperatures and either water-quenched, furnace-cooled, or air-cooled are given in Table V. The data shows that when the temperature and time of heat treatment are constant large variations in the cooling rate have no effect upon growth.

The appearances of a furnace cooled and a water-quenched specimen, Nos. 3U-29 and 3U-30 respectively, after $N=300$ are shown in Fig. 12. Upon comparison it is apparent that slow furnace cooling leads to

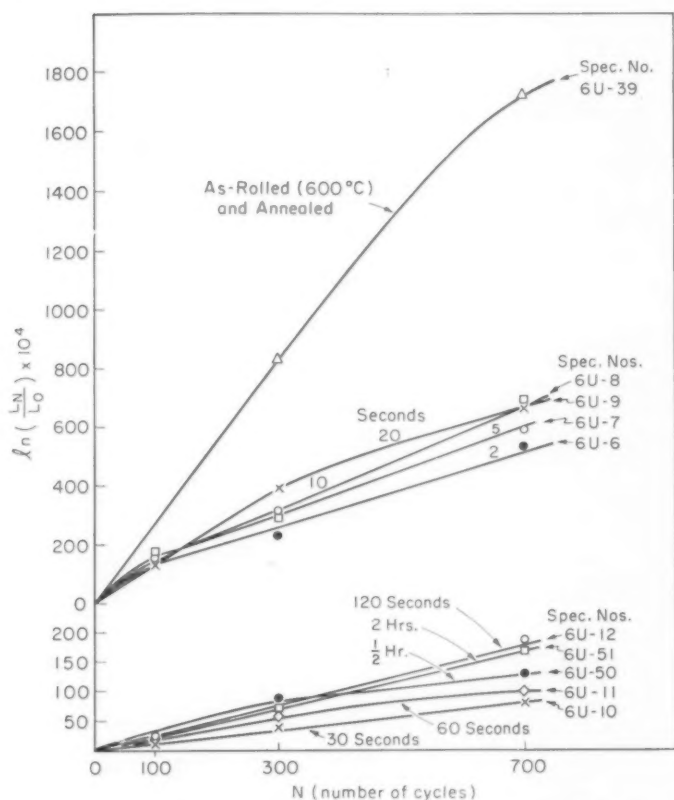


Fig. 8—Plot of $\ln(L_N/L_0)$ Versus N for Specimens Heat Treated for Varying Times at 700°C and Water-Quenched. (Material initially rolled at 600°C in schedule H-1).

more pronounced surface wrinkling. From metallographic evidence the more pronounced wrinkling is interpreted to be related to a coarser alpha-grain size as may be seen from comparison of the photomicrographs of specimens Nos. 3U-29 and 3U-30 in Fig. 13.

Prior Fabrication—In Fig. 9 the growth coefficient G_t at $N = 0$ of the beta-treated specimens (see Table IV) initially rolled at 300 and 600°C (570 – 1110°F) are plotted as a function of heat treating time at 700°C (1290°F). Fig. 9 shows that rolling temperature has no effect upon growth except perhaps when the heat treating times are very short, 2 to 10 seconds. For these times rolling at 600°C (1110°F) appears to relate to lesser growth. The appearances after $N = 700$ of the specimens initially rolled at 600°C (1110°F) are shown in Fig. 11.

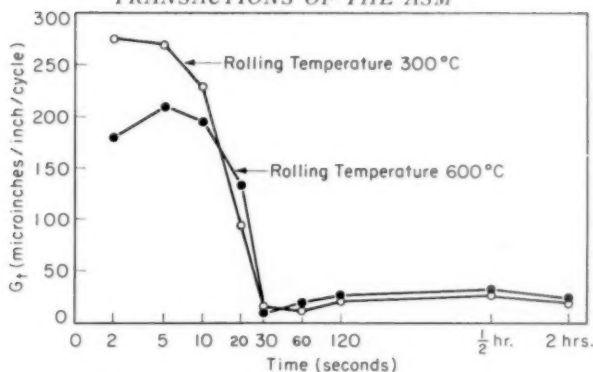


Fig. 9—Effect of Rolling Temperature on Growth Coefficient G_t at $N = 0$ of Beta-Phase Heat Treated (700 °C) Uranium (See Table IV).

From comparison of the specimens in Fig. 11 with those in Fig. 10 it can be seen that prior fabrication has no effect on wrinkling behavior.

Detailed in Table IV and plotted in Figs. 5 and 8 are growth data for the materials upon thermal cycling as-rolled and annealed (Spec. Nos. 3U-73 and 6U-39). Rolling at 600 °C (1110 °F) (above the recrystallization temperature) as opposed to 300 °C (570 °F) is again seen to lead to lesser growth.

Effects of Cycling Variables

In Table VI are data showing the influence of heating and cooling transfer times during thermal cycling upon the growth of beta-treated uranium. The data indicates that with a constant fast cooling transfer time (Spec. Nos. 9 and 7-1) a direct relationship exists between the heating transfer time and the coefficient of growth G_t . With increasing heating transfer time, i.e. slower heating, the coefficient changes from negative (shrinkage in lengths) to positive. With reversed conditions, i.e. with a constant fast heating time (Spec. Nos. 9 and 8-1) increasing the cooling transfer time has no effect on the coefficient, negative in both cases. With both slow heating and slow cooling (Spec. No. 7) the coefficient is practically zero.

SUMMARY AND DISCUSSION

A study has been made showing that the growth of uranium upon thermal cycling in the alpha-phase temperature range is dependent upon a number of variables upon fabrication, heat treatment, and thermal cycling. The growth of rolled rod is shown to be dependent upon rolling temperature, the amount of rolling reduction, and the condition of the material prior to rolling. The influence of rolling temperature is most marked upon thermal cycling to high alpha-phase temperatures

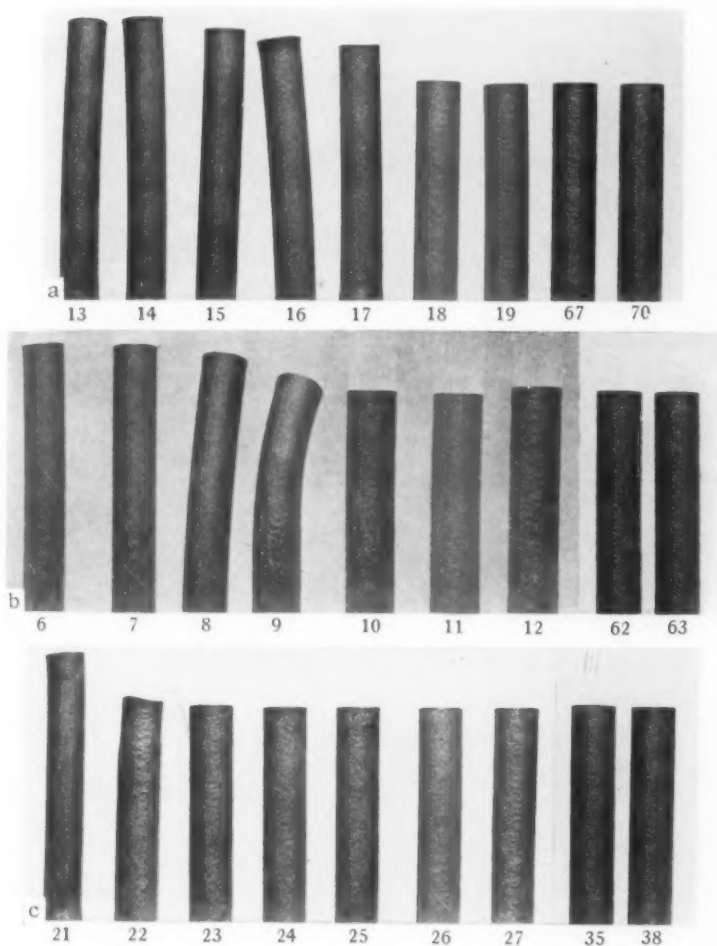


Fig. 10—Specimens Beta Treated for 2, 5, 10, 20, 30, 60, 120 Seconds and $\frac{1}{4}$ and 2 Hours (Left to Right) After 700 Cycles. (Material initially rolled at 300 °C in schedule H-2). a. 680 °C; Water-Quenched. b. 700 °C; Water-Quenched. c. 750 °C; Water-Quenched.

(above the recrystallization temperatures, see Fig. 2). On thermal cycling, however, below the recrystallization temperature, for which rates of growth are in any case small, rolling temperature appears to have no effect (see Fig. 3). In general, increasing amounts of reduction at 300 or 600 °C (570 or 1110 °F) progressively increase the rate of growth on cycling below the recrystallization temperature (see Fig. 3). For any definite amount of reduction, however, the rate of growth

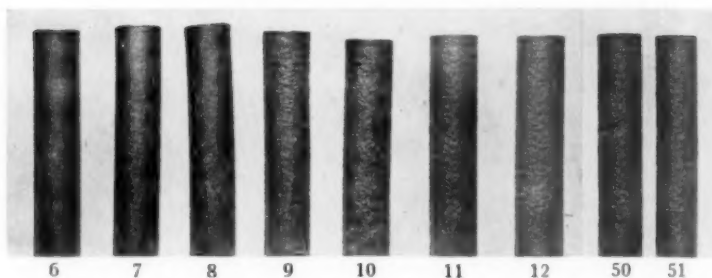


Fig. 11—Specimens Beta Treated for 2, 5, 10, 20, 30, 60, 120 Seconds and $\frac{1}{2}$ and 2 Hours (Left to Right) After 700 Cycles. (Material initially rolled at 600 °C in schedule H-1). 700 °C; Water-Quenched.

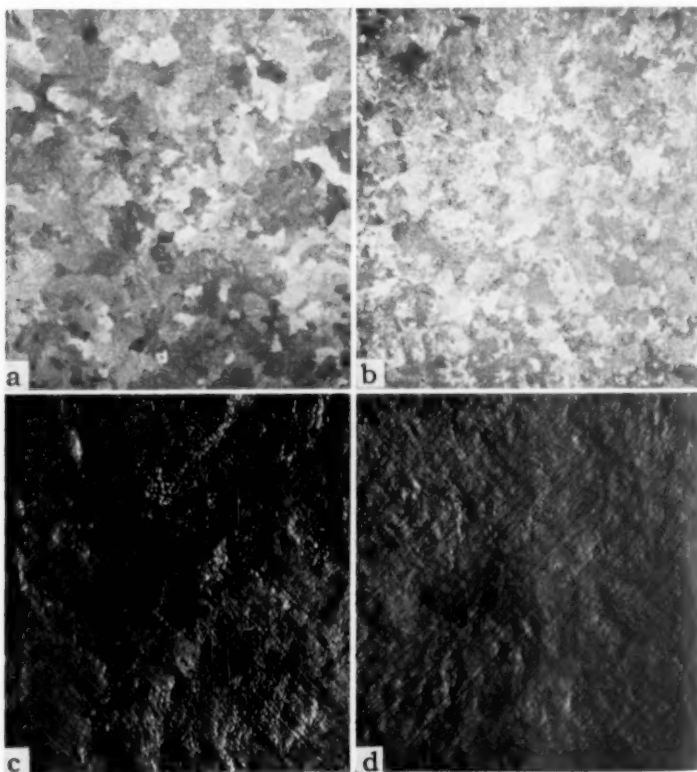


Fig. 12—Macro Grain Size and Surface Roughening of Beta-Treated Bars 3U-29 and 3U-30. (a and c) Specimen 3U-29: Slow furnace cooled after 2 hours at 720 °C. (a) As macroetched before cycling. $\times 7$. (c) Roughening after 300 cycles. $\times 7$. (b and d) Specimen 3U-30: Water-quenched after 2 hours at 720 °C. (b) As macroetched before cycling. $\times 7$. (d) Roughening after 300 cycles. $\times 7$.

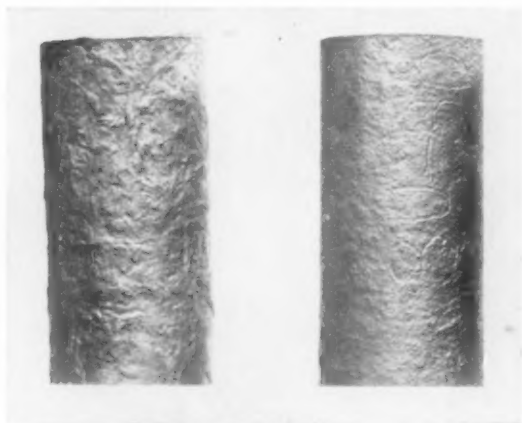


Fig. 12c—Roughening on Surfaces After 300 Cycles. (Left)—3U-29; Furnace-cooled. (Right)—3U-30; Water-quenched. $\times 2$.

is dependent upon the starting condition of the material. For material initially in a randomly oriented condition such as following a beta heat treatment the rate of growth is relatively lower than material having initially a strong preferred orientation. Superimposing rolling at 300 °C (570 °F) upon material previously rolled to high reductions at 300 and 600 °C (1110 °F) is clearly seen to increase growth (see Fig. 3).

Annealing of 300 °C (570 °F) rolled rod at high alpha-phase temperatures (above the recrystallization temperature) results in grain growth and also as shown by Mueller, et al. (5) in a change in the texture. The net effect of these changes is a decrease in the rate of growth as seen from the data in Table II.

The major variables influencing the growth of beta-treated uranium are shown to be those on the thermal cycling test itself. It is observed that either growth or shrinkage may occur dependent apparently only upon the rate of heating. The fact that both growth or shrinkage occurs suggests that some slight degree of preferred orientation may be present. With slow heating-slow cooling it is shown that the rate of growth approaches zero.

The effects of other variables upon the growth of beta treated uranium were studied upon cycling with essentially slow heating-slow cooling (5–7 minutes heating 20–25 minutes cooling). The data shows that growth is influenced only by the temperature of heat treatment (see Fig. 7). The time at temperature, cooling rate, and the fabrication of the material prior to heat treatment appear to have no effect. Surface wrinkling of beta-treated uranium appears dependent only upon the cooling rate during heat treatment. Slower cooling is seen to result in

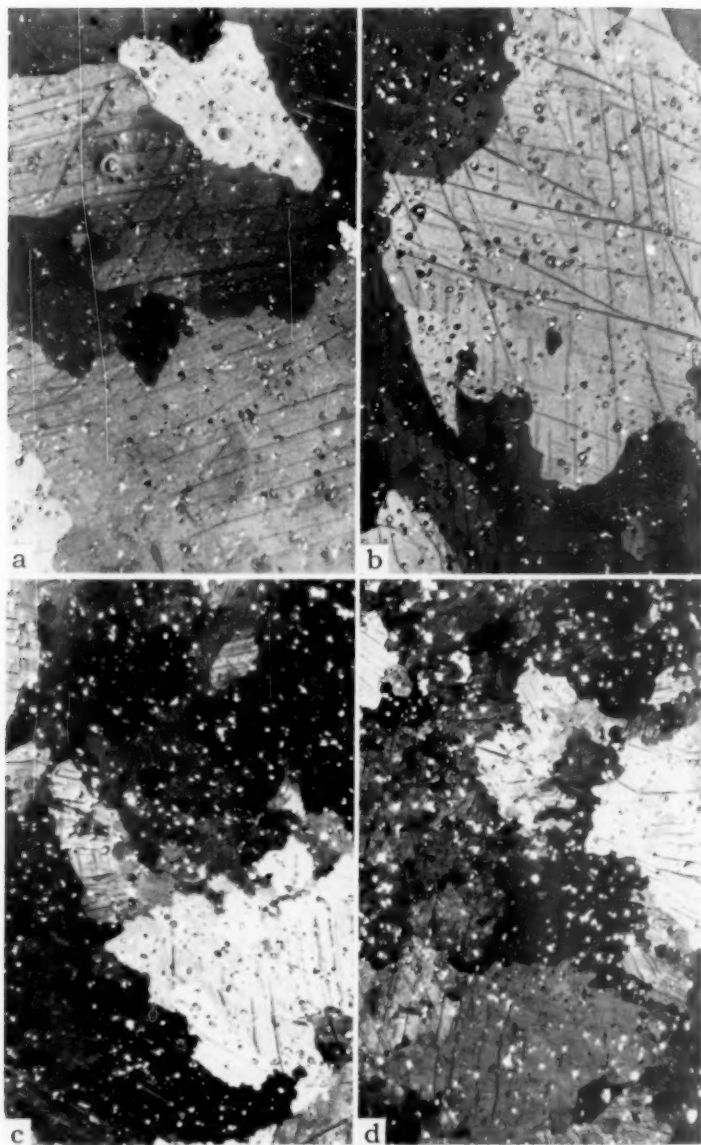


Fig. 13—Microstructure of Beta Heat Treated Specimens. (a) Edge of furnace-cooled specimen. $\times 100$. (b) Center of furnace-cooled specimen. $\times 100$. (c) Edge of water-quenched specimen. $\times 100$. (d) Center of water-quenched specimen. $\times 100$. (a and b) Specimen 3U-29. (c and d) Specimen 3U-30.

a coarser alpha grain size which relates in turn upon cycling to more pronounced wrinkling.

ACKNOWLEDGMENTS

The authors acknowledge the considerable effort of R. E. Macherey in the rolling of the materials. This paper is based upon work performed at the Argonne National Laboratory under the auspices of the Atomic Energy Commission.

References

1. F. G. Foote, "Physical Metallurgy of Uranium," Nuclear Metallurgy Symposium, American Institute of Mining and Metallurgical Engineers, October 1955.
2. H. H. Chiswik and L. R. Kelman, "Thermal Cycling Effects in Uranium," *Proceedings*, the International Conference on the Peaceful Uses of Atomic Energy, Report A/Conf. 8/557, U. S. A., June 29, 1955.
3. H. H. Chiswik, "The Plastic Deformation of Uranium on Thermal Cycling," *TRANSACTIONS*, American Society for Metals, Vol. 49, 1957, p. 622.
4. R. M. Mayfield and S. T. Zegler, "Thermal Cycling Equipment," ANL-4848, November 1, 1951.
5. M. H. Mueller, H. W. Knott and P. A. Beck, "Effect of Varying Reduction on the Preferred Orientation in Rolled Uranium Rods," ANL-5194, May 1954.

EFFECTS OF CYCLING VARIABLES UPON GROWTH RATE OF 300 °C ROLLED URANIUM

BY R. M. MAYFIELD

Abstract

Thermal cycling growth rate of 300 °C (570 °F) rolled uranium rods has been shown to be profoundly affected by cycling variables such as heating and cooling rate, temperature limits, temperature range, and holding times at temperature. For any appreciable growth to occur, the upper cycling temperature must be above 350 °C (660 °F). For a constant cycling temperature range, maximum growth rates per cycle are observed with slow heating and fast cooling. Minimum rates are obtained with fast heating and slow cooling, and equal rates yield intermediate values. In general, the greater the temperature range (ΔT), the greater the resulting growth. Likewise, for a given temperature range, the higher the temperatures the greater the growth. (ASM International Classification P10d, P11; U)

INTRODUCTION

THE PERMANENT dimensional changes that result from the thermal cycling of uranium in the orthorhombic phase have been the subject of extensive investigation. Chiswick (1)¹ has shown that the growth is dependent upon preferred orientation and grain size and several other papers covering a wide range of subjects are pending publication. In most cases these results were based on a constant thermal cycle due to equipment limitations. This paper deals with the effect of cycling variables, per se, on the growth of uranium upon thermal cycling in the alpha temperature range; all other variables being maintained as constant as possible. Cycling characteristics studied include (a) heating and cooling rates, (b) cycling temperature limits, (c) temperature range, and (d) holding times at temperature.

This investigation was prompted by the fact that in the early thermal cycling work, every method of cycling seemed to produce a different growth result making any correlation difficult, at best. In some cases, a similarly fabricated piece of uranium would grow twice as much in one cycling apparatus as in another, within the same temperature limita-

¹ The figures appearing in parentheses pertain to the references appended to this paper.

A paper presented before the Thirty-Ninth Annual Convention of the Society, held in Chicago, November 4-8, 1957. The author, R. M. Mayfield, is associated with the Argonne National Laboratory, Metallurgy Division, Lemont, Illinois. Manuscript received April 4, 1957.

tions. From results such as these, it became apparent that cycling variables must have a marked effect on the resulting growth. A detailed study was considered necessary to obtain data that would aid in the analysis and interpretation of results and also in the evaluation of proposed mechanisms of the growth phenomenon.

CYCLING METHODS

One of the more common methods of thermal cycling employs an open ended tube furnace into which the encapsulated specimen is suspended. After a predetermined time at temperature, the specimen is lowered out of the furnace into a blast of room temperature air. This procedure is noted for its simplicity and generally low cost. However, only a few specimens may be cycled at any one time and little flexibility of operation is possible. Temperature and holding time at temperature are about the only two possible variables.

At ANL, two cyclers were generally used for this type work, an induction cycler and a vertical tube cycler. The power source of the induction cycles is a high frequency spark gap converter. Specimens to be cycled are placed in a stainless steel container of the type shown in Fig. 1, and covered with NaK under an argon blanket, after which the whole assembly is placed in the work coil. When the specimens and container reach the preset upper temperature of the heating cycle, a microswitch on the recorder is activated, which opens the converter circuit and closes the fan circuit. The container is then air-cooled to the desired lower temperature, whereupon the cycle repeats itself. Operational temperatures, heating and cooling rates and coil design can be altered to a degree for special tests, but holding time at temperature is not feasible. A large number of specimens can be cycled at once, being a function, of course, of container and coil design.

A schematic diagram of the vertical tube cycler is shown in Fig. 2. The equipment consists of a vertical transfer tube filled with NaK which passes through the centers of two NaK filled tanks. Thermal cycling is accomplished by automatically transferring the specimens from the center of one tank to the center of another by a pair of drive motors operating through a differential. After the last sojourn in the hot temperature zone (upper tank) the sample is reeled up into the head assembly for cooling and later removal. On the left of the schematic drawing is a typical temperature survey in the transfer tube when the upper and lower tanks are at 550 °C and 100 °C, respectively. A flat temperature zone exists over most of each tank length (about 20 inches).

Extreme flexibility of cycling conditions is obtained by variations in temperature, holding time and transfer time.* Rates of cycling are

* Transfer time is defined as the time required to transfer the samples from the center of one tank to the center of the other. It is, therefore, essentially a measure of the heating or cooling rate of the specimens.

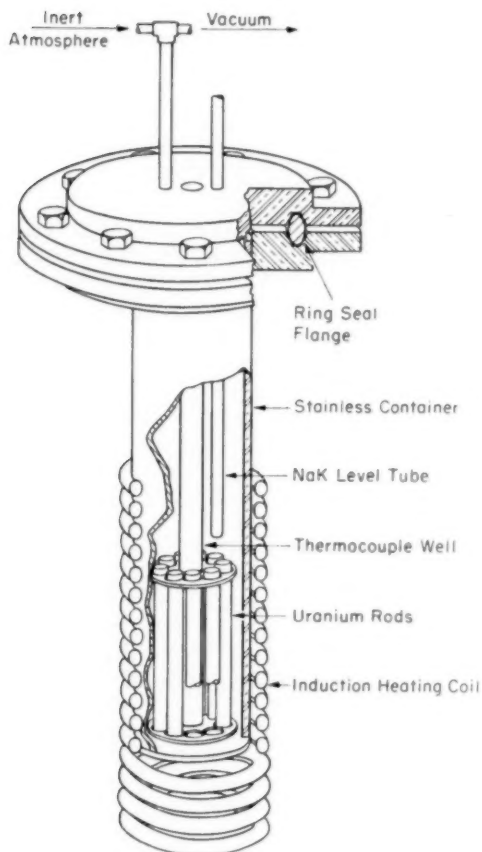


Fig. 1—Schematic Diagram of Bomb Used in Induction Thermal Cycling.

limited only by the rate of heating and cooling of the test pieces and considerable time saving may be effected over other cycling procedures. For the above reasons as well as from the standpoint of control accuracy and reproducibility, the vertical tube cyclers was considered ideally suited for an analysis of the effect of cycling variables upon the growth rate of uranium.

MATERIAL

The uranium used was 99.9+ weight % pure, the major impurity being carbon ranging from 0.05 to 0.07 weight %. The starting mate-

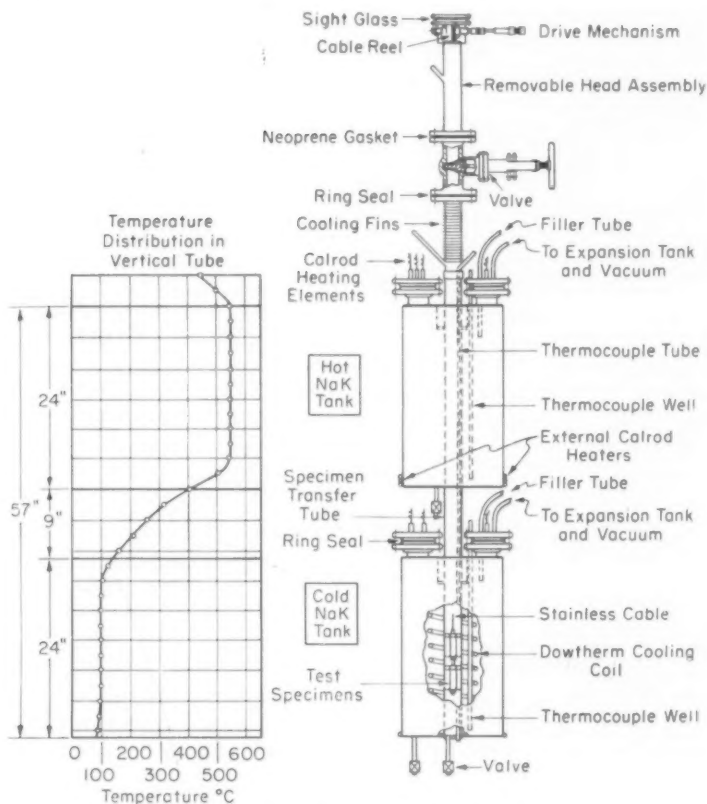


Fig. 2—Schematic Diagram of the Vertical Tube Cycling Unit.

rial was rolled from about $1\frac{3}{8}$ inch to about $\frac{1}{2}$ inch diameter at 300°C (570°F) in hand round passes, using an oil bath to control the rolling temperature. The 300°C (570°F) rolling was selected for two reasons: (a) better fabrication control, assuming constancy of texture and uniformity of results, and (b) high growth values that would permit higher accuracy of measurement, since under some cycling conditions, little dimensional change was to be expected.

The test specimens were about $\frac{3}{8}$ inch in diameter by slightly over 1 inch in length. Before cycling, all test pieces were annealed at 600°C (1110°F) for 2 hours in the cycler followed by 10 cycles between 50 and 600°C (120 – 1110°F) to remove any abnormal or nontypical dimensional changes that might occur in the first few test cycles. Each new group of material was tested under a standard set of thermal cy-

cling conditions to assure uniformity of results. Variation in growth over a large number of duplicate test pieces was found to be less than 2% under a standard set of cycling conditions, so for the most part, only one specimen was used for any one test.

The starting material was, in all cases, of uniform fine grain size, approximately 0.02 millimeter average grain diameter. The orientation of this material, based on the work of Chernock, Mueller and Beck (2,3), appears to consist of a duplex fiber texture in which the (010) poles are nearly parallel to the rolling direction in the major texture component and the (110) poles nearly parallel to the rolling direction in the minor texture. In both components, the (001) pole is perpendicular to the rolling direction. Recrystallization causes a decrease in the (110) component. The recrystallization texture may then be described as consisting of an approximate (140) component together with considerable spread especially towards and including the (010) component. Based on the results of Chiswick (1), the grain size and orientation must be maintained reasonably constant if the true effect of cycling variables is to be evaluated.

EXPERIMENTAL RESULTS

In comparing the thermal cycling growth of the specimens, the significant property is the growth per cycle per unit length at any given cycling level. The evaluation of the growth rate at a cycling level $N = N_a$ must, of course, be based on the length of the specimen corresponding to $N = N_a$ rather than on the original length of the specimen, thus taking into consideration the increments in length that had occurred in cycling between $N = 0$ and $N = N_a$. This "true" or "instantaneous" growth rate is given by the expression

$$G_t = 1/L(dL/dN) = d\ln L/dN$$

where L = length of specimen and N = number of cycles. The usual method of evaluating G_t is to plot $\ln(L/L_0)$ as a function of N , where L_0 = the initial length of the specimen. In this report, all the G_t values reported are based on 100 cycles. For this number of cycles, it has been assumed that $\ln(L/L_0)$ is a linear function of N , then

$$\ln(L/L_0) = G_t N$$

G_t , the thermal cycling growth coefficient, is expressed in microinches per inch per cycle.

Assuming G_t to be a constant and independent of N , the relationship between "percentage growth" and G_t is as follows:

$$\% \text{ growth } (G) = (L - L_0/L_0) \times 100 = (L/L_0 - 1) \times 100$$

$$\text{Now } \ln(L/L_0) = G_t N$$

$$L/L_0 = e^{G_t N}$$

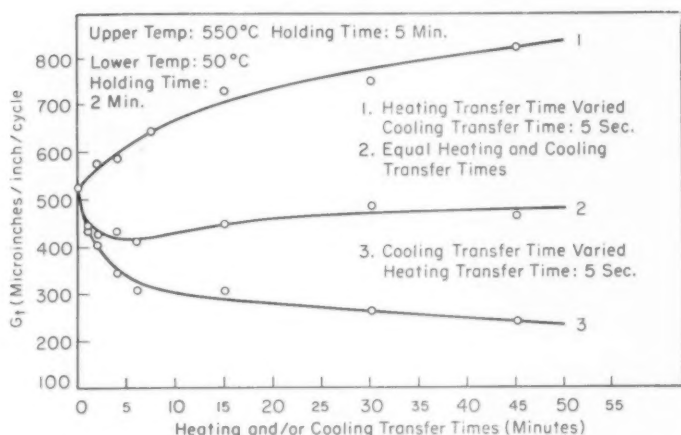


Fig. 3—Effect of Heating and Cooling Transfer Times Upon the Growth Coefficient of 300 °C (570 °F) Rolled Uranium.

Hence $\% \text{ Growth } (G) = (G_t N - 1) 100$
 or $\% \text{ Growth } (G) = (G_t N + \frac{1}{2} G_t^2 N^2 + \frac{1}{6} G_t^3 N^3 + \dots) \times 100$
 If G_t and N are small
 $\% G = 100 G_t N$

If G_t and N are large, the higher terms must be taken into consideration. The G_t value for heavily 300 °C (570 °F) rolled material used in this investigation remains fairly constant up to approximately 1000 cycles. Eventually porosity develops with increased cycling, and the growth rate decreases; however, the initial highly preferred orientation is only slightly randomized after 3000 cycles (4).

Heating and Cooling Transfer Times

The effect of variable heating and cooling transfer times upon the elongation coefficient of 300 °C (570 °F) rolled uranium is illustrated in Fig. 3. The greatest growth rates are obtained when slow heating is combined with fast cooling (Curve 1). Equal heating and cooling transfer times, over a wide range of values, yield intermediate growth rates (Curve 2) and minimum growth results from the combination of fast heating and slow cooling (Curve 3). (The fastest transfer time used in any case was 5 seconds and it is not intended for the curves to approach a zero transfer time.)

Based on the above results, it is difficult to say when the most deformation occurs, heating or cooling, since it will depend in either case on the heating and/or cooling rate involved and the over-all growth per cycle is the algebraic sum of both effects. The theory of dimensional changes due to temperature gradients during thermal cycling as out-

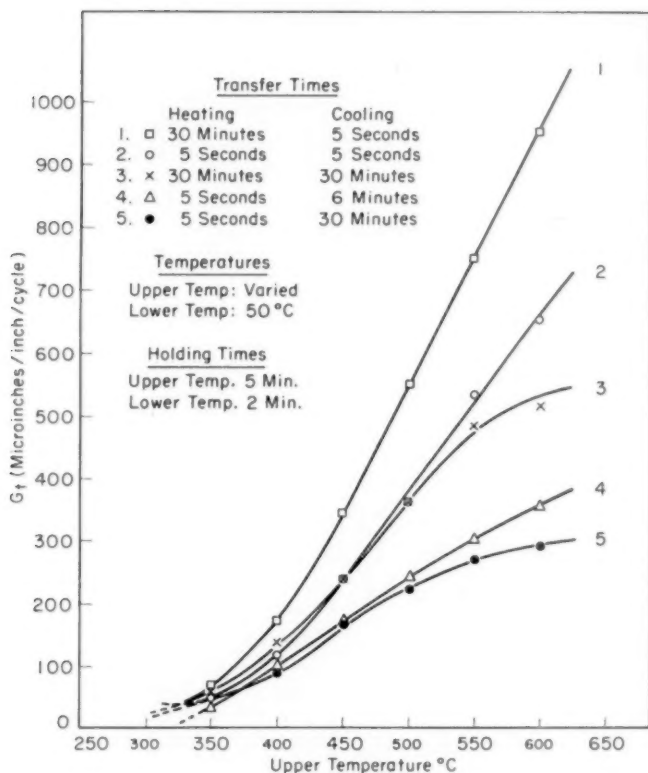


Fig. 4—Variation of the Growth Coefficient With Upper Temperature and Transfer Time.

lined by Woodrow (5) does not appear to be completely valid since on slow heating and cooling, thermal gradients developed in the specimen would be inconsequential; yet considerable growth results, as shown by Curve 2 of Fig. 3. No appreciable change in growth values is anticipated with even slower heating and cooling times.

If, however, grain boundary relaxation is employed in any way as an explanation of the growth phenomenon, then the temperature at which boundary relaxation becomes operative must be dependent upon heating and cooling rates.

Upper Cycling Temperature

With increasing upper cycling temperatures, above about 350 °C (660 °F), and constant lower temperatures, the growth rate increases as shown in Fig. 4. The curves verify the general relationship de-

scribed previously between growth rates and rates of heating and cooling. Maximum rates are obtained when slow heating and fast cooling are combined with a large temperature range of cycling.

Although the growth rate decreases with decreasing upper temperature, significant growths have been obtained as a result of exposing highly orientated uranium to an extremely large number of induction cycles below 350 °C (660 °F) as indicated by the results in Table I.

Table I
Growth of 300 °C Rolled Uranium As A Result
of Low Temperature Induction Cycling (6)

Fabrication & Heat Treatment	Test No.	100–550 °C G_t (100 cycles)	Test No.	20–300 °C G_t (2000 cycles)
300 °C Rolled	7B	280	2A	2.7
575 °C Annealed			5A	2.4
			6A	2.4

The growth rates obtained after 2000 cycles between 20–300 °C (70–570 °F) are low but significant, and appreciable elongation would, no doubt, result with continued cycling. The magnitude of the G_t value under standard conditions of induction cycling should be noted; the value reported is slightly less than $\frac{1}{2}$ of the 5 second heating and cooling transfer time value of Fig. 3.

Temperature Range (ΔT)

The effect of the temperature range upon the resulting growth rate is shown in Fig. 5. (Range is defined as the temperature difference over which the specimens are cycled.) The family of curves show conclusively, that for upper temperatures above about 350 °C (660 °F), the greater the cycling temperature range, the greater the growth. Further, for any given temperature range, the higher the temperature level, the greater the resulting growth.

The lower temperature curves are actually isotherms connecting appropriate range points on the upper temperature curves rather than being influenced by the location of experimental data points. (The shape of the 50 °C (120 °F) lower temperature curve agrees with the 5 second heating and cooling transfer time curve of Fig. 4, except here it is plotted against temperature range instead of upper temperature.) The effect of the temperature range variable is further illustrated in Fig. 6 using 5 second heating and 6 minute cooling transfer times; in all other respects, cycling conditions are the same as in Fig. 5. It is at once apparent that the G_t values have been depressed, as a result of the lowered cooling rate. Based on the effects of heating and cooling rates as illustrated by Figs. 3 and 4, this decrease in G_t values is in agreement with what should be expected.

The lower portion of the 600 °C (1110 °F) upper temperature curve of Fig. 6 is somewhat doubtful. The experimental points are shown as

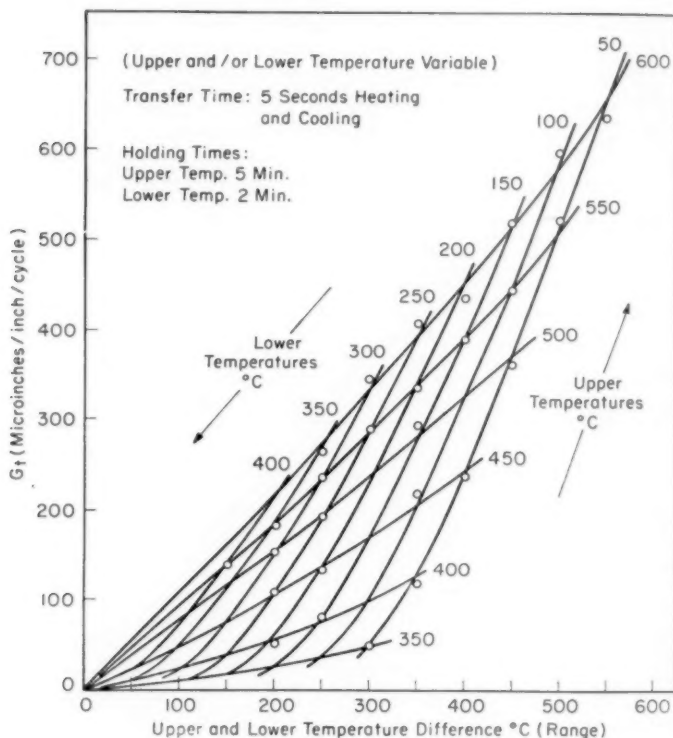


Fig. 5—Composite Effect of Temperature Range (ΔT) on the Growth Coefficient.

X's and are considerably below the 600 °C (1110 °F) curve. This is believed to be an equipment error. Thermal gradient disturbances may occur when both tanks are at relatively high temperatures. With fast transfer times, this condition may not be troublesome, but a variation in growth characteristics apparently results with slower transfer times.

A family of temperature range curves of the type shown in Figs. 5 and 6 can be constructed for any given conditions of heating and cooling rates as a first approximation requiring only a knowledge of the variation of G_t with the upper cycling temperature. This is accomplished by plotting the G_t values versus temperature range, and then connecting these points by straight lines to the origin. The intersections of upper and lower temperature curves then represent the approximate G_t one would obtain on cycling between the corresponding temperatures. This method would, however, be subject to increasingly greater error when the cycling conditions are such as to cause the G_t value to

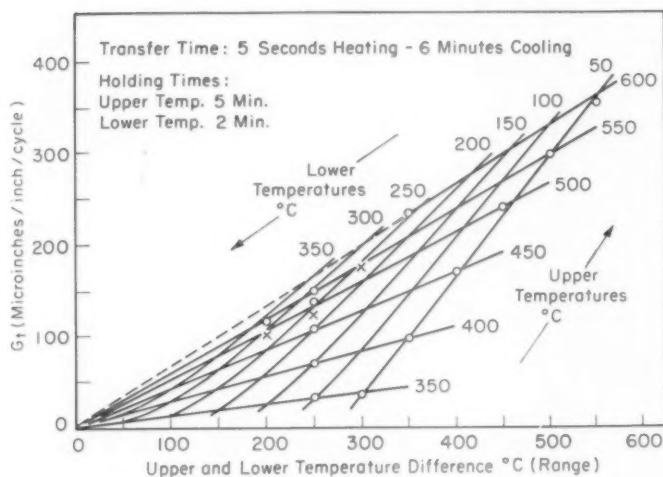


Fig. 6—Composite Effect of Temperature Range (ΔT) on the Growth Coefficient at Lower Cooling Rates.

drop off appreciably with increasing upper temperature. This condition would be most prevalent where slow cooling rates were employed. (See curves 3 and 5 of Fig. 4.)

Only limited work by other investigators on the effect of temperature range have been reported. Boas and Honeycombe (7) concluded that the deformations noted in cadmium as a result of thermal cycling were due to anisotropy of thermal expansion and that a theoretical estimation of the stresses showed that their magnitude was directly proportional to the temperature range employed.

Kelman (6) induction cycled 300 °C (570 °F) rolled uranium between 500 and 550 °C (930 and 1020 °F) for 2200 cycles with the following results:

Table II
Growth of 300 °C Rolled Uranium Due To Small Thermal Cycles at Elevated Temperatures

Fabrication & Heat Treatment	Test No.	100–550 °C G_t (100 cycles)	500–550 °C G_t (2200 cycles)
300 °C Rolled	40	200	3.0
575 °C Annealed	41	160	3.4

The G_t value obtained for a ΔT of 50 °C (120 °F), the upper and lower temperatures being 550 and 500 °C (1020 and 930 °F) respectively, is of slightly larger magnitude than those values reported in Table I where a 280 °C (505 °F) ΔT was employed but the upper temperature was 300 °C (570 °F).

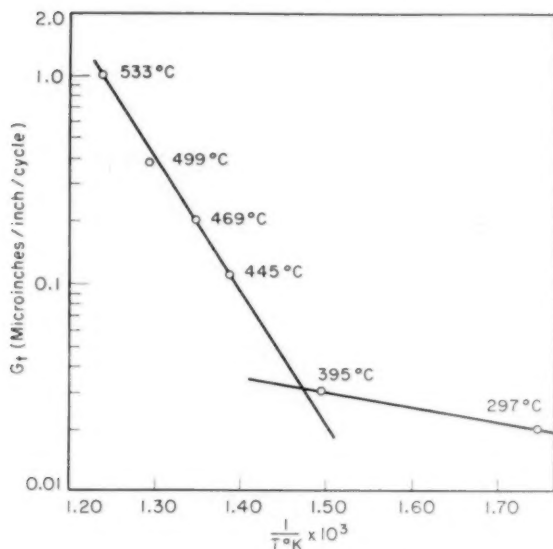


Fig. 7—Growth Rate Versus Reciprocal Absolute Temperature for 300 °C (570 °F) Rolled, Alpha Annealed Uranium, Thermal Cycled ± 2 °C About Various Mean Temperatures.

Muehlenkamp, Shober and Schwöpe (8) have found uranium to elongate when cycled over a ΔT of ± 2 °C. The effect of such a cycle at various mean temperatures is shown in Fig. 7.* (Measurable changes were obtained by using a large number of cycles; however, the results are reported for 100 cycles.) A transition temperature occurs at approximately 405 °C (760 °F) below which the growth is nearly independent of temperature. The activation energy for the upper curve is about 3 KCal/gram atom while the lower portion corresponds to an energy of 29 KCal/gram atom.

Because of this effect of a small ΔT , which may be caused by the on-off cycle of a temperature controller, some doubt is cast upon uranium creep test data and Muehlenkamp, Shober and Schwöpe (8) maintain that before the true creep properties of uranium can be obtained, a quantitative evaluation of the thermal cycling effect will have to be evolved, or true isothermal conditions will have to be maintained.

Holding Time

The growth rate is dependent upon the holding time at the upper cycling temperature as illustrated in Fig. 8. With increasing holding time above about 350 °C (660 °F), the growth rate increases rapidly

* The ordinate scale has been converted from percent deformation per 100 cycles $\times 10^3$ to G_t by use of the formula

$$G_t = \%G/100N \text{ or } \%G = 100G_tN$$

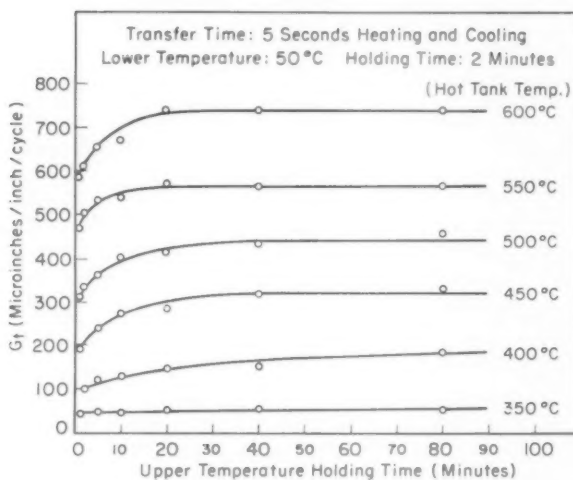


Fig. 8—Influence of Time at Temperature Upon the Growth Coefficient.

at first, then more slowly until it approaches a constant value. The higher the temperature, the shorter the time required for the growth rate to level off. This time-temperature dependence suggests that grain boundary relaxation at elevated temperature may offer a significant contribution to any plausible explanation of the growth phenomenon. Although not illustrated, increasing the time at lower temperature (up to 350 °C [660 °F]) had no measurable effect upon the resulting growth rates.

It should be noted that the constant growth rates obtained at the several upper temperatures of Fig. 8 are higher in all cases than the 5 minute holding time values of Figs. 3-6. This situation does not invalidate any of the results where 5 minute holding times were used; it merely lowers values from the constant growth rate value, at the same time effecting a considerable saving in time.

The result of plotting the constant growth rates of Fig. 8 versus the reciprocal of absolute temperature is illustrated in Fig. 9. A transition temperature occurs at about 415 °C (780 °F), which is in agreement with the results of Fig. 7 and also with internal friction and recrystallization studies (9,10). Below 415 °C (780 °F) grain boundary flow is restricted and less growth results. The activation energies have been computed to be 22 KCal/gram atom below the transition point while above 410 °C (770 °F), the temperature dependence of G_t corresponds to an activation energy of only 7 KCal/gram atom. The rate of growth cannot be expressed by a simple exponential rate equation of the type

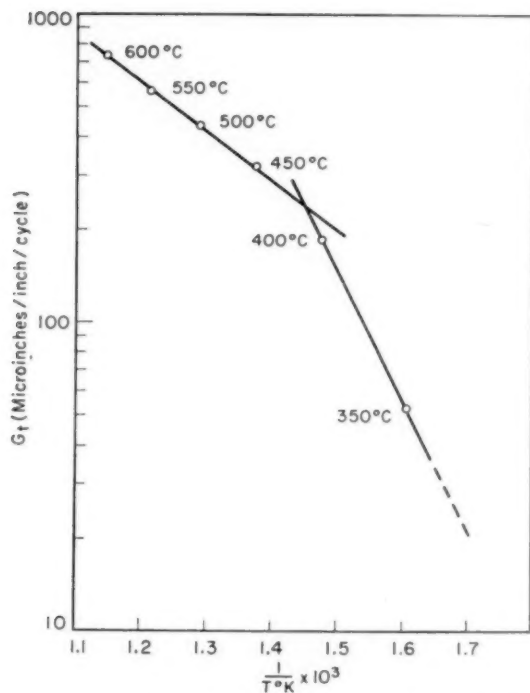


Fig. 9—Constant Growth Rate at Various Upper Temperatures Versus Reciprocal Absolute Temperature.

$G_t = A_e^{-Q/RT}$ because of this pronounced change in relationship at 415 °C (780 °F).

CONCLUSIONS

The dimensional changes that result from thermal cycling 300 °C (570 °F) rolled uranium in the alpha temperature range are profoundly affected by cycling variables such as heating and cooling rates, temperature limits, temperature range and holding time.

Transfer times (heating and cooling rates) exert a marked effect upon the growth characteristics, other factors being constant. Maximum growth is obtained when slow heating is combined with fast cooling; minimum growth results from a reversal of this combination and equal heating and cooling rates yield intermediate values.

Analysis of the temperature limits and temperature range effects, considered jointly indicates that little growth results if the upper temperature of the cycling range is below about 350 °C (660 °F). In

general, above this limiting condition, the greater the temperature range (ΔT) the greater the resulting growth. For a given temperature range, the higher the temperatures (upper and lower limits) the greater the growth.

The maximum amount of growth obtained is dependent upon the holding time at the upper cycling temperature. In general, as the upper temperature increases, the holding time required to reach a constant growth rate decreases.

Certain intrinsic operating or construction characteristics of the vertical tube cyler have made complete isolation of specific variables difficult. For instance, the actual time at temperature may be longer than the specified holding time when using slow transfers. It should be further realized that cycling values obtained in this study might not necessarily agree in magnitude with those obtained by vastly different means.

The effect of a cycling variable, per se, upon the growth characteristic has generally far outweighed any growth behavior that might be attributed to the overlapping of control variables. It is similarly anticipated that the effect of variables, herein described, would be apparent by other test means; granted, the actual magnitude of values would not necessarily be in agreement.

ACKNOWLEDGMENTS

The author acknowledges with thanks the advice and guidance of F. G. Foote, S. H. Paine, Jr. and H. H. Chiswik. Thanks are also due to R. E. Macherey for fabricating all test material; M. H. Mueller for texture analysis; D. C. Woodard for maintaining the electrical control devices and M. E. Monahan for preparing the graphs. This paper is based upon work performed at the Argonne National Laboratory under the auspices of the Atomic Energy Commission.

References

1. H. H. Chiswik, "The Plastic Deformation of Uranium on Thermal Cycling," *TRANSACTIONS, American Society for Metals*, Vol. 49, 1957, p. 622.
2. W. P. Chernock and P. A. Beck, "Quantitative Determination of Rolling and Recrystallization Textures in 600 °C and 300 °C Rolled Uranium Rods," ANL-4839, August 1951.
3. M. H. Mueller, H. W. Knott and P. A. Beck, "Effect of Varying Reduction on the Preferred Orientation in Rolled Uranium Rods," ANL-5194, 1954; AECD-4208.
4. L. T. Lloyd and R. M. Mayfield, "Microstructural Changes of Uranium Upon Thermal Cycling," *TRANSACTIONS, American Society for Metals*, This Vol., 1958, p. 954.
5. J. Woodrow, "The Axial Contraction of Irradiated Uranium Rods," Report No. AERE-EM-33, Feb. 9, 1950.
6. L. R. Kelman, "Dimensional Changes in Uranium Under Thermal Cycling," *Journal of Metals and Ceramics*, Issue #4, September 1949, TID-68.
7. W. Boas and R. W. K. Honeycombe, "The Anisotropy of Thermal Expansion as a Cause of Deformation in Metals and Alloys," *Proceedings of the Royal Society*, Vol. 188, Series A, 1947, p. 427-439.

8. G. T. Muehlenkamp, F. R. Shoher and A. D. Schwoppe, "Deformation of Uranium During Thermal Cycling and Under Constant Load," Battelle Memorial Institute, BMI-735, 1952.
9. G. T. Muehlenkamp, A. D. Schwoppe and L. R. Jackson, "Deformation of Uranium During Thermal Cycling," TID-5061, Vol. 1, Jan. 31, 1952, p. 235.
10. E. E. Hayes, "Recrystallization of Cold Rolled Uranium," *Journal of Metals and Ceramics*, TID-67, Issue #3, May 1949, p. 13.

DISCUSSION

Written Discussion: By S. F. Pugh, United Kingdom Atomic Energy Authority, Metallurgy Div., Atomic Energy Research Establishment, Harwell, Didcot, Berks., England.

Most of the quantitative data published in the paper was included in a Geneva paper by Chiswick and Kelman and I have used the data to obtain an activation energy for the thermally activated processes which occur at the upper cycling temperature and which contribute an essential part in the growth mechanism. The analysis follows the method evolved by Dorn based on the conditions that, (a) for any given stress the metallurgical structure developed during creep depends only on the strain history and (b) for a given stress the strain is a function of $te^{-Q/RT}$, where t is the time and T the temperature at which the stress is applied, since when these conditions are fulfilled an equation of state can be used.

The results shown in Fig. 8 of the paper by Mayfield are for constant lower cycling temperatures, therefore the stress within the specimen will increase as the upper cycling temperature increases since the temperature range of the cycling also increases. It is, however, possible to correct these results for constant internal stress history by using the relationship indicated in Fig. 5 namely that for a constant upper cycling temperature the growth is directly proportional to the temperature range of the cycle. Thus each of the curves in Fig. 8 can be corrected to constant ΔT and then pairs of curves can be used to give values of t and T which will result in the same growth at different upper cycling temperatures. These values of t and T can then be used to solve for Q in the following equation:

$$\ln t_1/t_2 = Q/R \{1/T_1 - 1/T_2\}$$

The value of 65 ± 10 K calories/gram atom is obtained by this method and is in good agreement with values deduced from diffusion measurements.

This method thus indicates that an essential part of the growth mechanism is a thermally activated process; the activation energy does not change significantly in the range 350–600 °C (660–1110 °F) and provides further support to Dorn's proposal that creep processes at higher temperatures are controlled mainly by self-diffusion processes.

Incidentally the method used by Mayfield to extract an activation energy from his growth data is quite invalid since he has not compared values of t and T for constant growth and constant internal stress. The results he obtains therefore have no real meaning.

Written Discussion: By R. E. Maringer, Battelle Memorial Institute, Columbus, Ohio.

Dr. Mayfield has provided, in this paper, a wealth of experimental data showing

in a very detailed way the sensitivity of the "growth" of uranium during thermal cycling on the experimental conditions. These are the kind of data necessary when testing an hypothesis concerning the underlying causes of the observed phenomena.

Plotting these data as the logarithm of G , versus the reciprocal of the absolute temperature, as the author does in Fig. 9, may, however, be misleading. The nature of the plot suggests that perhaps two mechanisms are operative and that there is a transition, near 400°C (750°F), from one to the other. From my own work on this problem, I would be happy to believe that such is the case. However, there is a simpler alternative that should be brought forth.

If one extrapolates the curves of constant minimum cyclic temperature in Fig. 5 (considering them as straight lines rather than the slight curves as shown) to zero growth rate, one obtains a temperature range (ΔT) which must be covered during a cycle to obtain growth. This is, of course, ignoring the very small growth rates observed even when the temperature change is below the defined ΔT .

It is interesting then to plot the observed ΔT versus the lowest temperature of the appropriate temperature cycle. This is shown in the accompanying graph.

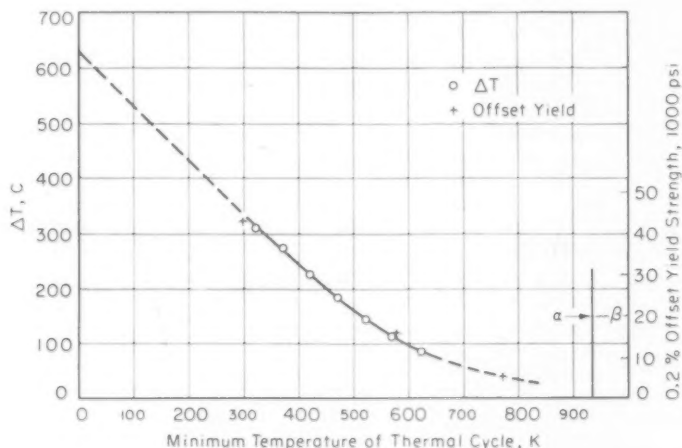


Fig. 10—Temperature Dependence of ΔT and 0.2% Offset Yield Strength in 300°C Rolled, Alpha-Annealed Uranium.

Included on the graph are three points representing the 0.2% offset yield strength of 300°C rolled, alpha annealed uranium. The pronounced similarity of the slopes of these curves suggests that the observed ΔT is the temperature range required to build up internal stresses (due to the anisotropic thermal expansion) of the magnitude of the yield stress. If this is true, the "transition" shown in Fig. 9 may be the result only of the method of plotting.

If one extrapolates the curve shown in the accompanying graph to lower temperatures, it appears that ΔT increases approximately as fast as the minimum cycling temperature decreases. Thus, lowering the minimum cycling temperature below 50°C might not increase the growth rate for a constant maximum cycling temperature. Are there any experimental data to this effect?

Author's Reply

The author wishes to thank the contributors of discussions to this paper. They should help immeasurably to clarify as well as further develop certain relationships and perhaps prompt additional work on areas of uncertainty.

Mr. Pugh's application of Dorn's temperature, compensated time, equations of state to this data is of considerable interest and of general fundamental significance. I have verified the activation energy values of 65 ± 10 K cal/gram atom obtained at most temperatures, but I have been unsuccessful in finding a significant diffusion value for uranium with which a comparison could be made. How a similar value was deduced from diffusion measurements on uranium would be of utmost importance if any real meaning were to be derived from the comparison. I also find it difficult to extract a satisfactory activation energy using the 350 °C (660 °F) data in Fig. 8 since there is little or no change in G_t with time; consequently, I feel it would be appropriate, at this time to limit the constant activation energy to the temperature range 400–600 °C (750–1110 °F).

I cannot disagree with Mr. Pugh's criticism of my method of extracting activation energies from the curve of Fig. 9. However, I should like to emphasize that two different processes operate at two different temperature levels and I attached no immediate significance to the activation energy values derived therefrom. Unfortunately, Fig. 9 contains too many variables. If the ΔT variable is removed, a similar relationship is obtained—with somewhat lower G_t values—the break is still evident.

Dorn has indicated that his method of analysis may apply, generally speaking, only when the temperature is above that for rapid crystal recovery and might not necessarily correlate with creep data obtained at lower temperatures. He therefore suggests that two alternate mechanisms for creep may exist, one predominating at the higher temperatures and the other predominating over the lower temperatures. Fig. 9 was offered in this same belief, namely, that there are two mechanisms in existence.

Mr. Maringer views this break in the curve of Fig. 9 as a possible consequence of the method of plotting and suggests an interesting alternate which I feel at this time may be somewhat oversimplified. The ΔT versus minimum temperature curve will change with both holding time at temperature and transfer times (heating and cooling rates). The latter might have to be disregarded in some cases due to the overlapping of control variables mentioned. How the yield strength would vary with strain rate would be of utmost significance at the temperatures indicated if a correlation were to exist. It may be possible that such is the case, however, a more complete analysis would be required before it would be possible to indicate that only one mechanism was involved here.

In answer to Mr. Maringer's question, there are no experimental data available at Argonne to indicate that minimum cycling temperatures below 50 °C might not increase the growth rate for a constant maximum cycling temperature as indicated from the extrapolation of Maringer's alternate ΔT vs min. temperature plot.

THE GROWTH OF URANIUM UPON THERMAL CYCLING

By J. E. BURKE AND A. M. TURKALO

Abstract

Uranium bars which are subjected to repeated cycles of heating and cooling may change shape: under extreme conditions the length may double or triple. This can lead to difficulty in the utilization of uranium. In this paper, a model for the process is described, and is shown to account qualitatively for the distortions observed in uranium.

The driving force is the stress that develops between differently oriented anisotropic uranium grains when the temperature is changed. At high temperatures this stress is relaxed by viscous flow at the grain boundary, and at low temperatures by crystallographic slip in some of the grains. The two mechanisms of relaxation are shown to combine to produce a "thermal ratchet" which causes continued elongation of textured polycrystalline uranium on thermal cycling. (ASM International Classification: P10d, P11; U)

THE ELONGATIONS which occur in uranium wires and rods when they are repeatedly cycled between room temperature and about 500 °C (930 °F) have been reported in the literature (1,2),¹ and the effects of temperature, heating and cooling rates, texture of the specimen, grain size and purity have been described. This irreversible behavior must be caused by stress relaxation processes which operate competitively in different parts of the thermal cycle. The mechanism for such a "thermal ratchet" was described by the present authors in 1952 (3) and was shown to explain the plastic distortions produced in zinc bicrystals by thermal cycling. In this paper the thermal ratchet is used to explain the growth under thermal cycling of polycrystalline uranium.*

THE MECHANISM OF THE THERMAL RATCHET

The ratchet proposed has as its two competitive mechanisms of deformation: (a) crystallographic slip at low temperatures and (b)

¹ The figures appearing in parentheses pertain to the references appended to this paper.

* Historically, the development was in the opposite order. H. Brooks and J. P. Howe pointed out in 1950 that some kind of a thermal ratchet must operate to produce the growth in uranium. Burke postulated the mechanism described here, and Burke and Turkalo confirmed its operation with the reported observations on zinc bicrystals.

A paper presented before the Thirty-Ninth Annual Convention of the Society, held in Chicago, November 4-8, 1957. The authors, J. E. Burke and A. M. Turkalo, are associated with General Electric Research Laboratory, Schenectady, New York. Manuscript received April 11, 1957.

viscous grain boundary flow at high temperatures. It is assumed to operate between a pair of anisotropic crystals joined at a grain boundary and the stresses responsible for the distortion have their origin in the difference in the coefficient of expansion of the two grains in a reference direction parallel to the grain boundary. This difference in expansion upon heating or cooling will produce a tensile stress in one grain and a compressive stress in the other. These stresses will resolve to different shearing stresses on the slip planes and in the slip directions of the two grains making up the bicrystal couple. Thus, the strengths of the two grains will appear to be different. In the discussion which follows, the grain which has the higher stress resolved on its slip system is called the weaker grain.

For simplicity we may assume that at any strain rate, there is a temperature, T_c , which appears to be a melting point for the grain boundary. Above this temperature the stress developed by the difference in expansion of the two grains is relaxed by viscous flow as fast as it develops. Below this temperature, the difference in expansion of the two grains is accommodated largely by plastic flow in the weaker of the two grains. Because the grain boundary flow is viscous, this temperature, T_c , is relatively high if the heating or cooling rate is high, and is low if the heating or cooling rate is low.

Consider a pair of grains in which the weaker one has the higher coefficient of expansion at a temperature just above T_c . Upon cooling, an elastic tensile stress develops in the weaker grain, and after cooling by ΔT , the stress is defined to become so high that plastic flow commences in the weaker grain, and the elastic stress thus will remain essentially constant. If cooling is continued until the temperature is $(T_c - 2\Delta T)$, and then the specimen is heated again, the tensile stress in the weaker grain gradually falls and reaches zero at $(T_c - \Delta T)$. Upon heating further to T_c , a compressive elastic stress is developed, and is relaxed at T_c by grain boundary flow. Now the weaker grain is longer than the stronger one. The stress and temperature are just what they initially were, so repetitions of this cycle will produce continued elongation of the weaker grain. We have thus described a thermal ratchet which can operate to produce a continuing change in shape of one grain in a two grain couple. On cooling the weaker grain is plastically distorted. On heating to T_c , flow occurs along the grain boundary, so that the stronger grain can take a new grip on the weaker one and cause it to distort more on the next thermal cycle. The weaker grain will always be distorted: it will lengthen if its coefficient of expansion is higher, and it will shorten if its coefficient of expansion is smaller than that of the stronger grain.

APPLICATION OF THE THERMAL RATCHET TO POLYCRYSTALLINE URANIUM

We assume that a polycrystalline specimen can be treated as an ag-

Table I
Effect of Texture on Growth Rate of Uranium Rod

No.	Cycling range: Room temperature to 550 °C (1020 °F) No. of cycles: 750		G X 10 ⁸
	Treatment	Texture	
1	Pseudo-single crystal	Almost perfect	0
2	"Beta-treated" crystal	Almost random	20-30
3	5% reduction at 300 °C (570 °F)	Slight—(010) poles parallel rolling direction	250
4	75% reduction at 300 °C (570 °F)	Strong—(010) poles parallel rolling direction	550
5	75% reduction at 600 °C (1110 °F)	(010) + (110) poles parallel rolling direction	200

gregate of bicrystal couples. The overall distortion of the specimen will be the algebraic sum of the distortions of the individual grains in the specimen.

The Effect of Texture

Typical values for the growth rate during thermal cycling of uranium as a function of texture are listed in Table I. The growth coefficient, *G*, is the true strain per cycle, and refers to an elongation parallel to the wire axis.

No growth occurs on thermal cycling a pseudo-single crystal (#1, Table I) since it is so nearly a perfect single crystal that essentially no stress is developed across the boundaries.

In "beta-treated" uranium (#2, Table I) which is polycrystalline but has practically no texture, the algebraic sum of all distortions is almost zero, so that a very small amount of growth occurs.

Textured rods (#3 and 4, Table I) with (010) poles approximately parallel to the rolling direction elongate on thermal cycling. This is in agreement with the described ratchet model. Grains which are precisely oriented with the [010] direction parallel to the rod axes have a negative coefficient of expansion in that direction. Furthermore, they are also the strong grains: the predominant slip system in uranium is (010) [100], so a tensile or compressive stress parallel to the rod axis will not be resolved as a shearing stress on the (010) slip plane of grains in the nominal (010) orientation, since the slip plane is 90 degrees to the stress direction. The tensile or compressive stress will be resolved as a shearing stress on the (010) slip planes of all grains which deviate from this nominal orientation. Thus, grains in the nominal orientation will be stronger than any of their neighbors which deviate from this orientation. All such slightly deviating grains have higher coefficients of expansion than the nominally orientated grains. It follows from the mechanism proposed that weaker grains having higher coefficients of expansion in a given direction are stretched in that direction. Thus it is predicted that textured rods having (010) poles oriented approximately parallel to the rolling direction will grow longer on thermal cycling. Of course, the more perfect the texture, the greater will be

the growth per cycle unless the texture becomes so perfect that the specimen is essentially a single crystal, when no growth occurs again.

Specimen 5 (Table I) worked at 600 °C (1110 °F) has a mixed (010) plus (110) texture. In the (110) component of the texture, the crystallographic pole which is parallel to the rod axis may deviate from (110) toward (100) or toward (120). When the deviation is toward (100) the coefficient of expansion is high (since [100] is the direction of maximum coefficient of expansion) and the strength of the grain is greater because the stress direction is nearly 90 degrees to the slip plane and nearly parallel to the slip direction. When the deviation is toward (120) the grain has a lower coefficient of expansion and is weaker because the stress direction is nearly 45 degrees to the (010) slip plane and to the [100] slip direction. Thus, the couples between all grains lying close to the (110) texture component will be between high expansion strong grains and low expansion weak grains. The ratchet model predicts that the weaker grains of these couples will shorten upon thermal cycling. However, since the (010) texture component predominates in uranium worked at 600 °C (1110 °F), the specimen as a whole elongates, but the negative contribution of the (110) texture leads to a smaller effect than that observed in Specimen 4 which has no (110) component.

Effect of Temperature

Most thermal cycling has been done between room temperature and some elevated temperature. Little growth occurs unless the elevated temperature is above 350 °C (660 °F). The ratchet model predicts that no growth will occur if cycling is carried out at temperatures below those at which atomic mobility and grain boundary sliding is appreciable. In zinc bicrystals it was found that no distortion occurred if cycling was conducted between room temperature and liquid nitrogen temperature. The "recrystallization temperature" provides a rough index of the temperature at which atomic mobility is appreciable. Since cold-worked uranium will not recrystallize in reasonable times at temperatures below 350 °C (660 °F), it seems probable that the reason no growth occurs on thermal cycling below this temperature is that no grain boundary flow occurs.

Effect of Heating and Cooling Rate

The ratchet model also predicts changes in the growth rate for a given specimen cycled over a constant temperature range if the ratio of the heating to the cooling rates is changed.

For example, if the bicrystal is heated much more rapidly than it is cooled, upon heating a step is produced between the grains at some temperature T_c when grain boundary flow starts, exactly as in the case of equal heating and cooling rates. However, if the specimen is cooled

very slowly, reverse flow on the grain boundary continues to a lower temperature (i.e., T_c is lower for cooling than for heating). This continued flow decreases the size of the step initially produced, and the amount of growth in that cycle is less than the amount which would have been produced by equal heating and cooling rates. If conditions are sufficiently extreme, the sign of the displacement may even be reversed.

On the other hand, if the bicrystal is heated much more slowly than it is cooled, a very large step may be produced, because grain boundary flow starts at a low temperature and continues over a large temperature range (i.e., T_c for this slow heating cycle is very low). Rapid quenching retains this large step because T_c is high. As a result, the amount of growth per cycle is greater than that produced by equal heating and cooling rates.

Thus, if a certain amount of growth occurs with equal heating and cooling rates the ratchet model predicts that the amount of growth will be greater if the cooling time is less than the heating time, and less if the cooling time is greater than the heating time.

This is exactly in agreement with the data reported by Chiswick, et al. (1) for variation of the growth coefficient, G , with different combinations of heating and cooling times. The data presented in Table II were read from their graph for an upper cycling temperature of 550 °C (1020 °F).

Table II
Effect of Heating and Cooling Times on Growth Rate of Uranium Rod

Heating Time	Cooling Time	$G \times 10^4$
30 minutes	5 seconds	750
5 seconds	5 seconds	540
30 minutes	30 minutes	490
5 seconds	30 minutes	275

Effect of Composition

Large amounts of carbide inclusions are reported to decrease the growth rate. This is logically attributed to the hindrance of grain boundary flow by the carbide particles.

DISCUSSION

Chiswick, et al. report that Bettman, Brown and Frankel criticized this model as: "being intuitively unsatisfactory for polycrystalline metals because the proposed differential dimensional changes of adjacent grains should be prevented by the surrounding matrix of interlocking grains". Certainly, a great part of this differential movement can be accounted for by grain boundary sliding. In addition, if local compressive or tensile stresses do develop that cannot readily be relaxed by grain boundary flow, they can be relaxed by diffusion if the cycling in-

terval is long, as proposed by Nabarro (4) and by Herring (5). Such diffusion has been repeatedly shown to be responsible for matter transport during sintering (6).

CONCLUSIONS

The ratchet model proposed provides satisfactory explanations for the growth of uranium as well as zinc. It explains in a semi-quantitative way the role of temperature of cycling, rate of cycling, kind and perfection of texture.

ACKNOWLEDGMENT

This work was done while the authors were employed at the Knolls Atomic Power Laboratory. The mechanism of the ratchet and its application to polycrystalline uranium was included as part of a Classified paper by J. E. Burke, J. P. Howe and C. Lacy, to which reference has been made in the open literature. We are indebted to J. P. Howe for helpful discussion and to R. L. Coble for reading this manuscript.

References

1. H. H. Chiswick, L. R. Kelman, R. M. Mayfield and S. T. Ziegler, "Thermal Cycling Effects in Uranium," International Conference on the Peaceful Uses of Atomic Energy-A/Cong. 8/ p. 557.
2. H. H. Chiswick, "The Plastic Deformation of Uranium During Thermal Cycling," *TRANSACTIONS, American Society for Metals*, Vol. 49, 1957, p. 622.
3. J. E. Burke and A. M. Turkalo, "Deformation of Zinc Bicrystals by Thermal Ratcheting," *Transactions, American Institute of Mining and Metallurgical Engineers*, Vol. 194, 1952, p. 651.
4. F. R. N. Nabarro, "Deformation of Crystals by Motion of Single Ions," Report Conference on the Strength of Solids, The Physical Society, 1948, p. 75.
5. C. Herring, "Diffusional Viscosities of a Polycrystalline Solid," *Journal of Applied Physics*, Vol. 21, 1950, p. 437.
6. G. A. Geach, "The Theory of Sintering," *Progress in Metal Physics*, Vol. 4, 1953.

DISCUSSION

Written Discussion: By John P. Howe, Chief, Research, Atomics International, A Division of North American Aviation, Inc., Canoga Park, California.

The discussion of the mechanism for the distortion of textured alpha-uranium during thermal cycling is an important addition to science associated with materials for nuclear reactors, and to metallurgy generally. The mechanism discussed has been demonstrated to be at least one, if not the sole, mechanism operating in this interesting phenomenon.

Besides criticizing the model proposed (other authors, particularly Frankel, in discussions and in AEC reports, have offered other models), it is quite true any pair of deformation mechanisms, which operate in different regions and which have differing rate-temperature relations, can produce a ratchet. So far as this reviewer is aware, however, no other pair has been shown explicitly to exist. Perhaps a slight generalization could be made that one mechanism must be the

phenomena associated with the yielding of the metal. Thus, slip may be supplemented by twinning. Similarly, mechanisms related to stress relaxation at high temperature may be involved, but clearly grain boundary movement must be most important. A fairly quantitative description is probably possible for selected bicrystals, and probably should be attempted. For the polycrystalline case, particularly with complex textures which exist in alpha-uranium, the qualitative description offered by the authors is quite satisfying.

Written Discussion: By S. F. Pugh, United Kingdom Atomic Energy Authority, Atomic Energy Research Establishment, Harwell, Didcot, Berks., England.

The experiments of Burke and Turkalo on thermal ratcheting in zinc were published many years ago and gave a very nice demonstration of the process of thermal ratcheting which was also observed in the early work of Boas and Honeycombe in cadmium and tin. The calculated growth to be expected on the basis of the differential thermal expansion of the component crystals in the thermal ratcheting experiments of Burke and Turkalo on zinc bicrystals is about two orders of magnitude greater than that observed. It is therefore deduced that a process other than grain boundary flow was responsible for most of the stress relaxation at the upper cycling temperature. This is supported by the statement of the authors that occasionally grain boundaries were found to stick at certain points and not to move during cycling.

The mechanism of growth in alpha uranium on thermal cycling has an efficiency more than an order of magnitude greater than that of the ratcheting process in zinc, and in alpha uranium grain boundary flow is even less likely to occur than in zinc partly because the grain boundaries in uranium are corrugated and because the temperature of the uranium is much further from the melting point than that of the zinc in the ratcheting experiments. The work of Lloyd and Mayfield reported in this volume also indicates that grain boundary movement is of minor importance in the distortion which occurs in uranium during cycling. For these reasons I feel that the mechanism described by Bettman, Brown and Frankel² is more likely to be the one applicable to the case of growth in uranium on thermal cycling. The mechanism merely postulates a change in relative strengths of the two textures in the direction of the axis of bars with temperature. The mode of deformation at low temperatures is essentially nonthermally activated whereas the mode of deformation at the higher temperature is thermally activated. The change in relative strengths can therefore be treated as a change from a yield criterion to a creep process on raising the temperature. The kinetics of the creep process can be analyzed by the method developed by Dorn using the quantitative data published by Mayfield in this volume to give an activation energy of 65 ± 10 K calories/gram mol.

Written Discussion: By F. N. Rhines, Aluminum Company of America Professor of Light Metals, Carnegie Institute of Technology, Pittsburgh.

In the period since the authors first developed their thermal ratchet model, the results of several studies upon grain boundary flow have been published.³ It has become quite clear, thereby, that the rate of flow diminishes with time and that

² M. Bettman, G. W. Brown, and J. P. Frankel, U.S.A.E.C. report MTA-36, December 1953, (Declassified Sept. 29th, 1955).

³ For example: F. N. Rhines, W. E. Bond and M. A. Kissel, "Grain Boundary Creep in Aluminum Bicrystals," *TRANSACTIONS, American Society for Metals*, Vol. 48, 1956, p. 919.

grain boundary shearing is therefore not viscous. This in no way vitiates the authors' plausible and well defended model of growth by thermal cycling, which involves only observed grain boundary behavior and not the property of viscosity. The existence of a threshold temperature of grain boundary flow is well recognized and its reason for existence understood; the elevation of the threshold temperature with rapid heating is predictable upon the basis of the localized recovery-flow model of grain boundary shearing. Although the assumption of viscous flow happens not to have affected adversely the present conclusions, it seems to me unwise to perpetuate the concept lest others be led astray.

Since long-time demonstrations of thermal cycling growth in the everyday use of metals are somewhat rare, I should like to offer an example which I can document to some extent.

The accompanying photograph exhibits edgewise the wrinkled nameplate on a combination electric hot-plate and toaster which is still in use after about 38 years



Fig. 1—Edgewise View of Nameplate on a Combination Electric Hot-Plate and Toaster in Use After About 38 Years of Service.

of service. The nameplate is evidently made of zinc sheet; it has grown approximately 10%, lengthwise between its two points of attachment. Owing to the nature of the use of the device it is possible to estimate the number of heating cycles to which it has been subjected as 8000, with an uncertainty of about 30%. The same considerations suggest also that the thermal cycle has been of the long, slow heating and relatively rapid cooling type, its range being from 75 °F to somewhere between 300 and 390 °F. Zinc sheet, as produced 40 years ago, may be expected to have had a strong texture. The observed growth is equivalent to a little more than half the maximum reported for zinc bicrystals, by Burke and Turkalo in 1952.

Written Discussion: By Hubert Bairiot, Belgian American Educational Foundation, New York City.

The fundamentals of the growth of uranium upon thermal cycling is described in two papers: L. T. Lloyd's present experimental data, J. E. Burke's thermal ratcheting theory. The author of the discussion had the opportunity to investigate the problem, both on the experimental and theoretical point of view, at the Massachusetts Institute of Technology and the Argonne National Laboratory. A paper will be issued soon.

High purity, coarse-grained uranium specimens are observed up to 100 cycles by microscopic examination and 200 cycles by x-rays. A fiducial grid helps to spot the deformations. The deformations appear to be born near the grain boundaries and extend only through the grains after many cycles. Considering the region near the grain boundary of two neighboring grains, one of them usually appears a "strong" grain, the other as a "weak" grain. This supports the thermal ratcheting picture. The grain boundary sliding appears, however, only as a minor effect, restricted to grains near the edge where interlocking by neighbors is negligible. The experiments lead to the same conclusion of creep-type deformation, as observed at the ANL. Strong evidence of polygonization, and later recrystallization, starting from grain boundaries, can be noticed.

The experimental results suggested a model very close to the thermal ratcheting, in which the grain boundary sliding is replaced by grain boundary creep. The temperature T_c appears as the equicohesive temperature, observed in creep testing. Comparison with extensively creep tested metals shows this equicohesive temperature to be between 300 and 500 °C (570 and 930 °F) for uranium, in good agreement with 350 °C (660 °F) indicated for T_c by J. E. Burke.

The performed mathematical development was based on two approximations: many grains have the (010) direction close to the considered direction, and only (010)-[100] slip is operative. Let θ be the most probable angle between the [010] directions and the growth direction in a polycrystalline specimen, and G_{max} the growth coefficient to be expected with very low heating and cooling rates; the values of G_{max} as a function of θ , calculated on now out-of-date mechanical data for uranium, was:

θ Degree	G_{max} ppm/cycle
60	40
30	120
10	500
5	700
3	10
2	0
1	-10
0	0

This is in good agreement with Table I of the paper.

The influence of the hot phase temperature and effective heating time (approximately the "hot temperature holding time") may also be accounted for quantitatively. The effect of cooling rates is an involved mathematical problem, not yet solved. Both effects of cooling and heating rates may be looked upon as due to the viscous behavior of high temperature creep, without taking into account a displacement of the equicohesive temperature. In fact, it is very questionable whether the energy stored near a grain boundary by fast heating or cooling may be sufficient to initiate a noticeable raise of this temperature.

Written Discussion: By J. P. Frankel, Engineering Department, University of California, Los Angeles.

The summary of the basic phenomena related to this important problem contained in this paper is an excellent brief compilation that will often be referred to in the future.

The possibility that the mechanism of the instability is related to grain boundary

sliding at high temperatures is logically stated. It is reasonable that part of the growth of uranium may be accounted for by this mode of deformation.

The study by Lloyd and Mayfield⁴, however, indicates that grain boundary sliding occurs only to a slight extent. In his discussion of their paper, the writer has indicated the difficulties which make significant grain boundary motion unlikely.

In their discussion, the authors assert that an alternative to grain boundary relaxation is the diffusion process proposed by Nabarro and Herring. Lloyd and Mayfield suggest as still a third alternative the possible importance of creep and relaxation phenomena. There does not seem to be experimental evaluation of the merits of these alternatives available in the current literature. In this regard, it is proper to mention that the creep relaxation mechanism is discussed at some length in MTA-36, an AEC report available from OTS.

On the other hand, the role of grain boundary relaxation must continue to be conjectural, at least until experimental verification on fine-grained material is obtained.

Authors' Reply

It is gratifying to have such a detailed and spirited discussion of our paper, and we should like to thank all those who contributed discussions.

The comments of Dr. Howe are particularly welcome since he was so closely associated with this work and made so many contributions to it. He emphasizes the importance of having two different mechanisms of deformation which have different rate-temperature relations to produce a ratchet. This is a clear requirement for any process to explain the observed distortion.

Mr. Pugh does not agree with the mechanism proposed, but he bases his disagreement on several misunderstandings and a few errors, in fact, which should be corrected: As was pointed out in some detail in our earlier paper, Boas and Honeycombe did not observe thermal ratcheting. They observed that stresses produced by differential thermal expansion could produce plastic slip. As Dr. Howe so clearly pointed out, two mechanisms of deformation are necessary for a thermal ratchet. Again the calculated growth to be expected in zinc bi-crystals is two to four *times* that observed, not two orders of magnitude as stated by Mr. Pugh. He further states that uranium grows when its temperature is much further below the melting point than the temperature at which zinc grows. In absolute temperature interval this is so, but in fractions of the melting point, the discrepancy is small. Uranium growth is observed at 0.59 of the melting point and the only temperature tested in zinc was 0.67 of the melting point. Grain boundaries are corrugated only in beta-treated uranium, which does not grow.

Since it is for these reasons that Mr. Pugh objects to the model we proposed, we feel his objections are not well taken.

The discussion of Mr. Frankel as well as that of Mr. Pugh refers to the fact that Lloyd and Mayfield claim that grain boundary sliding occurs only to a limited extent. Actually they show excellent photographic evidence for grain boundary flow; they state that the chief mechanisms of deformation are "intragranular slip and twinning, sub-grain formation, boundary migration and boundary sliding". Of these, we particularly invoke intragranular slip and boundary sliding as the components of the ratchet. Twinning will produce only limited deformation, sub-grain formation an amount exceedingly small compared to twin

⁴ Page 954-978, this volume.

boundary migration, and grain boundary migration can produce no deformation at all. Lloyd and Mayfield make no quantitative measurements of the distribution of distortion among these models, nor do they offer any mechanism as an alternative to the one we propose. Thus we feel that there is no experimental evidence to support the claim that grain boundary flow is unimportant in the growth of uranium.

The mechanism proposed by Mr. Pugh, that of a change in the relative strength of different texture components with temperature is interesting, but I believe wholly unsupported by any experimental evidence in any material. In order to seriously present it as an alternative mechanism, there should be at least some theoretical argument for supposing that such a behavior might be observed. It requires, of course, that there be some pair of grain orientations having the property that one grain is weaker at high temperatures and one is weaker at low temperatures.

Mr. Frankel also states that we propose Nabarro-Herring creep as an alternative to grain boundary flow. Actually, we proposed this diffusional process only as a secondary one to relax local stresses that cannot be readily relaxed by grain boundary flow.

It is comforting to read M. Bairiot's discussion, in which he confirms by direct observation the general principles of the ratchet we propose. We assume that the differentiation which M. Bairiot makes between "grain boundary sliding" and "grain boundary creep" is one of scale, with the flow appearing to occur in the close neighborhood of the boundary rather than right at it. We might here call attention to the fact that in many cases the grain boundary displays considerable mobility. Continuing grain-boundary flow on a grain boundary that is moving will spread the deformation over quite a wide area as was noted in our earlier paper. We look forward to the appearance of M. Bairiot's paper.

Finally we should like to thank Prof. Rhines for his very pleasant example of the thermal ratcheting process. We accept his criticism of our use of the term "viscous" to describe the flow properties of a grain boundary, and regret that his elegant work on grain boundary flow was not available when we were doing our original work on zinc.

In closing we should like to again thank those who contributed, and to summarize our position: The problem is to explain the growth of uranium; i.e., to explain why a cyclic stress causes it to elongate. Observations of mechanism of deformation do not answer the problem—it must also be shown that they may be coupled to produce a ratchet. We have proposed a coupling mechanism, have demonstrated experimentally that it works in zinc and have demonstrated that it accounts quantitatively for the relationship between texture and growth in uranium, and that it accounts qualitatively for all of the observed phenomena in the thermal cycling of uranium, and that the theory can be used to predict behavior.

MICROSTRUCTURAL CHANGES OF URANIUM UPON THERMAL CYCLING

BY L. T. LLOYD AND R. M. MAYFIELD

Abstract

Microstructural observations of thermal cycled uranium demonstrate that the macro growth embodies deformation phenomena similar to those occurring in creep. Coarse-grained specimens deform by slip, twinning, and localized interactions at the grain boundaries. Slip occurs prominently on the (010) plane along with cross-slip on (010)-(001) planes and limited slip on the {110} plane. For two adjoining grains, the extent of interaction is dependent upon the relative orientations of the grain boundary and the angle between the two (010) axes; the interaction increases as the angle increases. Fine-grained specimens deform by grain interaction and grain boundary migration, together with some intragranular slip and grain boundary sliding. (ASM International Classification Q24, 1-11, N5; U)

INTRODUCTION

THE MACROSCOPIC deformation of the uranium orthorhombic phase upon thermal cycling has received considerable attention from investigators associated with development and construction of nuclear reactors. Data have been reported by Chiswick (1),¹ Mayfield (2), and Zegler, et al. (3), as well as by many others in the nuclear metallurgy field. Most investigators agree that the dimensional instability arises from intercrystalline stresses developed during cycling due to thermal expansion anisotropy (4). Burke, Howe, and Lacy (5) proposed a "thermal ratcheting" mechanism which makes deformation irreversible. Textured polycrystalline uranium is pictured to consist of differently oriented grain couples with a stress developed across their boundaries. They postulate that the grain which is weaker, because of its crystallographic orientation, deforms by slip at low temperatures, whereas at high temperatures the intergranular stress is relieved by grain boundary sliding. In support of this mechanism they point to

¹ The figures appearing in parentheses pertain to the references appended to this paper.

A paper presented before the Thirty-Ninth Annual Convention of the Society, held in Chicago, November 4-8, 1957. Of the authors, L. T. Lloyd is group leader, Physical Metallurgy, and R. M. Mayfield is associated with the Metallurgy Division, Argonne National Laboratory, Lemont, Illinois. Manuscript received March 29, 1957.

experimental observations of grain boundary sliding in thermally cycled zinc (6). Bettman, Brown, and Frankel (7) have proposed that continued elongation may result from creep in the stronger grain of a similar couple at the high temperature part of the cycle, whereas the weaker grain may be deformed plastically in the low temperature part. A similar mechanism has been proposed by Maringer, Mangio, and Johnson (8).

Boas and Honeycombe (9,10,11) studied the microstructures of certain noncubic metals (zinc, cadmium, and tin) after thermal cycling over a relatively low temperature range. Three general types of phenomena were observed: (a) surface roughening accompanied by the grain boundaries becoming more pronounced; (b) deformation markings within grains brought about by slip and twinning; and (c) migration of grain boundaries in high purity metal. X-ray results indicated that the deformations occurred throughout the specimen and were not restricted to surface layers. Similar observations were noted by Burke and Turkalo (6) from thermally cycled bicrystals of zinc. In specimens cycled between 100 and 300 °C (210 and 570 °F) they observed intragranular slip, grain boundary sliding, boundary migration, and in some cases, recrystallization or subgraining immediately adjacent to grain boundaries. In specimens cycled between room temperature and -180 °C (-290 °F) they found no boundary migration or sliding, deformation within grains occurred by twinning and slip, and intragranular cleavage occurred in some cases.

Postulates of the thermal cycling growth mechanism in uranium have thus far been based upon studies of macro deformation. The present study concerned itself primarily with the microstructural changes during thermal cycling, particularly those pertaining to the magnitudes of grain boundary interactions as related to their relative orientations, and to the mechanisms of deformations within grains.

MATERIALS AND EXPERIMENTAL TECHNIQUES

The specimens studied were high purity uranium (99.99 + wt. %) with the exception of one sample of 99.9 + wt. % uranium (hereafter referred to as commercial grade); in both cases the major impurity was carbon. All materials were rod-rolled 75% reduction in area at 300 °C (570 °F), and annealed at 600 to 650 °C (1110 to 1200 °F). This fabrication and heat treatment resulted in highly textured rods (12).

Coarse-grained samples employed for comparative microstructural observations were prepared by grain coarsening techniques (13), whereas fine-grained specimens were obtained by normal recrystallization. Metallographic surfaces were polished by mechanical and electrolytic means (14) and examined in polarized light. Orthogonal scribe marks were placed on the polished surfaces with a Bergsman Hardness Tester; light indentations were used to prevent distortion and recryst-

Table I
Specimen Cycling Histories

Specimen Number*	Treatment Number	Number of Cycles	Low Temperature Holding Time** (minutes)	Transfer Time (seconds)	High Temperature Holding Time*** (minutes)
48	1	15	2	5	10
48	2	15	2	5	10
71	1	50	2	5	10
80	1	25	2	5	5
80	2	25	2	5	5
86	1	25	2	5	5
86	2	25	2	5	5
121	1	50	2	5	10
B-366-I	1	25	2	5	10
B-366-I	2	25	2	5	10
B-366-II	1	100	2	5	10
B-366-III	1	25	2	5	10
4A	—	3000	5	5	5
7A	—	3000	2	5	5

*Specimen 7A was of commercial purity—all other specimens were high purity uranium.

**Low cycling temperature was 50°C (120°F) for specimens 7A and 4A; all other samples were cycled to room temperature.

***High cycling temperature for specimen 4A was 550°C (1020°F) and for specimen 7A—600°C (1100°F); all other samples were cycled to 500°C (930°F).

tallization upon heating. These served as reference marks and were used to reveal displacement of adjoining grains.

Orientations of individual grains in the coarse-grained specimens were determined from back-reflection Laue photograms. Such data could not be procured from fine-grained specimens; however, in some cases, a measure of preferred orientation was obtained by x-ray techniques.

Individual samples used for comparative microstructural observations were wrapped in 0.002-inch thick tantalum sheet and sealed in Pyrex under a vacuum equal to, or better than, 5×10^{-5} millimeters of mercury. They were then thermally cycled in a small resistance furnace by raising the capsule into the 500°C (930°F) temperature zone, holding for a predetermined time, and then lowering into a room temperature air blast. Specimens 4A and 7A whose microstructures were observed during and subsequent to treatment were cycled in the vertical tube NaK cycler (2). Cycling histories of all specimens are given in Table I.

After predetermined numbers of cycles, the polished surfaces were examined metallographically. A portion of the samples were resealed in Pyrex, cycled a second time, and again observed for microstructure changes. Some specimens were repolished after final cycling to permit a detailed examination of microstructures under polarized light.

RESULTS

Coarse-Grained Specimens

Microstructures of five coarse-grained specimens were studied. Representative observations are presented for two of these in relation to their condition.

Table II
Orientation Relationship Data for Coarse-Grained Specimens

Spec. No.	Grains	Angle between common axis and—(degrees)			Rotation required about com- mon axis, δ —(degrees)	Angle be- tween [010] axes, σ —(degrees)	Degree of grain boundary inter- action*
		[100]— α	[010]— β	[001]— γ			
48	A-B	72	56	40	84	63	3
48	B-C	77	24	70	85	48	3
80	A-B	59	31	85	44	22	2
80	B-C	88	21	69	88	29	2
71	A-B	88	8	82	47	4	0
71	B-C	82	6	85	47	9	0
71	C-A	89	2	89	83	4	0
86	A-B	84	6	84	84	12	0-1
86	B-E	50	50	64	51	40	2
86	B-C	60	82	31	17	17	0-1
86	C-E	67	47	52	54	40	2
86	C-D	39	60	69	50	42	2
86	D-E	27	83	64	60	60	3
121	A-B	87	8.5	82	83	11	1
121	A-C	83	10	83	90	13.5	1
121	A-D	70	25	77	66.5	21	0-1
121	A-F	33	60	80	15	22	2
121	A-G	12	90	78	56	35	3
121	A-H	79	17	76	82	23	2
121	A-I	86	11	78	56	22	1
121	B-C	61	35	73	12.5	8	0-1
121	C-D	80	20	78	27	8	0
121	D-E	84	23.5	63	58	20	1
121	D-F	69	58	40	84	4	1
121	E-F	88	19	71	78	21	2
121	F-G	57	62	45	21	19	3
121	F-I	89.5	1	89.5	68	1	0
121	G-I	86	4	89	58	20	1
121	H-I	82	8	90	24	3	1

*Arbitrary scale of grain boundary interaction. (Deformation values were assigned after the first cycling treatment of each sample.)

0—negligible; 1—very slight; 2—moderate; 3—pronounced.

Initial Condition—Table II records data pertaining to the relative orientations of each pair of grains within individual samples. Angles α , β , and γ were measured from the axis common to both grains to the [100], [010], and [001] axes, respectively; δ is the magnitude of rotation of one grain about the common axis that brings it into coincidence with the other grain; and σ is the angle between the [010] axes. Fig. 1 is a stereographic plot of the principal poles of grains in specimens 48 and 80 relative to the scribed reference marks shown in Figs. 2b and 3a. For each specimen, the arrow of the stereographic plot is parallel to horizontal scribed lines and the head points in a direction corresponding to left.

Figs. 2a and 3a show samples 48 and 80 prior to thermal cycling; letters designate the various grains and numbers refer to twins. Traces 25, 26, 27, 28, and 29 of specimen 48 and traces 3 and 4 of specimen 80 were identified by pole-loci analyses as $\sim\{172\}$ type twins; all other traces are $\{130\}$ twins.

As-Cycled Condition—Specimens 48 and 80 after their first cycling

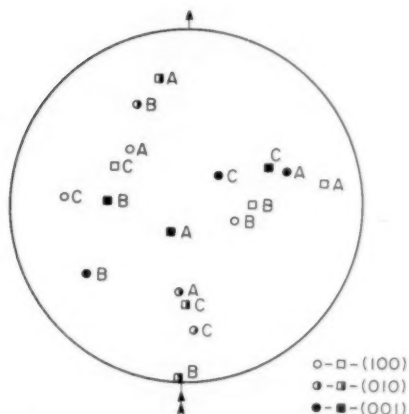


Fig. 1—Relative Orientation of Grains in Specimens 48 (circle) and (square) 80.

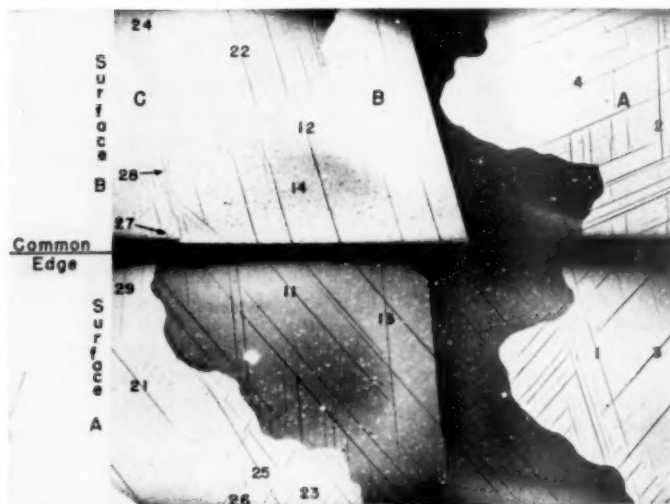


Fig. 2—Composite Photomicrographs of Two Polished Surfaces of Specimen 48 (121 degrees Included Angle Between Surfaces). Fig. 2a—Prior to Cycling (Polarized Light, $\times 20$).

treatment are shown in Figs. 2b and 3b. An obvious increase in $\{130\}$ twinned material has occurred in some grains (grain B, specimen 80—Fig. 3b). Frequently this appeared as thickening of twins which were present prior to cycling; however, some new traces were created. There

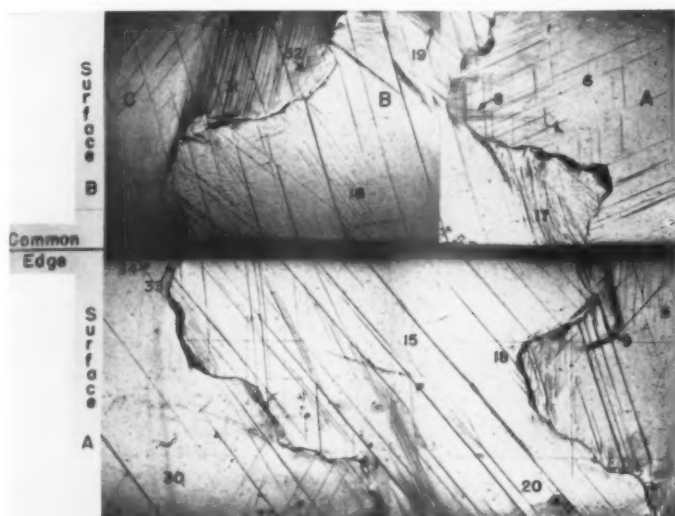


Fig. 2b—After 15 Cycles from Room Temperature to 500 °C (930 °F). (Bright Field— $\times 20$.)

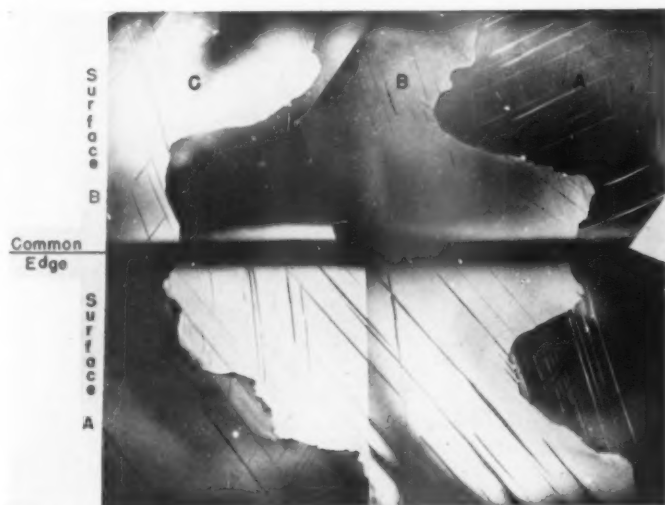


Fig. 2c—After Repolishing Subsequent to 30 Cycles. (Polarized light $\times 20$.)

were no changes in the $\sim \{172\}$ twins present prior to cycling, nor were other new twin trace directions found.

The major intragranular deformations occurred by slip mechanisms.

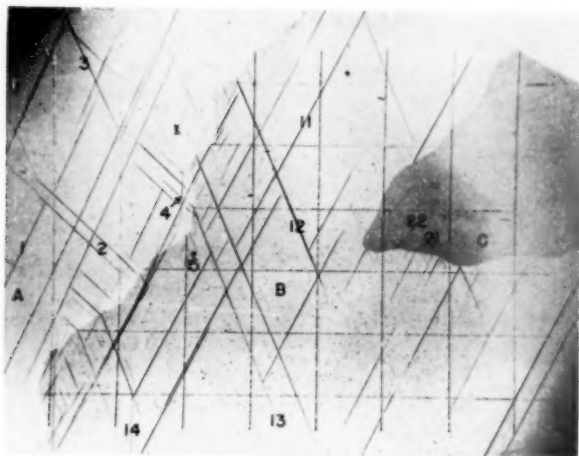


Fig. 3—Photomicrographs of Polished Surface of Specimen 80. Fig. 3a—Prior to Cycling. (Polarized light— $\times 40$.)



Fig. 3b—After 25 Cycles from Room Temperature to 500 °C (930 °F). (Bright field— $\times 40$.)

All coarse grains studied, except those for specimen 71, contained traces which were identified as (010)-[100] slip (see for example, grain B, traces 15 and 16, specimen 48—Fig. 2b; grain B, trace 16, specimen 80—Fig. 3b). Irregular slip markings whose appearance identified them as (010)-(001) cross-slip (15,16) were found in some grains (see for example, grain B, area 17, specimen 48—Fig. 2b; grain

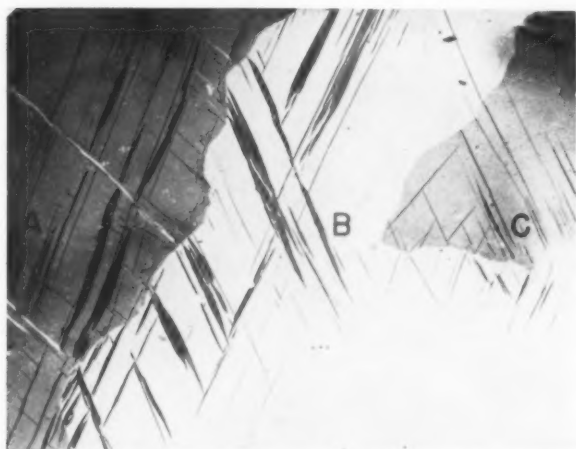


Fig. 3c—After Repolishing Subsequent to 50 Cycles. (Polarized light— $\times 40$.)

B, area 19, specimen 80—Fig. 3b). Other slip deformations were found in some grains; most of these were identified by pole-loci analyses as $\{110\}$ slip (see for example, grain A, trace 8, specimen 48—Fig. 2b).

The extent of intergranular interaction is manifested by slip deformations near the grain boundaries. Because the grain boundaries are irregular, this interaction is not uniform. It was, however, possible to obtain a measure of its extent according to an arbitrary scale of deformation; these values are recorded for each pair of grains in Table II.

The above observations are limited to the first cycling treatments of coarse-grained specimens; their appearance after the second treatment did not differ greatly. In general, increased cycling enhanced metallographic evidence of deformation but did not result in additional mechanisms.

As-Cycled and Repolished Condition: Subsequent to thermal cycling and repolishing, specimens 48 and 80 appeared as shown in Figs. 2c and 3c. Many of the twins present prior to cycling have disappeared, whereas others have increased in width and assumed irregular shapes. Comparison of these with trace directions prior to cycling showed their identity to be $\{130\}$ twins.

Regions immediately adjacent to grain boundaries, especially those where considerable distortion was observed in the as-cycled condition, exhibit sub-graining as shown in Fig. 5. The Laue photograph of Fig. 6 obtained from such an area in specimen 86 indicates the sub-grains to be systematically disoriented with respect to each other.

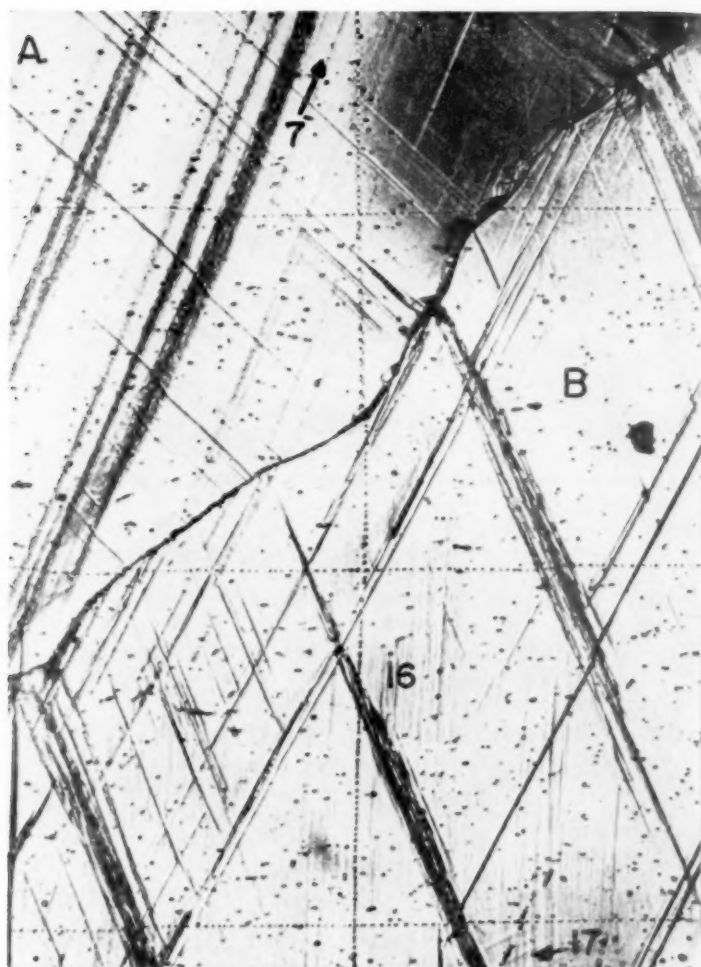


Fig. 4—Higher Magnification Photomicrograph of Specimen 80 in Same Condition as that of Fig. 3b. (Bright field— $\times 200$.)

FINE-GRAINED SPECIMENS

Two of the fine-grained specimens (B-336-I and B-336-II) used for comparative metallographic observations were thermal cycled in the alpha-annealed condition; sample B-366-III was cycled after a 4-minute beta phase treatment at 725°C (1335°F) followed by water quenching. All three specimens had an initial average grain diameter of ap-



Fig. 5—Higher Magnification Photomicrograph of Specimen 80 in Same Condition as that of Fig. 3c. (Polarized light— $\times 100$.)

proximately 0.05 millimeter. Because the individual grain orientations could not be obtained, it is impossible to associate deformations with specific mechanisms and correlate relative grain orientations with observed grain interaction. Observations of microstructures, however, do permit some generalizations with respect to cycling deformations.

Prior to thermal cycling, the alpha-annealed specimens appeared as equiaxed grains with little evidence of internal stressing as indicated by the presence of twins. Metallographic surfaces, subsequent to cycling, appeared as shown in Figs. 7a and 8. Internal stressing of the grains was indicated by slip and twin traces; observations subsequent to elec-

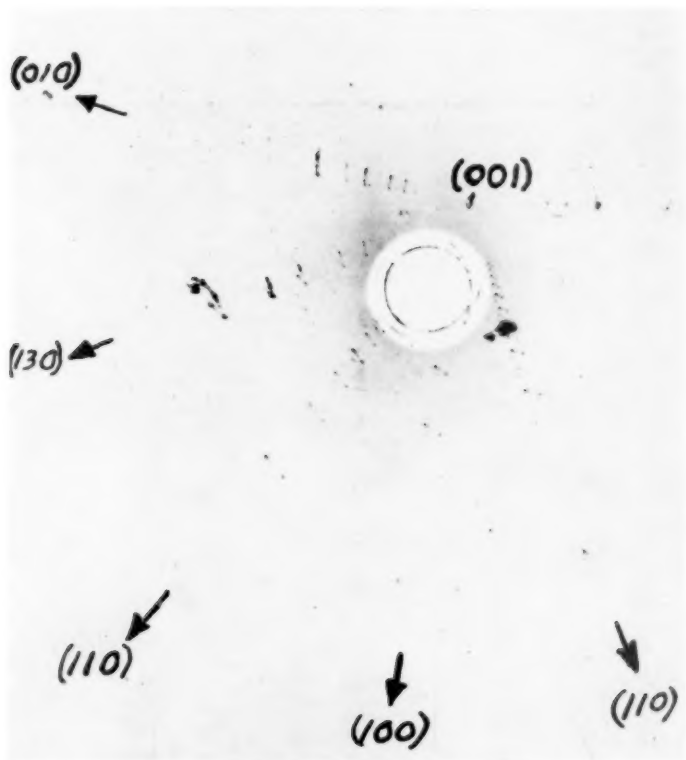


Fig. 6—Laue Photogram Taken from Subgrained Area Near Grain Boundary of Specimen 86. (Copper white radiation.)

tropolishing showed that only a small portion of these were caused by twins. Grain interaction was indicated by several factors: (a) A subgrained structure was created within grains as shown by oblique illumination in Fig. 8; this was substantiated by polarized light observations after electropolishing. (b) Some grain boundaries have migrated as shown by the series of irregular lines. (c) Some evidence of grain boundary sliding was observed because various grains have a difference in height and thereby cast shadows of varied width when viewed under oblique illumination.

Prior to thermal cycling, the beta-treated sample of Fig. 9a showed relatively large grains with extensive subgraining and some twins. The polished surface exhibited considerable deformation and some increase in the quantity of twins after cycling as shown in Fig. 9b. Extensive deformation occurred at grain boundaries and some interaction between

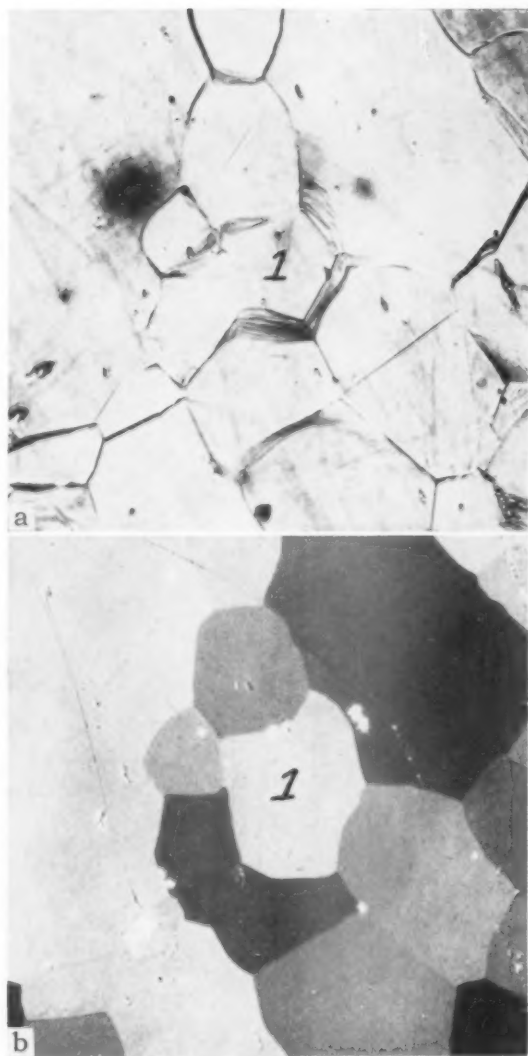


Fig. 7—Microstructures of Specimen B-366-I After 50 Cycles Between Room Temperature and 500 °C (930 °F). Fig. 7a—As Cycled (Bright Field— $\times 300$). Fig. 7b—Cycled and Repolished (Polarized Light— $\times 300$.)

subgrains was evident because they were clearly distinguishable under bright field illumination.

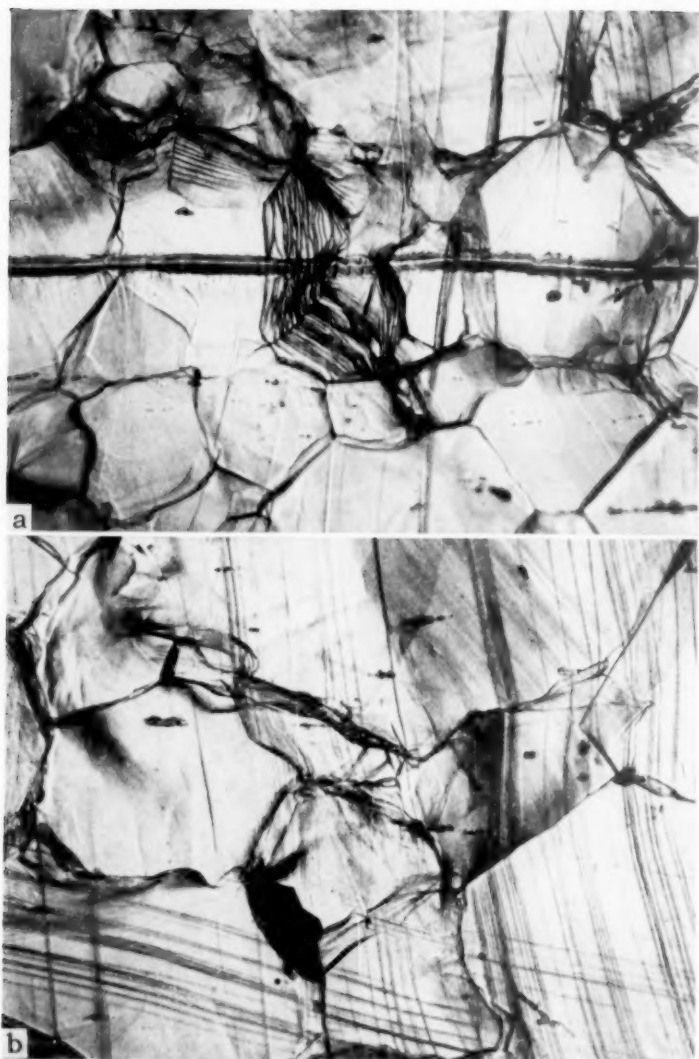


Fig. 8—Photomicrographs of Specimen B-366-II After 100 Cycles Between Room Temperature and 500 °C (930 °F). (Bright field— $\times 250$.)

General microstructural features of commercial-grade specimen 7A were observed on unrelated sections before and after 3000 cycles. The cycling treatment resulted in a unidirectional growth to approximately

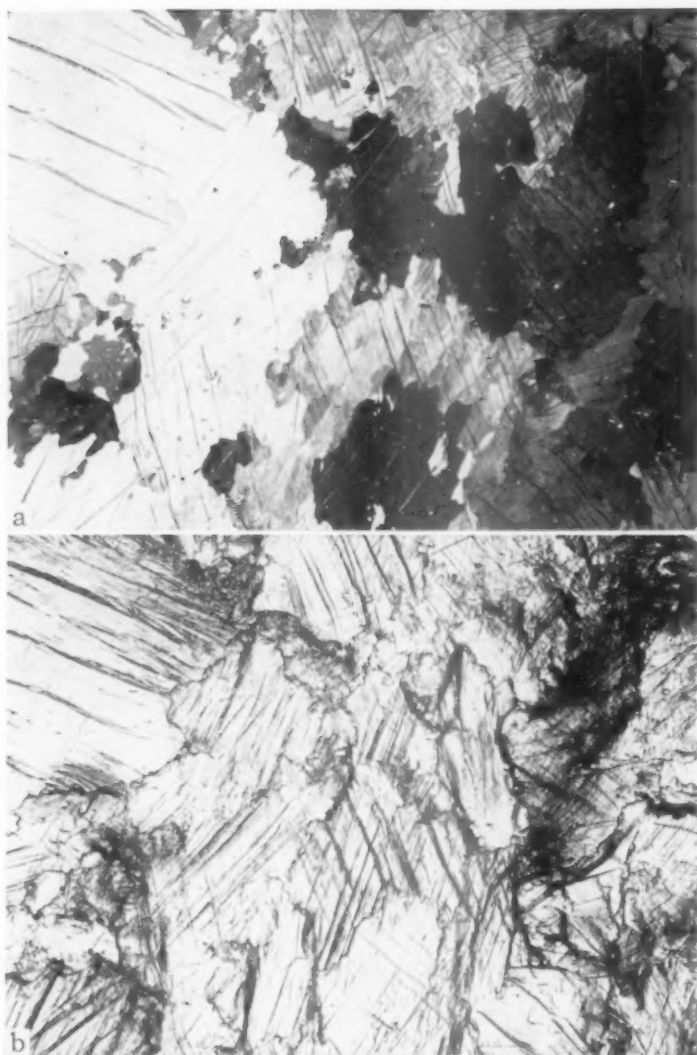


Fig. 9—Photomicrographs of Beta Treated Specimen B-366-III. Fig. 9a—Prior to Cycling (Polarized Light— $\times 50$). Fig. 9b—Same area as 9a. After Cycling 25 Times Between Room Temperature and 500 °C (930 °F). Bright field— $\times 50$.)

6 times the sample's original length. As illustrated in Fig. 10c, the outstanding structural change was the abundant formation of voids. Comparison of microstructures before and after 3000 cycles shows that

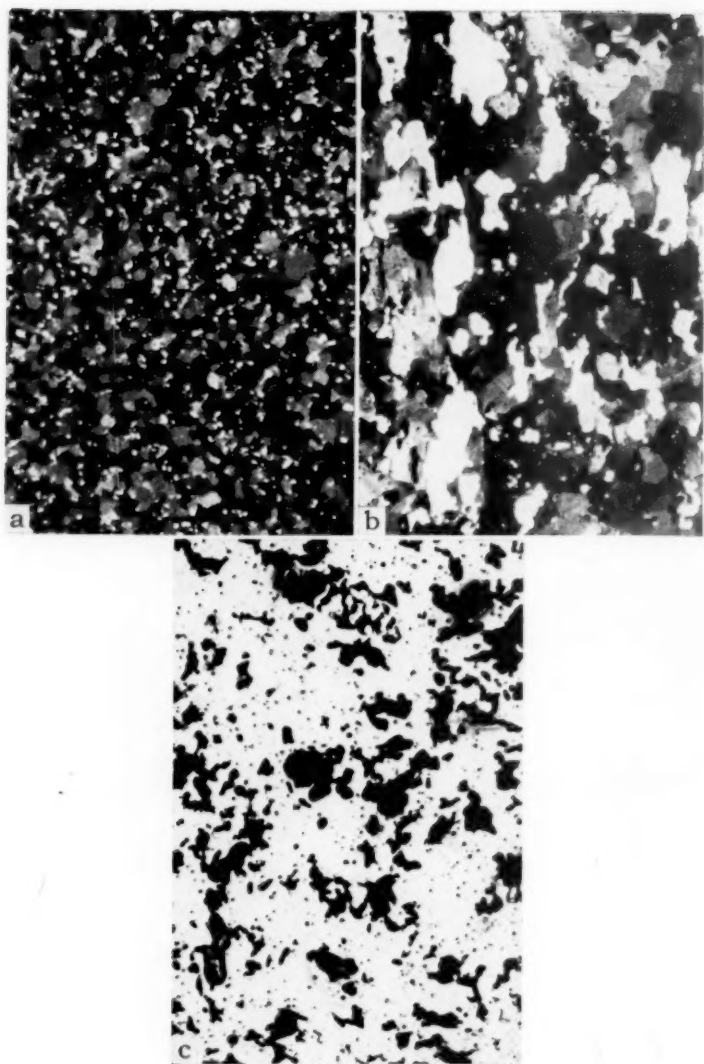


Fig. 10—Microstructures of Specimen 7A.

Fig. 10a—Relative Grain Size Prior to Cycling (Polarized light— $\times 100$).

Fig. 10b—Relative Grain Size After 3000 Cycles Between 50 °C (120 °F) and 600 °C (1110 °F). White areas represent voids. (Polarized light— $\times 100$.)

Fig. 10c—Appearance of Voids After Mechanically Polishing Subsequent to 3000 Cycles. (Bright field— $\times 100$.)

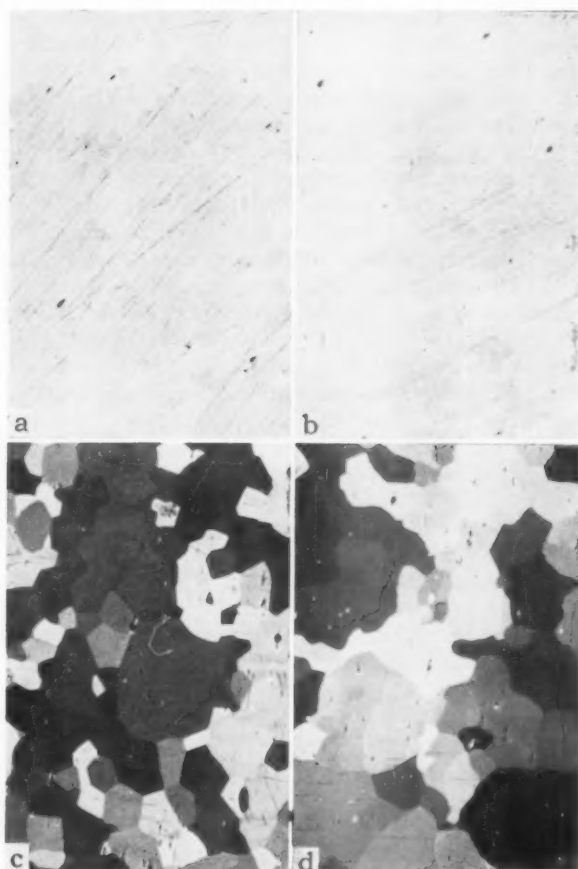


Fig. 11—Microstructures of Specimen 4A.

Fig. 11a—As Mechanically Polished Prior to Cycling. (Bright field— $\times 100$.)

Fig. 11b—As Mechanically Polished Subsequent to 2000 Cycles Between 50 and 550 °C (120 and 1020 °F). (Bright field— $\times 100$.)

Fig. 11c—Grain Structure Prior to Cycling. (Polarized light— $\times 100$.)

Fig. 11d—Grain Structure Subsequent to 3000 Cycles. (Polarized light— $\times 100$.)

grain size has increased. X-ray determinations of preferred orientation prior and subsequent to cycling indicated little change in texture; however, there appeared to be a slight increase in the degree of scatter.

Metallography of high purity specimen 4A sampled after various stages of cycling did not result in observations of void formation. To

prevent confusing electropolishing pits with voids, the specimens were examined "as mechanically" polished. The small number of black particles in Fig. 11a were identified at higher magnifications as inclusions. After 2000 cycles the number of particles increased slightly and they were somewhat larger as illustrated in Fig. 11b, but they could still be identified as inclusions; other samples cycled up to 3000 times were similar in appearance. The general grain structure prior to cycling is illustrated in Fig. 11c; after cycling 3000 times it appears as shown in Fig. 11d. The grain size has increased as a result of cycling; however, examination upon rotation in polarized light revealed the larger grains of Fig. 11d to be subgrained, with the subgrains being of approximately the same size as the original grains. The presence of low angle boundaries was observed for all samples, even one which was cycled only 200 times. Comparison of measured average grain sizes for the series of samples, taking into account all microscopically detectable subboundaries, showed no significant variation.

DISCUSSION

Crystallographic Deformation

Because of grain size and, therefore, capability of obtaining individual grain orientations, only the observations of coarse-grained specimens can furnish positive information concerning crystallography of thermal cycling deformations. This information then can be extrapolated to fine-grained specimens which more closely represent the type of material used in nuclear reactors.

Twinning—A detailed discussion of twin deformations in coarse-grained specimens and their changes upon thermal cycling is superfluous because observations of fine-grained samples indicated that they play an insignificant role in the unidirectional growth. This conclusion is based upon the fact that fine-grained specimens subsequent to thermal cycling and repolishing showed few, if any, twin traces as illustrated in Figs. 7b and 11d.

Slip—Slip deformations, however, were observed in both coarse- and fine-grained samples. Their origin can best be attributed to the linear thermal expansion anisotropy of the three principal orthorhombic alpha-uranium crystallographic directions. The coefficient of expansion in the [010] direction has been shown by x-ray diffraction lattice parameter measurements (4) and by dilatometric studies (12,17) to be negative upon heating above room temperature, whereas the coefficients are positive in the two mutually perpendicular directions. Stresses strong enough to bring about plastic deformation within individual grains can be established as a function of temperature and relative grain orientation. The relationships between stresses and relative grain orientations will be discussed in more detail later.

Stereographic analyses of slip traces in coarse-grained specimens demonstrate the most prominent mechanism to be slip on the (010) plane in the [100] direction. Fine-grained specimens present indirect evidence for this same mechanism. A horizontal line through the photographs of Fig. 8 is parallel to the rod rolling direction; the polished surface is also parallel to it. Consequently, the nearly vertical slip lines lie in a position almost perpendicular to the rolling direction. From considerations of texture determinations in similar samples (12), the (010) plane traces would occupy this position.

In addition to the prominent slip in coarse-grained specimens, there were several other slip markings. A portion of these had the appearance of cross-slip whose operative planes have been identified as (010) and (001), (16). Ten of the remaining 16 traces were identified by pole-loci analyses as originating in {110} plane slip—a mechanism reported by Cahn (15). These identifications were not confused by passage near {011} and (001) slip plane poles (16). Inability to clearly identify the other six traces may be attributed to one or both of two factors: (a) their short lengths made exact determinations of trace directions difficult; and (b) the areas where they appeared were heavily distorted. The latter would cause their orientations to be changed with respect to that of the original grains.

Fine-grained specimens also indicate the existence of slip deformations other than the (010)—[100] system. Photographs of Fig. 8 clearly show more than one trace direction in an individual grain. None of these would appear to represent twins; upon repolishing this specimen very few grains contained twin traces, and never was the number of parallel markings in an individual grain nearly as great as that found in the as-cycled condition. Some of the grains, particularly near grain boundaries, showed markings similar to (010)—(001) cross-slip deformations.

Interaction Between Grains

Coarse-Grained Specimens—Interaction deformation at grain boundaries is dependent upon two factors: (a) relative orientations of the grains; and (b) orientation of the grain interface with respect to the crystal structures. An approximate measure of the influence of these factors can be obtained by considerations of the relative dimensional change of two grains at the boundary between them.

Several assumptions must be made to obtain a simple mathematical expression for the differential expansion of two grains. Four general types of restraints may be imposed upon a grain boundary: (a) restraint on all sides, (b) restraint at the ends of the boundary, (c) restraint normal to the boundary, and (d) no external restraint. The following will consider the last condition because it is approximated by the coarse-grained samples; in general, grains passed completely through the specimens. There will be no component of stress perpendicular to the bound-

ary if it is planar in nature. If the analysis is limited to material located near the grain boundary, then the only source of stress application will be differential expansion of the two grains. By assuming the expansions in the $[100]$ and $[001]$ to be equal, the problem is simplified to a two-dimensional condition; this assumption is reasonably valid in light of data calculated from lattice parameter measurements (4). Finally, the

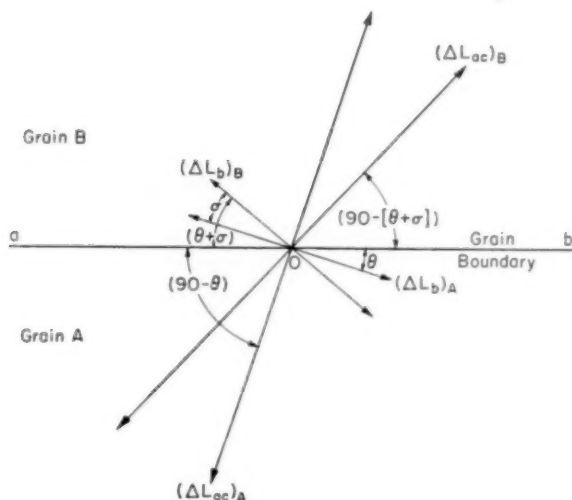


Fig. 12—Schematic Representation of Thermally Induced Dimensional Changes Acting Upon Grain Boundary.

analysis will be confined to the plane containing the $[010]$ axes of the two grains; effects on an inclined plane are a direct cosine function of the angle between the planes.

The problem is reduced to the situation depicted in Fig. 12 where grains A and B are externally unrestrained and separated by a boundary aob . The $[010]$ axis of grain A is inclined to the boundary by an angle θ and the dimension change as a result of temperature increase is ΔL_b . Dimension change cannot differentiate between a positive or negative direction, however, it may have a positive or negative value. The dimension change of grain A at right angles to the $[010]$ axis (ΔL_{ac}) is inclined at an angle $(90 - \theta)$. If the angle between the $[010]$ axes of grains A and B is σ , then the $[010]$ axis of grain B will be inclined at an angle $(\theta + \sigma)$ and the dimension change of grain B at right angles to the $[010]$ axis will be inclined at an angle $[90 - (\theta + \sigma)]$. An elemental portion of grain A adjacent to the grain bound-

ary will experience a dimension change for a given temperature change as shown in the following equation:

$$\Delta L_A = -\Delta L_b [\cos \theta - \cos (\theta + \sigma)] - \Delta L_{ac} [\cos (90 - \theta) - \cos (90 - [\theta + \sigma])]$$

where ΔL_A is the dimension change of A parallel to the boundary. Expansion of A relative to B will create compressive forces in A, and ex-

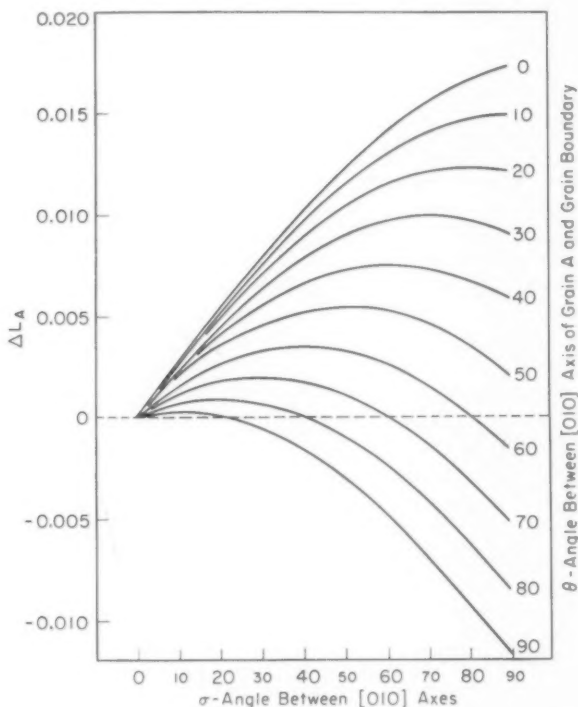


Fig. 13—Effect of Variation of the Angle θ and δ Upon the Differential Expansion of Grain A (ΔL_A) Adjacent to the Grain Boundary.

pansion of B relative to A will create tensile forces. Tensile forces in A are indicated by a positive value of ΔL_A and compressive forces are indicated by a negative value.

A series of curves plotting ΔL_A for different values of the angles θ and σ is shown in Fig. 13; ΔL_b and ΔL_{ac} between room temperature and 500 °C (930 °F) were taken as -0.0027 and 0.0145 inch per inch, respectively. These curves, even though they represent a greatly oversimplified condition, do show some interesting features. When σ is zero

there is no interaction between grains; this condition applies to a single crystal or a bicrystal where the $[010]$ axes are parallel. As σ increases the stress upon A, as indicated by differential expansion, increases; this stress attains its maximum value when σ is 90 degrees and θ is 0 degrees. Because ΔL_b and ΔL_{ac} do not know directionality, values for ΔL_A for angles of θ and σ less than 0 degrees or greater than 90 degrees are symmetrical about the 0 and 90-degree values, respectively. Finally, for certain combinations of angles θ and σ there will be no stress applied on A.

A direct correlation of the above dependency of stress induced within a grain upon the relative orientations of two grains and the position of the boundary between them with experimental observations in coarse-grained specimens is impossible because of simplifying assumptions. Experimentally, grain boundaries are not planar, but rather they are curved surfaces; this results in components normal to the boundary as well as parallel to it and contributes to local inhomogeneities of deformation. Observations of the microstructures, however, do agree with the relationship in two respects. Certain combinations of θ and σ result in no stress applied to A; this is substantiated experimentally, for along the length of irregular grain boundaries there are regions where no apparent interaction is observed within a specific grain. In spite of localized deformation inhomogeneities the relative interaction of two adjacent grains can be described on an arbitrary scale as given in Table II. Although the number of observations is small, the amount of interaction depends upon relative orientations of the grains as measured by the angle σ between the $[010]$ axes. When orientations of $[010]$ axes are quite close interaction is at a minimum and it increases with an increase in the value of σ . Rotation of the other two principal poles about the $[010]$ where σ is small for two adjoining grains appears to have little effect upon deformation behavior.

The nature of deformations resulting from grain interaction can best be understood by observations of coarse-grained specimens after cycling and repolishing. Deformed areas near grain boundaries show subgraining as illustrated in Figs. 3b and 5; their quantity appears to be directly correlated with the amount of deformation. Presumably this structure was created by a polygonization phenomenon. As the samples were heated, stress fields were established at grain boundaries so as to cause slip, bend the lattice, and create imperfections within it. Upon further heating these became mobile and migrated to form low angle boundaries or subgrains; further cycling enhanced this progress. The regularity of the misorientations indicate them to be associated with crystallographic deformations. The Laue photogram of Fig. 6 shows spots that are misoriented by a rotation about the $[001]$ axis (or (001) plane pole). This direction is perpendicular to the $[100]$ slip direction and in the (010) slip plane. Slip on this system may cause rotation

about the $[001]$; it also satisfies the same condition for $\{110\} - \langle 110 \rangle$ slip.

Two other boundary interactions were observed in coarse-grained specimens—boundary sliding and boundary migration. Evidence of boundary sliding was limited; however, there were some definite sharp offsets of scribed lines at grain boundaries (Fig. 4). One clear case of boundary migration was observed in specimen #121. The migration direction was such as to increase grain boundary radius of curvature and to make the angles between grain boundaries more nearly equal; these are normal grain growth phenomenon.

Fine-Grained Specimens—Lack of knowledge concerning individual grain orientations in fine-grained samples prevents any precise evaluation of relative orientation effects upon interaction deformations. Because the grains are restrained to a greater degree, these samples present more complicated conditions than those for coarse-grained samples. Metallographic observations, however, do show similarities in behavior between the two types of specimens, but to varying degrees.

Figs. 7a and 8 show grain boundary migration in fine-grained specimens; successive boundary locations are indicated by a series of lines. Each line probably represents the boundary location during an individual cycle. Information concerning migration direction can be ascertained by comparing the repolished structure of Fig. 7b to that of the as-cycled condition shown in Fig. 7a. Many of the indicated migrations are contrary to those found for normal grain growth. Instead of the grain boundary radius of curvature increasing some have decreased; in other cases, migration direction is away from the center of curvature; and some of the angles between grain boundaries have changed from near equilibrium values of 120 degrees to values larger and smaller than this. These behaviors can point only to deformation inhomogeneities in the various grains during cycling and, therefore, to strain induced boundary migration.

Figs. 8 and 11d clearly demonstrate the formation of subgrains during cycling of fine-grained specimens. Subgrain size in fine-grained material, in proportion to grain size, is considerably greater than that for coarse-grained specimens; however, actual sizes in the two cases are nearly equal as illustrated in Figs. 5 and 11d. The mobility of imperfections probably dictates the subgrain size; this, in turn, depends upon chemical composition and cycling variables such as rate of heating, maximum temperature, and time at maximum temperature.

The increase in grain size as a result of cycling specimen 7A can best be attributed to increased time at maximum heating temperature. Prior to testing, all other fine-grained specimens had been annealed in the alpha phase at temperatures above their high cycling temperatures. Specimen 7A, however, was annealed for 2 hours at 600 °C (1110 °F) and cycled to the same temperature; A similar grain size would prob-

ably have been created if the sample had been annealed for a longer time prior to cycling.

Metallographic observations of fine-grained samples do not permit positive identification of grain boundary sliding; however, relative motion along boundaries is demonstrated by differences in height of the various grains, as shown by shadows cast under oblique illumination in Fig. 8. Such variations in level could be created by localized lattice bending near the boundary. One would expect these deformations to be associated with subgraining and grain boundary migration; in many cases this is true. Boundary sliding may occur in fine-grained specimens; on a purely statistical basis some grain boundaries will yield more readily when subjected to shear stresses than will the grains on either side. This type of grain interaction, however, would appear to play a minor role in unidirectional growth.

The observations of the beta-treated sample substantiate the viewpoint of more liberal localized deformations being associated with randomization of orientation and large variations in σ values. Because no well-defined texture exists in this sample, there is no directionality of macrodeformation. In this respect, Chiswick (1) shows thermal cycling growth to increase as texture perfection of 300 °C (570 °F) rolled rods increases. Data reported by Zegler, et al. (3) indicate the same to be true for 600 °C (1110 °F) rolled rods.

Porosity was not observed in high purity uranium even for a fine-grained specimen cycled as many as 3000 times. Commercial purity material, however, does contain voids after an equal number of cycles. At what level of cycling these voids began to form and the reason for them being created in less pure material is not known. Chiswick (1) observes them to develop as early as 500 cycles. They cannot be correlated with grain size, preferred orientation, or magnitude of growth; nor can they be related to inclusions or grain boundaries.

Upon cycling specimen 7A little texture change was observed other than a slight increase in scatter; this is what would be expected as a result of subgraining. Thermal cycling of mechanically restrained samples, on the other hand, does cause texture changes because differences are observed in expansion coefficients prior and subsequent to cycling; this indicates that primary recrystallization has occurred due to the internal stressing.

Comparison of Thermal Cycling and Creep Studies

There is no visual evidence of a unidirectional dimensional change in the present work. The observed microstructure changes must, however, be used to explain growth. Texture characteristics of uranium and, more specifically, the disorientation between individual grains provide the stress upon cycling. The general types of deformational mechanisms observed here agree well with those reported by Boas and

Honeycombe (9,10,11) and Burke and Turkalo (6). Specifically, the deformations are: intragranular slip and twinning, subgrain formation, boundary migration, and boundary sliding. In many respects these mechanisms are similar to those reported in creep studies.* Primary creep is associated with intragranular deformations of slip and, in some cases, twinning. Secondary or steady state creep is accompanied by polygonization, grain boundary migration, and boundary sliding. A difference in deformation mechanisms appears to occur with grain size; greatly over-simplified, intragranular slip is the dominant mechanism of creep in coarse-grained specimens, whereas in fine-grained specimens grain boundary deformation becomes more prominent.

Supporting evidence for the similarity between thermal cycling growth and creep results can be presented from considerations of the effects produced by test conditions and metallurgical factors. Mayfield (2) reports small values of thermal cycling growth if the upper temperature is below 350 °C (660 °F). This would correspond to creep tests below temperatures where polygonization occurs. For upper temperatures above 350 °C (660 °F), the greater the cycling temperature range the greater the growth; this corresponds to increased stress of creep tests. The higher the upper cycling temperature, for a given temperature range, the greater the growth; likewise higher creep test temperatures cause greater creep rates. Finally, increased holding time at the upper cycling temperature increases growth; this directly correlates with results obtained by increasing creep test time.

Grain size appears to affect creep and thermal cycling in a similar manner. For samples of constant preferred orientation and varying grain size, the specimen with the smallest initial grain size results in the highest growth rate (1). Analogously, small grain size specimens show higher creep rates. Thermal cycling of large-grained materials resulted in refinement of grain size when account was taken of all visible subgrain boundaries as well as grain boundaries; the same is true for creep studies.

Voids are observed to form upon thermal cycling of less pure materials, whereas high purity uranium does not generate them, at least up to 3000 cycles. There are no good experimental data to explain this behavior; however, if similarities between thermal cycling and creep carry over to this phenomenon, the formation of voids is related to chemical purity. Creep studies have shown that, because of decreased grain boundary mobility, less pure materials develop fissures at triple points and grain boundaries more readily than do purer metals.

SUMMARY

Thermal cycling of both large and small grain size uranium speci-

* An excellent review paper which summarized most of the recent investigations of creep processes has been written by Sully (18).

mens results in the appearance of relief on the polished surfaces accompanied by the disclosure of grain boundaries as well as other surface deformation effects. Grain interactions and subsequent subgraining are caused by internally generated stresses; these may be ascribed to the amount of disorientation between adjoining grains and the relative position of the grain boundary between them. This explanation probably also accounts for deformation noted in fine-grained materials, but individual orientation data were lacking and consequently only qualitative statements can be made. Coarse-grained specimens reveal slip deformation mechanisms upon cycling; (010)-[100] slip system being the most predominant, with a second system of the {110}-<110> type, and evidence of (010)-(001) cross slip. Twinning plays a minor role in the deformation of coarse-grained materials and is almost nonexistent in fine-grained samples. Deformation of fine-grained specimens occurs by slip, grain boundary migration, and very limited grain boundary sliding. Because of the texture randomization and the accompanying large disorientation between adjoining grains, beta-treated material deforms extensively upon cycling.

Thermal cycling deformation of orthorhombic alpha-uranium produces microscopic changes similar to those observed in other metals under creep conditions. Effects of test conditions and metallurgical variables upon cycling behavior can be compared to the influence of similar factors upon creep. Therefore, thermal cycling macro growth may be closely related to creep relaxation phenomena.

ACKNOWLEDGMENTS

This investigation was carried out under the direction of F. G. Foote. E. S. Fisher, H. H. Chiswik, and P. A. Beck offered many suggestions with regard to technique and interpretation of results. R. J. Friddle, R. M. Scott, and M. D. Odie perfected most of the technical operations involved in specimen handling and preparation. This paper is based on work performed at Argonne National Laboratory under the auspices of the Atomic Energy Commission.

References

1. H. H. Chiswik, "The Plastic Deformation of Uranium on Thermal Cycling," *TRANSACTIONS, American Society for Metals*, Vol. 49, 1957, p. 622.
2. R. M. Mayfield, "Effects of Cycling Variables Upon Growth Rate of 300 °C Rolled Uranium," *TRANSACTIONS, American Society for Metals*, Vol. 50, 1958, p. 926.
3. S. T. Ziegler, R. M. Mayfield, and M. H. Mueller, "Effects of Fabrication and Heat Treatment Variables Upon the Thermal Cycling Behavior of Uranium," *TRANSACTIONS, American Society for Metals*, Vol. 50, 1958, p. 905.
4. J. R. Bridge, C. M. Schwartz and D. A. Vaughan, "X-Ray Diffraction Determination of the Coefficients of Expansion of Alpha-Uranium," *Transactions, American Institute of Mining and Metallurgical Engineers*, Vol. 206, 1956, p. 1282-1285.

5. J. E. Burke, J. P. Howe and C. F. Lacy, "Dimensional Instability of Uranium," Knolls Atomic Power Laboratory, TID-5044.
6. J. E. Burke and A. M. Turkalo, "Deformation of Zinc Bicrystals by Thermal Ratcheting," *Transactions, American Institute of Mining and Metallurgical Engineers*, Vol. 194, 1952, p. 651-656.
7. M. Bettman, G. W. Brown, and J. P. Frankel, "On the Dimensional Instability of Uranium and of Clad Plates Subjected to Thermal Cycling," California Research and Development Company, MTA-36, December 1953.
8. R. E. Maringer, C. A. Mangio and R. D. Johnson, "A Mechanism of the Thermal Deformation of Uranium," Battelle Memorial Institute, BMI-827.
9. W. Boas and R. W. K. Honeycombe, "The Plastic Deformation of Non-Cubic Metals by Heating and Cooling," *Proceedings of the Royal Society*, Vol. 186, Series A, 1946, p. 57-71.
10. W. Boas and R. W. K. Honeycombe, "The Deformation of Tin-Base Bearing Alloys by Heating and Cooling," *Journal, Institute of Metals*, Vol. 73, 1946-47, p. 433.
11. W. Boas and R. W. K. Honeycombe, "The Anisotropy of Thermal Expansion as a Cause of Deformation in Metals and Alloys," *Proceedings of the Royal Society*, Vol. 188, Series A, 1947, p. 427-439.
12. F. G. Foote, "Physical Metallurgy of Uranium," Nuclear Metallurgy, IMD Special Report Series, No. 1, American Institute of Mining and Metallurgical Engineers.
13. E. S. Fisher, "Preparation of Alpha-Uranium Single Crystals by a Grain-Coarsening Method," *Transactions, American Institute of Mining and Metallurgical Engineers*, Vol. 209, 1957, p. 882.
14. B. Blumenthal, "Melting of High Purity Uranium," *Transactions, American Institute of Mining and Metallurgical Engineers*, Vol. 203, 1955, p. 1199-1205.
15. R. W. Cahn, "Plastic Deformation of Alpha-Uranium; Twinning and Slip," *Acta Metallurgica*, Vol. 1, 1953, p. 49-70.
16. L. T. Lloyd and H. H. Chiswick, "Deformation Mechanisms of Alpha-Uranium Single Crystals," *Transactions, American Institute of Mining and Metallurgical Engineers*, Vol. 203, 1955, p. 1206-1214.
17. P. Lehr and J. P. Langeror, "Dilatometric Behavior of Alpha Uranium Single Crystals," *Comptes rendus*, Vol. 241, 1955, p. 1130-1133.
18. A. H. Sully, "Recent Advances in Knowledge Concerning the Process of Creep in Metals," *Progress in Metal Physics*, Vol. 6, 1956, p. 135-180, Pergamon Press.

DISCUSSION

Written Discussion: By J. P. Frankel, Engineering Department, University of California, Los Angeles.

The authors are to be complimented on the thorough study they reported. Particularly interesting are their observations on the role of grain boundary sliding as a mechanism of distortion. On the twenty-third page of the paper is reported that relative motion along boundaries (in fine-grained samples) is demonstrated by differences in height of the various grains. The implication is that such relative motion can occur only at the surface of the specimen, where such height differences are permitted due to lack of restraint in the direction normal to the surface.

It would appear that, at least when the grain size is so small that a grain does not completely cross the specimen, there is some question whether grain boundary slip can be important in the process studied.

Much less important is an error in viewpoint exhibited by the equation at the bottom of the nineteenth page of the paper. The stress set up between grains with

a common boundary depend not on displacements but strains. Thus the equation should read

$$\Delta L_A/L_A = -\Delta L_b/L_b [\cos^2\theta - \cos^2(\theta + \sigma)] - \Delta L_{ac}/L_{ac} [\sin^2\theta - \sin^2(\theta + \sigma)]$$

where the trigonometric functions have been squared, as is required by the theory of strain.² This equation can be simplified to read

$$(\Delta L/L)_A = (\Delta L/L)_b - (\Delta L/L)_{ac} [\sin^2(\theta + \sigma) - \sin^2\theta]$$

The curves of this equation (corresponding to Fig. 13 of the paper) would of course be different than those shown in Fig. 13; however, no significant change in the authors' analysis is anticipated.

Authors' Reply

The authors thank Dr. Frankel for his discussion to the paper.

Certainly we agree that grain boundary slip does not play an important role in alpha uranium thermal cycling deformation. It does not, however, appear reasonable to entirely discount its occurrence within the volume of fine grained material. A particular grain boundary may experience sliding with the relative displacements of the two grains being accommodated by trans-granular deformation of the surrounding grains.

The relationship between dimensional change and the angles σ and θ was presented as being purely qualitative in nature. Dr. Frankel is quite correct in pointing out that the stress set up between grains with a common boundary depend not on displacements but strains, and thus the equation should have squared trigonometric functions. The authors did not choose to use this relationship because a quantitative evaluation of the stresses and strains at a common grain boundary must take into consideration, among other things, a three dimensional model and the various mechanisms of plastic deformation. It was felt that the more simplified viewpoint would be further removed from a quantitative consideration and thereby accentuate its qualitative nature. Incidentally, the second equation given by Dr. Frankel should read:

$$(\Delta L/L)_A = [(\Delta L/L)_{ac} - (\Delta L/L)_b] [\sin^2(\theta + \sigma) - \sin^2\theta]$$

As was pointed out, this form of the equation does not result in any change in the interpretation of the qualitative feature shown by the equation in the paper.

² See for example A.E.H. Love, *Mathematical Theory of Electricity*, Dover, N.Y., 1944, (p. 39 in 4th Edition).

HYDROGEN-URANIUM RELATIONSHIPS

BY M. W. MALLETT AND M. J. TRZECIAK

Abstract

The relationships in the uranium-uranium hydride-hydrogen system were studied. These included the solubility of hydrogen in massive uranium, the sorption of hydrogen by powdered uranium, and equilibrium pressures for the plateaus of the pressure-composition isotherms. Phase diagrams were constructed from these data. Also, the rates of diffusion of hydrogen in alpha and beta uranium were determined. (ASM International Classification M24b, N15d; U, H)

INTRODUCTION

KNOWLEDGE of the solubilities and rates of diffusion of hydrogen in uranium and of the properties of its hydride enables one to use uranium more effectively. In general, the effect of hydrogen in uranium is deleterious. It causes porosity in castings and loss of ductility through the precipitation of hydride platelets. It also tends to diffuse to the surface of metal parts and disrupt protective coatings. Also, from a metallurgical aspect, a knowledge of phase relationships in the uranium-uranium hydride-hydrogen system is desirable. Therefore, a study of the above mentioned variables was made.

SOLUBILITY OF HYDROGEN IN URANIUM

Early in the Manhattan Project, Battelle (1)¹ reported solubilities of hydrogen in the alpha, beta, gamma, and liquid phases of uranium under one atmosphere hydrogen pressure. The manometric technique used involved measuring the amount of gas absorbed from a measured volume of hydrogen introduced into the system containing the uranium. A recent investigation by Matraw (2) raised questions as to the validity of these data. Consequently, a reinvestigation was made using hydrogen at one atmosphere pressure and employing different equipment but, in general, the same absorption technique. Good agreement with the previous data was obtained. The earlier study had indicated that the pressure dependency of solubility was according to Sieverts' law. Equations

¹ The figures appearing in parentheses pertain to the references appended to this paper.

Work performed under AEC Contract No. W-7405-eng-92.

Of the authors, M. W. Mallett is Consulting Physical Chemist; M. J. Trzeciak is assistant division chief, Battelle Memorial Institute, Columbus, Ohio. Manuscript received March 27, 1957.

Table I
Solubility Equations for Hydrogen in Uranium

Alpha: $\log (S/\sqrt{p}) = -388/T - 0.688$
Beta: $\log (S/\sqrt{p}) = -892/T + 0.408$
Gamma: $\log (S/\sqrt{p}) = -227/T - 0.052$
Liquid: $\log (S/\sqrt{p}) = -587/T + 0.426$
Dissociation pressure: $\log p = -4590/T + 9.39$
S, solubility, in ppm.
P, pressure in mm Hg.

for the solubility of hydrogen in the various allotropic forms of uranium are given in Table I. The limiting values for pressure in these equations are the plateau dissociation pressures of the uranium-uranium hydride mixtures at given temperatures.

An Apparent Anomaly

An extrapolation of the Battelle (1) data to the temperature 295 °C (560 °F) and a pressure (150 microns) used by Matraw gave a value of 0.004 ppm. This figure shows a thousand-fold difference from the 3.6 ppm of Matraw. He reported solubilities of hydrogen in powdered uranium at 295 °C (560 °F) at pressures of 26 to 150 microns. These solubilities were found to obey Sieverts' law and are expressed by $S = K\sqrt{p} = 3.30 \pm 0.22 \times 10^{-3}\sqrt{p}$ where S is solubility in standard cubic centimeter per gram of uranium, and p is the pressure in microns. Because of the enormous difference between the two sets of data an explanation was obviously required. Uranium hydride formation is ruled out since the operating experimental pressure (150 microns) was a hundred times lower than the dissociation pressure of uranium hydride (20,000 microns). Since powdered uranium was used by Matraw it is quite feasible that the high hydrogen sorption was related to the large surface area of the specimen.

A further investigation was made of the sorption of hydrogen on powdered uranium. Measurements were made at 250, 295, 350, 400, 450, and 500 °C (480, 560, 660, 750, 840, and 930 °F) at pressures ranging from 22 to 324 microns. The data are represented by the curves in Fig. 1. The slopes increase progressively with temperature from 250 to 350 °C (480 to 660 °F) and decrease from 400 to 500 °C (750 to 930 °F). The 500 °C (930 °F) isotherm is practically linear indicating lack of pressure dependency in this range. The lowered sorption at 500 °C (930 °F) is a function of elevated temperature and sintering which decreases the surface area. In massive uranium, solution of hydrogen is endothermic and increases with temperature. Therefore, the

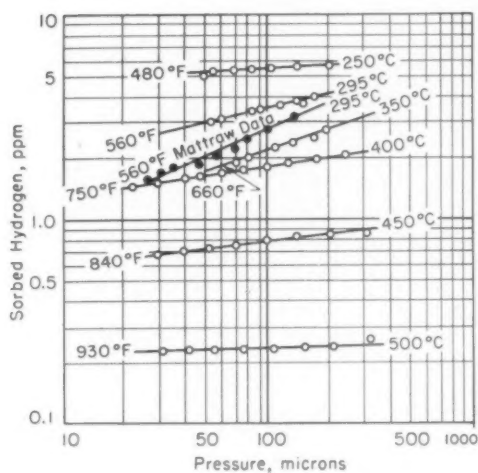


Fig. 1—Sorption of Hydrogen by Powdered Uranium.

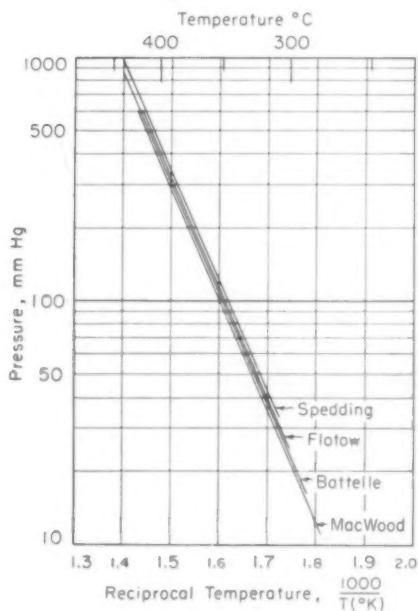


Fig. 2—Comparison of Various Dissociation Pressure Equations.

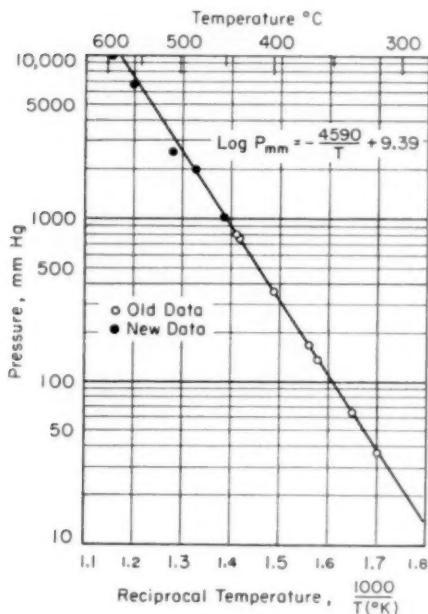


Fig. 3—Variation of Dissociation Pressure of UH_3 with Temperature.

decrease in hydrogen pickup by the uranium powder with increasing temperatures indicates that the main process is not solution.

Results of Matraw's experiment are indicated in Fig. 1 as the black dots. Order of magnitude agreement between the two sets of data is evident. Differences in surface areas between Matraw's samples and those of the present investigation would account for the small discrepancies. Uranium powder used in the present experiment was produced by decomposing UH_3 for three days at 250°C (480°F) in a vacuum. Matraw's UH_3 was decomposed in vacuum at 450°C (840°F) where some sintering took place. The lower sorption on his sample reflects the smaller surface area resulting from sintering.

It is evident that with powdered uranium the hydrogen is held (probably chemisorbed) on the surface of the metal. Consequently, the amounts of hydrogen taken up in these experiments are not directly comparable to true solubility data.

EQUILIBRIUM PRESSURES

Pressure-composition isotherms in metal-hydride systems exhibit plateaus at lower temperatures. Several measurements of the plateau

Table II
Solubilities for Hydrogen in Uranium at One Atmosphere Pressure

Temperature, (°C)	Hydrogen, (ppm)	Temperature, (°C)	Hydrogen, (ppm)
100	Alpha 0.0006*	769	Gamma 14.7
200	0.02*	800	15.0
300	0.2*	900	15.6
400	1.1*	1000	16.2
432	1.6	1100	16.7
500	1.8	1129	16.9
600	2.0		Liquid (Delta) 28.1
662	2.2	1129	29.3
	Beta 7.8	1200	31.1
662	8.5	1300	32.7
700	9.0	1400	
725	9.7		
769			

*Terminal solubilities; $P < 1$ atm.

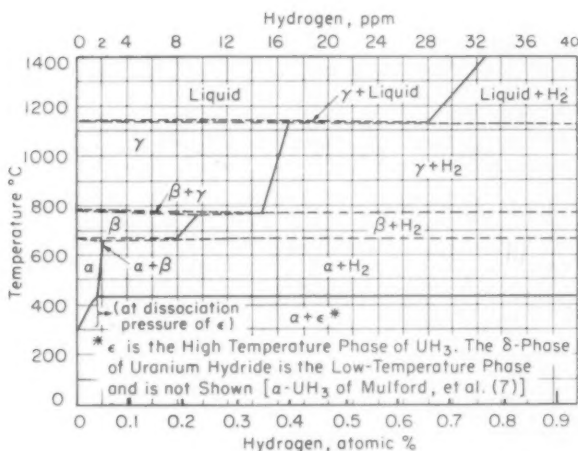


Fig. 4—Hydrogen-Uranium One Atmosphere Pressure Phase Diagram.

equilibrium pressures in the range up to atmospheric have been reported (1,3,4,5). The results of these measurements are plotted in Fig. 2. Agreement among the various equations is very good as the figure illustrates.

The authors recently extended the plateau equilibrium pressure measurements to the region of higher temperatures and pressures. Extrapolation between the old and the new data showed good agreement as seen in Fig. 3. It must be emphasized that these equilibrium pressure data are for partially decomposed uranium hydride and are the plateau pressures of the various isotherms. As hydrogen is withdrawn isothermally the pressure remains constant over the plateau range, the

Table III
Terminal Solubilities for Hydrogen in Uranium

Temperature, (°C)	Hydrogen, (ppm)	Pressure, (atm)	Temperature, (°C)	Hydrogen, (ppm)	Pressure, (atm)
100	Alpha 0.0006	0.000002	800	Gamma (continued) 195	170
200	0.02	0.0006	825	222	213
300	0.2	0.03	850	249	263
400	1.1	0.5	875	279	324
432	1.6	1.0	900	312	397
450	2.0	1.5	925	346	478
500	3.5	3.7	950	385	575
550	5.6	8.5	975	418	675
600	8.6	17.9	1000	457	793
662	13.5	39.7	1025	499	932
	Beta		1050	545	1100
662	49	39.7	1075	589	1260
700	68	61.6	1100	643	1470
725	81	81.2	1129	702	1740
750	97	104		Liquid	
769	111	129	1129	1170	1740
	Gamma		1200	1450	2450
769	168	129	1300	1940	3880
775	172	134	1400	2520	5880

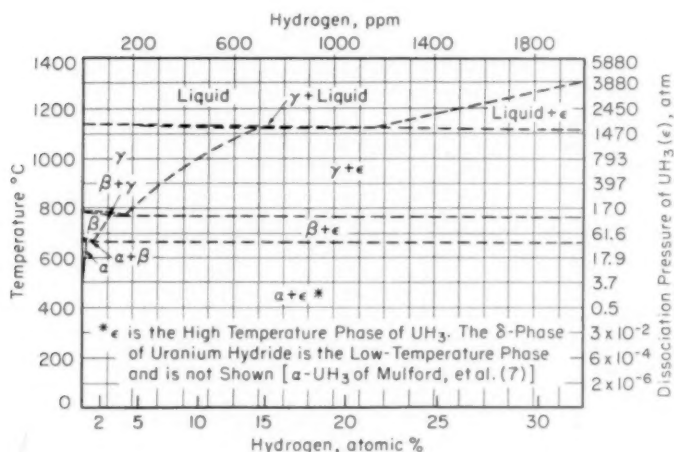


Fig. 5—Hydrogen-Uranium Dissociation Pressure Phase Diagram.

system exhibiting one degree of freedom. The condensed phases comprise a solid solution of hydrogen in uranium and a solid solution of uranium in uranium hydride.

PHASE RELATIONSHIPS

There are three allotropic modifications of pure uranium: alpha, beta, and gamma. The alpha-beta transformation occurs at 662 °C (1224 °F) and the beta-gamma transformation at 769 °C (1416 °F). The melting point of uranium is 1129 °C (2064 °F) (6). These temperatures were used in constructing phase diagrams. The uranium hy-

hydride phase, UH_3 , is designated in the diagrams by ϵ [the $\beta\text{-UH}_3$ phase of Mulford, et al. (7)]. No attempt has been made to show the low temperature δ phase (the $\alpha\text{-UH}_3$ phase of Mulford, et al.)

Solubilities at one atmosphere pressure calculated from the equations in Table I are listed in Table II. The solubility is seen to increase from 2.2 to 7.8 ppm in the transformation from alpha to beta, from 9.7 to 14.7 ppm in the beta to gamma transition, and from 16.9 to 28.1 ppm in the transformation from gamma to liquid. Fig. 4 shows the calculated

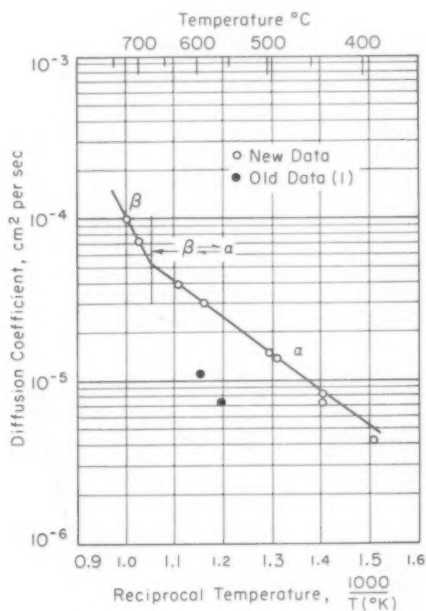


Fig. 6—Diffusion Coefficients for Hydrogen in Uranium.

solubilities plotted as a one-atmosphere phase diagram. Hydride formation occurs at one atmosphere hydrogen pressure below 432 °C (810 °F). Consequently, the solubility curve below this temperature was drawn to represent terminal solubilities, that is, solubilities at the dissociation pressure of the hydride. No precise knowledge was available on the exact location of the alpha plus beta, beta plus gamma, and gamma plus liquid regions when hydrogen is present. Therefore, an arbitrary isotherm 10 degrees below the transformation temperature was selected to which lines could be drawn in order to indicate the existence of these phases.

Table III lists terminal solubilities computed from the equations

Table IV
Diffusion Coefficients

Temperature, °C		D, cm ² per sec
	Alpha Uranium	
390		4.3×10^{-6}
440		8.2×10^{-6}
440		7.3×10^{-6}
490		1.4×10^{-5}
500		1.5×10^{-5}
590		3.0×10^{-5}
630		4.0×10^{-5}
	Beta Uranium	
700		7.3×10^{-5}
724		1.0×10^{-4}

mentioned above. Dissociation pressures were computed from the Equation 1, $\log p = -4590/T + 9.39$, derived from the data shown in Fig. 3. The terminal-solubility data are plotted as a phase diagram in Fig. 5. In addition to temperatures listed on the ordinate, the corresponding dissociation pressures are given.

It must be remembered that these diagrams represent present available data and are not complete. For example, more data are required to establish the position of the two-phase solid-solution region boundaries and the stability region for the δ phase. However, they show graphically the present status of the hydrogen-uranium system and are valuable in illustrating the relationship between hydrogen and the various phases of uranium.

DIFFUSION OF HYDROGEN IN URANIUM

Earliest estimates of the diffusion of hydrogen in uranium were made at Battelle (1) from degassing data. The two experimental diffusion coefficients thus obtained are shown in Fig. 6. The present study was based on a solution of Fick's linear diffusion law, $dc/dt = D d^2C/dX^2$, for radial diffusion in cylinders (8). The solution, which permits the determination of diffusion coefficients from degassing rate data, takes the form

$$R/R_0 = 32/\pi^2 \left[\sum_{n=0}^{\infty} \exp \left[\frac{-\pi^2 (2n+1)^2 Dt/l^2}{(2n+1)^2} \right] \right] \left[\sum_{n=1}^{\infty} \exp \left[\frac{-B_n^2 Dt/r^2}{B_n^2} \right] \right]$$

where,

- R/R_0 = fraction of gas remaining in cylinder at time t ,
- t = degassing time,
- l = length of cylinder,
- r = radius of cylinder,
- B_n = a root of Bessel's function of zero order,
- D = Diffusion coefficient.

Three basic assumptions are made in this application:

- (a) initially, hydrogen is distributed homogeneously throughout the uranium;

(b) the mechanism is simple diffusion of hydrogen through uranium;

(c) the concentration of hydrogen at the surface of the uranium during degassing is zero.

The above equation may be simplified where the degassing time is large. For the cylinder used, 3.81 centimeters long with a 0.487 centimeter radius, the equation simply becomes,

$$\log R/R_0 = -0.252 - 10.88 Dt.$$

A plot of $\log R/R_0$ versus t gives a slope equal to $-10.88D$, from which D in cm^2/sec is calculated. Results obtained using this method are listed in Table IV and are plotted in Fig. 6. The alpha-phase data are represented by the equation,

$$\log D = -2420 \pm 45/T(^{\circ}\text{K}) - 1.71.$$

Since the beta-phase data comprised only two points no equation was calculated. Diffusion coefficients determined from degassing data and involving desorption of molecular hydrogen may differ from those based solely on the movement of atomic hydrogen within the metal. However, in the present case the surface effect is believed to be small because of the relatively large diameter of the specimens used.

ACKNOWLEDGMENTS

Acknowledgment is made of the assistance of Messrs. W. M. Albrecht, D. F. Dilthey, A. F. Gerds, C. B. Griffith, and W. R. Hansen who contributed data for this paper.

References

1. J. J. Katz and F. Rabinowitch, "The Chemistry of Uranium," Part I, National Nuclear Energy Series, 1951, p. 183ff, McGraw-Hill Book Co., New York.
2. H. C. Matraw, "Low Pressure Hydrogen Solubility in Uranium," *Journal of Physical Chemistry*, Vol. 59, 1955, p. 93.
3. F. H. Spedding, A. S. Newton, J. C. Warf, O. Johnson, R. W. Nottorf, I. B. Johns, and A. H. Daane, "Uranium Hydride; Part I. Preparation, Composition, and Physical Properties," *Nucleonics*, Vol. 4, January 1949, p. 4.
4. G. E. MacWood and D. Altman, "The Thermodynamic Properties of Some Tuballoy Compounds," General Resume of Tuballoy Chemistry, Chemical Group, University of California Radiation Laboratory, *Report RL-4.7.600*, August 9, 1944.
5. H. Flotow and B. Abraham, "Dissociation Pressures of Uranium Hydride and Uranium Tritide," *Report No. AECD-3074*, January 5, 1951.
6. H. A. Saller and F. A. Rough, "Compilation of U. S. and U. K. Uranium and Thorium Constitutional Diagrams," Battelle Memorial Institute Report No. BMI-1000, 1955, p. 9.
7. R. N. R. Mulford, F. H. Ellinger and W. H. Zacharaisen, "A New Form of Uranium Hydride," *Journal, American Chemical Society*, Vol. 76, 1954, p. 297.
8. A. Demarez, A. G. Hock and F. A. Meunier, "Diffusion of Hydrogen in Mild Steel," *Acta Metallurgica*, Vol. 2, 1954, p. 214.

DISCUSSION

Written Discussion: By James T. Waber, University of California, Los Alamos Scientific Laboratory, Los Alamos, New Mexico.

The authors are to be complimented for having assembled a variety of information about the hydrogen-uranium system for presentation. However, in preparing this summary the authors apparently overlooked their earlier resume of the same material.² This inadvertence has led to some confusion between investigators which will be mentioned below, because of the similarity in titles.

The experimental method has not been described in detail either in Reference 1, in the authors' resume,² or in the present paper. It would be desirable to have the authors indicate which modifications of the method have been responsible for their obtaining the successively improved results.

The coefficients in the Sieverts' Law expressions

$$\log \frac{S}{\sqrt{p}} = \frac{-A}{T} + B \quad (a)$$

previously reported are different from the values in the present Table I so that the solubilities at one atmosphere pressure and the terminal solubilities are higher at low temperatures in the more recent data. Although the same equation for the decomposition pressures is cited in Table I of both reports, the pressure values employed by the authors are dissimilar. The following data for the terminal solubilities at 662 °C (1225 °F), the alpha beta transformation temperature,

	Alpha	Beta	Pressure
Previous	9.5 ppm	38.9 ppm	43.5 atm
Present	13.5	49	39.7

will illustrate the situation.

The authors indicate that the terminal solubilities; i.e., the boundaries between the uranium solid solution and the two solid phase regions, were obtained by equating the pressures in the Sieverts' Law expressions to the dissociation or plateau pressure equation at a given temperature. The decomposition pressure relations of three other investigators are cited. What would the spread in terminal solubilities be if the highest and lowest of these equilibrium pressures were used? Have any experimental checks of the solubility limits been made to ascertain which is more nearly correct?

The authors note that the adsorption of hydrogen on the surface of finely divided metal will increase the apparent solubility. How did the authors separate the two in deriving their solubility equations?

It would appear that the authors could estimate the heat of solution of hydrogen in the allotropes of uranium from their data. This may be seen by rewriting equation (a) in the form

$$\log p = 2A/T - 2B + 2 \log S \quad (b)$$

Since one obtains the partial molar heat of solution of hydrogen by plotting $\log p$ against the reciprocal of temperature at a given constant composition, ΔH is

² M. W. Mallett and M. J. Trzeciak, "Hydrogen-Uranium Phase Diagrams," Nuclear Engineering and Science Congress Preprint 333 (1956).

$-2(2.303)R.A.$ Thus, these heats of solution specifically are -3.55 Kcal for alpha, -8.16 Kcal for beta, -2.08 for gamma and -5.37 Kcal for the liquid, if the tabulated equations are based on log 10. All four appear to be negative in contrast to the statement of Matraw (Ref. 2).

The really important new information in this report is the diffusion coefficients.

Would the authors estimate for a series of temperatures and the minimum times to reduce the hydrogen content to 1% of its initial value? What would the minimum vacuum pressure be to achieve 0.1 ppm in the various phases? This would be useful information for practicing metallurgists.

Written Discussion: By W. D. Davis, Mass Spectrometry, Knolls Atomic Power Laboratory, Schenectady, New York.

This paper was especially interesting to the writer because similar work has been done at this Laboratory. A comparison of the authors' data on the solubility and diffusion of hydrogen in uranium with our own results (AEC Research and Development Report KAPL-1548, unclassified) shows that while in general the agreement is satisfactory, discrepancies do occur which need resolving.

The solubility was measured from 400–800 °C (750–1470 °F) at pressures from 100 to 650 mm by an absorption technique similar to that used by the authors. The results extrapolated to 1 atmosphere pressure are shown in the accompanying table. For temperatures of 600 °C (1110 °F) or greater, the agreement can be

Solubility of Hydrogen in Uranium at One Atmosphere Pressure

Temperature (°C)	(°F)	Solubility (ppm)
400	752	0.54
417	783	0.57
450	842	0.67
500	932	0.91
Alpha 525	977	1.07
550	1022	1.25
600	1112	1.65
650	1202	2.14
685	1265	2.5
Beta 700	1292	2.5
725	1337	2.5
750	1382	8.2
Gamma 800	1472	14.2

considered satisfactory but at lower temperature, the solubilities obtained at Battelle are considerably higher. An earlier classified report by the authors gave some results which agreed much more closely with our data. These results were obtained by saturating uranium specimens with hydrogen, quenching, and analyzing by vacuum fusion. I would like the authors to comment on the reason why these solubilities were not considered reliable. Our experience with this general method using rapidly flowing He to quench the saturated uranium and hot extraction for analysis has been satisfactory although temperatures other than 600 °C (1110 °F) have not been tried.

We observed an interesting anomaly in the solubility behavior of alpha-uranium which the authors apparently did not encounter. The solubility was found to be proportional to $P^{1/2}$, as expected, but extrapolation to zero pressure gave residual solubilities between 0.1–0.2 ppm., for all temperatures. A more detailed study at

600 °C (1110 °F) and pressures below 10 mm using both absorption measurements and the quenching-analysis method showing that the solubility increased rapidly with pressure up to about 4 mm and then changed to the lesser slope previously found for the higher pressures. All of these results were obtained with the ordinary grade of uranium of about 99.9% purity usually referred to as "biscuit" uranium. Solubility determinations on two other samples of uranium containing less impurities showed that this abnormal behavior had been eliminated or greatly decreased. Apparently, there is a trace of impurity in "biscuit" uranium which adds its own hydrogen absorption to that of uranium until it is saturated at about 4 mm following which the variation of solubility with pressure is characteristic of pure uranium. If this is true, the solubilities of the accompanying table are too large by an amount varying from about 0.2 ppm at 600 °C (1110 °F) to 0.1 ppm at 400 °C (750 °F).

In view of this behavior, additional information would seem to be necessary before, "it is evident that with powdered uranium, the hydrogen is held on the surface of the metal". Were any measurements made of solubility at low pressures and temperatures for massive uranium? What grade of uranium was used in this work? Instead of depending on extrapolation of temperature and pressure, a more direct comparison of powdered and massive uranium using the same grade of uranium should be made.

The diffusion constant for hydrogen in U was determined at this Laboratory both by diffusion out of 1/2-inch spheres and diffusion through membranes. In both cases, wide variations in rates were observed which appeared to be a function of the cleanness of the surface. The variation of permeability of the membranes with pressure was characteristic of surface poisoning. The high values for the diffusion constant obtained after treatments designed to remove the surface contamination were reasonably consistent and gave for the alpha-phase:

$$D(\text{cm}^2/\text{sec}) = 1.4 \times 10^{-8} e^{-3200/T^\circ \text{K}}$$

At the top of the alpha-range, our values for D are in agreement with the authors but at the lower temperatures are appreciably higher. The fact that our experience showed that dimensions as large as 1/2-inch were not sufficient to eliminate the surface effect suggests this as one possible reason for the discrepancy but certainly more evidence is needed to establish this point.

In the beta-phase, our results indicate a nearly constant D of about 5×10^{-8} cm²/sec., instead of a rapidly rising function. In the gamma-phase between 800-900 °C (1470-1650 °F), D was about 12×10^{-8} cm²/sec.

Authors' Reply

We thank the discussers of our paper for their interesting comments and additional observations on the subject.

Dr. Waber has drawn attention to the discrepancy between hydrogen solubility data presented in Nuclear Engineering and Science Congress (1955) Preprint 333 (see also Preprint 334, M. W. Mallett, M. J. Trzeciak, and C. B. Griffith, "A Review and Redetermination of Hydrogen-Uranium Relationships"). These preprints were unedited drafts of the material appearing in the present paper. Corrections and modifications have been made; therefore, apparent discrepancies will be observed. In the first draft solubility data by both the manometric (absorption) and vacuum-fusion analysis techniques were reported in a graph. In addition, the

analytical data were tabulated. Upon reconsideration, the lower analytical results were attributed to ineffective quenching of the analytical samples. Therefore, the manometric data are considered more nearly correct.

As to difference in equilibrium pressures calculated from the same equation listed in both papers, an error was discovered in the earlier calculations. All equilibrium pressures were recalculated and corrected where necessary.

In regard to the terminal solubilities calculated from the highest and lowest dissociation pressures (Fig. 2: Data of Spedding and Mac Wood respectively) the spread in results is about 10% at 300 and 400 °C (570 and 750 °F), the approximate experimental limits of these investigations. It is felt that if experimental checks of solubility limits were made, they would agree no better than this.

Since the authors' solubility measurements were made on massive specimens with small surface to mass ratios the amount of adsorbed hydrogen was quite small.

In view of Dr. Waber's interest in our diffusion coefficients we should like to mention that the sample equation for $\log R/R_0$ in the Nuclear Congress Preprint 334 contained an error which has been corrected in the present paper. This error did not affect other data.

It is recognized that degassing times, residual hydrogen concentrations, etc. can be calculated from the data presented in this paper. However, for the sake of brevity, tables, charts, and nomographs illustrating the use of the data have been omitted.

In reply to Dr. Davis, we have made no experiments which would either confirm or refute the hypothesis that at 400 to 600 °C (750 to 1110 °F), 0.1 to 0.2 ppm hydrogen is combined with impurities thus causing hydrogen solubilities for uranium to be high by these amounts. However, since uranium is usually saturated with oxygen, any metals capable of forming stable hydrides should already be combined with oxygen. Such oxides would be inert to hydrogen in the uranium.

We have observed that the solubility of hydrogen in massive biscuit uranium varies as the square root of hydrogen pressure. These findings appear in Ref. 1. On the basis of this, we believe that, "it is evident that with powdered uranium the hydrogen is held on the surface of the metal". For example, hydrogen solubility in massive uranium at 400 °C (750 °F) is 1.1 ppm at 360 mm of pressure. Extrapolating to 0.2 mm, a value of 0.03 ppm is obtained. Comparing this with the observed value of 2 ppm for uranium powder at the same temperature and pressure a difference of 1.97 ppm is found. This is much more than the 0.1 ppm said to be held by impurities. Also, the decrease of the amount of adsorbed hydrogen associated with the decrease in surface area due to sintering of the powder clearly points to a surface phenomenon.

GRAIN BOUNDARY MOVEMENT IN BICRYSTALLINE ALUMINUM

BY R. B. POND AND ELEANOR HARRISON

Abstract

An investigation of the plastic deformation of aluminum bicrystals having grain boundaries normal to the specimen axis is reported. Data indicate that these "free" boundaries behave quite differently than boundaries which contain the specimen axis and are therefore influenced by a grip effect. A technique for producing transverse boundaries is described. Stress-strain diagrams for such specimens are given which show that the index of strain hardening for bicrystals whose boundaries are free to translate is lower in the plastic region than the index for single crystals of the parent orientation. Examination of both tension and compression specimens having the [121] pole in the slip plane and 90 degrees from the specimen axis shows that the boundary does translate during deformation causing the bicrystal to assume a "V" shape. In tensile specimens this translation is away from the acute angle made by the intersection of the slip planes in the two grains; in compression specimens, toward it. There is no significant bending of the slip planes at the grain boundary in either. (ASM International Classification M27f, Q24; Al)

INTRODUCTION

THE MECHANICAL PROPERTIES of a metal are greatly dependent upon the size and relative orientations of the crystals composing the specimen being tested. In order to better understand the basic deformation characteristics, considerable attention has been given to the variation of mechanical properties and deformation mechanics with orientation variation for single crystal specimens. As a result of research in this direction, the basic concepts involved in the deformation phenomena can be explained and have been summarized in the literature (1-4)¹.

The information gleaned from the single crystal has been used to explain the more complex behavior of a polycrystalline specimen (5)

¹ The figures appearing in parentheses pertain to the references appended to this paper.

A paper presented before the Thirty-Ninth Annual Convention of the Society, held in Chicago, November 4-8, 1957. Of the authors, R. B. Pond is assistant professor; Eleanor Harrison, research assistant, Metallurgy Section of the Department of Mechanical Engineering, Johns Hopkins University, Baltimore. Manuscript received April 15, 1957.

and experiments have been designed to study the deformation of such specimens. Studies of specimens containing large, approximately equiaxed grains of random orientation have been made as well as studies of specimens containing crystals of controlled orientation and grain boundary position. Included among the second group of studies are those of Chalmers (6), Kawada (7), Gilman (8), Clark and Chalmers (9), Aust and Chen (10), Chen and France (11), and Davis, et al. (12). In all of these studies there have been two parameters which have remained constant, i.e., each specimen tested has been a bicrystal and all grain boundaries have extended along the longitudinal axis of the specimen.

It is not obvious that studies involving bicrystal specimens wherein the grain boundary contains the specimen axis will not be influenced by grip effects on the grain boundary. In such cases the grain boundary is held almost completely immobile to movements in the direction of the specimen axis. France (13) showed that when certain bicrystals of aluminum were extended to rupture the grain boundary moved considerably in a direction away from the specimen axis, see Fig. 1. Because of the above reasons the present investigation concerns itself with bicrystal specimens, the grain boundaries of which are situated normal to or approximately normal to the specimen axis. They are referred to as "free grain boundaries" since they are in no sense held within the grips of the testing device.

SPECIMEN PREPARATION

The specimens used in this investigation were square in cross section and measured either $\frac{1}{8}$ or $\frac{1}{4}$ inch on an edge. The bicrystalline specimen was produced from a single crystal specimen which had been grown by the modified Bridgman technique as described by Chen and Pond (14). The single crystals were cast from Alcoa high purity aluminum (99.99+ % purity). The technique which was devised for the manufacture of bicrystals contains three basic steps: 1) obtaining a small molten zone through a cross section of the specimen at its approximate midpoint, 2) rotating one end of the specimen relative to the other end about the specimen axis without rupturing the fluid coupling between the two ends, and 3) translating one end of the specimen toward the other end in the direction of the specimen axis. This is illustrated in Fig. 2a where the A section of the specimen is rigidly attached and the B section of the specimen is capable of being rotated in direction X and translated in direction Y. The operation of translation produces an ejection of the excess molten material from the molten zone M which flushes the bulk of the impurities which have been moved into the zone by sectional zone refining from the body of the specimen and also provides a space external to the body of the specimen for normal solidification shrinkage cavity which can be seen in the second view of Fig. 2a.



Fig. 1—Ruptured Surface of Aluminum Bicrystalline Specimens Containing Longitudinal Grain Boundaries Viewed Parallel to the Specimen Axis Showing Grain Boundary Movement for Two Specimens. (Actual size), after France (13).

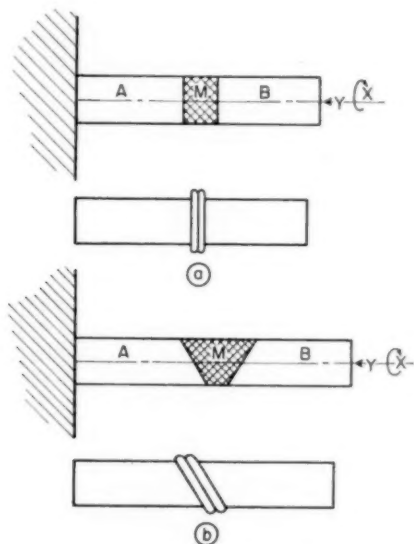


Fig. 2a—Schematic Illustration of Molten Zone and Movement Directions in Production of a Bicrystalline Specimen with a Free Grain Boundary.

Fig. 2b—Schematic Illustration of Molten Zone and Movement Directions Necessary to Produce a Bicrystalline Specimen with a Free Grain Boundary Being at an Angle to the Specimen Axis.

Subsequent to these operations, the ejected bead is carefully filed away, the specimen lightly sanded, drastically etched to remove surface re-

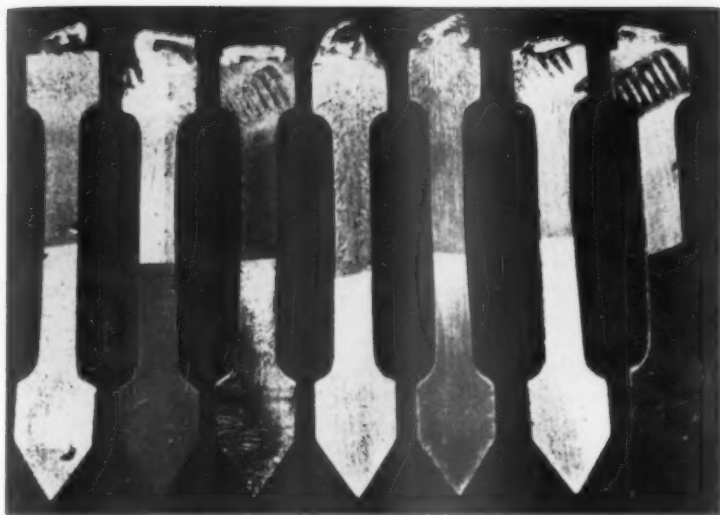


Fig. 3—Characteristic Array of Tensile Specimens Produced with Free Grain Boundaries.
($\times 2$.)

sidual stresses and then homogenized above recrystallization temperature.

Using this technique, approximately one hundred bicrystalline specimens of the type illustrated in Fig. 3 have been produced. The production of the molten zone is accomplished by use of an oxygen-acetylene torch with a tip suitable to concentrate the heat in the desired section for fusion without rupturing the fluid surfaces thereby avoiding the mechanical incorporation of oxide or impurities. It can easily be seen that by the proper selection of the original crystal orientation and control of the amount of rotation in the X-direction, one can develop either twist or tilt type boundaries using this technique.

In the cases to be discussed herein, all boundaries were approximately normal to the specimen axis and all rotations were of either 90 or 180 degrees since the specimens were square in cross section. It is very easy by this technique to develop free grain boundaries having an angle with the specimen axis of magnitudes up to 45 degrees by the simple expedient of controlling the shape of the molten zone and performing rotational operations in the X-direction of 180 degrees prior to translation along the specimen axis. This is illustrated in Fig. 2b. The molten zone is controlled to be trapezoidal in cross section so that upon rotation the liquid solid interface on the mobile end of the specimen is parallel to the liquid solid interface on the fixed end, both being at an angle to the specimen axis. Specimens having such grain boundary



Fig. 4—Ruptured Tensile Specimen Showing Translation of Free Grain Boundary and Disposition of Slip Planes ($\times 5$).

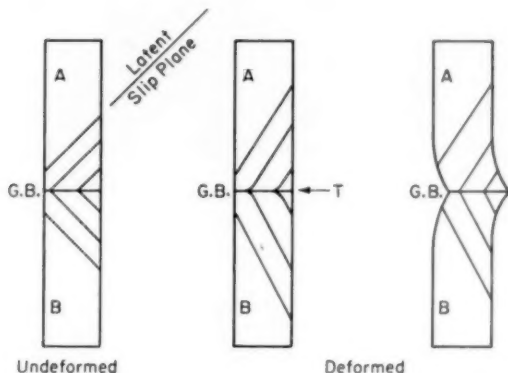


Fig. 5—Schematic Illustration Depicting Rotation of Segments of the Crystal with Deformation Producing Bending of the Slip Planes if Grain Boundary is Restricted or Translation of the Grain Boundary if Movement is Not Restricted.

situations have been produced although they were not used in the present investigation.

Orientations of all parent single crystals as well as the individual crystals of the bicrystal specimen were determined by standard x-ray back-reflection Laue methods.

RESULTS AND DISCUSSIONS

Upon extending specimens in tension having random parent crystal orientation and free grain boundaries, the general observation was made that in most cases the grain boundary seemed to be translated out of line. See Fig. 4. Close examination indicated that in all such specimens, the primary slip planes on either side of the grain boundary were located so that the grain boundary translation was in a direction included within and extending away from the acute angle made by the

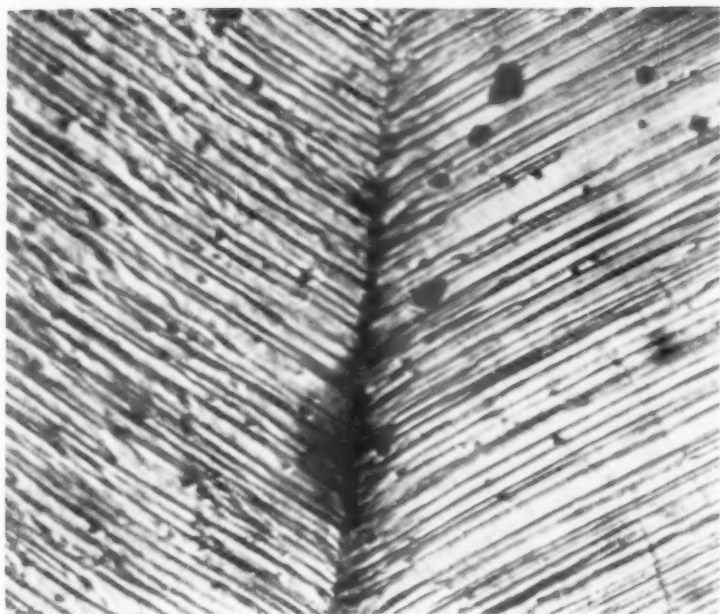


Fig. 6—Grain Boundary of Specimen Deformed in Tension Showing Lack of Bending of the Slip Planes at the Grain Boundary. $\times 325$.

intersection of the slip planes in the two grains. A postulation was made that the grain boundary translation was due to rotation of the crystal segments by the slip process and a subsequent translation of the grain boundary in the direction of rotation of the end of the slip planes adjacent to the grain boundary. If this postulate is to prove correct there should be virtually no bending of the slip planes in the vicinity of the grain boundary. This is illustrated in Fig. 5. Here the position of the latent slip planes is seen and the specimen is pictured having a force T applied at the grain boundary opposing what has been observed as the translation, thereby holding the grain boundary in alignment with the rest of the specimen and producing bending of the slip plane adjacent to the grain boundary. However, when this force is nonexistent, it can be seen that the slip planes do not bend at the grain boundary but translate the grain boundary. Fig. 6 is a characteristic photomicrograph of such a grain boundary showing the lack of distortion or bending of the slip lines at or in the vicinity of the grain boundary. It was further postulated that the bicrystalline specimen grain boundary desires to translate under deformation for specific orientations. If this translation were allowed both the index of strain hardening, (the slope of the stress-strain diagram) and the stress level for a given strain in the

advanced plastic region for such a specimen should be lower than for a single crystal of the same parent orientation. Therefore, specimens were produced having the $[121]$ pole which lies in the slip plane 90 degrees from the slip direction and is therefore the axis of rotation of the slipped segment of the specimen nearly perpendicular to the specimen axis. Such a specimen should produce a maximum amount of translation at

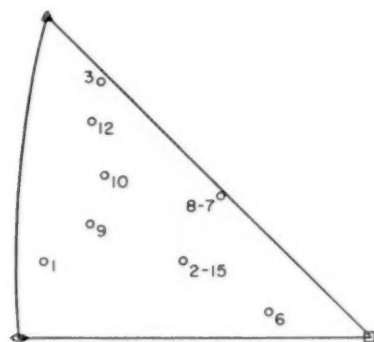


Fig. 7—Representation of the Orientation of Specimens Tested.

a given extension. Eight such specimens were produced; the specimen axis orientation is shown in a standard reference triangle of a stereographic plot in Fig. 7; the angle between the $[121]$ and the plane normal to the specimen axis being given in Table I.

Table I		
Specimen No.	Type of test	Angle versus $[121]$ and plane perpendicular to specimen axis
1	Tensile	26°
3	Tensile	18°
6	Tensile	17°
9	Tensile	18°
10	Compressive	18°
12	Tensile	22°
2-15	Compressive	3°
8-7	Compressive	2°

Fig. 8 is a characteristic plot of the tensile stress-strain relationships showing that although the proportional limit for the single crystal material is below that for the bicrystalline material, the two curves cross and the index of strain hardening as well as the stress level for a given strain of the bicrystalline specimen becomes considerably less than those of the single crystal. It is apparent that the grain boundary in the tensile specimen cannot translate too far out of line since the tensile grips and the length of the specimens will regulate to some ex-

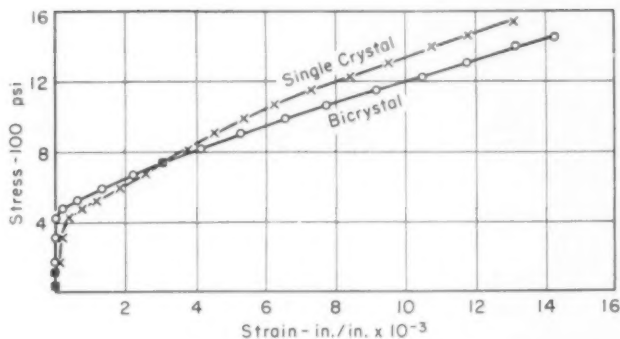


Fig. 8—Stress-Strain Relationships for Single Crystal and Bicrystal Specimens No. 1 Having the Same Parent Orientation When Deformed in Tension.

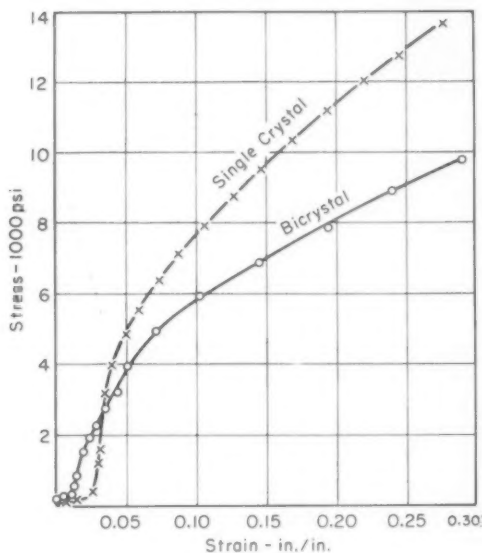


Fig. 9—Stress-Strain Relationships for Single Crystal and Bicrystal Specimens No. 2-15 Having the Same Parent Orientation When Deformed in Compression.

tent such movement. However, if a similar specimen were loaded in compression, the grain boundary translation should still occur although the movement should be a direction opposite that for the tensile specimen or toward the acute angle formed by the intersection of the primary

slip planes in the two grains. In this case, since there will be no bending of the slip planes at the grain boundary, the index of strain hardening and the stress level for a given strain should be considerably less than those of a single crystal of the same parent orientation. Since neither the length of the specimen nor the grips should have as much influence in the extent of translation, the index of strain hardening and the stress level for a given strain should maintain considerably lower values.

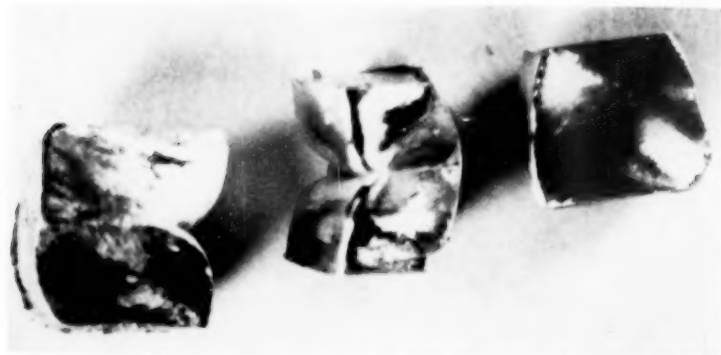


Fig. 10—Illustration of Translation of Grain Boundaries in Compression Specimens 8.7 and 2.15 as Compared with the Deformed Single Crystal of Same Parent Orientation. ($\times 7$)

Fig. 9 is a plot of the stress-strain relationships for such compressive test. Fig. 10 shows the translation in the compressive specimen grain boundaries as compared with the appearance of deformation in the single crystal.

It seems appropriate to use these observations as a basis for suggesting future work on the problem of deformation of the polycrystalline aggregate. If the force T in Fig. 5 required to prevent translation of the grain boundary can be accurately measured and a specimen can be manufactured wherein a small third grain is positioned at the grain boundary so that it does not interfere with the slip mechanics of the principle bicrystalline specimen and yet prevents grain boundary translation, a measure of the contribution to the increase of the strain hardening index and plastic stress level by this third grain could be indicated.

CONCLUSIONS

On the basis of the investigation described, we conclude:

- 1) the grip effect on all bicrystalline specimens having longitudinal grain boundaries cannot be ignored,
- 2) the index of strain hardening as well as the plastic stress level in free grain boundary bicrystalline specimens capable of maximum grain

boundary translation is lower than said index and stress level for single crystals having the same orientation as the parent crystal of bicrystalline specimens whether tested in tension or compression.

ACKNOWLEDGMENTS

This research was supported by the United States Air Force through the Air Force Office of Scientific Research of the Air Research & Development Command, under contract No. AF 18(600)-1587. Reproduction in whole or in part is permitted for any purpose of the United States Government.

References

1. C. S. Barrett, *Structure of Metals*, 2nd Edition, 1952, McGraw-Hill Co., New York.
2. E. Schmid and W. Boas, *Plasticity of Crystals*, 1950, F. A. Hughes and Co., Ltd., London.
3. A. H. Cottrell, *Dislocations and Plastic Flow in Crystals*, 1953, Oxford University Press, London.
4. R. Maddin and N. K. Chen, "Geometrical Aspects of the Plastic Deformation of Metal Single Crystals," *Progress in Metal Physics*, Vol. 5, 1954, Pergamon Press, London.
5. C. J. Taylor, "Plastic Strain in Metals," *Journal*, Institute of Metals, Vol. 62, 1938, p. 307.
6. B. Chalmers, "Influence of the Difference of Orientation of Two Crystals (Tin) on the Mechanical Effect of Their Boundary," *Proceedings*, The Royal Society, Vol. 162, Series A, 1937, p. 120.
7. T. J. Kawada, "On the Plastic Deformation of Zinc Bicrystal," *Physical Society of Japan*, Vol. 6, 1951, p. 363, 485.
8. J. J. Gilman, "Deformation of Symmetric Zinc Bicrystals," *Acta Metallurgica*, Vol. 1, 1953, p. 426.
9. R. Clark and B. Chalmers, "Mechanical Deformation of Aluminum Bicrystals," *Acta Metallurgica*, Vol. 2, 1953, p. 80.
10. K. T. Aust and N. K. Chen, "Effect of Orientation Difference on the Plastic Deformation of Aluminum Bicrystals," *Acta Metallurgica*, Vol. 2, 1953, p. 632.
11. N. K. Chen and L. L. France, "Interaction of Slip Bands with a Grain Boundary," *Technical Report #1*, O. O. R. Contract # D-36-034-ORD 1153RD, 1953.
12. R. S. Davis, R. L. Fleischer, J. D. Livingston and B. Chalmers, "Effect of Orientation on the Plastic Deformation of Aluminum Single Crystals and Bicrystals," *Journal of Metals*, Vol. 140, 1957, p. 136.
13. L. L. France "The Effect of a Grain Boundary on the Mechanical Properties of Aluminum Bicrystals of Controlled Orientation," Thesis, The Johns Hopkins University, 1955.
14. N. K. Chen and R. B. Pond, "Dynamic Formation of Slip Bands in Aluminum," *Transactions*, American Institute of Mining and Metallurgical Engineers, Vol. 194, 1952, p. 1085.

DISCUSSION

Written Discussion: By J. D. Livingston, General Electric Research Laboratory, Schenectady, New York.

I would like to compliment the authors on their interesting method of preparing bicrystal specimens. Although the method yields specimens in which the boundary

region has had a rather special freezing history, probably the subsequent high temperature anneal allows this region to approach more closely an equilibrium structure.

One study of the deformation of aluminum bicrystals with boundaries transverse to the stress axis has already been published² but I believe the authors' paper to be the first to attempt interpretation of stress-strain curves on such bicrystals. In Dr. Fleischer's discussion, which he has kindly allowed me to see before publication, he points out some of the difficulties inherent in such an attempt. I would like to make some further observations which I believe should also be borne in mind when comparing the authors' results to those on bicrystals with longitudinal grain boundaries.

Most of the bicrystals reported on here were formed by a rotation of 180 degrees about the grain boundary normal, which produces *symmetric* bicrystals. Such boundaries cause little disturbance of the slip processes in the crystals, and it has been shown that the stress-strain curves for symmetric longitudinal bicrystals are no higher than those of corresponding single crystals.³ Furthermore, during metallographic observation of various symmetric longitudinal bicrystals I have never observed any bending or distortion of slip lines at the boundary, so that in this latter respect the authors' symmetric transverse boundaries behave no differently than symmetric longitudinal ones. It would be of interest if the authors would report their observations on transverse bicrystals that were not symmetric.

It is to be hoped that the authors' work will stimulate further investigation of the "grip effects" involved in tensile deformation of single crystals and bicrystals. The points raised by Dr. Fleischer make it clear that the deformation behavior of bicrystals with *transverse* boundaries is intimately related to "grip effects", and that stress-strain curves obtained will depend sensitively on specimen length, type of loading (tension or compression) and length of the gage section. With *longitudinal* bicrystal specimens, on the other hand, one can presumably get data unrelated to "grip effects" by employing a gage section long compared to the cross sectional dimensions of the specimen but still well removed from the grips. This paper may stimulate a more critical examination of this supposition, which is inherent in most of the published work on longitudinal bicrystals.

Written Discussion: By R. L. Fleischer, Massachusetts Institute of Technology, Cambridge, Mass.

The authors' use of bicrystal specimens is a most interesting one. In interpreting the work in terms of grain boundary effects, however, certain difficulties arise. In the first place the nature of the stress-strain curve obtained for the bicrystals will vary depending on the gage section chosen for the measurement of strain. As an example, if the local strain near the grain boundary were less than the average over the whole sample, then by choosing a sufficiently short gage length one would find the bicrystal stress-strain curve above that for the single crystal. A second difficulty is that once deformation has begun, the nature of the applied stress for the bicrystal is different from that for the single crystal. This difference exists because of the freedom of translation in the plane of the boundary, which displaces the crystal so that its sides are no longer parallel to the applied stress.

² S. Karashima, "Studies on the Plastic Deformation of Two-Grained Aluminum Specimens," *Memoirs of the Institute of Scientific and Industrial Research*, Osaka University, Vol. 10, 1952, p. 78.

³ J. J. Gilman, "Deformation of Symmetric Zinc Bicrystals," *Acta Metallurgica*, Vol. 1, 1953, p. 426.

Hence, simple uniaxial tension or compression is no longer present and the meaning of the stress-strain curves is in doubt.

The experiments described can perhaps be most simply understood by approaching them as an examination of properties of single crystals. If the bicrystals are regarded as two single crystals, acting as each others grip at one end, then the stress-strain curves given show the effect of changing the grip constraints on single crystals. Thus the displacement of the grain boundary perpendicular to the original stress axis is a means of reducing the grip restraint. The work described here can now be seen to be analogous to that of Karashima,¹ who supplied bending moments to oppose those which normally arise during tensile deformation of single crystals. He too observed a lowering of the work hardening rate where the grip restraint was reduced.

Authors' Reply

Some excellent points have been brought out by these discussors and the discussions presented make evident to us that we should explain our method of determining the stress-strain curves reported.

The tensile curves were developed for the single crystal and the bicrystal simultaneously by attaching bonded wire, resistance strain gages, type A-8 over the grain boundary as well as at the mid-point of one single crystal end of the specimen, and reading the respective strains for each load applied. These tensile specimens were square in cross section, $\frac{1}{4}$ -inch on a side, and 3 inches long. The gage length for both the bicrystal and single crystal can now be seen to be only $\frac{1}{8}$ -inch.

The compression curves were developed independently for the bicrystal and single crystal specimens. These specimens were square in cross section, $\frac{1}{8}$ -inch on a side and $\frac{3}{8}$ -inch long. The gage length was taken as the specimen length in both specimens.

¹ S. Karashima, *Memoirs of the Institute of Scientific and Industrial Research*, Vol. 13, 1956, p. 35.

GROWTH OF CADMIUM FROM THE VAPOR

By J. E. McNUTT AND R. F. MEHL

Abstract

A technique is described for making continuous microscopic and interferometric observations of cadmium crystals while they are actually growing by deposition from cadmium vapor at constant temperature and supersaturation. Selected observations on the changes occurring on basal hexagonal surfaces during experiments with various supersaturations and deposit temperatures within 50 °C of the melting point are reported.

The propagation of steps across basal surfaces was the principal mechanism of growth observed at high deposit temperatures. These steps usually originated at edges of surfaces where adjacent crystals touched or at other boundaries and ranged from sub-interferometric heights (less than about 300 Å) to heights of more than 3000 Å. Their heights often changed during propagation, and there was no particular step height characteristic of a given substrate temperature or vapor supersaturation.

As the deposit temperature decreased there was an increasing tendency for growth to occur by the propagation of sloping growth fronts, which are probably tiers of irresolvably small, closely spaced steps, rather than by movement of apparently sharp higher steps.

New types of defects called trigonal wakes and ramps were found at the lowest substrate temperatures (274 °C). Other imperfections, designated as ridge boundaries, were found in deposits which had undergone large temperature changes. (ASM International Classification: N159, N3; Cd)

INTRODUCTION

OF THE several ways in which crystals of metals may be grown, that of deposition from the vapor phase is presumably the simplest mechanistically. Yet information is very scanty; reviews of this field (1,2,3)¹ show that theory has far outstripped experiment.

¹ The figures appearing in parentheses pertain to the references appended to this paper.

This paper is based on a thesis submitted by J. E. McNutt in partial fulfillment of the requirements for the degree of Doctor of Philosophy in the Department of Metallurgical Engineering at Carnegie Institute of Technology, Pittsburgh.

A paper presented before the Thirty-Ninth Annual Convention of the Society, held in Chicago, November 4-8, 1957. Of the authors, J. E. McNutt is now Research Engineer, Engineering Research Laboratory, E. I. du Pont de Nemours & Co., Inc., Wilmington, Delaware and R. E. Mehl is associated with the Department of Metallurgical Engineering, Carnegie Institute of Technology, Pittsburgh. Manuscript received September 17, 1956.

Observations of morphology and measurements of rates during growth under controlled conditions are needed; this paper recounts the first of a continuing series of efforts in which metal crystals are grown from the vapor at constant supersaturations and temperatures, whilst microscopic observations, including interferometric, are made continuously.

Cadmium was selected for study since its vapor pressure at moderate temperatures is high and supersaturation accordingly can be readily varied and because spirals which are presumably growth spirals have been observed on cadmium (4). Observations consisted in ordinary microscopic observation of the growing crystal, at a magnification of seventy-five diameters, in the use of interferometric fringes to assess height differences through fringe disregistry, and in the use of an optically imposed fiducial system to measure lateral dimensional changes. The sensitivity of the interferometric system used was about 300 Å in height at the best; any process whatsoever that occurred on a scale smaller than this was unobservable, and this is a limitation to the work. No easy method of measuring total displacement of a crystal surface in the direction normal to the surface was conceived and thus condensation coefficients could not be measured. Lateral dimensions were measured to ± 0.0003 centimeter. All observations were made on crystals that nucleated and grew as solids without intervening melting (except in a few special instances as noted); all measurements were made on small crystals in an aggregate of crystals, a circumstance which possibly, and even probably, provided special effects.

EXPERIMENTAL PROCEDURE

The cell shown in Fig. 1 was constructed in order that the growth of cadmium crystals from cadmium vapor, under controlled conditions of temperature and supersaturation, could be observed. All walls of the cell except the substrate and the graded seal were of pyrex. Kovar was employed as a condensation surface, (B, Fig. 1). The substrate temperature was measured with a prong-type iron-constantan thermocouple, using 0.01 inch-diameter wires. With the prong-type thermocouple, a relatively large portion of the substrate was made to serve as the hot junction, thus insuring valid temperature indications.

Supersaturation of the cadmium vapor was provided by maintaining the substrate at a temperature below that of the vapor source. Cooling of the substrate and temperature regulation were accomplished by blowing nitrogen against the inside end-surface of the Kovar piece. The substrate-thermocouple leads were connected to a recorder-controller which activated a solenoid valve that interrupted the nitrogen stream when the substrate cooled below the control temperature. With this arrangement, the substrate temperature fluctuated regularly through a range of 3 °C, with a period of several seconds.

The arm of the cell containing the vapor source was immersed in a tin bath. The source temperature was measured with an iron-constantan

thermocouple, fixed within a pyrex protection tube tied to the arm; this thermocouple was connected to a recorder-controller which regulated the current through the furnace windings. The source temperature could be held within 1.5°C of the control point.

No special efforts were made to keep the outer cell walls closer than about 5°C to the source temperature. A small tube furnace, concentric to the Kovar unit and flush with the window at one end, heated the walls outside the tin bath, except for the window. Current through the furnace was manually regulated. The experimental technique

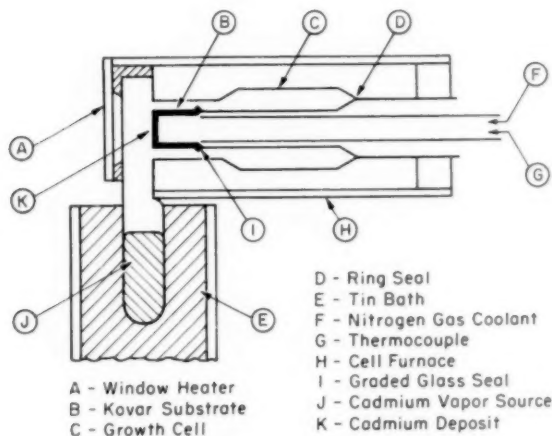


Fig. 1—Cross Section of Growth-Cell Assembly.

caused a temperature gradient to exist along the glass wall between the substrate and the ring seal. The temperature difference between these areas depended upon the particular experiment, the largest about 40°C , with the Kovar the coldest point in the system. It may be noted that in all experiments reported, deposition was chiefly restricted to the flat part of the substrate facing the window; in several instances the deposit also covered a small part of the lateral surfaces of the Kovar. The deposits were apparently uniform in character over the whole end of the Kovar.

The window was heated with a thin pyrex plate to which a transparent conducting coating had been applied by the Pittsburgh Plate Glass Company.* The plate was fixed approximately parallel to the window, with a slight separation to allow a small thermocouple bead to be held against the window. Current through the window heater was regulated manually.

* We owe this happy idea to Dr. Bruce Chalmers.

Prior to an experiment, the cell was outgassed through the arm containing the source crystals.

The cadmium used as a vapor source was the "Super Purity" grade (99.999+ % Cd, — "spectroscopically pure") of the New Jersey Zinc Company.

The microinterferometer designed and fabricated as part of this research was constructed according to standard principles and practices. A schematic diagram of the instrument is shown in Fig. 2. When light was cut off from the reference objective, the microinterferometer oper-

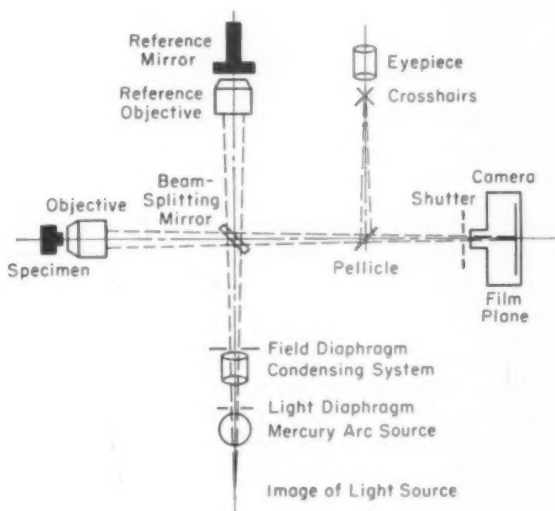


Fig. 2—Schematic Diagram of Interferometer.

ated as a simple microscope with vertical illumination. When the reference objective was illuminated, interference was effected between the images of the two objectives, resulting in a fringe pattern which could be used to determine relative heights in the field of view on the specimen. The principles of optics involved are reviewed in many physics texts; a complete discussion on use of fringe patterns in studies of topography has been made by Tolansky (5).

The camera consisted of a 35-millimeter camera from which the lens and shutter were removed, mounted on an independent shutter fixed to the interferometer. Cross-hairs within the eyepiece were fixed at the same distance from the pellicle as the film plane, so that an image in focus in the eyepiece was also in focus on the film. Cross-hairs were also fixed within the camera so as to cast shadows around the edges of each frame; these shadows served as a fiducial system for

measuring changes within the field of view between successive exposures.

There were two principal sources of continual fringe motion during an experiment. One was air convection before the window heater, which was sometimes as hot as 360 °C (680 °F). Variations of refractive index within the heated moving air caused irregular motion of the fringe pattern through distances that were small compared with the spacing of the fringes. The other source of fringe motion was the change in dimensions of the crystals and substrate concomitant with temperature variation around the control point. This motion was regular with a period of several seconds and caused the fringe pattern to shift back and forth across the field of view with an amplitude of more than one fringe spacing. Neither of these factors caused any apparent motion of the image when the interferometer was functioning as a simple microscope. With this experimental technique, there was no way to preclude these movements of the fringe patterns. As a result, it was necessary to use short exposures (1/10 to 1/5 second) to prevent blurring on the film.

The continual fringe motion prevented measurement of changes in absolute height of a crystal surface; otherwise the position of a single fringe could be followed over a long period of time; changes in position would indicate that the surface was growing and this growth would be susceptible to quantitative measurement. Thus, though the height of a detectable discontinuity on the surface and changes in height could be measured, the rates of perpendicular growth of the surfaces above and below the discontinuity could not be determined. This limitation could, of course, be circumvented by photographing the fringe patterns at a rate sufficiently rapid to permit tracing the position of individual fringes, and this is planned for subsequent work.

Under optimum conditions, heights of discontinuities of growing crystal surfaces could, as noted, be measured to within about 300 Å. Often sensitivity was poorer than this, owing to the difficult experimental conditions.

As soon as some crystal facets reached an appropriate size (about 0.1 millimeter or larger), photographs with and without fringes were taken at intervals depending upon the temperature and supersaturation of the particular experiment. Intervals ranged from 15 seconds to several hours. Whenever there was a possibility that the fringe shift at any surface discontinuity was more than the fringe spacing, two fringe patterns were photographed, one with the mercury green line (5461 Å) and one with the blue line (4358 Å). In most instances where there was doubt, the use of these two patterns allowed solution for the order of the fringe shift.

Conditions for the experiments reported here are summarized in Table I. Vapor pressures were arbitrarily calculated from the rela-

Table I

Experiment	Substrate Temp., °C.	Deposit Vapor Pressure, mm. Hg	Source Temp., °C.	Source Vapor Pressure, mm. Hg
15	317	0.089	356	0.35
10	317	0.089	347	0.26
11	317	0.089	335	0.18
16	317	0.089	325	0.12
14	296	0.038	328	0.14
22	296	0.038	320	0.10
12	296	0.038	315	0.081
23	296	0.038	302	0.048
17	274	0.015	307	0.059
18	274	0.015	301	0.046
19	274	0.015	301	0.046
20	274	0.015	289	0.027
21	274	0.015	288	0.026

tions between temperature and vapor pressure of cadmium given by Lumsden (6).

Nominal supersaturations such as might be calculated from the vapor pressures shown in Table I were not those actually operative during the experiments; effective supersaturations would be less than these, and evidence discussed below shows that the discrepancies were probably relatively large. In continuations of this work, effective supersaturations are being determined.

RESULTS

Thirteen experiments are reported here. These were preceded by several dozen preliminary, largely defective runs. In the final series of experiments, hundreds of crystals were studied and over 4000 sequential photographs were taken; of them, only a very few typical ones are reproduced here.

The deposits formed in the course of these experiments were compact aggregates of contiguous crystals, the basal surfaces of which were generally within a few degrees of normal to the axis of the interferometer—only those crystals with their basal planes approximately parallel to the substrate survived during growth, giving rise to a columnar structure. Selected observations on the growth of these crystals are reported below.

Ridge Boundaries

By "ridge boundary" is meant a discrete, straight boundary across a crystal which separates two regions differing slightly in orientation, as evidenced by a small angle between their basal surfaces.

The surfaces meeting at ridge boundaries are basal planes. Hexagonal symmetry of growth structures on both surfaces proved this many times. In several instances where this was not apparent, indents made with a needle indicated hexagonal symmetry of each surface.

A crystal with several ridge boundaries is seen in Fig. 3. Table II

Table II
Data on Boundaries in Fig. 3

Boundary No.	Angle	Surface Concave (Re-entrant) or Convex at Boundary
1	1°26'	Convex
2	1°26'	Convex
3	3°16'	Concave
4	2°42'	Convex
5	6°35'	Concave
6		Convex
7		Convex

gives the angles between adjacent basal surfaces at five of the boundaries and notes whether the surface is concave or convex (toward the window) at the boundaries; there was no consistency in this latter regard. Fifteen of the 18 boundaries observed were characterized by angles too small to be explained by twinning; the majority exhibited angles less than 1.5 degrees.

There was no consistency as to whether the surface was re-entrant at a ridge boundary, or not. When the surface was convex (to the viewer, i.e., not re-entrant), the boundary seemed to have no effect upon growth structures; Fig. 3 shows steps continuous across convex boundaries and this was found at all other such boundaries. When the surface was concave at a ridge boundary, however, several effects were noted. New steps often issued from such boundaries; steps were also seen to end there. Each circumstance is illustrated along boundary 5 in Fig. 3. The boundaries themselves did not move as growth progressed, nor did the angles at the boundaries change.

It has not been found that ridge boundary traces on basal surfaces follow rational crystallographic directions.

Ridge boundaries were seen only in those experiments where the substrate temperature had changed more than about 20 °C after a deposit had appeared. Because ridge boundaries existed only when large temperature changes had occurred and since twinned crystals were never present unless ridge boundaries were also observed, it has been concluded that they result from deformation of the crystals in the deposit. Temperature changes can introduce stresses into the crystals as a result of the anisotropy of thermal expansion, causing neighbors with nonparallel c-axes to interfere with each other, and because of the different thermal expansion coefficients of cadmium and Kovar. The ridge boundaries seem similar to the polygonization structures found by Holden (7) on zinc specimens which were cleaved, then annealed.

Growth at Steps

One of the features of crystal growth observed was the movement of

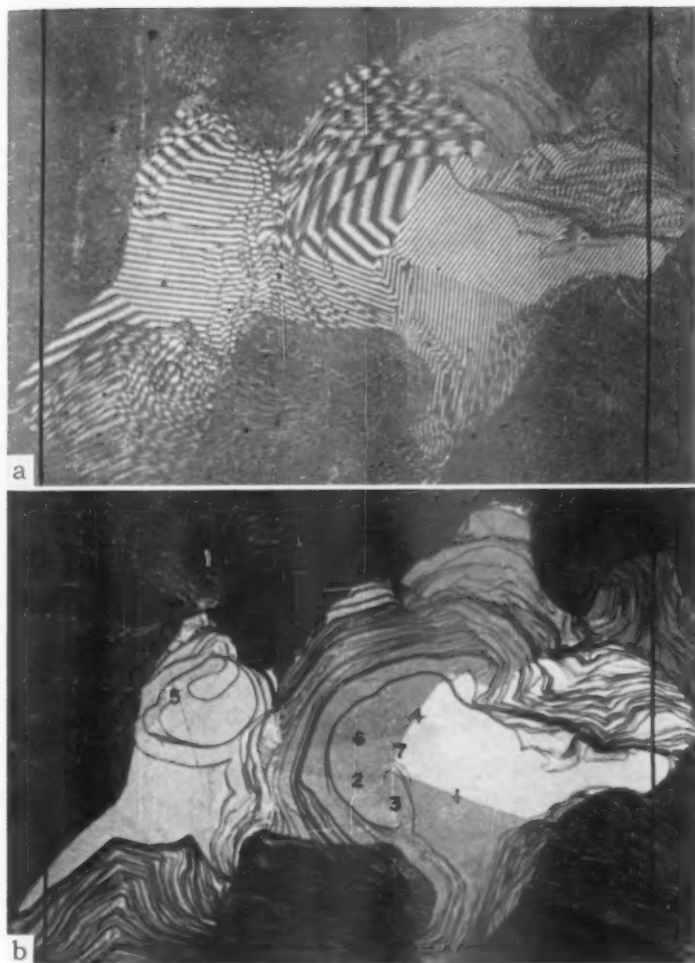


Fig. 3—Crystals with Ridge Boundaries. Experiment 10. $\times 90$.

discrete, detectable steps across basal surfaces. This was not the only way in which surfaces grew outward, nor was it even found under some experimental conditions; however, at the two higher substrate temperatures, growth of obvious steps appeared to be a dominant mechanism.

Origin of Steps—The classical theory of crystal growth predicts that new monolayers should be nucleated on homopolar crystals away

from edges and corners. On the majority of crystals observed in this work, however, steps appeared first at edges of basal surfaces where adjacent crystals touched. There was no periodicity in appearance of steps at crystal edges, nor was there usually a consistency in the height of new steps. This would be expected if the neighbors were of different orientations since then, as growth proceeded, the nature of the area of contact between them would change.

As noted above, new steps also appeared at concave ridge boundaries. This effect is probably related to that obtaining at the point where two neighboring crystals touch. Even at ridge boundaries, there is no rigorous chronological periodicity in the appearance of new steps, and no close uniformity in heights of the steps.

Sometimes steps formed independently of such edge effects. One instance was an experiment (No. 11) during which deposition took place on a continuous sheet of solid cadmium covering the end of the Kovar. This coating was obtained by allowing the substrate, on which a deposit had already formed, to heat above the melting point of cadmium; after the molten cadmium had spread out over the substrate, the temperature was again lowered, freezing the cadmium on the Kovar. Apparently, there were preferred points of layer nucleation in this coating, and after growth had proceeded for a time, mounds were built up around these points as new layers formed over them and grew out laterally. This was illustrated by the sequence of pictures in Fig. 4.

While visually observing growth in this experiment, the impression was obtained that large steps, such as visible in Fig. 4c arose as Volmer (8) suggested, that is, by smaller steps overtaking and joining steps below them. Small, barely discernible layers could be seen apparently continuously emanating from some point on a given mound; then suddenly a large step would begin to form, as if one of the small layers had been slowed down for some reason and successive layers began "piling up" on it. The large step would continue to propagate laterally and soon the process would be repeated above it. This did not happen at all sites, for as shown in Fig. 4d, some of the growth mounds exhibited no large steps, but had tapered sides probably composed of tiers of very small, individually irresolvable steps.

Discrete steps were also occasionally noted to form in growth fronts which took the form of microscopically smooth, irrational surfaces moving across the basal faces. Such growth fronts were seen frequently at the lower temperatures of growth and will be discussed in detail below; they are believed to be actually tiers of steps too small and too close together to be individually resolved. The formation of visible steps probably represents an aggregation of the small steps.

In summary, steps usually originated at edges of basal surfaces, either at ridge boundaries or where adjacent crystals touched. The appearance of new steps independent of these effects was noted only

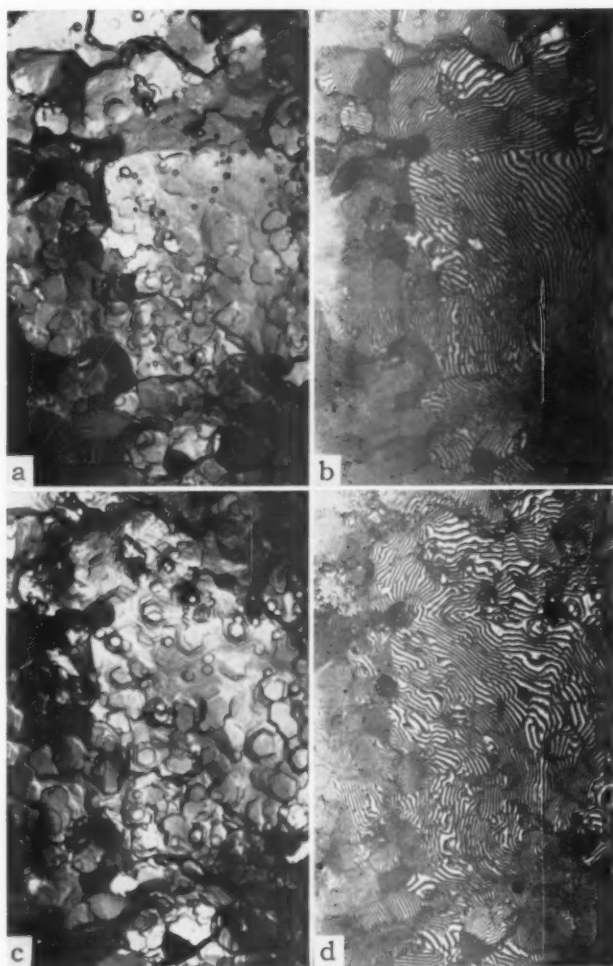


Fig. 4—Growth Structures on a Continuous Covering of Cadmium on the Substrate, Obtained by Melting Then Freezing a Previous Deposit. (c), 6 minutes after a. Experiment 11. $\times 50$.

occasionally as described above, and in these circumstances the origin of the steps was undetermined.

Development of Lattice Symmetry in Steps—According to the theory of growth of monatomic steps, lattice symmetry should not be apparent in growth from the vapor owing to the high mobility of adsorbed atoms. For cadmium, the symmetry on basal surfaces should be trigonal or hexagonal, if seen at all.

In the experiments with deposits held just below the melting point, the development of symmetry varied with supersaturation and step height. At the highest supersaturation (Experiment 15), there was no evidence for any steps assuming the lattice symmetry. At the lower supersaturations, small steps (about 250 to 1000 Å high) showed predominant development of hexagonal symmetry; as step height increased, the symmetry became less apparent, with corners between straight edges becoming more gradually rounded, until for heights of about 3000 Å only vestiges of straight sides remained.

At lower substrate temperatures, hexagonal symmetry was promi-

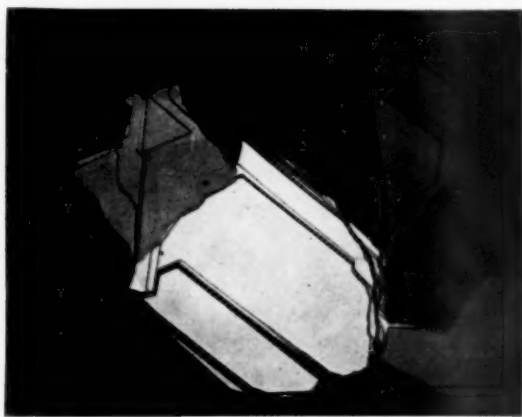


Fig. 5—A Crystal on Which Steps Are at Small Angles to Each Other. Experiment 18. $\times 80$.

nent even for high steps, with sharp corners between the straight sides. At the lowest temperature, it was occasionally noted that steps, though straight, were at slight angles to one another as shown in Fig. 5; this means that at least one of the steps follows an irrational direction. Such circumstances were transient.

Crystallography of Steps—The hexagonal symmetry, when developed in steps, indicates that they follow either $\langle 10\bar{1}0 \rangle$ or $\langle 11\bar{2}0 \rangle$ directions if rational. Previous work by Straumanis (1,9) and Stranski (10) and current theory (11,12) indicate that they should be in $\langle 11\bar{2}0 \rangle$ directions; this was verified in the present work by comparing step directions with traces of twins on the basal planes. Thus, if step faces are rational, they are probably $\{1010\}$ or $\{1011\}$ surfaces.

Rate of Step Propagation—At the higher temperatures and supersaturations, steps of various heights were observed to propagate laterally across the underlying basal surfaces and eventually cover them. This was not seen at low temperatures as discussed below.

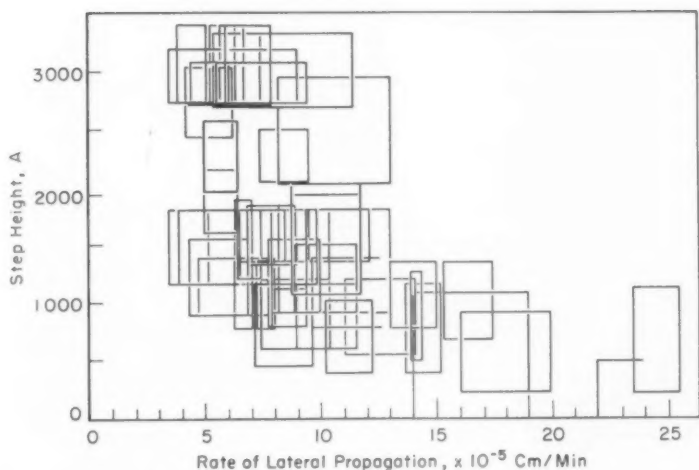


Fig. 6—Step Height vs. Rate of Lateral Propagation, Experiment 10.

For all experiments in which such information could be obtained, rates of lateral propagation of steps were determined together with step heights. Step movements were measured in directions normal to the step edges. Often the rates so determined were not uniform along the length of a step. Near the side of a crystal, a step would propagate sometimes more rapidly and sometimes more slowly than away from the edge—this could not be correlated with other observations. Step movement was affected by proximity to concave ridge boundaries. The propagation was always retarded as steps from different origins intersected and at the junction of two steps from the same source, an occasional occurrence to be discussed below. In such circumstances, only the rate of propagation along the apparently unaffected length of the step was considered.

The rate of propagation of a given step was apparently constant with time, apart from the conditions noted above. There was no instance in which a step accelerated or slowed down unless some external factor became influential on its progress or the step height changed.

Fig. 6 shows a plot of the data obtained from Experiment 10. Each datum is plotted as a rectangle, the horizontal dimension of which corresponds to twice the uncertainty in propagation rate, with the middle point of the line placed at the measured rate; the vertical side of each rectangle is equivalently defined. The true height and rate corresponding to the measured values would fall somewhere within the rectangle.

Fig. 6 shows the most apparent correlation between step height and rate of propagation; data from the other experiments were generally

characterized by too much scatter independently to show any trend. However, the data appear to show that the rate of lateral propagation increases as step height decreases. It was clear that a lower substrate temperature led to lower rates of step propagation. Rates of propagation exceeding 2×10^{-3} centimeters per minute were observed during Experiment 15.

From the experimental conditions given in Table I, it would be predicted that the steps observed in these experiments would propagate at rates greater than 10^{-3} centimeters per minute, on the basis only of direct collisions of atoms from the vapor on step faces and assuming a condensation coefficient of one, for which the evidence on metals is good (13-17). Except for the smaller steps observed in Experiment 15, the actual values are at least an order of magnitude less than the expected rates. This is a reason for believing that the effective supersaturations were lower than those calculated from source and substrate temperatures, for there is no other good basis for explaining these results.

Detectable lateral movement of steps was observed only on crystals growing at 317 °C (600 °F) and at 296 °C (565 °F) under the three highest supersaturations. The changes at steps in the other experiments are discussed below.

It is clear that there is no characteristic step height corresponding to given experimental conditions; in each experiment, a wide range of step heights was observed, and there is much evidence, to be discussed, that steps too small to be detected are important in growth.

Changes in Steps during Growth—Quite often increases in step height could be assigned to smaller steps, which move more rapidly, catching up to and joining larger steps. An example of this is shown in Fig. 7. Another process which occurred frequently can be noted in Fig. 7, namely, the splitting of a high step into two steps which are then separated owing to different rates of lateral propagation. This occurs in the large step which is joined by the smaller layer described above. The splitting-off of the smaller step is seen at an early stage in Fig. 7a and can be followed through the time of Fig. 7d. The height of the bottom step decreased between Fig. 7b and 7d and the step was invisible in Fig. 7e. Disappearance of the new step is not characteristic of the phenomenon. A clearer example of the process is shown in Fig. 8, where separation of steps may be seen at several places.

The growth front which moves away from a step is not always another smaller, discrete step, as shown in Fig. 9. In this sequence, a growth front about 1600 Å high, with a microscopically sloping edge, issues from the second uppermost step on the crystal. Here also the process seems to have begun at a single point in the parent step and then proceeded along its length. This may be evidence for a substructure in steps that appear to be simple at this degree of resolution.

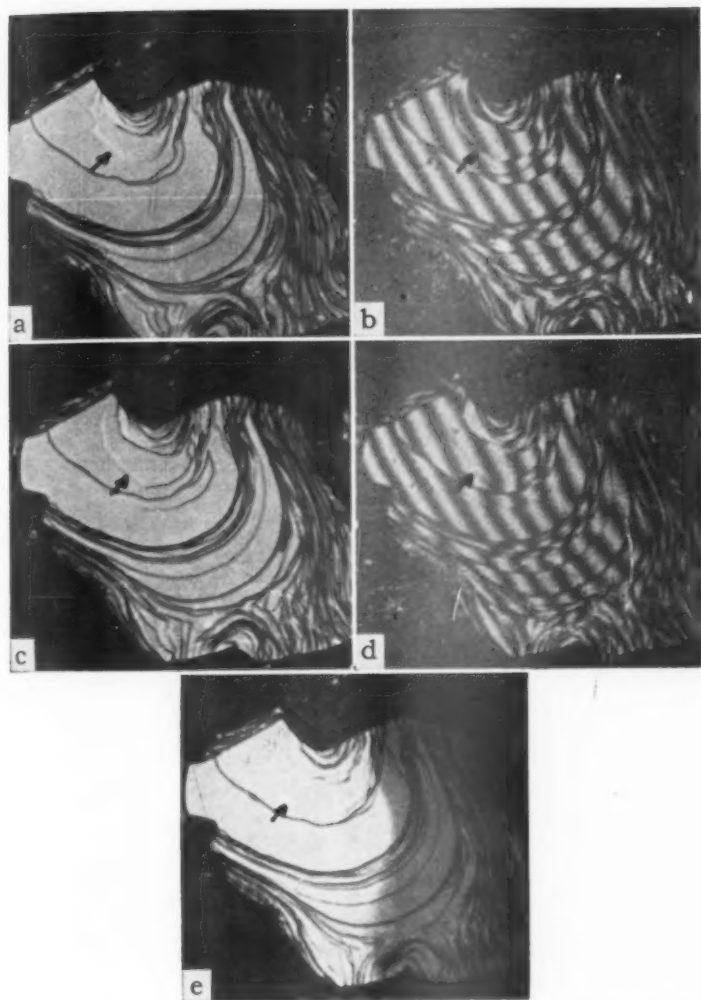


Fig. 7—A Crystal on Which a Step of Small Height Overtakes and Joins the Underlying, Higher Step. (c), 5 minutes after a. (e), 9 minutes after a. Experiment 11. $\times 150$.

As mentioned above, Fig. 7 shows that a step which split off from a higher one decreased in height and finally disappeared, within the limits of detection, before growing out to the edge of the surface. Such disappearance of a step also is of frequent occurrence, as illustrated on the same crystal in Fig. 10. At the time of Fig. 10b, the layer was about

1200 Å high and 3 minutes later 700 Å high. Actually, disappearance is believed to be a misnomer for the process, since it is thought that such dissipation of a layer occurs by very small steps growing away at a high rate from the bottom edge of the layer; thus, a vertical cross section of the crystal at successive times might appear as in Fig. 11. According to this idea, some small steps are able to dissociate themselves from a high step and, once this is accomplished, leave an apparently smaller, though still high, step behind; this high step meanwhile continues to propagate laterally. Unfortunately the experimental method

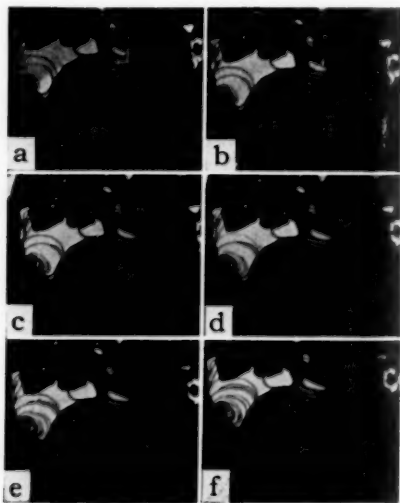


Fig. 8—A Crystal on Which Small Steps Split Away from Larger Steps. (b), 2 minutes; (f), 15 minutes after a. Experiment 16. $\times 75$.

did not make possible a direct verification of this postulated mechanism, since absolute height measurements were not possible, but there is much indirect evidence for the occurrence of such a mechanism.

Fig. 10d illustrates one kind of substantiation for this proposal, though it is somewhat equivocal. The fringes which do not meet the layer spreading across the top surface show a curvature which indicates that the surface slopes upward slightly in the vicinity of the small layer, as shown in outline 2 of Fig. 11. The fringes intersecting the layer are too short to show such a curvature. Fig. 12 is a better example of the evidence for the suggested mechanism. Although the surface seems to have a fairly simple structure in Fig. 12a, in the corresponding picture with green fringes, a very small growth front is barely apparent as a slight deviation in the fringes. This growth front, which probably consisted of a series of small, closely spaced steps, moved across the

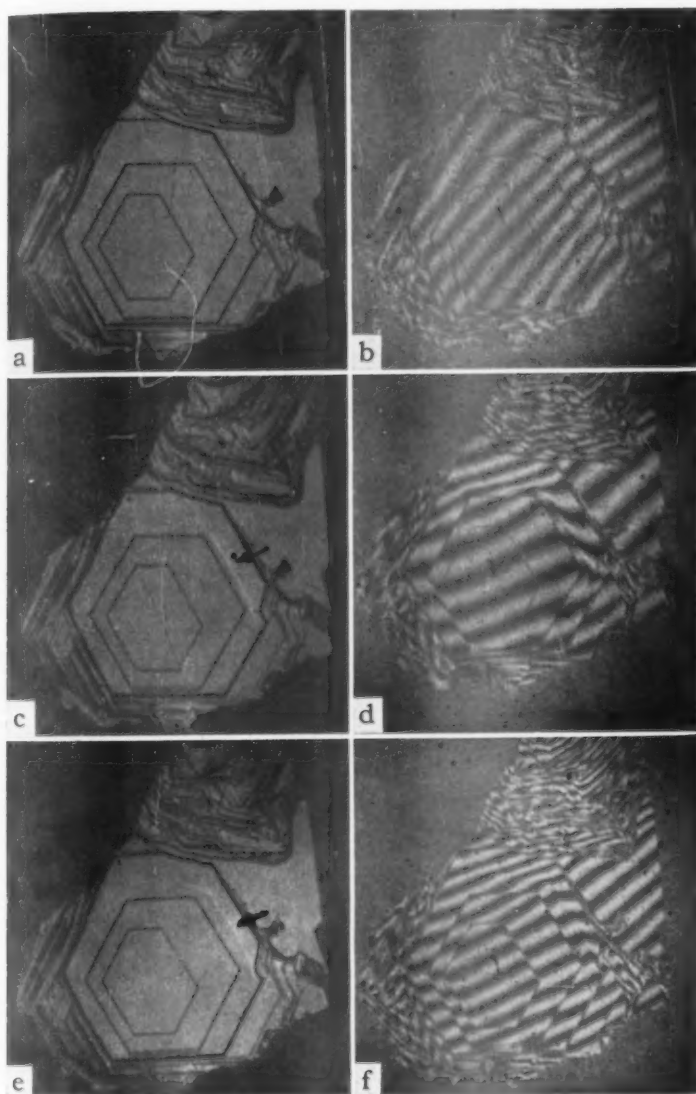


Fig. 9—A Crystal on Which a Growth Front Issues from a High Step. (c), 12 minutes after a. (e), 15 minutes after a. Experiment 22. $\times 100$.

surface very rapidly in accordance with expectation on the basis of the data on rates of lateral propagation for steps of various heights. Further, it can be seen in Fig. 12b that there is a small change in fringe

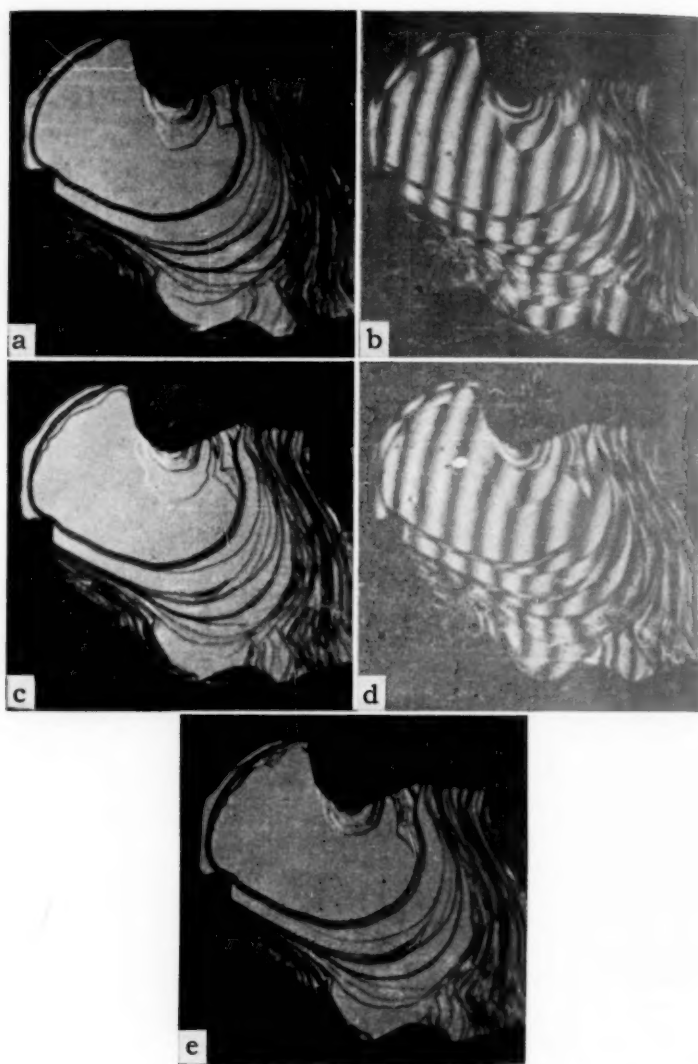


Fig. 10—A Crystal on Which a Small Layer Apparently Diminishes in Height as it Propagates Laterally. (c), 6 minutes after a. (e), 9 minutes after a. Experiment 17. $\times 150$.

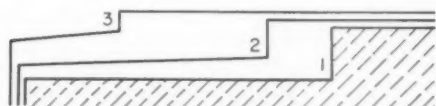


Fig. 11—Cross Section Through a Crystal on Which a Layer is Moving Laterally, With Decreasing Height, According to Suggested Mechanism.

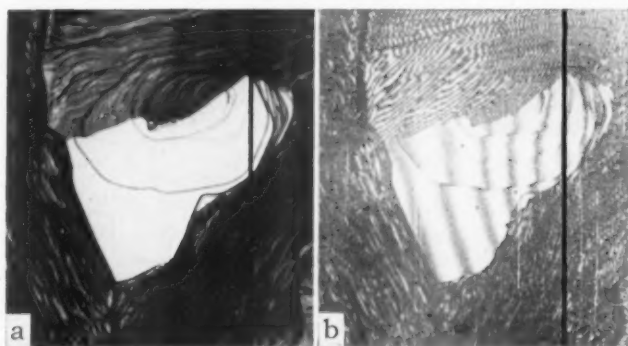


Fig. 12—A Crystal on Which Very Small Growth Fronts Are Active; These Can Only Be Detected by Slight Deviations in the Fringes. Experiment 10. $\times 90$.

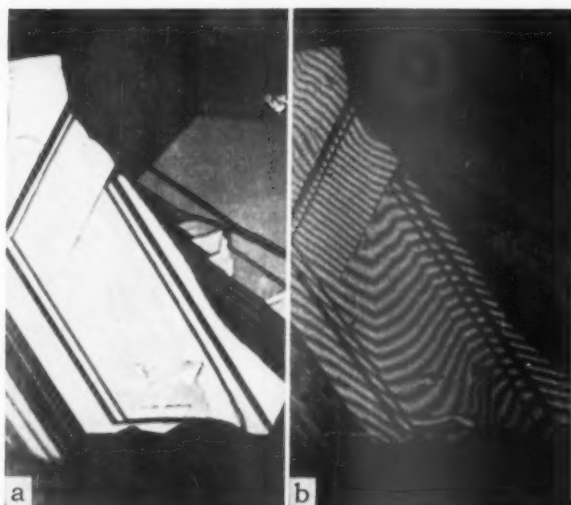


Fig. 13—A Crystal on Which Trigonal Structures Are Developed as Growth Fronts Issued from Steps. Experiment 18. $\times 85$.

orientation at the outermost step on this crystal; the change is such as to indicate that the upper surface slopes slightly upward relative to the face below the step, and thus there may be still other, smaller steps not obvious even in the fringe patterns that are moving across the upper surface. There were many other examples of such occurrences.

Frequently, evidence was obtained for the presence of steps too small to cause variations in the fringe patterns. This may be illustrated by changes in the two upper hexagonal structures on the crystal shown in Fig. 9. The heights of the steps bounding these structures were observed to vary widely while the fringes on all surfaces remained straight and parallel. To illustrate this, heights at successive times over a short interval are given in Table III; such changes may be followed in Fig. 9 also.

An explanation for these observations is that new, small steps were being continually generated on the top surface and growing out until

Table III
Heights of Two Uppermost Hexagons in Fig. 9, Prior to That Sequence

Minutes after Start	Height of top Hexagon	Height of Second Hexagon
0	2300	2500
4- $\frac{1}{2}$	2700	2700
9- $\frac{1}{2}$	2000	3000
16- $\frac{1}{2}$	2000	2700
23- $\frac{1}{2}$	1800	2800
45- $\frac{1}{2}$	3200	2300
58- $\frac{1}{2}$	2700	3200

they joined the step bounding the uppermost hexagonal layer, while simultaneously irresolvable steps were dissociating themselves from that layer and growing out to the edge of the second hexagon. No lateral propagation of any of the steps on the crystal described was detected during observation.

At the lowest substrate temperature used, measurable lateral propagation of steps in the sense of the preceding section was not observed. The usual changes in steps seemed akin to those discussed above; that is, new growth fronts issued from the steps. At this temperature, however, immobile steps seemed to wholly disintegrate into microscopically sloping growth fronts, probably actually tiers of smaller steps, which then progressed across the surfaces.

The above evidence indicates that high steps, though always observed, are not stable but represent a dynamic situation, with smaller growth fronts continually joining and issuing from the steps. If a step remains of about constant height, this probably indicates a balance between the two opposing processes. Nonetheless, the experimental observations seem to show that lateral propagation of high steps is a real process in crystal growth near the melting point and at temperatures as low as 295 °C (665 °F) when supersaturations are large.

Other Observations on Growth of Steps—In four of the experiments with low substrate temperatures (Numbers 17, 18, 19, 21), trigonal structures such as shown in Fig. 13 were encountered. These structures appeared when sloping growth fronts issuing from steps moved across a surface and have a shape that suggests the fronts had encountered points over which they could move and which then "cast a wake" as the growth front moved past them. The apex of the wake always pointed into the moving growth front; that is, opposite to the direction of propagation. Often the wakes were quite deep, the depth at the apex reaching as much as 8200 Å. They were accurately crystallographic, with the angle between sides 60 degrees. There were certain areas on each surface that seemed amenable to the formation of such structures. Sometimes these structures disappeared before becoming very deep and sometimes persisted until quite large; there was no consistency in the latter regard in the behavior of a given region. No explanation of this phenomenon is known. As mentioned, it would seem that a moving growth front had encountered a "poisoned" surface site. However, if the poisoned area were small, a pit should remain after the front had passed. There seems no reason to expect a small poisoned region to extend its effects along close-packed directions, as would be necessary to rationalize the observed structures. During continued growth the trigonal wakes disappeared and recurred in nearly the same locations.

Another phenomenon of low-temperature growth is the tendency for a high step to emit sloping growth fronts which seemingly cannot grow across a line in a close-packed direction following the extension of the parent step. The effect was sometimes so pronounced that "ramps" were built up on the sides of the growth front as it moved across the surface. Such a ramp is seen in Fig. 13, appearing as a line following the extension of one edge of the higher layer and coming to an end in the middle of the underlying surface. After a time, growth began to proceed outward normally from a ramp, which then gradually receded as the surface below grew upward through the progression of steps across it.

The irregularity of the surface apparent in Fig. 13b is due to the trigonal wakes and to complex growth fronts issuing from the steps on the crystal. It may be seen that these fronts did not move uniformly away from the steps and that a discontinuity existed on the surface above the ramp, at an angle of 30 degrees to the step direction, therefore in the less closely packed $\langle 10\bar{1}0 \rangle$ directions. Such discontinuities were transient and only rarely found, but there was much evidence for barriers to growth along $\langle 11\bar{2}0 \rangle$ directions.

Growth at Sloping Growth Fronts

As described above, at 317 and 296 °C (603 and 565 °F) the predominant mechanism of growth was the propagation of high steps across basal surfaces. However, concurrently with step propagation at

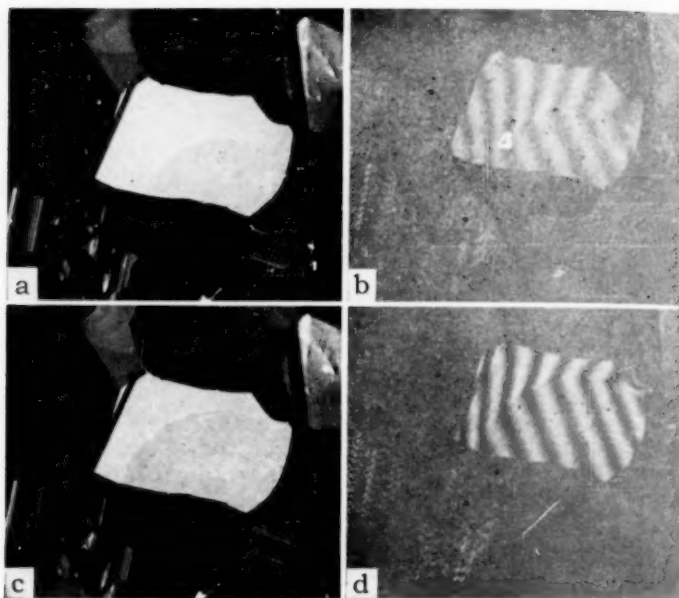


Fig. 14—A Crystal Across Which a Mesa is Progressing. (c), 4 minutes after a. Experiment 17. $\times 100$.

296 °C (565 °F) and exclusively at 274 °C (525 °F), the movement of sloping growth fronts became important in the deposition of new material.

Such growth fronts often occurred in the form of "mesas" such as shown in Fig. 14. As can be seen, they are characterized microscopically by slightly concave, sloping surfaces with flat tops, with the apparent line of farthest advance being curved; actually the only tenable model for such a structure seems to be a tier of irresolvably small, closely spaced steps.

Mesas appeared first at crystal edges, and probably the same considerations that apply for steps originating at edges apply here also. A number of growth fronts were seen which were apparently equivalent to mesas in all respects except that they did not have flat tops; this was presumably the result of continuous formation of new steps at the contact with a neighbor. These growth fronts seem to correspond to those that emerged from steps at the lower temperatures of deposition, as already described.

Sloping growth fronts showed no development of lattice symmetry in the sense that no straight edges were seen to appear in them while they were growing freely. However, their growth often tended to pro-

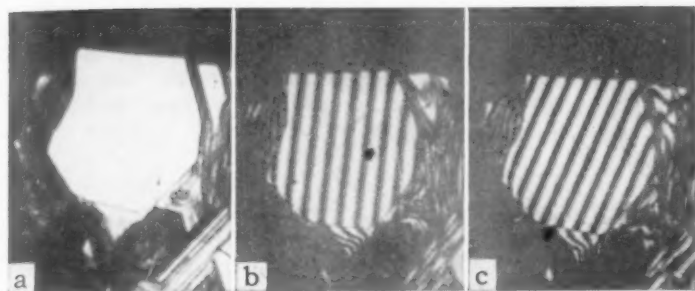


Fig. 15—A Crystal on Which Only Slight Changes in Fringe Patterns Indicate Any Growth Processes Over a Long Period of Time. (b), 5 minutes and c, 94 minutes after a. Experiment 20. $\times 150$.

ceed more rapidly in close-packed directions, in contrast to the mesa shown in Fig. 14, which grew fairly isotropically.

As yet it is unclear how the stepped crystals always seen at low temperatures arose, since growth seemed to occur only in sloping fronts. During observation the surfaces were usually found to simplify by the dissipation of steps rather than to add new steps.

No attempts were made to determine the rates of propagation of the steps composing sloping growth fronts, because it was impossible to establish the corresponding positions in the fronts at different times.

Sub-Interferometric Processes

Many of the observations made during this research can be explained only on the basis of processes occurring on a scale too small to be detected even by the sensitive techniques employed. Much of the evidence was of the kind already described; that is seemingly anomalous changes in step heights. Steps were seen to become higher and to shrink, even disappear, though no other changes in their neighborhoods were noted. The best explanation is that other steps too small to be detected either joined the steps which were seen or left, or perhaps both, at different rates. Sometimes these occurrences were detected or deduced from changes in fringe patterns, as already mentioned. If on this basis it is assumed that similar processes also took place on a sub-interferometric scale, then the otherwise inexplicable height changes and fringe patterns can be rationalized.

During the experiments on growth at 276°C (530°F), sometimes a flat surface was observed to remain largely inactive over a period of time, though slight fringe variations indicated that growth was actually proceeding. An example is shown in Fig. 15, where only small changes in the fringe deviations at edges of the surface indicate that anything was happening during the interval. In the central area, the fringes remained straight and parallel, so that only very small, undetected steps

could have been active; it seems impossible that no growth whatsoever was occurring. (The changes in fringe orientation have no significance with respect to growth on the surface, since this is caused artificially.) Such behavior was noted on several surfaces and was not restricted to growth at low temperatures.

Other Observations

The deposits formed during Experiments 21 and 23 were examined, after cessation of growth, with a metallograph to search for spirals resulting from screw dislocations; such structures would be most likely developed in these experiments. To minimize changes on the surfaces of the growing crystals, both the source and the substrate were rapidly cooled to room temperature when the experiments were terminated. The deposits were then removed by breaking the growth cell and examined using conventional microscopy, both to see if any spiral growth structures could be found at higher magnifications in this way, and to select crystals for study with multiple-beam interferometry. Surfaces unobstructed by neighboring crystals were examined by the conventional techniques for interferometry in reflection described by Tolansky (5). Good fringes (for reflection) were obtained, and probably discontinuities less than 200 Å high could have been detected. When it was impossible to place the reference mirror sufficiently near a surface to yield good fringes, the less desirable technique of effecting interference in a Canada balsam film was used. Attempts were also made to increase the visibility of surface structures by plasticine decoration as described by Forty (4).

On none of the surfaces, even those where growth had apparently occurred independently of edge effects, were spiral structures found; and none were observed during growth. This is not conclusive as to the activity of dislocation spirals, since it is quite possible that they were present but undetected. For instance, the spiral generated on a single screw dislocation with a Burgers vector of one might be estimated to have a slope of 4×10^{-5} relative to a basal plane; such a slope would be difficult to find even with multiple-beam fringes.

CONCLUSION

It is clear that studies at room temperature of the end products of crystal growth are of little help in understanding the mechanism of growth; continuous observation of the crystals while they are growing is necessary, as the above evidence indicates.

There is no step height characteristic of a given temperature and supersaturation, as suggested by Straumanis (9) and Graf (18,19). Instead, steps ranging from sub-interferometric heights (less than about 300 Å) to heights of 3000 Å or more are active on basal surfaces during deposition. Further, these steps may constantly change in

height: they can disintegrate into a series of smaller steps or may aggregate into larger ones. This is obviously not growth by the successive appearance of monatomic layers alone, though there is evidence for growth occurring on a sub-interferometric scale of unknown nature; nor is it growth by the operation of spiral growth forms originating in screw dislocations, for these large steps are simple layers and not spirals. In all but a few instances, new steps originated at the edges of crystal faces where neighboring crystals touched or at re-entrant angles on basal surfaces, where, to be sure, imperfections, possibly of the screw dislocation type, could have led to the nucleation of the observed layers. The tendency for development of hexagonal symmetry in steps increases as temperature decreases; when rational, steps follow $\langle 1120 \rangle$ directions.

Propagation of steps was observed under all conditions with a substrate temperature of 317 °C (603 °F), but only at the higher supersaturations when the substrate temperature was 296 °C (565 °F) and not at all when it was 274 °C (525 °F). Sloping growth fronts were active at the two lower temperatures. New types of imperfections, called ramps and trigonal wakes, were observed at the lowest substrate temperature. Ridge boundaries, another type of imperfection, were found only in those deposits which had been subjected to large temperature changes.

ACKNOWLEDGMENTS

Most of this work was sponsored by the Office of Ordnance Research, Contract No. DA-36-061-ORD-175.

The authors are grateful to E. I. du Pont de Nemours & Company for a fellowship awarded to one of them.

The authors also wish to thank the Pittsburgh Plate Glass Company for furnishing the transparent window heaters.

References

1. M. Straumanis, "Keimbildung, Kristallwachstum und Katalysis," *Handbuch der Katalyse*, Vol. IV: *Heterogene Katalyse I.*, Springer-Verlag, Wien, 1943.
2. R. F. Mehl, "The Growth of Metal Crystals," *The Solidification of Metals and Alloys*, 1951. American Institute of Mining and Metallurgical Engineers, New York.
3. F. C. Frank, "Crystal Growth and Dislocations," *Advances in Physics*, Vol. 1, 1952, p. 91.
4. A. J. Forty, "The Growth of Crystals of the Hexagonal Metals from their Vapours," *Philosophical Magazine*, Vol. 43, 1952, p. 949.
5. S. Tolansky, *Multiple-Beam Interferometry of Surfaces and Films*, 1948. Oxford Press.
6. J. Lumsden, *Thermodynamics of Alloys*, 1952. The Institute of Metals, London.
7. J. Holden, "Plastic Deformation Features on Cleavage Surfaces of Metal Crystals," *Philosophical Magazine*, Vol. 43, 1952, p. 976.
8. M. Volmer, "Zum Problem des Kristallwachstums," *Zeitschrift für Physikalische Chemie*, Vol. 102, 1922, p. 267.

9. M. Straumanis, "Das Wachstum von Metallkristallen in Metaldampf," *Zeitschrift für Physikalische Chemie*, Vol. B13, 1931, p. 316.
10. I. N. Stranski, "Zur Bestimmung der Reichweite der Zwischen den Gitterbausteinen in Homoöpolaren Kristallen Wirksamen Kräfte auf Grund von Kristallwachstumsformen," *Zeitschrift für Physikalische Chemie*, Vol. 38, 1938, p. 451.
11. W. K. Burton, N. Cabrera and F. C. Frank, "The Growth of Crystals and the Equilibrium Structure of their Surfaces," *Philosophical Transactions*, Royal Society of London, Series A, Vol. 243, 1951, p. 299.
12. S. Amelinckx, "Growth Spirals Originating from Screw Dislocations on Gold Crystals," *Philosophical Magazine*, Vol. 43, 1952, p. 562.
13. G. Wessel, "Messung von Dampfdrucken und Kondensationskoeffizienten an Eisen, Cadmium und Silber," *Zeitschrift für Physik*, Vol. 130, 1951, p. 539.
14. M. Volmer and I. Estermann, "Über den Verdampfungskoeffizienten von festen und flüssigen Quesksilber," *Zeitschrift für Physik*, Vol. 7, 1921, p. 1-12.
15. A. L. Marshall, R. W. Dorn and F. J. Norton, "The Vapor Pressure of Copper and Iron," *Journal, American Chemical Society*, Vol. 59, 1937, p. 1161.
16. H. L. Johnston and A. L. Marshall, "Vapor Pressure of Nickel and of Nickel Oxide," *Journal, American Chemical Society*, Vol. 62, 1940, p. 1382.
17. R. B. Holden, R. Speiser and H. L. Johnston, "The Vapor Pressures of Inorganic Substances—I. Beryllium," *Journal, American Chemical Society*, Vol. 70, 1948, p. 3897.
18. L. Graf, "Zum Aufbau der Metallkristalle," *Zeitschrift für Elektrochemie*, Vol. 48, 1942, p. 181.
19. L. Graf, "Das Lamellenwachstum der Kristalle," *Zeitschrift für Metallkunde*, Vol. 42, 1951, p. 336, p. 401.

GRAIN BOUNDARY SELF-DIFFUSION OF NICKEL

By W. R. UPTHEGROVE AND M. J. SINNOTT

Abstract

The diffusion of nickel-63 into controlled orientation bicrystal grain boundaries of nickel in the temperature range 700–1100 °C (1290–2010 °F) has been studied using autoradiographic techniques. The ratio of the grain boundary diffusion coefficient to the lattice diffusion coefficient has been shown to vary from 10^3 to 10^7 depending on the grain boundary angle and the temperature of diffusion; the largest ratios were obtained in boundaries of large misfit diffused at low temperatures. The activation energy for grain boundary self-diffusion was found to be 26 k-cal per gram mole for the one degree of freedom boundaries between 20 and 70 °; outside of these limits it appears to increase rapidly with decreasing misfit to 65.9 k-cal per gram mole, the value for lattice self diffusion. (ASM International Classification N1d; Ni)

THE PRESENT investigation was concerned with obtaining additional quantitative data on the phenomenon of grain boundary diffusion. Other studies have indicated the general outlines of the process but at the start of this program few self-diffusion grain boundary data were available; even lattice self-diffusion data had not yet been obtained on the nickel system (1–5).¹

The steps involved in this research were the preparation of suitable bicrystals with simple tilt boundaries of one degree of freedom expressible as a symmetrical angle of misorientation; the determination of the extent of diffusion at various temperatures; and the analysis of the data in terms of the existing theories of grain boundary diffusion.

EXPERIMENTAL PROCEDURES

Nickel bicrystals were produced by controlled solidification of vacuum melted electrolytic nickel of better than 99.95% purity with a common $\langle 100 \rangle$ axis. Single crystal seeds were rotated relative to one another about this axis to produce a simple symmetrical tilt boundary.

¹ The figures appearing in parentheses pertain to the references appended to this paper.

This paper is based on a thesis by W. R. Upthegrove submitted as partial fulfillment of the requirements for the degree of Doctor of Philosophy to the Rackham School of Graduate Studies, University of Michigan.

A paper presented before the Thirty-Ninth Annual Convention of the Society, held in Chicago, November 4–8, 1957. Of the authors, W. R. Upthegrove is assistant professor of Metallurgical Engineering, University of Oklahoma, Norman, Oklahoma; M. J. Sinnott is Professor of Metallurgical Engineering, University of Michigan, Ann Arbor, Michigan. Manuscript received April 5, 1957.

The angle of rotation between the two crystals is the grain boundary angle, θ , commonly termed the misfit angle. The growth of these bicrystals was carried out in an alundum boat, surrounded by a graphite susceptor, with energy supplied by a movable induction coil. This assembly was heated within a Vycor tube in a dynamic atmosphere of purified argon. The bicrystals, of dimension $4 \times 1\frac{1}{4} \times \frac{1}{2}$ inch, produced by this technique showed a strong lineage subgrain structure within each crystal of the bicrystal. These subgrains, on optical and x-ray examination, exhibited mutual rotational misfit about common

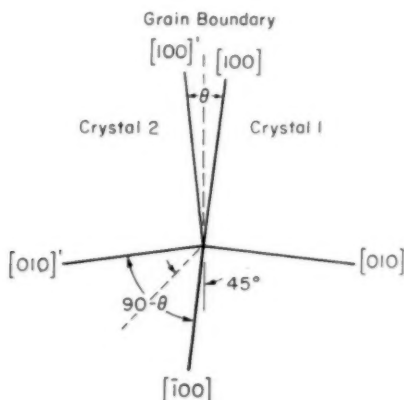


Fig. 1—The Effect of a 45 Degree Bend on a Simple Tilt Boundary.

$\langle 100 \rangle$ directions with the angle of rotation varying from 0 to 4 degrees. Variations in growth rates during solidification did not result in any appreciable change in type or quantity of substructure obtained and lineage structures were present in all the bicrystals that were used.

The boundary between the two crystals making up the bicrystal was normally straight in the growth direction but was seldom straight in the transverse direction. Neither this curvature nor the substructures were modified by prediffusion anneals which were given all boundaries prior to their use.

By careful selection of the boundary area it was possible to utilize the curved boundaries for angular values of both θ and $(90-\theta)$. Fig. 1 shows that if a boundary is sufficiently curved so that a segment of its surface is inclined 45 degrees to the position at which it is a symmetrical tilt boundary of θ , then this inclined segment is a symmetrical tilt boundary of $(90-\theta)$. By sectioning the diffused specimen along two planes which intersect the boundary at the proper positions along its curve

it is possible to measure grain boundary penetration at angles of both θ and $(90-\theta)$ on one bicrystal specimen. By the use of this technique it was possible to measure grain boundary diffusion at 19 values of θ over the range from 4 to 80 degrees using only 10 bicrystal ingots.

The crystallographic misorientation of the bicrystals was determined by x-ray back reflection methods. By aligning the x-ray beam so as to impinge on both crystals at the boundary, the patterns of both grains were obtained on one film. The measurements made on these films showed that the common cube axes along the growth direction were parallel within 4 degrees except for a few cases where as much as an 8 degree difference was observed. The data obtained on these latter samples showed no consistent deviation from those of the more perfectly aligned bicrystals.

Diffusion specimens were prepared by sectioning the bicrystal ingots perpendicular to the common $\langle 100 \rangle$ axes, etching the cut surfaces to remove the disturbed metal, then subjecting the specimens to a pre-diffusion anneal for 50–75 hours at 1050 °C (1920 °F) to eliminate residual stresses and to stabilize the boundary structures. Following this treatment the specimens were metallographically polished and subsequently chemically polished to produce a flat strain-free surface. A circular area of high activity nickel-63, $\frac{3}{8}$ inch in diameter, was then plated over the bicrystal boundary. A thickness of approximately one micron of active nickel was deposited from an ammoniacal sulphate solution. It was found that some blistering occurred on the rapid heating of these plated specimens to the diffusion temperatures but by degassing these samples under a dynamic vacuum of 1 micron for 2 hours at 230 °C (445 °F), immediately after plating, the blistering was eliminated.

The plated diffusion samples were sealed in Vycor capsules under an atmosphere of dried argon with a getter of either tungsten or tantalum. Diffusion anneals were carried out in a tubular muffle furnace maintained at the diffusion temperatures within ± 2 °C. Upon completion of the diffusion anneal the samples were quenched to room temperature by breaking the capsules under water.

All penetration measurements were made using the autoradiographic permeable base stripping film technique. These techniques have been standardized and are discussed at length in the literature (5,9). In this process the film is placed in contact with a one micron layer of protective plastic which covers the metal specimen surface, exposed, and processed intact with the metallographic surface so that subsequent examination of the microstructure may be made through the activated emulsion which is in perfect registry with the microstructure. Depths of boundary and lattice penetration were measured to a point where the silver emulsion grain density became visible above background. By maintaining the variables of exposure time and film processing at predeter-

mined values, the penetration measurements were made to a constant concentration. The value of this concentration was determined using small melts of nickel containing known concentrations of nickel-63 varying from 0.01 to 0.001%. It was found that a concentration of 0.005% radioactive nickel produced a photographic density that was distinguishable above background. This concentration was used as the visible end point for boundary diffusion.

Measurements of the depth of penetration were made on a Bausch and Lomb Research Metallograph using a calibrated eye-piece grid. This permitted measurements to be made to within 3 microns which was the degree of uncertainty of the end point of diffusion penetration. Two sections were cut from both the θ and the $(90-\theta)$ segments of each bicrystal boundary and duplicate autoradiographs were made on each section. Fig. 2 through 6 are typical autoradiographs of grain boundary and subboundary diffusion.

EXPERIMENTAL RESULTS

The experimental results of this work are presented in Table I and are graphically shown in Figs. 7 through 10. In some cases the grain boundary did not intersect the diffusion interface perpendicularly and these boundaries have been annotated in Table I and on the Figs. It was also noted, particularly in the 700 and 850 °C (1290–1560 °F) diffusion specimens, that some of the subboundaries of the nickel crystals were penetrated by the radioactive nickel. The depth of penetration along these subboundaries was usually considerably less than the depth along the regular grain boundaries, as shown in Figs. 5 and 6, but in some cases, when θ or $(90-\theta)$ were small angles, these depths were comparable. Measurements made on specimens in which subboundary penetration was observed have likewise been indicated in Table I and on Figs. 7–10.

ANALYSIS AND DISCUSSION OF DATA

Using Fick's laws of diffusion and assuming that the concentration of the diffusing material at the interface remains constant at a value of C_0 , the following solution is obtained for the case of lattice diffusion:

$$C/C_0 = \operatorname{erfc} y_L/2(D_L t)^{0.5} \quad \text{Equation 1}$$

$C =$ Concentration of diffusion material
at point y_L .

$y_L =$ Depth of lattice diffusion

$t =$ Diffusion time

$D =$ Lattice diffusion constant.

The assumption of constant C_0 is justifiable in view of the small amount of diffusion that has occurred. Under the conditions of this investigation C/C_0 had a constant value of 5×10^{-5} . It has been shown previously that a large experimental error in this value would have only a relatively small effect on the calculated diffusion coefficients (5).

Table I
Depth of Penetration of Radioactive Nickel
in the Grain Boundaries and Lattice of Nickel Bicrystals
(Measured autoradiographically from the original interface to a concentration of 0.005 per cent)

Diff. Cond. Temp. Time	Specimen Cut ARG*	Penetration along a Boundary of Misfit θ (microns)																76°	80°
		0°	4°	10°	14°	19°	21°	23°	27°	31°	32°	42°	48°	58°	59°	63°	67°	69°	
700 °C	I 1	0	0	—	81 ^b	172 ^b	—	—	129	165 ^b	250 ^b	229	290 ^b	274 ^b	299	114	262	170	105
15.8 hr.	II 1	0	0	93 ^b	102 ^b	112 ^b	—	166	112	142	230 ^b	237	240 ^b	273 ^b	301	160	24	179	118
850 °C	I 1	0	0	—	—	128 ^b	—	—	178	184 ^b	153	265	260	304	202	123	323	190 ^a	252 ^{a,b}
15.8 hr.	II 2	0	0	93 ^b	—	109	—	191	100	160	166	237	195	319	312	112	270	—	254 ^a
850 °C	I 1	3	3	54	86	81 ^b	120 ^a	129	109	123 ^a	106	234	208	142	86	116	120	204 ^a	148 ^b
15.8 hr.	II 1	3	—	42	—	—	184 ^a	126	90	112	104	194	203	176 ^b	109	92	104	167 ^a	299 ^{a,b}
850 °C	I 1	3	6	42 ^b	64	75 ^b	108 ^a	123	98	132	123	206	200	—	92	137	113	194	252 ^{a,b}
15.8 hr.	II 2	3	—	76 ^b	38	101	160	107	88	106	121 ^a	186	179	120	117	104	157	179	254 ^a
850 °C	I 1	5	—	—	—	135 ^b	—	—	—	—	—	—	—	—	—	—	—	—	—
35.8 hr.	II 1	5	—	—	—	—	—	—	214	—	—	—	—	—	—	—	—	—	—
850 °C	I 1	8	—	—	—	—	—	—	215	—	—	—	—	—	—	—	—	—	—
60.2 hr.	II 2	8	—	—	—	—	—	—	250	—	—	—	—	—	—	—	—	—	—
1050 °C	I 1	23	23	70	52	64 ^a	82 ^a	—	104	114	95	120	116	86	92	120	—	70	—
7.8 hr.	II 2	23	23	58	48	61 ^a	64 ^a	—	84	94	—	123	119	95	106	100	—	61 ^a	—
1100 °C	I 1	40	40	46	40	82	70 ^a	—	107	—	113	100	110	110	—	—	—	—	—
7.8 hr.	II 2	40	40	52	40	82	76 ^a	—	84	—	107	106	84	116	—	82	—	58	68
40	I 1	40	40	49	43	76	82 ^a	—	88	—	110	76	84	96	—	92	—	61	40
40	II 2	40	—	49	40	86	82 ^a	—	88	—	107	103	82	114	—	70	—	64	67 ^a
40	I 1	40	—	—	—	—	—	—	—	—	—	—	—	—	—	—	—	157	76
40	II 2	40	—	—	—	—	—	—	—	—	—	—	—	—	—	—	—	42	—
40	I 1	40	—	—	—	—	—	—	—	—	—	—	—	—	—	—	—	—	—
40	II 2	40	—	—	—	—	—	—	—	—	—	—	—	—	—	—	—	—	—

*ARG—autoradiograph. ^a—nonperpendicular boundary. ^b—subboundary penetration present.

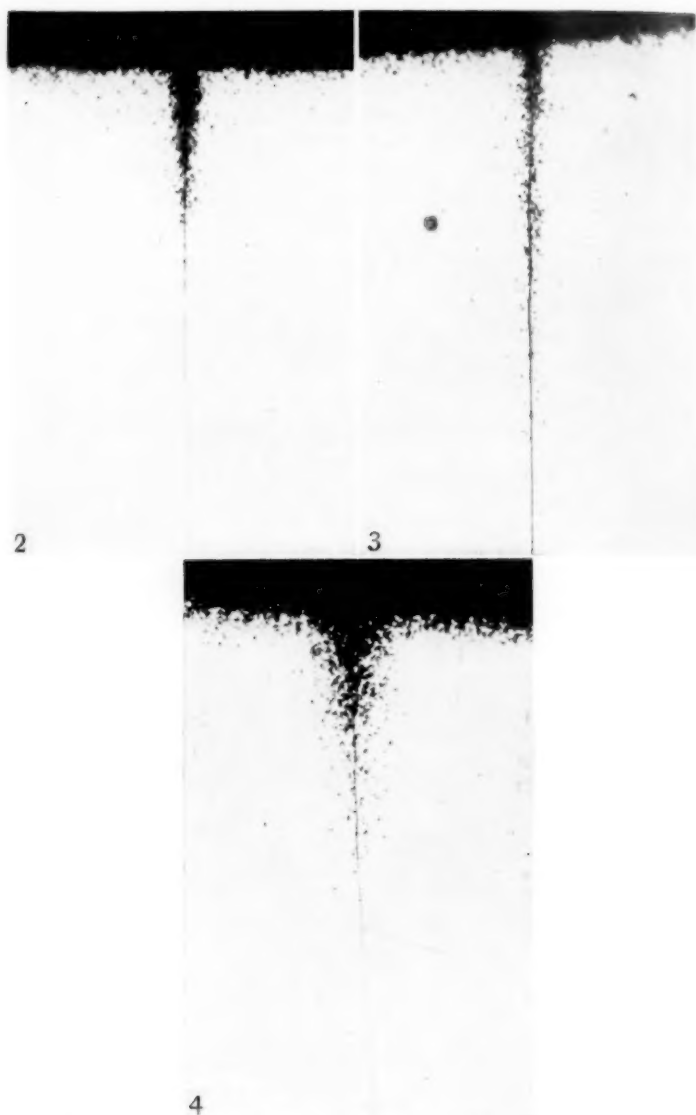


Fig. 2—The Diffusion of Radioactive Nickel into a Nickel Grain Boundary. $\theta = 14^\circ$, 15.8 hours at 850°C (1560°F), $\times 500$.

Fig. 3—The Diffusion of Radioactive Nickel into a Nickel Grain Boundary. $\theta = 31^\circ$, 15.8 hours at 850°C (1560°F), $\times 500$.

Fig. 4—The Diffusion of Radioactive Nickel into a Nickel Grain Boundary. $\theta = 42^\circ$, 7.8 hours at 1050°C (1920°F), $\times 500$.

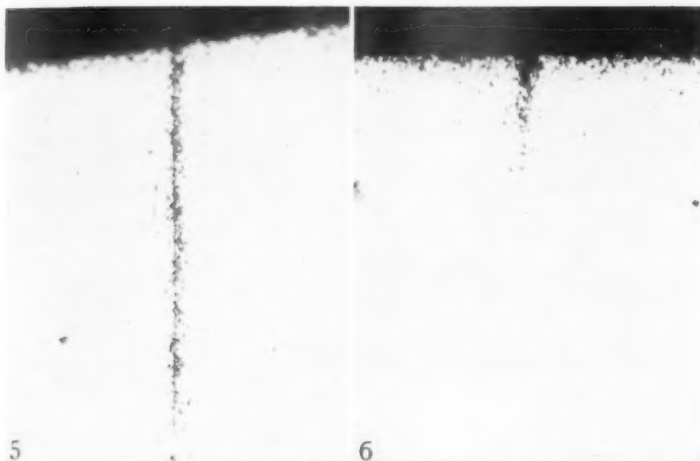


Fig. 5—The Diffusion of Radioactive Nickel into a Nickel Grain Boundary. $\theta = 58^\circ$, 15.8 hours at 700°C (1290°F), $\times 500$.

Fig. 6—The Diffusion of Radioactive Nickel into a Nickel Sub-Boundary. 15.8 hours at 700°C (1290°F), $\times 500$.

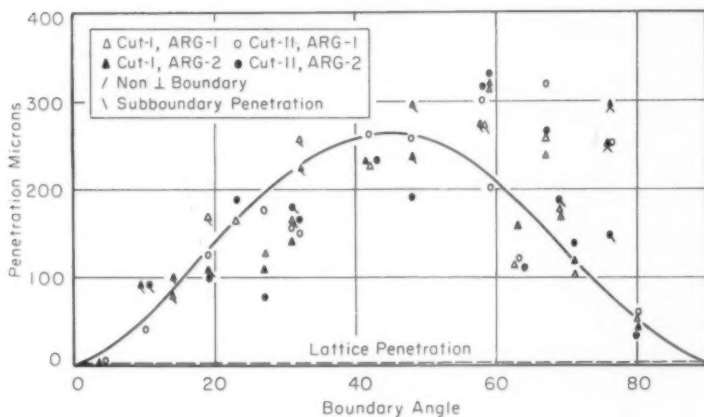


Fig. 7—The Penetration of Radioactive Nickel Along Nickel Bicrystal Grain Boundaries at 700°C (1290°F) as a Function of the Misfit Angle.

Lattice diffusion coefficients were computed from the data of Table I and have been plotted versus reciprocal temperature in Fig. 11. The linear regression of these data estimated by least squares give the expression:

$$D_L = 0.48 \exp (-65,900/RT) \text{ cm}^2/\text{sec}$$

The results of other investigations recently reported are also plotted

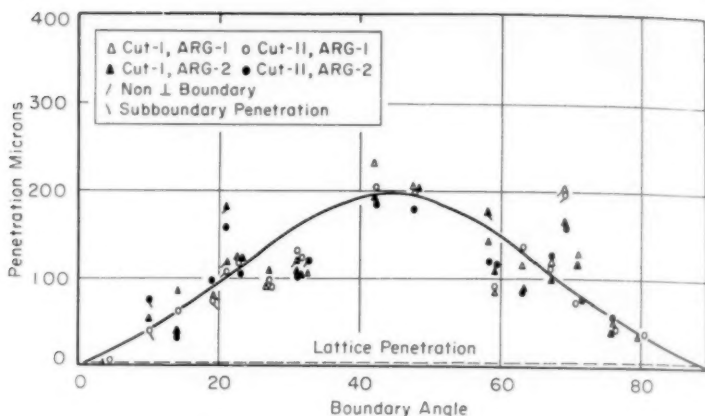


Fig. 8—The Penetration of Radioactive Nickel Along Nickel Bicrystal Grain Boundaries at 850 °C (1560 °F) as a Function of the Misfit Angle.

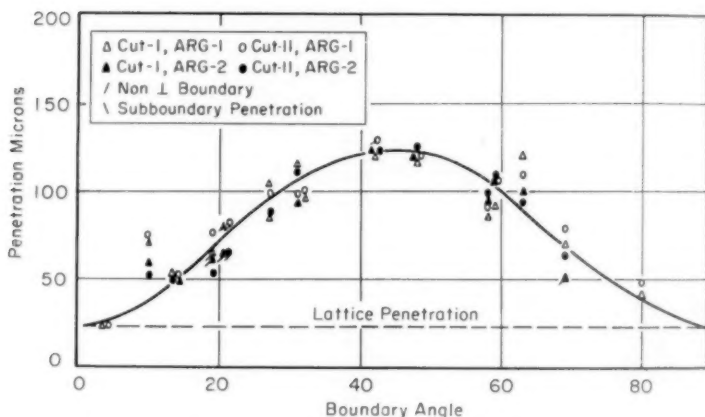


Fig. 9—The Penetration of Radioactive Nickel Along Nickel Bicrystal Grain Boundaries at 1050 °C (1920 °F) as a Function of the Misfit Angle.

in Fig. 11 and compared with present results in Table II. The agreement of these four investigations is very good, particularly when it is recognized that three different methods of measurement were utilized to determine these values in these investigations.

Because of the limited number of data points available for lattice diffusion from this research, as well as the relatively small diffusion distances measured, the equation given by Hoffman, et al. was used in the subsequent analysis of grain boundary diffusion (12). Their equation is based on 16 datum points determined by two different methods of

Table II
Comparison of Lattice Self-Diffusion Coefficients
and Activation Energies Reported in Various Investigations

Investigators	Ref.	Diffusion Coefficient at 1000 °C (cm ² /sec)	D (cm ² /sec)	Activation Energy (k cal/g mole)
This investigation	—	2.35×10^{-12}	0.48	65.9
Burgess and Smoluchowski	11	1.5×10^{-12}	—	61-65
Hoffman, Pikus and Ward	12	4.41×10^{-12}	1.27	66.8
Reynolds, Averbach, and Cohen	13	4.46×10^{-12}	0.40	63.8

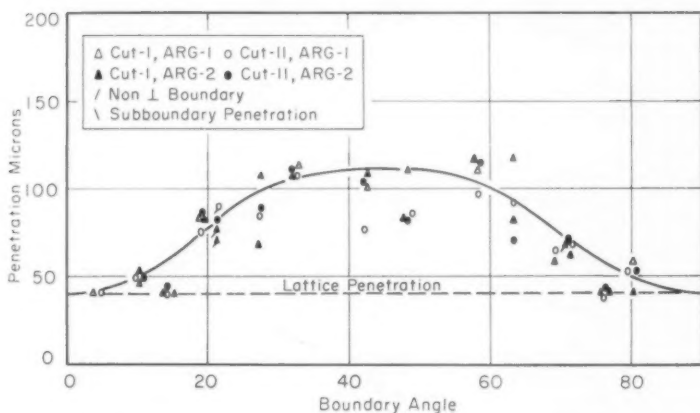


Fig. 10—The Penetration of Radioactive Nickel Along Nickel Bicrystal Grain Boundaries at 1100 °C (2010 °F) as a Function of the Misfit Angle.

measurement and for this reason it is believed that their result is probably more accurate.

Both Fisher and Whipple have presented solutions for the concentration curve resulting from combined grain boundary and volume diffusion (7,9). If these solutions are restricted to the boundary slab, the Fisher equation may be given as:

$$C/C_0 = \exp - [(4D_L/\pi t)^{0.5} y_B / (\delta D_B)^{0.5}] \quad \text{Equation 2}$$

while that of Whipple may be approximated as:

$$C/C_0 = 1.159 \beta^{0.55} \eta^{-0.67} \exp(-0.476 \beta^{-0.67} \eta^{-1.35} + 0.398 \beta^{-1.25} \eta^{0.67} + \dots) \quad \text{Equation 3}$$

C = Concentration of diffusion material at point y_B

C_0 = Depth of original interface

y_B = Depth of boundary penetration

D_B = Boundary diffusion coefficient

D_L = Lattice diffusion coefficient

t = Diffusion time

δ = Boundary width

$\beta = (\Delta - 1) \delta / 2(D_L t)^{0.5}$

$\Delta = D_B/D_L$

$\eta = y_B / (D_L t)^{0.5}$

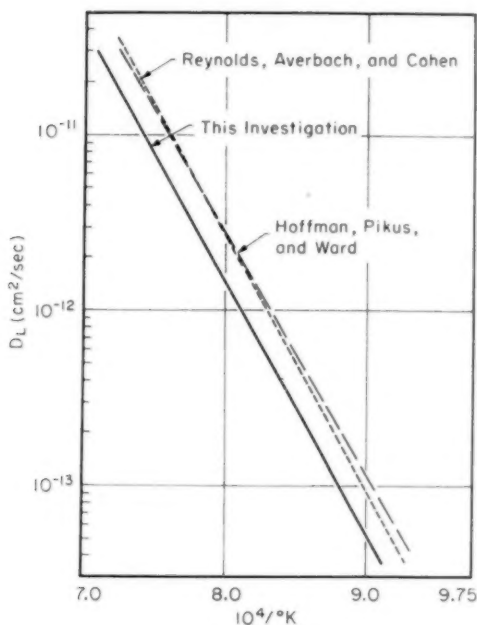


Fig. 11—The Lattice Self-Diffusion Coefficient, D_L , as a Function of the Reciprocal Temperature.

The relationship between these two solutions has been discussed by Turnbull and Hoffman and Yukawa and Sinnott and it has been shown that under the restricted conditions for which either solution is valid, they are essentially equivalent (1,5). It appears that both Fisher's and Whipple's solution represent limiting conditions which are approached as the boundary misfit, boundary diffusivity, and the ratio D_B/D_L approach very large values. They are only approximately correct for diffusion along low angle boundaries and for diffusion at high temperatures.

Fisher's equation can be simplified for calculation purposes by putting it in the logarithmic form:

$$\ln C/C_0 = -(4D_L/\pi t)^{0.5} y_B/p^{0.5} \quad \text{Equation 4}$$

where the parameter p has been substituted for $D_B\delta$. Using the known values of C/C_0 and D_L taken from the curves of Figs. 7 to 10 it is possible to calculate p . By assuming δ to be 5 Å a value of D_B may also be computed. These calculations are summarized in Table III.

A comparison of D_B computed from Fisher's equation and from Whipple's equation is shown in Table IV. These data show that the

Table III
Summary of Calculations of Grain Boundary Self-Diffusion
Coefficients of Nickel According to Fisher's Solution

	Misfit Angle (degrees)	Penetration (10^{-4} cm.)	$D = D_B g$ (cm^2/sec)	Boundary Diffusion Coefficient (cm^2/sec)	D_B/D_L
$D_L = 1.25 \times 10^{-13} \frac{\text{cm}^2}{\text{sec}}$ $t = 5.67 \times 10^4 \text{ sec}$ Temp. = 700 °C (1292 °F)	5	22	0.828×10^{-17}	1.65×10^{-18}	1.31×10^{-5}
	10	54	4.99	9.98	7.95
	20	141	34.0	68.0	54.1
	30	216	79.8	159	127
	40	260	116	232	185
	45	265	120	240	191
	50	259	115	230	183
	60	210	75.5	151	120
	70	129	28.5	57.0	45.5
	80	52	4.63	9.26	7.38
$D_L = 1.27 \times 10^{-13} \frac{\text{cm}^2}{\text{sec}}$ $t = 5.67 \times 10^4 \text{ sec}$ Temp. = 850 °C (1562 °F)	5	20	1.08×10^{-17}	2.16×10^{-18}	1.73×10^{-5}
	10	42	0.688×10^{-16}	1.37×10^{-17}	1.08×10^{-4}
	20	96	15.8	6.06	4.80
	30	154	40.8	31.6	25.0
	40	192	63.4	81.6	64.5
	45	194	64.7	127	100
	50	190	62.1	129	102
	60	148	62.1	124	98.0
	70	88	37.7	75.4	59.5
	80	38	13.3	26.6	21.0
$D_L = 1.17 \times 10^{-13} \frac{\text{cm}^2}{\text{sec}}$ $t = 2.81 \times 10^4 \text{ sec}$ Temp. = 1050 °C (1922 °F)	5	27	1.71×10^{-15}	3.42×10^{-16}	2.92×10^4
	10	38	3.3	6.78	5.80
	20	72	12.2	24.4	20.9
	30	104	25.4	50.8	43.5
	40	121	34.4	68.8	58.8
	45	123	35.5	71.0	60.7
	50	121	34.4	68.8	58.8
	60	100	23.5	47.0	40.2
	70	65	9.92	19.8	16.9
	80	38	3.39	6.78	5.80
$D_L = 2.95 \times 10^{-13} \frac{\text{cm}^2}{\text{sec}}$ $t = 2.81 \times 10^4 \text{ sec}$ Temp. = 1100 °C (2012 °F)	5	42	6.58×10^{-15}	1.32×10^{-15}	4.47×10^4
	10	49	8.96	1.79	6.06
	20	77	22.1	4.42	15.0
	30	103	39.5	7.90	26.8
	40	110	45.1	9.02	30.6
	45	111	46.0	9.20	31.2
	50	110	45.1	9.02	30.6
	60	101	38.1	7.62	25.8
	70	74	20.4	4.08	13.8
	80	49	8.96	1.79	6.06

Table IV
Comparison of Grain Boundary Self-Diffusion
Coefficients of Nickel Calculated by Whipple's
Equation and by Fisher's Equation

Temp. (°C)	Ratio of D^B (Whipple) to D_B (Fisher) for the indicated angles				
	10°	30°	45°	60°	80°
700	2.24	2.23	2.24	2.24	2.24
850	2.22	2.24	2.24	2.24	2.23
1050	—	2.09	2.10	2.06	—

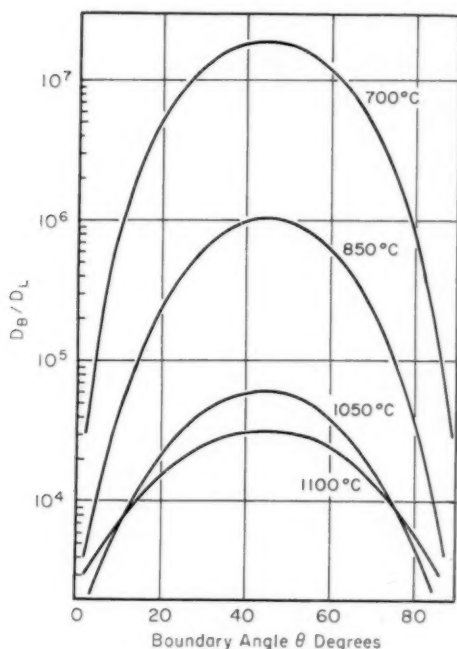


Fig. 12—The Influence of the Misfit Angle on the Ratio of the Grain Boundary Diffusion Coefficient to the Lattice Diffusion Coefficient, D_B/D_L .

values differ by an approximately constant factor of 2.2. This difference would seem to be negligible in view of the uncertainty in the value of δ , the grain boundary width, and the doubtful validity of either of these solutions for many of the data of this investigation.

The ratios of D_B/D_L for a δ of 5 Å are plotted as a function of the misfit angle in Fig. 12 which shows clearly the increasing importance of grain boundary diffusion with decreasing temperature. The anomalous behavior of the 1100 °C (2010 °F) curve at the very low or very high angles has been observed previously and is apparently due to the lack of validity of Fisher's equations for these conditions (5). In general the shape of the curves suggests that D_B is greater than D_L for all angles of θ . This concept is not inconsistent with the failure to detect preferential boundary penetration at low misfit angles in this investigation since D_B/D_L can be large and still result in preferential penetration of less than three microns, the resolution limit of this study.

Turnbull and Hoffman have proposed a grain boundary diffusion model consisting of dislocation pipes with a single characteristic diffusion coefficient D_P (1). D_P is postulated to be much greater than D_L

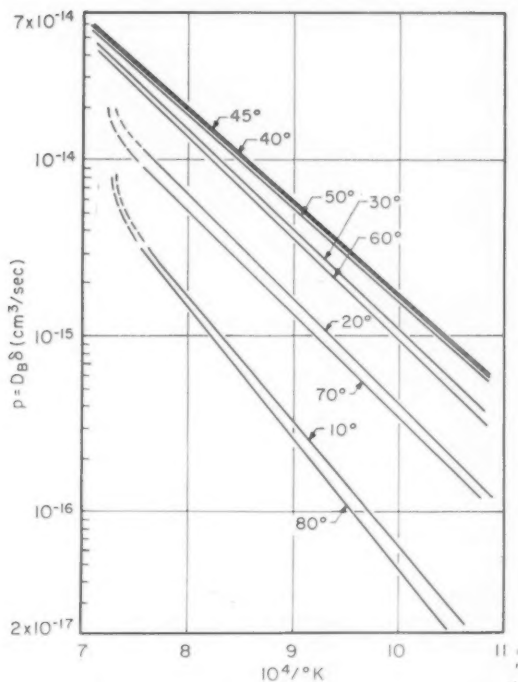


Fig. 13—The Grain Boundary Self-Diffusion Parameter, p , for Various Misfit Angles as a Function of Reciprocal Temperature.

with the regions between dislocation pipes within the boundary slab having a diffusion coefficient less than D_P but still greater than D_L . Assuming the effective diameter of a dislocation pipe to be ρ and expressing their spacing from one another, d , as a function of θ :

$$d = \lambda/2 \sin (\theta/2) \quad \text{Equation 5}$$

where λ is the lattice spacing. These authors have suggested that a variable effective grain boundary width $\delta(\theta)$ could be expressed as:

$$\delta(\theta) = \rho^2/d \quad \text{Equation 6}$$

which when combined with equation (5) results in

$$\delta(\theta) = 2 \sin (\theta/2)/\rho^2 \quad \text{Equation 7}$$

The diffusion coefficient within this effective width is D_P so that the parameter p becomes:

$$p = D_P \delta(\theta) = 2 D_P \sin (\theta/2)/\rho^2 \quad \text{Equation 8}$$

Table V
Self-Diffusion Coefficients of Nickel Along
Grain Boundary Dislocation Pipes According to
Turnbull and Hoffman's Theory

Misfit Angle (degrees)	D _p Value for the Indicated Diffusion Temperature (cm ² /sec)			
	700 °C	850 °C	1050 °C	1100 °C
10	5.72×10^{-9}	3.48×10^{-8}	3.89×10^{-7}	1.03×10^{-6}
20	19.6	9.11	7.02	1.27
30	30.8	15.8	9.82	1.53
40	33.9	18.5	10.0	1.32
45	31.4	16.9	9.82	1.20

and as such can be substituted for $D_{R\delta}$ in either Fisher's or Whipple's solution. The D_p values resulting from such a substitution in the Fisher equation are presented in Table V for various angles of misfit. These calculations indicate that the data of this investigation do not support the proposed theory that the coefficient for self-diffusion along single grain boundary dislocation pipes is independent of the boundary angle of misfit.

The temperature dependence of nickel grain boundary self-diffusion can be correlated by an Arrhenius-type equation. Fig. 13 shows the logarithms of the parameter p from Table III plotted against the reciprocal absolute temperature. This correlation is very good for the grain boundaries of large misfit ($30^\circ < \theta < 60^\circ$), but at lower misfit angles the data show deviations from a straight line plot, particularly at higher temperatures. Similar deviations have been noted for the nickel-copper system under these conditions (5). These departures appear to be due to the inadequacy of the mathematical solution for these conditions.

The activation energy for boundary self-diffusion was determined from the slopes of Fig. 13 and has been plotted as a function of the misfit angle θ in Fig. 14. It can be seen from the curve that the activation energy is effectively constant at a value of 26.0 ± 1.5 kcal/g mole for angular misfit of $20^\circ < \theta < 70^\circ$. This value is about twice that reported by Burgess and Smoluchowski (11). Their value was indirectly estimated from surface activity measurements with no direct verification of grain boundary diffusion and it appears to be of doubtful accuracy.

Because of the questionable validity of the mathematical analysis for low angle boundary misfit the shape of Fig. 14 is not conclusive. The marked dependence of grain boundary activation energy is in conflict with the grain boundary diffusion theory of Turnbull and Hoffman which suggests that boundary diffusion activation energy should be independent of misfit (1). On the other hand the data of the copper-nickel system also show a similar dependent relationship between activation energy and boundary misfit that is reported in this investigation (5). The striking similarity between Fig. 14 and the inverted plot of

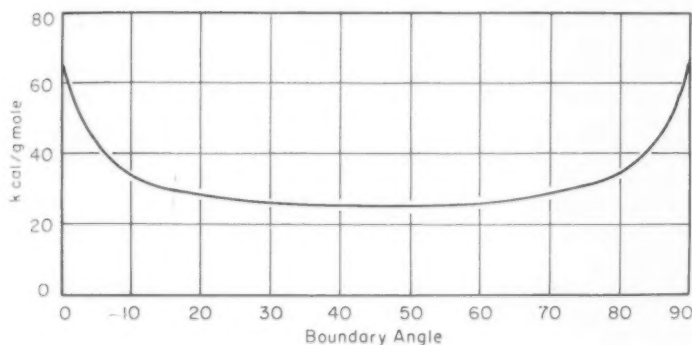


Fig. 14—The Activation Energy for Grain Boundary Self-Diffusion as a Function of the Misfit Angle.

the conventional curve relating grain boundary energy to misfit angle suggests that the activation energy for the diffusion process may be rather closely related to the interfacial energy of the boundary. Such an interrelationship may be expected since both energies are dependent upon the atomic binding forces within the boundary region. Additional experimental data and an improved mathematical analysis in the region of $0 < \theta < 20^\circ$ is needed to clarify this possible relationship.

CONCLUSIONS

The lattice self-diffusion coefficient of nickel in the temperature range $850\text{--}1100^\circ\text{C}$ ($1560\text{--}2010^\circ\text{F}$) has been determined and is expressible by the relationship:

$$D_L = 0.48 \exp(-65,800/RT)$$

The depth of penetration of radioactive nickel along the grain boundaries of nickel is dependent on the boundary orientation with the maximum penetration occurring at the maximum misfit angle.

The available mathematical solutions for the analysis of grain boundary diffusion represent the limiting conditions which are approached for boundaries of large crystallographic misfit at low diffusion temperatures. At higher temperatures and with decreasing boundary misfit these solutions are subject to an increasing degree of uncertainty.

The ratio of the grain boundary diffusion coefficient to the lattice diffusion coefficient, D_B/D_L , varies from 10^3 to 10^7 for boundary angles from 5° to 80° over the temperature range $700\text{--}1100^\circ\text{C}$ ($1290\text{--}2010^\circ\text{F}$). This ratio has been shown to increase with increasing angular misfit and with decreasing diffusion temperature.

The activation energy for grain boundary diffusion is independent of the misfit angle for $20^\circ < \theta < 70^\circ$ with a value of 26.0 ± 1.5 k cal/g

mole. Beyond these limits the activation energy appears to approach the value of 65.9 K cal/g mole, the lattice diffusion activation energy.

The grain boundary diffusion of nickel cannot be correlated in terms of a self-diffusion coefficient for dislocation pipes that is independent of the angle of misfit.

ACKNOWLEDGMENT

The authors wish to acknowledge the financial support of this investigation by the Michigan Memorial Phoenix Project and by the American Society for Metals Graduate Fellowship in Metallurgy. The many helpful discussions of this research with Dr. Lars Thomassen of the University of Michigan are gratefully acknowledged.

References

1. D. Turnbull and R. W. Hoffman, "The Effect of Relative Crystal and Boundary Orientations on Grain Boundary Diffusion Rates," *Acta Metallurgica*, Vol. 2, 1954, p. 419-426.
2. P. J. Fenshan, "Self-Diffusion in Polycrystalline Tin," *Australian Journal of Scientific Research*, Vol. 3, Series A, 1950, p. 105-108.
3. R. Flanagan and R. Smoluchowski, "Grain Boundary Diffusion of Zinc in Copper," *Journal of Applied Physics*, Vol. 23, 1952, p. 785-87.
4. R. Achter and R. Smoluchowski, "Diffusion in Grain Boundaries and Their Structure," *Journal of Applied Physics*, Vol. 22, 1951, p. 1260-64.
5. S. Yukawa and M. J. Sinnott, "Grain Boundary Diffusion of Nickel into Copper," *Transactions, American Institute of Mining and Metallurgical Engineers*, Vol. 203, 1955, p. 996-1001.
6. J. M. Burgers, "Geometrical Considerations Concerning the Structural Irregularities to be Assumed in a Crystal," *Proceedings, The Physical Society*, Vol. 52, 1940, p. 23-33.
7. J. C. Fisher, "Calculation of Diffusion Penetration Curves for Surface and Grain Boundary Diffusion," *Journal of Applied Physics*, Vol. 22, 1951, p. 74-76.
8. R. T. P. Whipple, "Concentration Contour in Grain Boundary Diffusion," *Philosophical Magazine*, Vol. 45, 1954, p. 1225-236.
9. H. J. Gombert, G. C. Towe and J. W. Freeman, "High-Resolution Autoradiography for Study of Grain Boundaries in Metals," U. S. Dept. of Commerce, Office of Technical Services, PB 111558, 1954.
10. K. T. Aust and B. Chalmers, "Energies and Structures of Grain Boundaries," *Metal Interfaces*, 1952, American Society for Metals, Cleveland, Ohio.
11. H. Burgess and R. Smoluchowski, "Note on Self-Diffusion of Nickel," *Journal of Applied Physics*, Vol. 26, 1955, p. 491-92.
12. R. E. Hoffman, F. W. Pikus and R. A. Ward, "Self-Diffusion in Solid Nickel," *Transactions, American Institute of Mining and Metallurgical Engineers*, Vol. 206, 1956, p. 483-5.
13. J. E. Reynolds, B. L. Averbach and M. Cohen, "Self-Diffusion and Inter-Diffusion in Gold-Nickel Alloys," *Acta Metallurgica*, Vol. 5, 1957, p. 29.

THE EFFECT OF OXIDE RECRYSTALLIZATION ON THE OXIDATION KINETICS OF A 62:38 COPPER-NICKEL ALLOY

BY J. A. SARTELL, S. BENDEL, T. L. JOHNSTON AND C. H. LI

Abstract

A study has been made of the oxidation behavior of a constantan-type 62:38 copper-nickel alloy at temperatures in the range of 620–927 °C (1150–1700° F) by using complementary gravimetric, marker movement, and metallographic techniques. During isothermal oxidation, two oxide layers are formed; an outer CuO layer whose growth is described by a single parabolic law and an inner layer, consisting of a mixture of Cu₂O and NiO, whose growth is described by two consecutive parabolic laws. The growth of the CuO layer requires the outward movement of cupric ions, while the oxide front of the inner layer moves forward by the nucleation and growth of NiO by an internal oxidation mechanism involving a rapid inward diffusion of oxygen from the CuO:Cu₂O interface to the Ni-Cu solid solution. The change in the parabolic rate constant associated with the growth of the inner NiO-Cu₂O layer is caused by recrystallization of the outer CuO layer. (ASM International Classification R1h; Cu, Ni)

INTRODUCTION

FROM A thermodynamic viewpoint, it is usually assumed that the system copper nickel is ideal for oxidation studies (1)¹. The two metals are mutually soluble throughout the entire range of composition; one is more active with respect to oxygen than the other and furthermore the respective oxides are insoluble in each other. The oxidation behavior of copper-rich Cu-Ni and nickel-rich Ni-Cu alloys has received adequate attention, and it has been found that Wagner's theory of oxidation of alloys is applicable (2). However, the authors are aware of only one paper, that of Pilling and Bedworth published in 1925 (3), which describes the oxidation behavior of alloys of intermediate composition. Since that time experimental techniques and theories have developed to such an extent that it seems reasonable to

¹ The figures appearing in parentheses pertain to the references appended to this paper.

A paper presented before the Thirty-Ninth Annual Convention of the Society, held in Chicago, November 4–8, 1957. The authors, J. A. Sartell, S. Bendel, T. L. Johnston, and C. H. Li, are associated with the Minneapolis-Honeywell Regulator Company Research Center, Hopkins, Minnesota. Manuscript received April 15, 1957.

expect that additional knowledge may be gained by re-investigation of these intermediate-composition alloys.

The occurrence of multiple oxides in this system complicates the analysis of oxidation behavior. One of the major difficulties is the determination of the rate-determining factors. Many theoretical analyses rely on the assumption that the cation movement is the sole rate-determining factor (4) but application of marker techniques has indicated that this assumption is not valid in general (5,6). In view of this, our kinetic studies have been complemented by marker and metallographic observations. For preliminary work, a constantan (62-38 Cu-Ni) alloy was chosen. For this particular alloy, it has been shown that strain induced recrystallization of an oxide layer plays an important role in oxidation behavior. The fact that the influence of changes in structure of an oxide is usually neglected has stimulated publication of this work before a survey of the oxidation characteristics of all the intermediate alloys has been completed.

EXPERIMENTAL PROCEDURE

30-gram ingots of a nominal 62:38 copper-nickel alloy were prepared by vacuum melting high purity copper (99.999%) and high purity nickel (99.999%) at pressures less than 10^{-3} millimeters of mercury. These ingots were then dripcast in vacuum and homogenized at 900 °C (1650 °F) in a purified helium atmosphere for five days. Metallographic examination showed that these ingots were homogeneous. They were then rolled down with intermediate anneals to the thickness appropriate to the kinetic studies, marker observations, and chemical analyses respectively. The latter showed that for $\frac{1}{2}$ gram samples taken from each end and the center of a strip obtained from a given ingot, the composition was uniform to within 0.5%.

Specimens were finally held at 900 °C (1650 °F) for 30 minutes to stabilize the grain size and chemically cleaned with 2 parts HNO₃, 1 part acetic acid, and 1 part water.

For the kinetic studies, a thermal balance (sensitivity 0.2 milligrams) similar to that of Horn (7) was used. The oxidation furnace was constructed in such a way that the specimen could be lifted from a low temperature region to the hot zone so that the time for heating the specimen up to the testing temperature was reduced in order to minimize nonisothermal oxidation.

Purified dry oxygen was passed continuously through the furnace at a constant rate (0.15 liters per minute) at atmospheric pressure at temperatures which were controlled to within 2 °C. For specimens with dimensions of $3 \times 1.5 \times 0.05$ centimeters the reproducibility of kinetic curves (weight-gain versus time at constant temperature) was quite satisfactory (see Fig. 1).

For the marker observations, gold-plated platinum wires of 0.0025

centimeters in diameter were employed. These wires were pressure welded on opposite surfaces of $0.6 \times 0.6 \times 0.17$ centimeter specimens at 650°C (1200°F) and sintered at 900°C (1650°F) for 30 minutes. The oxidation conditions were similar to those used for kinetic studies, in order that a correlation between marker movement and weight-gain could be made. Taking a polished section through the sample normal to the marker axes, the distance between the markers was measured

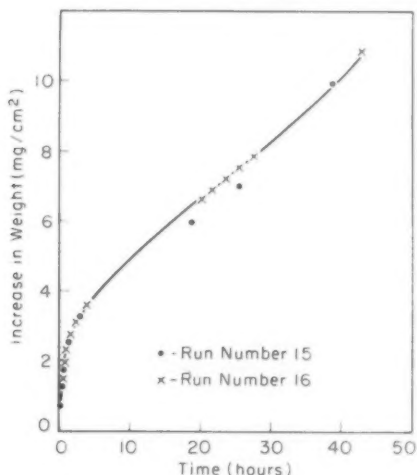


Fig. 1—Reproducibility of the Gravimetric Method Illustrated by Duplicate Oxidation Runs on the 62 Cu — 38 Ni Alloy at 732°C (1350°F).

both before and after oxidation with an accuracy of ± 0.00025 centimeters. The thickness of the oxide layers was also measured. Sachs (8) studied the influence of the size of the marker and found that if it was greater than a certain size, it would affect the micro-structure of the surrounding oxide. Experiments performed in our laboratory on the effect of the marker size showed that markers with 0.005 centimeters diameter or less had no effect other than reducing the local thickness of oxide.

To identify the oxidation products, the powder method and Geiger counter diffractometer method of x-ray diffraction were employed. Chemical analysis was frequently used for further checking.

EXPERIMENTAL RESULTS AND DISCUSSION

The oxidation kinetic curves plotted as the square of the weight-gain per unit area versus time at constant temperature are shown in Fig. 2. It will be noted that instead of a single parabolic time law, two con-

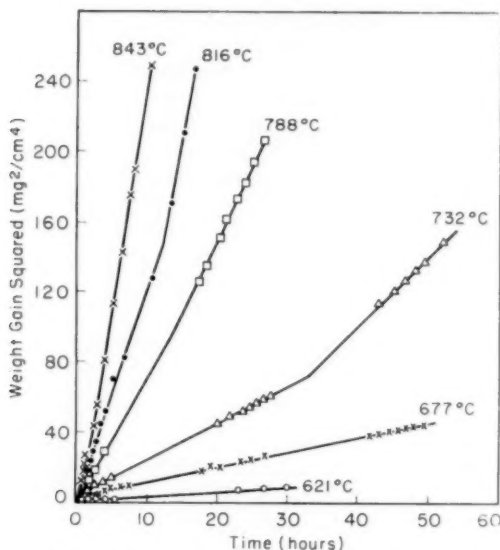


Fig. 2—Parabolic plot of the Oxidation Rates of a 62 Cu - 38 Ni Alloy Obtained Gravimetrically.

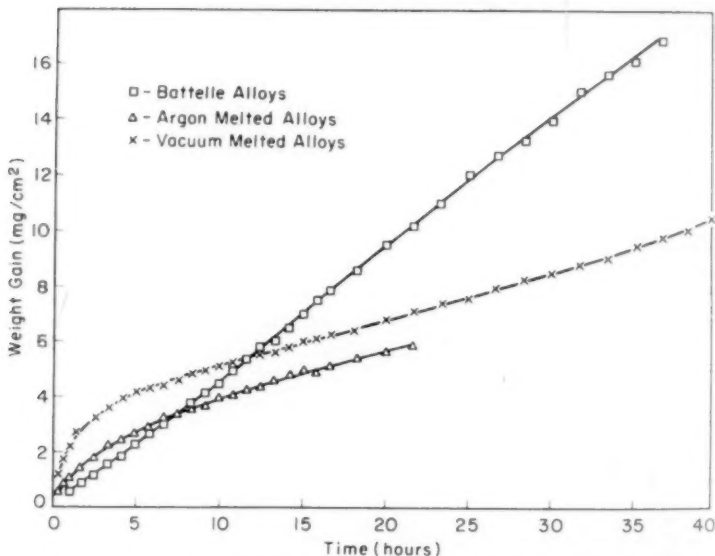


Fig. 3—A Comparison of Oxidation Rates of 62 Cu - 38 Ni Alloys Produced Under Different Conditions. The argon and vacuum melted alloys were made from materials of 99.999% purity and the Battelle alloy was made from commercially pure metals.

secutive parabolic laws were obeyed during oxidation: the rate constant during the second stage was greater than that for the initial period. These results are different from those of Pilling and Bedworth (3), who reported that oxidation followed a single cubic law. This discrepancy is probably due to differences in purity of the material used. According to Wagner (9), NiO and Cu₂O are metal-deficit oxides; small amounts of higher valency cations from the impurity atoms of the alloy itself would greatly increase the oxidation rate. In view of this, Argon-melted high purity and air-melted commercial purity Cu-Ni alloys were studied also, their respective oxidation behaviors were not the same as that of vacuum melted material (Fig. 3).

Examination of the micro-structure showed that the oxide was composed of two distinct layers: the outside layer was identified by x-ray diffraction as monoclinic CuO. It was fine-grained and frequently had a columnar structure. The substrate was identified as a mixture of cubic Cu₂O and cubic NiO. From lattice parameter analysis, there was no evidence of solid solubility between these oxides. The structure of this substrate consisted of a Cu₂O matrix in which NiO particles were dispersed in narrow bands lying parallel to the alloy surface (Fig. 4). In the alloy-substrate interface there were small isolated oxide particles which, after stripping off the oxide layers, were identified as NiO in a matrix of essentially pure copper by x-ray diffraction. The presence of CuO at these temperatures of investigation is not in agreement with Hickman and Gulbransen (10) nor with the theoretical considerations proposed by Wagner (1). However, Hickman and Gulbransen's experiments were performed with oxygen at a much lower pressure of 1 millimeter. Since the CuO is formed by the oxidation of Cu₂O, then the oxygen pressure must play an important role.

The Significance of Marker Studies

At all temperatures of investigation (760–927 °C), the platinum marker was always found at the interface between the two oxide layers. The marker acted as a barrier to the diffusion currents during oxidation, since the total thickness of the oxide layers in the immediate neighborhood of the marker was always somewhat smaller (Fig. 5). However, this did not complicate our measurements, since one could measure the movement of the boundary between the outside layer and substrate and assume that it indicated the movement of an infinitely small marker.

The fact that the marker was a barrier to the diffusion currents and was located between these two different oxide layers indicates that not only do copper ions diffuse outward to the surface but also oxygen ions diffuse inward to the metal substrate. A plot of the square of the increase in thickness of the respective oxide layers $(\Delta x)^2$ versus time at various temperatures shows that for each layer the parabolic relationship holds true, as shown in Figs. 6 and 7. It is interesting to note

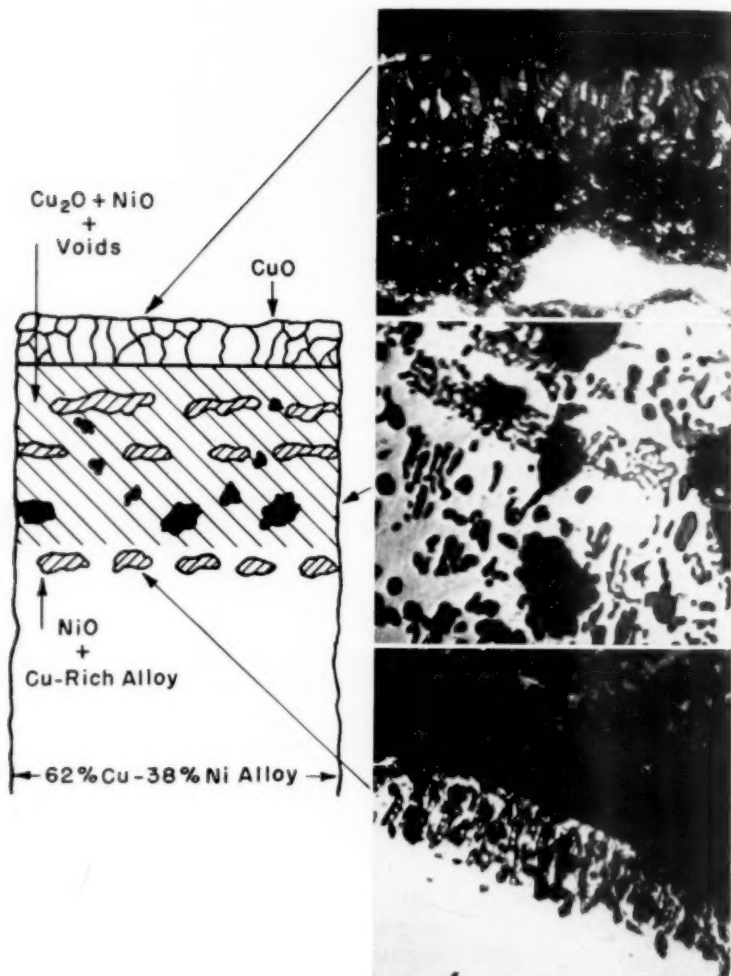


Fig. 4—The Alloy-Substrate-CuO Structure. $\times 750$.

that the growth of the outer layer (CuO) obeys a single parabolic time law, whereas the growth of the inner layer ($\text{Cu}_2\text{O} + \text{NiO}$) follows two parabolic time laws: one for the earlier and another for the later period of oxidation. The possible reasons for this behavior will be discussed below.

The activation energies associated with each parabolic time relation-

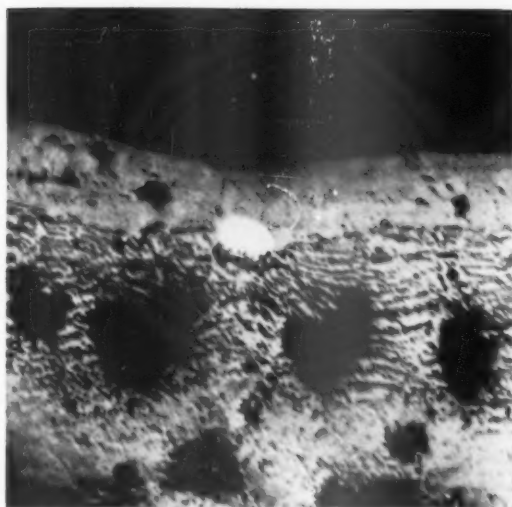


Fig. 5—A Platinum Marker Lying at the CuO—Substrate Interface. $\times 200$.

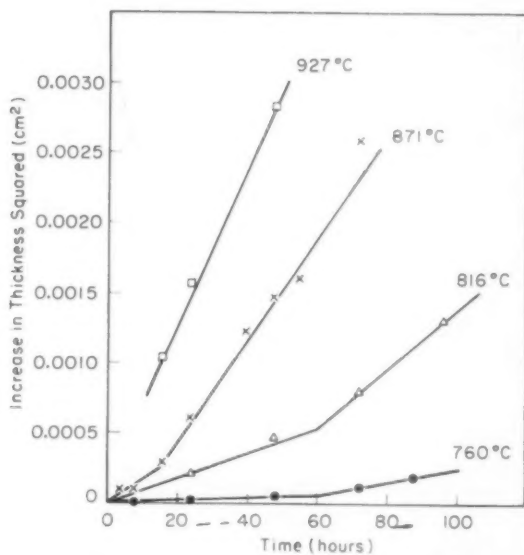


Fig. 6—The Growth Rates of the $\text{Cu}_2\text{O-NiO}$ Layer as Determined from Marker Measurements.

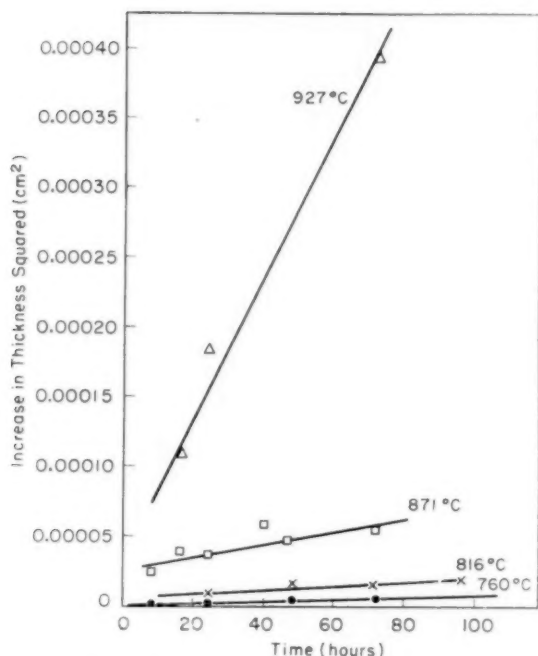


Fig. 7—The Growth Rate of the CuO Layer as Determined from Marker Measurements.

ship (based on marker observations) were found to be constant (Figs. 8 and 9). For the growth of CuO, the activation energy was 43,000 cal/mole. The value associated with the growth of the Cu_2O -NiO layer during the early part of oxidation was 44,000 cal/mole, whereas in the later part of oxidation, it changed to 21,000 cal/mole. The oxidation behavior can be summed up in Table I based upon the following equations:

$$(\Delta x)^2 = K'_p t$$

where K'_p , the parabolic rate constant, is related to temperature by the Arrhenius equation

$$K'_p = A e^{-Q/RT}$$

Table I			K'_p cm ² /hour		
°C	Temperature	°F	NiO-Cu ₂ O, 1st stage	NiO-Cu ₂ O 2nd stage	CuO
760		1400	9.7×10^{-7}		3.2×10^{-8}
816		1500	7.3×10^{-6}	2.2×10^{-5}	9.7×10^{-8}
871		1600	1.6×10^{-5}	3.6×10^{-6}	4.0×10^{-7}
927		1700		5.6×10^{-6}	6.1×10^{-7}

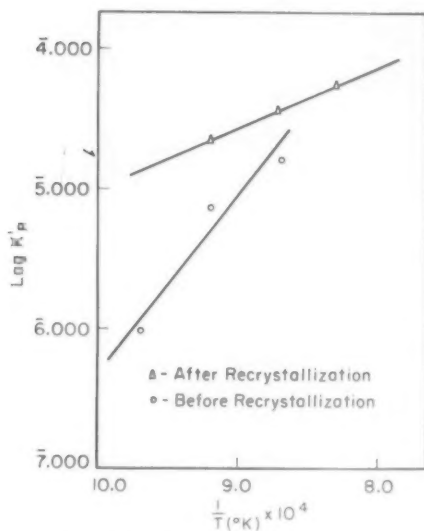


Fig. 8—The Temperature Dependence of the Growth Rates of the $\text{Cu}_2\text{O-NiO}$ Layer.

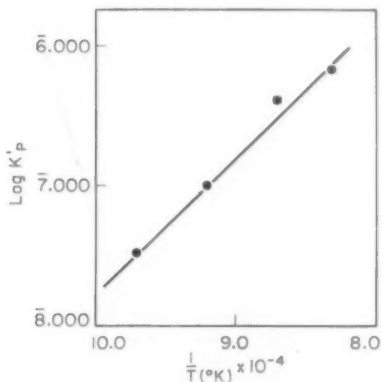


Fig. 9—The Temperature Dependence of the Growth Rate of the CuO Layer.

A possible explanation for the change in the growth rate of the $\text{NiO-Cu}_2\text{O}$ layer has evolved from a study of the CuO . As mentioned previously, when the CuO was formed, it had a fine-grained (and frequently columnar) structure (Fig. 10). This fine-grained CuO layer was replaced eventually during isothermal oxidation by a coarse equiaxed structure many of whose grains contained twins (Fig. 11).

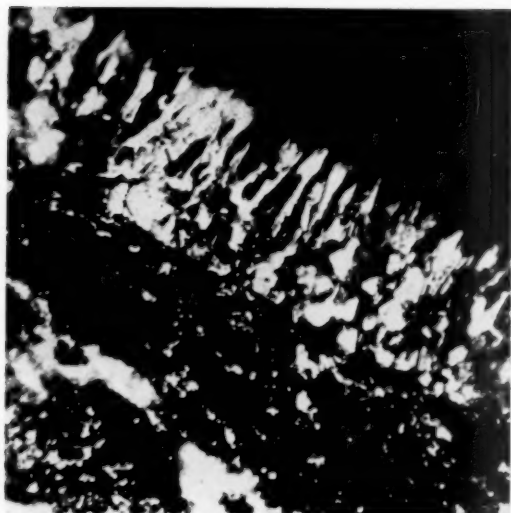


Fig. 10—The CuO Layer Shortly After the Onset of Recrystallization. Note the equi-axed grains at the base of the CuO. Specimen oxidized 72 hours at 760 °C (1400 °F). $\times 1000$.

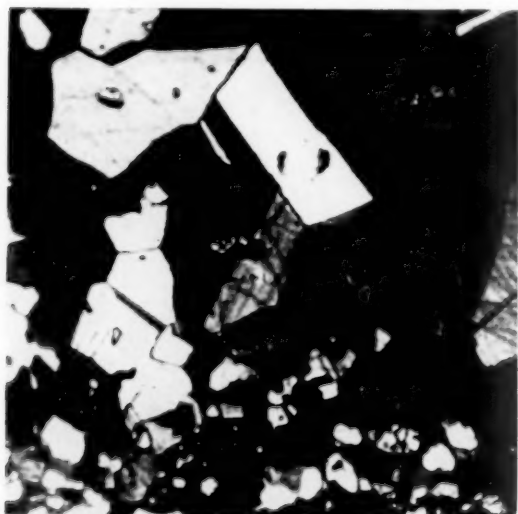


Fig. 11—The CuO Layer After Recrystallization. (Note twinning bands.) Specimen oxidized 48 hours at 871 °C (1600 °F). $\times 250$.

At the stage of oxidation shown in Fig. 11, the growth rate of $\text{Cu}_2\text{O} + \text{NiO}$ had already increased. It is clear that since no change of phase was involved, recrystallization must have taken place as a re-

sult of internal strain. This suggests that a state of stress existed at the $\text{Cu}_2\text{O}:\text{CuO}$ interface as soon as CuO was formed, possibly as a result of epitaxial growth. This does not seem to be unreasonable since the specific volume of Cu_2O is 23.3 and that of CuO , 12.2; and the oxides were observed to be very adherent to each other, no apparent microcracks were observed. Although the stress must have been equal and opposite across the interface, the gradient of stress in the respective oxide layers was not necessarily symmetrical. The recrystallization of CuO was shown to nucleate at the $\text{CuO}:\text{Cu}_2\text{O}$ interface (Fig. 10).

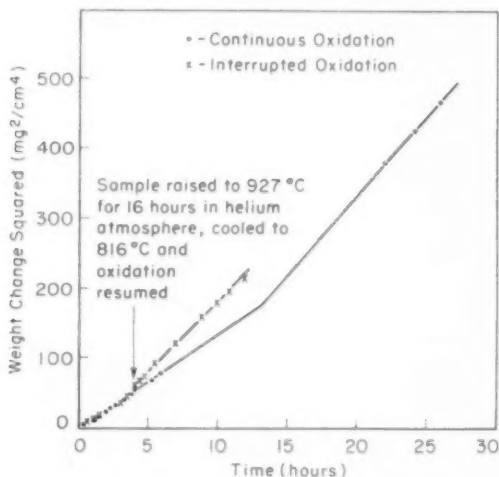


Fig. 12—The Premature Increase in the Oxidation Rate at 816 °C (1500 °F) Caused by Recrystallization of CuO Induced by a High Temperature Anneal in Helium.

Assuming that the oxide layers grow by the diffusion of oxygen and copper ions across the above interface (involving the movement of anion and cation vacancies), then the existence of stress at the interface may possibly modify the rate of oxidation in the following way: Williams (11) has pointed out that provided there are appropriate sources and sinks in a material, a stress gradient will cause a net flux of vacancies in the direction of the gradient. If this is so in the present case, the total flux of vacancies in each oxide will be the algebraic sum of that associated with the activity gradients of the diffusing ions and that associated with the stress gradients. It is reasonable to assume that the CuO layer is in tension at the interface so that the stress gradient is toward the interface while the Cu_2O is in compression so that the stress gradient in this oxide is away from the interface.

The increase in thickness of CuO probably depends upon the rate at which cupric ions reach the oxide/oxygen surface, and this requires

the diffusion of cation vacancies towards the interface. The vacancy movements associated with chemical and stress gradients respectively are additive. The transport of ions in this "transition conductor" type of oxide is very small because of the existence of equivalent concentrations of positive holes and negative interstitial electrons. The limited electronic conductivity that characterizes this type of oxide suggests that the transport of charge is a major factor in controlling the increase in thickness of the CuO layer and therefore it is not to be expected that the interaction of a stress gradient and the flux of cation vacancies will have an appreciable effect. This is consistent with the fact that no change in the rate of isothermal growth of the CuO layer was detected after its recrystallization.

Let us next consider the NiO:Cu₂O layer. Cu₂O is a cation-deficient semiconductor whose growth rate is controlled by ionic rather than electron transport. It will be emphasized later that the oxide front advances by the mechanism of internal oxidation in which oxygen diffuses rapidly into the alloy to form nuclei of NiO and that this process is controlled by the supply of oxygen to the Ni-Cu solid solution. This requires that a flux of anion vacancies in the Cu₂O is directed towards the Cu₂O:CuO interface which is in opposition to the effect of the stress gradient in Cu₂O which would drive vacancies away from the interface. In the present case this has a twofold effect, firstly the concentration of anion vacancies is reduced in the neighborhood of the interface and secondly, the energy required for an oxygen ion to squeeze into an anion vacancy will be higher. Each effect will reduce the rate at which oxygen can diffuse through Cu₂O away from the interface. It is suggested, therefore, that the higher rate constant in the parabolic relationship which describes the later period of oxidation is associated with the relaxation of stress in Cu₂O caused by the recrystallization of CuO. To demonstrate directly that such recrystallization is associated with the increase in growth rate, a specimen was oxidized at 815 °C (1500 °F) for 4 hours (at 815 °C (1500 °F), the increase in oxidation rate normally occurs after approximately 13-14 hours) and annealed at 925 °C (1695 °F) in helium in order to recrystallize the CuO without further oxidation. Metallographic examination of dummy specimens indicated that 16 hours at 925 °C (1695 °F) was sufficient for full recrystallization. Immediately after resumption of oxidation at 815 °C (1500 °F), the higher rate constant characteristic of this temperature was manifest, see Fig. 12.

It is a familiar fact that recrystallization is a function of plastic strain, temperature, and time, e.g., for a given degree of strain, the time required for recrystallization is inversely related to the temperature. Fig. 2 shows that the change in the oxidation rate is a function of time and temperature. The fact that the CuO, rather than the Cu₂O, layer recrystallized suggests that the epitaxial stresses involved in the growth

of CuO cause the latter to flow plastically (presumably, since it has a lower yield point than Cu_2O). In addition, differences in the elastic moduli of the respective oxides will be important; unfortunately, little information exists regarding their elastic and plastic properties.

It is now possible to put forward a tentative phenomenological description of the oxidation of the Cu-Ni alloy in question. The position maintained by the inert markers proves that the oxide front moves forward into the alloy by the rapid diffusion of oxygen through the Ni-Cu solid solution to nucleate particles of NiO which has the greatest free energy of formation of the three oxides formed (the values for NiO, Cu_2O , and CuO, respectively, are: $-32,900$, $-23,300$, and $-16,200$ cal/mol at 1000°C). The growth of a given NiO particle continues until the activity of nickel in the surrounding matrix is reduced to a value which is of the order of zero. The observation that in the advance front NiO particles are surrounded by almost pure copper is in agreement with Wagner's estimate (1) that the simultaneous existence of NiO and Cu_2O in a Cu:Ni alloy can only occur at a nickel concentration of 0.7% or lower. This means that the diffusion rate of oxygen must be higher than that of nickel in the solid solution.

After the copper-rich matrix has oxidized to Cu_2O by the local reaction of Cu^+ ions at the oxygen-rich surface, CuO is formed by further oxidation of Cu_2O and evidently grows by the diffusion of Cu^{++} ions to the free oxygen surface. The growth rate constant of the CuO remains essentially constant during isothermal oxidation and is unaffected by its recrystallization. The small value of the parabolic rate constant is a reflection of the low mobility of ions in a "transition conductor" type of oxide.

The continued advance of the NiO front is controlled by the rate of arrival of oxygen to the unchanged alloy, the former having to diffuse from the $\text{Cu}_2\text{O}:\text{CuO}$ interface through Cu_2O , Cu, and Cu-Ni solid solution respectively. Inasmuch as there is evidence that internal oxidation depends for its existence upon the ability of oxygen to diffuse through an alloy much more rapidly than the chemical diffusion rates of the respective metal atoms, the rate at which the anions diffuse through Cu_2O is that which is believed to control the rate at which new particles of NiO are nucleated. The low rate at which oxygen ions can diffuse through the outer CuO layer does not control the advance of the oxide front since the activity of oxygen in CuO at the $\text{Cu}_2\text{O}:\text{CuO}$ interface is always high enough to satisfy the needs of internal oxidation. The growth of the CuO and NiO- Cu_2O layers is regarded as two independent processes; at present no significance can be attached to the close similarity between the activation energies of the growth of CuO and the initial stage of the growth of the Cu_2O -NiO layer.

So far as the formation of CuO is concerned, it should be pointed out that its thickness is considerably greater than that on pure copper (12).

This is to be expected, since the constant K_p in the parabolic time law depends on the differences in the electro-chemical potentials at the interfaces. The potentials at the $(\text{NiO-Cu}_2\text{O})\text{:CuO}$ interface are certainly different from those at the $\text{Cu}_2\text{O}\text{:CuO}$ interface on pure copper. Unfortunately, there are no thermodynamic data available to calculate the specific differences.

ACKNOWLEDGMENTS

The authors are grateful to Drs. J. N. Dempsey and Van W. Bearinger for their encouragement and to Dr. Finn J. Larsen for permission to publish this paper.

References

1. C. Wagner, "Theoretical Analysis of the Diffusion Processes Determining the Oxidation Rate of Alloys," *Journal, Electrochemical Society*, Vol. 99, 1952, p. 369.
2. C. Wagner, "Theory of the Tarnishing Process," *Zeitschrift fur Physikalische Chemie*, Vol. 21, Series B, 1933, p. 25.
3. N. B. Pilling and R. E. Bedworth, "Oxidation of Copper-Nickel Alloys at High Temperatures," *Industrial Engineering Chemistry*, Vol. 17, 1925, p. 372.
4. O. Kubaschewski and O. von Goldbeck, "Oxidation of Nickel-Platinum Alloys," *Journal, Institute of Metals*, Vol. 76, 1949, p. 255.
5. M. H. Davies, M. T. Simnad and C. E. Birchenall, "On the Mechanism and Kinetics of the Scaling of Iron," *Journal of Metals*, Vol. 3, 1951, p. 889.
6. L. Himmel, R. F. Mehl and C. E. Birchenall, "Self-Diffusion of Iron in Iron Oxides and the Wagner Theory of Oxidation," *Transactions, American Institute of Mining and Metallurgical Engineers*, Vol. 197, 1953, p. 827.
7. L. Horn, "The Effect of Some Added Elements on the Oxidation of Nickel," *Zeitschrift fur Metallkunde*, Vol. 36, 1944, p. 142.
8. K. Sachs, "Marker Movement in Scale Layers," *Metallurgia*, Vol. 54, No. 321, 1956, p. 11.
9. C. Wagner, "Theory of Arranged Mixed Phases. III-Disarranged Phenomena in Polar Compounds as Basis for Ionic and Electronic Conduction," *Zeitschrift fur Physikalische Chemie*, Vol. 22, Series B, 1933, p. 181.
10. J. W. Hickman and E. A. Gulbransen, "An Electron-Diffraction Study of Oxide Films Formed on Copper-Nickel Alloys at Elevated Temperatures," *Transactions, American Institute of Mining and Metallurgical Engineers*, Vol. 180, 1949, p. 519.
11. R. O. Williams, "Diffusion of Vacancies Under a Stress Gradient," *Acta Metallurgica*, Vol. 5, No. 1, 1957, p. 55.
12. C. G. Cruzan and H. A. Miley, "Cuprous-Cupric Oxide Films on Copper," *Journal of Applied Physics*, Vol. 11, 1940, p. 631.

DISCUSSION

Written Discussion: By James T. Waber, Los Alamos Scientific Laboratory, Los Alamos, New Mexico.

This paper is extremely interesting since it represents one of the first papers dealing with marker studies made during the oxidation of alloys and certainly it is one of the few which discusses the possible role of recrystallization in oxide layers.

The enhancement in the growth of the cuprite (Cu_2O) layers is attributed to the reduction in stress in the oxide after recrystallization of the outer cupric oxide scale.

The CuO is assumed by the authors to be in tension with respect to cuprous oxide, however, it occupies approximately 1.05 the volume of ($\text{CuO}_{0.8}$). The contrary assumption would appear more correct.

The effect of stress on the diffusion of lattice defects is such that material flows towards a boundary in tension. Alternately the vacancy current moves towards a region under compression. The phrasing of the authors is ambiguous in this connection. This effect of stress would facilitate the transfer of matter across the metal-oxide interface into the alloy. Noting that the Pilling-Bedworth ratios of Cu_2O is 1.64 and of CuO is 1.72, the stress gradient would increase the vacancy current moving away from the alloy phase. This is contrary to the direction, the cation vacancies migrate in cuprous oxide since these vacancies are created at the Cu_2O - CuO interface. Relaxation of the stress at this interface would thus augment the vacancy flux and thus the oxidation rate.

The evidence supporting this argument, however, is circumstantial. Annealing the oxide scales in helium can also lead to a reduction in the concentration gradients across the films.

Presumably stress relief occurs before recrystallization. Is there evidence that the break in the kinetics occurs before recrystallization takes place? One can augment the interfacial stresses by oxidizing a curved specimen while under an axial load. Would the rate of oxidation be the same on the tension side of sample as on the compression side?

The authors mention anion vacancies being formed at the alloy- Cu_2O interface. Is there experimental evidence that any appreciable concentration of anion vacancies can exist in this oxide?

Since the use of markers make these oxidation experiments into Kirkendall diffusion experiments, is there a net motion of the markers with respect to the original interface? Why are voids formed during the oxidation of the alloy when they are not formed during the oxidation of pure copper?

The fact that the markers were buried under the cupric oxide layers is strong evidence that cation migration is dominant in this oxide, which is a fact that apparently has not been reported previously. At first sight, one might have expected it to be buried under the ($\text{Cu}_2\text{O} + \text{NiO}$) layer as well, since migration of the cations via vacancies has been established for cuprite. This makes the question of any net motion of the markers an important one.

The authors are to be complimented for presenting this provocative paper before the total study could be completed.

Written Discussion: By David J. Mack, Professor of Metallurgical Engineering, Department of Mining & Metallurgy, The University of Wisconsin, Madison, Wisconsin.

Any person who has worked with the metallography of oxide scales is well aware of the difficulties to be encountered. Hence my question to the authors may be pointless. Was any epitaxis observed between either alloy and oxide scale or between the two oxide layers? I should think it unlikely that any appreciable epitaxial layer should exist at the metal-oxide interface; it is more likely that one would be found between the two oxide layers. As the authors point out, the stresses due to such a coherent epitaxial layer may play an important part in the

recrystallization of the CuO layer. If no such layer exists, the origin of the stresses responsible for the recrystallization of the CuO must be found elsewhere.

Authors' Reply

The authors would like to thank both Professor Mack and Dr. Waber for their interest and discussion.

In answer to Professor Mack's question, subsequent x-ray diffraction work on both single and polycrystalline specimens, has shown the oxide layers to be preferentially oriented. The Cu_2O is oriented so that its (100) plane is parallel to the (100) plane in the alloy, while for the NiO particles the (111) plane is parallel to the (111) plane in the alloy. On the polycrystalline specimens the CuO layer is oriented with the (111) plane parallel to the oxide-oxide interface. Additional work is being done to determine the exact nature of these orientation relationships.

It is true, as Dr. Waber points out, that the stress pattern postulated by the authors is in opposition to that predicted by the Pilling-Bedworth ratio. It must be kept in mind, however, that no macroscopic quantity can successfully predict the stress configuration at the oxide-oxide interface. A determination of this configuration can only come from a knowledge of lattice-matching requirements across the interface, both as to planes and directions of matching.

Annealing the oxide scales could indeed lead to a reduction in the concentration gradients across the films, but these reduced gradients would result in a reduced reaction rate constant. An increased rate constant was observed subsequent to annealing, therefore any reduction in the concentration gradients must have been negligibly small.

We found no evidence that the break in reaction kinetics occurs before recrystallization.

The movement of anions through the cuprous oxide as shown by the marker position, is taken as indirect evidence for the existence of anion vacancies in this oxide, since the movement of oxygen ions through interstitial positions is extremely unlikely.

There was a net motion of markers with respect to the original interface, but the occurrence of considerable numbers of voids prevents the quantitative treatment of such movements. The voids are thought to be caused, at least in part, by the Kirkendall effect.

TEMPERATURE STRESSES IN THE TWO-PHASE ALLOY, WC-Co

By J. GURLAND

Abstract

Thermally induced stresses in the WC constituent of sintered WC-Co alloys were calculated from elastic theory and were measured by x-ray diffraction techniques. The compositions of the alloys ranged from 5 to 37% by volume cobalt. It was found that compressive stresses act on the dispersed carbide phase of high binder compositions but that tensile stress components become predominant in low binder alloys. (ASM International Classification Q25p; W, Co, 6-19)

INTRODUCTION

ALLOYS OF TWO phases contain stresses which are caused by the difference of coefficients of thermal expansion and elastic properties of the constituents. If, for instance, the microstructure consists of particles of one phase dispersed in a matrix of another phase, stresses appear in both the matrix and the dispersions during cooling to room temperature from a stress-free state at higher temperature. A method of calculation of such stresses, based on the approximation of a compound sphere, was developed by Laszlo (1)¹, and applied by Nielsen and Hibbard (2) to aluminum-silicon alloys. The latter confirmed the presence of both tensile and compressive stresses in the matrix of the alloy by measuring the width of x-ray diffraction lines. In general, the quantitative measurement of the stress magnitudes is made difficult by line broadening due to stresses of alternating signs and by mutual solid solubilities of the constituents.

The present work is concerned with the stresses induced in the tungsten carbide constituent of tungsten carbide-cobalt alloys. After sintering the alloys consist of two phases, namely, the carbide WC, and the binder, a cobalt-rich solid solution. Compositions were chosen to attain microstructures ranging from a fairly loose dispersion of WC particles in a matrix of the solid solution to an almost continuous aggregate of WC with only small amounts of binder phase. This alloy system is particularly suited for this type of study because the solubility

¹ The figures appearing in parentheses pertain to the references appended to this paper.

A paper presented before the Thirty-Ninth Annual Convention of the Society, held in Chicago, November 4-8, 1957. The author, J. Gurland, is Assistant Professor, Division of Engineering, Brown University, Providence, Rhode Island. Manuscript received December 4, 1956.

of Co in WC is so small at room temperature that it does not measurably alter the lattice constants of WC (3). In addition, the properties of the constituents (Table I) are sufficiently different to produce significant effects. Indications of stresses of high magnitude were found by Ritzau (4) by magnetic measurements on the binder, and by Pfau and Rix (5) by the observation of broadening of x-ray diffraction lines of WC. Both effects were attributed to thermally induced stresses. The magnitude and direction of such stresses will now be discussed in detail.

THEORY

The following calculations are carried out for the case of a spherical inclusion of material I surrounded by an infinite mass of material II. The computational method is outlined in the Appendix. The principal stresses in inclusion and matrix, due to a temperature change, are:

$$\sigma_{r1} = \frac{2E_1E_2(a_2 - a_1) T}{(1 + \nu_2) E_1 + 2(1 - 2\nu_1) E_2}$$

$$\sigma_{c1} = \sigma_{r1}$$

$$\sigma_{r2} = \sigma_{r1} \rho^3 / r^3$$

$$\sigma_{c2} = -\frac{1}{2} \sigma_{r1} \rho^3 / r^3$$

where: σ_{r1}, σ_{r2} = radial stress in materials I and II, respectively.

σ_{c1}, σ_{c2} = circumferential stress in materials I and II, respectively.

α = coefficient of linear expansion.

r = distance from center of spherical inclusion.

ρ = radius of spherical inclusion.

ν = Poisson's ratio.

T = Temperature range.

E_1, E_2 = Young's modulus of elasticity of materials I and II, respectively.

These results show that

- (a) The spherical inclusion is under hydrostatic tension or compression.
- (b) The radial and circumferential stresses in the matrix are of opposite sign.
- (c) The stresses in the matrix fall off according to the cube power of the distance from the inclusion.

In order to apply the above results to the calculation of the stress on WC particles, material II is made to take on the properties of WC-Co alloys ranging in composition from pure WC to pure cobalt. The required properties (E, ν, α) of a number of intermediate alloys

Table I
Properties of Tungsten Carbide, Cobalt and their Alloys

Composition Volume percent	Poisson's Ratio	Young's Modulus $\times 10^6$ psi	Coefficient of Linear Thermal Expansion $\times 10^{-6}$ in./in./ $^{\circ}$ C (20-800 $^{\circ}$ C)
100% WC	0.22	102	5.4
5% Co, 95% WC	0.22	94.5	5.5
10% Co, 90% WC	0.22	88.3	5.6
24% Co, 76% WC	0.22	76.3	6.8
31% Co, 69% WC	—	70.6	7.6
37% Co, 63% WC	—	66.4	7.8
100% Co	0.3	30	12.3

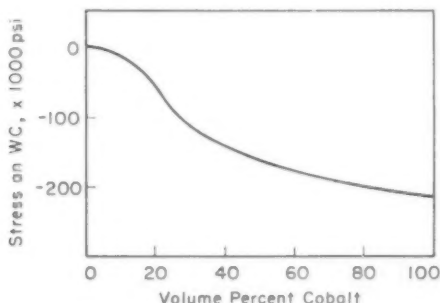


Fig. 1—Calculated Stress on Dispersed WC Particles in WC-Co Alloys.

are known (Table I). Although the sintering temperature is approximately 1400 $^{\circ}$ C (2550 $^{\circ}$ F), it was assumed that the shrinkage stresses of the matrix phase became effective at 800 $^{\circ}$ C (1470 $^{\circ}$ F). The arbitrary selection of this temperature was based on the loss of strength of sintered carbides near 800 $^{\circ}$ C (1470 $^{\circ}$ F).

The results of the calculations are shown in Fig. 1. The dispersed WC particles are under compression; the compressive stress increases with the percentage of cobalt in the alloy.

The above results do not take into consideration that the stress on the carbide phase may be less than the calculated maximum because of stress relaxation by plastic deformation in the matrix. An attempt to determine the order of magnitude of the actual stresses existing in the carbide phase of WC-Co compacts will be described in the following section.

EXPERIMENTAL DATA

The elastic strain in the WC phase was determined by comparing the interplanar spacings of WC in the sintered alloy with those in unalloyed WC powder. The sum of the principal stresses in the surface of sintered compacts is given by the relation:

$$\sigma_1 + \sigma_2 = (-E/\nu)(d_s - d_u/d_u)$$

where σ_1, σ_2 are principal stresses
 d_s, d_u are interplanar spacings in the stressed and unstressed states, respectively.

The (211) diffraction line of WC, ($\text{Cu K}\alpha, 2\theta = 117.2^\circ$) was found most suitable as to strength and sharpness. Both recording x-ray spectrometer and back reflection camera techniques were employed. The (224) line of tantalum carbide at $2\theta = 119.7^\circ$ was used as an internal standard of calibration. The surfaces of the sintered samples were pol-

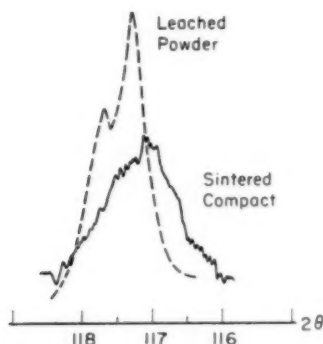


Fig. 2—Comparison of (211) Line of WC from Sintered Compact and from Leached Powder.

ished and etched with 10% potassium ferricyanide. The precision of measurement of the interplanar spacing was within 0.0001 Å.

1. Comparison of lattice of WC from sintered compact and from leached powder. The lattice spacing of WC was determined from the surface of a sintered compact of 63% WC and 37% Co. The compact was then crushed and leached with HCl, removing the cobalt. The spacing was again determined.

Condition	Lattice Spacing, d_{211}
Solid sintered alloy; 63% WC, 37% Co	0.9009 Å
Crushed powder, 63% WC, 37% Co	0.9007
Leached powder, WC	0.9003

The change of lattice spacing by the leaching operation indicated that the WC was under compression in the sintered compact. At the same time, the leaching resulted in considerable sharpening of the diffraction line (Fig. 2).

2. Effect of cobalt content on WC lattice spacing. The diffraction patterns of a number of sintered samples ranging in cobalt content from 5 to 37 volume percent were compared to that of WC powder (Table II). The grain size of WC was estimated

Table II
Lattice Spacing of Tungsten Carbide in WC-Co Alloys

Composition Volume percent	Grain Size of WC (microns)	Lattice Spacing d_{211} , (angstroms).
WC powder	2.5	0.9004
	4.0	0.9003
5% cobalt	2.0	0.9004
10% cobalt	1.7	0.8999
	1.9	0.9001
	2.5	0.9001
	3.0	0.9003
	4.4	0.9003
	5.1	0.9004
21% cobalt	2.0	0.9004
25% cobalt	1.5	0.9006
	3.3	0.9008
	5.1	0.9008
37% cobalt	1.8	0.9008
	2.2	0.9009
	4.8	0.9008

from photomicrographs of sintered samples. The stresses calculated from the x-ray data are plotted against the cobalt content in Fig. 3 for WC of particle size 2.0–2.5 microns. The overall result of increasing binder content is an increase of the compressive stress on the carbide phase. At low cobalt compositions the hydrostatic stress is tensile over a range of composition.

3. Effect of grain size of WC on lattice spacing of WC in sintered compacts. The change of lattice spacing with different grain sizes of WC is shown in Fig. 4 for a composition of 10% by volume of cobalt. The lattice spacing increases with grain size, indicating a reduction of the tensile stress. This effect is much less marked at higher cobalt contents.

The determination of interplanar spacings was possible in spite of the broadening of diffraction lines which occurred for all compositions. It was noted that the extent of line broadening increased with lower binder contents.

DISCUSSION

The results indicate the general nature of temperature stresses in two-phase alloys. It will be noted by comparing Figs. 1 and 3 that the experimentally determined stresses agree qualitatively with the calculated stresses in that range of compositions where the binder content is high, i.e., where the WC particles are well dispersed. No more than a qualitative agreement between theory and experiment is expected in view of the deviation of the alloy from the assumed ideal elastic, isotropic and homogeneous material. Additional unknown factors are the stresses introduced by the transformation of cobalt on cooling and by the anisotropy of WC crystals.

The concept of carbide particles dispersed in a matrix of binder phase does not apply to the low cobalt end of the alloy system. At 10% by

volume of binder, the sintered alloy consists of an aggregate of WC particles, the binder phase being concentrated within the interstices of the aggregate. Locally in the microstructure, areas of cobalt solid solution are surrounded, more or less completely, by a shell of WC. In that case, the WC is subject to a tensile stress perpendicular to the WC-Co interface (σ_{r2}), although the stresses parallel to the interface (σ_{e2}) remain compressive. The x-ray results represent a statistical average of

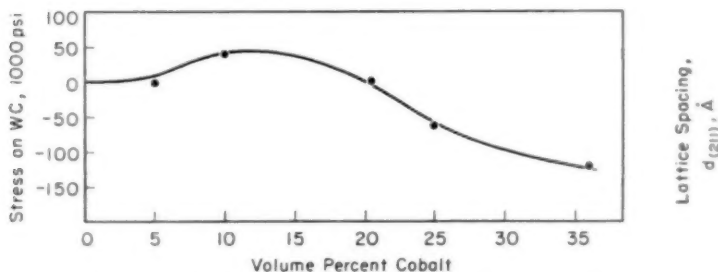


Fig. 3—Measured Stress on WC Phase in Sintered WC-Co Alloys.

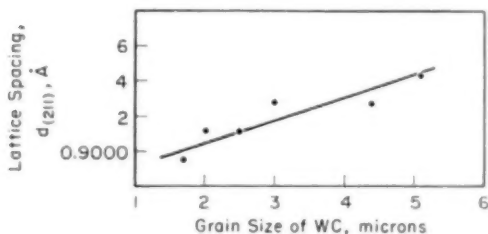


Fig. 4—Effect of Grain Size of WC on Lattice Spacing of WC in Sintered WC-Co Alloy (90% WC, 10% Vol. Co).

the strains in the carbide phase. Tensile stresses predominate in the low cobalt range, compressive stresses become more and more marked as the amount of binder is increased.

Within a compact the sign and magnitude of the stresses vary with the local distribution of the carbide phase. Compressive and tensile strains may be found in adjacent areas, producing the observed broadening of x-ray diffraction lines. The carbide phase is continuous over long distances in the microstructure of low binder compacts, and, therefore, the nonuniform distribution of the binder phase and the variations of internal stresses are more marked in low cobalt alloys.

The temperature stresses of the indicated magnitude must influence the mechanical behavior of the material. Just as the compressive stress on WC is beneficial, the tensile component is undesirable, since the car-

bide is stronger in compression than in tension. Also, the flow stress of the binder is altered by the tensile and compressive forces present in small areas.

ACKNOWLEDGMENT

Sponsored by the Office of Ordnance Research, U. S. Army. Preliminary data were obtained at Firth-Sterling, Inc., Pittsburgh. The author gratefully acknowledges the cooperation of Dr. E. Brown with the calculation of the internal stress system.

Appendix

Outline of Calculation of Stresses in and around a Spherical Inclusion due to a Uniform Temperature Change.

A homogeneous elastic sphere of radius ρ is set in an infinite mass of a second homogeneous elastic material. Subscripts 1, 2 refer to the sphere and the surrounding material, respectively.

A uniform temperature change T causes a change of stress σ . Because of geometrical symmetry there will be no shear stresses on radial and circumferential planes and the circumferential stress σ_c will be the same in all directions at a given radius. The radial stress will be σ_r . Also from symmetry there will be no circumferential displacements, but only a radial displacement u , positive away from the center of the sphere.

The equation of radial equilibrium is:

$$d\sigma_r/dr + 2\sigma_r/r - 2\sigma_c/r = 0 \quad \text{Equation 1}$$

Hooke's law gives:

$$du/dr = \sigma_r/E - 2\nu\sigma_c/E + \alpha T \quad \text{Equation 2}$$

$$u/r = (1 - \nu)\sigma_c/E - \nu\sigma_r/E + \alpha T \quad \text{Equation 3}$$

E , ν and α are, respectively, the Young's modulus, Poisson's ratio and the coefficient of linear expansion. Eliminating σ_c and σ_r from Equations 1-3:

$$d^2u/dr^2 + 2/r du/dr - 2u/r^3 = 0 \quad \text{Equation 4}$$

which restricts the radial displacement to the general form:

$$u = Ar + B/r^2 \quad \text{Equation 5}$$

The constants A and B have different values in the two materials. In order to avoid an infinite displacement at the center of the sphere, $B_1 = 0$.

Substitution of Equation 5 in Equations 2 and 3 gives expressions for the stresses. The condition that $\sigma_c \rightarrow \sigma_r \rightarrow 0$ when $r \rightarrow \infty$ requires that $A_2 = \alpha_2 T$. Expressions for A_1 and B_2 are obtained from the conditions of continuity of u and σ_r at the interface $r = \rho$. The displacement

is now known everywhere, and the stresses can be calculated from Equations 2 and 3.

References

1. F. Laszlo, "Tesselated Stresses," Part I, *Journal*, Iron and Steel Institute, No. 1, Vol. 147, 1943, p. 173.
2. J. P. Nielsen and W. R. Hibbard, "An X-Ray Study of Thermally Induced Stresses in Micro-Constituents of Aluminum-Silicon Alloys," *Journal of Applied Physics*, Vol. 21, 1950, p. 853.
3. P. Rautala and J. T. Norton, "Tungsten-Cobalt-Carbon System," *Transactions*, American Institute of Mining and Metallurgical Engineers, Vol. 194, 1952, p. 1045.
4. C. Ritzau, "Contribution to the Magnetic Analysis of Hard Metals," *Stahl und Eisen*, Vol. 60, 1940, p. 891.
5. H. Pfau and W. Rix, "On the Lattice Constant and Hardness of the Tungsten Carbide Crystal in Hard Metal Structure," *Zeitschrift für Metallkunde*, Vol. 43, 1952, p. 440.

DISCUSSION

Written Discussion: By C. J. Newton and H. C. Vacher, Metallurgy Division, National Bureau of Standards, Washington, D. C.

It is a pleasure to read this interesting paper by Professor Gurland concerned with thermal textural stresses in two-phase alloys. The author is to be congratulated for his contribution to this field, which has been somewhat neglected. We should like to take this opportunity to comment on his method of stress measurement and to mention some work we have done on a similar problem.

In the X-ray and Metallographic Laboratory of the Metallurgy Division of the National Bureau of Standards, we conducted a study in 1956 of thermal textural stresses in some two-phase alloys of brass and of steel.² We compared our experimental results with computed values based on Laszlo's formulas and found good agreement in the case of the brass and at least qualitative agreement in the case of the steel. As we reported, we used the two-exposure, normal and inclined incidence method, which measures a stress component in the surface without the necessity of possessing a stress-free standard.

We notice that Professor Gurland has in this study used the single-exposure method of making a lattice spacing measurement normal to the surface of his specimen of sintered alloy and has compared it with the measurement of the lattice spacing in an unalloyed powder. This makes necessary the assumption that the spacings would be precisely equal except for the effect of the stress one is trying to measure. No such assumption is called for in the two-exposure method, where no reference standard is used, and where true stresses are measured without the uncertainties introduced by possible changes in the unit cell volume at equilibrium. Furthermore, the change in observed data between the normal and inclined incidence exposures is greater than the change one has to detect in the single-exposure comparison method.

For these reasons, we now feel that the two-exposure method is preferable, although we also used the single exposure method, partly through necessity, in the study of residual stresses in sectioned bars of plastically deformed iron a few years

² C. J. Newton and H. C. Vacher, "An X-ray Study of Textural Stresses in Two-Phase Alloys," *Journal of Research*, National Bureau of Standards, Vol. 59, October 1957.

ago.³ In that work, also like Professor Gurland apparently, we made no correction for the partial relaxation at the surface of stresses parallel to the surface. Laszlo, however, has suggested a corrective factor of one minus Poisson's ratio, which we did apply to our later calculations of textural stresses.

When these precautions and other points of careful technique are observed, we feel that experimental values of the textural stresses arising from differences of coefficients of thermal expansion as expounded by Laszlo can be obtained with a degree of reliability sufficiently high to warrant their consideration in many problems of metallurgy.

Author's Reply

The author joins the discussors in the hope that more work in the field of temperature stresses in alloys will be forthcoming.

Undoubtedly, the two-exposure method reduces the error by eliminating the use of the unstressed material as reference standard. However, it is the difference of lattice parameters between the pure and the alloyed material which was of interest here and seemed to justify the method of direct comparison.

³ C. J. Newton and H. C. Vacher, "Residual Lattice Strains in Sectioned Bars of Plastically Deformed Iron," *Journal of Metals*, Vol. 7, 1955, p. 1193-1194.

THE TENSILE AND STRESS-RUPTURE PROPERTIES OF CHROMIUM

By J. W. PUGH

Abstract

The temperature dependence of the tensile and stress-rupture properties of chromium were evaluated up to 2200 °F (1215 °C). The chromium metal used was arc-melted, extruded, and swaged, but was not of special purity. Its ductile-brittle transition temperature for the testing procedure used was about 600 °F (315 °C). No yield points were observed, but some evidence of strain aging at intermediate temperatures was obtained. Both tensile and stress-rupture properties were inferior to those of molybdenum and tungsten tested in precisely the same way. In both cases the differences in the properties can be closely related to melting point differences. (ASM International Classification Q27a, Q3m; Cr)

INTRODUCTION

IT IS POSSIBLE that chromium-base alloys will become important high temperature materials. This suggestion is based primarily on chromium's abundance, moderately high melting point, and excellent oxidation resistance. However, chromium and chromium-base alloys are characteristically brittle at lower temperatures. It is this unpleasant condition which has made some investigators pessimistic about the future of chromium alloys (1)¹. However, progress is being made with respect to ductility (2) and alloy investigations continue (3). The purpose of this paper is to report the tensile and creep rupture properties so that some basis for comparing chromium with other refractory alloy bases may be established. It may in this way help to determine the prognosis of chromium's application as a high temperature alloy base.

METAL PREPARATION

Electrolytic chromium was treated for 20 hours at 2900 °F (1595 °C) in pure dry hydrogen. This treatment was effective in removing sufficient gaseous impurities (notably oxygen) so that a good quality arc-cast ingot might be made. Melting was accomplished in a furnace similar to one previously described (4). The treated electrolytic chromium

¹ The figures appearing in parentheses pertain to the references appended to this paper.

The author, J. W. Pugh, is associated with the General Electric Company Refractory Metals Laboratory, Lamp Wire and Phosphors Department, Cleveland. Manuscript received January 25, 1957.

flake was fed continuously into a 4-inch (diameter) water-cooled copper crucible and melted in a direct current arc. The water-cooled electrode was rotated over the molten chromium to insure adequate melting. This operation took place in a vacuum tight shell filled with argon at a positive pressure of 5 pounds per square inch.

The arc-melted ingot was scalped to 3.5 inches in diameter, and ex-

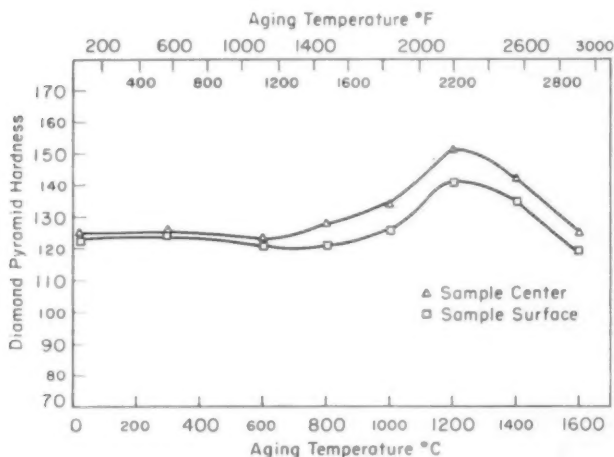


Fig. 1—Hardness Versus Aging Temperature.

truded to 1 inch in two passes at 2500 °F (1370 °C) using molten glass for a die lubricant. The extruded rod was scalped and swaged to 0.345-inch diameter at 2000 °F (1095 °C). One hour annealing treatment at 2900 °F (1595 °C) in pure hydrogen produced a uniform grain size of about 0.5 millimeter diameter. Chemical analysis of the bar was as follows:

Impurity	Weight %
Nitrogen	0.05 *
Oxygen	0.041 **
Hydrogen	0.0001 **
Carbon	0.01
Sulphur	0.02
Lead	0.001
Iron	0.05
Copper	0.01

Presumably, oxygen and nitrogen were added in considerable amounts during processing. The expected level of each after the 20-hour hydrogen purification treatment was about 0.001%.

* Kjeldahl.

** Vacuum fusion.

Fig. 1 shows the hardness response to heat treatment. Each sample represented here was annealed 1 hour in pure dry hydrogen and cooled rapidly. It is suggested that the maximum produced at about 2200 °F (1205 °C) results from the solution of nitrogen. This is supported by evidence that nitrogen in solution causes an embrittling effect as compared to precipitated nitride in chromium of the same composition (5).

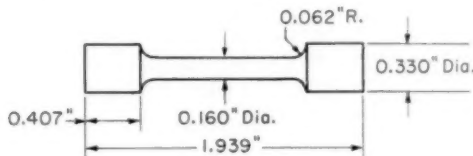


Fig. 2—Tensile Test Bar.

The nitrogen content is sufficient to form a saturated solution at 2200 °F (6). It is difficult to appraise its effect (if any) on test results in the range 1600 to 2200 °F (870 to 1205 °C). Dissolved nitrogen is probably sufficiently mobile in this range to preclude a strain aging interaction.

TESTING PROCEDURE

Tensile tests were made on an Instron machine at the rates 0.2 and 0.02 inch per inch per minute. Flow curves were recorded autographically. Specimens were protected from atmospheric contamination by testing them in a vacuum capsule. Temperatures were measured by means of a platinum, platinum-rhodium thermocouple resting on top of the specimen. Constant load stress-rupture tests were made in argon atmosphere at 1400, 1600, 1800, 2000, and 2200 °F (760, 870, 980, 1095, and 1205 °C). The machines used had specimen strings which were enclosed in vacuum-tight capsules. Fig. 2 shows the specimen used for both tensile and stress-rupture tests. More detailed descriptions of these test devices can be found elsewhere (7).

RESULTS AND DISCUSSION

Tensile Tests

The tensile parameters evaluated for chromium were yield strength at 0.2% offset, ultimate tensile strength, per cent elongation, strain hardening, and strain sensitivity. Strain hardening is expressed as the exponent m in the relation

$$\sigma = A\epsilon^m \bigg|_{\epsilon, T,}$$

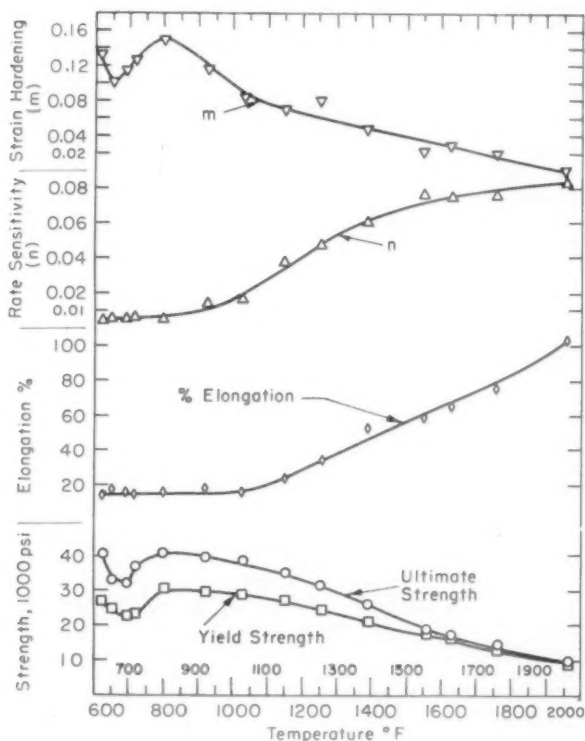


Fig. 3—Temperature Dependence of the Tensile Parameters.

which fits the true stress-strain curves fairly accurately. Here σ is the stress, ϵ is strain, A is stress at unit strain, T is temperature, and $\dot{\epsilon}$ is strain rate. Rate sensitivity was expressed as n where

$$n = \frac{\log \frac{\sigma_1}{\sigma_2}}{\log \frac{\dot{\epsilon}_1}{\dot{\epsilon}_2}} \bigg|_{\epsilon, T}$$

σ_1 and σ_2 are the stresses at the rates $\dot{\epsilon}_1 = 0.2 \text{ min}^{-1}$ and $\dot{\epsilon}_2 = 0.02 \text{ min}^{-1}$ respectively. These parameters are all shown as a function of temperature in Fig. 3. Note that there is a maximum in strength and strain hardening at 800 °F (425 °C), and that elongation and rate

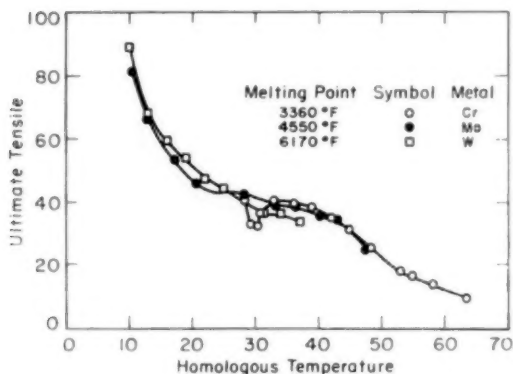


Fig. 4—Comparison of the Strength of Chromium, Molybdenum, and Tungsten.

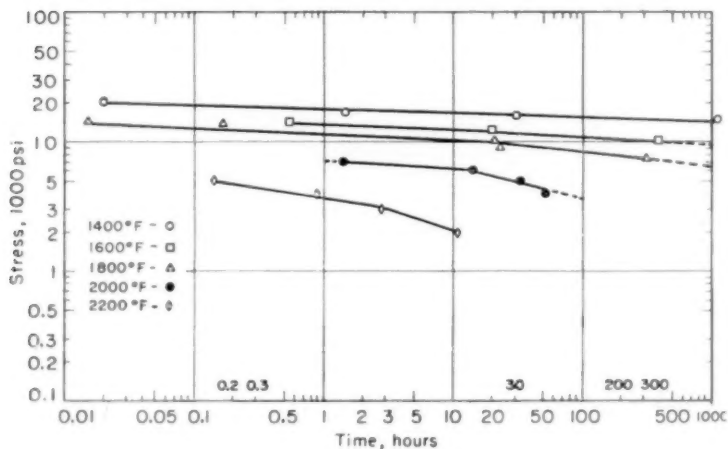


Fig. 5—Stress Rupture Life of Chromium.

sensitivity remains low and constant with temperature to about 1000 °F (540 °C). These observations are very probably indicative of strain aging in chromium.

By comparison with the higher melting refractory metals tungsten and molybdenum, chromium is decidedly inferior in strength. For example, the ultimate tensile strength of chromium at 2000 °F (1095 °C) is only 40% that of molybdenum (8) and 30% that of tungsten (9). This suggests that chromium's lower strength may be related to its lower melting point. In Fig. 4 ultimate tensile strengths

Table I

Temp °F	Yield Strength 1000 psi	Ultimate Tensile Strength 1000 psi	Per Cent Elongation	Strain Hardening m	Rate Sensitivity n
626	26.9	40.7	14.0	0.134	0.005
655	24.9	33.0	18.5	0.101	0.006
695	22.9	32.3	17.8	0.118	0.005
719	23.6	36.7	14.8	0.127	0.006
798	30.0	40.8	18.3	0.149	0.006
926	29.4	40.3	19.5	0.117	0.014
1032	28.8	38.2	17.3	0.084	0.018
1150	27.9	35.1	23.9	0.070	0.039
1256	24.9	31.2	33.8	0.080	0.048
1391	21.0	25.6	50.3	0.048	0.060
1556	17.5	18.2	58.8	0.022	0.077
1630	15.4	16.8	65.9	0.030	0.073
1758	13.7	14.0	75.9	0.020	0.073
1965	9.3	9.3	104.1	0.001	0.082

for chromium, molybdenum, and tungsten are plotted as a function of homologous temperature. Homologous temperature is defined as the test temperature in percent of the absolute melting point of the metal. Conditions of testing (i.e. specimen, rate, atmosphere, etc.) were identical for this comparison. It is obvious that chromium compares favorably on this basis.

The temperature dependence of strain rate sensitivity for chromium is comparable to that of tungsten and molybdenum, but rate sensitivity begins rising with temperature at lower temperatures for chromium than for tungsten or molybdenum. It is interesting to note that the rate sensitivities of chromium and molybdenum begin rising at the same percentage (38%) of the melting point on the absolute temperature scale. A rise in rate sensitivity is predicted for tungsten on this basis at about 2100 °F (1150 °C). No rise for tungsten was observed up to 2000 °F (1095 °C); data above 2000 °F are not available. The absolute magnitudes of rate sensitivity were similar at high and low temperatures.

The same sort of comparison may be made with respect to the temperature dependence of strain hardening. The maximum at 800 °F (425 °C) in this relationship for chromium appears at 33% of the absolute melting point, while similar maxima for molybdenum and tungsten are at 30 and 32% respectively. This is considered to be good correspondence in view of the difficulty in locating the exact temperature peak from the data available. In terms of absolute values for strain hardening, chromium has the smallest values, molybdenum has higher values, and tungsten has the highest.

The ductile-to-brittle transition temperature was approximately 600 °F (315 °C) for this material at a strain rate of 0.20 inch per inch per minute. Data for tests below 600 °F (315 °C) are not presented because the stress concentrations in the brittle range make these values unreliable. Tensile properties are summarized in Table I.

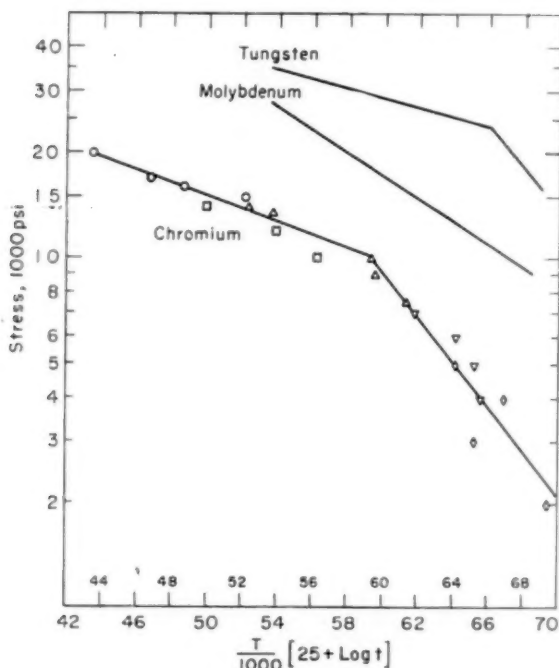


Fig. 6—Larson-Miller Parameter Versus Stress.

Stress Rupture Properties

Fig. 5 shows loading stress as a function of rupture life. Stress values for various rupture times are compared to those for tungsten and molybdenum tested under identical conditions in Table II. The superiority of the higher melting refractory metals is striking, but here again a comparison on a homologous temperature basis (not shown) indicates good correspondence. A graphical comparison of chromium, molybdenum, and tungsten is made in Fig. 6. The loading stress is plotted versus the Larson-Miller parameter (10),

$$P = T (C + \log t)$$

A value of $C = 25$ provided the best fit for the chromium data which are plotted in Fig. 6.

SUMMARY AND CONCLUSIONS

Chromium is easily arc-melted and fabricated by extrusion and swaging if the melting stock is first purified at 2900 °F (1595 °C) in pure dry hydrogen. Processing was observed to raise the oxygen and nitro-

Table II

Temp °F	Stress 10 Hours			1000 psi					
	Cr	Mo	W	100 Hours			1000 Hours		
				Cr	Mo	W	Cr	Mo	W
1400	16.9			15.8			14.7		
1600	12.5	28.0	35.0	10.9	22.0	33.0	9.5	17.0	31.0
1800	10.3	19.0	33.0	8.5	15.0	28.5	6.5	12.0	22.0
2000	6.2	14.5	29.3	5.6	11.5	22.0		9.0	15.5
2200	2.1		21.5						

gen levels significantly above those obtainable after hydrogen purification. These impurities probably do not affect the properties at the higher temperatures, however, they may be important with respect to strain aging, and they certainly affect the ductile-brittle transition temperature. This transition temperature was about 600 °F (315 °C).

An evaluation of the hardness response to annealing indicated that increased room temperature hardness results from treatments in the range 1600 to 2800 °F (870 to 1540 °C). It is suggested that this is caused by increased nitrogen in solution. It is not likely that this modified the properties evaluated perceptibly, since the solution of nitrogen would only take place at test temperatures above the range where nitrogen is expected to be effective.

No yield points were observed in the tensile flow curves, but the characteristic temperature dependence of the tensile parameters (Fig. 3) suggests strain aging. Yield points may be expected at temperatures lower than 600 °F (315 °C) and should be produced by chromium having a lower transition temperature.

A comparison of the tensile and rupture properties of chromium with

Table III
Stress Rupture Test Data

Temp °F	Stress 1000 psi	Rupture Life Hours	Total % Elongation
1400	20.00	0.02	40.4
1400	17.00	1.45	38.7
1400	16.00	31.10	29.9
1400	15.00	1122.23	13.7
1600	14.00	0.54	35.8
1600	12.00	15.02	12.8
1600	10.00	393.76	5.4
1800	14.00	0.015	31.8
1800	13.50	0.162	27.2
1800	10.00	20.91	12.2
1800	9.00	23.65	14.8
1800	7.50	131.86	20.2
2000	7.00	1.42	29.1
2000	6.00	14.39	19.1
2000	5.00	32.92	9.8
2000	4.00	50.73	10.9
2200	5.00	.14	20.7
2200	4.00	0.89	19.1
2200	3.00	2.78	22.6
2200	2.00	10.95	22.2

those of molybdenum and tungsten is an impressive demonstration of the relationship between strength and melting point. More fundamental relationships such as that of the heat content at the melting point undoubtedly exist with the properties evaluated here as they do with hot hardness (11). It is beyond the scope of this report to demonstrate these or to speculate about the fundamental etiology of these relationships. It can be pointed out, however, that chromium has a detriment or an advantage which is reflected by its melting point. On this basis, it is reasonable to expect chromium alloys to be most useful in a range below that of the higher melting refractory metals and above that of iron-nickel-cobalt base alloys. More specifically, it is estimated that chromium alloys, when they are developed, will be used mainly in the temperature range 1600 to 1800 °F (870 to 980 °C) and for those applications which utilize chromium's remarkable oxidation resistance.

References

1. A. H. Sully and E. A. Brandes, "The Properties of Cast Chromium Alloys at Elevated Temperature," *Journal, Institute of Metals*, Vol. 81, 1952-53, p. 578.
2. R. W. Fountain, "Ductility and Toughness of High Chromium Alloys," *Ductile Chromium and Its Alloys*, 1957, Chapter 20, American Society for Metals, Cleveland.
3. D. J. Maykuth and R. I. Jaffee, "The Mechanical Properties of Swaged Iodide-Base Chromium and Chromium Alloys," *Ductile Chromium and Its Alloys*, 1957, Chapter 19, American Society for Metals, Cleveland.
4. J. W. Pugh, R. L. Hadley and R. W. Hennig, "An Arc Furnace for Melting Refractory Metals," *METAL PROGRESS*, American Society for Metals, Vol. 64, March 1953, p. 70.
5. W. H. Smith and A. U. Seybolt, "Ductile Chromium," *Journal, Electrochemical Society*, Vol. 103, 1956, p. 347.
6. A. U. Seybolt and R. A. Oriani, "Pressure-Temperature-Composition Relation in the Cr-N Terminal Solid Solution," *Journal of Metals*, Vol. 8, May 1956, p. 556.
7. J. W. Pugh, "How to Test Refractory Metals," *Steel*, Vol. 137, No. 16, October 17, 1955, p. 114.
8. J. W. Pugh, "The Tensile Properties of Molybdenum at Elevated Temperatures," *TRANSACTIONS, American Society for Metals*, Vol. 47, 1955, p. 984.
9. J. W. Pugh, "Tensile and Creep Properties of Tungsten at Elevated Temperatures," to be published.
10. F. R. Larson and J. Miller, "A Time Temperature Relationship for Rupture and Creep Stresses," *Transactions, American Society of Mechanical Engineers*, Vol. 74, No. 5, 1952, p. 765.
11. J. H. Westbrook, "Temperature Dependence of the Hardness of Pure Metals," *TRANSACTIONS, American Society for Metals*, Vol. 45, 1953, p. 221.

THE TANTALUM-COLUMBIUM ALLOY SYSTEM

By D. E. WILLIAMS AND W. H. PECHIN

Abstract

The tantalum-columbium alloy system was investigated by means of x-ray, electrical resistance and metallographic methods.

The constitutional diagram is an unbroken series of solid solutions. No evidence of a solid transformation was found in any of the alloys. The solidus line rises smoothly from the melting point of columbium, 2420 °C (4388 °F), to the melting point obtained for tantalum, 2940 °C (5324 °F), and the liquidus was found to follow quite closely the path taken by the solidus.

Experimental results are given and equipment is described. (ASM International Classification M24b, Ta, Cb)

INTRODUCTION

THE INCREASED number of applications of high melting metals and alloys has created a need for information regarding their properties and their constitutional diagrams. With respect to the tantalum-columbium system, the literature contains little information. Bückle (1)¹ gave a lattice parameter-composition curve but no other information. The mechanical and physical properties of some tantalum-columbium alloys have been reported by several investigators, and other laboratories under contract to the AEC have reported that alloys containing from zero to 15% tantalum can be successfully fabricated.

The authors' investigation was undertaken to obtain information that would permit construction of a complete constitutional diagram.

THE PREPARATION OF THE ALLOYS

Materials—Both the tantalum and the columbium used in the preparation of the alloys were obtained from the Fansteel Metallurgical Corp. These materials were ordered as high purity sheet, the analyses of which are given in Table I.

Melting—The alloys were melted in a tungsten-electrode arc-furnace of the type described by Geach and Summers-Smith (2) and others. The water-cooled copper crucible used in this work is provided with three cavities, one of which is used for melting a getter charge prior

¹ The figures appearing in parentheses pertain to the references appended to this paper.

The authors, D. E. Williams and W. H. Pechin, are associated with the Institute for Atomic Research and Department of Chemistry, Iowa State College, Ames, Iowa. Manuscript received April 18, 1957. Work was performed in the Ames Laboratory of the U.S. Atomic Energy Commission.

Table I
Composition of Metals Used in Alloy Preparation¹

Impurity	Tantalum	Columbium
Tantalum	major	~ 1500
Carbon	< 100*	1000*
Iron	~ 40*	< 100
Titanium	~ 200*	< 100
Manganese	—	< 100
Aluminum	present	~ 70
Silicon	200	90
Copper	present	present
Magnesium	present	present
Calcium	present	present
Silver	present	present

¹All impurities reported in ppm.

*By chemical analysis, all others by spectrographic methods.

to melting the alloys. Zirconium was used as the getter material to purify the helium atmosphere of the furnace. Seventy- to eighty-gram charges of the materials to be alloyed were placed in the remaining cavities and melted several times. The ingots were turned over after each melting in an effort to make them as homogeneous as possible. The size of the resulting button-shaped ingot was about 1¼ inch in diameter and ⅜ inch thick. The difference in the weight of the charge before and after melting was seldom as much as 0.1 grams. All alloys are specified on the basis of their intended compositions.

Some of the ingots exhibited dendritic segregation which was not alleviated by annealing for 96 hours at 1400 °C (2550 °F). The cast alloys were brought into equilibrium by annealing at temperatures near their melting point. After being worked, the alloys were successfully homogenized by annealing at 2000 °C (3630 °F).

Fabrication—All alloys of the tantalum-columbium system were found amenable to fabrication. All compositions were swaged from ⅝ to 0.030 inch diameter wires with no intermediate annealing. Also, slabs of the ingots could be rolled to a thickness of 0.010 inch or less.

APPARATUS AND PROCEDURE

All work at elevated temperatures was done under a pressure of 10⁻⁶ millimeters mercury or less except arc melting which was carried out in a helium atmosphere.

The special equipment used in the investigation was that for the determination of melting points and for measurement of the change of electrical resistance with temperature. The other equipment, x-ray and metallographic, needs little explanation.

Melting Points—The solidus point determinations were made in the apparatus described by Williams (3). The samples were machined from slabs cut from the ingots and placed in the melting point furnace without preliminary heat treatment. The temperature was measured with an optical pyrometer sighted on a small hole drilled in the center of the necked-down portion of the melting point bar. The ratio of the

depth to diameter of the hole was made four or more to insure black body conditions. Temperature measurements were also made of the surface of the bar immediately adjacent to the hole. From these measurements a relationship between the surface or apparent temperature and the true temperature was found. The samples were heated to temperatures ranging from 2000 to 2400 °C (3630 to 4350 °F) by their own electrical resistance and held about 2 hours. After this annealing, the temperature of the specimen was increased slowly until the solidus temperature was reached which was indicated by the formation of liquid in the black-body hole. The temperature at which the bar melted completely in two was taken as the liquidus point.

Electrical Resistance—The change in electrical resistance from room temperature to 1000 °C (1830 °F) was measured potentiometrically with the type of apparatus described by Rogers and Atkins (4) except that the platinum current and potential leads were welded to the sample so as to be independent of the thermocouple.

Measurement of the electrical resistance from 1000 to 2000 °C (1830 to 3630 °F) was done in a manner similar to that employed in the lower temperature range except the temperature was measured with an optical pyrometer and the wire under test was heated by passing a measured direct current through it. The potential leads used in these experiments were 0.01 inch diameter tantalum wire. The relationship between surface and true temperatures obtained during the melting point determinations was used to correct the surface temperature measurements in the high temperature-resistance experiments.

X-Ray Diffraction Methods—Powders were taken from the annealed portion of the melting point samples for x-ray diffraction use. These powders were exposed to nickel-filtered, copper radiation in a Debye-Scherrer type camera with Straumanis film mounting.

Metallographic Procedure—A Vickers projection microscope and standard polishing equipment were used in the metallographic investigation of this alloy system. Polishing and etching the tantalum-columbium alloys were somewhat tedious since the surface was readily pitted in both operations. The most satisfactory polishing procedure found was the use of a lead lap charged with levigated alumina, then final polishing with diamond compound on microcloth. The etchant found most effective was a $\text{HNO}_3\text{-HF-H}_2\text{O}$ mixture of equal proportions.

RESULTS OF THE INVESTIGATION

The results of the investigation are expressed in the constitutional diagram for the tantalum-columbium alloy system shown in Fig. 1.

The Solidus—The solidus line was found to follow a smooth curve from the melting point of columbium to that of tantalum. The temper-

ature difference between the solidus and liquidus was so slight that it could not be detected with an optical pyrometer.

In order to be certain that the melting point samples had been brought into equilibrium by the annealing procedure previously described, a microscopic examination of the samples was made after melting. This examination indicated that all samples had attained equilibrium.

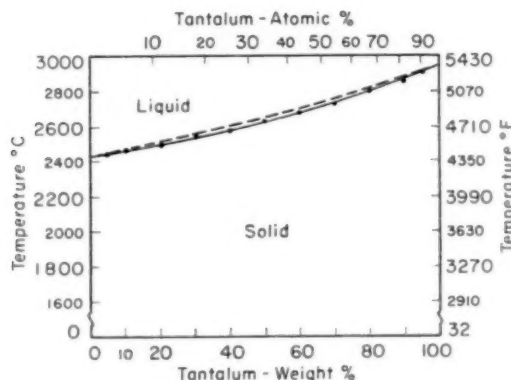


Fig. 1—The Constitutional Diagram of the Tantalum-Columbium System.

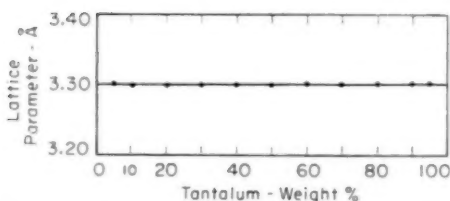


Fig. 2—Lattice Parameter-Composition Curve of Annealed Tantalum-Columbium Alloys.

X-Ray Results—X-ray diffraction patterns made on the alloys gave the lattice parameter curve shown in Fig. 2. The powders were filed from the annealed portion of the melting point samples, treated for the removal of iron, and annealed at 900 °C (1650 °F) for 72 hours then cooled slowly to room temperature. The lattice parameter-composition curve substantiates the idea of continuous solid solution by showing no deviation from a straight line drawn between the lattice-parameter values of tantalum and columbium. Two of the patterns made at room temperature are contained in Fig. 3.

X-ray patterns were made of the 25, 50 and 75 atomic % tantalum alloys that had been annealed at 900 °C (1650 °F) for 200 hours and

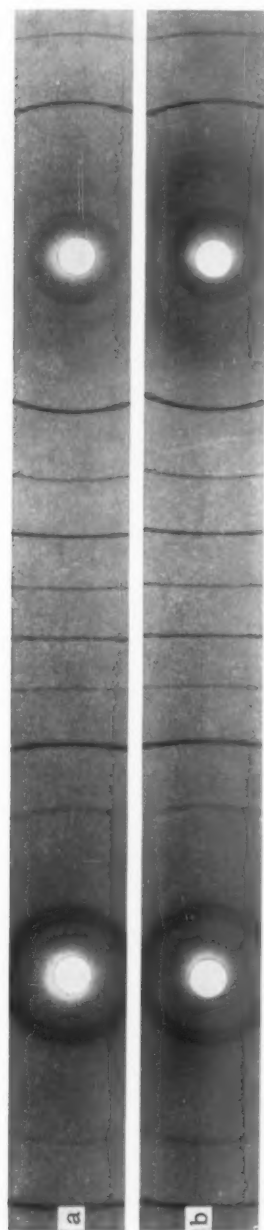


Fig. 3—X-Ray Diffraction Patterns of Annealed Tantalum-Columbium Alloys. (a) 40% tantalum, (b) 60% tantalum.

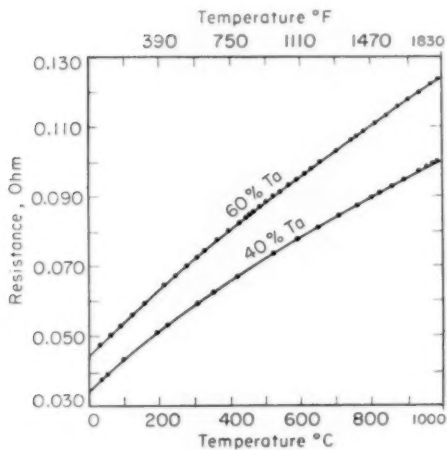


Fig. 4—Resistance-Temperature Curves of Two Tantalum-Columbium Alloys from Room Temperature to 1000 °C (1830 °F).

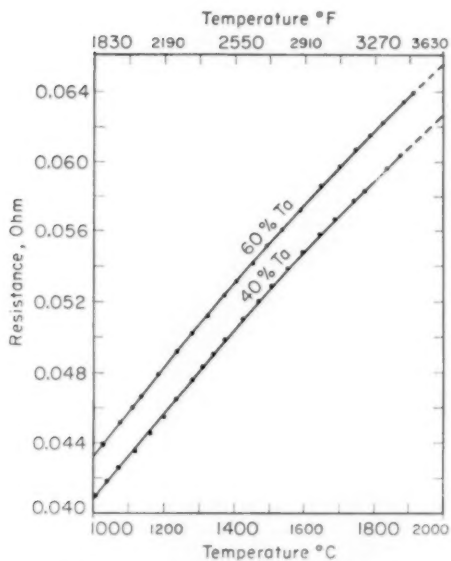


Fig. 5—Resistance-Temperature Curves of Two Tantalum-Columbium Alloys from 1000 to 2000 °C (1830 to 3630 °F).

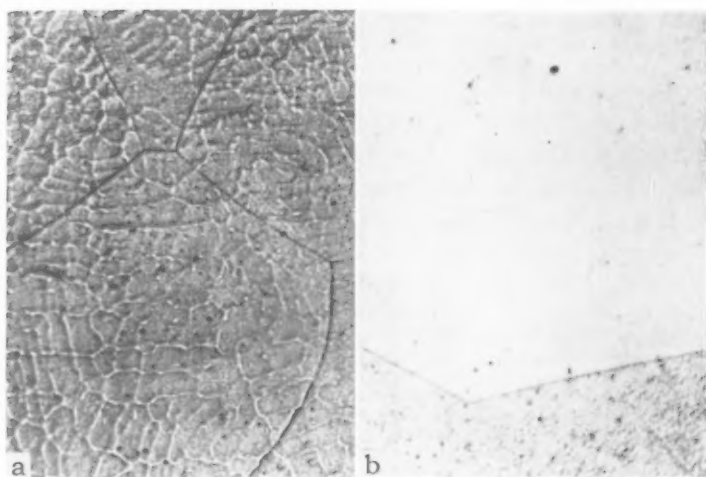


Fig. 6—The 30% Tantalum-Columbium Alloy in Two Conditions. Etched with $\text{HNO}_3\text{-HF-H}_2\text{O}$. $\times 120$. (a) as-cast, (b) after 12 hours at 2000°C (3630°F).

cooled slowly to room temperature. This was done in an effort to determine the presence of any intermediate solid transformation such as the order-disorder type. The patterns obtained from these samples yielded the same lattice parameter values as those obtained from alloys of other compositions after shorter periods of annealing. This fact refutes the existence of an intermediate phase.

Electrical Resistance Measurements—Measurements of the change of electrical resistance with temperature did not indicate a change in the solid state of any of the alloys within the temperature ranges investigated. If any order-disorder effects were present, they would most likely be found in the 25, 50 and 75 atomic % tantalum alloys, (39.4, 64.1 and 85.4 weight %). However, neither these alloys nor the 20, 40, 60 and 80 weight % tantalum alloys showed any irregularities in their resistance curves. Graphs for the 40 and 60 weight % tantalum alloys are shown in Figs. 4 and 5.

Metallography—The cast alloys exhibited a microstructure indicating dendritic segregation and as mentioned previously, efforts to homogenize them by annealing at 1400°C (2550°F) were unsuccessful. A series of samples which had been cold swaged to approximately 0.080 inch were annealed at 1400°C (2550°F) for 96 hours. They no longer showed coring, but did retain the worked structure. These wires were then swaged to 0.030 inch and annealed at temperatures of 2000°C (3630°F) and above. This heat treatment brought the alloys into equilibrium and produced a uniform single phase microstructure. Fig. 6

shows the 30% tantalum alloy in both the cast and the fully annealed conditions.

SUMMARY

The results of the investigation indicate that the tantalum-columbium alloy system has solid solubility in all proportions.

ACKNOWLEDGMENTS

The authors wish to thank Dr. B. A. Rogers for his interest in the investigation and Mr. O. D. McMasters who recorded some of the experimental data.

References

1. Helmut Bückle, "Aufbau und Mikrohärtigkeit der Zwei- und Dreistoffsysteme der Metalle Niob, Tantal, Molybdän und Wolfram," *Metallforschung*, Vol. 1, 1946, p. 53-56.
2. G. A. Geach and D. Summers-Smith, "A Laboratory Arc-Melting Furnace for Melting Alloys Containing the Refractory Transition Metals," *Metalurgia*, Vol. 42, 1950, p. 153-156.
3. J. T. Williams, "Vanadium-Zirconium Alloy System," *Transactions, American Institute of Mining and Metallurgical Engineers*, Vol. 200, 1955, p. 345-350.
4. B. A. Rogers and D. F. Atkins, "Zirconium-Columbium Diagram," *Transactions, American Institute of Mining and Metallurgical Engineers*, Vol. 203, 1955, p. 1034-1041.

DISCUSSION

Written Discussion: By F. N. Rhines, Metals Research Laboratory, Carnegie Institute of Technology, Schenley Park, Pittsburgh.

Among the pure metals and isomorphous systems, as a whole, I believe that it is usually found that there is little visible evidence of melting at the solidus, beyond a slight swelling at the grain boundaries when the volume change is substantial and positive. The most sensitive indicator of the onset of liquidation appears to be a loss of intergranular cohesion. For this reason, I would like to suggest that the solidus values here reported are probably too high, and that the error could be rather large. Since the liquidus is the temperature at which the last of the solid melts, it is also improbable that this point could be identified visually. Normally, the alloy will begin to flow while there remains a considerable quantity of unmelted solid particles in suspension. Thus, the temperature at which a bar of an intermediate alloy will melt, in two, may be expected to lie somewhat below the liquidus. I should expect, accordingly, that the liquidus, except at its ends, is probably somewhat low.

I offer these remarks, not to depreciate this work, which is much to be commended, especially in view of the extreme experimental difficulties involved, but only to assist in the interpretation of its valuable results.

Authors' Reply

The authors wish to thank Dr. Rhines for his discussion concerning the melting-point determinations. The limitations he mentioned do exist and perhaps should have been included in the paper.

The error introduced in melting-point determinations by measuring the temperature at which liquid is first observed has been determined and seems to be no greater than that of the optical pyrometer for the melting points of pure metals, solid-solution minima, and eutectic horizontals. If the temperature difference between the solidus and liquidus is small, or if the slope of the solidus curve is not extreme, a small temperature change above the melting point should produce an appreciable amount of liquid, in which case also the method is relatively accurate.

The tantalum-columbium alloys were found to melt in two almost immediately upon the first appearance of liquid. In most cases there was no measurable difference in the surface temperature when the liquid formation was observed and when the bar melted in two. For this reason and also since the solidus of the system is relatively flat, the authors believe the error introduced by the method employed is probably not much greater than that of the measuring device. Any liquidus determination using this method would have to be considered an approximation.

PARTIAL PHASE DIAGRAMS OF THE SYSTEMS Mg-Th AND Mg-Th-Zr

BY A. S. YAMAMOTO AND W. ROSTOKER

Abstract

A phase diagram for the Mg-Th system up to 70% Th has been constructed showing an intermediate phase Mg_5Th forming by a peritectic reaction and a eutectic reaction forming ($Mg + Mg_5Th$) from the melt at 42% Th and 582 °C. The maximum solid solubility of Th in Mg has been set at 4.5%. A tentative vertical section for Mg-Th-1% Zr has been outlined. A ternary peritectic reaction has been postulated to account for unusual cast microstructures. The limit of the Mg terminal solid solution does not appear to be appreciably altered by additions of Zr. (ASM International Classification M24b, M24c; Mg, Th, Zr)

THE CONSTITUTION of the magnesium-rich portions of these two systems is important to the development of a group of magnesium alloys which are currently arousing interest. Prior information on these systems is fragmentary and inconclusive.

Jones and Nash (1)¹ reported a simple eutectic diagram between the terminal magnesium solid solution and the first intermetallic compound, whose identity was not determined. In their work, liquidus and solidus curves were delineated; maximum solubility of thorium in magnesium at the eutectic temperature, 596 °C (1105 °F), was set at about 10%; approximate eutectic composition was reported in the vicinity of 35% thorium. The compound, theta, as they designated it, was inferred to contain about 55% thorium. The solidus temperature measurements published earlier by Leontis (2) show an intersection with the eutectic temperature (587 °C) at somewhere between 5.8 and 10.2% thorium. An intermediate eutectic temperature of 593 °C (1100 °F) was indicated by Hess' unpublished research (3).

As to the solvus curve, the only available data is from unpublished work by the Dow Chemical Company (4). It demonstrates a very sharp decrease of solubility of thorium in magnesium with decreasing temperature: about 5.5% Th at 593 °C (1100 °F) (eutectic temper-

¹ The figures appearing in parentheses pertain to the references appended to this paper.

Performed under Contract No. AF 33(616)-2571 for Aeronautical Research Laboratory of Wright Air Development Center, Wright-Patterson Air Force Base, Ohio.

The authors, A. S. Yamamoto and W. Rostoker, are associated with Metals Research Department, Armour Research Foundation of Illinois Institute of Technology, Chicago. Manuscript received March 6, 1957.

ature) to 0.1% thorium at 482 °C (900 °F). Very recently, it was reported that a 3.1% thorium alloy showed a quantity of second phase, after annealing 24 hours at 576 °C (1060 °F), which was identified by electron diffraction as a magnesium-thorium intermetallic compound (5). Even after a prolonged anneal of 96 hours at the same temperature, there was no change of the volume per cent of the undissolved phase. A more recent report under the same program attempted another rationalization of the presence of the undissolved compound (6). X-ray diffraction analysis indicated the existence of an oxygen-deficient ThO phase, which was assumed to exist as a layer enveloping those compound particles, thereby preventing their solution during prolonged annealing. A probable solubility limit of thorium at this temperature was estimated at about 2.5%. Other information by Fox (7) reported that a 1.2% thorium alloy had a second phase which showed no sign of any solution upon annealing for 24 hours at both 420 and 500 °C (788 and 930 °F). The alloy was prepared by reducing ThCl₄ with molten magnesium of 99.8% purity.

Leontis (2) reported the existence of two compounds in the alloy system. X-ray diffraction study confirmed that alloys of 10.2% thorium or less has only one compound, while an alloy containing 19.9% thorium indicated a trace of a second compound. However, the formula and crystal structure of these compounds were not reported in the paper. Table I summarizes all information obtained.

According to Leontis (8), thorium increases the solubility of zirconium in liquid magnesium. His alloys were melted at 730 °C (1345 °F) at which temperature the maximum solubility of zirconium in magnesium was reported as 0.69%. An increase in the thorium content raised the solubility of zirconium in the melt to 1.0%.

Table I
A Summary of Prior Information on the Mg-Th System

Liquidus Temperatures (1)		Solidus Temperatures, °C			
Th%*	T °C	Th%*	T °C(2)	Th%**	T °C (1)
4.98	647.5	0.97	637	5.0	621
5.73	646.5	2.1	624	6.0	635
9.58	642.5	3.2	616	6.3	635
15.6	615	5.8	597	7.5	621
25.9	619	10.2-49.9	587	10-55	593
28.9	617				
38.1	619				
Eutectic Temperatures		Solvus Boundary			
Th%	T °C	Th%	T °C		
~ 35	596 (1)	max. ~ 10			(1)
	593 (3)	max. ~ 6.6			(3)
49.9	587 (2)	max. 5.8-10.2			(2)
		6.6*		593	(4)
		~ 5.3*		582	
		4.1*		566	
		1.7*		538	
		0.6*		510	
		0.1*		482	

*analyzed

**nominal

MATERIALS

Magnesium used in this investigation was distilled by the supplier to a purity of 99.95% magnesium. Thorium, a calcium-reduced product, of 98% metal was added directly to melts or as a previously prepared master alloy of 45% thorium. The chief impurity in the thorium was ThO_2 ; the only metallics being 0.004% iron and <0.05% calcium. Zirconium was added as a master alloy containing 34.7% zirconium supplied by the National Lead Company. Unfortunately, late in the program it was discovered that the Mg-Zr master alloy was somewhat heterogeneous. Since only small pieces of this were added to any one melt, it is suspected that the heterogeneity was responsible for the somewhat erratic analyzed zirconium contents of the various alloys.

MELT PREPARATION AND HEAT TREATMENTS

In accordance with satisfactory prior experience, melts were produced in molybdenum crucibles. The crucibles were formed from 3 mil molybdenum sheet around a molybdenum or tungsten plug of 0.5 inch diameter. The sheet, formed into a tube with an interlocking seam, was bound to the plug as a bottom by alumel wire. It was demonstrated that there was no dissolution of the crucible metals at temperatures as high as 900 °C (1650 °F). Melting was performed in vertical tubular resistance heated furnaces dynamically purged with argon. A flux cover of LiF-3LiCl further protected the melt and minimized volatilization of magnesium. In order to minimize solution time, thorium or thorium-master alloys were less than $\frac{3}{16}$ inch mean dimension. The melts were periodically stirred with a $\frac{1}{8}$ inch molybdenum rod. All Mg-Th and Mg-Th-Zr alloys of less than 20% thorium were prepared using the 45% thorium master alloy. This was not necessary for melt homogeneity since thorium dissolves in molten magnesium readily but rather as an attempt to reduce the ThO_2 content of the more solid solution-rich alloys.

Both top and bottom portions of the chill cast ingots were discarded. To ensure homogeneity in the magnesium-rich alloys, the castings were mostly extruded to 3 millimeter wire. A routine for heat treatment was as follows. Specimens were wrapped in 1 mil molybdenum foil on which identification codes were stamped. Batches of such specimens were sealed in Pyrex bulbs with one atmosphere of argon.

METHODS OF CONSTITUTIONAL ANALYSIS

Thermal analysis, metallographic examination and x-ray diffraction were used in the construction of the phase diagrams.

Liquidus and eutectic temperatures were obtained directly from cooling curves using a mean cooling rate of about 8 °C per minute recording with a Leeds and Northrup Speedomax having a chart speed

of 2 inch per minute. Generally, solidus temperatures for the Mg/Mg + L boundary could not be read from the cooling curves and actually such values would probably be unreliable because of nonequilibrium solidification effects.

It is common practice to determine the solidus boundary of the type Mg/Mg + L by metallographic examination for incipient melting in pre-equilibrated specimens. This method did not prove very satisfactory in the systems under discussion because of the large spread between the composition of the solid and the liquid in equilibrium with it. The solidus boundary was also determined by differential thermal analysis on heating only, using pre-equilibrated specimens. A piece of pure magnesium was used as the nontransforming coupled sample.

For metallographic examination, specimens were mounted in a room temperature setting compound. Final polishing was performed in two stages using successively diamond powder with kerosene and sapphire powder (Linde B) with distilled water. The etchant used consisted of:

Glacial acetic acid	20 parts
Ethylene glycol	60 parts
Conc. nitric acid	1 part
Water	19 parts

Photomicrographs were taken immediately after etching.

A 14 cm diameter Debye-Scherrer powder camera was used for the x-ray diffraction analyses. Filtered characteristic copper radiation during 6-hour exposures produced satisfactory patterns. The -200 mesh powders for examination were prepared by filing, screening and sealing off in capillaries while in argon atmosphere by the use of a special apparatus described in a previous paper (9).

Most of the melts were chemically analyzed for the alloying elements. The thorium analysis distinguished between alloyed thorium and ThO₂.

THE SYSTEM MAGNESIUM-THORIUM

A list of the nominal and analyzed compositions of alloys prepared is given in Table II. As can be seen, the actual thorium contents are generally lower than the intended. These differences may result from the thorium oxide (ThO₂) which is inevitably present in alloys, partly from the original thorium metal and, it is assumed, partly from the melting operation. The latter origin probably became more serious in the preparation of higher thorium alloys since longer melting times and higher temperatures were required. Segregation on a macro scale did not prove serious because of the chill casting technique. A summary of measured thermal arrests is given in Table III. Thermal arrests could not be obtained for the steeply rising liquidus L/L + Mg₃Th between 45 and 55% Th. This is a common problem when the slope of the boundary is so steep. Heat treatments for determination of the solid solubility boundary involved a homogenization at 550 °C (1020 °F) for

Table II
Chemical Analyses of Magnesium-Thorium
Binary Alloys

Nominal Per Cent Thorium	Weight Per Cent	
	Thorium	Thoria (ThO ₂)
0.5	0.45	0.00
1	0.99	0.00
1.5	1.57	0.00
2	1.78	0.00
2.5	2.48	0.00
3	3.07	0.00
5	4.80	0.51
7	5.87	0.32
9	9.20	0.33
11	14.23	0.36
13	11.88	0.87
15	13.77	0.26
17	16.86	0.19
20	17.80	0.35
25	21.59	0.76
30	28.90	0.26
35	31.23	0.46
40	38.34	1.04
45	44.47	2.13
50	45.60	1.67
55	53.71	2.26
60	54.88	3.12
65	63.05	1.94
70	70.92	5.06

Table III
Thermal Analysis Data of the Magnesium-Thorium System

Alloy Composition % Th	Temperature, °C		
	Liquidus	Invariant Reaction	Solidus
0.99	646		—
1.78	651		—
2.48	650		—
3.07	632		—
4.80	648.5		579.5
5.87	643		582
9.20	640		582
11.88	641		576.5
13.77	637		581
14.23	635		580
17.80	637		577
21.59	632.5		580
28.9	622.5		581
31.21	612		582
38.34	597		581
41.56	597		583.5
45.03	—		580.5
53.71	—	772	583.5
54.74	—	778	584
63.05	812	773	582
70.92	813	772	582
2.37			635, 636
3.89			619

Two data points shown at the bottom of the table were obtained by differential thermal analysis.

at least 24 hours followed by final equilibration anneals for times of 72 hours (575 °C), 47 hours (550 °C), 120 hours (501 °C), 258 hours (452 °C), 353 hours (400 °C), 500 hours (351 °C) and 650 hours (303 °C). From the thermal arrest, differential thermal analysis and metallographic data the phase diagram of Fig. 1 has been constructed. An expanded view of the solid solubility region is shown in Fig. 2.

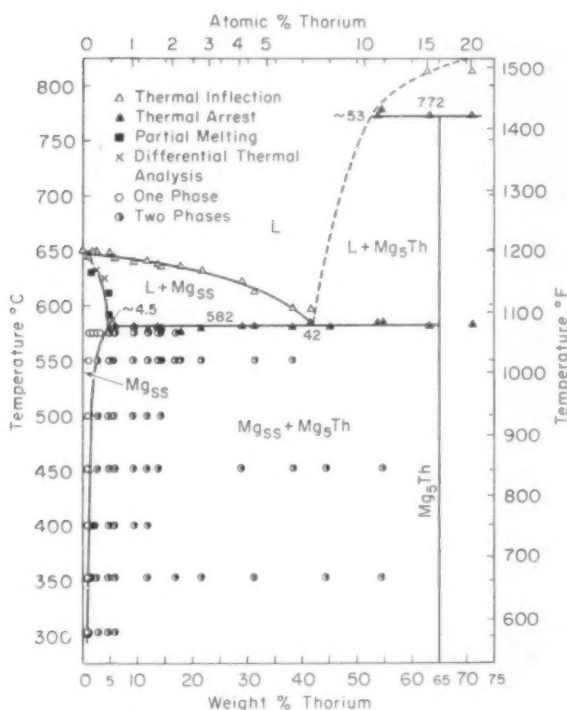


Fig. 1—Partial Diagram of the Magnesium-Thorium System.

Metallography showed that in the range 0–70% thorium one intermediate phase predominated. Vestiges of a second intermediate phase (or thorium terminal solid solution) appeared in the cast structures of alloys containing more than 53% thorium. There was never sufficient of this latter phase to identify it by x-ray diffraction. Thermal arrests confirmed that the first intermediate phase formed by peritectic reaction.

It was not found possible to produce an alloy containing only the first intermediate phase. The incomplete peritectic reaction could not be annealed out. The identity of the phase had to be made by extrapolation of lineal analysis data. These data, shown in Fig. 3, extrapolate to 16.5 atomic % thorium which corresponds to the formula Mg₅Th. Clear x-ray diffraction patterns of this phase have been obtained. The sequence of interplanar spacings can be fitted to a cubic lattice having unit cell dimensions of 14.24kX. Table IV compares measured and computed interplanar spacings. The density of the phase was determined by extrapolation of density measurements on the pure metal and three al-

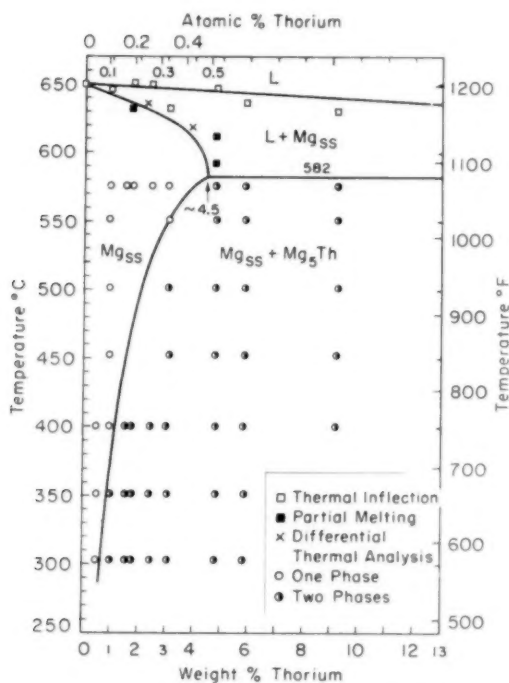


Fig. 2—Expanded Diagram of the Magnesium-Rich Region of the Magnesium-Thorium System.

Table IV
Summary of the Powder Pattern Lines of The First Intermediate Phase, Mg₅Th,
in the System Magnesium-Thorium

hkl	d observed (kX)*	d calculated (kX)**	I
111	8.216	8.221	w
200	7.128	7.120	vft
220	5.008	5.035	
222	4.106	4.111	vw
400	3.566	3.566	
331	3.262	3.267	vw
422	2.901	2.907	vft
511, 333	2.748	2.740	wm
440	2.520	2.517	ft
600, 442	2.373	2.373	
620	2.254	2.252	
711, 551	1.986	1.994	ft
731, 553	1.852	1.854	vft
800	1.780	1.780	
733	1.742	1.740	vft
822, 660	1.680	1.678	w
751, 555	1.646	1.644	vft
842	1.552	1.554	vft
664	1.521	1.518	vvft
844	1.467	1.453	
993, 771, 755	1.433	1.431	ft
1131, 971, 955	1.242	1.244	
1133, 973	1.207	1.208	

*Taken from pattern for 28.9% thorium alloy.

**Calculated on the basis of a cubic unit cell of edge dimension 14.24 kX. w = weak, vw = very weak, ft = faint, vft = very faint, vvft = very very faint.

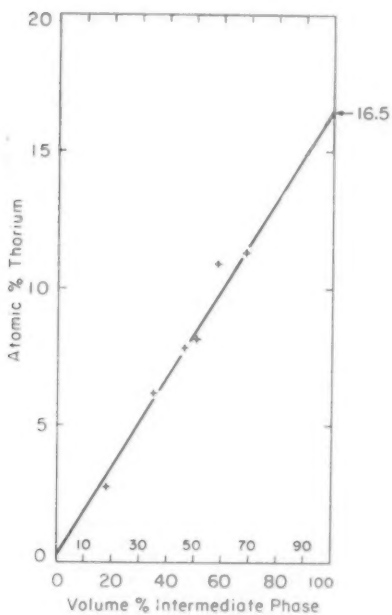


Fig. 3—Extrapolation of Composition of the First Intermediate Phase.

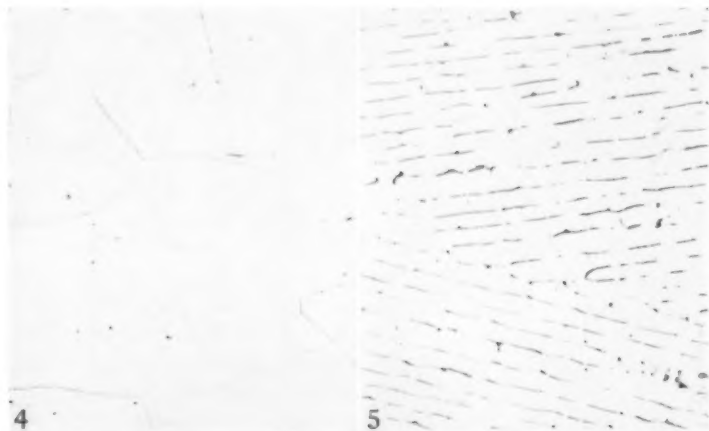


Fig. 4—A 3.07% Thorium Alloy Annealed at 550 °C (1020 °F), Nearly Single Phase Magnesium Solid Solution. $\times 250$.

Fig. 5—A 4.8% Thorium Alloy Annealed at 550 °C (1020 °F) Magnesium Solid Solution Plus Mg_3Th . $\times 250$.

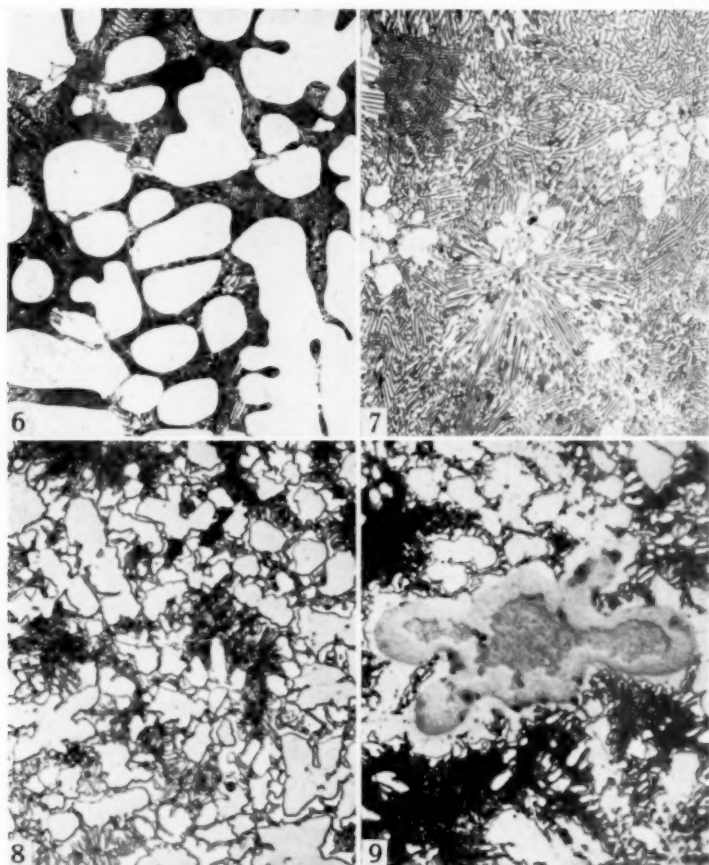


Fig. 6—A Nominal 25% Thorium Alloy, as Furnace-Cooled. Primary dendrites of Mg in a eutectic of (Mg + Mg₅Th). $\times 150$.

Fig. 7—A 41.95% Thorium Alloy, as Furnace-Cooled. Nearly complete eutectic of (Mg + Mg₅Th). $\times 150$.

Fig. 8—A 54.9% Thorium Alloy, as Chill Cast. Primary crystals of Mg₅Th plus eutectic of (Mg + Mg₅Th). $\times 750$.

Fig. 9—A 63.1% Thorium Alloy, as Chill Cast. Evidence of an incomplete peritectic reaction. A primary phase of unknown identity, a reaction product Mg₅Th and a eutectic (Mg + Mg₅Th). $\times 750$.

loys in the extruded and annealed condition containing 44.47, 45.60, 53.71% thorium, respectively. Using the derived density of 4.08 gm/cc and the formula Mg₅Th, the number of atoms in this large unit cell was computed to be 120.

A series of characteristic microstructures in Figs. 4 to 9 illustrate the essential structural characteristics encountered in this system. It

should be remembered that these alloys tend toward a segregated eutectic type structure. Only by furnace cooling can the conventional lamellar eutectic configuration be developed. It was decided that the third phase in the high thorium alloys (Fig. 9) could not be construed as undissolved thorium because the third phase frequently showed a clear dendritic shape.

The maximum solid solubility was determined as the 3-way intersection of the solidus and solvus boundaries and the eutectic line. The

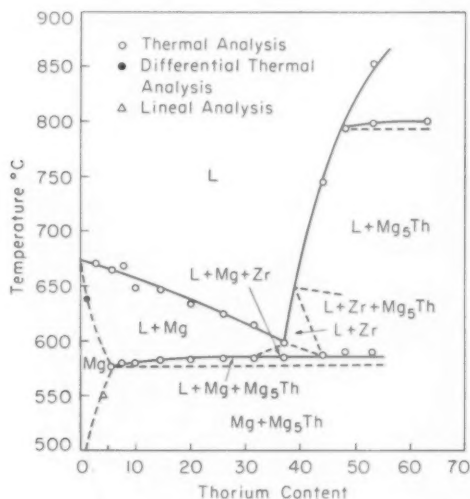


Fig. 10—A Tentative Vertical Section of the Magnesium-Thorium-1% Zirconium System.

derived solubility of 4.5% thorium is less than previous workers had estimated. Also, the decrease in solid solubility with temperature proved less drastic.

THE SYSTEM MAGNESIUM-THORIUM-ZIRCONIUM

The characteristics of this ternary system must derive from the interaction of the peritectic formation of magnesium and the steeply rising liquidus of the Mg-Zr system and the eutectic formation of (Mg + Mg₅Th) with the consequent initial depression of the liquidus of the system Mg-Th. Excluding for the moment the possible occurrence of ternary intermediate phases, it is to be expected that the most important feature of the ternary system would be the location of a steep liquidus surface demarking the solubility of zirconium in the liquid.

An attempt was made to analyze the form of this ternary system by

Table V
Chemical Analyses of Mg-Th-Zr Alloys Prepared

Analyzed Composition, %		Analyzed Composition, %		Analyzed Composition, %	
Th	Zr	Th	Zr	Th	Zr
1.67	0.57	1.62	0.28	2.34	1.04
3.42	0.48	3.87	0.02	3.51	0.03
5.97	0.80	4.91	0.65	5.85	0.88
5.70	0.66	8.29	0.68	7.88	1.00
7.27	0.61	10.39	0.86	10.01	0.95
11.78	1.74	12.35	0.73	11.44	0.91
10.46	0.99	15.81	0.74	14.75	1.11
13.01	0.80	21.36	0.73	19.89	1.06
17.97	1.00	25.14	0.68	26.13	0.91
22.96	0.75	26.75	0.71	31.46	0.95
27.88	0.83	33.38	0.66	37.04	0.99
34.84	1.29	41.51	0.72	34.31	1.02
41.19	0.51	46.38	0.72	44.25	0.98
46.19	0.46	50.45	0.71	48.31	1.07
55.58	0.38	58.88	0.69	53.62	0.61
59.25	0.46	62.28	0.70	58.83	0.78
61.88	0.44			63.11	0.99

a study of three vertical sections Mg-Th-0.5% Zr, Mg-Th-0.75% Th and Mg-Th-1.0% Zr. For each section, at least 16 alloys were prepared covering the range of 0-63% thorium. The analyzed compositions are summarized in Table V. The nominal 0.5% zirconium alloys showed more variation than desirable, but the analytical procedure is suspect since it was discovered later that the separation of thorium was critical to the accurate determination of zirconium. Some of the scatter must also be due to heterogeneity of the master alloy used. The variations in zirconium content, however, do not appear to complicate the problem badly because the pattern of liquidus and eutectic arrests for the three sections were indistinguishable even on the analyzed chemical composition basis. Fig. 10 is a construction of a vertical section at 1% zirconium (nominal) showing thermal arrest data points as well as other data points. Other facets of this diagram will be discussed in succeeding paragraphs.

Examination of as-cast structures revealed two important characteristics. Addition of zirconium reduces the thorium content of the eutectic compositions at 41.83% Th, 0.18% Zr and 38.77% Th, 0.64% Zr, respectively. Fig. 13 illustrates a type of as-cast structure found frequently in hypo-eutectic alloys of Mg-Th-Zr with thorium contents greater than about 30% thorium. One can distinguish the usual (Mg + Mg₅Th) eutectic and the primary dendrites of Mg plus a very coarse eutectic-like configuration reminiscent of the "Chinese Script" structures in aluminum alloys. The "Chinese Script" structure never occurs in binary Mg-Th alloys. Furthermore, in specimens where the "Chinese Script" abounds, x-ray diffraction identifies only magnesium and Mg₅Th. It is felt that the two configurations of (Mg + Mg₅Th) in conjunction with other evidence can be used to infer the phase reactions involved in the solidification of the Mg-Th-Zr alloys.

Fig. 14 graphically displays the liquidus arrests measured for a large

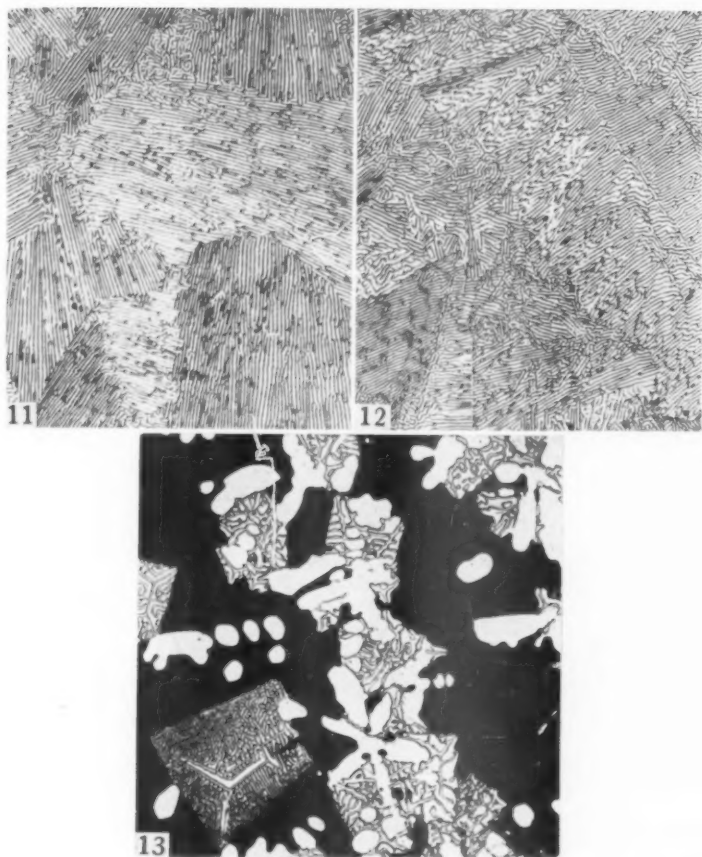


Fig. 11—A 41.83% Thorium, 0.18% Zirconium Alloy as Furnace-Cooled from the Melt Showing a Eutectic Structure. $\times 250$.

Fig. 12—A 38.77% Thorium, 0.64% Zirconium Alloy as Furnace-Cooled from the Melt Showing a Eutectic Structure. $\times 250$.

Fig. 13—A Nominal 37% Thorium, 0.5% Zirconium Alloy as Furnace-Cooled from the Melt Showing Primary Dendrites of Magnesium, "Chinese Scripts", and Eutectic ($\text{Mg} + \text{Mg}_5\text{Th}$). $\times 250$.

number of alloys. In this range of compositions, the liquidus surface appears to be roughly a flat plane. Alloys made up with more than 1% zirconium showed what appeared to be undissolved nodular residues congregating near the bottom of the ingots indicating that the liquid solubility limit for zirconium in Mg-Th alloys is in the neighborhood of 1% as Leontis (8) observed. The liquidus surface then seems to give the appearance of an inclined plane of negligible transverse slope joined

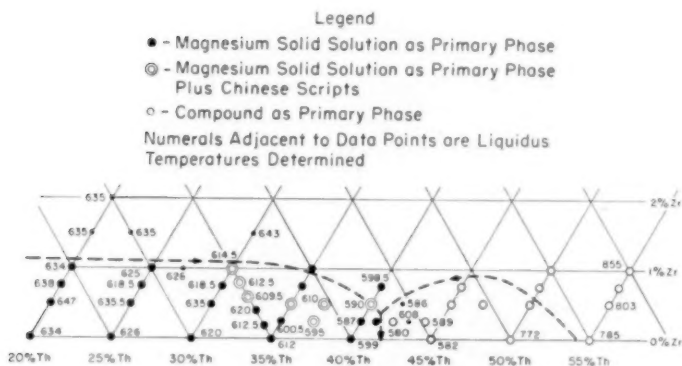


Fig. 14—Segment of Probable Liquid Surface of the Magnesium-Thorium-Zirconium System.

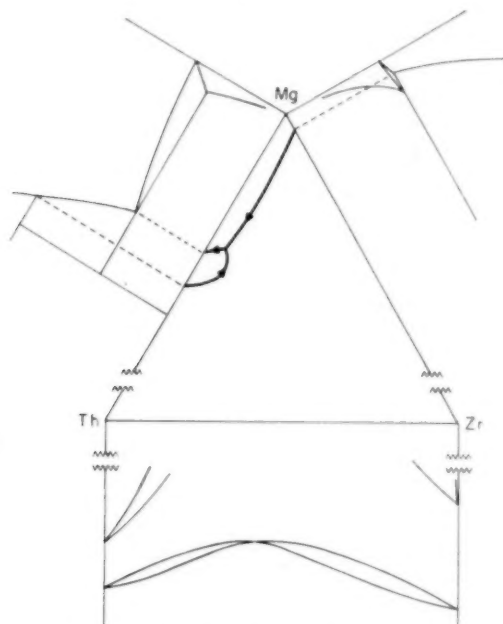


Fig. 15—Hypothetical Lines of Primary Crystallization (Diagrammatic) in the Magnesium-Thorium-Zirconium System.

sharply by a steeply rising surface at something above 1% zirconium.

The pertinent evidence on the solidification of Mg-Th-Zr alloys can be mobilized as follows:

(a) In all of the alloys studied only the phases Mg, Mg_5Th and the thorium-rich phase of the binary system (at high alloy levels) were identified. There appears to be no ternary intermediate phases. The Mg-Zr and Th-Zr systems also possess no intermediate phases.

(b) Binary invariant solidification reactions to be interrelated include: $L \rightarrow Mg + Mg_5Th$, $L + Mg_xTh \rightarrow Mg_5Th$, $L + Zr \rightarrow Mg$. The high temperature allotropes of thorium and zirconium are continuously miscible.

(c) The thermal arrest data indicate that the peritectic reaction of the Mg-Zr system moves towards the eutectic reaction of the Mg-Th system.

(d) The appearance of a "Chinese Script" structure in Mg-Th-Zr alloys containing 30-45% Th indicates the occurrence of a ternary invariant reaction.

With these observations in mind, the interrelation of the binary invariant reactions is assumed to be of the form shown in Fig. 15. The

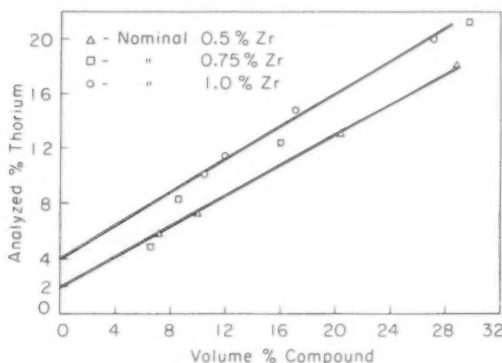


Fig. 16—Extrapolation of Terminal Solid Solubility at 550 °C (1020 °F) of the Magnesium-Thorium-Zirconium System by Lineal Analysis.

main point of question is whether the ternary invariant reaction is peritectic or eutectic. Because of the coarseness and configuration of the "Chinese Script" microstructure, the peritectic assumption is preferred. Ternary eutectics are generally much finer structures than the prior precipitating binary eutectics. Moreover, the "Chinese Script" structures are invariably attached to primary magnesium dendrites which indicates that they crystallized out before the binary eutectic.

The following hypothesis is advanced to account for the cast structures observed. Reference is made to Fig. 10, the Mg-Th-1% Zr section. On cooling a melt containing, for instance, 35% Th, primary magnesium is first rejected from the melt, followed at lower temper-

atures by the co-precipitation of magnesium and zirconium. Simultaneous rejection of the two solid phases during this period is likely to occur at the surface of the already formed magnesium primary dendrites. However, the zirconium phase thus formed is consumed by the ternary peritectic reaction: $L + Zr \rightarrow Mg + Mg_5Th$. During the reaction, the precipitated zirconium reacts with the melt surrounding it to produce more Mg and Mg_5Th , for the first time, until all of the zirconium is consumed. As a result, the co-deposition of magnesium and zirconium at the outset and the juxtaposed magnesium and Mg_5Th mixture in the end assume the appearance of "Chinese Script".

The remaining liquid solidifies over a temperature range by the joint crystallization of magnesium and Mg_5Th in a conventional eutectiferous configuration.

Because of the somewhat erratic zirconium analyses it was not possible to determine solid solubility limits very exactly. Instead, a lineal analysis of Mg_5Th in 12 alloys was run on specimens annealed at 550 °C for 48 hours. The alloys covered the composition range 6–30% thorium and 0.5–1% zirconium. The results shown graphically in Fig. 16 indicate that the binary solubility of 3% thorium at 550 °C is not appreciably altered by zirconium additions.

Alloys containing 8–60% thorium were annealed at 578, 550, 500, 400 and 302 °C for times of 48, 48, 120, 352 and 600 hours, respectively. Microstructures indicated no solid state reactions occurred.

SUMMARY

A phase diagram for the binary system Mg-Th has been constructed for the composition range 0–70% thorium. One intermediate phase has been identified as having the formula Mg_5Th . A thorium-rich phase exists but it could not be identified. Between magnesium and Mg_5Th , a eutectic occurs at 45% thorium and 582 °C. The Mg_5Th phase forms by a peritectic reaction at 772 °C between melt and the thorium-rich phase. The maximum solid solubility of thorium in magnesium has been set at 4.5% thorium.

A tentative vertical section for Mg-Th-1% Zr has been constructed. Lesser amounts of zirconium yield very similar sections. No ternary intermediate phases were found. A ternary peritectic reaction slightly above 582 °C: $L + Zr \rightarrow Mg + Mg_5Th$ has been postulated to account for a "Chinese Script" type microstructure encountered in cast alloys between 30–45% thorium. The solubility of zirconium in the melt is of the order of 1% zirconium. The terminal solid solution of magnesium is in equilibrium with a phase mixture of (Mg + Mg_5Th). The solid solubility of magnesium at 550 °C is not appreciably altered by zirconium.

ACKNOWLEDGMENT

This work has been performed under Contract with the Aeronautical Research Laboratory of the United States Air Force. This sponsorship and permission to publish are gratefully acknowledged. The metallography was conducted by E. Klimek.

References

1. A. Jones and R. R. Nash, "Magnesium Alloy Research," *WADC Technical Report 53-113*, Contract No. W33-038-ac 22542, Materials Laboratory, Wright Air Development Center, Ohio, October 1953.
2. T. E. Leontis, "Properties of Magnesium and Magnesium-Thorium-Cerium Alloys," *Transactions, American Institute of Mining and Metallurgical Engineers*, Vol. 194, 1952, p. 287-94.
3. J. B. Hess, unpublished research, The Dow Chemical Company.
4. "Principles of the Effect of Rare Earth Additions on the High Temperature Properties of Magnesium," Seventh Quarterly Report (Report No. 15657), The Dow Chemical Company, Contract No. AF 33(038)-16655, Aeronautical Research Laboratory, Wright Air Development Center, Ohio, December 1953.
5. "Creep Behavior of Magnesium Alloys," Second Quarterly Report (Report MT 16403), The Dow Chemical Company, Contract No. AF 33(616)-2511, Aeronautical Research Laboratory, Wright Air Development Center, Ohio.
6. "Creep Behavior of Magnesium Alloys," Third Quarterly Report (Report MT 16403), The Dow Chemical Company, Contract No. AF 33(616)-2511, Aeronautical Research Laboratory, Wright Air Development Center, Ohio, January 1955.
7. F. A. Fox, "A Note on the Influence of Additions of Thorium to Magnesium-Base Alloys," *Journal, Institute of Metals*, Vol. 73, 1947, p. 223-224.
8. T. E. Leontis, "Effect of Zirconium on Magnesium-Thorium and Magnesium-Thorium-Cerium Alloys," *Transactions, American Institute of Mining and Metallurgical Engineers*, Vol. 194, 1952, p. 633-642.
9. D. W. Levinson and D. J. McPherson, "Phase Relations in Magnesium-Lithium-Aluminum Alloys," *TRANSACTIONS, American Society for Metals*, Vol. 48, 1956, p. 689-705.

INDEX OF AUTHORS

VOLUME L

TRANSACTIONS OF AMERICAN SOCIETY FOR METALS

1958

A

Abrahamson, E. P. II.....705-721
Averbach, B. L.....517-540, 634-655
Avery, C. H.....814-829

B

Backofen, W. A.....478-497
Baldwin, W. M. Jr.....803-813
Bartholomew, E. L. Jr.....370-383
Beck, F. H.....759-772
Bendel, S.1047-1062
Berger, L. W.....384-397
Borik, F.242-257
Brown, Norman541-561
Burke, J. E.....943-953

C

Carlson, O. N.....348-369
Chapman, R. D.....242-257
Christakos, J.105-128
Chubb, W.298-304
Clark, Donald S.....14-20, 656-681
Cohen, M.517-540, 634-655

D

Day, D. L.....398-417
Dieter, G. E.....722-737
Domagala, R. F.....323-339
Dorn, J. E.....856-883
Douglass, D. L.....305-322
Dulis, E. J.....773-802
Duwell, E. J.....208-226

E

Eichelberger, T. W.....738-758
Elliott, R. P.617-633

F

Fontana, M. G.759-772
Fortney, R. E.....814-829

G

Gibson, E. D.....348-369
Grant, N. J.....705-721
Gurland, J.1063-1071
Gurry, R. W.105-128

H

Hagel, W. C.....184-207
Harmon, E. L.....418-437
Harrison, Eleanor994-1005
Hauser, F. E.....856-883
Hendrickson, J. A....498-516, 656-681
Hsiao, Chi-Mei773-802

J

Jaffee, R. I.....384-397
Johnston, T. L.....1047-1062
Jominy, W. E.....163-183, 242-257

K

Kalish, Herbert A.....272-297
Kessler, H. D.....398-417
Koistinen, D. P.....227-241
Kozol, J.418-437
Kramer, A.803-813

L

Lagerberg, G.141-162
Landon, P. R.....856-883
Lement, B. S.....141-162
Levinson, D. W.....323-339

Li, C. H.....	1047-1062	Ross, S. T.....	163-183
Liu, Tien-Shih	455-477	Rostoker, W.	617-633, 838-855, 1090-1105
Lloyd, L. T.....	954-980	Ruoff, M. N.....	184-207
Loomis, B. A.....	348-369		

M

McKinsey, C. R.....	438-454
McNutt, J. E.....	1006-1030
McPherson, D. J.....	323-339
Mallett, M. W.....	981-993
Manning, G. K.....	305-322
Marsh, L. L. Jr.....	305-322
Marshall, E. R.....	478-497
Martin, W. G.....	572-588
Mayfield, R. M.	905-925, 926-942, 954-980
Mehl, R. F.....	1006-1030
Mickelson, Robert	340-348
Mikus, E. B.....	682-704
Muehlenkamp, G. T.....	298-304
Mueller, M. H.....	905-925
Murphy, Daniel J.....	884-904

N

Newkirk, J. B.....	572-588
--------------------	---------

O

Owen, W. S.....	517-540, 634-655
-----------------	------------------

P

Paliwoda, E. J.....	208-226, 258-270
Parker, Earl R.....	46, 52-104
Pechin, W. H.....	1081-1089
Perkins, R. A.....	438-454
Peterson, David	340-348
Pond, R. B.....	994-1030
Powell, G. W.....	478-497
Pugh, J. W.....	1072-1080

R

Richards, R. S.....	398-417
Roberts, Earl C.....	129-140

S

Sartell, J. A.....	1047-1062
Schwoppe, A. D.....	298-304
Semchyshen, M.	830-837
Sernka, R. P.....	163-183
Siebert, C. A.....	682-704
Sinnott, M. J.....	1031-1046
Spachner, S. A.....	838-855
Sperry, Philip R.....	589-616
Steinberg, Morris A.....	455-477
Stern, M.....	438-454
Stricker, C. D.....	105-128

T

Thurman, J. W.....	208-226
Torgerson, C. S.....	830-837
Troiano, A. R.....	418-437
Trzeciak, M. J.....	981-993
Turkalo, A. M.....	943-953

U

Upp, J. R.....	759-772
Upthegrove, W. R.....	1031-1046

W

Wang, T. P.....	541-561
Williams, D. E.....	1081-1089
Williams, D. N.....	384-397
Williams, R. O.....	562-571
Wood, D. S.....	498-516, 656-681

Y

Yamamoto, A. S.....	1090-1105
---------------------	-----------

Z

Zegler, S. T.....	905-925
-------------------	---------

SUBJECT INDEX

- ASM Awards**.....12, 13, 19, 32, 47-52
ASM Educational Lecture Series.9, 10
ASM Foundation for Education and Research41-45
ASM Gold Medal.....51, 52
ASM Medal for Advancement of Research Award.....49, 50
ASM Periodicals.....29, 30
ASM Publications.....28, 30, 31, 37
Acid pickling of titanium
 hydrogen absorbed in.....438-454
Activation energy
 for grain boundary self-diffusion.....1039, 1044, 1045
 for recrystallization of
 Ti alloy RC55.377, 378, 380-383
 for release of a dis-
 location.....500, 505, 508, 514
 of creep and growth in
 uranium.....940, 942, 949
 of temper embrittlement.691, 695, 697
Age hardening
 classification of systems.....562-571
 in Ti-Cb alloys.....394-396
 in Ti-V alloys.418, 427, 428, 435, 437
 treatments for high temperature
 alloys738, 739
Aging
 of Cr-Mn-C-N steels.....775
 of iron-base alloy, hardened
 with Ti, effect of-cycles
 on properties738-758
 of Ti-4Al-3Mo-1V405-408, 412
 of Ti-V alloys.....427-437
 types of cycles used for high
 temperature alloys738, 739
Alcoholic extraction of carbides
 from steel105-128
Allotropic modifications
 of uranium986, 987
Alloys
 for high temperature use
 See High temperature alloys
 for nuclear reactors.271, 272, 298, 348
 for use at 800 °F.....398
Alloying elements
 in Al-1.25 Mn
 Alloying elements (cont.)
 in Al-1.25 Mn (cont.)
 distribution by lineal
 analysis593, 594
 in chromium, effect on
 BDT temperature705-721
 in magnesium
 effect on axial ratio...859, 877, 878
 effect on transition
 temperature880
 in temper embrittlement.683, 691, 695
Alloy steels, hypoeutectoid
 transformation structures .187-207
Alpha-gamma transformation
 in pure iron, sensitivity of
 hot hardness tester at....834, 835
Aluminum
 coefficient of work hardening....64
 strain induced growth in ab-
 sence of recrystallization....373
Aluminum, bicrystalline
 grain boundary movement..994-1005
 micrograph of grain
 boundary999
 plastic deformation in.....994-1005
 ruptured surface996, 998
 specimen preparation995-998
Aluminum, single crystal
 strain hardening in.....64
 stress-strain curve....64, 1000, 1001
Aluminum alloys, airframe
 structural
 effects of temperature-time his-
 tories on tensile
 properties814-829
 prediction of tensile
 properties827, 829
 sampling and analysis of
 variation815
**Aluminum alloys, trade designa-
 tions**
 2024-T3, alclad, effects of
 temperature-time histories
 on tensile properties....814-829
 3003 (3S), relation between
 constitution and ultimate
 grain size589-616

Aluminum alloys (cont.)

- 7075-T6, alclad, effects of
temperature-time histories
on tensile properties...814-829

Aluminum-1.25 Mn alloy

- hardness changes during proc-
essing591
microstructure592, 595-599
properties of, unhomogenized
and homogenized591
relation between constitution
and grain size.....589-616
solid solution composition as
affected by microstructure..592

Aluminum-silicon alloys

- thermally induced stresses in...1063

Andrade theory of creep.....79**Annealing**

- of austenitic stainless steels,
effect on tensile ductility at
various temperatures ...803-813
of ingot iron, stored energy
measured during549-554
of titanium and its alloys,
effect of temp. and time on
final grain size..371-373, 376, 380
of uranium, effect of alpha phase,
upon growth ..907-909, 914, 923

Annual Address of President....14-20**Apparatus for determining the**

- hardness of metals up to
3000 °F.830-837

Aqueous extraction of carbides

- in steel105-128

Argon in cathodic etching.....

-574, 576, 579-581, 587

Atomic diameters (Goldschmidt)

- table619

Austenite

- in Cr-Mn-C-N steels
hardening of794
stability of782-786, 797
in Fe-Cr-Ni alloys, effect on
intergranular corrosion..763-770
in stainless steel, stability of....
.....478, 489, 492, 495

Austenite, banded and retained

- in stainless steel, 431, effect
on transverse properties..730-736

Austenite transformation

- effect of tension, torsion and
compression strains on..493-496

Austenitic stainless steel

- See Stainless steel, austenitic

Austenitizing

- of high C steel, effect on prop-
erty-relationships163-183
of mild steel, effect of temps.
on critical stresses.....529-531

Autoradiography

- methods in685, 686
of carbon 14 in steel.....687-696
of intergranular microsegregation
of radioactive P in steel....698
of role of C in temper em-
brittlement687, 691, 696
of self diffusion of nickel..1033, 1034
photographs687, 691-694
resolution in700, 701, 703

Axial ratio (c/a)

- relation to prismatic slip in
Mg-Li alloys
..856, 859, 874, 877, 878, 881, 883

BDT of binary Cr-base alloys..705-721**BDT temperature**

- bend test for.....706, 707, 718
correlation with electron con-
figuration712, 713, 715-717
definition716
theory for.....716, 717

Becker theory of creep.....79, 80**Bend test for BDT.....706, 707, 718****Bens hot hardness tester..831, 834, 836****Beryllium**

- correlation of slip mechanisms
with axial ratios.....877, 883

Bicrystals from single crystals

- illustrations and schematic..996-998
specimen preparation995-998

Binary alloys

- Laves phases in, of transition
elements618-623

Brillouin zones

- in Laves phases..617, 618, 622, 628-630
theory878

Brass

- effect of grain size on creep
 - in 70-3089
- strain induced growth in absence
 - of recrystallization373
- thermal stresses in two-phase
 - alloys 1070

Brittle-ductile transition

See BDT

Brittle fracture

- contrasted with ductile.....
-661, 662, 678, 680
- Griffith-Orowan theory of.....
-635, 647, 651
- in chromium alloys.....705-721
- in mild steel
 - critical tensile stress for.673, 676
 - effect of notch geometry.....
 -656, 658, 675
 - effect of stress rate.....675
 - effect of temperature.675, 677, 680
 - initiation of656-681
 - under tension at -196°C ..635-655
 - relationship to crystal structure..657

Brittle fracture strength

- equation for857
- of magnesium858

Brittleness

- in austenitic stainless steel, and
 - carbide precipitation ...803-813
- in chromium, theories on.....853

Burger's mechanism of strain

- hardening65

Burger's vectors in slip...876, 877, 879**C-T diagrams**

- for Cr-Mo-V steel.....190
- for Ni-Cr-Mo steel.....190, 191
- for Ni-Mo steel.....189
- for 4340 steel.....202

Cadmium

- correlation of slip mechanisms
 - with axial ratios.....877
- growth of, from vapor....1006-1030

Campbell Memorial Lecture.46, 52-104**Campbell dislocation theory of**

- yield point502, 505, 508, 509, 512, 514

Carbide extraction

- data114, 115
- electrolyte 111-114
- equipment 106-111
- handling of residue.....118-123
- variations in conditions.....115-118
- variations in tempering
 - temp. 123-126

Carbide precipitation

- globular type in alloy steels.194, 200
- in austenitic stainless steels
 - brittleness and803-813
 - microstructure805, 810

Carbides, grain boundary

- in stainless steel, effect on
 - properties 734-736

Carbides, residual

- in Cr-Mn-C-N steels...780-782, 794

Carbides

- in carbon steel, extraction
 - method for105-128
- in steel, thermo-magnetic
 - properties 150

Carbon

- diffusion gradients in carbon
 - steels 201, 202, 206
- in case of a carburized steel....
-228, 233, 235, 240
- in cementite, Curie tempera-
 - ture analysis135, 136
- in Cr-Mn-C-N steels, stabilizing
 - effect of, on austenite.....
 -783, 784, 788, 789, 793
- in leaded steels, effect on
 - machinability266, 270
- in 3140 steel, temper embrittlement
 - and682-704
- in thorium, solubility of....340-347
- in uranium-low titanium alloys
 - 903, 904

Carbon 14

- in autoradiography of steel..685, 686

Carbon steel

- carbon diffusion gradients.....
-201, 202, 206
- extraction of carbides from..105-128
- temper embrittlement in.683, 699, 702

Carbon steel, high

- fracture behavior vs. hardness 163-183
- torsional strength and electron microstructure 163-183

Carburization of steel

- stress distribution in case...227-241
- x-ray diffraction study of...227-238

Cathode ion bombardment.....572**Cathodic etching572-588**

- argon used in.....574, 579, 587
- cathode cooling in...580, 581, 583, 587
- cathode shielding580, 581, 587
- conditions for several alloys...579
- equipotential lines in model.....581
- ionization efficiency in.....
-573, 574, 578-580, 584, 587
- krypton use in.....587
- magnetic field use in...578, 580, 585
- normal and oblique incidence.....
-582-585, 587
- of copper-2.5 iron alloy.....578
- of gold-nickel577
- of electroplated steel.....582-585
- of radioactive and nonradioactive materials585
- of sintered compacts.....579, 585
- of stainless steel.....577
- operation procedure575-578
- power supply575
- safety precautions575
- time and temperature characteristics582, 586, 587
- time-pressure elements, with and without magnetic field578, 586, 587
- vacuum equipment.573-576, 580, 581

Cathodic reaction to lessen

- corrosion in titanium.438, 440, 441

Cementite

- in high carbon steel...175-177, 179
- in steel, effect of Mn on Curie point129-140
- phase changes during quenching141-162
- thermo-magnetic properties150

Ceramic single crystals

- ductility at room temp.....100, 101

Chemistry

- of lead in leaded high S steels. 208-226

Chinese script structure

- in Mg-Th-Zr alloys.....
-1100, 1101, 1103, 1104

Chromium

- ductile-brittle transition.....
-843, 845, 854, 1077, 1079
- ductility with strain rate.....718
- effect of alloying elements on BDT temperature...705-721
- effect of contaminants on transition temperature838
- effect of Fe and W on transition temperature848
- effect of purity on ductility.....
-838, 847, 848
- Goldschmidt atomic diameter....619
- hardness vs. aging temperature...1073
- high temp. properties of forged842-847
- in Al-5 Mg alloy effect on recrystallization
-610-612
- in Cr-Mn-C-N steels, stabilizing effect of784, 799
- mechanical properties of forged838-855
- preparation of ingot.....1072, 1073
- rheotropic recovery in.....848-850
- strain rate sensitivity.....718, 720
- stress-rupture properties...1072-1080
- tensile properties1072-1080
- transition temperature848-850
- valencies used by different investigators630

Chromium alloys

- for high temperature use...1072, 1080

Chromium-aluminum alloys ..711, 712**Chromium binary alloys**

- BDT temperatures705-721
- electronic configuration and mechanical behavior ...705-721

Chromium-boron alloys711, 712**Chromium-beryllium alloys711, 713****Chromium-carbon alloys711, 712****Chromium-cobalt alloys708-710, 713-715**

- Chromium-columbium alloys** 709, 711, 713
Chromium-copper alloys 713
Chromium-hafnium alloys 713
Chromium-iridium alloys 708-710, 713-715
Chromium-iron alloys 708-710, 713-715
Chromium-manganese alloys 708-710, 713-715
Chromium-Mn-C-N stainless steel
 phase relationships in 773-802
Chromium-Mn-C steels
 isothermal section at 2100 °F. 781
Chromium-molybdenum alloys 709, 710, 713, 715
Chromium-Mo-V steel
 hardness with various quenching
 treatments 187, 206
 isothermal and cooling trans-
 formation curves 190
 transformation structures in 195, 196, 198
Chromium-nickel alloys 708-710, 713-715
Chromium-nitrogen 707, 712, 718
Chromium-oxygen 712
Chromium-palladium alloys 708-711, 713-715, 718, 720
Chromium-platinum alloys 708-710, 713-715
Chromium-rhenium alloys 708-710, 713-715
Chromium-rhodium alloys 708, 709, 713, 714
Chromium-ruthenium alloys 708-710, 713-715, 717, 719
Chromium-silicon alloys 711, 712
Chromium steels
 influence of Ni on intergranular
 corrosion of 18% Cr. 759-772
Chromium-tantalum alloys 709, 711, 713
Chromium-technetium alloys 713
Chromium-titanium alloys 709, 711, 713
Chromium-tungsten alloys 709, 710, 713
Chromium-vanadium alloys 709
Chromium-zirconium alloys 709, 711, 713
Clark-Wood yield theory 519, 533
Classification of precipitation systems 562-571
Coalescence in precipitation
 of Al-1.25 Mn alloy 601, 616
Cobalt
 coefficient of linear expan-
 sion 1065
 effect of, on WC lattice
 spacing 1066
 Goldschmidt atomic diameter. 619
 Poisson's ratio 1065
 valencies used by various inves-
 tigators 630
 Young's modulus 1065
Cobalt-base alloy, trade designation
HS-21 (effect of double aging
 on stress-rupture) 757, 758
S-816, hardness (70-2300 °F.)
 834, 835
Coefficient of expansion
 of cobalt 1065
 of uranium 954, 970
Coherency in precipitation 568, 569
Columbium
 effect on alpha and beta Ti. 384
 Goldschmidt atomic diameter. 619
 Laves phases in. 617-633
 plastic strain prior to abrupt
 yielding 536
 stress-strain prior to abrupt
 yielding 538
Composition
 of Cr-Mn-C-N steels, effect of
 solution treatments and, on
 hardness 788, 792, 795, 796
 of leaded steels (type A)
 effect on machinability
 261, 262, 264-267, 269
 of nonleaded open hearth free-
 cutting steel, effect on
 machinability 258
 of uranium, effect on thermal
 cycling growth 947

- Compression testing**
 of austenitic stainless steels.....
481, 488, 489, 496
- Constitution of Al-1.25 Mn alloy**
 effect on grain size.....589-616
- Constitutional diagram**
See Phase diagram
- Contaminants in chromium**
 effect on transition temperature..838
- Continuous cooling**
 microstructure of low alloy steel
 produced by244
- Cooling rates in thermal cycling**
 for uranium, effect on growth...
 ..912, 918, 919, 931, 932, 935,
 937, 938
- Cooling rates (quenching)**
 for U-low Ti alloys, effect of
 heat treatment and, on
 properties .888-896, 899, 903, 904
- Cooling transformations in steel**
See C-T diagrams
- Copper**
 creep rate vs. grain diameter
 in polycrystalline90
 Goldschmidt atomic diameter...619
 stress-strain curves for
 single crystal97
- Copper alloys**
 effect of electron concentration
 on yield strength.....97
 stress-strain curves for
 single crystal96, 97
- Copper-2.5 iron alloy**
 cathodically etched578
- Copper-nickel alloy (62:38)**
 oxidation behavior1047-1062
- Copper oxides (CuO) and (Cu₂O)**
 growth rates in oxidation-
 kinetics study on Cu-Ni
 alloy1051-1057
 orientation1062
- Corrosion rates for Fe-Cr-Ni
 alloys**763-770
- Corrosion resistance**
 of uranium898
 of U-low Ti alloys.....894, 897-899
- Corrosion tests on stainless
 steel**762, 763
- Cottrell atmosphere**
83, 92-94, 98, 500, 516, 537
- Cottrell-Bilby theory of initial
 dislocation release** ...500, 501, 514
- Cottrell mechanism of
 hardening**92-94
- Cottrell strain aging theory**.....878
- Cottrell theory of creep**.....83, 91, 92
- Creep**
 activation energy for87
 deformational mechanisms for...
976, 977
 effect of grain size on.....89, 90
 in high purity nickel.....85, 86
 in mild steel, in nonelastic
 deformation ..521, 522, 524, 534
 in uranium949, 951
 effect of temperature
 variation936, 940, 942
 shape of curves84-86
 theories of79-91
 Andrade79
 Becker79, 80
 Cottrell atmosphere
83, 91, 92, 94, 98
 exhaustion80, 81
 Kauzmann rate process81
 K₀83, 84
 Kochendorfer82, 83
 Nowick and Machlin rate.....82
 Orowan modification of
 Becker80
 recent84
 thermal cycling growth com-
 pared with954, 976-978
- Creep-rupture properties**
 of high temperature alloys,
 effects of aging treatments
 on738-758
 of iron-base alloy, hardened
 with Ti, effect of aging
 cycles on743, 744, 748-753
 effect of notched and plain
 bar tests743, 744, 748-753
- Critical size nucleus**739-741
- Crystal growth in cadmium**
 effect of temperature
1016, 1018, 1024, 1028, 1029
 hexagonal symmetry1016

- Crystal growth in cadmium (cont.)**
 mesa growth1026
 no screw dislocations in.....1028
 ridge boundaries1011-1013
 sloping growth fronts.....1025-1027
 step growth1012-1027
 trigonal wakes and ramps.1023, 1025
- Crystal growth from vapor**
 cadmium1006-1030
 continuous microscopic and interferometer observations during1001-1007
 defects appearing at low temperature1023, 1025, 1026
 equipment and process....1007-1011
- Crystal orientation**
 of copper oxides1062
 of titanium hydrides468, 474-476
- Crystal structure**
 in precipitation569
 relationship to brittle fracture657
- Crystallographic deformation**
 in uranium during thermal cycling970-976
- Crystallography**
 of zirconium hydride precipitation455-477
- Crystals, metallic**
 dislocation in f.c.c.95
 schematic diagram of dislocation in71
 strain hardening in.....62-72
- Crystals, nonmetallic**
 plastic properties in.....100, 101
- Cycling unit, vertical tube**929
- Debye-Scherrer powder camera**210, 211
- Defects in crystal growth from vapor**..1011-1013, 1023, 1025-1027
- Deformation**
 in ingot iron at low temps....541-561
 in Ti and Ti alloy, effect of amount on final grain size..371-375, 380, 382
 of alpha solid solutions of lithium in magnesium...856-883
- Deformation (cont.)**
 of various Mg alloys at 78 °K...861-864
 type or mode influencing transformation in stainless steel..485-496
- Delay time**
 in low C steel vs. tensile stress503, 511
 in mild steel, before fracture....640, 648, 649, 651, 654
 in yield phenomena....498, 499, 505-507, 513-516, 519, 535, 536
- Delta ferrite**
 in Cr-Mn-C-N steels.....774, 775, 778, 780, 797, 799
 in stainless steel 431 effect on transverse properties722-737
 microstructure728, 729
- Diffusion anneals of nickel**.....1033
- Diffusion**
 in oxidation kinetics of 62:38 Cu-Ni alloy....1057-1059, 1061
 of hydrogen into titanium.....441
 of hydrogen into uranium...987-993
 of nickel 63 into nickel....1031-1046
- Dimensional instability of uranium upon thermal cycling**905, 926, 943, 954
- Dislocation**54-62
 climb74, 75, 87-90
 density in ingot iron...553, 554, 560
 edge or line.....55, 56, 61
 in lithium fluoride crystal.....57
 in nucleation566, 567, 568
 loop58-60
 generation of500, 508, 514
 schematic at barriers.....88
 screw56, 61
 sessile71, 72
- Dislocation pile-up theory of fracture**634, 647, 651-653, 655
- Discontinuous grain growth**
 in Al-Mg alloys610, 615
- Discontinuous yield theories**..517, 518
 applied to mild steel.....498-516

- Discontinuous yielding**
in austenitic stainless steel.....
.....478, 483, 485, 486, 490-495
- Dissociation pressures**
of hydrogen-uranium
.....983-986, 988, 990
- Documentation**27
- Domain structure**
in zirconium-uranium alloys....
.....320, 321
- Double age**
advantages 738, 739
application to Fe-base alloy, hard-
ened with Ti.....749, 751, 757
definition738, 739
- Ductile-brittle transition**
See also BDT
- Ductile-brittle transition tem-
perature for chromium**.....
.....843, 845, 854, 1077, 1079
effect of grain size on.....850, 851
effect of impurities on.....848
effect of prestrain and strain
rate on848-851
- Ductile fracture vs. brittle**.....
.....661, 662, 678, 680
- Ductility**
of austenitic stainless steels
vs. strain rate at various
temperatures806, 807
of chromium...838, 845-848, 851-854
effect of strain rate845-847
of chromium alloys718
of Mg-Li alloys at low
temperatures856-883
of Ti-Cb alloys....388, 389, 391, 396
- Educational Lectures**9, 10
- Effect of manganese on the Curie
point of cementite**129-140
- Effect of oxide recrystallization
on oxidation kinetics of a
62:38 Cu-Ni alloy**....1047-1062
- Effect of percent tempered
martensite on endurance
limit**242-257
- Elastic limit**
definition517, 533
effect of temperature on.....534
- Elastic-plastic boundary around
notch in mild steel**
.....660, 665, 666, 668-677, 680
- Elastic-plastic stress analysis
of notched specimens of mild
steel**656-681
- Election of Officers**45, 46
- Electrical resistance**
of Ta-Cb alloys (30-1000 °C.)
.....1083, 1086, 1087
- Electro-etching**
of U-low Ti alloys.....903
- Electrolytic extraction of car-
bides from carbon steel**...105-128
- Electron: atom ratio**
for binary and ternary alloys...
.....622-628
calculated vs. theoretical.....
.....627, 628
- Electron configuration in
chromium alloys, correlation
with rate of transition tem-
perature change**705-721
- Electron microscopy**
of high carbon steel 51100.....
.....163-183
of hypoeutectoid alloy
steels184-207
of iron-base alloy hardened
with titanium754, 755
of role of carbon in temper em-
brittlement of steel682-704
of steel during quench-aging.141-162
of steel, phase identification....145
- Elongation in tensile fracture
behavior of mild steel at
-196 °C.**637, 641, 642
- Embrittlement**
in austenitic stainless steels
effect of microstructure on.803-813
extent after sensitization.....807
in steel, effect of P and N on....267
in alpha Ti and alpha Ti alloy..
.....455-477
in Ti-V alloys
.....418, 429, 431, 433, 435-437
- Endurance limit**
of steel vs. percent martensite..
.....242-257

- Energy (stored) from plastic deformation, release by**
 annealing 541-561
- Engineering Education** 14-16
- Etchants for revealing grain boundary segregation in steel**
 695, 701, 702
- Etching by gas ion bombardment**
 572-588
See also Cathodic etching
- Evaluation of a new titanium-base sheet alloy, Ti-4Al-3Mo-1 V**
 398-417
- Exhaustion theory of creep** 80, 81
- Extraction, electrolytic of carbides**
 from carbon steel 105-128
 cell for 106-111
 handling the residue 118-123
 methods 111-118
 variations in conditions 115-118
- Fabrication of uranium, effect of—**
 upon thermal cycling 905-925
- Fatigue strength of low alloy steel**
 effect of hardness on 255, 256
 effect of microstructure on 242-257
 effect of stress raisers on 255, 256
- Fatigue testing of low alloy steel**
 249-251
 need of statistical treatment in 256, 257
- Ferrite**
 decomposition of, during quench-aging 141-162
 in Fe-Cr-Ni alloys, effect on intergranular corrosion 763-770
 in stainless steel 431, effect on transverse ductility 726-730, 734, 735
 phase changes during quench-aging 141-162
- Ferromagnetism of cementite**
 effect of manganese on 129-140
 effect of temperature 130
- Fick's diffusion laws** 1034
- Fisher activation energy** 508, 513, 514
- Fisher diffusion formula** 1039-1041
- Fisher mechanism of hardening** 94, 96
- Flow and fracture**
 modern concepts of 52-104
- Flow curves for Ti-Cb alloys** 390, 391
- Forging of chromium** 841, 851
- Formability of**
 Ti-4Al-3Mo-1V 401, 411, 413, 415
- Fracture**
 dislocations in 99, 100
 in alpha solid solutions of
 Li in Mg 858-883
 in mild steel at -196°F 634-655
 in notched specimens of
 mild steel 667, 671, 674-678
 in 51100 steel 168
 in various Mg alloys at
 78°K 861-864
 resistance to initiation and
 propagation in 678-681
- Fracture strength**
 of Mg-Li alloys 871, 872
- Frank-Read sources** 56-60, 98
 in dislocation 654
 in low carbon steel 499, 500, 506, 508, 509, 514, 515
 in slip 875, 876
 in yield phenomena 534
- Free grain boundaries** 995
- Fringe motion in microinterferometry** 1010
- Gas ion bombardment etching** 572-588
- Genuine treatment**
 application to Fe-base alloy 749-751, 754-756, 758
 definition 739
- Gold nickel, cathodically etched compact** 577
- Goldschmidt atomic diameters table** 619
- Grain boundary**
 angle, defined 1032
 changes in 971-974
 flow in uranium, upon thermal cycling 944-953
 free 995
 movement in bicrystalline
 aluminum 994-1005
 illustrations of 998, 999, 1002
 self-diffusion of nickel 1031-1046

Grain boundary (cont.)

- self-diffusion of nickel (cont.)
 - calculation of coefficients
 - by various formulae..... 1039-1044
 - experimental procedures..... 1031-1034
 - parameter for various misfit angles vs. reciprocal temperature1043
- sliding or flow in thermal cycling of uranium...946, 947, 949, 951-953, 964, 971-976, 980
- transverse
 - method of
 - production....977, 998, 1004
 - translation in998, 999, 1002

Grain coarsening in titanium and various Ti alloys.370-383,459**Grain growth**

- in commercial Ti RC 55....370-383
- in superalloys during solution treatment758
- in Ti alloy TI-100A370-383

Grain refinement Al-1.25**Mn alloy**606, 614, 615**Grain size**

- effect on creep rate.....89, 90
- in Al-1.25 Mn alloy
 - effect of constitution on...589-616
 - effect of homogenization....
 - ...594, 595, 598, 601, 602, 605-610, 613
 - of precipitate in recrystallization605, 613-616
- in chromium, effect on ductility850, 851, 854
- in Cr-Mn-C-N steels
 - effect of solution treatment on782, 794
- in Mg-14.5 Li alloy
 - heat treatment and861
 - in flow and fracture stress...
 -872, 873
- in mild steel, effect on elastic limit and critical stresses526-529, 533, 534
- in pure magnesium, in flow and fracture stress872, 873

Grain size (cont.)

- in titanium and its alloys, effect of prior- to deformation on final size ..371-376, 380, 382, 383
- in tungsten carbide, effect of- on lattice spacing1067, 1068
- in uranium
 - during growth919, 922, 923
 - effect on creep977
 - effect on thermal cycling growth956-970, 975, 977
- in zirconium-uranium alloys287-289

Griffith-Orowan theory of brittle**fracture**635, 647, 651**Grip effect in tensile testing****on aluminum bicrystals.**994-1005**Growth**

- of cadmium from vapor...1006-1030
- of uranium upon thermal cycling ..905-925, 926-942,943-953, 954-980

Growth-cell assembly1007, 1008**sensitivity of**1007, 1010**Growth rate in thermal cycling**

- mathematical analysis930, 931
- proposed mechanisms for
 -954, 955, 976

Habit planes in precipitation for**titanium hydrides**468, 474-476**Hafnium**

- allotropy349
- atomic radius349, 367
- Goldschmidt atomic diameter...619
- Laves phases in.....617-633
- melting and transformation temperatures367
- physical properties349, 367

Hafnium binary alloys631**Hagg type pericarbide****.....163, 170, 179, 182, 183****Hardening**

- by interstitial and substitutional atoms98
- in Cr-Mn-C-N steels, effect of constituents on..786, 792-796
- in two phase systems.....99

Hardness

- of alloy steels.....205-207
- of Al-1.25 Mn alloy.....
 - ..591, 593, 595, 598, 600, 601, 604
- of austenitic steels, effect of composition on794-797
- of Cr-Mn-C-N steels
 - effect of composition and solution treatment on.....794-796
- of chromium versus aging temperatures...1073, 1074, 1079
- of ingot iron vs. annealing temperature557
- of iron-base alloy hardened with titanium
 - effect of aging cycles on.....744
 - effect of heating rate on.....745
- of low alloy steels
 - effect of on fatigue255, 256
 - vs. percent martensite246-249
- of mild steel at low temperatures, notched specimens...
 -668, 669, 671, 677
- of Mo and Mo-0.5 Ti alloy, correlation with creep-rupture properties835, 837
- of 51100 steel, vs. torsional yield strength167
- of thorium-carbon340, 345, 346
- of Ti-4Al-3Mo-1V414
- of Ti-Cb alloys....388, 389, 393, 396
- of uranium-low titanium alloys...
 -894-896, 898-901, 904
- of zirconium-uranium alloys...
 -298-304
 - isotherms in system302
 - table301
 - temperature relationships303

Hardness at elevated temperatures

See Hot Hardness

Hardness testing up to 3000 °F.

- equipment830-837
- variations in readings.....836

Heat of solution

- of hydrogen in uranium....990, 991

Heat resistant alloys

See High temperature alloys and Superalloys

Heating and cooling rates in

- thermal cycling of uranium,**
- effect of-on growth
 - 931, 932, 935, 937, 938, 946, 947, 951

Heat treatment

- of Al-1.25 Mn alloy, effect
 - on ultimate grain size...589-616
- of 430 chromium steel, effect on intergranular corrosion....
 -759, 760, 762, 764
- of high carbon steel, effect on property relationships..163-183
- of iron-base alloy, hardened with titanium, effect on properties
 -743, 744
- of magnesium alloys, grain sizes and861
- of stainless steel 304, to produce susceptibility to intergranular corrosion.759, 760, 762
- of stainless steel 431, effect on mechanical properties...722-737
- of thorium-carbon alloys....341, 342
- of thorium-hafnium alloys.....351
- of thorium-zirconium alloys....351
- of Ti-4Al-3Mo-1V399, 400, 402, 403, 405, 406, 410-412, 415
- of Ti-Cb alloys384-397
- of Ti-V alloys.418, 420-424, 431, 435
- of turbine blades, effect on microstructure and properties757, 758
- of uranium, effect of variables on growth910-922
- of uranium-low titanium alloys
 - effect on microstructure and properties888-901
- of zirconium-tin alloys,
 - effect on transformation kinetics ..323, 326, 334, 337, 338
- on zirconium-titanium alloys,
 - effect on transformation kinetics326, 330, 337, 338

Hexagonal symmetry in

- crystal growth**1015, 1016

High temperature alloys....1072, 1080

See also Superalloys

- cathodically etched584

High temperature alloys (cont.)

- effect of aging cycle on
 - properties738-758
- Ti-4Al-3Mo-1V398
- trade designations
 - GMR 235, cathodically etched.584

High temperature properties

- of chromium1072-1080
- of 62:38 Cu-Ni alloy.....1047-1062
- of forged chromium.....842-847
- of Fe-Cr-Mn-C-N alloys.....801
- of molybdenum1076-1078
- of Ti-4Al-3Mo-1V
 -398, 401, 408-410
- of tungsten1076-1078

High temperature X-ray analysis

- equipment352

Homogenization

- of Al-1.25 Mn alloy, effect on
 - ultimate grain size.....589-616
- of powdered compact alloys of
 - Zr-U271, 278-288, 292

Hot hardness

- of Fe-Cr-Mn-C-N alloys...795, 801
- of Zr-U system298-304

Hot hardness testing

- methods and equipment
 -299, 300, 800-837
- vacuum machine299, 300

Huey corrosion test on stainless

- steel762, 763

Hydride layer on titanium

- significance of449-451
- stability of446-448, 451

Hydride precipitation in alpha

- titanium and alpha titanium
 - alloys455-477

Hydrogen contamination in

- titanium438, 439

Hydrogen embrittlement

- in Ti and Ti alloys.....455-477
- surface hydride layer....449-451
- in zirconium457

Hydrogen

- in titanium
 - absorption and distribution
 - during pickling438-454

Hydrogen (cont.)**in titanium (cont.)**

- environmental factors affecting
 - absorption and distribution
 -438-454
 - metallurgical factors441
 - significance and stability of
 - hydride layer446-451
 - solubility in456, 472
- in uranium
 - absorption by powdered...982, 983
 - heat of solution990, 991
 - solubility in981-987, 990-992
- in zirconium, phase study.....457
- uranium relationships981-993

Hydrogenation treatment

- modified Sievert's apparatus...
 -460-462

Hypoeutectoid alloy steels

- transformation structures ...184-207

Impact brittleness in alpha Ti

- and alpha Ti alloys, hydride
 - precipitation and455-477

Impact properties

- of Ti-V alloys.....
 -420, 421, 425-427, 432-435
- of U- low Ti alloys.....894-896, 898

Impact transition curves for

- Ti- V alloys426, 427, 434

Impurities in chromium

- effect on properties...1072-1074, 1079

Inclusions in free-cutting steels

- effect on machinability...258-268, 270
- effect of size.....267, 268

Induction thermal cycling

- equipment927, 928

Ingot

- segregation in218, 219
- solidification in a large.....
 -213, 214, 216, 218

Ingot iron

See Iron, ingot

Inhibition of recrystallization

- in Al-1.25 Mn alloy.607-610, 613, 614

Intergranular corrosion

- in 18% chromium steels, effect
 - of nickel on.....759-772

- Intergranular corrosion** (cont.)
 in chromium steel 430, effect of
 heat treatment and stabilizing
 elements on760, 761
 in Fe-Cr-Ni alloys.....763-770
 in stainless steel 304, effect of
 heat treatment and stabilizing
 elements on760
- Intermediate phases in alloys of
 the transition elements**...617-633
- Iodide extraction of carbides
 from steel**105-128
- Ionization efficiency increased by
 use of magnetic field**
573, 578, 587
- Iron**
 Goldschmidt atomic diameter....619
 hardness (R.T.—2300 °F.) of
 pure834, 835
 in forged chromium.....848
 valencies used by various
 investigators630
- Iron, ingot**
 energy stored in, deformed by
 torsion541-561
 test method543-546
 plastic deformation by
 torsion549-560
 specific heat at various
 temperatures543, 547, 548
- Iron-base alloy, hardened with Ti**
 effect of aging on properties...
738-758
- Iron-carbon alloy**
 phase changes during quench-
 aging145-149, 158, 160
 thermo-magnetic analysis133
- Iron-carbon-nitrogen alloy**
 phase changes during quench-
 aging154-160
- Iron-Cr-Mn-C-N alloys**
 development of nickel-free
 steels for high
 temperature use773, 774
 high temperature properties801
 phase relationships in.....773-802
- Iron-Cr-Mn-N alloys**
 phase relationships in.....800
- Iron-nickel, single crystal**
 habit planes in precipi-
 tation475
- Iron-nitrogen alloy**
 phase changes during quench-
 aging149-154, 159, 160
- Iso-embrittlement diagrams
 for steels**699
- Isothermal annealing of
 titanium RC-55**376, 378, 379
- Isothermal and cooling transfor-
 mation**
 in Cr-Mo-V steel.....190
 in Ni-Cr-Mo steel190, 191
 in Ni-Mo steel189
 in 4340 steel202
 in Ti-V alloys420, 421
 in Zr-U alloys
305, 306, 308, 315-320
- Kauzmann rate process theory
 of creep**81, 82
- K_c analysis of creep**83, 84
- Kirkendall diffusion experiments** .
1061, 1062
- Kochendorfer theory of creep**...82, 83
- Krypton as etching agent**....572-588
- Larson-Miller parameter for rup-
 ture and creep tests**817
- Laszlo stress calculations**
1064, 1069, 1070
- Lattice constants**
 of thorium-carbon341-347
 of thorium-hafnium alloys...364, 365
 of thorium-zirconium alloys...
349, 356, 359
- Lattice parameters**
 of alloys containing transition
 elements620, 621
 of magnesium alloys862, 874
 vs. composition Ta-Cb alloy....1084
- Lattice self-diffusion coefficients
 for Ni 63 into Ni**..1034, 1037,
 1039, 1040, 1045, 1046
 effect of misfit angle on ratio
 of grain boundary diffusion
 coefficient to lattice diffu-
 sion coefficient1042

- Lattice spacing**
 of WC in WC-Co alloys...1066, 1067
 of WC leached powder.....1066
- Lattice symmetry in crystal growth**1015, 1016
- Laves phases**
 crystal structure in transition elements622
 general characteristics618
 in transition element alloys...617-633
 melting points of binary.....620
 miscibility ranges of, in quasi-binary systems624
 occurrences as function of diameter ratio621
 stability ranges of, in transition element alloys629
- Lead**
 in leaded high S steels
 effect of casting and rolling on dispersion213-222
 microdispersion208-226
 morphology and chemistry of208-222
 in leaded steels
 effect on machinability...258-270
- Liquid Metals, ASM Seminar Program**1, 2
- Lithium fluoride, dislocation in**....57
- Lithium in magnesium**
 effect on axial ratio (c/a)....877, 878, 881
 effect on lattice parameters874
 effect on low temperature ductility871, 880
 effect on strain hardening...866, 880
 effect on yield strength...866, 870, 871
- Lloyd-Mayfield creep and relaxation theory**949, 952
- Loading of mild steel**
 patterns, effect on yield point508, 511
 rate at -196°C ., effect on properties634, 638-642, 651
 time, effect on stress-strain curves521
 tests on notched specimens at low temperatures....664-667
- Low carbon steel (O, 17 C)**
 effect of stress rate and temperature on yield stress...498-516
 initiation of brittle fracture in656-681
 log. delay time vs. tensile stress...503
 upper yield point vs. stress rate...504
- Low microcrack theory of fracture**...634, 635, 646-648, 651, 652
- Low temperature deformation**
 in austenitic stainless steel481-489, 492
 in ingot iron541-561
 in mild steel517-540
- Low temperature properties**
 of low carbon steel.....498-516
 of magnesium-lithium alloys...856-883
 of mild steel634, 655-681
- Low temperature tensile testing of notched specimens of mild steel**656-681
- Low temperature yield stress of a low carbon steel, effect of variables on**498-516
- Lüders' bands in mild steel**
 at -196°C ...634-649, 651, 653, 654
 in dislocation509, 516
 in yield phenomena...517-520, 524-526, 531-533, 536-539
- Machinability**
 index of
 definition259
 formula based on percentage composition260-264, 269
 of steel208, 219, 224, 225
 of type A leaded steel.....258-270
 effect of P and N on.....267
 of free cutting steel.....258-270
 test method259, 260
- Macrostructure of uranium**922
- Magnesium**
 BDT with alloying.....875, 880
 brittleness at low temperatures...856, 858, 866, 867, 875, 879, 880
 coefficient of work hardening....64
 correlation of slip mechanisms and axial ratios887
 deformation in single crystal...859

- Magnesium** (cont.)
 heat treatment and grain sizes...861
 slip in875, 879
 strain hardening in single
 crystal879
- Magnesium-binary alloys**
 deformation in861-864
 stress-strain curves at
 78° F.861-864
- Magnesium-lithium alloys**
 axial ratios and prismatic slip
 in.856, 859, 874, 877, 878, 881, 883
 correlation of slip mechanisms
 and axial ratios.....877
 deformation and fracture in..856-883
 ductility and prismatic
 slip856-883
 ductile fracture in880
 heat treatment and grain
 sizes861
 stress-strain curves at low
 temperatures.....865, 866, 873
- Magnesium-14.8 Li alloy**
 grain sizes in861, 872, 873
 pole figures for882
 strain hardening and recovery
 in873, 874, 878
 stress-strain curve at
 78° K.873, 878
- Magnesium oxide**, ductility at
 room temperature of single
 crystals101
- Magnesium-thorium alloys**
 partial phase diagram....1095, 1096
 phase studies1090-1099
 preparation of alloys....1092, 1094
 survey of literature on
 phase analysis1090, 1091
- Magnesium-Th-Zr system**
 Chinese script structure...1103, 1104
 crystallization1102
 microstructure1101, 1103, 1104
 partial phase diagram1099, 1102
 phase studies1099-1104
 preparation of alloys.....1100
 segment of liquid surface of....1102
 solid solubility1103
- Magnetic behavior in austenitic
 stainless steels vs. strain rate
 at various temperatures**809
- Magnetic field used in
 cathodic etching**572-588
- Magnetic tests on Cr-Mn-C
 -N steels**775
- Manganese**
 effect on Curie point of
 cementite129-140
 Goldschmidt atomic diameter619
 in aluminum
 effect on recrystallization
 temperature589
 effect on grain size.....589, 608
 in Al-5 Mg alloy, effect on
 recrystallization
589, 592-594, 610-612
 in cementite, Curie temperature
 analysis134-136, 138
 in Cr-Mn-C-N steels, stabilizing
 effect on austenite.....
783, 784, 799-801
 in ferrite, Curie temperature
 analysis137, 138
 in leaded steels, effect on
 machinability266, 267
 valencies used by various
 investigators630
- Manganese sulphide in leaded high
 S steel**, morphology of....208-226
- Marker technique in oxidation**
 studies.....1048, 1049, 1061, 1062
 significance of1051-1054
- Martensite**
 in austenitic stainless steels
 contribution to strain har-
 dening482, 490-493
 density of482
 non-correlation with duc-
 tility807-809, 811
 volume produced by tension,
 torsion and compression..
485, 486, 488-490, 493, 494
 in Cr-Mn-C-N steel.....782, 786
 in steel
 effect on endurance limit....
242-257
 effect on impact properties....255

- Martensite** (cont.)
 in steel (cont.)
 methods to produce predetermined amounts of...245-249
 in U-low Ti alloys900-904
- Martensitic transformation**
 in austenitic stainless steels....
 478-498
 effect of tension, torsion
 and compression on...493-496
 effect of strain rate.....495
 in zirconium-uranium alloys....307
- Massive transformation**
 definition321, 322
- Mechanized Literature Searching Project**27, 28
- Mechanical properties**
 effect of orientation characteristics on994, 995
 of aluminum bicrystals,995
 of forged chromium.....838-855
 of stainless steel 431, effect
 of microstructure and heat
 treatment on722-737
 of Ti-Cb alloys.....384-397
 of Ti-V alloys.....418-437
 of uranium898
 of U-low Ti alloys.....894-899
 of Zr-Sn alloys.....333-335
 of Zr-Ti alloys.....328-330
- Melting of chromium**...840, 841, 854
- Melting points**
 of alloys of transition
 elements620
 of Ta-Cb alloys.1082, 1083, 1088, 1089
- Membership Award, Honorary**....49
- Mesa, growth front in crystal growth**1026
- Metal-hydrogen systems**
 interaction types456
- Metallography**
 See also Microstructure and
 Morphology
- Metallography**
 of Mg-Th alloys.....1093, 1095
 of oxide scales.....1061
 of Ta-Cb alloys.....1083, 1087
- Metallographic etching by gas ion bombardment**572-588
- Metallurgical Congress, Second World Program**10-12, 40, 41
- Metallurgical Engineering**
 Education14-16
- Metals Engineering Institute**....37, 38
- Metals for nuclear reactors**....272-298
- Microcracks**
 in brittle fracture.....679
 in mild steel at -196°C
 634, 635, 643-651, 653, 655
- Microcreep**
 at low temperatures, theories
 of518, 533
 in brittle fracture of mild
 steel at -196°C635
 in nonelastic deformation.....
 ...518, 521, 523, 532, 533, 539, 540
- Microdispersion of lead in steel**261, 264
- Microinterferometer in study of crystal growth**.....1009, 1010
- Microradiography**
 of leaded high S steel...209-213, 223
 definition208, 209
 sampling of ingot213, 214
 techniques209-213
 of leaded steels261-264
- Microstrain in stress-strain analysis at low temperatures**
 517, 518, 521, 523, 533, 534, 539, 540
- Microstructure**
 cathodic etching572-588
 of Al-1.25 Mn alloy.....592-606
 of austenitic stainless
 steel803-813
 of chromium, arc-melted.....839
 of Cr-Mn-C-N steels...785-793, 802
 of 62:38 Cu-Ni alloy.1051-1053, 1056
 of hydrogen pickup in
 Ti442, 444-446
 of ingot iron, plastic deformation by torsion....549, 556, 558
 of Fe-base alloy, hardened with
 titanium752-755
 of Fe-Cr-Ni alloys.....763-772
 of Mg-Li alloys.....867-870
 of Mg-Th alloys....1095, 1097, 1098
 of Mg-Th-Zr alloys.....1100-1104
 of mild steel at -196°C642-646

Microstructure (cont.)

- of stainless steel AM 350.....728
- of stainless steel 431.....722-737
- of steel

- effect on endurance limit...242-257
 - during quench-aging.....144, 145

- of Ta-Cb alloys.....1087

- of Th-C alloys.....343, 344, 346

- of Th-Hf alloys.....360-365

- of Th-Zr alloys.....353, 354

- of titanium RC 55.....372, 379

- of Ti alloy Ti-100A.....372, 377

- of Ti-4 Al-3 Mo-1 V...404, 416, 417

- of Ti-Cb alloys.....390-393

- of Ti-V alloys.....420, 435

- of uranium.....924

- during thermal cycling...954-980

- of U-low Ti alloys.....

-889-894, 898, 899, 902-904

- of Zr-U alloys.....

- ..280, 284-289, 291, 292, 308-319

- Misfit angle

- definition.....1032

- in grain boundary self-diffu-

- sion of nickel.....1037-1043

Modern concepts of flow and

- fracture.....52-104

Molybdenum

- Goldschmidt atomic diameter...619

- hardness (70-3000 °F.) of

- strain hardened.....834, 835

- plastic strain prior to abrupt

- yielding.....536

- stress-rupture properties

- vs. temperature.....1078

- stress-rupture strength of

- strain hardened.....835

- stress-strain relationship prior

- to abrupt yielding.....539

- tensile properties vs. temper-

- ature.....1076

Molybdenum-base alloys

- hot hardness tester (70-

- 3000 °F.) for.....830-837

Molybdenum-0.5 Ti alloy

- hot hardness of strain-

- hardened.....834-837

- stress-rupture strength

- at high temperatures.....835

Morphological and phase changes

- during quench-aging of ferrite
 - containing C and N.....141-162

Morphology

- of hypoeutectoid alloy steels

-184-207

- of lead in leaded high S

- steels.....208-226

Mott and Nabarro theory of

- creep.....80, 81, 91

Nabarro-Herring diffusion theory

- of growth during thermal

- cycling.....948, 952

Necking, multiple in

- austenitic stainless steel.....

-478, 483, 485, 486, 490-495

Nickel

- constant creep curves for high

- purity.....85, 86

- crystallographic misorientation

- of bicrystals.....1033

- diffusion of radioactive Ni

- into.....1035-1040

- Goldschmidt atomic diameter...619

- grain boundary self-diffu-

- sion of-into Ni.....1031-1046

- in 18% chromium steels, effect

- on intergranular corrosion

-759-772

- production of bicrystals...1031, 1032

- stress-strain curve of poly-

- crystalline.....76

Nickel oxide (NiO)

- growth rate in oxidation kinet-

- ics study of 62:38 Cu-Ni..

-1051-1056

- orientation.....1062

Nickel-Cr-Mo steel

- hardness with various quenching

- treatments.....187, 206

- isothermal and cooling trans-

- formation curves.....190, 191

- transformation structures in...

-192, 193, 198

Nickel-molybdenum steel

- hardness with various quenching

- treatments.....187, 206

- Nickel-molybdenum steel** (cont.)
 isothermal and cooling transformation curves189
 transformation structures in192, 193, 195, 196
- Nickel steels**
 temper embrittlement in....699, 702
- Niobium**
See Columbium
- Nitrides**
 in Cr-Mn-C-N alloys.....780-782
- Nitrogen**
 in chromium (forged).....
 838, 839, 842, 851, 853, 854
 in Cr-Mn-C-N steels, stabilizing
 effect on austenite.....
 783, 784, 788-793
 in Fe-Cr-Ni alloys, effect on
 intergranular corrosion772
 in leaded steel.....267
 in stainless steels, martensitic,
 effect on microstructure.....734
 in thorium-carbon alloys....346, 347
- Nonelastic strain in mild steel**
 518, 521, 529-534
 stages in518, 635
- Nonmartensitic structure in low
 alloy steel**, effect on endurance limit243, 251-256
- Notch**
 depth
 definition425
 in Ti-V alloys.....425, 435
 geometry, effect on brittle
 fracture in mild steel.....
 ..658, 660-666, 669, 670, 675, 681
 machining by generating
 process663, 664, 677
 plane hyperbolic658-664, 667
- Notch ductility**
 in martensitic stainless steel
 effect of microstructure on
 732, 735, 736
 of Ti-V alloys.....425, 426, 429
- Notch sensitivity**
 of Fe-base alloy, hardened with
 Ti, effect of aging on creep
 738-758
- Notch sensitivity** (cont.)
 of Ti-V alloys, effect of
 aging on425, 432-435
- Notch tensile properties**
 of Ti-V alloys.....421, 433
- Nowick and Machlin theory
 of creep**82
- Nuclear reactors**, metals and
 alloys for.....271, 272, 298, 348
- Nucleation**
 growth and, in yield phenomena.510
 in age hardening alloys.....739-741
 in precipitation
 complex563, 564, 566, 567
 discontinuous563, 564
 simple563, 566, 570
 strain energy and.....566
 in precipitation hardening.....
 739-741, 757
 in recrystallization607, 612
- Occurrence of Laves phases in
 transition elements**617-633
- Ordering**
 kinetics of568
 of matrix and precipitate.....
 563, 564, 568, 569
- Orowan-Becker theory of creep**....80
- Oxidation kinetics of 62:38**
- Cu-Ni alloy**.....1047-1062
 effect of temperature on...1055, 1058
 marker techniques in.....1048,
 1049, 1051, 1053, 1054, 1061, 1062
 orientation of oxide layers....1062
 procedure and equipment.....1048
 rate curves1049-1051
- Oxide scale**, metallography of....1061
- Oxygen in chromium**
 effect on transition temperature
 and other properties.....
 838-840, 853
- Padden and Cain apparatus for gas
 ion bombardment**
 572, 575, 580, 583, 586, 588
- Particle shape in precipitation**563, 567-569
- Passivation of titanium**.....438

- Peak sharpness in X-ray diffraction study of stress distribution**233-237
- Peierl's force to move a dislocation**876, 877, 883
- Pericarbide, Hagg-type, in high carbon steel**...163, 164, 166, 170-175, 179, 182, 183
- Phosphorus**
 in leaded steel267
 in temper embrittled steel, autoradiography of698
- Phase changes during quenching of ferrite**141-162
- Phase identification in U-low Ti alloys**...888-894, 898, 899
- Phase diagrams**
 of Mg-Th1095, 1096
 of Mg-Th-Zr1099, 1102
 of Ta-Cb1083, 1084
 of Th-Hf359, 360, 366
 of Th-Zr349, 353, 365
 of Ti-Cb385
 of U-H985, 986
 of U-Ti886, 898, 899, 904
 of Zr-U279, 285, 288, 294-297, 303, 305, 306
- Phase relationships**
 in austenitic Cr-Mn-C-N stainless steels773-802
 in 18% Cr-Fe base alloys, effect of Ni on763
 in Fe-Cr-Mn-N system800
- Phase studies**
 in precipitation569, 570
 of alloys of transition elements617-633
 of high carbon steel163-183
 of iron alloys by electron diffraction145
 of Mg-Th system1090-1099
 of Mg-Th-Zr system1099-1104
 of Ta-Cb alloys1083, 1084, 1088
 of Th-Hf alloys359-368
 of Th-Zr alloys353-357, 366, 368
 of Ti-Cb alloys384, 385, 388-393, 395, 397
 of Zr-U alloys279-285, 288, 291-294, 298-304
- Physical properties**
 See also Mechanical properties
- Physical properties**
 of Fe-base alloy, hardened with Ti, effect of aging on738-758
 of Zr-U alloys289-292, 297
- Plastic deformation**
 by torsion in ingot iron549-550
 in brittle fracture658-660
 in polycrystalline aggregates856-858
 measurement of stored energy in, survey541-543
 twinning in857, 858
- Plastic flow in mild steel at low temperatures**517-540
 influence of metallurgical variables526-531, 534
 metallography of525, 526, 533, 534
 strain measurement in519-526, 534
- Plastic properties of magnesium-lithium alloys**864-867
- Plastic stress level in free grain boundaries**1000, 1002
- Pole figures for Mg-14.8 Li alloys**...882
- Polycrystalline aggregates, plastic deformation theories**856-858
- Polycrystalline metals**
 creep in83, 88
 grain boundary shearing88
- Polygonization in uranium upon thermal cycling**974, 977
- Polyhedra in precipitation, definition**564
- Porosity in uranium after thermal cycling**964, 965, 968, 976, 977
- Powder metallurgy of zirconium-uranium alloys**271-297
- Precipitate**
 effect of size on recrystallization in Al-1.25 Mn alloy608, 613, 614
 effect on recrystallization in Al-1.25 Mn alloy600, 607-610, 613, 614
 in silver alloy608
- Precipitation**
 cellular564

- Precipitation (cont.)**
 coherency in568, 569
 degree of complexity in
 nucleation562-564, 566, 570
 inter-relationships of aspects....565
 kinetics of562, 564, 565
 nucleation in563, 564, 566, 570
 in quench-aging of steel....141-162
 of titanium hydrides455-477
 order in563, 564, 568, 569
 particle shape in.....563, 567-569
 polyhedra in564
 recrystallization564
 vacancies in567
- Precipitation hardening**
 general considerations739, 740
 of U-Ti alloys.....895-900
 treatments for738, 739
- Precipitation reactions**
 in alloys739, 740, 757, 758
 in Cr-Mn-C-N steels.....
 786-788, 797, 800, 801
- Precipitation systems**
 classification of562-571
 dependence of physical properties
 on characteristics of.....569
 illustrations of classifica-
 tions570, 571
 proposed classification563
 three early methods of
 classification562, 563
- Prediction of tensile properties
 in structural aluminum
 alloys**827, 829
- Preferred orientation in U**....916, 923
- President's Annual Address**....14-20
- Press forging of chromium**....841, 851
- Prestrain**
 effect on ductility and
 transition temperature
 of chromium849-851
- Pre-yield microstrain in mild steel**
 in brittle fracture at -196°C ...
 635, 637, 639, 647, 654
 in dislocation512, 515, 516
- Pre-yield phenomena**
 in mild steel at low tempera-
 tures517-546
 in other B.C.C. metals.....536, 537
- Prismatic slip in Mg-Li alloys**....
 859, 867-871, 874-876, 879, 881, 883
- Pyramid penetration hardness**
 (70 to 3000 $^{\circ}\text{F}$)
 equipment830-837
 reproducibility in testing....836, 837
- Quartz tube casting of
 chromium alloys**706
- Quench-aging**
 electron microscopy tech-
 niques143, 144
 internal friction tech-
 niques142
 of ferrite141-162
- Quenching**
 of stainless steels, water-,
 effect on intergranular corro-
 sion770, 771
 of steels, study of different
 media245, 248, 249
- Quinney-Taylor method of measur-
 ing stored energy**543-546
- Rate process theory of creep**81, 82
- Rate of transition temperature
 change in Cr alloys**.....705-721
- Recovery**72-79
 in deformed ingot iron during
 annealing555-559
 schematic559
 macrostructure of556, 558
 in zinc crystal72-75
 of heat in plastically de-
 formed ingot iron555-559
 schematic of dislocation
 climb75
 Washburn demonstration of...72-74
- Recrystallization**
 in Al-1.25 Mn alloy.594-600, 604-614
 effect of Mn.589, 592-594, 610-612
 effect of 2nd phase.....607, 610
 effect of Si594, 608, 614, 615
 effect of temperature605
 in ingot iron after defor-
 mation548, 549, 556, 558
 in oxidation kinetics of 62:38
 Cu-Ni....1055, 1056, 1058-1061
 in Ti (RC 55)370-383

- Recrystallization** (cont.)
 in Ti alloy (Ti-100A)370-383
Reversed age, definition739
Ridge boundaries in crystal
 growth1011-1013
 definition1010
 illustration1013
Rheotropic recovery in forged
 chromium848-850, 853, 855
Rolling of uranium
 effect of variables on
 growth906-910, 913-920
 reduction effects ...909, 910, 914-916
 temperature effects.906, 907, 913, 920
Ruthenium in chromium alloys,
 decrease in BDT temperature..
 707-711, 717, 719
- S-N curves**
 for Al single crystals and bi-
 crystals64, 1000, 1001
 for copper alloys96
 for Mg-Li alloys at low
 temperatures...863-866, 873, 878
 for mild steel77, 521
 for polycrystalline Ni.....76
 for solid solutions in Mg
 at 78 °K.861-864
 for stainless steel..301, 484, 485, 487
 for stainless steel..304, 483, 486, 487
 for steel 102077
 for steel 5140250
 for Ti-4 Al-3 Mo-1 V.....411, 412
 for zinc crystal67, 69, 70
Sapphire hardness penetrator831
Sauveur Achievement Award.....47-49
Second World Metallurgical
 Congress10-12
Secondary recrystallization
 in Al-5 Mg alloy.....610
 in Al-1.25 Mn alloy.....615
Secretary's Report25-41
Segregation in stainless steel,
 431, theory of temper embrit-
 tlement697, 698, 703, 735
Self-diffusion of Ni 63 into Ni
 at grain boundary1031-1046
Sensitization
 definition812, 813
- Sensitization** (cont.)
 of austenitic stainless steels,
 effect on tensile ductility...
 803-813
 relation to intergranular
 attack813
Sequence of transformations in case
 and core of carburized
 steels227-241
Sequential exposures (Temper-
 ature-Time) on airframe
 structural Al alloys
 compared to single824-826
 effect on tensile properties..823-827
 procedures815, 816
 question regarding random829
Shrinkage in sintering....275-277, 296
Sievert's apparatus for hydro-
 genation treatment460-462
Sigma phase
 in Cr-Mn-C-N steels.....
 788, 792-794, 797
- Silicon**
 in Al-1.25 Mn alloy, effect on
 microstructure..594, 608, 614, 615
 in leaded steels, effect on
 machinability265-267, 270
Silver alloy, single crystal,
 effect of precipitate on re-
 crystallization608
Single exposure (Temperature-
 Time) on airframe structural
 Al alloys,
 compared to sequential823-827
 effect on tensile properties...817-826
 procedures815, 816
Sintering of Zr-U alloys
 decomposition during296
 effect of temperature
 273, 275, 277-279, 281-283, 293
 oxygen pickup during..278, 295, 296
 shrinkage in275-277
Slack quenching of uranium-low
 Ti alloys902, 904
Slip
 in mild steel -196 °C.....645, 646
 in uranium upon thermal
 cycling..943, 944, 949, 958-
 960, 970, 971, 977, 978

Slip mechanisms in fracture

- correlation with axial ratios876-879
- effect of alpha solid solution alloying859
- in Mg-Li alloys867-870, 875, 879, 881
- in polycrystalline aggregates.857, 858
- work hardening and879

Sloping front in crystal

- growth1025-1027

Smith theory of creep.....80, 81**Solid solubility**

- in Al-1.25 Mn alloy592, 600-603, 608
- in Ta-Cb system1083, 1084, 1088
- of Th in Mg.....1096, 1099, 1104
- of Ti in U.....886-889, 903
- of Zr in Mg-Th.....1101, 1104

Solid state physics53**Solidification, ASM Seminar**

- Program1, 2

Solubility

- of C in Th340-347
- of Hf in Th.....365
- of H in massive uranium981, 982, 985-987, 990-993
- effect of purity of U.....992, 993
- of H in powdered U.....981, 982, 985-988, 990, 993
- of Th-Zr system ...352-355, 358, 359

Solution hardening

- by interstitial and substitutional atoms98
- Cottrell mechanism91, 92
- Fisher mechanism94, 95
- in two phase systems.....98
- mechanisms of91-96
- Suzuki mechanism93, 94

Solution treatments

- for Cr-Mn-C-N steels.....775, 779, 780, 794-796
- for Fe-base alloy, hardened with Ti, effect on properties743-745, 757, 758
- for Ti-4 Al-3 Mo-1 V, effect on properties..403, 405-412, 415
- for Ti-Cb alloys384, 393-395
- for Ti-V alloys.421-424, 431, 435, 437

Some relationships between

- torsional strength and electron microstructure in a high C steel163-183

Specific heat

- of ingot iron547, 548
- test method at various temperatures543-546

Stabilization

- in austenitic stainless steels782-786, 797
- of stainless steels, effect on intergranular corrosion....760, 761, 772

Stainless steel

- ductility of annealed and sensitized808-811

Stainless steel, austenitic

- carbide precipitation and brittleness803-813
- Cr-Mn-C-N, phase relationships in773-802
- classification by microstructure777
- development of Ni-free-for high temperature use773, 774
- intergranular corrosion, theories for760
- mechanical behavior478, 479
- strain hardening of478-498

Stainless steel, ferritic

- intergranular corrosion, theories for760, 761

Stainless steel, martensitic

- effect of microstructure and heat treatment on transverse properties722-737

Stainless steel, trade designations

- 17-4 PH, effect of microstructure on transverse properties....731
- 18-8, cathodically etched577
- influence of Ni on intergranular corrosion ..759-772
- 301, strain hardening478-498
- 302, carbide precipitation and brittleness in803-813

Stainless steel, trade**designations (cont.)**

304

carbide precipitation and

brittleness in803-813

influence of Ni on inter-

granular corrosion ...759-772

strain hardening478-498

AM 350

effect of microstructure and

heat treatment on transverse

properties728, 731, 735-737

tensile properties727

410, effect of microstructure and

heat treatment on transverse

properties731

414, effect of microstructure and

heat treatment on transverse

properties731

430 (18% Cr), influence of Ni

on intergranular corrosion

.....759-772

431

effect of microstructure and

heat treatment on me-

chanical properties ...722-737

transverse properties726, 727

Steel,

effect of Mn on Curie point of

cementite129-140

effect of martensite on endur-

ance limit242-257

hydrogen diffusion through....439

lead and machinability in...208, 219

residual stress in carburized

case227-241

stress-strain in aircraft77

thermo-magnetic analysis of,

containing low Mn....132, 133

Steel, Bessemer screw, machina-**bility**264, 270**Steel, electroplated with Cu-Ni-Cr,****cathodically etched**582, 583**Steel, free-cutting, effect of S and****Pb on machinability**264**Steel, leaded high sulphur**

effect of casting and rolling

on dispersion of Pb in...213-222

microradiography of209-223

Steel, leaded high sulphur (cont.)

morphology and chemistry of

lead in208-226

Steel, leaded type A, machina-**bility of**258-270**Steel, low alloy, effect of mar-****tensite on endurance limit** .242-257**Steel, mild**brittle fracture at -196°C ...634-655

effect of cold work on Charpy

curve78

effect of reheating on cold-

worked78

effect of stress rate and tem-

perature on yield stress...498-516

elongation vs. strain rate...641, 642

initiation of brittle fracture...656-681

physical properties at -196°C ...

.....636, 638

plastic strain prior to abrupt

yielding536

prediction of yield stress...498-516

preyield phenomena at low

temperatures517-540

quench-aging141-162

stress-strain curve77

stress-strain relationships prior

to abrupt yielding537

tensile fracture behavior636, 637

Steel, open hearth, machinability**of**267**Steel, rimmed, brittle fracture at** **-196°C** 634-655**Steel, ship, preyield phenomena****at low temperatures**517-540**Steel, two phase alloy, thermal****stresses in**1070**Steel, trade designations**

1018, carburized

microhardness236

residual stresses and

retained austenite in...234, 235

X-ray diffraction peak

sharpness234-236

1020, stress-strain curve.....77

1045, electrolytic extraction of

carbides from105-128

Steel, trade designations (cont.)

- 1118, carburized
 - residual stresses and retained austenite in234, 235
 - X-ray diffraction peak sharpness233, 234
- C 1213, machinability258-270
- 1340, effect of martensite on endurance limit242-257
- 3140, role of C in temper embrittlement682-704
- 4042, effect of martensite on endurance limit242-257
- 4340
 - C-T diagram202
 - effect of martensite on endurance limit242-257
 - hardenability203-205
 - hardness traverses204
 - transverse properties725, 726
- 5140
 - cooling curves of carburized..232
 - correlation of transition temperature and lattice parameter after various heat treatments701, 702
 - effect of martensite on endurance limit242-257
 - residual stresses and retained austenite in carburized... ..236, 237
- 80B40, effect of martensite on endurance limit242-257
- 8620, carburized
 - cooling curves232
 - residual stresses and retained austenite in ..229-233, 239, 240
- 51100
 - electron microstructure and torsional strength ... 163-183
 - isothermal transformation diagram165
- Step growth in crystals**1011-1027
 - changes in1018-1024
 - crystallography of1016
 - defects in. 1011-1013, 1023, 1025-1027
 - rate of propagation1016-1018

Stereoscopy in microradiography

- of alpha Ti and Ti alloy462
- of leaded high S steels215-218

Stored energy in ingot iron, re-

- leased during annealing...541-561
- calculated density of dislocations553, 554, 560
- 1st and 2nd stage releases.....554, 558, 560
- graphical results551-553
- mathematical analysis549
- recovery and recrystallization in554, 558, 560
- temperature difference curves... ..551-553

Strain-aging

- of chromium1074, 1077, 1079
- of ingot iron554, 555
- of molybdenum1077, 1078
- of tungsten1077, 1078

Strain hardening

- in aluminum single and bicrystals64, 1000, 1002
- in austenitic stainless steel...478-498
- in Cr846, 847, 1074, 1077, 1079
- in Mg and Mg alloys.....64, 867, 878-880
- in Mg-14.5 Li alloy with recovery873, 874, 878
- in Mo and W.....1077, 1078
- in tensile testing635, 648
- theories of62-72

Strain induced boundary mi-

- gration in Ti RC 55, deduced from micrographs.378-380

Strain induced martensitic transformation in Ti-Cb alloys...

-384, 389, 390, 393, 395

Strain induced recrystallization

- in 62:38 Cu-Ni alloy.....1048

Strain measurement during plastic

- flow in mild steel.519-526, 534, 536

Strain mechanism theory of temper embrittlement

-695, 696, 698, 700, 703

Strain pattern analysis at

- 196 °C., tensile fracture behavior of mild steel.....636-655

Strain rate

- in austenitic stainless steels
 - effect on magnetic behavior...809
 - effect on mechanical properties813
 - effect on strain hardening....
 - 478, 479, 481-483, 491, 492, 495
 - effect on tensile ductility...803-813
- in chromium, sensitivity
 - 716, 718, 720, 1077
- in forging chromium ...841, 842, 851
- effect on transition temperature848
- in mild steel at constant load.522, 523
- in Mo and W, sensitivity.....1077

Strain transformation in Ti-V

- alloys418, 436

Strength-ductility with various solution treatments for Ti-V alloys

-427-433, 437

Stress

- application rate effect on yield stress in a low C steel..498-516
- critical vs. ferrite grain size in mild steel527, 528
- distribution in carburized and quenched steel239
- in notched specimens of mild steel....667, 669, 671, 672, 675
- residual in carburized case..227-241

Stress analysis

- of mild steel at
 - 196 °C.637-639, 654
- of a notched specimen of mild steel..658-660, 665-670, 674, 675
- of two phase alloy, WC-Co.....
 - 1063-1071

Stress calculation in and around a spherical inclusion due to uniform temperature change

-1064, 1069, 1070

Stress-rupture properties

- of Cr, effect of temperature
 - on1076-1079
- of Mo and Mo-0.5 Ti alloy, correlation with hardness..
 - 835, 837

Stress stability

- in Ti-Al-Mo alloys.....416

Stress stability (cont.)

- in Ti-4 Al-3 Mo-1 V.....
 - 398, 401, 410-412, 415-417

Stress-strain curves

- See S-N curves

Stress-strain tests for transition

- temperature of chromium...843

Stroh-Petch theory of brittle

- fracture....634, 635, 646, 648, 655

Subcell structure in Zr-U

- alloys320, 321

Subgrain formation in U upon

- thermal cycling
 - 961, 963, 964, 970, 974-976

Sub-interferometric processes

-1027, 1028

Substructure, effect on stress-

- strain curves76, 77, 86

Sulphur in type A leaded steels,

- effect on machinability.....258-267

Superalloys

- See also High temperature alloys

Superalloys

- effect of aging cycles on
 - properties738-758
- effect of solution treatments
 - on properties757, 758
- trade designations
 - HS-21, effect of double aging
 - on stress-rupture properties757, 758

Surface roughening in U.905, 923, 925**Surface tension in alloys, effect of**

- alpha solid solution alloying
 - on858, 859

Suzuki mechanism of hardening.93, 94**TTT curves**

- for Ti-V alloys....420-424, 430, 433
- for Zr-U alloys308-310

Tantalum

- Goldschmidt atomic diameter...619
- Laves phases in617-633
- plastic strain prior to abrupt yielding537
- stress-strain relationships
 - prior to abrupt yielding....538

Tantalum-chromium

- Laves phases in631

- Tantalum-columbium system**.....
 1081-1089
 impurities in1082
 phase diagram1083, 1084
 preparation of alloys.....1081, 1082
 properties1082, 1083
- Technical Program, 39th Annual Convention**1-9
- Temper embrittlement**
 alloys with no683
 correlation of transition temperature and lattice parameter with702
 in alloy steels699
 in carbon steels683, 699, 702
 in nickel steels699, 702
 in steel, mechanism of682-704
 role of alloying elements in683, 695, 697
 role of carbon in682-704
 role of temperature in700
 segregation theories of697, 703
 strain mechanism theory of695, 696, 698, 700, 703
 theories of682-684
- Temperature**
 effect on tensile and stress-rupture properties of Cr..1072-1080
 effect on tensile ductility of austenitic stainless steels...
 803-813
 effect on upper yield stress of a low carbon steel.....498-516
 immunization for stainless steels and Fe-Cr-Ni alloys.....770
 in crystal growth in Cd.....
1016, 1018, 1024, 1028, 1029
 in oxidation kinetics of 62:38 Cu-Ni alloy1055, 1058
 in self-diffusion, effect on penetration of Ni 63.....
1035-1040, 1044, 1045
 stresses
 in Al-Si alloys1063
 in brass and steel1070
 in WC-Co alloys1063-1071
 calculated and experimental1064-1068
- Temperature (cont.)**
 time and, exposures of airframe structural Al alloys...814-829
 time and, variables in thermal cycling of U, effect on growth930-942
- Tensile ductility**
 of austenitic stainless steels
 803-813
 of stainless steels...302, 304, 803-813
- Tensile fracture behavior of mild steel at low temperatures**.....
 634-655, 656-681
- Tensile properties**
 of aluminum alloys, 2024-T3 and 7075-T6, both alclad...814-829
 prediction of827, 829
 of Al-1.25 Mn alloy.....591
 of chromium
 effect of temperature on.1074-1077
 forged847
 methods of test.....1074, 1075
 of Fe-base alloy, hardened with Ti, effect of constant strain rate746-748
 of Mo and W at high temperatures1076
 of stainless steels AM 350 and 431725-727, 731
 of Ti-4 Al-3 Mo-1 V
 effect of aging and heat treatment402-410, 415
 effect of welding.....414
 of Ti-Cb alloys387-389, 396
 of Ti-V alloys ...420, 424-435, 437
 of U-low Ti alloys.....901, 904
- Tensile stress in notched specimens of mild steel**.....666, 673, 675-678
- Tensile testing**
 of austenitic stainless steels.....
481-488, 495, 496
 of bicrystals of aluminum.....997
- Ternary alloys of transition elements, Laves phases in**.623-629
- Texture in uranium, effect on growth rate**945, 946, 953
- Thermal analysis**
 of Mg-Th alloys1092-1096
 of Mg-Th-Zr alloys.....1100

Thermal analysis (cont.)

of Ta-Cb alloys1082-1084

Thermal arrest

in martensitic transformation...307
in Th-Hf alloys.....360

Thermal cycling

growth in Cd, Sn and Zn...949, 955
growth in uranium...905-925, 926-942, 943-953, 954-980
comparison with creep...976-978
effect of cycling variables....
.....912, 913, 920, 923
effect of time and temperature
variables930-939, 941
equipment and procedure...927-929
microstructural changes...954-980
mechanisms for976

Thermal expansion anisotropy

in uranium954, 970

Thermal ratchet

applied to bicrystals...944, 946, 947
explains growth of U in
thermal cycling943-953
mechanisms of. 943, 944, 949, 952, 953

Thermal sluggishness

in Ti-7 Al-3 Mo.....417
in Ti-Cb alloys391

Thermally-induced stresses

in WC-Co alloys1063-1071
in two-phase alloys
Al-Si alloys1063
brass and steel1070

Thermo-magnetic analysis of

cementite in steel.....132, 133

Thorium

allotropy349
atomic radius349, 367
physical properties349, 367
solubility of C in.....340-347

Thorium-carbon alloys340-347

hardness340, 345, 346
heat treatment341, 342
lattice constants ...341-343, 345-347
microstructure343, 344, 346
nitrogen in346, 347
solubility of C in.....340-347
X-ray diffraction analysis...341-343

Thorium-hafnium alloys

heat treatment351

Thorium-hafnium alloys (cont.)

lattice constants364, 365
microstructure360-365
phase diagram359, 360, 366
phase studies359-368
solubilities in365
thermal arrest in360
X-ray diffraction analysis.....
.....352, 361-365

Thorium-zirconium alloys

heat treatment351
lattice constants349, 356-359
microstructure353, 354
phase diagram349, 353, 365
phase studies353-357, 366, 368
solid immiscibility loop359
solubilities in352, 354-359
X-ray diffraction analysis...354-358

Time-temperature-transformation

See TTT curves and Transformation

Titanium

alteration of cathodic reaction
minimizes H pickup.....438
correlation of slip mechanisms
with axial ratios.....877, 883
factors affecting absorption and
distribution of H in, during
acid pickling438-454
Goldschmidt atomic diameter...619
hydrides in polycrystalline....469
hydrides in single crystals....
.....463-466, 475
hydrogen absorption in....438-454
hydrogenation equipment ...460-462
in iron-base alloy
effect on heat treatment and
properties738-758
in uranium, effect on corrosion
resistance and mechanical
properties884-904
Laves phases in617-633
microscopy of hydrogenated
single crystals463-467
passivation to minimize
hydrogen pickup438
valency630
X-ray reflection pattern in
single crystals464

Twinning (cont.)

- in uranium in thermal cycling...
.....957, 958, 961, 964, 970, 978

Uranium

- coefficient of expansion....954, 970
- corrosion resistance884-904
- effect of composition and purity
on growth947, 992, 993
- effects of cycling variables on
growth912, 913, 926-942
- effect of grain size on
growth956-970
- effect of fabrication on growth...
.....906-910, 913-916, 919, 920
- effect of heat treatment on
growth907-912, 914-923
- growth upon thermal cycling...
.....905-925, 926-942, 943-953
- mechanical properties884-904
- microstructural changes upon
thermal cycling.....954-980
- orientation in coarse grained
specimens957
- phases in986
- solubility of hydrogen in.....
.....981, 982, 985-988, 990-993
- thermal ratchet model applied
to growth943-953
- X-ray photograms of958, 964
- Uranium hydride**, possible use in
alloy preparation.....
.....273-277, 293, 297
- Uranium-hydrogen relation-**
ships981-993
- Uranium-low-titanium alloys**
corrosion resistance884-904
- mechanical properties884-904
- Uranium-zirconium alloys**
See Zirconium-uranium alloys

Vacancies in nucleation567**Vacuum cathodic etching**572-588**Valencies**

- electronic, of transition
elements626, 629, 630
- mathematical calculation from
X-ray diffraction data on
phases in transition element
alloys617-633

Vanadium

- Goldschmidt atomic diameter....619
- valencies used by different
investigators630

Vanishing phase method, applied

- to Th-Zr system355-357

Virtual pressure in hydrogen

- diffusion through steel...439, 440

Wear test on tools...259, 260, 268-270**Weertman theory of creep**.....84**Welding of Ti-4 Al-3 Mo-**

- 1 V402, 413-415

Whipple diffusion formula.....

-1039-1041

Widmanstätten structure in defor-
mation of mild steel.....

-520, 529-533

Work hardening

- in Mg-14.5 Li alloys.....879
- in Ti-Cb alloys391
- slip mechanisms and879

Wrinkling behavior in U....922-925**X-ray diffraction analysis**

- of alloys of transition
elements619, 620
- of Laves phases620
- of Mg-Th system.....1093, 1096
- of peak sharpness in carburized
steels233-237
- of stress distributions in
carburized steels229-238
- of Ta-Cb alloys1083-1085
- of Th-C alloys.....341-343
- of Th-Hf alloys352, 361-365
- of Th-Zr alloys352-358
- high temperature equipment...352
- of WC phase in WC-Co alloys...
.....1065-1068
- single and two exposure
methods1070, 1071
- of Zr-U alloys307, 315
- X-ray photograms of U**....958, 964

Yield phenomena after plastic

- deformation**.517, 521, 522, 533, 534
- in B.C.C. metals509, 513
- in mild steel at low
temperatures517-540

- Yield phenomena after plastic deformation** (cont.)
 in tensile fracture of mild steel
 at -196°C . . . 637-642, 648, 651
 rate experiments for mild steel . . . 509, 510
- Yield strength**
 of Al alloys: 2024-T3 and 7075-T6, both alclad
 effects of single and sequential temperature-time exposures on . . . 814-829
 of chromium, effect of repeated strains on . . . 853
 of Mg-Li alloys . . . 870, 871, 874
 of stainless steel 431
 effect of retained austenite. . . 730-735
 of Ti-V alloys, ratio to tensile strength . . . 425
 of uranium, 0.2% offset . . . 941
- Yield stress**
 of a low carbon steel, effect of variables on . . . 498-516
 of mild steel specimens, notched and unnotched. 667, 671, 674-678
- Yokobori theory of dislocations.** . . . 505, 512-515
- Zener-Hollomon thermal spike theory** . . . 878, 879
- Zinc**
 brittle fracture at low temperature in polycrystalline . . . 858
 correlation of slip mechanisms with axial ratios . . . 877, 883
 growth on thermal cycling, thermal ratchet model for . . . 943, 946, 948-950, 952
- Zinc crystal**
 dimple, recovery of . . . 73, 74
 dislocation boundary . . . 63
 recovery after strain. . . 5, 72-74
 slip in . . . 66
 strain hardening and reversals in . . . 668-670
 stress-strain curves . . . 67, 70
- Zircaloy** . . . 298
- Zirconium**
 allotropy . . . 349
- Zirconium** (cont.)
 atomic radius . . . 349, 367
 correlation of slip mechanism with axial ratios . . . 87
 Goldschmidt atomic diameter . . . 619
 hydrogen embrittlement and precipitation in . . . 457, 475
 Laves phases in . . . 617-633
 mechanical properties with heat treatment . . . 326
 melting vs. transformation temperature . . . 367
 physical properties . . . 349
 transformation kinetics . . . 325, 326
- Zirconium-tin alloys**
 heat treatment . . . 323, 326, 334, 337
 mechanical properties . . . 333-335
 microstructure . . . 332, 334, 336, 337
 partial phase diagram . . . 331, 332
 transformation kinetics. 332, 333, 337
- Zirconium-titanium alloys**
 heat treatment . . . 326, 330, 337
 mechanical properties . . . 328-331
 microstructure . . . 327, 330
 transformation kinetics . . . 326-331
- Zirconium-uranium alloys**
 densification in sintering. . . 277-283
 density . . . 273-283, 289-293
 ductility . . . 292
 electrical resistivity . . . 289-292
 hardness . . . 289-292, 301
 heat treatment . . . 306, 307
 homogenization . . . 280-288, 292
 hot hardness survey . . . 298-304
 martensite transformation . . . 307
 microstructure . . . 280, 284-289, 292, 308-319
 phase diagram . . . 279, 285, 288, 294-297, 305, 306
 phase studies . . . 293-297
 powder metallurgy . . . 271-297
 production method . . . 272, 273
 properties . . . 289-292
 TTT diagrams . . . 308-310
 tensile strength . . . 291, 292, 296
 transformation kinetics . . . 305-322
- Zirconium-uranium-oxygen**
 tentative ternary section . . . 295, 297
- Zirconium-vanadium**
 Laves phase in . . . 631